# Proceedings Book of 17th International Foundrymen Conference: Hi-tech casting solution and knowledge based engineering

| | |
|---|---|
| **University of Zagreb**<br>**Faculty of Metallurgy**<br>**Sisak, Croatia** | |
| **University of Ljubljana**<br>**Faculty of Natural Sciences and Engineering**<br>**Ljubljana, Slovenia** | |
| **University North**<br>**Koprivnica, Croatia** | |
| **ELKEM AS**<br>**Norway** | |

# PROCEEDINGS BOOK

# 17th INTERNATIONAL FOUNDRYMEN CONFERENCE

# Hi-tech casting solution and knowledge based engineering

**Opatija, May 16th – 18th, 2018**

**ORGANIZERS**
University of Zagreb Faculty of Metallurgy, Sisak, Croatia
University of Ljubljana Faculty of Natural Sciences and Engineering, Ljubljana, Slovenia
University North, Koprivnica, Croatia
ELKEM AS, Norway

**PROCEEDINGS BOOK**
**17th INTERNATIONAL FOUNDRYMEN CONFERENCE**
Hi-tech casting solution and knowledge based engineering

**EDITORS**
Natalija Dolić, Zdenka Zovko Brodarac, Anita Begić Hadžipašić

**TECHNICAL EDITOR**
Anita Begić Hadžipašić

**PUBLISHER**
University of Zagreb
Faculty of Metallurgy
Aleja narodnih heroja 3
44000 Sisak
Croatia

**PRINT**
InfOmArt Zagreb d.o.o.
Nikole Tesle 10
44000 Sisak
Croatia

**ISSUE**
200 copies

**ISBN**
978-953-7082-31-4

-A CIP record is available in computer catalogue of the National and University Library in Zagreb under the number 000996420.

## PREFACE

Foundry industry as a base branch represents an important factor contributing to the economic potential of each country. Current market development as well as technical and economic objective, the production of high-quality, low-cost and environmentally friendly casting, requires application of recent and advanced materials, as well as production technologies, followed and supported by understanding of production process.

Production imperative is pointed into the recent technologies and improved materials for everyday usage in our homes, workplaces, as well as materials with special requirements for specific applications such as those for the automotive or space industry. Industrial activities, which are defined as strategic activities in the Republic of Croatia are Metal Casting and Production of Final Metal Products, recognized as "economic growth drivers" because they are expected to realize higher rates of growth and employment.

What does knowledge based engineering actually means? The following abstract indicate the definition:

*"The handling of knowledge represents the key to competitiveness, with company-specific product and process knowledge marking a unique position with respect to competition. Knowledge-based engineering (KBE) is a comprehensive application of artificial intelligence in engineering. It facilitates new product development by automating repetitive design tasks through acquisition, capture, transform, retention, share, and (re-)use of product and process knowledge. The idea behind KBE is to store engineering knowledge once by suitable, user friendly means and use it whenever necessary in a formal, well documented, repeatable and traceable process. It works like design automation. This chapter begins with the definition of knowledge in an engineering context and subsequently addresses the state-of-the-art in KBE research. Three particular areas of research are discussed in detail: knowledge structuring, maintainability of knowledge and KBE applications, and the technological progress and weaknesses of commercial KBE applications like KBE templates. From case study examples, various recent developments in KBE research, development and industrial exploitation are highlighted. By the resulting sequence optimization of the design process a significant time saving can be achieved. However, there are still notable drawbacks such as the complexity of KBE implementation and the adaptability of developed applications that need to be researched and solved. A view on KBE systems within the Concurrent Engineering context is synthesized, leading to the identification of future directions for research."*
[J. Stjepandić, W. J. C. Verhagen, H. Liese, P. Bermell-Garcia, Knowledge-Based Engineering, in Concurrent Engineering in the 21st Century Foundations, Developments and Challenges; J. Stjepandić, N. Wognum, W. J. C. Verhagen (Editors) Springer International Publishing Switzerland, 2015, DOI 10.1007/978-3-319-13776-6, Chapter 10, pp. 255 – 286]

Hi-Tech casting solution comprehends to recent technology and educated and skilled engineers. The Conference topics were designed as presentations of the current "state of the art" research in collaboration with industry, and production innovation with the aim to improve the competitiveness.

The scope of ***17th International Foundrymen Conference (IFC)*** covers scientific, technological and practical aspects concerning research, development and application of casting technology with the common perspective – increase of competitiveness. Special attention will be focused towards the competitiveness ability of foundries, improvement of materials features and casting technologies, environmental protection as well as subjects connected to the application of castings.

During this Conference 44 papers will be presented. Book of Abstracts of the 17th International Foundrymen Conference includes summaries of the papers. The Proceedings book consists of papers *in extenso* published in electronic format (CD). Full length papers have undergone the international review procedure, done by eminent experts from corresponding fields, but have not undergone linguistic proof reading. Sequence of papers in Proceedings book has been done by category of papers in following order: plenary lectures, invited lectures, oral and poster presentation, and inside the category alphabetically by the first author's surname.

Within the Conference Student section is organized. This is an opportunity for industry to meet and recruit human resources as a main potential for business development. Correlation of material knowledge based engineering and technology improvement known as Hi-Tech solutions, represent a knowledge transfer between industry and higher education institutions. Higher education at the Faculty of Metallurgy (HEI), conceived through the program and the learning outcomes, is based, inter alia, on promoting students' scientific and research work on applied topics, enabling ambitious and creative young people to become independent problem solvers, developing and supporting their curiosity, analytics and communication: Graduates like the labour market need!

This occasion represents the opportunity to discuss and increase the mutual collaboration between HEIs' and industry with the aim of information exchange related to advanced experience in foundry processes and technologies, gaining the new experience in presentation and / or teaching process within lifelong learning process.

The organizers of the Conference would like to thank all participants, reviewers, sponsors, auspices, media coverage and all those who have contributed to this Conference in any way.

President of Organizing Board

Assoc.Prof. Zdenka Zovko Brodarac, PhD

THE HEAD OF ORIENTAL GOD (ATIS?)
bronza
2nd century AD
SISCIA (modern Sisak, Croatia)

ILLYRIAN HELMET
iron
6th century BC

## UNDER THE HIGH AUSPICES

President of Croatia
Kolinda Grabar – Kitarović

## UNDER THE PATRONAGE

Ministry of Science and Education of the Republic of Croatia
Ministry of Economy, Entrepreneurship and Crafts of the Republic of Croatia
University of Zagreb
Croatian Foundry Association
AD KLASTER
Mittel Europäische Giesserei Initiative (MEGI)
Chamber of Commerce of Republic of Croatia
Sisak – Moslavina County
City of Sisak

## SPONSORED BY

**GOLDEN SPONSOR**

COMET d.o.o., Novi Marof (HR) & SWATYCOMET d.o.o., Maribor (SI)
KONTROLTEST INTERNATIONAL d.o.o., Zagreb (HR)
LABTIM ADRIA d.o.o., Sesvete (HR)
MIKROLUX d.o.o., Zaprešić (HR)

**BRONZE SPONSOR**

ANALYSIS d.o.o., Beograd (RS)
BL METAL d.o.o., Črnomelj (SI)
EKW – KREMEN d.o.o., Šentjerej (SI)
EDC d.o.o., Zagreb (HR)
HAGI GmbH, Pyhra (AT)
HEINRICH WAGNER SINTO MASCHINENFABRIK GmbH, Bad Laasphe (DE)
IDEF d.o.o., Zagreb (HR)
INDUCTOTHERM EUROPE Ltd., Worcestershire (UK)
LABEKO d.o.o., Zagreb (HR)
MECAS ESI s.r.o., Plzen (CZ) & TC LIVARSTVO d.o.o., Ljubljana (Sl)
SCAN d.o.o, Kranj (SI)
TCT TESIC GmbH, Iserlohn (DE)
TOPOMATIKA d.o.o., Zagreb (HR)

**MEDIA COVERAGE**

IRT 3000
Foundry Planet
Foundry Lexicon

**SUPPORTING ASSOCIATION AND COMPANIES**
Croatian Foundry Association
Slovenian Foundry Association

## ORGANIZING COMMITTEE

Zdenka Zovko Brodarac, president
Anita Begić Hadžipašić
Natalija Dolić
Gordana Gojsević Marić
Franjo Kozina
Stjepan Kožuh
Ladislav Lazić
Jožef Medved
Marin Milković
Primož Mrvar
Tomislav Rupčić
Mario Tomiša

## PROGRAM COMMITTEE

Hasan Avdušinović (BiH)
Branko Bauer (HR)
Anita Begić Hadžipašić (HR)
Ivica Buljeta (BiH)
Jaka Burja (SI)
Lidija Ćurković (HR)
Mile Djurdjević (AT)
Natalija Dolić (HR)
Peter Cvahte (SI)
Regina Fuchs-Godec (SI)
Dario Iljkić (HR)
Sebastjan Kastelic (SI)
Varužan Kervorkijan (SI)
Ivica Kladarić (HR)
Borut Kosec (SI)
Dražan Kozak (HR)
Stjepan Kožuh (HR)
Zoran Kožuh (HR)
Ladislav Lazić (HR)
Martina Lovrenić-Jugović (HR)
Srećko Manasijević (RS)
Dragan Manasijević (RS)
Jožef Medved (SI)
Daniel Novoselović (HR)
Mitja Petrič (SI)
Bojan Podgornik (SI)
Karlo T. Raić (RS)
Vera Rede (HR)
Zdravko Schauperl (HR)
Ljerka Slokar (HR)
Božo Smoljan (HR)
Tahir Sofilić (HR)
Davor Stanić (HR)
Sanja Šolić (HR)
Iveta Vaskova (SK)
Maja Vončina (SI)
Zdenka Zovko Brodarac (HR)
Irena Žmak (HR)

# REVIEW COMMITTEE

Ljubiša Balanović (RS)
Jakov Baleta (HR)
Branko Bauer (HR)
Anita Begić Hadžipašić (HR)
Ana Beroš (BiH)
Roberto Boeri (IT)
Ivan Brnardić (HR)
Ivica Buljeta (BiH)
Danko Ćorić (HR)
Diana Ćubela (BiH)
Lidija Ćurković (HR)
Natalija Dolić (HR)
Nenad Drvar (HR)
Aleksandar Durman (HR)
Tomislav Filetin (HR)
Mladen Franc (HR)
Regina Fuchs-Godec (SI)
Tomislav Galeta (HR)
Zoran Glavaš (HR)
Mirko Gojić (HR)
Gordana Gojsević Marić (HR)
Vesna Grekulović (RS)
Krešimir Grilec (HR)
Dragoslav Gusković (RS)
Tamara Holjevac Grgurić (HR)
Dario Iljkić (HR)
Ivan Ivec (HR)
Ivan Jandrlić (HR)
Zoran Jurković (HR)
Frankica Kapor (HR)
Varužan Kevorkijan (SI)
Ivica Kladarić (HR)
Borut Kosec (SI)
Ana Kostov (RS)
Saša Kovačić (HR)
Dražan Kozak (HR)
Stjepan Kožuh (HR)
Zoran Kožuh (HR)
Witold Kazimierz Krajewski (PL)
Ladislav Lazić (HR)
Martina Lovrenić-Jugović (HR)
Srećko Manasijević (RS)
Vilko Mandić (HR)
Jožef Medved (SI)
Aleš Nagode (SI)
Daniel Novoselović (HR)
Mitja Petrič (SI)
Žarko Radović (ME)
Mira Rajčić Vujasinović (RS)
Vera Rede (HR)
Iulian Riposan (RO)
Zdravko Schauperl (HR)
Peter Schumacher (AT)
Ivica Skozrit (HR)
Davor Stanić (HR)
Amir Šećerkadić (HR)
Snježana Šerbula (RS)
Nebojša Tadić (ME)
Zdenko Tonković (HR)
Ružica Udovičić (BiH)
Darja Volšak (SI)
Gotthard Wolf (DE)
Zdenka Zovko Brodarac (HR)

## CONTENTS

17th INTERNATIONAL FOUNDRYMEN CONFERENCE
Hi-tech casting solution and knowledge based engineering
Opatija, May 16th-18th, 2018
http://www.simet.hr/~foundry/

# FUNDAMENTAL QUALITY ISSUES IN CASTINGS

**John Campbell***

University of Birmingham, Department of Metallurgy and Materials, Birmingham, United Kingdom

**Plenary lecture**
*Subject review*

**Abstract**

Traditionally some of the main quality problems in castings were described as porosity (gas and shrinkage types), hot tears, cracks and poor and variable mechanical properties. All these defects occur because of the presence of more fundamental entities: *entrainment defects* in the form of bifilms and bubbles. During the surface turbulence associated with stirring and pouring of liquid metals, the oxide surface is *entrained* into the bulk liquid. The entrainment mechanism involving the impingement of drops or splashes is one which guarantees that the top dry oxide surface on one liquid mass impinges on a similar top dry oxide surface of another liquid mass, with the result that a non-bonded interface consisting of a double oxide film (a 'bifilm') is formed between them. Bifilms act as cracks in the liquid. Turbulent pouring fills the liquid with bifilm cracks and air bubbles. Air bubbles are very damaging to the liquid as a result of the long oxide trails which they leave behind. However, bubbles can at least be easily seen. Bifilms are often so thin (although relatively large area) that they are often invisible, being only nanometers thick. The bifilms degrade properties, but can also be expanded by diffusion of gas to form gas porosity, or expanded by strain to form shrinkage porosity. They are the universal initiators of tears and cracks. Interestingly, there is evidence that the bifilm is the most important, and possibly the only, crack-initiating mechanism in metals. Novel casting techniques to eliminate entrainment defects have been proven to deliver essentially defect-free, consistent and reliable castings. A revolution in metallurgy and engineering now seems within the control of the foundry industry.

***Keywords**: bifilm, casting, entrainment, defect, properties*

*Corresponding author (e-mail address): jc@campbelltech.co.uk

*Emeritus Professor of Casting Technology*

# Fundamental Quality Issues in Castings

*Opatija, Croatia 2018*

John Campbell
University of Birmingham UK

# Top gated turbulent filling

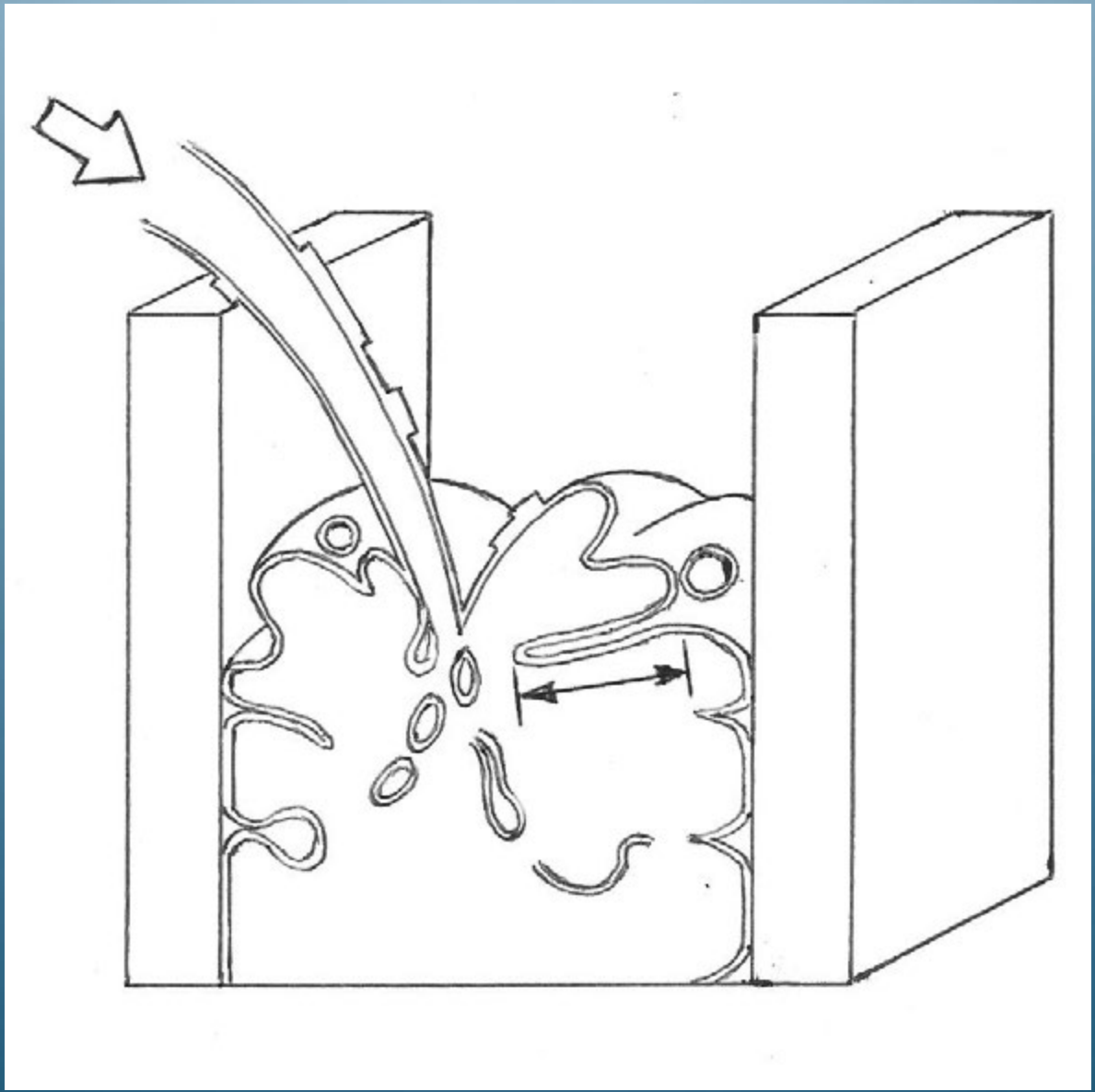

# Bottom gated laminar filling

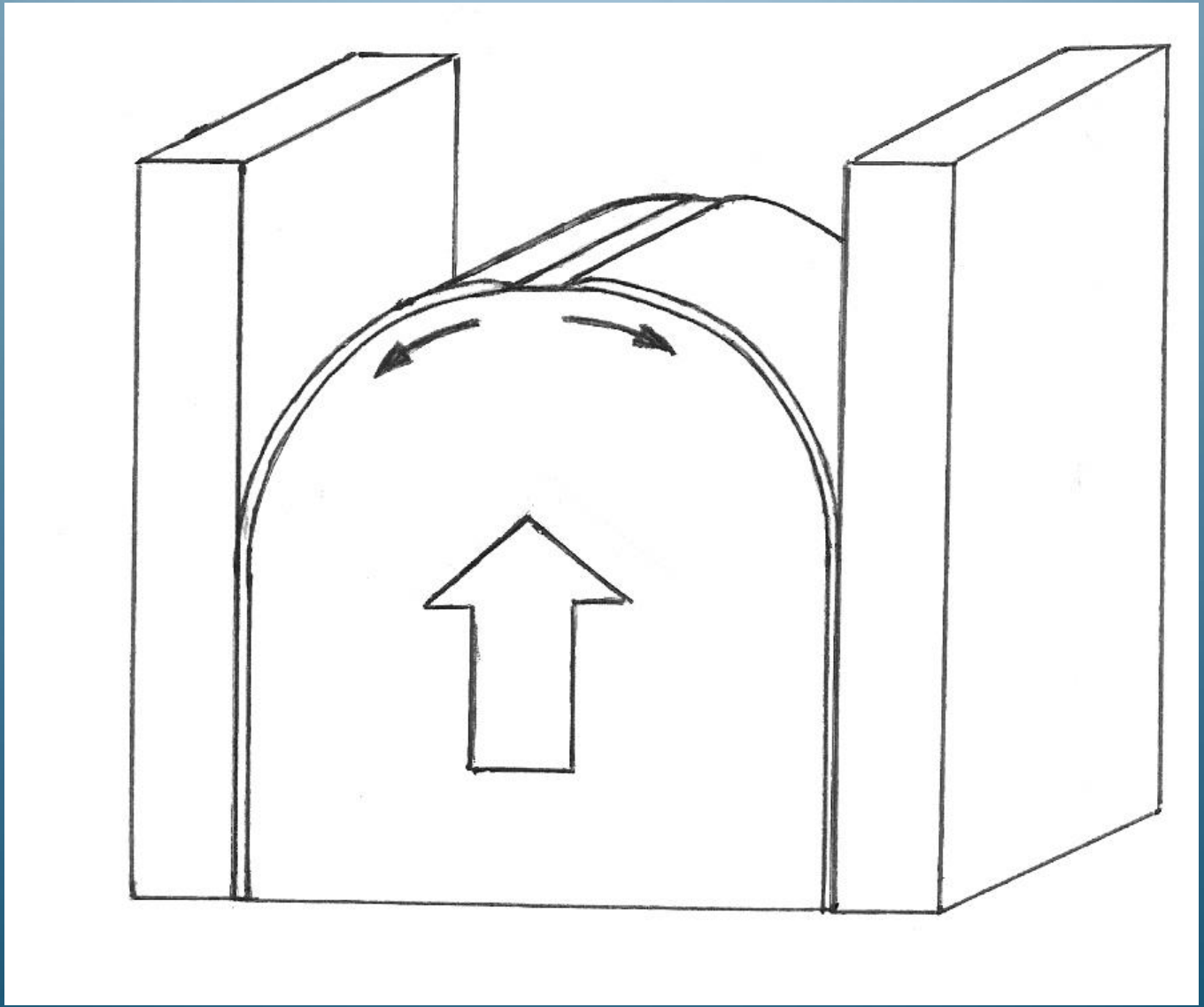

# The range of ingate velocities

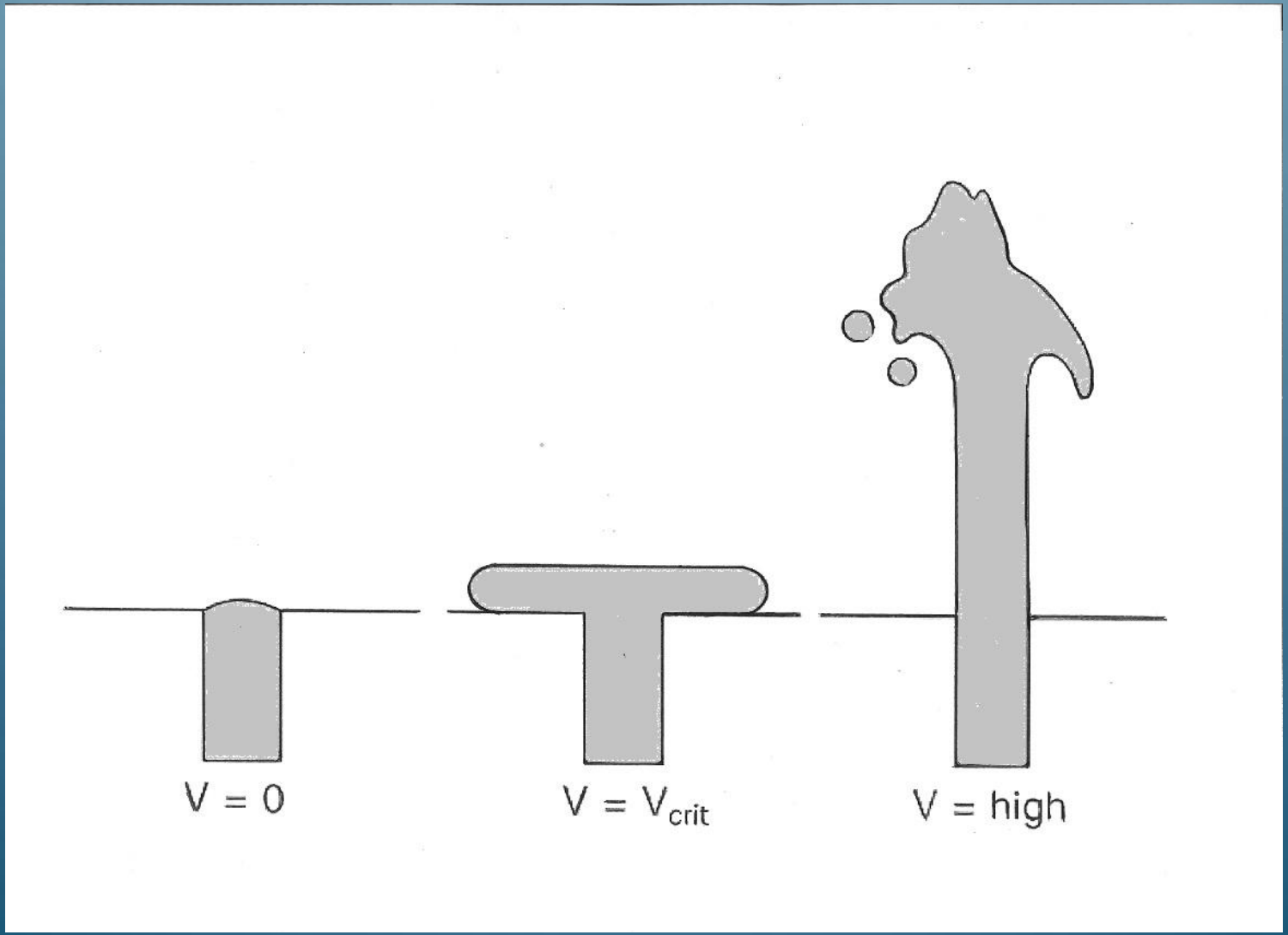

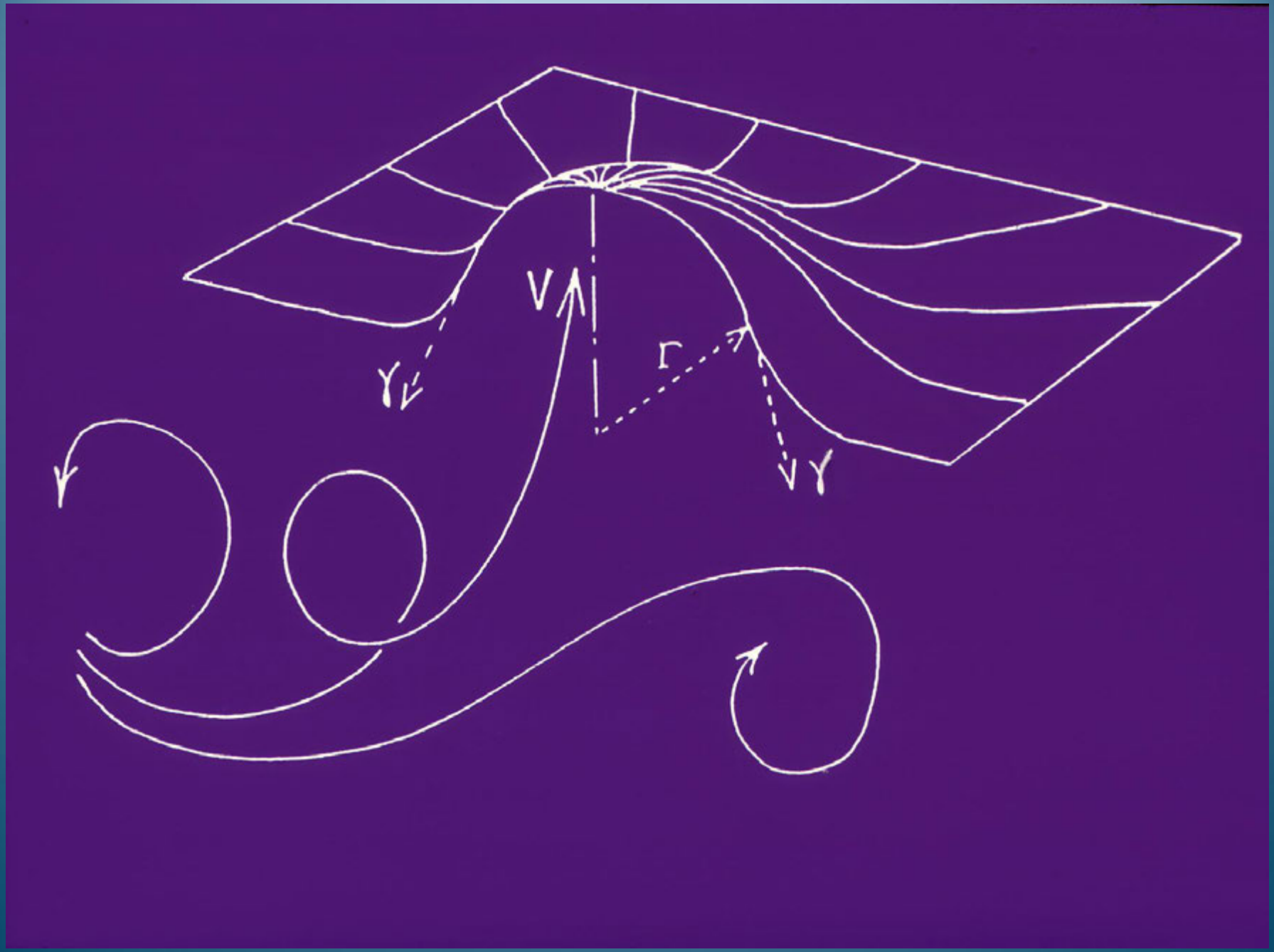
V
Γ

# Balance of pressures at the surface of the liquid metal

Inertial Pressure = Surface tension pressure

$$\rho V^2/2 = 2\gamma/r$$

$$V = 2\{\gamma/\rho r\}^{1/2}$$

$$= 0.4 \text{ m/s for Fe alloys}$$

$$= 0.5 \text{ m/s for Al alloys}$$

$$= 0.6 \text{ m/s for Mg alloys}$$

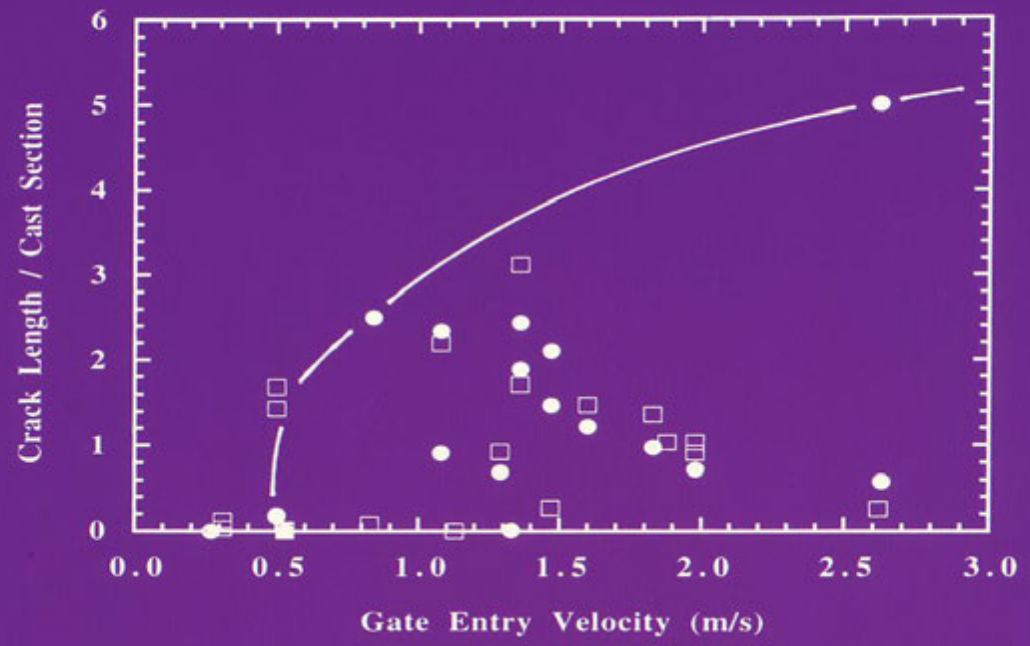
Crack Length / Cast Section
0
1
2
3
4
5
6
0.0
0.5
1.0
1.5
2.0
2.5
3.0
Gate Entry Velocity (m/s)

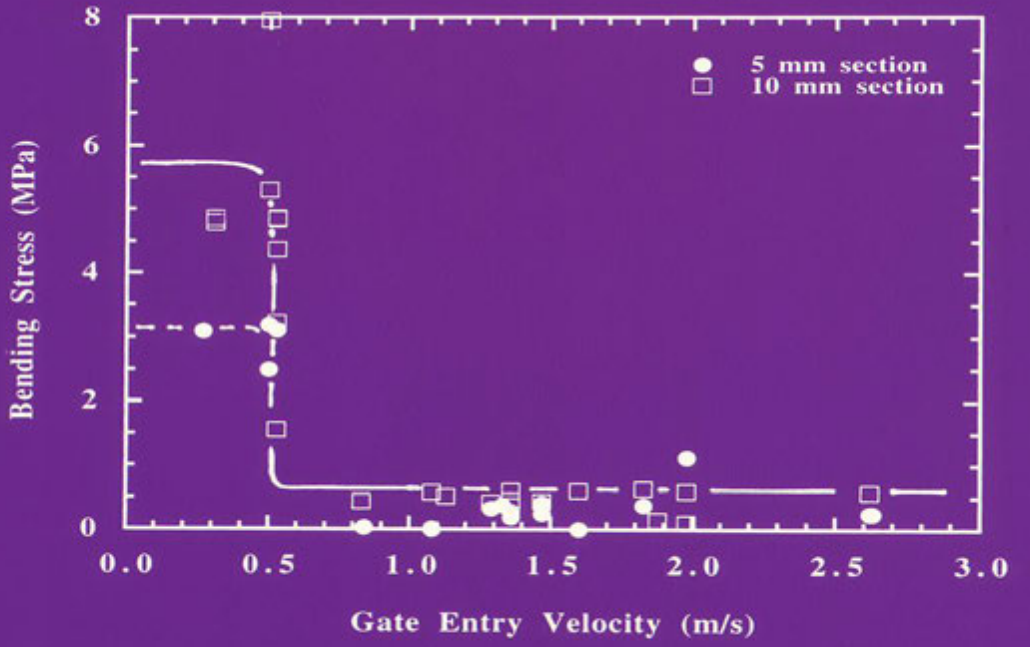
Bending Stress (MPa)
0
2
4
6
8
5 mm section
10 mm section
0.0
0.5
1.0
1.5
2.0
2.5
3.0
Gate Entry Velocity (m/s)

# “Before and after”

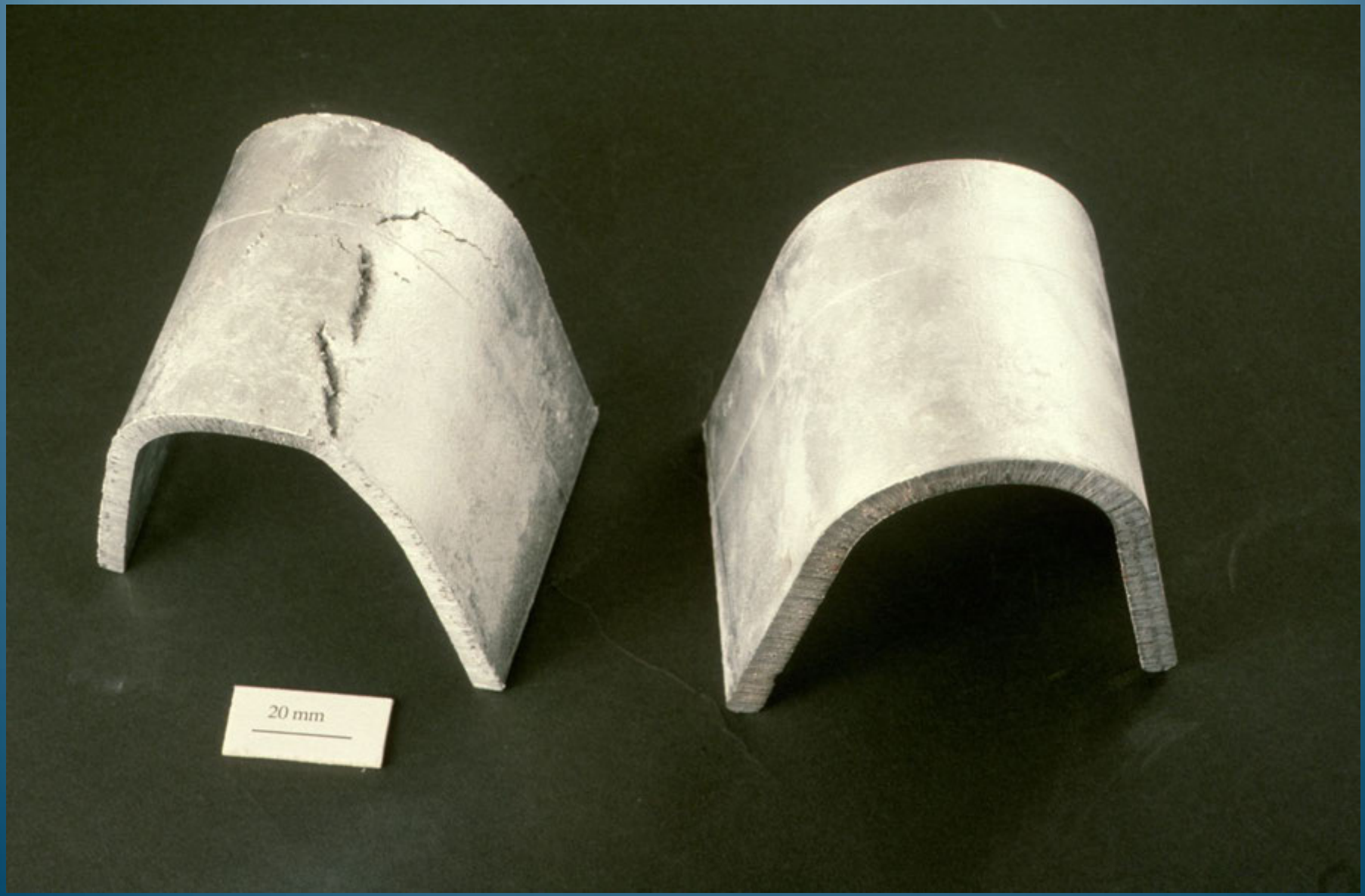

# Entrainment Defects

1. Bifilms
2. Bubbles

- A tangled network of oxide films in a turbulently filled casting

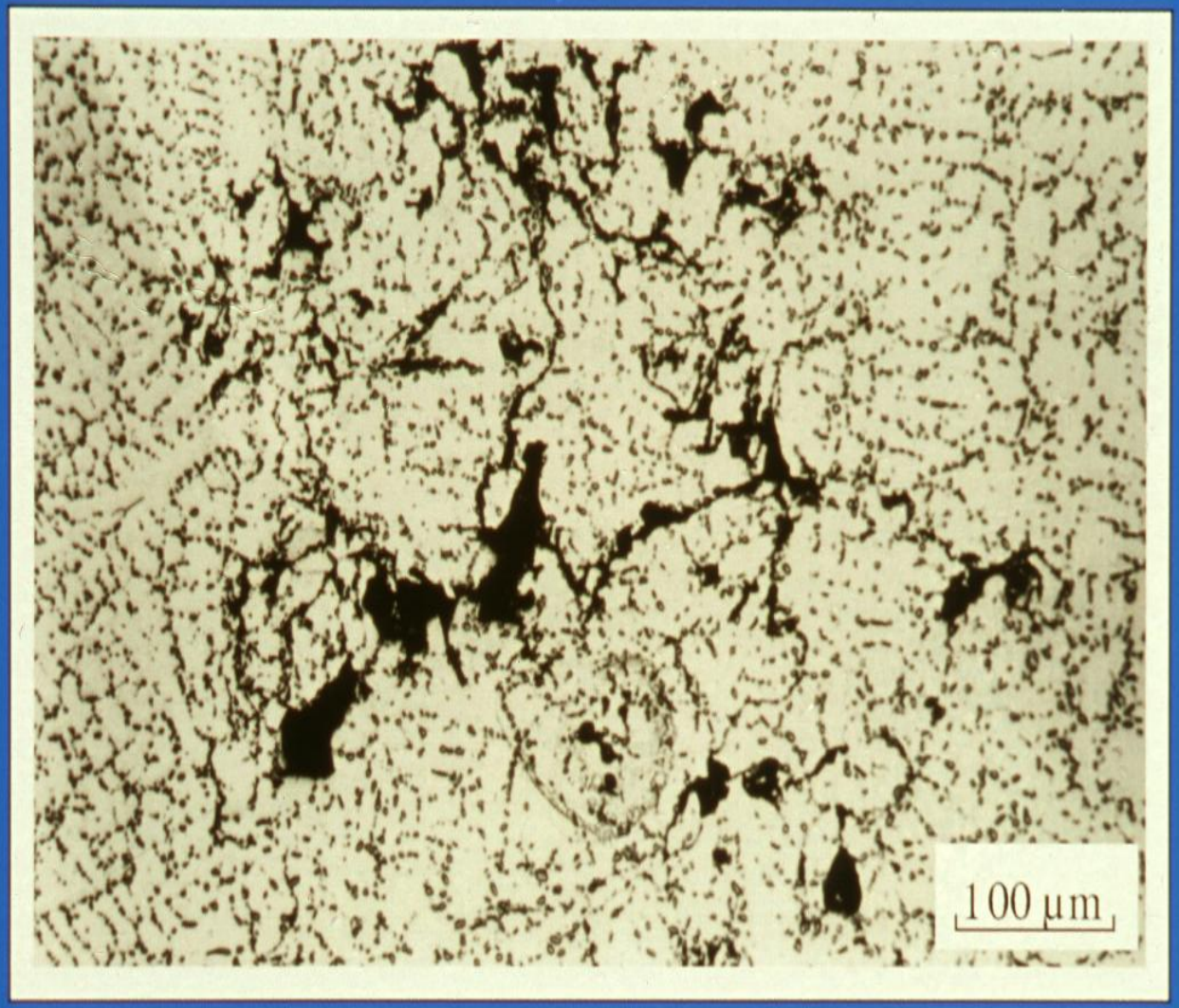

# RPT Before and After Reduced Pressure

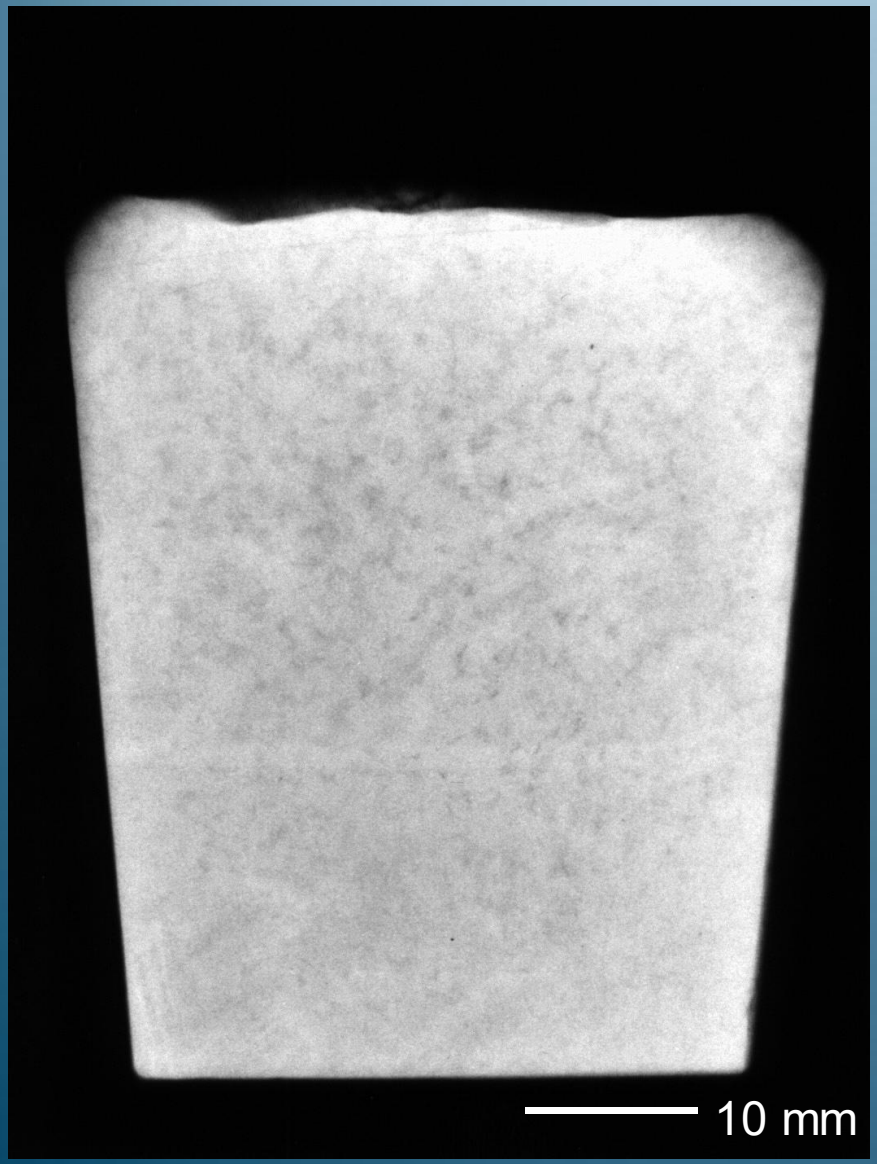


# Elongation and Yield Strength of A201/6

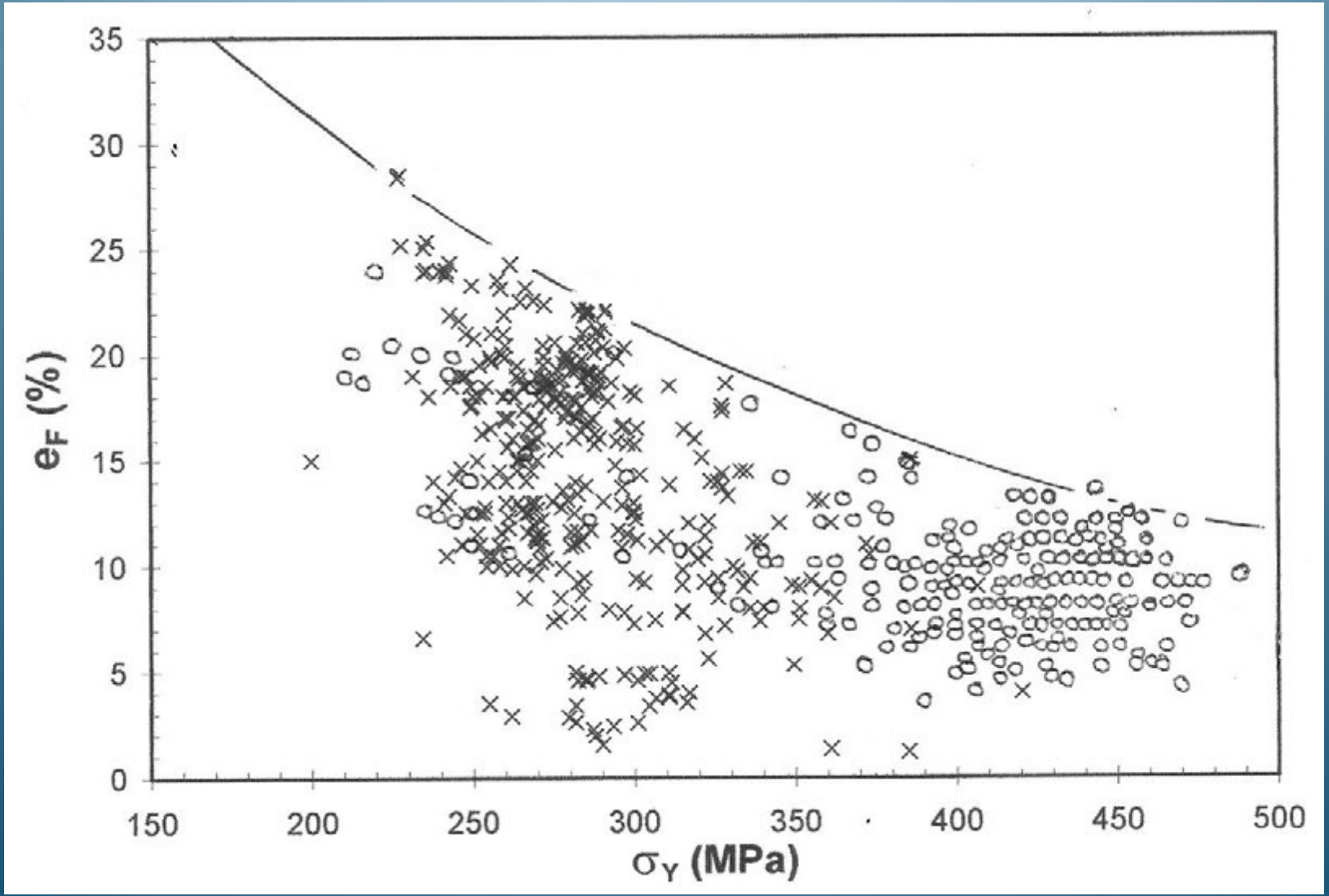

# αFe + βFe formed on bifilms

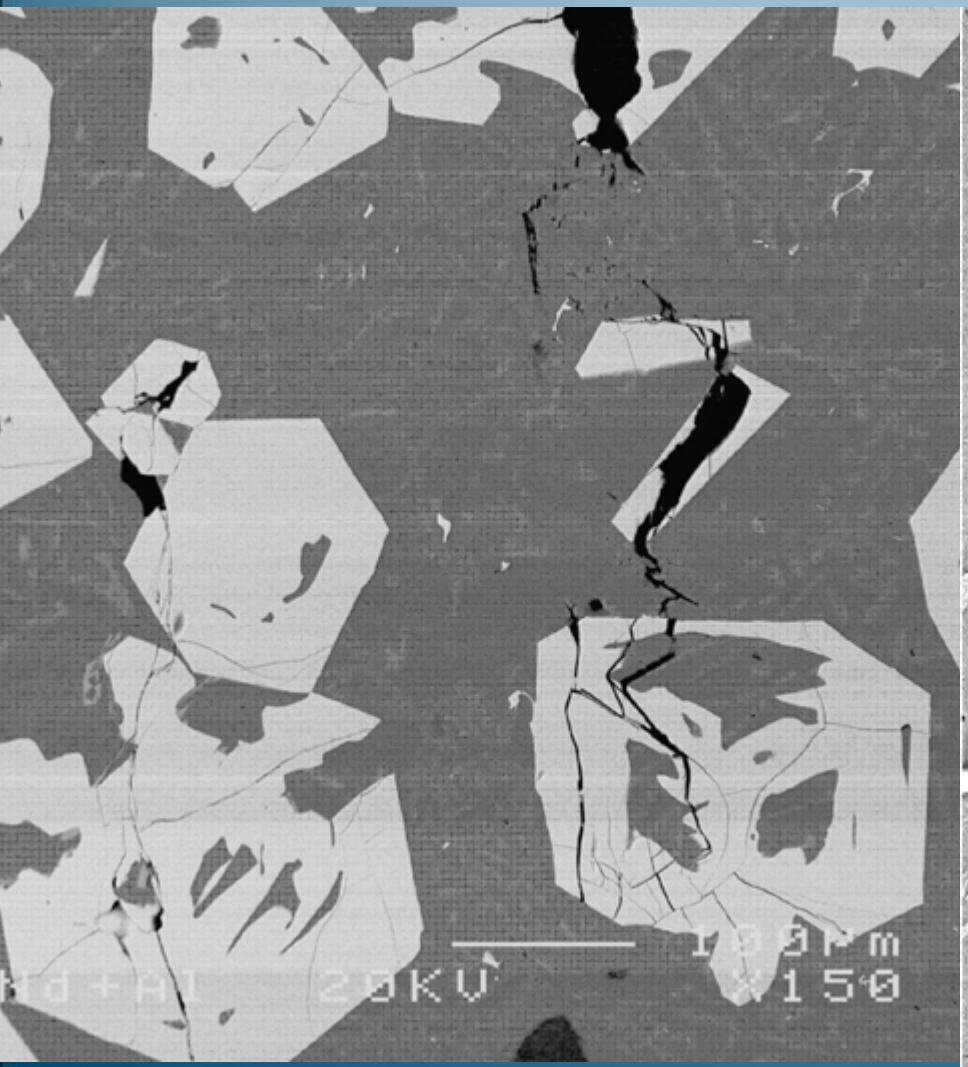


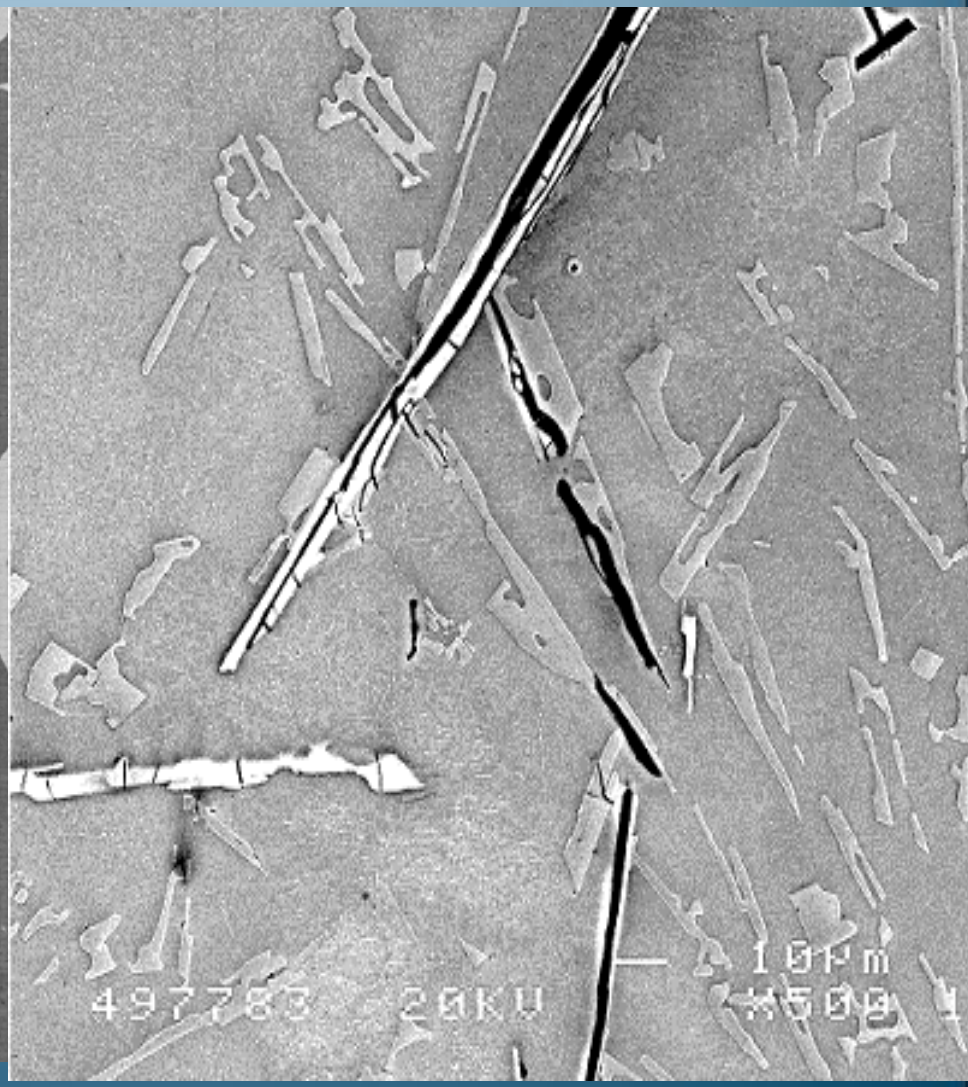

# Gravity Filling Systems

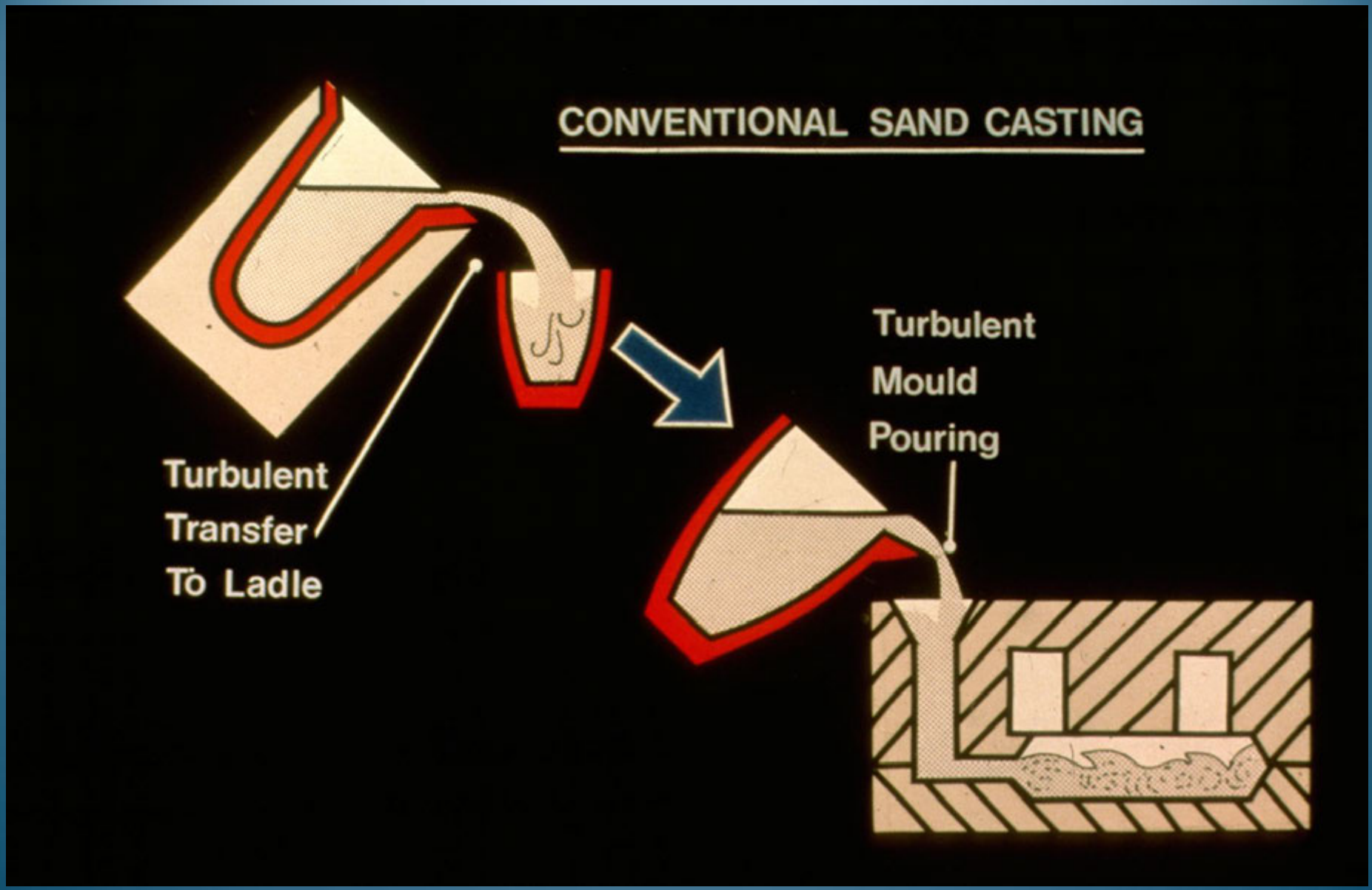
CONVENTIONAL SAND CASTING
Turbulent
Transfer
To Ladle
Turbulent
Mould
Pouring

# Top Pour

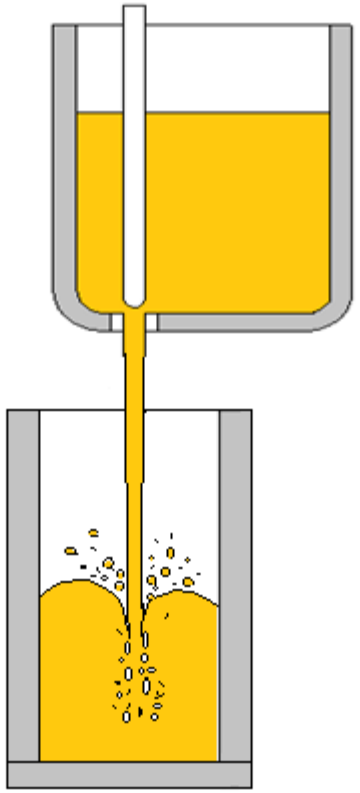

# Top Pour

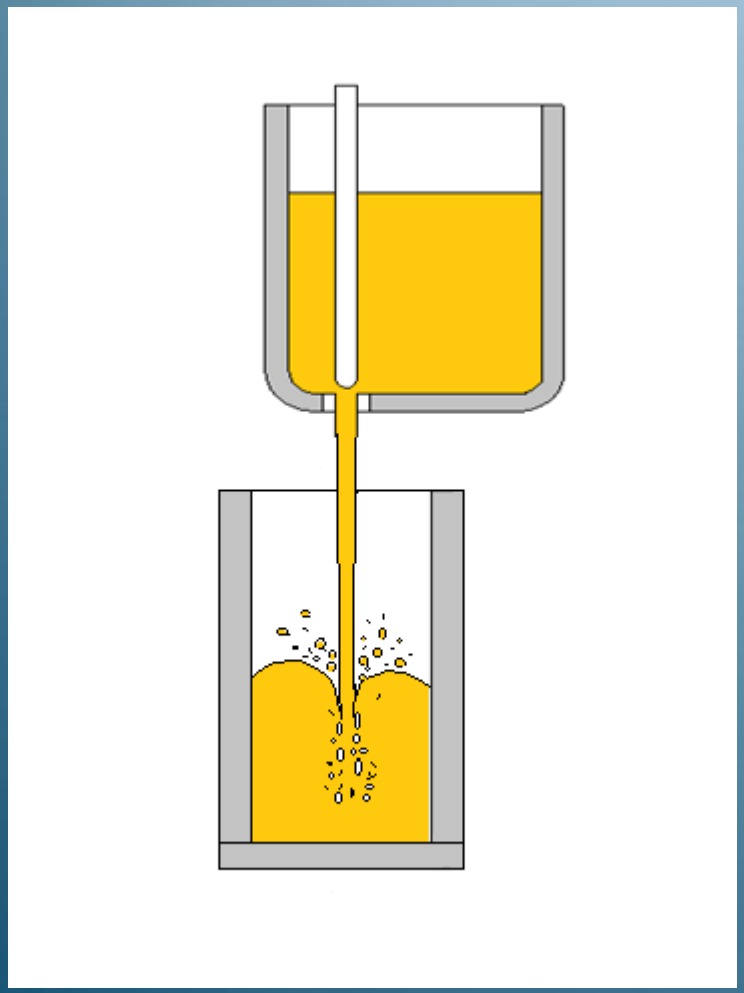

# Bottom Gate

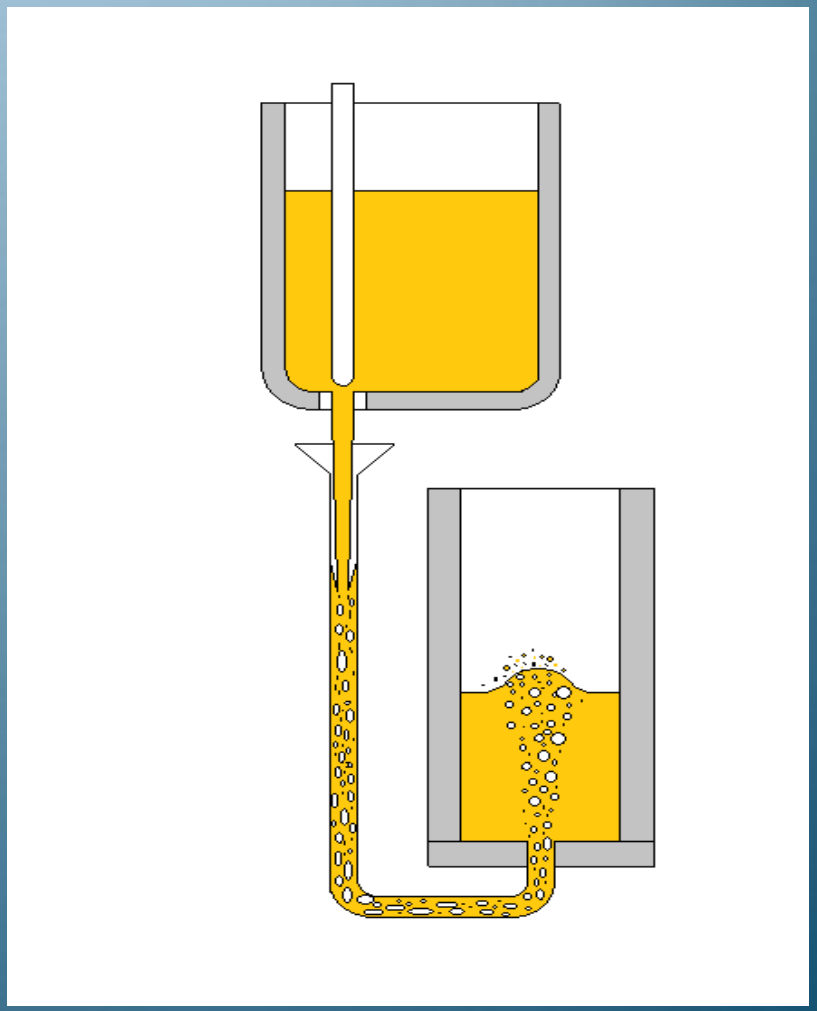

# Top Pour

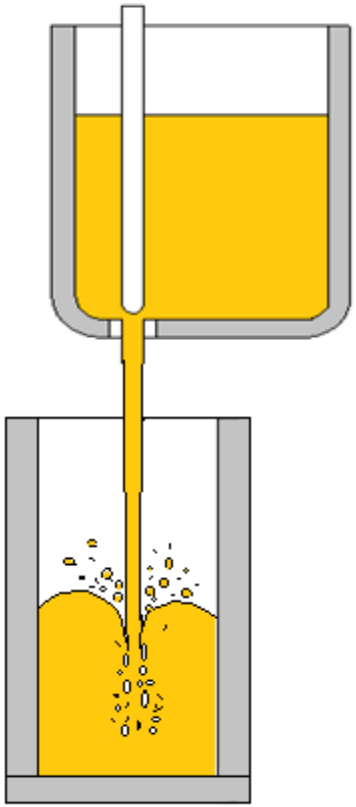

# Bottom Gate

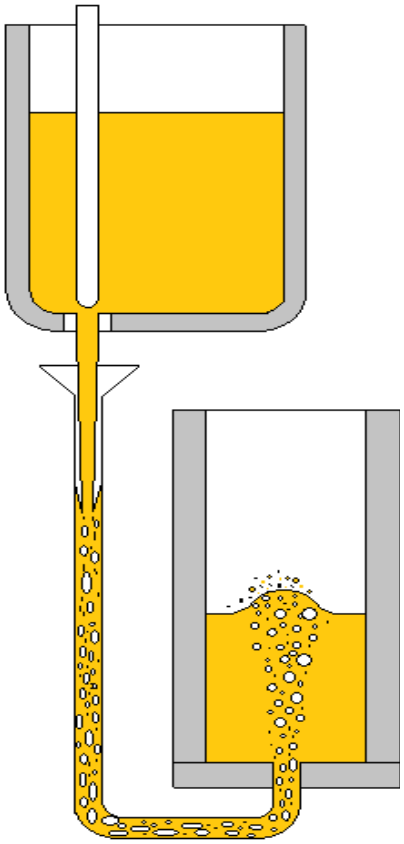

# Contact Pour

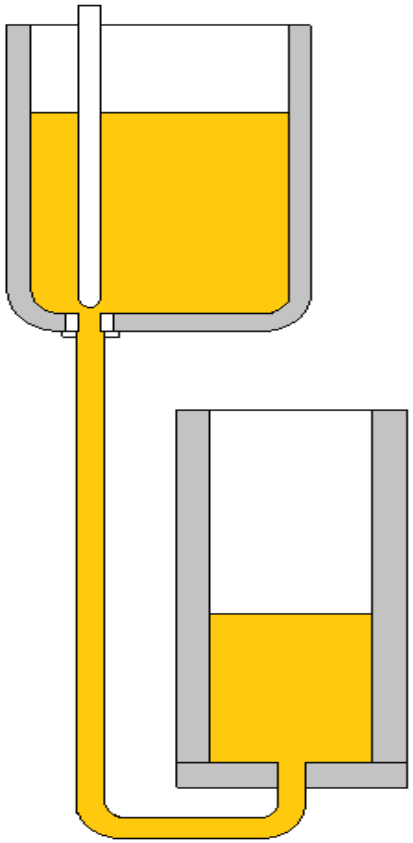


Contact surface
Wind Turbine
Fatigue Failure
(a)
WECs

Ni-base CY40

# Highly ductile Ni-base alloy CY40 tensile test piece (with bifilms!)

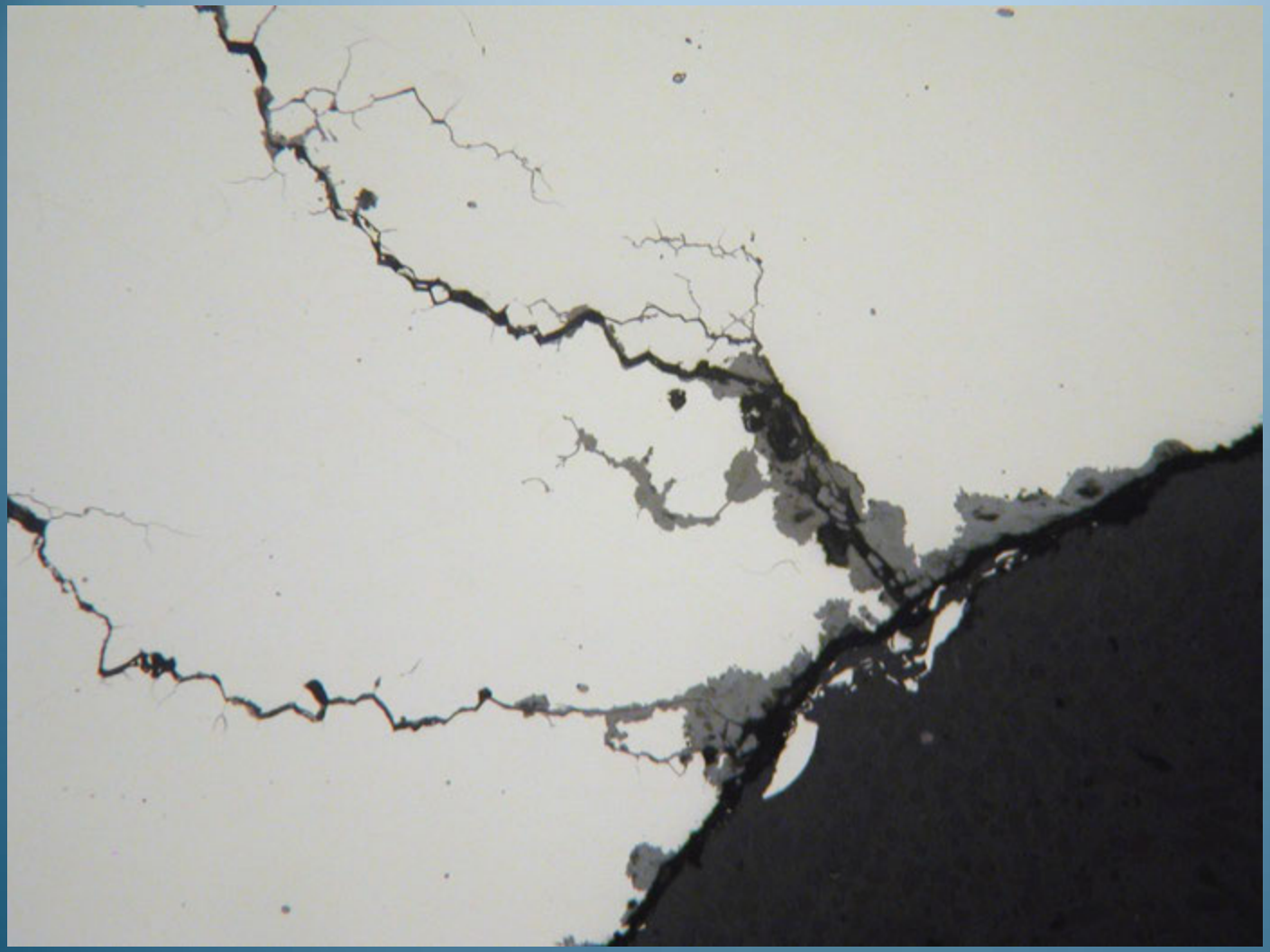

ETCH PIT
(formed where bifilm intersects surface)

*Image courtesy Metallurgical Associates Inc 2015*

# 10 Rules

***(The 10 Commandments by JC)***

1. Use good metal
2. Not too fast (no turbulence)(0.5m/s)
3. Not too slow (no stopping)
4. No entrained bubbles
5. No core blows
6. Feed shrinkage if necessary
7. Avoid convection
8. Avoid segregation
9. Avoid stress
10. Provide pick-up locations

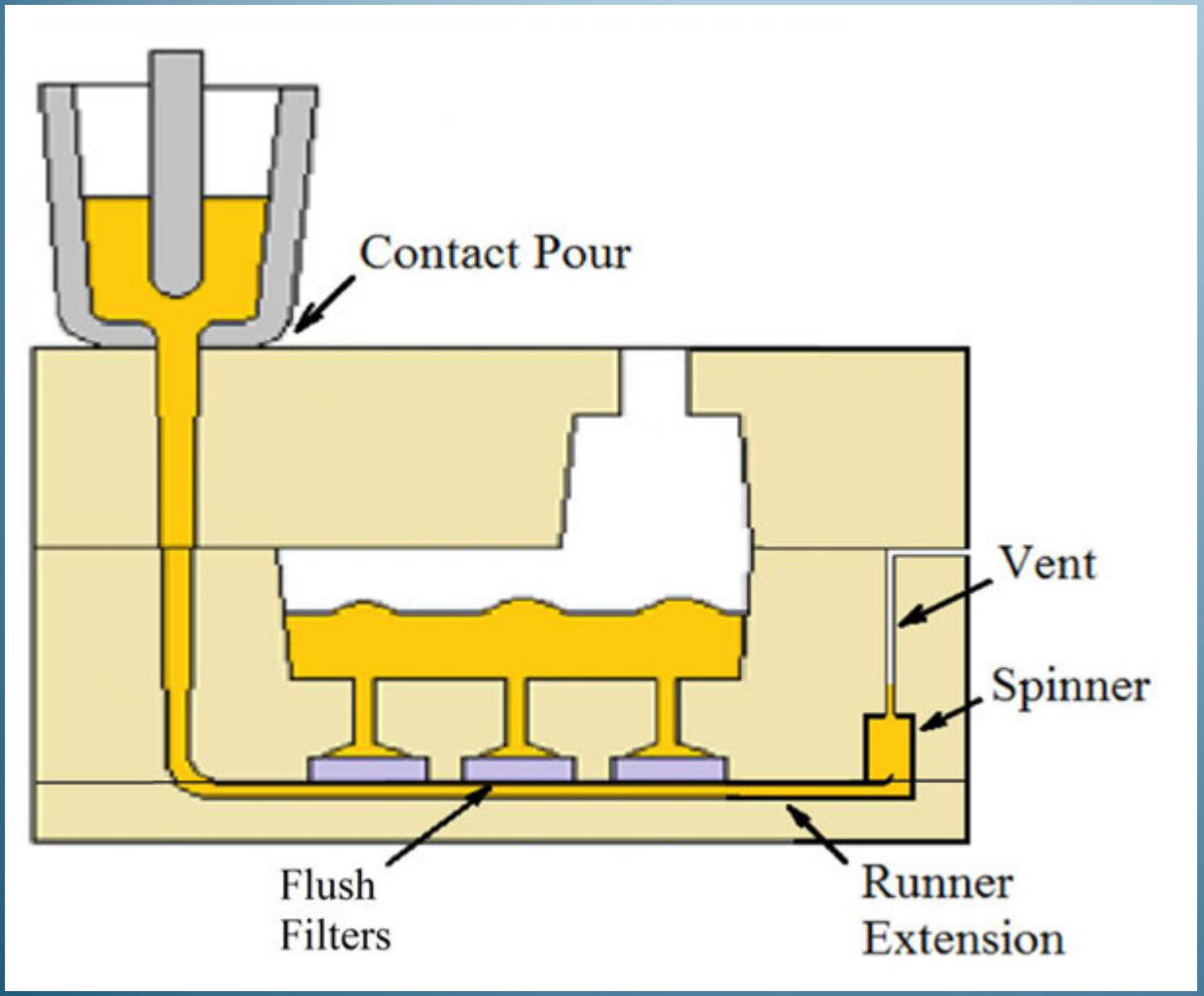


The latest development in gravity pouring to achieve a defect-free casting

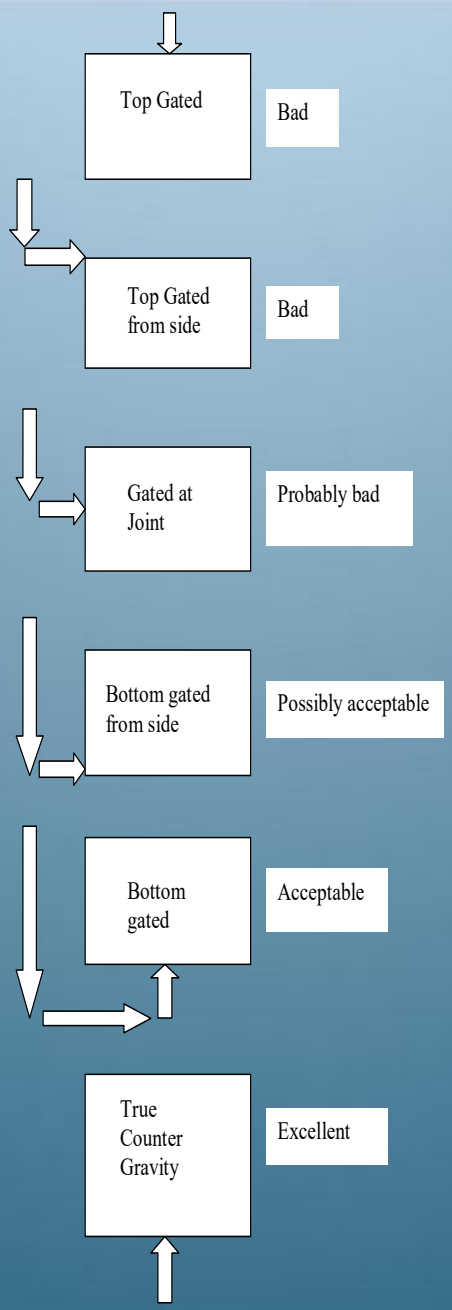
Top Gated
Bad
Top Gated from side
Bad
Gated at Joint
Probably bad
Bottom gated from side
Possibly acceptable
Bottom gated
Acceptable
True Counter Gravity
Excellent

# Counter-gravity Filling Systems

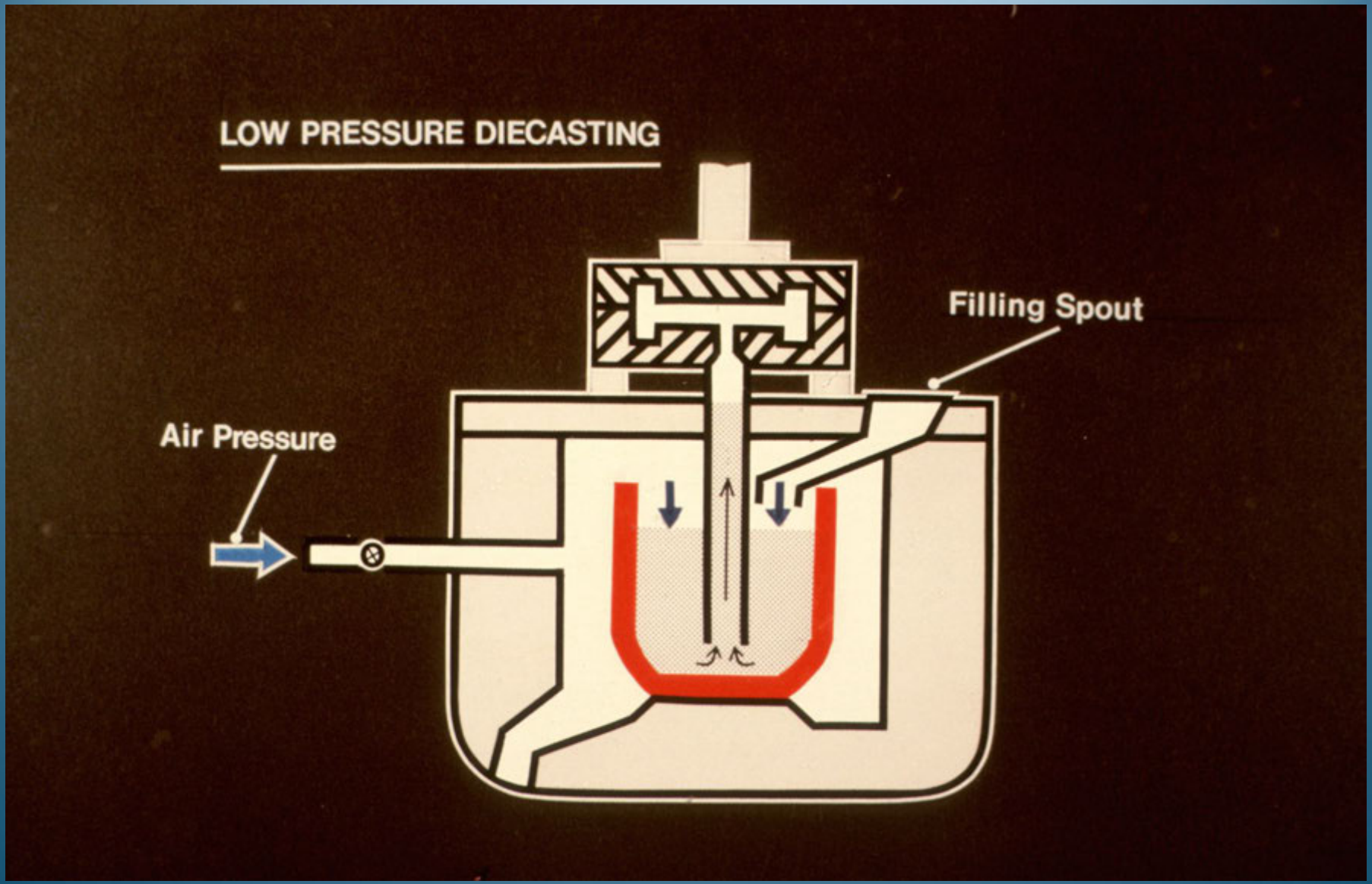
LOW PRESSURE DIECASTING
Filling Spout
Air Pressure

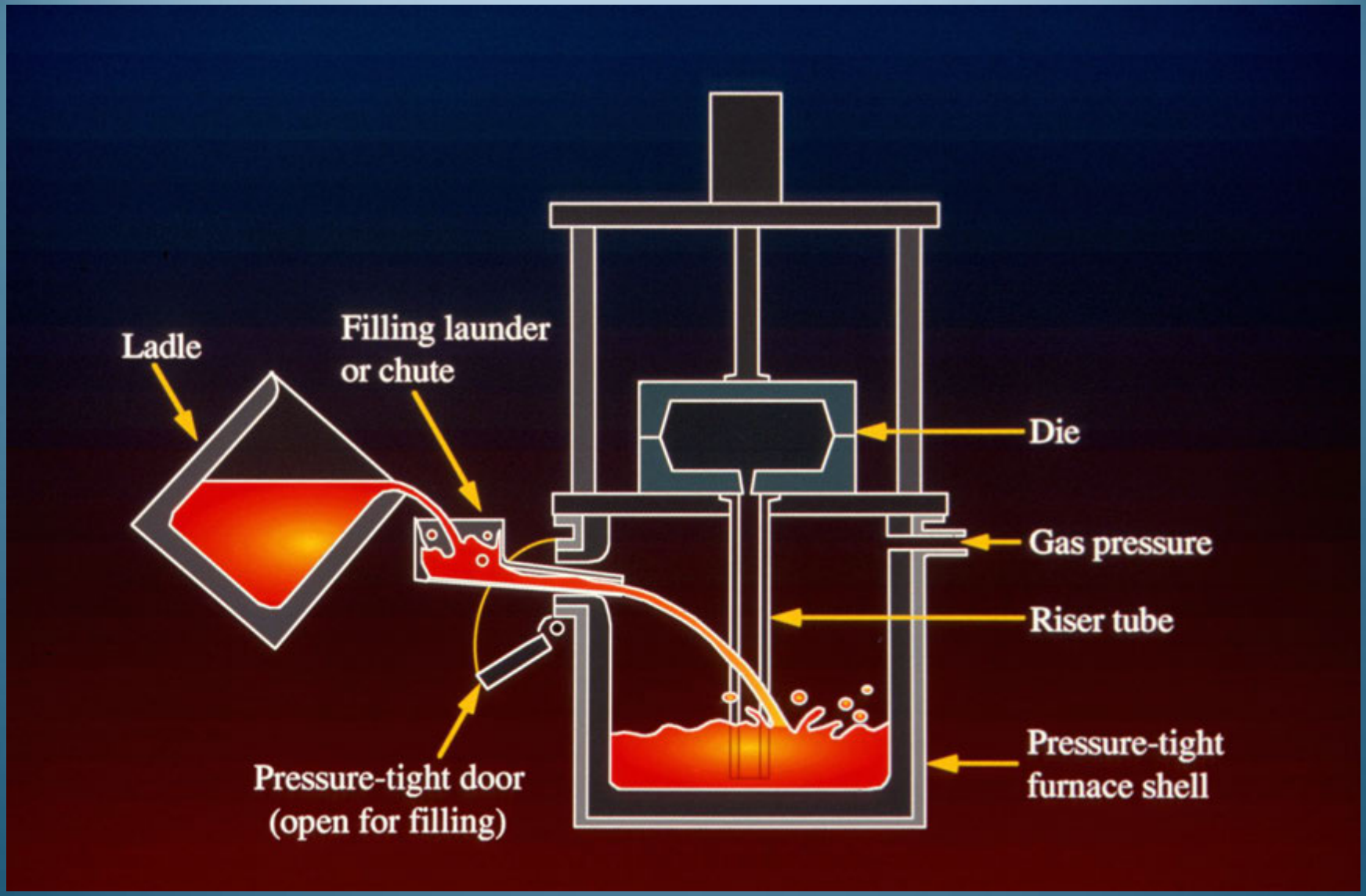


# Low Pressure Die Casting

# THE COSWORTH PROCESS

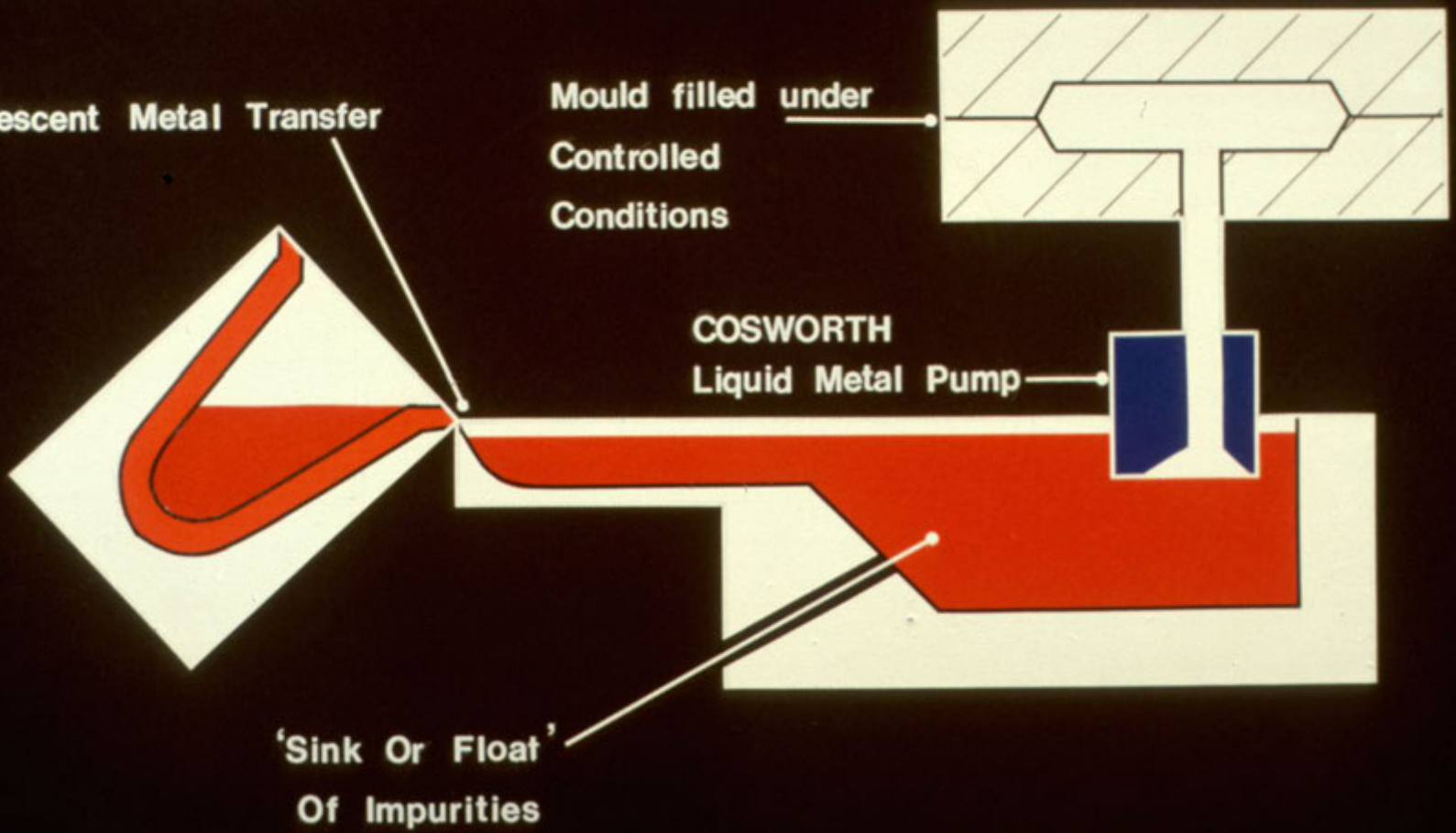

# Cosworth Mark II

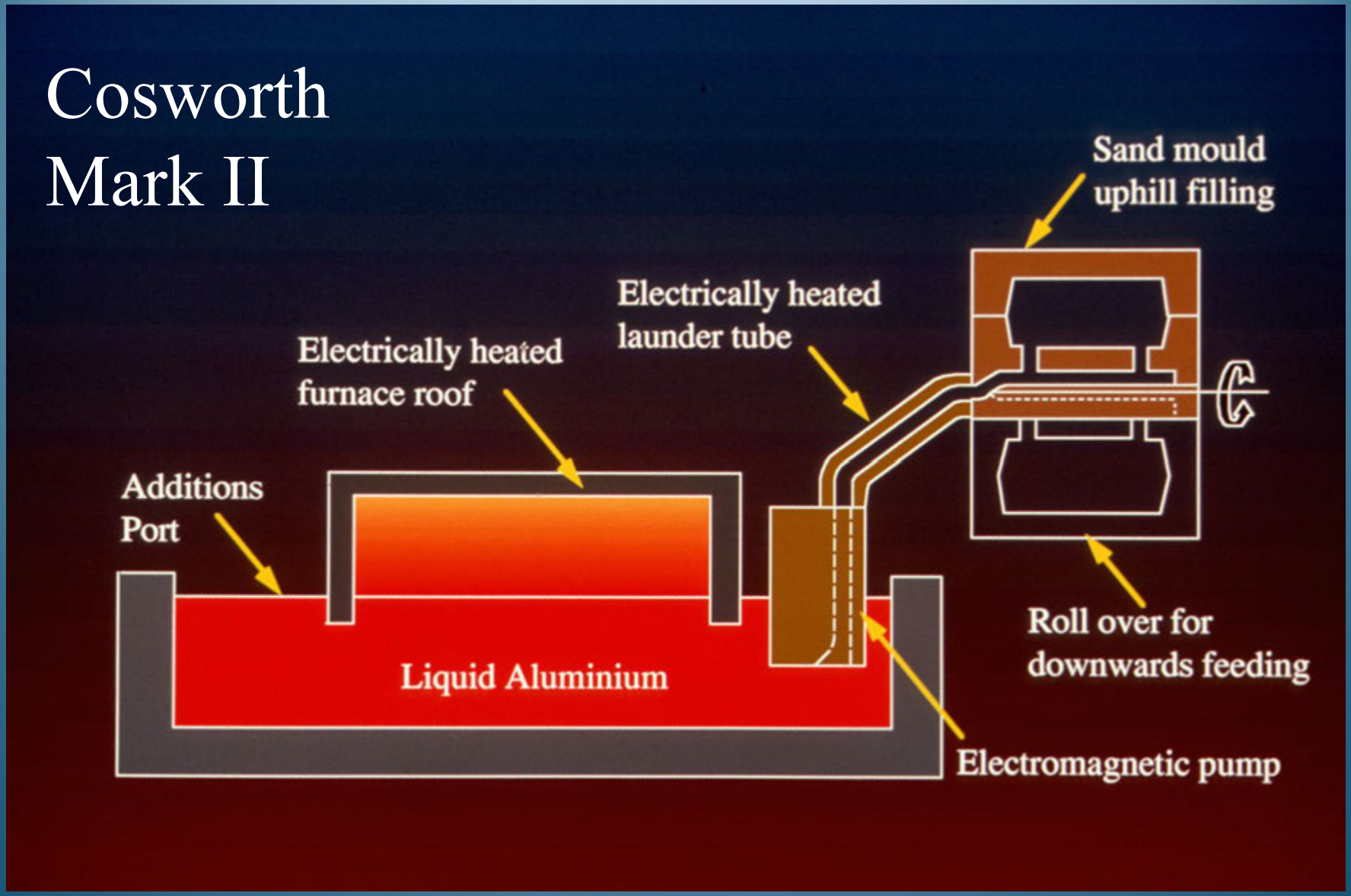

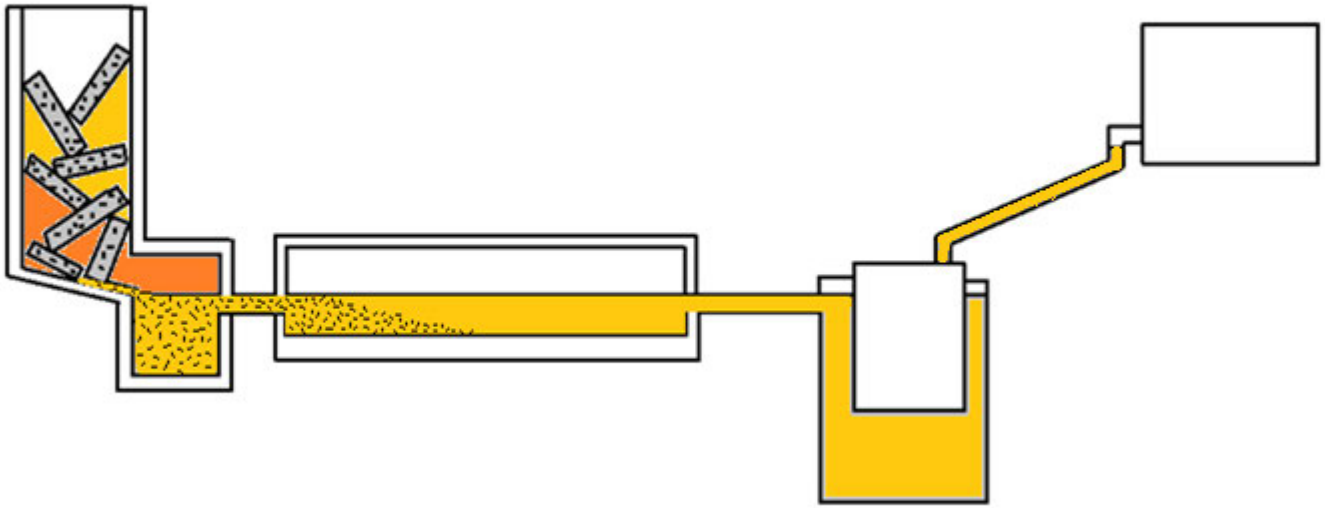

# Al Alloy Continuous Production of Castings using Sedimentation

# Theoretical Basis of Crack Formation

1. Griffith: An Energy criterion
   No specified geometry

2. Barenblatt: A geometrical model
   A region of zero cohesion edged by strong cohesion

# A History of Metallurgy

**Atoms**
1900

Point entities
0-D

# A History of Metallurgy

**Atoms**
1900

Point entities
0-D

**Dislocations**
1950

Line Defects
1-D

(Control Plasticity)

# A History of Metallurgy

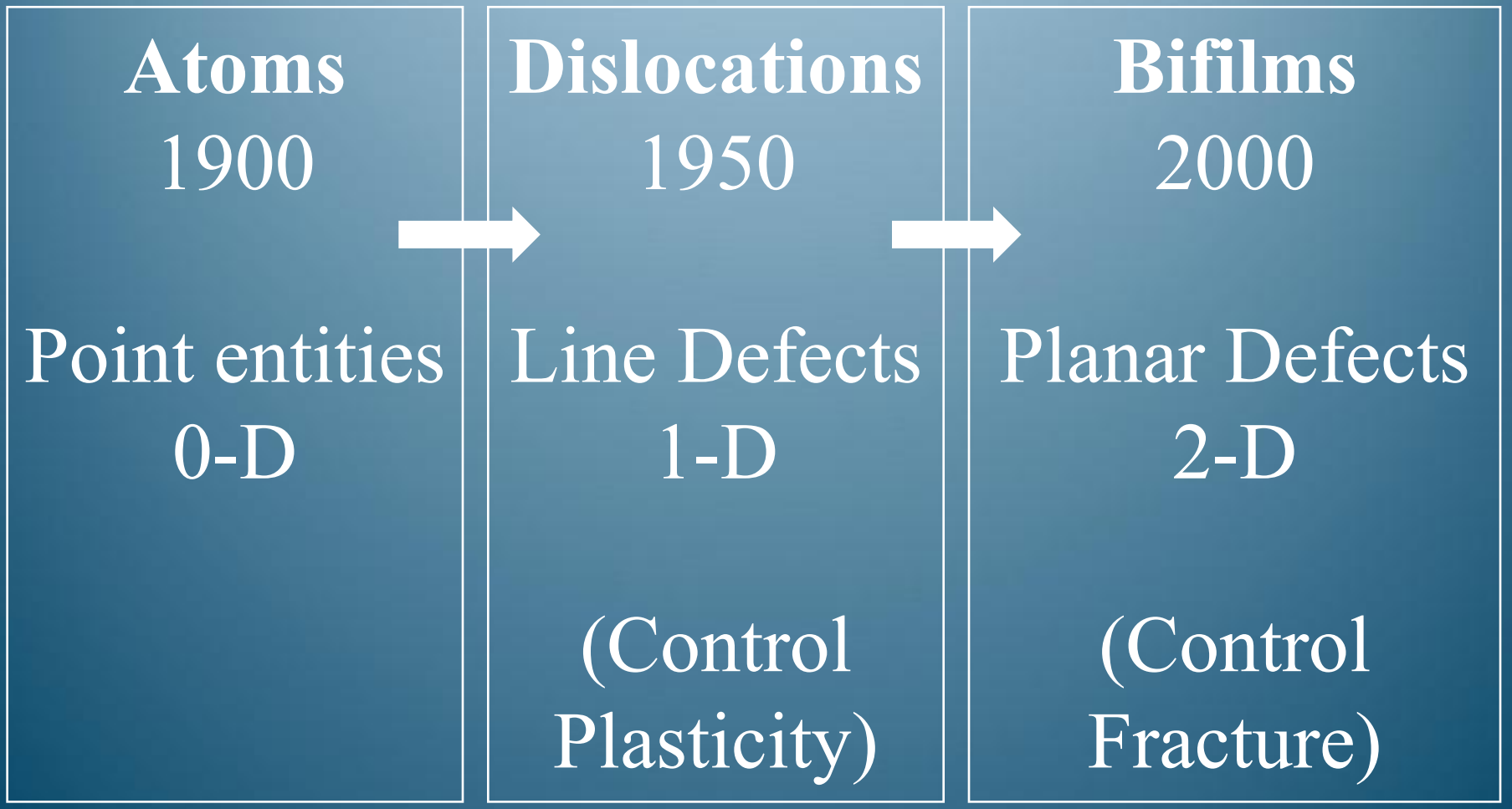

17th INTERNATIONAL FOUNDRYMEN CONFERENCE
Hi-tech casting solution and knowledge based engineering
Opatija, May 16th-18th, 2018
http://www.simet.hr/~foundry/

# TOWARDS STRUCTURAL AND DIMENSIONAL STABILITY OF SELECTED AlZn-BASED CAST ALLOYS

**Witold Kazimierz Krajewski[1]*, Alan Lindsay Greer[2], Paweł Krzysztof Krajewski[1]**

[1] AGH University of Science and Technology Faculty of Foundry Engineering, Krakow, Poland
[2] University of Cambridge, Department of Materials Science & Metallurgy, Cambridge, United Kingdom

**Plenary lecture**
*Original scientific paper*

**Abstract**

The present paper is devoted to modification of the AlZn based cast alloys aimed at improving their mechanical properties and structural stability. The examined alloys belong to high aluminium-zinc group represented here by Zn-(20-30) wt% Al – 1-3 wt% Cu (HAl-Zn) and to high zinc-aluminium group represented here by Al-(20-30) wt% Zn – 1-3 wt% Cu (HZn-Al). It was stated that reducing Cu content to 2-2.5 wt% and/or its partial replacing by Ti in the HAl-Zn alloys or with Mn in the HZn-Al alloys allows avoiding dimensional changes long time after supersaturation and quenching.

***Keywords***: *AlZn-based foundry alloys, structure modification, grain refinement, dimensional changes*

*Corresponding author: *krajwit@agh.edu.pl*

## INTRODUCTION

Nowadays foundry industry is aimed at developing cast alloys of good mechanical and service properties. The alloys composed on aluminium-zinc system satisfy these requirements. They have good strength, tribological and damping properties [1-15]. Thanks to their comparatively low melting temperatures they are among those which are classified as energy-saving and environmentally friendly. That is why interest in these alloys is still increasing [16]. It should be noted that the sand cast HAl-Zn and HZn-Al alloys solidify naturally with coarse dendrites of $\alpha$(Al) solid solution which decreases their elongation. For this reason the mentioned alloys are grain-refined with the addition of Ti-containing master alloys [16-18] which significantly increases grain population in the mentioned alloys – Fig. 1. It should be noted that the mentioned alloys with copper addition show instability of structure and dimensions caused by phase transformations which take place in solid alloys over long periods of time after casting [19]. Cu addition in a range of 4-5 wt% increases strength and wear

properties on one hand, but on the other it builds the metastable ε-$CuZn_4$ phase. The latter takes part in the so-called four-phase reaction to form a stable T'-$Al_5Cu_4Zn$ phase. The transformation ε – to - T' prolongs more than one year after casting and it causes significant dimensional changes [19-24].

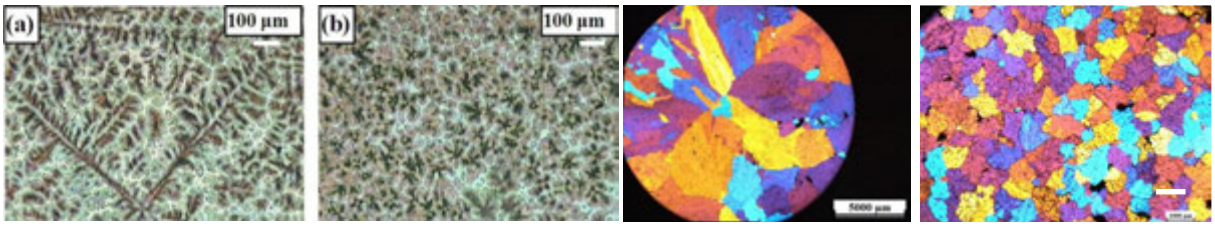


Figure 1. (a) and (b) Example of the initial and refined Zn-25 wt% Al alloy after addition of ZnTi-based master alloy [12]; (c) and (d) Example of the initial and refined Al-20 wt% Zn after addition of AlTi-based master alloy [9]

This problem can be solved by partial replacing Cu with other elements, e.g. Ti or Mn [25-27]. This work presents examinations of long-term dimensional changes of the high-zinc aluminium alloys of reduced Cu content.

## MATERIALS AND METHODS

The materials, melting and casting procedures, sample preparation and measurements techniques were the same as described previously, e.g. in [19, 21-27]:
The examined alloys Zn-26 wt% Al-2.2 wt% Cu (Zn-26Al-2.2Cu), Zn-26 wt% Al-1 wt% Cu-1.5 wt% Ti (Zn-26Al-1Cu-1.5Ti), Al-30 wt% Zn-2 wt% Cu-1 wt% Mn (Al-30Zn-2Cu-1Mn) and master alloys Al-12.5 wt% Ti (Al-12Ti) and Al-33 wt% Cu (Al-33Cu) were melted from electrolytic aluminum (minimum purity 99.96 %), electrolytic zinc (99.995 %), electrolytic copper (minimum purity 99.95 %) and titanium sponge (98-99.8 %, from Johnson Matthey Alfa). The Zn-Al, Zn-Al-Cu and Al-Zn-Cu alloys were melted in an electric resistance furnace, in an alumina crucible of 2-litre capacity. The Al-12Ti master alloy was melted in a Balzers induction furnace with a protective argon atmosphere. The obtained ingot of the Al-12Ti master alloy was the source of the Ti. The melts of Zn-Al and Zn-Al-Cu alloys were superheated to about 600 $^{o}$C and the Al-12Ti master alloy was added to give an overall titanium content of approx. 1.5-1.6 wt% Ti. The Al-30Zn based alloys were superheated to about 720-740 °C. Mn was added into melt with Al-12 wt% Mn master alloy (Al-12Mn, prod. Alumetal, Poland). The melted charges were flushed with pure argon for 10 min. Then, 10 min after finishing the flushing, the dross was removed from the melt surface. Five minutes after the Al-12Ti or Al-12Mn addition, the bath was stirred for 2 minutes with an alumina rod, and the alloys were cast into a metal mould with vertical cylindrical cavity ∅12 x 90 mm. From these castings samples ∅5 x 35 mm were cut for dimensional examinations. The samples used in the dilatometry

examinations in the state after supersaturation were homogenized in air, in the annealing furnace at 370-380 °C for 48 h and then quenched in water at room temperature. The dilatometry measurements were carried out at room temperature using screw-micrometer of accuracy of 0.001 mm. Results of, at least, 3 repeatable measurements were registered. From the castings ∅12 x 90 mm samples about 25 mm high were cut for structural SEM-EBSD examinations. Optical light metallography (LM) was performed using Zeiss Axio Imager A2m light microscope. The samples for LM examinations were ground on abrasive papers (grit 200-1000) and then were polished using sub-microscopic aluminium oxide in a water-alcohol suspension. The LM samples were etched using Barker's etchant. SEM/EBSD measurements were carried out using Quanta 3D FEG microscope. Chemical composition of the analyzed phases was obtained using SUTW-Sapphire detector and EDAX ZAF procedure. 2D EBSD maps were acquired in low vacuum conditions at a water vapor pressure of 0.45 Torr using the EDAX Hikari camera. The operating parameters of the electron beam were as follows: an accelerating voltage was set to 20 kV and beam current to 8 nA. Diffraction patterns were analyzed at a rate of 50-100 patterns per second.

## RESULTS AND DISCUSSION

Figure 2 (a) and (b) shows microstructures of the Zn-26Al-2.2Cu and Zn-26Al-1Cu-1.5Ti alloys [12, 22] while (c) shows long-term dimensional changes of these alloys. Figure 3 (a) and (b) shows microstructures of the Al-30Zn-3Cu alloy with coarse grain structure and Al-30Zn-2Cu-1Mn with highly refined grains, while (c) shows long-term dimensional changes of these alloys. From Figs 2 (a) and (b) it can be seen that Ti addition causes refinement of the $\alpha$(Al) primary dendrites of solid solution of zinc in aluminium. The observed refinement should be beneficial for increasing ductility of the examined high-aluminium zinc alloys. From Fig. 2(b) it can be also seen that intermetallic Ti-based particles are visible in the structure. As it was previously reported in [12] these particles can play role of the bearing phases improving tribological properties.

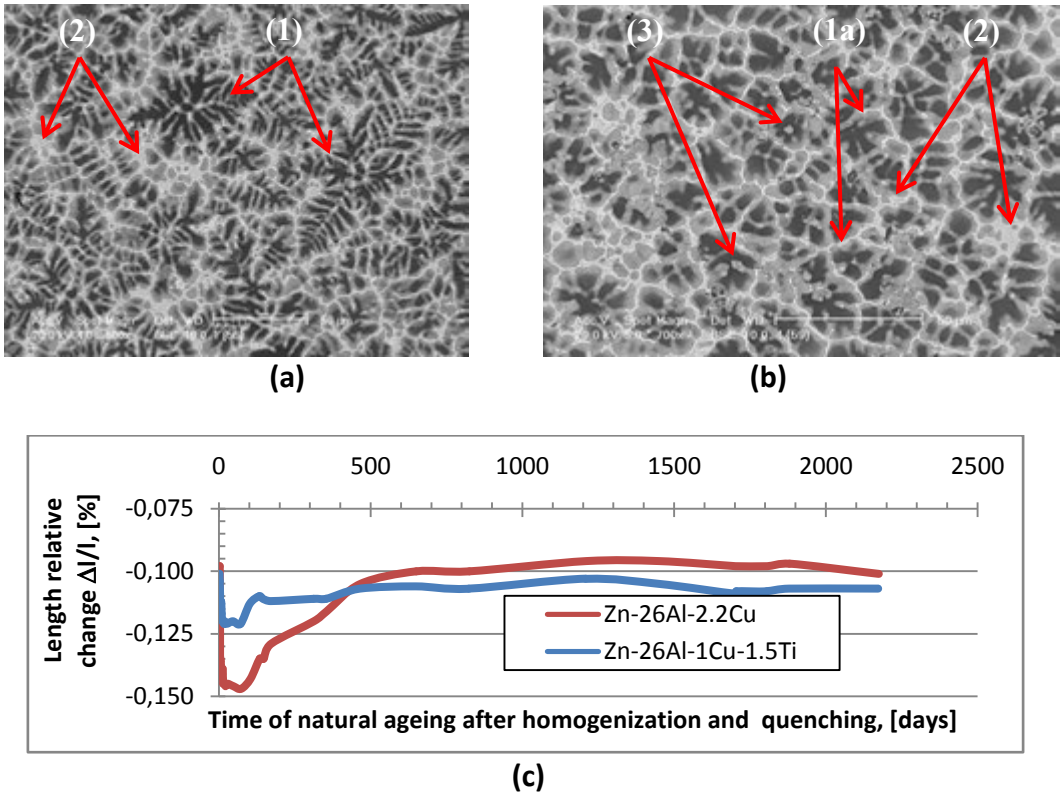


Figure 2. SEM microstructures of the examined sand cast high-aluminium zinc alloys: (a) Sample Zn-26Al-2.2Cu alloy with coarse α(Al) dendrites (1) and eutectics (2); (b) Sample Zn-26Al-1Cu-1.5Ti alloy with refined α(Al) dendrites (1a), eutectics (2) and visible Ti-based intermetallic phases (3); (c) dimensional changes of the examined alloys

It should be also noted that Ti presence in the α(Al) solid solution can retard its grain growth while small Ti-based particles can serve as substrate of its heterogeneous nucleation. This double role is beneficial for shaping good plastic properties. And finally, partial replacing Cu with Ti significantly decreases range of dimensional changes during natural ageing of the homogenized and quenched samples – which is clearly seen in Fig. 2(c). Summing up, the addition of Ti allows obtaining alloy of improved structural stability and mechanical properties which is a positive effect of the implemented modification.

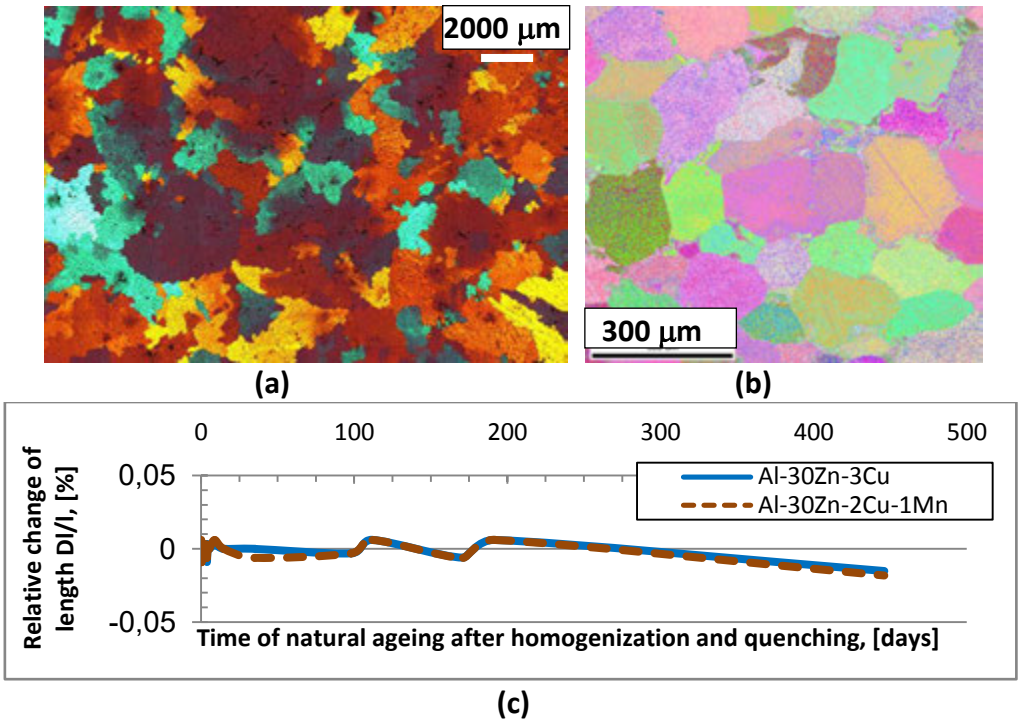


Figure 3. Microstructures of the examined sand cast high-zinc aluminium alloy: (a) Al-30Zn-3Cu alloy with coarse grain structure, LM picture; (b) Al-30Zn-2Cu-1Mn alloy with refined structure, 2D inverse pole figure (IPF) EBSD map; (c) dimensional changes of the examined alloys [24]

From Fig. 3 (a) and (b) one can see that partial replacing of Cu with Mn causes significant structure refinement while range of dimensional changes remains practically preserved. It was also stated that the observed structure refinement positively influences plastic properties of the alloy doped with Mn [27]. This role of Mn should be subject of additional detail examinations and it will be discussed elsewhere.

## CONCLUSIONS

On the basis of the presented results the following conclusions can be drawn:
High aluminium zinc alloys. Partial replacement of Cu with Ti significantly decreases dimensional changes over long time after supersaturation and quenching. At the same time Ti addition causes refinement of the alloy matrix which should positively influence ductility of the examined alloys.
High zinc aluminium alloys. Partial replacement of Cu with Mn significantly increases grain population of the alloy matrix which should positively influence ductility of the examined alloys. Mn addition does not influence dimensional changes during the 1.5 year of natural ageing after supersaturation and quenching. The reported dimensional changes are very low, i.e. below $\pm$ 0.02 % in relation to the initial length, which are in the accuracy range of

the measurement instrument. The examined Al-30Zn-2Cu-1Mn alloy appears to have stable structure and improved wear properties [24] which is a positive achievement of this replacement.

## REFERENCES

[1] I. G. Ritchie, Z-L. Pan, High damping metals and alloys, Metallurgical Transactions A, 22A (1991) pp. 607-616.
[2] W. Krajewski, The Effect of Ti Addition on Properties of Selected Zn-Al Alloys, Physica Status Solidi (a), 147 (1995), pp. 389-399.
[3] W. K. Krajewski, Structure and properties of high-aluminium zinc alloys inoculated with Ti addition (retrospective coverage), Archives of Foundry, 5 (2005) 15, pp. 231-240.
[4] W. K. Krajewski, Shaping Surface Wear Properties of the ZnAl-based MMCs, Metallurgia Italiana, 11-12 (2006), pp. 27-30.
[5] W. R. Osorio, J. E. Spinelli, N. Cheung, A. Garcia, Secondary dendrite arm spacing and so-lute redistribution effects on the corrosion resistance of Al–10 wt% Sn and Al–20 wt% Zn alloys, Materials Science and Engineering, A, 420 (2006), pp. 179-185.
[6] W. K. Krajewski, J. Buras, M. Żurakowski, A. L. Greer, Structure and properties of grain-refined Al-20wt% Zn sand cast alloy, Archives of Metallurgy and Materials, 54 (2009) pp. 329-334.
[7] G. Purcek, O. Saray, I. Karaman, M. Haouaoui, Microstructural evolution and mechanical response of equal-channel angular extrusion-processed Al-40Zn-2Cu alloy, Metallurgical and Materials Transactions A, 40A (2009), pp. 2772-2783.
[8] Y. Alemdag, T. Savaskan, Mechanical and tribological properties of Al–40Zn–Cu alloys, Tribology International, 42 (2009), pp. 176-182.
[9] K. Haberl, W. K. Krajewski, P. Schumacher, Microstructural features of the grain-refined sand cast alloy AlZn20, Archives of Metallurgy and Materials, 55 (2010), pp. 837-841.
[10] W. K. Krajewski, J. Buras, M. Zurakowski, A. L. Greer, M. N. Mancheva, K. Haberl, P. Schumacher, Development of environmentally friendly cast alloys. High-zinc Al alloys, Archives of Materials Science and Engineering, 45 (2010) 2, pp. 120-124.
[11] W. K. Krajewski, K. Haberl - Faerber, J. Buras, P. K. Krajewski, Damping Properties vs. Structure Fineness of the High-zinc Aluminium Alloys, Archives of Foundry Engineering, 12 (2012) 3, pp. 63-66.
[12] W. K. Krajewski, A. L. Greer,P. K. Krajewski, Trends in developments of high-aluminium zinc alloys of stable structure and properties, Archives of Metallurgy and Materials, 58 (2013), pp. 859-861.
[13] A. F. Abd El-Rehim, M. S. Sakr, M. M. El-Sayed, M. Abd El-Hafez, Effect of Cu addition on the microstructure and mechanical properties of Al–30 wt% Zn alloy, Journal of Alloys and Compounds, 607 (2014), pp. 157-162.

[14] S. S. Shin, K. M. Lim, I. M. Park, Characteristics and microstructure of newly designed AlZn-based alloys for the die-casting process, Journal of Alloys and Compounds, 671 (2016), pp.517–526.
[15] S. S. Shin, K. M. Lim, I. M. Park, Characteristics and microstructure of newly designed Al-Zn-based alloys for the die-casting process, Journal of Alloys and Compounds, 671 (2016), pp. 517–526.
[16] W. K. Krajewski, A. L. Greer, P. K. Krajewski, G. Piwowarski, Grain refinement of zinc-aluminium based foundry alloys, Proceedings of 71st World Foundry Congress, World Foundry Organization, 19-21 May 2014, Bilbao, Spain.
[17] W. Krajewski, Phases of Heterogeneous Nucleation in the ZnAl25 Alloy Modified by Zn-Ti and Al-Ti Master Alloys, Zeitschrift für Metallkunde, 87 (1996), pp. 645-651.
[18] W. K. Krajewski, A. L. Greer, EBSD Study of ZnAl25 Alloy Inoculated with ZnTi4 Master Alloy, Materials Science Forum, 508 (2006), pp.281-285.
[19] W. K. Krajewski, P. L. Zak, J. Orava, A. L. Greer, P. K. Krajewski, Structural Stability of the High-aluminium Zinc Alloys Modified with Ti Addition, Archives of Foundry Engineering, 12 (2012) 1, pp. 61-66.
[20] R. Ciach, J. Krol, K. Wegrzyn-Tasior, Studies on Four Phases Transformation in AlZn78 Alloy Containing 1-3 per cent of Copper, Bulletins of the Polish Academy of Sciences - Ser. Techn., 17 (1969) 4, pp. 13-18.
[21] W. Krajewski, The Effect of Ti Addition on the Kinetics and Enthalpy of the Supersaturated ZnAl Alloy Phase Transformation, Physica Status Solidi (a), 142 (1994), pp. 75-79.
[22] W. K. Krajewski, A. L. Greer, J. Orava, P. K. Krajewski, E. Tyrala, Dimensional Stability of the High-aluminium Zinc Alloys Modified with Ti Addition, Proceedings of 12th International Foundrymen Conference of Sustainable Development in Foundry Materials and Technologies, University of Zagreb – Faculty of Metallurgy, May 24th-25th, 2012, Opatija, Croatia, Abstract Book, pp. 24.
[23] W. K. Krajewski, A. L. Greer2, P. K. Krajewski, Long-term dimensional changes of the high-aluminium zinc alloys modified with Ti addition, Proceedings of 13th International Foundrymen Conference Innovative Foundry Processes and Materials, University of Zagreb – Faculty of Metallurgy, May, 16 - 17, 2013, Opatija, Croatia (pp. 1-6, on CD).
[24] P. K. Krajewski, A. L. Greer, M. Faryna, W. K. Krajewski, Structural Stability of Novel Multicomponent AlZn-Based Cast Alloy, Materials Science Forum, (submitted in 2018).
[25] W. K. Krajewski, J. Buras, P. K. Krajewski, A. L. Greer, K. Faerber, P. Schumacher, New developments of Al-Zn cast alloys, Materials Today: Proceedings, 2 (2015), Part A, pp. 4978-4983.
[26] W. K. Krajewski, A. L. Greer, J. Buras, G. Piwowarski, P. K. Krajewski, Development of new multicomponent high-zinc aluminium cast alloys, Proceedings of International Conference on Frontiers in Materials Processing Applications, Research and Technology, FIMPART'17, 9-12 July 2017, Bordeaux, France, Abstract Book (on USB), Session E2, Light Alloys.
[27] W. K. Krajewski, A. L. Greer, J. Buras, G. Piwowarski, P. K. Krajewski, New developments of high-zinc Al-Zn-Cu-Mn cast alloys, Materials Today: Proceedings, (2017) (in printing).

**Acknowledgements**

The authors are grateful to the NCN Polish Science National Centre for financial support under grant No. UMO-2015/18/M/ST8/00038. The AGH University of Science and Technology, Krakow, Poland – Faculty of Foundry Engineering and The University of Cambridge, UK – Department of Materials Science and Metallurgy are warmly acknowledged for provision of laboratory facilities.

17th INTERNATIONAL FOUNDRYMEN CONFERENCE
Hi-tech casting solution and knowledge based engineering
Opatija, May 16th-18th, 2018
http://www.simet.hr/~foundry/

# HIGH Si / Si-Mo DUCTILE CAST IRONS

**Iulian Riposan*, Stelian Stan, Mihai Chisamera**

Politehnica University of Bucharest, Bucharest, Romania

**Plenary lecture**
*Subject review*

**Abstract**

A review of Si / Si-Mo alloyed ductile iron data in the first part of the paper shows that Si promotes ferrite, increases the strength and reduces the elongation and toughness by solid solution hardening. The instability of a mixed ferrite-pearlite matrix (Si < 3%), could be replaced with more predictable and controllable ferritic grades (3.2 – 4.3%Si), with reduced hardness variation (± 4HB), increased cutting tool life, and consistently better mechanical properties ($R_m$=450-650MPa; $R_{p0.2}$=350–500MPa; A=10-20%). Mo additions in high Si ferritic grades (3.5–5.5%Si, 0.2–2.0%Mo) favours superior mechanical properties ($R_m$=450-550MPa; $Rp_{0.2}$=275 – 440MPa; A=4 – 10%) and improved resistance to oxidation and corrosion at high temperatures. Some important new knowledge was identified: Si segregation pattern and typical content to reach the maximum strength and ductility; graphite degeneration (Si & Al effects); tolerance levels for other elements; increasing the strength and maximum working temperature up to 900-1000°C (Al, Ni, Co, Cr, V, Ti, Zr, etc supplementary alloying); carbides and phases characteristics; effects of Si and Al on transformation temperature and the oxide layer thickness; CGI–SiMoAl efficient application; specific corrosion and fatigue behaviour in different media; crack growth mechanisms, etc.
Experiments studied the solidification pattern of three ductile iron compositions [2.5%Si; 4%Si and 4%Si-1.6%Mo (Si:Mo=2.5)], for 0.35–0.45%Mn and controlled on minor elements content. The influence of Si and Si-Mo content and inoculation on the representative temperatures and undercooling during the eutectic reaction and at the end of solidification was observed. Without inoculation a supplementary high Mo addition decreased the beneficial effect of Si on decreasing undercooling. Despite that, Si is known to favour chunky graphite formation, effective inoculation decreased the sensitivity to form a dark coloured porous region in the thermal centre of castings and ensured desirable graphite nodularity and nodule count. It was found that inoculation is important for high-Si but particularly so for Si-Mo alloyed irons, requiring a high efficiency inoculation.

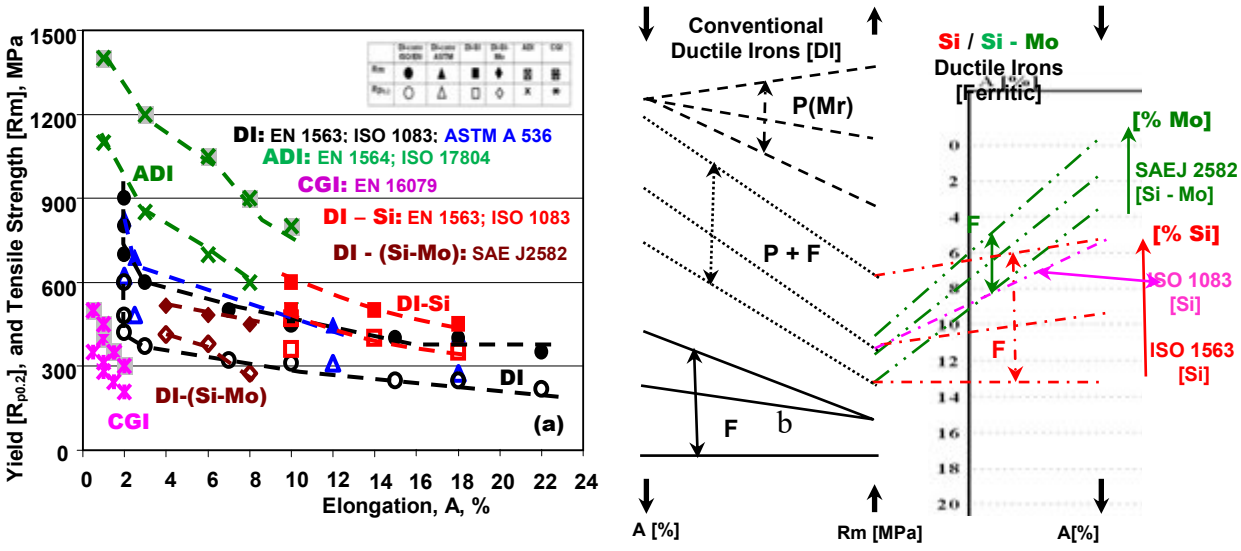


***Keywords***: *ductile iron, Si, Si-Mo, alloying, inoculation, thermal analysis, structure, graphite, ferrite*

*Corresponding author (e-mail address): *iulian.riposan@upb.ro*

# HIGH Si / Si-Mo DUCTILE CAST IRONS

**Iulian RIPOSAN, Stelian STAN, Mihai CHISAMERA**

**POLITEHNICA University of Bucharest,**

**RO - 060042 Bucharest, ROMANIA**

# RESEARCH PROGRAM

## SOLIDIFICATION PATTERN OF SILICON ALLOYED DUCTILE CAST IRONS

- **To review the new generation ductile cast irons with 3.0 ... 6.0% Si:**
  - strongly increasing demand, especially in the automotive industry:
    - instability of a mixed ferritic-pearlitic matrix could be replaced with more predictable *and* controllable Si-alloyed ferritic grades, at reduced machining cost
      - the maximum working temperature could be increased from $700^0$C up to 900 - $1000^0$C
- **To identify the differences in the solidification pattern of ductile irons:**
  - conventional [2.5%Si] / high Si [4%Si] / high Si - Mo [4%Si - 1.6%Mo, lower Si / Mo=2.5 ratio]
  - un-inoculated and inoculated cast irons [selected inoculants]
  - large range of the cooling modulus [solidification cooling rate] samples

---

* Thermal / Cooling Curves Analysis, conventional ceramic cup, 0.75cm cooling modulus
* Micro–structure analysis [graphite, carbides, ferrite / pearlite, specific phases]
* Macro – structure / fracture analysis [central porous area sensitiveness]
* Shrinkage and Micro-shrinkage tendency
* Simultaneous Thermal / Contraction-Expansio Analysis – new equipment

# WORLD ALLOY TRENDS OF A HALF CENTURY

## [1966 / 2016, tonnage]

**Grey Iron [GI]** [While still the highest produced alloy has deceased from over three - quarters of the pie to less than half]

**Ductile Iron [DI]** & **Aluminum [Al]** - grown considerably; **Steel** – decreased

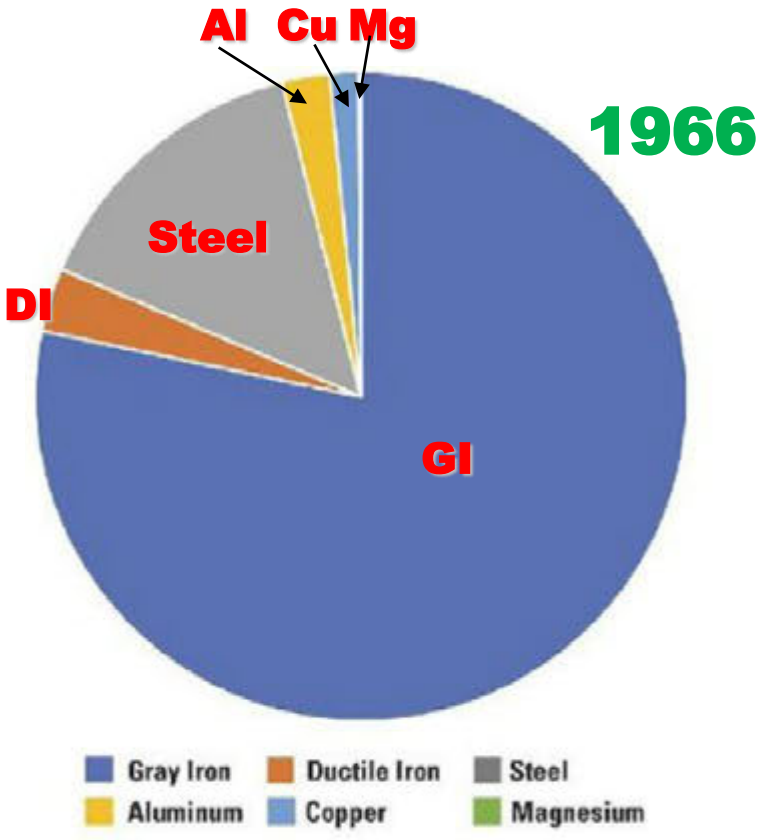


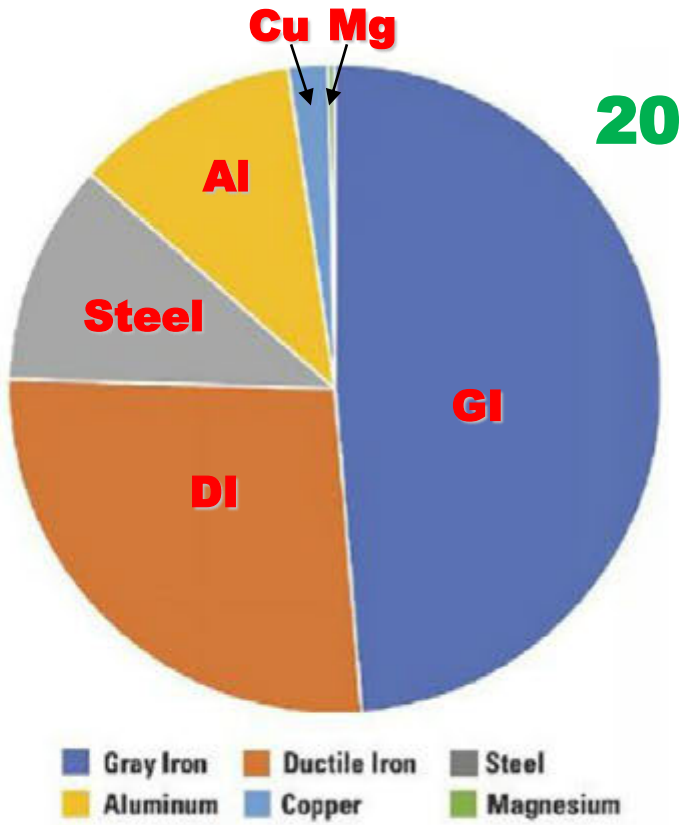


*[Modern Casting, December 2017, pp. 24 - 28]*

# Minimal values of Tensile Strength [Rm, MPa], Yield Strength [$Rp_{0.2}$, MPa], Elongation [A, %]

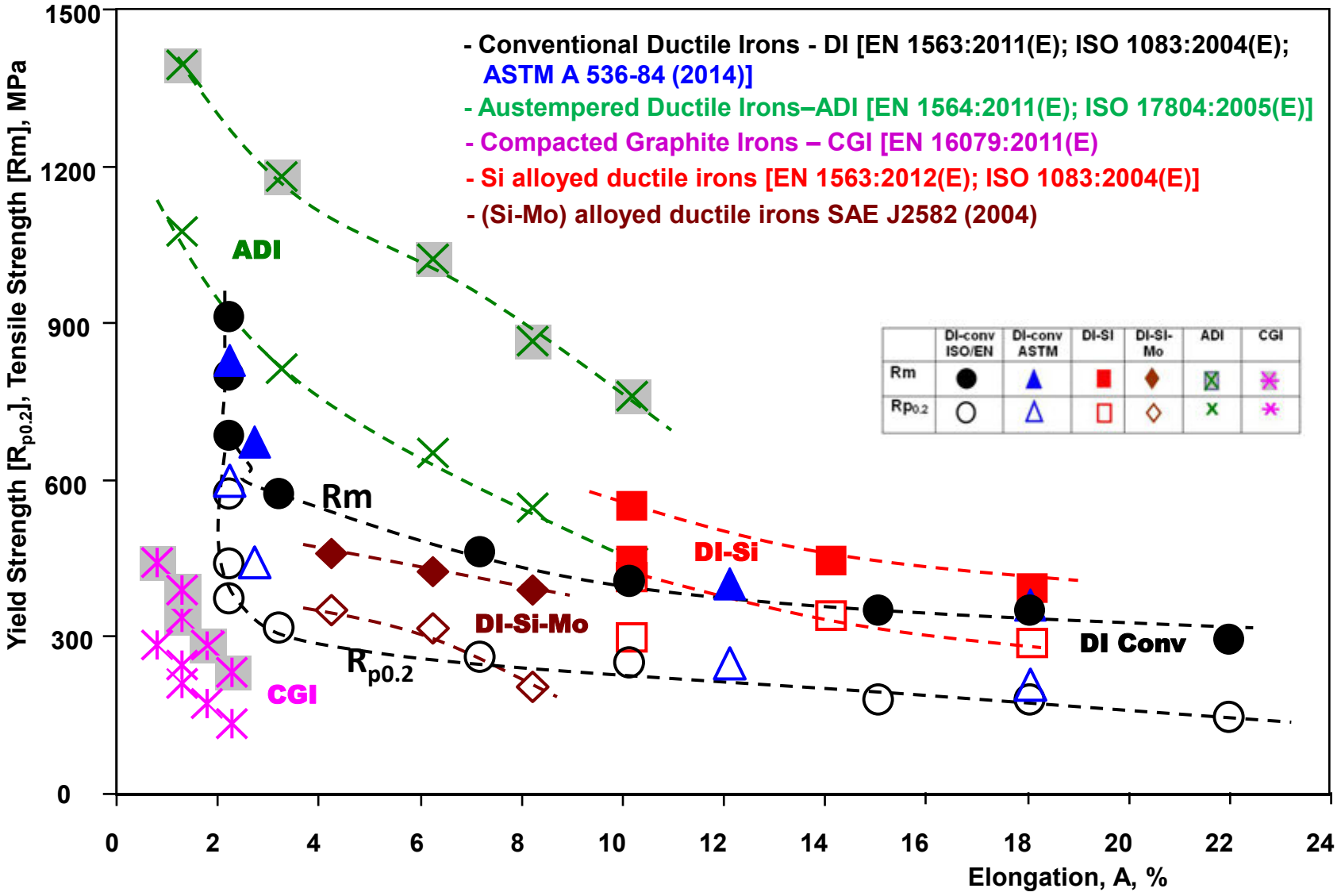

**Conventional Ductile Irons**
**ISO 1083 [2004]**
**ISO 1563 [2011]**
**[ P / P + F / F ]**

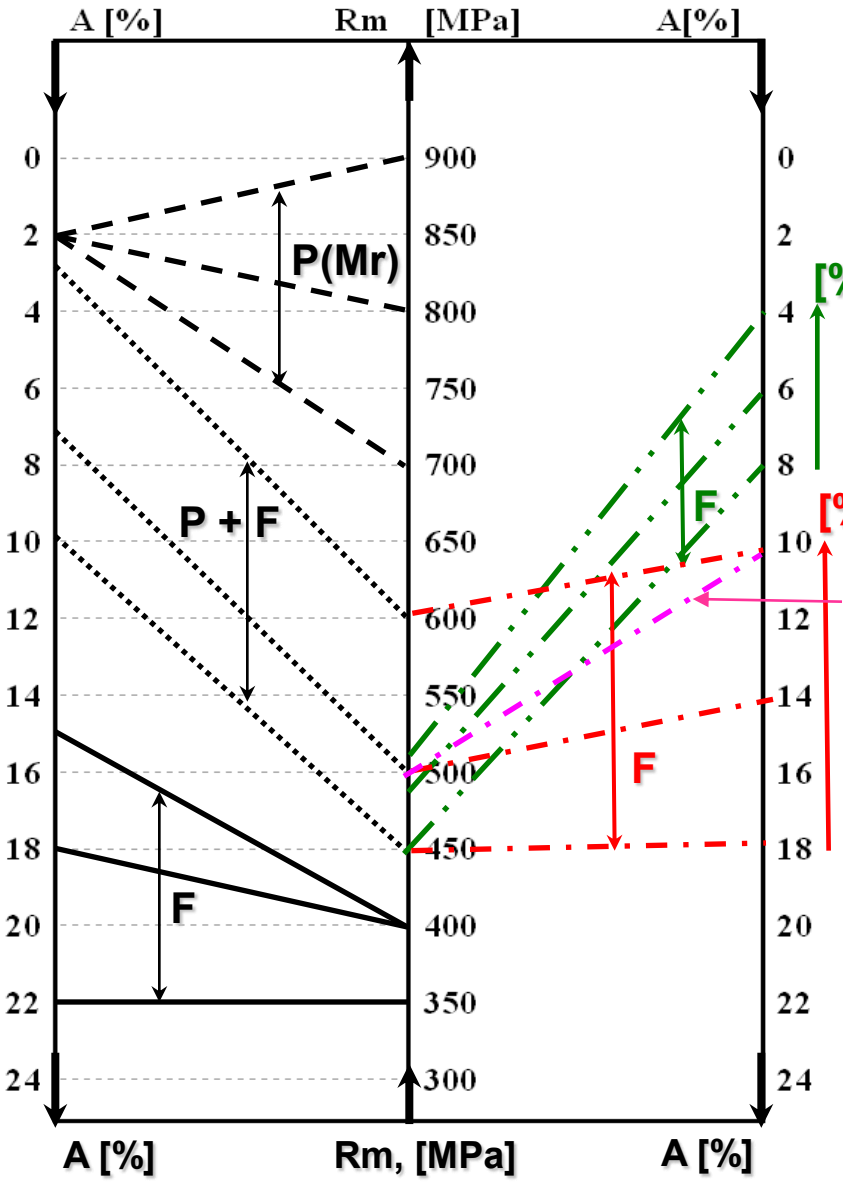


**Si / Si - Mo alloyed Ductile Irons [ Ferritic ]**

**[% Mo]**

**SAEJ 2582 [2004]**
**[ Si - Mo ]**

**[% Si]**

**[Si] ISO 1083 [2004]**

**[Si] ISO 1563 [2011]**

# New important knowledge in research and production – literature review

[I. Riposan et al, 122nd AFS Metalcasting Congr., April 2018, Fort Worth, TX, USA, Paper 18-022]

## [I. Si – alloyed Ductile Cast Irons]

* 2.5 - 4.6 %Si: changes the ferrite lattice parameter by (– 0.00185 Å) / % Si:
  - Si - strengthened ferrite
* Si highly segregation around nodules:
  - The origin of the initiation & propagation of cracks fracture
  - Conventional Ferritic Ductile Irons: the best impact strength;
  - High Si – DI: Si favors brittle cleavage; higher Si, lower impact strength
  - Fracture Toughness: Ferritic high Si-DI *and* the Pearlitic DI are similarly low
* Supplementary alloying beneficial effects in mechanical properties (Ni, Al)
  - 1.5%Ni + 0.3%Al to EN-GJS-500-14 grade [3.8%Si]: Rm = 650 MPa at 15% elongation

# Silicon influence on the mechanical properties of ductile cast irons

## [High-Si Ferritic Ductile Cast Irons]

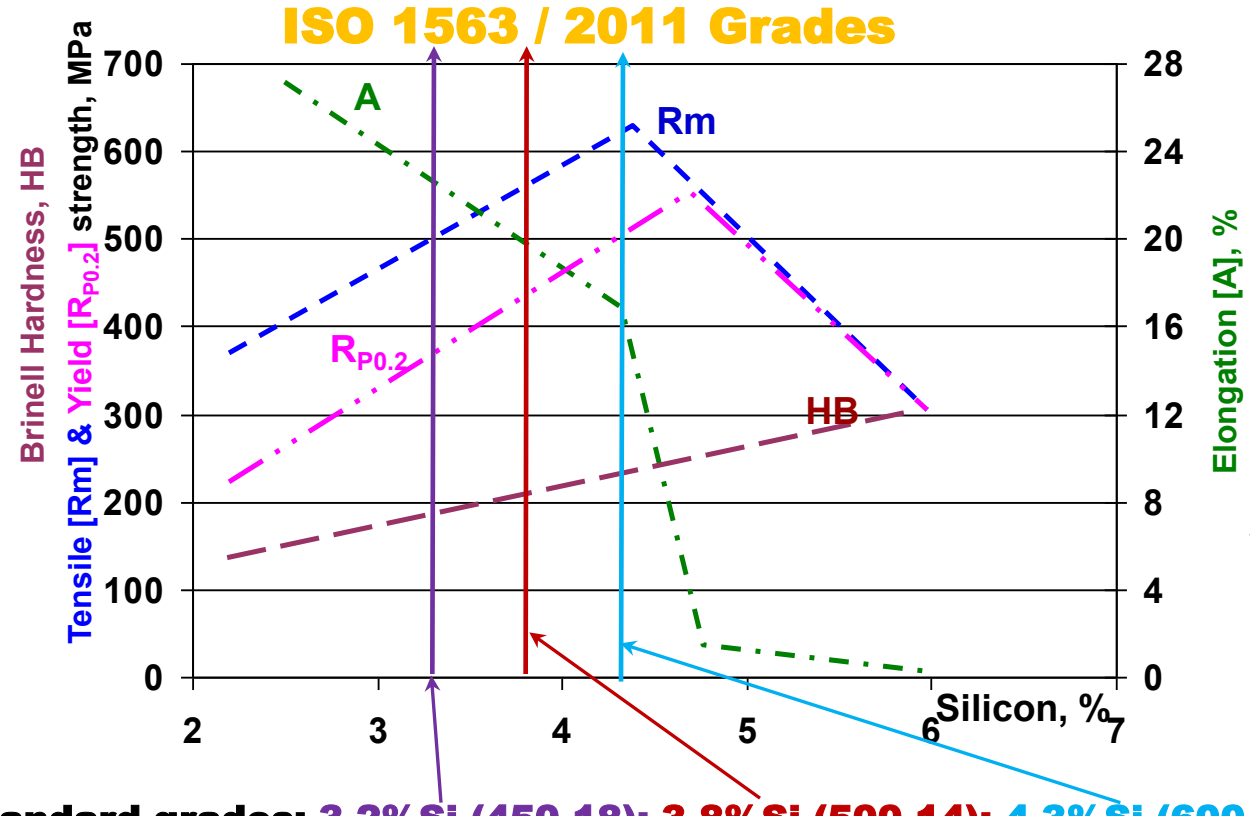


*[Stets, W., Loblich, H., Gassner, G., Schumacher, P., The 2013 Keith Millis Symp. on DI, Nashville, TN, pp. 283-292 (2013)]*

**Standard grades: 3.2%Si (450-18); 3.8%Si (500-14); 4.3%Si (600-10) - ISO 1563/2011**

## *Typical Si content:

- **To reach the maximum**: Tensile Strength [4.2 - 4.4%Si]; (+128 MPa) / %Si

  Yield Strength [4.6 - 4.8%Si]; (+ 118 MPa) / %Si

- Elongation [E] decreasing: (- 5% E / %Si) < 4.3%Si; (- 30% E) / %Si, 4.3 up to 4.8%Si

- Continue hardness [HB] increasing: (+ 45 HB) / %Si, for 2.5 – 6%Si [150 to 310 HB]

*** Tolerance of higher amounts of pearlite & carbide stabilizing elements**

- *Statistics:* 2.3 - 5.3%Si DI, 200 production heats, 20 years, 500-14 *versus* 600-10 grades
  - 500 -14 grade, less variation in elongation, than 600-10 grade;
  - 600 -10 grade, a little effect on ductility by tramp elements if below 0.3%
  - 500-14 grade tolerates up to 4%Si, 0.4%Mn and 0.04%P.

*Obs. Different limited values in different works*

- such as 0.6-1.0%Mn, 0.3-0.6%Cr, 0.26%V…….

*** Fully ausferritic structure, into a Si - solution strengthened matrix:**

- severe Si segregation reduces the stability of C-stabilized austenite
  - and leads into compromised machinability.

*** Chunky graphite sensitivity: Si - one of the influencing elements [Si, Ni, Ca, Ce]**

- necessity of special treatments to preserve spheroidal graphite compactness

# Si - Mo – alloyed Ductile Cast Irons

*** > 4.0%Si and > 0.2%Mo enhances the performance at elevated temperatures**

- **Si:** by stabilizing the ferritic matrix and forming a Si-rich surface layer which inhibits oxidation
- **Mo** additions (up to 2%), superior mechanical properties and resistance to oxidation

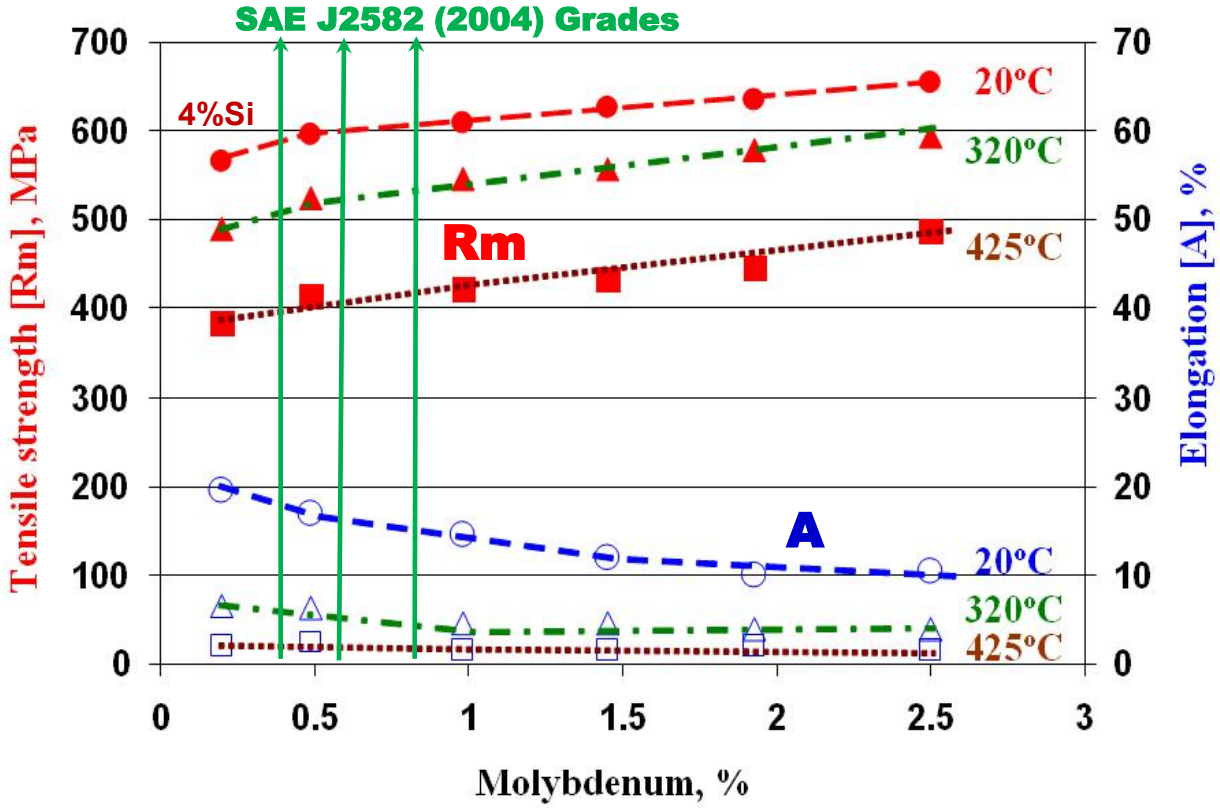


*[ASM-American Society of Materials Handbook, Vol. 1A: Cast Iron Science and Technology, Doru M. Stefanescu Vol. Editor, Sept. 2017, pp. 692-693]*

* Maximum working temperature increased from 700 - 750$^0$C up to 900 - 1000$^0$C

- by supplementary alloying, **with Al** and contribution of Ni, Co, Cr, V, Ti, Zr… **[SiMoAl-X DI]**
- specific effects of **Si** and **Al** (transformation temperature, the oxide layer thickness, formed phases)
  - **Si** and **Al** association: **to improve** the durability of the protective oxide layer *but with a*
    - **negative effect** on the spheroidal graphite morphology, increasing the iron embrittlement
- economics of compacted graphite **CGI –SiMoAl** application

* Information on carbide formation (physical, chemical, distribution characteristics)

- predominantly ferritic matrix, with a Mo carbide-rich phase at the eutectic cell boundaries
- as cast state, Mo forms metastable carbidic grain boundary precipitates with Fe, Si, C
  - these transform into stable MoC precipitates during sustained exposure to temperature
- there are finely dispersed Mo containing precipitates found in the matrix

* Specific corrosion and fatigue behavior in dry and humid air and diesel exhaust gas

* Crack growth mechanisms in different oxidation and corrosion media

# EXPERIMENTAL PROCEDURE

*Coreless induction furnace melting (10kg, 8000Hz)

*Tundish-Cover Mg-treatment [2.0wt.% addition, FeSiCaMgRE alloy]

*Ladle Inoculation [0.3wt.% Ca,Ce,S,O-FeSi alloy]

| Treatment Alloy [wt.%] | | Si | Ca | Al | TRE* | Mg | S** | O** | Fe |
|---|---|---|---|---|---|---|---|---|---|
| Role | Type | | | | | | | | |
| Nodulizer | FeSiCaMgRE | 43.03 | 1.87 | 1.35 | 1.10 | 10.35 | | | Bal |
| Inoculant | Ca,Ce,S,O-FeSi | 70 - 76 | 0.75-1.25 | 0.75-1.25 | 1.5-2.0 | | X | X | Bal |
| Si-alloying | FeSi | 70.9 | 0.038 | 0.06 | | | | | Bal |

*TRE-total rare earth elements; **addition of S and O bearing compounds totaling less than 1%

FeSiCaMgRE

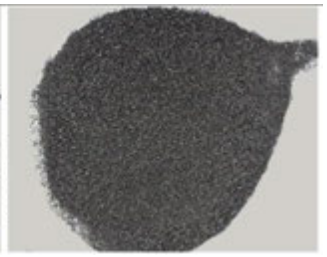

Ca,Ce,S,O-FeSi

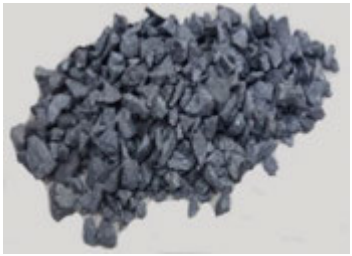

FeSi

* 20mm diameter bar (furan resin sand mold / micro - structure analysis)

* $W_1$, $W_2$ and $W_3$ wedge samples – ASTM A 367 [furan resin sand mold / macro & micro structure]

* Thermal (Cooling Curves) Analysis - ceramic cup [CM=0.75 cm Cooling Modulus (0.45 $^0$C/sec)]

# EXPERIMENTAL PROCEDURE

## *Thermal (Cooling Curves) Analysis - ceramic cup

[CM=0.75 cm (0.30 in) Cooling Modulus [0.45 $^0$C/sec]

$\Delta T_1$ = TEU – Tmst; $\Delta T_1 < 0$ – carbides; $\Delta T_1 > 0$ - graphite

WI MI GI

$\Delta T_2$ = TER – Tmst; $\Delta T_2 < 0$ – carbides; $\Delta T_2 > 0$ - graphite

$\Delta T_3$ = TES – Tmst; $\Delta T_3 < 0$ *or* $\Delta T_3 > 0$

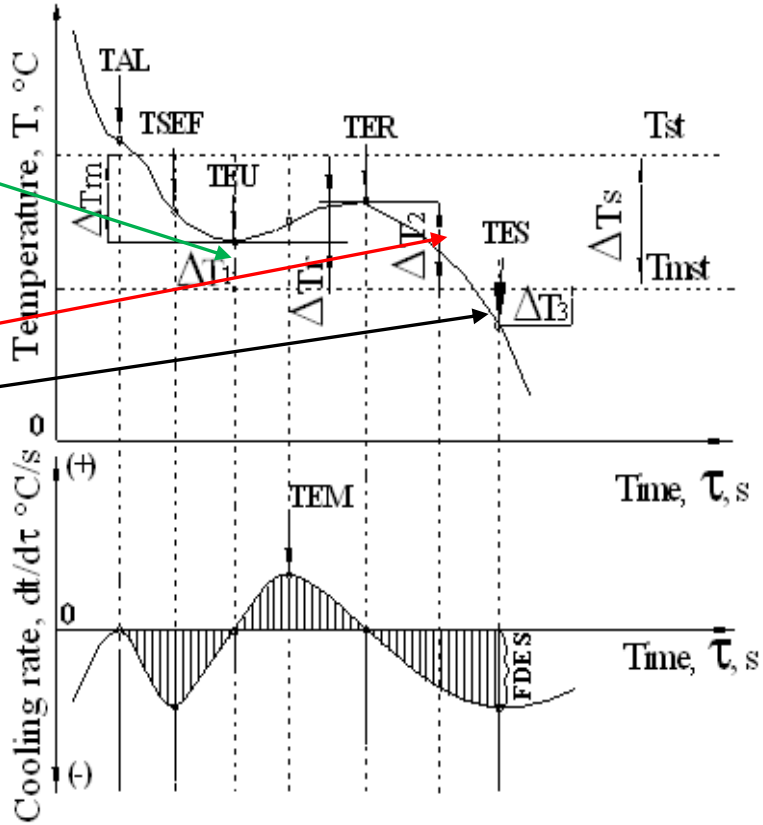


**Tmst** = 1142.6 ($^0$C) - 11.6 (%Si) - 0. 75 [% Sol. Mn] – 46.2 (%P) – 1.4 (%Cu) – 1.1 (%Ni) – 0.7 (%Co) – 1.8 (%Al) – 14.5 (%Mo) + 5.9 %Cr) – 6.0 (%Sn) –
5.1 (%Sb) – 2.8 (%W) + 0 (%Nb) + 3.3 (%V) – 26.0 (%B)

**TEG [Tst]** = 1149.1 ($^0$C) + 4.7 (%Si) - 4.0 [%Sol. Mn] – 44 (%P) + 2.7 (%Cu) + 1.0 (%Ni) + 1.8 (%Co) + 13.9 (%Al) - 17.7 (%Mo) – 10.5 (%Cr) – 9.3 (%Sn) – 5.2 (%Sb) – 6.1 (%W) – 3.7 (%Nb) – 14.8 (%V) – 80.3 (%B)

*[Kanno, T., Fukuda, Y., Morinaka, M., Nakae, H., J. JFS vol. 70, pp. 465–470 (1998)]*

# RESULTS

*The base chemical composition of tested cast irons and control factors*

| Si level | Alloying element | Heat | Chemical composition, wt. % | | | | | | Chemistry control factors | | |
|---|---|---|---|---|---|---|---|---|---|---|---|
| | | | C | Si | Mn | S | Mg | Mo | CE* (%) | K** | $P_x$*** |
| Normal | - | I | 3.20 | 2.55 | 0.38 | 0.011 | 0.032 | 0.012 | 4.03 | 0.16 | 1.34 |
| High | Si | II | 3.08 | 4.20 | 0.45 | 0.015 | 0.057 | 0.011 | 4.42 | 0.18 | - 2.77 |
| | Si – Mo | III | 2.76 | 4.10 | 0.34 | 0.014 | 0.036 | 1.66 | 4.06 | 0.14 | - 2.85 |

***CE = carbon equivalent** [CE = %C+0.3 (%Si + %P) – 0.03 %Mn + 0.4%S];**K= 4.4 (%Ti) + 2.0 (%As) + 2.4 (%Sn) + 5.0 (%Sb) + 290 (%Pb) + 370 (%Bi) + 1.6 (%Al); ***$P_x$ = 3.0 (%Mn) – 2.65 (%Si - 2.0) + 7.75 (%Cu) + 90 (%Sn) + 357 (%Pb) + 333(%Bi) + 20.1 (%As) + 9.60 (%Cr) + 71.7 (%Sb)

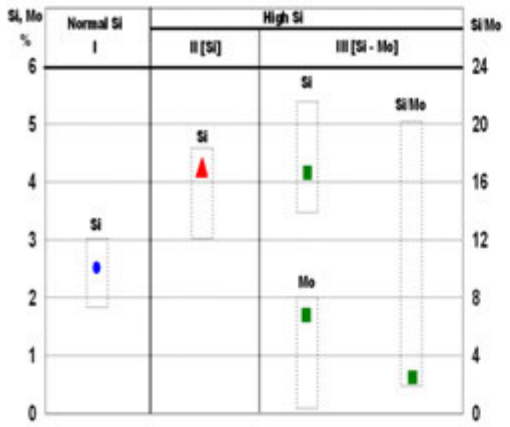


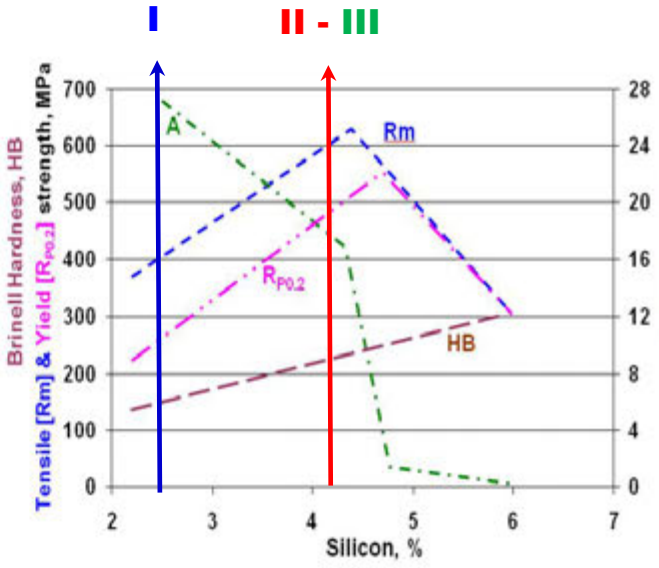


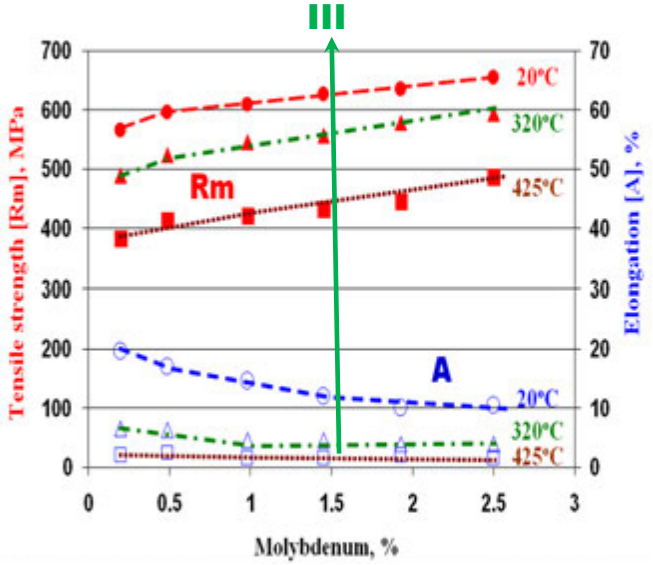

# Effects of alloy elements on eutectic temperature of stable [$t_{EG}$ / Tst] and metastable [$t_{EM}$ / Tmst] systems

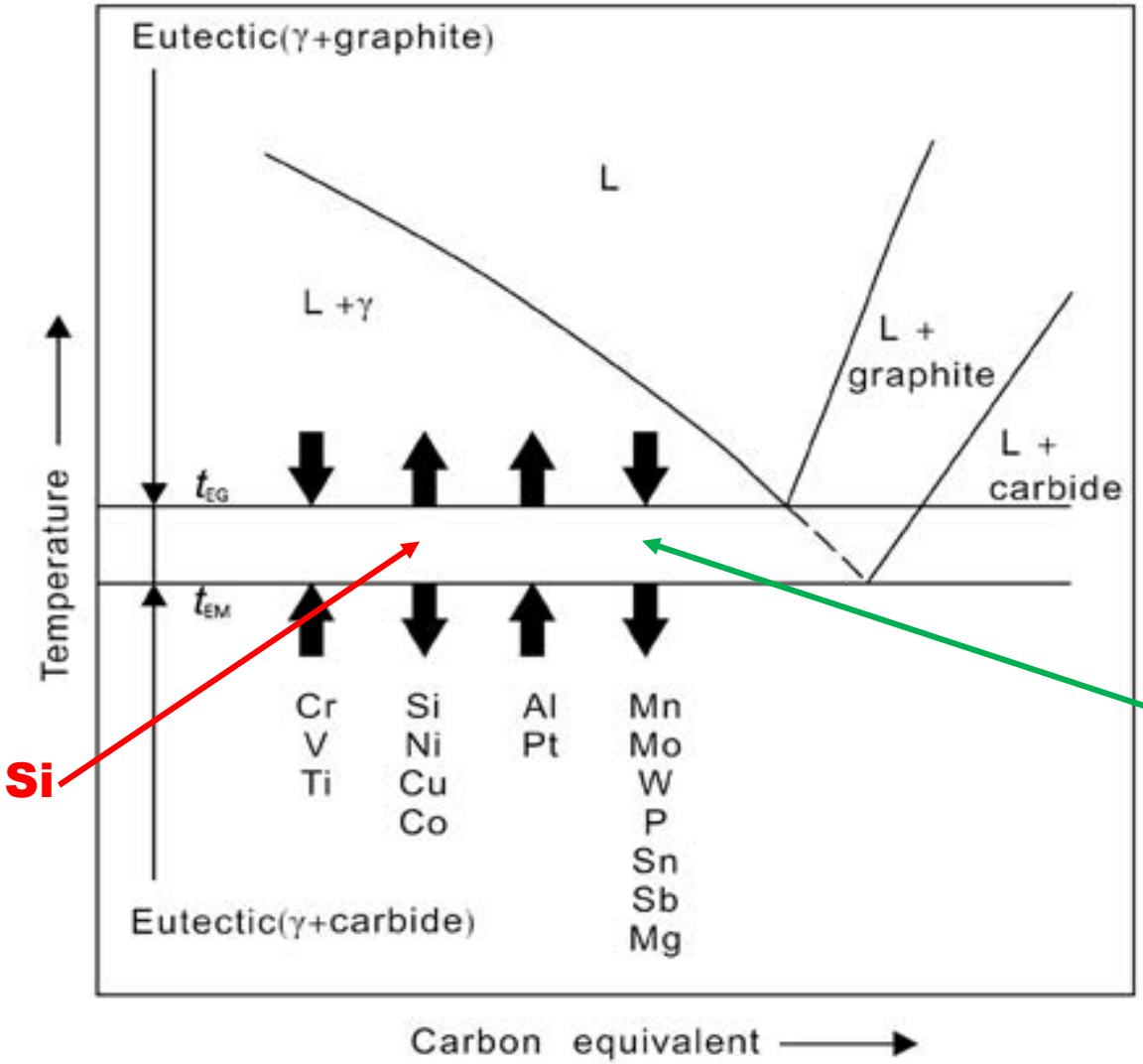


$\Delta Ts = Tst\ [t_{EG}] - Tmst\ [t_{EM}] =$

**5 ..... 50°C**

**[1.0 – 3.0%Si]**

*[Janovak J. F., Gundlach R. B., AFS Trans., 90, 847—863 (1982); Zhou Jiyang, China Foundry, 6 (1), 57-69 (2009)]*

# Undercooling degrees ($^0$C) of un-inoculated (UI) and inoculated (Inoc) ductile irons, **at the beginning ($\Delta T_1$)** and **at the end of eutectic reaction ($\Delta T_2$)** and **at the end of solidification ($\Delta T_3$)**

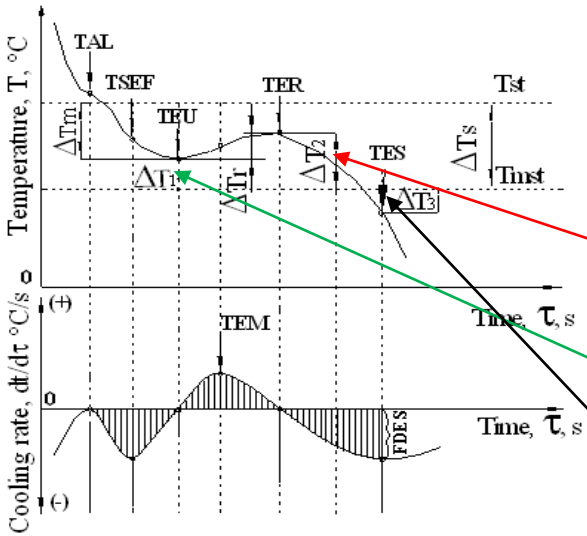


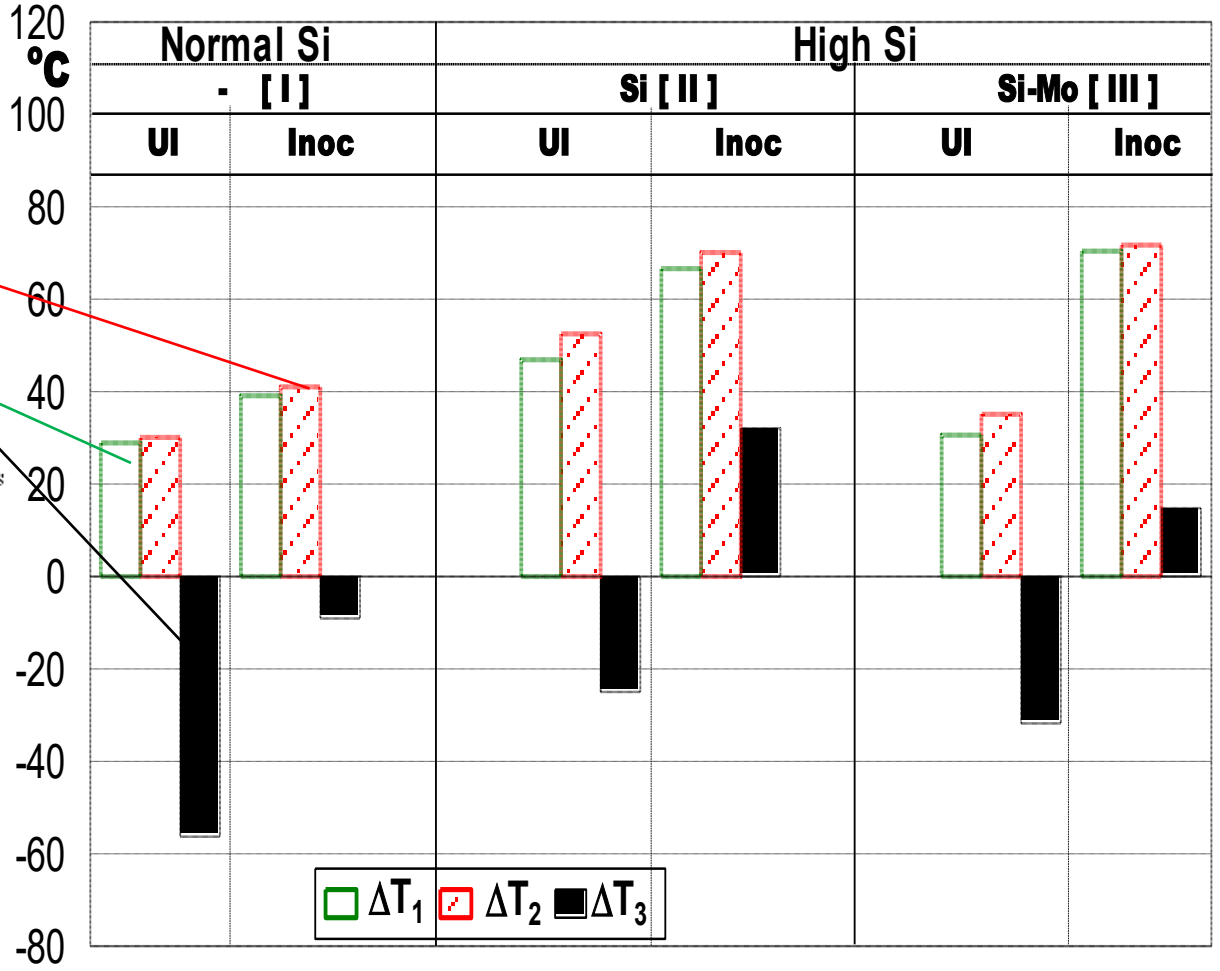

# Representative graphite forms [ISO 945] characterized by Roundness Shape Factor [RSF]

$RSF = 4.A_G / \pi.F^2_{max}$

**F - Feret**
min / mean / max

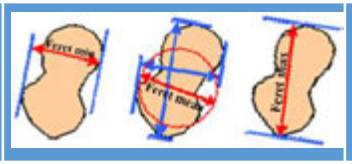

The minimum / mean / maximum distance of parallel tangents at opposing measured particle borders

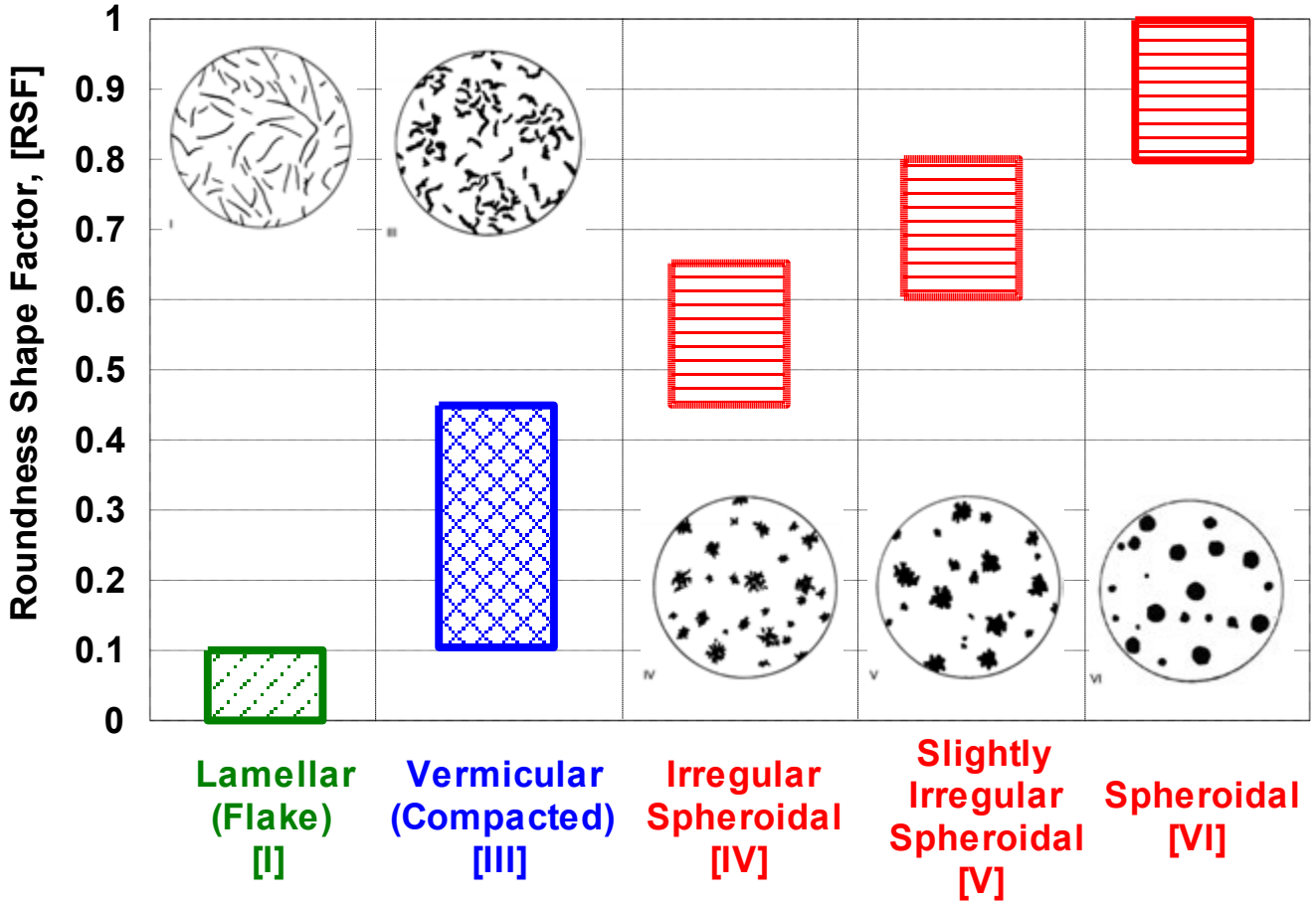

# GRAPHITE PHASE CHARACTERISTICS

**[20mm dia samples, furan resin sand mold, standard analysis – ISO 945]**

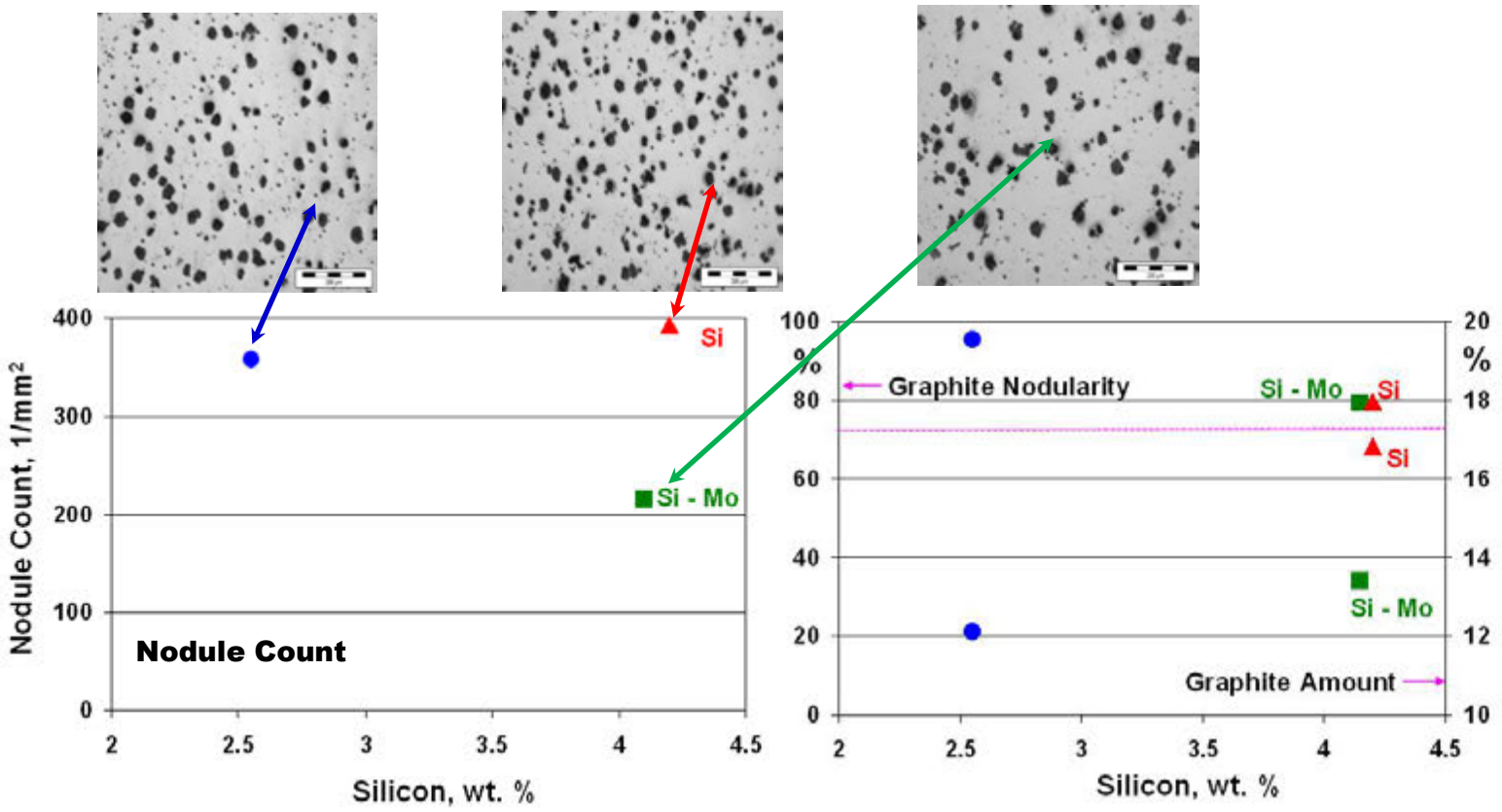


$$NG_{[ISO\ 945]} = 100\ [(\Sigma A_{particles\ (RSF \geq 0.80)} + 0.9\ \Sigma A_{particles\ (RSF = 0.60 - 0.80)})\ /\ \Sigma A_{all\ particles}]$$

[ISO 945] [VI] [V]

$$RSF = 4.A_G / \pi.F^2_{max}$$

# GRAPHITE PHASE CHARACTERISTICS

**NG** - Graphite Nodularity [%]; **AG** – Graphite Amount [%]; **NC** – Nodule Count [1/mm$^2$]

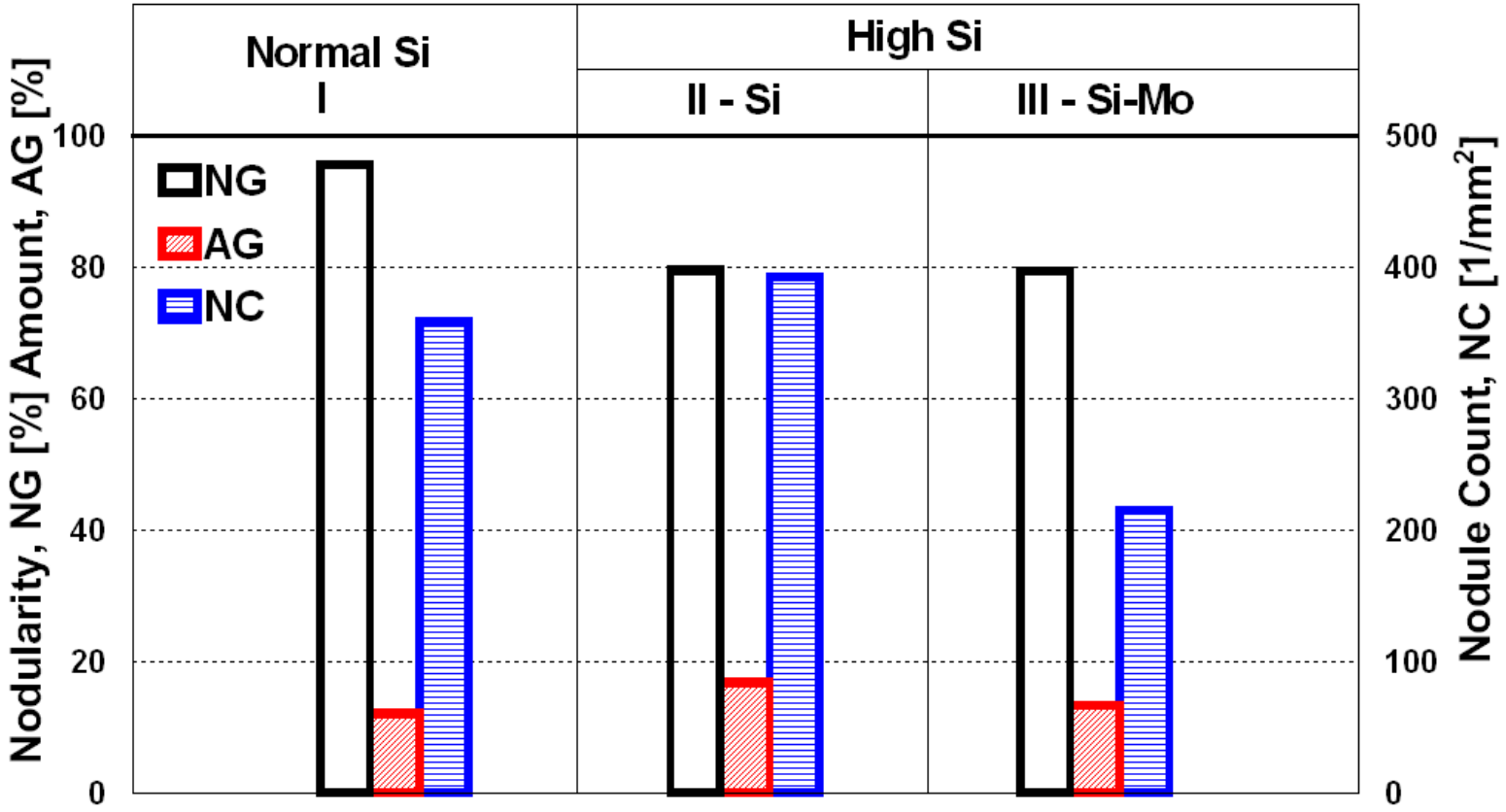

# METAL MATRIX CHARACTERISTICS

## [20mm dia samples, furan resin sand mold, standard analysis]

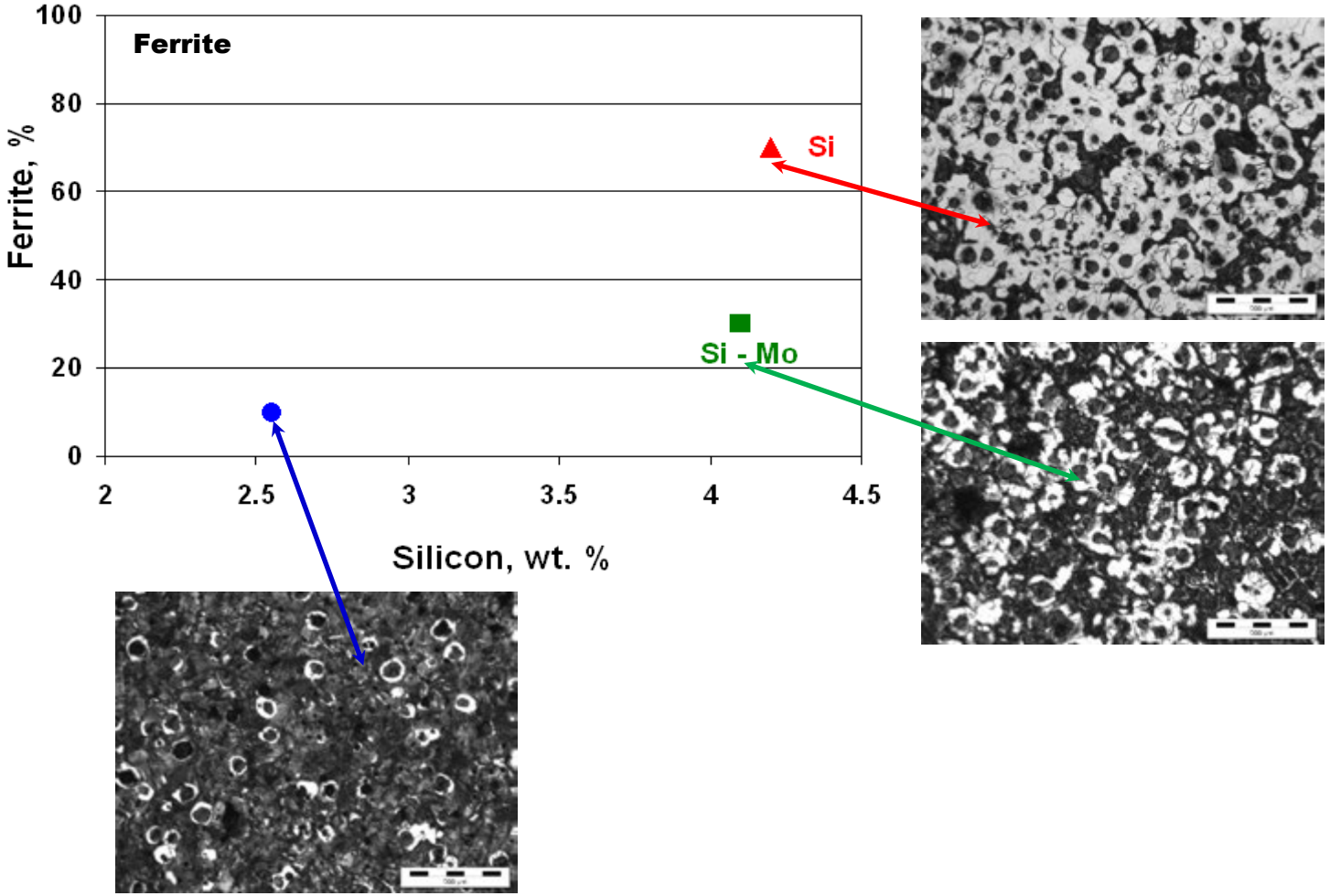

# CONCLUSIONS

**•Three groups of High - Si - Ferritic ductile irons [3 – 20%Si] are very attractive for their specific applications:**

**(a) Si-strengthened ferritic materials [3.2 – 4.3%Si],** typically for automotive ind.

- to replace conventional ferrite - pearlite grades [Si < 3%] [EN GJS 450-10, 500-7, 600-3]
- with drastically reduced hardness variation / increased cutting tool life,
- better mechanical properties [Rm = 450 - 650 MPa; $Rp_{0.2}$ = 350 – 500 MPa); A = 10 - 20%]

**(b) Si-Mo ferritic grades (3.5 – 5.5%Si, 0.2 – 2.0%Mo)**

- improved resistance to oxidation and corrosion at high temperatures [700 – 1000$^0$C]
- superior mechanical properties [Rm = 450 – 550MPa; $Rp_{0.2}$= 275 – 440MPa); A = 4 – 10%)]
- typically used in automotive industry, especially for exhaust manifolds parts

**(c) corrosion resistance cast irons, especially for more than 14%Si**

- **Thermal analysis identified important differences in the solidification pattern of 2.5%Si / 4%Si / 4%Si - 1.6%Mo DIs**

***Increasing Si content increased the eutectic interval ΔTs**

**-** *and* **decreased the undercooling during the eutectic reaction,**

**-** *and* **up to the end of solidification,**

**in both un-inoculated and inoculated ductile cast irons.**

***Mo additions at higher levels in high Si ductile iron**

**- decreased the ΔTs eutectic interval** *and*

**- led to increased undercooling over the entire solidification period,**

**in un-inoculated irons.**

***Inoculation of Si-Mo ductile irons**

**- compensates for the negative effect of Mo mainly during the eutectic reaction.**

- **As it was expected, the increasing of the Si content:**
  - **the increasing of the graphite amount,**
  - but high **Mo** addition in high **Si-ductile iron**
    - limited the graphitizing effect of **Si**,
      - with graphite amount remaining higher compared with **conventional Ductile Iron**
- **A similar evolution for graphite nodule count:**
  - **with the highest level for Si-alloying,**
  - while **Si-Mo** iron has lower nodule count compared with referred iron.
- **Graphite nodularity negative affected by Si content**
  - **it decreases,** but remains at the accepted level for general applications
  - **it would be insufficient** to be accepted as high performance ductile cast irons
- **High Si & Si-Mo DI: graphite nodularity, carefully considered**
  - **by including a minimum limit of the accepted Sphericity Shape Factor [SSF]**
    - *graphite real perimeter considered,*
    - *instead of maximum Feret, such as in Roundness Shape Factor [RSF, ISO 945]*
- **Increasing of the %Si led to a prevalent Ferritic matrix**
  - **Mo addition at the upper limit in Si-Mo affected the ferritic effect of Si,**
    - resulting an intermediary ferrite and pearlite mixture.

- **Inoculation appears to be important**

  **- not only in conventional ductile iron** *but also*

  **- in High – Si irons, with the greatest effect in Si-Mo ductile irons,**

  **in controlling solidification undercooling** *and* **structure**

- **Inoculation must be a high priority for these materials,**

  **- The high Si-ductile irons, > 4%Si, medium quality graphite phase,**

  **- with prevalent form V - ISO 945 graphite, inclusively in inoculated cast irons**

  **More experiments are necessary to find a specific inoculant,**

  **- with prevalent action on the graphite particles compactness degree,**

  **- especially to promote VI graphite form**

  **- in terms of inoculant power and inoculation technique.**

# ACKNOWLEDGMENTS

**This work was partially financed by a grant of the Romanian National Authority for Scientific Research and Innovation, CNCS/CCCDI - UEFISCDI, project number PN-III-P2-2.1-PED-2016-1793, within PNCDI III.**


THANK YOU

17th INTERNATIONAL FOUNDRYMEN CONFERENCE
Hi-tech casting solution and knowledge based engineering
Opatija, May 16th-18th, 2018
http://www.simet.hr/~foundry/

# THE GLOBAL CASTINGS INDUSTRY

**Andrew Turner***

The World Foundry Organization Ltd., United Kingdom

**Plenary lecture**
*Subject review*

**Abstract**

This paper will give an overview of the World Foundry Organization and how it works with member associations from around the world, covering the working groups and the World Foundry Congress and Technical Forum.
It will then give a comment on the global industry and in particular the production output from the worlds leading foundry nations, looking at the individual countries production and their challenges and opportunities.
Finally there will a look at the global challenges that face the industry in particular reference to macro economics and geopolitical instability.

***Keywords:*** *production, WFO, challenges*

*Corresponding author (e-mail address): *andrew@thewfo.com*

# THE GLOBAL CASTINGS INDUSTRY

**Eur Ing Andrew Turner FICME**
General Secretary– The WFO

# TO BE ADDRESSED IN PRESENTATION:

- Overview of the World Foundry Organization
- General Thoughts on the Global castings Industry
- Specific Statistics on the leading nations
- Thoughts for the future

# WORKING GROUPS


- Now represents 31 Countries
- Including 9 of the top 10 producing nations and all of the top 8 producing countries
- Financially supported by 10 of the worlds leading foundry supply businesses and foundries
- Producing high quality global statistics – The Foundry Nations Report
- Managed by top executives from industry and academia in 11 countries
- Working to a renewed 3 year strategic plan
- Significant social media penetration and profile

WFO

# WORKING GROUPS

- Training and Professional Development
- Energy Saving and the Environment
- Cast Composites
- Non Ferrous Metals
- Ferrous Metals
- Moulding Materials

# GLOBAL INDUSTRY

**We should remember that our industry:**

- Metalcasting is the oldest production process
- It fascinates those people who involved in it
- It is unique in its ability to recycle
- Exhibits a level of passion from those who are working in it
- Virtually every nation in the world has a casting industry
- Worldwide output of castings now exceeds 103M tons
- Metalcasting is key to the improvement in the standard of living
- Metalcasting is vital to the drive in both aerospace and automotive for fuel efficiency

# Global Industry

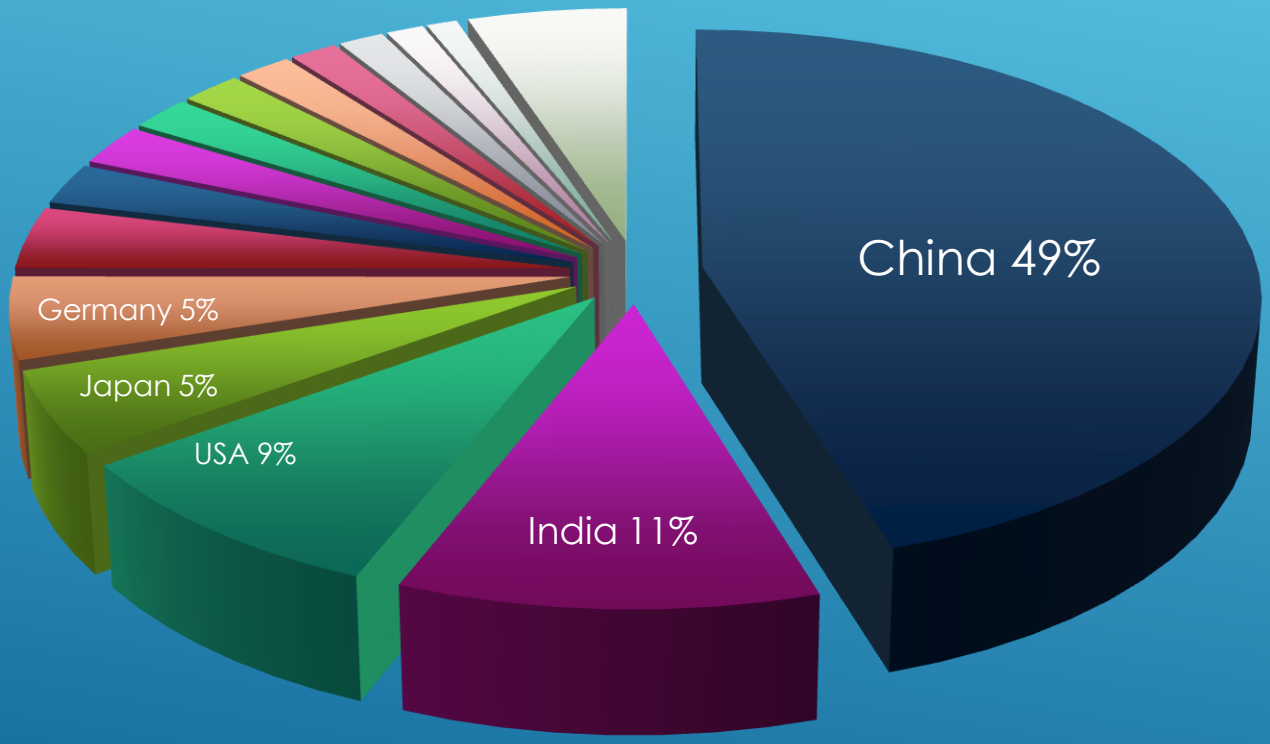


- China
- India
- USA
- Japan
- Germany
- Russia
- Korea
- Mexico
- Brazil
- Italy
- Turkey
- France
- Ukraine
- Spain
- Poland

Figures from Modern Castings Dec 2017.

WFO

# GLOBAL INDUSTRY (Million Tonnes)

1 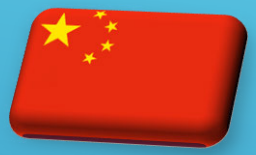

**China** 47.2

12th for Efficiency

2 

**India** 11.4

8th for Efficiency

3 

**USA** 9.4

2nd for Efficiency

4 

**Japan** 5.2

7th for Efficiency

5 

**Germany** 5.2

1st for Efficiency

6 

**Russia** 3.9

4th for Efficiency

7 

**Korea** 2.6

5th for Efficiency

8 

**Mexico** 2.6

6th for Efficiency

9 

**Brazil** 2.1

9th for Efficiency

10 

**Italia** 2.1

11th for Efficiency

11 

**Turkey** 1.9

10th for Efficiency

Figures from Modern castings Dec 2017.
Efficiency is tonnage / No of plants

WFO

# GLOBAL INDUSTRY

## Effects on regional production

- Affected by Build near demand
- Mercedes JLR and BMW Cars in China
- Bombardier Aircraft in China
- Hyundai Cars in India
- Construction vehicles in India

WFO

# GLOBAL INDUSTRY

## Influences on Export Markets

- Currency effects – Strong Euro
- Energy costs in Europe double that of USA

- Devaluation in BRICS Countries


- Growth of New Developing  Countries

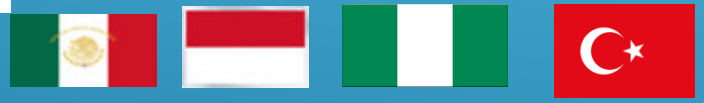

- Brexit Effects – Devaluation of the £

- European Uncertainties

# GLOBAL INDUSTRY

## Automotive Industry Impact

- More than half of castings produced are for the automotive industry
- This will increase with electrification
- Increasing customer demand for comfort, technology and performance
- Cars need bigger engines, bigger fuel tanks and stiffer chassis all adding weight
- Casting Industry meets weight reduction challenge with:

  * material substitution
  * thinner walls
  * converting fabrications to castings

# COUNTRY SPECIFICS

## China

- New Government initiatives for development and growth in the sector
- Heavily influenced by the 13th 5 year plan
- Industry will have access to support for the achievement of improvements in 9 key areas
- Foundries will be closed or merged due to program to push for high productivity & productivity as well as greater focus on quality.

# GLOBAL INDUSTRY

## India

- 11.4 Million Tonnes produced in 2016
- Of which 9.1 Million Tonnes Ferrous castings
- 2016 has 4500 foundries significantly down in number since 2010
- During same time 45% Growth in tonnage output
- New Governmental influences assisting industry. Re-use of energy subsidy

# GLOBAL INDUSTRY

## India

- Significant investment in infrastructure to boost demand
- Revenue worth $18 Billion
- Of which only 15% is export
- Expectations for doubling of output in next 5 years

# GLOBAL INDUSTRY

## Europe

- **Low GDP Growth**
- **High Unemployment ( Italy 13% & 43% of Youth )**
- **High Energy Costs**
- **EU Commission Influences**
- **Recognizes need for:**
  - **Industrial Renaissance**
  - **Solid Manufacturing base to provide growth and employment**
  - **The centrality of manufacturing & competitive integration**

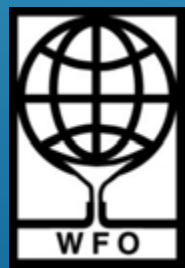

# COUNTRY SPECIFICS

## Europe

- 15.2 M T  current production similar to 2013
- 5000 Foundries value of €41.3 B
- Automotive Sector driver for non ferrous output
- Overall the number of foundries is falling as is employment.
- However in the Aluminum sector the trend is upwards - unit numbers stable and manpower growing.

# COUNTRY SPECIFICS

## Europe

- 85% of castings made in Europe used in Europe
- 15% direct export
- High growth for castings 2014 – 2018 from Automotive, General Engineering and Construction
- Difficult time for ferrous foundries
- Future growth driven by:

  * development of substitution
  * trend to electric vehicles
  * smart engineering
  * additive manufacturing

# COUNTRY SPECIFICS

## USA

- 9.4 M T produced by 1960 foundries €32 B
- Additional 2.6 M T Mexico and .65 M T Canada
- 2008 – 2010 falling output due to off shoring and high energy costs
- 2010 – 2016 recovering output but still below the 2008 figure
- Currently optimistic with high growth forecasts due to:
    * low energy costs
    * high productivity
    * reduced shipping costs
    * trend toward re-shoring

# THOUGHT FOR THE FUTURE

- in 2001 the German car industry made 50% of its cars in Germany and 50% in rest of the world
- By 2017 that was 30% made Germany 70% ROW
- Electrification of cars is a positive not a negative, higher volumes of cars with more aluminium castings
- In Europe Casting production saw little change between 2004 and 2016 in China they had 100% growth and in India 140% growth to 11.4 M te
- Casting is still the most important process for manufacturing net shape products
- We still don't really understand the physics / chemistry of the casting process. Great opportunities still available
- Huge potential for improvement in all aspects of foundry production
- Still areas for research available into Die and Tool life, simulation of mechanical properties


# THOUGHT FOR THE FUTURE

- The industry needs Track, watch, and respond to industry trends. Success in the past is no guarantee
- China has significant governmental control over foundry development
- India developing regional clusters for services, which is highly efficient Training, Testing, Simulation, re-cycling
- Global output predicted to be 107 M T in 2018 a small but real growth
- The Foundry Industry in general is more efficient than many national economies


WFO

# FORWARD THINKING SPONSORS



Also Supported by Foseco, Imerys, ASK Chemicals and ABP Induction

WFO

# THE GLOBAL CASTINGS INDUSTRY

## Thanks for your attention

**Eur Ing Andrew Turner FICME**
General Secretary – The WFO

17th INTERNATIONAL FOUNDRYMEN CONFERENCE
Hi-tech casting solution and knowledge based engineering
Opatija, May 16th-18th, 2018
http://www.simet.hr/~foundry/

# OPTIAl-AN INDUSTRIAL GENERIC TOLL FOR DATA-DRIVEN MODELLING OF PRODUCTION CHAIN AND PROPERTIES OF THE END-PRODUCTS APPLICATION IN WROUGHT ALUMINIUM ALLOYS DEVELOPMENT AND PRODUCTION OF SEMIS

**Varužan Kevorkijan[1]*, Peter Cvahte[1], Sara Hmelak[2], Vukašin Dragojević[1], Borislav Hostej[1], Irena Lesjak[1], Branko Hmelak[2], Darja Volšak[1]**

[1] Impol Aluminium Industry, Slovenska Bistrica, Slovenia
[2] Alcad d.o.o., IT Company, Slovenska Bistrica, Slovenia

**Invited lecture**
*Preliminary note*

**Abstract**

Prior to the successful industrialization of the new recycling-friendly wrought aluminium alloys it will be necessary to develop and apply advanced tools and techniques for their virtual modelling.
An industrial tool developed within the Impol Aluminium Group for such modelling is OPTIAl. It is the cognitive computing algorithm for (i) **extracting structured data** (process parameters, concentrations of alloying elements, and mechanical properties), (ii) **finding the correlations** between the individual processing paths and the end-product properties, and (iii) **performing the predictions** on the composition of new alloys and the processing parameters for matching the required mechanical properties.
The algorithm was validated in an industrial environment by ***predicting the properties*** of more than 250 production lots of the alloy AA 6110 processed by the different technological paths, and by ***predicting the processing paths*** for the production of semis with required mechanical properties. In both cases the matching was better than 90%.
In the case of the non-standard compositions derived from the alloy AA 6110, it was found that either the processing paths or the mechanical properties can be predicted with a typical accuracy of 60 to 80%, which is a promising starting point for further optimizations and development of new alloys.

***Keywords***: *data-driven modelling, OPTIAl, correlations, prediction of properties, prediction of processing paths*

*Corresponding author (e-mail address): varuzan.kevorkijan@impol.si

## INTRODUCTION

The so-called recycling-friendly wrought aluminium alloys are generally perceived as ***new alloys*** with broader concentration intervals for some of the ***critical*** alloying elements (e.g., Fe, Si) and impurities, but still able to provide the customer-required combination of properties. The recycling concept is based on the expectation that the required quality of these alloys will be assured by modifying the rest of the processing path (alloying elements and processing parameters).

In contrast to the existing standard wrought aluminium alloys, the compositions of which correspond to the purity level of the primary aluminium, the recycling-friendly alloys are designed with a consideration of the common purity of the ***recycled*** metal after refining.
However, prior to the successful industrialization of the new recycling-friendly wrought aluminium alloys, it will be necessary to develop and apply advanced tools and techniques for their virtual modelling.

The missing **key knowledge**, necessary for the modelling of such alloys and the processes of their production, are ***correlations*** (not necessarily functional) established between the various processing paths (formulated by the chemical composition and the processing parameters) and the properties of the end-product, and vice-versa.
Such correlations could become very useful in the further optimization of the existing, standard wrought aluminium alloys, often based on the existing empirical or semi-empirical knowledge.

Therefore, the purpose of this presentation is to show the progress that Impol Aluminium Industry has made in this area over the past few years.

## ALGORITHM FOR MODELLING THE ALLOY COMPOSITION, THE PRODUCTION PROCESS AND THE PROPERTIES OF THE END-PRODUCT

In principle, the modelling of wrought aluminium alloys with the desired combination of properties is based on finding the surjective and inverse correlation T (C, PP) $\leftrightarrow$ P between the properties, P, of the final product and the different technological paths T (C, PP) capable of providing it (and vice-versa), as illustrated in Fig 1. Here, C represents the chemical composition of the alloy and PP is the processing parameters. The algorithm presented here is based on the functional equivalency of two different technological paths, T1 and T2, able to provide the same combination of properties, written as P(T1) = P(T2), where P(T1) and P(T2) represent the properties obtained using the various paths T1 and T2 in the vector space. The selection of the best among the functionally equivalent technological paths, T, was performed by applying the minimum-cost criterion.

The cognitive system applied in this work includes the tools for (i) extracting structured data (process parameters, concentrations of alloying elements, and mechanical properties), (ii) finding the correlations between the individual processing paths and the end-product properties, and finally, (iii) a learning process for the algorithm so it can perform the predictions on the composition of new alloys and the processing parameters for matching the required mechanical properties. The additional principles of the modelling of aluminium alloys can be found in Refs. [1-5].

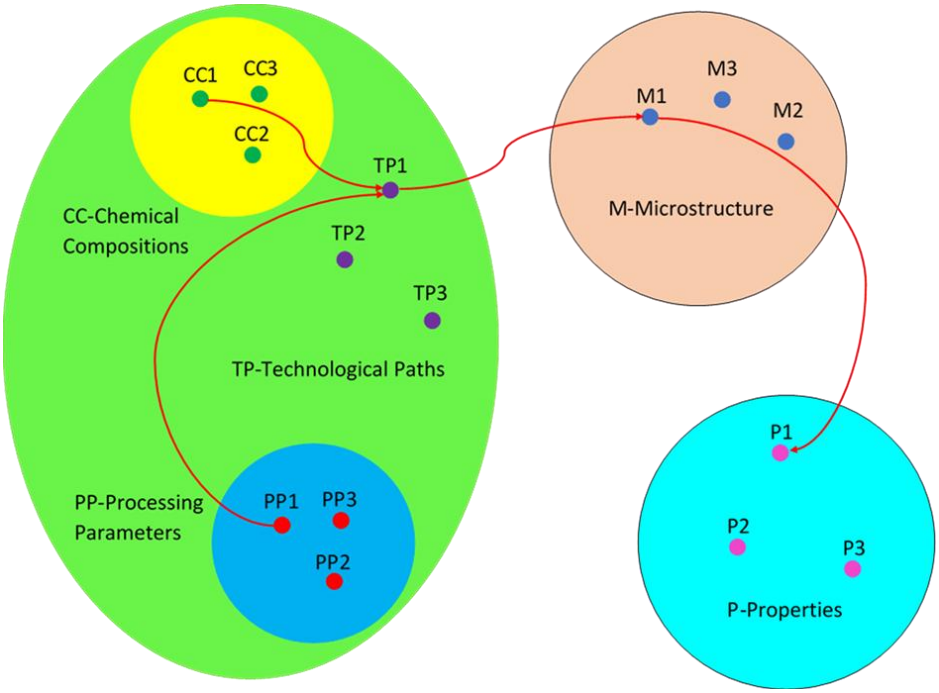


Figure 1. Schematic presentation of the relations existing between the technological path (TP), the microstructure and the properties of the end-product

The purpose of the algorithm developed in this work is to search for correlations between the processing paths and the properties of the end-products. The processing paths are determined by the concentrations of the alloying elements (all the elements that appeared in the alloy) and the processing parameters (all the parameters that influence the production process), while the properties are defined as a group of selected properties with individual values.

The big-data system used in this work consisted of various wrought aluminium alloys, the production and processing paths for end-products and the corresponding set of (combination of) properties achieved in the end-products (and/or at various intermediate stages).

Mathematically, the processing paths are expressed by the appropriate vectors of the processing path in which the vector components appear as the concentration of chemical elements and the various processing parameters.
Analogously, the set of properties achieved in the end-products are expressed with the corresponding vectors of the properties, consisting of the individual properties of the particular vector components.

## THE ORGANIZATION OF THE BIG-DATA SYSTEM

Let us propose that the vector $\overrightarrow{pp_i}$ represents the processing path *i*. Because each processing path is determined by the concentrations of *l* alloying elements and *m* processing parameters, the corresponding vector $\overrightarrow{pp_i}$ should be with m= l+f components. Denoting the individual concentrations of the alloying elements with $c_{ij}$ and the individual processing parameters with $pp_{ij}$, we can write:

$$\overrightarrow{pp_i} = \left(c_{i1}, c_{i2}, c_{i3}, \ldots . c_{il}, pp_{il+1,} pp_{il+2}, pp_{il+3} \ldots . pp_{im}\right) \quad (1)$$

Following the same methodology, the vector $\vec{P}_i$ with *k* components will be used to describe the group of *k* selected properties:

$$\vec{P}_i = (P_{i1}, P_{i2}, P_{i3}, \ldots . P_{ik}) \quad (2)$$

In this way the big data can be written using the following two matrices: $\left[pp_{ij}\right]_{nxm}$ and $\left[P_{ij}\right]_{nxk}$. Here, the matrix $\left[pp_{ij}\right]_{nxm}$ represents n different processing paths with m components, while the matrix $\left[P_{ij}\right]_{nxk}$ represents n groups of k identically selected properties:

$$\begin{bmatrix} c_{11}, c_{12}, c_{13} & \cdots & c_{1l}, pp_{1l+1}, pp_{1l+2}, pp_{1l+3} \ldots . pp_{1m} \\ \vdots & \ddots & \vdots \\ c_{n1}, c_{n2}, c_{n3} & \cdots & c_{nl}, pp_{nl+1}, pp_{nl+2}, pp_{nl+3}, \ldots , pp_{nm} \end{bmatrix} \rightleftarrows \begin{bmatrix} P_{11}, P_{12}, P_{13} & \cdots & P_{1k} \\ \vdots & \ddots & \vdots \\ P_{n1}, P_{n2}, P_{n3} & \cdots & P_{nk} \end{bmatrix} \quad (3)$$

Generally, we can state that the vectors $\overrightarrow{pp_i}$, $i \in (1..n)$ determine the coordinates of n different points (processing paths) in an m-dimensional vector space and, in analogy with this, that the vectors $\vec{P}_i$, $i \in (1..n)$ determine the coordinates of n different points (groups of selected properties) in a k-dimensional vector space.

## THE DIFFICULTIES OF MODELLING PROCESSING PATHS AND PROPERTIES

The modelling of processing paths and the end-product properties based on data taken from regular production often faces the following two difficulties: (i) the collinearity of the group

of data (e.g., the collinearity of the multicomponent vectors describing the processing paths or sets of properties) and (ii) the surjective behaviour (character) and/or even surjective nature of the multi-component data structures (e.g., vectors) and the data-driven predictions based on them.

Due to the fact that the processing-path vectors that describe the industrial processes usually consist of a few tens or hundreds of components, modelling of the end-product properties with such multi-component processing path vectors is always difficult and demanding.

The same, or even more demanding, is the reverse predicting of the processing paths with a set of end-product properties, a vector with typically no more than 3–4 components.

Because of the large number of vector components, the computing procedure in both cases required very large processor power and a long time. In spite of the high computing costs, the accuracy of such predictions is usually poor.

However, the multi-component data (e.g., vectors) taken from the regular production are, due to the high stability of industrial processes, usually collinear. Since the data system used for modelling is actually the group of collinear (i.e., not independent) vectors, this could reduce the potential of the prediction, but, on the other hand, it could also be an opportunity for significant mathematical simplifications, as will be discussed in the next sections.

The same is the case with the surjective nature of some of the multi-component data-driven predictions. Because of the surjective transformations, the equity of two vectors (e.g., two processing paths or sets of properties), which is a mathematically more demanding criterion, becomes less important for the right prediction than their ***equivalency*** (i.e., the ability of the different processing paths to result in the required set of properties). For this reason, further mathematical simplifications are possible, as will also be discussed.

Regarding the quality of the predictions, it always depends on the mutual strength of the relation established between the processing paths and the sets of properties, and vice-versa. Therefore, the ability to define such relations inside the considered data system is of key importance for high-quality predictions. The way of finding the relationship between the processing paths and the set of properties of the end-products (and vice-versa) that is strong enough for the proper prediction, which is the basic part of the predicting algorithm, will be discussed in detail, with a particular emphasis paid to simplifications and the cost-effectiveness of computing.

## THE DESCRIPTOR: AN EFFECTIVE WAY OF DESCRIBING THE INDIVIDUAL MULTICOMPONENT VECTORS INSIDE THE GROUP OF VECTORS

A possible solution for the above-listed difficulties might be in quantifying (and describing) such complex processing paths with the much simpler but properly selected mathematical structures consisting of just 1–2 variables. Such structures, called **descriptors**, are used to replace the complex processing paths, expressed as multicomponent vectors, with just one or two variables.

In our case the variable used for defining the processing path is ***the position*** of the selected relative to the average processing path. With reference with this, it is important to note that for the group of collinear vectors, the simplest way to position one of them to the average vector is by calculating the difference, $D_i$ or $d_i$ between them. Because all the vectors in the vector group are collinear, the vector difference can be expressed as the scalar distance. This is **the descriptor of the first order** and can be written as $\boldsymbol{DESC}(D_i)$ for the processing path *i*, and $\boldsymbol{DESC}(d_i)$ for the set of properties *i*. For both kinds of descriptors of the first order, we can write:

$$\boldsymbol{DESC}(D_i) = D_i \tag{4}$$

$$\boldsymbol{DESC}(d_i) = d_i \tag{5}$$

However, for the group of non-collinear vectors it is necessary to add the ***orientation***. The orientation is defined by the angle $\theta_i$ or $\varphi_i$ between the selected and the average vector inside that group of vectors. Therefore, an appropriate descriptor for that case will have two components: the distance and the angle. This is **the descriptor of the second order**, written as $\boldsymbol{DESC}(D_i, \theta_i)$ for the processing path *i*, and as $\boldsymbol{DESC}(d_i, \varphi_i)$, for the corresponding set of properties. Note also that in this case both descriptor components are scalars, which additionally simplifies the computing process.

Generally, the descriptors of the second order are vectors having two components: the **distance** and the **angle** between the selected and the average vector of a group of vectors.

The way of calculating $D_i, \theta_i, d_i$ and $\varphi_i$ is explained in detail in the section The Big-Data Analytics.

It is important to note that the main purpose for introducing the descriptors in predictive algorithm considered in this work is their simple form, able to replace (under well-defined conditions) the multicomponent vectors of the processing path and the set of properties. For example, the descriptor of the first order is scalar, while the descriptor of the second order is a vector having only two components. In addition, the predictions made by our algorithm are based on determining the most probable events. Therefore, the most effective way of predicting is to consider the descriptors as ***events*** that appear in such a predictive algorithm.

## THE EQUIVALENCET OF TWO PROCESSING PATHS AND TWO SETS OF PROPERTIES

Mathematically, two processing paths, expressed as vectors with *m* components, and two sets of properties, written as vectors with *k* components are ***equal or identical*** if the vector differences between both pairs of corresponding vectors are equal to zero.

However, from the point of view of practical modelling, it is more important to introduce the non-exact mathematical criterion under which two processing paths or two sets of properties are ***equivalent*** and not necessarily identical.

Generally, two processing paths are equivalent if both result in the set of properties acceptable to the customer.

In the algorithms considered for the industrial modelling of processes and alloys, the equivalency of two processing paths and sets of properties (i.e., two different vectors) is measured by comparing their ***positions*** with respect to the average processing path and the average set of properties. The position of the individual vector from the big data in reference to the average vector is defined just by their distance (if all vectors in the big data are collinear) or by the distance and the angle if the vectors in the big data have a different orientation.
Therefore, based on all the above mentioned, two processing paths or two sets of properties are equivalent when they have the same descriptors.

## THE METHODOLOGY FOR ESTABLISHING THE DATA-DRIVEN RELATIONS

As already mentioned, the first step in data-analytics is determining the average processing path and the average set of properties.
The main assumption is that the average processing path will result in the average set of properties and vice-versa. This transformation is considered as a certain event with the probability P=1.
An additional assumption is that every processing path from the big-data, arbitrarily positioned to the average processing path, will result in a set of properties, also properly positioned with respect to the average set of properties. In other words, for every processing path, either the real one – taken from the big-data or modelled – based on the existing paths, it will be possible to find the most probable set of properties – either among all those listed in the big data or those artificially generated (computed).

## THE BIG-DATA ANALYTICS IN THE GROUP OF COLLINEAR VECTORS

As already discussed, the main characteristic of the big data created using real data from production (i.e., obtained by mining in the industrial environment) is in the fact that the differences between the real processing paths will be minimal. In other words, due to the highly repeatable production (Industry 4.0), most of the processing paths will be almost identical, with differences caused only by the fluctuations allowed in production procedures. Consequently, the selected properties of the end-products will also be similar.
Mathematically, the vector differences, $\Delta\vec{D}$, between a group of vectors describing the processing paths, and a group of vectors describing the properties of the end-products, $\Delta\vec{d}$, will be small and with similar intensity and directions compared to the zero level (the starting point) of each group of vectors in the big data. This situation is illustrated in Fig. 2.

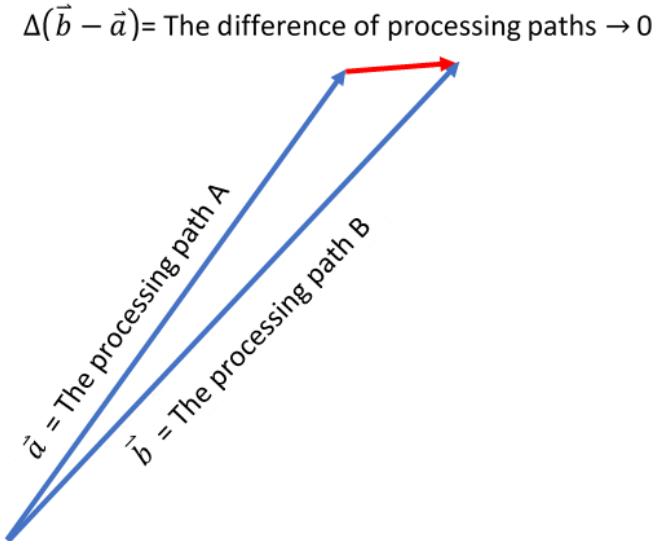


Figure 2. The difference between the vectors of the processing paths

If the difference between the vectors of the processing path is sufficiently low then these vectors are almost collinear and with almost the same intensity. The same is true for the vectors of the set of properties. This approximation enables a significant mathematical simplification of the computing procedure for both functional and cognitive predicting.
The zero level for the group of vectors of the processing paths is an average of these vectors and the same is applied for the properties of the group of vectors.
For this reason, and to simplify the calculation, it is helpful to introduce the vector of the average processing path, $\overrightarrow{\overline{pp}}$ and the vector of the average values of the selected (combination of) properties, $\vec{\bar{P}}$. The basic idea is to replace the demanding computing procedure for finding the functional relation between the corresponding vectors, $\overrightarrow{pp_i}$ and $\vec{P}_i$, with a significantly easier procedure, based on calculating the deviation of the processing path and the properties from the corresponding average values. The main advantage of such an approach is in the fact that the measure of the deviation is the distance from the average, which is a scalar and appears as a single variable, in contrast to the vectors (especially the vector of the processing path) defined with so many components.
Avoiding detailed mathematical explanations, we can write that the vector of the average processing path and the vector of the average combination of properties are:

$$\overrightarrow{\overline{pp}} = \left(\bar{c}_1, \bar{c}_2, \bar{c}_3, \ldots\ldots \bar{c}_l, \overline{pp}_{l+1}, \overline{pp}_{l+2}, \overline{pp}_{l+3} \ldots\ldots \overline{pp}_m\right) \quad (6)$$

$$\vec{\bar{P}} = (\bar{P}_1, \bar{P}_2, \bar{P}_3, \ldots\ldots \bar{P}_k) \quad (7)$$

where the average of each vector component (e.g., $\bar{c}_1$) represents the arithmetic average of the *n* corresponding values from the big data (e.g., $\bar{c}_1 = \frac{1}{n}\sum_{i=1}^{n} c_{i1}$).
To follow the above-explained methodology, it is necessary to calculate the corresponding average distances, $\bar{D}$, and $\bar{d}$, between the previously introduced average vectors $\overrightarrow{\overline{pp}}$ and $\vec{\bar{P}}$

and the so-called zero or ort vectors $\overline{\overline{pp}}(0, 0, 0,\ldots 0)$ and $\bar{\bar{P}}(0,0,0,\ldots,0)$. These distances or deviations are defined as the lengths of the corresponding average vectors:

$$\bar{D} = \left|\overline{\overline{pp}}\right| = \sqrt{\overline{\overline{pp}} \cdot \overline{\overline{pp}}} \tag{8}$$

$$\bar{d} = \left|\bar{\bar{P}}\right| = \sqrt{\bar{\bar{P}} \cdot \bar{\bar{P}}} \tag{9}$$

Finally, the distance or the deviation, $D_i$, between the vector representing the *i* processing path, $\overrightarrow{pp}_i$, and the vector representing the average processing path $\overline{\overline{pp}}$ , is expressed as:

$$D_i = \left|\overrightarrow{pp}_i - \overline{\overline{pp}}\right| = \sqrt{\left|\overrightarrow{pp}_i - \overline{\overline{pp}}\right| \cdot \left|\overrightarrow{pp}_i - \overline{\overline{pp}}\right|} \tag{10}$$

Eq. (11) defines the corresponding distance between the vector of the *i* group of properties, $\vec{P}_i$, and the vector of an average value of properties, $\bar{\bar{P}}$:

$$d_i = \left|\vec{P}_i - \bar{\bar{P}}\right| = \sqrt{\left|\vec{P}_i - \bar{\bar{P}}\right| \cdot \left|\vec{P}_i - \bar{\bar{P}}\right|} \tag{11}$$

The so-called critical distances $D^*$ and $d^*$, which also appear in the model and determine the transition from the functional to the surjective transformations, are defined empirically as:

$$D^* =\leq -10 - 20\%\ of\ \bar{D} \tag{12}$$

$$d^* =\leq 5 - 10\%\ of\ \bar{d} \tag{13}$$

**THE BIG-DATA ANALYTICS IN THE GROUP OF NON-COLINEAR VECTORS**

As differences between the vectors inside the same group of vectors in the big data become significant, they must be expressed by the non-collinear vectors. In that case, for an appropriate description of the individual multicomponent vectors inside the group of non-collinear vectors it is necessary to use the descriptor of the second order. Such a descriptor consists of the following two components: the distance of the individual vector to the average vector and the angle between them.

Also, in that case, the distance or the deviation, $D_i$, between the vector representing the *i* processing path, $\overrightarrow{pp}_i$, and the vector representing the average processing path $\overline{\overline{pp}}$, is expressed by Eqs. (9) and (10).

The angle $\theta_i$ between vectors $\overrightarrow{pp}_i$ and $\overline{\overline{pp}}$ is defined by Eq. (13):

$$cos\theta_i = \overrightarrow{pp}_i \cdot \overline{\overline{pp}} \Big/ \left|\overrightarrow{pp}_i\right| \cdot \left|\overline{\overline{pp}}\right| \tag{14}$$

In a same way, the angle $\varphi_i$ between vectors $\vec{P}_i$ and $\vec{\bar{P}}$ is expressed as:

$$cos\varphi_i = \overrightarrow{PP_i} \cdot \overrightarrow{\overline{PP}} \Big/ \left|\overrightarrow{PP_i}\right| \cdot \left|\overrightarrow{\overline{PP}}\right| \tag{15}$$

## THE SURJECTIVE BEHAVIOUR OF REAL AND DATA-DRIVEN MODELLED PROCESSES

First, it is very important to distinguish between the surjective behaviour of the real (e.g., metallurgical) processes, caused by their physical and chemical nature, and the surjective behaviour observed in the modelled (e.g., virtual) processes, in which case the surjection is caused by the predictions themselves.

## THE SURJECTIVE NATURE OF PREDICTIONS

Mathematically, non-functional relation appears when a single descriptor transforms into two or more predictors. In the case of a transformation of processing paths into a desired set of properties of the end-product, or vice-versa, surjection happens when, for a single descriptor of the processing path, there are several predictors of the set of properties, or vice-versa. In that case, the ***predicted*** most probable set of properties is not only one, but two or more sets can be predicted with similar or almost the same probability.
In other words, following the same processing path considered in the virtual model might result in end-products with different sets of properties (i.e., “the same original is transformed into two or more different pictures”).
It is important to note that such surjective behaviour also appears in the big data that is almost collinear but prevails in systems with non-collinear vectors.
The tendency of surjective behaviour for a group of data is to increase with increasing distance of the selected data from the average value and is also influenced by the nature of the data. For example, the transformation of the properties into the processing paths is more surjective than the opposite – the transformation of the processing path to the corresponding set of properties.

## THE SURJECTIVE NATURE OF THE REAL (METALLURGICAL) PROCESSES

Although additional investigations should be necessary for a final explanation of the surjective nature of such systems, it is already clear that the surjective transformations in the production chain for wrought aluminium alloys and their processing to final products are a consequence of the so-called “chaotic” behaviour of some of the main variables (chemical elements and processing parameters) involved in the system. In that sense these variables are particularly important, with small deviations causing significant differences in the final

properties of the end-product (typical examples of such variables are trace elements). An additional explanation might be in the statistical or stochastic nature of the production processes, caused by the simultaneous fluctuations of numerous processing variables. Moreover, it is also possible that some of the processing parameters (e.g., trace elements or some of the parameters from the production) are not considered as relevant and incorporated into the big data. However, a more accurate analysis confirmed that they influence, quite significantly, the repeatability of the production process. In other words, to reduce the surjective behaviour, it is necessary to enhance the big data and, in parallel, to verify its quality.

## THE PREDICTOR: THE PREDICTION THAT THE SELECTED PROCESSING PATH WILL RESULT IN A PARTICULAR SET OF PROPERTIES AND VICE-VERSA

**The first step** in finding a correlation between the processing paths and the set of properties as ***pairs of events***, and vice-versa, is to calculate the ***conditional probabilities*** $\boldsymbol{\pi_i}$ of all the available ***pairs***, either taken from the regular production and/or virtually generated. This conditional or posterior probability $\boldsymbol{\pi_i}$ is actually the probability that the vector of the processing path $\overrightarrow{pp_i}$ will result in a set of properties given by the appropriate vector $\vec{P}_i$ if the processing path is realized. Therefore, one can write the conditional probability:

$$\boldsymbol{\pi_i} = P(\vec{P}_i \backslash \overrightarrow{pp_i}) = {P(\overrightarrow{pp_i} \backslash \vec{P}_i) P(\vec{P}_i)} \Big/ {P(\overrightarrow{pp_i})} \tag{16}$$

as the posterior probability, i.e., the probability of $\vec{P}_i$ given $\overrightarrow{pp_i}$ , i.e., after $\overrightarrow{pp_i}$ is observed. This is what we want to know: the probability of a hypothesis given the available evidence.

The result of the first step is the set of pairs $(\overrightarrow{pp_i} \leftrightarrow \vec{P}_i)$, each with the corresponding conditional probability $\boldsymbol{\pi_i}$ that this will happen, which can be written as triples $\left[(\overrightarrow{pp_i} \leftrightarrow \vec{P}_i), \boldsymbol{\pi}_i \right]$ and called the predictor. The predictor $\boldsymbol{PRED}(\overrightarrow{pp_i}, \vec{P}_i, \boldsymbol{\pi}_i)$ is a triplet of data giving the probability $\boldsymbol{\pi}_i$ that the processing path $\overrightarrow{pp_i}$ will result in a particular set of properties $\overrightarrow{P_i}$. Therefore, we can write:

$$\boldsymbol{PRED}(\overrightarrow{pp_i}, \vec{P}_i, \boldsymbol{\pi}_i) = \left[(\overrightarrow{pp_i} \leftrightarrow \vec{P}_i), \boldsymbol{\pi}_i\right] \tag{17}$$

Of course, if the vector of the processing path and the vector of the set of properties are replaced with the appropriate descriptors $\boldsymbol{DESC}(D_i, \theta_i)$ and $\boldsymbol{DESC}(d_i, \varphi_i)$, we can write the following formula of the predictor:

$$\boldsymbol{PRED}(\overrightarrow{pp_i}, \vec{P}_i, \boldsymbol{\pi}_i) = \boldsymbol{PRED}(\boldsymbol{DESC}(D_i, \theta_i), \boldsymbol{DESC}(d_i, \varphi_i), \boldsymbol{\pi}_i) = \left[(\boldsymbol{DESC}(D_i, \theta_i) \leftrightarrow \boldsymbol{DESC}(d_i, \varphi_i)), \boldsymbol{\pi}_i \right] \tag{18}$$

For the descriptors of the first order $D_i$ and $d_i$, this formula for the predictor is as follows:

$$\boldsymbol{PRED}\left(\overrightarrow{pp}_i, \vec{P}_i, \boldsymbol{\pi}_i\right) = \boldsymbol{PRED}(D_i, d_i, \boldsymbol{\pi}_i) = [(D_i \leftrightarrow d_i), \boldsymbol{\pi}_i] \quad (19)$$

As already explained, each of these two events is described (and replaced in the algorithm) by the corresponding descriptors. Generally, for the group of the non-collinear vectors, we should select the descriptors of the second order, $\boldsymbol{DESC}(D_i, \theta_i)$ and $\boldsymbol{DESC}(d_i, \varphi_i)$, of the processing paths and the set of properties.
Therefore, in that general case, the conditional probability for the selected ***i*** pair of events is expressed by the Bayes' formula:

$$\pi[\boldsymbol{DESC}(d_i, \varphi_i) \backslash \boldsymbol{DESC}(D_i, \theta_i)] = P[\boldsymbol{DESC}(D_i, \theta_i) \backslash \boldsymbol{DESC}(d_i, \varphi_i)] P[\boldsymbol{DESC}(d_i, \varphi_i)] \Big/ P[\boldsymbol{DESC}(D_i, \theta_i)] \quad (20)$$

However, for the group of collinear vectors, we can write:

$$\boldsymbol{\pi}[\boldsymbol{DESC}(d_i) \backslash \boldsymbol{DESC}(D_i)] = P[\boldsymbol{DESC}(D_i) \backslash \boldsymbol{DESC}(d_i)] P[\boldsymbol{DESC}(d_i)] \Big/ P[\boldsymbol{DESC}(D_i)] \quad (21)$$

or, taking into consideration that $\boldsymbol{DESC}(D_i) = D_i$ and $\boldsymbol{DESC}(d_i) = d_i$, in a short form:

$$\boldsymbol{\pi}(d_i \backslash D_i) = P(D_i \backslash d_i) P(d_i) \Big/ P(D_i) \quad (22)$$

which is the well-known Bayes' formula.
The triples obtained in that case will be: $[(d_i \leftrightarrow D_i), \boldsymbol{\pi}_i]$.
The Bayes' formula derives the posterior probability as a consequence of two antecedents, a prior probability and a "likelihood function" derived from a statistical model for the observed data, where \ means "event conditional on" (so that $(d_i \backslash D_i)$ means $d_i$ given $D_i$.
$d_i$ stands for any hypothesis whose probability might be affected by the data (called evidence below). Often, there are competing hypotheses (i.e., surjective processing paths), and the task is to determine which is the most probable.
The evidence $D_i$ corresponds to new data that were not used when computing the prior probability.
$P(d_i)$, the prior probability, is an estimate of the probability of the hypothesis $d_i$ before the data $D_i$, the current evidence is observed.
$\boldsymbol{\pi}(d_i \backslash D_i)$, the posterior probability, is the probability of $d_i$ given $D_i$, i.e., after $D_i$ is observed.
$P(D_i \backslash d_i)$ is the probability of observing $D_i$ given $d_i$. As a function of $D_i$ with $d_i$ fixed, this is the likelihood; it indicates the compatibility of the evidence with the given hypothesis. The likelihood function is a function of the evidence, $D_i$, while the posterior probability is a function of the hypothesis, $d_i$.
$P(D_i)$ is sometimes termed the marginal likelihood or "model evidence". This factor is the same for all possible hypothesis being considered (as evident from the fact that the

hypothesis $d_i$ does not appear anywhere in the symbol, unlike for all the other factors), so this factor does not enter into determining the relative probabilities of different hypotheses. Note that for different values of $d_i$, only the factors $P(d_i)$ and $P(D_i \backslash d_i)$, both in the numerator, affect the value of $P(d_i) \backslash D_i$ – the posterior probability of a hypothesis is proportional to its prior probability (its inherent likeliness) and the newly acquired likelihood (its compatibility with the new observed evidence). Based on that, the Bayes' rule can be finally written as follows:

$$\boldsymbol{\pi}(D_i \backslash d_i) = \left[ P(d_i \backslash D_i) \Big/ P(d_i) \right] P(D_i) \tag{23}$$

where the factor $P(d_i \backslash D_i) \Big/ P(d_i)$ can be interpreted as the impact of $d_i$ on the probability of $D_i$.

## THE FUNCTIONAL RELATION BETWEEN THE DESCRIPTORS OF THE PROCESSING PATH AND THE PROPERTIES

To find the strong enough relationship between the processing paths and the set of properties, or vice-versa, it is necessary to recognize and select only those triplets (i.e., predictors), within all those possible, having a probability of achievement higher than that required in the model, $P_{required}$ , (usually higher that 95%). The result is a set of triplets we call the relation between the descriptor of the processing path $D_i$ and the descriptor of the set of properties $d_i$:

$$\begin{gathered} REL(D_i \leftrightarrow d_i) = \{ [(D_i \leftrightarrow d_i), \boldsymbol{\pi}_i \geq P_{required} \ ] \} = \\ \{ \boldsymbol{PRED}(D_i, d_i, P_{required}) \} = \boldsymbol{F(D_i, d_i)} \end{gathered} \tag{24}$$

It is important to point out that the relation that existed between the descriptor of the processing path and the descriptor of the set of properties (or vice-versa) will become ***functional*** (only when) since the probabilities of the individual transformations $D_i \leftrightarrow d_i$ exceed some critical value ($P_{required}$ ). Below that value, the individual transformations $D_i \leftrightarrow d_i$ are expressed only as a bijective or, even, surjective relation, with a significantly lower quality (potential) of the prediction.

## THE PREDICTION OF THE PROCESSING PATH FOR THE DESIRED SET OF PROPERTIES AND VICE-VERSA

This is the final step in the data-driven modelling and the main result the algorithm should provide to the end-users in an industrial environment.
The entire process of the prediction can be written as follows:

$$\begin{array}{ccc} (D_i, \theta_i) & \overset{F}{\leftrightarrow} & (d_i, \varphi_i) \\ \downarrow & & \downarrow \\ \overrightarrow{pp_i} & \leftrightarrow & \vec{P}_i \end{array} \tag{25}$$

In the first step, the counterparts of the descriptors $(D_i, \theta_i)$ and $(d_i, \varphi_i)$ are related by the functional transformation ***F*** that exists between them (the procedure is described in the previous section). Later, for the independently selected descriptor of the set of properties, the appropriate (i.e., functionally dependent) descriptor of the processing path, necessary for providing such a set of properties, can be calculated using the known function ***F***. Finally, due to the fact that both descriptors are within the functional range of the transformations, they can be replaced (by performing the data-driven searching procedure) with the corresponding vectors of the processing path, $\overrightarrow{pp_i}$, and the set of properties, $\vec{P}_i$.
Determining these two vectors is the final aim of the predictive algorithm.

## RESULTS AND DISCUSSION

### The structure of the big data and the data-mining procedure

The big data applied in this work consisted of different technological paths (concentrations of the 35 alloying elements and the 80 processing parameters) resulted in the achieved combination of properties (ultimate tensile strength, yield strength and elongation) of the end-products.
The data mining from the regular industrial production and quality control was applied to collect the results for the large number of technological paths of the AA 6110A alloy and the corresponding standard, room-temperature tensile tests.
The measurements of the mechanical properties were performed in the T1, T5 and T6 conditions using standard, room-temperature tensile tests. The chemical compositions of the samples were analysed using optical emission spectroscopy (OES), with an average accuracy of ±10 ppm.

### The quality of the big data and its influence on the alloy modelling

Generally, the quality of the big data applied for the modelling of wrought aluminium alloys depends on: (i) **the quality of the measurement** (i.e., the accuracy, precision, repeatability

and reproducibility) of the individual data involved in the big data and (ii) **the ability to effectively filter the data** (i.e., the recognition and removal of the uncertain data).
Sufficient quality of the big data is crucial for the successful learning and predictability that is shown by example in Fig. 3. As expected, the highest predictability is achieved by the algorithm learning with the most accurate experimentally available data – in that particular case the data of UTS and YS, determined by the lowest relative error of the measurement (approx. ±1.5%). In contrast, the predictability of the elongation was much worse due to the approximately three-times higher relative error of the measurement for that particular parameter (approx. ±4). The above findings indicate a rather exponential decrease in the quality of the prediction with an increase of the relative error of the individual data in the big data and vice-versa, which additionally demonstrates the importance of the quality of the big data in the cognitive prediction of an alloy's properties.

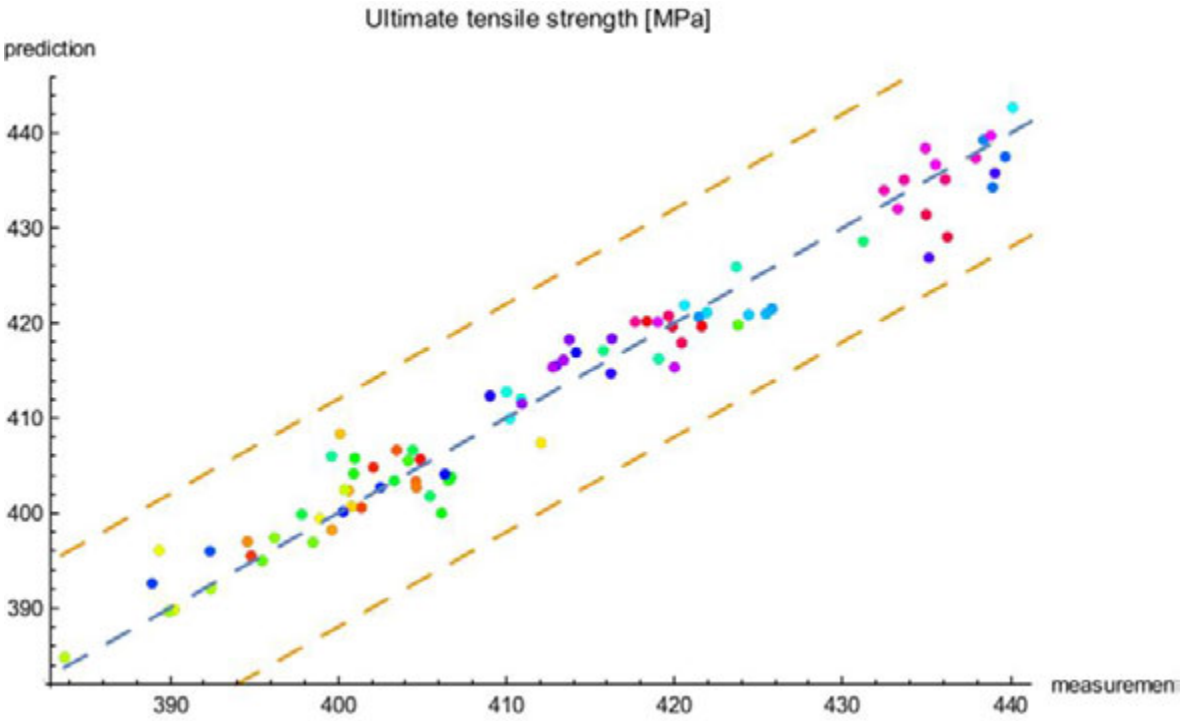

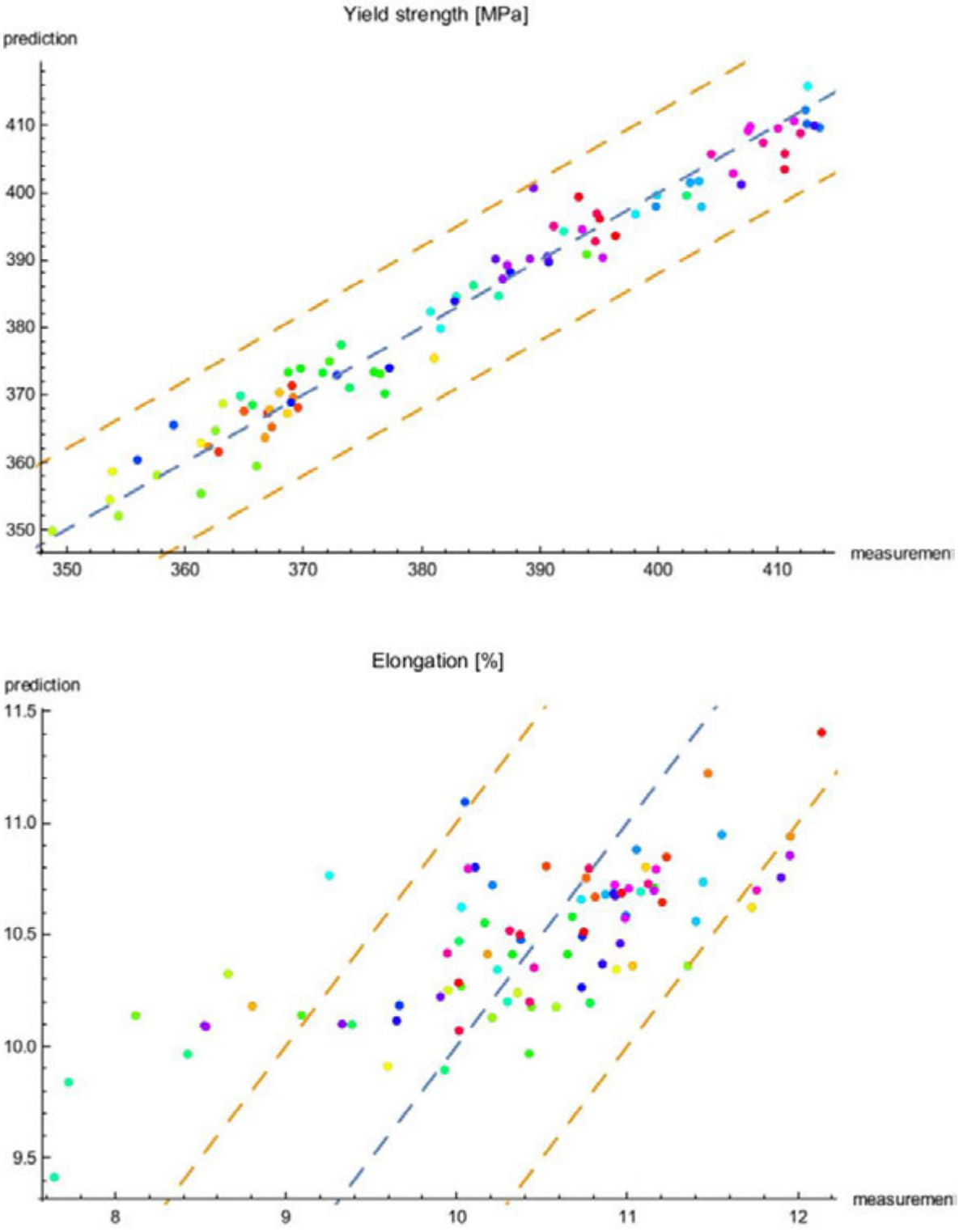


Figure 3. Influence of the quality of the **non-filtered** big data on the predictability of the selected alloy properties

**The correlations between the properties and the technological path and vice-versa**

Based on the accumulated data obtained for all three tempers, the required combinations of correlations between the properties and the technological path were established following the methodology of the functional and/or the data-driven computing [3].

**The modelling of the technological path and the properties of the end-product**

Finally, the correlation between the properties and the technological path established previously was applied for the modelling of the technological paths (compositions and processing parameters) so as to enable us to provide the desired end-product properties and vice-versa, including standard and some non-standard alloys from the base alloy AA6110.

The modelled data are proprietary and are beyond the scope of this publication. However, some data-driven alternative, non-standard compositions are presented in Table 1, without the corresponding processing parameters, all resulting in the required combination of end-product properties.

Table 1. Standard chemical composition of the alloy AA6110 and some cognitive-computed alternative compositions

| Alloy | Si | Fe | Cu | Mn | Mg | Cr | Zn | Ti | Zr | Others Each | Others Total |
|---|---|---|---|---|---|---|---|---|---|---|---|
| | wt% | wt% | wt% | wt% | wt% | wt% | wt% | wt% | wt% | wt% | wt% |
| 6110 | 1.00-1.10 | 0.14-0.25 | 0.40-0.50 | 0.70-0.80 | 0.75-0.85 | 0.15-0.25 | 0.20 | 0.02-0.10 | 0.12-0.15 | 0.05 | 0.15 |
| Com1 | 1.10-1.15 | O.25-0.28 | 0.40-0.50 | 0.70-0.80 | 0.85-0.95 | 0.15-0.25 | 0.20 | 0.05-0.15 | 0.12-0.15 | 0.05 | 0.15 |
| Com2 | 1.15-1.20 | 0.28-0.30 | 0.40-0.55 | 0.80-0.90 | 0.95-1.05 | 0.15-0.25 | 0.25 | 0.05-0.15 | 0.15-0.18 | 0.06 | 0.18 |
| Com3 | 1.20-1-30 | 0.30-0.33 | 0.50-0.60 | 0.90-0.95 | 1.05-1.15 | 0.15-0.30 | 0.25 | 0.05-0.20 | 0.15-0.18 | 0.07 | 0.21 |

The main advantage of the non-standard compositions predicted by the cognitive computing is in the higher upper concentrations of some of the main alloying elements (Fe, Si, Mg) and most of the trace elements, in this way enhancing the amount of scrap that could be involved in the pre-melting mixture. An additional advantage is a reduction in the minimal amount of the primary aluminium prerequisite for the alloy's production.

The cognitive predicted relations between the technological paths and the mechanical properties indicate that both the chemical composition and the processing parameters have a considerable influence on the properties of the end-product. However, the influence of some of the alloying and trace elements in the non-standard alloy compositions was found to be stronger and, in some cases, even dominant, when compared with the main processing parameters of the extrusion and the heat treatment. In addition, the cognitive modelling clearly proved that, with the appropriate adoption and the optimization of the processing parameters, particularly the heat treatment, it is possible to compensate or, at least, significantly reduce the negative influences of the non-standard alloy composition on the

mechanical properties. The result of such cognitive adopting is, *if it exists*, the proper technological path for achieving the required combination of properties. However, it is also important to note that at the same time, some other important properties that are out of the scope of those required (e.g., electrical conductivity, corrosion resistance, etc.) might be affected, which should be considered and improved, if necessary, by further modelling.

## VALIDATION OF THE QUALITY OF THE PREDICTION

The quality of the prediction is evaluated by determining the Precision, the Recall and the F-Measure. In principle, there are four outcomes of the quality of predictions when the data is evaluated:

- True positive,
- True negative,
- False positive,
- False negative.

True positive and true negative are events or predictions the algorithm identified correctly. False positives are recognized as wasted time and resources, while false negatives are categorized as missed opportunities.
Therefore, generally we can write:

$$Precision = {}^{True\ positives}\Big/_{(True\ positives + False\ Positivies)} \tag{26}$$

$$Recall = {}^{True\ positives}\Big/_{(True\ positives + False\ Negative)} \tag{27}$$

$$F - Measure = 2 * {}^{(Precision * Recall)}\Big/_{(Precision + Recall)} \tag{28}$$

The algorithm was validated by predicting the properties of randomly selected samples taken from the 150 different technological paths of the standard alloy AA 6110 and vice-versa, by predicting the chemical composition of the samples with known mechanical properties.
Typically, for the standard alloy AA 6110, the following quality of prediction was achieved:

$$Precision = \ approx. 90\%$$
$$Recall = \ approx. 65\%$$
$$F - Measure = approx. 75\%$$

In the case of the non-standard alloy compositions derived from the alloy AA6110, the validation was performed through production of the end-products in accordance with the

limited number (3–5) of computed processing paths and the comparison of the achieved and the predicted properties. It was found that by applying the data-driven computing methodology on the properly filtered big-data set of experimentally determined values, either the chemical composition or the mechanical properties can be predicted. However, due to the limited number of a non-standard processing paths considered in that work, a significantly lower quality of prediction was achieved:

$$Precision = approx. 70\%$$
$$Recall = approx. 50\%$$
$$F - Measure = approx. 58\%$$

which is a promising starting point for further optimizations.
Generally, the accuracy of the prediction exponentially decreases when increasing the distance calculated in the vector space of the predicted set of parameters (the technological path or the required combination of properties) from an average (the zero vector).

## CONCLUSION

A cognitive algorithm for finding a correlation between the properties of wrought aluminium alloys, the chemical composition and the processing parameters was developed and validated on the AA 6110A alloy.

The main concept of the recycling-friendly alloys, based on the expectation that the desired combination of the properties can still be achieved even when increasing the concentration of some of the alloying elements and the level of impurities if the rest of the processing parameters are properly modified, has been proven. Moreover, the developed modelling tool even enables the opposite engineering steps – the modelling of ***new*** processing paths to achieve ***superior*** mechanical properties for wrought aluminium alloys.

## REFERENCES

[1] V. Kevorkijan, Modelling of alternative compositions of recycled wrought aluminium alloys, JOM, 65 (2013) 8, pp. 973-981.
[2] V. M. Kevorkijan, P. Cvahte, B. Hmelak, S. Hmelak, V. Dragojević, M. Jelen, M. Lažeta, U. Kovačec, Scrap-intensive wrought aluminium alloys of standard quality, Light Metals 2015, (Editor M. Hyland), John Wiley & Sons, Inc., 20.2, 2015, Hoboken, USA, pp. 237.
[3] V. M. Kevorkijan, B. Hmelak, P. Cvahte, S. Hmelak, V. Dragojević, U. Kovačec, M. Jelen, D. Volšak, Algorithm for finding the correlation between the properties of wrought aluminium alloys, the chemical composition and the processing parameters, Light Metals 2017, (Editor A. P. Ratwik), Springer, 13.3, 2017, Chaim, Switzerland, pp. 259.

[4] J. Zander, R. Sandström, Modelling technological properties of commercial wrought aluminium alloys, Materials & Design, 30 (2009) 9, pp. 3752-3759.
[5] P. W. Staar, P. KI. Barkoutsos, R. Istrate, A. Cristiano, I. Malossi, I. Tavernelli, N. Moll, H. Giefers, C. Hagleitner, Costas Bekas, A. Curioni, Stochastic matrix-function estimators: scalable big-data kernels with high performance, 2016 IEEE International parallel & Distributed Processing Symposium, IEEE, 2016, Los Alamitos, pp. 812.

17th INTERNATIONAL FOUNDRYMEN CONFERENCE
Hi-tech casting solution and knowledge based engineering
Opatija, May 16th-18th, 2018
http://www.simet.hr/~foundry/

# INDUSTRY CHALLENGES CONNECTED WITH DIGITAL TRANSFORMATION

**Vladimír Krutiš***

Mecas ESI as subsidiary of ESI GROUP, Plzen, Czech Republic

**Invited lecture**
*Subject review*

**Abstract**

The next several years will be about the "digital Transformation" of manufacturing industries. This will touch nearly every aspect of business as existing systems, jobs, and business processes are instrumented, redefined, and optimized with artificial intelligence. This transformation will be widespread and far reaching. Information technology (IT), operational technology (OT), engineering technology (ET), supply chain, asset management, services, and customer-facing systems will all be impacted. Discrete manufacturing, process industries, utilities, energy, infrastructure, and more are already beginning the transformation.
The transformation will affect all stages from product development, manufacturing processes and also product in operation. In order to develop smarter products, and the emerging class of autonomous products, designers and engineers must anticipate multiple unknowns and associated risks. Among these are the somewhat unclear ways different sensors and systems, upon which "intelligent" products rely, may interact and function/dysfunction together. Furthermore, it becomes increasingly critical to be able to predict system faults, that can result from design weaknesses, fabrication defects, or wear and tear, and to mitigate detrimental consequences right from the conception phase.
There are the main points which are going to be a momentum for an industrial transformation:

- autonomous robots,
- simulation,
- horizontal and vertical system integration,
- industrial internet of things,
- cybersecurity,
- cloud,
- additive manufacturing,
- virtual and augmented reality,
- big data and analytics.

All mentioned aspects will be discussed in relation to manufacturing processes including foundry technology.

***Keywords***: *digital transformation, simulation, Industry 4.0*

*Corresponding author (e-mail address): *Vladimir.Krutis@esi-group.com*

# 17th INTERNATIONAL FOUNDRYMEN CONFERENCE

## INDUSTRY CHALLENGES CONNECTED WITH DIGITAL TRANSFORMATION

Ing. Vladimír Krutiš, Ph.D.
ESI Group

get it right®

www.esi-group.com

# Content

- Industrial new challenges
- The context of digital transformation
- Virtual Engineering
- Hybrid Twin™ concept

# Lighweight, autonomous, electric vehicles, new material …
# …..accelerate our world's transformations…

- Engines, gas, drivers

Environment
Safety

- Motors, batteries, occupants


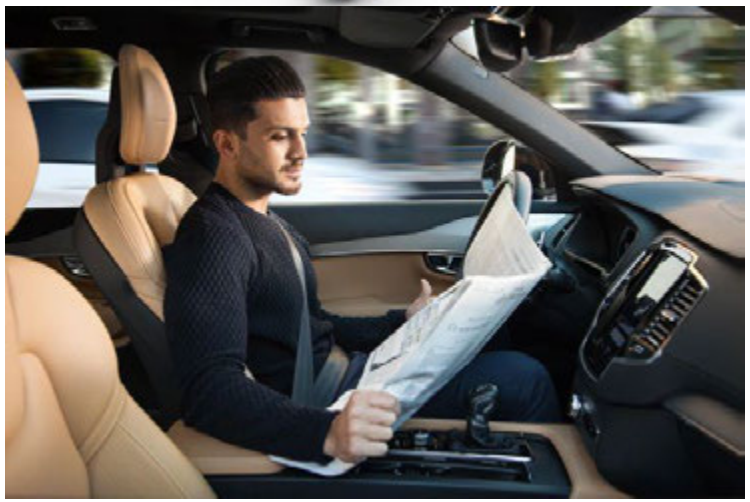


Volkswagen plans $40 billion investment in EVs over next five years, will introduce 15 new cars worldwide

November 17, 2017

Ford plans $11 billion investment, 40 electrified vehicles by 2022

Toyota is racing to commercialize a breakthrough battery technology during the first half of the 2020s with the potential to cut the cost of making electric cars.

January 14, 2018

# The Digital Transformation - Industry 4.0 – Smart factory

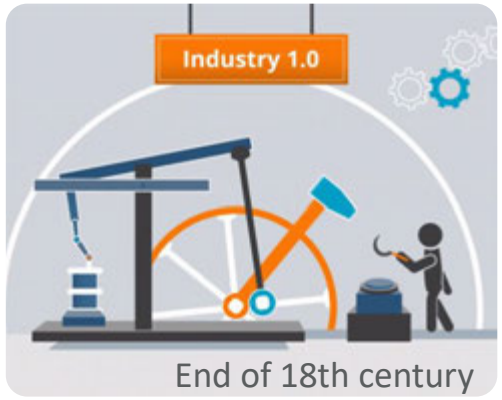


*Mechanization, water power, steam power, craft build*

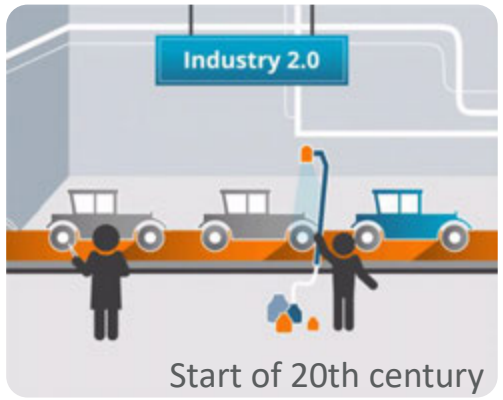


*Mass production, assembly line, electricity, repetitive tasks*

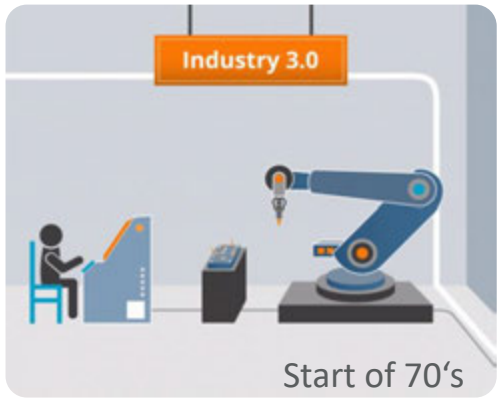


*Computer simulation, automation, Ad-Hoc human interaction*

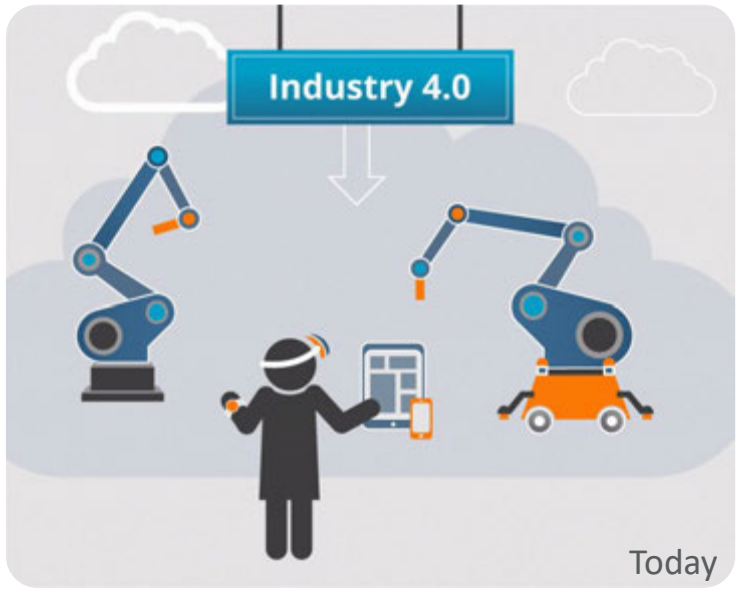


*Cyber physical systems*

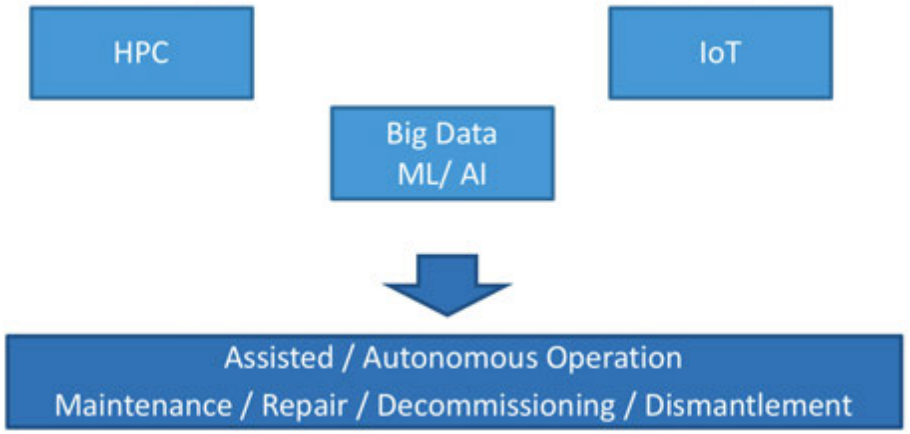

# The context of the Digital Transformation – Industry Disruption

| Product | ‘Nominal’ | ‘in-Life’ |
|---|---|---|
| Technology | HPC  | IoT / Cloud |
| Manufacture | Robotics | Smart Factory |
| Delivery | Certified  | In Operation  |

Hybrid Twin™

***PLM***
***Product Lifecycle Management***

***PPL***
***Product Performance Lifecycle***

# Accelerating Industrial Transformation

## International Initiatives heralding the impact of ICT and IoT

**Industry 4.0**

Fourth industrial revolution for the virtualization of manufacturing

**'Industrie du futur'**:
Transform the industrial model by digital technology

**'Innovate UK':**
Innovation agency to drive the science and technology innovations

**'Horizon 2020':**
Funding program to support and foster research

**'Manufacturing 2025'**:
Transition from '*made*' in China to '*design*' in China

National Network for Manufacturing Innovation (**NNMI**)
Improve US Manufacturing Competitiveness

*ICT*: Information & Communication Technologies – IoT*: Internet of Things*

# Toward an accelerated industrial transformation

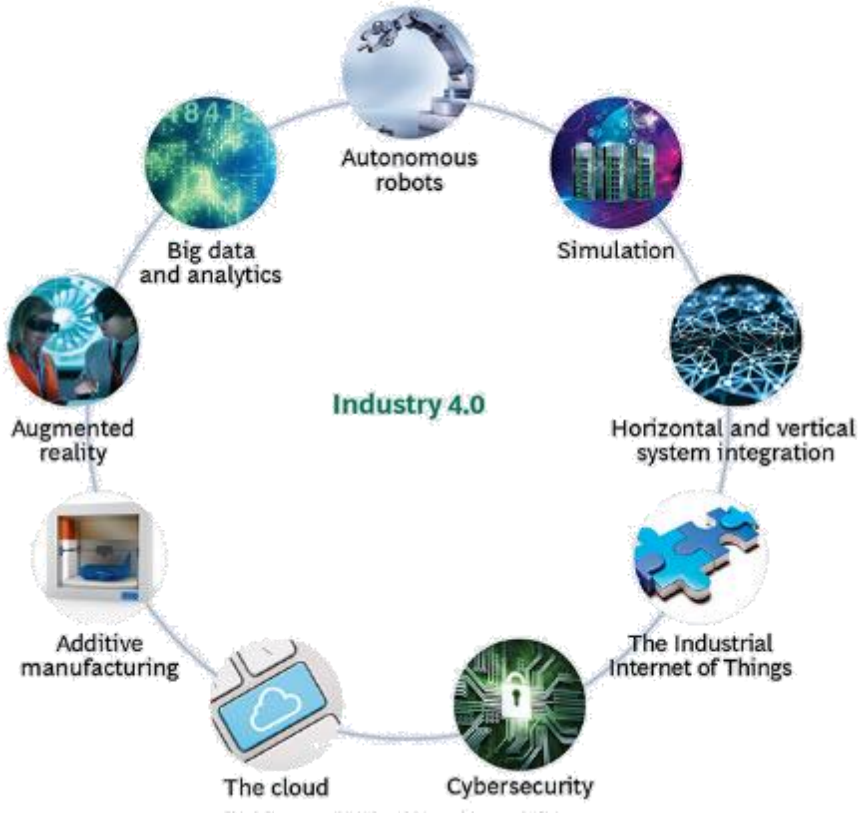


Nine technologies are transforming industrial production:

- autonomous robots,
- **simulation,**
- horizontal and vertical system integration,
- industrial internet of things,
- cybersecurity,
- cloud,
- additive manufacturing,
- virtual and augmented reality,
- big data and analytics.

# Toward an accelerated industrial transformation

## Product Lifecycle Management (PLM)

### ANALYSIS & SIMULATION

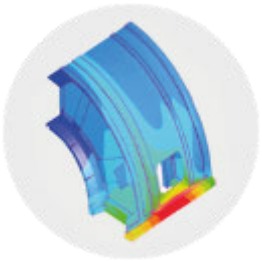

Conduct design checks

**Benefits x1**

### VIRTUAL TESTING

Replace real tests

**Benefits x10**

## Immersive Virtual Engineering

### VIRTUAL PROTOTYPE

Replace real prototypes

**Benefits x 100**

## Product Performance Lifecycle (PPL)

### HYBRID TWIN

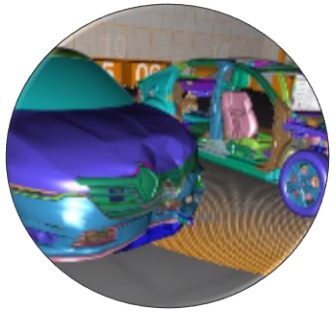

Pilot product performance in operation

### AUTONOMOUS PROTOTYPE

Communicate, Assist & Autonomize

**Benefits x +++**

# How Virtual prototyping can help?

- **Predict** the impact of new materials and advanced processes (i.e: hot forming, centrifugal casting, high pressure die casting…)
- **Optimize** simulations across domains, facilitated by use of a single-core model.
- Master lightweight engineering without compromising on performance.
- Efficiently **evaluate** all aspects of vehicle, occupant and pedestrian safety and achieve virtual pre-certification.
- **Innovate** in various domains, including active / passive safety, while controlling cost and managing time.
- **Explore** all aspects of passenger comfort necessary to deliver the best possible driving experience.

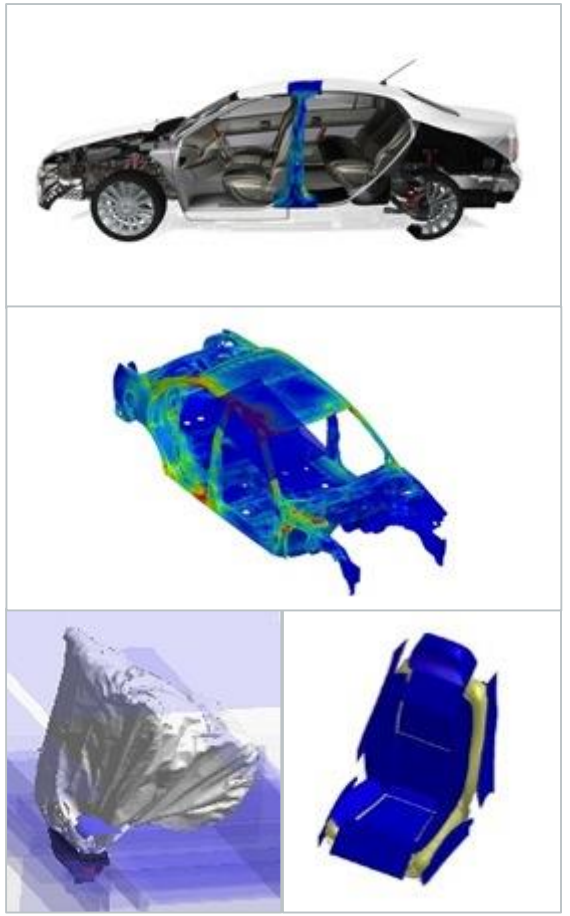

# 1. Building for Specific Application

## Industry and Domain Specific Apps

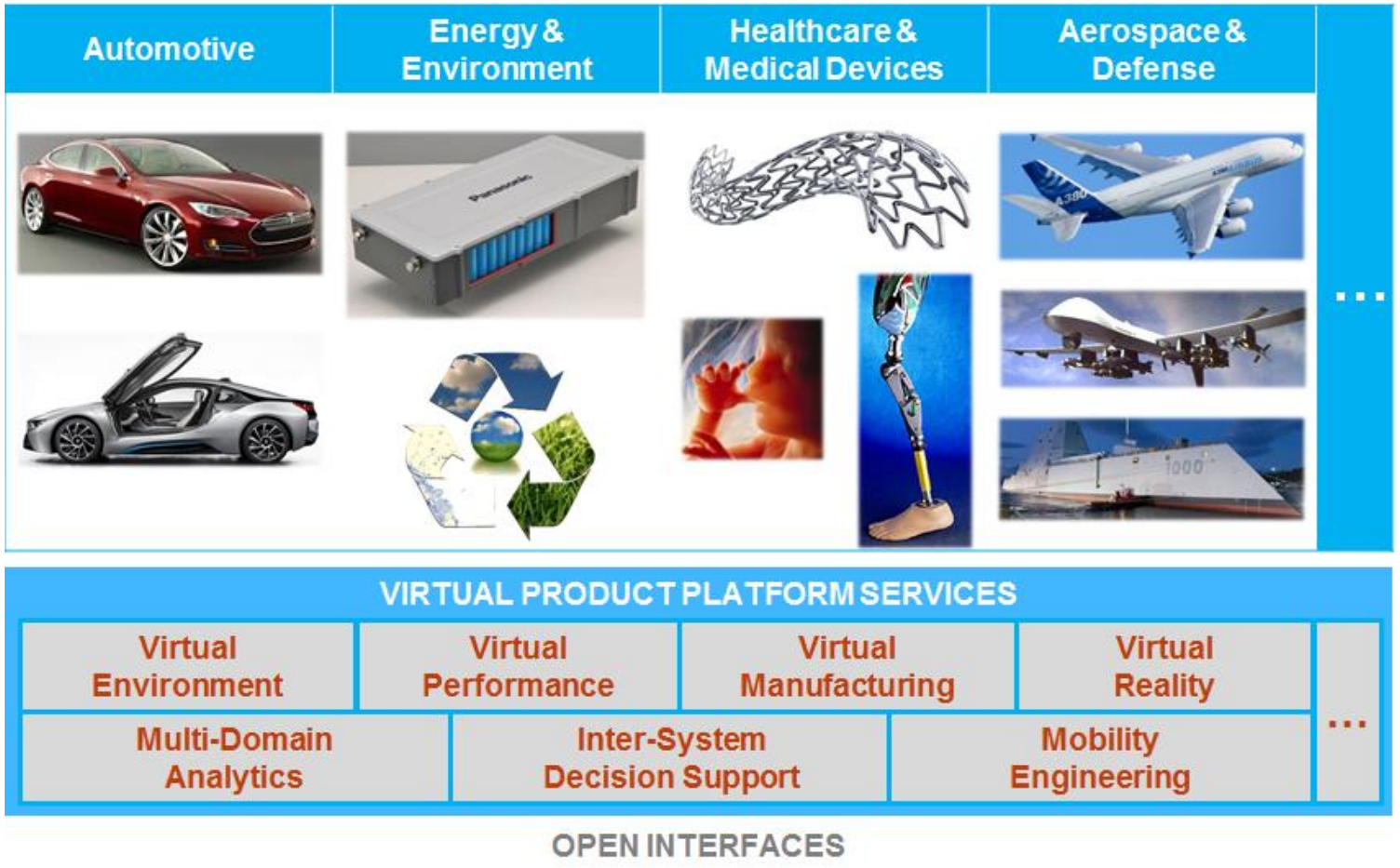


*Meeting the needs of industry and ultimately consumers*

# 2. Encapsulating Process Knowledge

## From Requirements to Performing Products

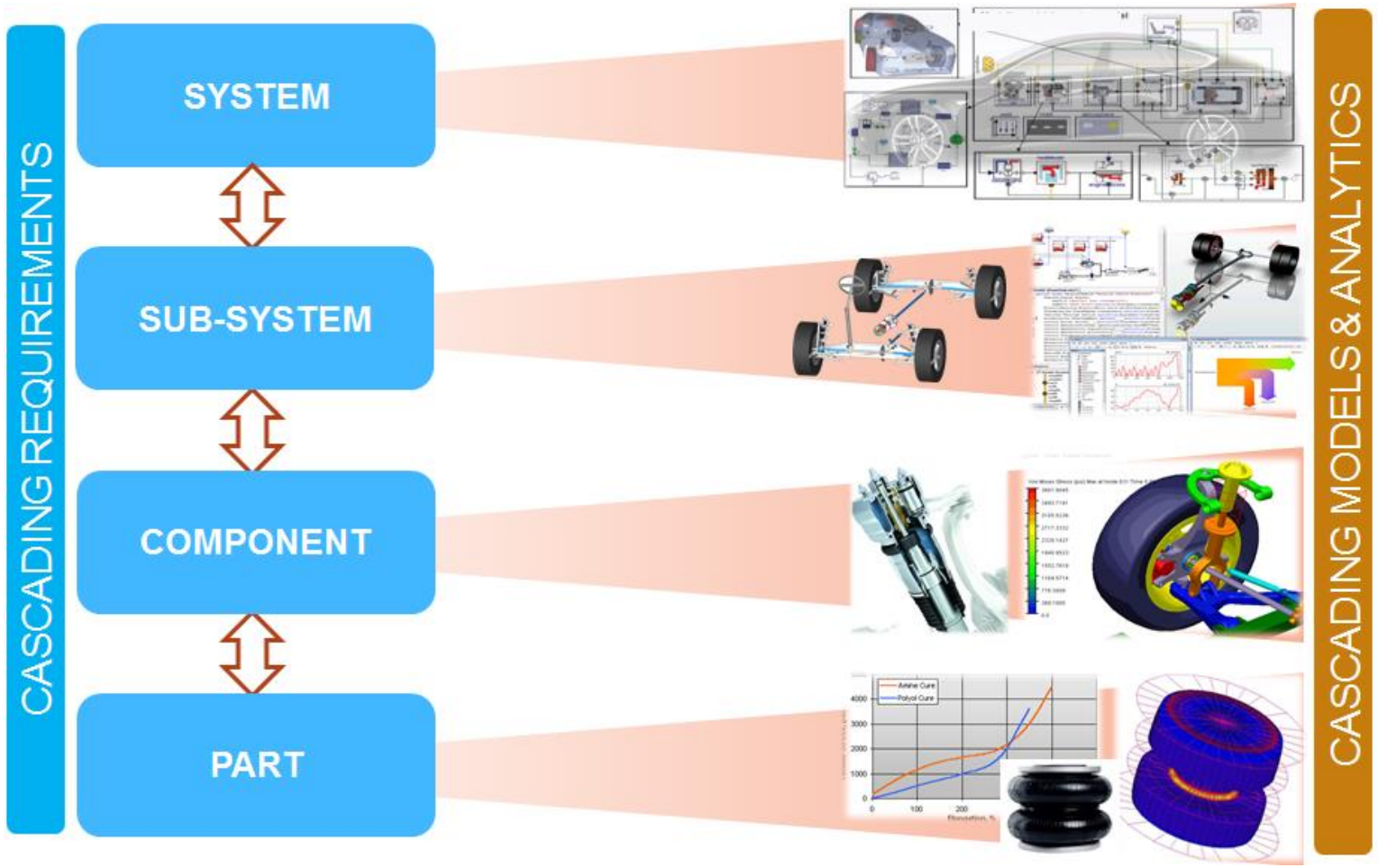

# Virtual manufacturing – chaining simulation

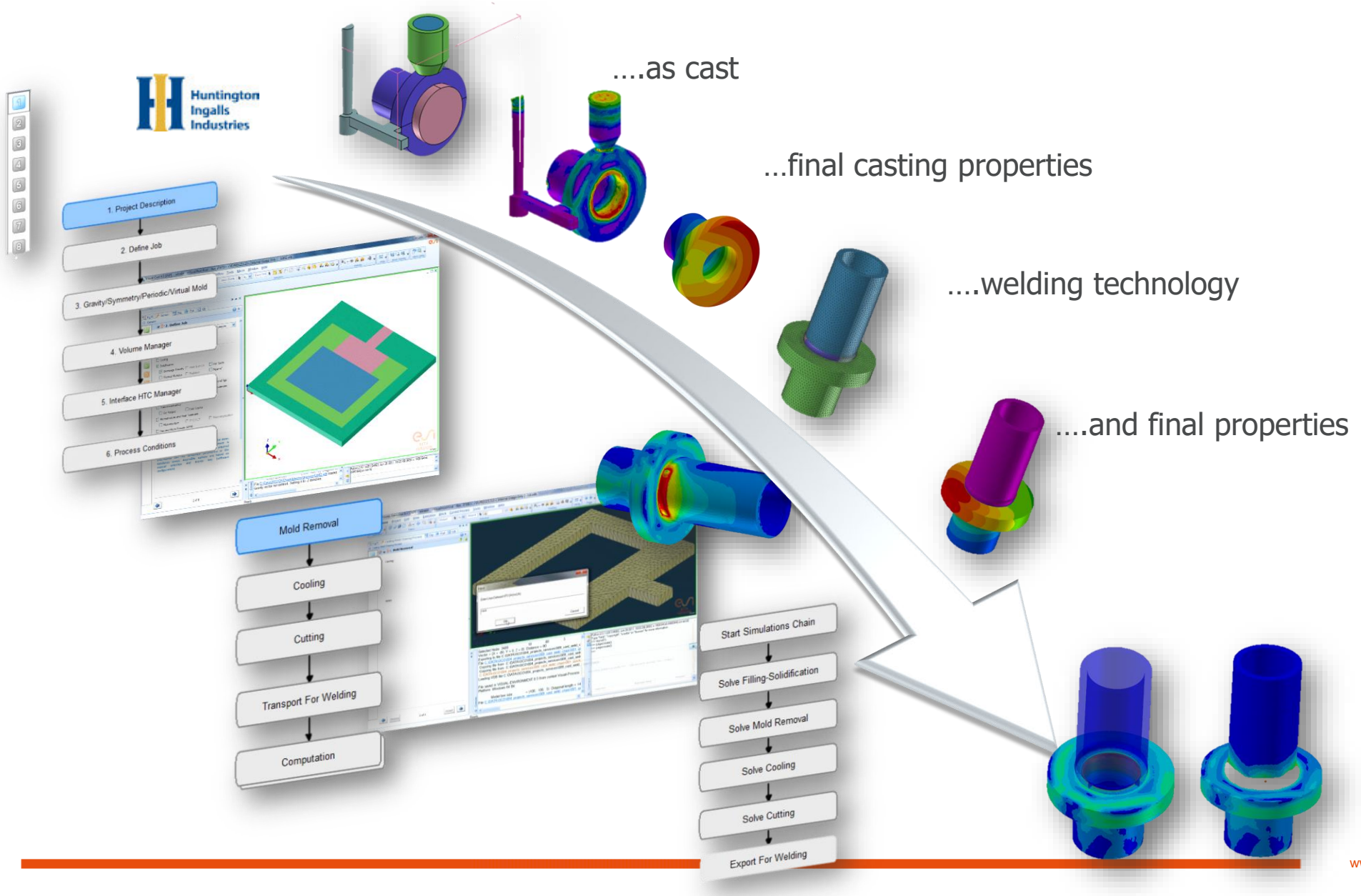

# Chained simulations

## Casting simulation coupled with heat treatment simulation

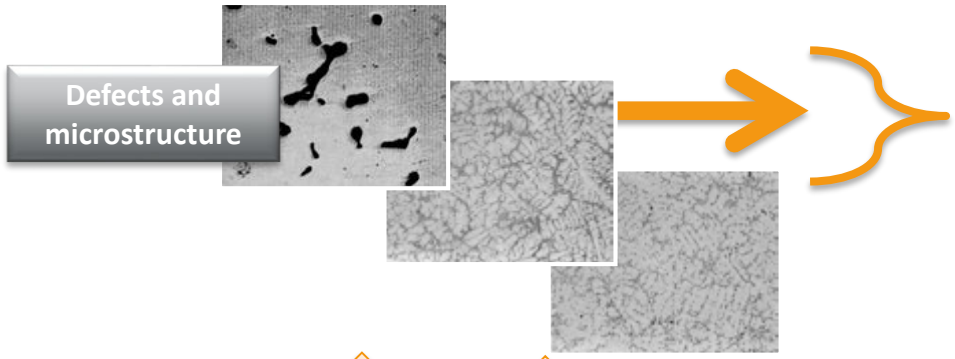



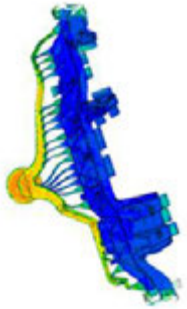

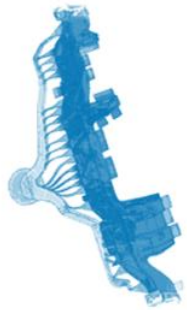


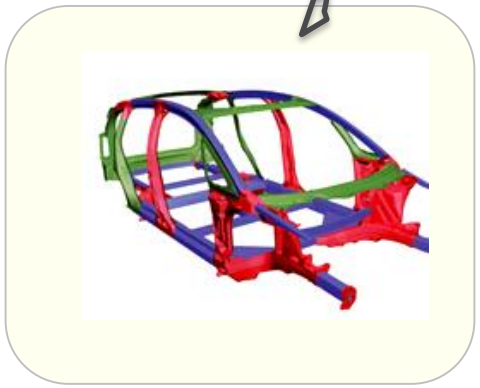

Die design | Casting | Heat treatment | Car assembly | Crash and safety tests

Processes

The objective is to follow a product throughout its whole manufacturing process by calculating at each stage the structures, defects, properties, states and dimensions and transferring the data from one application to the next one.

# 3. Bringing More Science

## Enabling the use of “exotic” and “designed” materials

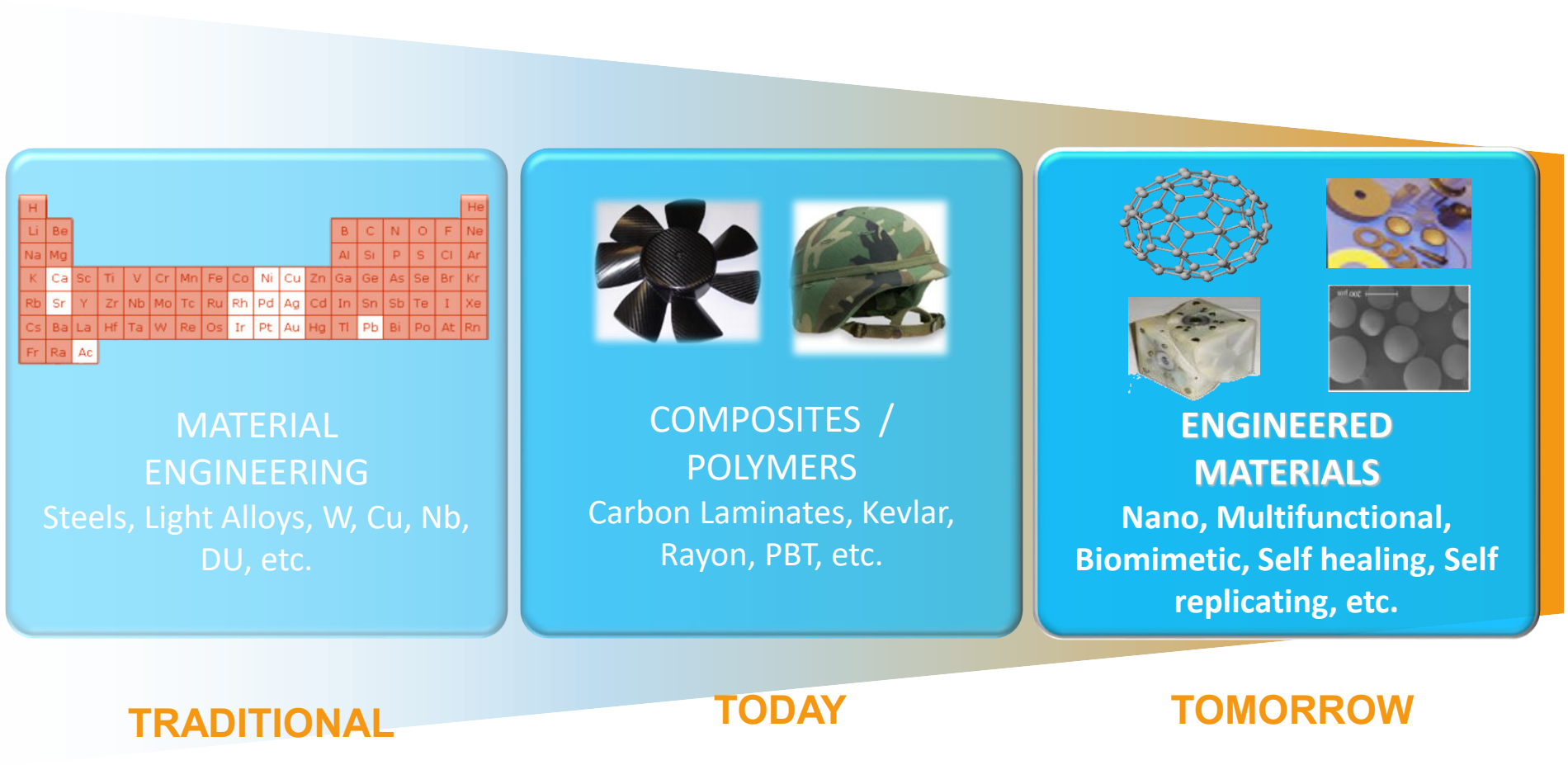

# and ... 4. Changing the Experience – new team work approach

**ENABLE PRODUCT COMPANIES …**

- Turn Requirements to Functioning Product naturally
- Experience : Build, Analyze, Improve – in real time

**DELIVER VALUE TO MORE STAKE HOLDERS …**

- Changing from Engineering “Jargon” to natural language and intuition
- Changing from on premise to Anyplace/Anytime

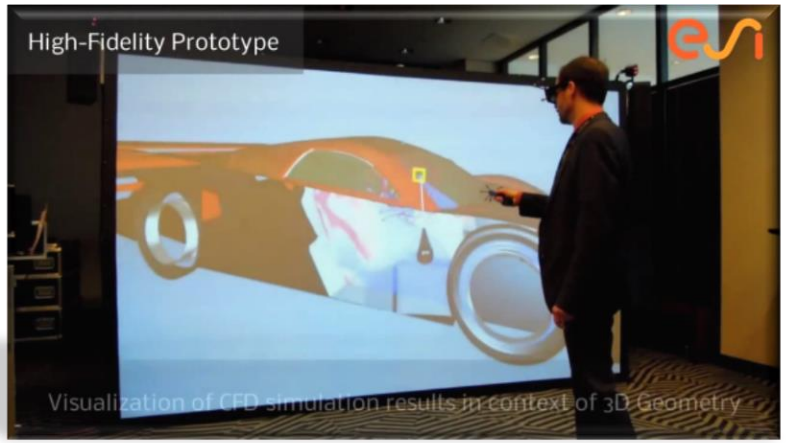


*Virtual Reality: CFD Performance*

*Virtual Reality: Manufacturing*

*Immersive Virtual Product Development*

# Hybrid Twin ™ concept

get it right®

www.esi-group.com

# Key Components of Hybrid Twin™ Solution

- **Physic Modeling and Simulation**
  - Multiphysics dynamic systems: System modeling + Fault modeling & augmentation
  - Single physics component or processes: 3D Modeling + Model order reduction
  - System + ROM combinations

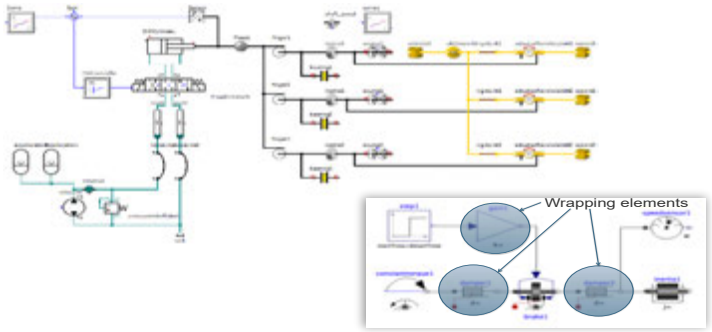


- **Data Science**
  - Data ingest and visualization: Links to IOT data historian, Filtration, signal/image processing, statistical analysis
  - Data analytics & ML: regression & time series analytics, clustering, classification

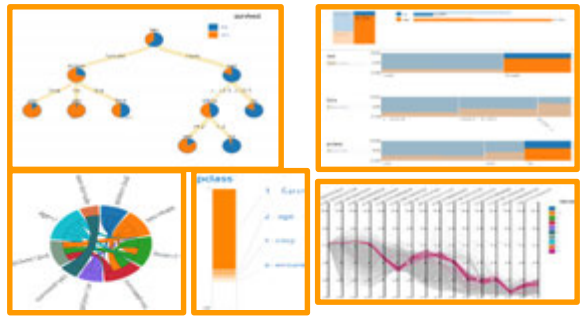

- **Hybrid Twin™ Solution Enabling:**
  - System or component:  anomaly detection, pattern recognition, classifiers, state estimators development using simulation and operational data
  - UI, dash board, and workflow prototyping per application

- **Simulation & Analytics Platform**
  - 3D & 1D simulation execution and data and work flow management
  - Data analytics and ML execution and visualization

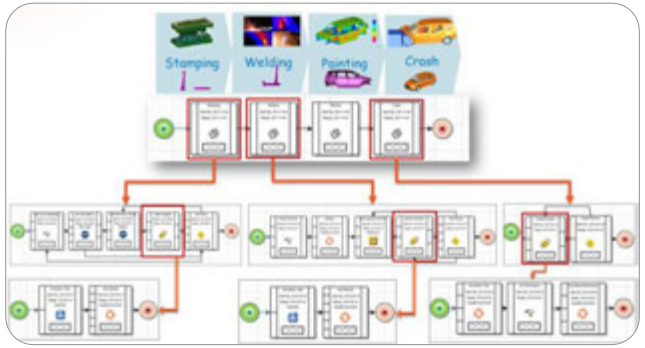

# Thanks for your attention

get it right®

17th INTERNATIONAL FOUNDRYMEN CONFERENCE
Hi-tech casting solution and knowledge based engineering
Opatija, May 16th-18th, 2018
http://www.simet.hr/~foundry/

# INCREASING THE VALUE OF CASTINGS BY APPLYING SURFACE ENGINEERING PROCESSES AND KNOWLEDGE BASED ENGINEERING

**Darko Landek***

University of Zagreb Faculty of Mechanical Engineering and Naval Architecture, Zagreb, Croatia

**Invited lecture**
*Preliminary note*

**Abstract**

The paper presents the concept of application of surface engineering on castings and permanent metal molds. The procedures for modifying and coating the surface of castings and permanent metal molds have been mentioned and the effects of their application on increasing durability and lowering production costs. The importance of the application of knowledge based engineering and materials selection in the design of castings and molds for application of surface engineering processes has been described. For a practical example, a duplex process with plasma nitriding and PACVD coating has been applied to extend the exploitation life of the die-cast mold.

***Keywords***: *knowledge based engineering, material selection, surface engineering, PACVD coating*

*Corresponding author (e-mail address): *darko.landek@fsb.hr*

## INTRODUCTION

Hard coatings applied to permanent metal molds significantly increase their duration or replace a more expensive tool material with a cheaper one [1]. Also, hard coating together with strength and ductile support layer increases their wear or corrosion resistance of some types of metallic casting. For both purposes duplex layer and a multilayer coating deposited at lower temperature are the most appropriated [2]. The primary application of hard coatings includes protection of tool surface against thermal fatigue, wear (to adhesion, abrasion, erosion, and tribo-corrosion) and corrosion as well as friction reduction and maintenance of high quality surface obtained by the initial grinding and polishing [2, 3, 4]. Also, the protection tasks primarily focused to the increasing wear and corrosion resistance can be obtained on the surface of some sorts of castings made of steels, ductile irons and aluminum alloys [5, 6]. The listed combinations of the surface layer properties can be obtained by a multilayer hard coating applied to the hardened substrate of selected tool steel used in mold or on the surface of casted components after its final machining [2, 3, 7,

8, 9]. The base condition for application of a hard multilayer coating is the deposition temperature similar or lower than the temperature of the previously heat treatment of the substrate. The good adhesion of the multilayer coating to the substrate and also of one layer of the coating to the other can be achieved by the physical vapour deposition (PVD) and plasma-assisted vapour deposition (PACVD) processes together with the pre-treatment of the substrate (e.g. plasma sputtering, plasma nitriding). The other potential surface engineering processes for producing hard and wear resistant coatings on the molds made from the hot work tool steel should be the laser or electron beam cladding processes, plasma spraying processes and ion implantation processes. Using the listed processes also increases the service life and productivity of molds [2, 3, 8, 10]. Application of the specific surface engineering processes should be taken into consideration at the beginning of the design of die-cast mold and casting part when the material selection has been conducted.
The first part of the paper describes the current trends of knowledge based software application in the selection of material and production processes. The second part of the paper presents an example of application of duplex surface coating resistant to wear and corrosion deposited on hot work tool steels for die-cast molds.

## AN INTEGRATED DEVELOPMENT OF PARTS WITH COMPUTER-ASSISTED MATERIAL AND PROCESS ENGINEERING

The number of materials available to the engineer is very large, over 120,000. And although standardization help to reduce the number, the continuing development and appearance of new materials with novel, exploitable, properties expands the options further [11]. How, then, does the engineer choose, from this large menu, the optimal material to the specific purpose? In the past, this was done on the basis of experience and recommendations. Today, modern methods of selecting materials are developed based on a systematic comparison of characteristics and quantitative values of the required properties. The question “Which material is optimal for the specific construction part or tool?” has to be addressed at a number of levels, corresponding to the stage the design has reached. At the beginning the design all materials must be considered. As shape of a part or tool takes geometrical dimensions, the selection criteria sharpen and the list of acceptable materials becomes shorter. Then more accurate data are required and a different way of analysing the selection must be used. In the final stages of design, precise data are needed, but for still fewer materials, is number of cases only one. The selection of material cannot be made independently of the selection of production process by which the material is to be casted, finished, heat treated or surface protected. Cost enters, both in the selection of material and in the production processes by which the material will be processed. The design starts from the identification of a market need, specified as a list of design requirements. Then a base concept is defined. The next step is embodiment of requirements into specific shape and dimensions of product and a detailed analysis according specifications are conducted [11]. Modern computer systems for the selection of materials (e.g. Granta Desing software CES) contain a database of material properties and a database of production processes

characteristics used for processing a particular material. In addition to these databases, a knowledge base with a description of the application of materials and production processes is incorporated into the material selection system. The material selection is performed by comparing the properties and characteristics of the material according to a set of criteria (structural, production, economic, etc.). The selection criteria (constrains) to obtain some specific product's function can be given in the table, bar chart or graphical form as shown in Figure 1. They can be used in any order and any combination but the final subset of selected materials depend form the order of selection. Also it is possible to minimize or maximize achieving of the specific constrains.

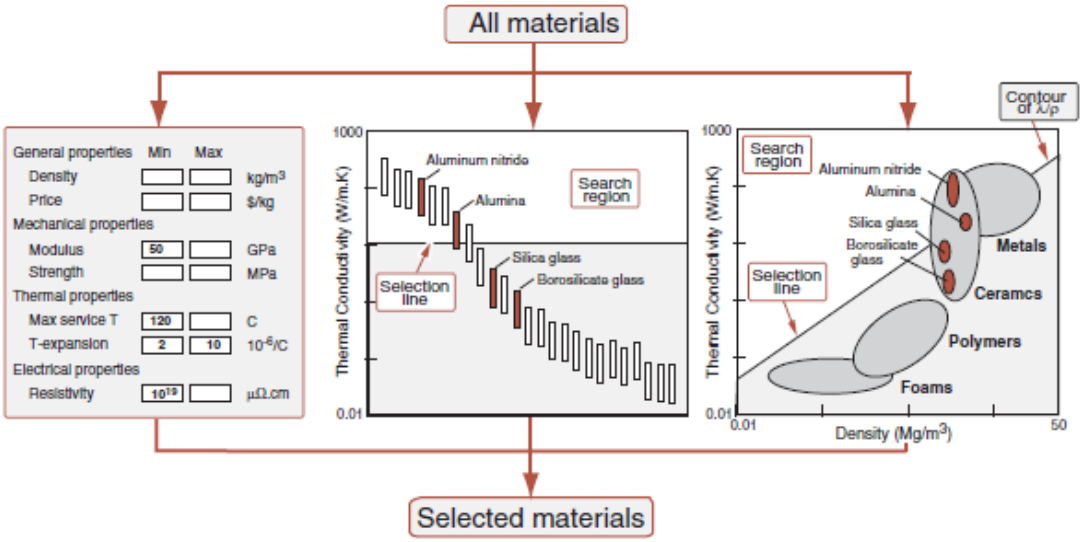


Figure 1. The schematic shows the three types of selection window in computer-aided selection software CES [11]

At the same time, with the choice of production materials, a selection process for its production can be carried out. Strategy for selection of optimal manufacturing processes consists from the following steps: translation design requirements, screening using constrains, ranking processes using objective functions and search for supporting information about selected process and its variants.

After materials and manufacturing processes are selected for designed components the Integrated Computational Materials Engineering (ICME) simulation can be applied to build virtual product performance analysis and manufacturing simulation before planning of the physical manufacturing starts. The ICME discipline allows fundamental research to be transferred to industrial application. ICME refers to the use of computer simulations that integrate mathematical models of metallurgical processes with computer-aided design (CAD) and computer-aided manufacturing (CAM) used in both product design and manufacturing process development with numerical tools such as Finite Element Analysis (FEA) and Computational Fluid Dynamics (CFD) [12]. The behavior of materials is modeled on different scales (micro-, meso- and macroscopic) in chemical composition – processing –

microstructure – property relationships linked with thermodynamic phase equilibria databases (e.g. DICTRA, Thermo-Calc). A well-documented example of the application of this concept is found in the literature [12, 13] is development the computer-aided engineering tools for virtual aluminum casting (VAC) of power train components and implemented in Ford Motor Company. The flow chart of virtual aluminum casting methodology is showed in Figure 2. The VAC program is consisted from four independent parts [13, 14, 15]:

- Accurate simulation of the thermal history of an component during casting and heat treating process,
- Prediction of the microstructure that form during casting and heat treatment processes at all locations in a casting,
- Prediction of critical local mechanical properties caused by locally formed microstructure,
- Coupling predicted local properties with new developed residual stresses, fracture mechanic and FEA models to predict the durability of engine components.

This modeling methodology combines several programs in a common program framework: MAGMASOFT, proCAST and FEA software ABAQUS. Implementation of VAC provides rapid development of high quality motor blocks and heads at the lowest possible cost with the reduced product development time. The developed ICME models had been validated over different microstructure and mechanical properties prediction.

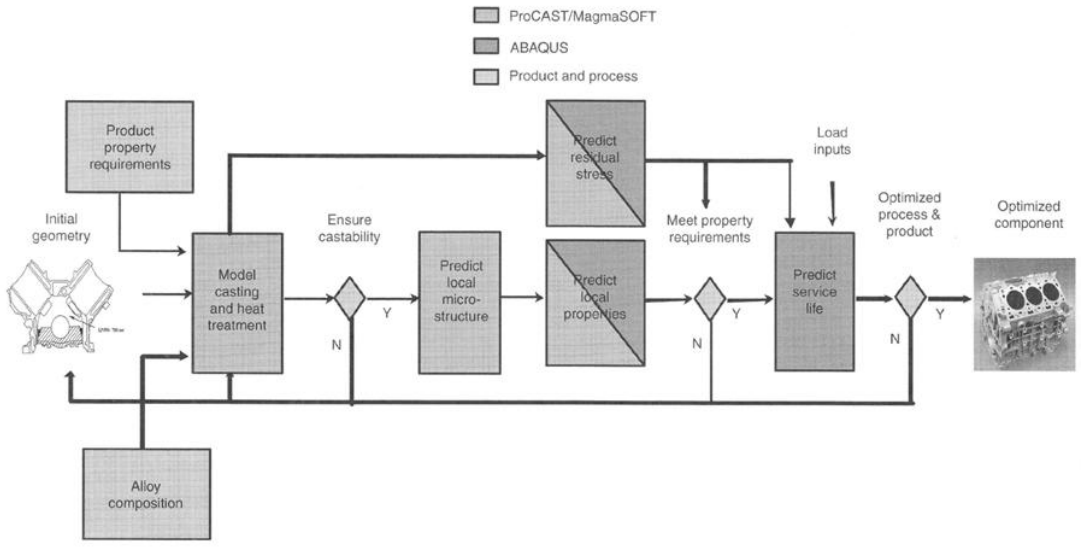


Figure 2. Virtual aluminum casting methodology flowchart [12, 15]

On the other hand, the design and manufacture of durable molds for optimized castings also requires the use of computer-assisted material selection and selection of machining processes as well as optimization of the process of heat treatment and surface protection. The choice between different surfaces treatments can be done based on the surface engineering methodology suggested in [16] and showed with own corrections in Figure 3.

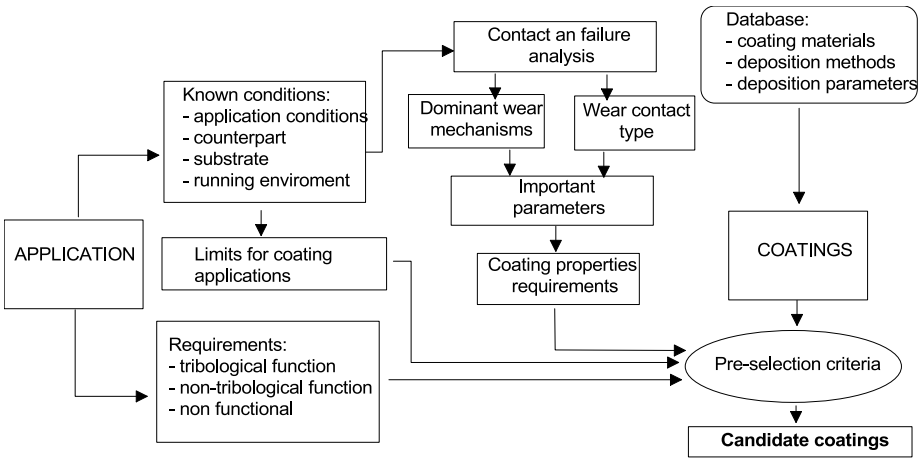


Figure 3. Coating pre-selection process

Pre-selection criteria for optimal coating or duplex surface layer can be defined at different ways, but it must include some of properties connected with substrate, some with surface layer and interface between coating and substrate as well as some comparable variables as is show in in Figure 4. The subset of selected coatings and duplex layers which fulfilled the required properties is further evaluated by laboratory conducted tribological and corrosion tests under the relevant conditions to find an appropriate surface layer for developed mold. The universal computer support programs for comparison of coatings properties and simulation of deposition process are still under development. So the application of surface engineering processes in improvement of properties of selected permanent molds is conducted as case studies.

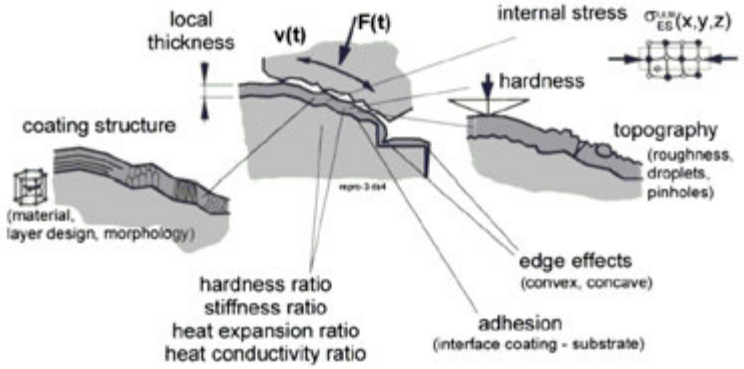


Figure 4. Important properties of the substrate and the surface modified layer [17]

In this respect, the coating properties are essentially determined by the composition and structure of the coating as well as the chemical composition, microstructure and substrate properties. For coatings applied to increase wear resistance and corrosion resistance, this relationship between coating and substrate properties is even more pronounced than other coatings. Only the optimum properties of the substrate and the coating through their

synergistic effect can be expected to significantly extend the life of the product. Therefore, prior to coating, it is necessary to adapt the technology of basic heat treatment of the substrate and subsequent modification and coating of the surface layer. Therefore, for a successful production of a product, it is necessary to keep the proper order of heat treatment procedures [8, 9, 17, 18].

## EXPERIMENTS WITH PACVD COATING DEPOSITED ON HOT WORK TOOL STEELS

Procurement of new equipment for plasma nitriding and coating process PACVD in the international IPA IIIc project "ARISE - Advanced Research, Innovation and Technology Transfer in Surface Engineering" and establishing a new Surface engineering laboratory on FMENA in University of Zagreb provided the use of modern technology applied to modification and coating metals in plasma. Deposition of hard coatings by the plasma-assisted chemical vapour deposition (PACVD) process is carried out at temperatures between 450 °C and 650 °C in an atmosphere of chemically active plasma. Multiple layers of the coating increase the hardness and toughness of the coating and its resistance to the adhesive and the abrasive wear, but also increase resistance to the thermal fatigue and high temperature corrosion. The PACVD coatings usually have the thickness between 1 to 10 µm, but a coating with smaller thickness has a better adhesion to the substrate [3, 8, 9].
For the preparation and implementation of laboratory and industrial research, the analysis of thermal, mechanical and tribological conditions in molds for pressure cast aluminum was performed. In the Granta Design software CES computer program, the choice of the most heavily loaded mold segments was carried out. In experimental investigation a two commercially available hot work tool steels X38CrMoV5-3 and X37CrMoV5-1 were used. Test samples for tribological investigations were manufactured from tool steel X37CrMoV5-1, while part of molds was manufactured from very similar tool steel X38CrMoV5-3. On testing samples and parts of molds for aluminum die-cast a conventional heat treatment, vacuum hardening and double tempering was carried out as shown in Figure 5.a After hardening and high temperature tempering the hardness value 51 ± 2 HRC was obtained on test samples and molds parts. After heat treatment, all the test samples were wet fine-ground with sandpaper and polished with diamond paste [18]. Using the selection method shown in Figure 3, the choice of coating on the surface of the mold segment was performed. For the testing of properties and behavior in the exploitation, the surface layers nitrated in plasma and duplex coatings produced by PACVD: TiN / TiCN and TiN / TiBN were chosen. This paper describes the results of the TiN / TiCN coating application. The coated samples and molds parts were plasma nitrided (at 500 °C/6 hours) and PACVD coated (at 500 °C/8 hours). The structure of PACVD coating is showed in Figure 5c.

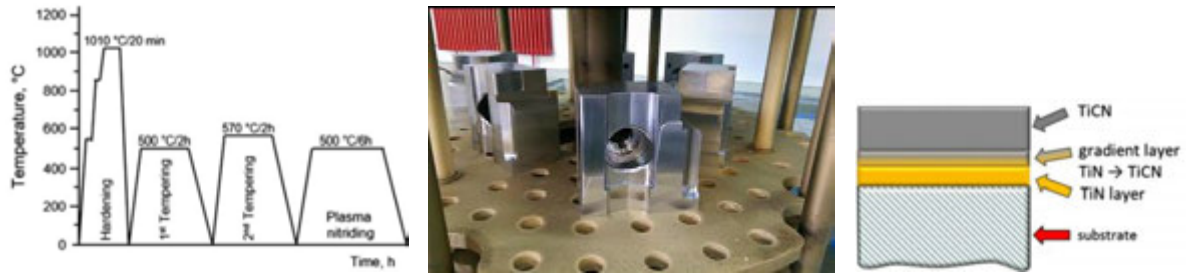


a) b) c)

Figure 5. Heat treatment and coating of the hot work tool steels [18]: a) Diagram of the base heat treatment of hot work tool steel X37CrMoV5-1, b) Tool segments for aluminum die-casting mold, c) The structure of a gradient layer TiN/TiCN coating

The surface roughness of samples was tested with five repetitions using an electromechanical device with a stylus, i.e. the TR200/210/220 surface roughness tester. The length on which the readings of the roughness parameter measurements were obtained was 4.00 mm; the Gauss filter was used for data filtering ($\lambda_c$= 0.8 mm). The thickness of the multilayer TiN/TiCN coating was determined by the calotest used on five different spots on the samples. For the thickness testing, a commercial device, TRIBOtechnic Calotester, was used. The adhesion of coatings was determined by the Rockwell-C indentation test and was validated according to the VDI 3198 method. Tool segments without coatings, only plasma nitrided segments and plasma nitrided and PACVD coated segments were incorporated into a cast-die mold and subjected to exploitation tests in manufacturer Lipovica d.o.o. The tool segments are simultaneously exposed to the same working conditions of pressure casting of aluminum radiators and the condition of their surface is monitored on a daily basis.

## RESULTS AND DISCUSSION

Test results of the surface roughness (expressed by $R_a$ and $R_z$) before and after the PACVD process are shown in Table 1.

Table 1. Roughness parameters of the tested samples before and after the deposition of the multilayer TiN/TiCN coating applied by PACVD

| Substrate | Surface layer | $\overline{Ra} \pm \sigma$, [µm] | $\overline{Rz} \pm \sigma$, [µm] |
|---|---|---|---|
| X38CrMoV5-3 | Non-coated surface | 0.043±0.002 | 0.423±0.045 |
| | Multilayer TiN/TiCN | 0.061±0.006 | 0.914±0.195 |
| X37CrMoV5-1 | Non-coated surface | 0.047±0.003 | 0.528±0.089 |
| | Multilayer TiN/TiCN | 0.086±0.013 | 1.222±0.304 |

From these results, it is observed that the initial state of low surface roughness with the maximum height less than 1 μm was achieved by fine sanding and polishing. The PACVD coating process increases the surface roughness on both steels as a result of formation coating with own roughness.

Results of the calotest showed that the thickness of the supportive TiN sublayer on the both tool steel was 0.6 ± 0.1 μm (mean value ± standard deviation). The total thickness of the TiN/TiCN coating on the X38CrMoV5-3 tool steel was 3.98 ± 0.94 μm and on the tool steel X37CrMoV5-1 the total thickness was 3.81 ± 0.55 μm.

The indents made on the multilayer coatings in the Rockwell-C indentation test are shown in Figure 6. On both coatings, one can note the delamination of the coating around the indent together with a small number of radial micro cracks. According to the VDI 3198 method, the appearance of the indents indicates slightly weaker adhesion and increased brittleness of both coatings. The weaker adhesion of HF = 3 corresponds to the acceptable class. From the results of the examination it follows that PACVD processes produced a multilayer gradient coating TiN/TiCN with acceptable adhesion and surface roughness.

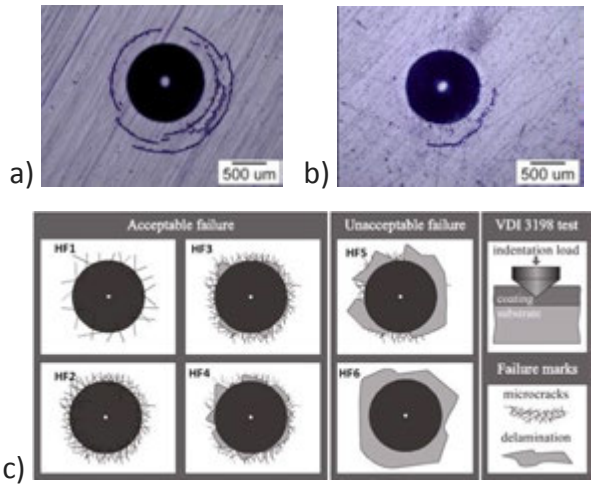


Figure 6. Micrographs of Rockwell-C indents on the multilayer PACVD TiN/TiCN coating deposited on the tool steel substrate: a) X38CrMoV5-3; b) X37CrMoV5-1, c) classification of indent due to the norm VDI 3198 method

In the exploitation investigation, the various heat treated tool segments are embedded in the same casting mold for high pressure aluminum die-casting of heating elements and exposed to casting cycles. Figure 7a shows a segment of mold for pressurized aluminum alloys coated with duplex coating TiN / TiCN. The appearance of damage and cracks on the surface of the segments will immediately become apparent on the surface of the castings, but until the end of the ARISE project, segment have withstood 60,000 spill cycles without the appearance of significant damage to the surface as was shown in Figure 7b. According to the foundry experience, the usual lifetime of untreated segments is about 30,000 leaking cycles.

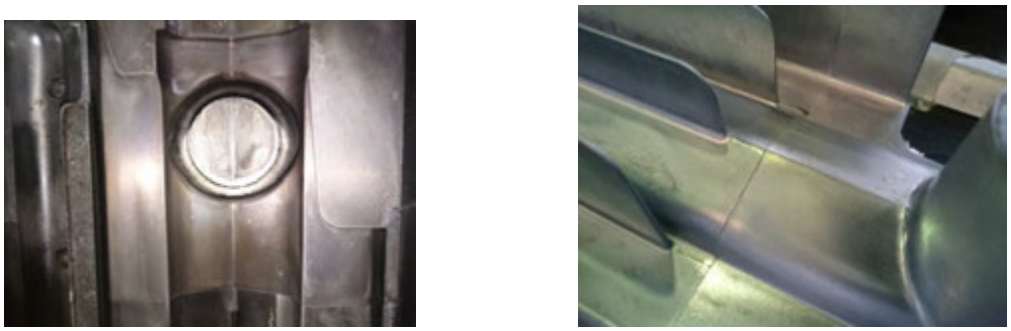

a) b)

Figure 7. Tool segment for aluminium die-casting of heating elements made from hot work tool steel X38CrMoV5-3 after 60.000 cycles: a) tool surface of duplex layer composed of a plasma nitriding and TiN/TiCN coating; b) part of surface of die-casting heating element with very good surface quality

## CONCLUSIONS

Increasing the value of castings should be done in three ways: with the addition of a new value to subsequent surface treatment by surface engineering methods, with a reduction in investment costs in tool development and with the prolongation of the service life of the tools by applying heat treatment and surface engineering procedures.
Significantly reduction in investment together with shortening of tool development time should be obtained by using a modern computer-assisted materials and process selection and optimization. The additionally possibility is using the integrated computational materials engineering simulation for development a virtual product performance analysis and manufacturing simulation before physical manufacturing starts.
Using the surface engineering methodology for surface layer design and selection a significantly increasing in wear and corrosion resistance can be obtained. Application of surface engineering processes will be successful if all specialties of materials and components or tools are taken into account in its preparation and implementation, taking into account the sequence of technological operations and the mutual impact of the previous procedure in the next operation in series. This means that the parameters of the basic heat treatment, the selection of treatment procedure and parameters of the modification and / or coating processes should be harmonized.
The availability and application of discussed procedures and computer programs enables the production of quality products with significantly greater durability and market value.

## REFERENCES

[1] T. Bell, H. Dong, Y. Sun, Realising the potential of duplex surface engineering, Tribology International, 31 (1998) 1-3, pp. 127-137.
[2] K. Holmberg, A. Matthews, Coatings Tribology: Properties, Mechanisms, Techniques and

Applications in Surface Engineering, Elsevier, Amsterdam, 2009.
[3] M. Stoiber et. al., Plasma-assisted pre-treatment for PACVD TiN coatings on tool steel, Surface and Coatings Technology, 174 -175 (2003) pp. 687-693.
[4] C. Mitterer et. al., Industrial applications of PACVD hard coatings, Surface and Coatings Technology, 163-164 (2003) pp. 716-722.
[5] C. M. Taylor, Automobile engine tribology- design considerations for efficiency and durability, Wear, 221 (1998) pp. 1-8.
[6] Th. Lampe, S. Eisenberg, E. R Cabeo, Plasma surface engineering in the automotive industry—trends and future prospectives, Surface and Coatings Technology, 174-175 (2003) pp. 1-7.
[7] C. Donnet, A. Erdemir, Historical developments and new trends in tribological and solid lubricant coatings, Surface and Coatings Technology, 180-181 (2004) pp. 76-84.
[8] M. Shengli, X. Kewei, J. Wanqi, Plasma nitrided and TiCN coated AISI H13 steel by pulsed dc PECVD and its application for hot-working dies, Surface & Coatings Technology, 191 (2005) pp. 201-205.
[9] S. Kovačić, F, Cajner, D. Landek, Wear Resistance of TiN/TiCN and TiN/TiBN Multilayer Coatings Applied on Hot Work Tool Steel, Key Eng. Materials, 674 (2016) 1, pp. 257-262.
[10] O. Durst, J. Ellermeier, C. Berger, Influence of Plasma-Nitriding and Surface Roughness on the Wear and Corrosion Resistance of Thin Films (PVD/PECVD), Surface and Coatings Technology, 203 (2008) 5-7, pp. 848-854.
[11] M. F. Ashby, Materials Selection in Mechanical Design, 3rd Edition, Elsevier, Oxford, 2005.
[12] J. E. Allison, M. Li, X. Su, Integrated Computational Materials Engineering in ASM Handbook Fundamentals of Modeling for Metals Processing, ASM International, 22A (2009) pp. 7-14.
[13] J. E. Allison, D. Backman, L Christodoulon, Integrated Computational Materials Engineering: A New Paradigm for the Global Materials Profession, JOM, 58 (2006) 11, pp. 25-27.
[15] J. E. Allison, M. Li, C. Wolverton, X. M. Su, Virtual Aluminium castings: An Industrial Application of ICME, JOM, 58 (2006) 8, pp. 28-35.
[16] D. B. Luo, V. Fridrici, Ph. Kapsa, A systematic approach for the selection of tribological coatings, Wear, 271 (2011) pp. 2132-2143.
[17] C. Frierrich, et. al., Reliable PVD coatings on components, Surface and Coatings Technology, 112 (1999) pp. 152-161.
[18] S. Kovačić, F. Cajner, D. Landek, Influence of Steel Substrate on the Properties of PACVD Gradient Multilayer TiCN Coating, Materials Performance and Characterization, 6 (2017) 5, pp. 860-870.

17th INTERNATIONAL FOUNDRYMEN CONFERENCE
Hi-tech casting solution and knowledge based engineering
Opatija, May 16th-18th, 2018
http://www.simet.hr/~foundry/

# EXPERIMENTAL AND NUMERICAL MODELING OF HETEROGENEOUS MATERIALS

**Tomislav Lesičar[1], Zdenko Tonković[1]*, Jurica Sorić[1], Predrag Čanžar[2]**

[1] University of Zagreb Faculty of Mechanical Engineering and Naval Architecture, Zagreb, Croatia
[2] Končar - Electrical Engineering Institute, Zagreb, Croatia

**Invited lecture**
*Original scientific paper*

**Abstract**

Heterogeneous and composite materials are nowadays widely used for engineering applications. Nodular cast iron is used as a material of many engineering structural components due to its high strength and ductility. The realistic description of its deformation responses demands an accurate modeling at both macroscopic and microscopic scales. In this paper experimental and numerical modeling of nodular cast iron is conducted by investigating the influence of the microstructure on the overall mechanical behaviour. In the experimental measurements, comprehensive study of the nodular cast iron fatigue behaviour is performed, for various production techniques. For numerical modeling a two-scale computational approach employing the homogenization scheme based on the small strain nonlocal continuum theory is presented. Discretization of the macro- and microstructure is performed by means of the $C^1$ continuity finite element based on the nonlocal continuum. Basic relations of the scale transition procedure, and the homogenization procedure performed at the microlevel are described. The results obtained are employed at each material point of the macroscale model predicting the structural deformation response. All algorithms derived have been embedded into the finite element program ABAQUS. The performance and accuracy of the proposed numerical method has been verified in an example, where the microstructure of a nodular cast iron is modeled by an academic representative volume element.

***Keywords**: heterogeneous materials, nodular cast iron, second-order homogenization, $C^1$ finite element, nonlocal continuum theory*

*Corresponding author (e-mail address): zdenko.tonkovic@fsb.hr

## 1 INTRODUCTION

Almost all engineering materials are heterogeneous, and referred to as multi-phase materials, composite or heterogeneous materials. From an engineering point of view, they are desirable by taking advantage of particular properties of each constituent. For example,

nodular cast iron is widely used as a material for structural components in mechanical engineering. It consists of graphite spheroids or nodules, positioned in a ductile ferritic matrix. The size, shape, spatial distribution and volume fraction of the nodules has a significant impact on the overall material properties.

In recent years study of the relations between mechanical properties of material and its microstructure became very attractive. Due to microstructural heterogeneities, size effects can be observed [1]. Unfortunately, the classical continuum theory cannot capture such effects, since it does not contain an internal length scale. Therefore, higher-order continuum theory has been proposed. Important developments in higher-order theories were achieved during the 1960's [2]. In the last few decades higher-order theory has been used as a remedy in modeling of gradient material elastoplasticity and for the damage modeling, resolving loss of ellipticity of the governing equations. For a detailed overview of the higher-order theories the reader is referred to [3]. In order to find numerical solutions of the problem described by the nonlocal theory, a higher interpolation scheme is required, satisfying $C^1$ continuity. This brings necessity for additional degrees of freedom [4], increasing structural complexity of the element [5]. There are attempts trying to avoid requirement for $C^1$ interpolations, such as [6, 7]. Unfortunately, they often result in locking and unphysical results.

To accurately predict the mechanical response of the evolving microstructure, the multiscale approach is required. Using the multiscale setting allows development of the constitutive models through application of computational homogenization methods. The computational homogenization allows incorporation of the microstructure into a standard continuum model. The macroscopic properties are determined by the homogenization process acting on the effective, homogenized sample of material called statistically Representative Volume Element (RVE) [8]. The resulting effective material is supposed to represent all macroscopic properties of the microheterogeneous structure. First-order homogenization techniques are built within the standard local continuum mechanics. Unfortunately, the first-order micro-macro computational approaches suffer from several disadvantages. Hence, the second-order computational homogenization procedure, as an extension of the classical computational homogenization has been proposed [9], employing the nonlocal continuum theory at the macroscale and local theory on the RVE. In this way, the first and the second gradient of the displacement field at the macrolevel are prescribed through the essential boundary conditions on the RVE.

In this paper, a new multiscale algorithm employing the nonlocal second-order computational homogenization is presented. The modified strain gradient elasticity theory [10], assuming the linear elastic material behaviour and small strain, has been adopted. The discretization at both scales has been performed by the $C^1$ triangular finite element derived in [11]. A consistent nonlocal homogenization scheme has been proposed. The performance and accuracy of the proposed approach has been verified on the three-point bending test. The microstructural RVE describes a nodular cast iron structure in an academic way.

The paper is organized as follows. In Section 2 experimental investigation of the nodular cast iron microstructure is described in more detail. In Section 3 basic relations of nonlocal continuum are presented, along with the finite element derivation. In Section 4, nonlocal

homogenization approach is described. The numerical example is presented in Section 5. Finally, concluding remarks are presented in Section 6.

## 2 MICROSTRUCTURAL INFLUENCE ON MATERIAL PROPERTIES OF NODULAR CAST IRON

One of highly heterogeneous materials with wide application in industry is the nodular cast iron, due to low production cost and weight reduction of the structural components. It is widely used in energy equipment and transportation and nuclear industries. The nodular cast iron consists of spheroidal graphite nodules distributed in the ferrite and/or pearlite matrix. Ductile iron with the ferritic matrix displays the lower yield and tensile strength, but higher elongation and toughness. The pearlite matrix has the opposite effect to the mechanical properties. Besides the matrix microstructure, the fatigue strength of the nodular cast iron is strongly influenced by the graphite morphology [12].
The results of experimental investigations on the mechanical behaviour of the nodular cast iron EN-GJS-400-18-LT depending on the material microstructure are contained in the previous authors' publications [13]. The cyclic deformation and fatigue behaviour under uniaxial loading of four types of cast iron produced by different techniques are considered. Herein, some results for two types of the cast iron produced by flotret (Type 200) and inmould (Type 400) techniques are presented. The graphite morphology of the casting types is shown in Fig. 1, while the microstructural data are presented in Table 1. Material type 200 produced by the flotret process has larger nodules with low density distribution than the type 400. Besides, the material type 200 has graphite nodules with the lowest circularity. On the other hand, the material type 400 produced by the inmould process has smaller ferrite grains and smaller nodules, more spherical and regular in shape than those in the material type 200.

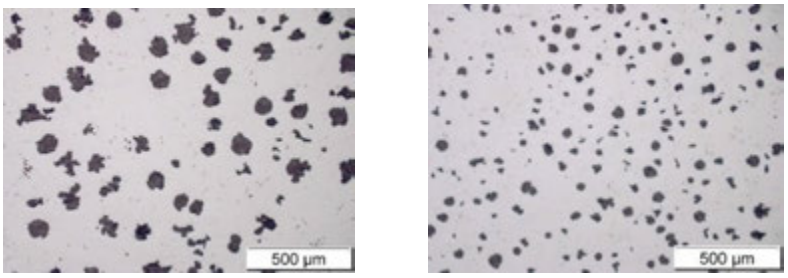


(a) (b)

Figure 1. The microstructure of the nodular cast iron: (a) type 200 and (b) type 400 [14]

Table 1. Metallographic characteristics of nodular cast iron [14]

| Material type | Graphite nodules | | | Pearlite | |
|---|---|---|---|---|---|
| | Number ($mm^{-2}$) | Average size ($\mu m^2$) | Circularity | Area ($\mu m^2$) | % |
| 200 | 57 | 1 416.80 | 0.57 | 49 925.41 | 4.99 |
| 400 | 81 | 837.09 | 0.66 | 69726.31 | 6.97 |

The tests have been conducted on the fatigue testing machines Walter Bai LFV 50-HH and MESSPHYSIK BETA 50-5 with a servo-hydraulic control system and a load capacity of ±50 kN. Fig. 2 shows the representative stress–strain hysteresis loops obtained from the symmetrical tests on a cylindrical specimen prepared according to the ASTM E606 standard. Both types of material have a similar hardening rate and their major difference is achieving maximum stress in first and all subsequent half-cycles.

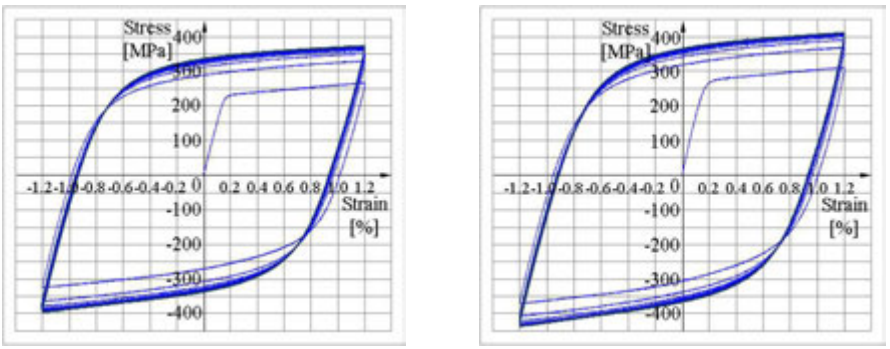


(a) (b)

Figure 2. Stress–strain hysteresis loops for: (a) type 200 and (b) type 400 [14]

The next part is concerned with the fatigue crack initiation and propagation testing. Fig. 3 shows the cracked specimen with exposed nodular cast iron microstructure. As can be seen, the direction of crack growth is towards the graphite nodules which act as a crack arrester. The fatigue cracks propagate in a zig–zag manner in the ferrite matrix but linearly in the pearlite matrix. In addition, the fatigue cracks always start at the interface between the graphite nodule and the surrounding ferrite matrix.

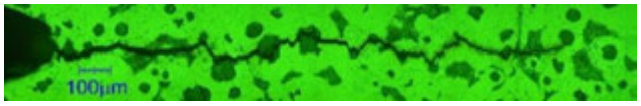


Figure 3. Microstructural crack exposure [14]

Fig. 4 illustrates the variation of the crack length ($a$) versus the applied cycles of loading ($N$) for different load ratios ($R$). The fatigue load is applied in a sinusoidal form with the frequency of 10Hz, defined by the maximum load of 12kN and the load ratio $R$. The specimens are subjected to two different loading regimes ($R$=0.1 and $R$=0.5). The crack length is measured in real time by a measuring system Aramis 4M using a novel technique proposed in [15]. For the load ratio $R$=0.1, there is the most pronounced difference in material types considering crack propagation. Material type 200 shows the least crack resistance, while the material type 400 lasts approximately 2.5 times longer. It can be concluded that the material with a large number of smaller and regularly shaped graphite nodules has larger fatigue threshold, compared to a small number of large irregularly shaped graphite nodules [16].

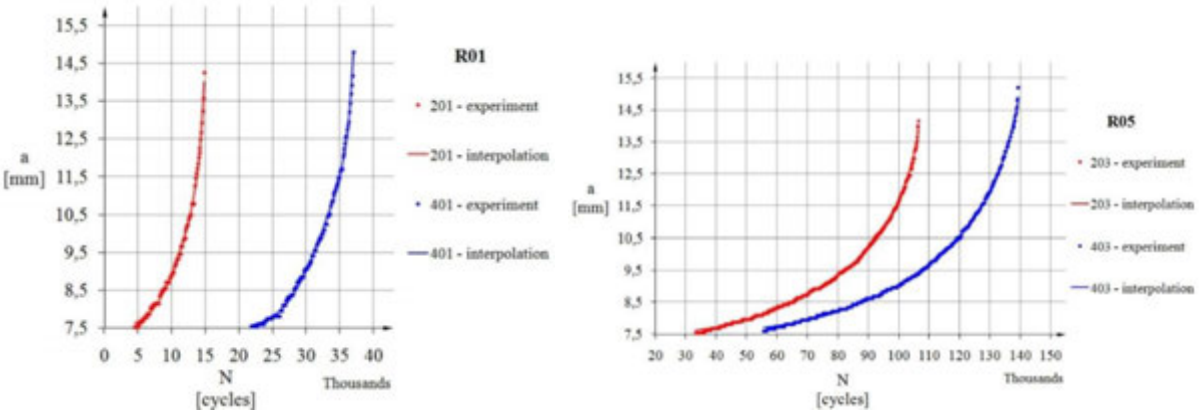


(a) (b)

Figure 4. Crack length *a* versus applied cycles of loading *N* for: a) *R*=0.1 and b) *R*=0.5 load ratio [17]

From the presented results, it can be concluded that the morphology, size and distribution of graphite particles do not have significant influence on cyclic hardening, but they play a great role in the crack initiation and propagation process.

## 3 $C^1$ FINITE ELEMENT FORMULATION

### 3.1 Basic relations of the nonlocal continuum

In nonlocal theory, besides the strain tensor $\boldsymbol{\varepsilon}$ which is defined as symmetric gradient of the displacement field $\mathbf{u}$, the second-order strain $\boldsymbol{\eta}$ is introduced. $\boldsymbol{\eta}$ is the third-order tensor, representing gradient of $\boldsymbol{\varepsilon}$

$$\boldsymbol{\eta} = \nabla \otimes \boldsymbol{\varepsilon} . \tag{1}$$

The variation of the strain energy density function is expressed as

$$\delta W = \frac{\partial W}{\partial \boldsymbol{\varepsilon}} : \delta \boldsymbol{\varepsilon} + \frac{\partial W}{\partial \boldsymbol{\eta}} \vdots \delta \boldsymbol{\eta} = \boldsymbol{\sigma} : \delta \boldsymbol{\varepsilon} + \boldsymbol{\mu} \vdots \delta \boldsymbol{\eta} . \tag{2}$$

In Eq. (2), $\boldsymbol{\sigma}$ and $\boldsymbol{\mu}$ represent the Cauchy and the double stress tensors, respectively. Using straightforward mathematical manipulations, as explained in [11], the internal work variation can be defined as

$$\begin{aligned} \delta W^{\text{int}} = & \int_A \left[ \mathbf{n} \cdot \left( \boldsymbol{\sigma} - \left( \nabla \cdot \boldsymbol{\mu} \right) \right) \cdot \delta \mathbf{u} \right] \mathrm{d}A + \int_A \left[ \left( \nabla^A \cdot \mathbf{n} \right) \otimes \mathbf{n} \cdot \left( \mathbf{n} \cdot \boldsymbol{\mu} \right) \cdot \delta \mathbf{u} \right] \mathrm{d}A - \\ & \int_A \left[ \nabla^A \cdot \left( \mathbf{n} \cdot \boldsymbol{\mu} \right) \cdot \delta \mathbf{u} \right] \mathrm{d}A - \int_V \left[ \nabla \cdot \left( \boldsymbol{\sigma} - \left( \nabla \cdot \boldsymbol{\mu} \right) \right) \cdot \delta \mathbf{u} \right] \mathrm{d}V + \int_A \left[ \left( \mathbf{n} \cdot \boldsymbol{\mu} \cdot \mathbf{n} \right) \cdot \left( D \otimes \left( \delta \mathbf{u} \right) \right) \right] \mathrm{d}A. \end{aligned} \tag{3}$$

In Eq. (3), $\mathbf{n}$ represents unit outward normal, while $\nabla^A$ and $D$ denote surface and normal gradient operators, respectively. The variation of the external work is written in the form

$$\delta W^{\text{ext}} = \int_A (\mathbf{t}\cdot\delta\mathbf{u})\,\mathrm{d}A + \int_A \left[\boldsymbol{\tau}\cdot\left(D\otimes(\delta\mathbf{u})\right)\right]\mathrm{d}A, \tag{4}$$

with $\mathbf{t}$ and $\boldsymbol{\tau}$ denoting the surface traction and the double surface traction, respectively

$$\mathbf{t} = \mathbf{n}\cdot\left(\boldsymbol{\sigma} - (\nabla\cdot\boldsymbol{\mu})\right) + \left(\nabla^A\cdot\mathbf{n}\right)\otimes\mathbf{n}\cdot(\mathbf{n}\cdot\boldsymbol{\mu}) - \nabla^A\cdot(\mathbf{n}\cdot\boldsymbol{\mu}),\ \boldsymbol{\tau} = \mathbf{n}\cdot\boldsymbol{\mu}\cdot\mathbf{n}. \tag{5}$$

From the principle of virtual work, the equilibrium equation is derived

$$\nabla\cdot\left(\boldsymbol{\sigma} - (\nabla\cdot\boldsymbol{\mu})\right) = \mathbf{0}. \tag{6}$$

For more details on the derivation of the aforementioned relations, refer to [18].

### 3.2 Finite element derivation

The nonlocal theory is implemented into finite element method by means of the displacement-based $C^1$ triangular finite element, and embedded into FE software ABAQUS. The proposed strain gradient finite element is shown in Fig. 5.

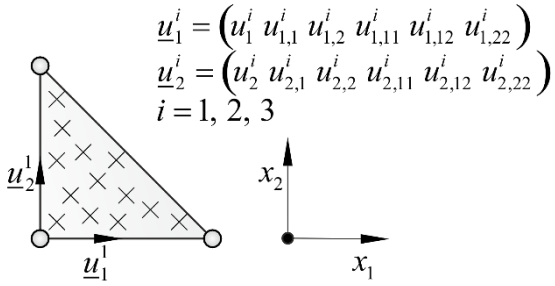


Figure 5. $C^1$ triangular finite element

The element consists of three nodes and twelve degrees of freedom (DOF) per node. The nodal degrees of freedom are two displacements and their first and second order derivatives with respect to the Cartesian coordinates. The element displacement field is approximated by the condensed fifth-order polynomial. The weak form of Eq. (6) expressed through the principle of virtual work may be presented as

$$\int_A (\boldsymbol{\sigma}:\delta\boldsymbol{\varepsilon} + \boldsymbol{\mu}\vdots\delta\boldsymbol{\eta})\,\mathrm{d}A = \int_s (\mathbf{t}\cdot\delta\mathbf{u})\,\mathrm{d}s + \int_s \left[\mathbf{T}:\left(\nabla\otimes(\delta\mathbf{u})\right)\right]\mathrm{d}s, \tag{7}$$

where *s* represents closed boundary line of the surface area *A*. Also, in the second integral term on the right side of (7), the double traction tensor $\mathbf{T}=\boldsymbol{\tau}\otimes\mathbf{n}$, is introduced. The displacement field $\mathbf{u}$ inside an element may be expressed by well-known relation as

$$\mathbf{u}=\mathbf{N}\mathbf{v}. \tag{8}$$

In Eq. (8), $\mathbf{N}$ is the shape functions matrix, and $\mathbf{v}$ is the vector of the nodal degrees of freedom. The strain $\boldsymbol{\varepsilon}$ and the higher-order displacement gradient $\boldsymbol{\eta}$ are obtained by the shape function derivatives using the following relations

$$\boldsymbol{\varepsilon}=\begin{bmatrix}\varepsilon_{11}\\ \varepsilon_{22}\\ 2\varepsilon_{12}\end{bmatrix}=\mathbf{B}_{\varepsilon}\mathbf{v},\ \boldsymbol{\eta}=\begin{bmatrix}\eta_{111}\\ \eta_{222}\\ \eta_{221}\\ \eta_{112}\\ 2\eta_{121}\\ 2\eta_{212}\end{bmatrix}=\begin{bmatrix}u_{1,11}\\ u_{2,22}\\ u_{1,22}\\ u_{2,11}\\ 2u_{1,21}\\ 2u_{2,12}\end{bmatrix}=\mathbf{B}_{\eta}\mathbf{v}, \tag{9}$$

where $\mathbf{B}_{\varepsilon}$ and $\mathbf{B}_{\eta}$ are the matrices containing appropriate interpolation polynomials derivatives. For solving of relation (7) in an incrementally-iterative procedure, the constitutive updates of the stress and double stress are computed by the linearized incremental constitutive relations

$$\Delta\boldsymbol{\sigma}=\mathbf{C}_{\sigma\varepsilon}:\Delta\boldsymbol{\varepsilon}+\mathbf{C}_{\sigma\eta}\vdots\Delta\boldsymbol{\eta},\ \Delta\boldsymbol{\mu}=\mathbf{C}_{\mu\varepsilon}:\Delta\boldsymbol{\varepsilon}+\mathbf{C}_{\mu\eta}\vdots\Delta\boldsymbol{\eta}. \tag{10}$$

Herein $\mathbf{C}_{\sigma\varepsilon}$, $\mathbf{C}_{\sigma\eta}$, $\mathbf{C}_{\mu\varepsilon}$ and $\mathbf{C}_{\mu\eta}$ are the consistent material tangent stiffness matrices providing correlations among corresponding stress and strain variables. Using the standard finite element mathematical procedures, the usual linearized finite element equation is obtained

$$\mathbf{K}\mathbf{v}=\mathbf{F}_{\mathrm{e}}-\mathbf{F}_{\mathrm{i}}. \tag{11}$$

In this paper Aifantis form of the constitutive behaviour has been adopted [19], where the stress tensors are defined as

$$\Delta\boldsymbol{\sigma}=\mathbf{C}:\Delta\boldsymbol{\varepsilon},\ \Delta\boldsymbol{\mu}_{x_1}=l^2\left(\mathbf{C}:\Delta\boldsymbol{\varepsilon}_{x_1}\right),\ \Delta\boldsymbol{\mu}_{x_2}=l^2\left(\mathbf{C}:\Delta\boldsymbol{\varepsilon}_{x_2}\right). \tag{12}$$

In the constitutive relations (12), $\boldsymbol{\varepsilon}_{x_1}$ and $\boldsymbol{\varepsilon}_{x_2}$ represent strain gradients with respect to the Cartesian coordinates $x_1$ and $x_2$, while $\boldsymbol{\mu}_{x_1}$ and $\boldsymbol{\mu}_{x_2}$ are their work conjugates.

## 4 SCALE TRANSITION METHODOLOGY

In the presented scheme, the microstructure is described by the strain gradient elasticity theory assuming the linear elastic material behaviour and the small strains. In the following, the subscript "m" is appointed to the microlevel variables and the subscript "M" represents the macrolevel quantities.

### 4.1 Macro to micro scale transition

In the macro-to-micro transition RVE displacement field is depending on the macroscale displacement gradients, expressed as

$$\mathbf{u}_{\mathrm{m}} = \boldsymbol{\varepsilon}_{\mathrm{M}} \cdot \mathbf{x} + \frac{1}{2}\left[\mathbf{x} \cdot \left(\nabla \otimes \boldsymbol{\varepsilon}_{\mathrm{M}}\right) \cdot \mathbf{x}\right] + \mathbf{r}\,. \tag{13}$$

In Eq. (13), $\mathbf{r}$ represents the microfluctuation displacement field. The microfluctuations are short-wavelength displacements representing contribution of the microconstituents to the macrolevel displacement field. As known, the volume average of the microscale quantities must be equal to their macroscale conjugates. Enforcing this principle between the macrolevel and microlevel strains, the microfluctuation constraints arise

$$\frac{1}{V}\int_{\Gamma}\left(\mathbf{n} \otimes \mathbf{r}\right)\mathrm{d}\Gamma = \mathbf{0}\,,\ \frac{1}{V}\int_{\Gamma}\left(\mathbf{n} \otimes \left(\nabla_{\mathrm{m}} \otimes \mathbf{r}\right)\right)\mathrm{d}\Gamma = \mathbf{0}\,, \tag{14}$$

where $\Gamma$ represents the RVE boundary, as shown in Fig. 6. Enforcement of the constraints (14) is easily achieved by means of the appropriate boundary conditions on the RVE. In this paper gradient generalized periodic boundary conditions will be utilized. In the case of periodicity assumption, it is easy to prove that (14) is fulfilled. Eq. (13) can be reformulated in matrix form to express the nodal degrees of freedom of an *i*th node along the RVE boundaries, which gives the following expression

$$\mathbf{u}_i = \mathbf{D}_i^T \boldsymbol{\varepsilon}_{\mathrm{M}} + \left(\mathbf{H}_1^T\right)_i \left(\boldsymbol{\varepsilon}_{,1}\right)_{\mathrm{M}} + \left(\mathbf{H}_2^T\right)_i \left(\boldsymbol{\varepsilon}_{,2}\right)_{\mathrm{M}}. \tag{15}$$

In (15), $\mathbf{D}$, $\mathbf{H}_1$ and $\mathbf{H}_2$ are the coordinate matrices.

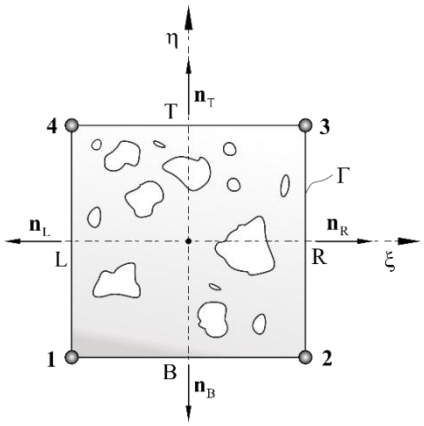


Figure 6. Representative Volume Element

### 4.2 Micro to macro scale transition

After resolving the microlevel boundary value problem, the stress tensors and the constitutive behaviour are required for the macroscale computation. In the scale transition, the energy equivalence principle is fulfilled through the Hill-Mandel condition

$$\frac{1}{V}\int_V \left(\boldsymbol{\sigma}_{\mathrm{m}} : \delta\boldsymbol{\varepsilon}_{\mathrm{m}} + \boldsymbol{\mu}_{\mathrm{m}} \vdots \left(\nabla_{\mathrm{m}} \otimes \delta\boldsymbol{\varepsilon}_{\mathrm{m}}\right)\right) \mathrm{d}V = \boldsymbol{\sigma}_{\mathrm{M}} : \delta\boldsymbol{\varepsilon}_{\mathrm{M}} + \boldsymbol{\mu}_{\mathrm{M}} \vdots \left(\nabla \otimes \delta\boldsymbol{\varepsilon}_{\mathrm{M}}\right). \tag{16}$$

a lengthy procedure, explained in [20], one can obtain homogenized stress tensors relations

$$\boldsymbol{\sigma}_{\mathrm{M}} = \frac{1}{V}\int_V \boldsymbol{\sigma}_{\mathrm{m}}\, \mathrm{d}V\,,\ \boldsymbol{\mu}_{\mathrm{M}} = \frac{1}{V}\int_V \left(\boldsymbol{\mu}_{\mathrm{m}} + \boldsymbol{\sigma}_{\mathrm{m}} \otimes \mathbf{x}\right) \mathrm{d}V\,. \tag{17}$$

On the macroscale, the generalized constitutive relations are derived as

$$\begin{aligned}
\Delta\boldsymbol{\sigma}_{\mathrm{M}} &= \mathbf{C}_{\sigma\varepsilon} : \Delta\boldsymbol{\varepsilon}_{\mathrm{M}} + \mathbf{C}_{\sigma\varepsilon_{x_1}} \vdots \Delta\left(\boldsymbol{\varepsilon}_{,1}\right)_{\mathrm{M}} + \mathbf{C}_{\sigma\varepsilon_{x_2}} \vdots \Delta\left(\boldsymbol{\varepsilon}_{,2}\right)_{\mathrm{M}}\,,\\
\Delta\left(\boldsymbol{\mu}_{x_1}\right)_{\mathrm{M}} &= \mathbf{C}_{\mu_{x_1}\varepsilon} : \Delta\boldsymbol{\varepsilon}_{\mathrm{M}} + \mathbf{C}_{\mu_{x_1}\varepsilon_{x_1}} \vdots \Delta\left(\boldsymbol{\varepsilon}_{,1}\right)_{\mathrm{M}} + \mathbf{C}_{\mu_{x_1}\varepsilon_{x_2}} \vdots \Delta\left(\boldsymbol{\varepsilon}_{,2}\right)_{\mathrm{M}}\,,\\
\Delta\left(\boldsymbol{\mu}_{x_2}\right)_{\mathrm{M}} &= \mathbf{C}_{\mu_{x_2}\varepsilon} : \Delta\boldsymbol{\varepsilon}_{\mathrm{M}} + \mathbf{C}_{\mu_{x_2}\varepsilon_{x_1}} \vdots \Delta\left(\boldsymbol{\varepsilon}_{,1}\right)_{\mathrm{M}} + \mathbf{C}_{\mu_{x_2}\varepsilon_{x_2}} \vdots \Delta\left(\boldsymbol{\varepsilon}_{,2}\right)_{\mathrm{M}}\,.
\end{aligned} \tag{18}$$

Accordingly, the nine constitutive operators are derived by the static condensation procedure, as explained in [20]. The homogenized constitutive matrices are expressed through the condensed RVE stiffness $\tilde{\mathbf{K}}_{\mathrm{bb}}$ and the coordinate matrices as

$$\mathbf{C}_{\sigma\varepsilon}=\frac{1}{V}\mathbf{D}\tilde{\mathbf{K}}_{\mathrm{bb}}\mathbf{D}^{T},\ \mathbf{C}_{\sigma\varepsilon_{x_1}}=\frac{1}{V}\mathbf{D}\tilde{\mathbf{K}}_{\mathrm{bb}}\mathbf{H}_1^{T},\ \mathbf{C}_{\sigma\varepsilon_{x_2}}=\frac{1}{V}\mathbf{D}\tilde{\mathbf{K}}_{\mathrm{bb}}\mathbf{H}_2^{T},$$
$$\mathbf{C}_{\mu_{x_1}\varepsilon}=\frac{1}{V}\mathbf{H}_1\tilde{\mathbf{K}}_{\mathrm{bb}}\mathbf{D}^{T},\ \mathbf{C}_{\mu_{x_1}\varepsilon_{x_1}}=\frac{1}{V}\mathbf{H}_1\tilde{\mathbf{K}}_{\mathrm{bb}}\mathbf{H}_1^{T},\ \mathbf{C}_{\mu_{x_1}\varepsilon_{x_2}}=\frac{1}{V}\mathbf{H}_1\tilde{\mathbf{K}}_{\mathrm{bb}}\mathbf{H}_2^{T},\tag{19}$$
$$\mathbf{C}_{\mu_{x_2}\varepsilon}=\frac{1}{V}\mathbf{H}_2\tilde{\mathbf{K}}_{\mathrm{bb}}\mathbf{D}^{T},\ \mathbf{C}_{\mu_{x_2}\varepsilon_{x_1}}=\frac{1}{V}\mathbf{H}_2\tilde{\mathbf{K}}_{\mathrm{bb}}\mathbf{H}_1^{T},\ \mathbf{C}_{\mu_{x_2}\varepsilon_{x_2}}=\frac{1}{V}\mathbf{H}_2\tilde{\mathbf{K}}_{\mathrm{bb}}\mathbf{H}_2^{T}.$$

## 5 NUMERICAL EXAMPLE

The presented micro-macro procedure is verified on a problem of three-point bending test. The deformed macromodel with boundary conditions is presented in Fig. 7. The dimensions of the test specimen are $100\times20\times10\,\mathrm{mm}$ with a notch radius of 0.08 mm according to the standard ASTM E1820 and used from [14]. The support-span is 79 mm and consists of two rigid support rollers with a diameter of 8 mm.

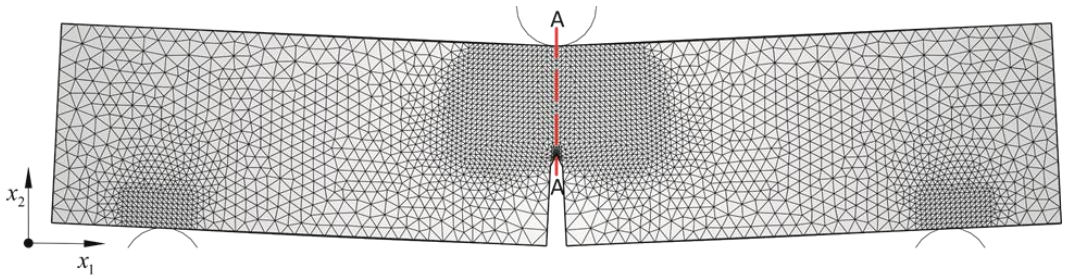


Figure 7. Three-point bending test specimen

The force of 10 kN has been applied over the loading roller. Material considered in the example is an academic interpretation of the linear elastic nodular cast iron with 13% of porosities. The Young's modulus of the matrix is 210 GPa and the Poisson's ratio is set to 0.3. The porosities represent graphite nodules, which are omitted, due to their negligible stiffness. The microstructure is represented by the RVE of the side length $L=0.2\,\mathrm{mm}$, as shown in Fig. 9(a). The constant discretization mesh has been kept along the red line A-A displayed in Fig. 7. The material constitutive matrices are computed by the homogenization prior to the analysis. Since only linear elastic behaviour is considered, the stress tensors are calculated according to relations (18). Only a few elements in front of the notch inside the red line in Fig. 8 are computed in the multiscale setting attaching the RVE to their material points.

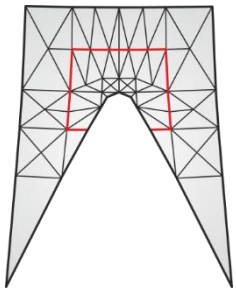

Figure 8. Mesh around notch root

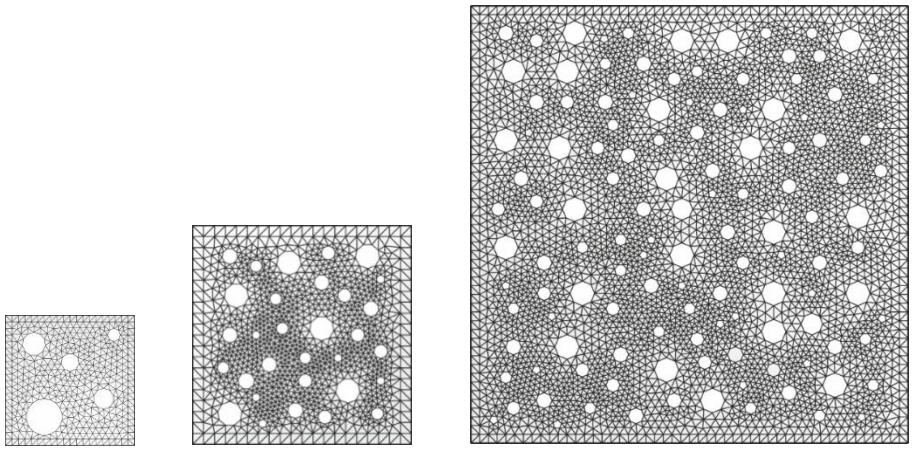


Figure 9. RVE with side length: (a) 0.2 mm, (b) 0.5 mm, (c) 1 mm

To prove that the RVE in Fig. 9(a) is statistically representative, two larger RVEs, with side lengths $L = 0.5\,\mathrm{mm}$ and $L = 1\,\mathrm{mm}$ have been considered (Figs. 9 (b) and (c)). Due to nonlocality effects induced by the RVE size, to ensure comparability, the appropriate combination of the RVE size and microstructural parameter $l$ has been chosen, as discussed in [20]. In the Figs. 10-12 the distribution of the relevant displacement gradient in front of the notch, along the line A-A is presented. In these diagrams, the ordinate represents the distance from the notch tip in the vertical direction, denoted as *H.* For the bending pattern exhibited here the dominant gradients of displacements are $u_{1,1}$ which opens the notch, $u_{1,21}$ describing trapezoidal deformed shape and $u_{2,11}$ representing curvature. The multiple analyses have been conducted for various values of the microstructural parameter $l$. As expected, the highest gradients appear in the vicinity of the notch, due to the geometrical discontinuity. Moving away from the notch tip the peak areas the gradients rapidly drop and disappear in the inner part of the specimen. With the increase of $l$, the general behaviour is preserved, but the stiffness of the material is increased due to larger nonlocal influence. Furthermore, Fig. 13 shows Von Mises stress on the RVE of side length 1 mm located at the notch tip for $l^2 = 0\,\mathrm{mm}^2$. On this RVE the gradient displacement boundary conditions are utilized. It can be seen that the RVE is elongated. Due to the mixed second-order derivative

$u_{1,21}$, the trapezoidal deformation mode is visible. The curvature, which is the result of $u_{2,11}$ is not expressed in large extent, but it is observable. Also, the stress concentrations around pores representing the graphite nodules can be observed.

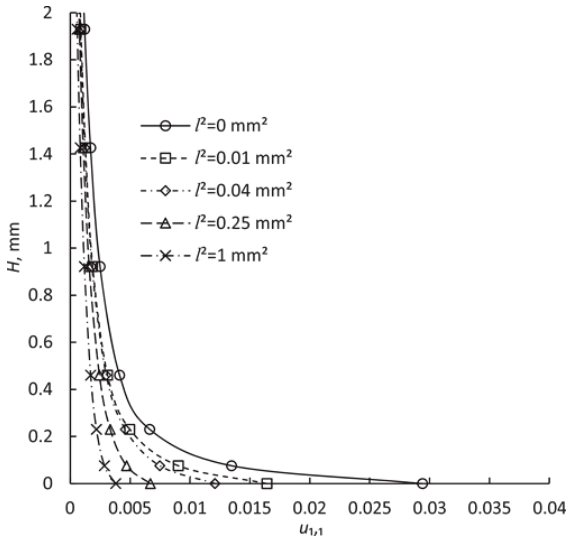


Figure 10. Distribution of $u_{1,1}$ along line A-A

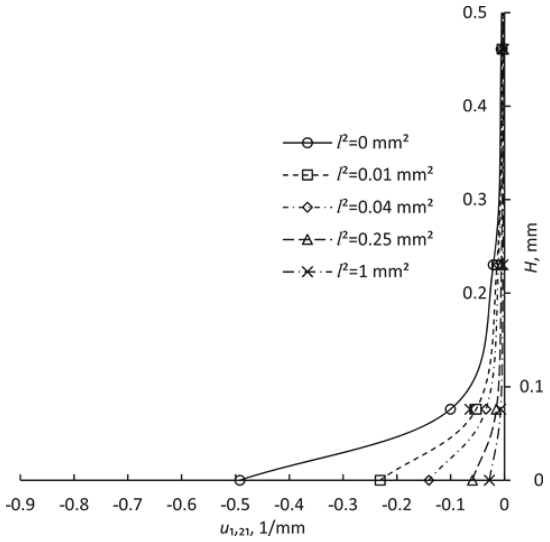


Figure 11. Distribution of $u_{1,21}$ along line A-A

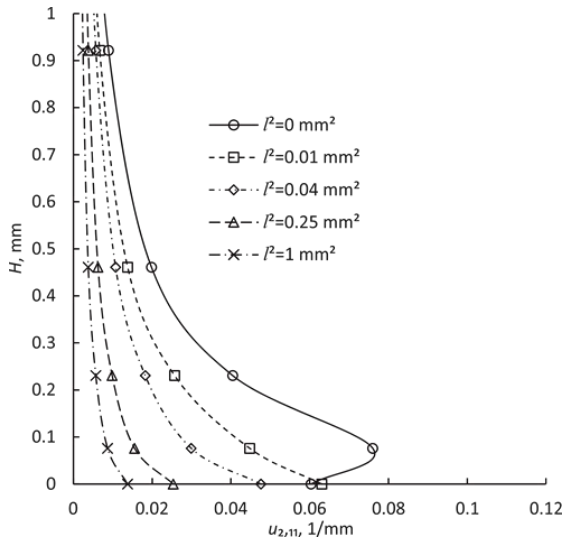


Figure 12. Distribution of $u_{2,11}$ along line A-A

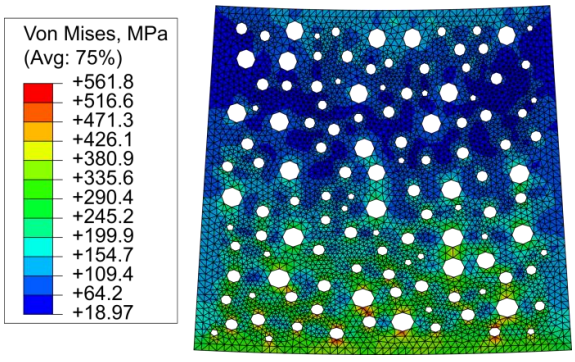


Figure 13. Distribution of Von Mises stress

## 6 CONCLUSION

The paper presents a numerical approach for modeling of heterogeneous engineering materials. The nodular cast iron, which is widely used in engineering structural components, is briefly studied. It is shown that influence of the heterogeneity represented by graphite nodules has significant influence on the load carrying capacity. For precise numerical modeling, consideration of both macro- and microscale is required. The second-order computational homogenization scheme employing the strain gradient elasticity theory at macro- and microlevel is presented. The formulation of the nonlocal theory is embedded into the finite element framework using the $C^1$ continuity three node triangular plane strain finite element. All algorithms developed are implemented into the FE software ABAQUS. The capabilities of the presented procedure are tested on the three-point bending test. The influence of the RVE size as well as the microstructural parameter on the material behaviour are analysed and discussed.

## REFERENCES

[1] N. A. Fleck, J. W. Hutchinson, A phenomenological theory for strain gradient effects in plasticity, J Mech Phys Solids, 41 (1993) 12, pp. 1825-57.
[2] R. D. Mindlin, H. F. Tiersten, Effects of couple-stresses in linear elasticity, Arch Ration Mech Anal, 11 (1962) 1, pp. 415-48.
[3] G. A. Maugin, A. V. Metrikine, Mechanics of Generalized Continua, (Maugin G. A, Metrikine A. V, editors), Advances in Mechanics and Mathematics, Vol. 21, Springer, 2010.
[4] J. H. Argyris, I. Fried, D. W. Scharpf, The TUBA family of plate elements for the matrix displacement method, 1968.
[5] R. Clough, J. Tocher, Finite element stiffness matrices for analysis of platebending, Finite Elem stiffness matrices Anal plate Bend, 1965, pp. 515-45.
[6] H. Askes, T. Bennett, E. C. Aifantis, A new formulation and C0-implementation of dynamically consistent gradient elasticity, Int J Num. Meth. Eng, 72 (2007) 1, pp. 111-26.
[7] J. Y. Shu , W. E. King, N. A. Fleck, Finite elements for materials with strain gradient effects, Int J Numer Methods Eng, 44 (1999) 3, pp. 373-91.
[8] M. Stroeven, H. Askes, Lj. Sluys, Numerical determination of representative volumes for granular materials, Comput Methods Appl Mech Eng, 193 (2004) 30-32, pp. 3221-38.
[9] O. van der Sluis, P. H. J. Vosbeek, P. J. G. Schreurs, H. E. H. Mei, Homogenization of heterogeneous polymers, Int J Solids Struct, 36 (1999) 21, pp. 3193-214.
[10] C. Ru, E. Aifantis, A simple approach to solve boundary-value problems in gradient elasticity, Acta Mechanica, 101 (1993) 1-4, pp. 59-68.
[11] T. Lesičar, Z. Tonković, J. Sorić, A second-order two-scale homogenization procedure using C1 macrolevel discretization, Comput Mech, 54 (2014) 2, pp. 425-441.

[12] N. Costa, N. Machado, F. S. Silva, Influence of Graphite Nodules Geometrical Features on Fatigue Life of High-Strength Nodular Cast Iron, J Mater Eng Perform, 17 (2008) 3, pp. 352-62.
[13] P. Čanžar, Z. Tonković, Nodular Cast Iron – Fatigue Crack Measurement and Simulation, Key Eng Mater, 577-578 (2014), pp. 473-476.
[14] P. Čanžar, Z. Tonković, J. Kodvanj, Microstructure influence on fatigue behaviour of nodular cast iron, Mater Sci Eng A, 556 (2012) 0, pp. 88-99.
[15] P. Čanžar, Experimental and Numerical Modelling of Fatigue Behaviour of Nodular Cast Iron, Faculty of Mechanical Engineering and Naval Architecture, University of Zagreb, PhD Thesis, 2012 (in Croatian).
[16] G. Hütter, L. Zybell, M. Kuna, Micromechanisms of fracture in nodular cast iron: From experimental findings towards modeling strategies – A review, Eng Fract Mech, 144 (2015) pp. 118-41.
[17] P. Čanžar, Z. Tonković, A. Bakić, J. Kodvanj, Experimental and Numerical Investigation of Fatigue Behaviour of Nodular Cast Iron for Wind Turbine Applications, Key Eng Mater, 488-489 (2011) pp. 182-185.
[18] T. Lesičar, J. Sorić, Z. Tonković, Large strain, two-scale computational approach using $C^1$ continuity finite element employing a second gradient theory, Comput Methods Appl Mech Eng, 298 (2016) pp. 303-324.
[19] E. C. Aifantis, Strain gradient interpretation of size effects, Int J Fract, 95 (1999) 1-4, pp. 299-314.
[20] T. Lesičar, Z. Tonković, J. Sorić, Two-scale computational approach using strain gradient theory at microlevel, Int J Mech Sci, 126 (2017) pp. 67-78.

**Acknowledgements**

The work has been supported in part by Croatian Science Foundation under the project "Multiscale Numerical Modeling of Material Deformation Responses from Macro- to Nanolevel" (2516).

17th INTERNATIONAL FOUNDRYMEN CONFERENCE
Hi-tech casting solution and knowledge based engineering
Opatija, May 16th-18th, 2018
http://www.simet.hr/~foundry/

# EVALUATION OF MICROSTRUCTURE AND TRANSFORMATION TEMPERATURES OF THE Cu-Al-Mn SHAPE MEMORY ALLOYS

**Dragan Manasijević[1]*, Tamara Holjevac Grgurić[2], Ljubiša Balanović[1], Milan Gorgievski[1], Uroš Stamenković[1], Nikola Kostić[1], Mirko Gojić[2]**

[1] University of Belgrade Technical Faculty in Bor, Bor, Serbia
[2] University of Zagreb Faculty of Metallurgy, Sisak, Croatia

**Invited lecture**
*Original scientific paper*

**Abstract**

Four ternary Cu-Al-Mn shape memory alloys with 10.0-13.4 wt.% of aluminium and 3.6-7.8 wt.% of manganese were prepared by arc melting. Microstructures of the bulk alloys were investigated in the as-prepared state and after homogenization annealing at 850 °C followed by slow cooling using SEM-EDS technique. Transformation temperatures of the investigated alloys were analyzed using DSC technique. The results of present study represent contribution to the better understanding of the properties of investigated alloys in different thermal conditions.

***Keywords***: *shape memory alloy, Cu-Al-Mn alloy, microstructure, martensitic transformation*

*Corresponding author (e-mail address): *dmanasijevic@tfbor.bg.ac.rs*

## INTRODUCTION

Shape memory alloys (SMAs) are metallic materials which exhibit the ability to return to some previously defined shape when subject to the appropriate treatment [1]. SMAs are often used as sensors, actuators, pipe couplings, high damping materials and in smart devices and structures [2]. The main types of these alloys are Ni-Ti alloys, Cu-based and Fe-based alloys [1,3]. Cu-based shape memory alloys (SMAs) possess high electrical and thermal conductivity, low cost and are easier to produce than Ni-Ti-based SMAs [4,5]. Among several Cu-based SMAs, Cu-Al-Mn ternary alloys are characterized by excellent ductility which makes them commercially attractive [6].
The shape memory effect is based on martensitic transformation (MT) which is a diffusionless and reversible solid state phase transformation [5,7,8]. It occurs between the high-temperature austenite phase and the low-temperature martensite phase [5,7,8].

During cooling, the martensitic transformation (MT) starts at a temperature $M_s$ (martensite start) and continues to evolve until a temperature $M_f$ (martensite finish) is reached. Similarly, during the heating cycle, the reverse transformation (martensite-to-austenite) begins at the temperature $A_s$ (austenite start), and ends at $A_f$ (austenite finish) when the material is fully austenite [8].
In this work four Cu-Al-Mn alloys with 10.0-13.4 wt.% of aluminium and 3.6-7.8 wt.% of manganese were prepared by arc melting of pure metals. Microstructure of the alloys was investigated in the as-prepared state and after homogenization annealing followed by furnace cooling using scanning electron microscopy with energy dispersive spectroscopy (SEM-EDS). Differential scanning calorimetry (DSC) was used for determination of transformation temperatures.

## MATERIALS AND METHODS

The investigated Cu-Al-Mn ternary alloys were prepared by melting of calculated quantities of pure copper (99.99%), aluminium (99.95%) and manganese (99.95%) in an electric arc furnace. The melting of alloys was performed in vacuum to avoid contamination. Each alloy was melted four times to improve compositional homogeneity. The cylindrical shaped ingots (15 mm diameter and 30 mm length) were prepared and studied by SEM-EDS and DSC methods.

Microstructures of the Cu–Al–Mn alloys after arc melting were analyzed using SEM-EDS. Average overall chemical compositions of the investigated samples obtained by EDS analysis are presented in Table 1.

Table 1. Overall compositions of the investigated alloys

| Sample | Experimentally determined composition with calculated standard uncertainties (wt.%) | | |
|---|---|---|---|
| | Cu | Al | Mn |
| 1 | 83.0±0.2 | 13.4±0.1 | 3.6±0.1 |
| 2 | 84.2±0.1 | 10.4±0.1 | 5.4±0.1 |
| 3 | 80.4±0.4 | 11.8±0.1 | 7.8±0.1 |
| 4 | 85.6±0.4 | 10.0±0.2 | 4.4±0.1 |

After the analysis of samples in as-prepared condition, the samples were homogenized at 850 °C for two hours, cooled inside the furnace and again studied by SEM-EDS method.
For microstructure investigation samples were mechanically grinded and polished. Etching was done using a solution containing 2.5 g $FeCl_3 \cdot 6H_2O$ and 1 ml HCl in 48 ml methanol.
TESCAN VEGA3 scanning electron microscope with energy dispersive spectroscopy (EDS) (Oxford Instruments X-act) was used for microstructure investigation of the prepared alloys and the measurements were carried out at 20 kV.

Thermal analysis of the investigated samples was performed on a SDT Q600 (TA Instruments). The masses of the investigated samples were about 40 mg and the heating rate 10 °C/min. Heating was done from room temperature up to 1100 °C in a nitrogen atmosphere. The reference material was empty alumina crucible.

## RESULTS AND DISCUSSION

### Microstructure analysis of the investigated Cu–Al–Mn alloys

Characteristic SEM micrographs of the investigated bulk alloys after arc melting and after the annealing at 850 °C followed by slow cooling inside the furnace are shown in Figs. 1-4.
It can be seen that SEM images of all 4 as-prepared samples display characteristic martensitic structure (Fig1a, Fig2a, Fig3a, Fig4a). The fine plate- or spear-like martensitic groups (most probably $\beta_1$' martensite) are visible in the microstructures of all 4 investigated alloys. However, the observed microstructures of the investigated alloys after annealing at 850 °C and slow cooling inside the furnace are quite different. Microstructure of the slowly cooled sample 1 (Fig. 1b) shows characteristic lath type morphology. According to the results of previous investigations the identified lath type morphology is due to bainite formation [9,10].

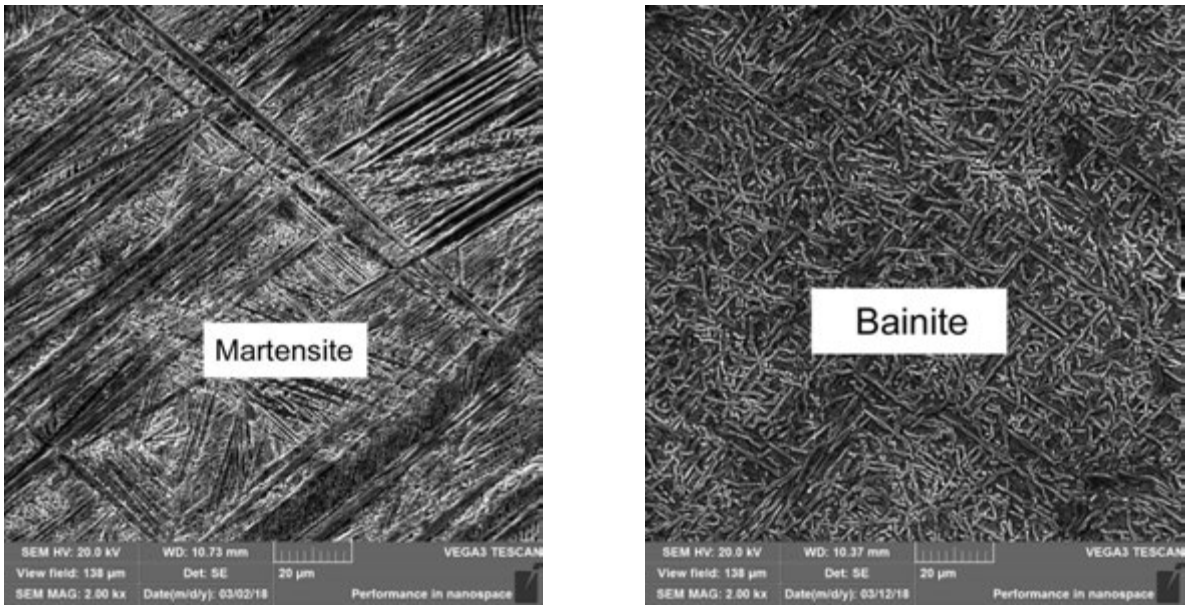


(a) (b)

Figure 1. SEM micrographs of the sample 1:
(a) as-prepared; (b) annealed at 850 °C for 2 h and slowly cooled

Two co-existing phases can clearly be noticed in the microstructure of the slowly cooled sample 2 (Fig. 2b): grey austenite phase in the matrix and light Cu-rich grains of α precipitates.

Average chemical compositions of identified phases were determined using EDS analysis and shown in Table 2. The grey matrix phase has lower amount of copper and higher amount of aluminium and manganese than the light phase.

Table 2. Chemical compositions of co-existing phases after homogenization annealing at 850 °C for 2 hours and slow cooling determined by EDS analysis

| | Phase | Cu (wt.%) | Al (wt.%) | Mn (wt.%) |
|---|---|---|---|---|
| Sample 2 | Austenite ( dark phase) | 82.0±0.3 | 11.6±0.2 | 6.4±0.1 |
| | α phase (bright phase) | 87.4±0.3 | 8.2±0.2 | 4.4±0.2 |

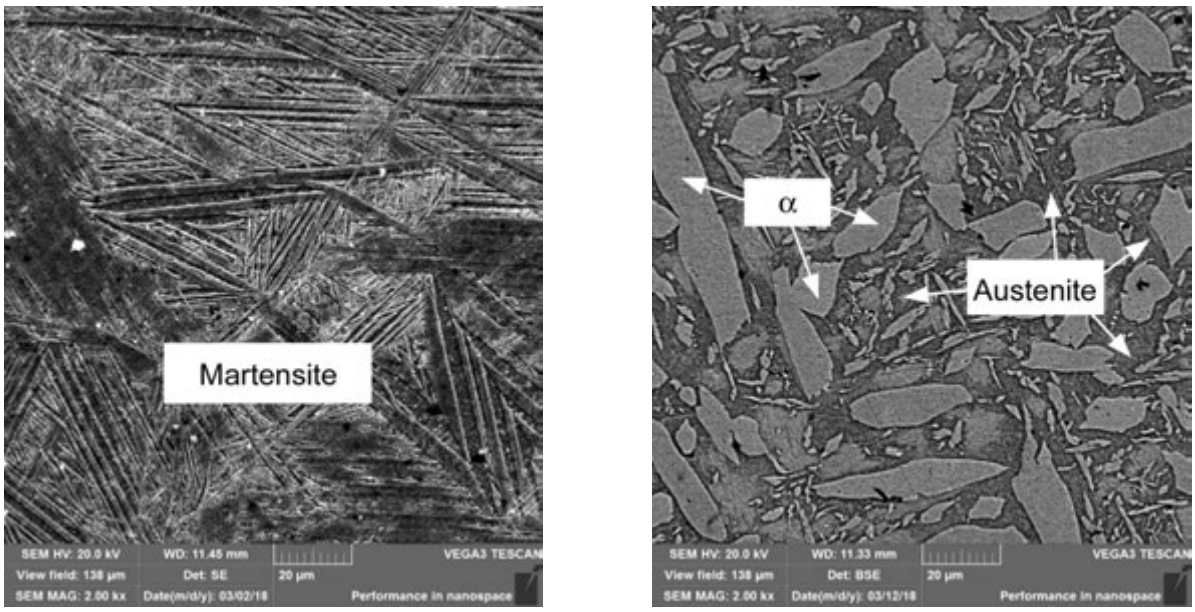


(a) (b)

Figure 2. SEM micrographs of the sample 2:
(a) as-prepared; (b) annealed at 850 °C for 2 h and slowly cooled

SEM image of the slowly cooled sample 3 (Fig. 3b) reveals the existence of 3 phases: martensite in the base (dark phase) and two types of precipitate phases: bainite as the thin light plates inside the martensitic grains and very fine α precipitates along the grain boundaries of martensitic grains.

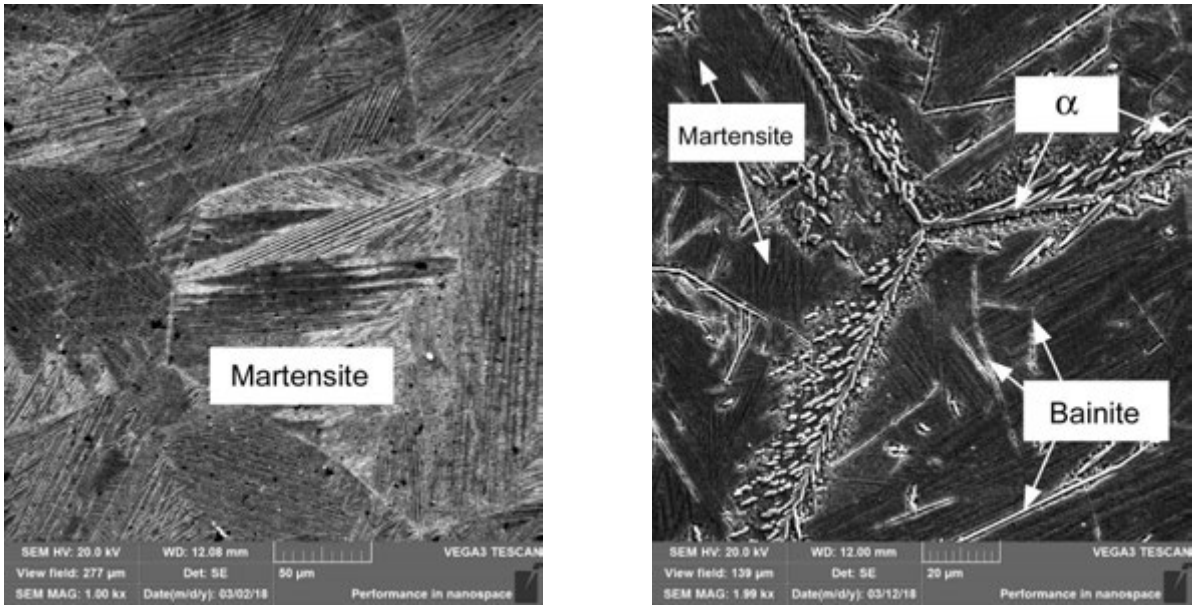


(a) (b)

Figure 3. SEM micrographs of the sample 3:
(a) as-prepared; (b) annealed at 850 °C for 2 h and slowly cooled

Microstructure of slowly cooled sample 4 consists of α precipitates as dark grains and bainite as thin light plates in the austenite matrix (grey phase) (Fig. 4b).

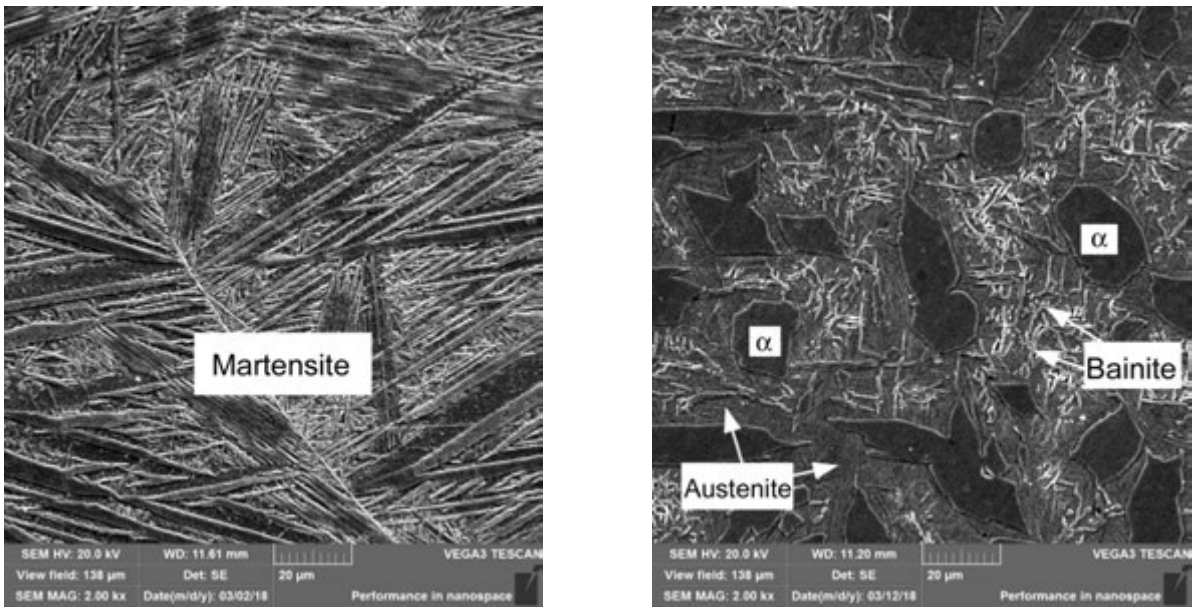


(a) (b)

Figure 4. SEM micrographs of the sample 4:
(a) as-prepared; (b) annealed at 850 °C for 2 h and slowly cooled

Average chemical compositions of the precipitate phase and matrix were determined by EDS area and point analysis (Fig. 5) and the obtained results are presented in Table 3.

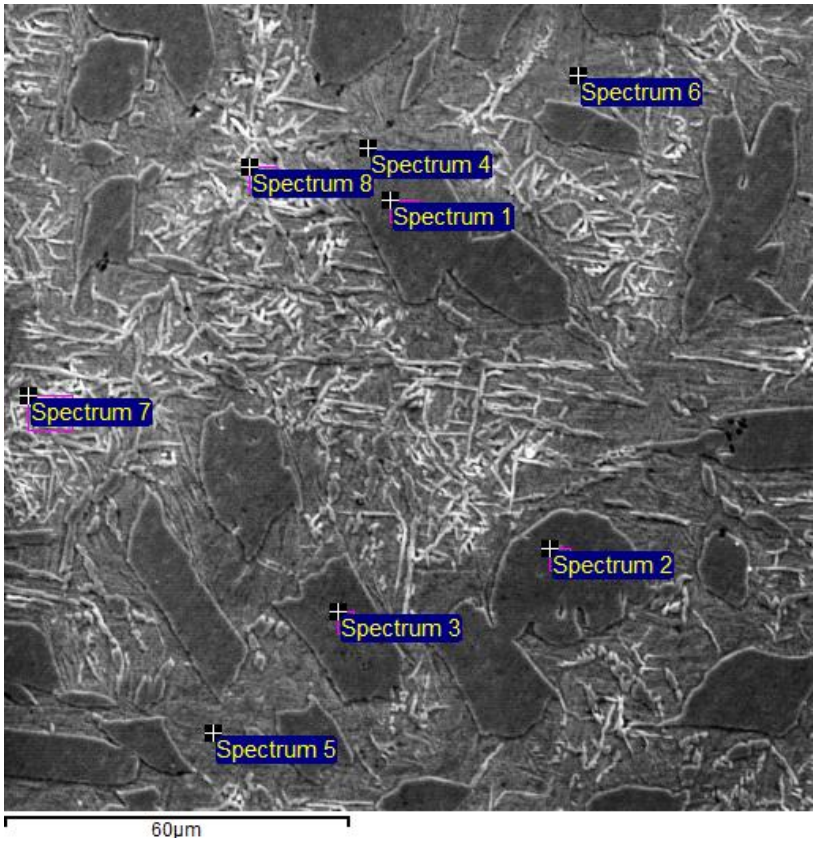


Figure 5. Example of EDS analysis for the sample 4

Table 3. Chemical compositions of co-existing phases after homogenization annealing at 850 °C for 2 hours and slow cooling determined by EDS analysis for the sample 4

| | Phase | Cu (wt.%) | Al (wt.%) | Mn (wt.%) |
|---|---|---|---|---|
| Sample 4 | Dark phase- α phase | 88.6±0.3 | 7.8±0.2 | 3.6±0.1 |
| | Matrix | 85.3±0.3 | 9.6±0.2 | 5.1±0.2 |

**Experimental investigation of transformation temperatures for the as-quenched alloys**

Phase transformation temperatures for the four investigated Cu-Al-Mn alloys in the as-prepared condition were measured using DSC method.
Summary of the obtained results is presented in Table 4.

Table 4. Phase transformation temperatures determined by DSC method

| Sample | Phase transformation temperatures, °C | | | | |
|---|---|---|---|---|---|
| | Austenite transformation | | Order-disorder transformation of austenite | Solidus | Liquidus |
| | $A_s$ | $A_f$ | | | |
| 1 | 139.2 | 269.7 | 504.3 | 1018.4 | 1030.7 |
| 2 | 129.9 | 276.6 | 499.1 | 1003.6 | 1023.5 |
| 3 | 149.7 | 273.6 | 487.3 | 976.4 | 997.7 |
| 4 | 131.7 | 272.9 | 499.6 | 1003.9 | 1024.9 |

Three endothermic peaks are identified on DSC heating curves of all four investigated alloys. First detected endothermic peak at low temperature is due to martensite/austenite phase transformation (Fig. 6). Austenite start ($A_s$) and austenite finish ($A_f$) transformation temperatures were determined as the onset and the endset temperatures of the first peak obtained on heating (Fig. 6). Second transformation occurs at the temperature close to 500 °C for all four investigated samples. This transformation can be explained by order-disorder transition of austenite phase [11]. The last and the largest endothermic peak at high temperatures represents melting of the alloy (Fig. 7).

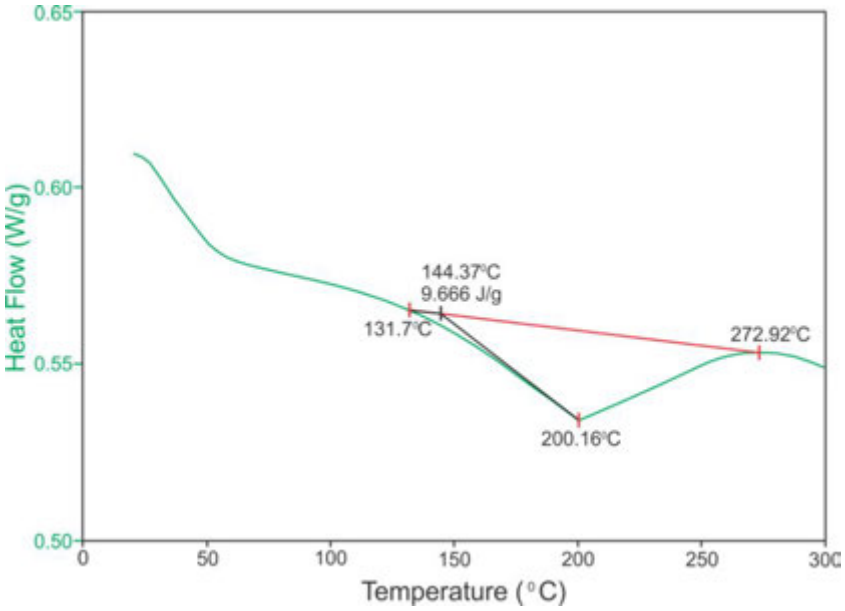


Figure 6. Part of the DSC heating curve for the sample 4 in the temperature range of the first detected endothermic peak related to martensite/austenite transformation

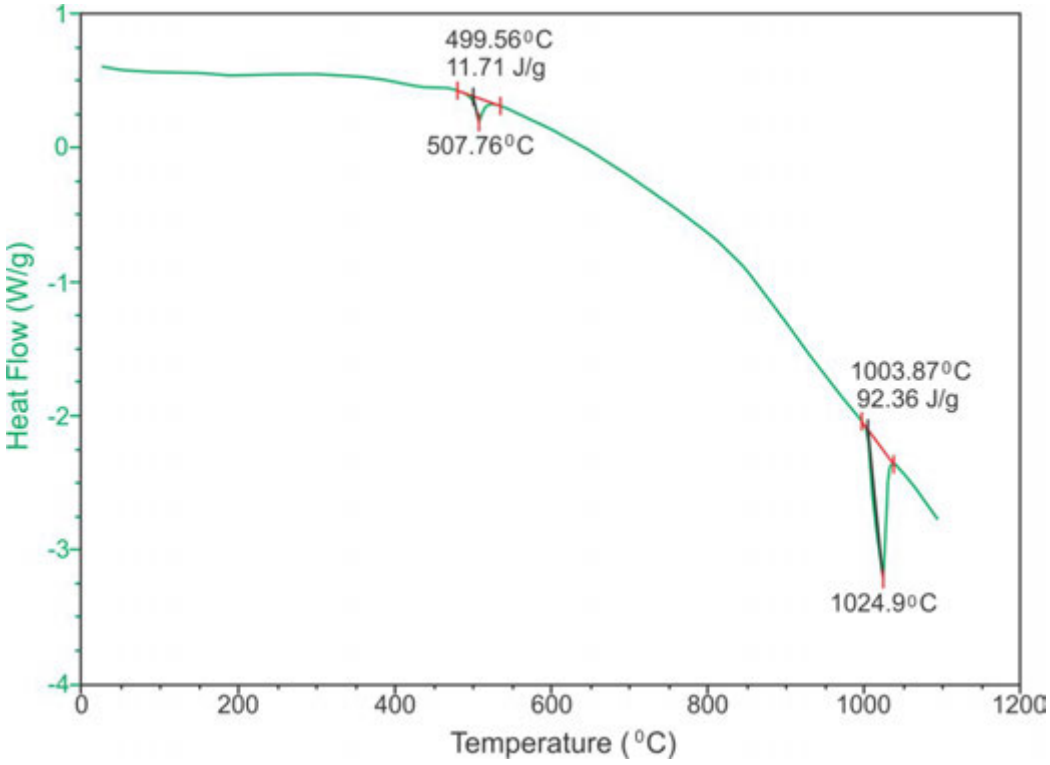


Figure 7. DSC heating curve for the sample 4

**CONCLUSIONS**

Based on the obtained results of SEM-EDS and DSC analysis following conclusions can be made:

1) All four Cu–Al–Mn alloys in the as-prepared condition exhibit martensitic structure.

2) After homogenization annealing at 850 °C and slow cooling microstructures of the investigated alloys show different co-existing phases. Microstructure of the sample 1 consists of bainite phase. Microstructure of the sample 2 includes α and β phases. Martensite in the base, small fraction of bainite precipitates inside martensite grains and fine α precipitates along the martensite grain boundaries are identified in the microstructure of sample 3. Microstructure of sample 4 includes α precipitates, β phase in the base and significant fraction of fine bainite precipitates in the matrix.

3) Phase transformation temperatures of four investigated Cu–Al–Mn alloys in the as-prepared condition were measured using DSC technique.

Three characteristic phase transformations were determined for each investigated alloy. First transformation at the lowest temperature represents martensite to austenite transformation. Second phase transformation at about 500 °C represent order/disorder transformation of austenite and the last detected endothermic peak is associated with melting of the alloy.

**REFERENCES**

[1] M. Gojić, S. Kožuh, I. Ivanić, M. Selanec, T. Holjevac Grgurić, B. Kosec, D. Ćubela, O. Beganović, Microstructural characterization of Cu82.3Al8.3Mn9.4 shape memory alloy after rolling, Metallurgical and Materials Engineering, 23 (2017) 3, pp. 281-289.
[2] U. S. Mallik, V. Sampath, Influence of aluminum and manganese concentration on the shape memory characteristics of Cu–Al–Mn shape memory alloys, Journal of Alloys and Compounds, 459 (2008), pp. 142-147.
[3] C. Lexcellent, Shape-memory Alloys Handbook, New York, John Wiley&Sons, 2013.
[4] Z. Wang, X. Zu, Y. Fu, Review on the temperature memory effect in shape memory alloys, International Journal of Smart and Nano Materials, 2 (2011) 3, pp. 101-119.
[5] R. Dasgupta, A look into Cu-based shape memory alloys: Present scenario and future prospects, Journal of Materials Research, 29 (2014) 16, pp. 1681-1698.
[6] Y. Sutou, T. Omori, R. Kainuma and K. Ishida, Materials Science and Technology, 24 (2008) 8, pp. 896-901.
[7] M. Blanco, J.T.C. Barragan, N. Barelli, R.D. Noce, C.S. Fugivara, J. Fernández, A. V. Benedetti, On the electrochemical behavior of Cu–16%Zn–6.5%Al alloy containing the β'-phase (martensite) in borate buffer, Electrochimica Acta, 107 (2013), pp. 238- 247.
[8] M. Ahlers, Martensite and equilibrium phases in Cu-Zn and Cu-Zn-Al alloys, Progress in Materials Science, 30 (1986) 3, pp.135-186.
[9] Y. Sutou, N. Koeda, T. Omori, R. Kainuma, K. Ishida, Effects of ageing on bainitic and thermally induced martensitic transformations in ductile Cu–Al–Mn-based shape memory alloys, Acta Materialia, 57 (2009), pp. 5748-5758.
[10] Y. Sutou, N. Koeda, T. Omori, R. Kainuma, K. Ishida, Effects of aging on stress-induced martensitic transformation in ductile Cu–Al–Mn-based shape memory alloys, Acta Materialia, 57 (2009), pp. 5759-5770.
[11] S. Stanciu, L. G. Bujoreanu, R. I. Comanenci, N. Cimpoesu, I. Ionita, V. V. Moldoveanu, Particularities of phase transitions in thermomechanically processed Cu-Al-Mn shape memory alloys, Proceedings of 8th European Symposium on Martensitic Transformations ESOMAT, 07-11. September, Prague, 2009, pp. 1-6.

**Acknowledgements**

This study was supported by the Ministry of Education, Science and Technological Development, Republic of Serbia, under Project ON 172037. This work has been supported in part by Croatian Science Foundation under the project IP-2014-09-3405.

17th INTERNATIONAL FOUNDRYMEN CONFERENCE
Hi-tech casting solution and knowledge based engineering
Opatija, May 16th-18th, 2018
http://www.simet.hr/~foundry/

# MASTER OF THE COMPLEX CASTINGS IN THE TECHNOLOGY OF HIGH PRESSURE DIE-CASTING

**Primož Mrvar[1]*, Grega Gorše[2], Almir Mahmutovič[3], Mitja Petrič[1]**

[1] University of Ljubljana Faculty of Natural Sciences and Engineering, Ljubljana, Slovenia
[2] LTH Castings d.o.o., Ljubljana, Slovenia
[3] TC Livarstvo, Ljubljana, Slovenia

**Invited lecture**
*Subject review*

**Abstract**

In contemporary high pressure die casting (HPDC) foundries the mastery of each sequence in production cycle is the most important, where the strive to reliable master, as well as planning of composed molten metal, pouring and solidification process, ejection of castings, transport to the cooling place and cutting of gating system and overflows were done. For castings with a complex geometry and dimensional accuracy, the appropriate planning of pouring and feeding elements according to a heat economy of casting, rapid tooling and prototyping and then reliable manufacturing which includes the mastery of all the edge conditions in the process chain. In the work the example of virtual analysis of casting from Al alloy will be presented with choosing of appropriate foundry technology HPDC, calculation of casting process which includes the filling process of cold chamber, model description of three phases at HPDC, flow of molten metal, solidification with considering the temporary air gap formation between the casting and tool, formation of stress and relaxation of it into deformations in each sequence, cooling in water or on air and after cutting off the gating system. It is not always possible to produce the castings according to the principle of unidirectional solidification with a traditional approach, for the individual areas, the local squeezing process is performed in the sequence of the semi-solid state of the region. The location of the impression is marked by a local increase of pressure and a plastic deformation of the already solid part of the casting (solid shell). Comparisons will be made with calculations of volume defects, casting dimensions and deformations with experimentally obtained castings produced from LTH Castings' industrial technology practice. Proven complete master of high-pressure die-casting have the result an important financial effect and decreasing of required time to start of serial production of castings.

***Keywords**: aluminium alloy, high pressure die casting (HPDC), complex geometry, virtual analysis, squeezing process*

*Corresponding author (e-mail address): *primoz.mrvar@omm.ntf.uni-lj.si*

# Master of the complex castings in the technology of high pressure die-casting

P. MRVAR[1], G. GORŠE[2], A. MAHMUTOVIČ[3], M. PETRIČ[1]

[1]*Department of Materials and Metallurgy, FNT, University of Ljubljana (SI),*
[2]*LTH Castings d.o.o. (SI),* [3]*TC livarstvo d.o.o.* (SI);

University of Ljubljana
Faculty of Natural Sciences and Engineering
Department of Materials and Metallurgy

Aškerčeva 12, 1000 Ljubljana, Slovenia

***Opatija, 14. 05. 2018***

# Casting, technology

- Permanent mold ( GDC, GDTC, HPDC; LPDC;)
- Sand or ceramic mould (GSC, INV, )

•Gravity (G, T)
•Pressure (HPDC, LPDC)←
•Centrifugal (H, V)
•Vacuum
•Continues,..

**Casting technology** ( selection of technology, calculation of gating system, selection of cold chamber set, determining the technological process window, application of LS, …)

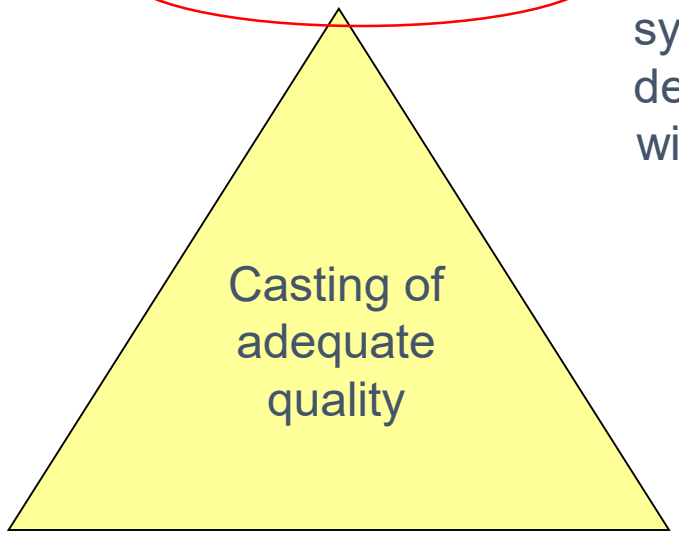


**Alloy**
(raw material, degree of recycling, melt treatment, way of pouring, Chemical composition, NP)

**Type of the p. mould**
(selection of different hot working toll steel, W-alloy,.. heat tretment, properties, ..)

# HPDC

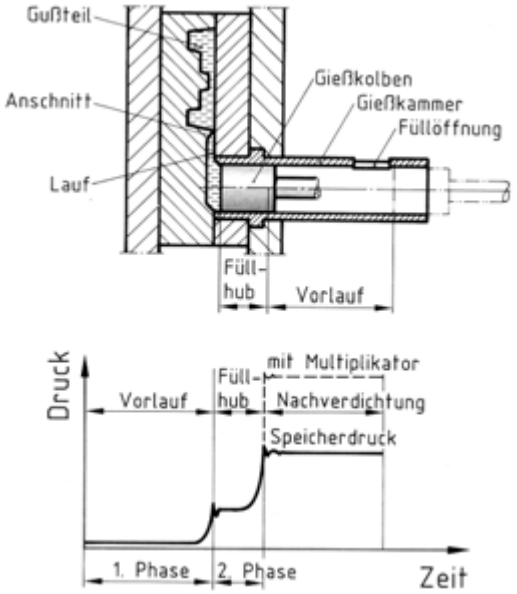


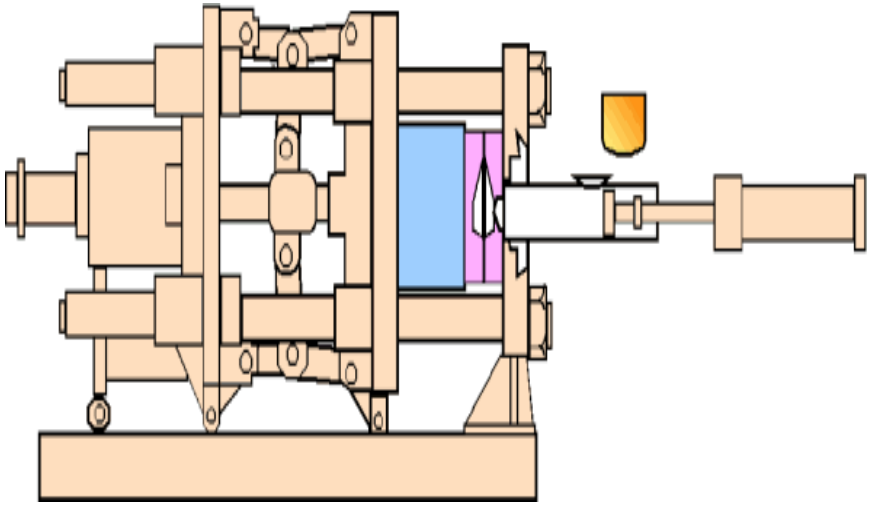

1 Piston motion

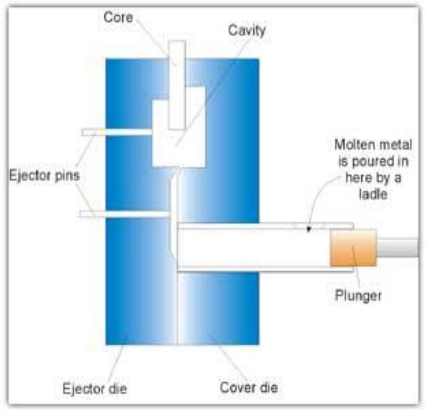


2 Die cavity filling

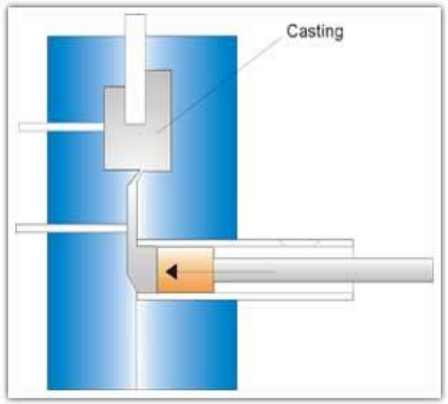


3rd phase effect

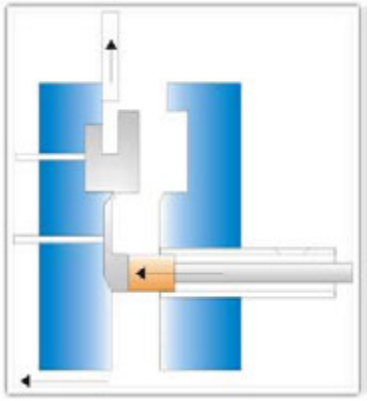

# HPDC- Cold chamber

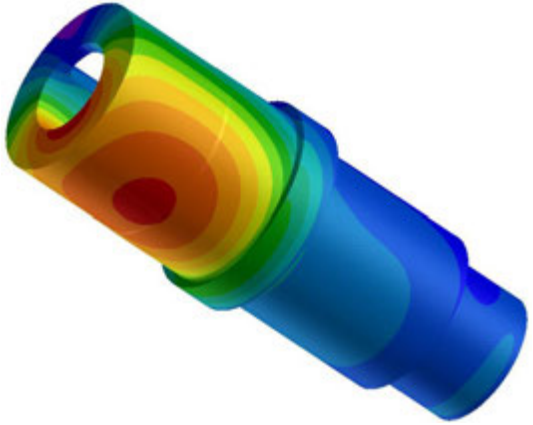

1. - What is the main problem to pour the molten Al alloy?

   - Solubility of iron in Al alloys
   - Cycle time

2. - How to increase the efficiency of working the c. chamber?

   - Decreasing the solidification of molten alloy in chamber (t for stage I and II have to be short, T of chamber high)……development of hot chamber machine for Al ?
   - This cause the new situation which is connect with time for shot (II. Stage)
   - Increasing the life time of sleeve and piston
   - Increasing of yield of molten metal

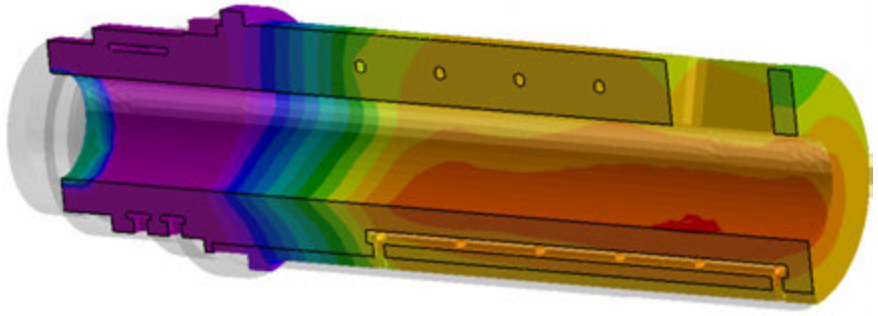

# HPDC- Cold chamber

1. - What is the  main problem to prepare the accurate calculation of casting process for HPDC?

   - It is necessary to choose and/or calculate or measure  the real materials data
     - Tl, Ts, fs-f(T), ρ-f(T), ŋ_f(T), E, ..
   - The calculation should start in the stage 0
   - The description of stage I to III is required for accuracy
   - The boundary conditions have to be set properly (T, HTC, t..)
   - The geometry should be describe with fine mash
   - Technological process window should reflect the real (experimental) data input

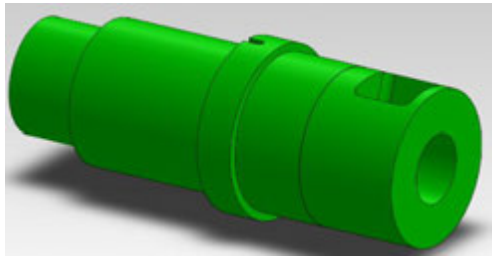

# Calculation of melt flow and melt temperature drop from furnace to casting chamber

- Measurements of melt temperature in the casting chamber before the first stage starts

Sacrificial thermocouples

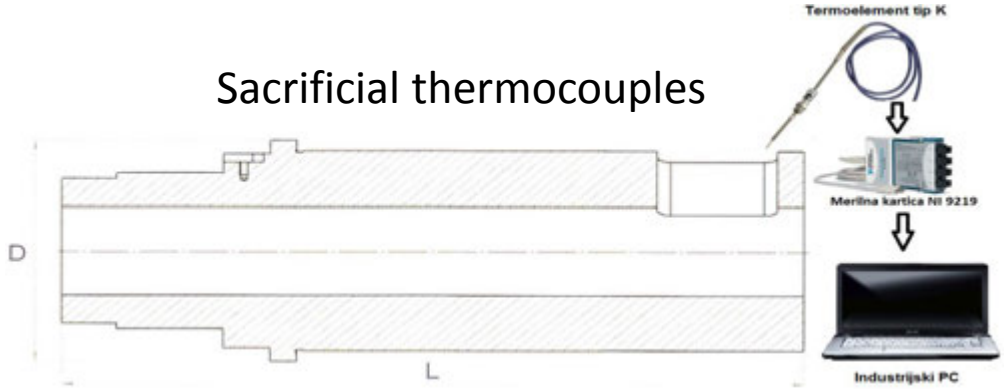


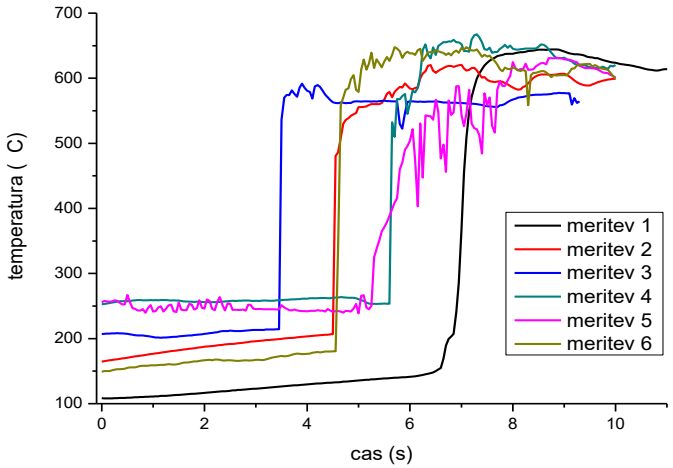

- **Simulation of melt flow and melt temperature drop from furnace to casting chamber**

- Filing of casting chamber calculation compered with experimentaly determined temperatures.

- Temperature in the chamber before the shot at 650 °C, temperature of the melt in the casting furnace 677 °C ⇒ temperature drop 20 - 30°C.

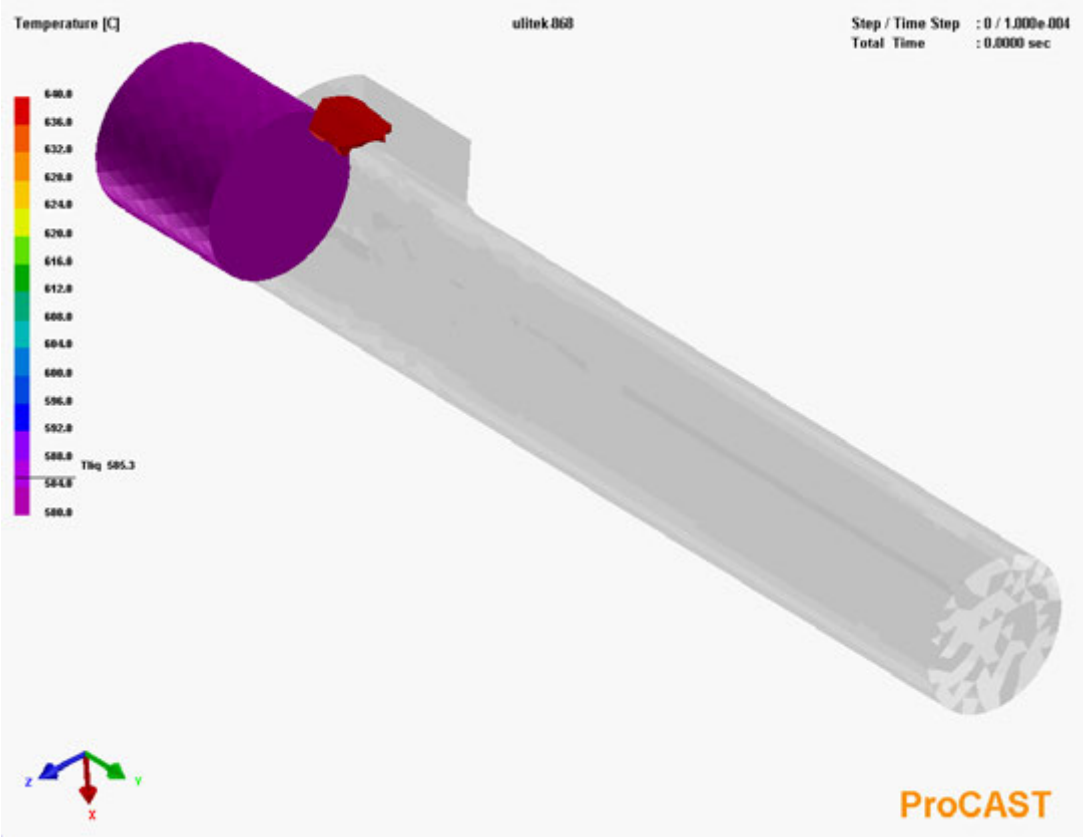

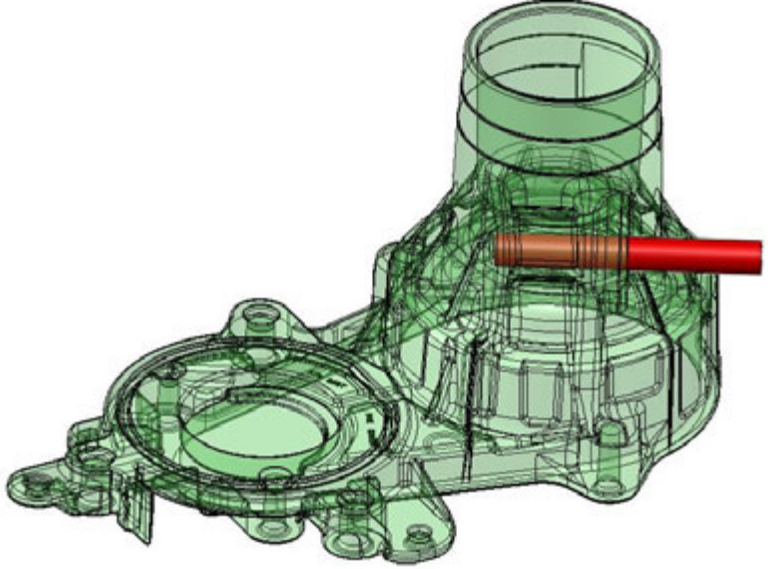

# Example 1: Investigated geometry of casting and their gating system

- **Material**
  - **Alloy: AlSi9Cu3**
    - $T^{liquidus}$ =588°C
    - $T^{Solidus}$ =508°C
  - **Pouring temperature 660 °C**

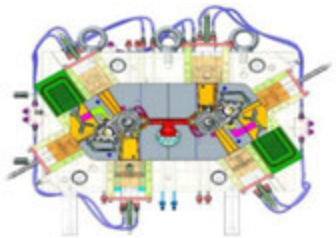

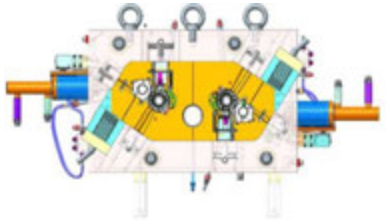

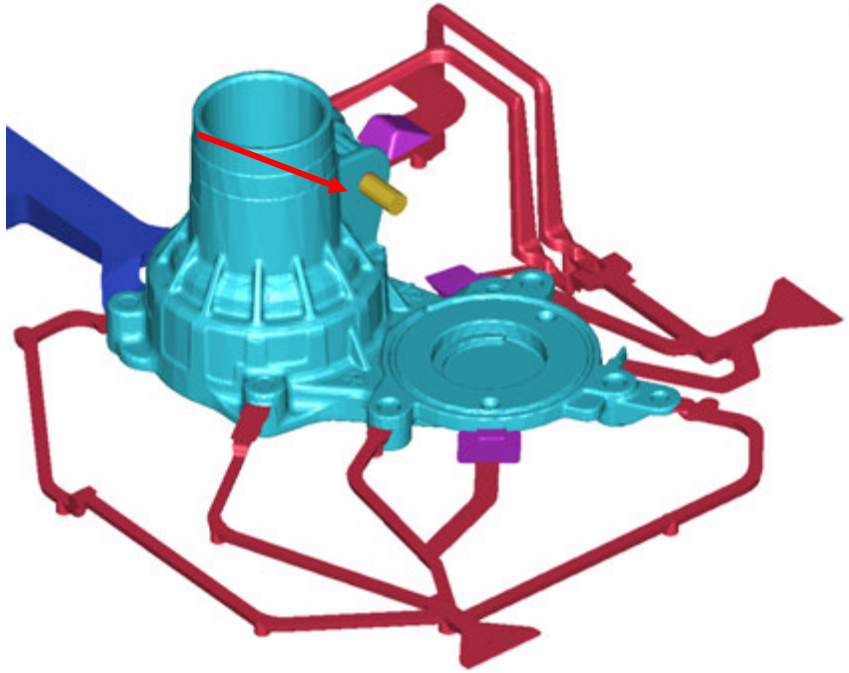

- **Brut weight of shot (2 castings): 3,1 kg**
- **Net weight of casting: 0,8 kg**

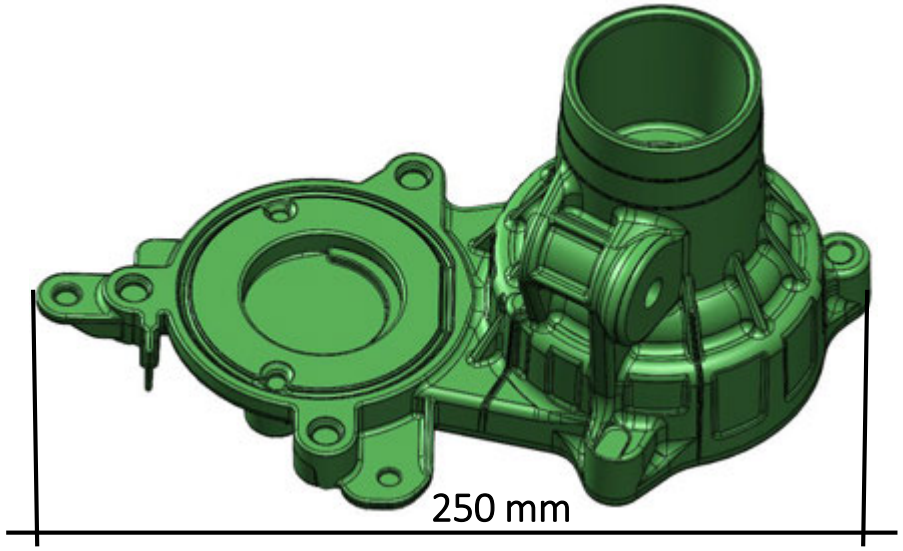

# Geometry of toll assembled with cold chamber set

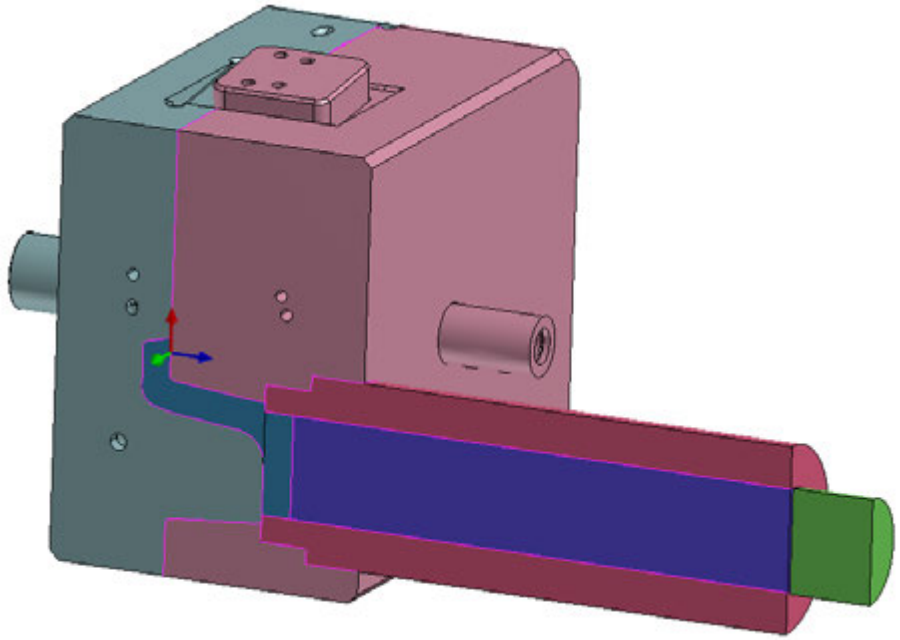

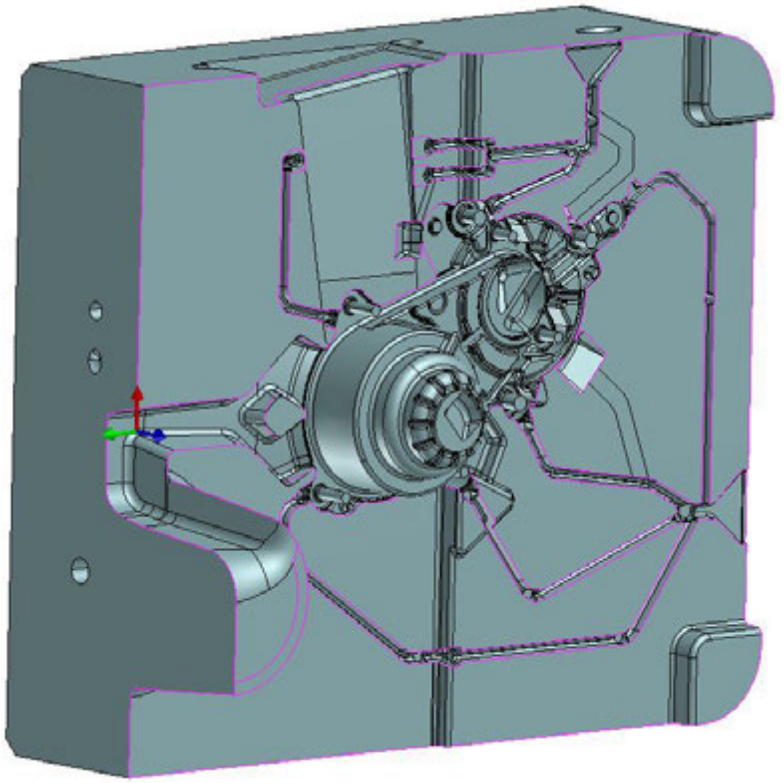

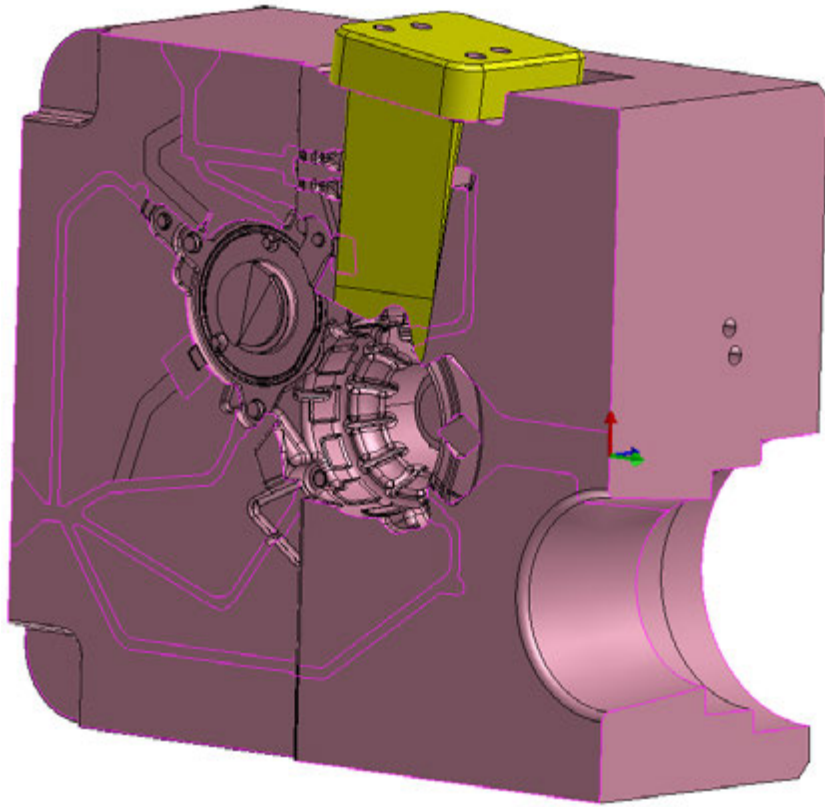

Casting distributor

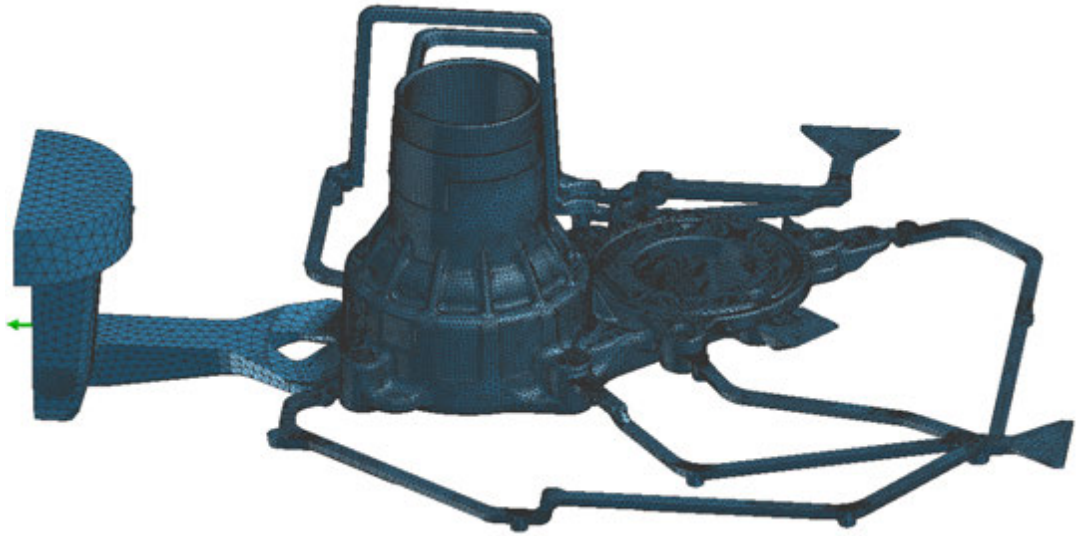

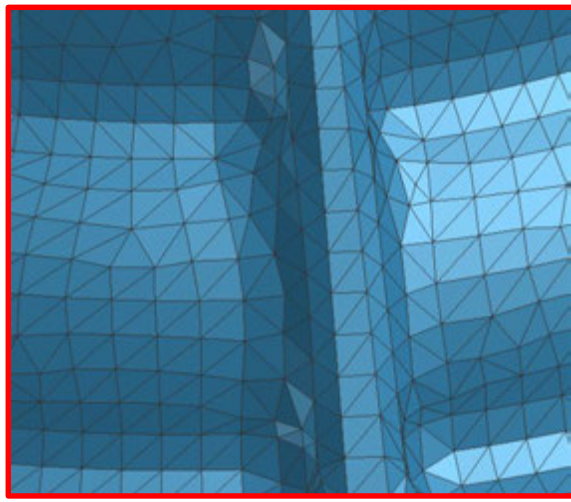

- **The origin layout of Cooling and heating channels**

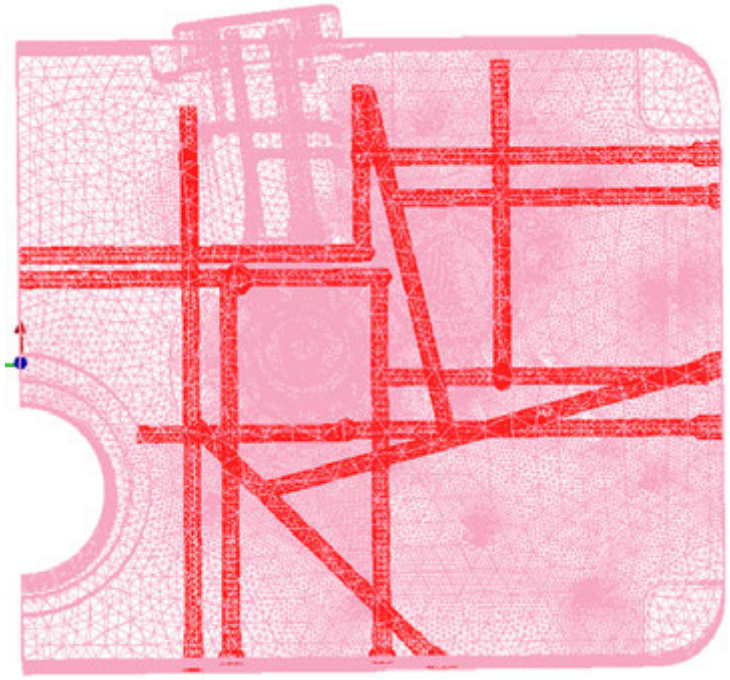

| Property | Type | Value | | Temp | | Time | |
|---|---|---|---|---|---|---|---|
| Film Coeff | V... | 2.0000e+003 | W/m^2k | | C | | sec |
| Emissivity | V... | | | | C | | sec |
| Ambient Te... | V... | 1.8000e+002 | C | | | | sec |
| Heat Flux | V... | | W/m^2 | | | | sec |
| View Factor | | OFF | | | | | |

Fixed side of die; T-oil 180°C

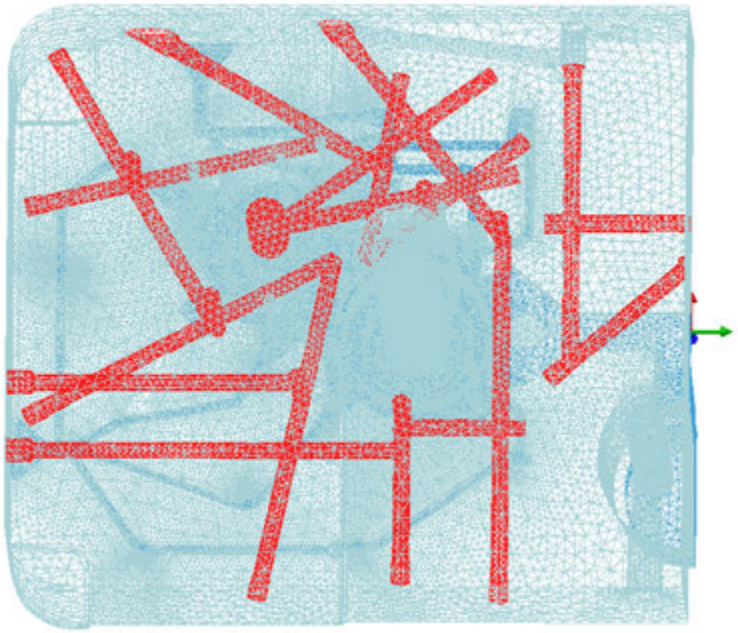

| Property | Type | Value | | Temp | | Time | |
|---|---|---|---|---|---|---|---|
| Film Coeff | V... | 2.0000e+003 | W/m^2k | | C | | sec |
| Emissivity | V... | | | | C | | sec |
| Ambient Te... | V... | 1.6000e+002 | C | | | | sec |
| Heat Flux | V... | | W/m^2 | | | | sec |
| View Factor | | OFF | | | | | |

Moveable side of die; T-oil 160°C

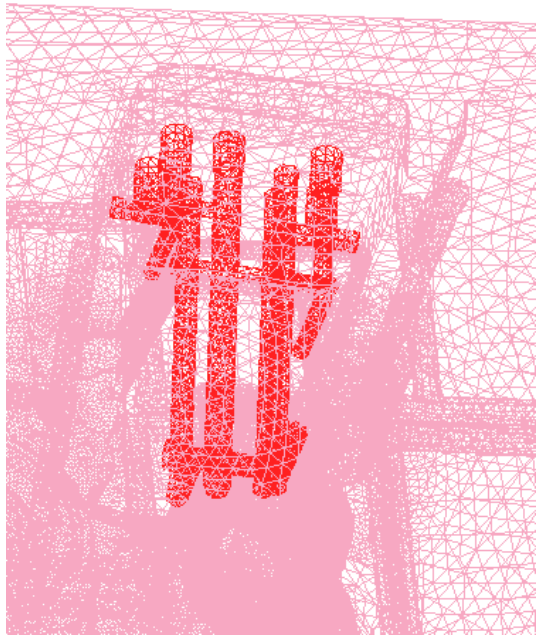

| Property | Type | Value | | Temp | | Time | |
|---|---|---|---|---|---|---|---|
| Film Coeff | V... | 2.0000e+003 | W/m^2k | | C | | sec |
| Emissivity | V... | | | | C | | sec |
| Ambient Te... | V... | 1.6000e+002 | C | | | | sec |
| Heat Flux | V... | | W/m^2 | | | | sec |
| View Factor | | OFF | | | | | |

Side core of die; T-oil 160°C

- **Example of optimization the sequence I ; Cooling of molten metal in the cold chamber in the first stage**

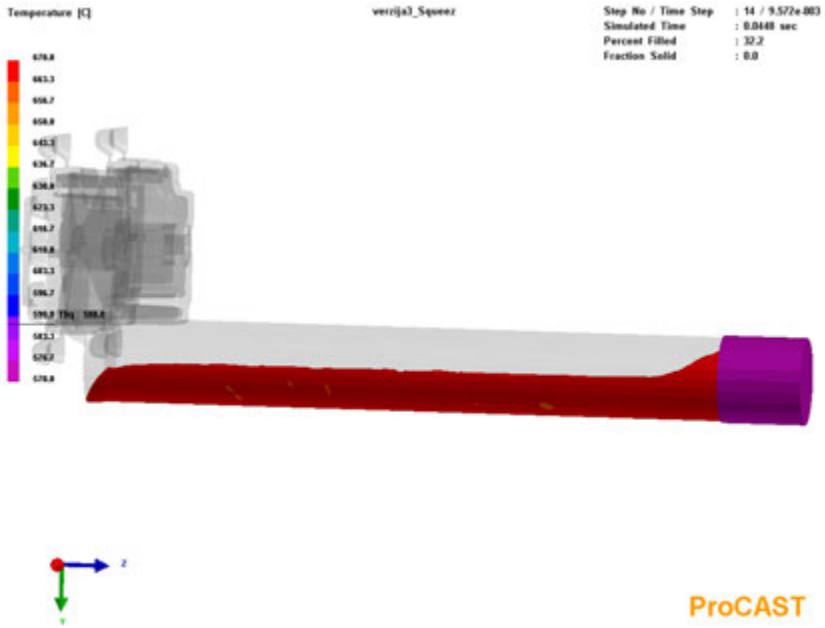


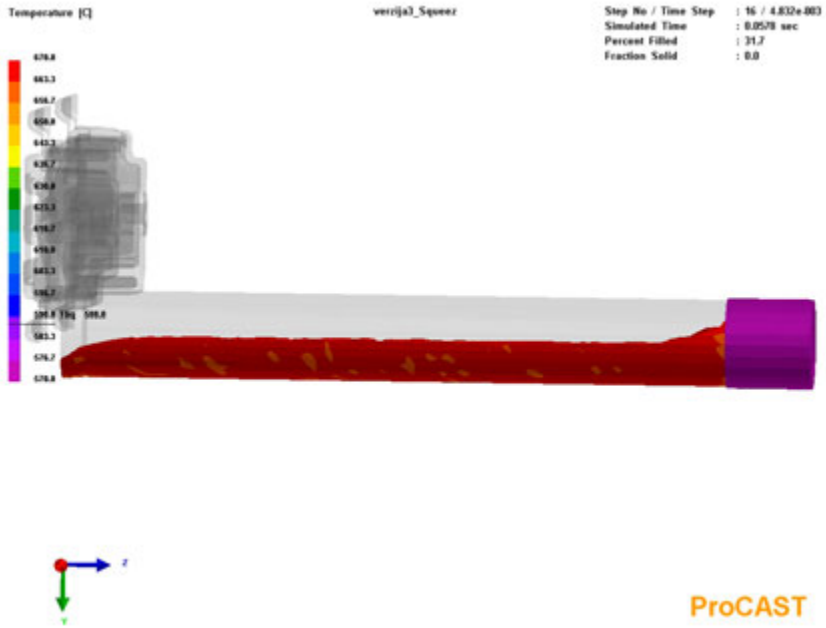


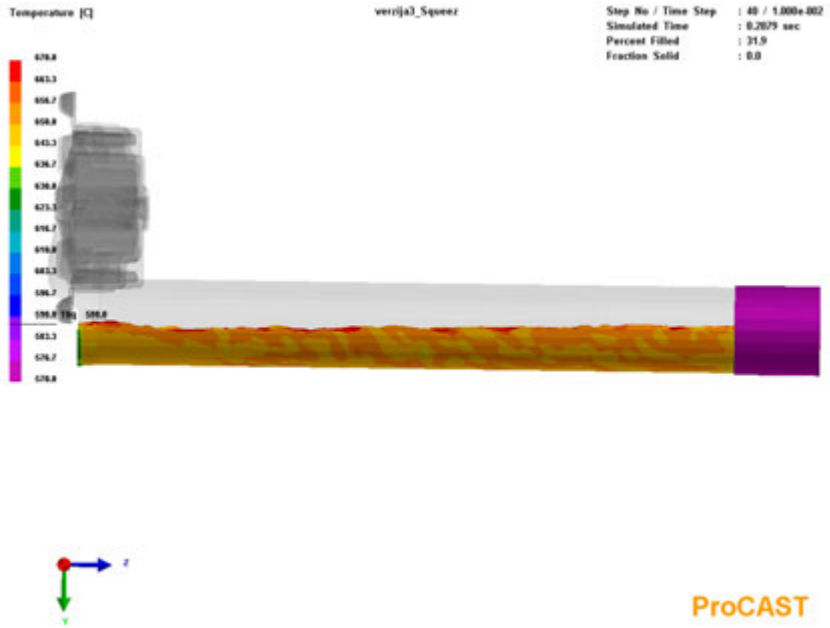


**V1= 0,6 m/s**

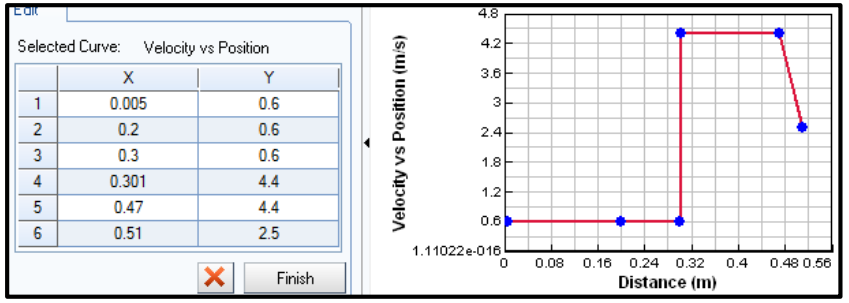


**V1= 0,3 m/s**

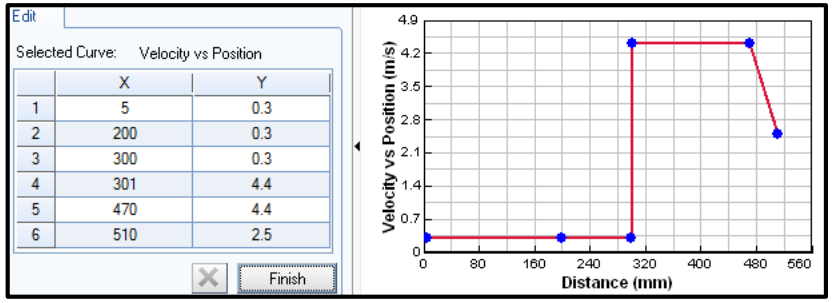


**V1= 0,07 m/s**

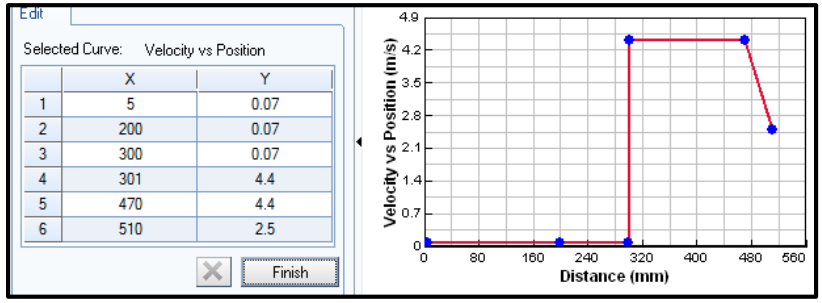

# Sequence of piston moving

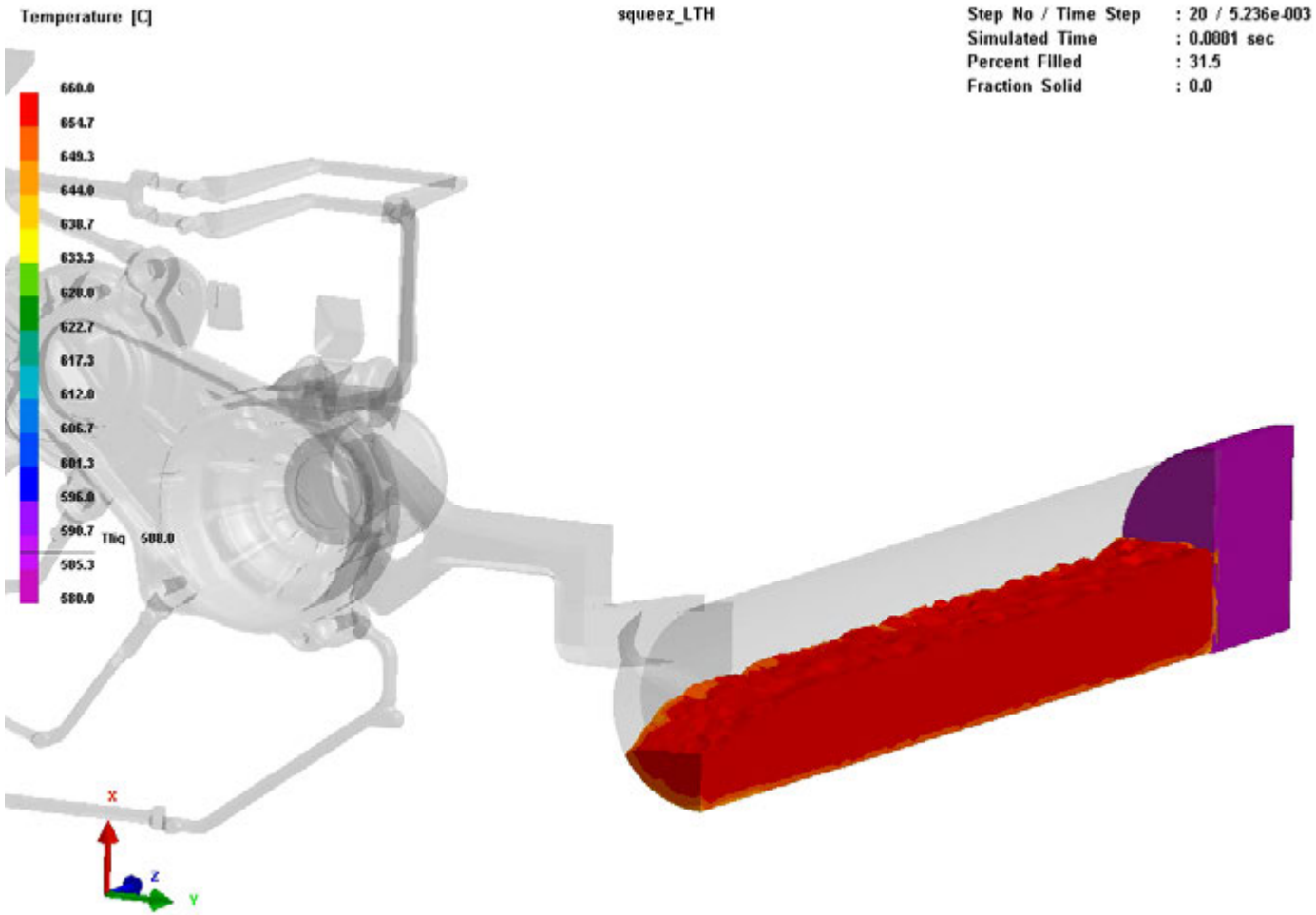


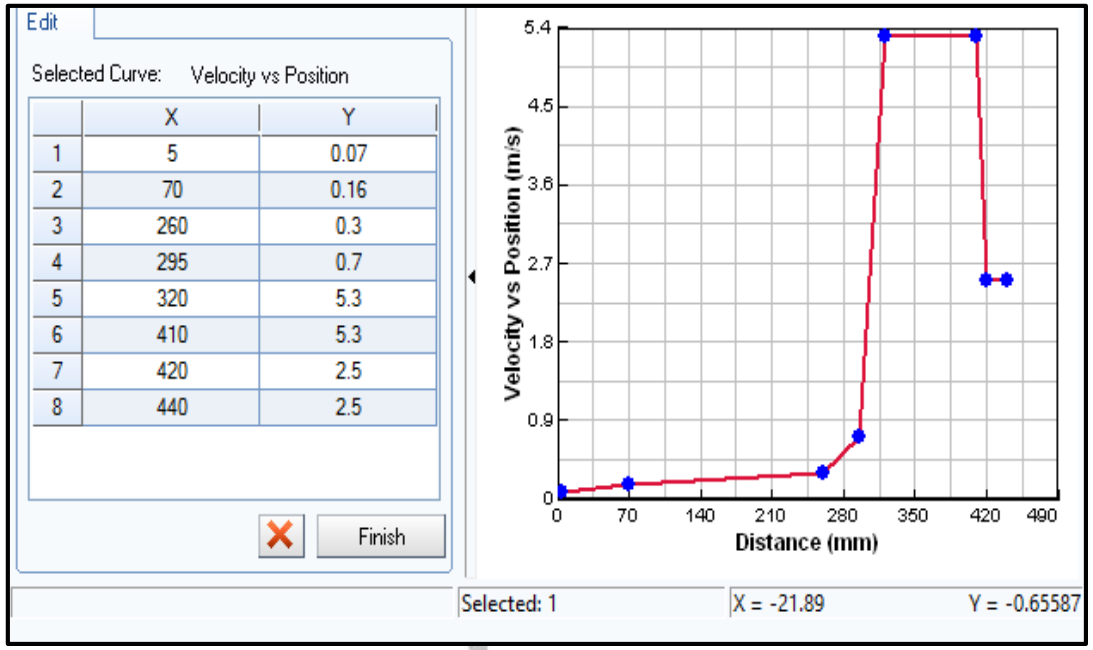


**Way - Velocity**

ProCAST

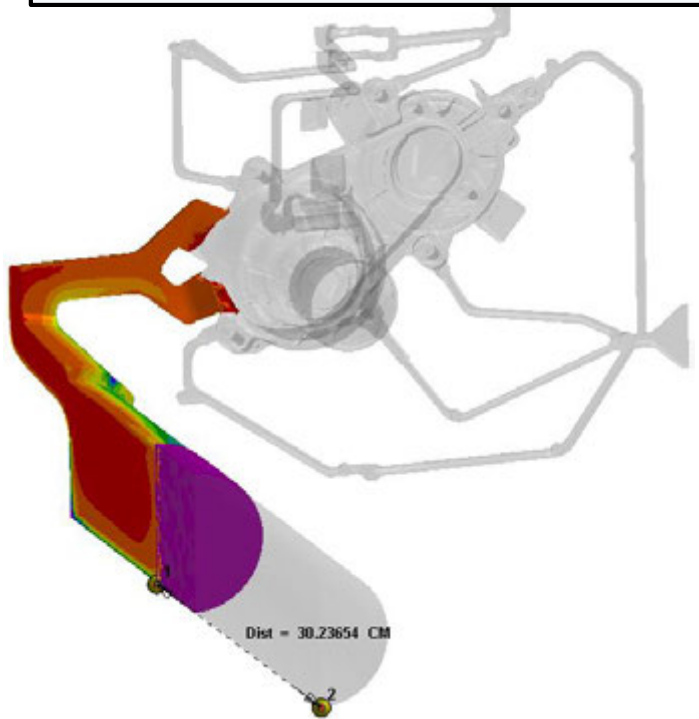

- **Calculation of filing**

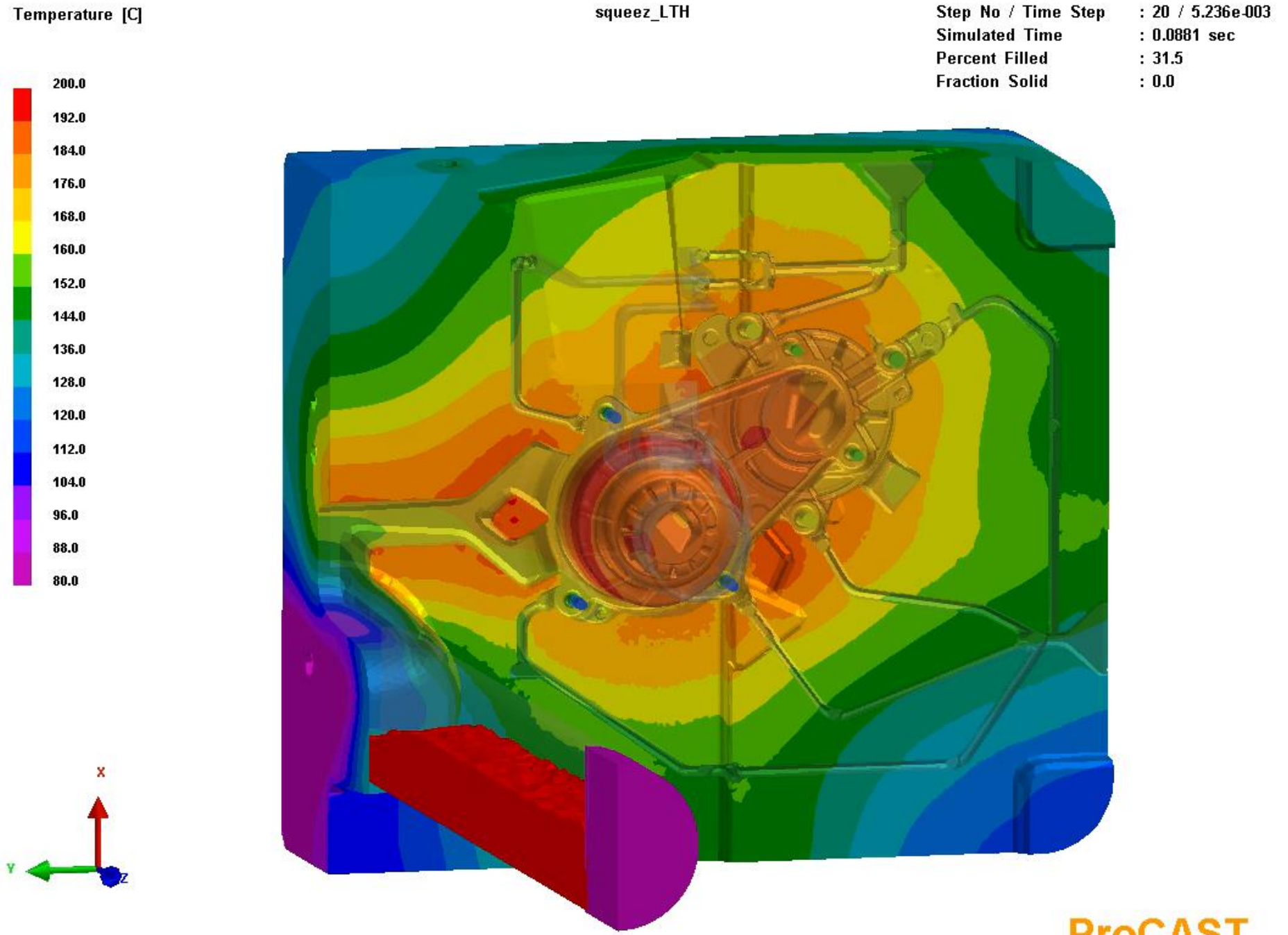

# Comperation between calculated temperature field and experimentally determined; movable side of die

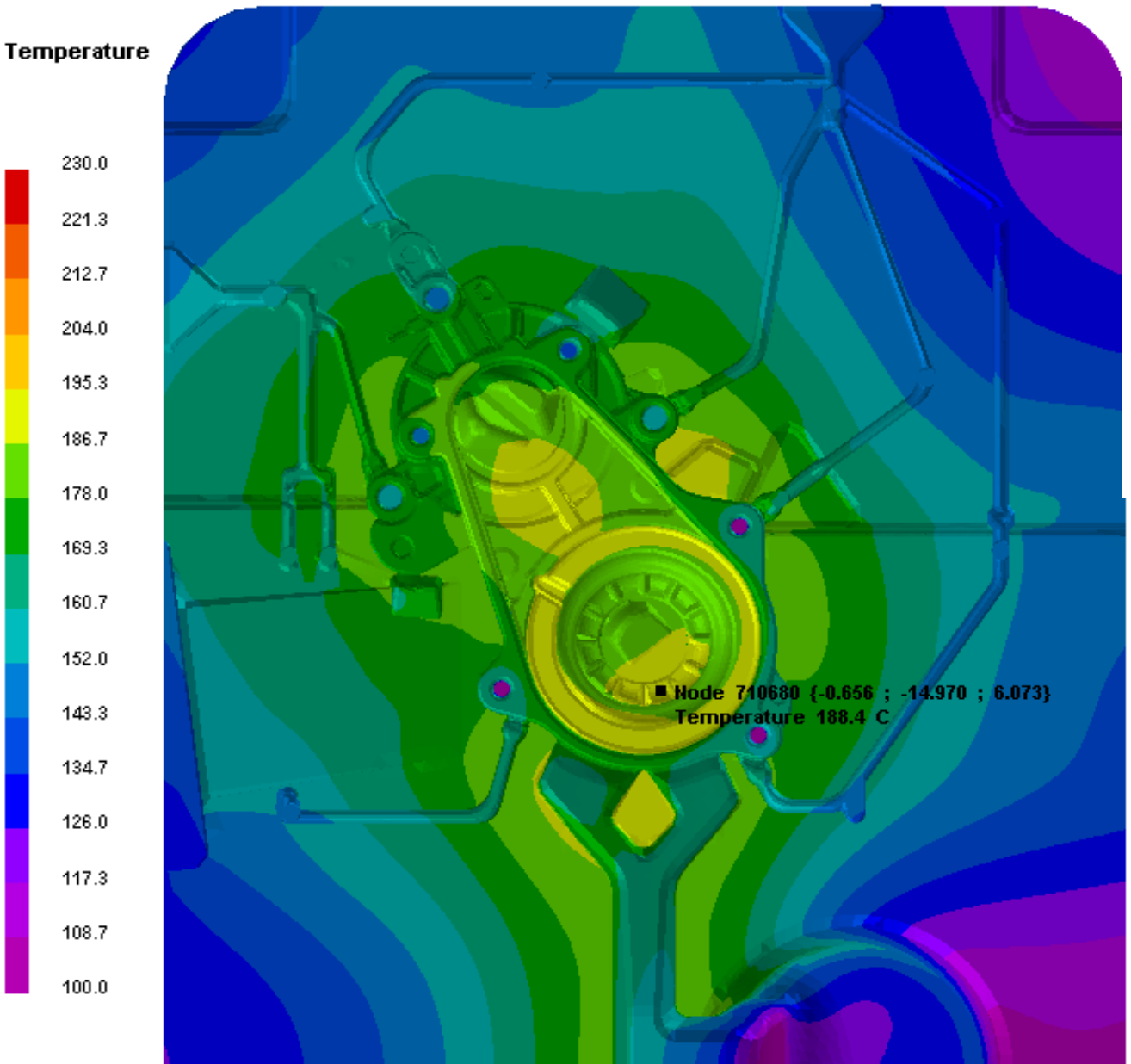


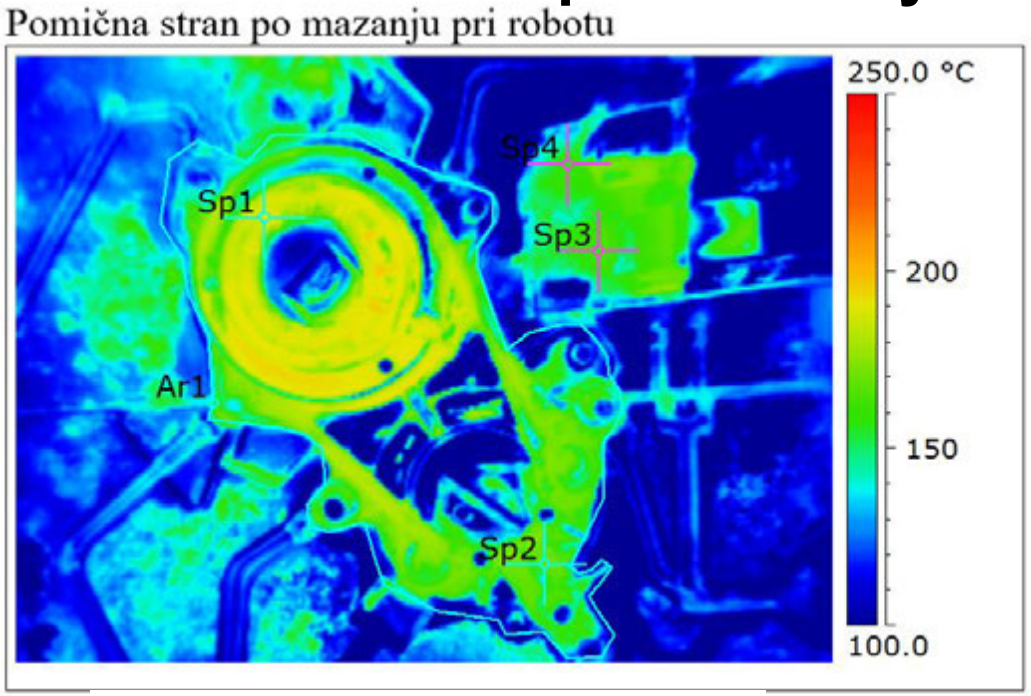


| | |
|---|---|
| Date | 11.04.2016 |
| Filename | IR_14818.jpg |
| Image Time | 12:27:22 |
| Sp1 Temperature | 187.6 °C |
| Sp2 Temperature | 166.9 °C |
| Sp3 Temperature | 160.5 °C |
| Sp4 Temperature | 160.0 °C |
| Ar1 Min. Temperature | 78.2 °C |
| Ar1 Max. Temperature | 195.7 °C |
| Ar1 Average Temperature | 150.0 °C |
| Sp1 Emissivity | 0.80 |
| Sp2 Emissivity | 0.80 |
| Sp3 Emissivity | 0.80 |
| Sp4 Emissivity | 0.80 |

# Movable side of die: Cycling calculation on die which is cooled by Jet Cooling system

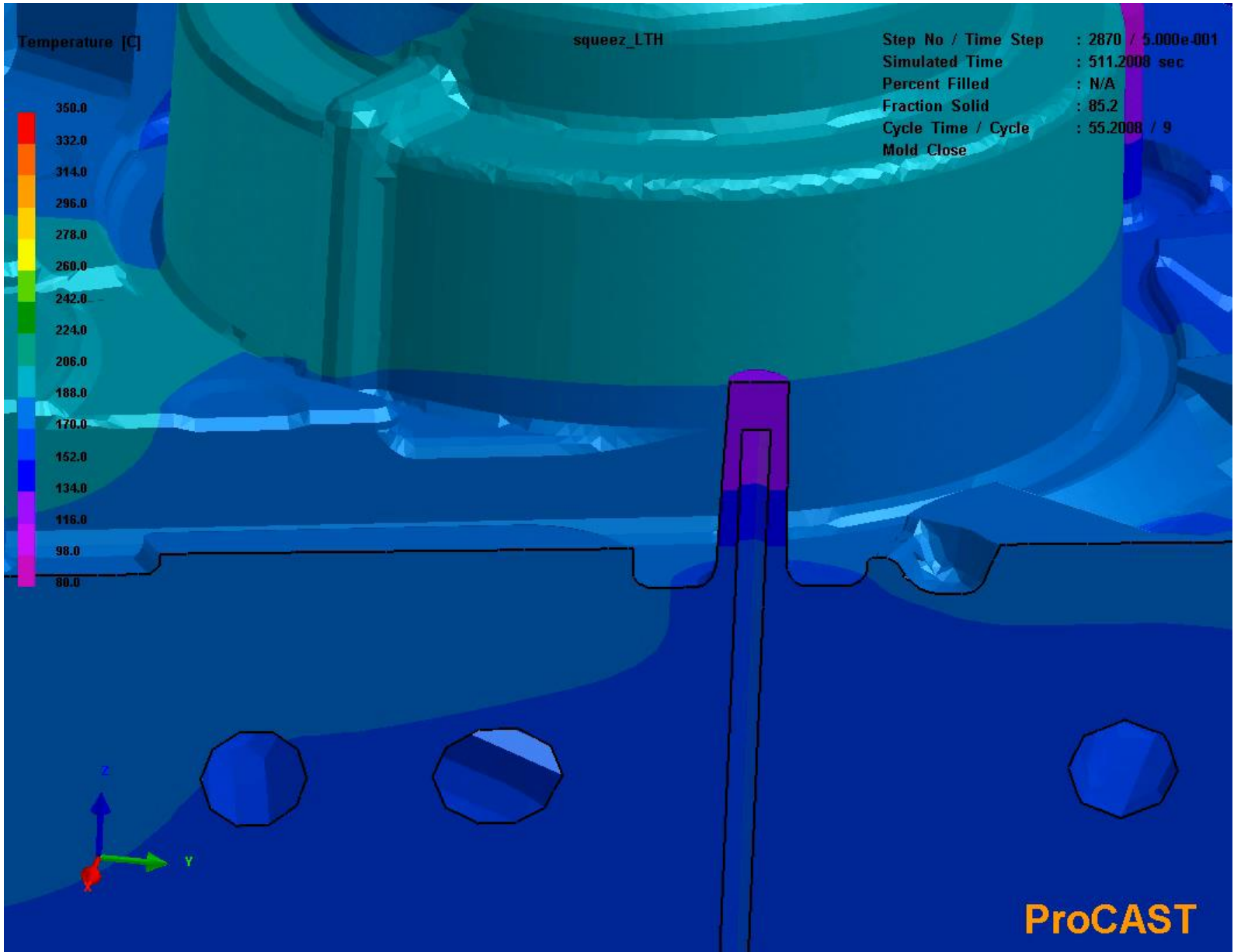

- **Calculation of temperature field on die surface which is cooled with Jet Cooling**

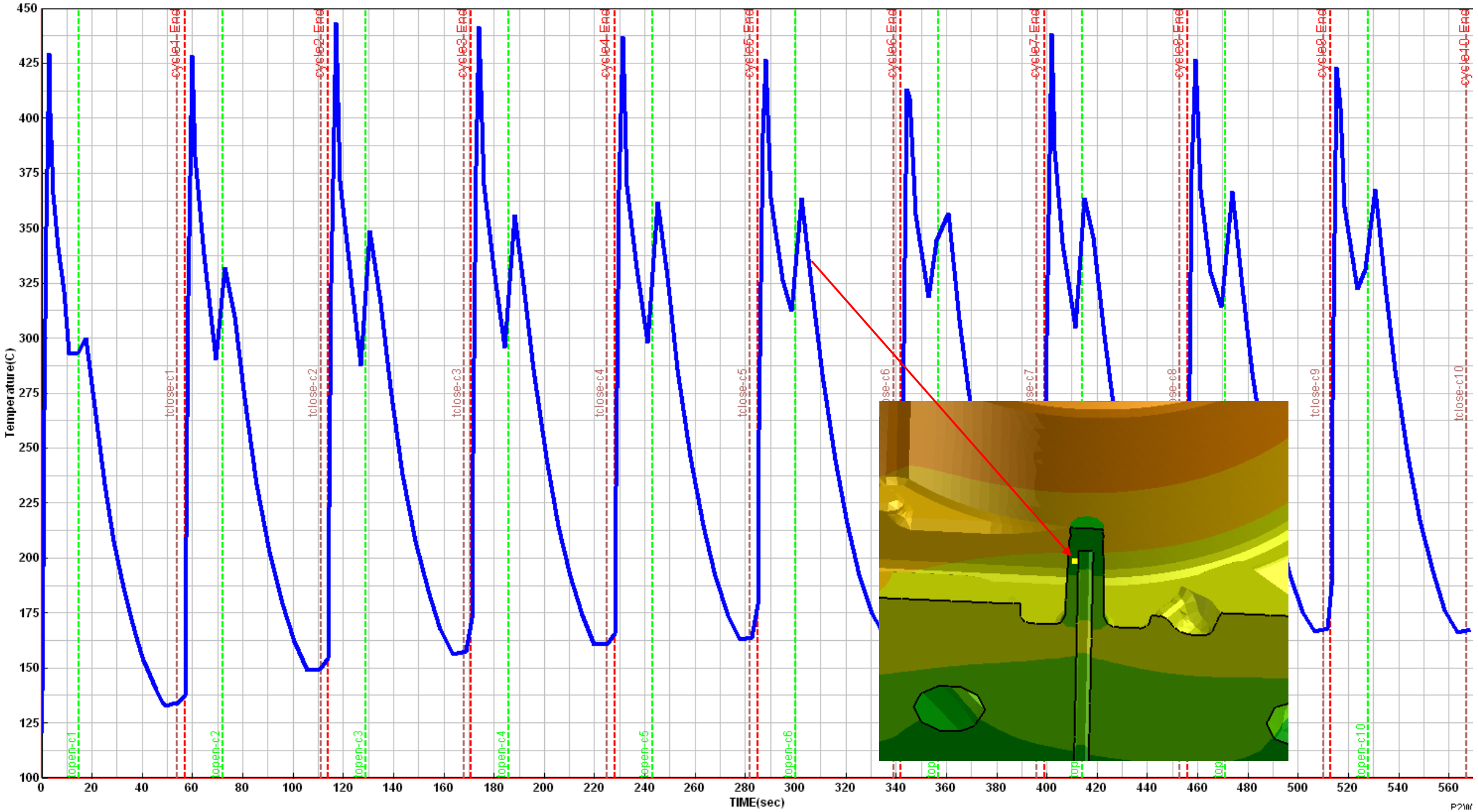

Fixed side of die; The temperature field was stabilized after 10 cycles

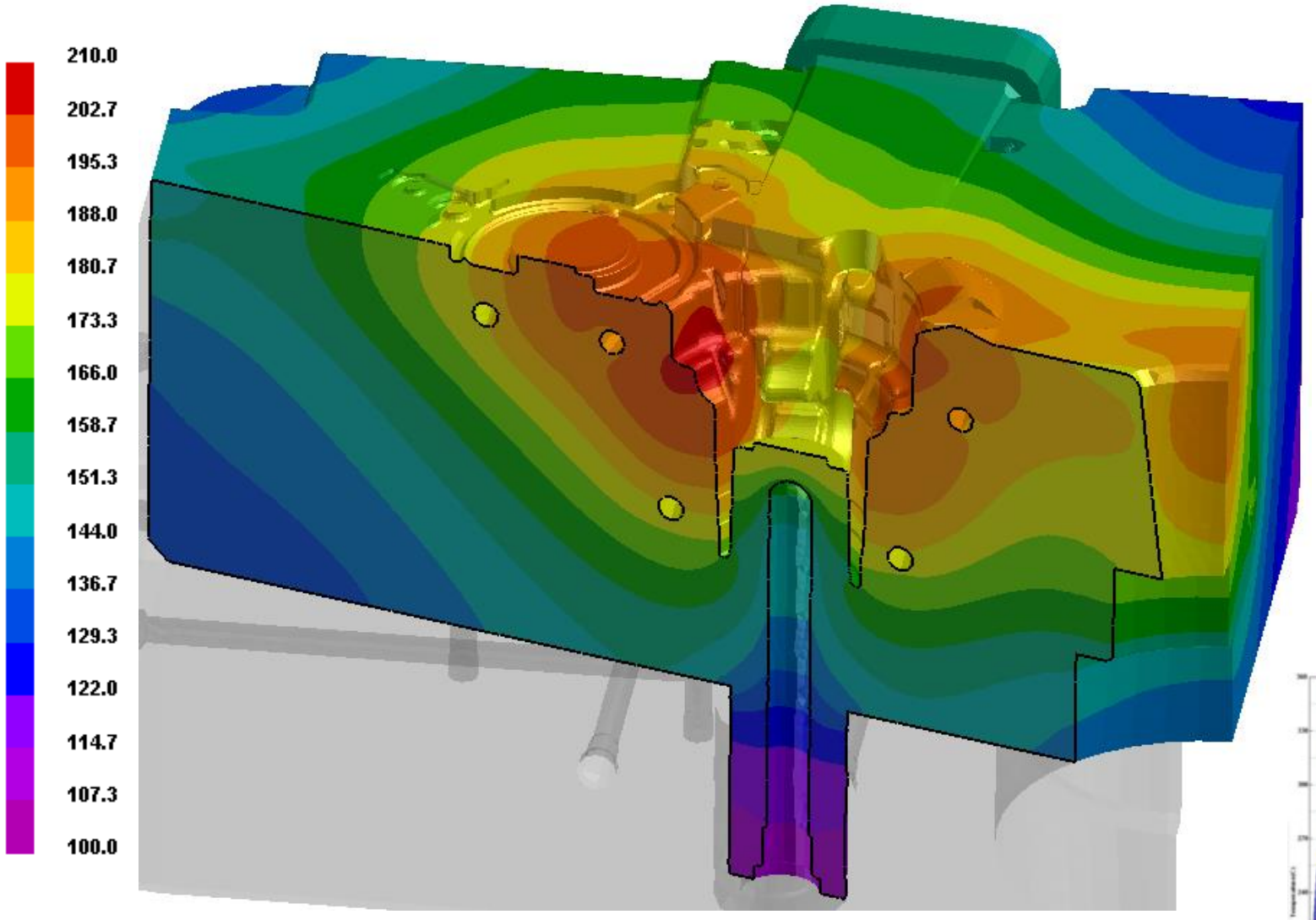


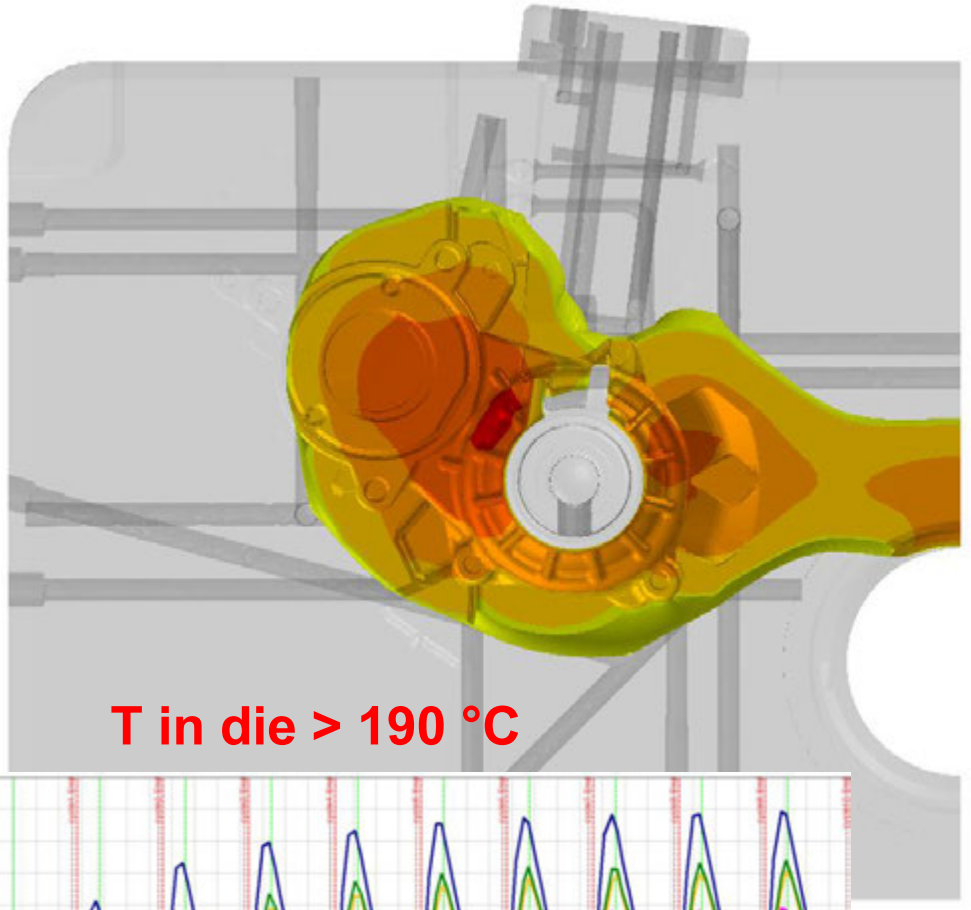


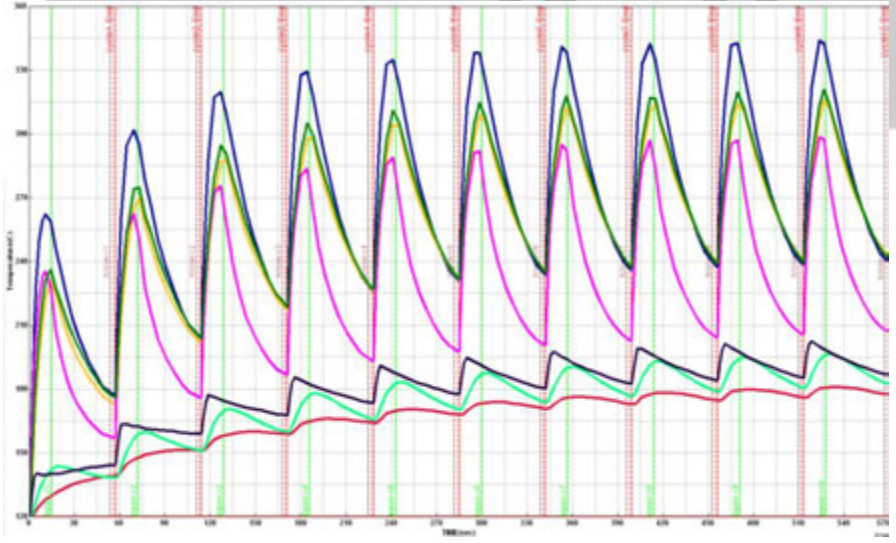

- **Calculation of solidification sequence**

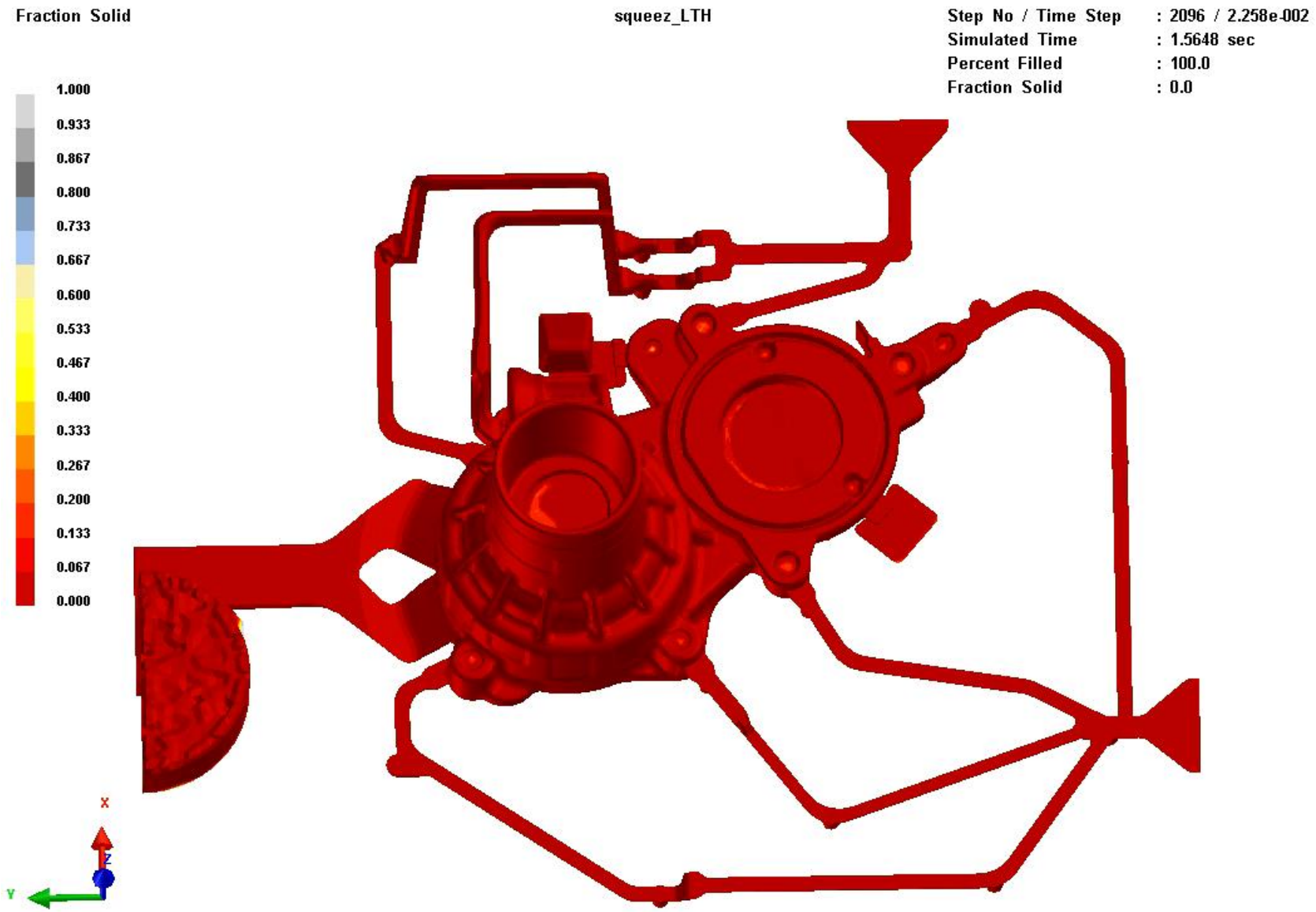


- **Unidirectional solidification is not possible**

# *Calculation of solidification sequence versus time / Last solidified areas in the casting

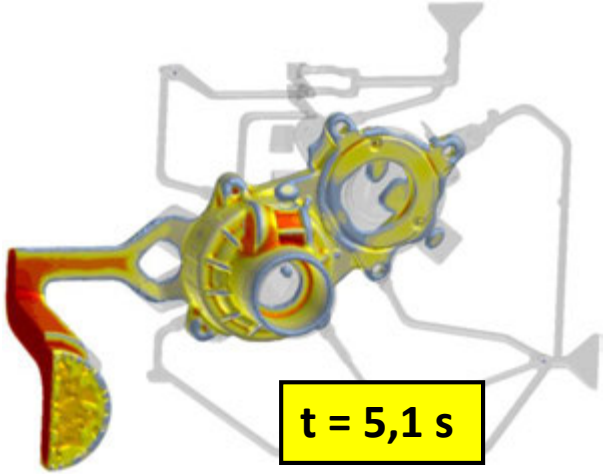

t = 5,1 s

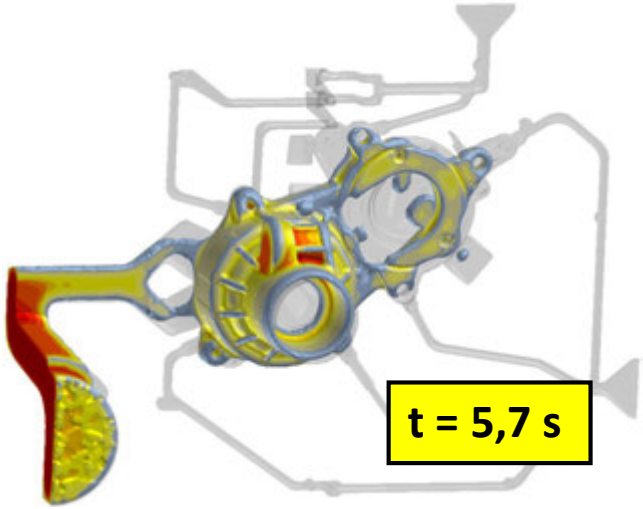

t = 5,7 s

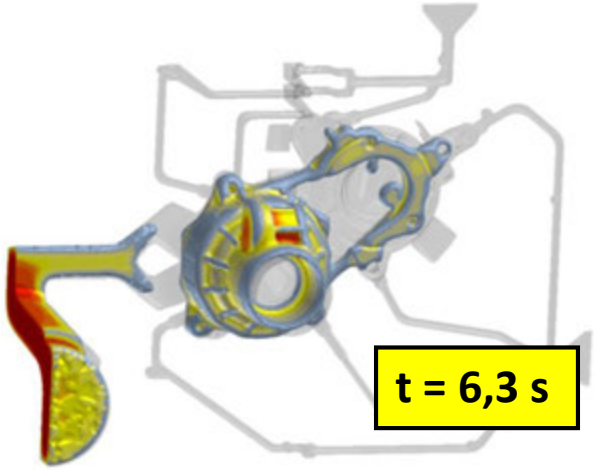

t = 6,3 s

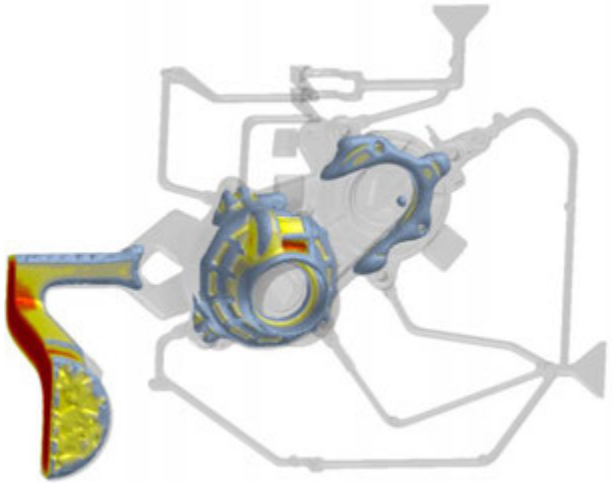

t = 7,6 s

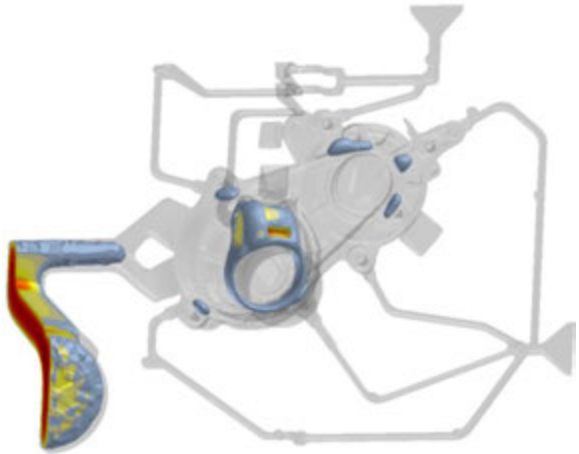

t = 10,1 s

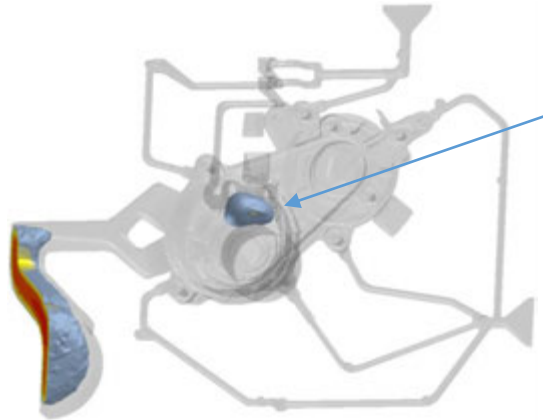

t = 14,9 s

- Critical area

# Calculation of porosity with out of LS / hole in the as cast state

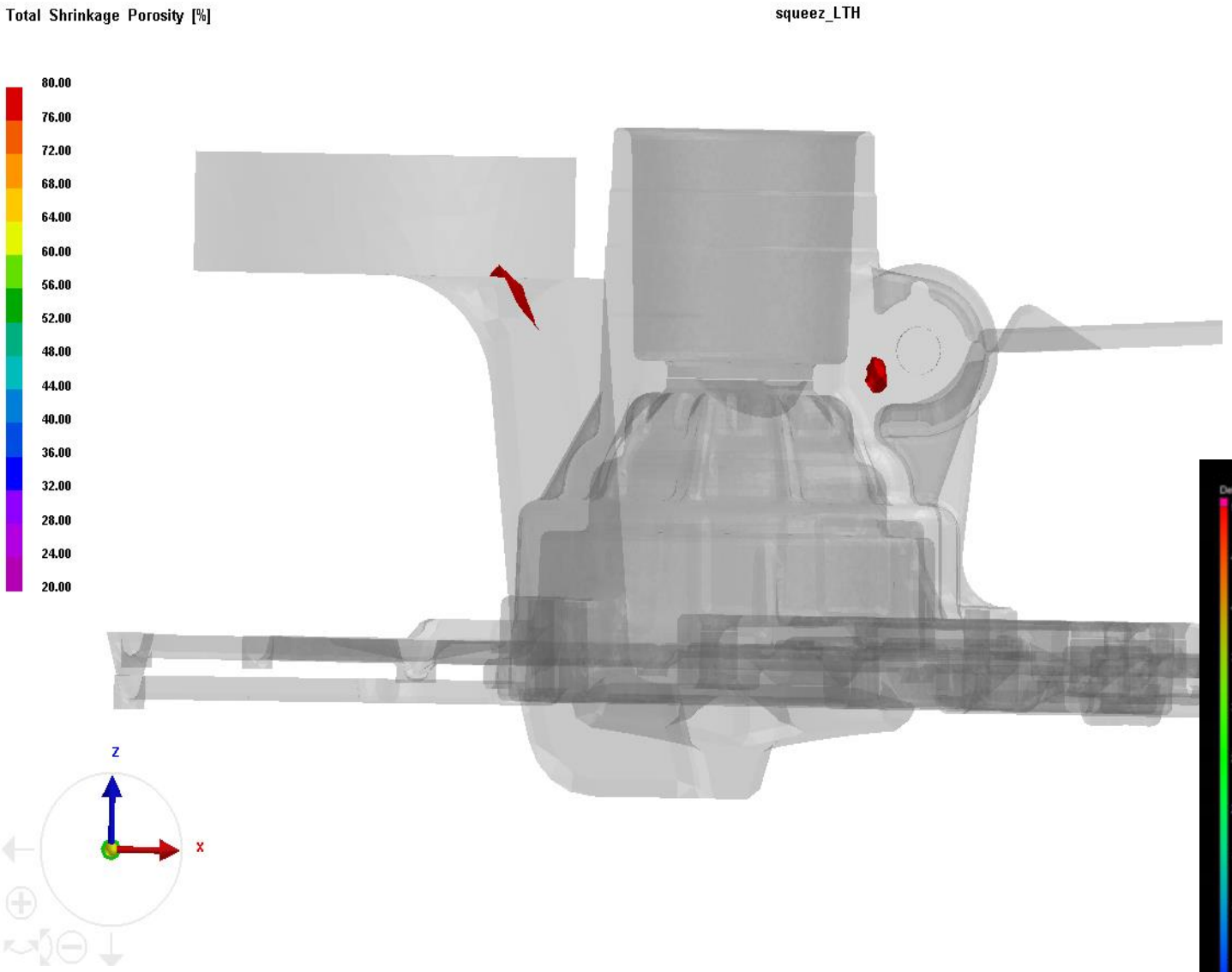


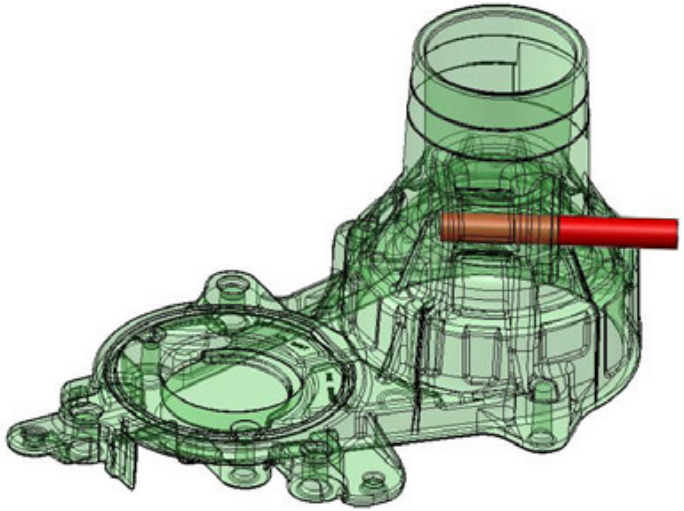

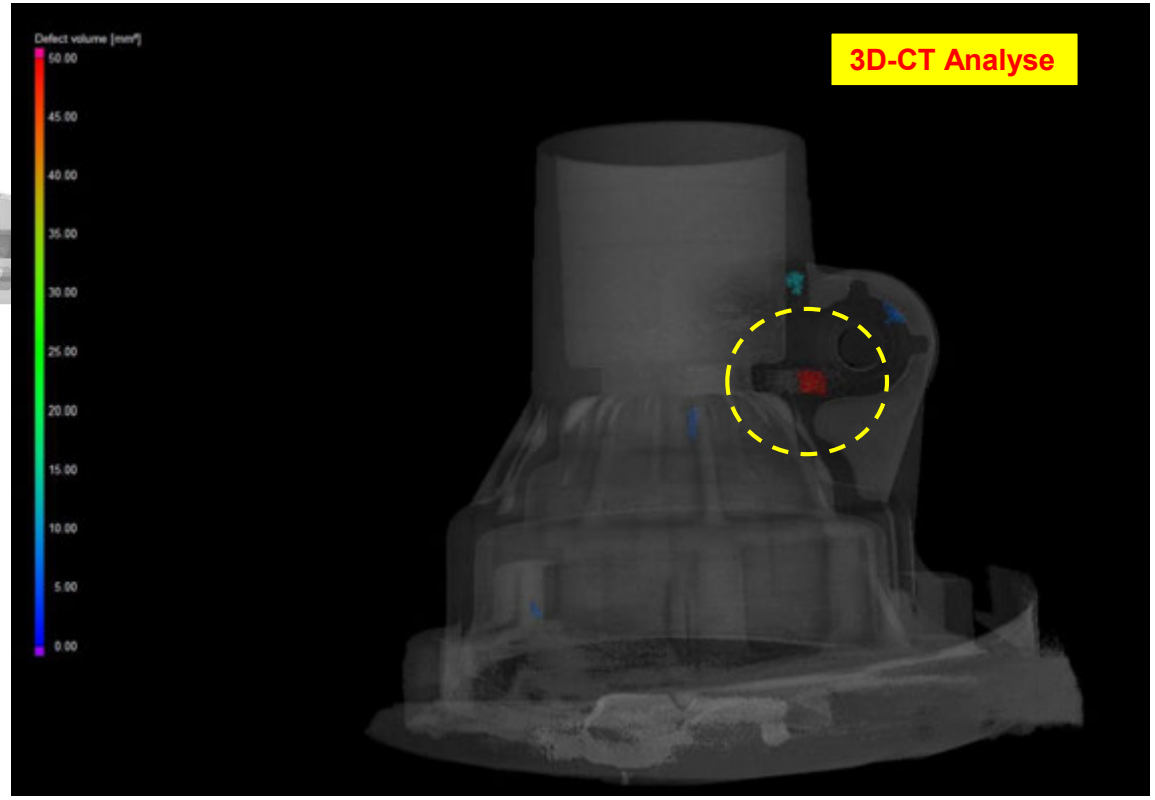


*Presented shrinkage porosity areas are not allowed, with help of the local squeezing can be eliminate

# • Parameters of loc. squeezing

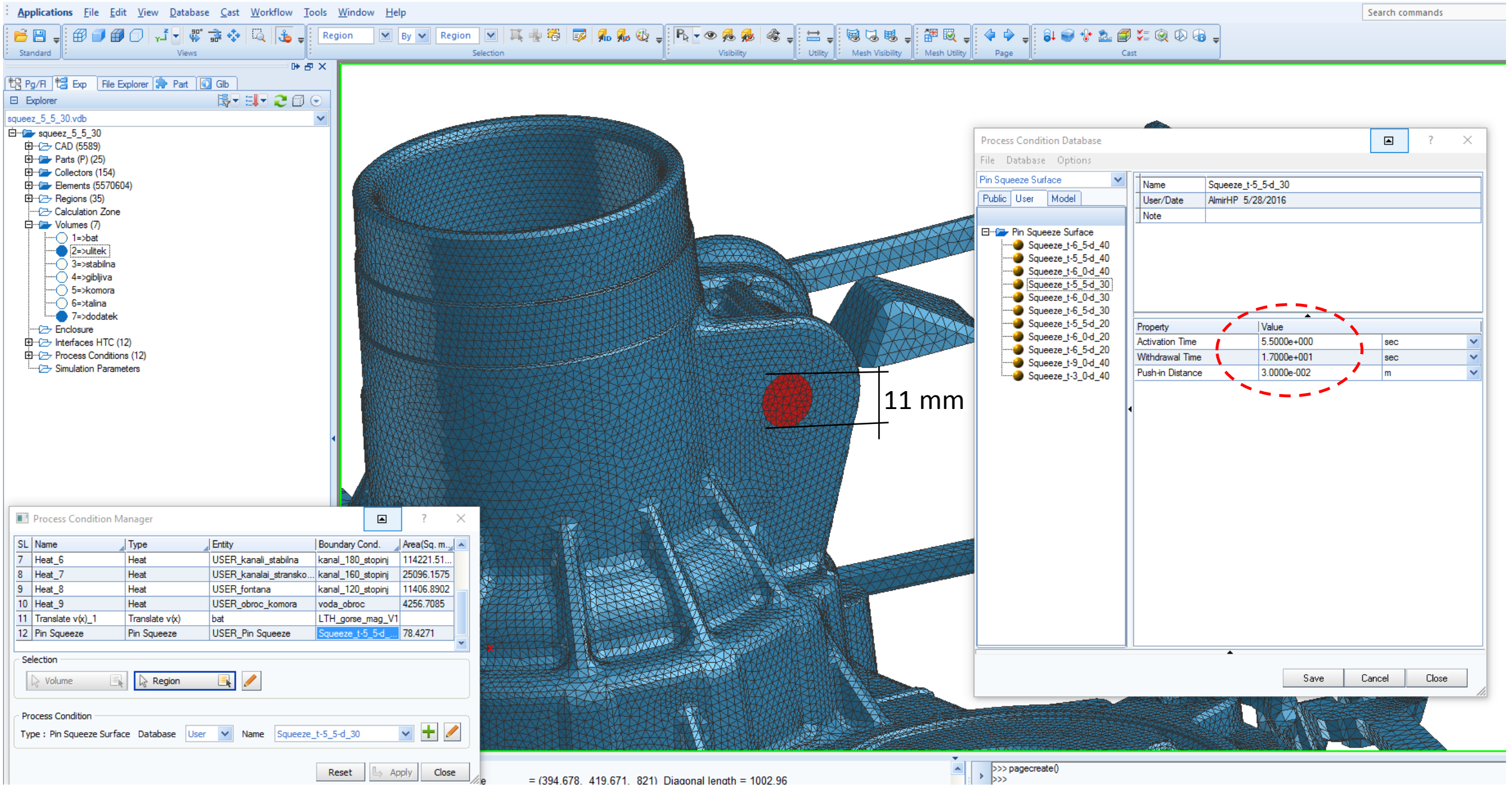

# Calculation of s. porosity

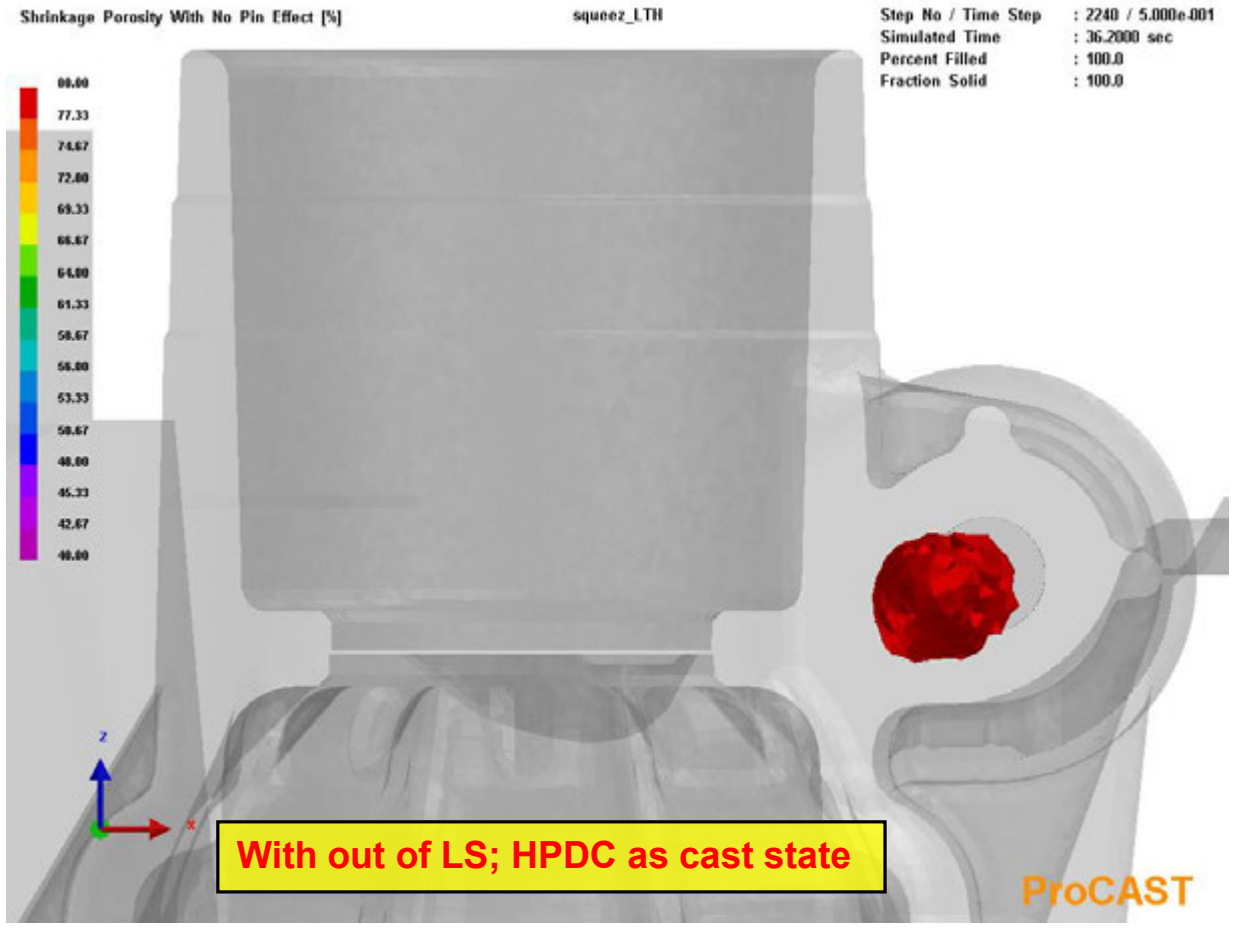


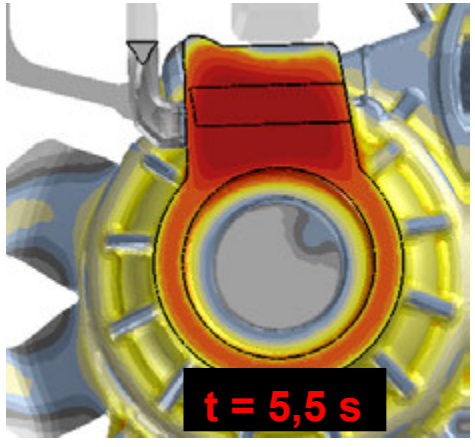


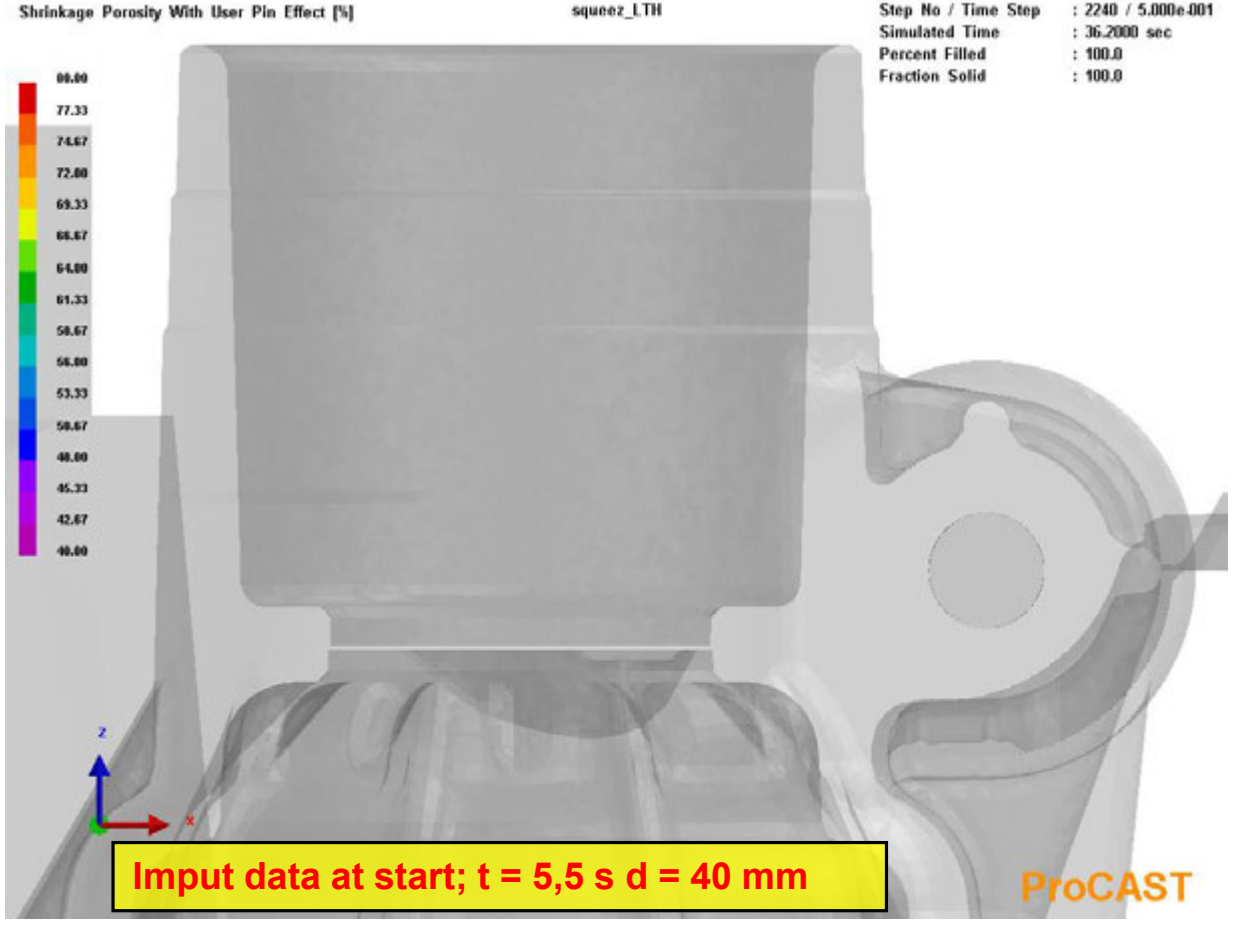

# Calculation of porosity

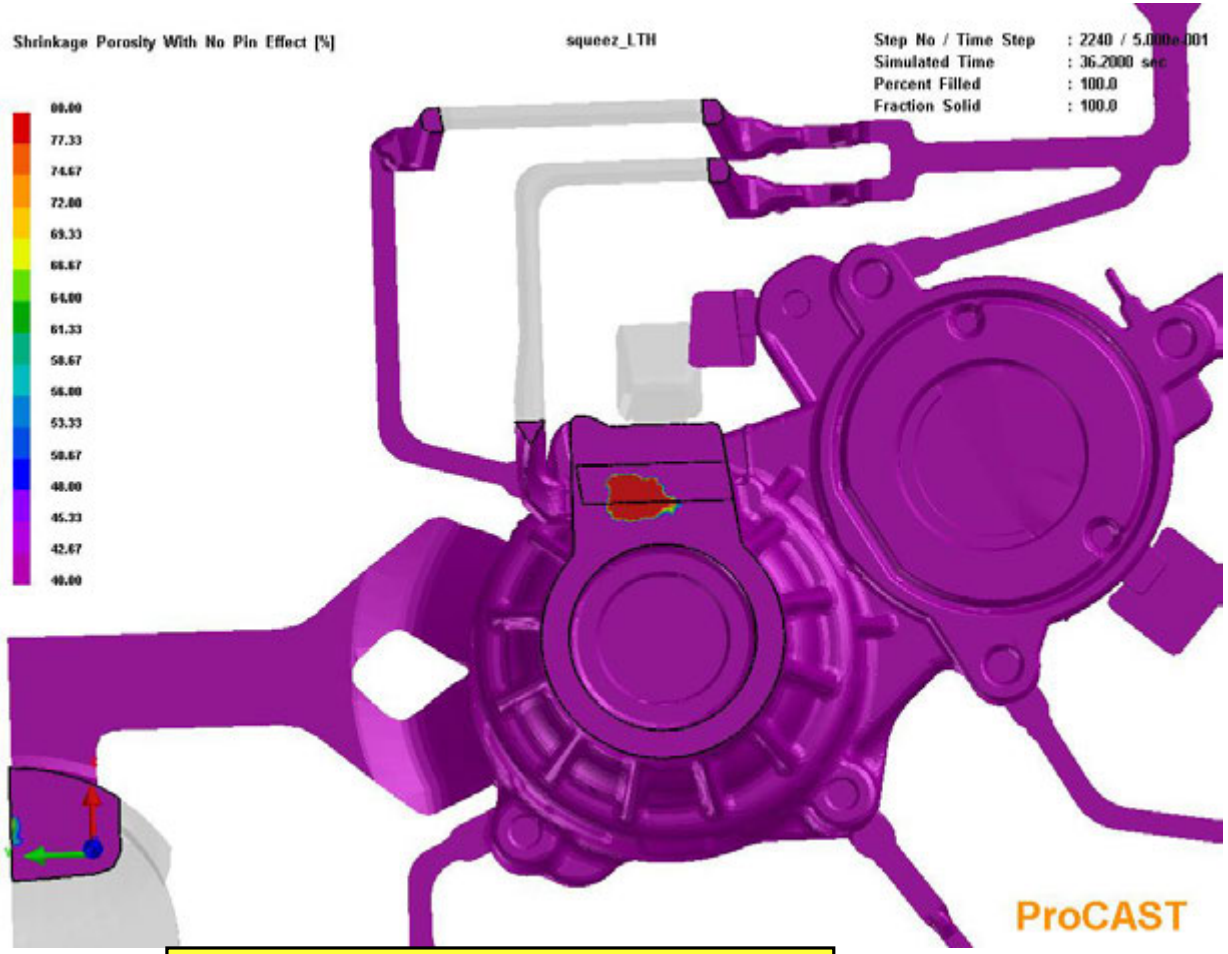


With out of LS; HPDC as cast state

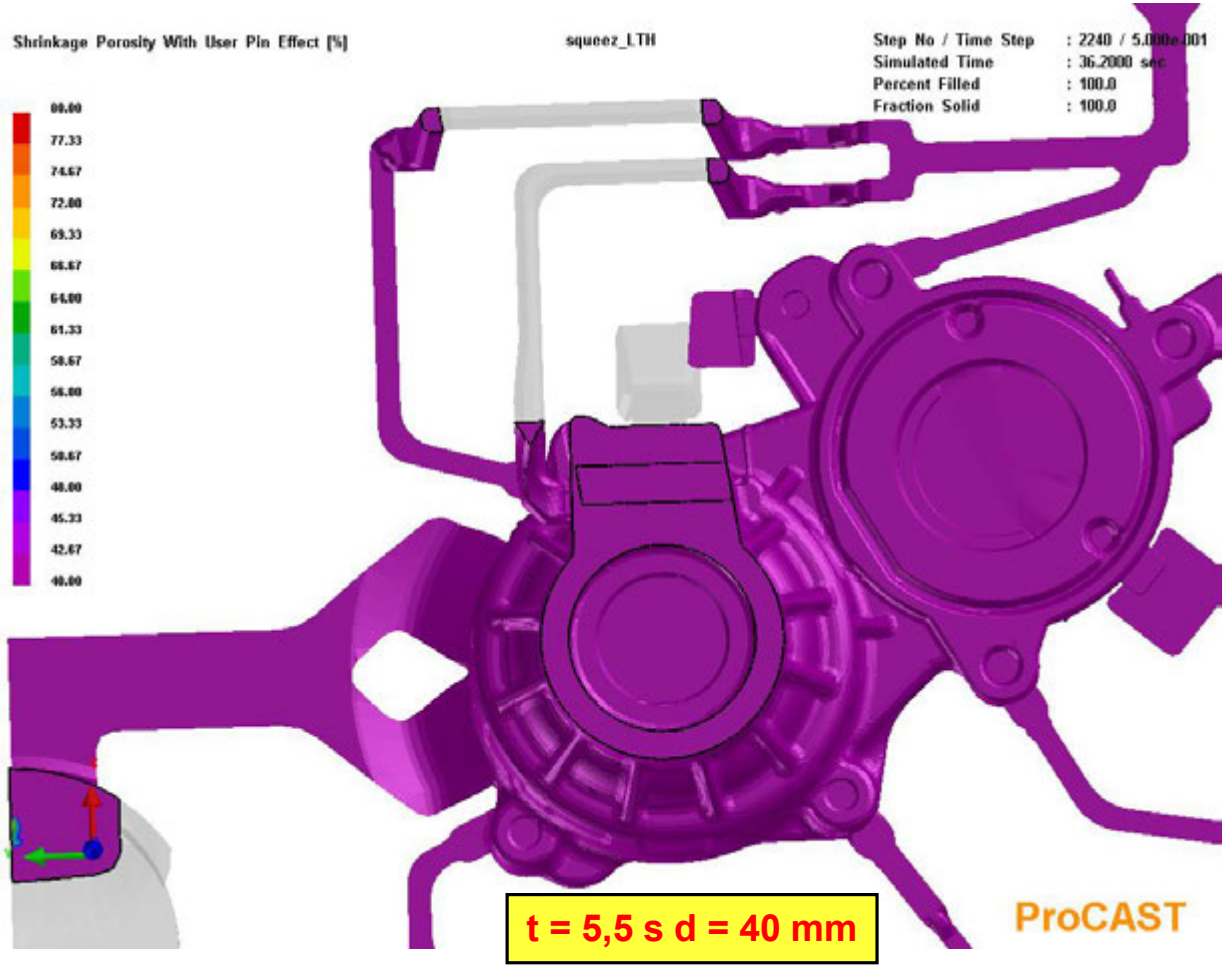


t = 5,5 s d = 40 mm

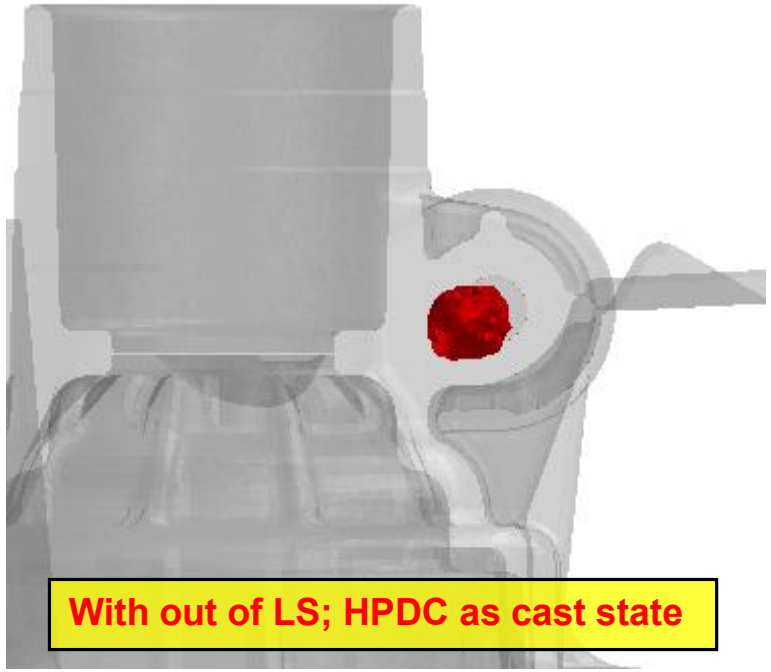


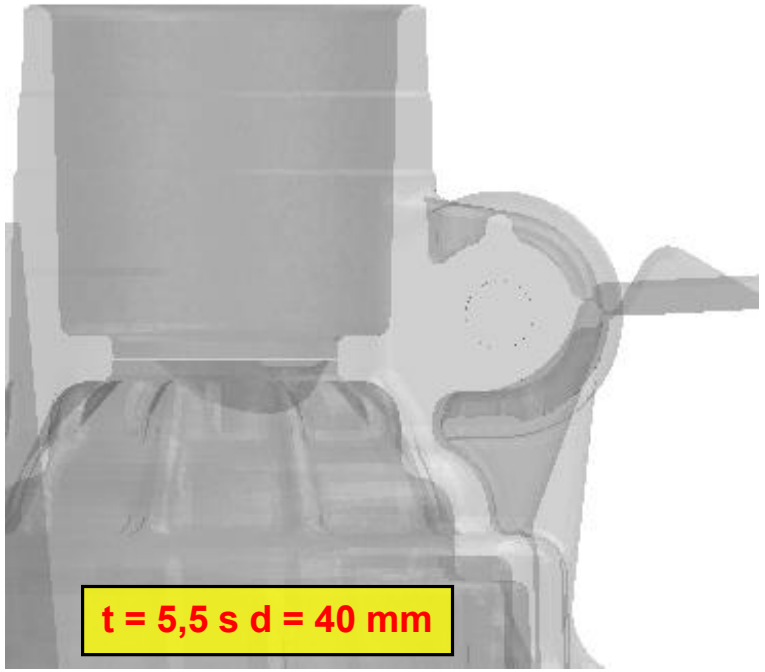


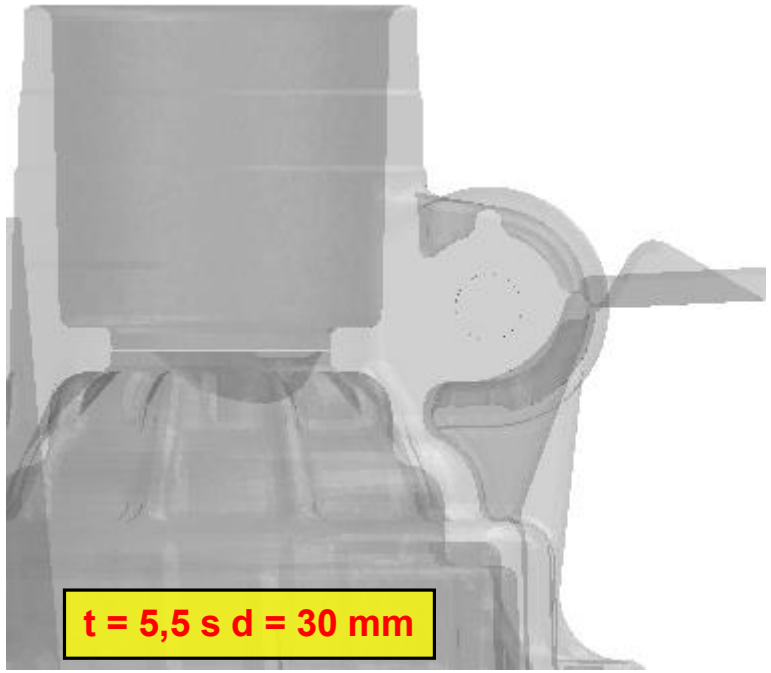


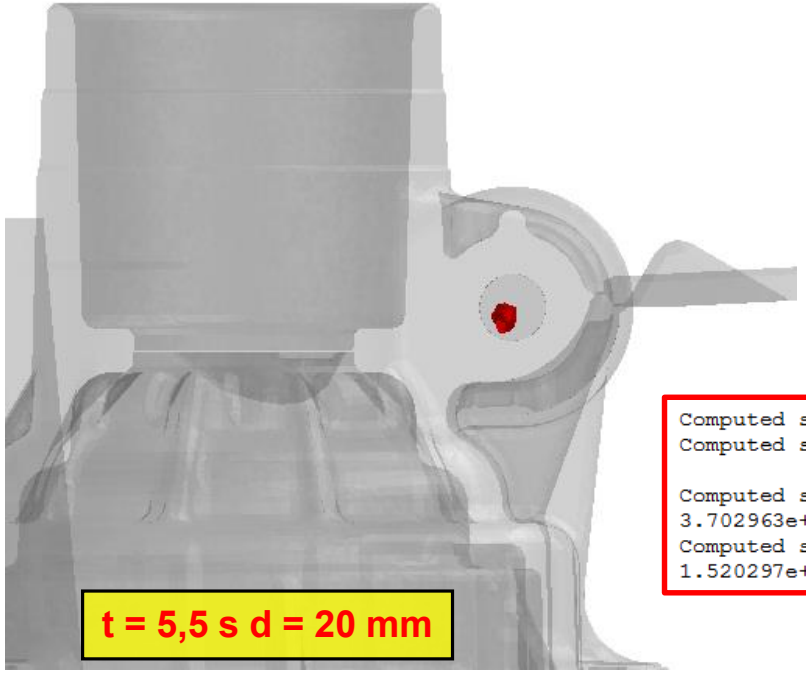


- **Calculation of s. porosity; t= const., path distance is changing**

**Optimal parameters**

```
Computed squeeze pin activation time = 5.199998e+00 seconds
Computed squeeze pin withdraw time   = 1.670001e+01 seconds

Computed squeeze pin activation time (after filling) =
3.702963e+00 seconds
Computed squeeze pin withdraw time   (after filling) =
1.520297e+01 seconds
```

- **Calculation of porosity; - path distance = const., - time is changing**

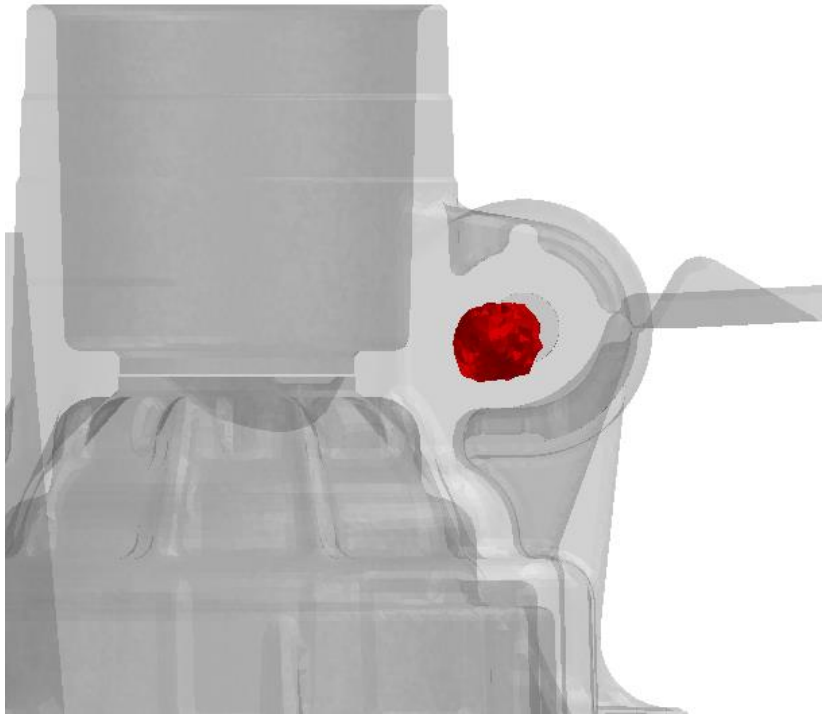

t = 3,0 s d = 40 mm

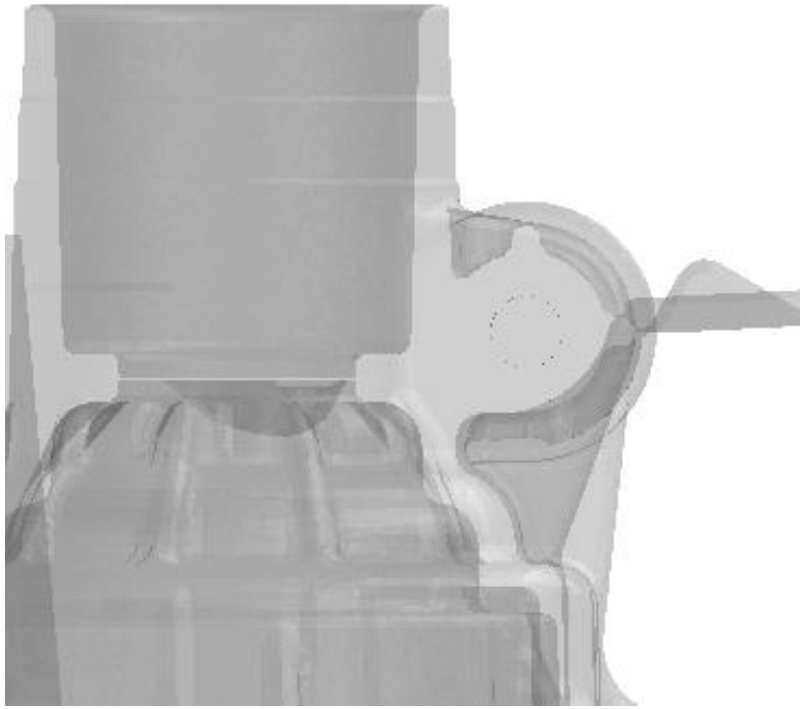

t = 5,5 s d = 40 mm

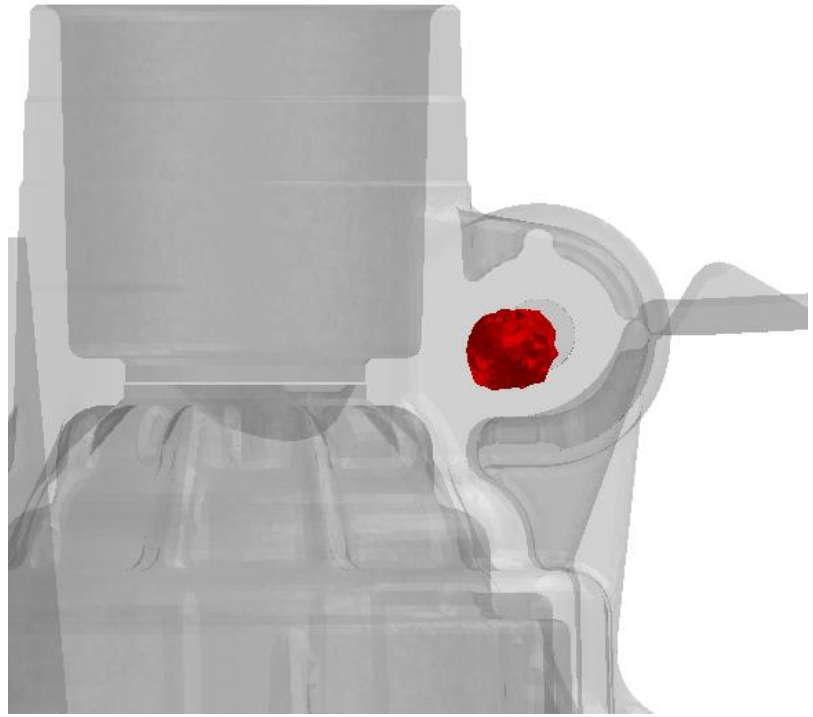

t = 9,0 s d = 40 mm

- Measurements of pressure at LS process

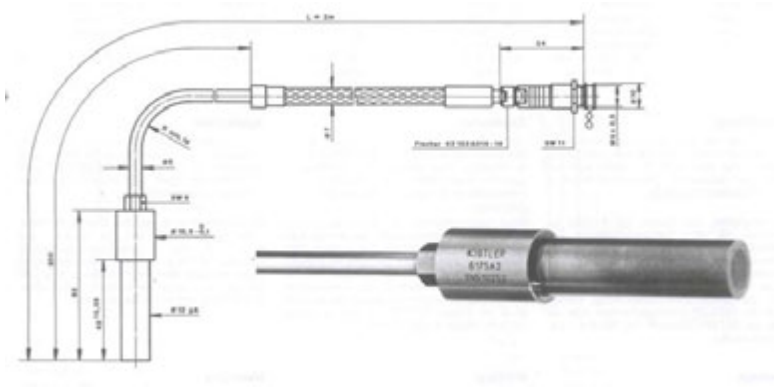

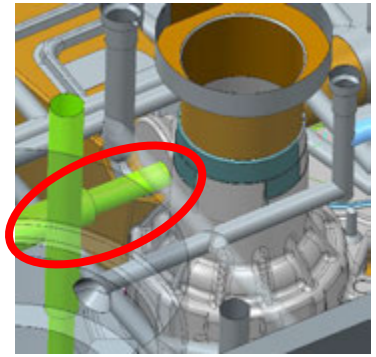

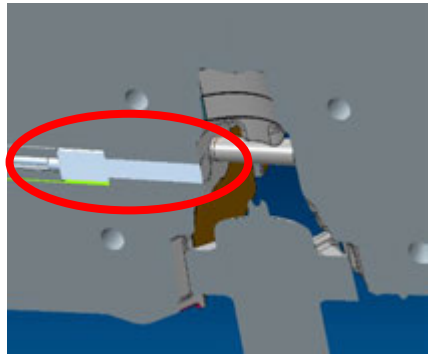

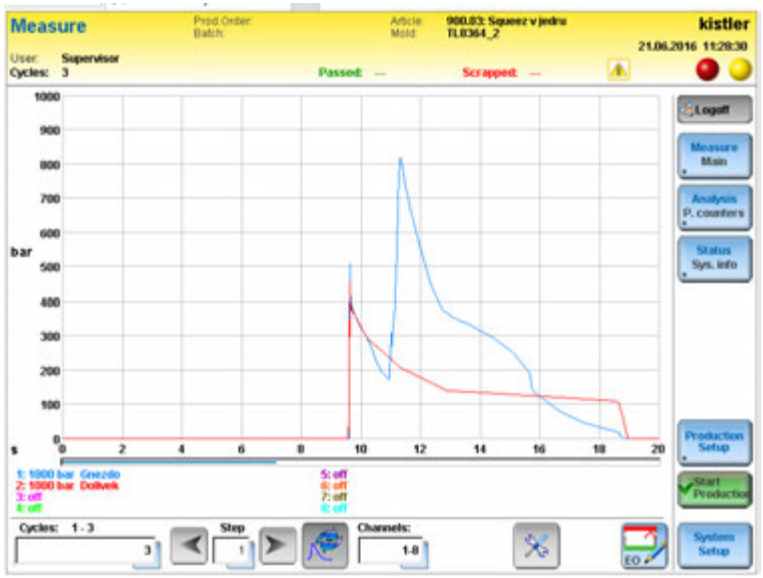


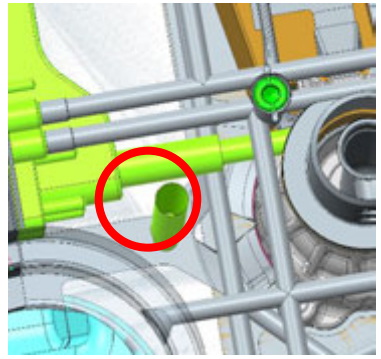

2 Pressure sensors was implemented on gating system and on local squeezing area

- without squeeze pin (as cast state)

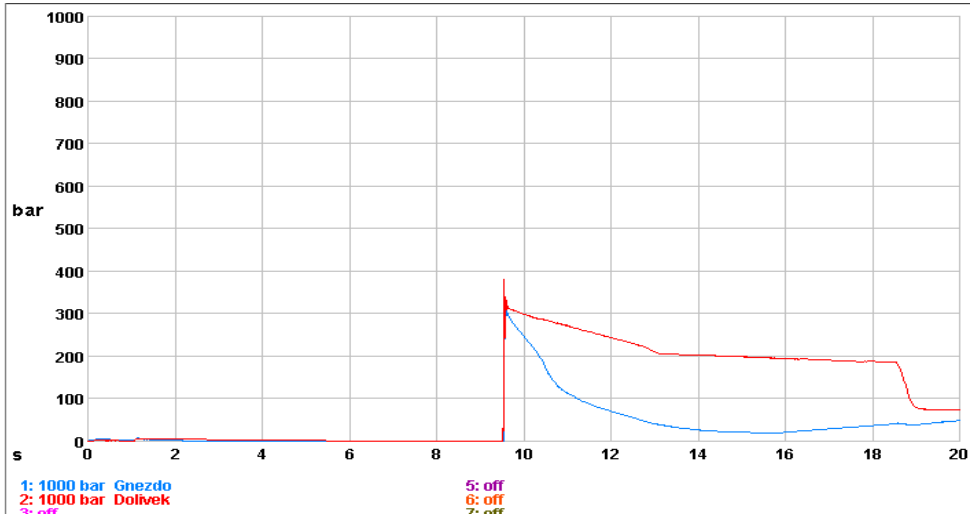


- 0,5 s squeeze pin start delay after change from II to III sequence

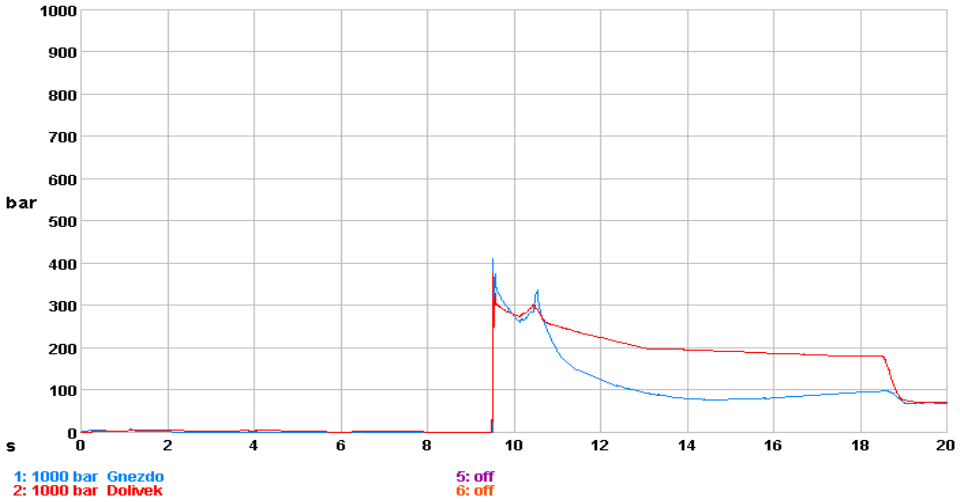


- 2s squeeze pin start delay after change from II to III sequence

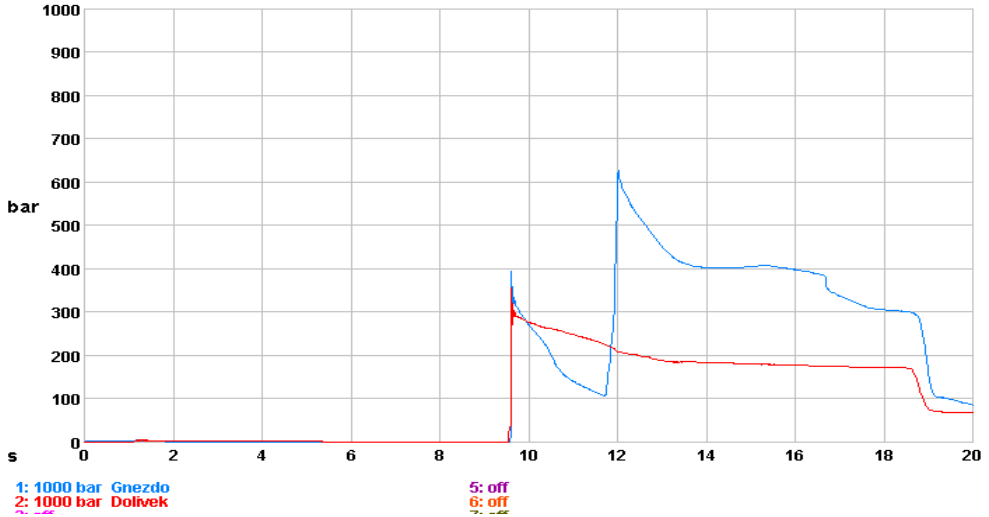


- 4,5s squeeze pin start delay after change from II to III sequence

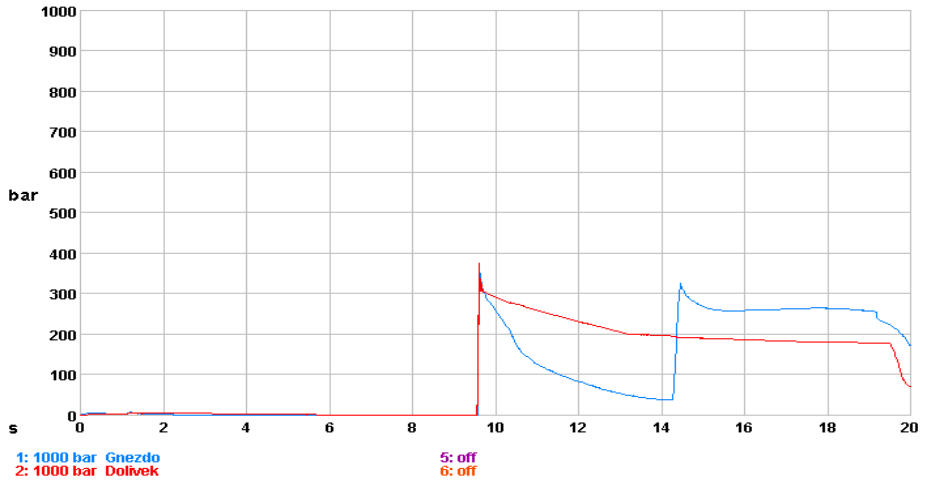

Time of squeeze pin start delay after change from II to III sequence

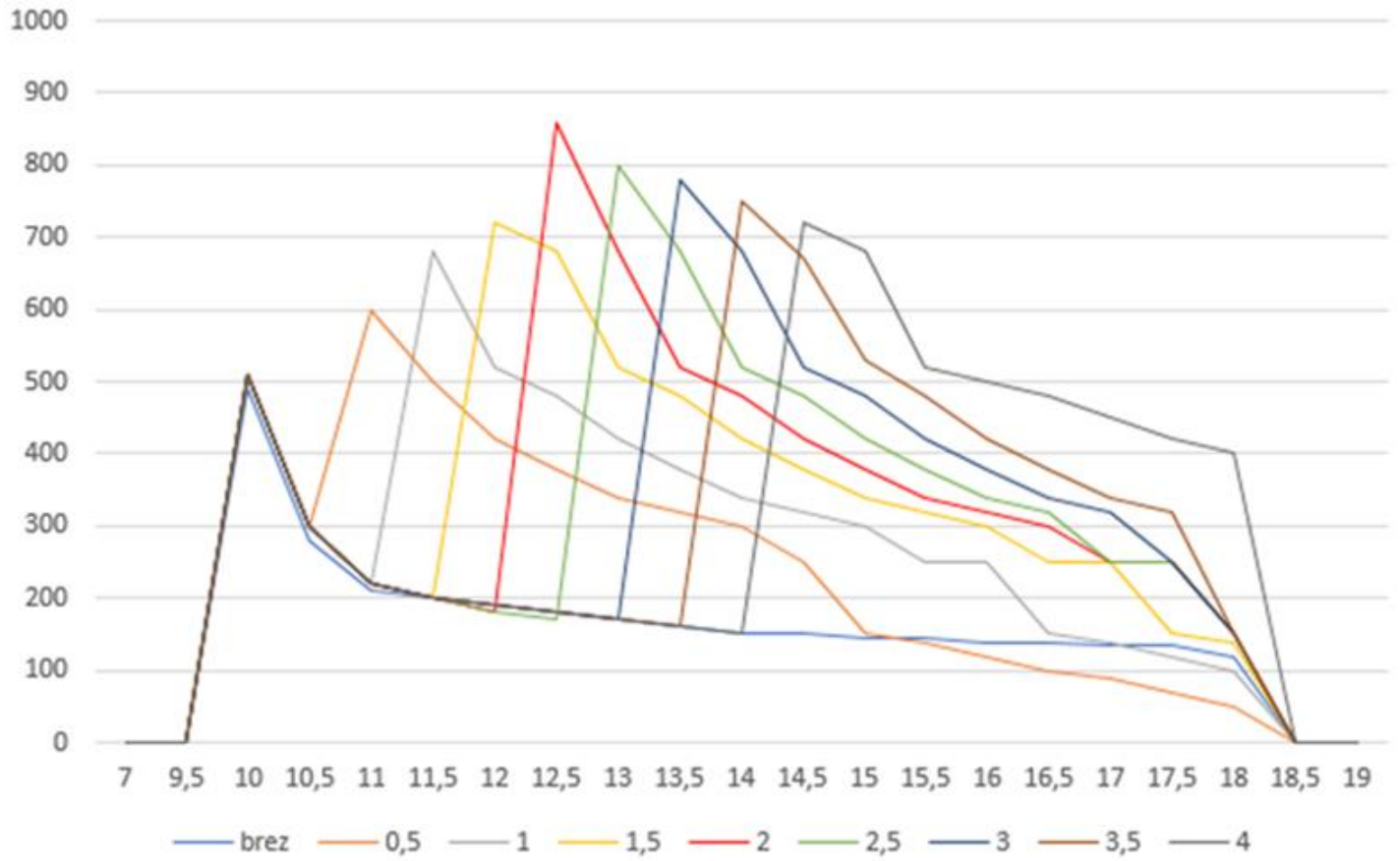

- Depth of squeeze pin implementation (path of LS pin)

| Number of experiment | 1 | 2 | 3 | 4 | 5 | 6 | 7 | 8 | 9 | 10 |
|---|---|---|---|---|---|---|---|---|---|---|
| Time of delay after end of II. seq. [s] | 0,5 | 1,0 | 1,5 | 2,0 | 2,5 | 3,0 | 3,5 | 4,0 | 4,5 | 6,0 |

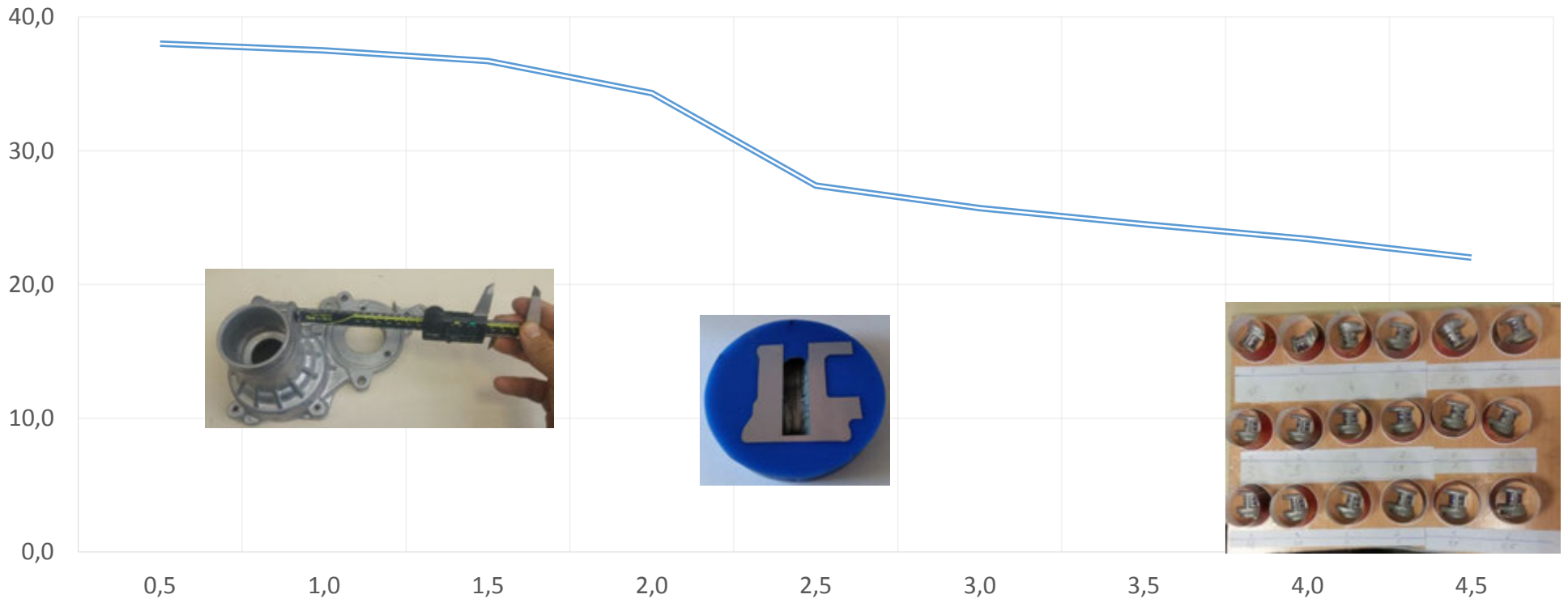

$t_{LSP}$ = 0,5 s

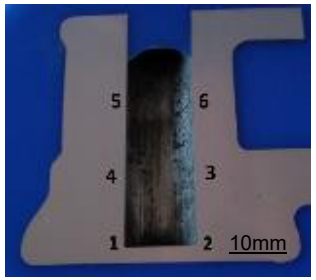


| Mesto 5 | Mesto 6 |
|---|---|
| 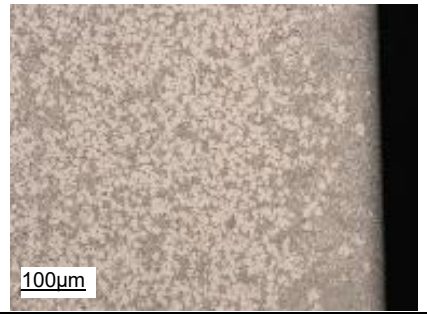  | 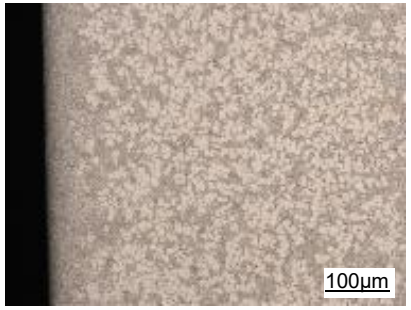  |
| Mesto 4 | Mesto 3 |
| 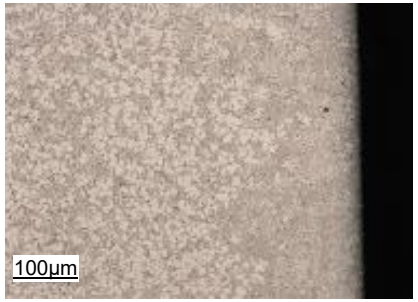  | 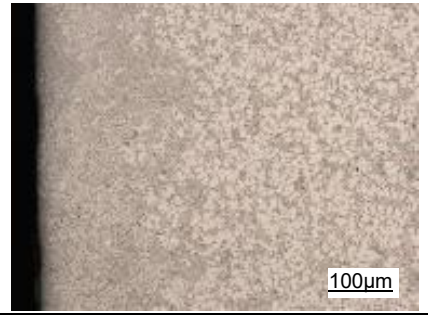  |
| Mesto 1 | Mesto 2 |
| 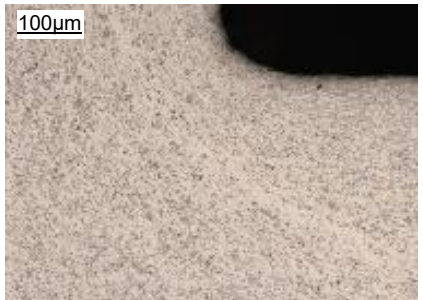  | 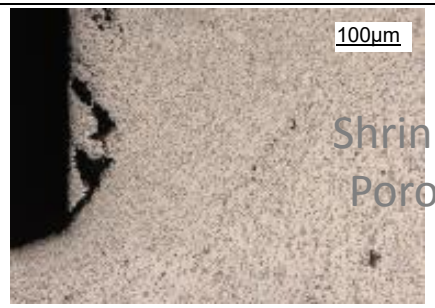  |

Shrinkage Porosity

$t_{LSP}$ = 1 s

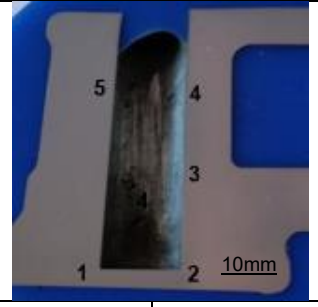


| Mesto 5 | Mesto 4 |
|---|---|
| 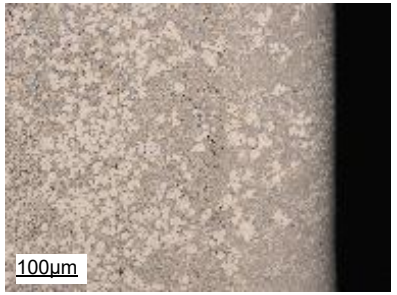  | 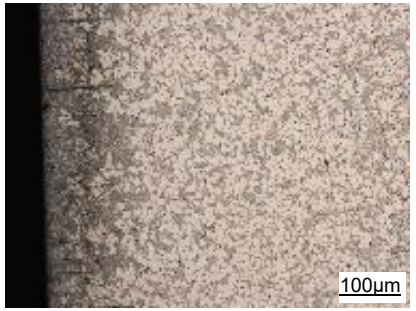  |
| | Mesto 3 |
| | 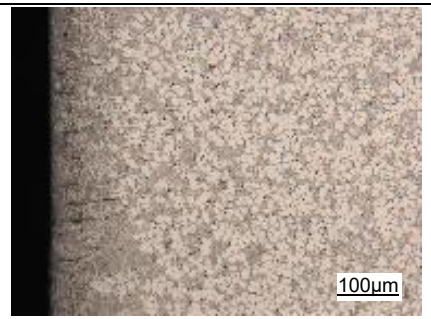  |
| Mesto 1 | Mesto 2 |
| 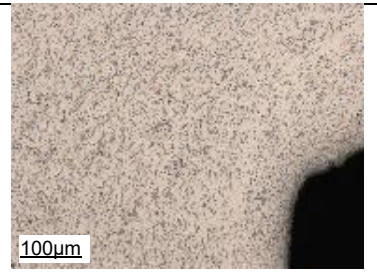  | 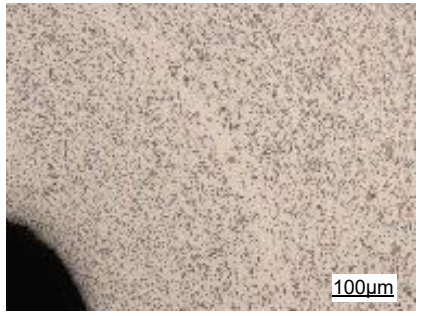  |

$t_{LSP}$ = 2 s

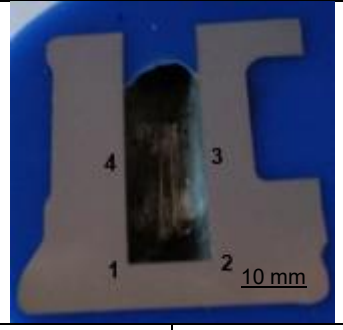


Mesto 4

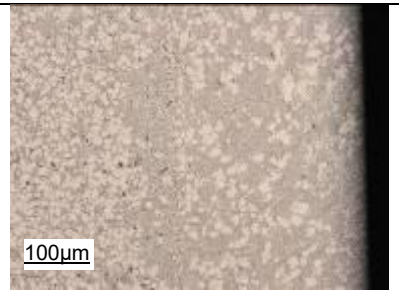


Mesto 3

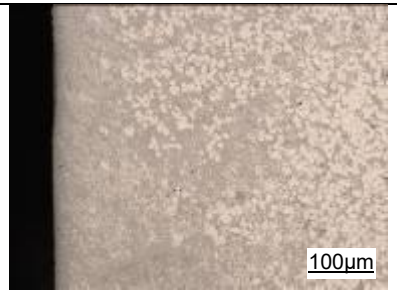


Mesto 1

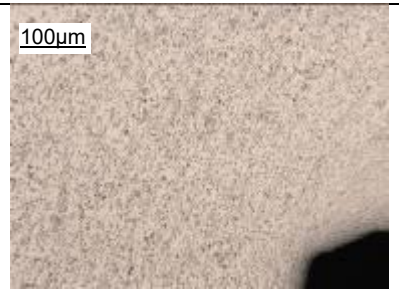


Mesto 2

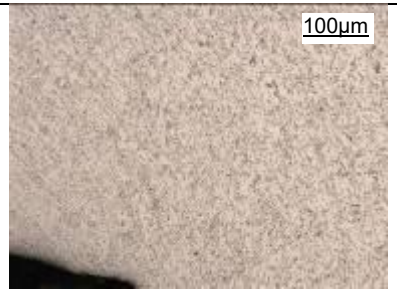


$t_{LSP}$ = 4,5 s

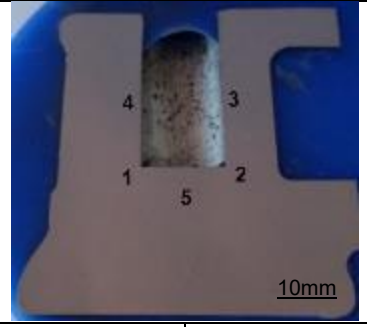


Mesto 4

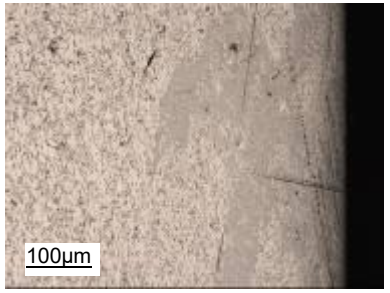


Mesto 3

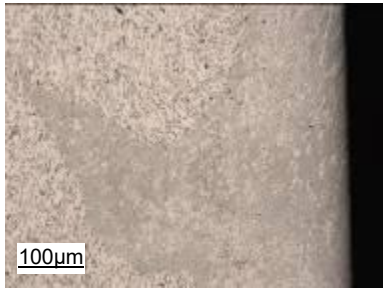


Mesto 1

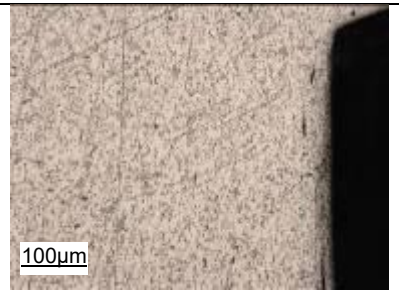


Mesto 2

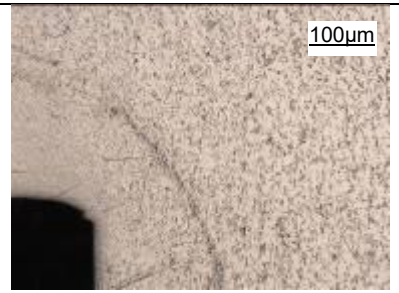


Mesto 5

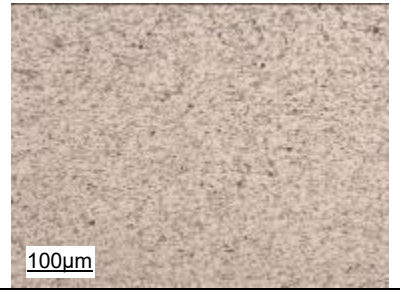

- Microstructure of casting on area where LS occurred; 226

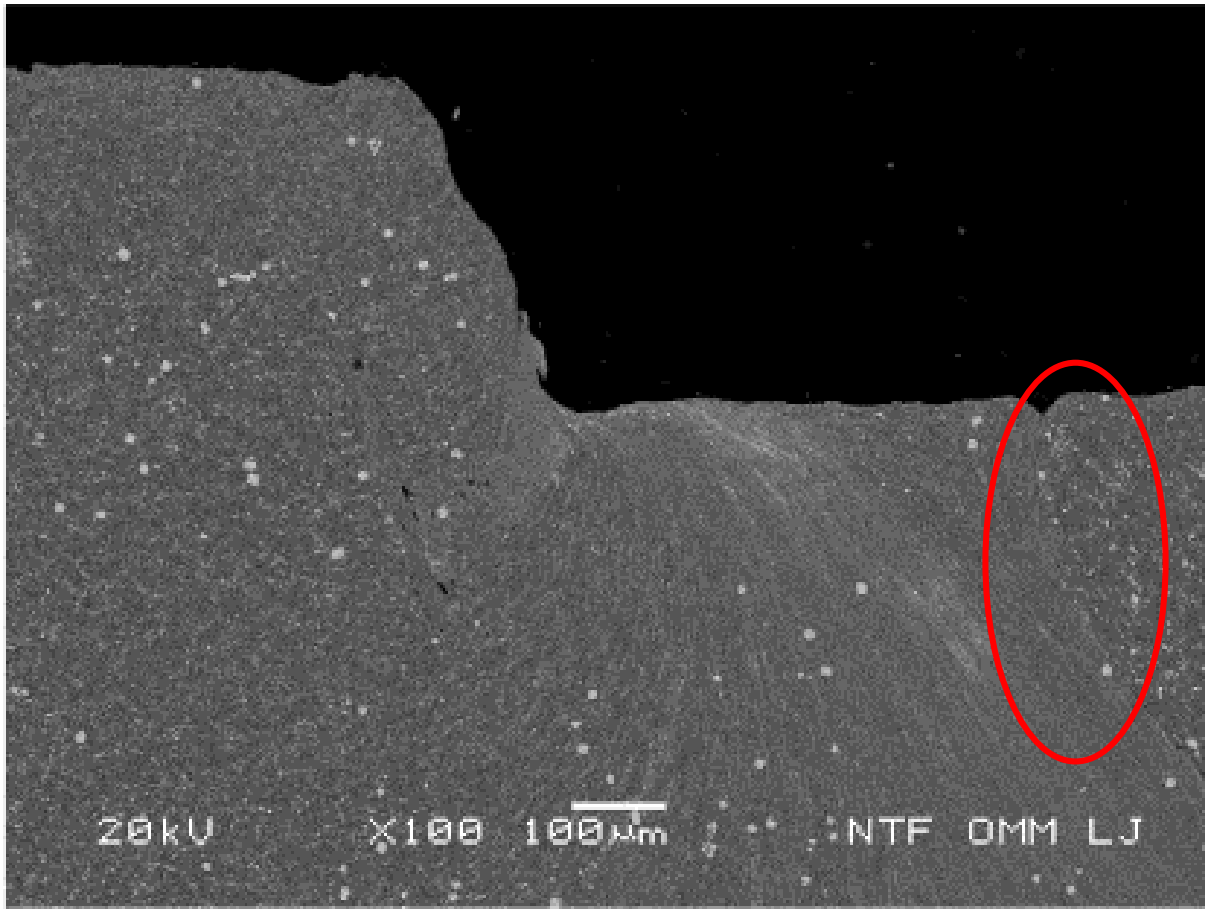


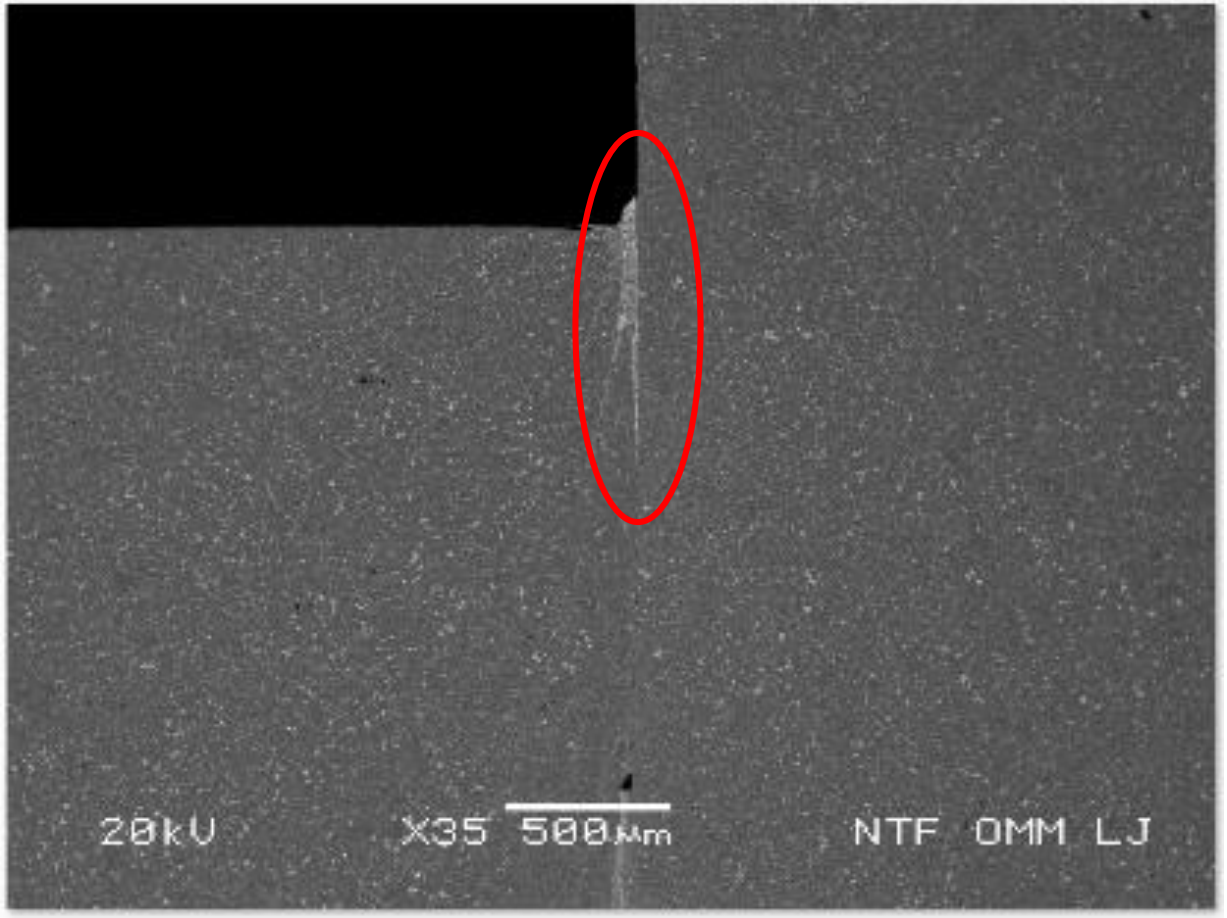


- Cold laps,
- Flow lines

# • Effective cooling

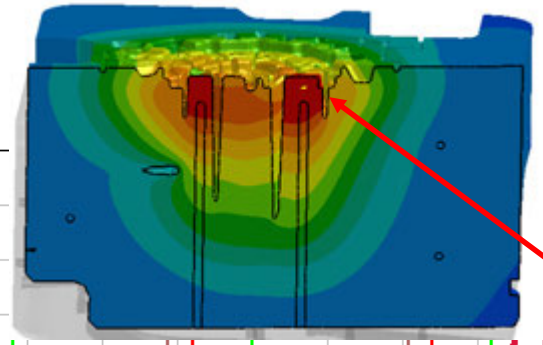

# The calculation of normal stresses in the tool

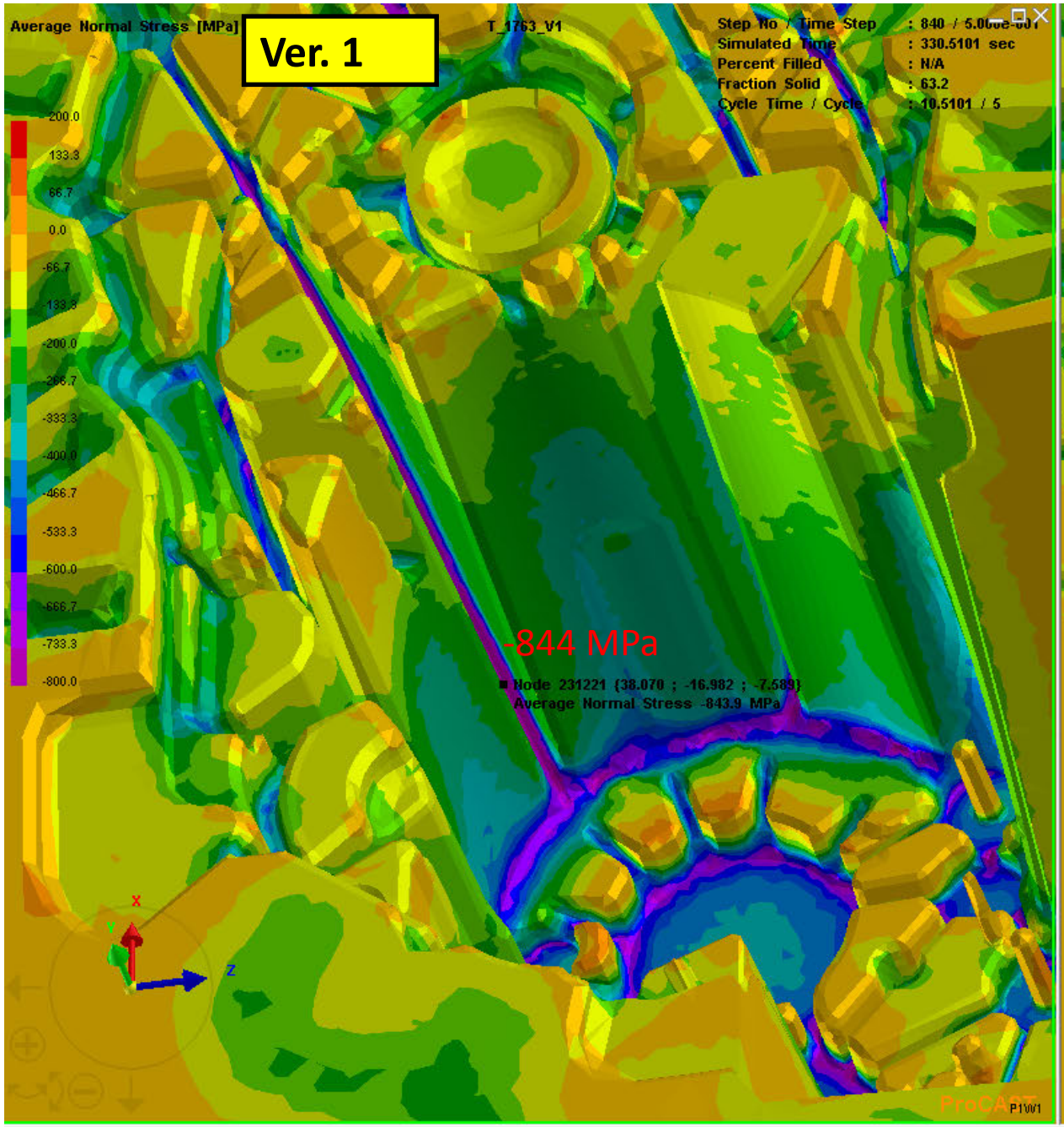


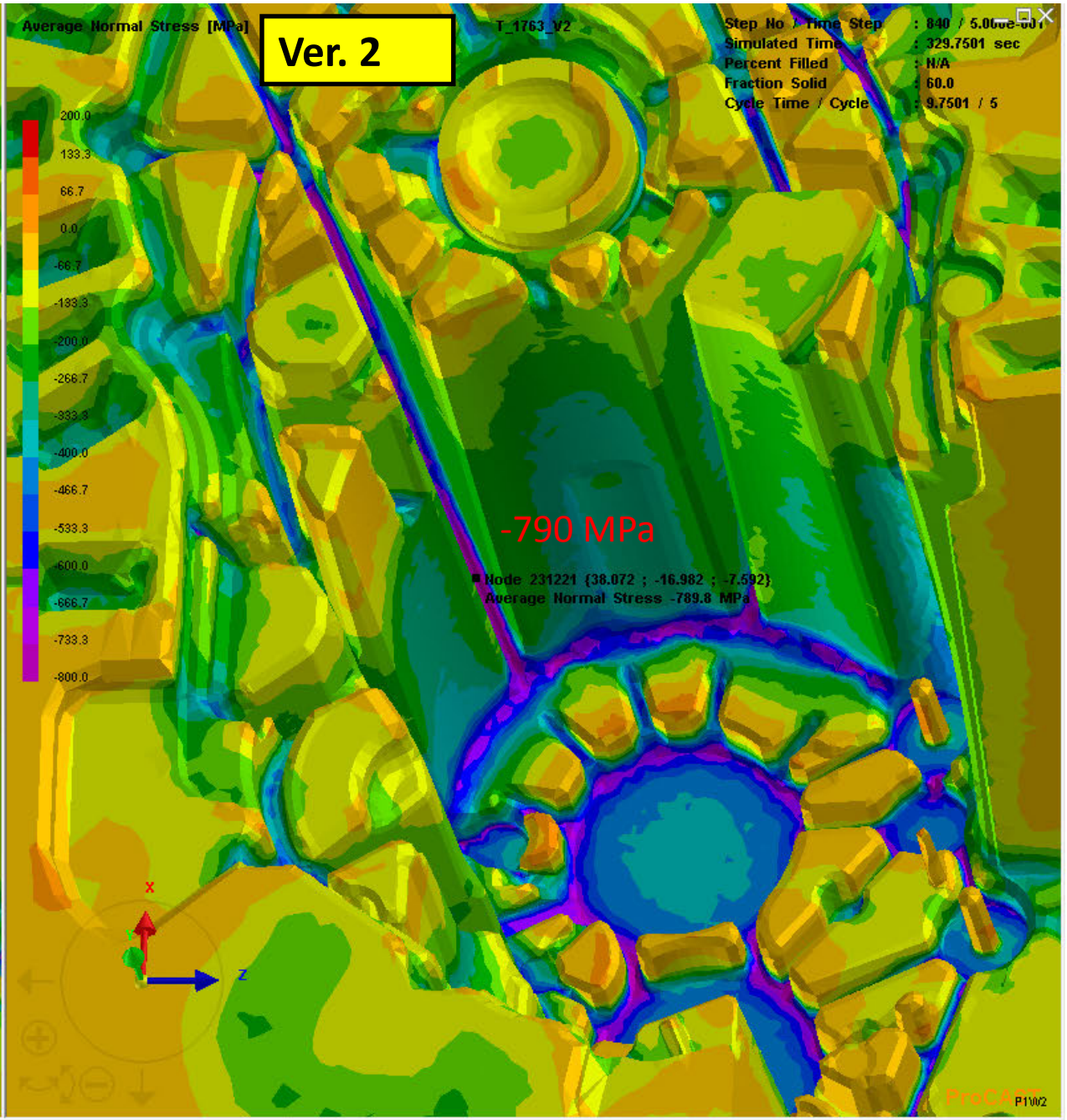

# Example 2: Technology optimization - distributor

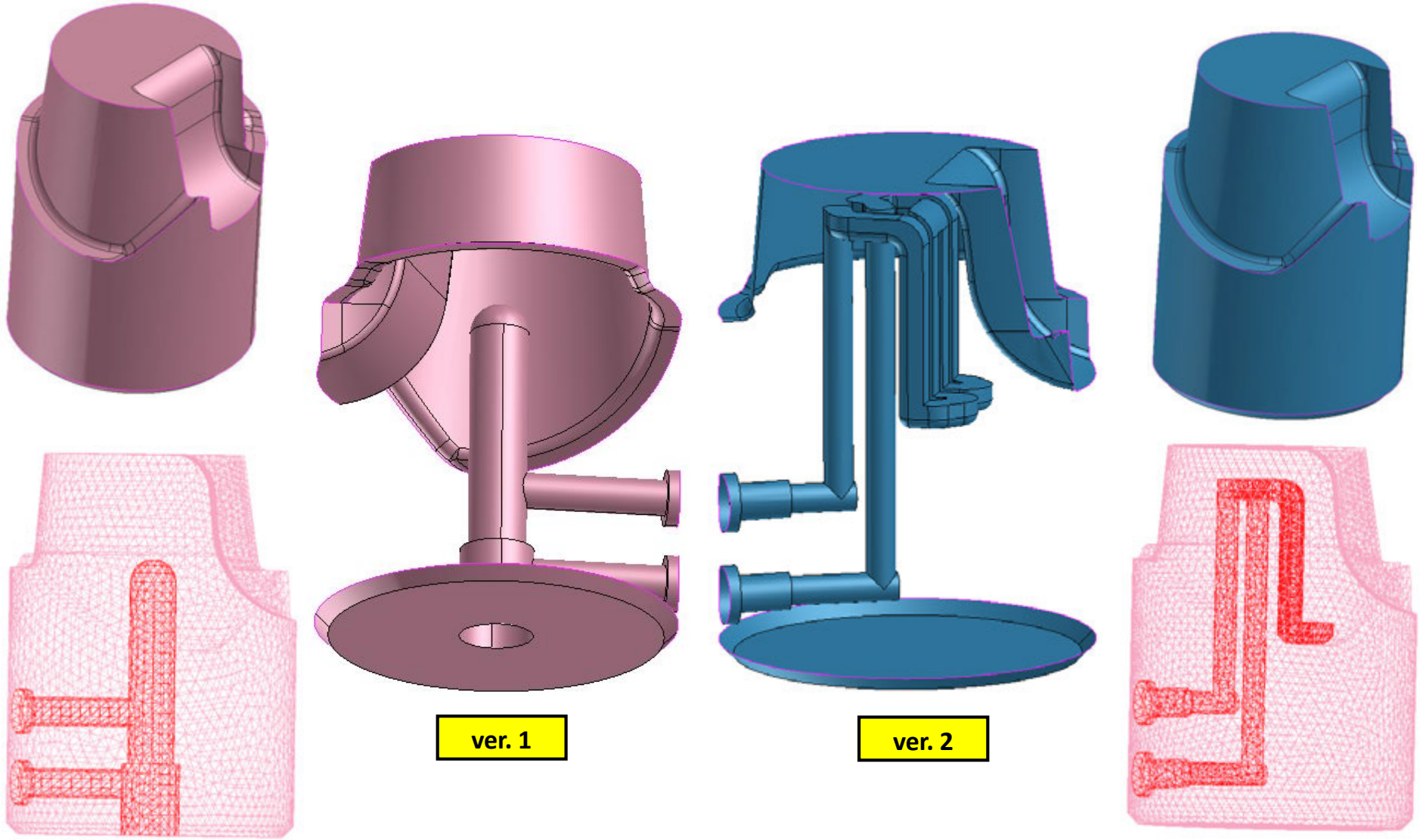

ver. 1

ver. 2

# Technology optimization - distributor

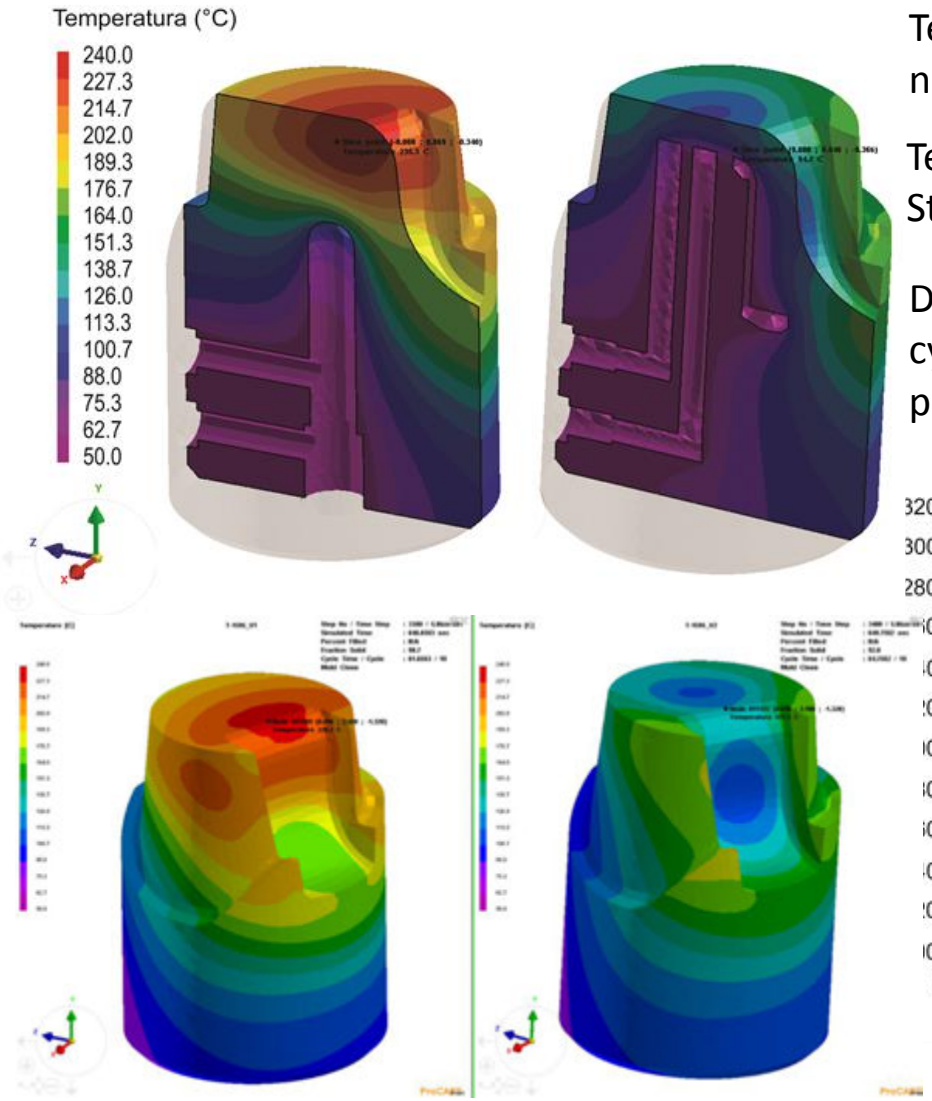


Temperature in critical area was in ver. 1- 235,3 °C, with new cooling system the temperature was 94,7 °C

Temperature drop with new cooling system was 60 %. Stresses with new  cooling system were lower for 47 %.

Distributor with version 1 cooling system made 65.080 cycles, new distributor made 79.129 cycles. Life time prolongated for 21 %.

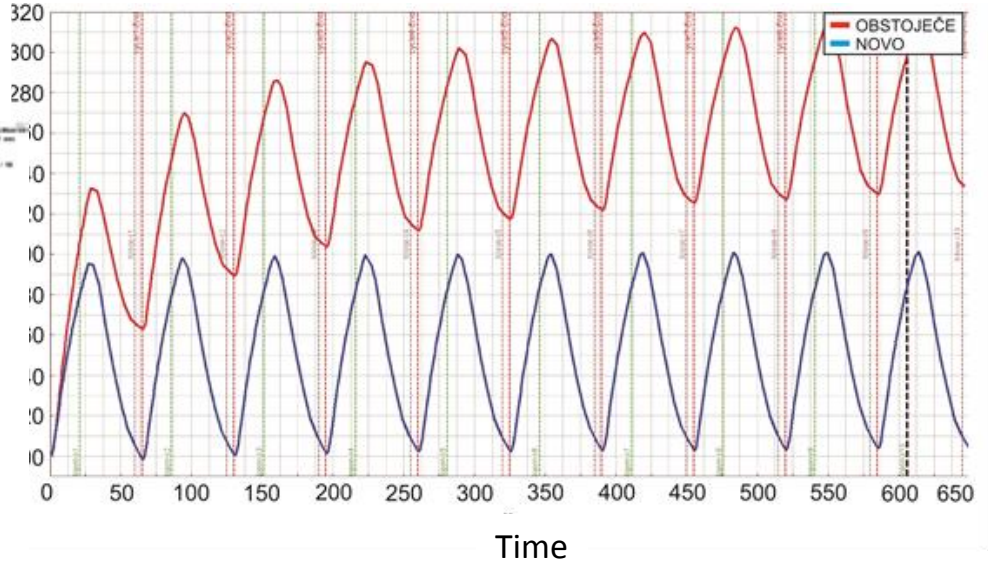

# Short conclusions

- Including advanced numerical simulations in early technology development phase can reduce costs:

- optimal casting technology can be defined before real testing
- casting defects under acceptable limits
- finding critical areas during design phase

- With adequate process and technology optimization it is possible to:

- prolong the dies lifetime
- shorten production cycle of casting

- With displacement of internal cooling and heating channels near the casting cavity surface the temperature field and also stresses are decreased

- Experimentally determined dl values vs. T can be usefully applied for prediction of total contraction in HPDC part

- With help of calculation of casting process it is possible to realize the technology and technological process window before the toll is manufactured

- When the unidirectional solidification is not possible the use of LS can be accepted.

- Time of delay have to be calculate for each geometry and depended from local fracture solid. Calculated and experimentally obtained values are practical the same value.

- Microstructure analyses show that according to technological process window no critical areas was found.

- Pressure of III. sequence can be generally decrease what cause lover residual stress.

# SREČNO!

# Good luck!

17th INTERNATIONAL FOUNDRYMEN CONFERENCE
Hi-tech casting solution and knowledge based engineering
Opatija, May 16th-18th, 2018
http://www.simet.hr/~foundry/

# FROM IDEA TO PATENT: DEVELOPMENT OF INNOVATIVE BIOMEDICAL MATERIAL FOR DENTAL IMPLANTS

**Zdravko Schauperl[1]*, Amir Ćatić[2], Mateja Šnajdar[1], Martin Balog[3], Peter Križik[3]**

[1] University of Zagreb Faculty of Mechanical Engineering and Naval Architecture, Zagreb, Croatia
[2] University of Zagreb School of Dental Medicine, Zagreb, Croatia
[3] Slovak Academy of Sciences Institute of Materials and Machine Mechanics, Bratislava, Slovakia

**Invited lecture**
*Subject review*

**Abstract**

One of the main issues concerning dental, but also all other implants, arises from their Young's modulus being considerably higher than that of bone. This can lead to stress shielding, bone resorption, and poor osseointegration of dental implants. Therefore, intensive activities are directed to lowering Ti implants Young's modulus while preserving sufficient values of other mechanical properties. Most of them are oriented at β-type Ti alloys, but recently some other metal matrix composites appear as a possible solution.
This presentation report on the development of the titanium-magnesium (Ti–Mg) bioactive metal-metal composite designed concretely for a fabrication of dental implants. The biomedical Ti-12vol. %Mg composite is manufactured using a cost effective approach, where a mixture of elemental Ti and Mg powders is extruded at low temperature to sound profiles. Microstructure of composite comprises filaments of biodegradable Mg component, which are arrayed along extrusion direction and are homogenously distributed within permanent, bioinert Ti matrix. Compared to Ti Grade 4, the reference material used for dental implants, the properties of as-extruded composite include significantly reduced Young's elastic modulus (92.1 GPa) and low density (4.12 g/cm$^3$), while the mechanical strength of Ti Grade 4 is maintained (at values required for dental implants). Dynamic testing of dental implants fabricated from as-extruded composite, realized to follow the ISO 14801 standard for endosseous dental implants, confirms fatigue performance of Ti-Mg implants equal to the one of the reference material. Exposure of as-extruded composite samples to Hank's solution, realized to simulate behavior in human body over the time after implantation, yields gradual dilution of Mg from composites surface and volume. Corroded Mg leaves at prior Mg filament sites pores within Ti matrix, which remains intact. This provides further decrease of Young's modulus and enhances macro and micro roughness at implants surface. As a result, newly developed Ti-Mg composite shows improved mechanical compatibility (i.e., reduction of stress-shielding) and better osseointegration potential.

***Keywords**: dental implants, powder metallurgy, Ti-Mg composite, low modulus of elasticity*

*Corresponding author (e-mail address): *zdravko.schauperl@fsb.hr*

# FROM IDEA TO PATENT: DEVELOPMENT OF INNOVATIVE BIOMEDICAL MATERIAL FOR DENTAL IMPLANTS

Zdravko Schauperl[1], Amir Ćatić[2], Mateja Šnajdar[1], Martin Balog[3] , Peter Križik[3]

[1] Faculty of Mechanical Engineering and Naval Architecture, University of Zagreb, Ivana Lučića 5, HR – 10000 Zagreb, Croatia
[2] School of Dental Medicine, University of Zagreb, Gundulićeva 5, HR – 10000 Zagreb, Croatia
[3] Institute of Materials and Machine Mechanics, Slovak Academy of Sciences, Dúbravská cesta 9/6319, 845 13 Bratislava, Slovakia

***What I'm going to talk about:***

- Biomedical problem
- Idea
- Materials, technology, testing results
- In vivo testing
- What next

## *What I'm going to talk about:*

- ✓ ***Biomedical problem***
- ➢ Idea
- ➢ Materials, technology, testing results
- ➢ In vivo testing
- ➢ What next

# *Requirements on biomaterials:*

- Biocompatibility
- Chemical stability
- Mechanical properties
- Physical properties
- Surface condition

Materials in biomedicine:

- METALS (stainless steel, Ti alloys, Co alloys, Mg)
- POLYMERS (PEHD, PMMA…)
- CERAMICS (Al2O3, ZrO, SiC, HAP….)
- COMPOSITES (PMC, MMC, CMC)

***There is still no bulk (single) material that fully meets the two aspects of biocompatibility:***

1. Mechanical incompatibility (stress shielding effect) *
2. Compatibility of Implant and Tissue Surface (oseintegration) **

---

- LL. Hench, I.Thompson: Twenty-first century challenges for biomaterials, J Roy Soc Interface, 7 (2010), 379–391

** R. B. Ashman: Elastic modulus of trabecular bone material, Journal of Biomechanics, 21(1988), 177–181

# *STRESS SHIELDING EFFECT*

Result of the difference in the stiffness of the implant material and bone tissue

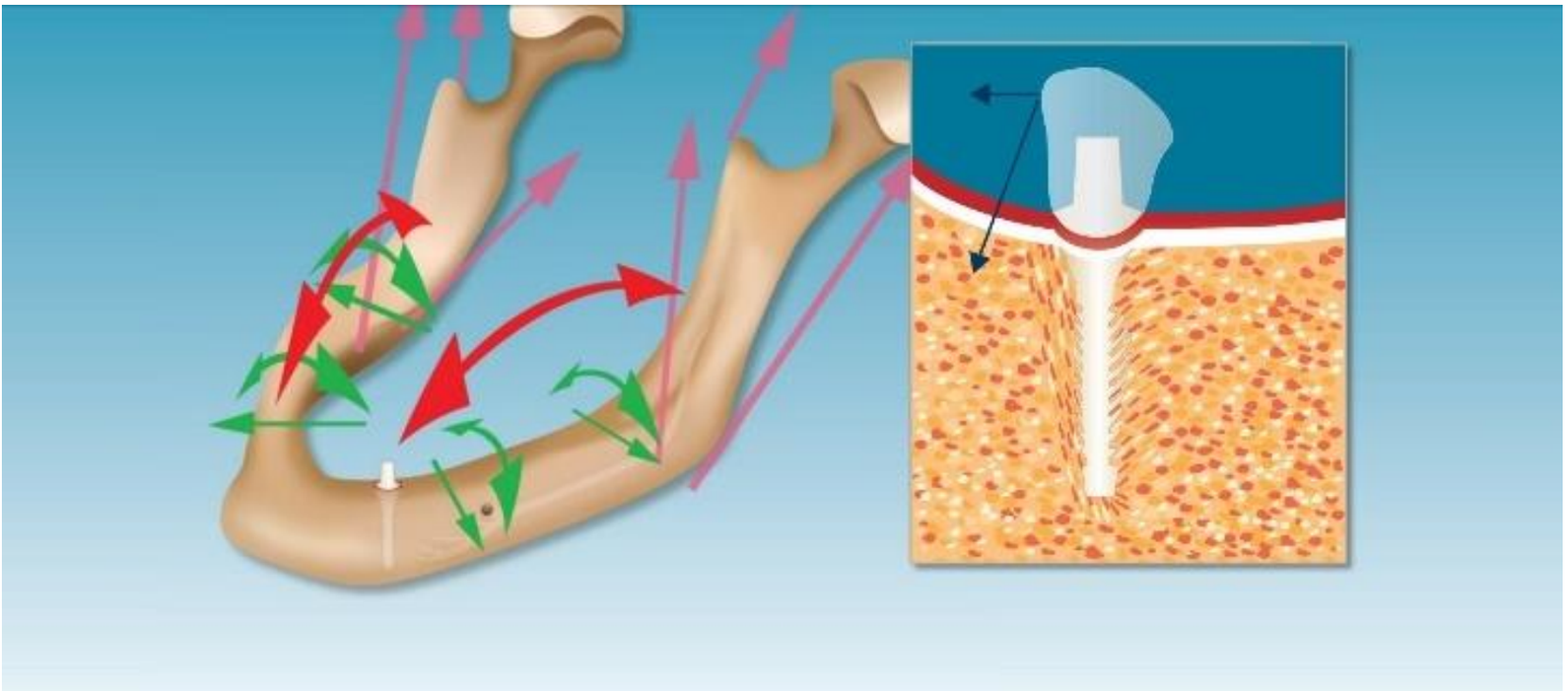

| Material | E, GPa |
|---|---|
| Bone | 10-50 |
| Ti | 110 |
| Stainless steel | 210 |
| $Al_2O_3$ | 380-410 |
| HAP | 80-120 |

**β-type Ti alloys 60 GPa to 85 GPa** (non-toxic stabilizers such as Nb,Zr,Ta,Sn,Mo: TiMo6Zr2Fe, Ti15Mo5ZrAl, Ti15Mo3Nb3O, Ti13Nb13Zr)

**Porous Ti implants**

---


Niinomi M, Nakai M. Int Journal Biomater. 2011.

P. Roach, D. Eglin, K Rohde, C. C. Perry: Modern biomaterials: a review—bulk properties and implications of surface modifications, Journal of Materials Science: Materials in Medicine,18 (2007), 1263-1277

# *OSEOINTEGRATION*

Forming a direct structural and functional link between the bone tissue and the surface of the implant

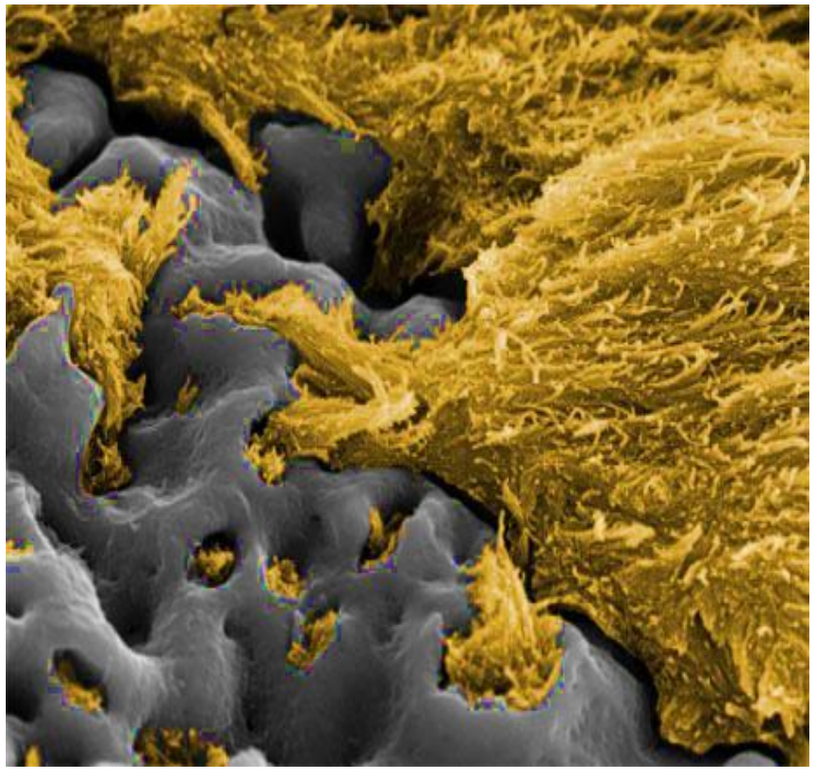

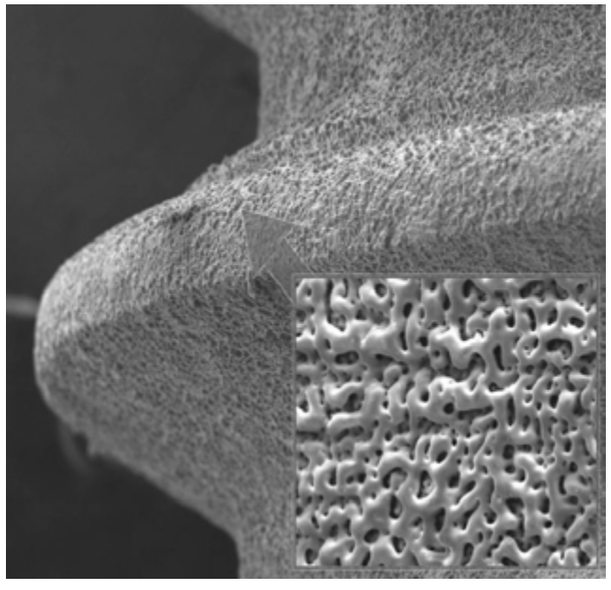

**Surface modification** (machining, sandblasting,acid etched surface, anodized surface, Laser modified micro- and nano-structured surface, Calcium phosphate coatings, plasma spraying, sputter deposition, Bioactive glass coatings…)

---

http://www.bocindia.org/osseointegration/

## *What I'm going to talk about:*

- ✓ Biomedical problem
- ✓ ***Idea***
- ➢ Materials, technology, testing results
- ➢ In vivo testing
- ➢ What next

# *IDEA: Ti-Mg composite*

**Titanium:**

+: high strength to weight ratio, resistance to crack propagation, fatique resistance, outstanding corrosion resistance, biocompatibility

-: modulus of elasticity, bio-inertness (slower osseointegration), $Ti^{4+}$ ion release (affect the vitality of osteoblastic, osteoclastic and gingival epithelial cells; some allergic events *)

**Magnesium:**

+: Low modulus of elasticity (40GPa), biodegradability (resortpion), great osteogenic potential, osteoinductive and osteoconductive properties.

---

Lopez-Jornet et al. Journal of materials science Materials in medicine. 2014.

Sicilia et al. Clinical oral implants research. 2008.

# *IDEA: Ti-Mg composite*

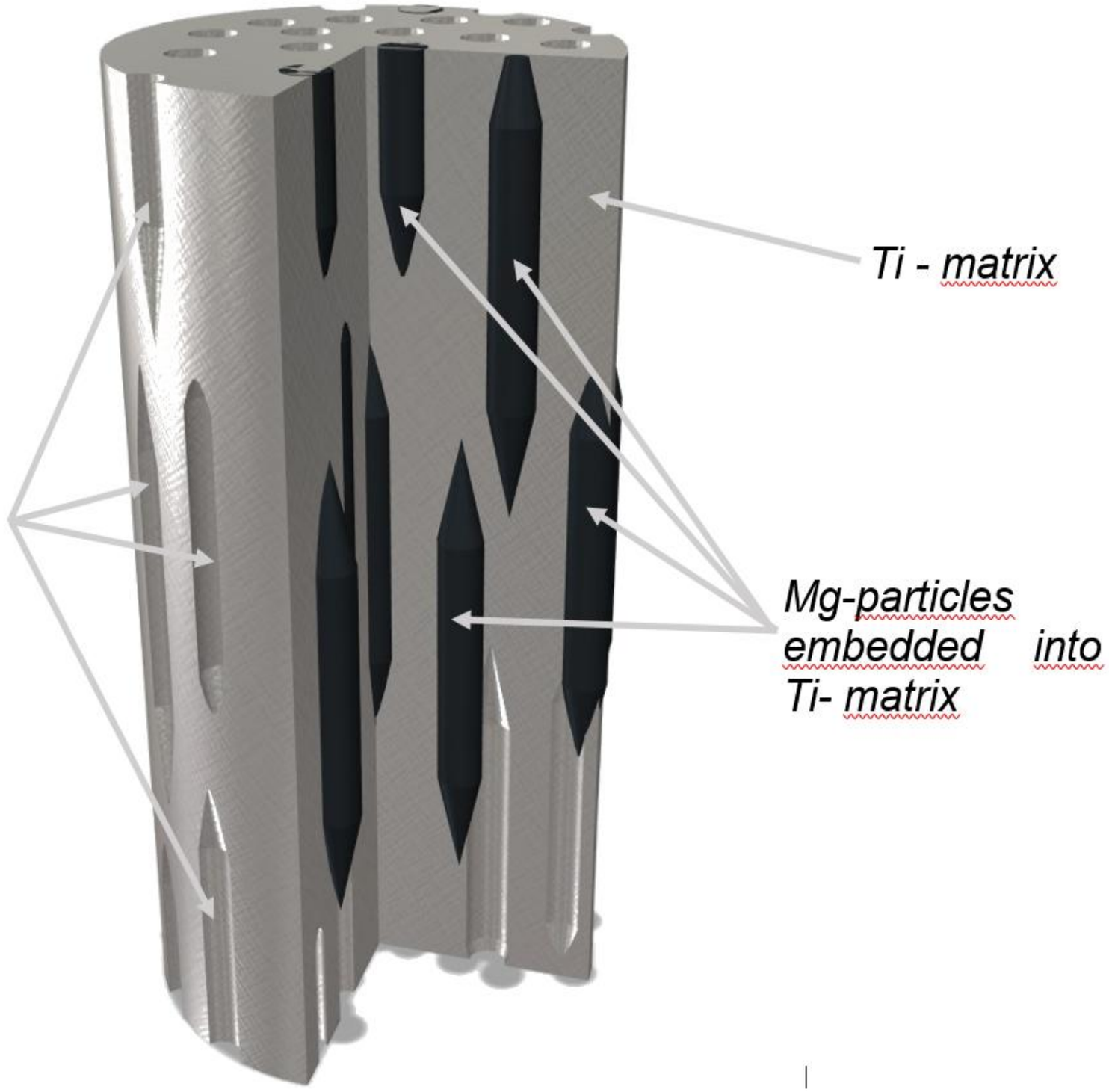

## ***What I'm going to talk about:***

- ✓ Biomedical problem
- ✓ Idea
- ✓ ***Materials, technology, testing results***
  - ➢ In vivo testing
  - ➢ What next

# *Materials and technology*

**Cooperation with Institute of Materials & Machine Mechanics, Slovak Academy of Sciences (http://www.umms.sav.sk/)**

Material:

HDH Ti99.4% powder <150μm
atomized Mg99.8% powder d50=30μm

Technology:

Powder metallurgy (combinationa of CIP, HIP, hot extrusion)

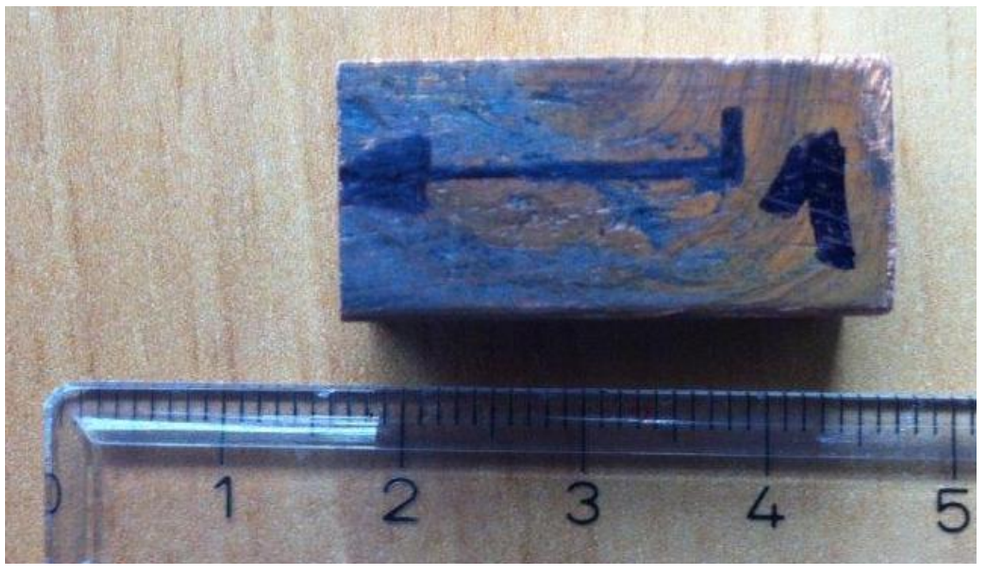

10wt. % Mg

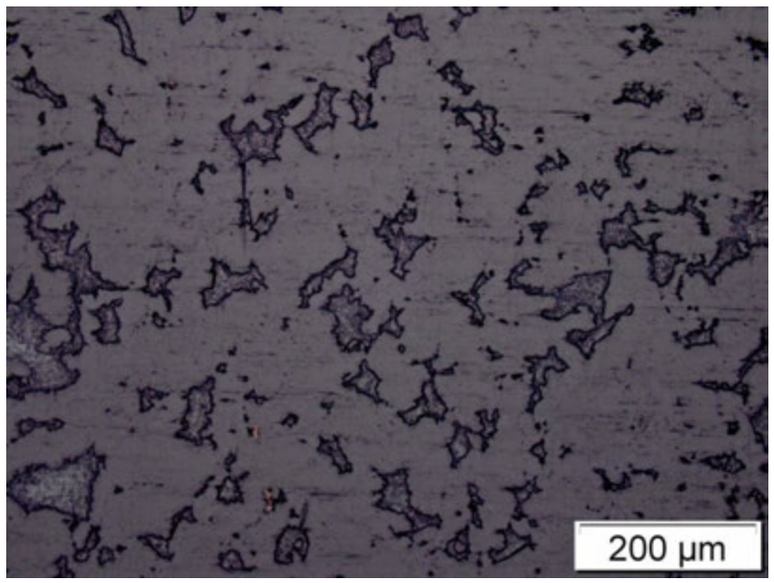


129 HV5

20 wt. % Mg

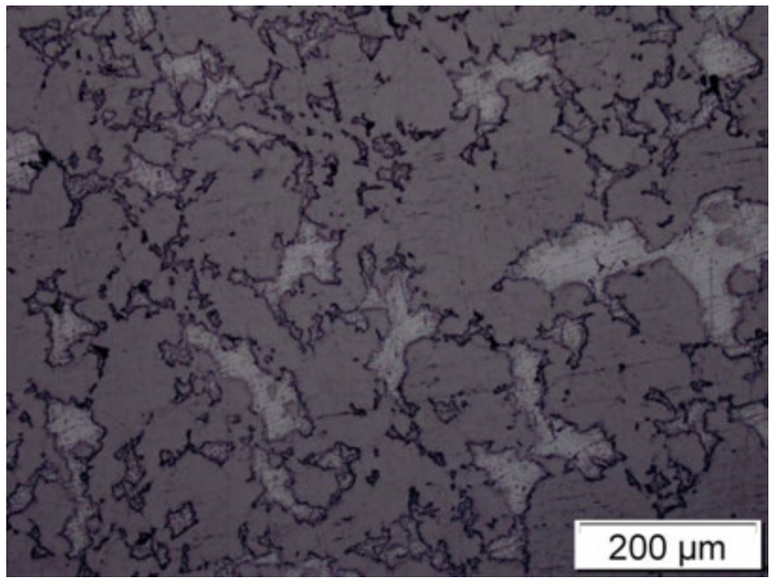


86 HV5

30 wt. % Mg

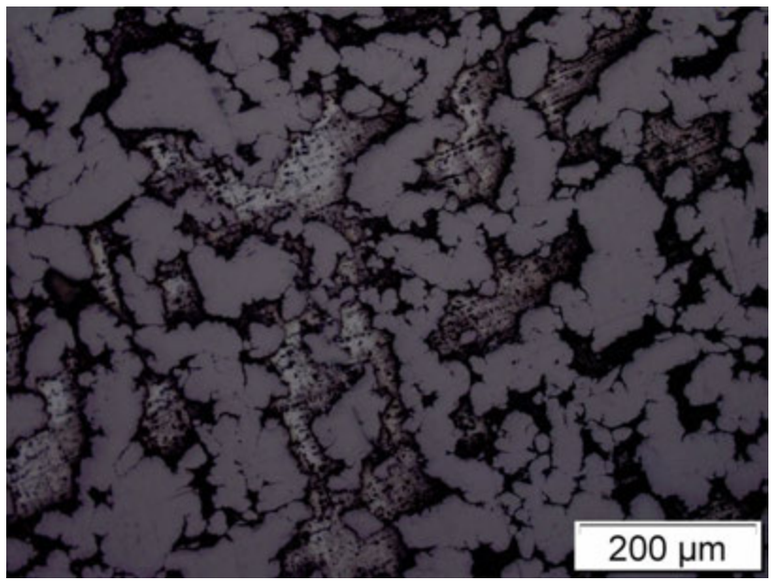


67 HV5

# 10wt.% Mg
# Surface after 35 days into distilled water

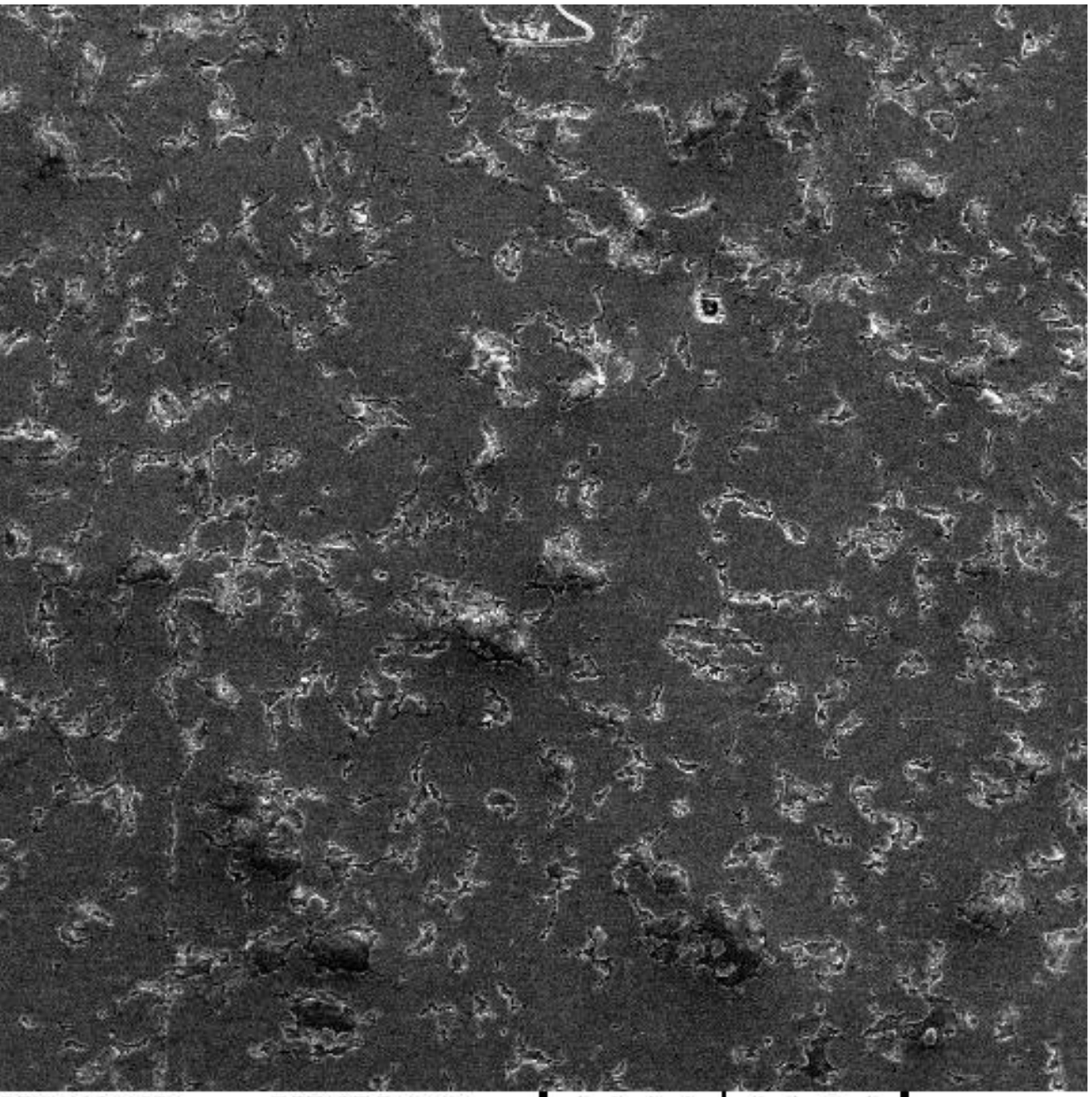


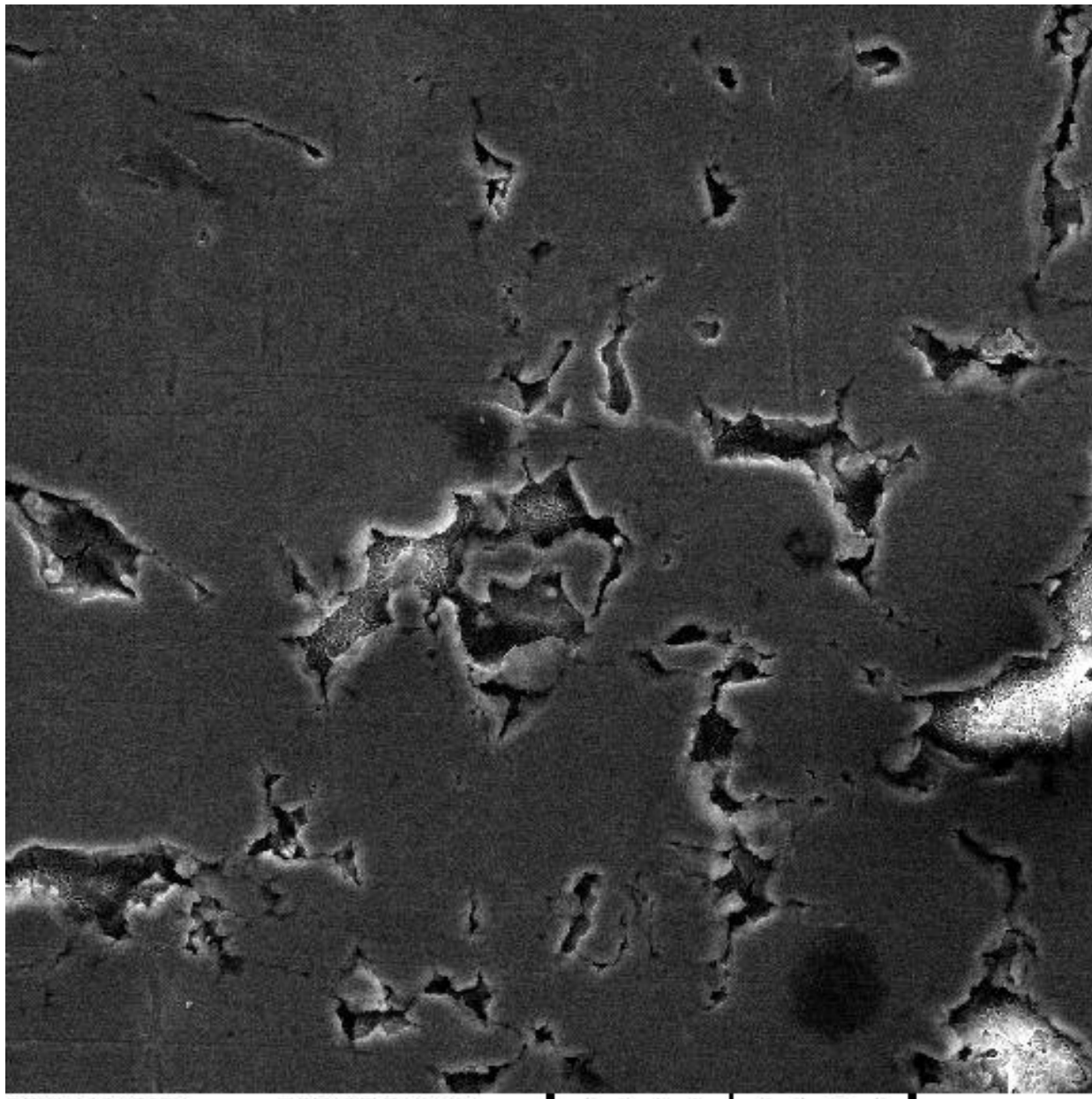

# 10wt.% Mg
# Cross section after 35 days into distilled water

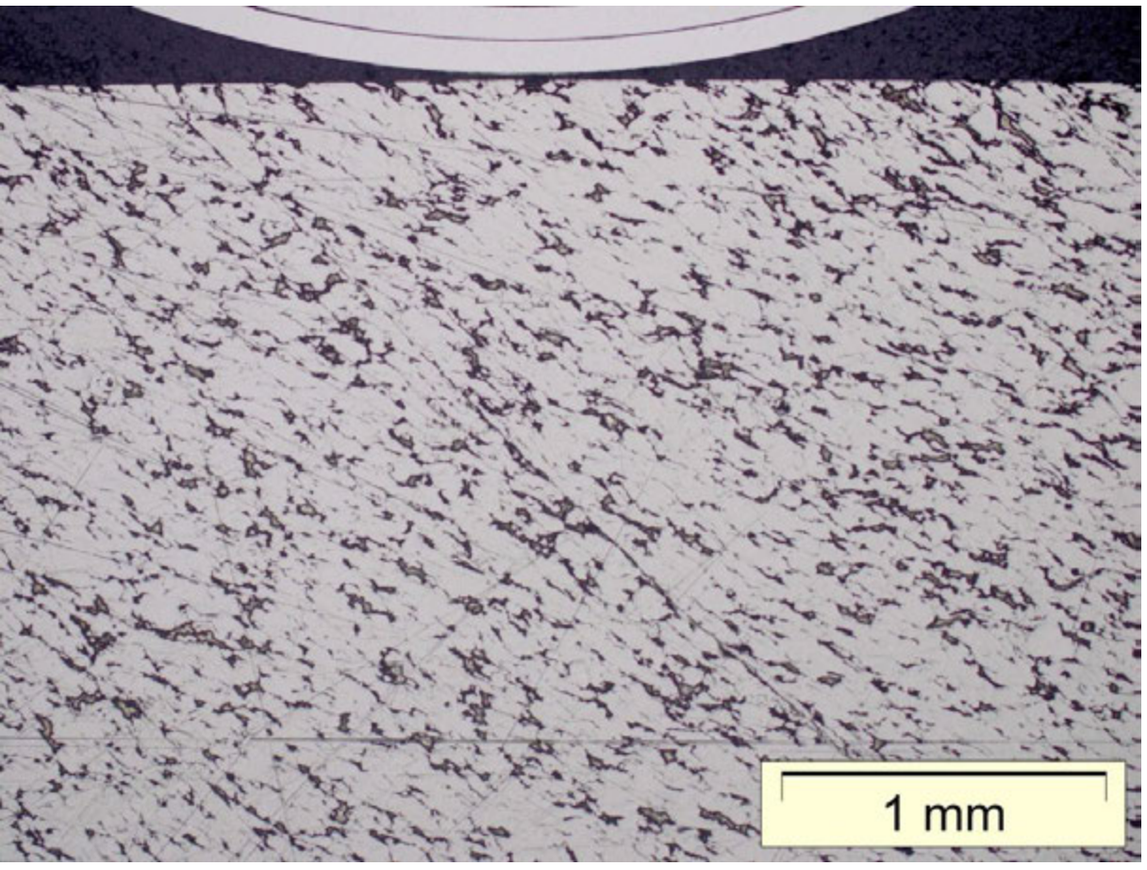


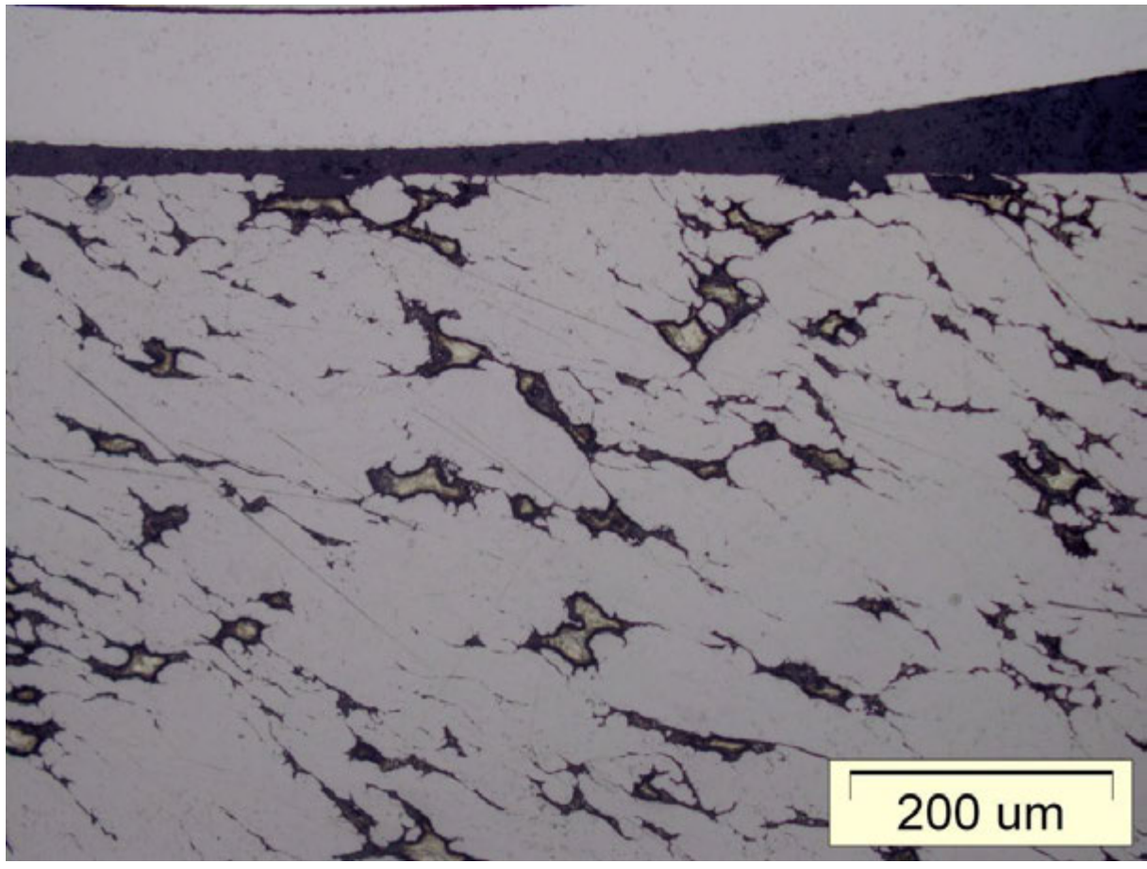

# 20wt.% Mg
# Surface after 35 days into distilled water

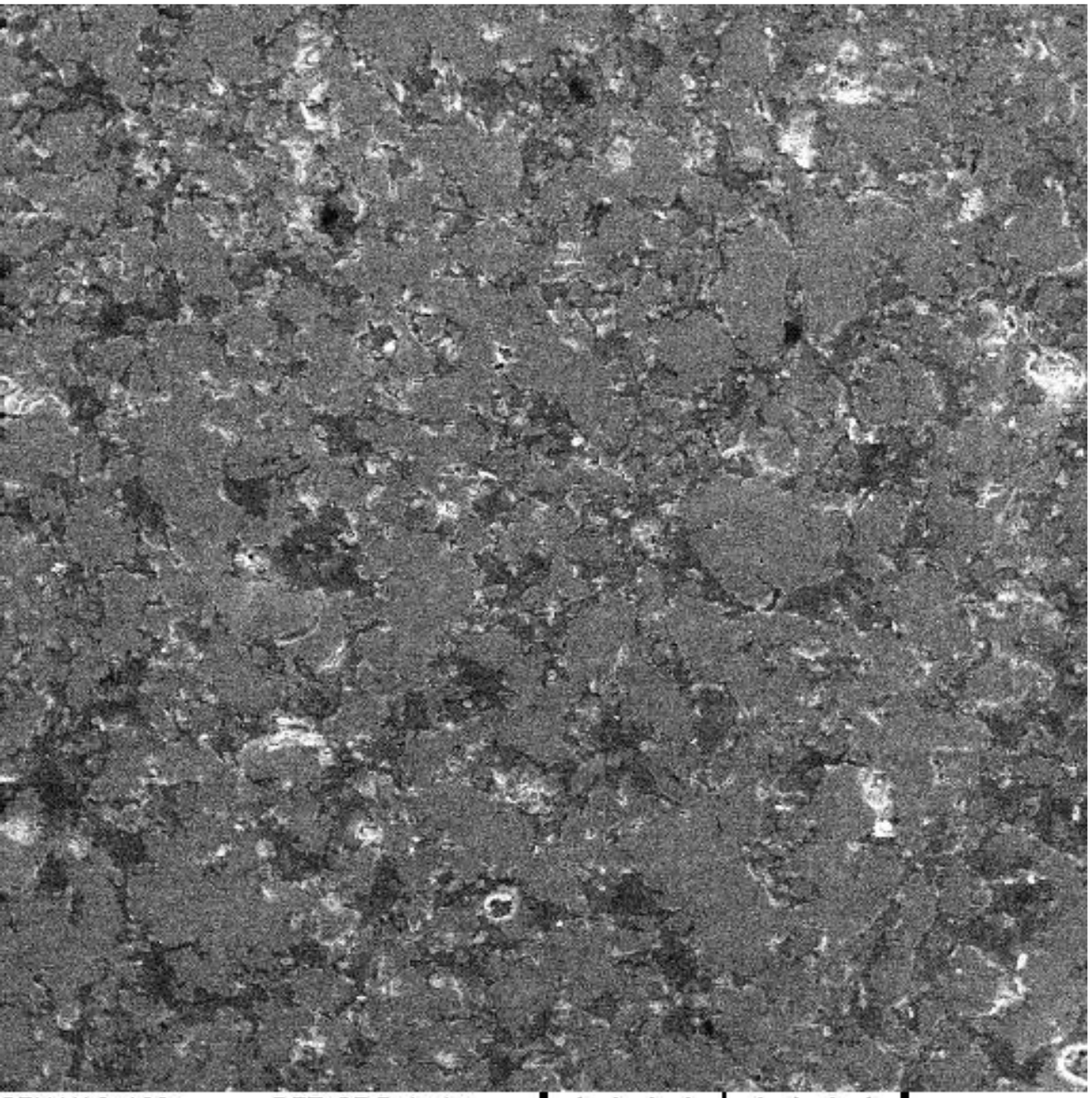


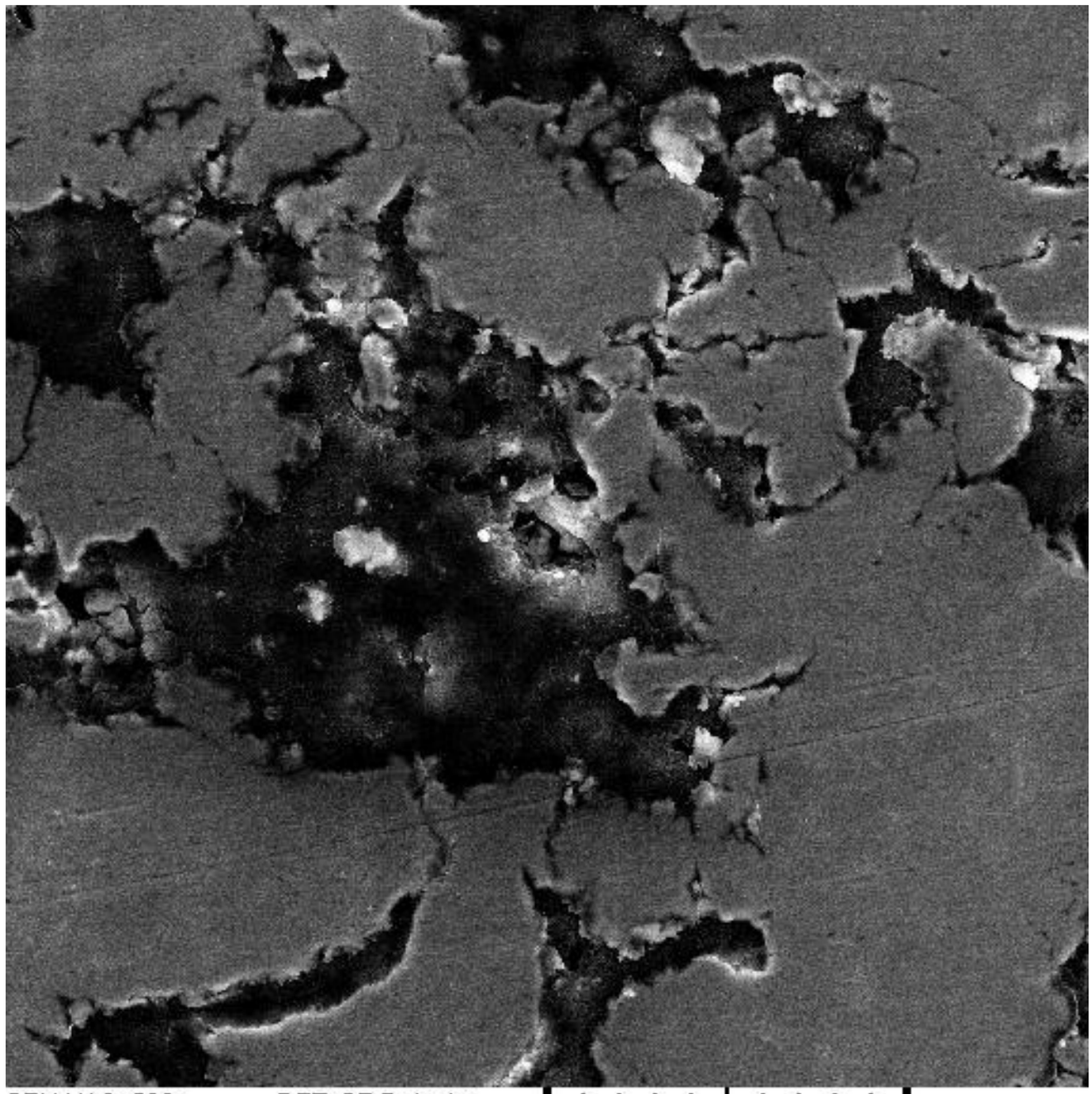

# 20wt.% Mg
# Cross section after 35 days into distilled water

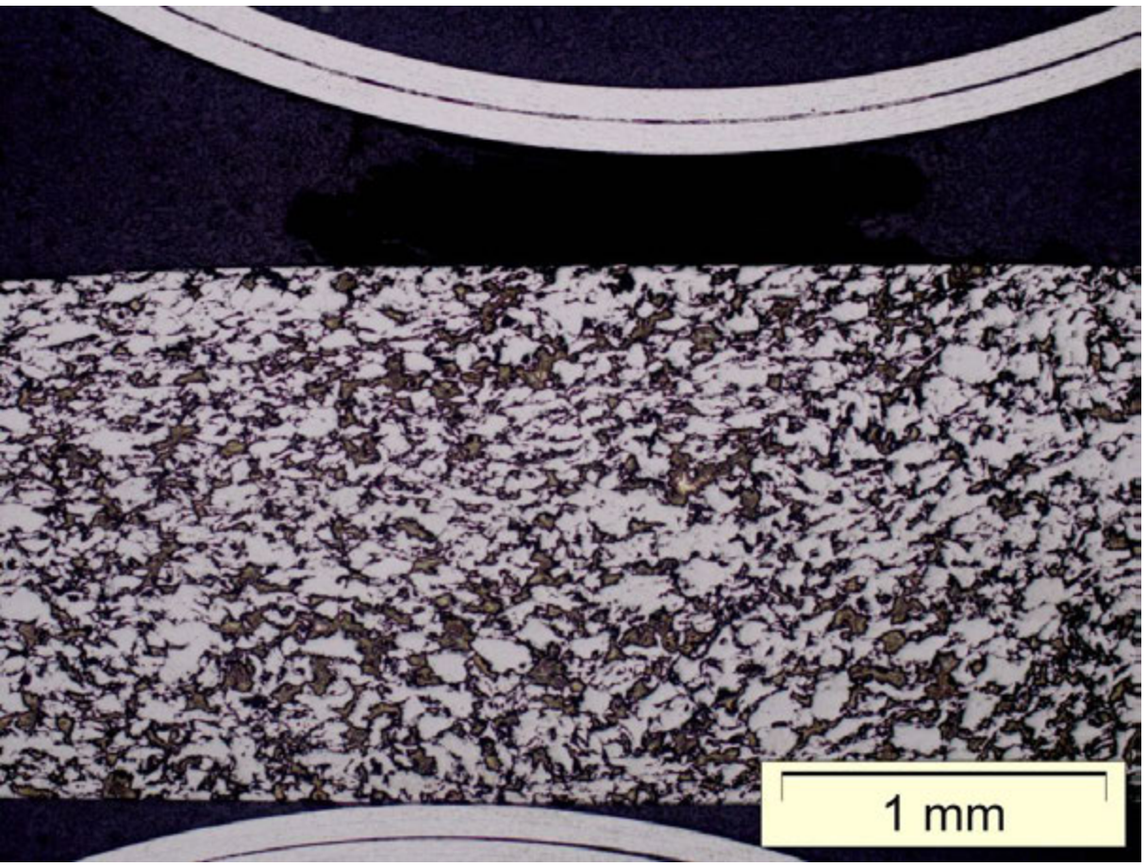


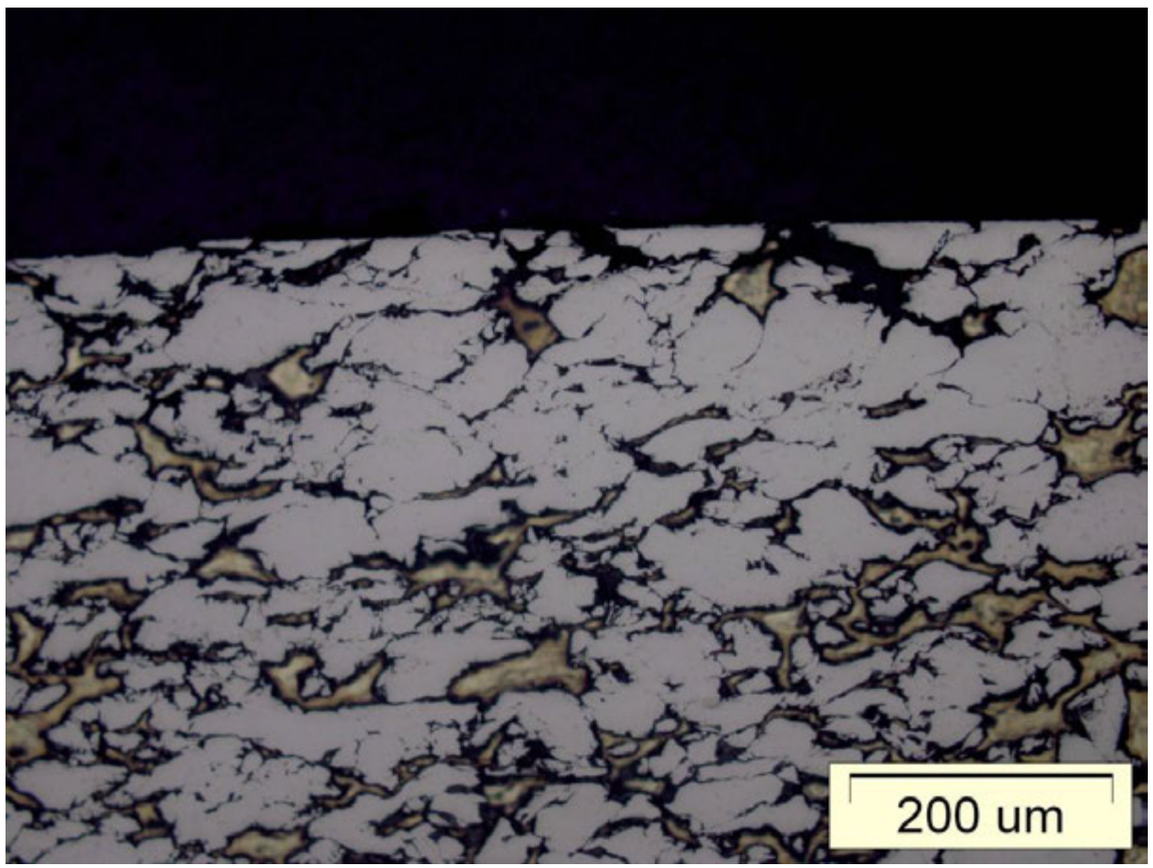

# 30wt.% Mg
# Surface after 35 days into distilled water

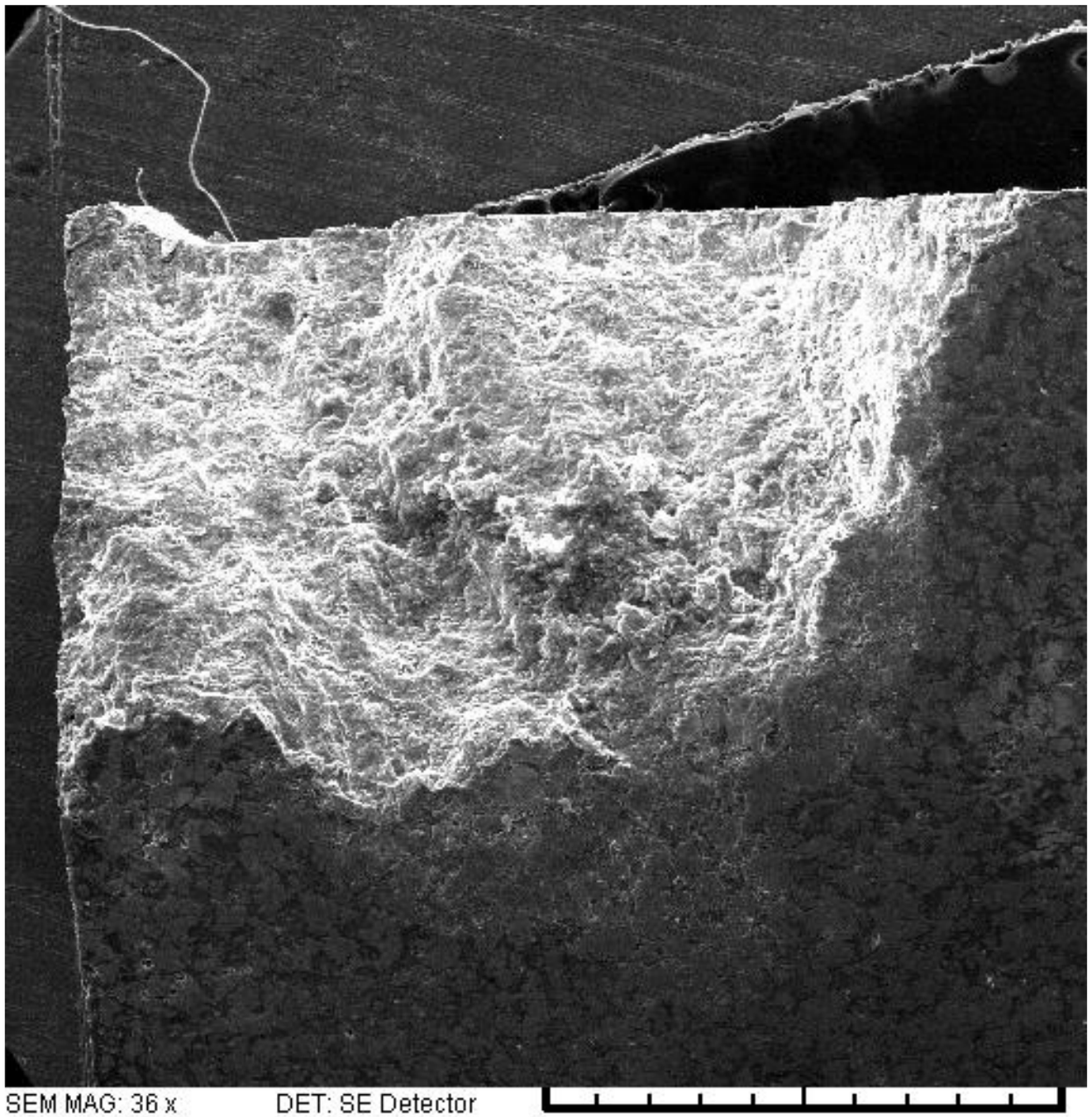


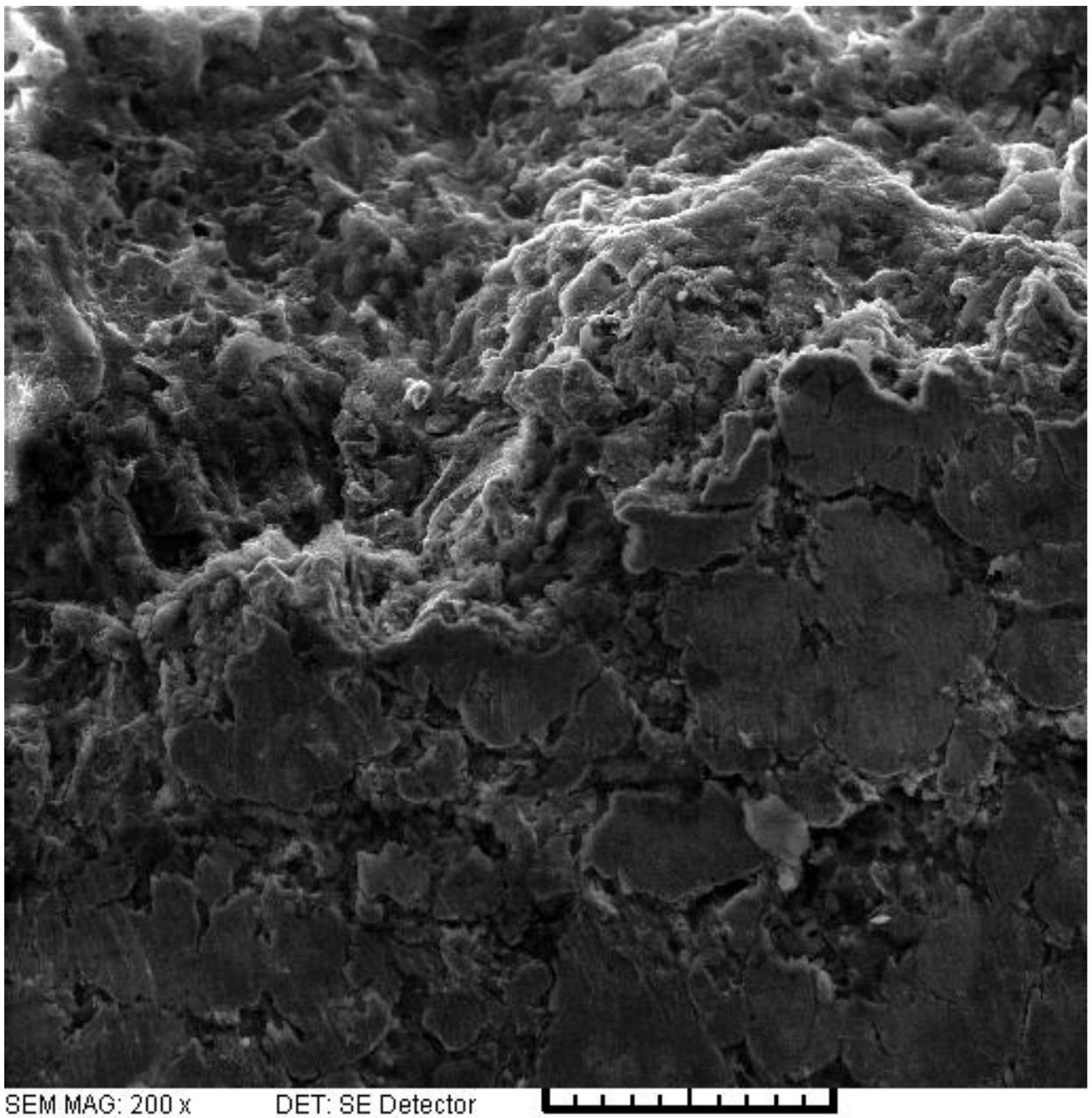

# 30wt.% Mg
# Cross section after 35 days into distilled water

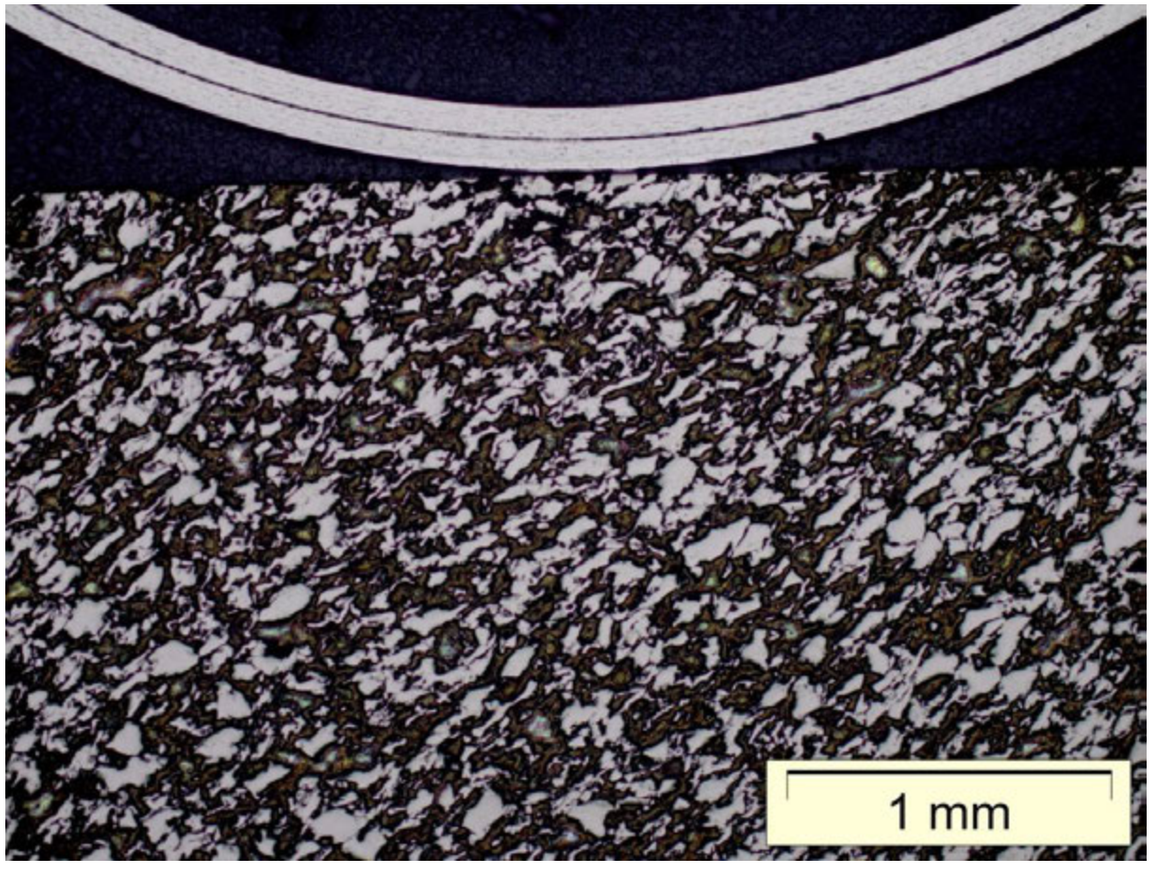


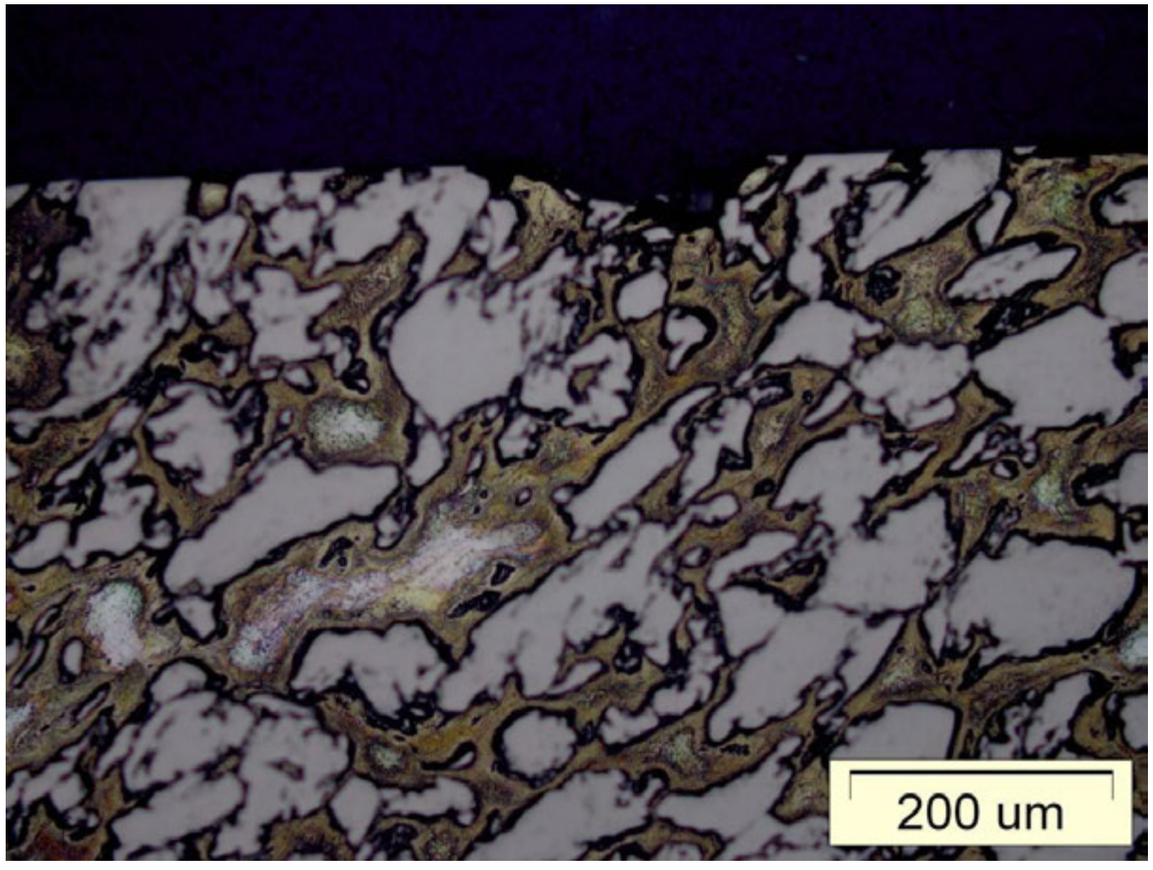


**Conclusion:** 30, 20 wt.% Mg- **TOO MUCH Mg!**

**Composite Ti + 10 wt.% Mg:** Density: 3.83 g/cm3; porosity 1.32 %  E = 68.9 GPa

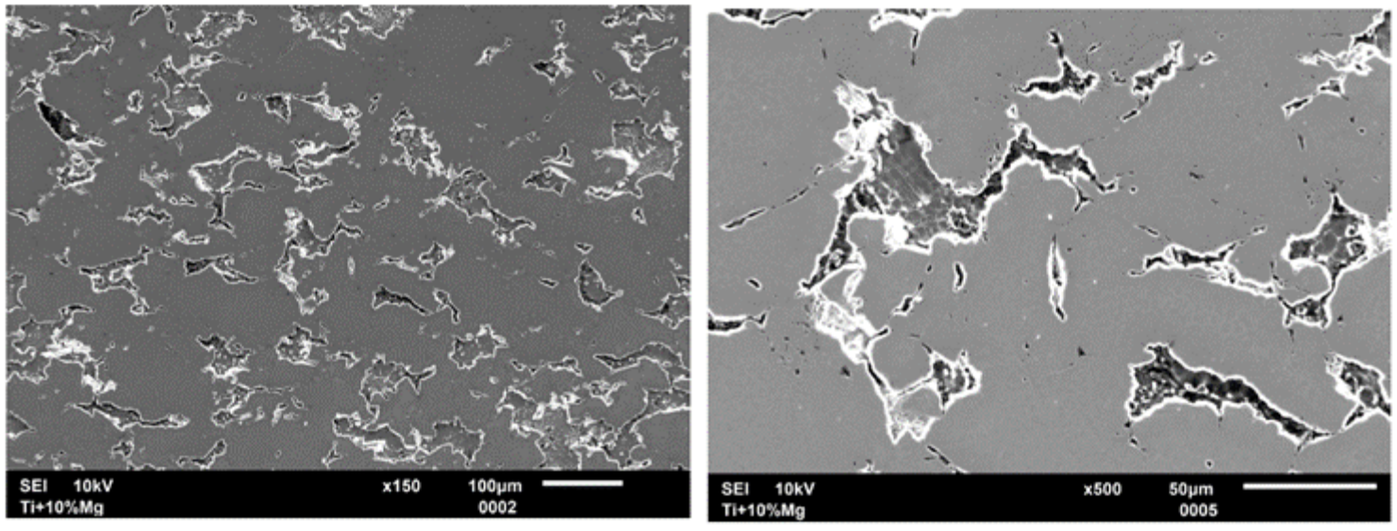


**Composite Ti + 5 wt.% Mg:** Density: 4.15 g/cm3; porosity 0.44 %  E = 74.8 GPa

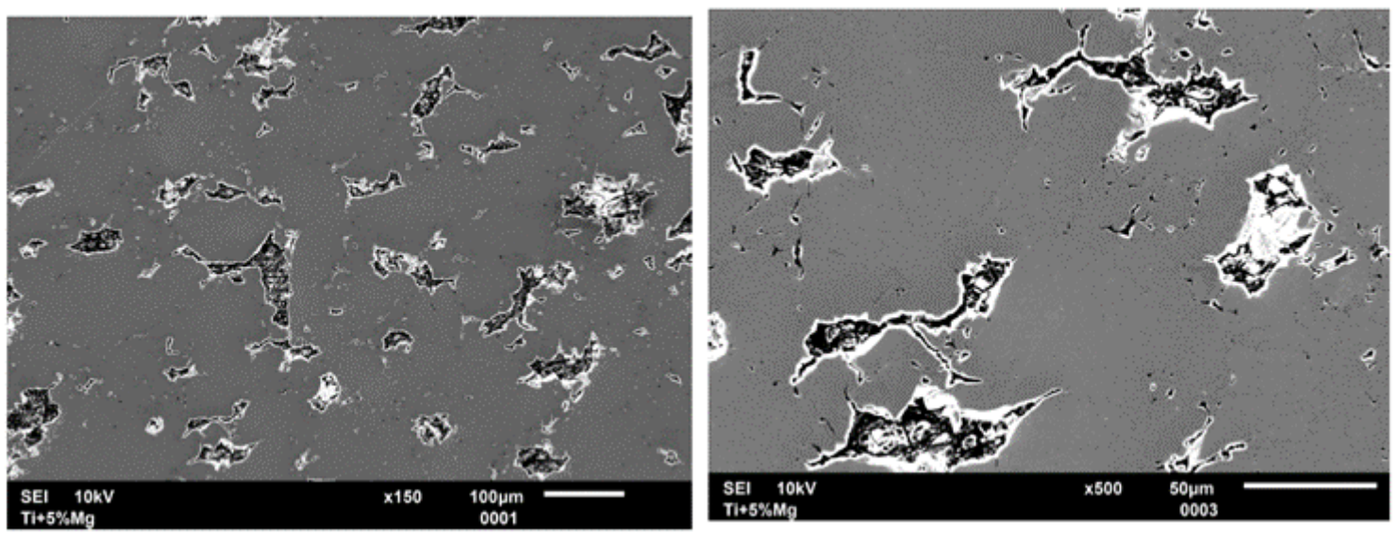

**Compressive test (** diameter 5.5 mm, leght 8.5 mm)

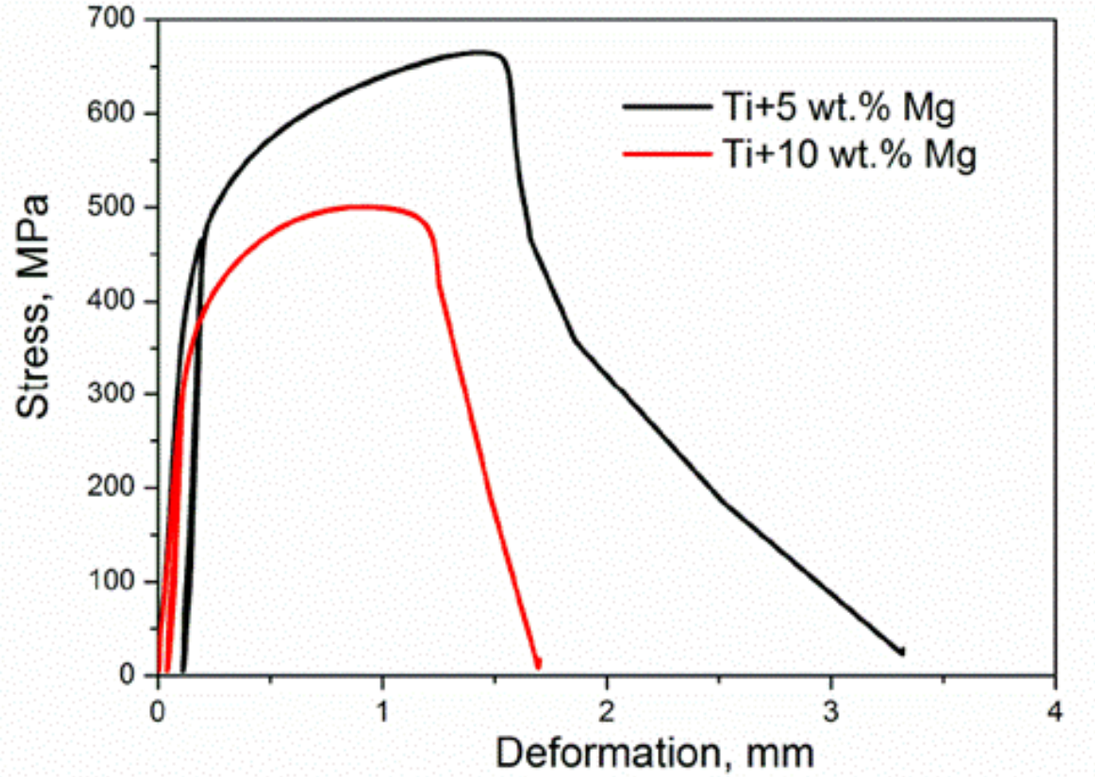


Compressive strength: Ti+5 %Mg - 665 MPa
Ti+10 %Mg - 490 MPa

## Tensile test:

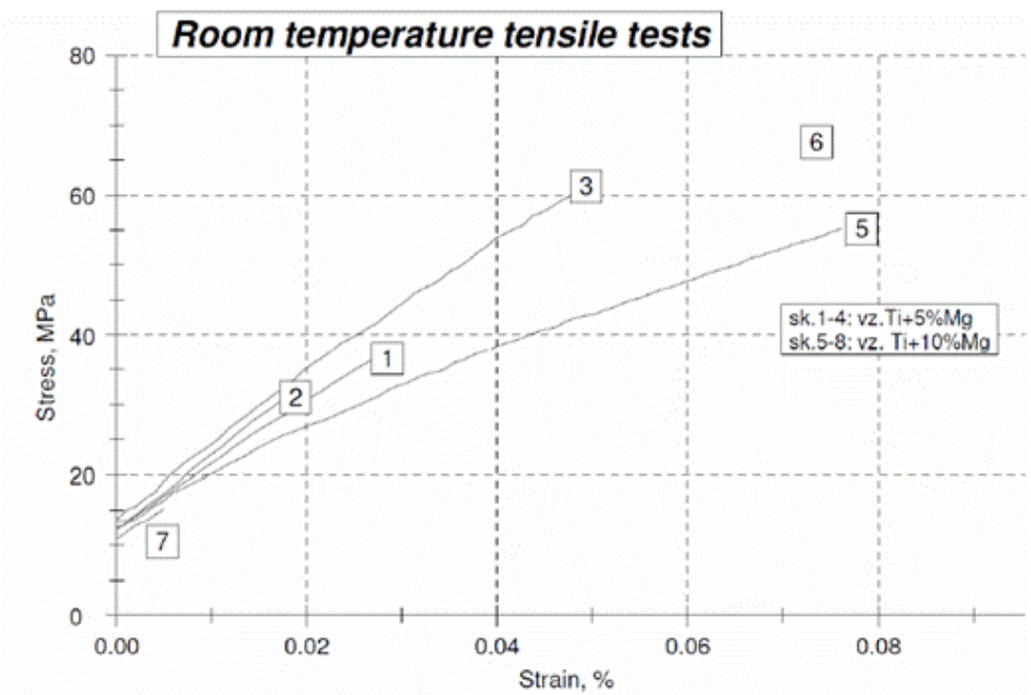


The reproducibility of the results is low, the samples were fractured by brittle manner. The obtained ultimate tensile strength is very low.

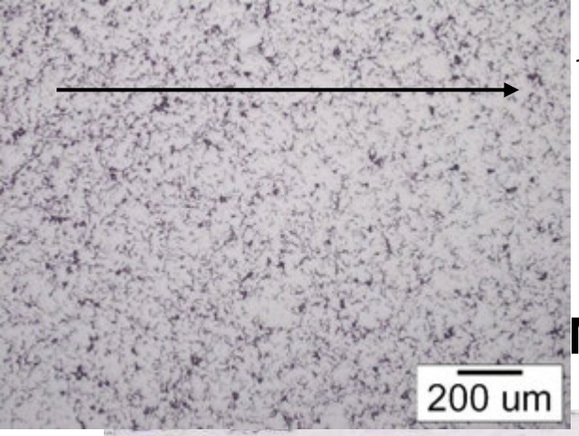


*wders, changes in technology and process parameters*

**Mg:** Density: 4.12 g/cm3; porosity 0.86 %

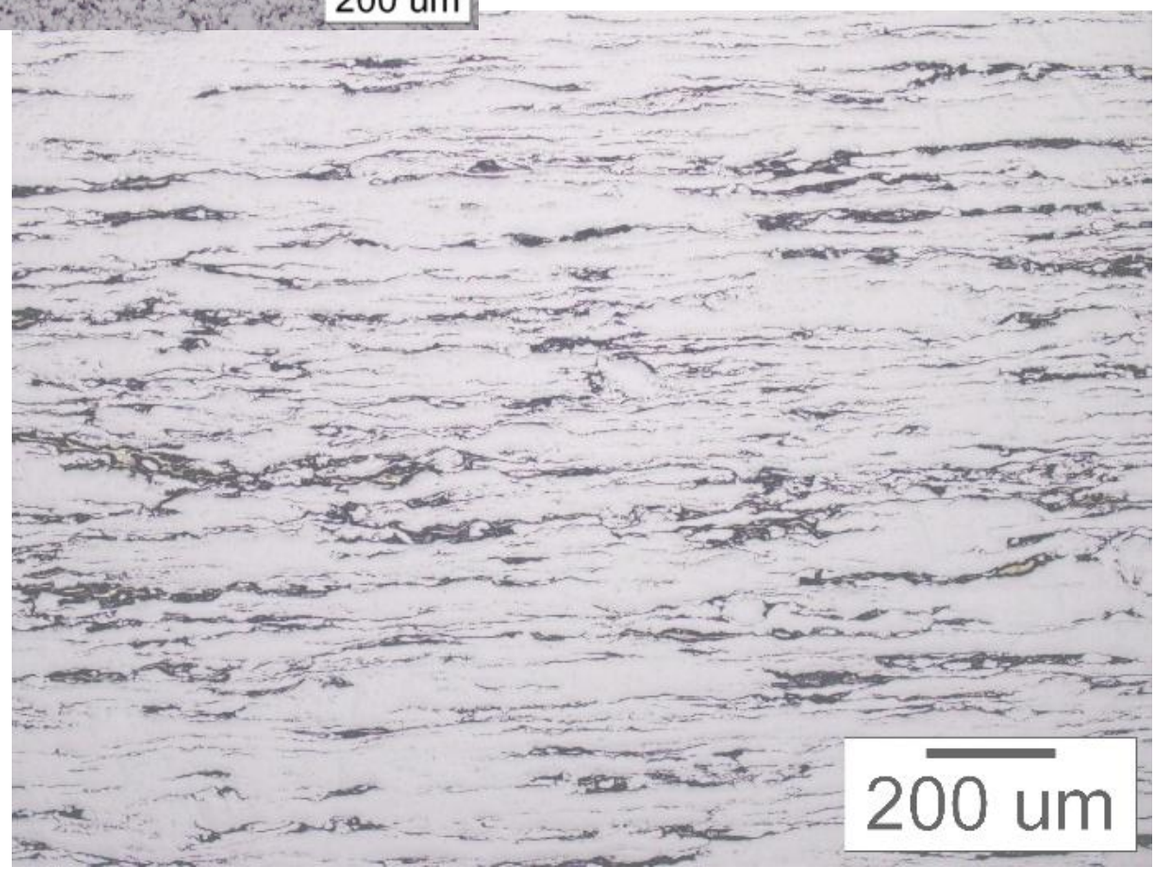


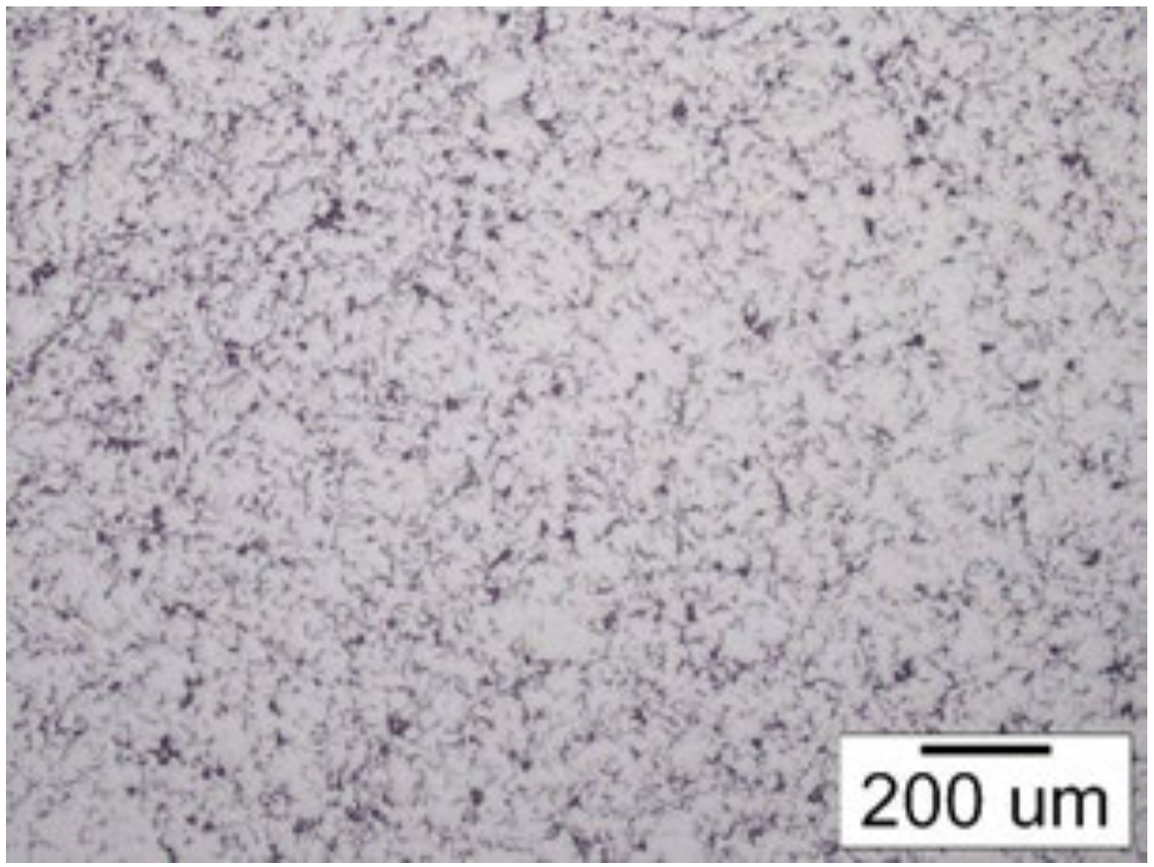


| | UTS, MPa | $YS_{0.2}$, MPa | ε, % | E, GPa |
|---|---|---|---|---|
| **Ti + 5 wt.% Mg** | 529 ± 7 | 450 ± 12 | 1.4 ± 0.3 | 92.1 ± 0.6 |
| **CP Ti Grade 4 minimum** | 550 | 483 | 15 | 105 |

**Fatigue test ISO 14801 standard for fatigue testing of endosseous implants**
**Corrosion tests**

## ***What I'm going to talk about:***

- ✓ Biomedical problem
- ✓ Idea
- ✓ Materials, technology, testing results
- ✓ ***In vivo testing***
- ➢ What next

# *ro implant made of Ti+5 wt.% Mg*

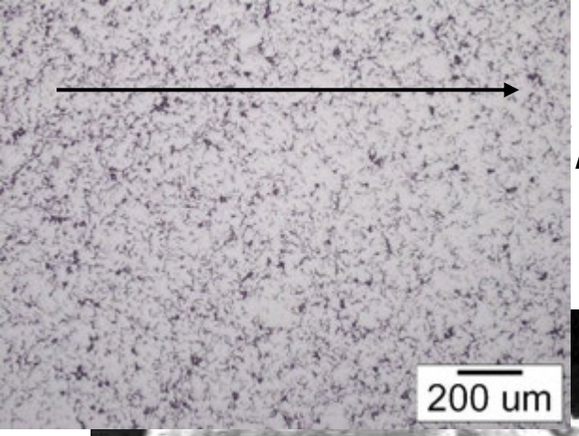


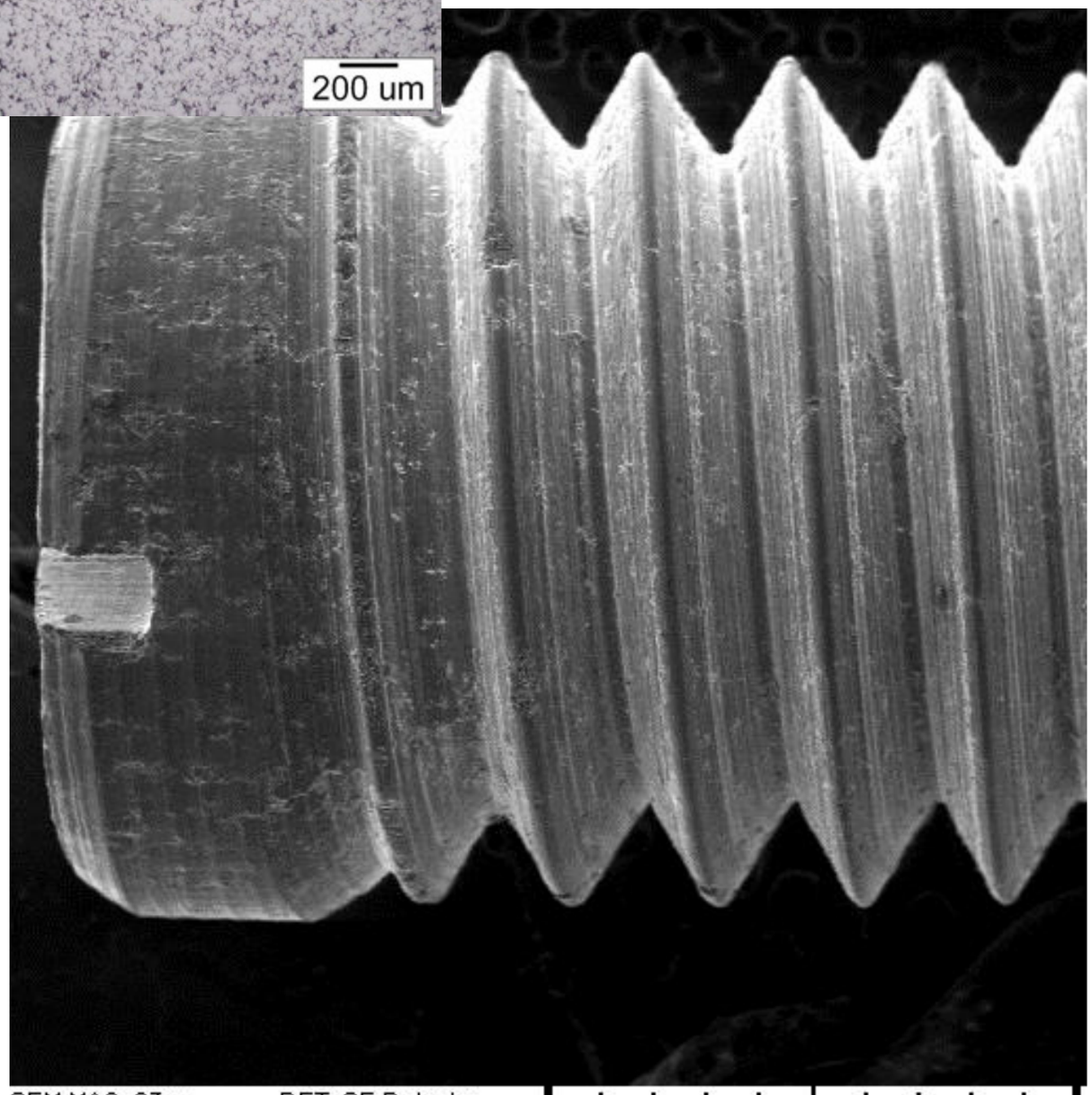


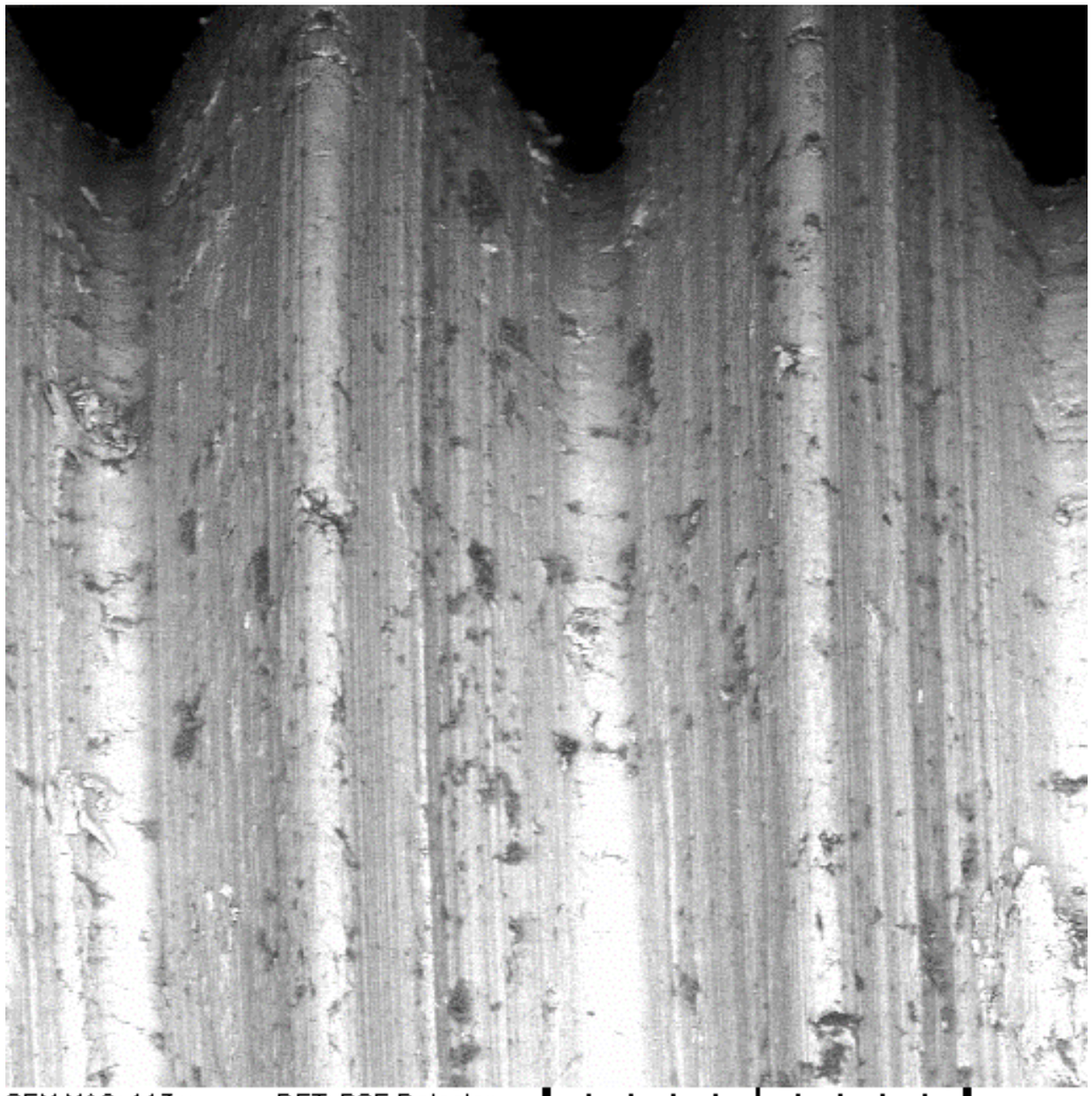

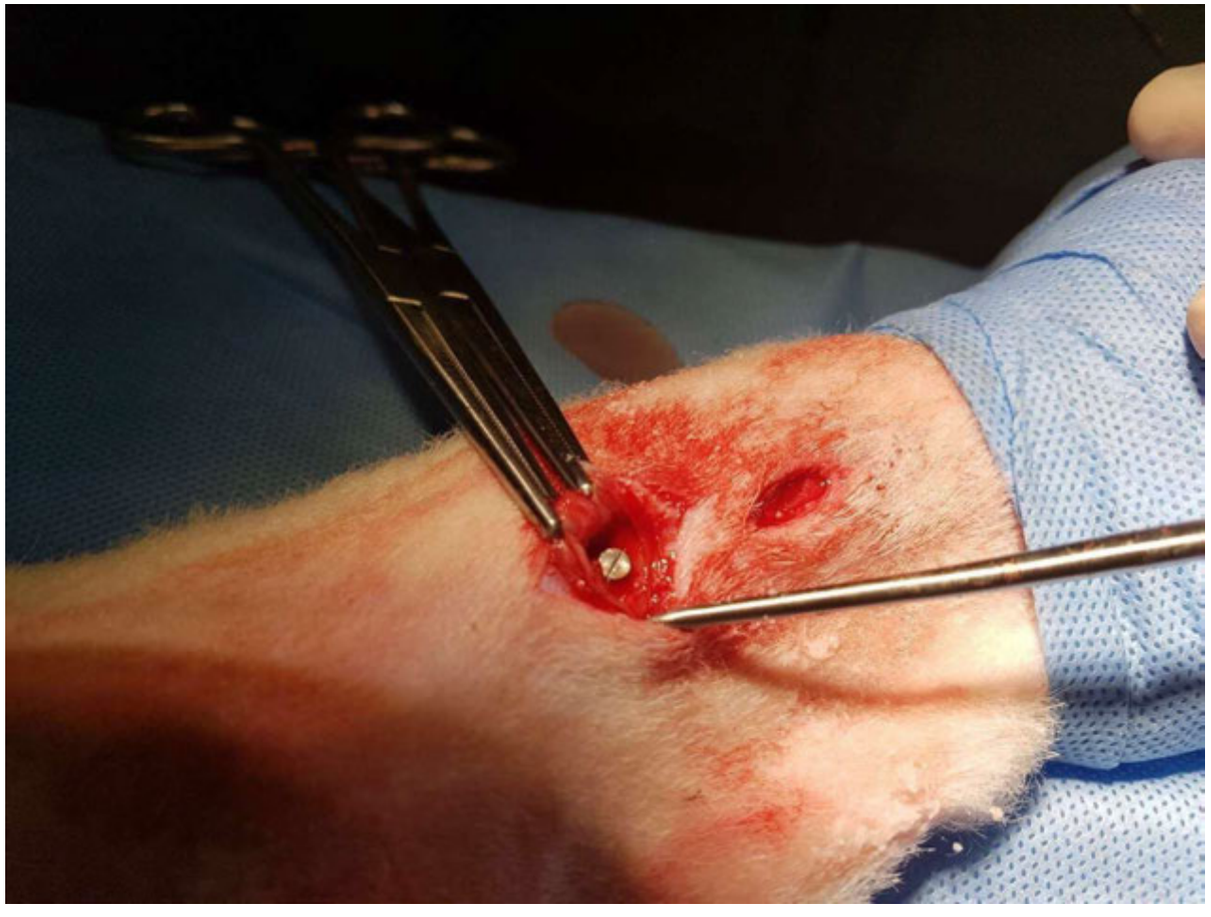


ge cart
Report
FCR PRIMA V Console Viewer
odify Study
Other
ed, dark
cm
ASUS

# *Implant into bone after 4 weeks*

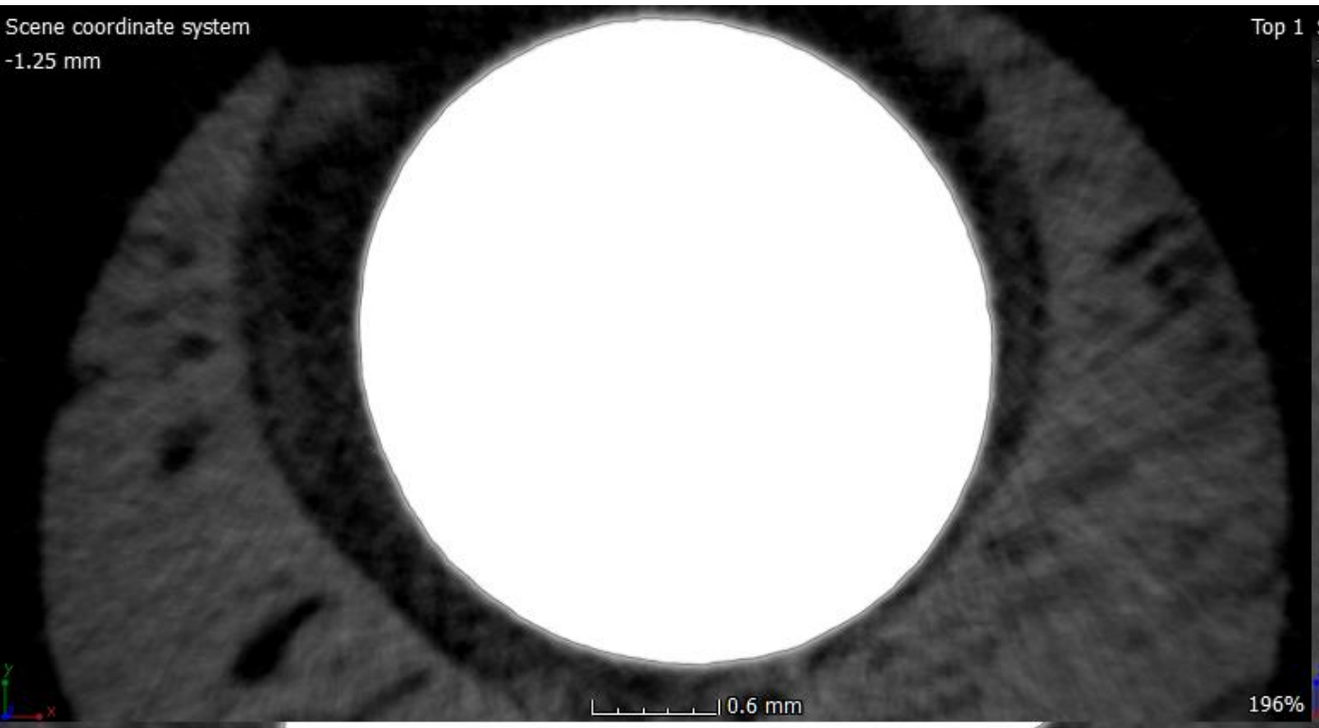


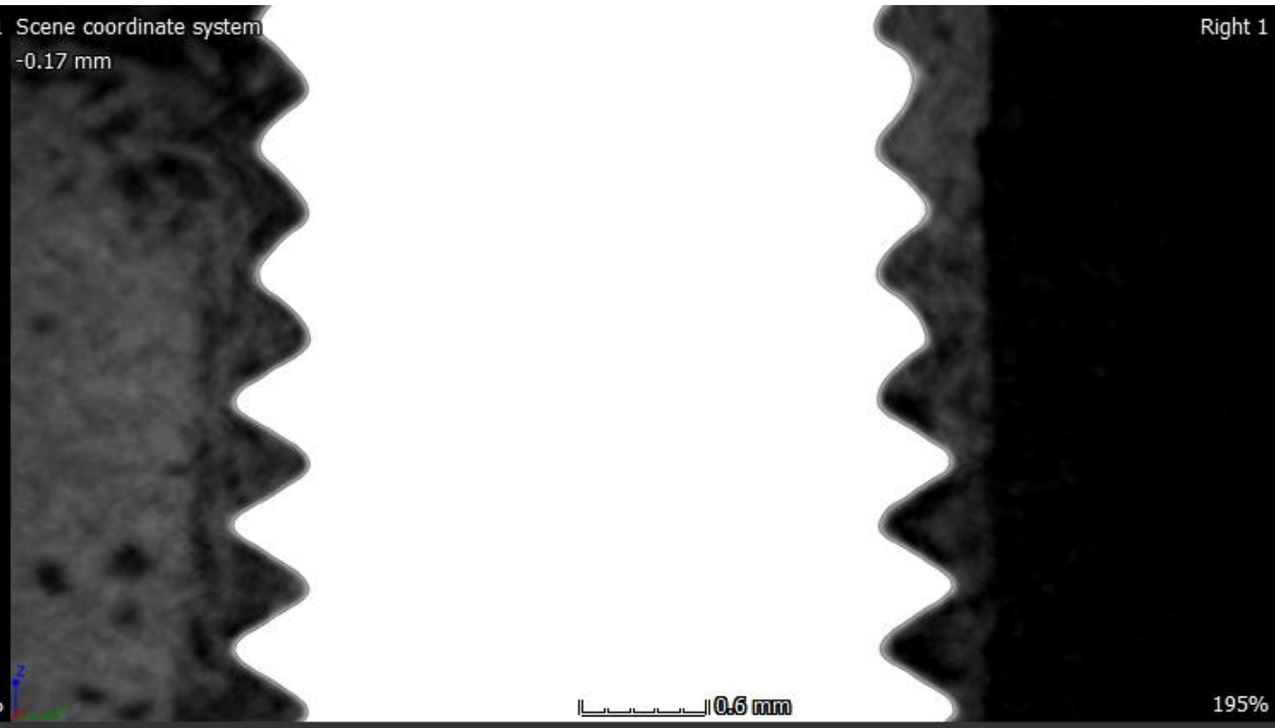


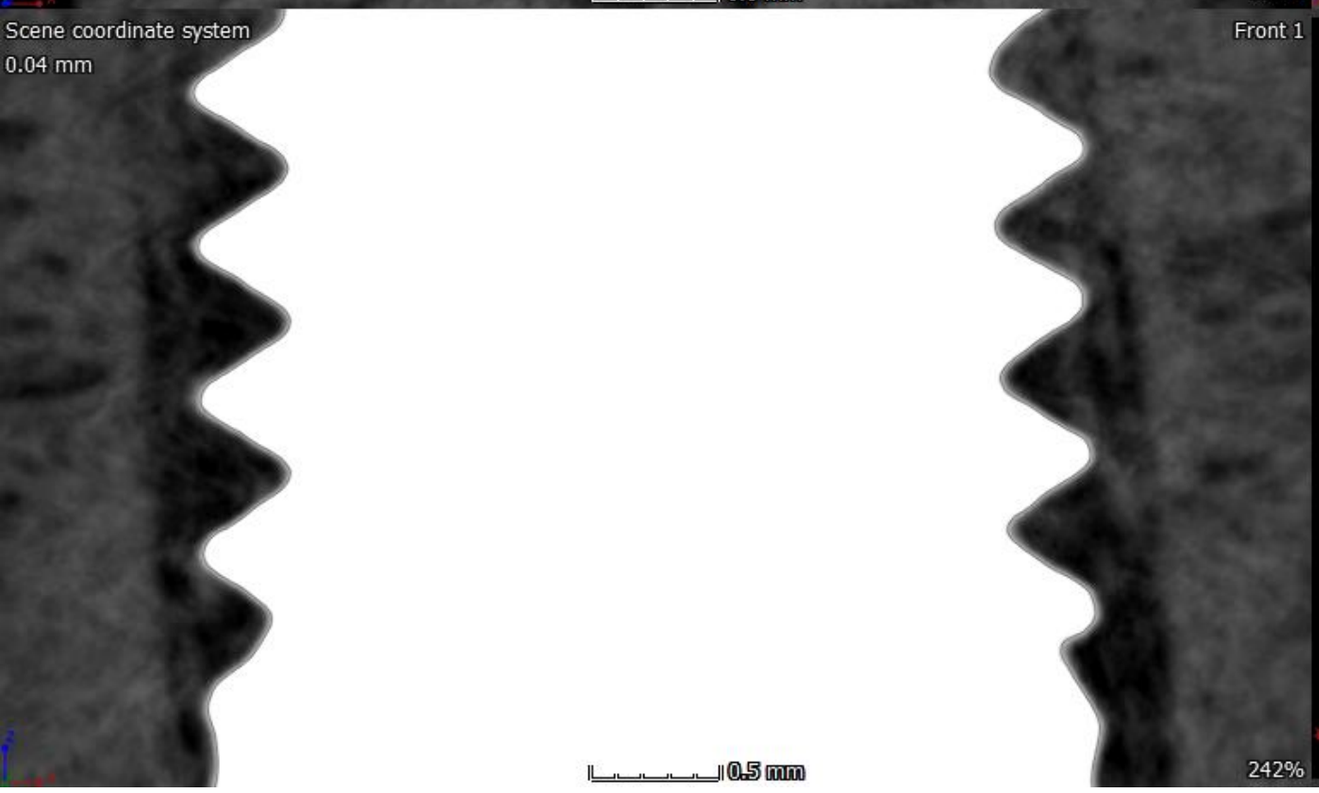


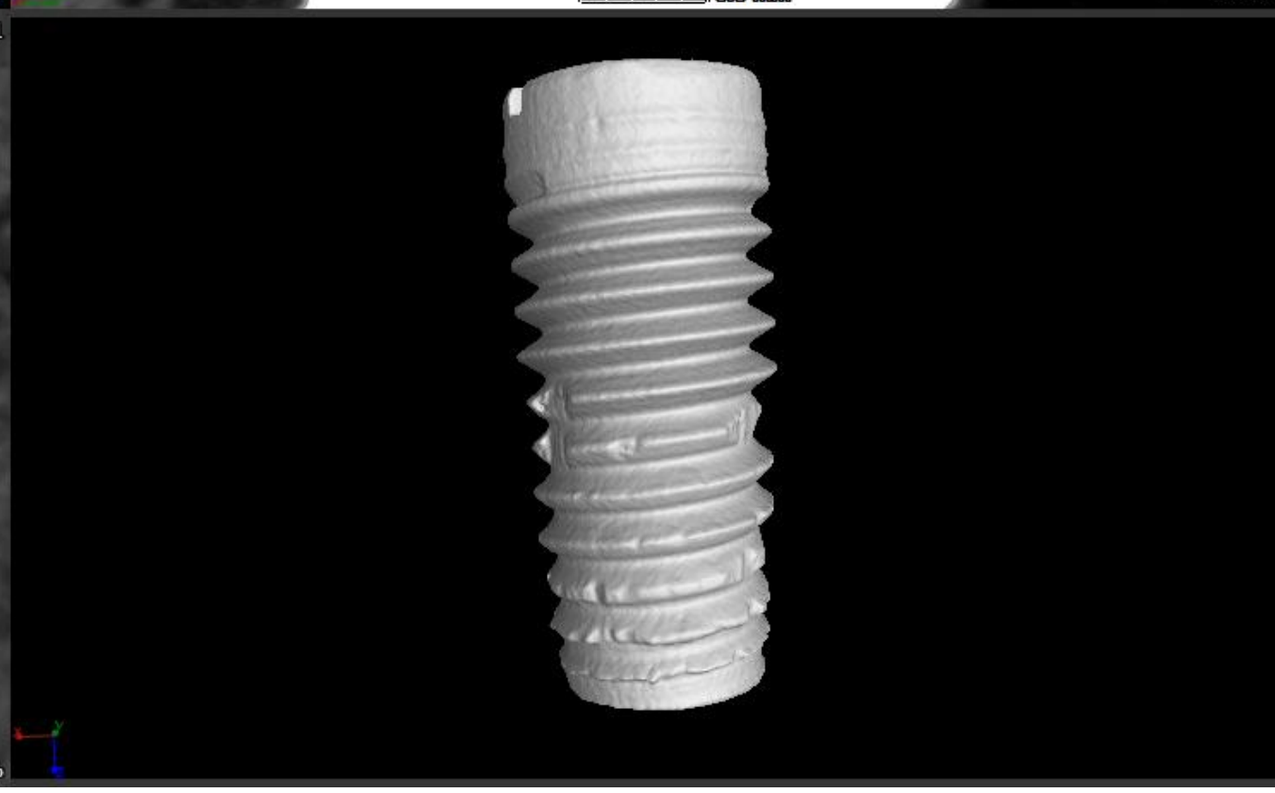

# *Implant into bone after 16 weeks*

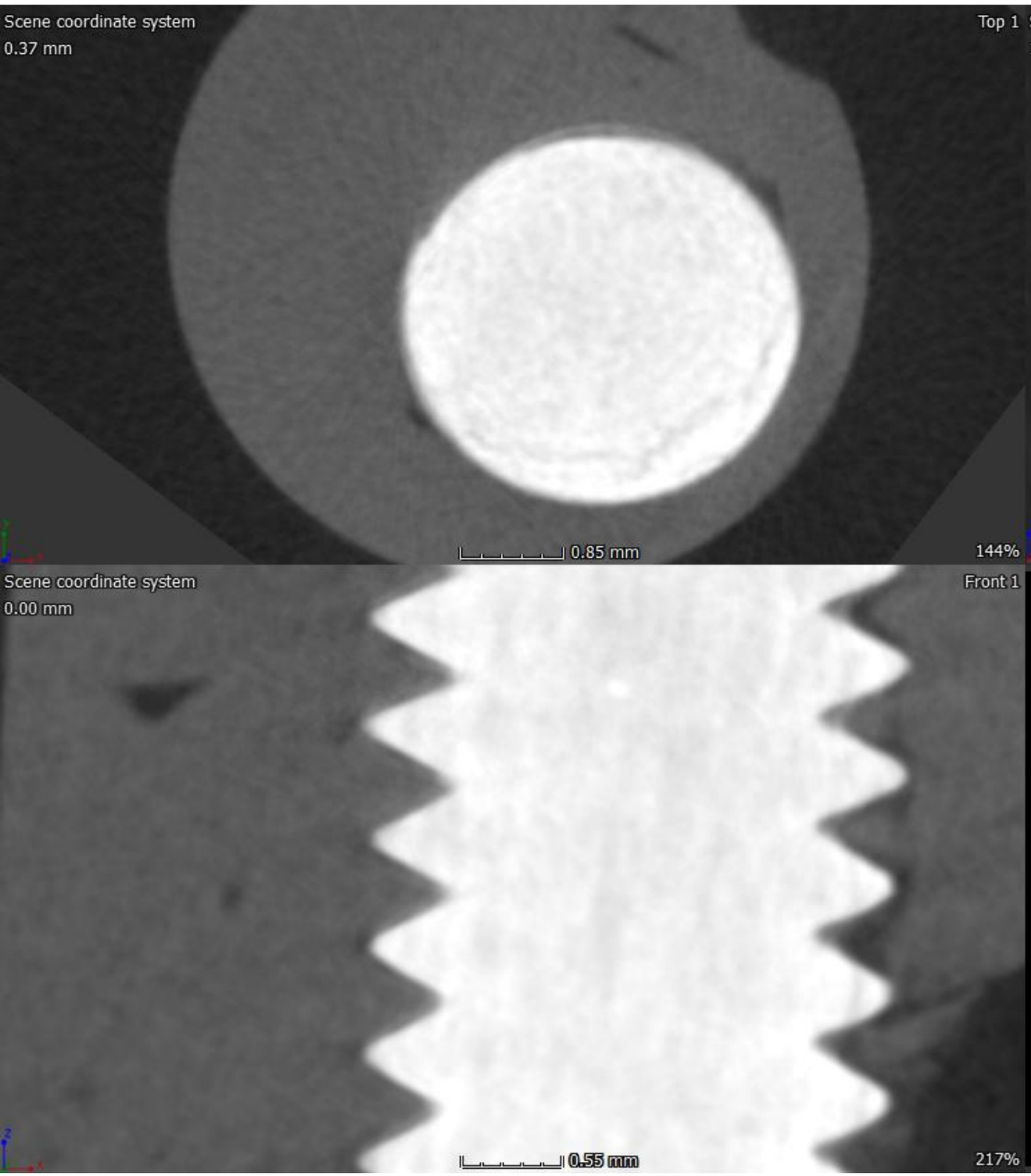


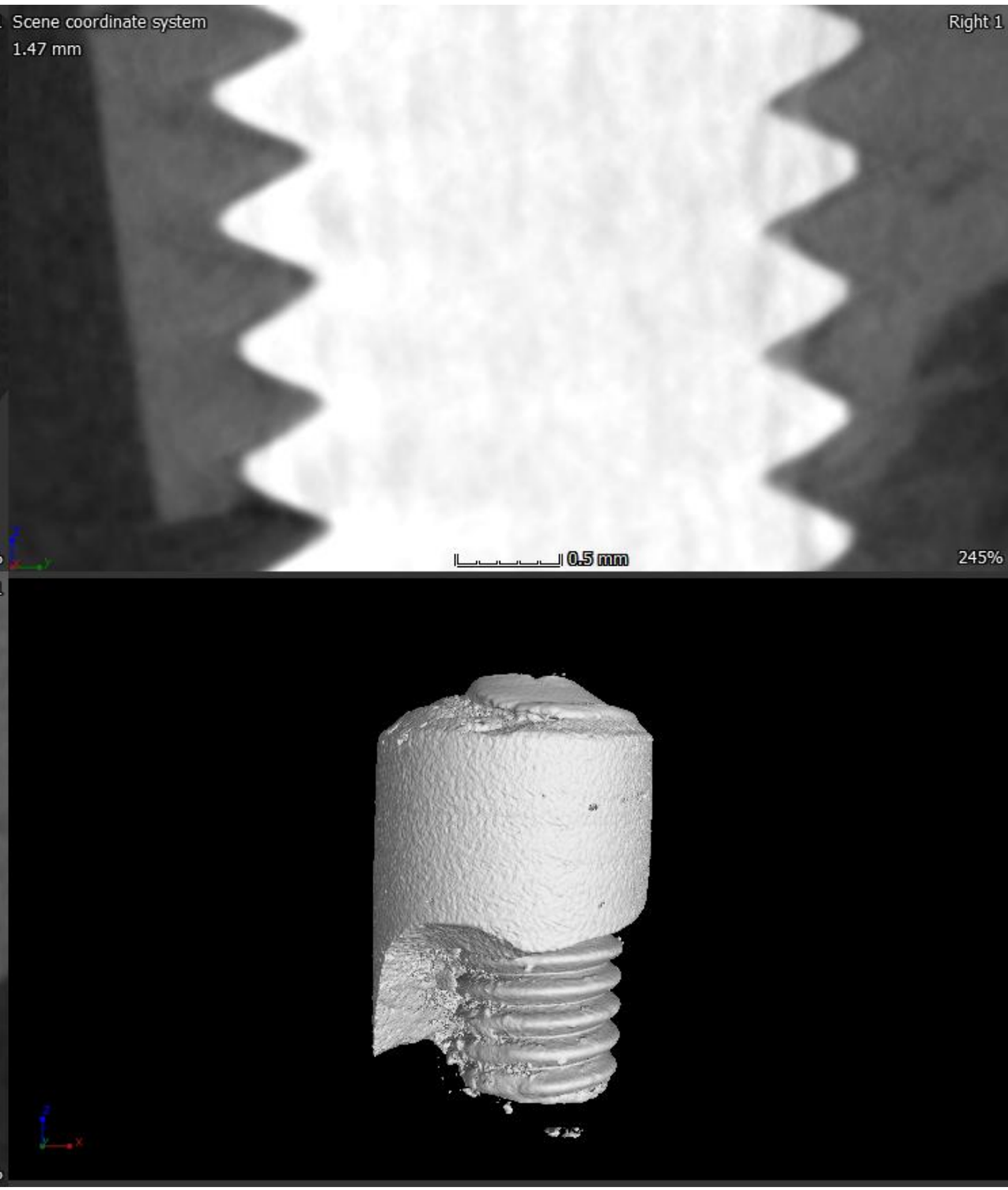

## ***What I'm going to talk about:***

- ✓ Biomedical problem
- ✓ Idea
- ✓ Materials, technology, testing results
- ✓ In vivo testing
- ✓ ***What next***

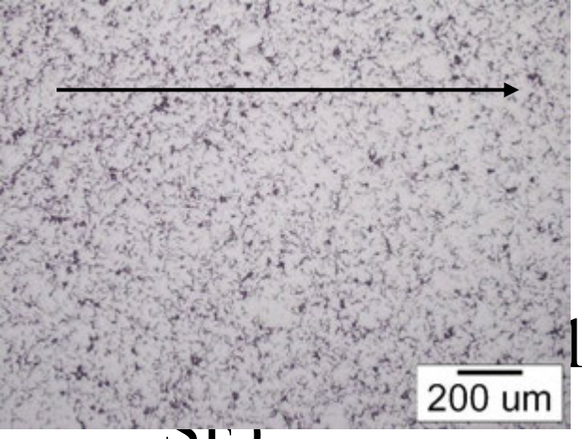


# *What next ????*

l disertation (Two finished: Mateja Šnajdar - FSB, Zlatko Stanec - SF)

- ❖ Patent application (EU application No./Patent No 16763311.4-1109 Composite material for implants, its use and method of its production)
- ❖ From research to application (IRI projekt ZRINSKI AG)

**Acknowledgment**:
BICRO (PoC5_1_3 Ti-Mg legura za zubne implantate)
Slovak Scientific Agency under the APVV-16-0527 project, the VEGA 2/0114/18 project and the CONICET-SAS RD 2017 project

17th INTERNATIONAL FOUNDRYMEN CONFERENCE
Hi-tech casting solution and knowledge based engineering
Opatija, May 16th-18th, 2018
http://www.simet.hr/~foundry/

# COMPUTER SIMULATION OF CONTROLLED COOLING OF CONTINUOUS CASTED AND ROLLED STEEL BAR

**Božo Smoljan[1], Dario Iljkić[2]*, Sunčana Smokvina Hanza[2], Lovro Štic[2], Luciano Gržinić[3], Goran Vratović[4]**

[1] Polytechnic of Pula College of Applied Sciences, Pula, Croatia
[2] University of Rijeka Faculty of Engineering, Rijeka, Croatia
[3] ULJANIK Mechanical Engineering Diesel JSC, Pula, Croatia
[4] Plazma tehnika d.o.o., Galižana, Croatia

**Invited lecture**
*Original scientific paper*

**Abstract**

Numerical model of controlled cooling in production of steel continues casting hot rolled bars was developed. By numerical model of controlled cooling is possible to predict a transient temperature field, microstructure evolution and hardness of rectangular steel bars during their cooling in cooling beds.
The numerical model of transient temperature field is based on control volume method. The algorithm for prediction of hardness and microstructure distribution in steel bars is based on continues cooling transformation (CCT) diagrams and real chemical composition. The numerical model and algorithm is completed to solve problems in controlled cooling of hot rolled bars in cooling beds. The controlled cooling is performed by special placement of hot rolled bars on cooling beds.
Numerical model and computer program was experimentally verified by simulation of real industrial production of low-alloyed steel bars. The verification of developed numerical model was performed by comparison of simulated hardness with experimentally evaluated results.

***Keywords***: *computer simulation, controlled cooling, continuous casting, rolling, steel, hardness, microstructure*

*Corresponding author (e-mail address): *darioi@riteh.hr*

## INTRODUCTION

Continuous casting is the process whereby molten steel is solidified into a semifinished billet, bloom, or slab for subsequent rolling in the finishing mills. Continuous casting has evolved to achieve improved yield, quality, productivity and cost efficiency. Steel from the electric or

basic oxygen furnace is tapped into a ladle and taken to the continuous casting machine. The ladle is raised onto a turret that rotates the ladle into the casting position above the tundish. Liquid steel flows out of the ladle into the tundish and then into a water-cooled copper mould. Solidification begins in the mould and continues through the First Zone (secondary cooling) and Strand Guide. In this configuration, the strand is straightened, torch-cut, then discharged for intermediate storage or hot charged for finished rolling. The product end-use dictates the quality, grade and shape of the cast product (billet, bloom, slab, beam blank, and/or round). Quality and grade considerations are utilized in determining various design parameters of the casting machine such as its length, vertical height, curved or straight mould, water versus water/air secondary cooling, electromagnetic-stirring, etc. Billets have cast section sizes up to about 7 inches square. Bloom sections sizes typically range from approximately 7 inches square to about 15 inches by 23 inches. Round castings include diameters of approximately 5 to 20 inches. Slab Castings range in thickness from 2 to 16 inches, and over 100 inches wide. Beam Blanks are shaped like dog bones, and are subsequently rolled into I-Beams. The width-to-thickness ratio, referred to as the "Aspect Ratio", is used to determine the dividing line between blooms and slabs. An Aspect Ratio of 2.5:1 or greater constitutes an as-cast product referred to as a Slab. After straightening, the strand is transferred on roller tables to a cut off machine, which cuts the product into ordered lengths. Sectioning can be achieved either via torches or mechanical shears. Then, depending on the shape or grade, the cast section will either be placed in intermediate storage, hot-charged for finished rolling or sold as a semi-finished product. Prior to hot rolling, the product will enter a reheat furnace to adjust its thermal conditions to achieve optimum metallurgical properties and dimensional tolerances.

Rate of steel specimen cooling essentially depends on workpiece geometry and characteristic physical properties of cooled steel and way of cooling. Relevant physical properties about which cooling rate depends are specific heat capacity of steel, heat conductivity coefficient of steel, steel density and heat transfer coefficient of steel body surroundings. For precise mathematical modelling these variables must be precisely estimated. These variables can be predicted by inversion method based on achieved cooling results and qualitative analysis of cooling curve [1-5].

In the developed computer program of simulation of hardness and microstructure distributions are calculated by using both, the CCT diagram and thermo-kinetic equations for evaluation of kinetic microstructure transformations.

## MATHEMATICAL MODELLING OF HEAT TRANSFER

The transient temperature field in an isotropic rigid body with coefficient of heat conductivity, $\lambda$/Wm$^{-1}$K$^{-1}$, density, $\rho$/kgm$^{-3}$ and specific heat capacity, $c$/Jkg$^{-1}$K$^{-1}$, without heat sources can be described by Fourier's law of heat conduction:

$$\frac{\delta(c\rho T)}{\delta t} = div\,\lambda\, grad T \qquad (1)$$

Characteristic boundary condition is:

$$-\lambda\frac{\delta T}{\delta n}\bigg|_{s}=\alpha\left(T_{s}-T_{f}\right) \tag{2}$$

where $\alpha$/Wm$^{-2}$K$^{-1}$ is heat transfer coefficient of body surroundings, $T_s$/K is surface temperature, $T_f$/K is temperature of body surroundings. Calibration of input data should be done according to achieved experimental results. If the variables $\rho$ and $c$ were accepted from other literature, variables $\lambda$ and $\alpha$ must be estimated, i.e., calibrated according to variables $\rho$ and $c$, based on experimental results. The input values of heat transfer coefficient can be optimized using Crafts-Lamont diagrams [6, 7].
The Equation (1) can be solved by using the finite volume method [8-10]. For example, 2-D finite volume formulation of the transient temperature field in an isotropic rigid body can be defined by [8]:

$$T_{ij}^{1}\left(\sum_{m=1}^{2}b_{\mathrm{I}(i+n)j}+\sum_{m=1}^{2}b_{\mathrm{J}i(j+n)}+b_{ij}\right)=\sum_{m=1}^{2}\left(b_{\mathrm{I}(i+n)j}T_{(i+k)j}^{1}+b_{\mathrm{J}i(j+n)}T_{i(j+k)}^{1}\right)+b_{ij}T_{ij}^{0} \tag{3}$$
$$i=1,2,...,i_{\max},\quad j=1,2,...,j_{\max},\quad n=2-m,\quad k=3-2m$$

where $T_{ij}^{0}$/K is the temperature in the beginning of time step $\Delta t$/s, $T_{ij}^{1}$/K is the temperature in the end of time step $\Delta t$/s, $b_{ij}$ = $(\rho_{ij}c_{ij}\Delta V_{ij})/\Delta t$, $\Delta V_{ij}$/m$^3$ is the volume of the control volume, $b_{\mathrm{I}(i+n)j}$ = $W_{\mathrm{I}(i+n)j}^{-1}$ and $b_{\mathrm{J}i(j+n)}$ = $W_{\mathrm{J}i(j+n)}^{-1}$, where variables $W_{\mathrm{I}(i+n)j}$ and $W_{\mathrm{J}i(j+n)}$ are the thermal resistances for $x$ axis. For example, $W_{\mathrm{I}(i+n)j}$ is thermal resistance between $ij$ and $(i-1)j$ volume for $n$=0, and for $n$=1, $W_{\mathrm{I}(i+n)j}$ is equal to thermal resistance between $ij$ and $(i+1)j$. The same nomenclature exists for $y$ axis.
Discretization system has $N$ linear algebraic equations with $N$ unknown temperatures of control volumes, where $N$ is total number of control volumes. Time of cooling from $T_a$ to specific temperature in particular volume of cooled specimen is determined as sum of time steps, and in this way, the diagram of cooling curve in every grid-point of a specimen is possible to found out.

$$t_{M}=\sum_{m=1}^{M}\Delta t_{m} \tag{4}$$

where $M$ is the number of time steps to the specific temperature.

## MATHEMATICAL MODELLING OF HARDNESS AND MICROSTRUCTURE COMPOSITION

Transformed part of microstructure, $X$ at some temperature, $T$ for time, $t$, can be calculated by Avrami's isothermal equation:

$$X = 1 - \exp(-k \cdot t^n) \tag{5}$$

For purpose of numerical analysis by computer, it is convenient to study the kinetic of austenite decomposition by Avrami's isothermal equation defined in an incremental form [11]:

$$\frac{dX}{dt} = n \cdot k^{\frac{1}{n}} \cdot \left( \ln \frac{1}{1-X} \right)^{1-\frac{1}{n}} \cdot (1-X) \tag{6}$$

Equation (6) can be written in an incremental form and the volume fraction $\Delta X$ of austenite transformed in the time interval $\Delta t_i$ at temperature $T_i$ can be calculated as follows:

$$\Delta X_{(N)} = n \cdot k^{\frac{1}{n}} \cdot \left( \ln \frac{1}{1-X_{(N-1)}} \right)^{1-\frac{1}{n}} \cdot \left(1-X_{(N-1)}\right) \cdot \Delta t_{(N)} \tag{7}$$

Kinetic parameters $k$ and $n$ from Equation (7) can be determined inversely by using a data from IT diagrams.

If IT diagrams is using, in accordance to the Scheil's additivity rule, characteristic microstructure transformation is completed when transformed part of microstructure, $X$ is equal to one [11, 12]:

$$\int_0^t \frac{dt}{\tau(X_0, T)} = 1 \tag{8}$$

where $\tau(X_0,T)$ represent the isothermal transformation time for $X = X_0$ at a temperature $T$, and $t$ is the total transformation time. Time of isothermal transformation, $\tau$ could be calculated by thermo-kinetic equations or could be found out by using IT diagram [12]. According to the additivity rule, the non-isothermal transformation kinetics during continues cooling can be described as the sum of series of the small increments of isothermal transformations.

Figure 1 shows the scheme for microstructure prediction based on cooling curve and IT diagram. In Figure 1, the temperature range is divided into a series of small finite steps. Maintaining the time interval, $\Delta t_i$ to sufficiently short times permits the assumption that the conditions are isothermal over each time step. It was assumed that each time step produces such a transformation as occurs in the IT diagram at the same temperature and microstructure composition.

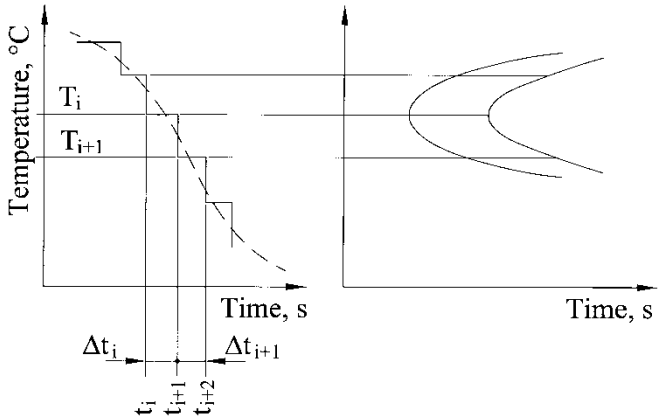


Figure 1. Prediction of microstructure composition from cooling curve and IT diagram

When using CCT diagrams, hardness can be estimated by drawing the cooling curve in the CCT diagram [11]. This is a very simple method which is often used. Also, hardness at different specimen points can be estimated by the conversion of the calculated cooling time $t_{8/5}$ to the hardness by using CCT diagram [11]. Differences between the actual chemical composition of steel and chemical composition of standard steel for which CCT diagram was prepared should be taken in account. In this work, it was done by using Equations (5) to (8).

## MATERIALS AND METHODS

The experiment was performed on two steel bars. First one was of 48 mm in diameter and 6000 mm long made of steel EN 30CrNiMo8. The chemical composition of steel EN 30CrNiMo8 was: 0.30 %C, 0.27 %Si, 0.44 %Mn, 0.015 %P, 0.004 %S, 1.93 %Cr, 0.36 %Mo, 1.90 %Ni. The second studied bar was of 20 mm thick, 60 mm wide and 6000 mm long made of steel EN 51CrV4. The chemical composition of steel EN 51CrV4 was: 0.51 %C, 0.33 %Si, 0.92 %Mn, 0.009 %P, 0.003 %S, 1.00 %Cr, 0.03 %Mo, 0.14 %Ni, 0.11 %V, 0.13 %Al, 0.19 %Cu.

Table 1 shows the comparison of the experimental and computer simulations results of cooling curves for studied bars. The results of the transient temperature field were measured at rolling bed which was adjusted for the numerical model needs. The round bar of 48 mm in diameter made of steel EN 30CrNiMo8 in Table 1 is referred to the case when one, separated bar was cooled alone. The rectangular bar of 20 mm thick, 60 mm wide made of steel EN 51CrV4 in Table 1 is referred to the case when two bars were cooled together, placed one above another. The second bar was placed after time step of 15 s. Measuring of temperature was performed by the M90R-1 pyrometer. The range of pyrometer is from 700 °C up to 2000 °C. For lower temperatures thermocamera can be used.

Table 1. Cooling curves of studied bars

| EN 30CrNiMo8 | | | EN 51CrV4 | | |
|---|---|---|---|---|---|
| Temperature/°C | Time/s | | Temperature/°C | Time/s | |
| | Experimental | Simulation | | Experimental | Simulation |
| 930 | 0 | 0 | 832 | 0 | 0 |
| 884 | 28 | 30.8 | 802 | 10 | 14.8 |
| 860 | 49 | 52.1 | 788 | 17 | 25.5 |
| 823 | 74 | 84.4 | 778 | 25 | 33.6 |
| 801 | 99 | 103.8 | 763 | 32 | 46.3 |
| 778 | 119 | 125.0 | 755 | 43 | 53.4 |
| 756 | 144 | 146.7 | 746 | 56 | 61.7 |
| 733 | 168 | 170.8 | 741 | 65 | 66.4 |
| 717 | 188 | 188.6 | 726 | 75 | 81.1 |
| 703 | 202 | 205.0 | 709 | 87 | 99.0 |
| Hardness HV | 367 | 398 | Hardness HV | 295 | 288 |

**APPLICATION**

By the numerical model, the hardness distributions and microstructure compositions in the steel bars after cooling were predicted. Numerical simulations are made by using the computer software BS-QUENCHING [8]. The developed model was applied in computer simulation of cooling of rectangular bar made of steel EN 42MnV7 with chemical composition: 0.44 %C, 0.25 %Si, 1.65 %Mn, 0.03 %P, 0.02 %S, 0.32 %Cr, 0.02 %Mo, 0.11 %Ni, 0.10 %V, 0.06 %Cu. Dimension of steel bars was of 25 mm thick, 250 mm wide and 6000 mm long. Numerical simulation was done for case when one, separated rectangular bar was cooled alone and for cases when two bars were cooled together, placed one above another. Starting temperature, $T_{start}$ of the steel bars in cooling bed was equal to 920 °C. For packed bars time step $t_{step}$ when second bar was placed to the cooling bed was equal to 25 s. Temperature of air, $T_{air}$ was equal to 30 °C.

The hardness and microstructure distributions of the steel bars after cooling and packed in different ways are shown in Figure 2 to 11.

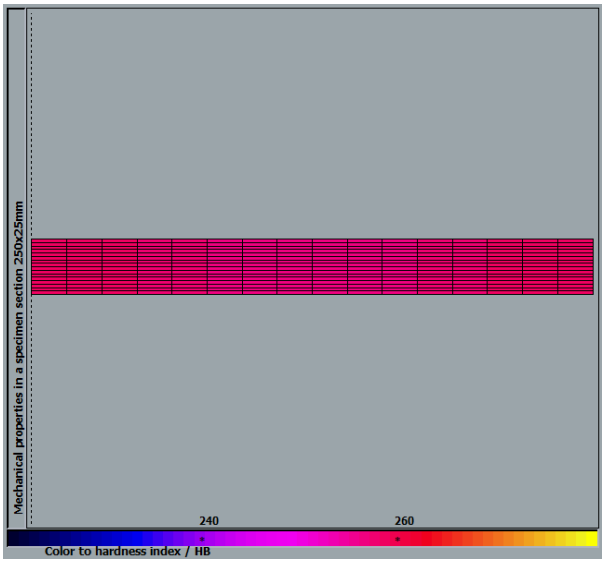


Figure 2. Hardness distribution of steel bar

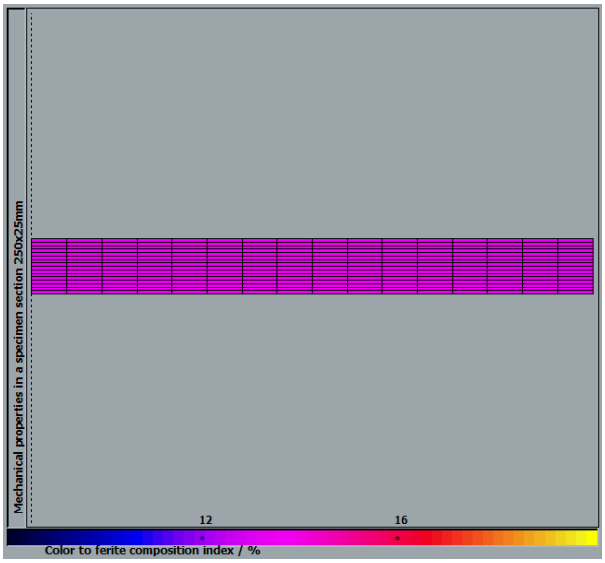


Figure 3. Ferrite distribution of steel bar

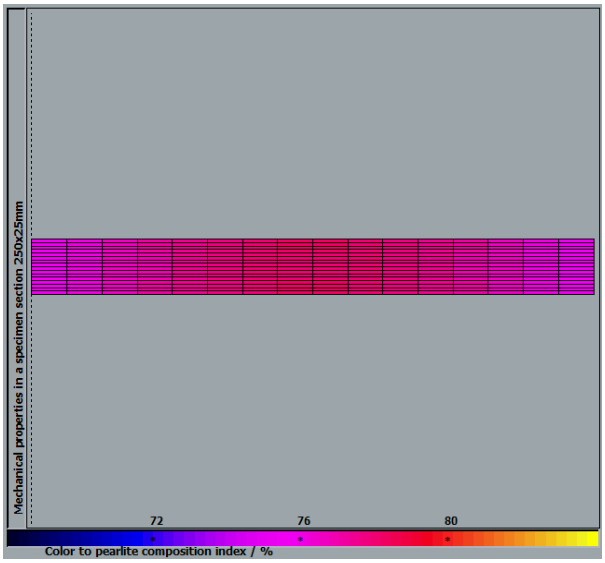


Figure 4. Pearlite distribution of steel bar

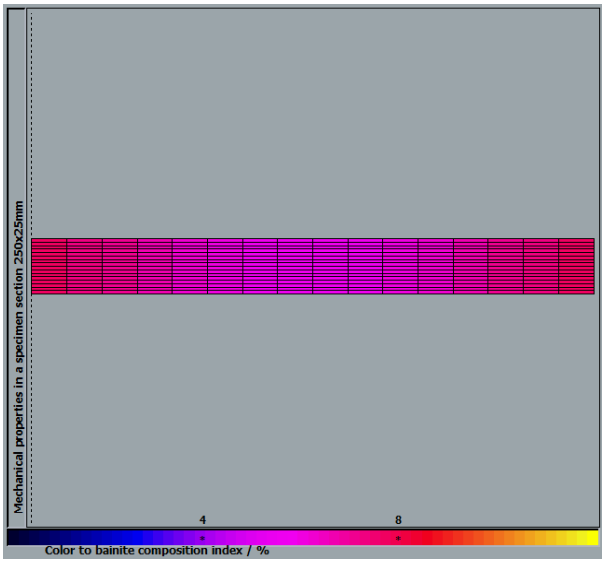


Figure 5. Bainite distribution of steel bar

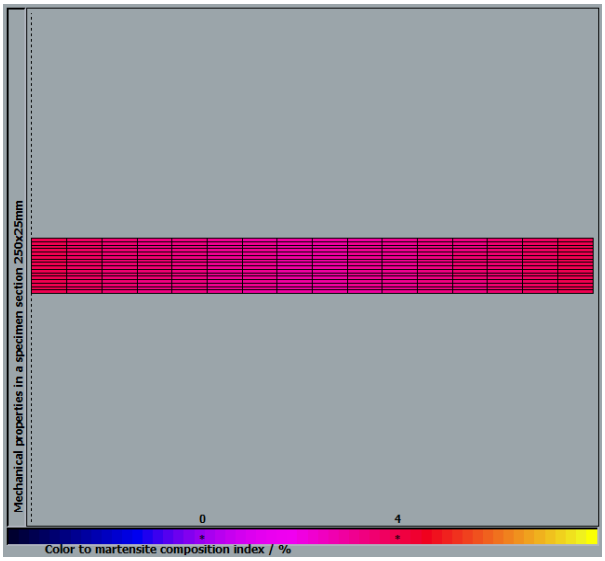


Figure 6. Martensite distribution of steel bar

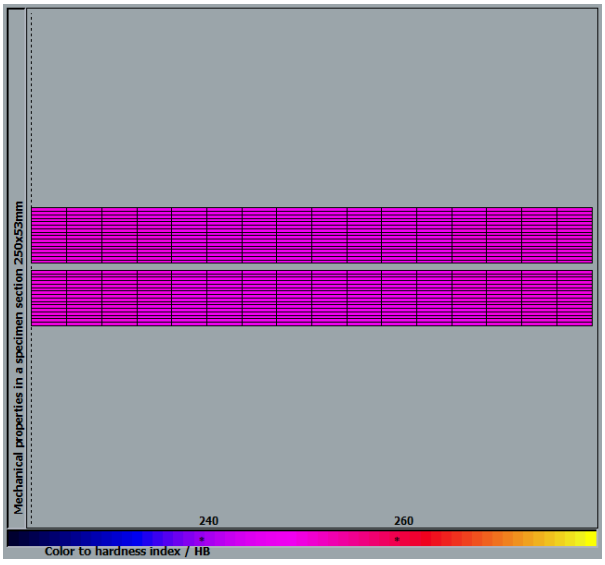


Figure 7. Hardness distribution of steel bars

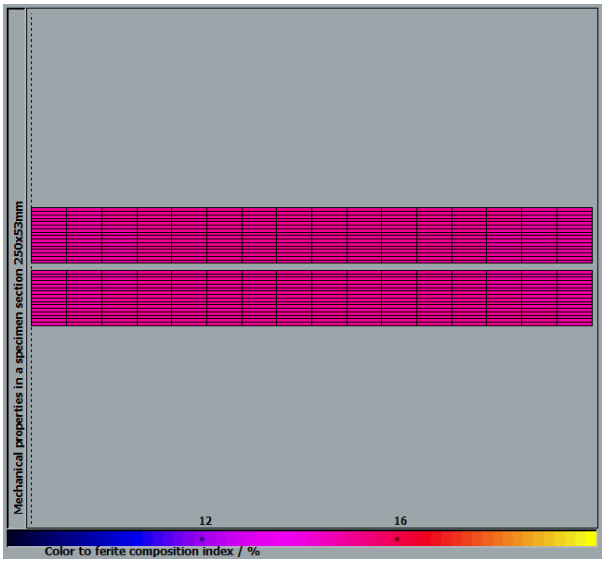


Figure 8. Ferrite distribution of steel bars

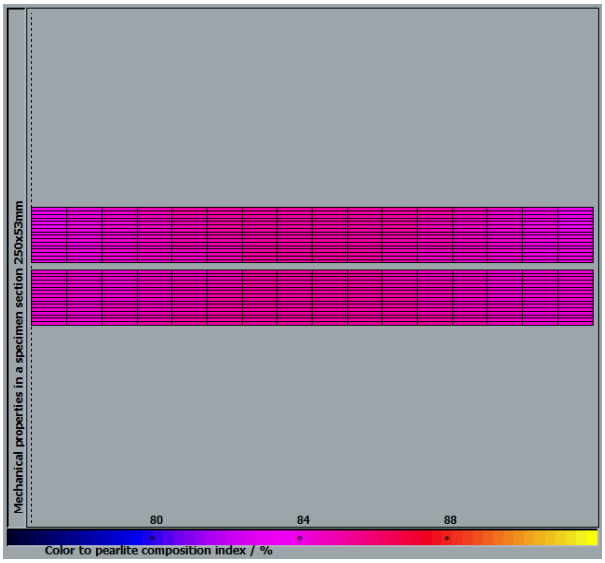


Figure 9. Pearlite distribution of steel bars

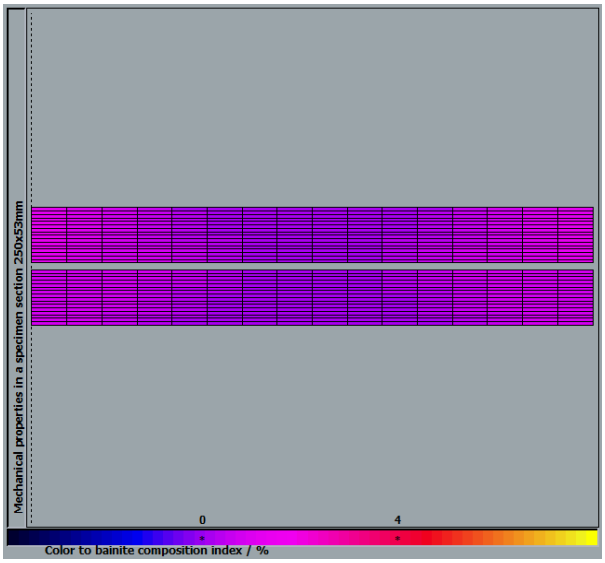


Figure 10. Bainite distribution of steel bars

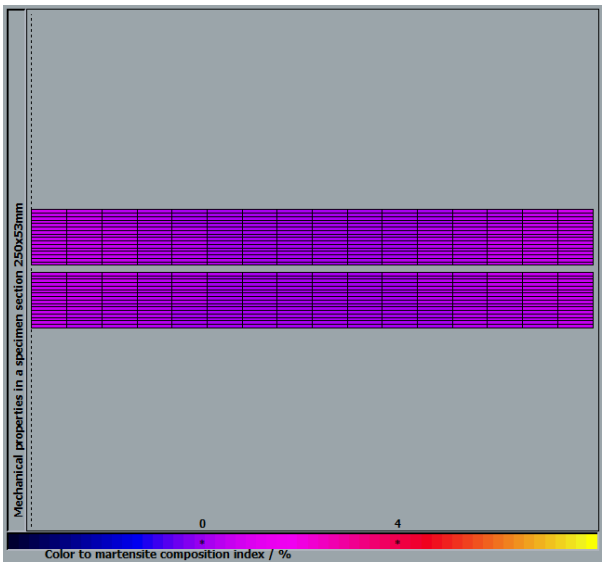


Figure 11. Martensite distribution of steel bars

## CONCLUSIONS

The 2-D numerical model of controlled cooling of steel bars in cooling beds in production of steel by continues casting and rolling was developed. The developed numerical model is consisted of prediction of a transient temperature field, microstructure evolution and hardness of round and rectangular steel bars during their cooling in cooling beds.

The numerical model of cooling is based on finite volume method. The algorithm for prediction of hardness and microstructure distribution in steel bars is based on continues cooling transformation, (CCT) diagrams of steel. The results was be improved by taking in account a real chemical composition of steel.
The verification of developed numerical model was performed by comparison of simulated cooling curves and hardness with experimentally evaluated results.
Established model was applied in two cases of controlled cooling of different packed rolling bars in cooling beds. The minimum hardness with minimum content of bainite and martensite was achieved when two bars were packed together.
Based on achieved results it can be concluded that by developed computer software is possible to predict a transient temperature field, microstructure composition and hardness distribution of steel bars during them controlled cooling in cooling beds.

**REFERENCES**

[1] E. Just, Verguten—Werkstoffbeenflussung durch Harten und Anlassen, VDI, Bericht, 256 (1976) pp. 124-140.
[2] B. Liščić, System for Process Analysis and Hardness Prediction When Quenching Axially-Symmetrical Workpieces of Any Shape in Liquid Quenchants, Materials Science Forum, 638-642 (2010) pp. 3966-3974.
[3] I. Felde, T. Réti, Evaluation of Cooling Characteristics of Quenchants by Using Inverse Heat Conduction Methods and Property Prediction, Materials Science Forum, 659 (2010) pp. 153-158.
[4] B. Smoljan, The Calibration of the Mathematical Model of Steel Quenching, in: M. Salehi (Ed.), Proc 5th World Seminar on Heat Treatment and Surface Engineering IFHT'95, Isfahan, Iran, 1995, pp. 709-715.
[5] D. Iljkić, A Contribution to the Development of the Mechanical Properties Prediction of Quenched and Tempered Steel and Cast Steel, Doctoral Thesis, Department of Materials Science and Engineering, Faculty of Engineering, University of Rijeka, (2010) (in Croatian).
[6] H. Bhadeshia, Material Factors, in Handbook of Residual Stress and Deformation of Steel, G. Totten, M. Howes, T. Inoue (eds.), ASM International, 2002.
[7] B. Smoljan, D. Iljkić, Computer Modeling of Mechanical Properties and Microsructure of Quenched Steel Specimen, Proc 5th International Conference on Thermal Process Modeling and Computer Simulation, 16-18 June 2014, Orlando, USA.
[8] B. Smoljan, Numerical Simulation of As-Quenched Hardness in a Steel Specimen of Complex Form, Communications in Numerical Methods in Engineering, 14 (1998) 1, pp. 277-285.
[9] S. Patankar, Numerical Heat Transfer and Fluid Flow, McGraw Hill Book Company, New York, 1980.
[10] J. P. Holman, Heat transfer, McGraw Hill Book Company, 1986.

[11] B. Smoljan, D. Iljkić, B. Senčić, R. Vertnik, Numerical model of controlled cooling of steel hot rolled bars, Proceedings of the 29th ASM Heat Treating Society Conference & Exposition, "Heat Treat 2017", 24-26. October 2017, Columbus, Ohio, USA.
[12] S. Smokvina Hanza, Mathematical modeling and computer simulation of microstructure transformations and mechanical properties during steel quenching, Doctoral Thesis, Department of Materials Science and Engineering, Faculty of Engineering, University of Rijeka, Rijeka, 2011, (in Croatian).

**Acknowledgements**

This work has been supported in part by Croatian Science Foundation under the project 5371.

This work has been supported in part by University of Rijeka, Support No 13.09.1.1.02.

17th INTERNATIONAL FOUNDRYMEN CONFERENCE
Hi-tech casting solution and knowledge based engineering
Opatija, May 16th-18th, 2018
http://www.simet.hr/~foundry/

# INFLUENCE FACTORS ON STORAGE ABILITY OF INORGANIC CORES

**Iveta Vasková*, Martin Conev**

Technical University of Košice Faculty of Materials, Metallurgy and Recycling, Košice, Slovakia

**Invited lecture**
*Original scientific paper*

**Abstract**

Use of inorganic binders based on alkali silicate solutions for core and mold production in the foundry industry represents the most environmental friendly technology. During the core and mold production or during the casting no odors and emissions are released, which is compared to the organic binder systems the great advantage. Nevertheless, the use of inorganic binders based on alkali silicate solutions brings along some technological drawbacks. In this paper the effect of storage conditions of cores with alkali silicate binder cured by dehydration is evaluated as well as the influence of sand granularity on storage ability. Test bars made with different mixtures were stored in climatic chamber with three different storage condition set ups. Bending strength of test bars was measured in certain time interval within 24 hours, free water content in test bars was also measured by the use of halogen moisture analyzer in order to express reverse reaction. From the obtained results, storage conditions with absolute humidity of 9.21 g/cm$^3$ were evaluated as ideal, storage conditions with absolute humidity 14.97 g/cm$^3$ were evaluated as critical with limited storage time and storage conditions with absolute humidity 27.31 g/cm$^3$ as not suitable storage conditions for inorganically bound cores and mold. Results also showed that finer sands are more sensitive for storage conditions with higher air humidity.

***Keywords**: inorganic binders, storage ability, granularity, sand core, automotive industry*

*Corresponding author (e-mail address): *iveta.vaskova@tuke.sk*

## INTRODUCTION

With the increasing number of laws and regulations (Figure 1) for the environmental protection, interest in inorganic binders based on alkali silicate solutions is also increasing [1]. Using the inorganic binders for mold and core production still represents technology that is the least harmful to the environment. On the other hand, using the inorganic binders based on alkali silicate solutions brings along some technological problems such as low sand flowability and moisture resistance, poor knock-out properties or sand reclamation

compared to the resin-bonded sands, which release emissions and related odor not only during casting but also during core production process [2-5].

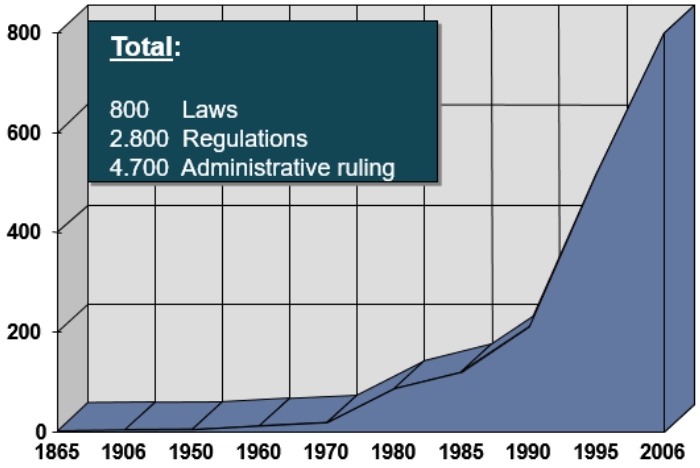


Figure 1. Intensification of the environmental protection in Germany [1]

There are two basic ways of alkali silicate solutions hardening [6,7]:

- Creation of gel by chemical irreversible reaction (1)

$$Na_2O{\times}mSiO_2{\times}nH_2O + \frac{CO_2}{H_2CO_3} \rightarrow \frac{Na_2CO_3}{NaHCO_3} + Si(OH)_4 \quad (1)$$

- Creation of gel by physical reversible curing (2)

$$Na_2O{\times}mSiO_2{\times}nH_2O \overset{\pm H_2O}{\longleftrightarrow} Na_2O{\times}mSiO_2 + nH_2O \quad (2)$$

According to the nature of hardening different character of gel is reached. Result of chemical way of curing is a gel disrupted by crystalline formations, which are causing internal stress in gel. Gel is then brittle, cohesive forces are low as well as compression strength. On the other hand, gel created via physical curing is creating intact and coherent layer which results in higher strength properties and cohesive forces. The curing reaction (2) is partly reversible, which means that with the input of water and energy, backward reaction can take place. This results into removal of silicate network and thus cores losing the strength. Loss of the strength can cause cores to collapse, break or bend, which can affect dimensions and quality of the final product - casting. Figure 2 shows the SEM images of binder bridge created by chemical reaction (1a) and by physical curing (1b) [7].

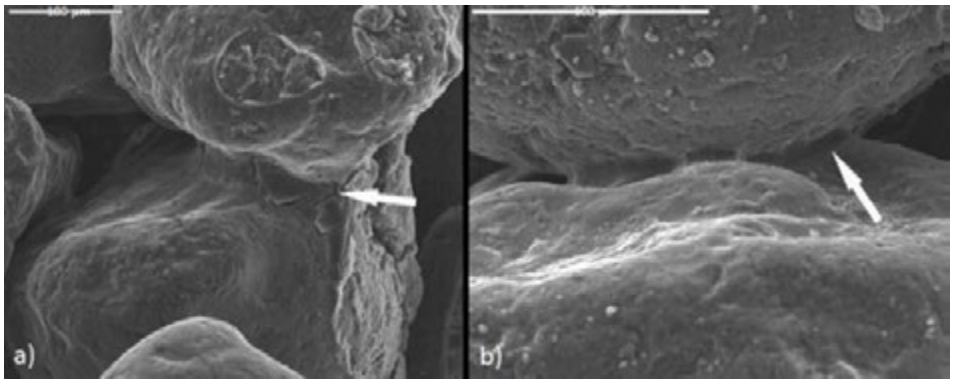


Figure 2. SEM image of binder bridge created by a) chemical reaction, b) physical curing [7]

Requirements of foundries and their customers for technological improvement of inorganic binder systems resulted into the development of new hot-curing binders based on alkali silicate solutions, which were introduced by the leading manufacturers at GIFA in 2003. These binder systems are working mainly on the physical way of hardening by dehydration process in heated tools with assistance of hot air purge, although a chemical reaction can be also triggered. In order to compensate already mentioned disadvantages of alkali silicate binders, the new hot-curing binder systems and processes are working with additives and adjuvants which are contained in a binder itself or added in liquid or powder form to the sand mixture. Additives are delaying reverse reaction and improving the moisture resistance. Through the reactive groups, particle of additive combines the individual binder particles with one another and forms a silicate framework in the shape of a three-dimensional network [8,9]. In Figure 3 there is a scheme of silicate particles connected through the particle of additive [10].

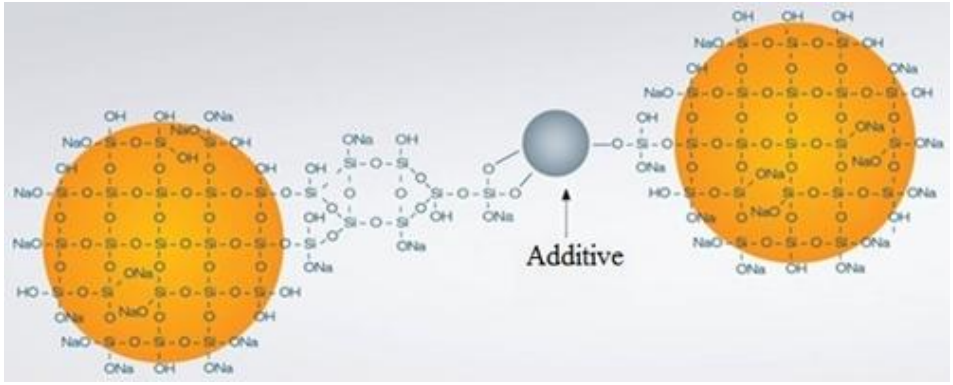


Figure 3. Effect of additive on three-dimensional silicate network creation [10]

## MATERIALS AND METHODS

Purpose of this paper was to examine the effect of storage conditions on strength of cores with hot cured alkali silicate binder system and influence of sand granularity on storage ability of cores. In order to accomplish this objective, materials and methodology described below were used.

Test bars for measurement of bending strength were produced on laboratory core blowing machine using method and parameters described in author´s previous paper [11]. Silica sand from Slovak locality was used in all cases, coarse sand with middle grain size 0.38 mm and fine sand with middle grain size 0.20 mm. Composition of tested core mixtures is shown in the Table 1 and Table 2.

Table 1. Composition of tested mixtures – effect of storage conditions

| R. | Sand [%] | | Binder | | Additive | |
|---|---|---|---|---|---|---|
| | Coarse | Fine | Type | Amount [%] | Type | Amount [%] |
| 1 | 100 | - | A | 2.2 | 1 | 0.8 |
| 2 | 100 | - | B | 2.4 | 2 | 0.8 |
| 3 | 20 | 80 | B | 2.4 | 3 | 2.0 |

Table 2. Composition of tested mixtures – influence of $d_{50}$

| R. | Sand [%] | | | Binder | | Additive | |
|---|---|---|---|---|---|---|---|
| | Coarse | Fine | $d_{50}$ [mm] | Type | Amount [%] | Type | Amount [%] |
| 4 | 100 | - | 0,38 | A | 2.4 | 1 | 1,1 |
| 5 | - | 100 | 0,20 | A | 2.4 | 1 | 1,1 |
| 6 | 70 | 30 | 0,33 | A | 2,4 | 1 | 1,1 |
| 7 | 20 | 80 | 0,22 | A | 2.4 | 1 | 1,1 |

Produced test bars were putted into the climatic chamber with stable conditions of temperature and relative humidity. Three different condition set ups were used in examination of effect of storage conditions in order to test ideal conditions with low temperature and low relative humidity, conditions with increased relative humidity and extreme conditions with increased temperature and very high relative humidity as described in the Table 3. For second examination of the influence of sand granularity on storage ability, conditions No. 2 were used in order to see differences between tested mixtures.

Table 3. Conditions in the incubator

| No. | Temperature [°C] | Rel. humidity [%] | Abs. humidity [g/m$^3$] |
|---|---|---|---|
| 1 | 25 | 40 | 9,21 |
| 2 | 25 | 65 | 14,97 |
| 3 | 30 | 90 | 27,31 |

Bending strength of the test bars was measured after 1, 2, 4, 6, 12 and 24 hours of storage in the climatic chamber on LRu-2e strength machine. Besides strength measurement, water

content in test bars was also measured using halogen moisture analyzer HR73 in order to express kinetics of backward reaction (2) in examined conditions. All results are the average of three measurements.

## RESULTS AND DISCUSSION

Figures 4, 5 and 6 present the strength behavior of three tested mixtures in different storage conditions with low temperature and relative humidity (Figure 4), with increased relative humidity (Figure 5) and with increased temperature and very high relative humidity (Figure 6). From the graphs on Figure 4 it can be stated, that storage in the conditions of 25 °C, 40% relative humidity and 9.21 g/cm$^3$ absolute humidity doesn´t negatively affect strength behavior over at least 24 hours. This statement also supports measurement of free water content, where the amount of free water after 24 hours didn´t exceed 0.03% from original 0.01% what can signify that the backward reaction (2) is taking place very slowly. Conditions of 25 °C and 40% RH can be, based on obtained results, evaluated as ideal for storage of cores bonded by alkali silicate solutions cured by dehydration for minimum storage time of 24 hours and based on the not changing trend of strength behavior assumption of even longer storage time is possible.

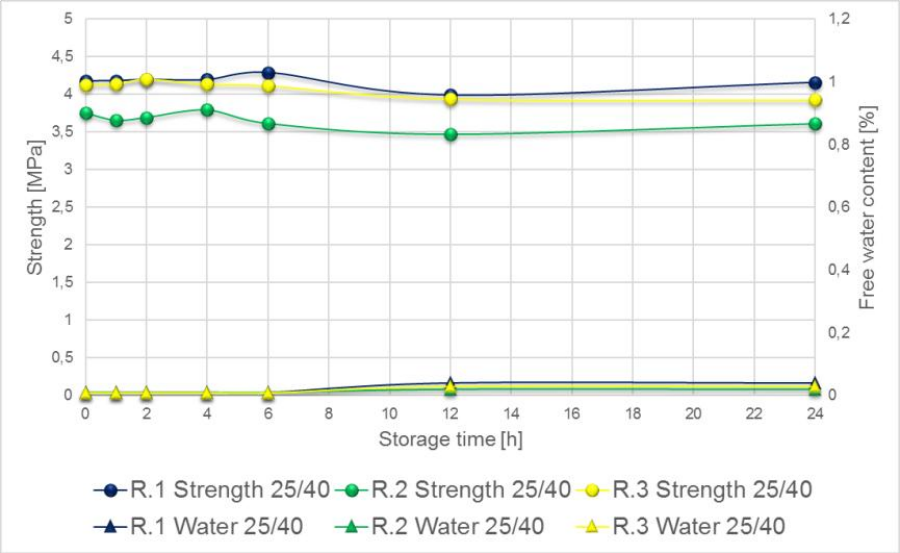


Figure 4. Strength behavior after storage in conditions 25 °C and 40 %RH

Graphs on the Figure 5 show strength behavior in the conditions of 25 °C and 65% relative humidity, absolute humidity in this case is 14.97 g/cm$^3$. It can be seen that after one hour of storage time there is slight decrease of strength and after 4 – 6 hours the drop is significant, which can result in bending or collapsing of cores with very complex geometry (e.g. water jacket cores). Free water content in first 6 hours corresponds with loss of strength. Between 12 and 24 hours of storage time, strength is not changing significantly, as well as free water

content. These conditions can be evaluated as critical with limited storage time. Mixture No. 3 seems to be more sensitive to the storage conditions than the others tested, since the free water content after 24 hours and also the loss of strength is the highest. Mixtures No. 1 and No. 2 are comparable.

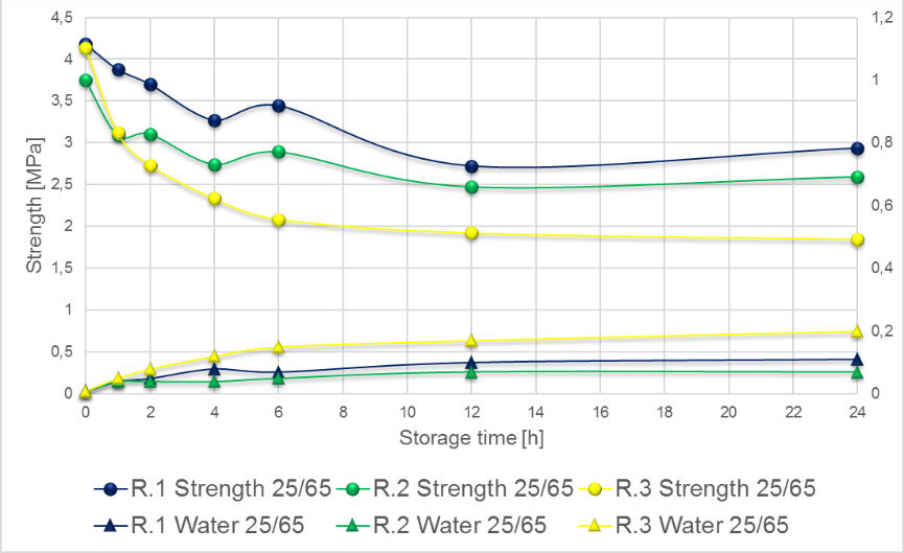


Figure 5. Strength behavior after storage in conditions 25 °C and 65 %RH

Figure 6 presents results of strength and free water measurement after storage in conditions of 30 °C and 90% relative humidity. Absolute humidity in these conditions is 27.31 g/cm$^3$. From the graphs it can be seen than in these conditions, test bars are losing strength rapidly in first hour of storage. This also corresponds with the free water content soaked back to the system, which indicates fast backward reaction (2). These conditions can be evaluated as not at all suitable for the inorganic cores cured by dehydration.

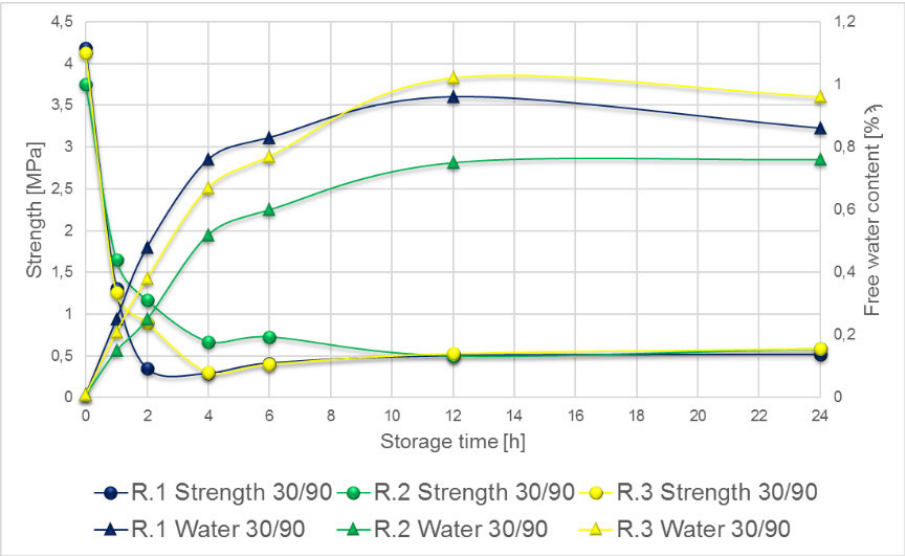


Figure 6. Strength behavior after storage in conditions 30 °C and 90 %RH

Figure 7 shows strength behavior and free water content over 24 hours of storage in conditions 25 °C and 65 %RH for mixtures with different middle grain size. Figure 8 presents drop of strength after 1 and 24 hours for these mixtures. From the results it can be seen, that finer sands are less moisture resistant compared to coarse sands. Drop of strength after 1 hour for mixture 4 with coarse sand is by 7% and for mixture 5 with fine sand is by 33%, which is significant difference. Explanation for this can be in larger surface of finer sands, that in case of mixture 4 is 61.45 $cm^2/g$ and in case of mixture 5 is 118.24 $cm^2/g$. With smaller grains higher porosity of core occurs which can lead to higher sorption of air humidity [12,13].

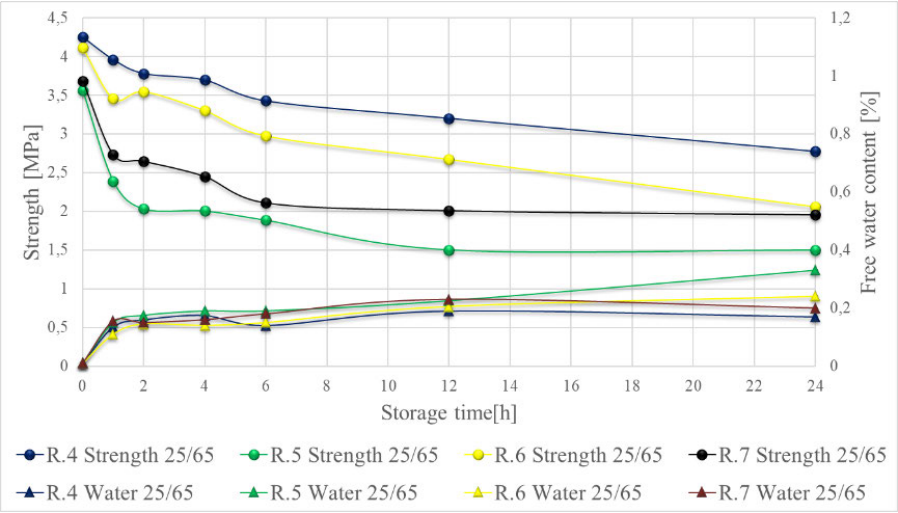


Figure 7. Strength behavior of mixtures with different middle grain size in conditions 25°C and 65 %RH

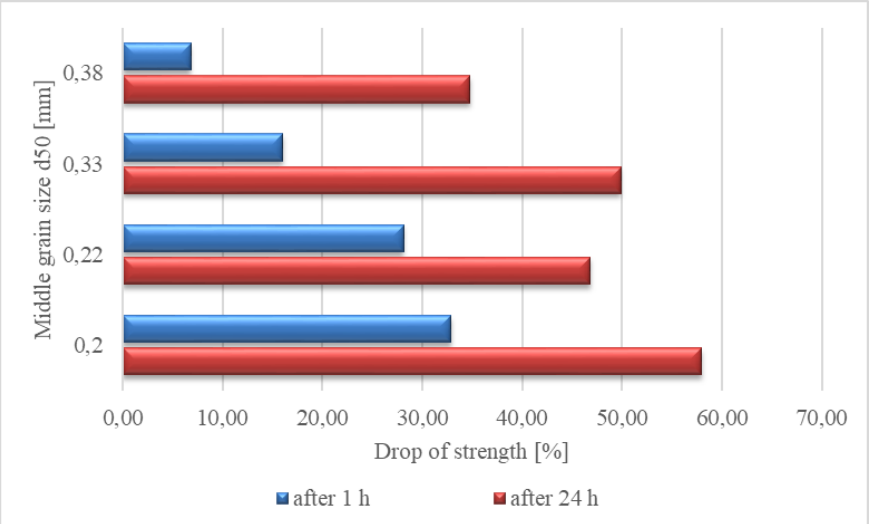


Figure 8. Influence of $d_{50}$ on drop of strength after 1 and 24 hours of storage

## CONCLUSIONS

From the performed investigation and obtained results, following conclusions can be stated, that storage conditions with 9.21 g/cm$^3$ absolute humidity can be evaluated as ideal, where strength behavior and free water content are stable within 24 hours. Conditions with 14.97 g/cm$^3$ were evaluated as critical with limited storage time. When exceeding the critical limit, which is more or less dependent on the core geometry, bending or collapsing of cores is possible. Storage conditions with 27.31 g/cm$^3$ were evaluated as not suitable for the cores bonded with alkali silicate solution cured by dehydration. Backward reaction takes place very quickly in such conditions and cores are losing their strength within one hour. In places with very high relative humidity it can be recommended using some air drying devices in cores storage areas. Influence of sand granularity was observed, from the results it was clearly seen that mixture with smallest medium grain size had the lowest moisture resistance than mixtures with larger grains, this can be explained by larger surface of grains and higher porosity of cores made of fine sand that leads to a higher sorption of air humidity.

## REFERENCES

[1] R. Boehm, Viel versprechende Ergebnisse Erfahrungen bei der Regenerierung neuer anorganischer Binder, Giesserei – Erfahrungsaustausch, (2008) 11, pp. 4-8.
[2] I. Izdebska-Szanda, A. Palma, M. Angrecki, M. Żmudzińska, Environmentally Friendly Mould Technology, Archives of foundry engineering, 13 (2013) 3, pp. 37-42.
[3] M. Stechman, D. Różycka, A. Baliński, Modification of aqueous sodium silicate solutions with morphoactive agents, Polish Journal of Chemical Technology, 5 (2003) 3, pp. 47.
[4] P. Jelínek, R. Škuta, Modified sodium silicates – a new alternative for inorganic foundry binders, Materials Enginering, 10 (2003) 3, pp. 283.
[5] I. Vasková, L. Bobok, Some knowledge of the water glass modification by the phosphate compounds, Acta Metallurgica Slovaca, 8 (2002) 2, pp. 161-167.
[6] R. Škuta, Dehydration processes of alkaline silicates hardening, TUKE -FBERG 2014.
[7] M. Stachowicz, K. Granat, D. Nowak, K. Haimann, Effect of hardening methods of moulding sands with water glass on structure of bonding bridges, Archives of Foundry engineering, 10 (2010) 3, pp. 123-128.
[8] H. Polzin, Inorganic Binders for mould and core production in the foundry, Fachverlag Schiele und Schön GmbH, Berlin, 2014.
[9] L. Zaretskiy, Modified silicate binders new developments and applications, International Journal of Metal casting, 10 (2016) 1, pp. 88-99.
[10] C. Wallenhorst, Grundlagen zum Verständnis der anorganischen Kernfertigung, Giesserei-Praxis, (2010) 6, pp. 181-184.
[11] M. Conev, I. Vasková, M. Hrubovčáková, Impact of Silica Sand Granulometry on Bending Strength of Cores Produced by ASK Inotec Process, Manufacturing Technology, 16 (2016) 2, pp. 327-334.

[12] P. Jelínek, E. Marko, P. Lichý, M. Cagala, Cooling Effect of Foundry Moulds from Mixtures with Non-quartz Base Sands, Hutnické listy, LXII (2009) 5, pp. 75-80.
[13] N. Kaźnica, J. Zych, Role of Sand Grains in Sorption Processes by Surface Layers of Components of Sand Moulds, Archives of Foundry Engineering, 17 (2017) 1, pp. 87-92.

17th INTERNATIONAL FOUNDRYMEN CONFERENCE
Hi-tech casting solution and knowledge based engineering
Opatija, May 16th-18th, 2018
http://www.simet.hr/~foundry/

# HOT TEARING TESTING OF ALUMINIUM ALLOYS USING RING CASTING METHOD

# ISPITIVANJE SKLONOSTI ALUMINIJSKIH LEGURA TOPLIM PUKOTINAMA METODOM LIJEVANJA PRSTENOVA

**Branko Bauer*, Ivana Mihalic Pokopec, Ines Mance, Ivan Marasović, Boris Crnobrnja**

University of Zagreb Faculty of Mechanical Engineering and Naval Architecture, Zagreb, Croatia

**Oral presentation**
*Preliminary note*

**Abstract**

Hot tearing is a serious and quite common casting defect therefore they are a good indicator of an alloy's castability. Most significant factors that influence overall susceptibility to hot tearing of an alloy are: chemical composition, grain size, pouring temperature and cooling rate. Ring casting test in green sand mould was carried out to determine susceptibility to hot tearing for AlSi12, AlSi9Mg and AlMg1 alloys. Outer ring diameter was kept constant in every trial while the ring width that defines the test severity varied depending on a metal core dimension. A steel core was used to inhibit ring shrinkage and therefore inducecrack occurrence. At the same time mould filling and ring solidification simulations were conducted. AlMg1 alloy showed high susceptibility to hot tearing and should not be cast using permanent moulds that that doesn't allow for shrinkage during solidification. Alloys AlSi12 and AlSi9Mg showed no tendency to hot tearing.

***Keywords:*** *aluminium alloys for casting, hot tearing, ring casting method*

*Corresponding author (e-mail address): *branko.bauer@fsb.hr*

**Sažetak**

Tople pukotine su česta i ozbiljna greška u ljevačkim legurama te jedan od glavnih pokazatelja koji definiraju livljivost neke legure. Na sklonost određene legure prema nastanku toplih pukotina utječu razni čimbenici, a najvažniji su; kemijski sastav legure, veličina zrna, temperatura ulijevanja i brzina ohlađivanja. U ovom radu provedeno je ispitivanje sklonosti legura AlSi12, AlSi9Mg i AlMg1 prema nastanku toplih pukotina metodom lijevanja prstenova. Legure su lijevane u jednokratne pješčane kalupe. Vanjski promjer prstena je bio konstantan, a širina prstena R koja ujedno definira strogost probe, varirana je promjenom radijusa metalne jezgre. Metalna jezgra korištena je kako bi spriječila stezanje prstena i izazvala pukotine. Nakon lijevanja provedena je simulacija punjenja kalupa i

skrućivanja prstena. Legura AlMg1 vrlo je sklona nastanku toplih pukotina i ne smije se lijevati u kalupe koji ne dopuštaju slobodno stezanje prilikom skrućivanja. Legure AlSi12 i AlSi9Mg nisu sklone nastanku toplih pukotina.

***Ključne riječi:*** *ljevačke aluminijske legure, tople pukotine, metoda lijevanja prstenova*

## UVOD

Tople pukotine nastaju u zadnjoj fazi skrućivanja u temperaturnim područjima blizu solidusa, a nalaze se unutar ili na površini odljevka [1]. Najveći dio dosadašnjih istraživanja toplih pukotina temelji se na proučavanju mehanizma njihovog nastanka. Međutim, točan mehanizam još uvijek nije do kraja razjašnjen. Općenito je prihvaćeno da se tople pukotine počinju stvarati u posljednjoj fazi skrućivanja u temperaturnom području u blizini solidusa. Jedan od uzroka njihova nastanka mogu su dodatna naprezanja u odljevku koja nastaju kada kalup ne dozvoljava skupljanje odljevka prilikom skrućivanja, a nastaju uslijed nedovoljne deformabilnosti dendritne mreže te nedovoljnog i neadekvatnog međudendritnog napajanja u širokoj kašastoj zoni. Mjesta njihove inicijacije u pravilu su granice dendritnih zrna obavijene tankim filmom rastaljenog metala [1-3].
Posebno su osjetljive aluminijeve legure sa širokim intervalom skrućivanja i kašastim načinom skrućivanja gdje još uvijek postoji tanki film rastaljenog metala po granicama dendritnih zrna koji u posljednjoj fazi skrućivanja pogoduju stvaranju toplih pukotina. U kasnim fazama skrućivanja tijekom stezanja razvijaju se sve veća naprezanja što dovodi do toga da se nastajuća mreža dendrita uslijed tih naprezanja sve više deformira, a zbog prisustva tankog filma rastaljenog metala oslabljena je povezanost među dendritima te može lako doći do njihovog odvajanja, tj. nastanka pukotina između njih. [2,4,5]. Mjesta na odljevku koja zadnja skrućuju su mjesta na kojima dolazi do koncentracije naprezanja i toplih pukotina.
Ukoliko je omogućen dotok rastaljenog metala na mjesto inicijacije pukotine može se spriječiti njen nastanak. Čak se i već nastala topla pukotina može popuniti ako je u područje razdvajanja omogućeno dotjecanje rastaljenog metala. Popravljena pukotina može se naknadno ponoviti jer skrutnuti ostatak rastaljenog metala koji je dotekao, zbog segregacije i mogućih uključaka u sebi, može imati smanjenu čvrstoću [6].
Za razliku od mreže dendrita oko kojih je prisutan tanak sloj rastaljenog metala, koherentna dendritna mreža zbog dovoljne čvrstoće može podnijeti i oduprijeti se djelovanju koncentriranih naprezanja tijekom stezanja bez nastanka pukotina. Iako dolazi do plastične deformacije mreže, veze između dendrita su dovoljno jake da ne dođe do pucanja istih, odnosno do nastanka pukotine [2,4].
Na sklonost određene legure prema nastanku toplih pukotina utječu razni čimbenici, među kojima svakako treba izdvojiti kemijski sastav legure, veličinu zrna, temperaturu ulijevanja te brzinu ohlađivanja [7].
Tople pukotine ostaju u odljevku nakon lijevanja te uzrokuju značajne gubitke u proizvodnji. Da bi se smanjili gubici uzrokovani pojavom toplih pukotina, tijekom godina su razvijani razni

modeli kojima bi se predvidjela pojava pukotina te metode ispitivanja sklonosti metalne legure prema nastanku toplih pukotina. Mnoge su od tih metoda kvalitativne prirode, dok su modeli ograničeni s obzirom na nedostatak kvantitativnih informacija, podataka te baza znanja, tako da još uvijek nema standardizirane i pouzdane kvantitativne metode ispitivanja sklonosti legure prema nastanku toplih pukotina ni pouzdanog modela kojim bi se mogla predvidjeti pojava toplih pukotina u određenoj leguri [1,2].
Većina metoda temelji se na istim principima. Legura se ulijeva u kalup u kojem se na određenim mjestima ograničava slobodno skupljanje odljevka tijekom skrućivanja. Sklonost prema nastanku toplih pukotina određuje se vizualnom kontrolom skrutnutog odljevka i proučavanjem nekoliko otvorenih pukotina uočenih na površini odljevka. Na ovakav se način provodi metoda lijevanja u kalup oblika „pseće kosti“ te metoda lijevanja prstena. Glavni su nedostaci navedenih metoda to što su kvalitativne te što se određivanje sklonosti uglavnom temelji na proučavanju otvorenih pukotina uočenih na površini odljevka, dok se unutarnje pukotine zanemaruju [1,2,5,8].
Osim ovih potpuno vizualnih metoda postoje i metode kod kojih se mjerenjem i praćenjem određenog parametra tijekom skrućivanja određuje sklonost legure prema nastanku toplih pukotina. Vrlo su česte metode u kojima se tijekom skrućivanja mjeri porast čvrstoće legure tijekom skrućivanja, vlačna naprezanja koja se razvijaju tijekom stezanja, sila stezanja odljevka tijekom skrućivanja, itd. Tijekom skrućivanja pomoću uređaja za mjerenje opterećenja očitaju se i snimaju stezanja koja se razvijaju u odljevcima tijekom skrućivanja. Na temelju dobivenih pukotina na odljevcima te snimljenih krivulja zaključuje se o povezanosti određenog opterećenja s nastankom toplih pukotina [9, 10].
Za preliminarna istraživanja u ovom radu, izabrana je metoda lijevanja prstenova.

## MATERIJALI I METODE

U ovom radu provedeno je ispitivanje sklonosti legura AlSi12, AlSi9Mg i AlMg1. U tablici 1. prikazan je kemijski sastav ispitivanih legura dobiven pomoću spektrometra Leco GDS 850A.

Tablica 1. Kemijski sastav ispitivanih legura

| Legura | mas. % | | | | | | | | | |
|---|---|---|---|---|---|---|---|---|---|---|
| | Si | Fe | Cu | Mn | Mg | Cr | Ni | Zn | Ti | Al |
| AlSi12 | 13 | 0,03 | 0 | 0,02 | 0,04 | <0,001 | <0,01 | 0,03 | 0,013 | ostatak |
| AlSi9Mg | 9,10 | 1,25 | 0,72 | 0,09 | 1,30 | 0,06 | 0,08 | 0,41 | 0,054 | ostatak |
| AlMg1 | 0,49 | 0,07 | 0 | 0,006 | 1,17 | 0,005 | 0,006 | 0,008 | 0,003 | ostatak |

Za ispitivanje sklonosti nastanku toplih pukotina korištena je metoda lijevanja prstenova različitih unutarnjih promjera. Metodu su razvile I. Spektrova i T.V. Lebedewa, 1950. godine. Legure su lijevane u jednokratne pješčane kalupe, Slika 1. Vanjski promjer prstena je bio konstantan i iznosio je 107 mm, a širina prstena R koja ujedno definira strogost probe, varirana je promjenom radijusa metalne jezgre. Korištene su jezgre radijusa 55 mm, 65 mm, 75 mm i 85 mm. Visina prstena iznosila je 5 mm. Metalna jezgra korištena je kako bi spriječila

stezanje prstena i izazvala pukotine. Uvjeti su pooštreni dodavanjem hladila polukružnog oblika. Veći promjer jezgre uzrokuje veće naprezanje. Kao mjera za tople pukotine služi kritična širina prstena R kod koje se prvi put pojavila pukotina. Što je širina prstena R veća to je legura sklonija nastanku toplih pukotina.

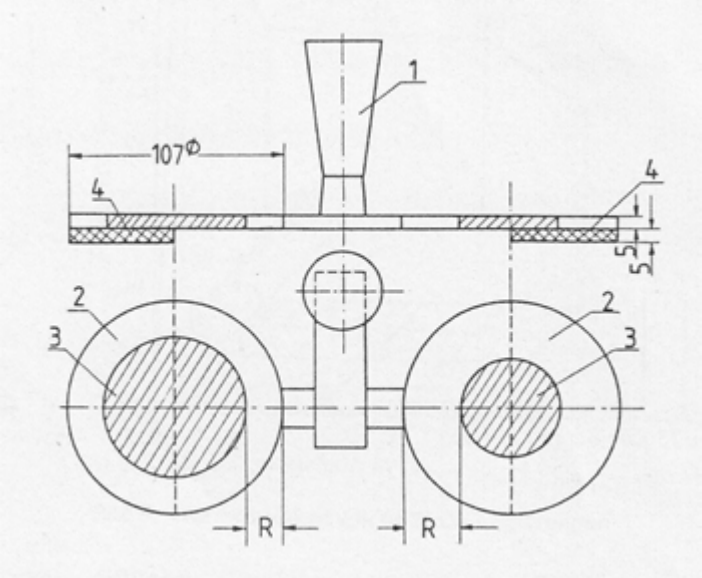


Slika 1. Konstrukcija kalupa za određivanje sklonosti toplim pukotinama
1-spust, 2-odljevak, 3-metalna jezgra promjenjivog promjera, 4-hladilo,
R-promjenjiva širina prstena [11]

Za svaku leguru napravljena su četiri različita kalupa od kojih dva s hladilom i dva bez, slika 2. Hladila su polovice valjaka promjera 107 mm i visine 5 mm, a smještena su s donje strane prstena, suprotno od ušća.

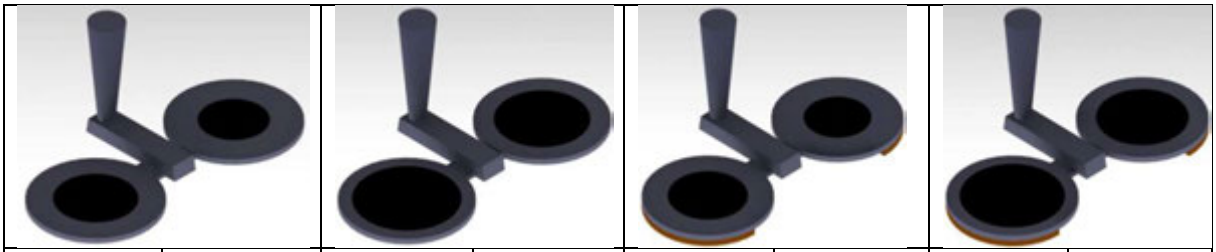

| | | | | | | | |
|---|---|---|---|---|---|---|---|
| R=21 mm | R=26 mm | R=11 mm | R=16 mm | R=21 mm | R=26 mm | R=11 mm | R=16 mm |
| Bez hladila | | | | Sa hladilima | | | |

Slika 2. Izgled odljevka s jezgrom i hladilima, R - širina prstena

Na slici 3 prikazan je model u gornjaku, a na slici 4 hladila u donjaku.

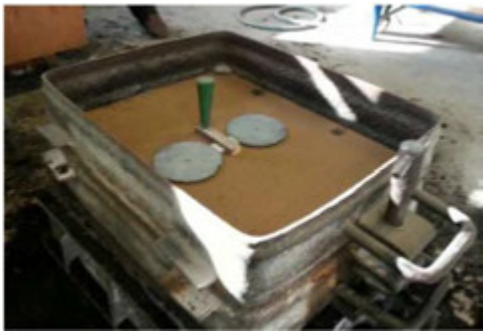

Slika 3. Model u gornjaku

Slika 4. Hladila u donjaku

Temperatura ulijevanja legure AlSi12 iznosila je 680 ˚C, legure AlSi9Mg, 690 ˚C, a legure AlMg1, 710 ˚C. Za simulaciju lijevanja i skrućivanja korišten je program QuikCAST. Brzina ulijevanja iznosila je približno 0,5 m/s.

**REZULTATI I RASPRAVA**

Prvo su napravljeni pokusi bez hladila. Topla pukotina pojavila se kod legure AlMg1 i to samo kod prstena sa najmanjom širinom R=11 mm. Najmanja širina prstena predstavlja najstrožu probu jer je stezanje na jezgru najveće. Pukotina se nalazi kod ušća, slika 5, širi se u radijalnom smjeru i ne prolazi po cijeloj širini prstena. Na prstenima širine 16, 21 i 26 mm nisu se pojavile tople pukotine.

Slika 5. Topla pukotina na prstenu širine 11 mm, legura AlMg1

Kod legura AlSi12 i AlSi9Mg nije došlo do pojave toplih pukotina kod ni jedne širine prstena R.

S ciljem pooštravanja uvjeta ispitivanja u pokus su uvedena hladila. Svrha hladila je usmjeravanje skrućivanja prema ušćima, kako bi na ušću dobili toplo mjesto eng. “hot spot“

koje će zadnje skrutnuti. Tople pukotine pojavile su se kod legure AlMg1 kod svih širina prstenova, slika 6. Tople pukotine pojavile su se bliže hladilu, a ne na području ušća kao što je očekivano i kao što je to bio slučaj bez hladila. Kod prstenova širine 16 i 26 mm pojavila se jedna pukotina, dok je kod prstenova širine 11 i 21 mm došlo do pucanja prstena s obje strane. Uvjeti za nastanak pukotine su se pojavili prije dosezanja toplog mjesta u blizini ušća.

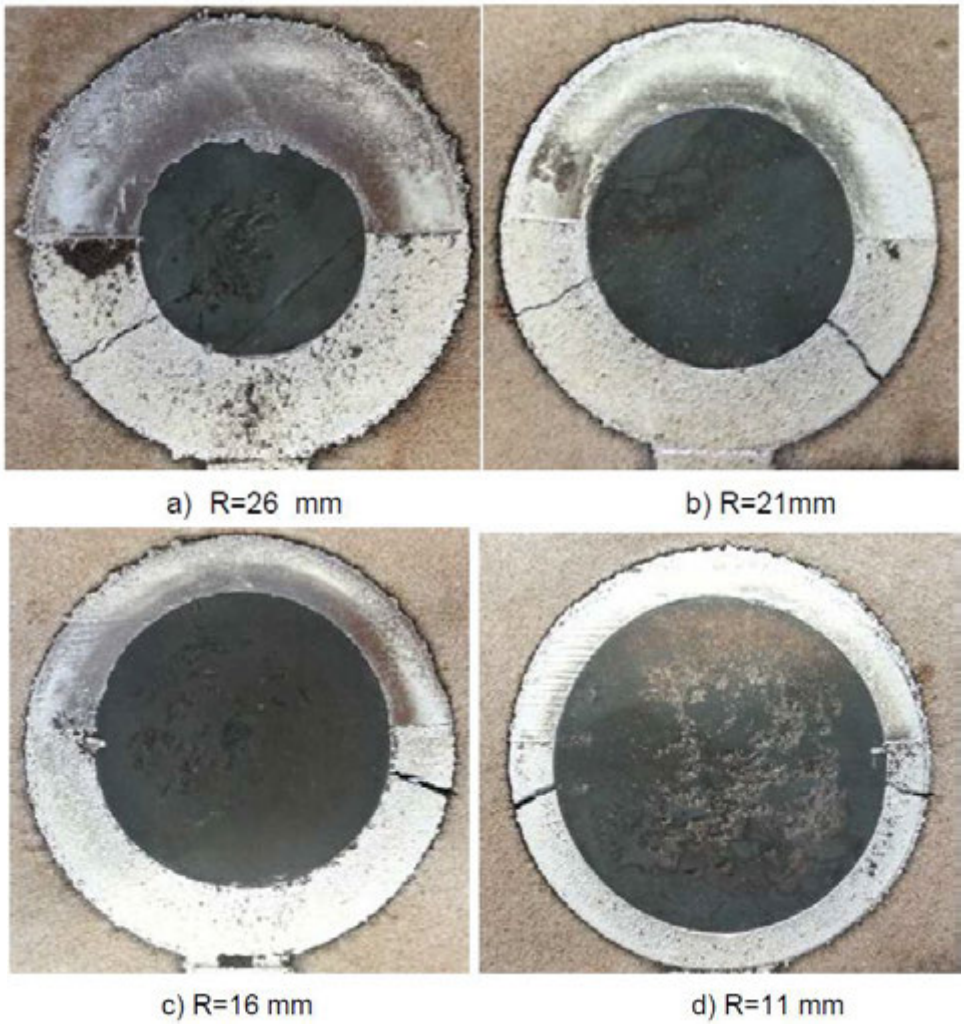


Slika 6. Tople pukotine kod legure AlMg1 za sve širine prstenova

Kod legura AlSi12 i AlSi9Mg nije došlo do pojave toplih pukotina kod ni jedne širine prstena R.

Rezultati pokazuju da je legura AlMg1 vrlo sklona nastanku toplih pukotina i ne smije se lijevati u kalupe koji ne dopuštaju slobodno stezanje legure prilikom skrućivanja. Legure AlSi12 i AlSi9Mg nisu sklone toplim pukotinama.

Na slici 7 prikazana je simulacija punjenja kalupne šupljine kod varijante sa hladilom i najstrožije probe s najmanjom širinom prstena.

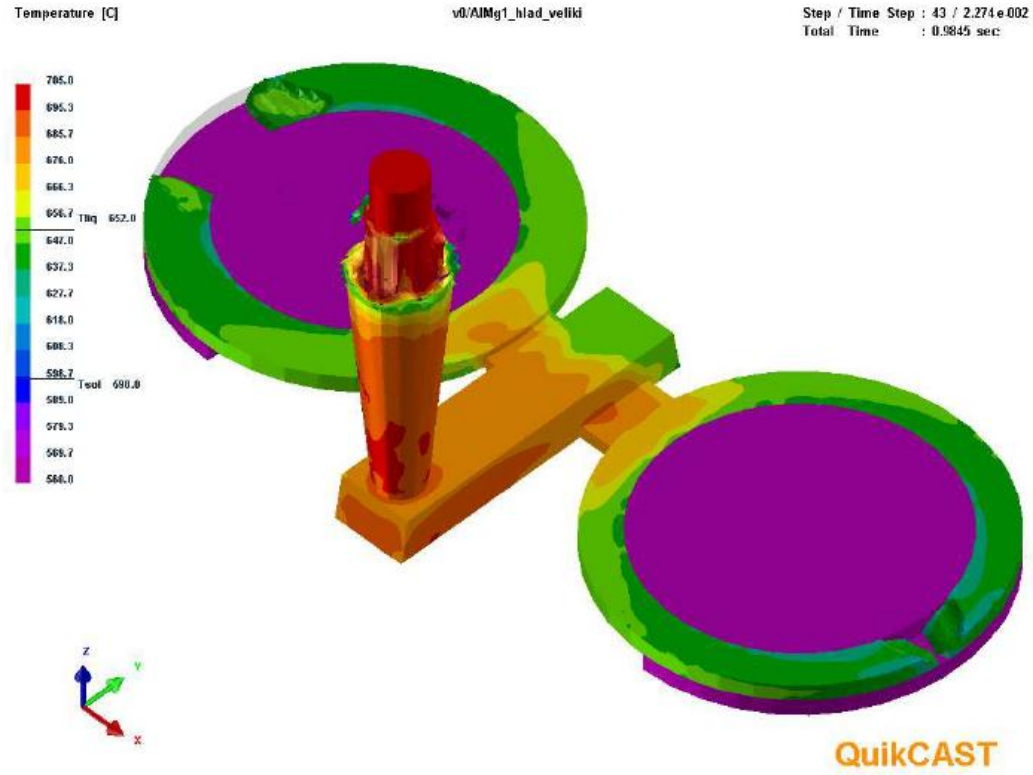


Slika 7. Prikaz punjenja kalupa

Na slici 8 prikazana je simulacija hlađenja prstenova od legure AlMg1. Na temelju položaja pukotina dobivenih eksperimentom i solidus temperature na tom mjestu blizu koje dolazi do pucanja, određeno je vrijeme nastanka pukotine. Pretpostavljeno je pucanje blizu solidus temperature te je položaj solidus temperature na simulaciji vizualno usklađen sa položajem pukotine u eksperimentu. Zatim je očitano vrijeme proteklo od početka skrućivanja t. Širi prstenovi sporije se hlade pa je vrijeme do nastanka pukotine duže.

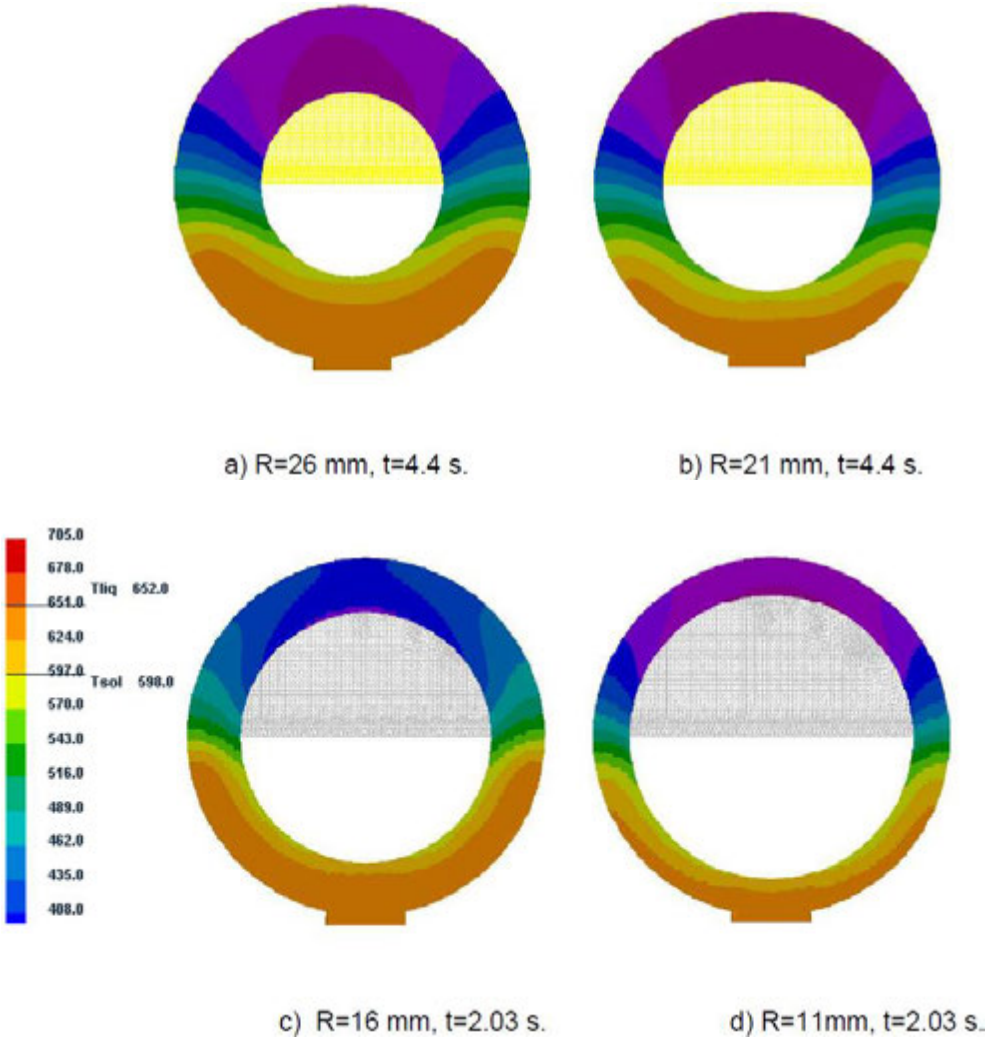


Slika 8. Simulacija položaja pukotine na solidus liniji, legura AlMg1 s hladilima, R-širina prstena, t-vrijeme proteklo od početka skrućivanja

**ZAKLJUČAK**

U radu je provedeno ispitivanje sklonosti nastanku toplih pukotina aluminijevih legura AlSi12, AlSi9Mg i AlMg1. Korištena je metoda prstenova kod koje se koristi metalna jezgra za dobivanje šupljine u prstenu. Prstenovi se stežu oko metalne jezgre što izaziva dodatna naprezanja. Ukoliko je materijal sklon toplim pukotinama dolazi do loma. Vanjski promjer prstena je konstantan a mijenja se unutarnji promjer prstena. U užem prstenu odnosno prstenu sa većim unutarnjim promjerom javlja se veće naprezanje prilikom hlađenja i skrućivanja. Što je uži prsten to je stroža proba. Još strožija proba postiže se primjenom hladila.

Na temelju vizualnog pregleda prstenova širina 26, 21, 16 i 11 mm, može se zaključiti da legure AlSi12 i AlSi9Mg nisu sklone nastanku toplim pukotinama jer na niti jednom prstenu

nije došlo do pojave pukotine. Legura AlMg1 vrlo je sklona nastanku toplih pukotina što je utvrđeno još u pokusu bez hladila gdje se pojavila pukotina na prstenu širine 11 mm. Povećanjem strogosti probe uvođenjem hladila došlo je do pojave pukotina na svim širinama prstena. Simulacijom je provjereno popunjavanje kalupa i skrućivanje odljevaka te je utvrđeno da su pukotine kod širih prstenova nastale 4,4 s od početka skrućivanja, a kod užih 2,03 s. Rezultati pokazuju da je legura AlMg1 vrlo sklona nastanku toplih pukotina i ne smije se lijevati u kalupe koji ne dopuštaju slobodno stezanje legure prilikom skrućivanja.

## LITERATURA

[1] S. Li, K. Sadayappan, D. Apelian, Hot Tearing of Aluminium Alloys – a Critical Literature Review, Ph.d Thesis, Metal Processing Institute, Worcester, 2011.
[2] …, ASM Handbook, Volume 15 – Casting, Materials Park, Ohio, 2008, pp. 375-379.
[3] M. Li, H. Wang, Z.Wei, Z. Zhu, The effect of Y on the hot-tearing resistance of Al-5 wt.%Cu based alloy, Materials and Design, 31 (2010) 5, pp. 2483-2487.
[4] N. Hatami, R. Babaei, M. Dadashzadeh, P. Davami, Modeling of hot tearing formation during solidification, Journal of Materials Processing Technology, 205 (2008) 1-3, pp. 506-513.
[5] H. Kamguo Kamga, D. Larouche, M. Bournane, A. Rahem, Hot tearing of aluminium-coper B206 alloys with iron and silicona additions, Materials Science and Engineering, 527 (2010) 27-28, pp. 7413-7423.
[6] S. Hasse, Pogrješke na odljevcima, HULJ, Zagreb, 2003, pp. 286-295.
[7] I. Mihalic, N. Ivetić, I. Mance, B. Bauer, Sklonost ljevačkih aluminijskih slitina k toplim pukotinama, 12th International Foundryman Conference, (N. Dolić, Z. Glavaš, Z. Zovko Brodarac (ed.)), Metalurški fakultet, 24.-25. svibanj, 2012, Opatija, Hrvatska, pp. 268-281.
[8] T. Pabel, S. Bozorgi, C. Kneissl, K. Haberl, P. Schumacher, Einfluss von Kupfer-und Magnesiumgehalt auf die Warmrissneigung bei AlSi7MgCu-Legierungen, Giesserei-Praxis, 12 (2010) pp. 388-394.
[9] B. Niroumand, M. Karbasi, H. Bagherpoor-Torghabe, Effects of Gating System Design on Hot Tearing susceptibility of A206 Alloy, Ljevarstvo, 53 (2011) 3-4, pp. 93-97.
[10] M. R. Nasr Esfahani, B.Niroumand,Study of hot tearing of A206 aluminium alloy using Instrumented Constrained T-shaped Casting Method, Materials Characterization, 61 (2010) 3, pp. 318-324.
[11] S. Nikitin, R. Ellerbrok, S. Engler, Vorstellung einer in der UdSSR verbreiteten Probe zur Messung der Warmrißneigung von Leichtmetallen, Giesserei, 76 (1989) 9, pp. 297-299.

17th INTERNATIONAL FOUNDRYMEN CONFERENCE
Hi-tech casting solution and knowledge based engineering
Opatija, May 16th-18th, 2018
http://www.simet.hr/~foundry/

# INFLUENCE OF MEDIUM AND MICROSTRUCTURE ON CORROSION BEHAVIOR OF GRAY CAST IRON

# UTJECAJ MEDIJA I MIKROSTRUKTURE NA KOROZIJSKO PONAŠANJE SIVOG LIJEVA

**Anita Begić Hadžipašić[1]*, Sandra Brajčinović[1], Gordana Gojsević Marić[2], Zdenka Zovko Brodarac[1]**

[1] University of Zagreb Faculty of Metallurgy, Sisak, Croatia
[2] ELKEM AS Podružnica u Sisku, Sisak, Croatia

**Oral presentation**
*Original scientific paper*

**Abstract**

This paper investigated the corrosion resistance of gray cast iron in the medium of artificial rain and 0.5 M $H_2SO_4$ medium and the effect of microstructure on its corrosion behavior in the mentioned media. By Tafel's extrapolation of the polarization curves, it was found that the examined gray cast iron shows an extremely high corrosion rate in the acidic medium, as opposed to the artificial rain test, where the corrosion rate is much lower. However, compared with the results of earlier researches obtained for nodular cast iron these values are three times higher, indicating that the nodular cast iron is more corrosion-resistant to atmospheric corrosion and therefore more acceptable for the manufacture of parts for agricultural machines. The obtained results were confirmed by the method of electrochemical impedance spectroscopy, where in the medium of artificial rain lower value of charge transfer resistance of gray cast iron was registered in opposite to nodular cast iron. These points to the fact that a thin layer formed on the gray cast iron, which represents a weak barrier to penetrating aggressive ions from the solution. The corrosion behavior of the gray cast iron in the tested media can also be related to its microstructure. Namely, aggressive ions from the applied media attack the metal matrix of the examined materials, while the graphite retains its original form. When compared to nodular cast iron, the nodules seems to be a more favorable form of precipitated graphite due to better sample surface covering and therefore the insulation in electrochemical corrosion process.

***Keywords***: *gray cast iron, corrosion rate, impedance, artificial rain, microstructure*

*Corresponding author (e-mail address): *begic@simet.hr*

**Sažetak**

U ovom radu ispitana je korozijska otpornost sivog lijeva u mediju umjetne kiše i mediju 0,5 M $H_2SO_4$ te utjecaj mikostrukture na njegovo korozijsko ponašanje u navedenim medijima. Tafelovom ekstrapolacijom polarizacijskih krivulja je ustanovljeno da ispitani sivi lijev pokazuje izrazito veliku brzinu korozije u kiselom mediju za razliku od ispitivanja u mediju umjetne kiše, gdje brzina korozije poprima znatno manju vrijednost. Međutim, u usporedbi s rezultatima ranijih istraživanja dobivenim za nodularni lijev te su vrijednosti trostruko veće, što upućuje na činjenicu da je nodularni lijev ipak korozijski otporniji u uvjetima atmosferske korozije te stoga i prihvatljiviji za izradu dijelova za poljoprivredne strojeve. Dobiveni rezultati su potvrđeni i metodom elektrokemijske impedancijske spektroskopije, pri čemu je u mediju umjetne kiše za sivi lijev registriran manji otpor prijenosu naboja od nodularnog lijeva. To ukazuje na činjenicu da se na sivom lijevu formirao tanji sloj, koji predstavlja slabu barijeru prema prodiranju agresivnih iona iz otopine. Dobiveno korozijsko ponašanje sivog lijeva u ispitanim medijima može se povezati i s njegovom mikrostrukturom. Naime agresivni ioni iz primijenjenih medija napadaju metalnu osnovu ispitanih materijala, dok grafit zadržava svoj prvobitni oblik. Pri usporedbi s nodularnim lijevom, nodule su se pokazale kao povoljniji oblik izlučenog grafita jer bolje prekrivaju površinu uzorka i slijedom navedenog izoliraju uzorak u procesu elektrokemijske korozije.

***Ključne riječi:*** *sivi lijev, brzina korozije, impedancija, umjetna kiša, mikrostruktura*

## UVOD

Sivi lijev pripada skupini željeznih ljevova koji imaju grafitnu mikrostrukturu, odnosno kod kojih je ugljik izlučen u obliku grafita. Naziv je dobio zbog prisutnosti grafita, jer se veći dio ugljika izdvaja u obliku listića (lamela) grafita, a manji dio kao cementit tako da je prijelomna površina sive boje. Mehanička i fizikalna svojstva sivog lijeva ovise o njegovom kemijskom sastavu i mikrostrukturi, jer kemijski sastav utječe na oblik grafita i strukturu metalne osnove. Sadržaj ugljika u sivom lijevu obično se kreće od 2,03% do 4,5% [1]. Porastom sadržaja ugljika u sivom lijevu opada vlačna čvrstoća, a poboljšava se livljivost taline. Stoga, u sivom lijevu je vrlo važan omjer silicija i ugljika, jer je silicij jak grafitizator koji promovira stvaranje grafita [2, 3]. Utjecaj mangana je suprotan od silicija. Mangan u sivom lijevu potpomaže stvaranje perlita i karbida, zbog čega se naziva karbidotvorcem. Njegova najvažnija uloga je vezanje sumpora u stabilne MnS uključke, čime se sprječava izlučivanje FeS uključaka po granicama zrna i pojava krhkosti [4-8]. Isto tako, MnS uključci djeluju kao potencijalna mjesta za nukleaciju grafita. Što se tiče fosfora u kemijskom sastavu sivog lijeva dozovoljeno je do 1% fosfora, jer utječe na stvaranje steadita, nisko topljivog fosfidnog eutektika. Steadit ima visoku tvrdoću i otežava strojnu obradu odljevaka od sivog lijeva [9]. K tome, kod sivog lijeva na mehanička svojstva velik utjecaj ima oblik izlučenog grafita, dok npr. kod vermikularnog lijeva glavnu ulogu ima metalna osnova.
Tehnološka svojstva sivog lijeva su: dobra rezljivost i slaba zavarljivost zbog male istezljivosti i visokog postotka ugljika, mogu se lijevati odljevci svih masivnosti te je vrlo dobra livljivost, odnosno linearno skupljanje iznosi oko 1%. Mehanička svojstva su: relativno niska vlačna

čvrstoća, visoka tlačna čvrstoća i slaba žilavost. Iz svega navedenoga, može se zaključiti da su prednosti sivog lijeva: visoka toplinska vodljivost, dobra strojna obradljivost, visok stupanj prigušenja vibracija, izvanredna livljivost i tlačna čvrstoća te ekonomičnost [4-6].
Drugim riječima, mehanička svojstva sivog lijeva ovise o količini, veličini i raspodjeli grafita. Mikrostruktura sivog lijeva uglavnom se sastoji od primarne strukture, tj. nakupine listića grafita i željezne osnove koja može biti feritna, perlitna ili feritno-perlitna uz moguću pojavu slobodnog cementita [5,6]. Područje primjene sivog lijeva najzastupljenije je u strojogradnji, za postolja i dijelove strojeva kućišta, izradu kućišta elektromotora, turbina, kliznih ležajeva te u poljoprivredi za izradu traktora i njegovih dijelova poput blokova motora s unutrašnjim izgaranjem, zupčanika, ramenica, mjenjačkih kutija i sjetvenih noževa.
Navedeni dijelovi mogu biti izloženi nepovoljnim uvjetima koji mogu prouzročiti nastanak korozije, a naročito se to odnosi na materijale koji se upotrebljavaju u poljoprivredi i izloženi su brojnim štetnim čimbenicima. Čimbenici koji uzrokuju stvaranje korozije mogu biti: kemijski, fizikalni, biološki, električni te kompleksni čimbenici koji su uzrokovani promjenom klime, tla, vode i radnih uvjeta. Korozija je štetno i nepoželjno trošenje materijala, a uglavnom se pojavljuje zbog kemijskog dijelovanja plinova, para ili kapljevina iz okoliša [10]. Kod procesa korozije u neelektrolitima ili kemijske korozije, atom metala iz kristalne rešetke direktno reagira s nekom molekulom iz okoline i tako nastane molekula spoja. Kod korozije u elektrolitima ili elektrokemijske korozije, atom se gubitkom elektrona pretvara u slobodni ion. Drugim riječima, elektrokemijska korozija metala odvija se u elektrolitima, tj. medijima s ionskom vodljivošću [11-13].
Korozija skraćuje vijek trajanja industrijske opreme, smanjuje masu i proizvodnu vrijednost materijala pa time dolazi do posljedica poput poskupljivanja održavanja, smanjivanja proizvodnih kapaciteta te zastoja u radu. Poljoprivredni strojevi i oprema su naročito izloženi atmosferskim uvjetima koji doprinose nastanku korozije. Atmosferska korozija se odvija u vodenom adsorbatu ili kondenzatu koji zbog vlažnosti zraka nastaju na površini metala i imaju svojstvo elektrolita [10]. Elektrokemijska korozija je veoma raširena, jer su mnogi industrijski strojevi često izloženi vodi, otopinama, vlažnom tlu ili vlažnoj atmosferi.
S obzirom da su konstrukcijski dijelovi poljoprivrednih strojeva izrađeni od sivog lijeva i prilikom korištenja izloženi su utjecajem različitih medija koji mogu prouzročiti nastanak korozije, u ovom radu je proučavan utjecaj medija koji simulira umjetnu kišu i medija 0,5 M $H_2SO_4$ te mikrostrukture na korozijsko ponašanje tog materijala. Primjenom elektrokemijskih ispitivanja u navedenim medijima te primjenom metalografske analize ispitanih materijala prije i nakon korozije dobiveni su korozijski parametri koji daju uvid u korozijsko ponašanje ispitanog uzorka sivog lijeva. Dobiveni rezultati su uspoređeni s ranijim istraživanjima korozijskog ponašanja nodularnog lijeva, koji se također primjenjuje za izradu dijelova poljoprivrednih strojeva.

## MATERIJALI I METODE

### Materijali

Ispitivanje utjecaja medija i mikrostrukture na korozijsku otpornost sivog lijeva provedeno je na atipičnom uzorku sivog lijeva nominalne kvalitete EN GJL-150, čiji kemijski sastav je prikazan u tablici 1.

Tablica 1. Kemijski sastav ispitanog uzorka sivog lijeva (mas. %)

| C | Si | Mn | P | S | Mg | Cr | Ni | Mo | Cu | Sn | Ti | V | Al | Fe |
|---|---|---|---|---|---|---|---|---|---|---|---|---|---|---|
| 3,750 | 2,350 | 0,335 | 0,025 | 0,035 | 0,006 | 0,037 | 0,035 | 0,005 | 0,193 | 0,008 | 0,008 | 0,005 | 0,005 | ostatak |

### Metode ispitivanja

**Elektrokemijska ispitivanja ($E_{corr}$, EIS, Tafel)**

Elektrokemijska korozijska ispitivanja omogućavaju primjenu raznih elektrokemijskih tehnika za određivanje intenziteta korozije. Za dobivanje podataka o korozijskom ponašanju za uzorak sivog lijeva korištena je metoda za određivanje korozijskog potencijala $E_{corr,}$ elektrokemijska impedancijska spektroskopija (EIS) i metoda Tafelove ekstrapolacije. Prije svake serije elektrokemijskih mjerenja uzorci su pripremljeni strojnim brušenjem i poliranjem, kako je opisano u nastavku.

***Određivanje korozijskog potencijala $E_{corr}$***

Za uzorak sivog lijeva prvo je provedeno ispitivanje ovisnosti korozijskog potencijala o vremenu. U svrhu određivanja potencijala kod otvorenog strujnog kruga $E_{ocp}$ ispitanih uzoraka sivog lijeva kao funkcije vremena uzorci su pripremljeni prešanjem u konduktivnu masu pomoću uređaja za vruće prešanje uzoraka (SimpliMet® 1000), strojnim brušenjem (gradacije No. 240, 400, 600 i 800) i poliranjem na Microclouthu sa suspenzijom $Al_2O_3$ u vodi na automatskom uređaju za brušenje i poliranje (Büehler), nakon čega su isprani u destiliranoj vodi i odmašćeni u etanolu [12].

Za provođenje elektrokemijskih ispitivanja korištena je troelektrodna staklena ćelija u kojoj su bile smještene radna elektroda, protuelektroda i referentna elektroda te potenciostat i računalo pomoću kojeg su se mjerili i bilježili podaci. Radna elektroda predstavlja ispitni uzorak koji je uronjen u radni medij. Kao radni medij u elektrokemijskim eksperimentima korištene su dvije otopine: 0,5 M $H_2SO_4$ i umjetna kiša. Otopina umjetne kiše pripremljena je od 0,2 g/l $Na_2SO_4$ i 0,2 g/l $Na_2HCO_3$. Protuelektroda je vodič koji zatvara strujni krug, a za provođenje ovih eksperimenata korištena je Pt elektroda kao protuelektroda. Referentna elektroda je elektroda poznatog potencijala i ne sudjeluje u strujnom krugu, već se pomoću nje mjeri potencijal radne elektrode. U laboratorijskim uvjetima uglavnom se koristi zasićena kalomel elektroda, standardnog elektrodnog potencijala +0,242 V s obzirom na vodikovu elektrodu. Stabilizacija potencijala kod otvorenog strujnog kruga $E_{ocp}$ je izvedena pri (19±2) °C uz pomoć računalom upravljanog potenciostata/galvanostata (Parstat 2273).

Prije početka polarizacijskog mjerenja potrebno je stabilizirati sustav metal-elektrolit. Korozijski potencijal ili potencijal otvorenog strujnog kruga određuje se na način da se strujni krug između radne elektrode i protuelektrode drži otvorenim te se mjeri razlika potencijala između radne elektrode i protuelektrode u vremenskom periodu od 1800 sekundi. Nakon određenog vremena, uspostavlja se približno stacionarno stanje na nekoj vrijednosti potencijala. Praćenjem vremenskih promjena stacionarnog potencijala otvorenog strujnog kruga $E_{ocp}$ dobiju se podaci o korozijskom ponašanju uzorka u ispitivanom mediju. Naime, ako su pozitivne vrijednosti $E_{ocp}$ smatra se da je elektroda stabilna, odnosno da je uzorak imun u ispitanom mediju. Negativne vrijednosti $E_{ocp}$ ukazuju na koroziju, odnosno nestabilnost elektrode, jer dolazi do otapanja uzorka. Postoji i opcija da se vrijednosti izmjenjuju, od negativnih do pozitivnih što predstavlja spontanu pasivaciju [14].

***Određivanje korozijskih parametara primjenom elektrokemijske impedancijske spektroskopije (EIS)***

Elektrokemijska impedancijska spektroskopija (EIS) je jedna od metoda mjerenja korozijskih parametara koja se temelji na primjeni izmjenične struje. Kod elektrokemijskih tehnika koje koriste izmjeničnu struju ne dolazi do narušavanja sustava, stoga se ova metoda koristi za istraživanje reakcije na granici faza. Metoda se zasniva na odzivu strujnog kruga na izmjenični napon ili struju kao funkciju frekvencije. Princip metode je da se na elektrodu dovodi izmjenično promjenjiv potencijal male amplitude (5 mV). Mjerenje impedancije u svrhu istraživanja granice faza elektroda/elektrolit izvodi se u području opsega frekvencije od 100 kHz do 10 mHz. Parametri impedancije analizirani su pomoću softvera ZSIMPWin 3.21. primjenom odgovarajućih modela električnog kruga [12,14,15]. Analizom rezultata dobivaju se vrijednosti sljedećih parametara: otpor elektrolita $R_{el}$, konstantno fazni element dvosloja $Q_{dl}$, mjera heterogenosti površine $n$ i otpor prijenosu naboja $R_{ct}$. Pomoću navedenih parametara dolazi se do informacija o elektrokemijskim parametrima površine elektrode te do podataka o korozijskim procesima i njihovim mehanizmima. Nakon elektrokemijske impedancijske spektroskopije izvedena je potenciodinamička polarizacija ispitanog uzorka sivog lijeva.

***Određivanje korozijskih parametara primjenom metode Tafelove ekstrapolacije***

Metoda Tafelove ekstrapolacije koristi se u svrhu dobivanja korozijskih parametara (korozijski potencijal $E_{corr}$, brzina korozije $v_{corr}$, anodni nagib $b_a$ i katodni nagib $b_c$) tako što se izvodi potenciodinamička polarizacija u području potencijala od -250 mV do +250 mV vs $E_{corr}$, uz brzinu promjene potencijala od 1 mV/s, a korozijski parametri su određeni pomoću softvera PowerCorr™ primjenom Tafelove metode ekstrapolacije i Faradayevih zakona [15,16]. Nakon što se elektroda polarizira na određeni potencijal, snimaju se anodne i katodne krivulje. Ekstrapolacijom anodnih i katodnih Tafelovih pravaca određuju se vrijednosti gustoće struje $j_{kor}$ i korozijskog potencijala $E_{corr}$ [14]. Dobiveni podaci daju uvid u korozijsko ponašanje materijala u ispitivanom elektrolitu.

**Metalografska ispitivanja**

Priprema ispitivanog uzorka sivog lijeva sastojala se od rezanja i prešanja uzorka u konduktivnu masu pomoću uređaja za vruće prešanje uzoraka (SimpliMet® 1000) [9,10]. Uzorak je zatim strojno brušen vodootpornim brusnim papirima gradacije No. 240, 400, 600 i 800 i poliran na Microclouthu suspenzijom glinice ($Al_2O_3$) u vodi na automatskom uređaju za brušenje i poliranje (Büehler). Nakon poliranja, izbrusak uzorka ispran je u destiliranoj vodi, odmašćen u etanolu i sušen u struji toplog zraka. Tako obrađeni uzorak promatran je na optičkom mikroskopu s digitalnom kamerom (Olympus GX 51) i sustavom za automatsku obradu slike (AnalySIS® Materials Research Lab) prije i poslije korozije u ispitnom mediju [12].

**REZULTATI I RASPRAVA**

Ovisnosti potencijala kod otvorenog strujnog kruga o vremenu za ispitani sivi lijev u oba medija prikazane su na slici 1. Dobiveni Nyquistovi EIS-spektri za ispitani uzorak i njihove analize provedene su primjenom odgovarajućeg modela električnog kruga, što je prikazano na slikama 2-6. Modeliranjem EIS spektara dobiveni su parametri impedancije: otpor elektrolita $R_{el}$, konstantno fazni element dvosloja $Q_{dl}$, mjera heterogenosti površine $n$ i otpor prijenosu naboja $R_{ct}$ te su navedeni u tablici 2.

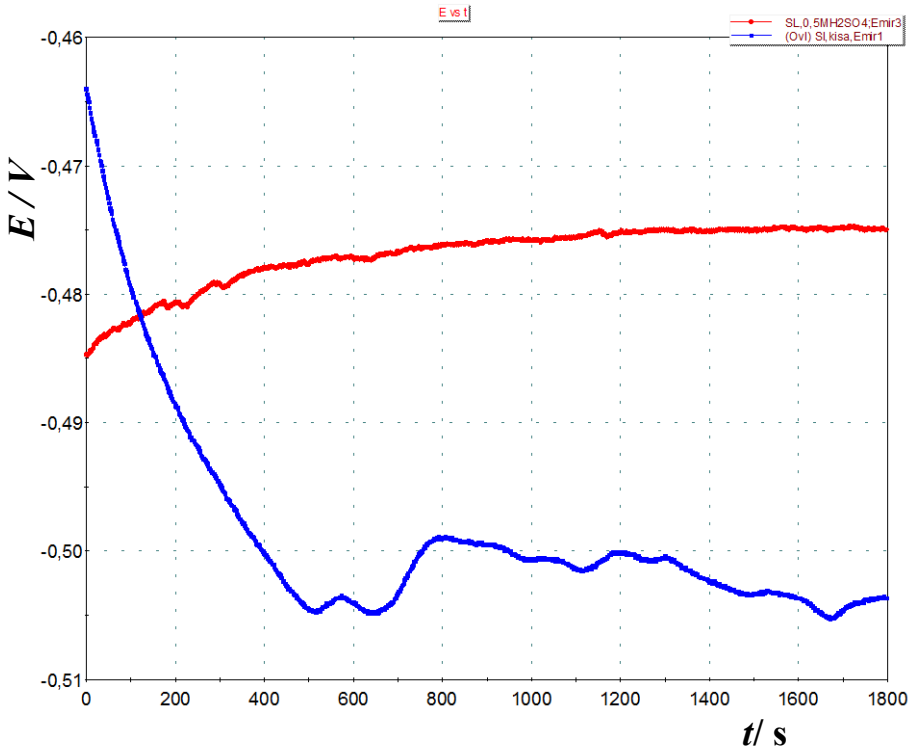


Slika 1. Ovisnost mirujućeg potencijala o vremenu za ispitani sivi lijev u mediju umjetne kiše i mediju 0,5 M $H_2SO_4$

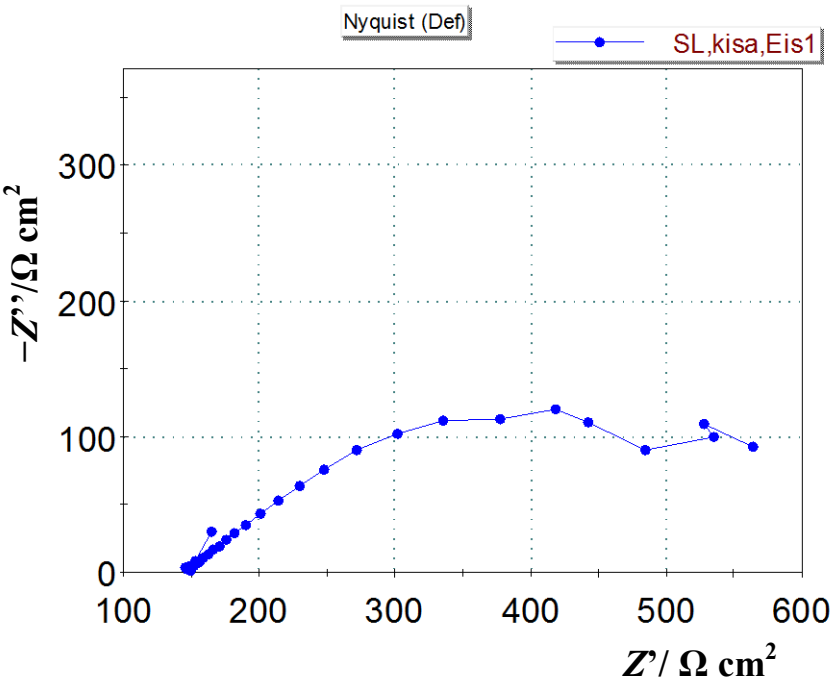


Slika 2. Nyquistov impedancijski prikaz ispitanog uzorka sivog lijeva u mediju umjetne kiše

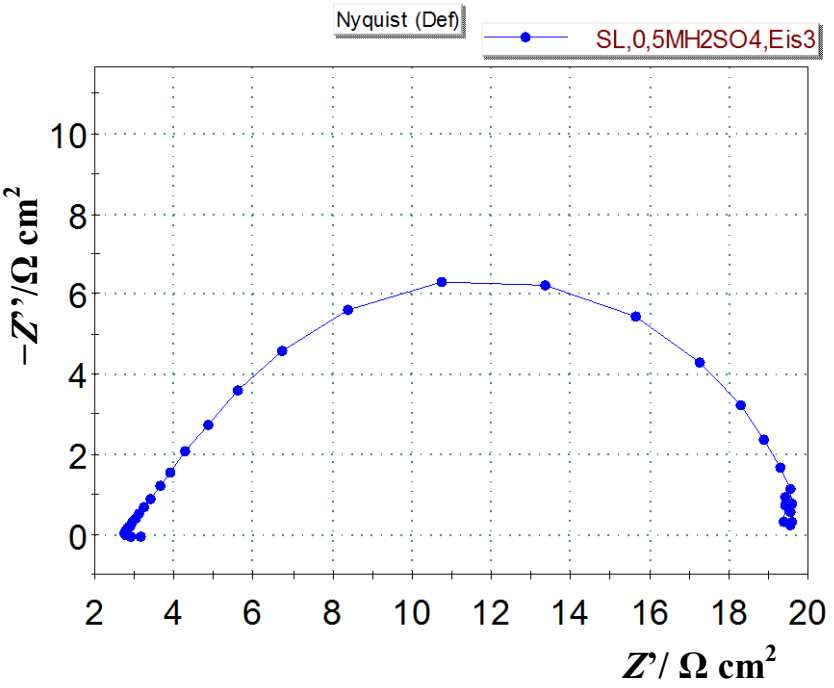


Slika 3. Nyquistov impedancijski prikaz ispitanog uzorka sivog lijeva u mediju 0,5 M $H_2SO_4$

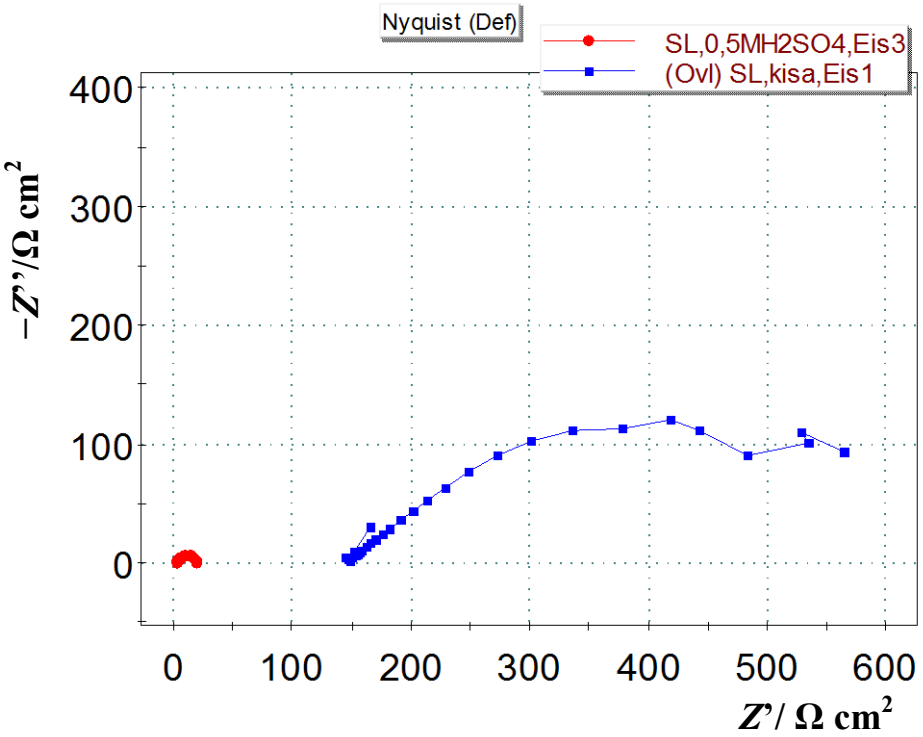


Slika 4. Komparativni prikaz Nyquistovih EIS spektara dobivenih za sivi lijev ispitan u mediju umjetne kiše i 0,5 M $H_2SO_4$

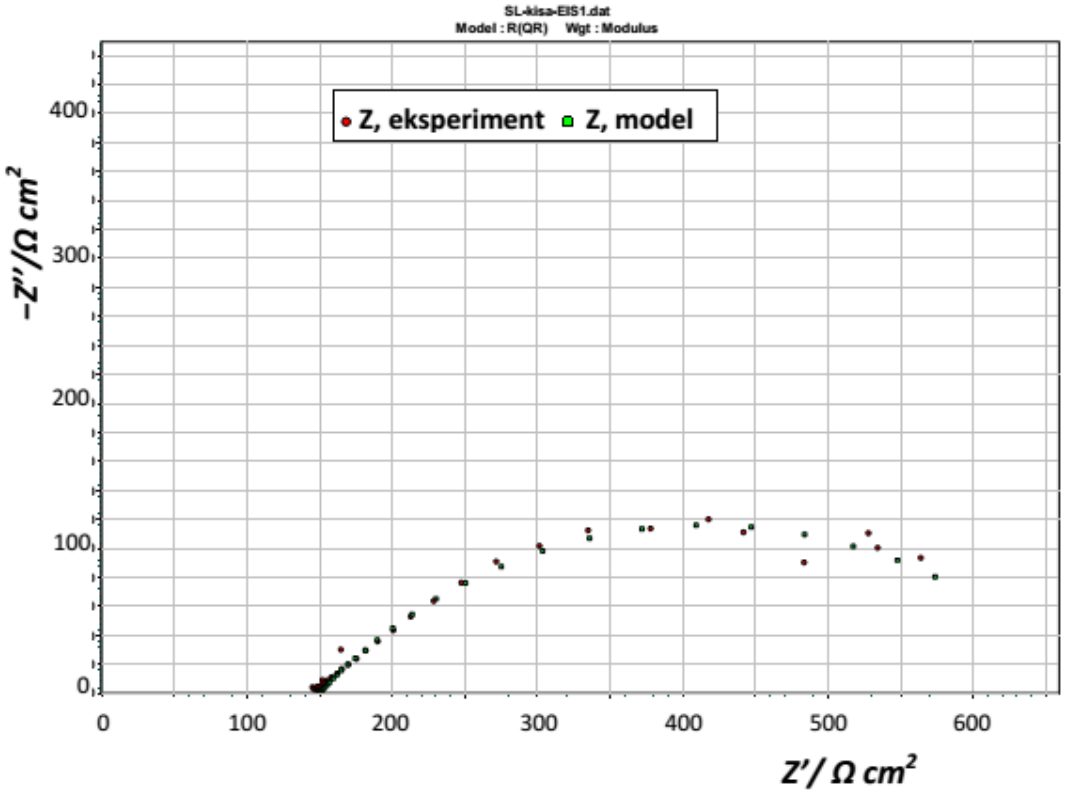


Slika 5. Modeliranje dobivenog Nyquistovog EIS spektra za sivi lijev u mediju umjetne kiše

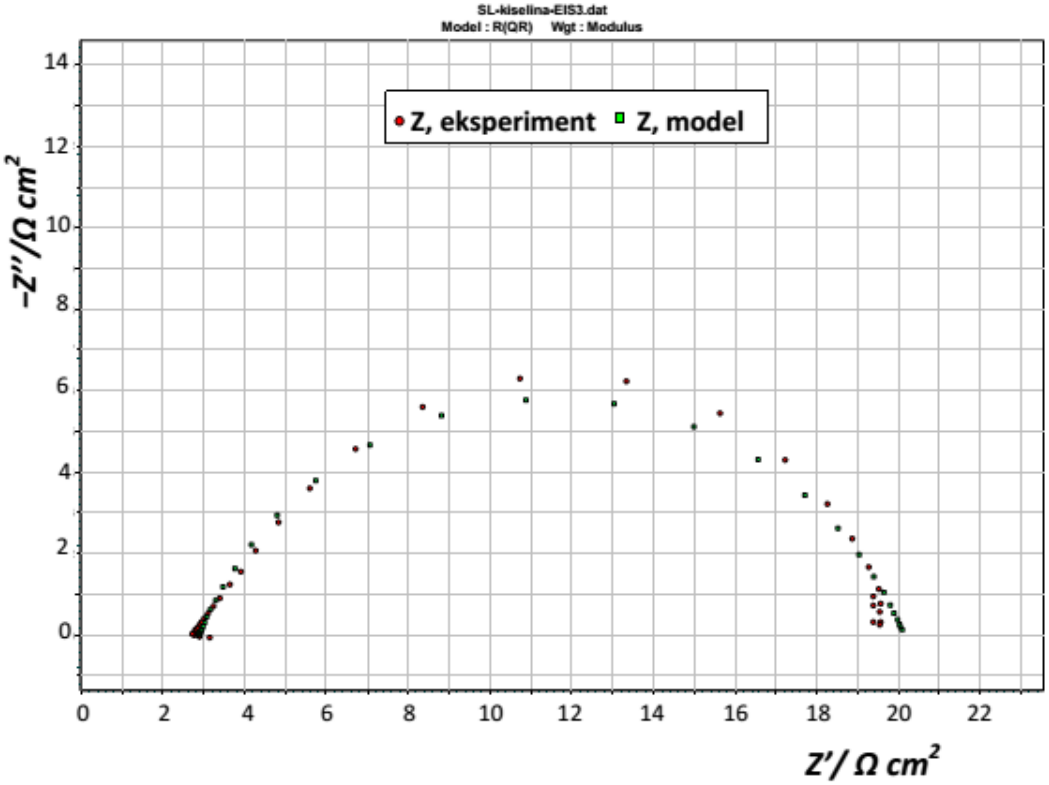


Slika 6. Modeliranje dobivenog Nyquistovog EIS spektra za sivi lijev u mediju 0,5 M $H_2SO_4$

Tablica 2. Parametri impedancije ispitanog sivog lijeva u oba medija

| Medij | $P$ | $E_{corr}$ vs. SCE | $R_{el}$ | $Q_{dl}\times10^6$ | $n$ | $R_{ct}$ |
|---|---|---|---|---|---|---|
| | $cm^2$ | mV | $\Omega cm^2$ | $\Omega^{-1}s^n cm^{-2}$ | | $\Omega\ cm^2$ |
| Umjetna kiša | 0,45 | −504,0 | 149,7 | 2497,0 | 0,52 | 534,1 |
| 0,5 M $H_2SO_4$ | | −475,0 | 2,89 | 4011,0 | 0,75 | 17,2 |

Iz slike 1 je vidljivo da sivi lijev u oba ispitana medija brzo postiže svoj mirujući potencijal, tj. potencijal kod otvorenog strujnog kruga. Na slikama 2 i 3 su prikazani Nyquistovi EIS spektri, koji predstavljaju ovisnost imaginarne komponente impedancije Z'' o realnoj komponenti imedancije Z' za svaku izmjerenu frekvenciju. Iz slika se može uočiti tendencija sivog lijeva ka stvaranju polukruga u oba ispitna medija. Međutim, iz komparativnog prikaza na slici 4 vidljivo je da sivi lijev ima veću širinu Nyquistovog polukruga u mediju umjetne kiše te je polukrug pomaknut ka većim impedancijskim vrijednostima, što bi trebalo ukazivati na činjenicu da bi sivi lijev u umjetnoj kiši trebao pokazati veće vrijednosti otpora prijenosu naboja $R_{ct}$ u odnosu na kiseli medij, a time i veću korozijsku otpornost. Modeliranje dobivenih EIS spektara je provedeno korištenjem najjednostavnijeg električnog kruga R(QR), što je prikazano na slikama 5 i 6. Iz modeliranih EIS spektara vidljivo je da se simulirane krivulje dobro podudaraju s eksperimentalnim pri čemu je registrirano odstupanje reda veličine $10^{-3}$. Također, može se uočiti da obje krivulje pokazuju samo jednu kapacitivnu petlju

depresivnog izgleda, što je karakteristično za čvrste elektrode [17]. Iz impedancijskih parametara dobivenih modeliranjem EIS spektara (tablica 2) može se uočiti da je sivi lijev u mediju umjetne kiše pokazao daleko veći otpor prijenosu naboja $R_{ct}$ od onog u kiselom mediju. To znači da se u mediju umjetne kiše formirao deblji oksidni sloj na sivom lijevu koji ima zaštitnu ulogu, jer predstavlja barijeru daljnjem prodiranju agresivnih iona iz otopine. S druge strane, manje vrijednosti otpora prijenosu naboja registrirane u kiselom mediju mogu se povezati s lakim razvijanjem vodika i stvaranjem oksidnog sloja manje debljine na površini ispitanog sivog lijeva. Nadalje, može se uočiti da je u kiselom mediju registrirana veća vrijednost konstantno faznog elementa dvosloja $Q_{dl}$, što ukazuje na činjenicu da nastali pasivni sloj, koji raste na površini sivog lijeva u kiselom mediju, nije dovoljno kompaktan te zbog toga dolazi do porasta kapaciteta na međupovršini metal/oksidni sloj ili unutar pasivnog sloja [18].
Rezultati dobiveni metodom elektrokemijske impedancijske spektroskopije podudaraju se i s korozijskim parametrima dobivenim metodom Tafelove ekstrapolacije. Potenciodinamička polarizacija u području potencijala od −250 mV do +250 mV vs. $E_{corr}$ izvedena je u svrhu određivanja korozijskih parametara, koji su navedeni u tablici 3. Polarizacijske krivulje ispitanog uzorka sivog lijeva u oba ispitna medija prikazane su na slici 7.

Tablica 3. Korozijski parametri ispitanog sivog lijeva u oba ispitana medija

| **Medij** | ***P*** | ***E*$_{corr}$ vs. SCE** | ***b*$_a$** | ***b*$_c$** | ***v*$_{corr}$** |
|---|---|---|---|---|---|
| | $cm^2$ | mV | mV $dec^{-1}$ | mV $dec^{-1}$ | mm $god^{-1}$ |
| Umjetna kiša | 0,45 | −515,4 | 257,7 | 268,9 | 1,4 |
| 0,5 M $H_2SO_4$ | | −469,8 | 161,2 | 194,6 | 34,9 |

Iz tablice 3 može se uočiti vrlo velika vrijednost brzine korozije $v_{corr}$ registrirana za sivi lijev u kiselom mediju, koja je čak oko 25× veća od one dobivene u mediju umjetne kiše. Stoga, može se zaključiti da ispitani sivi lijev je vrlo podložan koroziji u kiselom mediju te se ne preporučuje za takvu primjenu. S druge strane, mala vrijednost brzine korozije u umjetnoj kiši upućuje na činjenicu da bi se sivi lijev mogao primjenjivati za izradu konstrukcijskih elemenata i elemenata za poljoprivredne strojeve, koji su izloženi nepovoljnim atmosferskim uvjetima.
Također, vidljivo je da su anodni i katodni nagibi veći u mediju umjetne kiše, što znači da su u tom mediju dominantnije reakcije na anodi i katodi, nego u kiselom mediju. Drugim riječima, više su izražene anodna reakcija otapanja metala i katodna reakcije redukcije otopljenih iona iz primijenjenog medija.

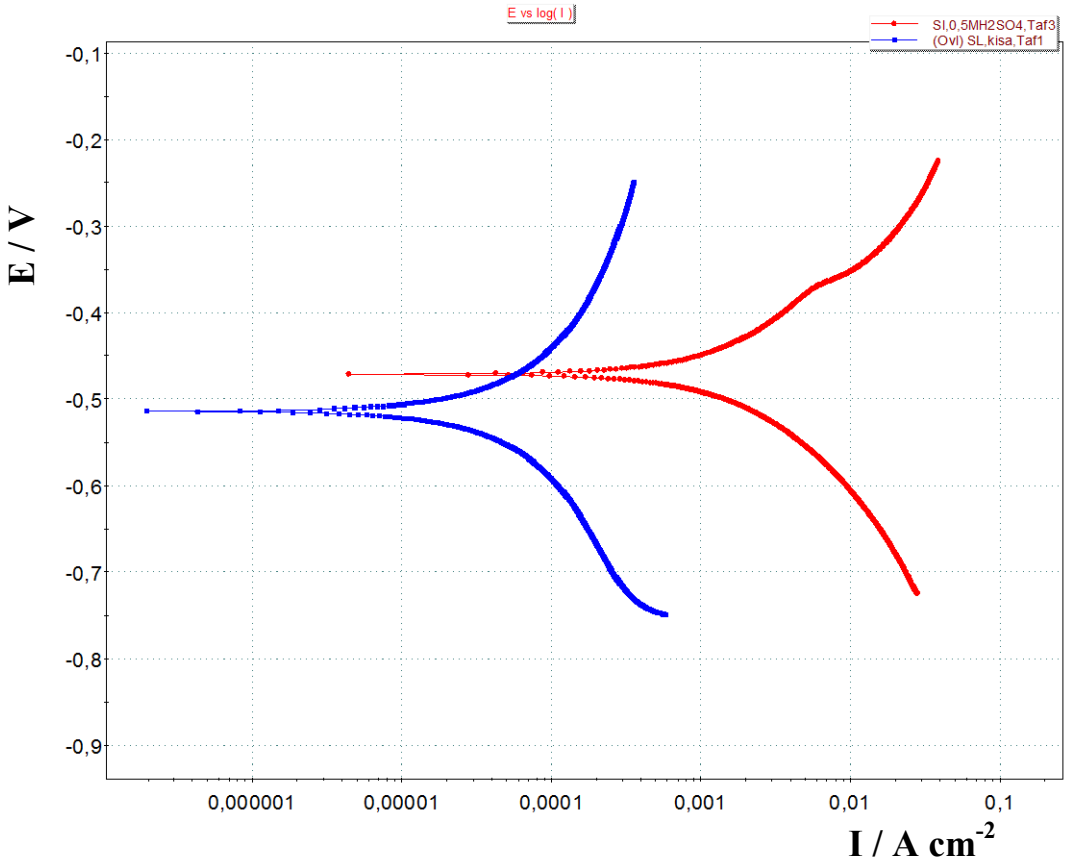


Slika 7. Polarizacijske krivulje sivog lijeva u oba ispitna medija

Usporedbom impedancijskih parametara dobivenih u ovom radu za sivi lijev i onih dobivenih u ranijim istraživanjima za nodularni lijev kvalitete EN-GJS-400-18-LT [12] može se zaključiti da se nodularni lijev pokazao korozijski otpornijim od sivog lijeva u mediju umjetne kiše. O tome svjedoče veći iznosi otpora prijenosu naboja za nodularni lijev koji se kreću od 602-620 Ω $cm^2$, zavisno o tome radi li se o nodularnom lijevu s više ili manje nodula po jedinici površine [12]. Također, rezultati dobiveni potenciodinamičkom polarizacijom nodularnog lijeva u mediju umjetne kiše pokazali su skoro trostruko manju vrijednost za brzinu korozije (0,5 mm $god^{-1}$) [12] od one izmjerene za sivi lijev u ovom radu (1,4 mm $god^{-1}$). Iz svega navedenog može se zaključiti da je nodularni lijev korozijski otporniji u mediju umjetne kiše od sivog lijeva te se može primijeniti kao prikladniji materijal za izradu dijelova za poljoprivredne strojeve koji će biti izloženi nepovoljnim vremenskim uvjetima. To se može pripisati povoljnijoj mikrostrukturi nodularnog lijeva u kojem se grafit izlučuje u obliku kuglica/nodula. Naime, nodule imaju ulogu izolatora zbog oksidnog sloja koji se stvara između grafita i metalne osnove te je manja korozijska otpornost registrirana kod nodularnog lijeva s manjom prekrivenošću površine nodulama [12].
U svrhu utvrđivanja mikrostrukturnih promjena ispitanog sivog lijeva, uzorak je pripremljen strojnim brušenjem i poliranjem te snimljen optičkim mikroskopom prije (slika 8) i poslije izlaganja mediju umjetne kiše i 0,5 M $H_2SO_4$ (slika 9).

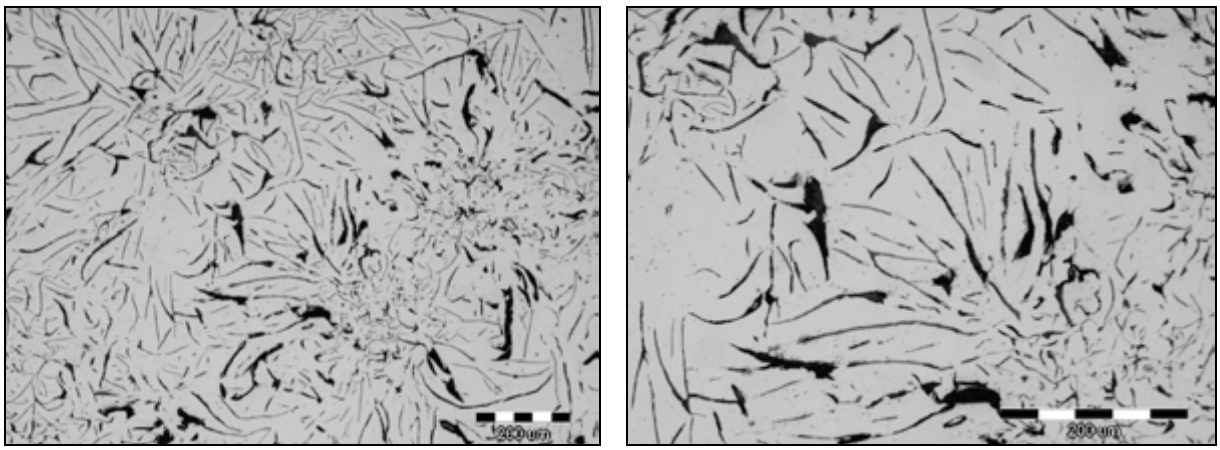

a) snimljeno pri povećanju 100× b) snimljeno pri povećanju 200×

Slika 8. Mikrostruktura ispitanog sivog lijeva prije izlaganja korozivnim medijima

Budući da se radi o atipičnom uzorku sivog lijeva, mikrostruktura ukazuje na izdvajanje grafita u obliku listića (oblik I), ali u širokoj paleti tipova od kojih su najuočljiviji tipovi A, B i C. Metalna osnova ispitanog sivog lijeva je feritno-perlitna s udjelom ferita u metalnoj osnovi od 30 %. Stoga, s obzirom na prisutnost više tipova grafita u ovom sivom lijevu, cilj ovoga rada bio je ispitati utjecaj oblika izlučenog grafita i metalne osnove na korozijsko ponašanje ispitanog sivog lijeva te ga usporediti s korozijskim ponašanjem nodularnog lijeva u istim medijima.
Izlaganjem sivog lijeva mediju umjetne kiše i 0,5 M $H_2SO_4$ dolazi do različitog djelovanja medija na mikrostrukturni izgled ispitanog materijala. Na slici 9 prikazana je morfologija površine sivog lijeva nakon izlaganja ispitnim medijima.

Iz slike 9 može se uočiti da u kiselom mediju kiselina izrazito napada metalnu osnovu sivog lijeva te su korozijski produkti ravnomjerno raspoređeni po površini uzorka. Međutim, korozijski produkti nisu kompaktni i nemaju zaštitnu ulogu u korozijskom procesu, što potvrđuju i rezultati dobiveni elektrokemijskim mjerenjima. U umjetnoj kiši je vidljivo slabije djelovanje medija pri čemu morfologija listićavog grafita ostaje nenarušena, kao što je bilo i očekivano.

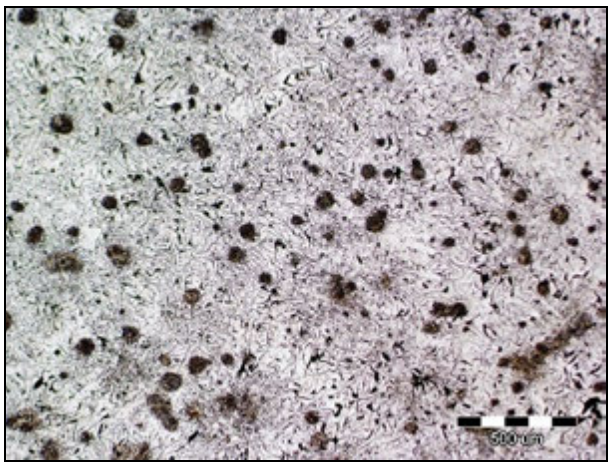

a) umjetna kiša: snimljeno pri povećanju 50×

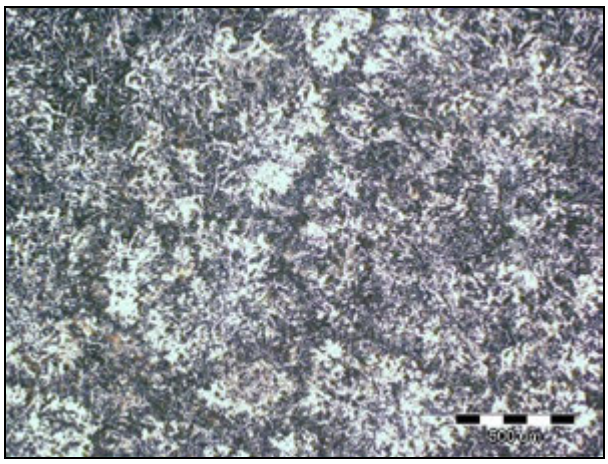

c) 0,5 M $H_2SO_4$: snimljeno pri povećanju 50×

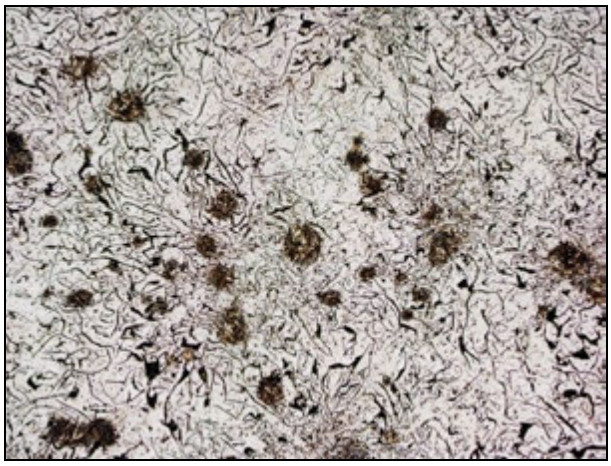

b) umjetna kiša: snimljeno pri povećanju 100×

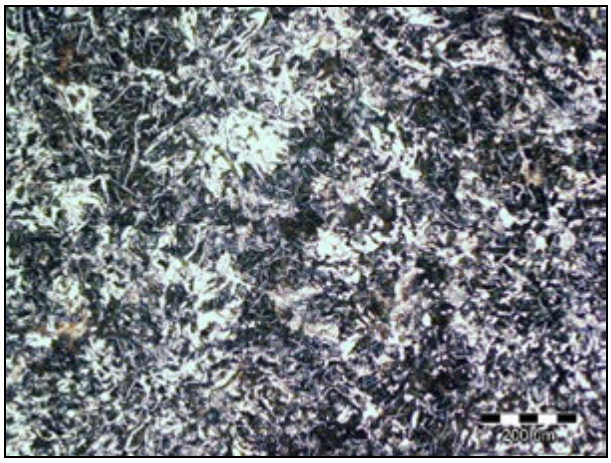

d) 0,5 M $H_2SO_4$: snimljeno pri povećanju 100×

Slika 9. Mikrostruktura sivog lijeva nakon korozije u mediju umjetne kiše i 0,5 M $H_2SO_4$ pri različitim povećanjima

U usporedbi s nodularnim lijevom iz ranijih istraživanja [12] može se zaključiti da su nodule u usporedbi s listićima grafita pogodniji oblik izlučenog grafita jer bolje prekrivaju površinu uzorka i djeluju kao obrana od korozijskih napada. Stoga, prema svim navedenim rezultatima nodularni lijev je prihvatljiviji i prikladniji za izradu konstrukcijskih dijelova i dijelova poljoprivrednih strojeva izloženih nepovoljnim atmosferskim uvjetima.

## ZAKLJUČAK

Elektrokemijskim mjerenjima ispitana je korozijska otpornost sivog lijeva u mediju umjetne kiše i mediju 0,5 M $H_2SO_4$ te se na osnovu dobivenih rezultata može zaključiti sljedeće:

1. Potenciodinamičkom polarizacijom sivog lijeva u mediju umjetne kiše registrirana je 25× manja brzina korozije od one dobivene u kiselom mediju, što znači da se sivi lijev ne preporučuje za primjenu u jako kiselom mediju. S druge strane, mala vrijednost brzine korozije u umjetnoj kiši upućuje na činjenicu da bi se sivi lijev mogao primjenjivati za izradu konstrukcijskih elemenata koji bi bili izloženi nepovoljnjim atmosferskim uvjetima.
2. Iz impedancijskih parametara dobivenih modeliranjem EIS spektara zabilježena je daleko veća vrijednost otpora prijenosu naboja $R_{ct}$ u mediju umjetne kiše, što znači da se u tom mediju formirao deblji oksidni sloj na sivom lijevu koji ima zaštitnu ulogu, jer predstavlja barijeru daljnjem prodiranju agresivnih iona iz otopine.
3. Promatrajući morfologiju površine uzoraka nakon korozijskih mjerenja uočen je izrazito velik utjecaj kiselog medija koji napada metalnu osnovu, a nastali korozijski produkti za razliku od onih nastalih u umjetnoj kiši, nemaju zaštitnu ulogu u borbi protiv daljnjeg napredovanja korozije.
4. Usporedbom rezultata dobivenih u ovom radu za sivi lijev i onih dobivenih u ranijim istraživanjima za nodularni lijev kvalitete EN-GJS-400-18-LT može se zaključiti da se nodularni lijev pokazao korozijski otpornijim od sivog lijeva u mediju umjetne kiše, o čemu svjedoče veći iznosi otpora prijenosu naboja i skoro trostruko manje vrijednosti za brzinu korozije za nodularni lijev. To se može pripisati povoljnijoj mikrostrukturi nodularnog lijeva u kojem se grafit izlučuje u obliku kuglica, koje u usporedbi s listićima grafita predstavljaju pogodniji oblik izlučenog grafita jer bolje prekrivaju površinu uzorka i djeluju kao izolatori u procesu elektrokemijske korozije.
5. Iz svega navedenog može se zaključiti da je nodularni lijev korozijski otporniji u mediju umjetne kiše od sivog lijeva te se preporučuje kao prikladniji materijal za izradu konstrukcijskih dijelova i dijelova za poljoprivredne strojeve koji će biti izloženi nepovoljnim vremenskim uvjetima.

**LITERATURA**

[1] K. G. Budinski, M. K. Budinski, Engineering Materials, Properties and selection, 9th Edition, Pearson, 2010.
[2] I. Gabrić, S. Šitić, Materijali I, Konstrukcijsko strojarstvo, Split, 2012.
[3] J. Sugishita, S. Fujiyoshi, The effect of cast iron graphites on friction and wear performance I: Graphite film formation on grey cast iron surfaces, Wear, 66 (1981) 2, pp. 209-221.
[4] T. Fugal, G. M. Goodrich, V. Patersson, M. Mroczek, J. Ward, G. Goodrich, C. Callison, C. A. Bhaskaran, L. Helm, A. Shturmakov, J. Way, Introduction to gray cast processing, American Foundry Society, Des Plaines, Illinois, SAD, 2000.
[5] T. Filetin, F. Kovačiček, J. Indof, Svojstva i primjena materijala, Fakultet strojarstva i brodogradnje, Zagreb, 2002.
[6] F. Unkić, Z. Glavaš, Lijevanje željeznih legura, skripta, Metalurški fakultet, Sisak, 2008.

[7] D. Bartocha, K. Janerka, J. Suchoń, Charge materials and technology of melt and structure of gray cast iron, Journal of Materials Processing Technology, 162–163 (2005) pp. 465-470.
[8] M. Ramadan, M. Takita, H. Nomura, Effect of semi-solid processing on solidification microstructure and mechanical properties of gray cast iron, Materials Science and Engineering: A, 417 (2006) 1–2, pp. 166-173.
[9] J. Keller, V. Fridrici, Ph. Kapsa, S. Vidaller, J. F. Huard, Influence of chemical composition and microstructure of gray cast iron on wear of heavy duty diesel engines cylinder liners, Wear, 263 (2007) 7-12, pp. 1158-1164.
[10] E. Stupnišek-Lisac, H. Otmačić Ćurković, Korozija i okoliš, skripta, Fakultet kemijskog inženjerstva i tehnologije, Zagreb, 2015.
[11] P. Marcus, J. Oudar, Corrosion mechanisms in theory and practice, Marcel Dekker, Inc, New York, 1995.
[12] S. Mitić, A. Begić Hadžipašić, G. Gojsević Marić, Z. Zovko Brodarac, Utjecaj medija i mikrostrukture na korozijsko ponašanje nodularnog lijeva, 16th International Foundrymen Conference, Opatija, 2017, str. 173-188.
[13] B. Jarić, A. Rešetić, Korozija – Elektrokemijske osnove i katodna zaštita, Korexpert, Zagreb, 2003.
[14] Juraga, V. Alar, I. Stojanović, Korozija i zaštita premazima, Fakultet strojarstva i brodogradnje, Zagreb, 2014.
[15] I. Esih, Z. Dugi, Tehnologija zaštite od korozije I, Školska knjiga, Zagreb, 1990.
[16] Stojanović, Utjecaj tehnoloških parametara na zaštitna svojstva vodorazrjedivih premaza, Fakultet strojarstva i brodogradnje, Zagreb, 2011.
[17] M. A. Quraishi, A. Singh, V. K. Singh, D. K. Yadav, A. K. Singh, Green approach to corrosion inhibition of mild steel in hydrochloric acid and sulphuric acid solutions by the extract of Murraya koenigii leaves, Materials Chemistry and Physics, 122 (2010) pp. 114-122.
[18] S. Kožuh, M. Gojić, M. Kraljić Roković, The effect of PWHT on electrochemical behaviour of AISI 316L weld metal, Chemical and Biochemical Engineering Quarterly, 22 (2008) 4, pp. 421-431.

**Zahvala**

Ovaj rad je financiran sredstvima Sveučilišta u Zagrebu u okviru Financijske potpore istraživanju „Dizajn i karakterizacija inovativnih inženjerskih legura“, šifra: TP167.

17th INTERNATIONAL FOUNDRYMEN CONFERENCE
Hi-tech casting solution and knowledge based engineering
Opatija, May 16th-18th, 2018
http://www.simet.hr/~foundry/

# TOOL STEELS - CLASSIFICATION AND BASIC PROPERTIES

# ALATNI ČELICI – PODJELA I OSNOVNA SVOJSTVA

**Sandra Brajčinović[1]*, Anita Begić Hadžipašić[1], Jožef Medved[2]**

[1] University of Zagreb Faculty of Metallurgy, Sisak, Croatia
[2] University of Ljubljana Faculty of Natural Sciences and Engineering, Ljubljana, Slovenia

**Oral presentation**
*Review*

**Abstract**

This paper presents an overview of metallurgical processes of advanced metallic materials. The thermodynamic characteristics of the process include the conditions under which it is possible to follow the process in the desired direction and kinetics of the process. Tool steels belong to a group of advanced metallic materials, which are required by special properties such as high hardness and wear resistance, high strength stability at elevated temperatures, good behavior during heat treatment, high corrosion resistance etc. Achieving good properties is enabled by alloying with chromium, tungsten, vanadium, molybdenum or cobalt. It is very important to what extent the alloying elements are added and how the process of production proceeds, because the compounds formed during the production can be altered, and thus affect the transformation processes, and secreted in an undesirable form. Alloying elements are most often combined with carbon in carbides but can also be partially substituted in the iron crystal lattice and create undesirable intermetallic compounds. In order to improve the properties of tool steels, the aim is to find an adequate chemical composition to enable obtaining stable thermodynamic parameters.

***Keywords**: tool steels, metallurgical processes, thermodynamics, kinetics, alloying elements*

*Corresponding author (e-mail address): *smitic@simet.hr*

**Sažetak**

U ovom radu dan je pregled proučavanja metalurških procesa naprednih metalnih materijala. Termodinamičke karakteristike procesa obuhvaćaju uvjete prema kojima je moguće pratiti odvijanje procesa u željenom pravcu te kinetiku odvijanja procesa. Alatni čelici pripadaju skupini naprednih metalnih materijala od kojih se zahtijevaju posebna svojstva poput visoke tvrdoće i otpornosti na trošenje, postojanost čvrstoće kod povišenih temperatura, dobro ponašanje pri toplinskoj obradi, korozijska otpornost i dr. Postizanje dobrih svojstava omogućeno je legiranjem kromom, volframom, vanadijem, molidbenom ili kobaltom. Veoma je bitno u kojoj mjeri se dodaju legirajući elementi i

kako teče proces proizvodnje, jer spojevi koji nastaju tijekom proizvodnje mogu se mijenjati i tako utjecati na transformacijske procese te se izlučiti u nepoželjnom obliku. Legirajući elementi se najčešće spajaju s ugljikom u karbide, ali također mogu dijelom supstituirati u kristalnu rešetku željeza te stvarati nepoželjne intermetalne spojeve. U svrhu poboljšanja svojstava alatnih čelika, teži se pronalasku adekvatnog kemijskog sastava kako bi se omogućilo dobivanje stabilnih termodinamičkih parametara.

***Ključne riječi:*** *alatni čelici, metalurški procesi, termodinamika, kinetika, legirajući elementi*

## UVOD

Alatni čelici se ubrajaju u visokougljične ili legirane čelike. Ugljični alatni čelici sadrže visok udio ugljika koji se kreće od 0,6 do 2,06%. Najčešći elementi koji se koriste za legiranje alatnih čelika su: krom, kobalt, vanadij, volfram i molidben. Alatni čelici pripadaju skupini naprednih metalnih materijala od kojih se zahtijevaju posebna svojstva poput visoke tvrdoće i otpornost na trošenje, postojanost čvrstoće kod povišenih temperatura, dobro ponašanje pri toplinskoj obradi itd. [1,2].
Kod proizvodnje alatnih čelika važno je utvrditi optimalan kemijski sastav s kojim bi se postigla otpornost materijala u svakodnevnoj upotrebi. Stoga se pri samoj proizvodnji provodi klasifikacija prema kemijskom sastavu bazirana na analizama taline. Ispitivanjem kemijskog sastava čelika u procesu lijevanja dobiva se željeni kemijski sastav, odnosno, precizni rezultat sadržaja određenih prisutnih elemenata.
Alatni čelici primarno se koriste u izradi različitih alata, stoga su podvrgnuti raznim procesima opterećenja i trošenja te se od njih zahtijeva maksimalna trajnost uz minimalno održavanje. Najčešća primjena alatnih čelika je u raznim industrijskim postrojenjima kao što su: toplinski strojevi i uređaji, kemijska i procesna industrija, termo i nuklearne elektrane, rakete i svemirski brodovi, alati za oblikovanje metala i keramike u kojima se rad pri povišenim i visokim temperaturama ne može izbjeći zbog čega zahtjeva velika izdržljivost i otpornost materijala [3].
U ovom radu obrađena je podjela i pregled najtraženijih zahtjeva, koji se odnose na alatne čelike. Također, opisan je pregled utjecaja elemenata, koji mogu sudjelovati u termodinamičkim metalurškim procesima proizvodnje alatnih čelika.

## PODJELA ALATNIH ČELIKA PREMA NAMJENI

Alatni čelici mogu biti nelegirani, niskolegirani i visokolegirani, a prema namjeni dijele se u četiri skupine [2,4]:
1. ugljični alatni čelici,
2. alatni čelici za hladni rad – $\vartheta r$ (radna temperatura) < 200°C,
3. alatni čelici za topli rad – $\vartheta r$ (radna temperatura) > 200°C i
4. brzorezni čelici.

Na slici 1 prikazana je podjela alatnih čelika prema namjeni. Ugljični alatni čelici sadrže 0,6-1,4% C. Karakteristika ove grupe alatnih čelika je visoka tvrdoća (60-64 HRC) [5]. Imaju dobru otpornost pri trošenju, ali samo do temperature 150°C i zbog toga se od ugljičnih alatnih čelika ne izrađuje alat za veće brzine rezanja. Karakteristika im je dobra žilavost, stoga je ova grupa čelika prihvatljiva za izradu alata koji su izloženi jačim udarnim opterećenjima.
Alatni čelici za hladni rad obuhvaćaju skupinu čelika koja je namijenjena za oblikovanje i mehaničku obradu do 200°C. Mogu biti nelegirani ili niskolegirani. Nelegirani čelici za hladan rad sadrže 0,5-1,3% C, imaju nisku prokaljivost i bolju žilavost u odnosu na druge alatne čelike. Namijenjeni su za izradu alata manjih presjeka i jednostavnijih oblika.
Niskolegirani čelik za hladan rad ima znatno bolja svojstva što se postiže dodavanjem legirajućih elemenata: krom, volfram, vanadij i molidben. Svrha legiranja je postizanje toplinski postojanih karbida koji omogućavaju dobru žilavost, zadržavanje visoke tvrdoće pri povišenim radnim temperaturama te dimenzijsku postojanost [6].
U ovoj skupini alatnih čelika postoje i viskolegirani alatni čelici za hladan rad kod kojih je glavni legirajući element krom i njegov udio je veći od 5%. Ova skupina alatnih čelika namijenjena je za proizvodnju alata koji su skloni koroziji, a kromom se postiže otpornost na koroziju. Uz krom, također su prisutni sljedeći legirajući elementi: V, Mo i W. Najvažniji zahtjevi za alatne čelike za rad u hladnom stanju su: otpornost na trošenje i otpornost na udarce [7].

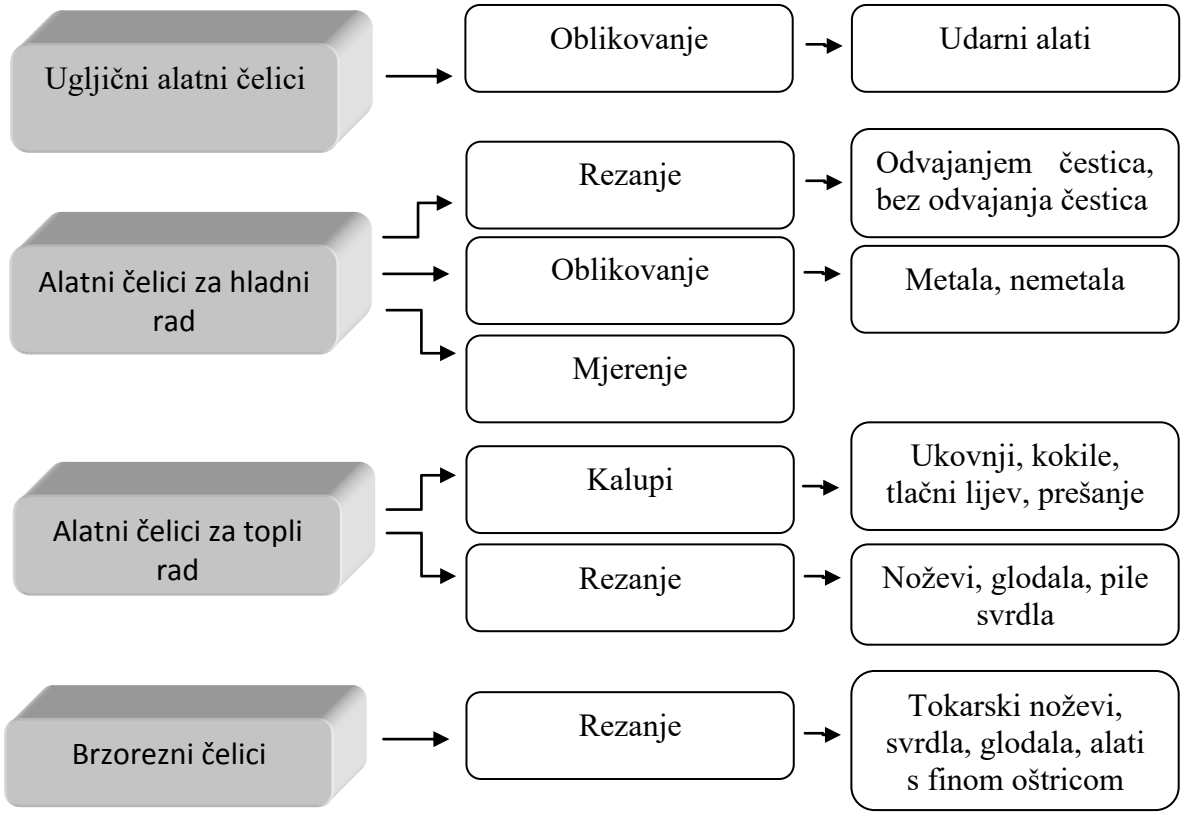


Slika 1. Podjela alatnih čelika prema namjeni

Alatni čelici za topli rad primjenjuju se pri temperaturama višim od 200°C. Osnovni legirajući

elementi kod ove skupine čelika su krom, molidben i vanadij, a često se dodaje i volfram. Ovisno o prisustvu legirajućih elemenata dijele se na grupe čelika tipa: W-Cr-V i Co-Mo-Cr-V. Kod ovih čelika najtraženije svojstvo je otpornost na popuštanje [8]. Naime, kod povišenih temperatura može doći do smanjenja tvrdoće, mikrostrukturnih promjena i toplinskog zamora. Za ovu skupinu alatnih čelika postavljaju se i dodatni zahtjevi poput: otpornost na trošenje, viskotemperaturnu koroziju, pojavu plastičnih deformacija i udarnog opterećenja. Legiranje karbidotovorcima omogućava stvaranje karbida koji povećavaju otpornost na popuštanje i otpornost na trošenje. Niskim sadržajem ugljika (0,35-0,45% C) postiže se dobra žilavost i otpornost na toplinski umor. Silicij se dodaje zbog poboljšanja dinamičke izdržljivosti, a nikal kako bi se povećala žilavost i prokaljivost [1,9].
Brzorezni alatni čelici su otporni na visoke temperature pa tako zadržavaju visoku tvrdoću i otpornost na trošenje pri temperaturama do 650°C [4,10]. Brzorezni čelici spadaju u skupinu visokolegiranih čelika, a osnovni legirajući elementi su volfram i moldben koji osiguravaju temperaturnu postojanost. Dodatkom kobalta i vanadija postiže se visoka tvrdoća pri povišenim temperaturama. Karakteristika ovih čelika je da omogućavaju četiri puta veće brzine rezanja u odnosu na ugljične čelike. Ovisno o udjelu legirajućih elemenata, ova skupina se dijeli na molidbenske, volframske i kobaltne brzorezne čelike [11].

## ZAHTJEVI PRI PROIZVODNJI ALATNIH ČELIKA

Primarni zahtjevi za alatne čelike su: otpornost na trošenje (adhezija i abrazija) i otpornost na popuštanje (žilavost). Sekundarni zahtjevi pri proizvodnji alatnih čelika su: mogućnost obrade alata, što viša zakaljivost i prokaljivost, a manja sklonost pogrubljenju zrna prilikom austenitizacije, što manja sklonost razugljičenju kod toplinske obrade, manje deformiranja u kaljenju te veća mogućnost za poliranje (otpornost na koroziju).
Alatnim čelicima se smanjuje vijek trajanja zbog trošenja, najviše abrazijom, tj. mikrorezanjem. Mehanizam abrazijskog trošenja nastaje pri direktnom fizičkom kontaktu između dviju površina te ukoliko se abrazivno sredstvo zaglavi između dviju površina u trenju (slika 2). Pri tome, neravni dijelovi hrapave i tvrde površine klize po mekšoj površini i pritom se pojavljuju oštećenja površine. Tvrde čestice koje djeluju na oštećenje alata mogu biti: tvrdi intermetalni spojevi, tvrdi organski spojevi, nečistoće u obrađivanom predmetu, karbidi u obrađivanom predmetu. Da bi se postiglo svojstvo otpornosti na trošenje, teži se postići prikladna funkcija mikrostrukturnog stanja čelika, tj. martenzitna struktura i što viši udio kvalitetnih karbida. Čelici koji su legirani s jakim karbidotvorcima (krom, volfram, mangan) imaju vrlo visoku otpornost na abrazijsko trošenje [1,3].

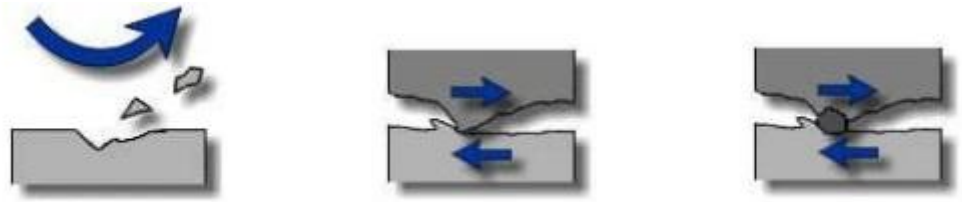

Slika 2. Abrazijsko trošenje alata [12]

Za primjer rješavanja problema trošenja može se navesti TD postupak, odnosno, termoreaktivni-difuzijski postupak oblaganja alata vanadijevim karbidom. Vanadij s ugljikom na površini alata stvara stabilan karbid $V_8C_7$. Karbidni sloj na površini raste tijekom procesa difuzije ugljika iz površinskog sloja čelika prema karbidnom sloju (slika 3). Pritom, određena količina karbidnog elementa difundira kroz nastali karbidni sloj u površinski sloj čelika. Ovaj postupak omogućio je postizanje visoke tvrdoće pri povišenim temperaturama posebno za alatne čelike za rad u toplom stanju, kao što su kalupi koji se koriste za lijevanje aluminija. Vanadij karbid obloga ne reagira s aluminijem i tako sprječava interakciju legura za lijevanje i kalupa [13]. Iako se postupak provodi u odgovarajućim uvjetima za koje je potrebna solna kupka odgovarajućeg sastava i visoke temperature (950-1050°C), glavni doprinos za nastajanje karbidnog sloja ovisi o kemijskom sastavu alatnog čelika što potvrđuje da se postizanjem odgovarajućeg kemijskog sastava mogu dodatno unaprijediti svojstva čelika te produžiti vijek trajanja alata.

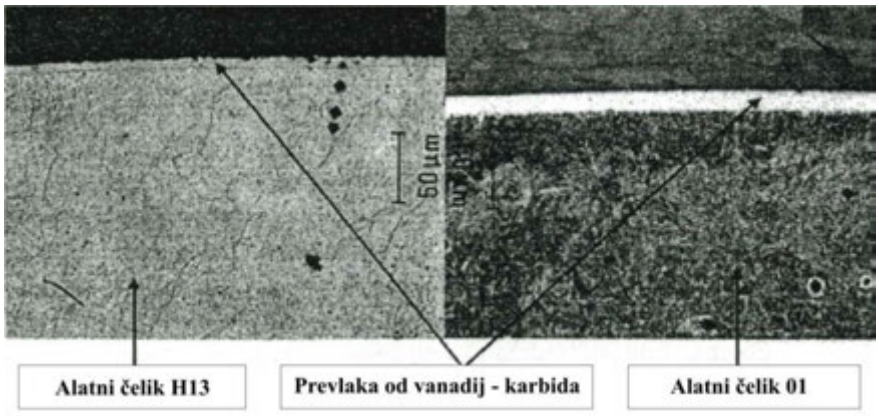


Slika 3. Prikaz nanešenog sloja vanadij karbida na alatnim čelicima za rad u hladnom (AISI 01) i toplom stanju (AISI H13) [13]

Otpornost na popuštanje važna je za alate (slika 4) koji se koriste pri povišenim temperaturama (oko 600°C). Takvi alati pretežito su rezni alati koji postižu visoke temperature dok su u funkciji rada, zatim kokile ili ukovnji. Povišena temperatura dovodi do slabe otpornosti na trošenje te do pada čvrstoće i tvrdoće, a elementi koji doprinose otpornosti na popuštanje su legirajući elementi: volfram, molidben, vanadij i krom [4,6]. Otpornost na popuštanje najviše pokazuju alatni čelici za topli rad i brzorezni čelici. Kod

kalupa koji su namijenjeni za topli rad može doći do toplinskog umora zbog toplinskih naprezanja, jer se prilikom rada alati naizmjenično zagrijavaju pa hlade. Otpornost na popuštanje se može iskazati kod razlika u vrijednosti tvrdoće nakon kaljenja i tvrdoće nakon popuštanja pri određenoj temperaturi, a vrijednost se naziva dekrement tvrdoće [1,10].

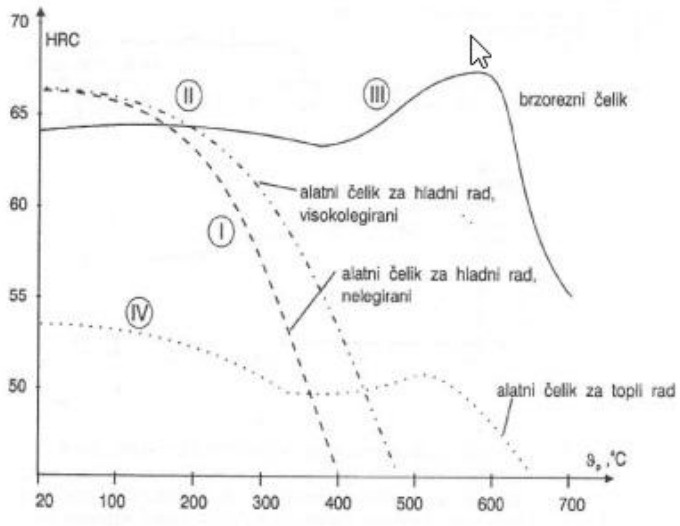


Slika 4. Dijagram popuštanja osnovnih skupina alatnih čelika [14]

**METALURŠKI PROCESI**

Metalurškim procesima smatra se proces dobivanja metala koji se zasniva na nizu odvijanja složenih fizikalno-kemijskih procesa koji se istovremeno ili postepeno odvijaju u metalurškim agregatima. Kod svakog metalurškog procesa prerađuje se sirovina u cilju dobivanja određenog produkta, a pritom se izvode fizikalne, kemijske i fizikalno-kemijske transformacije u određenoj mjeri, kako bi se omogućilo dobivanje željenog svojstva produkta, koji će biti prikladan za daljnju preradu. Metalurški procesi praćeni su pretvorbom elemenata, tj. kemijskim reakcijama čija brzina određuje efekte proizvodnje kao što su produktivnost, specifična potrošnja energije, izvadak i dr. [15].
Ravnotežu reakcije proučava termodinamika koja omogućuje predviđanje da li je neki proces moguć i kako ga ostvariti. Pritom se polazne sirovine pretvaraju u konačne produkte, ali ponekad tvari slabo ili uopće ne reagiraju. Stoga je potrebno za odvijanje metalurških procesa poznavati vrijeme u kojem će se neka reakcija ostvariti. To područje proučava kemijska kinetika [16]. Tako se lakše može protumačiti koje reakcije su poželjne u proizvodnji, a koje treba na vrijeme usporiti.
Visoke temperature u elektropećima omogućavaju legiranje čelika s teško taljivim metalima. Kako bi se dobila tražena svojstva materijala poput: otpornost na koroziju, otpornost na trošenje, prokaljivost, vatrootpornost i dr., posebna pažnja se pridodaje odabiru adekvatnog kemijskog sastava, stoga se dodaju legirajući elementi i tako se postiže traženo svojstvo materijala. Osim toga, u proizvodnji su prisutne i prateće primjese elemenata koji mogu

imati negativan utjecaj na kvalitetu čelika te je njihov maseni udio potrebno svesti na minimum. Primjese u čeliku mogu biti zastupljene kao prateći elementi, skriveni ili slučajni elementi [17].

Stoga se općenita podjela elemenata koji su u sastavu čelika može svrstati na:

- korisne elemente – legirajući elementi (Cr, Ni, Mo, Cu, W, V, Al ,Ti),
- štetne elemente – (Si, Mn, P, S, N, H, O, te nemetalni uključci).

Naročito se pri proizvodnji izbjegavaju štetni plinovi poput kisika, vodika, dušika koji narušavaju svojstva proizvoda. Kao primjer može se navesti pojava starenja koju uzrokuje dušik, stoga se dodaju elementi Al, Ti, Nb pa dušik iz čvrste otopine prelazi u nitride i tako čelik postaje otporan na starenje. Vodik u kombinaciji sa željezom tvori intersticijske mješance te dovodi do pojave vodikove krhkosti, tj. vodik iz atomarnog stanja prelazi u molekularno stanje u obliku sitnih mjehurića. Kisik djeluje tako da uzrokuje pojavu krhkosti čelika [9,18].
Nemetalni uključci uzrokuju smanjenje žilavosti, čvrstoće i pad duktilnosti. U kojoj mjeri će utjecati na svojstva čelika ovisi o njihovoj vrsti (oksidni, sulfatni ili silikatni), količini i rasporedu.
Osim prethodno navedenih elemenata, među najznačajnije štetne elemente ubrajaju se sumpor i fosfor. Sumpor sa željezom tvori FeS koji je nepoželjan, jer se pojavljuje na granicama zrna. Fosfor također sa željezom tvori supstitucijski kristal mješanac i utječe na pojavu krhkosti kod čelika [19].

## UTJECAJ LEGIRAJUĆIH ELEMENATA NA SVOJSTVA ALATNIH ČELIKA

Ugljik (C) se smatra najvažnijim elementom koji utječe na svojstva čelika. Maseni udio ugljika u čeliku iznosi do 2,03%. Visok udio ugljika utječe na porast čvrstoće i granice razvlačenja, dok se pritom smanjuje žilavost i duktilnost. Kod čelika s martenzitnom strukturom, sadržaj ugljika je viši, jer se pritom omogućava toplinska obrada [1,4,10]. Krom u kombinaciji s ugljikom stvara karbide koji povećavaju otpornost na trošenje čime se produžuje vijek trajanja alata. Također, krom djeluje na povišenje toplinske čvrstoće, vatrootpornost i otpornost na djelovanje vodika. Da bi se postigla korozijska otpornost, potrebno je legiranje s minimalno 12% Cr [3, 16]. Molidben povećava prokaljivost i čvrstoću čelika, stvara karbide i povećava otpornost i trošenje čelika te uz krom, povećava otpornost prema koroziji. Vanadij je jak karbidotvorac i omogućava stvaranje VC ili $V_4C_3$ karbida koji su poželjni pri proizvodnji alatnih čelika za rad pri povišenim temperaturama. Wolfram stvara karbide koji su otporni na trošenje i zbog toga je nužan legirajući element za brzorezne čelike [2,12].
Mangan se dodaje zbog lakšeg oblikovanja čelika u toplom stanju, povećava prokaljivost, čvrstoću i žilavost. Sposobnost mangana očituje se u tome da štiti čelik od sumporne kiseline i sumpornih koncentrata. Koristi se kao dezoksidator i desulfurizator tijekom proizvodnje čelika. Zajedno sa sumporom stvara sulfid MnS pri čemu se sprječava negativno djelovanje sulfida.

Nikal ima slab afinitet prema ugljiku i zbog toga ne stvara karbide. Dodatkom nikla stvara se austenitna struktura koja doprinosi održavanju visoke čvrstoće i duktilnosti. Također daje otpornost prema koroziji, ali zbog svoje visoke cijene uglavnom se upotrebljava u manjoj količini i to u kombinaciji s elementima sličnih svojstava.
Kobalt se u pojedinim legurama dodaje zbog povećanja vlačne čvrstoće i postojanosti na popuštanje pri povišenim temperaturama. Najčešće se koristi kod alatnih, brzoreznih i konstrukcijskih čelika. Ne smije se koristiti njegovo dodavanje pri izradi čelika za dijelove nuklearnih energetskih postrojenja zbog stvaranja radioaktivnog izotopa ($^{60}$Co) [1,5].
Količina karbida određena je sadržajem ugljika i legirajućih elemenata. Čelik se legira s određenom količinom nekog elementa kako bi mu se poboljšalo svojstvo ili kombinacija svojstava, ali pritom je važno u kojem postotku se dodaju legirajući elementi i u kojoj kombinaciji su prisutni.
Ako promatramo afinitet prema ugljiku, legirajući elementi u čeliku mogu biti [12,20]:

1. karbidotvorci (Cr, Mo, V, W, Ta, Ti);

2. nekarbidotvorci (Mn, Ni, Co).

Struktura alatnih čelika veoma je složena i ovisi od uvjeta legiranja i od stanja termičke obrade. Metalna osnova kod visokog sadržaja ugljika je perlitna te se može pojaviti i udio ferita. Ovisno o sadržaju ugljika i legirajućih elemenata, alatni čelici se mogu podijeliti na [4,10]:

1. nadeutektoidne čelike,

2. eutektoidne čelike,

3. ledeburitne čelike i

4. čelike s intermetalnim ojačanjem.

Količina karbidnih faza kod nadeutektoidnih čelika iznosi 5-12%, a kod ledeburitnih čelika 25-30%. Karbidne faze u čeliku stvaraju određenu koncentraciju ugljika i legirajućih elemenata pri čemu se omogućava prokaljivost, visoka tvrdoća i otpornost prema trošenju. Osnovna karbidna faza je cementit $Fe_3C$ koji ima visoku tvrdoću i na sobnoj temperaturi je magnetičan [21].
Karbidne faze mogu se podijeliti na tri grupe [1, 3]:

1. grupa su karbidi označeni tipom MC (TiC, VC, TaC, NbC),

2. grupa su karbidi označeni tipom $M_2C$ ($Mo_2C$, MoC, $W_2C$, WC) i

3. grupu čine karbidi $M_3C$ ($Fe_3C$, $Mn_3C$), $M_6C$, $M_{23}C_6$.

Metalne karbidne faze se skraćeno označavaju simbolima MC, a indeks označava broj atoma koji pripada jednoj atomskoj rešetci. Razlika u rasporedu karbidnih faza – cementita je više izražena kod ugljičnih čelika nego kod legiranih čelika. Strukturna građa čelika, odnosno granica zrna ima veliki utjecaj na svojstva čelika. Karbidne faze koje su prisutne u alatnim čelicima uglavnom su smještene na granicama zrna. Mogu biti izražene u obliku mreže oko

metalnih zrna pri čemu dolazi do slabljenja granica zrna što se negativno održava na udarnu žilavost [12,22].

Kod visokih temperatura uslijed kaljenja i sekundarnog otvrdnjavanja pri otpuštanju dolazi do slabljenja granice zbog krupnozrnate strukture. To znači da je rast zrna nepovoljan gdje je prisutna martenzitna struktura, jer dolazi do povećanog sadržaja ugljika u martenzitu, a kao posljedica toga je pad čvrstoće i udarne žilavosti. Ukoliko u strukturi alatnog čelika postoje pojedinačna krupna zrna karbida, ona neće u velikoj mjeri utjecati na osobine alata, ali problem se javlja ukoliko se krupna zrna karbida pojavljuju u grupama i u većem broju. Nastankom sitnozrnate strukture karbidnih čestica na granicama zrna veći je otpor prema stvaranju pukotina i loma [23].
U toku plastične deformacije, dimenzije karbidnih faza se smanjuju, ali nakon izvedene plastične deformacije ne postoji više utjecaj na formiranje veličine karbida [3,24]. Ipak, na nastanak krupnih karbida najviše utječu procesi pri proizvodnji, odnosno sastav čelika, dimenzija odljevka, kristalizacija i dr. Karbidna zrna su uglavnom ovalnog oblika, iako se u strukturi alatnih čelika mogu pojaviti uglati karbidi koji nepovoljno djeluju na svojstva alatnih čelika (slika 5).

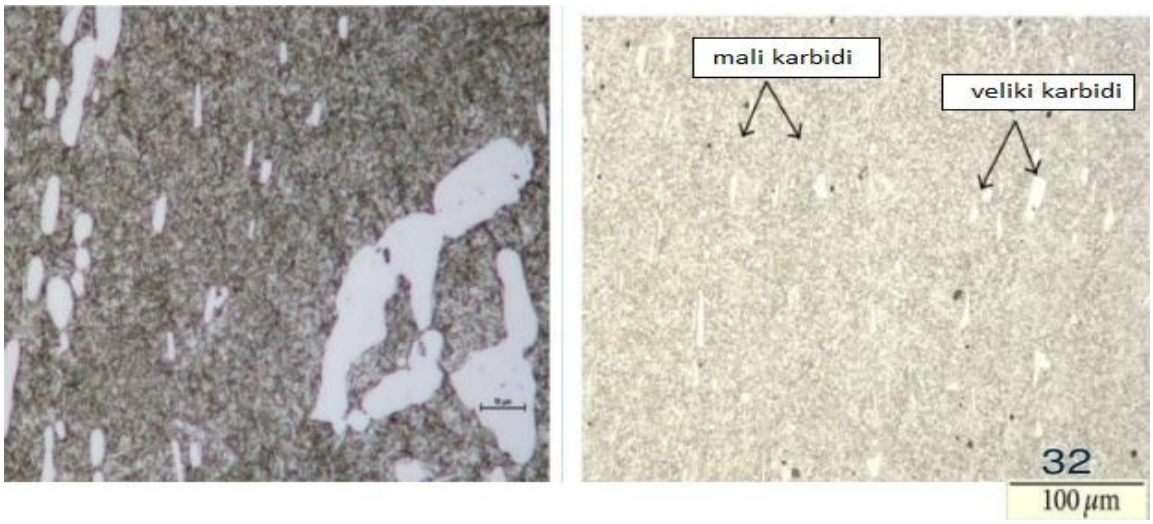


Slika 5. Nejednolika raspodjela karbida u alatnom čeliku [25]

Kako je navedeno, legirajući elementi, tzv. karbidotovorci se najčešće spajaju s ugljikom u karbide $Cr_7C_3$, $Cr_{23}C_6$, $W_2C$, WC, $Mo_2C$, VC, $V_4C_3$, TiC, TaC, NbC, $Fe_3C$ i dr., ali mogu također supstituirati u kristalnu rešetku željeza te stvarati intermetalne spojeve, odnosno faze sa strukturom različitom od strukture polaznih metala.
Krom je sklon formiranju intermetalnih faza koje djeluju negativno na svojstva alatnih čelika. U kombinaciji s ugljikom i dušikom može jako povisiti čvrstoću, a smanjiti žilavost i korozijsku postojanost. Nikal utječe na kinetiku nastanka intermetalne faze iako ne promiče njihovo formiranje. Intermetalne faze pojavljuju se u primarnoj kristalizaciji i njihov raspored formiran je pri lijevanju. Raspored intermetalnih faza je uglavnom ravnomjeran, dimenzije čestica faza su male, ali kao i kod karbidnih faza, zadržava se rast zrna. Slika 6 prikazuje

kristalnu rešetku u kojoj je vidljivo kako se atomi jednog elementa mogu zamijeniti atomom drugog elementa. Intermetalni spojevi nastaju kada su fizikalne osobine legura različite od njihovih osobina kod komponenata. Kod metalurških procesa legure reagiraju kao smjesa komponenata, dok u procesu isparavanja legure dolazi do raspada intermetalnog spoja na njegove sastavne komponente [26].

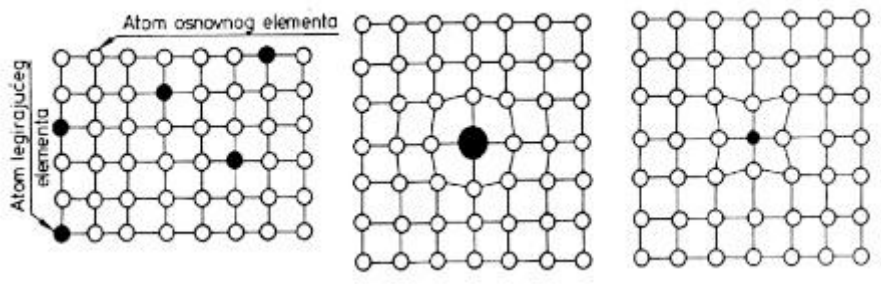


Slika 6. Formiranje intermetalne faze [26]

Najznačajnije intermetalne faze koje mogu biti prisutne u alatnim čelicima su [3,12,23]:
a) tip $(Fe, Co)_7(W,Mo)_6$ pojavljuje se kod alatnih čelika koji su legirani kobaltom, volframom i molidbenom;
b) tip $Fe_3W(Fe_3Mo_2)$ pojavljuje se također u alatnim čelicima kao i kod prethodnog tipa;
c) tip $(NiFe)_3Ti$ pojavljuje se u alatnim čelicima koji su legirani niklom i titanom;
d) tip $(Ni,Fe,Cr)_3(Ti,Al)$ pojavljuje se u čelicima legiranim niklom, kromom, titanom i aluminijem;
e) tip $(Fe,Ni, Co)_7(Mo,W)_6$ pojavljuje se u čelicima sistema Fe-Co-Mo niklom i titanom, a
f) tip $(Fe,Ni,Co)_2Mo$ može biti prisutan najčešće kod martenzitnih čelika.

## ZAKLJUČAK

U ovom radu dan je pregled utjecajnih elemenata pri termodinamičkim metalurškim procesima alatnih čelika. Za razvoj naprednih materijala potrebno je težiti strukturnoj stabilnosti, dobrim mehaničkim i korozijskim svojstvima. Odabirom odgovarajućeg kemijskog sastava može se izbalansirati udio elemenata koji sudjeluju u procesu proizvodnje alatnih čelika te tako postići što kvalitetnija svojstva. Jedan od osnovnih razloga zbog čega se legiraju alatni čelici su postizanje kvalitetnijih i toplinski stabilnijih karbida koji doprinose kvaliteti, odnosno daju višu tvrdoću i otpornost na trošenje u radnim uvjetima. Osim radnih zahtjeva, alatni čelici su izloženi povišenim temperaturama koje mogu nepovoljno djelovati na svojstva alatnog čelika, odnosno mogu prouzročiti pad čvrstoće i tvrdoće, što je još jedan razlog zašto bi se trebalo težiti ostvarenju prikladnog kemijskog sastava te pritom omogućiti dodatno oplemenjivanje različitim tehnikama obrade ukoliko se to prema propisima proizvodnje zahtjeva. Zbog toga, važno je nastaviti istraživanja u smislu poboljšanja svojstava alatnih čelika, jer moderan razvoj industrije bez ovih materijala bio bi gotovo nezamisliv. Tako bi se osigurala bolja kvaliteta i duži vijek trajanja alata, ali i omogućili manji troškovi u proizvodnji.

**LITERATURA**

[1] G. Roberts, G. Krauss, and R. Kennedy, Tool Steels, 5th ed., ASM International, Materials Park, 1998.
[2] M. Novosel, F. Cajner, D. Krumes, Alatni materijali, Strojarski fakultet u Slavonskom Brodu, Slavonski Brod, 1996.
[3] P. M. Novotny, M. K. Banerjee, Tool and Die Steels Introductory Article, Reference Module in Materials Science and Materials Engineering, 2016, Current as of 30 March 2016.
[4] T. Kostadin, Čelici i željezni ljevovi, Materijali II, Interna skripta, Karlovac, 2017.
[5] W. E. Bryson, Heat treatment, selection and application of tool steels, 2nd Edition, Hanser Publications, Cincinnati, 2013.
[6] R. W. Staehle, Engineering with advanced and new materials, Materials Science and Engineering: A, 198 (1995) 1-2, pp. 245-256.
[7] A. Molinari, M. Pellizzari, S. Gialanella, G. Straffelini, K. H. Stiasny, Effect of deep cryogenic treatment on the mechanical properties of tool steels, Journal of Materials Processing Technology, 118 (2001), 1-3, pp. 350-355.
[8] K. Hofmann, F. Neubauer, M. Holzer, V. Mann, F. Hugger, S. Roth, M. Schmidt, Effect of Laser Beam Alloying Strategies on the Metallurgical and Mechanical Properties of Hot Forming Tool Steels, Physics Procedia, 83 (2016) pp. 264-276.
[9] L. Ugrin, Dobivanje, svojstva i upotreba čelika, Završni rad, Split, 2016.
[10] T. Filetin, Pregled razvoja i primjene suvremenih materijala, Hrvatsko društvo za materijale i tribologiju, Zagreb, 2000.
[11] I. Zdelarec, Utjecaj dubokog hlađenja na pojave pri popuštanju brzoreznog čelika, Završni rad, Zagreb, 2010.
[12] B. Dobranić, Trošenje dijelova građevinskih strojeva, Diplomski rad, Fakultet strojarstva i brodogradnje, Zagreb, 2012.
[13] Ž. Stojanović, S. Stanisavljev, S. Radosavljević, Primena postupka vanadiranja u funkciji produženja radnog veka delova, Zaštita materijala, 54 (2013) 2, pp. 266-271.
[14] D. Landek, Autorizirane podloge za predavanja iz područja alatnih materijala, Sveučilište u Zagrebu Fakultet strojarstva i brodogradnje, Zagreb, 2016.
[15] D. R. Gaskell, Introduction the Thermodynamics of Materials, Washington, DC, Taylor and Francis, 1995.
[16] N. Birks, G. H. Meier, F. S. Pettit, Introduction to the high-temperature oxidation of metals, 2nd Edition, University of Pittsburgh, Cambridge, 2006.
[17] R. De Hoff, Thermodynamics in Material Science, Taylor and Francis Group, New York, USA, 2006.
[18] J. O Andersson, T. Helander, L. Höglund, P. Shi, Bo Sundman, Thermo-Calc & DICTRA, computational tools for materials science, Calphad, 23 (2002) 2, pp. 273-312.
[19] R. Duan, J. X. Deng, X. Ai, Y. Y. Liu, H. Chen, Experimental assessment of derivative cutting of micro-textured tools in dry cutting of medium carbon steels, International Journal of Advanced Manufacturing Technology 92 (2017) 9-12, pp. 3531-3540.

[20] D. C. Ko, S. G. Kim, B. M. Kim, Influence of microstructure on galling resistance of cold-work tool steels with different chemical compositions when sliding against ultra-high-strength steel sheets under dry condition, Wear, 338 (2015) pp. 362-371.
[21] S. J. Huang, Tribological properties of the low-carbon steels with different micro-structure processed by heat treratment and severe plastic deformation, Wear, 271 (2011) pp. 705-711.
[22] N. S. Kalsi, R. Sehgal, V. S. Sharma, Cryogenic Treatment of Tool Materials: A Review, Materials and Manufacturing Processes, 25 (2010) pp. 1077-1100.
[23] H. Kim, J. Kang, D. Son, T. Lee, K. Cho, Evolution of carbides in cold-work tool steels, Original Research Article, Materials Characterization, 107 (2015), pp. 376-385.
[24] D. Tobola, W. Brostow, K. Czechowski, P. Rusek, Improvement of wear resistance of some cold working tool steels, Wear, 382 (2017) pp. 29-39.
[25] U. Tahir, Cold Work Tool steel, presentation, NED University of Engineering and Technology, 2014.
[26] N. Haračić, Savremeni materijali za mašinogradnju, Univerzitet u Zenici Fakultet za metalurgiju i materijale, Zenica, 2012.

**Zahvala**

Ovaj rad je financiran sredstvima Sveučilišta u Zagrebu u okviru Financijske potpore istraživanju „Dizajn i karakterizacija inovativnih inženjerskih legura“, šifra: TP167.

17th INTERNATIONAL FOUNDRYMEN CONFERENCE
Hi-tech casting solution and knowledge based engineering
Opatija, May 16th-18th, 2018
http://www.simet.hr/~foundry/

# HARDNESS AND FRACTURE TOUGHNESS OF A CEMENTED CARBIDE

# TVRDOĆA I LOMNA ŽILAVOST NANOSTRUKTURIRANOG TVRDOG METALA

**Danko Ćorić, Matija Sakoman*, Božo Renić**

University of Zagreb Faculty of Mechanical Engineering and Naval Architecture, Zagreb, Croatia

**Oral presentation**
*Original scientific paper*

**Abstract**

In this paper the hardness and fracture toughness values for nanostructured cemented carbides were tested and analyzed. The experimental part included the testing of three samples: WC with 5% cobalt (WC-5Co), WC with 10% cobalt (WC-10Co) and WC with 15% cobalt (WC-15Co). Hardness was tested by Vickers method (HV30) according to HR EN ISO 6507-1: 2005, and fracture toughness was determined by the Palmqvist method according to ISO 28079: 2009. Palmqvist's method uses the length of cracks that propagate from the tip of the Vickers pyramid imprint to determine fracture toughness. The results show that by increasing the amount of cobalt in cemented carbides hardness values drop, and the fracture toughness increases. They also indicate that using nanostructured cemented carbides increases hardness with a slight change in toughness.

***Keywords**: nanostructured cemented carbides, hardness, fracture toughness*

*Corresponding author (e-mail address*): matija.sakoman@fsb.hr*

**Sažetak**

U ovom radu ispitivane su i analizirane vrijednosti tvrdoće i lomne žilavosti nanostrukturiranih tvrdih metala. Eksperimentalni dio uključivao je provođenje ispitivanja na tri uzorka: s 5% kobalta (WC-5Co), 10% kobalta (WC-10Co) odnosno 15% kobalta (WC-15Co). Tvrdoća je ispitana metodom po Vickersu (HV30) sukladno normi HR EN ISO 6507-1:2005, a lomna žilavost određena je Palmqvistovom metodom sukladno normi ISO 28079:2009. Kod Palmqvistove metode mjerene su duljine pukotina koje propagiraju iz vrhova otiska. Rezultati pokazuju da se s povećanjem udjela kobalta u tvrdom metalu smanjuje tvrdoća, a lomna žilavost povećava. Također ukazuju da se primjenom nanostrukturiranih tvrdih metala, povećava tvrdoća uz neznatnu promjenu lomne žilavosti.

***Ključne riječi**: nanostrukturirani tvrdi metali, tvrdoća, lomna žilavost*

## INTRODUCTION

Cemented carbides are metal composites that represent the most widely-known powder metallurgy product. The microstructure of cemented carbides consists of a higher portion of tungsten carbide (WC) and possibly smaller portions of titanium and tantalum carbides, mutually linked to a binder phase that is cobalt (Co). The cobalt matrix usually provides toughness, and carbides are here to provide high hardness and wear resistance. Their outstanding properties are: high compressive strength and high rigidity, high melting point, satisfactory mechanical properties at elevated temperatures, resistance to thermal shocks, good corrosion resistance and high thermal and electrical conductivity. These materials are most commonly used for the production of cutting tools for metal and stone processing, and tools for the oil and gas drilling industry. Cutting tools made from cemented carbides generally have better properties than high-speed steel ones [1].
With the advancement of industrial methods of consolidation and production of powders, small grain powders are used on a larger scale, which has led to the development of ultrafine (0.2 - 0.5 μm) and nanostructured (<0.2 μm) cemented carbides, Figure 1.

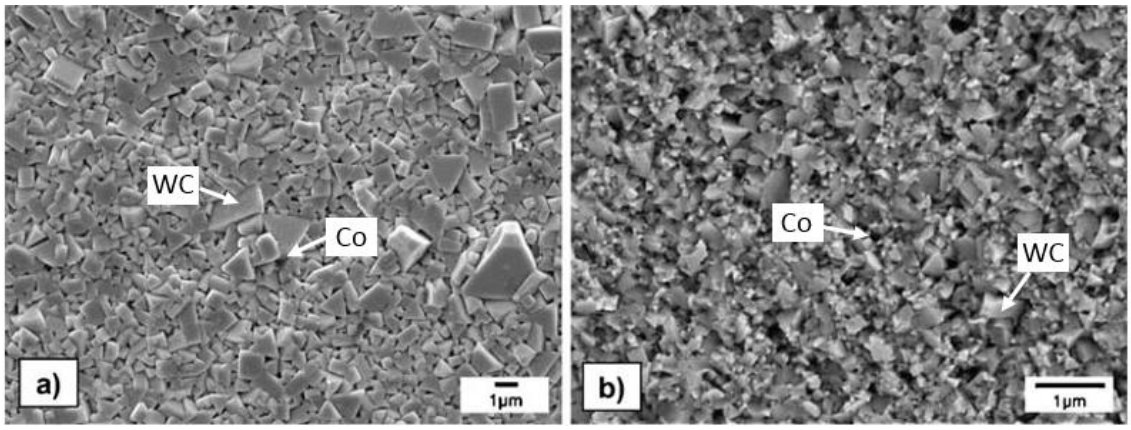


Figure 1. SEM images of WC-Co cemented carbides:
(a) submicron and (b) nano-grained WC-Co cemented carbide [2]

Nanoparticle sized powders can nowadays be consolidated into homogeneous microstructures of extremely high strength, hardness and satisfactory fracture toughness, Figure 2.

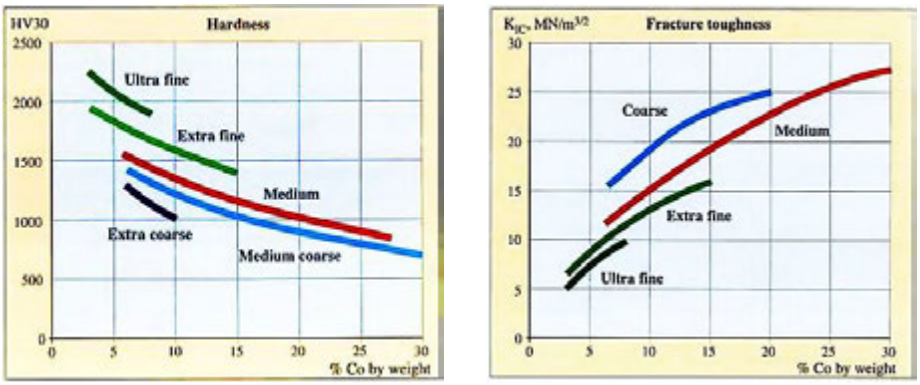


a) b)

Figure 2. (a) Hardness and (b) fracture toughness
as a function of the Co content for various WC grain sizes [3]

This allows longer service life of a cutting tool, application at higher cutting speeds and less tolerances of a machined part [4, 5]. Fracture toughness ($K_{IC}$) is a property that describes the ability of the material to endure the occurrence and spreading of a crack [6]. The properties of these metals are also largely determined by the amount of Co-binder, peculiarly when it comes to mechanical properties such as hardness and fracture toughness.

## MATERIALS AND METHODS

The tests were conducted on cemented carbide samples consolidated by sinter / HIP process as shown in Figure 3. The pre-compacted mixture of cobalt and tungsten carbide powders was sintered in vacuum and pressed by hot isostatic procedure in a protective atmosphere of inert gas (argon). Using this process, samples with 5% Co (WC-5Co), 10% Co (WC-10Co) and 15% Co (WC-15Co) were sintered.

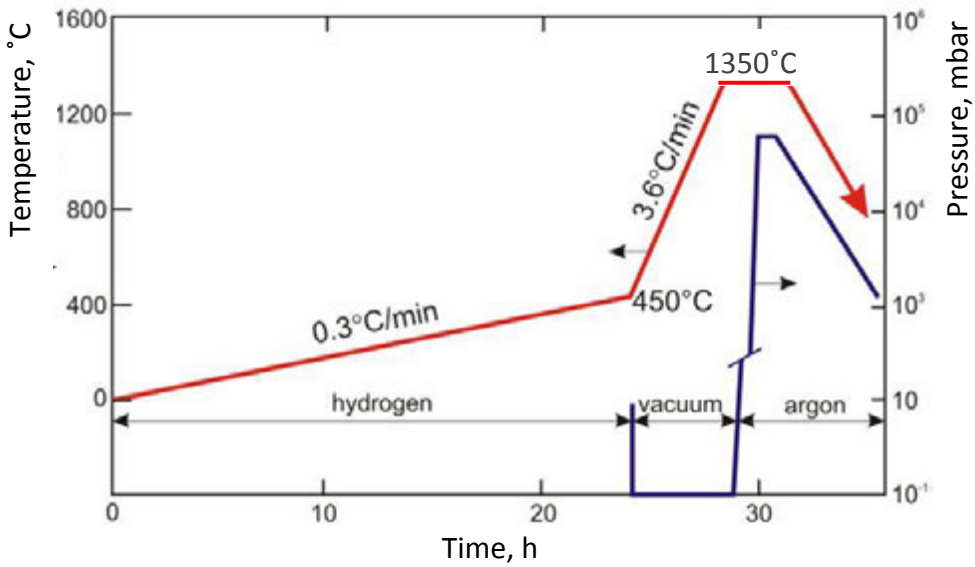


Figure 3. Sinter/HIP cycle

Hardness and fracture toughness of nanostructured cemented carbides requires a carefully prepared test surface to minimize the effect of residual stresses affecting the results [7, 8]. For this reason samples were subjected to metallographic preparation through several grinding and polishing stages:

1. grinding with diamond-abrasive MD-Piano 120 with water cooling,
2. fine grinding with MD-Allegro with a 9 µm granular diamond paste with coolant lubricant (alcohol and water),
3. fine grinding with MD-Largo with 3 µm granular diamond paste with cooling with lubricant,
4. polishing with MD-Dac 3 micron granulated diamond paste with coolant lubricant,
5. finial polishing with MD-Chem tile with colloidal paint.

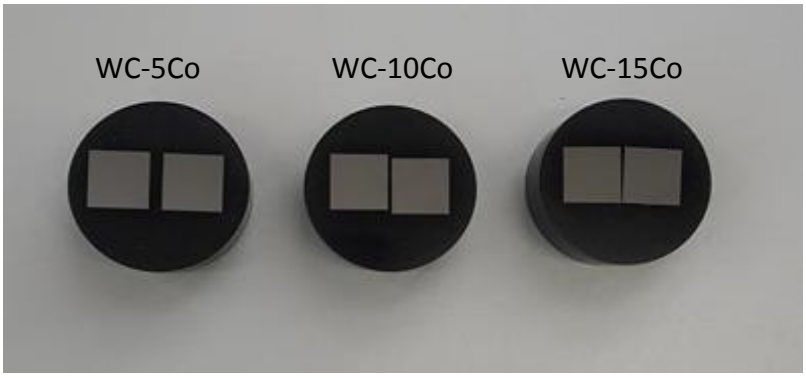


Figure 4. Samples of cemented carbides

Hardness and fracture toughness tests were performed on metalograficly prepared samples shown in Figure 4. Hardness was measured by Vickers method at reference hardness tester (manufactured by Indentec, United Kingdom, type: 5030 TKV) with a load of 294.20 N (HV30). On each sample, a total of 15 measurements were made. The hardness values for Viceks methods were calculated by the following equation:

$$HV = 0{,}1891 \cdot \frac{F}{d_{sr}^2} \tag{1}$$

where:

$d_{sr}$ – mean value of the indentation imprint diagonal, $d_{sr} = \frac{d_1+d_2}{2}$ [mm],

$F$ – indentation force [N].

Fracture toughness was determined by the indentation technique method. Compared to classical test methods this method has a number of advantages, such as simple and fast measurement that does not require sophisticated measurements of cracks, small sample dimensions, and minimum sample preparation at a low price [9, 10]. Indentation technique is based on measuring the length of cracks extending from the tip of the Vickers pyramid imprint, Figure 5.

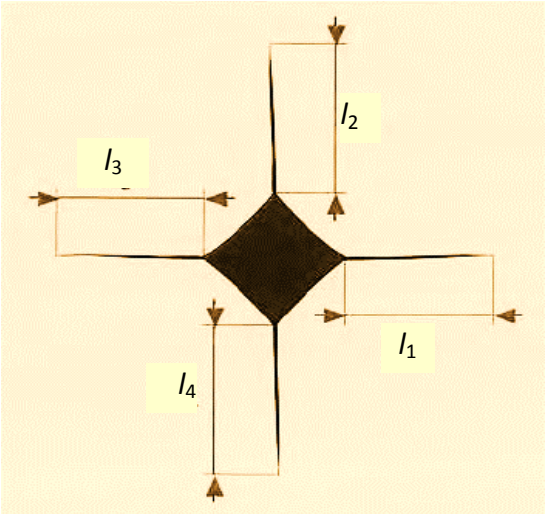


Figure 5. Vickers indentation and cracks occuring in cemented carbide materials

Nowadays, various mathematical models that describe Vickers indentation fracture toughness, such as the Anstis, Niihari, Casellas or Palmqvist models [11] are known. This paper uses Palmqvist's method of calculating fracture toughness which in the calculation includes the values of hardness, indentation force and the length of the cracks originating from the tip of the Vickers imprint. The crack lengths $l_1, l_2, l_3, l_4$, were measured using a

metallographic inverted Olympus GX51F-5 microscope with an integrated DP25 digital camera and an associated image analysis program. The toughness of Palmqvist was determined from the equation [12]:

$$W_K = A \cdot \sqrt{HV} \cdot \sqrt{W_G} \quad (2)$$

where:

$W_K$ [MPa m$^{1/2}$] – fracture toughness,
$A$ – constant (0,0028),
$HV$ – Vickers hardness,
$W_G$ [N/mm] – load and crack length ratio $T$ ($T = l_1 + l_2 + l_3 + l_4$).

Fracture toughness tests were performed with 15 repetitions on each sample.

## RESULTS AND DISCUSSION

Figure 6 shows the imprints of the Vickers pyramid embedded in the surface of the nanostructured cemented carbide WC-5Co, WC-10Co and WC-15Co after testing. Vickers pyramid diagonals are marked with the yellow colour, and the red colour shows the length of the cracks that extend from the tip of the imprint.

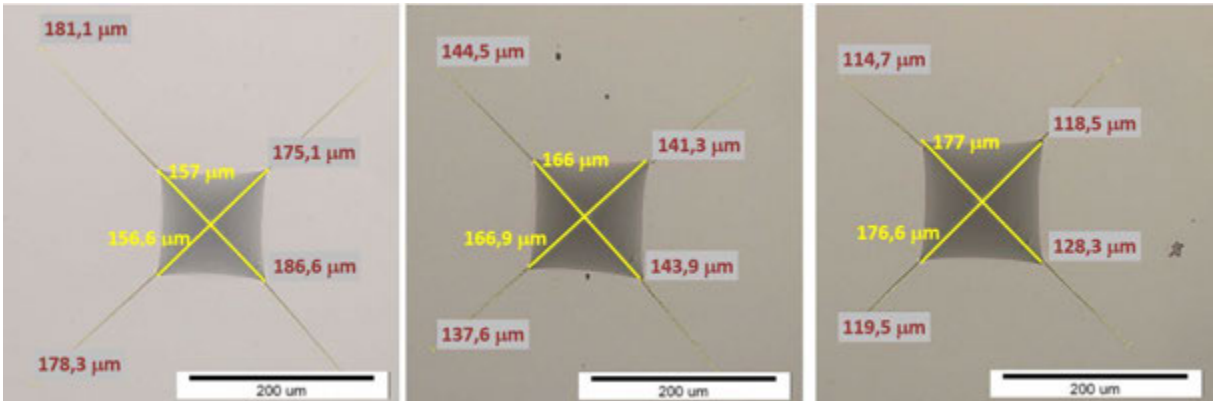


a) b) c)

Figure 6. The Optical micrograph of the Vickers indentation and cracks on the sample: (a) WC-5Co,(b) WC-10Co,(c) WC-15Co

Table 1 shows the mean hardness value from 15 measurements together with the measurement uncertainty and standard deviation. The measurement uncertainty is expressed as the half of the maximum and minimum deviation range.

Table 1. Hardness measurement results

| Sample | Hardness mean value, HV | Measurement uncertenty, HV | Standard deviation, HV |
|---|---|---|---|
| WC-5Co | 2263 | 28.0 | 15.2 |
| WC-10Co | 2014 | 25.6 | 12.3 |
| WC-15Co | 1779 | 12.6 | 6.0 |

It is visible that the hardness values are significantly decreasing with the increase in cobalt content. The difference in hardness of the sample with the 5% and 15% Co is around 500 HV. The dissipation of the hardness measurement results is very small which indicates a relatively homogeneous microstructure of the tested samples. The average hardness value as a cobalt share function is graphically shown in Figure 7.

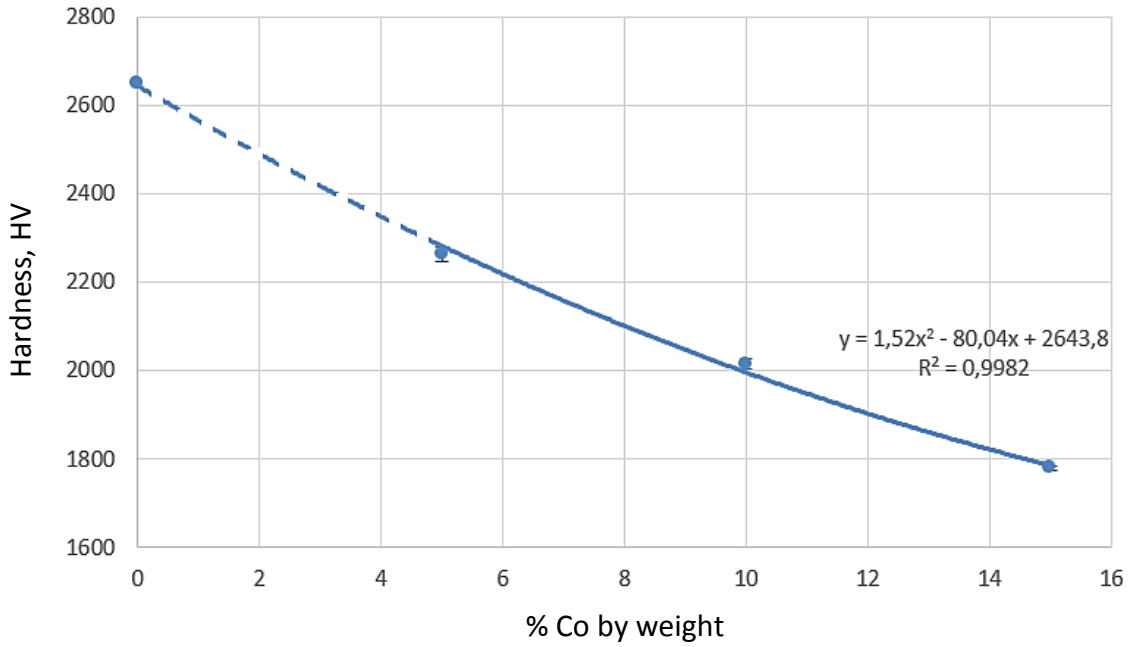


Figure 7. Hardness as a function of the Co content

The regression curve can be described by the exponential equation $Y=1.52 \cdot X^2-80.04 \cdot X+26438$ with a high coefficient of correlation ($R^2$ = 0.9982). If the curve was theoretically prolonged to 0% Co, the result would be the hardness of a WC consistent with

the literature data [13]. By comparing the measured hardness values shown in Figure 2a, the investigated samples are harder than the extra-fine and ultra-fine cemented carbides, which goes in favour of the results carried out earlier that indicate a nanostructured material.

Table 2 contains the mean values of the fracture toughness with the associated measurement uncertainty and standard deviations for all three samples.

Table 2. Fracture toughness measurement results

| Sample | Fracture toughness mean value, MPa·m$^{1/2}$ | Measurement uncertainty, MPa·m$^{1/2}$ | Standard deviation, MPa·m$^{1/2}$ |
|---|---|---|---|
| WC-5Co | 8.39 | 0.15 | 0.10 |
| WC-10Co | 9.03 | 0.16 | 0.07 |
| WC-15Co | 9.35 | 0.15 | 0.09 |

Results clearly show that the values of fracture toughness increase with increasing cobalt content. The dependence of the fracture toughness and cobalt content is shown in Figure 8.

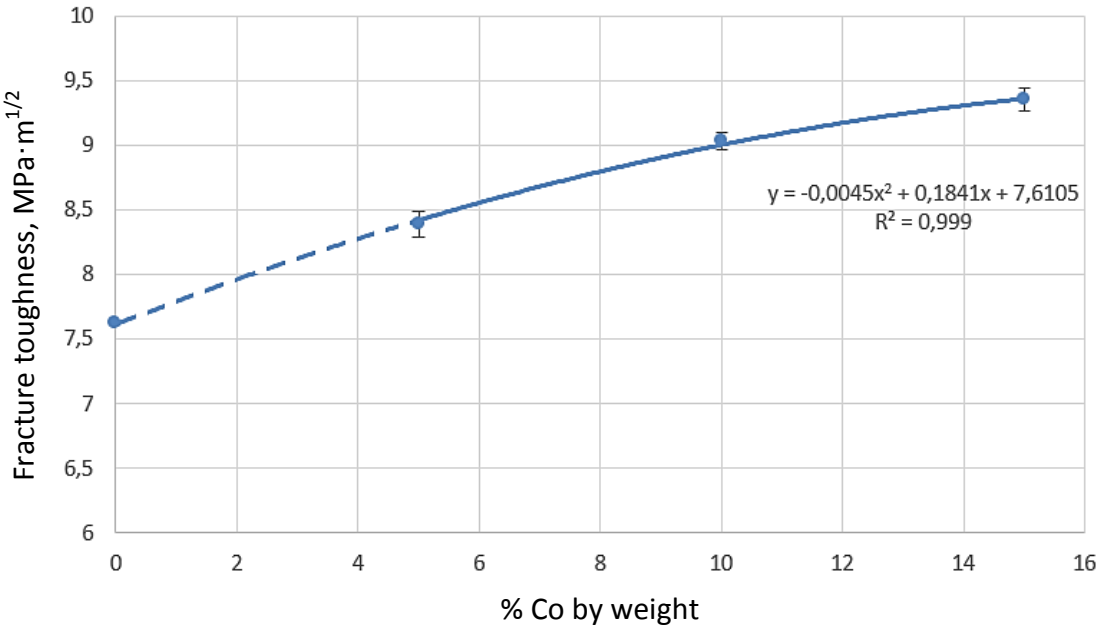


Figure 8. Fracture toughness as a function of the Co content

The obtained regression curve with high correlation coefficient ($R^2$ = 0.999) shows the trend of fracture toughness dependence on the cobalt content in a cemented carbide from 5% to

15% cobalt. Regression equation can be successfully applied to the lower contents of Co since the starting point of the curve point is 7.63 which corresponds to the fracture toughness of the WC which, according to the available literature, is approximately 7.6 MPa·$m^{1/2}$ [13]. When comparing the fracture toughness of extra-fine and ultra-fine cemented carbides with the same Co content (see Figure 2b), the existence of extremely small nano-sized grain is confirmed.

## CONCLUSION

Cemented carbide consolidation by sinter / HIP process has proven to be very successful in the production of nanostructured WC-Co composites of exceptional mechanical properties. Thanks to the simultaneous application of high pressure at high temperature, sintered cemented carbides have much better properties than those obtained from classic compacting and subsequent sintering processes.

All the results obtained on the composite WC-Co system indicate the importance of the Co binder, which means that the matrix share significantly influences the hardness and fracture toughness of the WC-Co material. The test results showed that the hardness of the test material was significantly reduced by the increase in cobalt content. With 1% of cobalt percentage reduction, the reduction in hardness is approximately 50 HV. As opposed to that at higher Co contents the fracture toughness increases, and this is more visible at lower Co amount, while at a higher contents the trend the milder.

Based on the above it can be concluded that the hardness and fracture toughness properties of the tested samples are inversely proportional, and harder WC-Co materials are more likely to form cracks that are will unstably spread in the surface. WC-Co systems with more cobalt content are tougher and thus more resistant to initiation of cracks, but have a lower hardness. Since cemented carbide cutting tools often require high hardness and high fraction toughness, it is necessary to find a compromise between these two properties and choose the appropriate cobalt content that provides the optimal combination of toughness and hardness for a particular application.

Alongside the chemical composition, cemented carbide properties are largely determined by the size of the WC grain. From the results presented and comparing with already known hardness and fracture toughness of ultra-fine and extra-fine cemented carbides, it can be concluded that the investigated materials are nanostructured materials. This is also confirmed by the results of earlier metallographic investigations. The nano size of the grain in these samples provides high hardness, higher than that of large grained cemented carbide. High hardness with good fracture toughness are two dominant features of nanostructured cemented carbides especially when it comes to their application for cutting tools because they allow for faster, cheaper and higher quality production.

**REFERENCES**

[1] D. Ćorić, Special Metallic Materials - Part III, textbook, Faculty of Mechanical Engineering and Naval Architecture University of Zagreb, Zagreb, 2017.
[2] M. Brieseck, W. Lengauer, B. Gneiß, K. Wagner, S. Wagner, A straightforward method for analysing the grain-size distribution in tungsten carbide - cobalt hardmetals, Microchimica Acta, 168 (2010) 3-4, pp. 309-316.
[3] Sandvik Hard Materials, Understanding Cemented Carbide, Available online: http://allaboutmetallurgy.com/wp/wp-content/uploads/2016/12/UnderstandCementedCarbide.pdf (Downloads 12.03. 2018.)
[4] V. Bonache, M. D. Salvador, D. Busquets, P. Burguete, E. Martinez, F. Sapina, E. Sanchez, Synthesis and processing of nanocrystalline tungsten carbide: Toward cemented carbides with optimal mechanical properties, Int. J. Refract. Met. Hard Mater., 29 (2011) pp. 78-84.
[5] T. Aleksandrov Fabijanić, Ž. Alar, D. Ćorić, Influence of consolidation process and sintering temperature on microstructure and mechanical properties of near-nano and nanostructured WC-Co Cemented Carbides, Int. J. Refract. Met. Hard Mater., 54 (2015) pp. 82-89.
[6] D. Ćorić, Ž. Alar, Selected chapters from the mechanical properties of the material, textbook, Faculty of Mechanical Engineering and Naval Architecture University of Zagreb, Zagreb, 2016.
[7] D. K. Shetty, I. G. Wright, P. N. Mincer, A. H. Clauer, Indentation fracture toughness of WC-Co cermets, J. Mater. Sci., 20 (1985) pp. 1873-1882.
[8] M. W. Barsoum, Series in Material Science and Engineering Fundamentals of Ceramics, Taylor & Francis: Abingdon, UK, 2003.
[9] F. Sergejev, M. Antonov, Comparative study on indentation fracture toughness measurements on cemented carbides, Proc. Estonian Acad., Sci. Eng., 12 (2006) pp. 388-398.
[10] S. Sheikh, R. M'Saoubi, P. Flasar, M. Schwind, T. Persson, J. Yang, L. Llanes, Fracture toughness of cemented carbides: Testing method and microstructural effect, Int. J. Refract. Met. Hard Mater., 49 (2015) pp. 153-160.
[11] G. D. Quinn, Fracture toughness of ceramics by the Vickers indentation crack lenght method: A critical review, National Institute of Standards and Technology, Gaithersburg, 2006.
[12] International Standard Organisation. ISO 28079:2009: Hardmetals-Palmqvist Toughness Test. Available online: https://www.iso.org/obp/ui/#iso:std:iso:28079:ed-1:v1:en (Downloads 15.12.2017).
[13] R. W. Armstrong, The Hardness and Strength Properties of WC-Co Composites, Materials, 4 (2011) pp. 1287-1308.

17th INTERNATIONAL FOUNDRYMEN CONFERENCE
Hi-tech casting solution and knowledge based engineering
Opatija, May 16th-18th, 2018
http://www.simet.hr/~foundry/

# COMPARISON OF PHOTOCATALYST PREPARATION BY $TiO_2$ DEPOSITION ON A SUPPORT USING DIFFERENT METHODS

# USPOREDBA PRIPRAVE FOTOKATALIZATORA NANOŠENJEM $TiO_2$ NA NOSAČ RAZLIČITIM METODAMA

**Igor Jajčinović[1]*, Matija Borošić[1], Ivan Brnardić[1], Ivana Grčić[2], Stanislav Kurajica[3]**

[1] University of Zagreb Faculty of Metallurgy, Sisak, Croatia
[2] University of Zagreb Faculty of Geotechnical Engineering, Varaždin, Croatia
[3] University of Zagreb Faculty of Chemical Engineering and Technology, Zagreb, Croatia

**Oral presentation**
*Original scientific paper*

**Abstract**

The issue of water protection has long been one of the most important environmental issues. When it comes to the micropollutants, one of the greatest problems is pharmaceuticals. Their detection is not only a consequence of the development of analytical methods but also of the massive use of pharmaceuticals and their increasing concentration in the environment. In this paper, advanced photocatalysts were prepared and characterized by two different processes of titanium dioxide immobilization ($TiO_2$) on the support through sol-gel method. Immobilization was performed by the classical and microwave-assisted drying, and the catalysts were characterized by scanning electron microscopy (SEM), energy dispersion X-ray spectrometry (EDS) and X-ray diffraction analysis (XRD). The photocatalyst activity was tested through the photocatalytic degradation of salicylic acid (SA) in the pilot reactor, monitoring the degradation by the UV-vis spectrometry.

**Keywords**: *titanium dioxide, imobilization, sol-gel, photocatalysis*

*Corresponding author (e-mail address): *jajcinovic@simet.hr*

**Sažetak**

Problematika zaštita voda već dugo je jedna od najvažnijih tema zaštite okoliša. Kada se govori o mikroonečišćenjima u vodi jedan od najvećih problema su farmaceutici. Utvrđivanje njihove prisutnosti nije samo posljedica razvoja analitičkih metoda nego i masovne uporabe farmaceutika te njihove sve veće koncentracije u okolišu. U ovom radu su pripremljeni i karakterizirani napredni fotokatalizaori dobiveni kroz dva različita postupka imobilizacije titanijeva dioksida ($TiO_2$) na nosač sol-gel metodom. Imobilizacija je provedena klasičnim i mikrovalnim sušenjem te su katalizatori karakterizirani pretražnom elektronskom mikroskopijom (SEM), energijsko disperzivnom

rendgenskom spektroskopijom (EDS) i rendgenskom difrakcijskom analizom (XRD). Aktivnost fotokatalizatora je ispitana kroz sposobnost fotokatalitičke razgradnjom salicilne kiseline (SA) u pilot reaktoru, čija je razgradnja praćena UV-ViS spektrometrom.

***Ključne riječi**: titan dioksid, imobilizacija, sol-gel, fotokataliza*

## UVOD

Onečišćenje okoliša i njegovo uništavanje je veoma ozbiljan problem s kojim se suočava današnji čovjek [1,2]. Veliki problem u zaštiti okoliša su onečišćenje voda i vodenih tokova. Ovim problemom znanost se već dugo bavi, ali konstantno se pokušava inovativnim i poboljšanim metodama podići pročišćavanje voda na novu razinu. Uz pitke vode pročišćavaju se industrijske otpadne vode, napojne vode za termoelektrane, rashladne vode za industrijska postrojenja i komunalne otpadne vode.

Brzi razvoj industrije, poljoprivrede i rasta broja stanovništva uzrokuje smanjenje kvalitete vode odnosno njezino onečišćenje. Onečišćenje vode uzrokuje neravnotežu u okolišu koja se očituje na ljudsko zdravlje, nedostatke vode, na cijenu vode i slično [3]. Pojava mikroonečišćujućih tvari u pročišćenim otpadnim vodama te vodama za piće potaknula je znanstvenu zajednicu da usmjeri svoj rad prema pronalasku rješenja uklanjanja istih. U mikroonečišćujuće tvari se ubrajaju humani i veterinarski lijekovi (farmaceutici), kemikalije iz industrije te pesticidi koji uslijed kontinuiranih proizvodnih procesa stalno pronalaze svoje mjesto u okolišu. Zbog svojih fizikalno-kemijskih svojstava mnoge od tih supstanci ili njihovih bioaktivnih metabolita mogu završiti u vodama gdje akumulacijom izazivaju neželjene učinke kod kopnenih ili vodenih organizama [4,5].

Važnost problema prisutnosti mikrooneišćenja u vodenim tokovima lako je vidljiva kad se pogledaju „farmaceutski profili“ voda koji pokazuju da u jednoj litri otpadne vode može biti do više desetaka mikrograma farmaceutika što je zabrinjavajuće jer su lijekovi dizajnirani da budu učinkoviti pri malim koncentracijama [6]. Trenutno se na industrijskoj razini u svijetu koriste dva postupka pročišćavanja voda od mikroonečišćujućih tvari, adsorpcija na aktivni ugljen i ozonacija. S obzirom na skupoću navedenih postupaka znanstvenici rade na pronalasku jeftinijih rješenja, a jedno od njih je napredni oksidacijski postupak, fotokataliza gdje dolazi do potpune razgradnje onečišćenja (mineralizacije). U tu svrhu koriste se fotokatalizatori, a jedan od njih je titanijev dioksid ($TiO_2$) [7]. $TiO_2$ je najčešće korišteni fotokatalizator zbog njegove niske cijene, kemijske i termičke stabilnosti, niske toksičnosti te relativno visoke katalitičke aktivnosti [8,9]. UV/$TiO_2$ zračenjem fotokatalizatora $TiO_2$ nastaju hidroksilni radikali, •OH [10] koji kao neselektivni oksidansi svojim oksidacijskim potencijalom gotovo potpuno pretvaraju organsku tvar u vodu i $CO_2$, to jest uzrokuju mineralizaciju vode [11,12]. Zahvaljujući ovoj činjenici, $TiO_2$ fotokataliza je u novije vrijeme našla primjenu u obradi otpadnih voda pri čemu površina prekrivena $TiO_2$ ostaje čista nakon UV ozračivanja [13,14]. Iako se $TiO_2$ najčešće koristi u suspendiranom obliku, imobilizacija

katalizatora smatra se korisnijom zbog lakšeg uklanjanja $TiO_2$ iz sustava i mogućnosti višekratnog korištenja imobiliziranog katalizatora [15]. Ideja o imobilizaciji fotokatalizatora na inertni nosač privukla je pažnju zbog mogućnosti smanjenja troškova u separacijskim procesima nakon fotokatalize. Količina fotokatalizatora korištena u imobiliziranom stanju značajno je manja u odnosu na fotokatalizator korišten u suspenziji što iziskuje izradu posebnih oblika reaktora.

Imobilizacija $TiO_2$ je do sada postignuta na različitim nosačima uključujući staklo, silikagel, metal, keramiku, polimere, aktivni ugljen i itd. [16,17]. Za industrijsku primjenu, od fotokatalizatora se očekuje mogućnost recikliranja i upotreba u više ciklusa što se postiže kemijskim vezanjem $TiO_2$ na nosač. Stoga, kako učinkovito imobilizirati $TiO_2$ putem kemijske veze te zadržati visoku fotokatalitičku aktivnost u upotrebi za više ciklusa postalo je predmet mnogih istraživanja. Kao jedan od načina imobilizacije $TiO_2$ na nosač ističe se sol-gel metoda [18,19,20].

Cilj ovog rada je usporediti dva različita načina priprave fotokatalizatora imobilizaciom $TiO_2$ na nosač sol-gel metodom uporabom klasičnog ili mikrovalnog sušenja. Nakon priprave fotokatalizatori su vagani, karakterizirani te su ispitana njihova fotokatalitička svojstva.

## MATERIJALI I METODE

Za pripremu imobiliziranog sloja korišten je $TiO_2$ (Aeroxide® P25, Evonik, Njemačka) nanošenjem na staklenu mrežicu (CM 300/300, $\rho$= 610 g/m$^2$) sol-gel metodom. Staklene mrežice su izrezane na dimenziju rektora i izvagane. Suspenzija iz koje se nanosi $TiO_2$ na staklenu mrežicu pripravljena je miješanjem $TiO_2$ s destiliranom vodom i etanolom (voda:etanol = 1:1) na magnetskoj miješalici. pH vrijednosti suspenzije podešavana je dodavanjem octene kiseline uz miješanje do pH 1,5-2. Nakon postizanja željene pH vrijednost, nastavilo je miješanje suspenzije u periodu od 15 minuta, nakon čega je provedena homogenizacija ultrazvukom u trajanju od 3 minute (ultrazvučna kupelj snage 120 W, frekvencija 40 kHz). Slijedilo je dodavanje tetraetoksisilana (TEOS, VWR Cemical, SAD) i dalje miješanje u periodu od 60 minuta pri temperaturi od 50°C. U tako priređenu suspenziju uranjane su staklene mrežice te su sušene. Sušenje se provodilo na dva načina; u sušioniku na 70°C 30 minuta i u komercijalnoj mikrovalnoj pećnici pri snazi 900 W 3 minute. Postupak uranjanja i sušenja mrežica ponavljan je 5 puta. Priređene mrežice su ostavljene na zraku 7 dana, nakon čega su ispirane destiliranom vodom, osušene i izvagane kako bi se odredila masa nanesenog sloja. Čiste mrežice i mrežice s $TiO_2$ dobivene opisanim postupkom snimane su pretražnim elektronskim mikroskopom (SEM, TESCAN VEGA 5136MM) opremljenim detektorom za energijsku disperzivnu rendgensku spektroskopiju (EDS) sa svrhom ispitivanja kemijskog sastava. Mrežice za SEM/EDS analizu su prethodno učvršćene na nosač pomoću dvostrane samoljepljive vodljive ugljikove trake te naparene slojem zlata-platine. Utjecaj sušenja na kristalnu strukturu $TiO_2$ je ispitan rendgenskom difrakcijskom analizom (Shimadzu XRD 6000 difraktometar). Fotokatalitička svojstva katalizatora su

ispitana kroz razgradnju salicilne kiseline (SA, Kemika, Hrvatska) u pripremljenoj 0,2 mmol/dm$^3$ modelnoj otopini. Za praćenje reakcije fotokatalitičke razgradnje korišten je UV-VIS spektrofotometar (Perkin Elmer LAMBDA 35, 200-700 nm uz brzinu snimanja od 480 nm/min). Ispitivanja fotokatalitičkih svojstava provodila su se u šaržnom pilot fotoreaktoru pravokutne geometrije (dimenzija 4,5 x 17,5 cm) uz recirkulaciju pomoću peristaltičkih pumpi s protokom od 48 cm$^3$/min. Izvor simuliranog sunčevog zračenja (UV-B 2%/13 W) postavljen je 7 cm iznad površine reakcijske otopine te je natkriven sjenilom/reflektivnom površinom od Al-lima s ciljem ravnomjernog osvjetljavanja reaktorskog prostora.

Mrežica s imobiliziranim fotokatalizatorom postavljena je na dno reaktora te je dodana modelna otopina SA 100 cm$^3$. Na početku postupka uzet je uzorak SA 2 cm$^3$ nakon čega je reaktor ostavljen u mraku 30 minuta te je ponovljeno uzimanje uzorka. Po završetku faze u mraku uključen je izvor simuliranog sunčevog zračenja te su uzorci uzimani periodički 15, 30, 60, 90, 120 i 150 minuta. Isto tako provela su se ispitivanja slijepe probe bez katalizatora, odnosno utjecaja svjetlosnog zračenja na potencijalnu fotolizu salicilne kiseline.

## REZULTATI I RASPRAVA

Kako bi se dokazala prisutnost $TiO_2$ na površini staklenih mrežica uzorci su snimani SEM-om (slika 1).

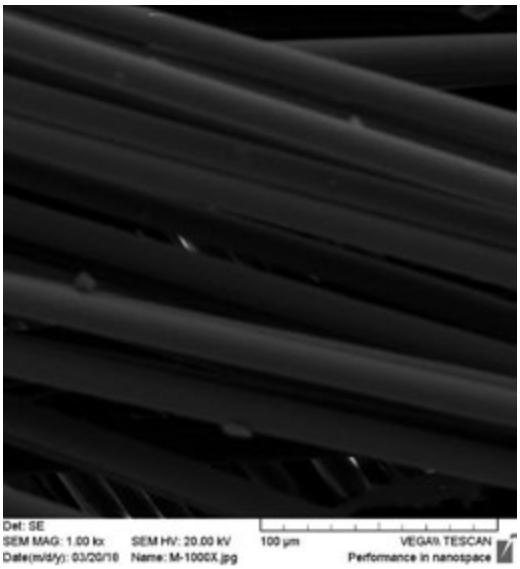


(a)

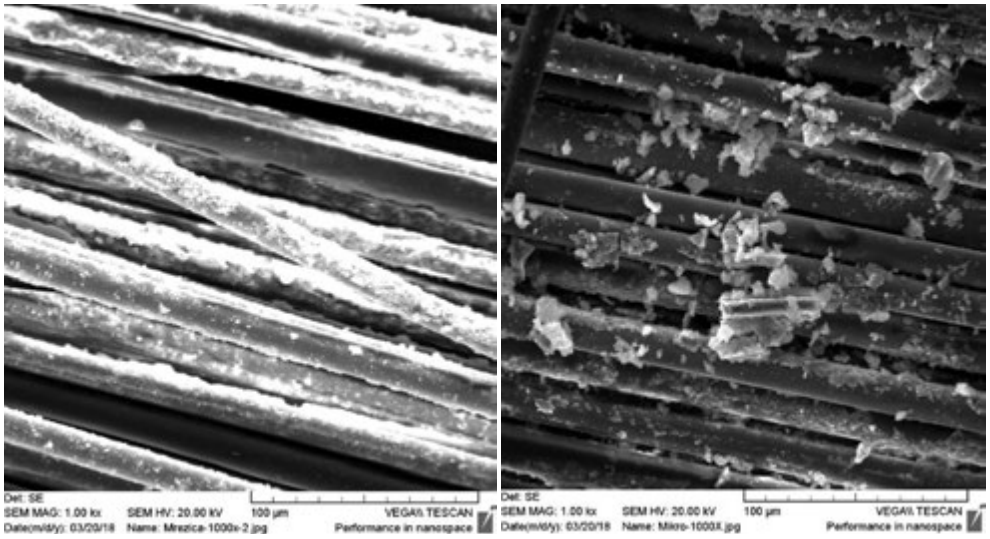


(b) (c)

Slika 1. SEM snimke staklenih mrežica: (a) bez $TiO_2$, (b) s $TiO_2$ sušene klasičnim načinom, (c) s $TiO_2$ sušene mikrovalovima

Usporedbom slika 1a, 1b i 1c može se zaključiti da je došlo do vezanja fotokatalizatora $TiO_2$ na staklene mrežice te je uočena i razlika u veličini vezanih čestica. Čestice većih dimenzija vezane na staklena vlakna su nastale prilikom primjene mikrovalnog sušenja.
Pomoću EDS analize utvrđena je prisutnost $TiO_2$ na nosaču nakon imobilizacije. Primjer rezultata EDS analize za imobilizaciju provedenu uz pomoć mikrovalnog sušenja prikazan je na slici 2, gdje je crnom crtom označeno područje provedene analize.

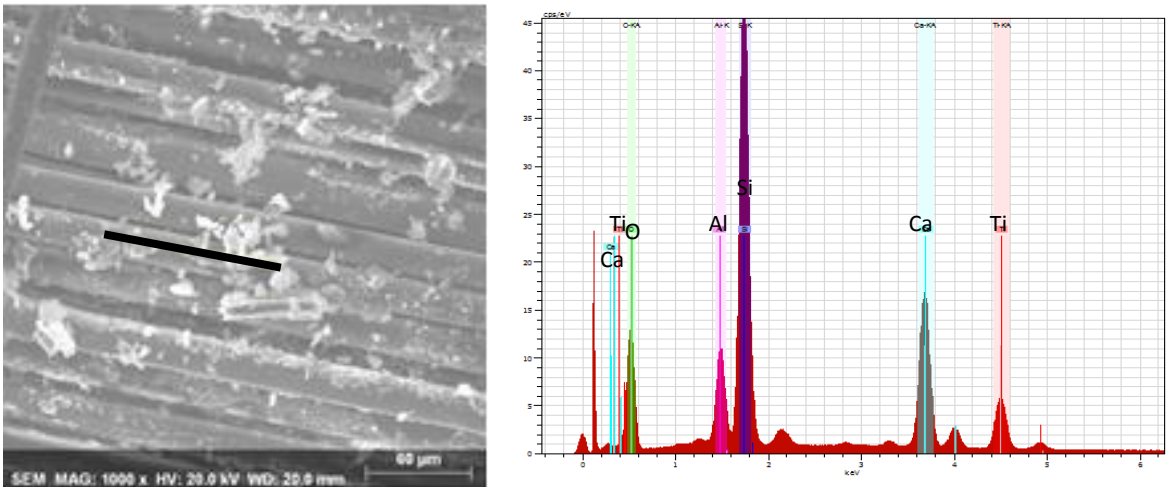


(a) (b)

Slika 2. SEM/EDS analiza: (a) SEM slika područja provodene EDS analize, (b) EDS rezultati

Mase mrežica prije i nakon nanošenja $TiO_2$ su dane u tablici 1 te je masa imobiliziranog $TiO_2$ izračunata stehiometrijski iz mase nanesenog sloja.

Tablica 1. Mase staklenih mrežica prije i nakon nanošenja $TiO_2$

| - | m (staklene mrežice), g | m (staklena mrežica + $TiO_2$), g | m (nanesenog sloja), g | $m_{stehiometrijski}$ ($TiO_2$ na mrežici), g |
|---|---|---|---|---|
| $m_K$ | 7,5953 | 7,9781 | 0,3828 | 0,2647 |
| $m_M$ | 8,4088 | 8,9649 | 0,5561 | 0,3845 |

$m_K$ – mrežica sušena klasičnim načinom; $m_M$ – mrežica sušena pomoću mikrovalova

Iz tablice 1 se vidi da je masa imobiliziranog sloja kod mikrovalnog sušenja za oko 30% veća u usporedbi s masom dobivenom klasičnim sušenjem.
Utjecaj mikrovalnog sušenja na $TiO_2$ ispitan je rendgenskom difrakcijskom analizom te su rezultati prikazani na slici 3 gdje su uspoređeni difraktogrami $TiO_2$ P25 i $TiO_2$ nanesenog pomoću silana na nosač sušenog mikrovalovima.

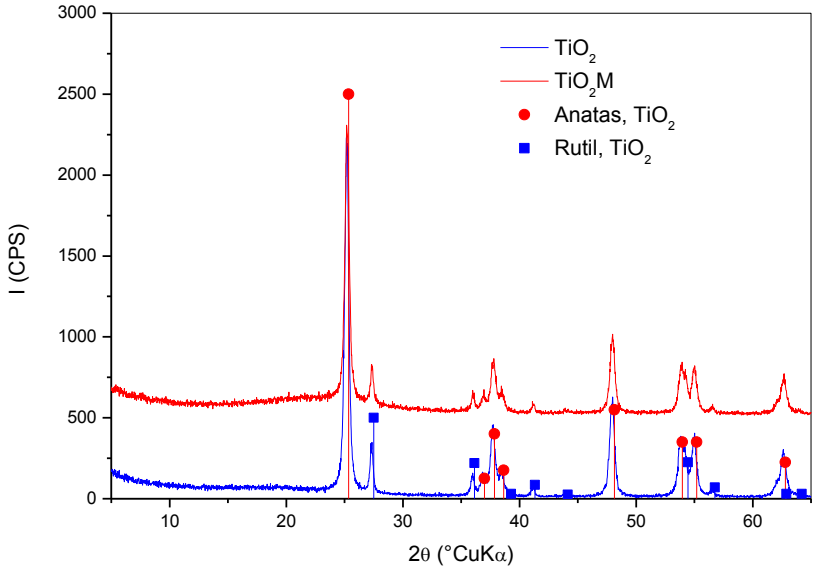


Slika 3. Difraktogrami $TiO_2$ i silanom vezanim $TiO_2$ M uz sušenje mikrovalovima

Na temelju lokalnog porasta bazne linije primjetnog na difraktogramu uzorka nanesenog pomoću silana može se zaključiti da je u uzorku prisutna amorfna faza nastala hidrolizom TEOS-a. Prisutnost ove faze smanjuje relativni udio anatasa i rutila te utječe na smanjenje specifične površine. Zajedno sa slikama dobivenih SEM analizom kroz usporedbu slika 1b i 1c dolazimo do istog zaključka.

Ispitivanje fotokatalitičke aktivnost pripravljenih fotokatalizatora su provedena u šaržnom reaktoru gdje je praćena razgradnja salicilne kiseline. Na slici 4 su uspoređeni rezultati fotokatalize bez i s fotokatalizatorima dobivenih klasičnim (K) i mikrovalnim (M) sušenjem.

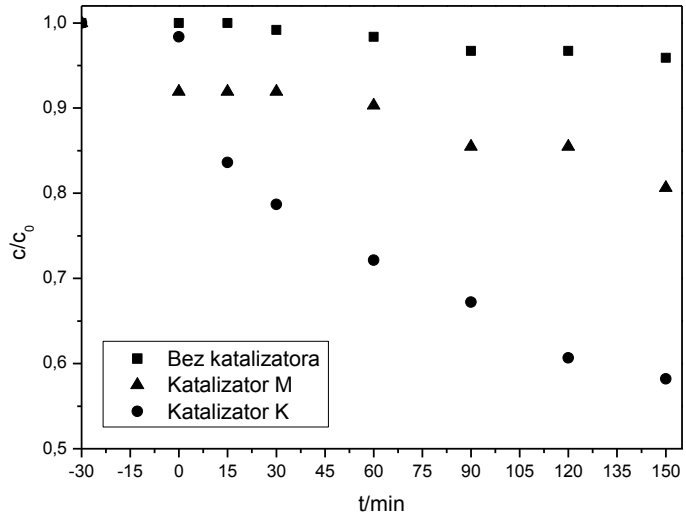


Slika 4. Fotokatalitička razgradnja SA bez katalizatora te katalizatorom K i M

Usporedbom rezultata fotokatalitičke razgradnje salicilne kiseline zaključuje se da je najbolji rezultat postignut prilikom upotrebe fotokatalizatora pripravljenog klasičnim sušenjem. Kao što je i očekivano razgradnja salicilne kiseline pod utjecajem svijetla bez prisutnosti fotokatalizatora je gotovo zanemariva. Slabiji rezultati dobiveni za fotokatalizator pripravljen mikrovalnim sušenjem su u korelaciji s rezultatima dobivenih SEM i XRD analizom.

## ZAKLJUČAK

U radu je provedena imobilizacija $TiO_2$ na nosač sol-gel metodom kroz dva različita načina, upotrebom klasičnog i mikrovalnog sušenja. Nakon imobilizacije fotokatalizatora provedena je karakterizacija i ispitana su fotokatalitička svojstva. SEM i EDS analizom dokazana je prisutnost $TiO_2$ na staklenim mrežicama, te je vidljivo da su kod mikrovalnog sušenja čestice $TiO_2$ nešto veće nego kod klasičnog sušenja. Usporedbom masa imobiliziranog sloja vidimo da je kod mikrovalnog sušenja oko 30% veća masa imobiliziranog sloja što rezultira i većom masom $TiO_2$. Veća masa $TiO_2$ trebala bi rezultirati s boljim fotokatalitičkim svojstvima, no utvrđeno je upravo suprotno što može biti rezultat mikrovalnog sušenja. Ta hipoteza je potvrđena rendgenskom difrakcijskom analizom, a rezultati su u korelaciji s rezultatima dobivenim elektronskom mikroskopijom.
Iz dobivenih rezultata možemo zaključiti da je uporaba klasičnog sušenja za pripremu imobilizirano fotokatalizatora sol-gel metodom bolja od uporabe mikrovalova. Uporaba mikrovalova rezultira većom masom $TiO_2$, ubrzava proces pripreme fotokatalizatora što rezultira uštedom energije i vremena, ali narušava fotokatalitička svojstva. Daljnja istraživanja će biti usmjerena prema pronalaženju načina uporabe mikrovalova kroz smanjenje snage i pronalaženje optimalnog vremena za mikrovalno sušenje.

## LITERATURA

[1] N. Khalid, A. Majid, M. Bilal Tahir, N. A. Niaz, S. Khalid, Carbonaceous-$TiO_2$ nanomaterials for photocatalytic degradation of pollutants: A review, Ceramics International, 43 (2017) pp. 14552-14571.
[2] J. Schneider, M. Matsuoka, M. Takeuchi, J. Zhang, Y. Horiuchi, M. Anpo, D. W. Bahnemann, Understanding $TiO_2$ Photocatalysis: Mechanisms and Materials, Chem. Rev., 114 (2014) pp. 9919-9986.
[3] N. Emmanuel, D. Duranoğlu, B. C. Beniamin, New Challenges Of Water Pollution In Europe And Their Socioeconomical, Economic Science Series, 25 (2016) pp. 67-74.
[4] Y. Luoa, W. Guo, H. H. Ngo, L. D. Nghiem, F. I. Hai, J. Zhang, S. Liang, X. C. Wang, A review on the occurrence of micropollutants in the aquatic environment and their fate and removal during wastewater treatment, Science of The Total Environment, 474 (2014) pp. 619-641.
[5] P. M. Thomas, D. G. Foster, Tracking acidic pharmaceuticals, caffeine, and triclosan through, Environmental Toxicology and Chemistry, 24 (2005) pp. 25-30.

[6] V. Vrček, Farmakoekologija – okolišna sudbina lijekova, Kem. Ind., 66 (2017) 3-4, pp. 135-144.
[7] J. Altmann, A. S. Ruhl, F. Zietzschmann, M. Jekel, Direct comparison of ozonation and adsorption onto powdered activated carbon for micropollutant removal in advanced wastewater treatment, Water Research, 55 (2014) pp. 185-193.
[8] B. Plavac, I. Grčić, I. Brnardić, V. Grozdanić, S. Papić, Kinetic study of salicylic acid photocatalytic degradation using sol–gel anatase thin film with enhanced long-term activity, Reaction Kinetics, Mechanisms and Catalysis, 120 (2017) pp. 385-401.
[9] H. D. Traid, M. L. Vera, A. E. Ares, M. I. Litter, Porous titanium dioxide coatings obtained by anodic oxidation for photocatalytic applications, Procedia Materials Science, 9 (2015) pp. 619-626.
[10] D. Mukherjee, S. Barghi, A. K. Ray, Preparation and Characterization of the $TiO_2$ Immobilized Polymeric Photocatalyst for Degradation of Aspirin under UV and Solar Light, Processes, 2 (2014) pp. 12-23.
[11] P. R. Gogate, A. B. Pandit, A review of imperative technologies for wastewater treatment I: oxidation technologies at ambient conditions, Advances in Environmental Research, 8 (2004) pp. 501-551.
[12] Y. Wang, Y. He, Q. Lai, M. Fan, Review of the progress in preparing nano $TiO_2$: An important environmental engineering material, Journal of environmental sciences, 26 (2014) pp. 2139-2177.
[13] J. M. Dostanić, Proučavanje fotodegradacije arilazo piridonskih boja, doktorska disertacija, Tehnološko-metalurški fakultet, Univerzitet u Beogradu, 2012.
[14] G. Lusvardi, C. Barani, F. Giubertoni, G. Paganelli, Synthesis and Characterization of $TiO_2$ Nanoparticles for the Reduction of Water Pollutants, Materials, 10 (2017) 1208.
[15] S. Souzanchi, F. Vahabzadeh, S. Fazel, S. N. Hosseini, Performance of an Annular Sieve-Plate Column photoreactor using immobilized $TiO_2$ on stainless steel support for phenol degradation, Chemical Engineering Journal, 223 (2013) pp. 268-276.
[16] L. Y. Cherif, I. Yahiaoui, F. Aissani-Benissad, K. Madi, N. Benmehdi, F. Fourcade, A. Amrane, Heat Attachment Method for the Immobilization of $TiO_2$ on Glass Plates: Application to Photodegradation of Basic Yellow Dye and Optimization of Operating Parameters Using Response Surface Methodology Eng. Chem. Res., 53 (2014) pp. 3813-3819.
[17] D. Mukherjee, S. Barghi, A. K. Ray, Preparation and Characterization of the $TiO_2$ Immobilized Polymeric Photocatalyst for Degradation of Aspirin under UV and Solar Light, Processes, 2 (2014) pp. 12-23.
[18] I. Ivanova, J. Schneider, H. Gutzmann, J. O. Kliemann, F. Gärtner, T. Klassen, D. Bahnemann, C. B. Mendivea, Photocatalytic degradation of oxalic and dichloroacetic acid on $TiO_2$ coated metal substrates Catalysis Today, 209 (2013) pp. 84-90.
[19] Z. Essalhi, B. Hartiti, A. Lfakir, M. Siadat, P. Thevenin, Optical properties of $TiO_2$ thin films prepared by Sol Gel method J. Mater. Environ. Sci., 7 (2016) pp. 1328-1333.
[20] Q. Yin, J. Xiang, X. Wang, X. Guo, T. Zhang, Preparation of highly crystalline mesoporous $TiO_2$ by sol–gel method combined with two-stepcalcining process Journal of Experimental Nanoscience, 11 (2016) pp. 1127-1137.

17th INTERNATIONAL FOUNDRYMEN CONFERENCE
Hi-tech casting solution and knowledge based engineering
Opatija, May 16th-18th, 2018
http://www.simet.hr/~foundry/

# ANALYSIS OF THE LOW ENERGY LAYERING FRACTURE IN Al-2.5Mg-0.7Li ALLOY

**Franjo Kozina[1]*, Zdenka Zovko Brodarac[1], Mitja Petrič[2]**

[1] University of Zagreb Faculty of Metallurgy, Sisak, Croatia
[2] University of Ljubljana Faculty of Natural Science and Engineering, Ljubljana, Slovenia

**Oral presentation**
*Original scientific paper*

**Abstract**

The mechanism of nucleation and propagation of low energy layering fracture, observed during thermo-mechanical testing of Al-2.5Mg-0.7Li alloy in as cast condition, was analyzed. Since the low energy layering fracture is affected by Li segregations and microstructural constituents' development, solidification sequence of Al-2.5Mg-0.7Li alloy was investigated in equilibrium and non-equilibrium conditions. Results of the investigations have shown that Mg has more pronounced effect on low energy layering fracture due to reducing solubility of Li in liquid phase and $\alpha_{Al}$, maximizing precipitation of hardening ($Al_3Li$) δ' phase, ternary ($Al_2LiMg$) T phase and ($Al_8Mg_5$) β phase, and reducing ductility by solid solution hardening.

***Keywords***: *Al-Mg-Li alloy, phase precipitation, Li solubility, solidification sequence, low energy delamination fracture*

*Corresponding author (e-mail address): *fkozin@simet.hr*

## INTRODUCTION

Density reduction, stiffness increase [1], increase in fracture toughness [2], fatigue crack growth resistance [3] and crack propagation behavior [4] (nucleation and growth of small [5] and long [6] cracks) as well as enhanced corrosion resistance [7] are considered to be the benefits of aluminum-magnesium-lithium (Al-Mg-Li) alloy application. The mechanical properties of Al-Mg-Li alloys are the result of microstructural constituents' development during solidification and/or thermo-mechanical processing [8]. Microstructural constituents characteristic for Al-Mg-Li alloys are nature and volume fraction of strengthening precipitates [9], amount of coherent precipitates that alter the planar slip deformation behavior [10], content, size and distribution of coarse and angular equilibrium precipitates [9] as well as formation and widening of low precipitation frequency zone (PFZ) [1].

Microstructural constituents' developed during solidification are influenced by chemical composition, thermodynamic parameters and processing parameters.
Each weight percent of Li added decreases the density by approximately 3 % [11] and increases Young's modulus by 6 % [12], for the additions up to 4 wt. % [13]. However, maximum strength is obtained in the range of 1.1-1.3 wt.% Li [14]. Increasing of Li content above 1.3 wt.% will result in yield and tensile strength decrease, respectively [15]. Furthermore, according to [16, 17] alloys with Li content greater than 1 wt.% are prone to low energy layering fracture. Layering fracture is characterized by the failure along the grain boundaries [18]. Low energy layering fracture is attributed to Li segregations at grain boundaries [18, 19], high frequency of grain boundary precipitates [20] followed by the formation of PFZ at the grain boundaries [21] and planar slip band formation [22]. The grain boundary segregation and non-uniformly distributed precipitates are result of coarse grain structure developed during solidification. Developed coarse grain structure has a preferred crystallographic orientation or texture with respect to ingot geometry. A preferred crystallographic orientation and evaluated texture cause anisotropy of mechanical properties [23]. Since the grain boundary area is small, high volume fraction of grain boundary precipitates form a continuous film. Formation of continuous film weakens grain boundaries enabling nucleation and propagation of cracks along the grain boundaries [20]. PFZ is formed during the reaction between grain boundary precipitates and pockets of bulk liquid. Widening of PFZ is a result of phase precipitation in the solid solution [24]. The low precipitation frequency increases plasticity and stress around grain boundary precipitates leading to the vacancy nucleation [25]. Additionally, the vacancy nucleation is facilitated by the planar slip bands impinging on the grain boundaries [26].
The solidification surface in the Al corner of the Al-Li-Mg system is given in Figure 1. The corresponding invariant reactions are given in Table 1.

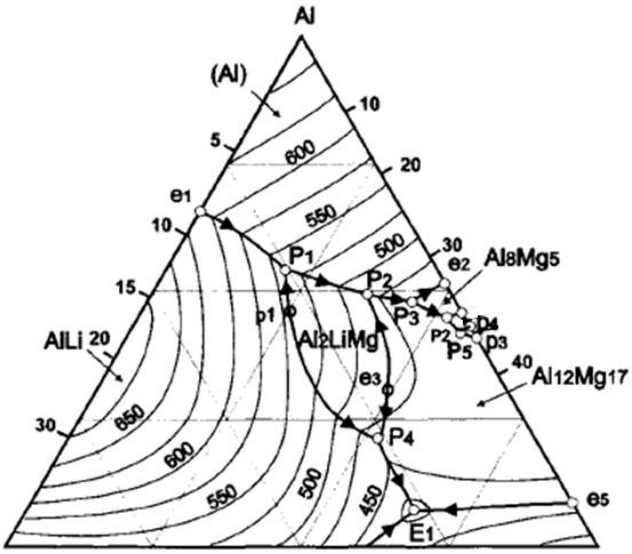


Figure 1. Liquids projection in the Al corner of Al-Li-Mg ternary phase diagram [27]

Table 1. Invariant equilibrium reactions in the Al corner of Al-Li-Mg phase diagram [27]

| Point in Figure 1 | Reaction | Concentration in liquid phase, at. % | | Temperature, °C |
|---|---|---|---|---|
| | | Li | Mg | |
| e1 | $L \rightarrow \alpha_{Al}+AlLi(\delta)$ | 7.5 | - | 602 |
| P1 | $L+AlLi \rightarrow \alpha_{Al}+Al_2LiMg(T)$ | 19.4 | 14.6 | 536 |
| P2 | $L+Al_2LiMg(T) \rightarrow \alpha_{Al}+Al_{12}Mg_{17}(\gamma)$[32] | 10.8 | 27.7 | 483 |
| P3 | $L+\alpha_{Al}+Al_{12}Mg_{17} \rightarrow Al_8Mg_5(\beta)$ | 6.0 | 33.5 | 458 |
| P4 | $L+Al_2LiMg \rightarrow AlLi+ Al_{12}Mg_{17}$ | 20.1 | 40.1 | 464 |
| e2 | $L \rightarrow \alpha_{Al}+Al_8Mg_5(\beta)$ | - | 34 | 450 |

Based on the liquids projection in the Al corner following phases are in equilibrium with the $\alpha_{Al}$ solid solution: AlLi (δ), $Al_2LiMg$ (T), $Al_{12}Mg_{17}$ (γ) and $Al_8Mg_5$ (β) (Figure 1). According to the Table 1, solidification begins with the eutectic reaction at 602°C involving primary $\alpha_{Al}$ dendrite network development and precipitation of stable δ phase (e1). Ternary T phase precipitates during peritectic reaction between stable δ phase and bulk liquid phase enriched in Mg (P1). T phase is the only ternary phase in this system existing in the range of 10.3 % to 11.3 % of Li and 27.1 % to 24.0 % of Mg respectively [28]. It has a complex cubic lattice and tends to precipitate at high angle grain boundaries [29]. Since stable δ phase is dissolved, precipitation of T phase leads to formation of PFZ. The low precipitation frequency areas have a low crack resistance and contribute to the formation of cracks at the grain boundaries. The creep and crack resistance is additionally reduced by precipitation of γ phase [30] (P3) and secondary eutectic β phases [31] (e2). The additions of Li narrow the composition range of β phase and widen homogeneity of γ [27] phase area. Consequently, γ phase stays in equilibrium with $\alpha_{Al}$ (P4) longer. The irregular coarse particles of β phase precipitate at the grain boundaries as a secondary eutectic phase [27].
The solid solubility of Li and Mg in $\alpha_{Al}$ related to temperatures is given in Figure 2. The mutual solid solubility of Li and Mg in $\alpha_{Al}$ at 470°C, 430°C and 200°C is indicated in Table 2.

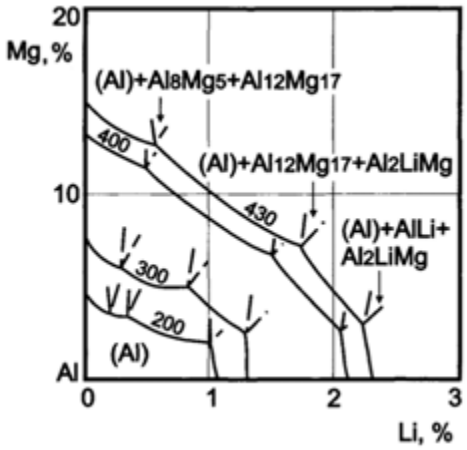


Figure 2. Solid solubility of Li and Mg in $\alpha_{Al}$ related to temperatures [33]

Table 2. Mutual solid solubility of Li and Mg in $\alpha_{Al}$ at different temperatures [27]

| T, °C | $\alpha_{Al}+Al_{12}Mg_{17}+Al_8Mg_5$ | | $\alpha_{Al}+Al_{12}Mg_{17}+Al_2LiMg$ | | $\alpha_{Al}+AlLi+ Al_2LiMg$ | |
|---|---|---|---|---|---|---|
| | Mg,% | Li, % | Mg,% | Li, % | Mg,% | Li, % |
| 470 | 14.0 | 0.8 | 9.3 | 1.4 | 3.8 | 3.0 |
| 430 | 12.5 | 0.55 | 7.2 | 1.72 | 3.0 | 2.25 |
| 200 | 3.6 | 0.19 | 3.4 | 0.32 | 2.0 | 1.0 |

Mg reduces solubility of Li resulting in the formation of high volume fraction of Al-Li based precipitates, mainly δ and T phase [33]. Despite precipitation of γ and β phase, solid solution of $\alpha_{Al}$ stays enriched in Mg (Table 2). Consequently, Mg enrichment enhances lattice of $\alpha_{Al}$ causing solid solution strengthening [34].

Thermodynamic parameters, mainly cooling rate, significantly influence solidification sequence. Equilibrium solidification of 1420 alloy, containing 5.5 % Mg and 2.0 % Li, involves only formation of $\alpha_{Al}$ dendrite network. The δ and T phase precipitate in solid state. However, in real, non-equilibrium conditions, solidification require transformation of $\alpha_{Al}$ dendrite network and eutectic precipitation of stable δ phase [35]. Ternary T phase precipitates during peritectic reaction between stable δ phase and liquid phase. Since stable δ phase is dissolved, precipitation of T phase causes formation of low precipitation frequency areas. Since Mg reduces solubility of Li in $\alpha_{Al}$ high volume fraction of δ and T phase is expected. By the end of solidification sequence, $\alpha_{Al}$ lattice stays enhanced due to the Mg enrichment [32].

Taking into account all interactions, the possible causes of low energy layering fracture represent a synergy of Li segregations at grain boundaries, high frequency of grain boundary precipitates, formation of PFZ at the grain boundaries and planar slip band formation. Layering fracture is unlikely caused by Li segregations because of its reduced solubility in liquid phase (Table 1, point e1, e2, P1, P4) and $\alpha_{Al}$ (Table 2). Since Mg significantly reduces solubility of Li in $\alpha_{Al}$, Mg has more pronounced effect on microstructural constituents' development and mechanical properties.

The goal of this research is to understand mechanism of layering crack formation observed during thermo-mechanical testing of Al-2.5Mg-0.7Li alloy in as cast condition. Solidification sequence under equilibrium conditions was identified using Computer Aided Thermodynamic Diagram Calculation (CALPHAD). CALPHAD enabled tracking interactions of Li and Mg with bulk $\alpha_{Al}$ as well as solidification sequence prediction and reactions in both liquid and solid state respectively. Microstructural constituents development under non-equilibrium conditions was identified using differential scanning calorimetry (DSC), metallographic analysis and X-ray diffraction (XRD).

## MATERIALS AND METHODS

The Al-2.5Mg-0.7Li alloy was synthesized in an induction melting furnace under protective atmosphere of argon (Ar) and crucible cover. The alloy was cast into a permanent steel mold

without protective atmosphere. Chemical composition of synthesized alloy was determined using ARL™ 4460 Optical Mass Spectroscope.
Application of CALPHAD enabled identification of solidification sequence under equilibrium conditions. Significant temperatures of phase transformations and precipitations were determined using DSC method. The samples were tested using heating and cooling rates of 50, 10, 2 K/min. Comparison of significant temperatures of phase transformations and precipitations with results from XRD and metallographic analysis enabled determination of solidification in non-equilibrium conditions.
Samples for metallographic analysis were prepared using grinding/polishing machine Pheonix Beta Biller SAD. In order to observe grain boundaries and precipitates, samples were etched using Poulton's, Keller's and Weck's etching solutions. Macrostructure was observed using stereo microscope Olympus SZ11. The Olympus GX51 inverted metallographic microscope was used to perform light microscopy. Electron microscopy was done on Tescan, Vega TS 5136 MM equipped with energy dispersive spectrometer (EDS). Since EDS does not have a possibility for Li identification, exact prediction of present phases was done by XRD method using Philips PANalyticalX'Pert PRO X-ray diffractometer.
Compression testing was conducted on GLEEBLE 1500 D machine. The sample in as cast condition was tested at room temperature. The force of 1.3 N was applied with strain rate of 230 mm/min.

## RESULTS AND DISCUSSION

Phase transformation and precipitations under equilibrium conditions, determined using Thermo-Calc software support, are given in Figure 3.

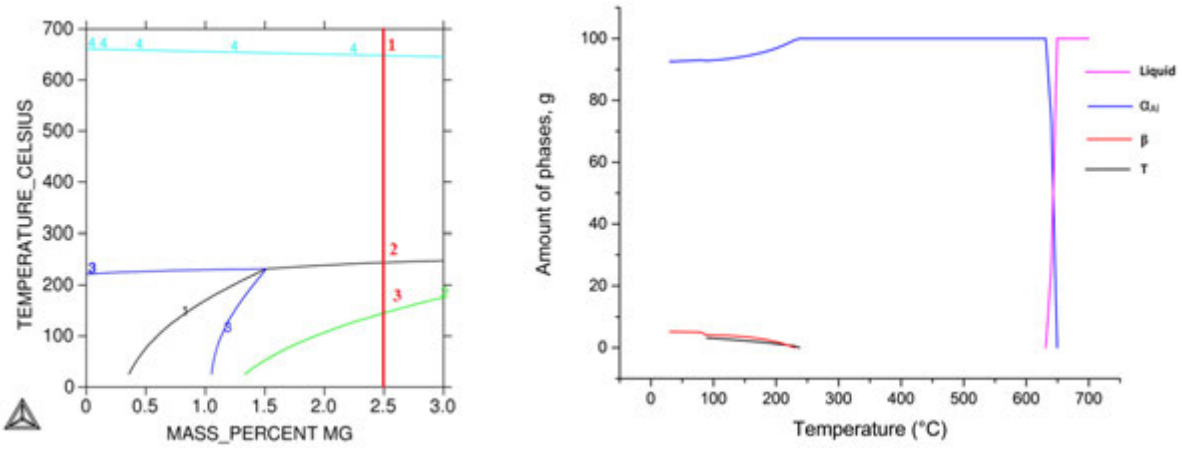


a) b)

Figure 3. The Al-rich corner of Al-Mg-Li ternary diagram:
a) Al-Li-Mg ternary phase diagram with respect to Mg,
b) Amount of phases developed during solidification

Solidification sequence according to the equilibrium phase diagram is given in Table 3.

Table 3. Solidification sequence according to Thermo-Calc calculations diagram in Figure 3 a

| Reaction No. | Reaction | Temperature, °C |
|---|---|---|
| 1 | $L \rightarrow \alpha_{Al}$ | 640 |
| 2 | $\alpha_{Al} \rightarrow \alpha_{Al}' + Al_2LiMg$ (T) | 230 |
| 3 | $\alpha_{Al}' \rightarrow \alpha_{Al}'' + Al_8Mg_5$ (β) | 146.5 |

According to Thermo-Calc calculations, equilibrium solidification begins with transformation of $\alpha_{Al}$ dendritic network at 640°C (Figure 3 b). Ternary T phase and β phase precipitate in solid solution (Figure 3 a, b). The T phase precipitates at 230°C during eutectoid reaction followed by decrease in the amount of $\alpha_{Al}$ (Figure 3 b). Solidification sequence, under equilibrium conditions ends with the precipitation of β phase. The β phase precipitates from bulked $\alpha_{Al}'$ at 146.5°C.
The amount of components in liquid (L) phase is given in Figure 4.

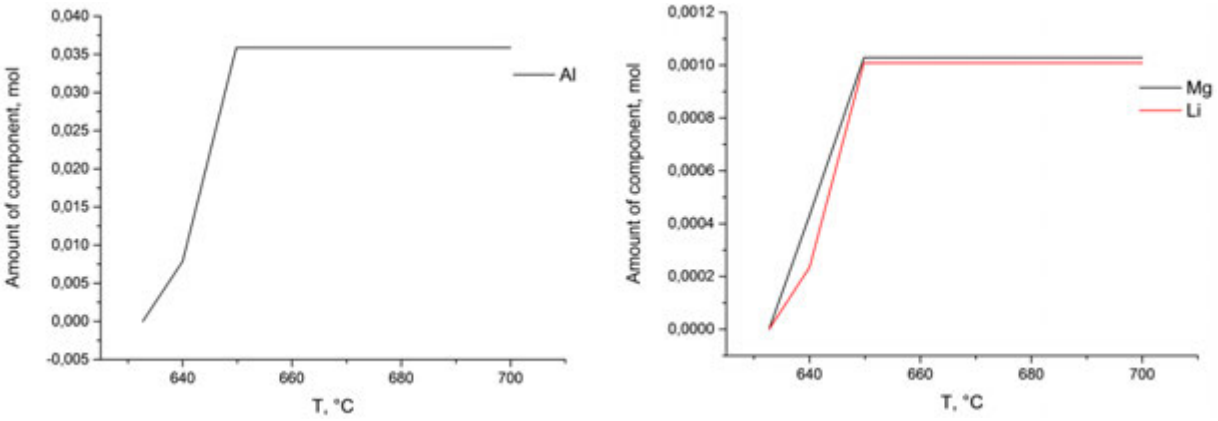


Figure 4. Component ratio in L: a) Al and b) Mg and Li

The average content of Al in L phase (0.03588 mol) stays constant until the temperature of 640°C when it starts to drop rapidly. The rapid drop is caused by phase transformation resulting in dendritic network development ($\alpha_{Al}$) (Figure 4 a). The changes in the amount of Mg (0.00103 mol) and Li (0.00101 mol) in L phase behave similarly (Figure 4 b).
The amount of components in $\alpha_{Al}$ is given in Figure 5 a and b.

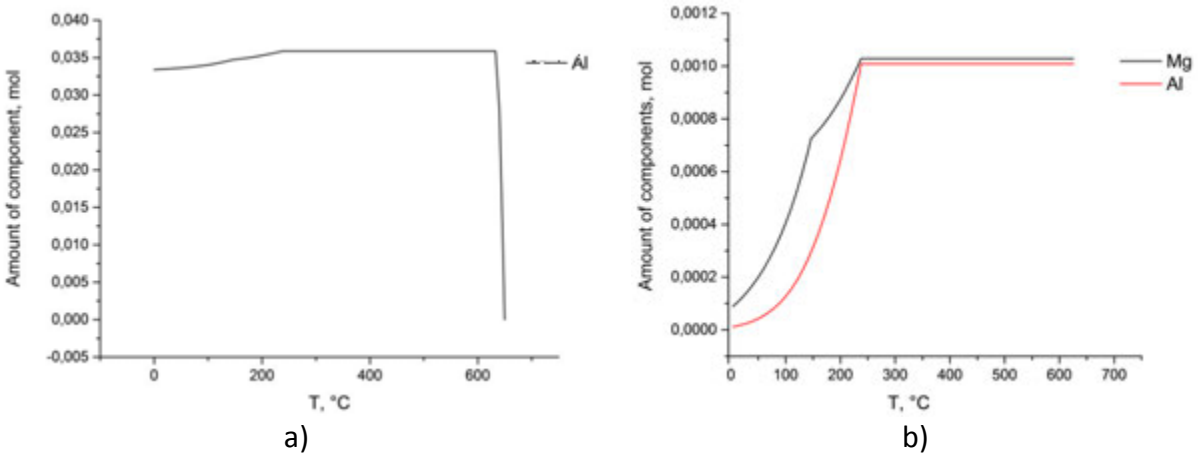


Figure 5. Component ratio in $\alpha_{Al}$: a) Al and b) Mg and Li

Based on the Figure 5 a, two changes in the average amount of Al (0.03588 mol) in $\alpha_{Al}$ can be found. The first drop in the average amount of Al is caused by eutectoid precipitation of ternary T phase at 230°C. The second drop in average amount of Al (0.037574 mol) is a result of precipitation of β phase at 146.5°C. At the end of solidification sequence, the average amount of Al in $\alpha_{Al}$ is 0.03341 mol. Starting average content of Mg is 0.00103 mol and Li is 0.00101 mol in $\alpha_{Al,}$ at 632.7°C respectively. The average amount of Li in $\alpha_{A}$ is rapidly reduced during the precipitation of ternary T phase because of the Mg influence and reduced solubility. At the end of solidification the average content of Li in $\alpha_{Al}$ is $1.04706e^{-5}$ (Figure 5 b). During precipitation of ternary T phase at 230°C the average content of Mg in $\alpha_{Al}$ decreases to $9.93495e^{-4}$. However, the pronounced change in the amount of Mg in $\alpha_{Al}$ is caused by precipitation of β phase at 146.5°C (Figure 5 b). The average content of Mg in $\alpha_{Al}$, at the end of solidification sequence is $8.30476e^{-5}$.
The amount of components in T phase is given in Figure 6 a and b.

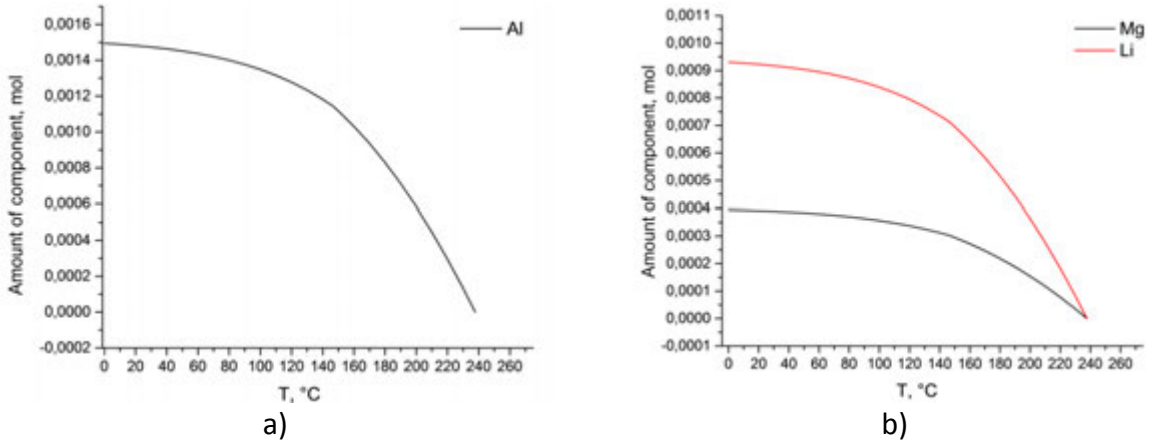


Figure 6. Component ration in T phase: a) Al and b) Mg and Li

The average content of Al in ternary T phase grows from starting 1.32877e$^{-4}$ mol at 230°C to 0.00149 mol at the end of solidification (Figure 6 a). Since Mg reduces solubility of Li in $\alpha_{Al}$, the amount of Li in T phase grows exponentially from the starting 8.27349e$^{-5}$ mol until the temperature of 146.5°C (Figure 6 b) and precipitation of β phase. The average content of Li at the end of solidification sequence is 9.3045e$^{-4}$ mol. After precipitation of β phase begins at 146.5°C, the amount of Mg in ternary T phase grows slowly from starting 3.50997e$^{-5}$ to 3.94737e$^{-4}$ (Figure 6 b).
The amount of components in β phase is given in Figure 7 a and b.

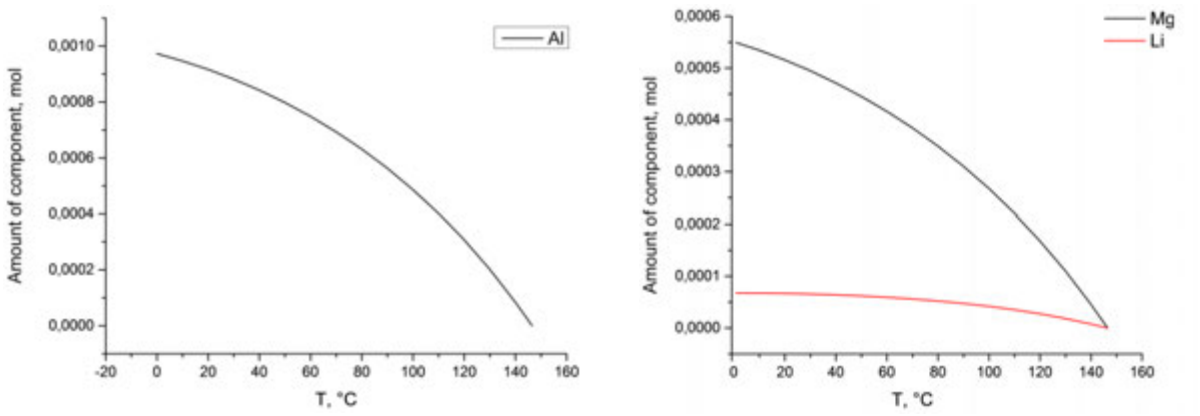


a) b)

Figure 7. Component ration in β phase: a) Al and b) Mg and Li

The starting average content of Al is 8.35005e$^{-5}$ mol and Mg is 4.53609e$^{-5}$ mol in β phase at 146.5°C respectively. At the end of solidification sequence, β phase contains in average 9.7274e$^{-4}$ Al and 5.50811e$^{-4}$ Mg. The average content of Li in β phase grows from starting 7.72156e$^{-6}$ mol to 6.75787e$^{-5}$ mol at the end of solidification sequence.
Calculation of Al-2.5Mg-0.7Li alloy under equilibrium conditions, involves only transformation of $\alpha_{Al}$ phase (Figure 5 a). Ternary T phase and β phase precipitate from the solid solution of $\alpha_{Al}$ phase (Figure 5 b). The reduced solubility of Li in $\alpha_{Al}$ phase causes precipitation of T phase leading to the significant depletion of Li from $\alpha_{Al}$ (Figure 5 b and Figure 6 b). Even due Mg is depleted from $\alpha_{Al}$ during precipitation of T phase, the amount of Mg is more significantly reduced during precipitation of β phase (Figure 5 b and Figure 6 b).
The influence of heating and cooling rates on the solidification sequence of Al-2.5Mg-0.7Li alloy is shown in Table 4.

Table 4. Influence of heating and cooling rate on solidification sequence

| Heating rate, K/min | | | Cooling rate, K/min | | | Reaction |
|---|---|---|---|---|---|---|
| 50 | 10 | 2 | 50 | 10 | 2 | |
| 659.9 | 666.0 | 651.0 | 639.7 | 643.1 | 643.8 | $L \rightarrow \alpha_{Al}$ |
| 612.7 | 647.3 | 620.0 | 588.4 | 638.8 | 635.1 | $L + \alpha_{Al} \rightarrow \alpha_{Al} + Al_3Li$ (δ') |
| -- | 608.1 | 605.8 | 540.8 | 594.2 | 617.8 | $\alpha_{Al} + \delta' \rightarrow \alpha_{Al}' + \delta$ |
| -- | 356.8 | 492.5 | -- | -- | 546.1 | $\alpha_{Al}' + \delta' \rightarrow \alpha_{Al}'' + T$ |
| -- | 313.8 | 368.5 | -- | -- | -- | $\alpha_{Al}'' \rightarrow \alpha_{Al}''' + \beta$ |

Solidification sequence of Al-2.5Mg-0.7Li alloy under non-equilibrium conditions begins with transformation of $\alpha_{Al}$. Reduced solubility of Li in remaining L phase, and already formed $\alpha_{Al}$ leads to eutectic reaction resulting with precipitation of metastable δ' inside the $\alpha_{Al}$ grains. Precipitation of δ' is aided by constitutional undercooling due to the Mg influence. With further temperature decrease, stable δ phase nucleates on the grain boundaries of $\alpha_{Al}$. Stable δ phase evaluated by reaction of previously precipitated $\alpha_{Al}$ and metastable δ' phase. Dissolution of δ' phase causes formation of PFZ near the grain boundaries. Elongated ternary phase precipitates due to the reaction of Mg from bulk $\alpha_{Al}$' and already precipitated δ' phase. Precipitation of T phase leads to the further reduction of precipitation frequency. Solidification sequence ends with precipitation of secondary eutectic β phase followed by decrease in Mg content of $\alpha_{Al}$''.
The microstructure of Al-2.5Mg-0.7Li is given in Figure 8. The individual phases were identified using literature survey comparison.

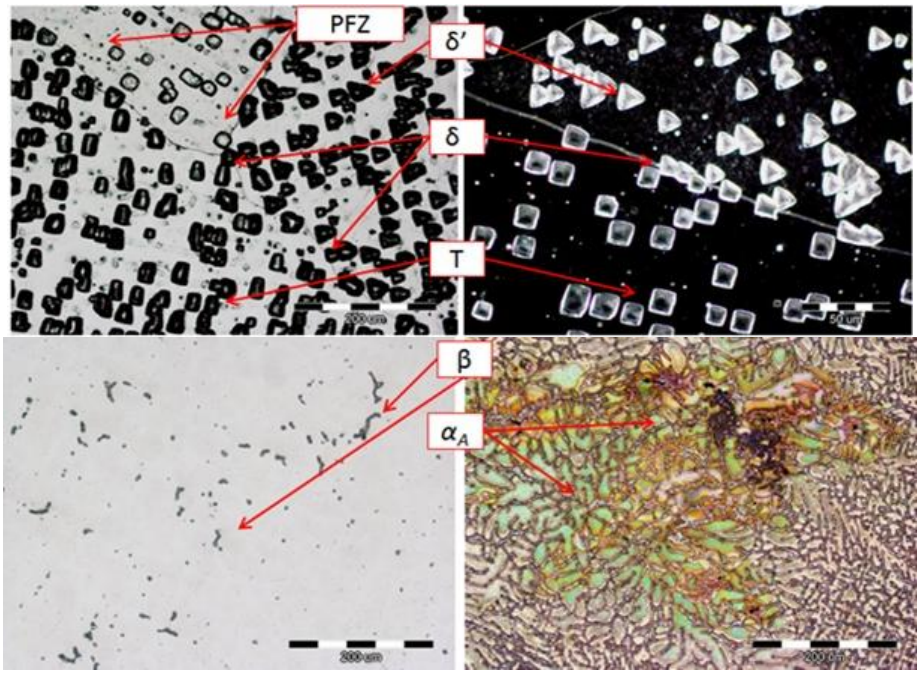


Figure 8. Microstructure of Al-2.5Mg-0.7Li

Particles of metastable δ' are found inside the grains of $\alpha_{Al}$ (Figure 8). The metastable δ' phase is a main strengthening precipitate in Al-Mg-Li alloys. It interacts with dislocations and leads to the formation of microstructural texture [11]. Stable δ phase can be found on grain boundaries. Precipitation of stable δ phase caused formation of PFZ near the grain boundaries (Figure 8). Ternary T phase can be found on the grain boundaries as well as inside the grains. Precipitation of T phase led to the further decrease of precipitation frequency (Figure 8) near the grain boundaries. Irregular coarse particles of secondary eutectic β phase can be found in the last solidifying areas (Figure 8).

The scanning electron image (SEI) and following mapping analysis are given in Figure 9 a and b. The positions for EDS quantitative analysis are indicated in Figure 9 a. The EDS is performed on characteristics phases at grain boundary as well as on different distances from it.

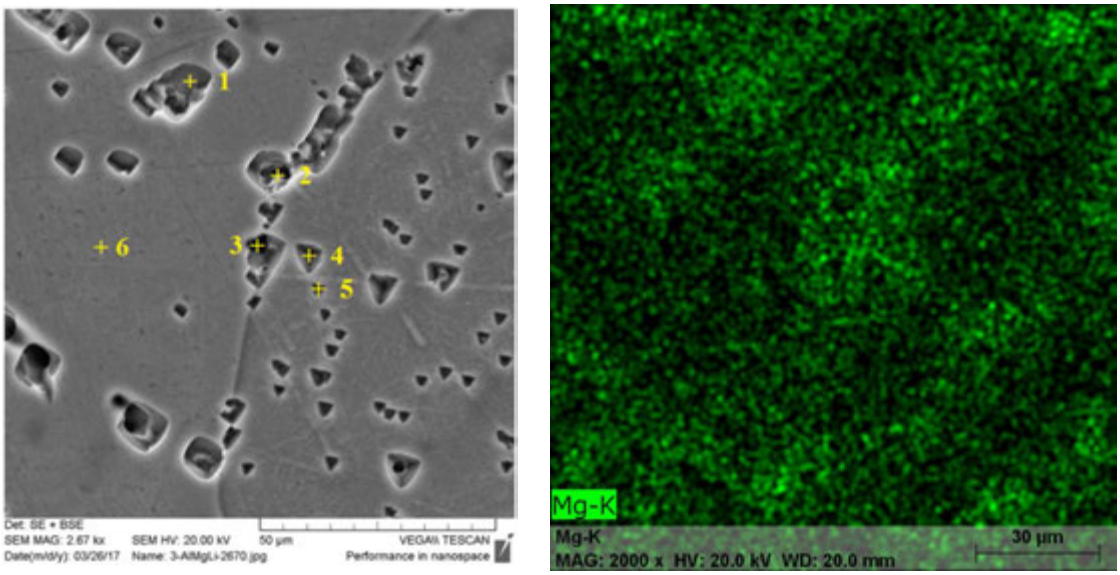


a) b)

Figure 9. SEI of:
a) Al-2.5Mg-0.7Li alloy with marked EDS analysis points
b) Mapping analysis of Mg content

Figure 9 a shows SEI of densely distributed phases in $\alpha_{Al}$ matrix. Results of mapping analysis show significant variations in color intensity concerning Mg content (Figure 9 b). Based on the mapping analysis, highest concentration of Mg can be found near grain boundaries. Results of additional EDS quantitative analysis are given in Table 5.

Table 5. Results of EDS quantitative analysis

| Location | Al, wt.% | Mg, wt.% |
|---|---|---|
| 1 | 94.59 | 5.41 |
| 2 | 94.11 | 5.89 |
| 3 | 39.79 | 6.21 |
| 4 | 95.01 | 4.99 |
| 5 | 97.54 | 2.46 |
| 6 | 97.59 | 2.41 |

Since the measurements taken at the position 1-5 indicate the occurrence of different phases, measurements taken at the position 6 confirm the existence of residual Mg in bulk $\alpha_{Al}$''.

Macrostructure of the sample's perpendicular quarter-section before compression testing is given in Figure 10 a. Microstructure of the sample in as cast condition is given in Figure 10 b.

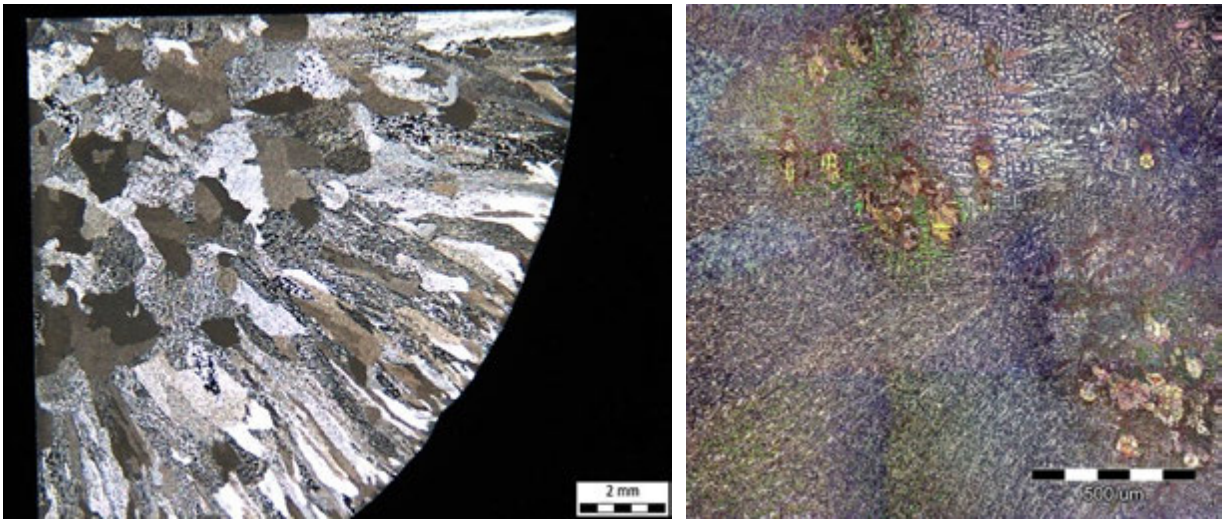


a) b)

Figure 10. Sample's quarter section perpendicular to the testing direction:
a) Macrostructure of the sample in as cast condition,
b) Microstructure of sample before compression testing, Multiple Image Alignment (MIA)

Sample exhibits typical structure for permanent mold castings. Formation of thin chill zone is followed by formation of columnar grains zone. Coarse equiaxed grains can be found in the middle of the sample (Figure 10 a).
Dendrites of $\alpha_{Al}$ developing in columnar zone have preferred orientation (Figure 10 b). The $\alpha_{Al}$ dendrites developing in equiaxed zone are coarse and filamentary (Figure 10 b).
Macrostructure of the sample after compression testing is given in Figure 11.


a)


b)

Figure 11. Macrostructure of the sample after compression testing:
a) Surface perpendicular to the testing direction,
b) Surface along the testing direction

The compression testing led to the significant texture development, as shown in Figure 11 a. Macrostructure of the surface parallel to the testing direction reveals significant cracking (Figure 11 b). The crack nucleated at the surface of the sample and propagated towards the center.
MIA of the area of the defects is given in Figure 12.

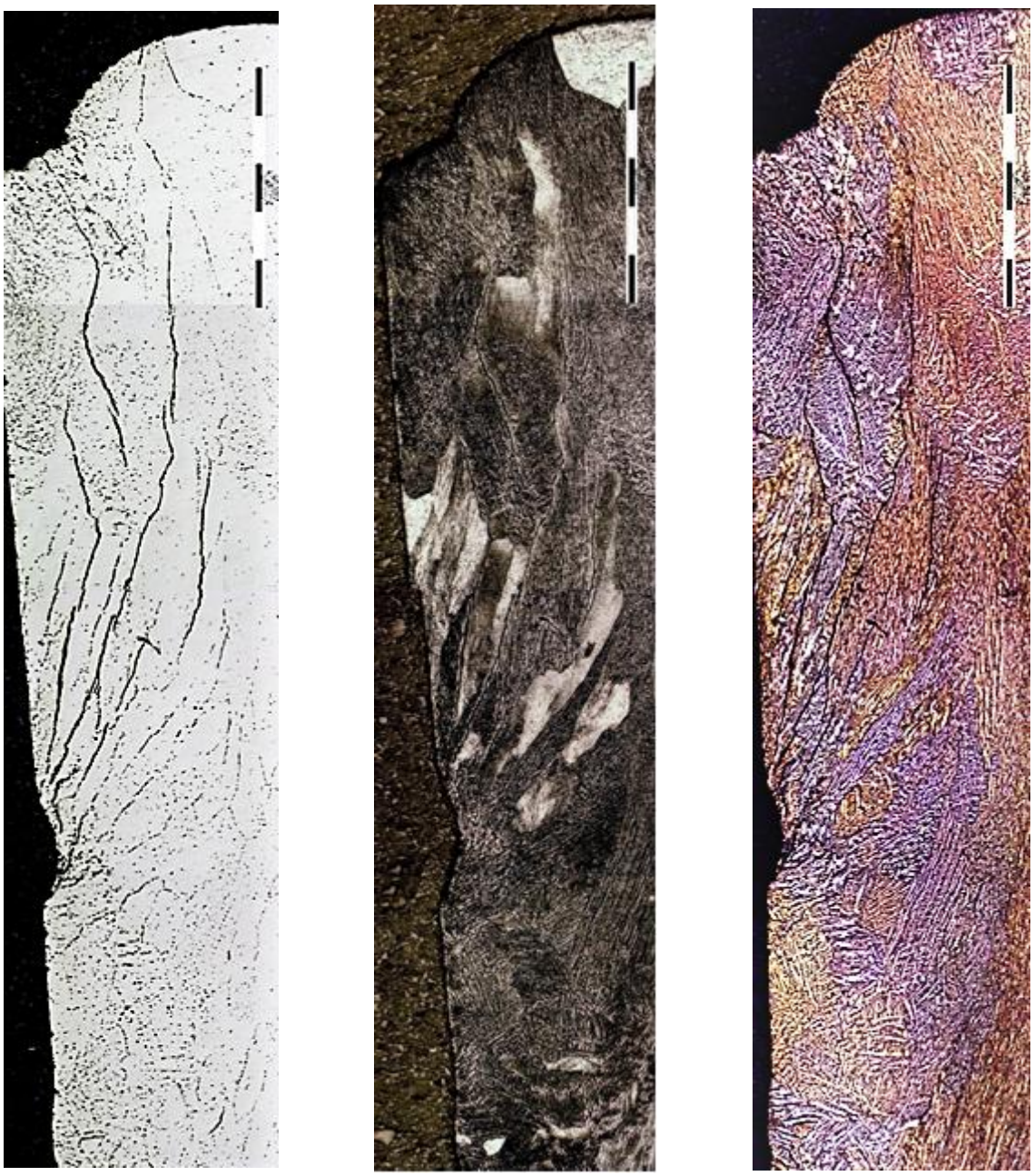

a) b) c)

Figure 12. MIA of the affected area in: a) As polished condition,
b) After etching with Poulton's etching solution,
c) After etching with Wecks's etching solution

The cracks nucleate at the surface defect and propagate towards the center of the sample, as shown in Figure 12 a. Etching to reveal the grain structure enabled identification of the defect as a failure along the grain boundaries (Figure 12 b). Result of color etching, given in Figure 12 c, indicated significant texture development in the area of the interest.

## CONCLUSIONS

The mechanism of nucleation and propagation of low energy layering fracture, observed during thermo-mechanical testing of Al-2.5Mg-0.7Li alloy in as cast condition, was analyzed. Low energy layering fracture is influenced by Li segregations and microstructural constituents' development. Both, changes in the amount of components (Al, Li and Mg) in individual phases and solidification sequence of Al-2.5Mg-0.7Li alloy were investigated in equilibrium and non-equilibrium conditions.

Solidification sequence in equilibrium conditions involves transformation of $\alpha_{Al}$ followed by the precipitation of ternary T phase and β phase. The amount of Li in $\alpha_A$ is rapidly reduced during the precipitation of ternary T phase due to the reduced solubility and Mg influence.

Changes in solidification sequence under non-equilibrium conditions are a result of reduced solubility of Li in L phase and $\alpha_{Al}$. Solidification sequence begins with transformation of $\alpha_{Al}$ dendritic network. Reduced solubility of Li in remaining L phase and $\alpha_{Al}$ leads to precipitation of metastable δ' inside the grains of $\alpha_{Al}$. With temperature decrease, stable δ phase nucleates at the grain boundaries of $\alpha_{Al}$. Stable δ phase grows on the account of previously precipitated $\alpha_{Al}$ and metastable δ' phase and leads to formation of PFZ near the grain boundaries. Precipitation of T phase widens the PFZ. Solidification sequence ends with precipitation of β phase at the grain boundaries.

Metallographic analysis of the sample, after compression testing, revealed low energy layering fracture as a failure along the grain boundaries. Interaction between δ' phase and dislocations caused textured development in the affected area. Precipitation of δ and β phase weakens the grain boundaries. Segregations of Mg at the grain boundaries led to the solid solution strengthening and ductility decrease.

The conducted investigations indicated that Mg has more pronounced effect on low energy delamination fracture development by:

- Reducing solubility of Li in L phase and $\alpha_{Al}$,
- Maximizing precipitation of hardening δ' phase particle,
- Precipitation of ternary T phase and widening PFZ,
- Precipitation of irregular β phase particles at the grain boundaries.
- Solid solution hardening.

## REFERENCES

[1] R. J. Rioja, J. Liu, The evolution of Al-Li based products for aerospace and space applications, Metallurgical and Materials Transactions A, 43 (2012) 9, pp. 3325-3337.
[2] D. Tsivoulas, P. B. Prangnell, The effect of Mn and Zr dispersoid-forming additions on recrystalization in Al-Cu-Li AA2198 sheet, Acta Materialia, 77 (2014) 1, pp. 1-16.
[3] E. M. Rodrigues, A. Matias, L. B. Godefroid, F. L. Bastian, K. S. Al-Rubaie, Fatigue crack growth resistance and crack closure behavior in two aluminum alloys for aeronautical applications, Materials Research, 8 (2005) 3, pp. 287-291.

[4] K. V. Jata, E. A. Starke, Fatigue crack growth and fracture toughness behavior of an Al-Li-Cu alloy, Metallurgical Transactions A, 17 (1986) 6, pp. 1011-1026.
[5] R. K. T. Venkateswara, W. You, R. O. Ritchie, Fatigue crack propagation in aluminum-lithium alloys 2090: Part II. Small crack behavior, Metallurgical Transactions A, 19 (1988) 3, pp. 563-569.
[6] R. K. T. Venkateswara, W. You, R. O. Ritchie, Fatigue crack propagation in aluminum-lithium alloys 2090: Part I. Long crack behavior, Metallurgical Transactions A, 19 (1988) 3, pp. 549-561.
[7] K. I. Moore, J. M. Sykes, S. C. Hogg, P. S. Grant, Pitting corrosion of Spray Formed Al-Li-Mg alloys, Corrosion Science, 50 (2008) 11, pp. 3221-3226.
[8] Z. W. Wang, P. B. Prangnell, Microstructure refinement and mechanical properties of severely deformed Al-Mg-Li alloys, Material Science and Engineering, A 328 (2002) 1-2, pp. 87-97.
[9] N. A. Belov, D. G. Eskin, A. A. Aksenov, Multicomponent phase diagrams: Application for commercial aluminum alloys, Elsevier Science, 2005.
[10] A. A. Csontos, E. A. Starke, The effect of inhomogeneous plastic deformation on the ductility and fracture behavior of age hardenable aluminum alloys, International Journal of Plasticity, 21 (2005) 6, 1097-1118.
[11] N. E. Prasad, A. A. Gokhale, P. R. Rao, Mechanical behavior of aluminum-lithium alloys, Sadhana, 28 (2003) 1-1, pp. 209-246.
[12] R. J. Rioja, Fabrication methods to manufacturing isotropic Al-Li alloys and products for space and aerospace applications, Material Science and Engineering, A 257 (1998) 1, pp. 100-107.
[13] R. K. Gupta, N. Nayan, G. Nagasireesha, S. C. Sherman, Development and characterization of Al-Li alloys, Material Science and Engineering, A 420 (2006) 1-2, pp. 228-243.
[14] K. K. Sankaran, N. J. Grant, The structure and properties of splat-quenched aluminum alloy 2024 containing lithium additions, Material Science and Engineering, A 44 (1980) 2, pp. 213-227.
[15] T. Dursun, C. Soutis, Recent developments in advanced aircraft aluminum alloys, Materials and Design, 50 (2014) 1, pp. 862-871.
[16] A. Bois-Brochu, F. A. T. Goma, C. Blais, D. Larouche, R. Gauvin, J. Boselli, Al-Li alloy 2099-T83 Extrusions: Static Mechanical Properties, Microstructure and Texture, Advanced Material Research, 409 (2011), pp. 29-34.
[17] H. Babel, J. Gibson, M. Tarkanian, C. Parrish, M. Prietto, A. Ordonez-Chu, H. Haberl, R. Clark, J. Ogren, O. S. Es Said, 2099 Aluminum-lithium with key-locked inserts for aerospace applications, Journal of Materials Engineering and Performance, 16 (2007) 5, pp. 584-591.
[18] S. P. Lynch, B. C. Muddle, T. Pasang, Ductile - to – brittle fracture transition in 8090 Al-Li alloys, Acta Materialia, 49 (2001) 15, pp. 2863-2874.
[19] S. P. Lynch, Fracture of 8090 Al-Li plate I. Short transverse fracture toughness, 136 (1991) pp. 25-43.

[20] C. Schlesier, E. Nembach, Strengthening of aluminum-lithium alloys by long-range ordered δ'-precipitates, Acta Metallurgica et Materialia, 43 (1995) 11, pp. 3983-3990.
[21] S. Suresh, A. K. Vasudevan, M. Tosten, P. R, Howell, Microscopic and macroscopic aspects of fracture in lithium-containing aluminum alloys, Acta Materialia, 35 (1987) 1, pp. 25-46.
[22] H. Garmastani, S. R. Kalidindi, L. Williams, C. M. Bacaltchuk, C. Fountain, E. W. Lee, O. S. Es-Said, Modeling the evolution of anisotropy in Al-Li alloys: application to Al-Li 2090-T8-E41, International Journal of Plasticity, 18 (2002) 10, pp. 1373-1393.
[23] J. E. Gruzleski, Microstructure development during metalcasting, American Foundrymen's Society, Illinois, 2000.
[24] J. Augustyn-Pieniažek, H. Adrian, S. Rzadkosz, M. Choroszynski, Structure and mechanical properties of Al-Li alloys as cast, Archives of Foundry Engineering, 13 (2013) 2, pp. 5-10.
[25] A. Williamd, Microstructural analysis of aluminium alloy 2093 as a function of heat treatment, School of Metallurgy and Materials, The University of Birmingham, 2010.
[26] H. J. McQueen, Mechanisms in creep and hot working to high strain; microstructural evidence, inconsistencies. Part I: substructure evolution; grain interactions, Metallurgical Science and Technology, 28 (2010) 1, pp. 12-21.
[27] B. Dubost, P. Bombard, I Ansara, Experimental study and thermodynamic calculations of Al-Li-Mg equilibrium phase diagram, Journal de Physique Colloques, 48 (1987) 3, 473-479.
[28] L. F. Mondolfo, Aluminum alloys: Structure and properties, Elsevier, Amsterdam, 2013.
[29] A. Mogucheva, R. Kaibyshev, Microstructure and mechanical properties of an Al-Li-Mg-Sc-Zr alloy subjected to ECAP, Metals, 254 (2016) 6, pp. 1-14.
[30] H. Zang, S. L. Shang, Y. Wang, A. Saengdeejing, L. Q. Chen, Z. K. Liu, First-principles calculations of the elastic, phonon and thermodynamic properties of $Al_{12}Mg_{17}$, Acta Materialia, 58 (2010) 11, pp. 4012-4018.
[31] Z. Z. Brodarac, F. Unkic, J. Medved, P. Mrvar, Determination of solidification sequence of the AlMg9 alloy, Kovove Materialy-Metallic Materials, 50 (2012) 1, pp. 59-67.
[32] Materials Science International Team (MSIT), Light metal ternary system: Phase diagrams, crystallographic and thermodynamic data, Springer-Verlag, Berlin Heidelberg, 2005.
[33] N. Prasad, A. Eswara, A. Gokhale, R. J. H. Wanhill, Aluminium–lithium alloys, Aerospace Materials and Material Technologies, Butterworth-Heinemann, Oxford, 2013.
[34] S. Betsofen, M. Chizhikov, Quantitative Phase Analysis of Al-Mg-Li and Al-Cu-Li Alloys, Aluminium Alloys, 794 (2014) 1, pp. 915-920.
[35] W. J. Poole, M. A. Walls, D. J. Lloyd, Crystal analysis of nonequilibrium $\delta_{non}$-phase in Al-Li-Mg alloys, Materials Science Forum, 519-521 (2006) pp. 259-264.

**Acknowledgements**

This investigation has been performed in the frame of financial support for investigation of University of Zagreb: “Design and characterization of innovative engineering alloys” (TP167) and support of scientific research projects within the joint Croatian-Slovenian collaboration “Design and characterization of innovative aluminium – magnesium – lithium alloy” (2018-2019) financed by Ministry of Science and Education, Republic of Croatia.

17th INTERNATIONAL FOUNDRYMEN CONFERENCE
Hi-tech casting solution and knowledge based engineering
Opatija, May 16th-18th, 2018
http://www.simet.hr/~foundry/

# GRAPHITE SHAPE DETERMINATION BY ELECTRICAL RESISTIVITY MEASUREMENTS OF CAST IRONS

**Mitja Petrič[1]*, Primož Mrvar[1], Sebastjan Kastelic[1,2]**

[1] University of Ljubljana Faculty of Natural Sciences and Engineering, Ljubljana, Slovenia
[2] TC Livarstvo d.o.o., Ljubljana, Slovenia

**Oral presentation**
*Preliminary note*

**Abstract**

The paper describes the possibility of electrical resistivity measurement in order to determine the state of the microstructure of grey cast irons.
Electrical resistivity is a property of materials which is changed by temperature and it depends also on microstructure. In cast irons the microstructure first consists from austenite dendrites and eutectic graphite which can be lamellar, nodular etc. Austenite is later transformed to pearlite and ferrite. The involved phases and amounts of phases and also the shape of graphite have big influence on electrical resistivity of material. In this manner it is possible to determine the solidification path of melt and the state of microstructure of cast irons.
Electrical resistivity measurements were performed on lamellar and nodular cast iron melts. A four probe technique was applied for the measurements of electrical resistivity in a sand mould made through Croning process. The temperature was measured simultaneously. Microstructures were investigated by optical microscopy to determine the shapes and amounts of graphite and to determine the matrix as well.
Results are showing that electrical resistivity of nodular cast iron is decreased during solidification but in lamellar cast iron it is rising during the solidification and decreasing after the solidification. From such phenomena one can conclude that such measurements are appropriate for graphite shape determination.

***Keywords***: *grey cast iron, electrical resistivity, graphite shape*

*Corresponding author (e-mail address): *mitja.petric@omm.ntf.uni-lj.si*

## INTRODUCTION

Simple thermal analysis is well established method for solidification path monitoring of metals and alloys especially in aluminium and cast iron foundry industry. The results give us information of solidified microstructure in terms of phase fractions, shapes of

microstructural constituents, presence of carbides, inclusions, etc. The measurement is based on heat release during solidification which is exothermal process. The heat release can be connected to individual phase or eutectic and in this way the microstructure can be predicted.

Electrical resistivity is a property of materials which is changed by temperature and it depends also on microstructure in terms of shape and size of phases [1, 2]. The involved phases and amounts of phases and also the shape of phases have big influence on electrical resistivity of material. It is reported for the case of aluminium alloys that shape and size of present phases has important influence on the electrical resistivity of material. If the phases are large and acicular or lamellar the electrical resistivity is higher because there are more interfaces – barriers for electrons to overcome. On the other hand if phases are smaller and more rounded the electrical resistivity of material is lower [3, 4].

In cast irons the microstructure usually first consists from austenite dendrites and eutectic of austenite and graphite. Graphite can be lamellar, nodular etc. Austenite is later transformed to pearlite and/or ferrite. It is similar in cast irons as written above. Electrical resistivity must be affected by the shape and size of graphite and the matrix as well. Very few reports about it have been found in literature. Stefanescu et al. [5] reported that electrical resistivity of lamellar grey cast irons is higher than the one of nodular cast irons. There is also stated that the matrix also influences the electrical resistivity and it is higher if it is pearlitic than ferritic [6] since pearlite consists from two phases and there are a lot of interfaces present.

There are also very few sources found describing the change of electrical resistivity of melt during solidification and this is the case to be studied.

## MATERIALS AND METHODS

Electrical resistivity measurements were performed on different lamellar and nodular cast iron melts during the range of solidification and further cooling. The sample markings and chemical compositions are given in Table 1. The ″in situ″ measurement during solidification and cooling was performed in a sand mould made through the Croning process. The shape of a casting is a 210 mm long bar with square cross-section of 330 $mm^2$. Electrical resistivity was measured using four probe technique and the temperature was measured simultaneously as described in literature [7]. The samples were metallographically investigated by light microscopy in order to evaluate the microstructure. Samples were etched by 2% NITAL.

Table 1. Chemical composition of investigated alloys

| | C | Si | Mn | S | Cr | Cu | P | Mg |
|---|---|---|---|---|---|---|---|---|
| **Lamellar** | 3.95 | 1.82 | 0.259 | 0.048 | 0.04 | 0.026 | 0.031 | 0.005 |
| **Nodular-1** | 3.7 | 2.54 | 0.324 | 0.008 | 0.039 | 0.029 | 0.026 | 0.036 |
| **Nodular -2** | 3.79 | 2.54 | 0.348 | 0.01 | 0.039 | 0.029 | 0.026 | 0.045 |
| | **Ni** | **Mo** | **V** | **Ti** | **Sn** | **Al** | **Bi** | **Ni** |
| **Lamellar** | 0.017 | 0.002 | 0.004 | 0.009 | 0.021 | 0.004 | 0.003 | 0.017 |
| **Nodular -1** | 0.019 | 0.003 | 0.004 | 0.008 | 0.053 | 0.006 | 0.004 | 0.019 |
| **600-2** | 0.019 | 0.004 | 0.004 | 0.008 | 0.056 | 0.007 | 0.005 | 0.019 |

## RESULTS AND DISCUSSION

### Metallography

Metallographic observations showed the shapes of graphite in all three samples. Sample of Lamellar alloy obtained directly from cupola furnace showed flake shape of graphite or form A. It is observed that also some rosette flake graphite (form B) and undercooled graphite (form D) are present in microstructure since the melt was not treated and inoculated. Samples of ductile iron have mainly nodular shape of graphite, but since the melt was not completely treated before pouring – it was pre-inoculated but it was not in-stream inoculated – the shape of graphite is not perfect form VI but it is degraded to some extent. Microstructures are given in in Figure 1. Figure 2 is presenting etched microstructures where it is seen that in Lamellar sample the matrix is nearly totally pearlitic but in sample Nodular-1 there is approximately 30 area % of ferrite and in sample Nodular-2 approximately 20 area % ferrite.

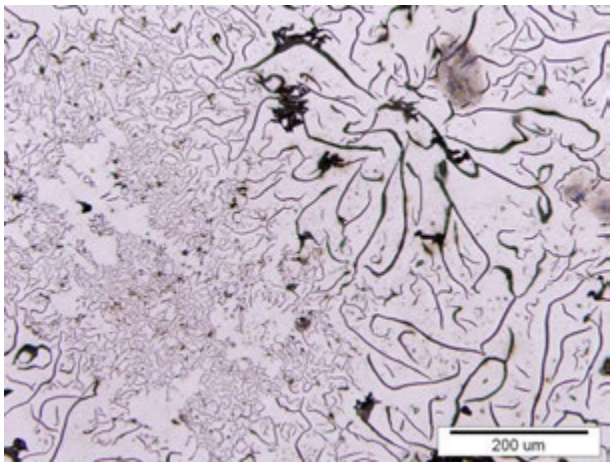


a)

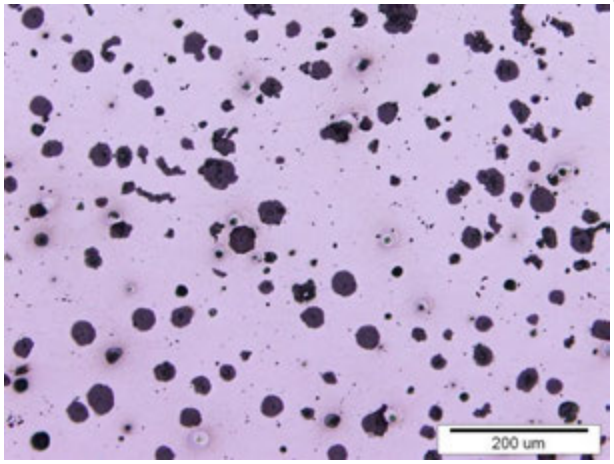


b)

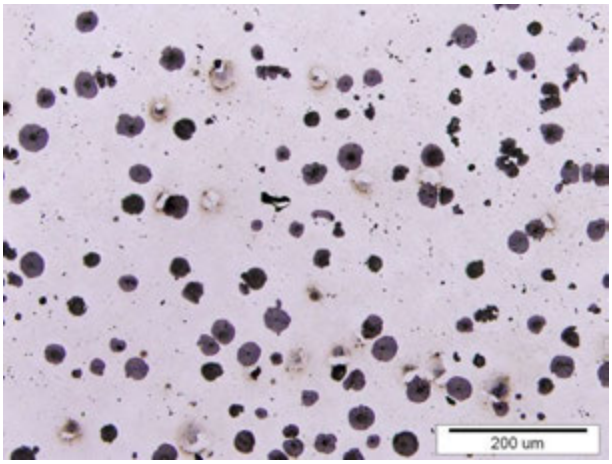


c)

Figure 1. Microstructures of polished samples: Lamellar (a), Nodular-1 (b) and Nodular-2 sample (c)

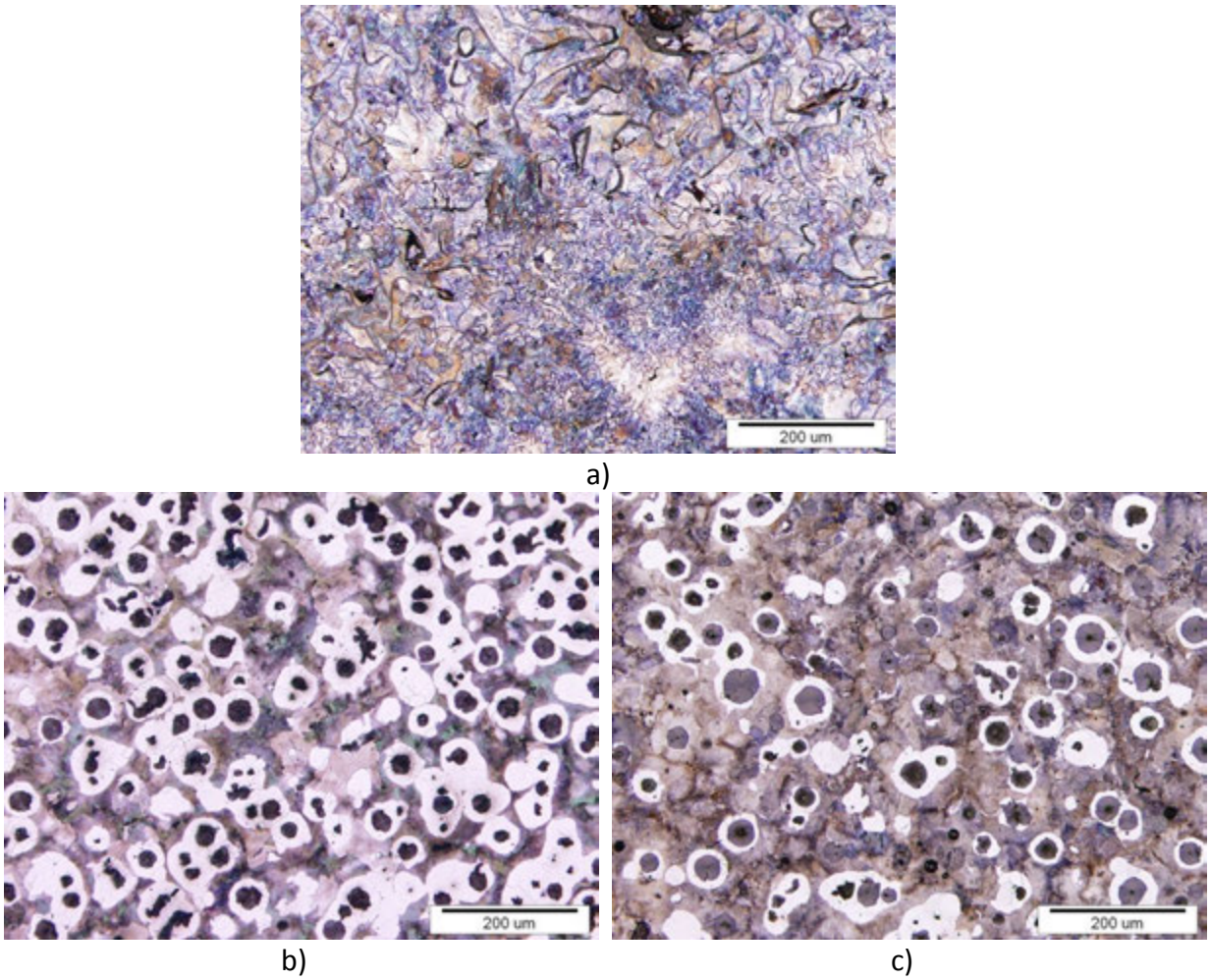


a)

b) c)

Figure 2. Microstructures of etched samples: Lamellar (a), Nodular-1 (b) and Nodular-2 sample (c)

**Electrical resistivity**

Results of measurements are given in Figures 3 and 4. It is seen that the electrical resistivity (ρ) of lamellar cast iron is decreasing in liquid but when the solidification starts it is suddenly increased since first lamellas of graphite appear. When solidification is finished the resistivity reaches a plateau after which eutectoid transformation takes place and after it decreases. At nodular cast iron the shape of the electrical resistivity curve is similar to those of pure metals since graphite nodules do not much affects the conduction electrons. After the solidification starts the curve decreases faster and after solidification it slows down. At eutectoid reaction at approx. 300 – 400 s there is a small plateau and then decreases continuously with temperature.

From the results one can easily notice a difference in two curves which go separate ways when the shape of graphite is a question. If the lamellar graphite is formed during solidification the resistivity is increased and at nodular graphite solidification the resistivity is decreased during solidification.

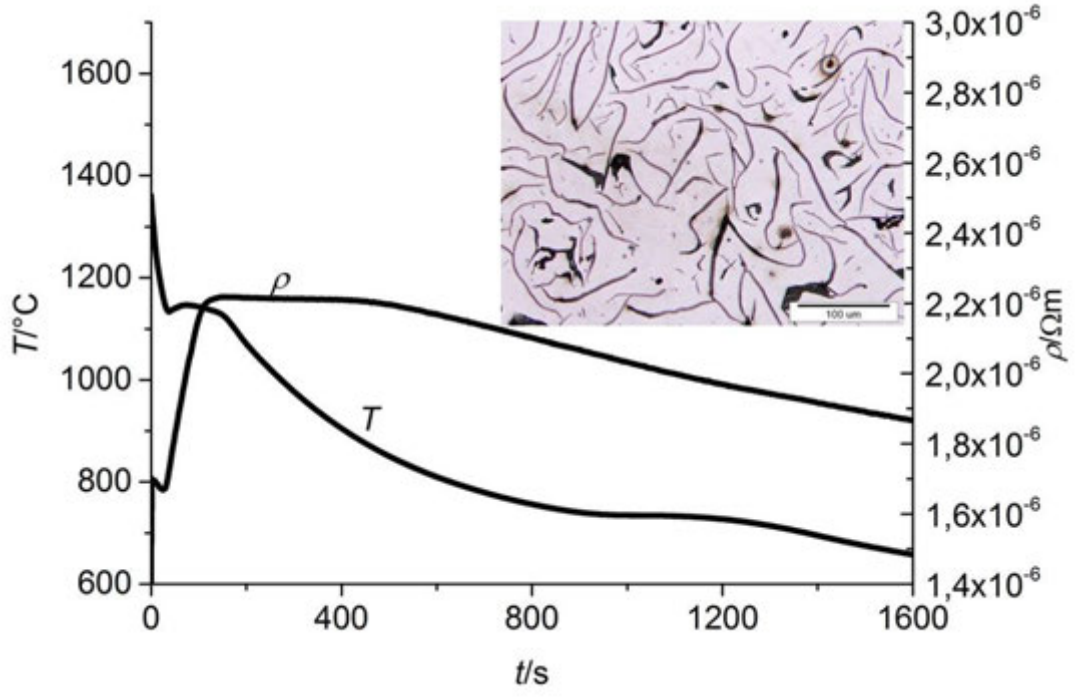


Figure 3. Measured curves of electrical resistivity and cooling curve of Lamellar sample

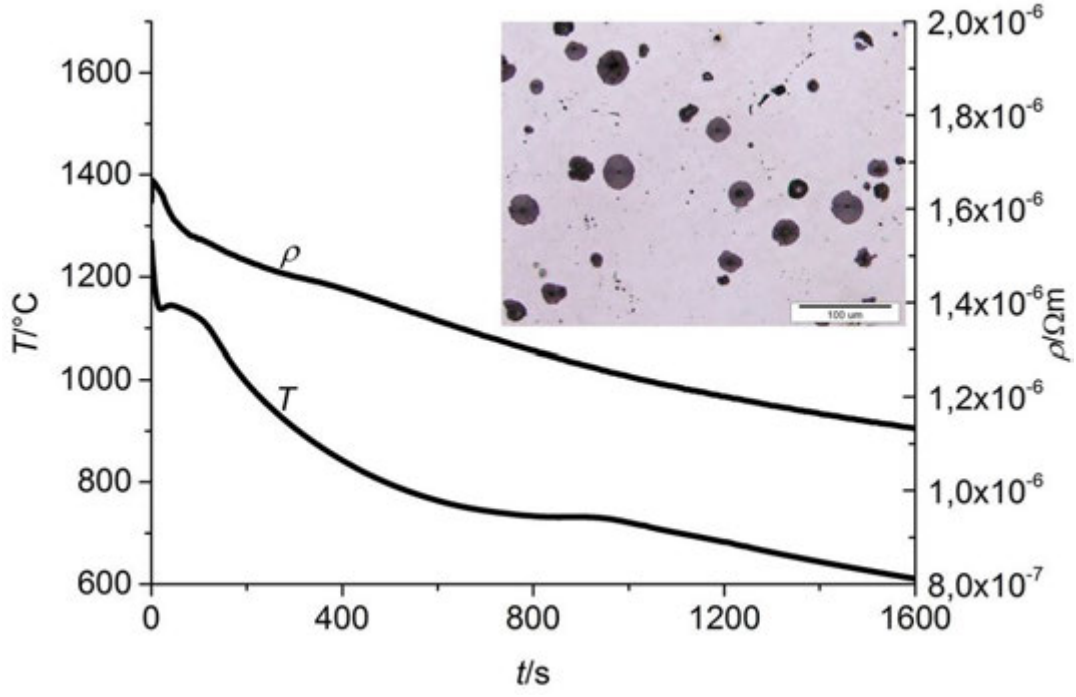


Figure 4. Measured curves of electrical resistivity and cooling curve of Nodular-1 sample

## CONCLUSIONS

The paper presents the measurements of electrical resistivity during solidification and cooling for different cast irons. Results have shown that the electrical resistivity is different for lamellar graphite cast irons from nodular cast irons. The electrical resistivity of lamellar graphite cast irons is increasing during solidification as a consequence of high electron scattering on lamellas of formed graphite. In nodular graphite cast iron it is the opposite way where electrical resistivity is decreasing during solidification since the electron scattering is lower at nodular graphite

From obtained results it can be concluded that such measurements can provide information about graphite shape already in early stage of a measurement.

## REFERENCES

[1] A. R. Sinigoj, Basics of Electromagnetics, Publisher of Faculty of Electrical engineering and Faculty for Computer and Information Science, Ljubljana, 1999 (in Slovenian).
[2] T. E. Faber, An introduction to the theory of liquid metals, Cambridge University Press, New York, 1972.
[3] L. Weber, C. Fischer, A. Mortensen, On the influence of the shape of randomly oriented, non-conducting inclusions in a conducting matrix on the effective electrical conductivity, Acta Materialia, 51 (2003) pp. 495-505.
[4] L. Weber, J. Dorn, A. Mortensen, On the electrical conductivity of metal matrix composites containing high volume fractions of non-conducting inclusions, Acta Materialia, 51 (2003) pp. 3199-3211.
[5] D. M. Stefanescu, S. T. Craciun, Bestimmung der graphitform im gusseisen durch messung des spzifischen elektrischen widerstandes waehrend der erstarrung, Giesserei-praxis, 11 (1973) pp. 197-200.
[6] D. M. Stefanescu, H. Weingert, Einfluss des graphits und der metallischen grundmasse auf den spezifischen elektrischen widerstand von gusseisen mit lamellen-bzw. kugelgraphit, Giesserei-praxis, 14 (1971) pp. 256-261.
[7] M. Petrič, S. Kastelic, P. Mrvar, Selection of electrodes for ˝in situ˝ electrical resistivity measurements of molten aluminium, J. Min. Metall. Sect. B-Metall., 49B (2013) 3, pp. 279-283.

17th INTERNATIONAL FOUNDRYMEN CONFERENCE
Hi-tech casting solution and knowledge based engineering
Opatija, May 16th-18th, 2018
http://www.simet.hr/~foundry/

# MICROSTRUCTURE CHARACTERISTICS OF GOLD ALLOYS AND PROCEDURES FOR CORROSION PROTECTION

**Rebeka Rudolf[1,2]*, Lidija Zorko[1,2], Dragana Stojić[3], Vesna Štager[1], Peter Majerič[1,2]**

[1] Zlatarna Celje d.o.o., Celje, Slovenia
[2] University of Maribor Faculty of Mechanical Engineering, Maribor, Slovenia
[3] Zlatarna Celje d.o.o., Belgrade, Serbia

**Oral presentation**
*Original scientific paper*

**Abstract**

The aim of this work is to present the microstructure characteristics and microhardness of different gold alloys (yellow, white and rose). This is connected closely to achieving proper coatings on these alloys with the goal to protect their surface against corrosion. We show some results of development in coating production, where it is extremely important that the difference in the colour of the gold alloy and the applied coating is not noticeable to the naked eye. Particular attention was focused on 2 production approaches of coatings: Electro-galvanization and the PVD process, in order to avoid different effects of reflection and inappropriate aesthetic performance (colour mixing). For this purpose, we show the results of colour measurements of different produced coatings on Au alloys with the use of the CIELAB system.
The assessment of the resulting coatings` layers is performed with FIB analysis, which was used to measure the deposited layers on various gold alloys. Investigations showed that the thickness of coatings layers varies according to the process, from 800 nm obtained by electro-deposition to 50 nm obtained by the PVD process.

***Keywords***: *gold alloys, galvanic layers, corrosion protection, colour stability*

*Corresponding author (e-mail address): *rebeka.rudolf@um.si*

## INTRODUCTION

The trends in the development of gold (Au) alloys are aimed at the study [1,2], development and improvement of existing processes in order to achieve the appropriate mechanical properties of these alloys [3-5], and, recently, also in the corrosion protection of products from these alloys for the needs of jewellery [6,7], industrial products (brazes, wires, strips), as well as for various biomaterials (dental alloys, implants, etc.). In Zlatarna Celje d.o.o. (ZC), which has more than 170 years of tradition, activities in this field are also being carried out

with the aim of introducing various new approaches in the manufacture, thermo-mechanical processing and finishing of precious metal products [8-10]. The research work focuses on the development and improvement of the electro-galvanization process, which enables obtaining the desired aesthetic effect of these products, as well as ensuring high corrosion resistance. Electro-galvanization of Au alloys in ZC is carried out under an electric current, where the protective layer of coating is formed on the metal cathode (product) [11, 12]. In this case, the cationic metal forming the layer is added to the galvanic bath as soluble salts. The process serves as a tool with which it is possible to produce an effective aesthetic and protective anti-corrosion layer on various products from Au alloys manufactured by ZC under various production programmes.

Gold and Au alloys are used greatly in the development of industry, especially in dentistry [13-15], electronics, due to their excellent electrical conductivity and simultaneous excellent chemical passivity; in optics, due to the excellent reflection of infrared light and, recently, in organic chemistry due to the catalytic properties of gold nanoparticles. Nevertheless, gold is still used mostly for making jewellery, while silver is used in the conductor industry. The amount of gold used for making jewellery is 58-60% of the world's annual production of gold mines. For making silver jewellery, the amount used is about 25% of the world's silver production. When pure, precious metals, such as gold and silver, have poor mechanical properties, extremely low hardness and high ductility. Pure gold is a very soft metal (25 HV), has a very low limit of plasticity under pressure of about 0.2% (30MPa) and a large elongation (45%). As such, gold is not useful, and needs to be alloyed with the following alloying elements - silver, platinum, palladium, copper, zinc, etc. Depending on the alloying element and its amount, the parameters of the technological process also change, which influence the change of mechanical and functional properties and increases the scope of use. The tensile strength and hardness, as well as increased wear resistance, have a decisive importance for jewellery. Particular attention should be paid to these mechanical properties in the technological process. By changing the composition and the casting temperature, a change in the structure or microstructure occurs and a change in the colour of the alloy. Given that the basic metal phase of the alloy affects the mechanical properties of the material, and, hence, its use controlling the conditions of the production process can improve the microstructure significantly and, thus, the mechanical and functional properties. During the technological process of production, unstable phases are formed that tend to transform into a stable state; these are so-called metastable phases. In addition to unstable phases with non-stoichiometric composition, other irregularities may also exist in the microstructure, such as porosity, non-homogeneity, linear defects (dislocations, grain boundaries), etc. → all of this presents irregularities that contribute to an increase in the degree of metastability. The aim of thermo-mechanical treatment is to remove the defects in the structure in order to achieve a more stable state. The metastable state of precious metals is not desirable because it increases the likelihood of corrosion and, thus, reduces the quality of the products themselves.

In this paper, we will present the results of investigations of newly formed deposits on various substrates from Au alloys. We took into account the fact that the resulting coating must have a high gloss and a colour resembling the basic alloy of the product as much as

possible (the difference in the reflection of the two surfaces must not be perceptible to the human eye) [15]. On the basis of these requirements, various baths with a high degree of purity (99.99%) were prepared, with which we have prepared a combination of protective layers aimed at the production of a "sandwich" structure of the coating. According to theory for composite materials, a coating structure consisting of several layers is expected to have substantially better mechanical and strength properties, and high corrosion resistance. The developed "sandwich" coating therefore represents an innovation in this field of Au golden alloys. Various characterization techniques were used to characterize the resulting layers: SEM + FIB, XRF technology, which allowed us to measure the thickness of the resulting corrosion coatings and evaluate their microstructure also at the contact with the base material. This is important for raising the level of understanding of anti corrosion phenomena, which we will use to determine the corrosion protection of ZC products.

## MATERIALS AND METHODS

Table 1 presents Au alloys` description (composition in wt. %) and coating methods used in this research for protection of their surfaces. Au alloys were marked according to the visual appearance (name). All alloys were cleaned in ultrasound, washed and degreased prior to coating.

Table 1. Au alloys and coating methods

| Sample name | Sample mark | Coating method |
|---|---|---|
| **Yellow Au**<br>Chemical composition:<br>Au 57 wt.%<br>Ag 29 wt.%<br>Cu 14 wt.% | Yellow Au0 | Control sample (without coating) |
| | Yellow Au1 | Hard Au coating |
| | Yellow Au2 | Hard Au coating<br>Colour Au coating |
| | Yellow Au3 | PVD process - Au coating with JEOL JFC-1100E Ion Sputter |
| **White Au**<br>Chemical composition:<br>Au 56 wt.%<br>Ag 8 wt.%<br>Cu 23 wt.%<br>Zn 6 wt.%<br>Pd 7 wt.% | White Au0 | Control sample (without coating) |
| | White Au1 | Pd/Rh coating 2× |
| | White Au2 | PVD process - Pt coating with JEOL JFC-1100E Ion Sputter |
| **Rose Au**<br>Chemical composition:<br>Au 59 wt.%<br>Ag 1 wt.%<br>Cu 39 wt.%<br>Zn 1 wt.% | Rose Au0 | Control sample (without coating) |
| | Rose Au1 | ROSE coating |

Metallographic samples were prepared in accordance with the appropriate Standards for metallographic preparation (brushing, polishing, etching). After cutting, the metallographic sample is polished on felts for polishing of varying fineness with a suitable polishing paste. After completion of the polishing and washing of gold samples, the dried sample is etched with an etchant, namely 1 part: 1 g KCN + 10 ml $H_2O$ and 2 parts: 1.1 g $(NH_4)_2S_2O_8$ + 10 ml $H_2O$. The etching time of gold samples was 180 s. For all samples, a metallographic examination was performed in the longitudinal and transversal directions. The samples were observed with light microscopy – Nikon Epiphot 200 at different magnification.

For identification of grain size, we used the Standard ASTM E112 – 12 Intercept method, which involves an actual count of the number of grains intercepted by a test line, or the number of grain boundary intersections with a test line, per unit length of test line, used to calculate the mean lineal intercept length, ℓ. ℓ is used to determine the ASTM grain size number, *G*. The precision of the method is a function of the number of intercepts or intersections counted. A precision of better than ±0.25 grain size units can be attained with a reasonable amount of effort. Results are free of bias; repeatability and reproducibility are less than ±0.5 grain size units.

On the samples, the HV1 micro-hardness was also measured on a ZWICK 3212 device with 9,804 N applied force and 20s load time. On each sample, the measurement was carried out in the longitudinal and transversal directions. In this way, minor or greater differences in the results were found.

In addition, samples with formatted coatings were observed with electron microscopy. The following equipment was used: Environmental Scanning Electron Microscope (FEI Quanta 200 3D), which is equipped with an Ion gun – FIB (Focused Ion Beam) and a system for platinum deposition. The ion gun generates focused Ion stream Ga ions, which may be composed of individual layers of atoms to crop a cross-section of the sample in the micro area. The application of platinum is to protect the area or make a conductive layer.

A Spectrophotometer Datacolor SF600 plus was used for measuring the colour parameters of Au samples with coatings. The instrument allows measuring of the remission spectrum of incident light in 10 nm intervals within the visible part of the spectrum (360 – 700 nm).

## RESULTS AND DISCUSSION

### MICROSTRUCTURE OF GOLD ALLOYS

Table 2-4 presents microstructures and grain size of the gold alloys used in this research.

Table 2. Yellow gold microstructure

| Cross section | Longitudinal section |
|---|---|
| 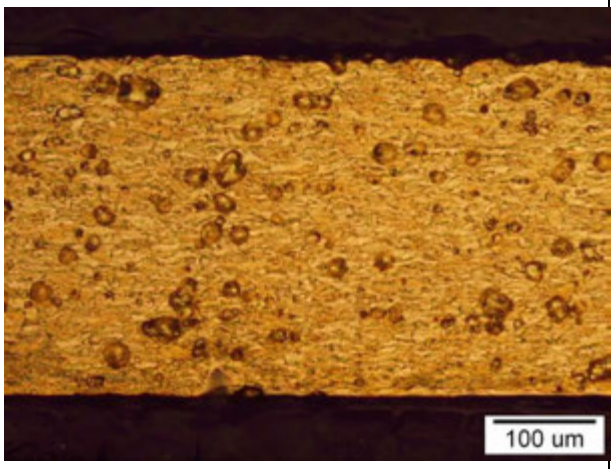  | 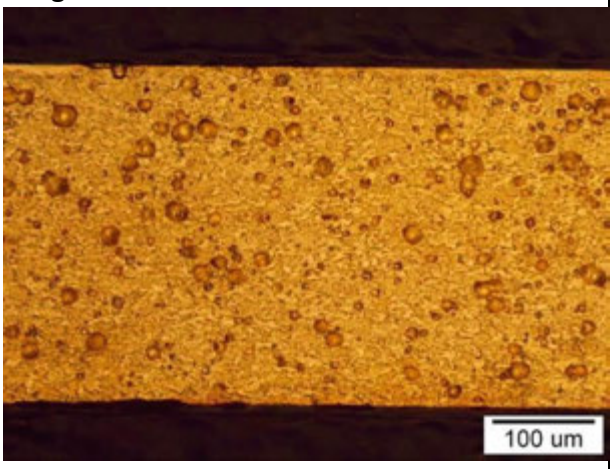  |
| 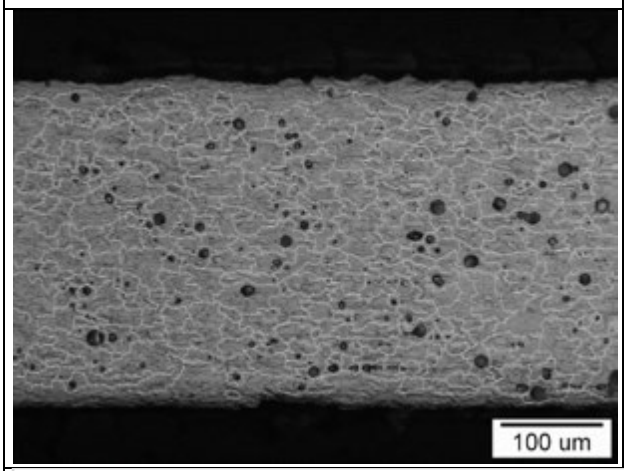  | |

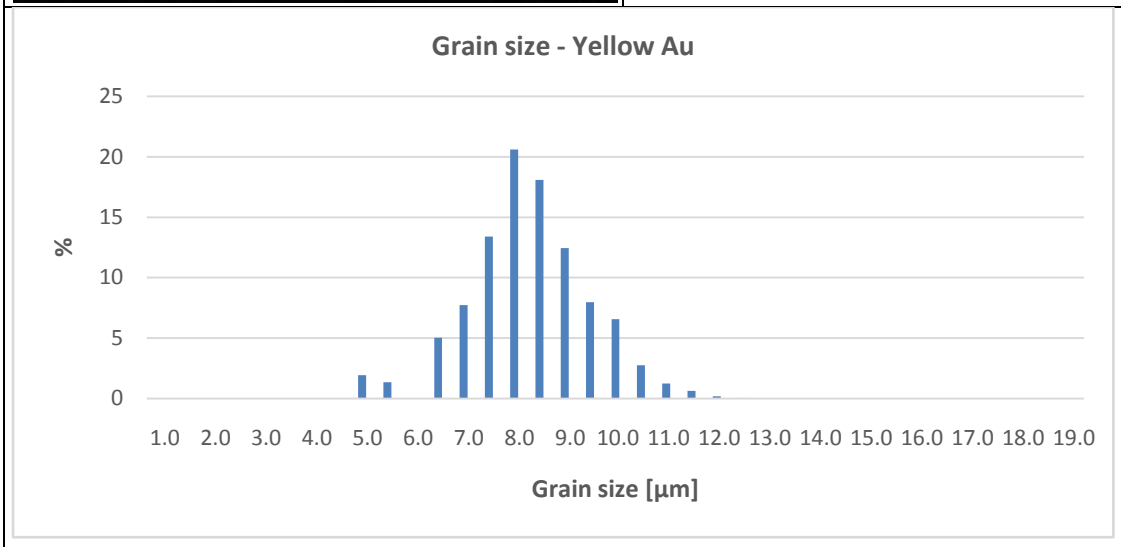

Table 3. Rose gold microstructure

| Cross section | Longitudinal section |
|---|---|
| 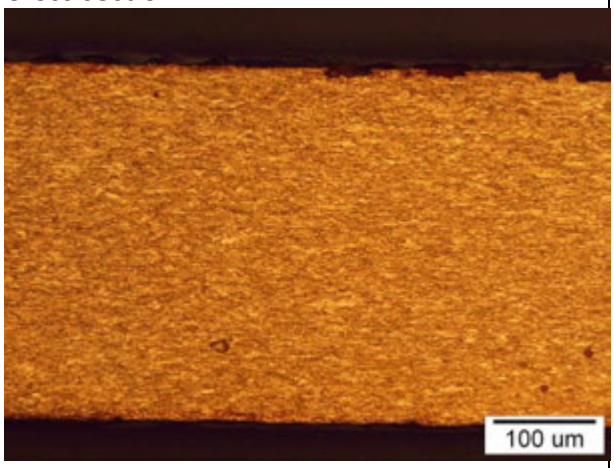  | 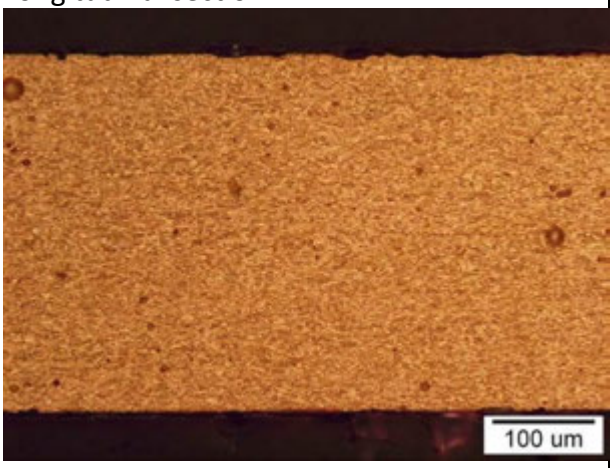  |
| 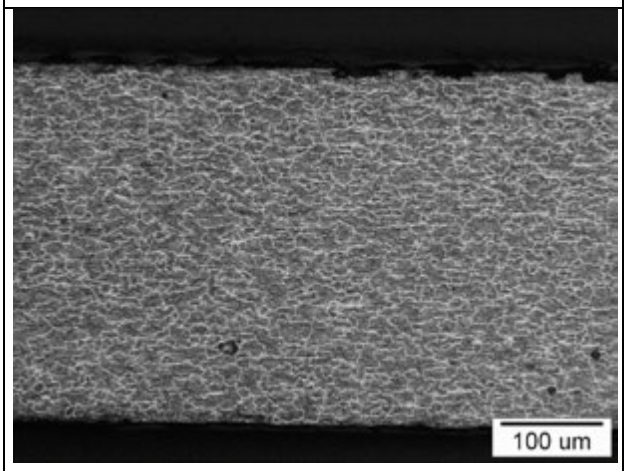  | |

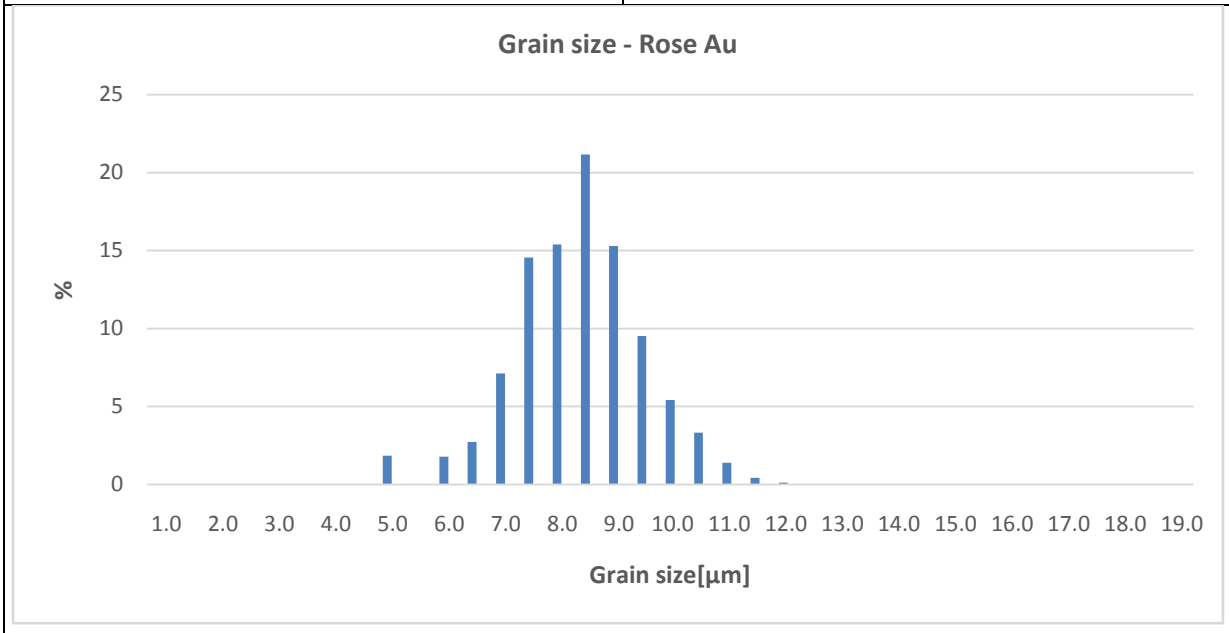

Table 4. White gold microstructure

| Cross section | Longitudinal section |
|---|---|
| 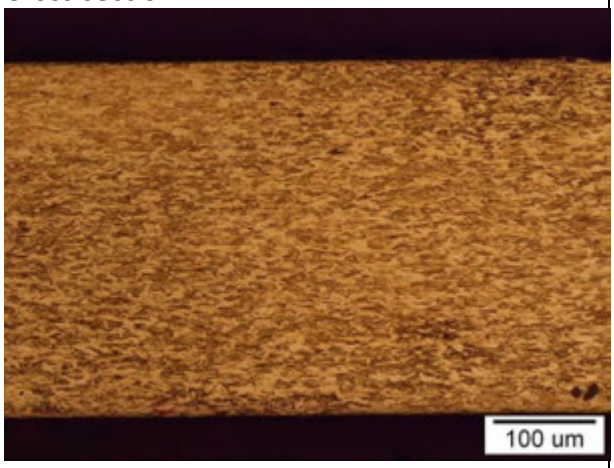  | 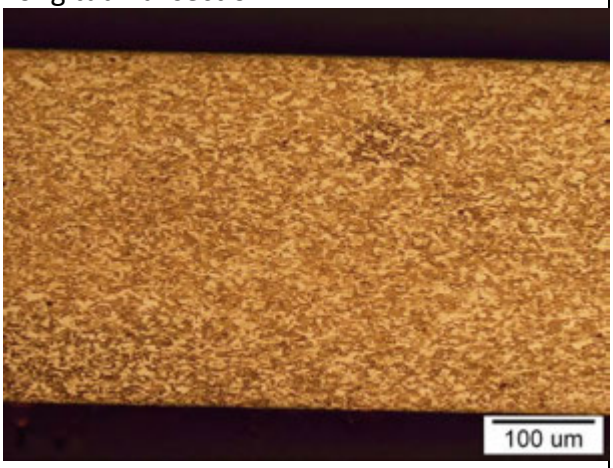  |
| 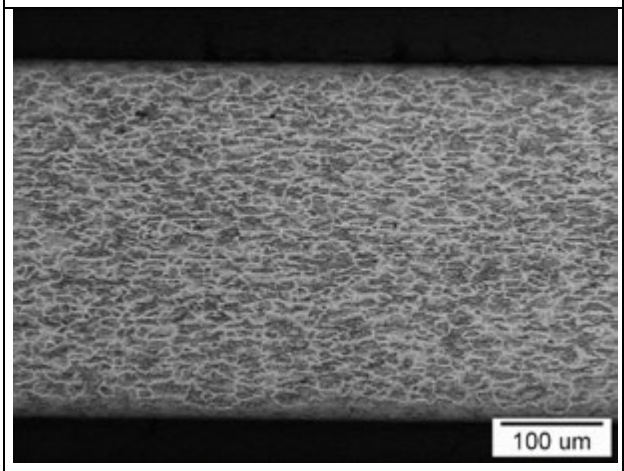  | |

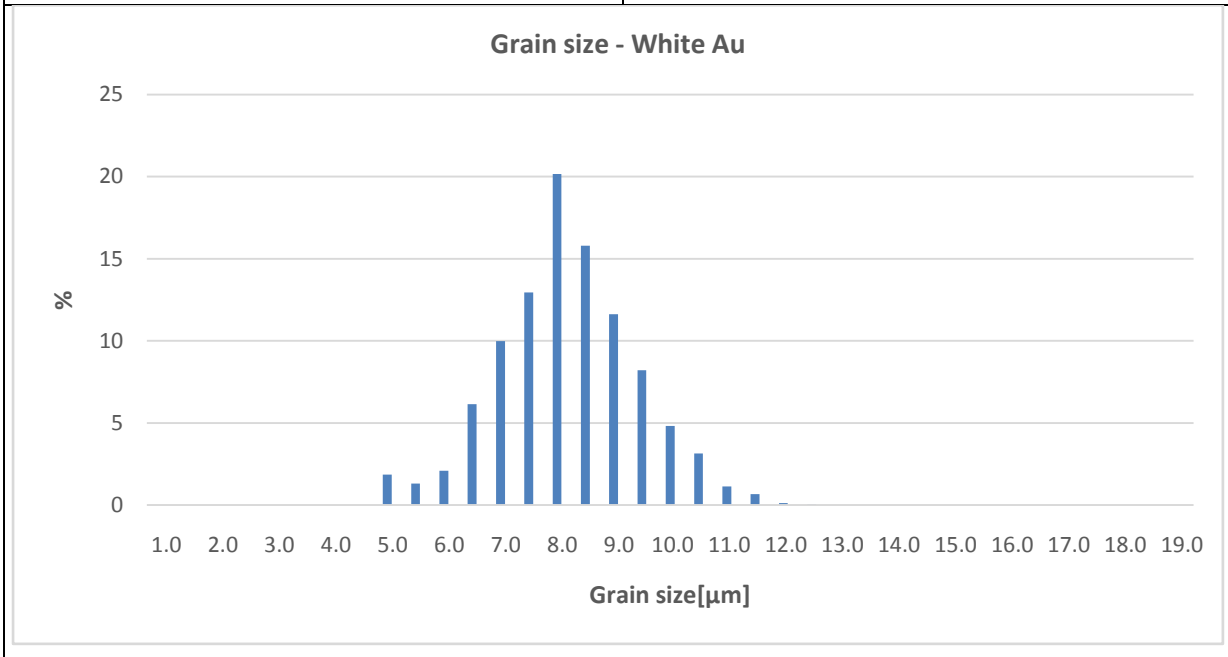

The metallographic examination of the yellow gold sample has shown oxidation traces at the grain boundaries, a larger grain size compared to the other two samples, and the appearance of holes on the surface, which may be due to the preparation of the sample, and although the pink gold sample has the highest percentage of copper, there was no oxidation at the grain boundaries. Of all the three samples, the structure of the white gold sample is the most homogeneous and finely grained. Measuring grain size is a complex process that depends on several factors, since the three-dimensional grain size is not constant, and the grain cross- section is random. Test methods include assessment procedures and rules for expressing the average grain size of a material, which consists essentially of only one phase. When comparing the grain size, the largest grain size was in a white gold sample (10.05 µm), and the smallest in a pink gold sample (9.84 µm).

## MICROHARDNESS OF GOLD ALLOYS

Table 5. Micro-hardness results

| **Yellow gold alloy** | | |
|---|---|---|
| | Cross-section | Longitudinal section |
| Mean value | 235 | 225 |
| **Rose gold alloy** | | |
| | Cross-section | Longitudinal section |
| Mean value | 278 | 269 |
| **White gold alloy** | | |
| | Cross-section | Longitudinal section |
| Mean value | 297 | 295 |

When we compare the measurement results of gold samples presented in Table 5, we see that the white gold sample has the highest HV1 micro-hardness value (297 in the transverse, or 295 in the longitudinal direction), compared with samples from yellow and pink gold, and the yellow gold sample has the lowest value (235 in the transverse, or 225 in the longitudinal direction). The reason for these micro-hardness measurements results is the fact that, in white gold, the composition includes elements that increase the hardness (rhodium); there is also an intermetallic mixture of copper and gold, which increases the strength, in contrast to the yellow gold, where there is a high percentage of gold, and hardness increases only with an intermetallic compound that forms from gold with copper.

**COATING MEASUREMENT RESULTS**

This section presents the coating layer measurements of Au alloys.
Figure 1 shows the FIB analysis of the yellow Au1 sample. With this sample, according to the yellow Au0 reference sample, another layer of gold is applied to the prepared surface. The results showed that the average layer thickness for this sample was 216 nm.

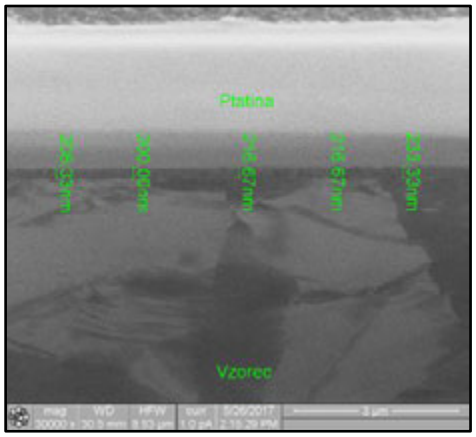


Figure 1. FIB analysis – sample Yellow Au1

In the Yellow Au2 sample - Figure 2, in contrast to Yellow Au1, one gold layer was applied, but with different parameters. Measurements of layer thickness were carried out in three places with 5 measurements. The average layer thickness of this sample is 218 nm.

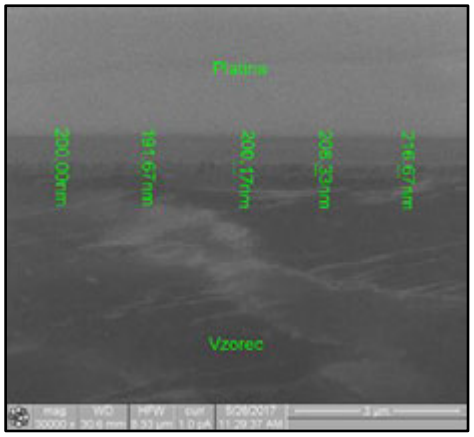


Figure 2. FIB analysis – Yellow Au2

Figure 3 shows the thickness measurements of the yellow Au3 sample. On the surface of this sample, nanoparticles were deposited using the PVD process. Unlike the other two samples, on this sample we measured layer thickness in four places with 5 measurements. Measurements showed that the average layer thickness is 47 nm.

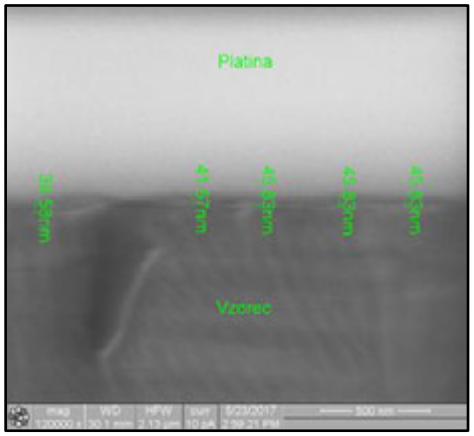


Figure 3. FIB analysis – Yellow Au3

If we compare the layer thicknesses of samples Yellow Au1 and Yellow Au2 with sample Yellow Au3, the smallest layer thickness is observed in the sample Yellow Au3.
On the basis of the results of the measurements, it was found that the maximum layer thickness is at the Yellow Au2 sample (218 nm), and the minimum layer thickness at the Yellow Au3 sample (47 nm). Such measurement results are expected, since two gold layers with different process parameters are applied to the Yellow Au2 sample, while in the yellow Au3 sample, gold is applied with the PVD process. The essence of the PVD process is to use it to apply extremely thin layers.
A layer of Pd/Rh/Pd/Rh is applied to the surface of the White Au1 sample – Figure 4, in accordance with the corresponding process parameters. For this sample, the layer thickness is measured at four places with 4 or 5 measurements. The results showed that the average thickness of the surface layer is 228 nm.

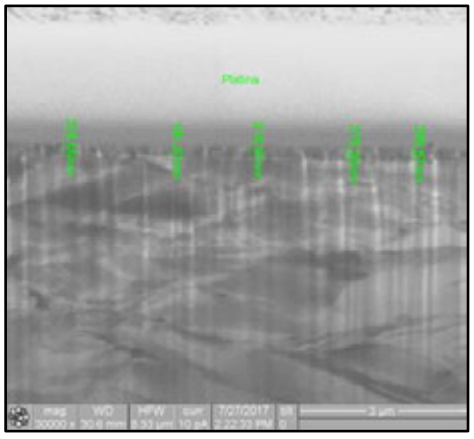

Figure 4. FIB analysis – White Au1

Figure 5 shows the layer thickness measurement on the White Au2 sample. Measurement of the layer thickness was carried out in four places with 5 measurements. The average layer thickness for this sample is 27 nm.

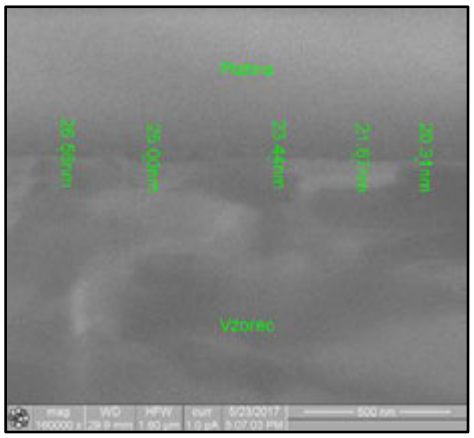


Figure 5. FIB analysis – White Au2

The measurement results of the layer thickness of the White Au1 and White Au2 samples showed that the layer thickness in the White Au1 sample was larger with respect to the layer thickness of the White Au2 sample. The results of the FIB analysis of these samples are in accordance with the surface treatment method, since four layers are deposited on the White Au1 sample, and only one layer was applied to the White Au2 sample with the PVD method.
Measurements of layer thickness on the Rose Au1 sample – Figure 6, were carried out in three places with 5 measurements. The results showed that the average surface layer thickness is 799 nm. In rose gold, given that the colour of the jewellery is of exceptional importance, another layer is applied to the surface of the sample.

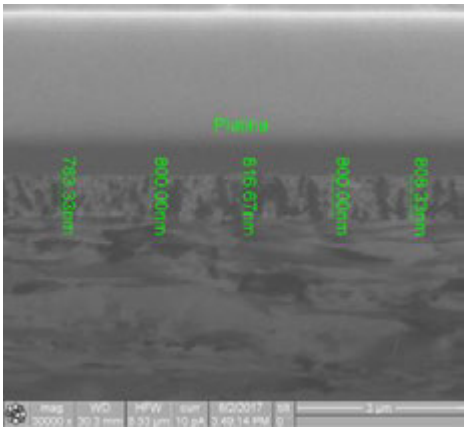


Figure 6. FIB analysis – Rose Au1

Samples were analyzed from yellow gold (Yellow Au1, Yellow Au2 and Yellow Au3), white gold (White Au1 and White Au2) and rose gold (Rose Au1).
The results showed that the smallest layer thickness was in the samples where the PVD process was used, where gold is deposited in the form of nanoparticles (Yellow Au3) and platinum nanoparticles (White Au2). The layer thickness in this case was 47 nm (Yellow Au3) and 27 nm (White Au2). Such results were expected, as the PVD method is used to apply a thin layer of material.
The results showed that the largest layer thickness occurred in samples in which two layers of gold (Yellow Au2), or more rhodium layers and palladium are applied alternately (White Au1). The precise data, as well as the process parameters themselves, are shown in Table 1.
Based on the obtained results of the FIB analysis it is assumed that, for samples with the smallest surface layer thickness, the ions will emerge from the base material into the medium, or to minor or major damage to the layer.
Electro-galvanization is used as a form of protection against corrosion, which can deposit a layer of pure metals (Au, Ag, etc.) to the prepared surface in order to avoid contact of the base alloy with oxidizing agents from the atmosphere. FIB analysis was used to measure the coating layer thickness on samples from yellow, white and rose gold alloys. The principle of the FIB is based on the same principle as the SEM, with the exception that it uses a beam of ions, usually gallium, instead of an electron beam. The primary gallium ion beam hits the surface of the sample, releasing a small amount of secondary ions from the surface (electrons or protons) or as neutral atoms. Secondary electrons ($e^-$) can also be obtained by means of a primary beam. While the ion beam acts on the surface of the sample, the signal from the scattered secondary electrons is collected as an image. Due to scattering, FIB is used as a tool for micro or nano levels to change or convert the material on a micro- or nano-level. FIB analysis was carried out on white gold (White Au-2) and yellow gold samples (Yellow Au-3). For a good analysis of the sample, it is necessary for the sample to be prepared properly. A sample of the base material was cleaned in an ultrasonic bath and then rinsed. The sample was then degreased and rinsed again. A layer of palladium was applied to such a prepared surface. When the palladium layer was finished, the sample was rinsed, followed by applying a layer of rhodium. Then the rinsing was repeated, followed by applying a palladium layer, rhodium layer, and, finally, rinsing the sample again. The parameters of the palladium and rhodium coating are the same for both layers. Finally, when the sample was rinsed, a platinum layer was applied by PVD. Based on the thickness measurements results of the White Au-2 sample, it ranges from 20.00 nm to 31.67 nm. The average thickness of the layer is 27.5 nm. Preparation of the Yellow Au-3 sample differs from the White Au-2 sample. After the repeated procedure (cleaning, rinsing, degreasing, strengthening according to the same process parameters and rinsing), the layer was "coloured". A layer of Au was deposited with the PVD process. In the White Au-2 sample, the thickness of the layer was found to be smaller (mean value of 27.5 nm) with respect to the Yellow Au-3 sample (mean value 47.9 nm). After measuring the thickness of the layer on the sample with a pink coating, it can be seen that the thickness is from 150 to 200 nm thick and the average value is 179.20 nm

**COLOUR MEASUREMENT**

The measurement procedure includes calibration with black and white after the device is started, followed by each start-up when changing the measuring opening and every 8 hours of measurements. This eliminates the effect of ageing the xenon flash on the measurement results. Each sample is placed and fixed with a special holder against the measuring aperture of the instrument. The sample is highlighted from the light source placed inside the instrument. The instrument measures the wavelengths of reflected and absorbed parts of the incident light. Measured data are stored into a computer database, and can be used by the special computer software for sorting and calculating the values of the colour parameters necessary for defining colour, whiteness, or computer colour matching.
Table 6 presents the colour measurement results of gold alloys. 9 samples were measured. The diagrams presented in Figure 7 show the position of the colour of the samples in the a * - b * CIELAB colour space. This colour shows the colour tone. From the sample position, it can be seen that all samples are pale yellow (very low value a *, and different value b *).

Table 6. Colour measurement results

| Sample | | a* | b* | C* | L* |
|---|---|---|---|---|---|
| RoseAU-0 | | 9.5754 | 15.88882 | 18.55109 | 84.29803 |
| RoseAU-1 | | 11.28459 | 14.22381 | 18.15651 | 83.02971 |
| WhiteAU-0 | | 1.42613 | 10.79617 | 10.88996 | 83.42687 |
| WhiteAU-1 | | 1.29849 | 3.37571 | 3.616835 | 86.73586 |
| WhiteAU-2 | | 12.66137 | 34.55458 | 36.80121 | 57.96297 |
| YellowAU-0 | | 2.27392 | 27.69907 | 27.79225 | 86.17391 |
| YellowAU-1 | | 5.71829 | 30.43739 | 30.96988 | 79.99106 |
| YellowAU-2 | | 1.4205 | 34.75325 | 34.78227 | 86.66601 |
| YellowAU-3 | | 7.49382 | 36.16143 | 36.92975 | 81.28143 |

Gold alloys contain silver, copper and other elements, in addition to gold. Silver and copper react easily with many sulphur compounds and form sulphides. A very thin layer of sulphides appears as coloration from intense yellow to red, brownish and even black at certain thicknesses. Pure gold and high carat alloys (18 carats and more) do not react with sulphur compounds, and are, therefore, resistant to staining. Usually, 14 carat alloys are resistant to staining, except in the case of severe exposure to hydrogen sulphide. Lower carat alloys (10 carat and less) behave like silver and copper, and darkening is a natural phenomenon. Not only sulphur, but also other substances, cause oxidation. The worst "enemy" of gold alloys of all purities is mercury.

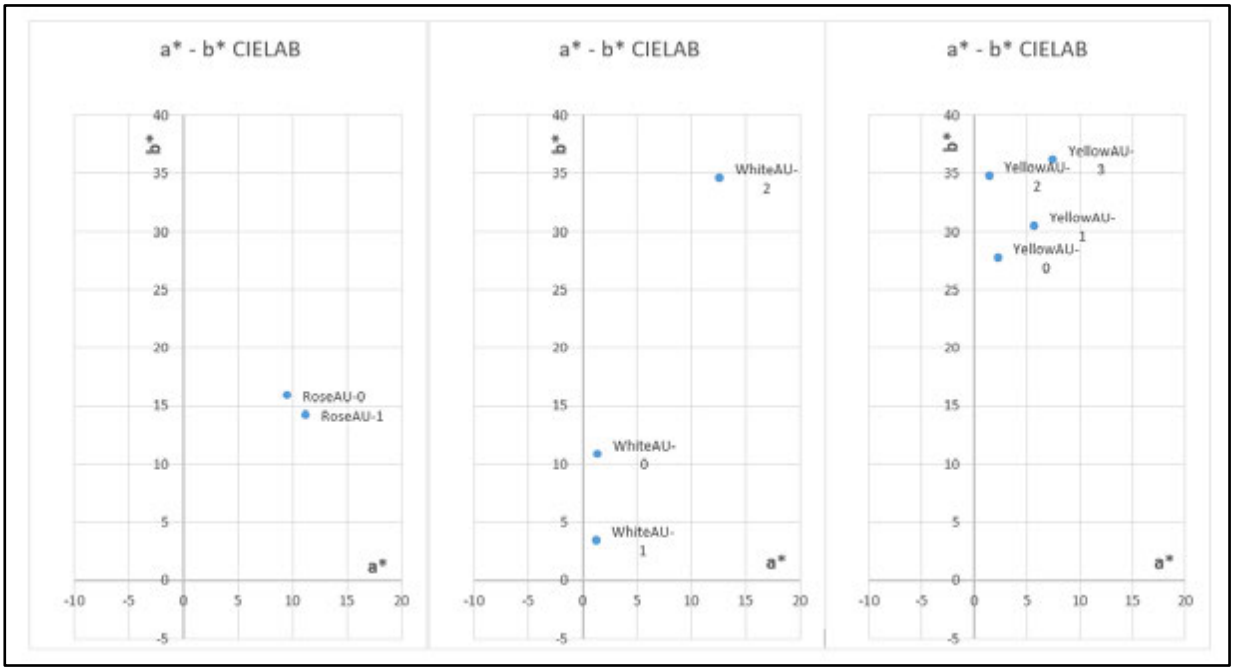


Figure 7. a * - b * CIELAB color space diagrams

If by chance jewellery comes in contact with mercury (even very small amounts), it turns into a brownish to dirty white or gray colour in a very short time. If small quantities are present, it turns brown, but if there is more mercury, a gold amalgam is formed, and the surface becomes dirty white to grey. Contact with mercury can occur when a thermometer breaks or with dental amalgams (fillings), or in a room where a halogen lamp containing mercury vapours breaks. A mercury "contaminated" gold alloy needs to be refined. In the case of gold alloys, special types of corrosions occur due to numerous metallurgical effects, among which are chemical composition, the preparation of melt and casting, thermal treatment and phase transformations. All of this affects changes in the microstructure, which is the basis for understanding the metallurgical effect of corrosion, which is present on the surface of products (jewellery, dental and industrial programmes). The corrosion of alloys follows a complicated mechanism: Oxidation of the alloy, the transfer of electrons to the reduction site of the oxidant on the surface, and the corresponding flow of cations and anions into the electrolyte and reduction of the oxidant. Corrosion cannot be avoided completely, but corrosion processes can be slowed down significantly, reduced in quantity, or the type of corrosion changed. The technological solution for this purpose is to determine the optimum conditions of the electro galvanization process (appropriate preparation of the product surface, time, temperature, voltage, choice of the appropriate anode or salt, bath dimensions, concentration, etc.), which ensures the formation of high quality and sustainable coatings on the surfaces of various products.

## CONCLUSIONS

From the experiments performed and the carried out characterizations, we can conclude the following:

- Microstructure of all three Au alloys is the most homogeneous and finely grained. The largest grain size was in a white gold sample (10.05 μm), and the smallest in a pink gold sample (9.84 μm).
- The white gold alloy has the highest HV1 micro-hardness value (297 in the transverse, or 295 in the longitudinal direction), compared with yellow and pink gold alloys, while the yellow gold sample has the lowest value (235 in the transverse, or 225 in the longitudinal direction).
- The results showed that the largest layer thickness occurred in gold alloy with rose coating (799 nm), or in the case of more rhodium and palladium layers (228 nm).
- The results showed that the smallest layer thickness was obtained by the PVD process. The layer thickness in this case of Au was 47 nm and by Pt about 27 nm. Such results were expected, as the PVD method is used to apply a thin layer of material.
- From the colour measurement it can be seen that all Au alloys belong to pale yellow (very low value a *, and different value b *).
- Corrosion cannot be avoided completely, but corrosion processes can be slowed down significantly.

## REFERENCES

[1] R. Rudolf, M. Anžel, E. Marković, M. Čolić, D. Stamenković, Gold in the past, today and future, Metalurgija, 51 (2012) 2, pp. 261-264.
[2] R. Rudolf, I. Anžel, D. Stamenković, Dental materials - challenge and usage of the latest inventions, Metalurgija, 14 (2008) 2, pp. 135-142.
[3] C. W. Corti, Metallurgy of Microalloyed 24 Carat Golds, Gold Bulletin, 32 (1999) 2, pp. 39-47.
[4] C. W. Corti, Strong 24 carat Golds: the Metallurgy of Microalloying, Gold Technology, 33 (2001) pp. 27-36.
[5] C. W. Corti, Microalloying of High Carat Gold, Platinum and Silver, Proceeding of the 2nd International Conference on Jewellerly Production Technology (JTF) Vicenza, 2005, Italy.
[6] C. W. Corti, R. J. Holliday, D. T. Thompson, Developing new industrial applications for gold: gold nanotechnology, Gold Bulletin, 35 (2002) pp. 111-117.
[7] R. Rudolf, J. Kramberger, H. T. Zupančič, D. A. Marić, V. Lazić, New gold dental alloy for metal-ceramic restorations, Stomatološki glasnik Srbije, 53 (2006) 4, pp. 236-245.
[8] A. Križman, R. Rudolf, B. Albreht, Melting and casting of dental alloys with high Au-content, Livarski vestnik: glasilo Društva livarjev Slovenije, 53 (2006) 1, pp. 19-31.

[9] R. Rudolf, H. T. Zupančič, I. Anžel, P. Mrvar, J. Medved, D. Stamenković, Characterisation of a new dental alloy with high Au content, RMZ - Materials and geoenvironment: periodical for mining, metallurgy and geology, 54 (2007) 3, pp. 303-318.
[10] R. Rudolf, H. T. Zupančič, L. Kosec, A. Todorović, B. Kosec, I. Anžel, Mechanical properties and microstructure characterisation of Au-Pt dental alloy, Metalurgija, 47 (2008) 4, pp. 317-323.
[11] R. Rudolf, B. Budič, D. Stamenković, M. Čolić, A. Ivanič, B. Kosec, Rhodium platings - experimental study, Metalurgija, 52 (2013) 3, pp. 337-340.
[12] K. Raić, R. Rudolf, B. Kosec, I. Anžel, V. Lazić, A. Todorovič, Nanofoils for soldering and brazing in dental joining practice and jewellery manufacturing, Materiali in tehnologije, 43 (2009) 1, pp. 3-9.
[13] V. Lazić, D. Stamenković, A. Todorović, R. Rudolf, I. Anžel, Investigation of mechanical and biomedical properties of new dental alloy with high content of Au, Metalurgija, 14 (2008) 2, pp. 121-134.
[14] M. Čolić, D. Stamenković, I. Anžel, G. Lojen, R. Rudolf, The influence of the microstructure of high noble gold-platinum dental alloys on their corrosion and biocompatibility in vitro, Gold bulletin, 42 (2009) 1, pp. 34-47.
[15] R. Rudolf, H. T. Zupančič, D. Stojić, Optička svojstva nove dentalne legure sa visokim procentom Au i značaj pripreme površine dentalne legure pre pečenja opaker-a OP5, Stomatolog, 84 (2010) pp. 10-13.

## Acknowledgements

This study was supported by the Infrastructure Programme I0-0029 and Research Core Programme P2-120 financed by the Slovenian Research Agency ARRS. Thanks also to the Ministry of Education, Science and Sport, Republic of Slovenia (Program MARTINA, OP20.00369) and project 391-00-16/2016-16/Zlatarna Celje d.o.o. Beograd, which enabled the research with co-financing.

17th INTERNATIONAL FOUNDRYMEN CONFERENCE
Hi-tech casting solution and knowledge based engineering
Opatija, May 16th-18th, 2018
http://www.simet.hr/~foundry/

# WEAR BEHAVIOUR OF TiAlN COATING DEPOSITED ON DEEP CRYOGENIC TREATED HIGH SPEED STEEL SUBSTRATE

# OTPORNOST NA TROŠENJE TiAlN PREVLAKE NA PODLOZI DUBOKO HLAĐENOG BRZOREZNOG ČELIKA

**Sanja Šolić[1]*, Bojan Podgornik[2], Zdravko Schauperl[3], Matjaž Godec[2], Vlado Tropša[1]**

[1] University North, Department of Mechanical Engineering, Varaždin, Croatia
[2] Institute of Metals and Technology, Ljubljana, Slovenia
[3] University of Zagreb Faculty of Mechanical Engineering and Naval Architecture, Zagreb, Croatia

**Oral presentation**
*Original scientific paper*

**Abstract**

The aim of the research was to investigate the influence of deep cryogenic treatment on the load-carrying capacity of the high speed steel substrate and the wear resistance, hardness and coefficient of friction of the PVD TiAlN hard coating. Deep cryogenic treatment in combination with classic heat treatment shows a significant improvement in wear resistance of high speed steel tools. Also extending tool durability by reducing friction and wear is achieved by applying hard thin coatings to the tool surface. The results showed that deep cryogenic treatment influenced the properties of the substrate which resulted in higher hardness, reduction of friction coefficient and better wear resistance of the deposited TiAlN coating.

***Keywords**: deep cryogenic treatment, PVD coating, load-carrying capacity, coefficient of friction, wear resistance*

*Corresponding author (e-mail address): *ssolic@unin.hr*

**Sažetak**

Svrha provedenog istraživanja je ispitivanje utjecaja dubokog hlađenja na nosivost brzoreznog čelika kao podloge za nanošenje tanke tvrde PVD TiAlN prevlake te utjecaj nosivosti podloge na otpornost na trošenje, tvrdoću i faktora trenja same prevlake. Primjena postupka dubokog hlađenja kao segmenta u toplinskoj obradi pokazala je značajno povećanje otpornosti na trošenje alata od brzoreznih čelika. Također, produljenje trajnosti alata smanjenjem trenja i trošenja postignuto je nanošenjem tvrdih tankih prevlaka na njihovu površinu. Rezultati istraživanja pokazali su značajan utjecaj dubokog hlađenja na poboljšanje svojstava brzoreznog čelika kao podloge čime je TiAlN

prevlaka ostvarila povećanje tvrdoće, smanjenje faktora trenja te bolju otpornost na trošenje pri dva različita primijenjena opterećenja.

***Ključne riječi:*** *duboko hlađenje, PVD prevlaka, nosivost podloge, faktor trenja, otpornost na trošenje*

## UVOD

Produljenje trajnosti alata smanjenjem trenja i trošenja postignuto je nanošenjem tankih tvrdih prevlaka na njihovu površinu. Glavne prednosti nanošenja tankih tvrdih prevlaka proizlaze iz smanjenja trenja što rezultira manjim zagrijavanjem alata i smanjenjem sila rezanja, manjom adhezijom prema materijalu obratka, a uslijed čega je manji prijelaz materijala u tribosustavu alat – prevlaka - obradak. Povećanje tvrdoće površine alata utječe na smanjenje trošenja abrazijom, a smanjeno je i difuzijsko trošenje zbog kemijske stabilnosti prevlake koja predstavlja difuzijsku barijeru [1 - 3].
Da bi zadovoljio tražena svojstva materijal prevlake mora imati nisku adheziju prema materijalu obratka, ali visoku prema osnovnom materijalu alata, dobru otpornost na abrazijsko trošenje, visoku kemijsku postojanost i visoku tvrdoću. Sekundarni zahtjevi na prevlaku su sitnozrnata mikrostruktura, tlačna unutarnja naprezanja i glatka površina.
Tanke tvrde karbidne i nitridne prevlake nanesene postupcima fizikalnog i kemijskog prevlačenja iz parne faze (PVD i CVD postupcima) zbog svojih se svojstava vrlo uspješno primjenjuju za tu namjenu već nekoliko desetljeća [2, 4].
Tvrde PVD prevlake su zbog sitnozrnate mikrostrukture i velikih unutarnjih tlačnih naprezanja znatno otpornije na nastanak mikro pukotina od CVD prevlaka. Relativno niska temperatura nanošenja onemogućava nastanak krhke η-faze u površinskom sloju tvrdog metala pa stoga ne dolazi do oslabljenja rezne oštrice alata. Učinkovitost alata zaštićenog tvrdom PVD prevlakom ne ovisi samo o svojstvima obrađivanog materijala već i u najvećoj mjeri o adheziji prevlake na podlogu te o mehaničkim, toplinskim i tribološkim svojstvima prevlake i podloge na koju se nanosi [1, 3 - 5].
Prva prevlaka za zaštitu reznih alata nanesena PVD postupkom bila je TiN prevlaka koja se zbog svojih dobrih svojstava koristi i danas. Primjerena je za obradu manje zahtjevnih materijala pri manjim brzinama rezanja. Za obradu tvrdih i žilavih materijala pri manjim brzinama rezanja i s prekidima jako dobra se pokazala Ti(C,N) prevlaka. Odlikuje se niskim faktorom trenja pri niskim temperaturama. Odvojena čestica je stoga glatka i klizi preko rezne oštrice.
(Ti, Al)N prevlaka donijela je veliki napredak u primjeni za rezne alate jer je osim vrlo visoke tvrdoće, za razliku od Ti(C,N) prevlake, i oksidacijski postojana. Iz tog razloga pogodna je za zaštitu alata za obradu vrlo abrazivnih materijala, kao što su Fe ljevovi i legure Al-Si, a pri čemu se razvija visoka temperatura na reznoj oštrici. Za razliku od Ti(C,N) prevlake (Ti,Al)N ima veći faktor trenja, ali slabiju toplinsku vodljivost. Zbog toga odvojena čestica uzrokuje velika naprezanja na reznoj oštrici što dovodi do odlamanja prevlake. S druge strane (Ti,Al)N zadržava visoku tvrdoću pri visokim temperaturama, oksidacijski je postojana i daleko bolji toplinski izolator od TiN prevlake. Radi toga se općenito smatra da je preporučena brzina

obrade alata prevučenog (Ti,Al)N prevlakom za 30% veća od iste preporučene za alat s TiN prevlakom. Pri obradi odvajanjem čestica, na površini alata s (Ti,Al)N prevlakom nastaje tanki pasivacijski sloj aluminijevog oksida $Al_2O_3$, koji štiti samu prevlaku od daljnje oksidacije. Ukoliko dođe do skidanja tog sloja, sloj će se obnoviti u kratkom vremenu [1].
Aluminijev oksid se također odlikuje slabom toplinskom vodljivosti, tako da se veći dio topline koja se razvija na reznoj oštrici odnosi s odvojenom česticom iz sustava i ne prelazi na sam alat. Upravo razvijanje tog tankog sloja $Al_2O_3$ povećava trajnost alata. Glodala prevučena (Ti,Al)N prevlakama imaju 60% veću trajnost od istih prevučenih Ti(C,N) prevlakama i tri puta veću od TiN [6-9].
Dosadašnja istraživanja [1-10] pokazala su da odlučujuću važnost za učinkovitost tribosustava «osnovni materijal /prevlaka /obradak» ima tzv. adhezijski spoj točnije adhezijska veza tj. zona između prevlake i osnovnog materijala. Kvaliteta adhezijske veze direktno utječe na učinkovitost tvrde prevlake u kontaktu s materijalom obratka. Osnovni zahtjev adhezijske veze je dobra prionjivost tj. adhezivnost prevlake jer ukoliko ne postoji dovoljna adhezivnost prema podlozi sva ostala svojstva prevlake neće doći do izražaja.
Karakteristike prevlake (debljina, kemijski sastav, mikrostruktura, topografija itd.) određene su parametrima postupka nanošenja (temperatura podloge, karakteristike plazme, vrijeme nanošenja, prednapon podloge itd.), ali u značajnoj mjeri i svojstvima osnovnog materijala (kemijski sastav, mikrostruktura, topografija, itd.) [4].
Osnovni materijal tj. podloga primarno utječe na nukleaciju i način rasta prevlake kao i na njenu topografiju. Uslijed toga, svojstva materijala podloge te priprema površine (hrapavost) osnovnog materijala ključni su za topografiju i adhezivnost tj. prionjivost prevlake te njenu učinkovitost u primjeni. U konačnici o karakteristikama prevlake ovise njena mehanička, toplinska, kemijska i tribološka svojstva [1, 4].
Cilj ovog istraživanja bio je ispitati utjecaj dubokog hlađenja brzoreznog čelika proizvedenog metalurgijom praha na tvrdoću, otpornost na trošenje te faktor trenja TiAlN prevlake nanesene na duboko hlađenu podlogu. Željelo se istražiti da li će, i u kojoj mjeri promjena primijenjene toplinske obrade brzoreznog čelika utjecati na svojstva prevlake, prvenstveno na tvrdoću i faktor trenja, te na otpornost na trošenje u uvjetima suhog kliznog trošenja.

## MATERIJALI I METODE

Ispitivanje je provedeno na brzoreznom čeliku proizvedenom metalurgijom praha oznake PM S390 MC. Kemijski sastav čelika prikazan je u tablici 1.

Tablica 1. Kemijski sastav ispitivanog čelika PM S390 MC

| % C | % Si | % Mn | % Cr | % Mo | % V | % W | % Co | % Fe |
|---|---|---|---|---|---|---|---|---|
| 1,64 | 0,60 | 0,30 | 4,80 | 2,00 | 4,80 | 10,40 | 8,00 | ostalo |

Ispitivanja su provedena na ispitnim uzorcima dimenzija ϕ22 mm x 4 mm. Toplinska obrada provedena je u vakuumskoj peći Ipsen. Uzorci su do temperature austenitizacije prošli tri predgrijavanja: 650 °C / 30 min, 850 °C / 20 min, 1050 °C / 15 min.

Brzina ugrijavanja do temperature austenitizacije bila je 5 °C/ min. Nakon austenitizacije u trajanju od 6 min uzorci su gašeni u struji dušika, p = 1050 mbar. Parametri toplinske obrade te oznake uzoraka prikazani su u tablici 2.

Tablica 2. Parametri provedene toplinske obrade

| Oznaka | Austenitizacija, °C / min | Duboko hlađenje, °C / h | Popuštanje, °C / h |
|---|---|---|---|
| C | 1130 / 6 min | - | 520 / 520 / 490 / 2h |
| DCT | 1130 / 6 min | - 196 / 24 h | 520 / 2h |

Nakon gašenja ispitni uzorci su kontroliranom brzinom uronjeni u tekući dušik te ostavljeni 24 h. Ostali uzorci su popušteni tri puta.
Nakon provedene toplinske obrade na ispitnim uzorcima provedena su temeljita ispitivanja mehaničkih i triboloških svojstava te karakterizacija mikrostrukture ispitnih uzoraka, a rezultati su objavljeni [10].
Provedena ispitivanja [10] pokazala su da je duboko hlađenje utjecalo na mikrostrukturu čelika što se očitovalo kroz povećanje tvrdoće (917 HV1 za klasično obrađene uzorke te 945 HV1 za duboko hlađene uzorke), neznatno je povećana tlačna čvrstoća te granica stlačivanja te je kod duboko hlađenih uzoraka došlo do značajnog povećanja otpornosti na intenzivno adhezijsko trošenje.
Nakon provedene toplinske obrade uzorci su polirani (Ra = 0.05–0.10 µm) te mehanički i kemijski očišćeni prije smještanja u uređaj za nanošenje prevlake. Prije samog prevlačenja u uređaju je provedeno ionsko nagrizanje u trajanju od 30 min pri čemu je s površine odstranjen sloj debljine oko 0,1 µm. Nagrizanje je provedeno u smjesi 90% argona i 10% kryptona. U postupku je na temperaturi od 450 °C nanesena standardna komercijalna TiAlN prevlaka debljine 6 µm. Parametri i uvjeti nanošenja TiAlN prevlake detaljno su opisani u [5]. U istom radu detaljno su navedeni rezultati karakterizacije prevlake.
U ovom istraživanju faktor trenja i otpornost na trošenje ispitano je metodom „ball-on-flat“ na CSM tribotesteru s dva primijenjena opterećenja, 850 MPa i 1 GPa. Kuglica ϕ32 mm od WC korištena je kao protutijelo, a ispitivanje je provedeno pri sobnoj temperaturi u uvjetima suhog trenja uz prosječnu brzinu klizanja kuglice od 0,12 m/s i ukupnu duljinu klizanja 250 m. Amplituda kuglice pri ispitivanju bila je 4 mm, frekvencija ispitivanja 15 Hz. Parametri ispitivanja prikazani su na slici 1. Na svakom ispitnom uzorku napravljena su tri traga trošenja s jednim opterećenjem, a dobiveni rezultat faktora trenja i volumena trošenja predstavlja srednju vrijednost tri ispitivanja po pojedinom opterećenju.

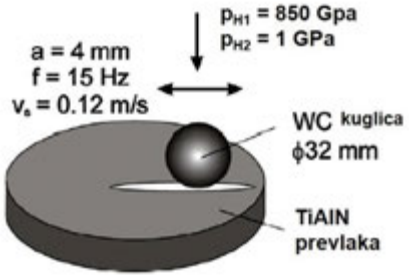


Slika 1. Shema ispitivanja trošenja metodom „ball-on-flat“ s primijenjenim parametrima

Tragovi trošenja prevlake analizirani su na FE skenirajućem elektronskom mikroskopu JEOL JSM6500F. Tvrdoća prevlake ispitana je na uređaju Vickers nanohardness tester, Fisherscope H100C, raspon opterećenja 0,4 mN – 1 N (40 mg – 100 g), opterećenjem od 50 mN i 100 mN. Prije ispitivanja tvrdoće uzorci su lokalno polirani dijamantnom pastom promjera abraziva 1 µm. Primijenjena opterećenja pri ispitivanju tvrdoće odabrana su na temelju dubine utiskivanja indentora obzirom na debljinu prevlake kako dubina utiskivanja indentora ne bi premašila jednu desetinu debljine prevlake čime je dobivena stvarna tvrdoća prevlake bez utjecaja tvrdoće podloge na rezultat ispitivanja. Za svako opterećenje napravljeno je deset mjerenja te rezultat predstavlja njihovu srednju vrijednost.

## REZULTATI I RASPRAVA

Na slici 2 prikazana je mikrostruktura TiAlN prevlake na poprečnom prijelomu ispitnih uzoraka. Na slikama je vidljiva TiAlN prevlaka na podlozi brzoreznog čelika te uniforman rast prevlake na obje podloge. Rezultati karakterizacije prevlake te tribooloških svojstava prevlake prikazani su u [10].

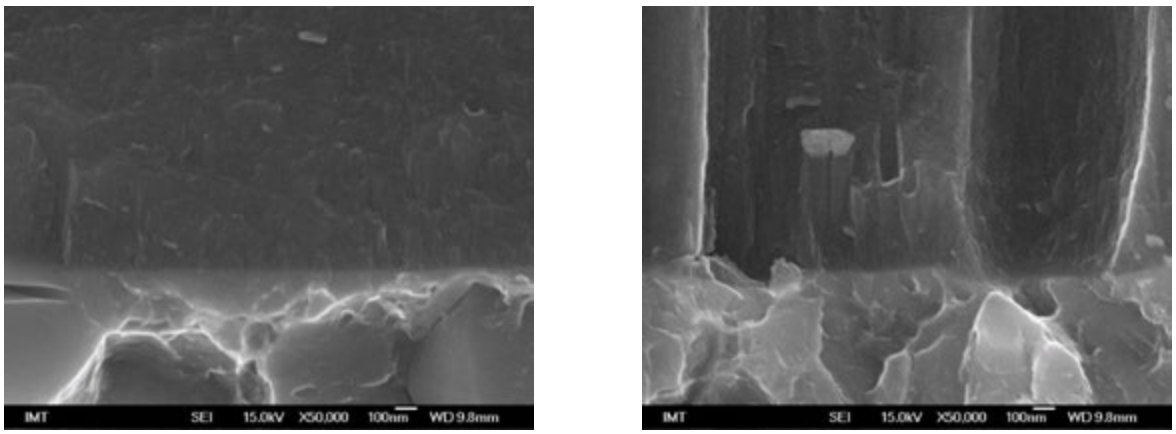


Slika 2. Poprečni prijelom ispitnih uzoraka: a) uzorak C, b) uzorak DCT

U dijagramu na slici 3 prikazani su rezultati ispitivanja tvrdoće TiAlN prevlake nanesene na dvije različito toplinski obrađene podloge. Iz rezultata je vidljivo da je na uzorcima koji su duboko hlađeni tvrdoća TiAlN prevlake veća za oba primijenjena opterećenja. Kako tvrdoća prevlake ne predstavlja njezino unutrašnje svojstvo već ovisi o čitavom nizu utjecajnih faktora [2, 4], pa tako i o svojstvima podloge koja svojom mikrostrukturom i svojstvima utječe na rast prevlake, vrstu adhezijske veze te prionjivost prevlake, rezultati ispitivanja pokazuju kako je duboko hlađenje brzoreznog čelika značajno utjecalo na tvrdoću prevlake. Prema [11] najveći utjecaj dubokog hlađenja može se pripisati plastičnoj deformaciji primarnog martenzita koja prati martenzitnu pretvorbu, djelomičnom otapanju karbida te formiranju ugljičnih klastera. Analogno tome pretpostavlja se da plastična deformacija primarnog martenzita kombinirana sa smanjenim udjelom ugljika u martenzitnim rešetkama

te precipitacija homogenijih karbida malih dimenzija utječe na porast tvrdoće kod duboko hlađenog uzorka, a što je utjecalo i na porast tvrdoće TiAlN prevlake na takvoj podlozi.

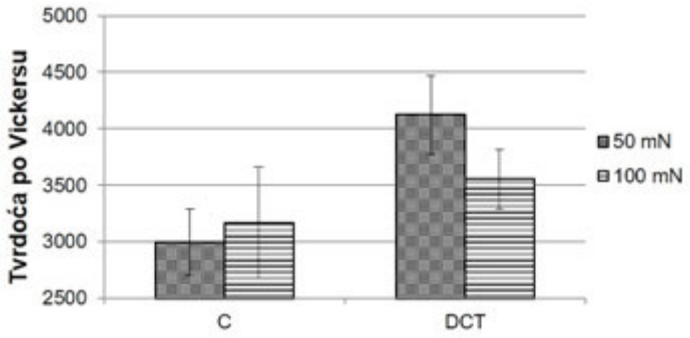


Slika 3. Tvrdoća po Vickersu TiAlN prevlake

U dijagramu na slici 4 prikazani su rezultati ispitivanja trošenja prevlake metodom „ball-on-flat“.

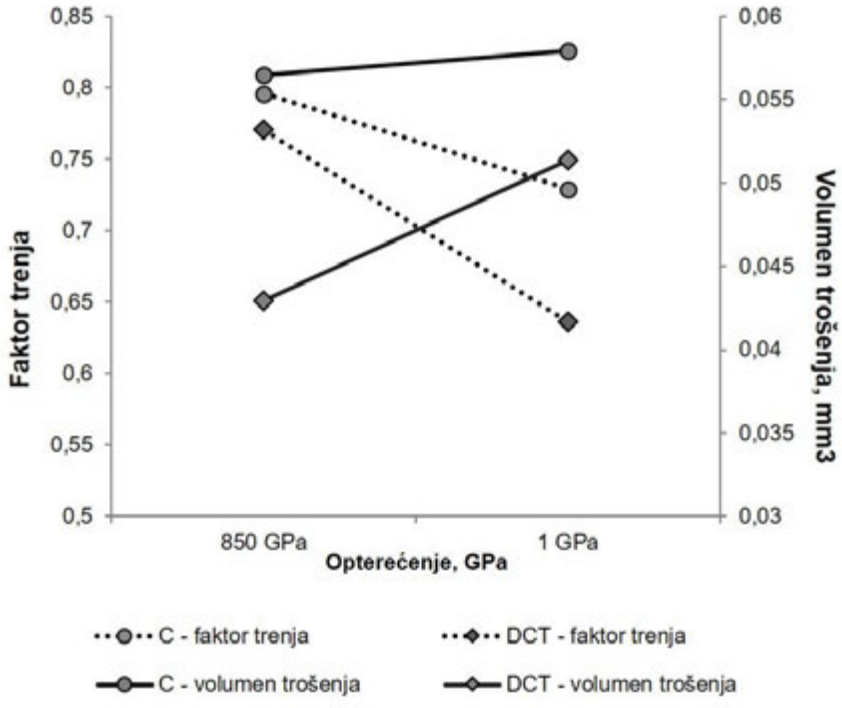


Slika 4. Volumen trošenja i faktor trenja TiAlN prevlake

Dijagram prikazuje faktor trenja TiAlN prevlake za dva primijenjena opterećenja te volumen trošenja prevlake. Rezultati ispitivanja pokazuju da je duboko hlađenje brzoreznog čelika utjecalo na smanjenje faktora trenja TiAlN prevlake u uvjetima suhog kliznog trošenja za oba primijenjena opterećenja s padom faktora trenja s povećanjem opterećenja. Volumen

trošenja TiAlN prevlake u uvjetima suhog kliznog trošenja manji je također na uzorku koji je bio duboko hlađen. S porastom opterećenja ispitivanja došlo je do porasta volumena trošenja prevlake, ali je volumen trošenja na duboko hlađenom uzorku još uvijek bio manji 10 % u odnosu na klasično toplinski obrađen uzorak.
Svojstva materijala podloge mogu značajno utjecati na nosivost sučelja prevlaka/podloga te utjecati na smanjenje pojave trošenja prevlake što je prikazano u više ispitivanja [12-15].
U svrhu određivanja mehanizama trošenja koji su se pojavili na pojedinom uzorku, tragovi trošenja analizirani su na FE SEM-u. Slika 5 prikazuje tragove trošenja ispitnih uzoraka u uvjetima suhog kliznog trošenja pri opterećenju 850 MPa. Slika 6 prikazuje tragove trošenja ispitnih uzoraka u uvjetima suhog kliznog trošenja pri opterećenju 1 GPa.

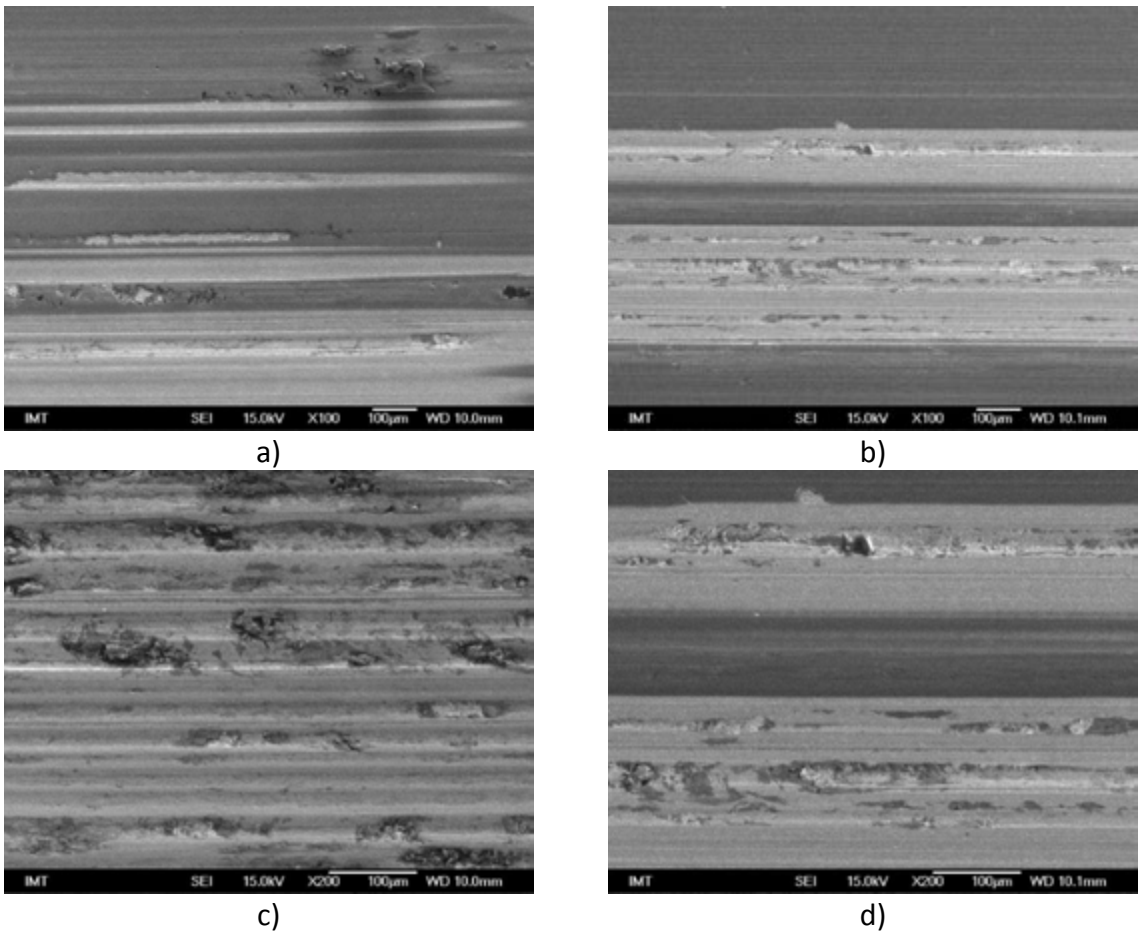


Slika 5. Tragovi trošenja TiAlN prevlake pri opterećenju 850 MPa: a) i c) uzorak C manje i veće povećanje, b) i d) uzorak DCT manje i veće povećanje

Na slici 5 a i c kod uzorka C (klasična toplinska obrada) vidljiva su brazde na površini prevlake što ukazuje na intenzivno abrazijsko trošenje tijekom ispitivanja te je vidljivo da je došlo do stvaranja naljepaka što ukazuje i na pojavu adhezijskog trošenja. Pri većem povećanju također su vidljive i pukotine na površini prevlake. Na uzorku DCT (duboko hlađenje), slika 5 b i d, vidljivo je da su tragovi trošenja slabije izraženi nego kod uzorka C što je u skladu s

manjim faktorom trenja koji je ova prevlaka imala pri ovom ispitivanju, te s manjim volumenom trošenja koji je postignut.
Također, analizom su uočeni samo tragovi trošenja koji ukazuju na pojavu mehanizma abrazije, ali bez značajne pojave adhezijskog mehanizma i stvaranja naljepaka. Nastanak pukotina na uzorku C u skladu je s [2] i rezultatima ispitivanja tvrdoće jer je dokazano da povećanje tvrdoće podloge povećava opterećenje koje prevlaka može podnijeti bez pojave pukotina, radi povećanja otpornosti prevlake na deformaciju (ugibanje) [2].

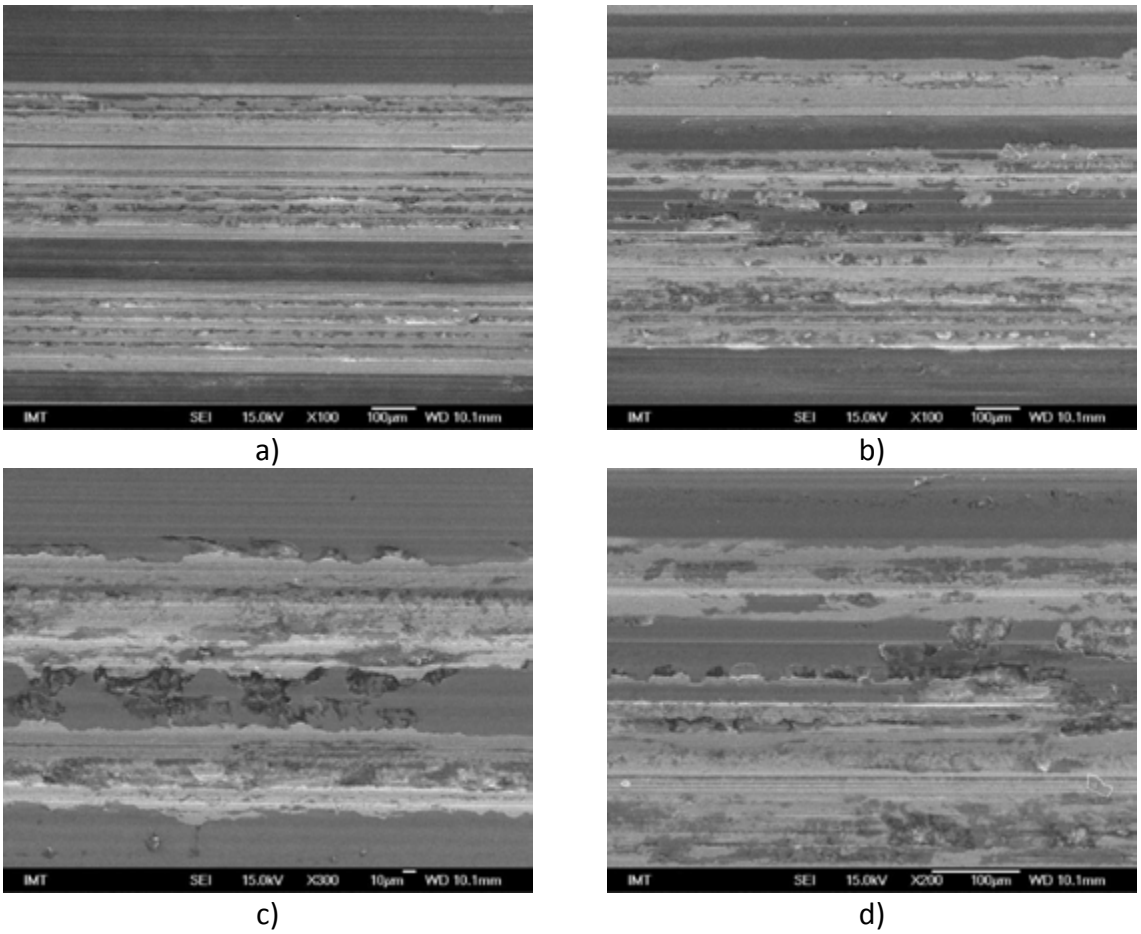


Slika 6. Tragovi trošenja TiAlN prevlake pri opterećenju 1 GPa: a) i c) uzorak C manje i veće povećanje, b) i d) uzorak DCT manje i veće povećanje

Na slici 6 vidljivo je da je kod uzorka DCT (sl. 6 b i d) također došlo do intenzivnijeg trošenja uz pojavu i adhezijskog mehanizma te stvaranja naljepaka. Također su vidljive delaminirane čestice prevlake te pojava pukotina. Na uzorku C (sl. 6 a i c) vidljivo je također intenzivno trošenje abrazijskim i adhezijskim mehanizmom uz dijelove s kojih je došlo do ispadanja čestica prevlake, te intenzivno zaglađenih područja. Zaglađena područja u tragu trošenja vidljiva su i na DCT uzorku. Pri većem opterećenju kuglice u uvjetima klizanja po površini tvrde prevlake, trenje koje nastaje uslijed smicanja prevlake i brazdanja rezultira vlačnim naprezanjem koje nastaje iza kuglice i tlačnim naprezanjem te gomilanjem materijala ispred

kuglice [2]. Intenzivnim kliznim kretanjem kuglice po površini prevlake u takvim uvjetima doći će do mjestimičnog zaglađivanja tragova trošenja što je vidljivo i na slici 6.

## ZAKLJUČAK

U radu su prikazani rezultati ispitivanja tvrdoće, faktora trenja i otpornosti na trošenje u uvjetima suhog kliznog trošenja TiAlN prevlake nanesene na podlogu od brzoreznog čelika. Na mikrostrukturu podloge utjecalo se provođenjem dubokog hlađenja umjesto dva visoko temperaturna popuštanja pri postupku toplinske obrade brzoreznog čelika.
Iz provedenih ispitivanja moguće je zaključiti da duboko hlađenje brzoreznog čelika utječe na poboljšanje svojstava brzoreznog čelika kao podloge za nanošenje TiAlN prevlake. Tvrdoća prevlake pri opterećenju 50 mN na duboko hlađenoj podlozi veća je gotovo 25 %, a pri opterećenju 100 mN, 12,5 %. U uvjetima suhog kliznog trošenja duboko hlađenje podloge utjecalo je na smanjenje faktora trenja prevlake od oko 15 % pri većem primijenjenom opterećenju 1 GPa. Volumen trošenja duboko hlađenog uzorka je 30 % manji od uzorka s klasično toplinski obrađenom podlogom pri manjem primijenjenom opterećenju, dok je pri većem opterećenju volumen trošenja duboko hlađenog uzorka manji oko 15 %. Rezultati analize tragova trošenja pokazali su pojavu mehanizama trošenja u skladu s rezultatima ispitivanja. Na uzorcima koji nisu duboko hlađeni uočeni su intenzivniji tragovi trošenja te pojava adhezijkog trošenja i stvaranja naljepaka već pri manjem primijenjenom opterećenju.
Dobiveni rezultati dokazuju da svojstva podloge na koju se nanose tanke tvrde prevlake imaju ključan utjecaj na svojstva sučelja prevlaka/osnovni materijal, na formiranje i rast prevlake te posljedično na mehanička i tribološka svojstva prevlake te njezino ponašanje u uvjetima trošenja, a što je u skladu i s literaturnim izvorima [2, 4-15].

## LITERATURA

[1] S. Šolić, Utjecaj mikrostrukture brzoreznog čelika na tribološka svojstva reznih alata, doktorska disertacija, Sveučilište u Zagrebu, Fakultet strojarstva i brodogradnje, 2011.
[2] K. Holmberg, A. Matthews, Coatings Tribology, Elsevier Science B. V., Amsterdam, 1994.
[3] M. Soković, B. Barišić, S. Sladić, Model of quality management of hard coatings on ceramic cutting tools, Journal of Materials Processing Technology, 209 (2009) pp. 4207- 4216.
[4] P. Panjan, M. Čekada, Zaščita orodij s trdimi PVD – prevlekami, Institut „Jožef Stefan“, Ljubljana, 2005.
[5] S. Šolić, F. Cajner, P. Panjan, Influence of deep cryogenic treatment of high speed steel substrate on TiAlN coating properties, Mat.-wiss. u.Werkstofftech, 44 (2013) 12, pp. 950- 958.

[6] P. C. Jindal, A. T. Santhanam, U. Schleinkofer, A. F. Shuster, Performance of PVD TiN, TiCN, and TiAlN coated cemented carbide tools in turning, International Journal of Refractory Metals & Hard Materials, 17 (1999) pp. 163-170.
[7] W. Kalss, A. Reiter, V. Derflinger, C. Gey, J. L. Endrino, Modern coatings in high performance cutting applications, International Journal of Refractory Metals & Hard Materials, 24 (2006) pp. 399-404.
[8] L. A. Dobrzanski, D. Pakuła, A. Križ, M. Soković, J. Kopač, Tribological properties of the PVD and CVD coatings deposited onto the nitride tool ceramics, Journal of Materials Processing Technology, 175 (2006) pp. 179-185.
[9] D.-Y. Wang, C.-L. Chang, K.-W. Wong, Y.-W. Li, W.-Y. Ho, Improvement of the interfacial integrity of (Ti,Al )N hard coatings deposited on high speed steel cutting tools, Surface and Coatings Technology, 120–121 (1999) pp. 388-394.
[10] S. Šolić, F. Cajner, V. Leskovšek, Effect of deep cryogenic treatment on mechanical and tribological properties of PM S390 MC high-speed steel, Materials Testing, 54 (2012) 10, pp. 688-693.
[11] A. I. Tyshchenko, W. Theisen, A. Oppenkowski, S. Siebert, O. N. Razumov, A. P. Skoblik, V. A. Sirosh, Yu. N. Petrov, V. G. Gavriljuk, Low-temperature martensitic transformation and deep cryogenic treatment of a tool steel, Mater. Sci. Eng. A, 527, (2010) pp. 7027-7039.
[12] X. Huang, I. Etsion, T. Shao, Effects of elastic modulus mismatch between coating and substrate on the friction and wear properties of TiN and TiAlN coating systems, Wear, 338-339 (2015) pp. 54-61.
[13] A. F. Rousseau, J. G. Partridge, E. L. H. Mayes, J. T. Totona, M. Kracica, D. G. McCulloch, E. D. Doyle, Microstructural and tribological characterisation of a nitriding/TiAlN PVD coating duplex treatment applied to M2 High Speed Steel tools, Surface & Coatings Technology, 272 (2015) pp. 403-408.
[14] B. Podgornik, I. Paulin, B. Zajec, S. Jacobson, V. Leskovšek, Deep cryogenic treatment of tool steels, Journal of Materials Processing Technology, 229 (2016) pp. 398-406.
[15] B. Podgornik, M. Sedlaček, M. Čekada, S. Jacobson, B. Zajec, Impact of fracture toughness on surface properties of PVD coated cold work tool steel, Surface & Coatings Technology, 277 (2015) pp. 144-150.

17th INTERNATIONAL FOUNDRYMEN CONFERENCE
Hi-tech casting solution and knowledge based engineering
Opatija, May 16th-18th, 2018
http://www.simet.hr/~foundry/

# INFLUENCE OF THE DIAMETER OF THE BORE OF THE COMBUSTIBLE MIXTURE ON THE TEMPERATURE FIELD IN THE AGGREGATE FOR THE MELTING OF ALUMINUM WASTE – SKIMS

**Augustín Varga[1], Ján Kizek[1], Gustáv Jablonský[1], Ladislav Lazić[2]*, Róbert Dzurňák[1]**

[1] Technical University of Košice Faculty of Materials, Metallurgy and Recycling, Košice, Slovakia
[2] University of Zagreb Faculty of Metallurgy, Sisak, Croatia

**Oral presentation**
*Original scientific paper*

**Abstract**

At the present time aimed at increasing the use of recycled material and reducing waste generation, specific aggregates are used to achieve this goal. Efforts to increase the efficiency of the facility lead to improvements in heat exchange in the system the flue gases – the batch – the lining. When heat is exchanged, the temperature of the heat source, its distribution in the working space, the way of the flue flow around the batch and others are decisive. The paper deals with the influence of the diameter of the combustion outlet of the combustible mixture for the temperature distribution in the working space, which is realized using mathematical modeling in the ANSYS simulation program. Based on the realized modeling, it is possible to predict the possibilities of adjusting the burner system to improve the heat exchange, thus shortening the heating time, respectively melting aluminum waste.

***Keywords***: *combustion, heat exchange, skims, tilting rotary melting furnace*

*Corresponding author (e-mail address): *lazic@simet.hr*

## INTRODUCTION

The production of aluminium from bauxite is a very demanding energy process and therefore, more emphasis is now being placed on the use of secondary aluminium production processes in the industrial sphere. At present, the dominant secondary aluminium recovery process is the recycling of aluminium scrap and its subsequent remelted in rotary tilting furnaces. Compared to the primary method of producing aluminium from natural raw materials, it is possible to save up to 95% of energy per tonne of aluminium produced from recycled material.

The batch material of the rotary tilting furnace is the skims or aluminium scrap with high alumina and aluminium. Aluminium skims is generated during the production of primary aluminium by electrolysis in the production of aluminium and aluminium alloys. Aluminium scraps consist of metallic aluminium, aluminium oxide, chlorides, fluorides and other impurities and impurities. The aim is to homogenize the input material so that the final product does not change the chemical composition. Particularly problematic are paints and varnishes, as they contribute to metal losses in the melting process and create chemical compounds that need to be trapped on filtration devices.
Aluminium dross is due to the high affinity of aluminium to oxygen on the surface of the molten aluminium. This dross contains a considerable amount of metallic aluminium. Other type of dross produced in the refining of aluminium, such dross comprising addition of the alumina (aluminium oxide is present in a smear in an amount 7-15%), aluminium metal, nitrides and carbides of aluminium salts and the cover formed by the chlorides and fluorides. Their processing is mainly focused on the production of aluminium, the content of which in steroids is about 10 to 35% [1].
In order to increase the efficiency of the thermal aggregates is in the present used oxygen in the process of combustion in the melting furnaces. The use of oxygen in the melting of non-ferrous metals has been known since 1920 when the first tests of oxygen were carried out in the Georgsmarienhütte in Germany. At the time, however, the benefits of using oxygen did not cover the economic costs of its production. The development of oxygen production technology has now led to an increase in the use of oxy-combustion technology in thermal aggregates, with the assumption that in future the use of oxygen will continue to increase in order to increase the ability of the enterprise to compete [2].
Another way to increase thermal efficiency is to optimize the diameter of the bore of the combustion mixture. By optimization of the diameter of the bore of the combustible mixture we can influence the shape of the flame in the furnace. It leads to the shift of the temperature field closer to the batch materials and also to the increase of the radiation intensity at a greater distance from the burner nozzle. There is almost no knowledge available in the field of research. In the study, we have developed CFD model in software ANSYS to model the distribution of temperature field in rotary tilting furnace.

## ANALYSIS OF THE FLAME LENGTH

Combustion in furnace has the character of kinetic combustion. Kinetic combustion is characterized by combustion of a previously prepared combination of natural gas and an oxidizing agent. The rate of combustion of the mixture is therefore influenced by diffusion processes of mixing. It is mainly influenced rate of chemical reactions which depends on temperature, pressure, gas concentration and the properties of the combustion mixture. On ignition of the combustible mixture takes place the process of flame spread affected by the rate of heat transfer from the flame zone to the preheat zone, that is, the normal rate of flame spread un. Because the normal speed is different for laminar and turbulent flow, the

proper course of combustion kinetic is also influenced by the speed of outflow combustion mixture from the burner [3].
Medium flow velocity of a combustion mixture in the bore $v_{0,pr}$ is calculated by the following formula:

$$v_{0,pr} = \frac{V}{\pi \cdot r_h^2} \tag{1}$$

where
$V$ - the flow rate of the mixture ($m^3.s^{-1}$),
$r_h$ - radius of bore (m).

The flame length is determined by the distance on the axis of the flame from bore to the place where the chemical reaction does not occur. $L$ for the length of the flame can be in laminar kinetic combustion considering the height of the cone $h$ [3].

$$L = h = r_h \cdot \sqrt{\left(\frac{v_{0,pr}}{u_n}\right)^2 - 1} \tag{2}$$

where
$r_h$ - radius of bore (m),
$v_{0,pr}$ - the mean flow velocity of a combustion mixture in the bore ($m.s^{-1}$),
$u_n$ - normal rate of flame spread ($m.s^{-1}$).

Results are show in Figure 3.

## MATHEMATICAL MODELLING

Combustion processes involve complex phenomena of momentum, heat and mass transfer, which play important roles in reaction kinetics. CFD modeling is a popular tool for combustion analysis because it allows you to monitor flow, turbulence, chemical kinetics, turbulent chemical interactions, heat transfer by radiation, and the formation of emission components at the same time. In the study, the mathematical model was based on an industrial tilting rotary furnace shown in Figure 1.
Furnace has dimensions inner diameter was 1.6 m and 3.2 m in length. The model was divided into two zones by interface plane. Combustion zone consists of a gas region with turbulent flow and combustion as well as radiative heat transfer in upper part of the furnace. Melting zone was suppressed to simplify calculation. The study was followed by the distribution of the temperature field at the interface. The rotation of the furnace was not included in this model. Analysis of the temperature field at the interface can therefore be considered as transient heat transfer through plane wall.

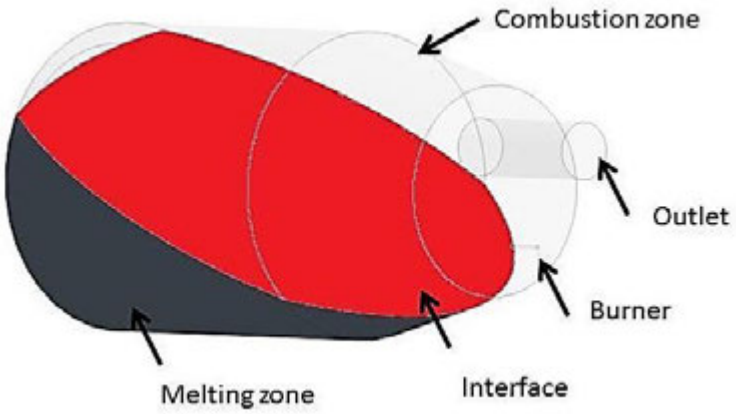


Figure 1. Model of rotary tilting furnace used for mathematical simulation

To calculate the melting rate of the aluminium dross we can use numerical model invented by Zhou (2003).This model was firstly conducted for a single aluminium particle melting in the molten metal. The melting process of a scrap particle is dependent on the properties of the particle (such as the size, shape, composition, and initial temperature) and the properties of the bulk melt [4]:

$$\frac{\partial T}{\partial t} = \alpha_i \left[\frac{\partial^2 T}{\partial r^2} + \frac{2}{r}\frac{\partial T}{\partial r}\right] \quad (3)$$

where are:

$T$- temperature (K),
$t$- time (s),
$\alpha_i$- thermal conductivity on the interface (W.m$^2$.K$^{-1}$),
$r$ - particle radius (m).

As part of monitoring the distribution of achieving temperature field in this article focus was on the interface plane, which represents the interface between the combustion zone and zone melting. If we assume that the heat loss will be the same depending on changes in the bore of the combustion mixture so increase in surface temperature of the layer will be reflected in shortening the time required for melting the material.

## RESULTS AND DISCUSSION

The results of computer simulation, presented in Figure 2, show the temperature field inside the furnace. The temperature in the combustion zone the temperature reaches 3000 °C for all the diameters of the nozzle, the temperature of the leaving flue gas is about 850-900 °C. Temperature field with the highest temperature is concentrated at the mouth of the burner.

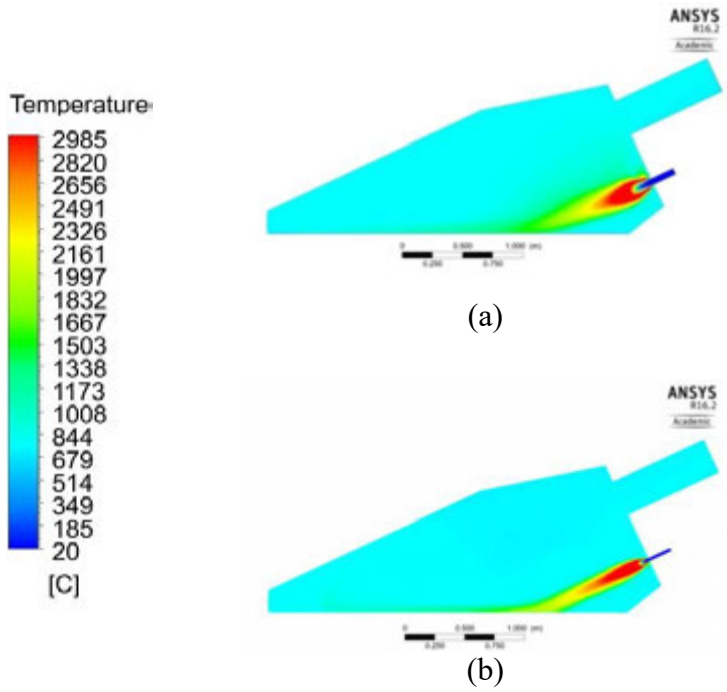


Figure 2. Mathematical simulation of the temperature field rotary tilting furnace using the diameter of burner nozzle of 50 mm (a) and 20 mm (b)

Figure 3 denotes the relationship between the average temperature at the interface plane and the flame length. Achieving temperature field spread over the interface plane is directly proportional to the flame length. The mean temperature on the interface plane is about 24.5% higher at the nozzle diameter of 20 mm than at 50 mm.

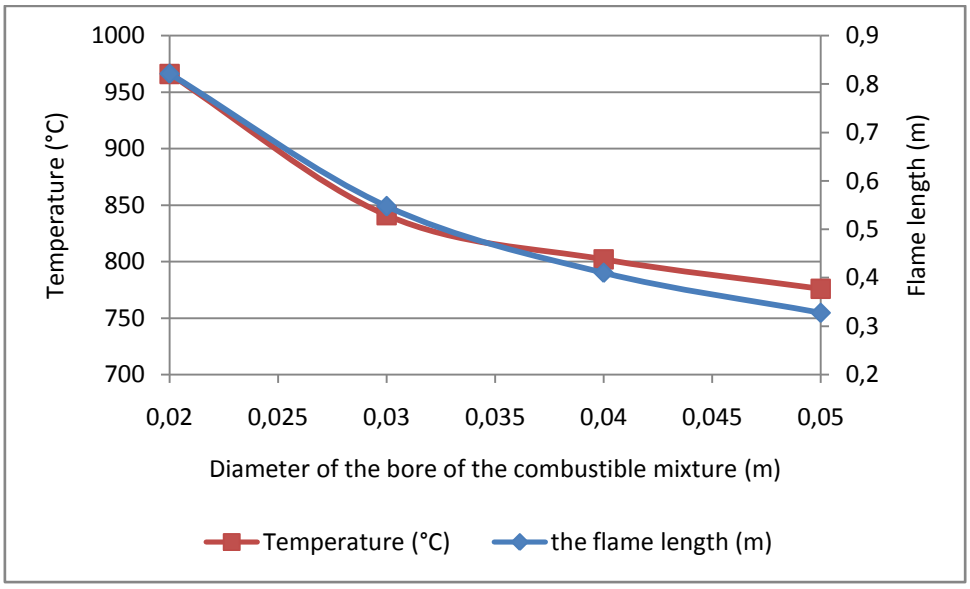


Figure 3. Dependence of average temperature and flame length from diameter of the bore of combustible mixture in interface plane

Figure 4 shows the distribution of the temperature field on the interface plane in the dependence from the distance from the burner. The influence of different flame lengths had a greater impact on the temperature reached in the axis of the mathematical model. The area of the highest temperatures is maintained at a distance of 0.5 to 1 m from the heat of the burner. By changing the diameter of the borehole there is a 46% increase in temperature in the area.

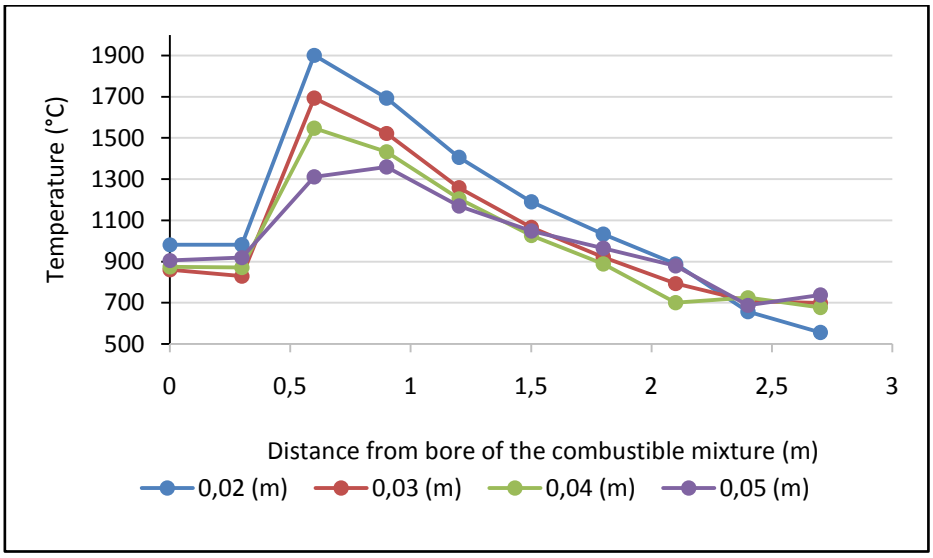


Figure 4. Dependence of temperature from distance of the bore of combustible mixture in interface plane

## CONCLUSIONS

The results of computer simulations have confirmed the effect of the nozzle to the flame length in the combustion chamber in rotary tilting furnace. The prolongation of flame increases temperature of the flame on batch material, resulting in intensive heat transfer on the batch along the furnace. By changing the diameter of the bore we can achieve a 30% reduction of time in the melting mode. The increase in heat exchange intensification in thermal aggregates increases efficiency, which reflects in the positive direction on the economy of the whole process. The submitted information is only partial results of the dissertation work.

## REFERENCES

[1] O. Velgosová, A. Miškufová, M. Laubertová, Príprava kompozitov na báze, Al Acta Metallurgica Slovaca, 14 (2008) 1, pp. 103-112.
[2] CH, Baukal, Oxygen-enhanced combustion, Second edition, CRC, press llc, 2013.

[3] G. Jablonský, M. Pástor, R. Dzurňák, Obohacovanie horľavej zmesi kyslíkom v praxi,1. vyd. - Košice: TU 2015.
[4] B. Zhou, Y. Yang, M. A. Reuter, U. M. J. Boin, Modelling of aluminium scrap melting in a rotaty furnace, Minerals Engineering, 19 (2006) pp. 299-308.

**Acknowledgements**

This work was supported by the project VEGA 1/0578/16 and obtained results are part of the solution from this grant project.

17th INTERNATIONAL FOUNDRYMEN CONFERENCE
Hi-tech casting solution and knowledge based engineering
Opatija, May 16th-18th, 2018
http://www.simet.hr/~foundry/

# THE INFLUENCE OF TIRON ON THE RHEOLOGICAL PROPERTIES OF ALUMINA SUSPENSIONS WHICH CONTAIN WASTE ALUMINA POWDER

**Milan Vukšić*, Irena Žmak**

University of Zagreb Faculty of Mechanical Engineering and Naval Architecture, Zagreb, Croatia

**Oral presentation**
*Original scientific paper*

**Abstract**

Ceramic materials are already a well-known and widely used group of technical materials. Convenient properties such as density and strength, high hardness as well as high temperature and corrosion resistance provide the ability to use ceramic materials for many technical purposes. During the green machining of the green body, a certain amount of waste ceramic powder is generated which remains unused. In addition, the waste ceramic powder should be disposed as a non-hazardous waste in a legally prescribed manner.
In this paper, the commercial dispersant 'Tiron' is investigated for the stabilization of highly concentrated alumina suspensions with three different composition of waste (secondary) alumina powder. The dispersant amount was varied and the rheological curves were recorded, in order to determine the optimal amount of the dispersant. The amount of the dispersant required for the minimum viscosity to obtain stable alumina suspensions with different addition of waste alumina powder was determined to be in range from 0.05 to 0.06 expressed on dry weight basis (dwb %) of alumina powder for each suspension.
The viscosity of all suspensions suggests that the waste alumina powder may be used to prepare new ceramic products, like less complex shapes produced via the direct casting process. According to the measured viscosity, the amount of waste alumina powder of 15 % wt., with the optimal amount of the dispersant, indicates possible applications in the production of new ceramics products, with acceptable properties.

***Keywords**: alumina suspensions, waste alumina, slip casting, rheology*

*Corresponding author (e-mail address): *milan.vuksic@fsb.hr*

## INTRODUCTION

Alumina ceramics are interesting materials for researchers due to their excellent properties like high hardness, thermal and chemical stability [1]. The properties of alumina ceramics are controlled by the microstructure. Different microstructure parameters such as density, grain

size and presence of heterogeneities in the microstructure are carefully managed to improve the properties and reliability of ceramics [2].

Colloidal shaping methods including slip casting, gel-casting and direct coagulation casting have been suggested as methods to produce high quality ceramic green body [3-5]. Understanding the mechanism of particle interactions is necessary for process optimization and best plan of the initial formulations. The first step in these methods is the preparation of a well-dispersed suspension of high solids loading with reasonably low viscosity to facilitate the mold filling process. Therefore, the rheological properties of the concentrated suspensions have a key role in controlling the shape forming behavior and subsequently, green body properties. Stability of a colloidal suspension is reflected in the property of a green compact, which also affects the property of a sintered material. Modifying of the surface properties of the ceramic powders and choosing the suitable dispersant as well as optimizing its content offer a route to reduce viscosity but require additional processing costs [6].

According to DLVO (Derjaguin-Landau-Verway-Overbeek) theory [7], the stability of colloidal sized particles depends essentially on the balance of attractive and repulsive forces surrounding the suspended particles. Electrostatically stabilized suspension has four major parameters that control the stability of the suspension such as surface potential (zeta potential), electrolyte concentration, particle size and Hamaker constant. The Hamaker constant is function of dielectric responses and distance of separation between particles which describes particle interactions including coagulation, flotation and dispersion. Steric stabilization is achieved by adsorbing a polymeric layer onto the particles. The adsorbed polymer layer more or less extends into the dispersion medium and the particles become stabilized due to the repulsion of the extended polymer layers in the continuous phase. Electrosteric stabilization can be achieved by using a polyelectrolyte polymer which at certain pH values enables a dual stability. Accordingly, controlling the pH of an aqueous suspension can develop charges on the particle surface. In most cases, these charges may not provide enough energy barrier between particles to overcome the Van der Waals attractive force between the particles. So these particles tend to flocculate. Because of that a dispersant agent is necessary to build up an electrical double layer and to generate enough repulsive force and consequently, to increase the particles dispersibility [7-9].

Dispersants which are primarily polyelectrolyte or polyvalent salts are often used to prepare well disperse ceramic suspensions. There are numerous and different kinds of dispersant used in the ceramic processing [10-13]. Studies on dispersing alumina in aqueous medium using the effect of the molecular structure of low molecular weight organic dispersants such as Tiron have been reported [14-17]. One of the studies has suggested the mechanism of the stabilization of the suspensions molecules via Tiron. According to this mechanism molecules of Tiron adsorb onto the alumina particles and produce a negative charge upon the surface of the particles. Any amount of the dispersant, above the optimum concentration, which remains in the aqueous phase results with agglutination of polymeric layers and thus reduces the range and strength of the double layer repulsion, and hence increases the viscosity [16].

The concept of combining coarse and fine particles for the achievement of better particle packing during slip casting has been employed by several researchers [18-20]. First of them were Hampton at al. [20], they have found that a mixture of coarse and fine powders produced the cast specimens with the highest green density. Okada at al. [19] have investigated the impact of bimodal size distributed alumina powder mixtures on slip casting process. When the difference between the average particle sizes was small an insufficient dispersion of the fine particles (high viscosity) has been detected which resulted with the low packing density but the packing structure was uniform. When the difference between the average particle size was large, the packing density was high but the packing structure was not uniform.
In this study the rheological measurements were conducted to investigate the influence of commercial dispersant Tiron (4,5-dihydroxy-1,3-benzenedisulfonic acid disodium salt monohydrate) on the stabilization of high concentrated alumina suspensions with different weight ratio of waste (secondary) alumina powder which is obtained after green machining in factory production of ceramics.

## MATERIALS AND METHODS

Waste (secondary) alumina powder which is obtained after green machining and high-purity $Al_2O_3$ powder with the average particle size 300-400 nm (Alcan Chemicals, USA) were used in this study. Mixtures of $Al_2O_3$ – $Al_2O_3$ (waste) with three different compositions were prepared. A commercial dispersant Tiron (4,5-dihydroxy-1,3-benzenedisulfonic acid disodium salt monohydrate) manufactured by Sigma-Aldrich Chemie GmbH, Germany was used to stabilize highly concentrated alumina suspensions.

### *Slip preparation*

Different amounts of dispersant were mixed with deionized water and added into the grinding jar of the planetary ball mill, after which 70 wt. % of dry alumina powders was added into the grinding jar. Dry alumina powders were prepared previously by mixing different weight ratios of waste alumina powder to high-purity alumina powder (Table 1). Ten alumina balls were used for the mixture homogenization, which lasted for 90 minutes at a speed of 300 rpm. The wear resistance of the used alumina balls is high and the assumption is that the impact of possible alumina wear debris in stated conditions of mixing is negligible. Alumina balls are separated from the suspension after the homogenization using a strainer. The suspension underwent an ultrasonic treatment for 15 min in an ultrasonic bath – BRANSONIC 220 (Branson Ultrasonics Corp., USA) to remove the air bubbles and achieve better homogeneity. After the homogenization, the pH-value was measured. For each dispersant the pH-values were from 8 to 9 (Table 2).

Table 1. Composition of prepared suspensions

| Dispersant | High-purity $Al_2O_3$ dry powder content (wt. %) | Waste $Al_2O_3$ dry powder content (wt. %) | Water content (wt. %) | *Dispersant content (dwb %) |
|---|---|---|---|---|
| Tiron (4,5-dihydroxy-1,3-benzenedisulfonic acid disodium salt monohydrate) | 55 | 15 | 30 | 0.04-0.1 |
| | 50 | 20 | 30 | 0.04-0.1 |
| | 45 | 25 | 30 | 0.04-0.1 |

*expressed on dry weight basis (dwb) of alumina powder

***Determination of rheological properties***

Rheological properties were determined using a rotational viscometer DV-III Ultra (Brookfield Engineering Laboratories, Inc., USA) in a small sample chamber with spindle SC4-18. Pre-shearing has been performed for 2 min at a shear rate of 100 $s^{-1}$ followed by a 2 min rest period in order to provide a common and consistent shear history for the system. The shear rate was gradually increased from 0.1 to 160 $s^{-1}$ and then reduced back to 0.1 $s^{-1}$. The shear rate increase/decrease interval was divided in equal time frames. Rheological measurements were conducted just before each shear rate change.

Temperature was kept constant at 25±1 °C using a thermostatic bath Lauda EcoRE 415 (LAUDA-Brinkmann, LP, USA). Flow curves were recorded for each $Al_2O_3$ – $Al_2O_3$ (waste) mixture and each dispersant concentration.

## RESULTS AND DISCUSSION

In this paper we investigate the influence of Tiron dispersant on the stability of highly concentrated alumina ($Al_2O_3$ – $Al_2O_3$ (waste)) suspensions. The prepared suspensions contained in total 70 wt. % of alumina powder, 30 wt. % of deionized water and the concentrations of dispersant varied from 0.04 – 0.1 dwb % expressed on dry weight basis (dwb) of alumina powder (Table 2).

***Viscosity of highly concentrated alumina ($Al_2O_3$ – $Al_2O_3$ (waste)) suspensions***

The suspension stability must be well achieved in order to establish the complete control over suspension rheological properties. Viscosity measurements and sedimentation tests are often used for the suspension stability estimation. In this paper, suspension stability was estimated by the measurements of viscosity for all prepared suspensions at two shear rates, γ; 50 and 100 $s^{-1}$. Obtained values are listed in Table 2.

Table 2. Measured viscosity of all prepared suspensions

| Waste $Al_2O_3$ dry powder content wt. % | Tiron % dwb | pH | η (mPa s) | |
|---|---|---|---|---|
| | | | γ = 50 $s^{-1}$ | γ = 100 $s^{-1}$ |
| 15 | 0.04 | 8.78 | 22.63 | 20.04 |
| | 0.05 | 8.79 | 19.32 | 17.20 |
| | 0.06 | 8.75 | 17.93 | 15.97 |
| | 0.1 | 8.64 | 20.40 | 17.76 |
| 20 | 0.04 | 8.86 | 27.09 | 23.55 |
| | 0.05 | 8.89 | 24.63 | 21.11 |
| | 0.06 | 8.86 | 26.71 | 22.83 |
| | 0.1 | 8.72 | 29.17 | 23.99 |
| 25 | 0.04 | 8.96 | 43.33 | 35.16 |
| | 0.05 | 8.98 | 39.71 | 32.21 |
| | 0.06 | 8.92 | 36.48 | 29.34 |
| | 0.1 | 8.80 | 43.10 | 34.01 |

The shear rate usually achieved during the gravity slip casting is 50 $s^{-1}$. From the Table 2 we can see that the viscosity decreased with the share rate increase, for all suspensions. The influence of increasing the content of Tiron dispersant on the viscosity of 70 wt. % alumina suspensions with three different composition of waste alumina powder at a constant shear rate of 50 $s^{-1}$ is shown on Figure 1.

Results presented in Table 2 and Figure 1 indicate the optimal amount of Tiron dispersant suitable for the slip casting is in range from 0.05 to 0.06 % dwb for all of the three different composition of prepared suspensions.

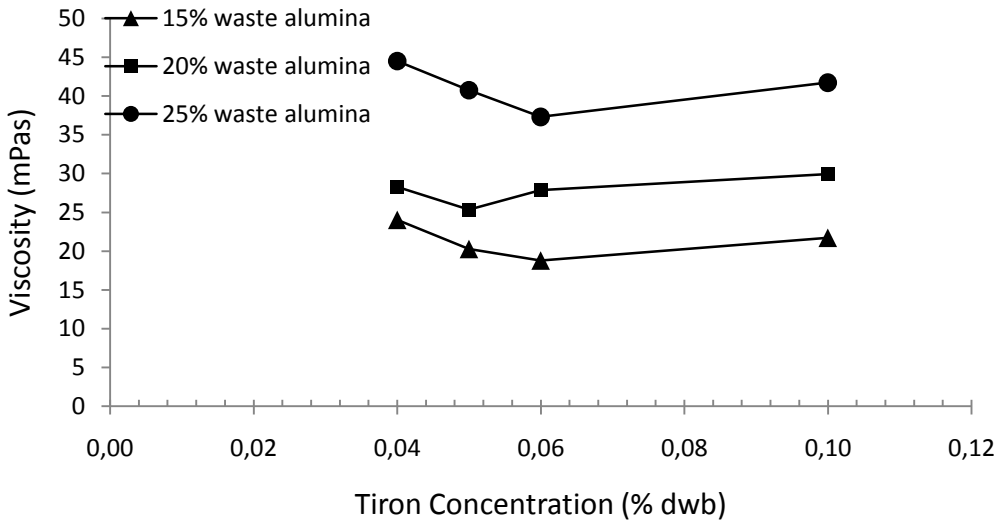


Figure 1. Viscosity of alumina 70 % wt. suspensions with three different composition of waste alumina powder as a function of Tiron concentration (% dwb)

***Rheological flow curves of highly concentrated alumina ($Al_2O_3$– $Al_2O_3$ (waste)) suspensions***

Rheological flow curves are often used instead of viscosity measurements when evaluating the stability of concentrated suspensions. Rheological flow curves show the dependence of shear stress (τ) on viscosity (η) as well as on shear rate (γ), and can be used for predicting of the nature of interactions among particles in the suspension. The alumina suspensions flow curves, with optimal amount of dispersant, are shown in Figure 2 and 3. Flow curves, expressed as a dependence of viscosity (Figure 2) and shear stress (Figure 3) on the applied shear rates, are shown for each optimal amount of dispersant.

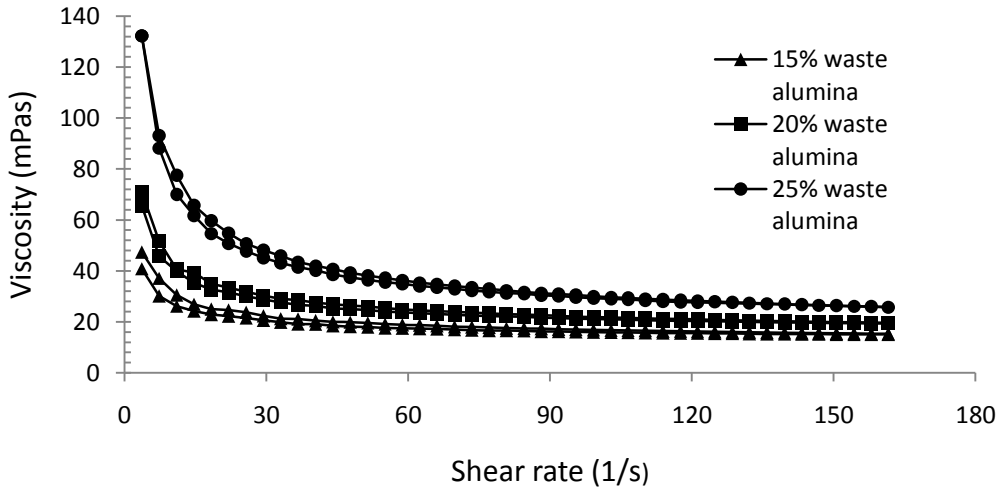


Figure 2. Variation of viscosity of 70 % wt. suspensions with three different composition of waste alumina powder as a function of shear rate

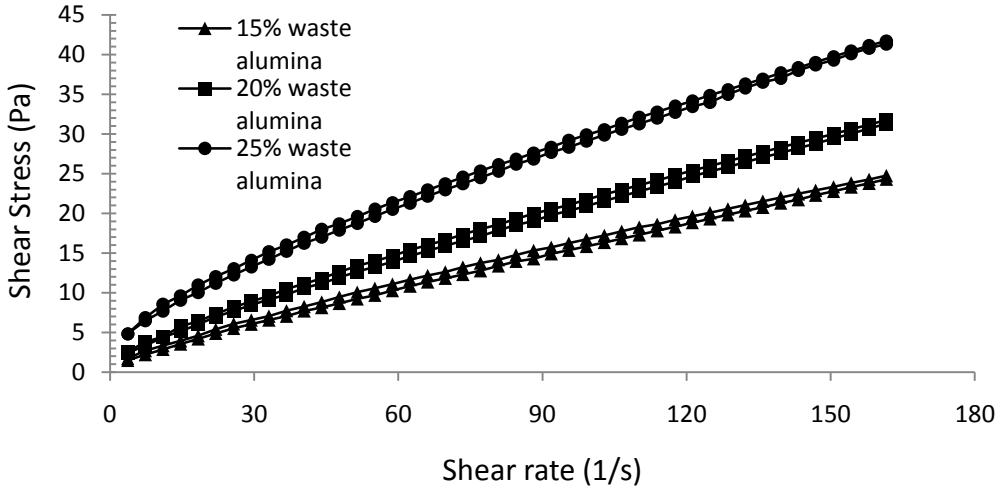


Figure 3. Variation of shear stress of 70 % wt. suspensions with three different composition of waste alumina powder as a function of shear rate

The obtained results showed that the suspensions viscosity decrease with increasing the shear rate (Figure 2). This is characteristic for the non-Newtonian behavior of fluids, more precisely for pseudoplastic behavior [21].
Figure 3 shows that shear stress increases with increasing shear rate for all suspensions, which also confirms the pseudoplastic behavior. Investigated suspensions with the addition of 25 % of waste alumina show higher viscosity values at smaller shear rates, while the viscosities are similar for the suspensions with the addition of 20 % and 15 % of waste alumina. Flow curves show no significant difference for different additions of waste alumina powder at higher shear rates. Shear stress values are quite similar at very low shear rates for all suspensions. However, shear stress values for the suspension with the addition of 15 % of waste alumina powder are notably smaller at higher shear rates than those for additions of 20 and 25 % of waste alumina powder.

## CONCLUSIONS

The commercial dispersant Tiron was investigated for the stabilization of highly concentrated alumina suspensions with three different composition of waste alumina powder: 15, 20 and 25 % wt. The dispersant amount was varied between 0.04 to 0.1 % dwb, and the rheological curves were recorded, in order to determine the optimal amount of dispersant.
The optimum amount of the dispersant required for the minimum viscosity to obtain stable alumina suspensions with different addition of waste alumina powder was determined to be in range from 0.05 to 0.06 % dwb for each suspension. Any percentage higher or lower than the optimum range increased the viscosity, hence the instability of suspensions. A too small amount of the dispersant resulted in the increase of the viscosity, which is due to the agglomeration of particles. To much of the dispersant caused also an increase of the viscosity, which may be explained by the overcrowding of the dispersant on the particle surface. Obviously this phenomenon is also unfavorable for the stability of the suspension. Basically, the amount of the dispersant which gives the lowest viscosity for the alumina suspensions corresponds to the situation where virtually all of the dispersant molecules are adsorbed onto the alumina particles. Therefore, the aqueous continuous phase remains free of, or with a negligible amount of the dispersant molecules (Tiron).
A well-dispersed suspension with low viscosity facilitates the mold filling process. The achieved viscosity of all suspensions suggests that the waste alumina powder may be used to prepare new ceramic products with non-highly complex shapes via the direct casting process. The lowest investigated composition of waste alumina powder of 15 % wt., with the addition of the optimal amount of dispersant, according to the measured viscosity, indicates the possible application in the production of new technical ceramics products, with acceptable properties.

**REFERENCES**

[1] E. G. Zemtsova, A. V. Monin, V. M. Smirnov, B. N. Semenov, N. F. Morozov, Formation and mechanical properties of alumina ceramics based on $Al_2O_3$ micro- and nanoparticles, Physical Mesomechanics, 18 (2015) 2, pp. 134-138.
[2] K. Bodišová, D. Galusek, P. Švančárek, V. Pouchlý, K. Maca, Grain growth suppression in alumina via doping and two-step sintering, Ceramics International, 41 (9, Part B) (2015) pp. 11975-11983.
[3] H. L. Calambás Pulgarin, L. B. Garrido, M. P. Albano, Rheological properties of aqueous alumina–alumina-doped Y-PSZ suspensions, Ceramics International, 38 (2012) 3, pp. 1843-1849.
[4] F. S. Ortega, R. H. R. Castro, D. Gouvêa, V. C. Pandolfelli, The rheological behavior and surface charging of gelcasting alumina suspensions, Ceramics International, 34 (2008) 1, pp. 237-241.
[5] J. Yu, J. Yang, Y. Huang, The transformation mechanism from suspension to green body and the development of colloidal forming, Ceramics International, 37 (2011) 5, pp. 1435-1451.
[6] W. J. Tseng, C. H. Wu, Sedimentation, rheology and particle-packing structure of aqueous $Al_2O_3$ suspensions, Ceramics International, 29 (2003) 7, pp. 821-828.
[7] Y. Yang, W. M. Sigmund, A new approach to prepare highly loaded aqueous alumina suspensions with temperature sensitive rheological properties, Journal of the European Ceramic Society, 23 (2003) 2, pp. 253-261.
[8] K. Shqau, Electrosteric Dispersant Used in the Colloidal Processing of Ceramics, Ohio State University, 2004, pp. 1-17.
[9] Y. Hirata, Theoretical aspects of colloidal processing, Ceramics International, 23 (1997) 1, pp. 93-98.
[10] B. P. Singh, S. Bhattacharjee, L. Besra, D. K. Sengupta, Evaluation of dispersibility of aqueous alumina suspension in presence of Darvan C, Ceramics International, 30 (2004) 6, pp. 939-946.
[11] B. P. Singh, S. Bhattacharjee, L. Besra, D. K. Sengupta, Electrokinetic and adsorption studies of alumina suspensions using Darvan C as dispersant, Journal of Colloid and Interface Science, 289 (2005) 2, pp. 592-596.
[12] A. Tsetsekou, C. Agrafiotis, I. Leon, A. Milias, Optimization of the rheological properties of alumina slurries for ceramic processing applications Part II: Spray-drying, Journal of the European Ceramic Society, 21 (2001) 4, pp. 493-506.
[13] K.-S. Chou, L. J. Lee, Effect of Dispersants on the Rheological Properties and Slip Casting of Concentrated Alumina Slurry, 1989.
[14] A. L. Penard, F. Rossignol, H. S. Nagaraja, C. Pagnoux, T. Chartier, Dispersion of alpha-alumina ultrafine powders using 2-phosphonobutane-1,2,4-tricarboxylic acid for the implementation of a DCC process, Journal of the European Ceramic Society, 25 (2005) 7, pp. 1109-1118.
[15] L. Jiang, L. Gao, Effect of Tiron adsorption on the colloidal stability of nano-sized alumina suspension, Materials Chemistry and Physics, 80 (2003) 1, pp. 157-161.

[16] B. J. Briscoe, A. U. Khan, P. F. Luckham, Optimising the dispersion on an alumina suspension using commercial polyvalent electrolyte dispersants, Journal of the European Ceramic Society, 18 (1998) 14, pp. 2141-2147.
[17] J. J. Gulicovski, L. S. Čerović, S. K. Milonjić, Stability of alumina suspensions in the presence of Tiron, Ceramics International, 34 (2008) 1, pp. 23-26.
[18] J. M. F. Ferreira, Role of the clogging effect in the slip casting process, Journal of the European Ceramic Society, 18 (1998) 9, pp. 1161-1169.
[19] S. Taruta, Y. Sakurai, N. Takusagawa, K. Okada, N. Otsuka, Slip Casting of Alumina Powder Mixtures with Bimodal Size Distribution, Journal of the Ceramic Society of Japan, 108 (2000) 3, pp. 254-260.
[20] J. Holly D. Hampton, S. Savage, R. Drew, Experimental Analysis and Modeling of Slip Casting, Journal of the American Ceramic Society, 71 (1988) 12, pp. 1040-1045.
[21] M. Majić Renjo, M. Lalić, L. Ćurković, G. Matijašić, Rheological properties of aqueous alumina suspensions, Materialwissenschaft und Werkstofftechnik, 43 (2012) 11, pp. 980-982.

**Acknowledgements**

This work has been fully supported by Croatian Science Foundation under the project IP-2016-06-6000: Monolithic and Composite Advanced Ceramics for Wear and Corrosion Protection (WECOR).

17th INTERNATIONAL FOUNDRYMEN CONFERENCE
Hi-tech casting solution and knowledge based engineering
Opatija, May 16th-18th, 2018
http://www.simet.hr/~foundry/

# PREVENTION OF CHUNKY GRAPHITE FORMATION AND OPTIMISING THE PRODUCTION OF FERRITIC DUCTILE CAST IRON WITH HIGHER CONTENT OF SILICON

**Matic Žbontar*, Jernej Kovačič**

Livar d.d., Ivančna Gorica, Slovenia

**Oral presentation**
*Professional paper*

**Abstract**

In this paper, the optimisation of production for ferritic ductile cast iron with higher content of silicon is presented. Due to problems with achieving mechanical properties and achieving proper microstructures for material qualities EN-GJS-500-14 and EN-GJS-600-10 possible affecting factors were researched. In the beginning-as it also says in this paper-insufficient mechanical properties were connected with chunky graphite in the microstructure. Further, carried out a couple of experiments were carried out with different additions into the melt to try to avoid chunky graphite.

***Keywords***: *ductile iron, chunky graphite, high silicon content, ferritic ductile iron*

*Corresponding author (e-mail address): *matic.zbontar@livar.si*

## INTRODUCTION

One of the most harmful and most frequent forms of degenerated graphite in thick-wall ductile iron castings from is chunky graphite. Although the term chunky graphite was first mentioned in the 60s exact mechanism of formation and growth still was not clearly defined. Consequently, there still haven't been found any affecting factors due to which nodular graphite starts growing as chunky [1].
It is known that chunky graphite in forming at smaller cooling speeds with increased wall thicknesses. That is also the main reason for formation of other degenerated forms of graphite.
Chunky graphite in most frequently present in thermic center of casting and causes decreasing of mechanical properties- tensile strength (Rm) and elongation (A). Depending on content of chunky graphite the values for Rm can decrease for 20-25% and values of elongation can only achieve 20-30% of elongation of castings without chunky graphite [1].

The effect of chunky graphite on mechanical properties in shown in the Table 1.

Table 1. Effect of chunky graphite on mechanical properties by different authors [1]

| Source | Rm (N/cm$^2$) | | A (%) | |
|---|---|---|---|---|
| | nodule | chunky | nodule | chunky |
| Gagné et. al | 440 | 345 | 25 | 5 |
| Källbom | 500 | 440 | 20 | 3 |
| Urike et. al | 405 | 315 | 22 | 4.5 |
| Ferro et. al | 400 | 321 | 11,5 | 3.4 |

Chunky graphite is intercrystal eutectic graphite. It can be seen with the naked eye on the cut surface castings as darker area, which is shown in Figure 1.

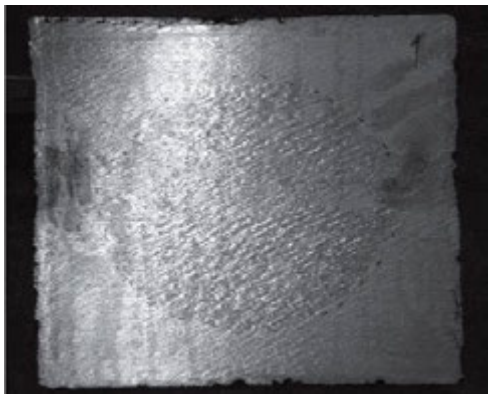

Figure 1. Surface with chunky graphite [1]

When inspecting surfaces of chunky graphite using optical microscope it can be seen that the microstructure consists of relatively large connected eutectic cells of chunky graphite surrounded with nodes of right shape.
It seems that chunky graphite appears in the shape of isolated units but that is not the case after detailed inspection on electronic microscope, significant connections can be visible. With the use of electronic microscope on analyzed samples 3 - dimensional structure of chunky graphite can be seen (Figure 2).

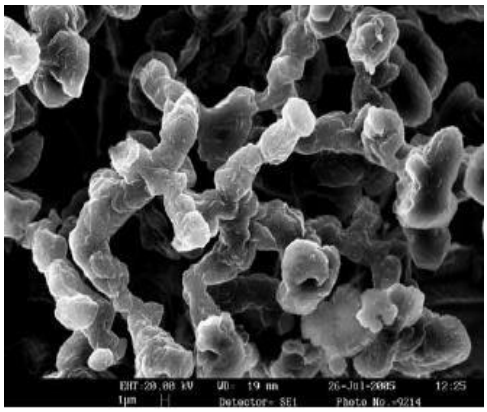

Figure 2. Microstructure of chunky graphite as seen on electronic microscope [1]

From most of the theories regarding the growth of chunky graphite it follows that it grows with the direct connection of the tops with the left over melt during eutectic solidification. Still it comes to the disagreements about if chunky graphite starts to emerge in the early stages of eutectic solidification or at the last stages. It also isn't yet known if first there is forming nodular or chunky graphite [1].
The aim of this work was to establish:

- How to prevent the emergence of chunky graphite,
- Which is the optimal content of silicon to achieve the quality material,
- Which inoculant and additions are optimal,
- How does the oxygen affect the emergence of chunky graphite,
- How to optimize the base melt.

## MATERIALS AND METHODS

Considering the problems with achieving mechanical properties and microstructure on material qualities EN-GJS-500-14 and EN-GJS-600-10 research was directed to some crucial factors.
Tests on material in the foundry were carried out. From each test chemical composition (base melt and from the end material) was checked, microstructure was analyzed and tensile strength and elongation was analyzed as well. The metallography was carried out on optical microscope Olympus BX 61 on the samples from the broken tensile strength test bars. Mechanical properties were analyzed on tensile stress machine Instron 5985. Test bars were made or machined out of a V shaped probes.
Seven different procedure of melt preparation was performed, as follows:

### Test No. 1

The objective was to discover the influence of rare earths on chunky graphite formation. Rare earths were present in the melt in the form of nodulating additive. Testing started with

the nodulating additive FeSiMg 7311 from ELKEM, which we also use regularly in production. It contains approximately 1% of RE.

Procedure:

- Sample No. 1 – added 1.1% FeSiMg 7311
- Sample No. 2 – added 0.9% FeSiMg 7311
- Inoculation with 0.15% barinoc into treatment ladle
- Y probe casting

**Test No. 2**

The objective of the test number 2 was to determine the influence of inoculant and oxygen (rust) on chunky graphite formation.

Procedure:

- Adding FeSi 75 ELKEM (traces of Ca and Al) into the electric furnace
- Added FeSiMg 7311 – 0.9% into treatment ladle
- Added 1 dose of rust after alloying (nodulation)
- Inoculated with 0.15% barinoc while pouring from electric furnace into treatment ladle
- Sample No. 3 – Y probe – inoculated with 5g zircinoc inoculant

Sample No. 4 – Y probe – non-inoculated

**Test No.3**

The objective of the test number 3 was to determine the influence of ultraseed inoculant with Bismuth. For test number 3 no rust was added at any time during material preparation.

Procedure:

- Added FeSiMg 7311 – (0.85%)
- Inoculated with 0.15% when pouring from electrical furnace
- Cast Y probes- Sample no. 5 was from 29mm Y probe non-inoculated, No.6 from 29mm Y probe inoculated with ultraseed Bi, No.7 was from 25mm Y probe inoculated with ultraseed Bi

**Test No. 4**

The purpose of test number 4 was to once again see if inoculant ultraseed Bi helps us with elimination of chunky graphite and also which inoculant (ultraseed Bi or zircinoc) works better.

Procedure:

- FeSiMg 7311 – (0.9%)
- Added 1 dose of rust after alloying
- Inoculated with 0.15% barinoc while pouring from the electrical furnace
- Cast 2 Y probes one was inoculated with 5g Bi (sample No.8) the other with 5g Zr (sample No.9)
- After that the leftovers from the ladle were poured back into the furnace along with FeSi75 ELKEM
- After the chemical analysis again FeSi75 ELKEM was aded

- FeSi Mg 7311 – (0.85%)
- Added double dosage of rust after alloying
- Inoculated 0.15% barinoc while pouring from the electric furnace into a ladle
- Another 2 Y probes was cast- sample No.10 inoculated with 5g ultraseed Bi and No.11 inoculated with 5g zircinoc

**Test No. 5**

The objective of test number 5 was to produce castings (samples) on DISAmatic vertical forming line from the material EN-GJS-600-10.

Procedure:

- FeSiMg 7311 – (1.1%)
- FeSi ELKEM
- Added 2 doses of rust after alloying
- Inoculated with 0.15% barinoc while pouring from the electrical furnace

**Test No. 6**

The aim of test number 6 was to produce two different samples of castings from material EN-GJS-600-10 on horizontal forming line. It was also for the first time that nodulating additive FeSiMg 8310 from ELKEM was used which has lower content of rare earths.

Procedure:

- FeSiMg 8310 – (8% Mg; 0.83% RE)
- Added 2 cups of rust after alloying
- Inoculated with 0.15% barinoc + some rust while pouring from the electric furnace

**Test No. 7**

From the conclusions that were collected during this project, a zero series was produced on horizontal molding line from material EN-GJS-600-10, the results are shown below.

## RESULTS AND DISCUSSION

The results of performed tests and theirs' discussion are presented in the order of appearance.

**Test No. 1**

Mechanical properties obtained from the sample cast by Test No.1 is shown in Table 2.

Table 2. Mechanical properties results (from casted Y probe)

| Sample No. | $R_{p0,2}$ | $R_m$ | A (%) |
|---|---|---|---|
| 1 | 484 | 581 | 7.3 |
| 2 | 485 | 603 | 14.4 |

Metallographic features obtained at samples cast by Test No.1 are shown in Figures 3 and 4.

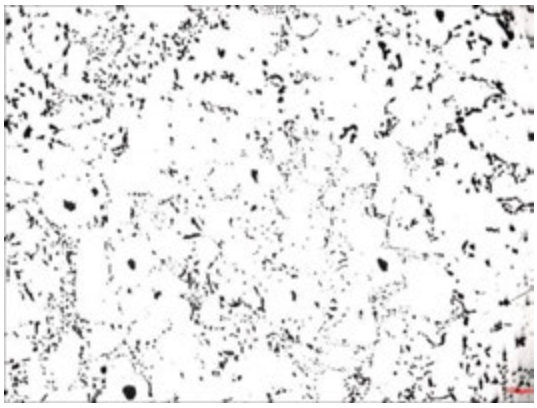

Figure 3. Microstructure of sample No. 1 – 1.1 % FeSiMg 7311

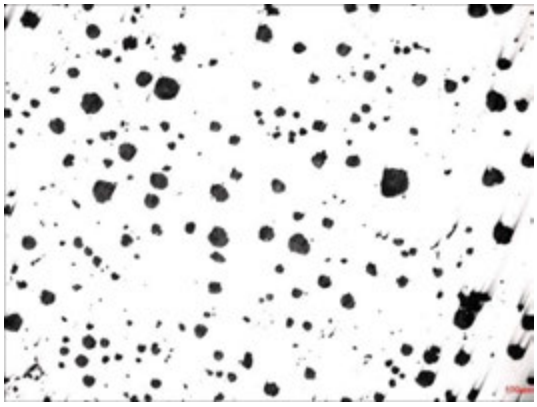

Figure 4. Microstructure of sample No. 2 – 0.9 % FeSiMg 7311

The first discovery was that rare earths are affecting the formation of chunky graphite. Microstructure of the sample containing 1.1% of additive with RE has chunky graphite (Figure 3). In the microstructure with less RE there is no chunky graphite (Figure 2).

**Test No. 2**

Mechanical properties obtained from the sample cast by Test No.2 are shown in Table 3.

Table 3. Mechanical properties results (from casted Y probe)

| Sample No. | $R_{p0,2}$ | $R_m$ | A (%) | Nodulation % | Ferite:pearlite |
|---|---|---|---|---|---|
| 3 | 465 | 598 | 15.8 | 90-95 | 85:15 |
| 4 | 448 | 578 | 9.7 | 50-70 | 75:25 |

Metallographic features obtained at samples cast by Test No.2 are shown in Figures 5 and 6.

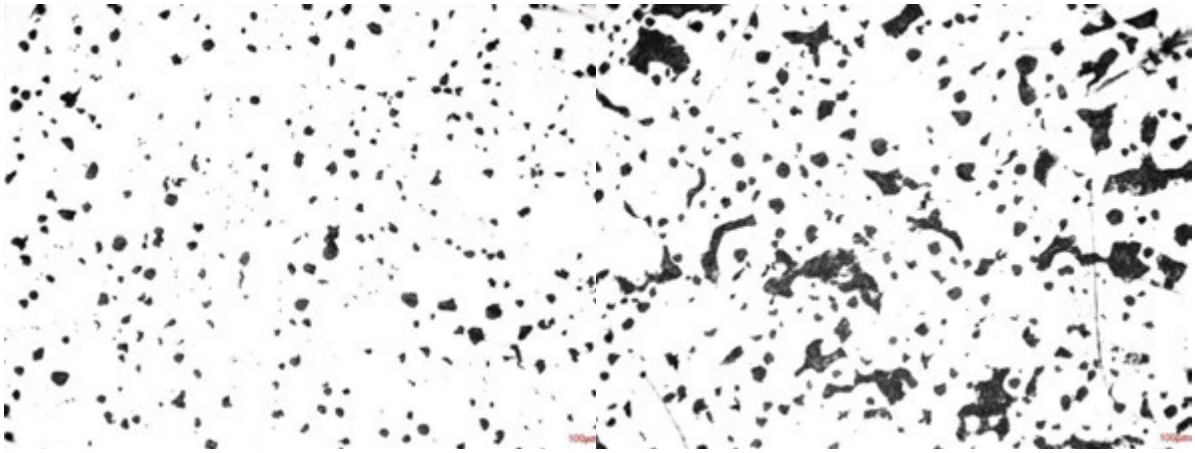

Figure 5. Microstructure of sample No. 3

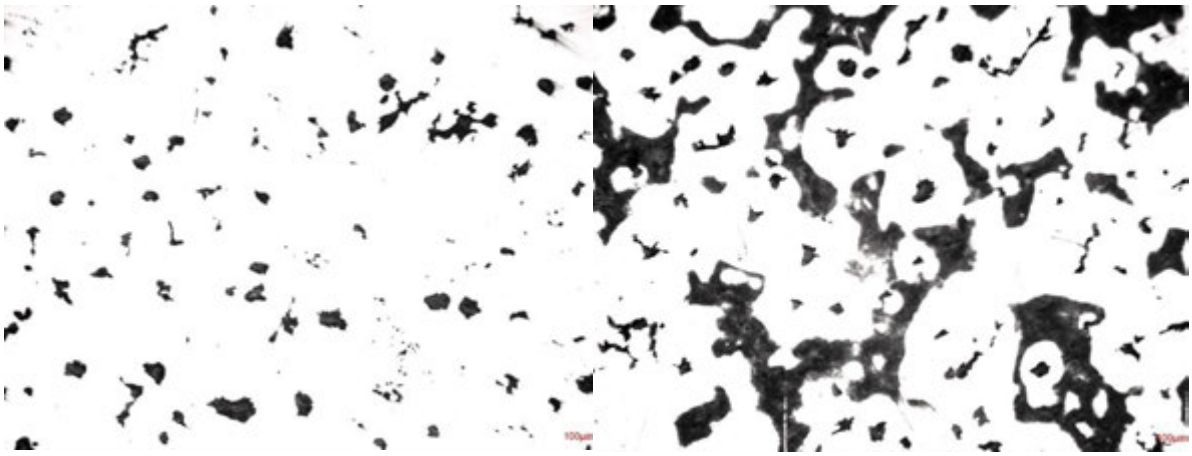

Figure 6. Microstructure of sample No. 4

It was found out from test number 2 that the inoculation of melt during pouring is mandatory (pouring Y probe), that it is needed to increase the percentage of Si for higher values of tensile strength ($R_m$). On the other side the content of Sn has to be reduced in order to achieve lower pearlite.

**Test No.3**

Mechanical properties obtained from the sample cast by Test No.3 are shown in Table 4.

Table 4. Mechanical properties results (from casted Y probe)

| Sample No. | $R_{p0,2}$ | $R_m$ | A (%) | Note |
|---|---|---|---|---|
| 5 | 503 | 610 | 11.2 | Non-inoculated |
| 6 | 528 | 620 | 7.75 | inoculated – 5g Bi |
| 7 | 534 | 621 | 6.76 | inoculated – 5g Bi |

Metallographic features obtained at samples cast by Test No.3 are shown in Figures 7 to 9.

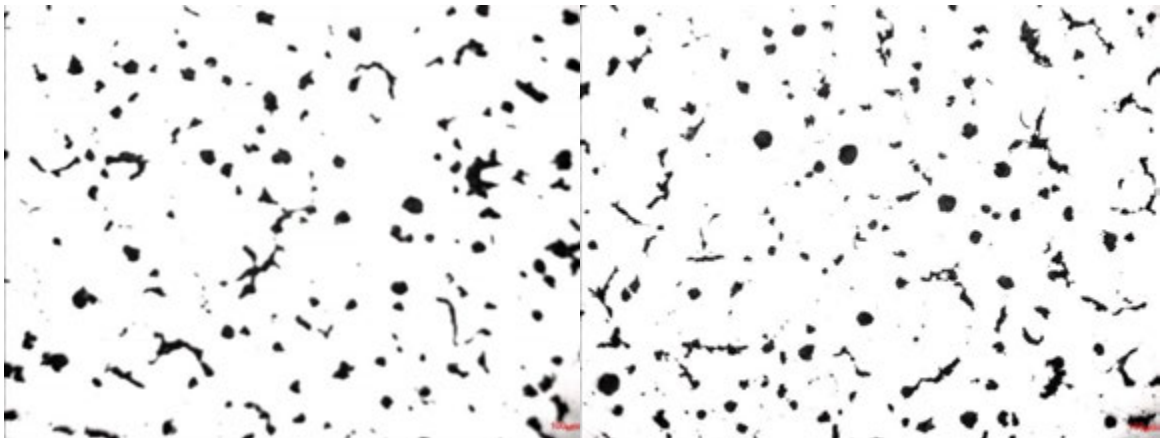

Figure 7. Microstructure from sample No. 5

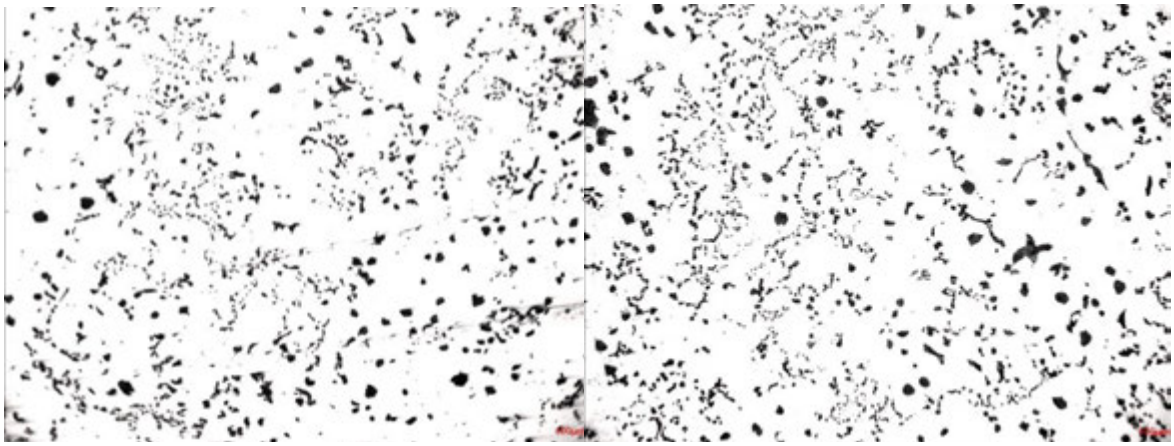

Figure 7. Microstructure from sample No. 6

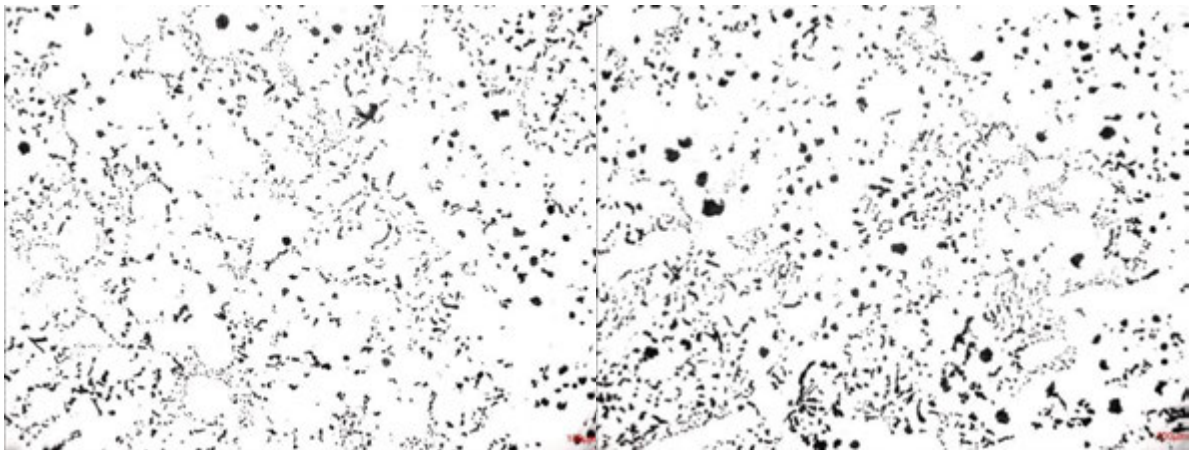

Figure 8. Microstructure from sample No. 7

It was found from test number 3 that from the non-inoculated Y probe the chunky is not present as it can be seen from Figure 7 (sample No. 5) - there is some vermicular type of graphite in the microstructure however. On the other hand, chunky graphite can be detected on the Figures 8 and 9 - inoculated Y probes or samples No.6 and No.7. It can be concluded that that inoculant Ultraseed containing bismuth did not prevent the formation of chunky graphite. The inoculant is therefore the promotor of chunky graphite but it is needed for the nodule count of ductile iron. It was concluded from tests No. 2 and No. 3 that adding oxygen in the form of rust is mandatory.

**Test No. 4**

Mechanical properties obtained from the sample cast by Test No. 4 are shown in Table 5.

Table 5. Mechanical properties results- Y probes

| Sample No. | $R_{p0,2}$ | $R_m$ | A (%) | alloy | Note |
|---|---|---|---|---|---|
| 8 | 432 | 539 | 13.1 | 500-14 | Inoculant 5g Bi |
| 9 | 434 | 543 | 16.5 | 500-14 | Inoculant 5g Zr |
| 10 | 499 | 599 | 10.2 | 600-10 | Inoculant 5g Bi |
| 11 | 493 | 593 | 10.0 | 600-10 | Inoculant 5g Zr |

Metallographic features obtained at samples cast by Test No. 4 are shown in Figures 10 to 13.

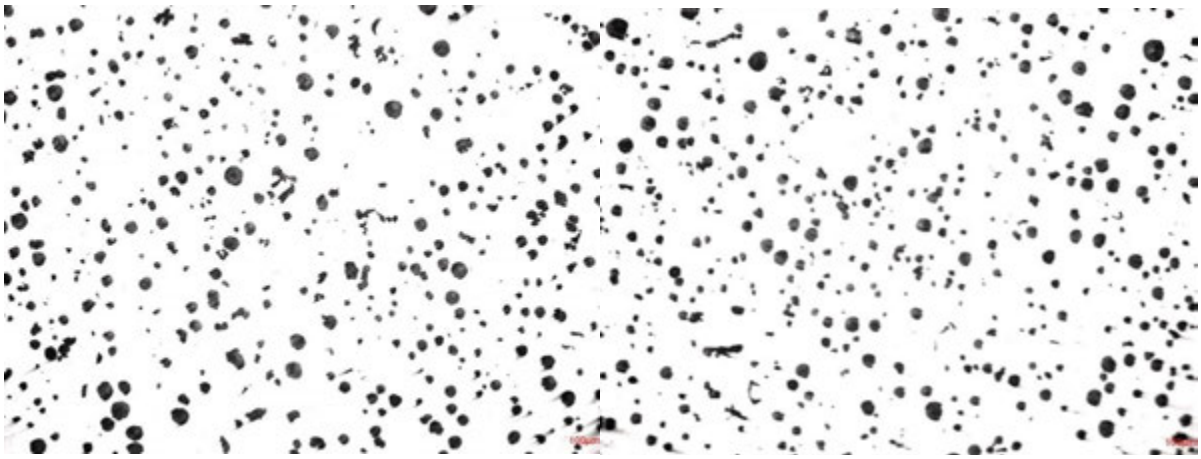

Figure 9. Microstructure of sample No. 8 – inoculated with Bi

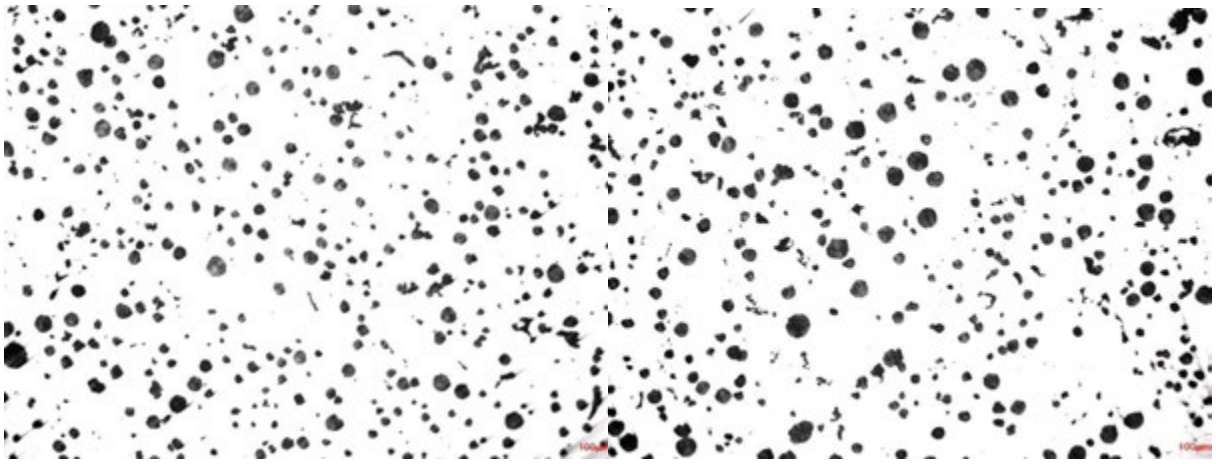

Figure 10. Microstructure of sample No. 9 - inoculated with Zr

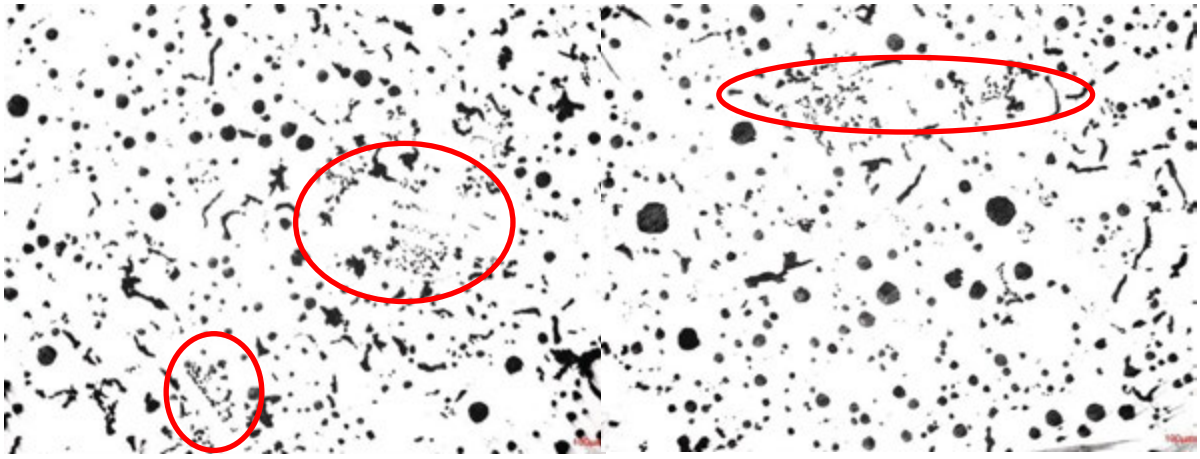

Figure 11. Microstructure of sample No. 10 – inoculated with Bi

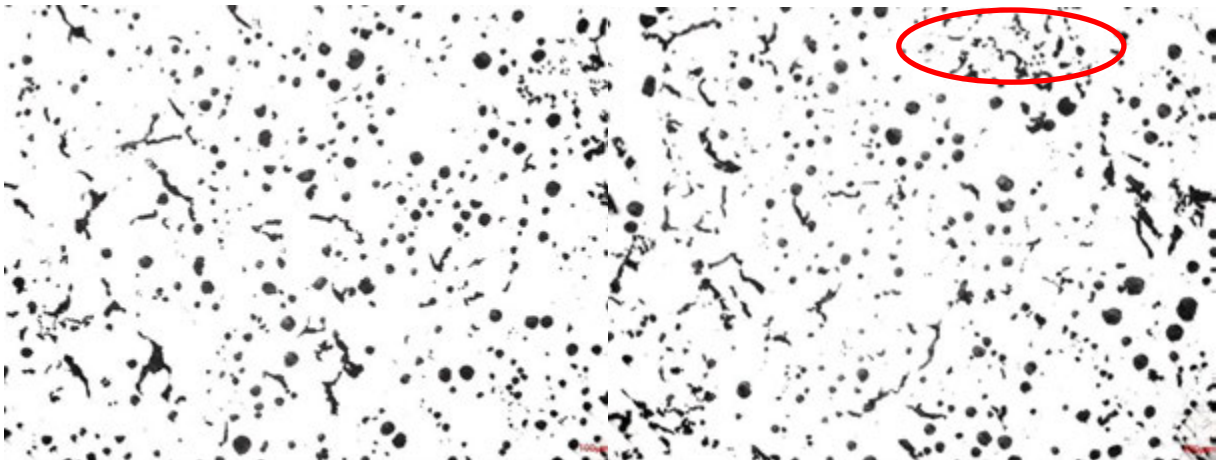

Figure 12. Microstructure of sample No. 11 – inoculated with Zr

Metallographic features analysis obtained at samples cast by Test No. 4 are shown in Table 6.

Table 6. Metallographic analysis results of samples cast by Test No. 4

| Sample No. | Nodulation % | Nodules size |
|---|---|---|
| 8 | 90-95 | 7.6 |
| 9 | 90-95 | 7.6 |
| 10 | 60-70 | 6.8 |
| 11 | 60-80 | 6.8 |

The outcomes of test number 4 is that the material 500-14 is sound, without chunky graphite present in the microstructure (samples No.8 and 9). Better mechanical properties were achieved from the Y probe inoculated with Zr. The material 600-10 is on the other hand not sound (samples No.10 and 11), chunky graphite has been identified in the microstructure. Chunkier graphite in microstructure was noticed when melt was inoculated with Bi. This appears due to leftovers of the melt returns from first two Y probes into the electric furnace (therefore there was less O and S in the furnace). Recommendation is to increase oxygen addition (rust) for material 600-10.

**Test No. 5**

Mechanical properties obtained from the sample cast by Test No. 5 are shown in Table 7.

Table 7. Mechanical properties results

| Sample | $R_{p0,2}$ | $R_m$ | A (%) | Note |
|---|---|---|---|---|
| Y | 472 | 599 | 12.8 | 5g Zr |
| From cast part | 484 | 609 | 13.7 | |

Metallographic features obtained at samples cast by Test No.5 are shown in Figures 14 and 15.

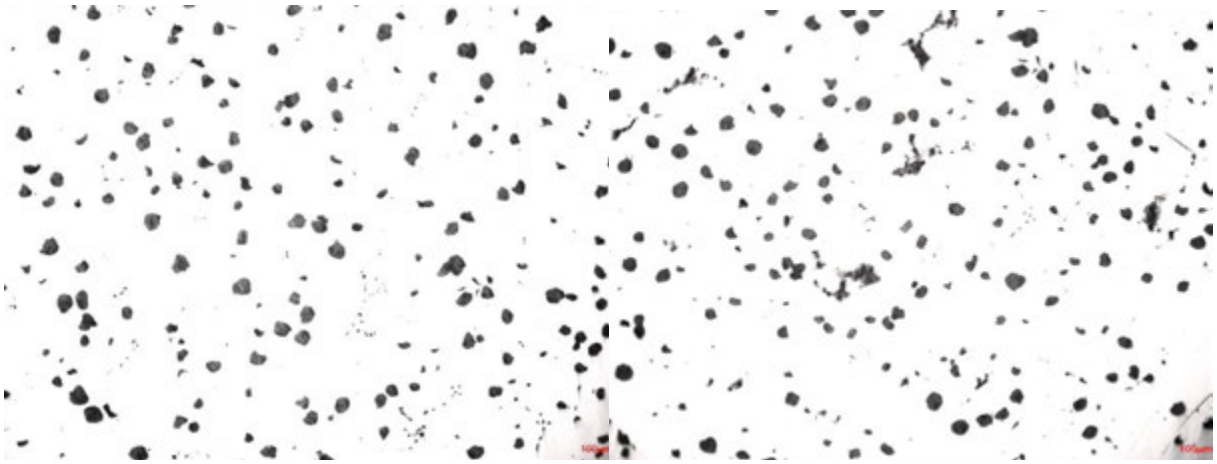

Figure 13. Microstructure from the Y probe

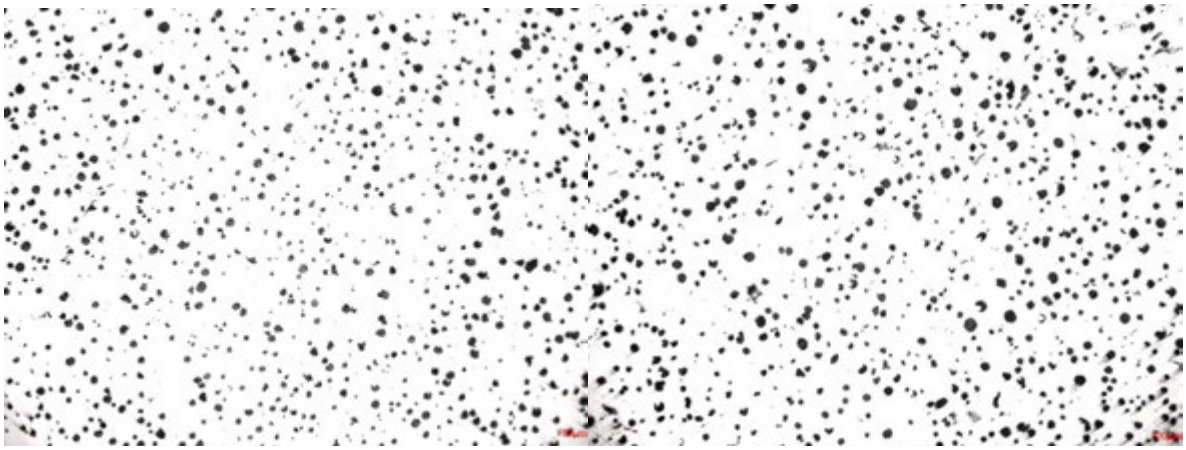

Figure 14. Microstructure from cast part

The mechanical properties and metallographic analysis both from Y probe and from the cast samples were arguably sound. Better mechanical properties were achieved in samples from the cast parts.

**Test No. 6**

Mechanical properties obtained from the sample cast by Test No.6 are shown in Table 8.

Table 8. Mechanical properties results

| Position | $R_{p0,2}$ | $R_m$ | A (%) | Note |
|---|---|---|---|---|
| Casting 1 | 497 | 619 | 16.3 | from cast part |
| Casting 2 | 495 | 615 | 12.5 | from cast part |

Microstructures were analyzed on the test bar samples after testing on tensile stress appliance in our lab with internally programed app to determine microstructure properties. Metallographic features and theirs analysis of samples cast by Test No.6 are shown in Figures 16 and 17.

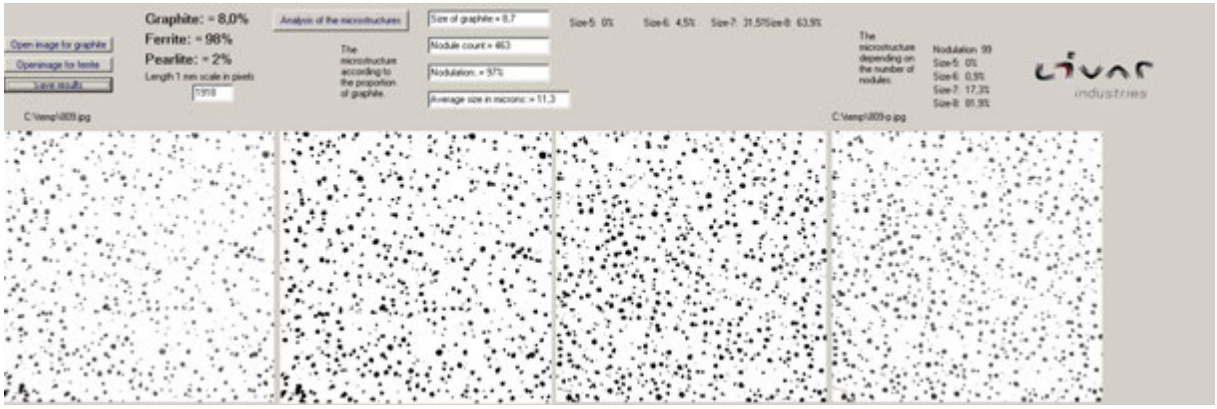


Figure 15. Metallographic analysis from casting 1

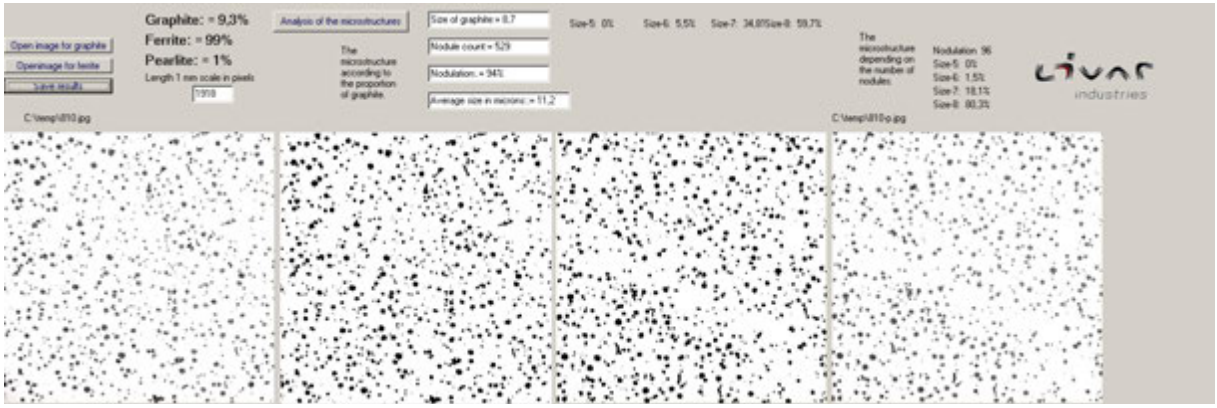


Figure 16. Metallographic analysis from casting 2

Casting microstructure with the additive FeSiMg 8310 is acceptable. Additives had better influence on mechanical properties (better that those achieved by additive FeSiMg 7311).

**Test No. 7**

Mechanical properties obtained from the sample cast by Test No. 7 are shown in Table 9 and Figure 18.

Table 9. Mechanical properties results

| Sample | $R_{p0,2}$ | $R_m$ | A (%) | Note |
|---|---|---|---|---|
| Sample 1 | 510 | 646 | 15.2 | from cast part |
| Sample 2 | 511 | 647 | 15.1 | from cast part |

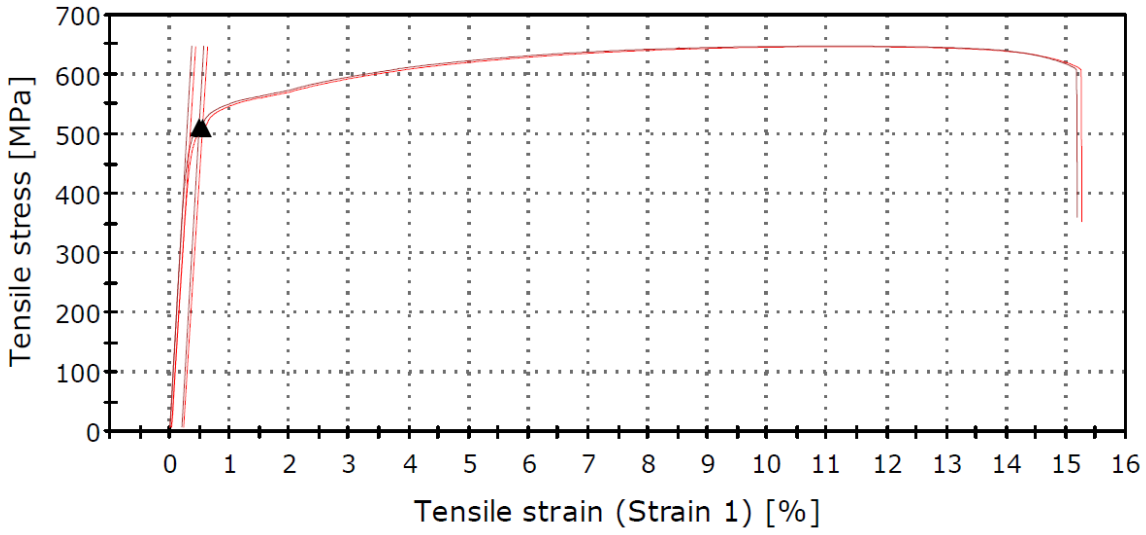


Figure 17. Mechanical properties diagram for both samples 1 and 2

Metallographic features and theirs analysis of samples cast by Test No. 7 are shown in Figure 19.

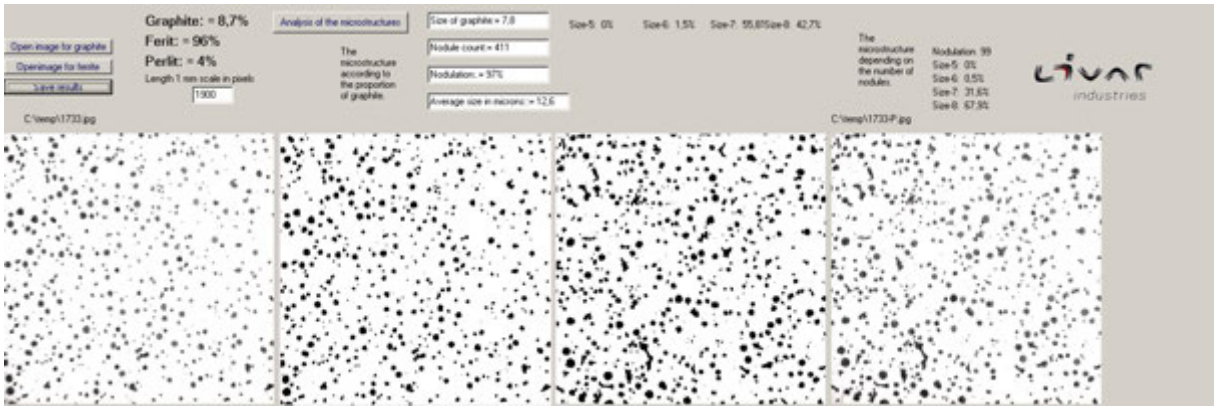


Figure 18. Metallographic analysis from casting

Microstructure analysis of samples cast by Test No. 7 confirmed that the additive FeSiMg 8310 is appropriate for production of ferritic ductile cast iron with higher content of silicon.

## CONCLUSIONS

Mechanical and metallographic analysis of ductile cast iron EN-GJS-500-14 and EN-GJS-600-10 with different production procedure indicate that melt preparation with higher %Si require following addition:

- FeSi 75ELKEM, because of lower content of Al and Ca
- FeSiMg 8310 for treatment, because of lower content of rare earth elements (RE)
- For further testing FeSiMg 6083 (0.0 – 0.1 RE) was ordered- the 8310 is not in the regular production of ELKEM
- Inoculation with 0.15% barinoc while pouring from treatment ladle into the pouring ladle
- Mandatory addition of oxygen (rust)
- For 500-14 alloy – 1 dose of rust per 1t of melt
- For 600-10 alloy – 2 doses of rust per 1t of melt

Recommendation of melt preparation indicated adequate mechanical properties and avoidance of chunky graphite in microstructure.

## REFERENCES

[1] I. Mihalic Pokopec, Utjecaj brzine hlađenja i dodatka cerija i bizmuta na morfologiju grafita u debelostijenim odljevcima od nodularnog lijeva, Doktorski rad, Zagreb, 2016.

## Acknowledgements

This work was supported by the foundry LIVAR d.d.

17th INTERNATIONAL FOUNDRYMEN CONFERENCE
Hi-tech casting solution and knowledge based engineering
Opatija, May 16th-18th, 2018
http://www.simet.hr/~foundry/

# ATMOSPHERIC CORROSION OF CORTEN STEEL IN THE RURAL, INDUSTRIAL AND MARINE ATMOSPHERE

# ATMOSFERSKA KOROZIJA CORTEN ČELIKA U RURALNOJ, INDUSTRIJSKOJ I MORSKOJ ATMOSFERI

**Bojan Bašić*, Vera Rede, Zrinka Švagelj**

University of Zagreb Faculty of Mechanical Engineering and Naval Architecture, Zagreb, Croatia

**Poster presentation**
*Professional paper*

**Abstract**

Corten steel is a trade name for a group of low alloy structural steels, which have an increased resistance to atmospheric corrosion. The carbon content for these steels is not greater than 0.2 % and the amount of alloying elements is not more than 5 %. Corten steel does not belong to a group of corrosion-resistant steels, but at exposure to atmospheric conditions as a corrosion product creates a surface oxide layer, which to some extent, protects the base material against further corrosion propagation. Due to the presence of alloying elements, especially copper, the oxide layer evenly covers the surface and has an attractive, red-brown color that takes darker tones over time. For this reason, Corten steel is very interesting to the architects and artists who use it in their projects.

The paper presents the results of the comparison of the oxide layers formed on the surface of the Corten steel plates after 200 days of exposure to the rural, industrial and marine environment. The thickness, homogeneity and color of the resulting oxide layers on the surface of the samples were significantly different. The thinnest oxide layer was measured in the sample exposed to the rural atmosphere, and the surface was uniformly covered with oxides. The sample exposed to marine atmosphere was most damaged by corrosion. In this sample, the largest thickness of the oxide layer and the greatest inequality of propagation of corrosion by depth were measured. Furthermore, surface was unevenly covered with oxides and had the darkest shades of brown-red color. For samples exposed to the industrial atmosphere, the surface coverage of oxides is similar to that of rural atmosphere and the thickness of the oxide layer is about 30 % higher.

***Keywords**: Corten steel, atmospheric corrosion, microstructure, oxide layer*

*Corresponding author (e-mail address): *b.basic2@gmail.com*

**Sažetak**

Corten čelik je trgovački naziv za grupu niskolegiranih konstrukcijskih čelika koji imaju povišenu otpornost na djelovanje atmosferske korozije. Kod ovih čelika udio ugljika nije veći od 0,2 %C i udio legirnih elemenata nije veći od 5 %. Corten čelik ne pripada skupini korozijski postojanih čelika, već on pri izloženosti atmosferskim uvjetima kao produkt korozije stvara površinski oksidni sloj koji u određenoj mjeri, štiti osnovni materijal od daljnjeg prodiranja korozije. Zbog prisustva legirnih elemenata u sastavu čelika, a pogotovo bakra, oksidni sloj ravnomjerno prekriva površinu i ima atraktivnu, crveno-smeđu boju koja s vremenom poprima tamnije tonove. Zbog toga je ovaj čelik vrlo zanimljiv arhitektima i umjetnicima koji ga koriste u svojim projektima.
U radu su prikazani rezultati usporedbe oksidnih slojeva nastalih na površini ploče od Corten čelika u ruralnom, industrijskom i morskom okruženju kroz 200 dana. Razlike u debljini, homogenosti i boji nastalih oksidnih slojeva na površini uzoraka su velike. Najtanji oksidni sloj izmjeren je kod uzoraka koji su izloženi djelovanju ruralne atmosfere, a površina je ujednačeno prekrivena oksidima. Uzorci izloženi djelovanju morske atmosfere najviše su oštećeni korozijom. Kod njih je izmjerena najveća debljina oksidnog sloja i najveća neravnomjernost prodiranja korozije po dubini. Površina im je neujednačeno prekrivena oksidima i ima najtamniju nijansu smeđe-crvene boje. Kod uzoraka izloženih djelovanju industrijske atmosfere prekrivenost površine oksidima je slična kao kod uzoraka iz ruralne atmosfere, a debljina oksidnog sloja im je za oko 30% veća.

***Ključne riječi**: Corten čelik, atmosferska korozija, mikrostruktura, oksidni sloj*

## UVOD

Konstrukcijski materijali podložni su nenamjernim štetnim promjenama, tj. pojavama i procesima koji smanjuju njihovu uporabnu vrijednost. Proces koji najčešće zahvaća konstrukcijske materijale je korozija koja razara materijal nakon čega on postaje neupotrebljiv za namjenu radi koje je nastao. Korozija je proces nenamjernog razaranja materijala, uzrokovan fizikalnim, kemijskim ili biološkim djelovanjem [1]. Faktori koji utječu na brzinu i vrstu korozijskih procesa dijele se na unutarnje (kemijski sastav i struktura materijala, stanje površine i sl.) i vanjske faktore (sastav medija, temperatura i sl.).
Korozijski procesi izazivaju velike novčane gubitke svjetskom gospodarstvu. Troškovi uzrokovani djelovanjem korozije nastaju zbog ranije zamjene korodiranih dijelova, provedbe mjera antikorozivne zaštite, zastoja u proizvodnji, gubitka proizvoda, onečišćenja okoliša i sl. Neke procjene govore da gubitci uzrokovani djelovanjem korozije u industrijskim zemljama iznose 3 do 5 % godišnjeg bruto domaćeg proizvoda (BDP-a) [2].
Budući da se atmosfera sastoji od zraka koji je jednolika smjesa plinova (oko 80 % dušika i 20 % kisika) za različito korozijsko ponašanje u različitim sredinama odgovorne su manjinske komponente atmosfere. Atmosferska korozija nastaje kao rezultat istovremenog djelovanja vlage i kisika iz zraka te ukoliko jedan od ta dva faktora nedostaje, atmosferska korozija neće nastupiti. Na brzinu atmosferske korozije utječe temperatura, sastav metala (legure), pasivni filmovi, sastav elektrolita i fizikalna svojstva, debljina filma elektrolita i produkti korozije. Proces korozije se teško može potpuno spriječiti ali se može dovoljno usporiti korištenjem

korozijski otpornih materijala, površinskom zaštitom materijala i nekim drugim postupcima [3, 4].
Corten čelik je trgovački naziv za grupu niskolegiranih konstrukcijskih čelika koji imaju povišenu otpornost na djelovanje atmosferske korozije. Corten naziv dolazi kao spoj dva najvažnija svojstva ovog čelika, a to su otpornost na atmosfersku koroziju (COR - corrosion resistance) i vlačna čvrstoća (TEN - tenssile strenght) [5]. U skupinu niskolegiranih konstrukcijskih čelika spadaju čelici koji imaju udio ugljika manji od 0,2 % te udio legirnih elemenata ne veći od 5 %. Ova vrsta čelika razvijena je iz razloga da se smanji potreba za bojanjem, te se najčešće koristi u arhitekturi za unutarnje i vanjske obloge (npr. zamjena za fasadu) i u umjetnosti za izradu umjetničkih djela. Neke od prednosti Corten čelika su jednostavno održavanje konstrukcije, niski troškovi održavanja konstrukcije, nema štetnih zaštitnih premaza i boja, zanimljiv estetski izgled, manje opasnih poslova za radnike pri održavanju jer nije potrebno čišćenje i bojanje konstrukcije, jednostavnije inspekcije i dr. [6]. Kako bi se postigla željena svojstva, ovaj čelik se legira bakrom (Cu), kromom (Cr) i niklom (Ni). Corten čelik ne pripada skupini korozijski postojanih čelika. Ako je izložen djelovanju atmosfere na njegovoj površini stvara se oksidni sloj koji ipak ima znatno bolja svojstva od oksidnog sloja na ugljičnim konstrukcijskim čelicima. Zbog prisustva specifičnih legirnih elemenata u sastavu čelika, a pogotovo bakra ovaj sloj na određeni način štiti osnovni materijal i kontrolira intenzitet korozije [7].
U normalnim atmosferskim uvjetima stvaranje površinskog oksidnog sloja traje od 18 do 36 mjeseci [5]. Na brzinu stvaranja sloja najviše utječe koncentracija vlage, ugljikovog dioksida ($CO_2$), sumporovog dioksida ($SO_2$) i morske vode u atmosferi u kojoj se čelik nalazi [8]. Stvoreni oksidni sloj naziva se patina. Tijekom tog perioda Corten čelik doživljava postupnu promjenu boje. Pri izlaganju Corten čelika normalnim atmosferskim uvjetima on prvo poprima prljavo žutu boju, koja s vremenom tamni i prelazi u crveno-smeđu boju. Ta promjena je najizraženija u prve 2 godine [8].
Corten čelik ima u nekim uvijetima bolju otpornost prema mikrobiološkoj koroziji od ugljičnog čelika, ali i od nehrđajućih austenitnih čelika [9].
U radu su prikazani rezultati usporedbe oksidnih slojeva nastalih na površini ploče od Corten čelika u ruralnom, industrijskom i morskom okruženju nastalih kroz 200 dana izlaganja.

## MATERIJALI I METODE

Sva ispitivanja provedena su na uzorcima izrezanima iz čelične ploče debljine 20 mm. Čelična ploča od Corten čelika standardne oznake S355J0WP+AR iz koje su izrezani uzorci dobivena je vrućim valjanjem i u takvom stanju je isporučena iz čeličane. Navedeni čelik spada u grupu niskolegiranih konstrukcijskih čelika s povišenom otpornosti na atmosfersku koroziju. Prema kemijskom sastavu i mehaničkim svojstvima čelik S355J0WP (brojčane oznake 1.8945) spada u skupinu Corten-A čelika, a prema američkom ASTM standardu ima oznaku A242 [8, 10]. Najčešće se koristi pri gradnji dimnjaka i mostova, kao obloga na zgradama i kućama te za izradu umjetničkih skulptura.
Kemijski sastav materijala prikazan je u tablici 1.

Tablica 1. Kemijski sastav čelika S355J0WP

| Element | C | Cr | Cu | Ni | Al | Mn | Si | P | S | Fe |
|---|---|---|---|---|---|---|---|---|---|---|
| maseni udio, [%] | 0,08 | 0,33 | 0,27 | 0,11 | 0,037 | 0,8 | 0,30 | 0,07 | 0,004 | ostatak |

Za potrebe ispitivanja ukupno su izrezana tri uzorka čije su sve površine obrađene glodanjem.
Na slici 1 prikazani su uzorci prije izlaganja djelovanju različitih atmosfera.

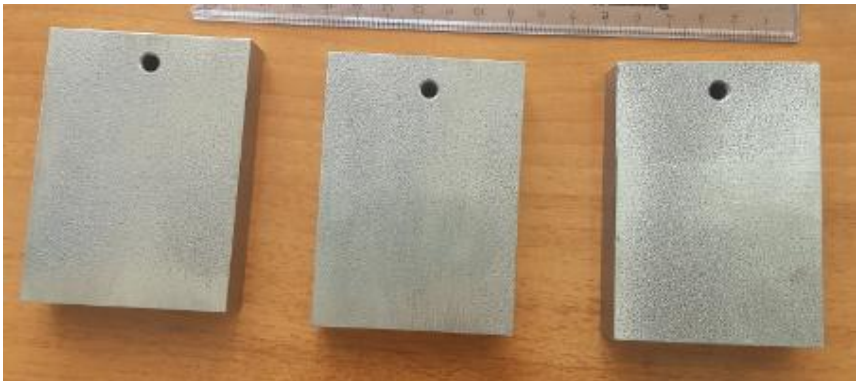

Slika 1. Izrezani uzorci prije izlaganja djelovanju različitih atmosfera

Uzorci su bili izloženi djelovanju različitih atmosfera u trajanju od 200 dana (od 25.02. do 12.09.2017. godine) na tri lokacije u Republici Hrvatskoj:

1. Šemovci (selo u Koprivničko-Križevačkoj županiji) – ruralna atmosfera,
2. grad Zagreb – industrijska atmosfera,
3. grad Pula – morska atmosfera.

Na slici 2 prikazane su navedene lokacije na karti.

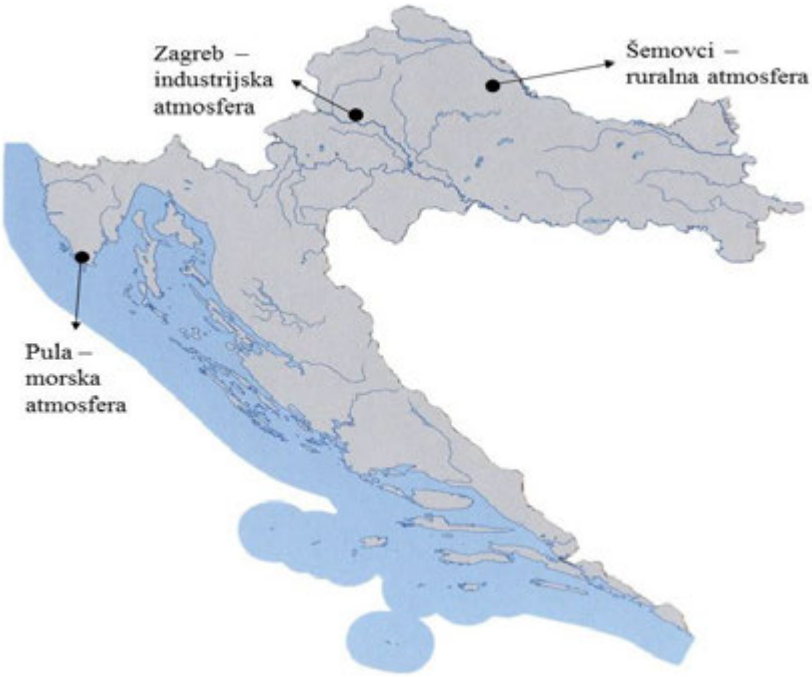


Slika 2. Lokacije na kojima su bili izloženi uzorci

Nakon izlaganja uzoraka djelovanju različitih atmosfera napravljena je analiza i usporedba nastalih oksidnih slojeva na površinama uzoraka. Analiza uzoraka započela je vizualnom kontrolom i usporedbom oksidiranih površina svih uzoraka.
Nakon toga provedena je analiza mikrostrukture materijala i analiza nastalog oksidnog sloja na površinama uzoraka pomoću svijetlosnog mikroskopa Olympus GX51 te skenirajućeg elektronskog mikroskopa Tescan Vega TS5136LS. Analiza mikrostrukture provedena je u poliranom i nagriženom stanju. Kako bi se utvrdio sastav nastalog oksidnog sloja napravljena je i EDS analiza.

## REZULTATI I RASPRAVA

Vizualnim pregledom utvrđena je velika razlika u intenzitetu korozije i izgledu oksidiranih površina uzoraka s različitih lokacija. Uzorak koji je bio izložen djelovanju morske atmosfere je puno neujednačenije korodirao u odnosu na druga dva uzorka. Oksidi su mjestimice dublje prodrli u površinu materijala što je rezultiralo neujednačenom bojom površine. U odnosu na druga dva uzorka, boja je zagasitija i manje atraktivna. Uzorci koji su bili izloženi djelovanju ruralne i industrijske atmosfere su relativno slični, površina im je ravnomjerno i skoro u potpunosti prekrivena tankim slojem oksida lijepe, crveno-smeđe boje. Na slici 3 prikazani su uzorci nakon 200 dana izlaganja.

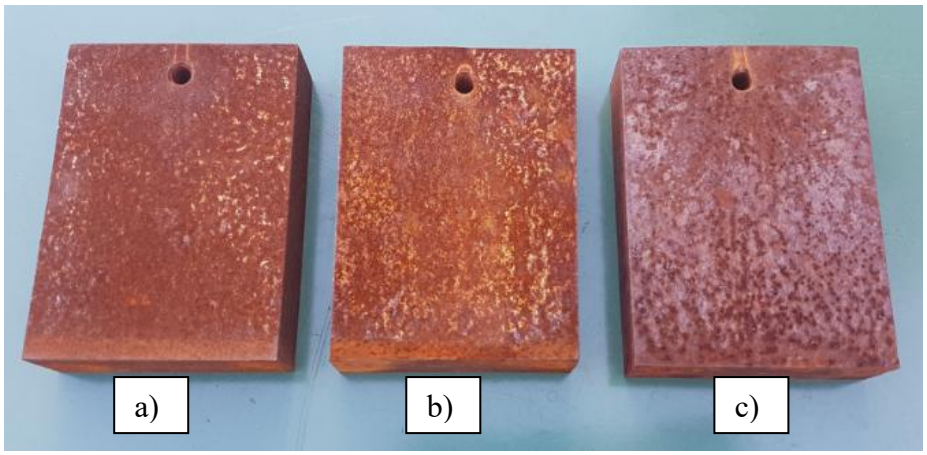


Slika 3. Osnovni materijal nakon 200 dana izlaganja u ruralnoj (a), industrijskoj (b) i morskoj atmosferi (c)

Nakon 200 dana izlaganja djelovanju atmosfere iz osnovnih uzoraka izrezani su i pripremljeni metalografski uzorci za analizu mikrostrukture (po dva uzorka za svaku lokaciju). Materijal je analiziran u smjeru valjanja i smjeru okomitom na smjer valjanja.
Mikrostruktura uzoraka je analizirana u poliranom i nagriženom stanju. Posebna pozornost posvećena je oksidnom sloju koji je nastao na površinama uzoraka tijekom izlaganja djelovanju različitih atmosfera.
Na slikama 4, 5 i 6 prikazan je oksidni sloj na površini uzoraka snimljen na svjetlosnom mikroskopu.

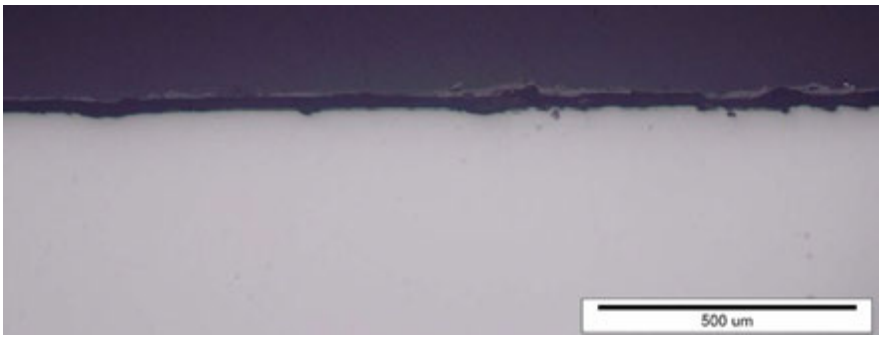


Slika 4. Oksidni sloj na površini uzorka iz ruralne atmosphere

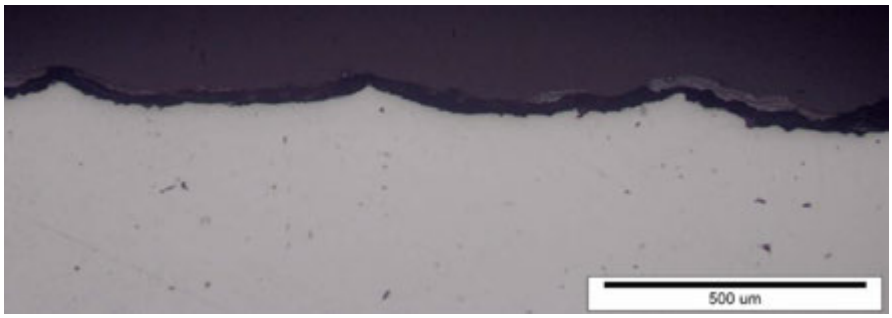


Slika 5. Oksidni sloj na površini uzorka iz industrijske atmosfere

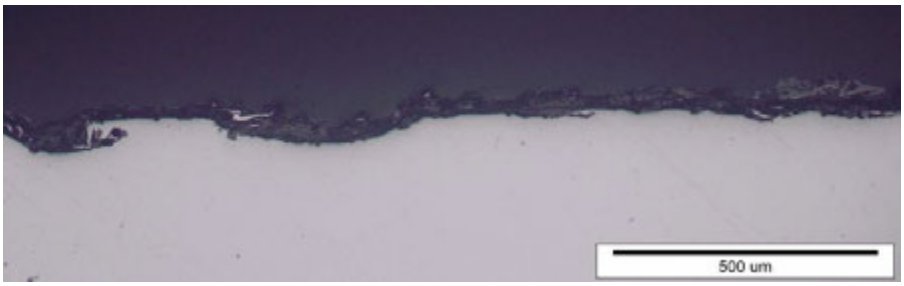


Slika 6. Oksidni sloj na površini uzorka iz morske atmosfere

Na uzorku koji je bio izložen djelovanju ruralne atmosfere, debljina oksidnog sloja na površini materijala iznosila je oko 0,03 mm (30 µm). Uzorak koji je bio izložen djelovanju industrijske atmosfere ima 30-ak % veću debljinu oksidnog sloja od uzorka izloženog ruralnoj atmosferi. Najdeblji oksidni sloj (oko 0,059 mm) izmjeren je kod uzorka koji je bio izložen djelovanju morske atmosfere. Hrapavost površine kod uzorka iz morske atmosfere je puno izraženija nego kod drugih uzoraka što znači da je korozija dublje prodrla u materijal. U poliranom stanju nisu uočene nikakve nepravilnosti u mikrostrukturi materijala.
Na slici 7 prikazana je mikrostruktura materijala u nagriženom stanju okomito na smjer valjanja (lijevo) i u smjeru valjanja (desno).

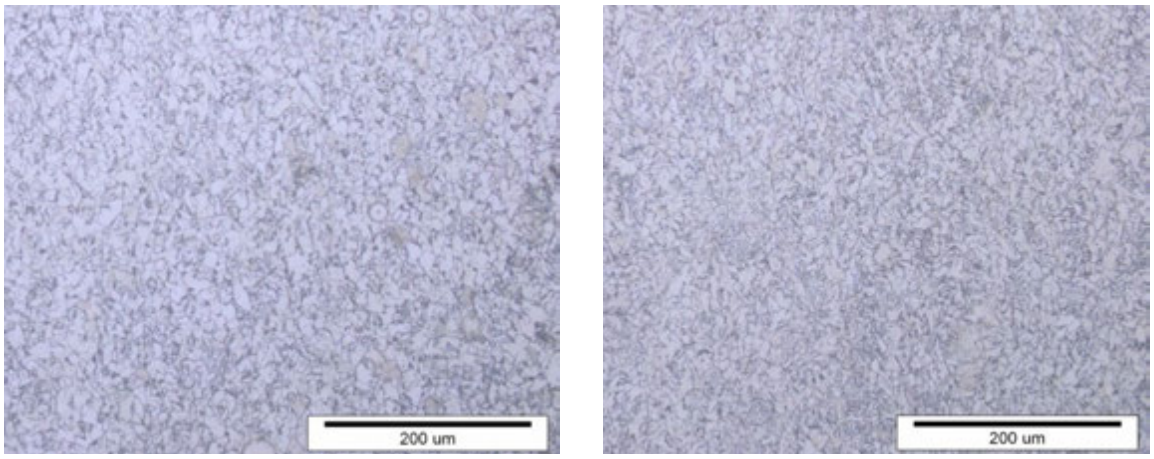


Slika 7. Mikrostruktura materijala okomito na smjer valjanja (lijevo) i u smjeru valjanja (desno)

Analiza mikrostrukture čelika S355J0WP+AR pokazala je da se mikrostruktura sastoji od ferita i perlita. Udio ferita je puno veći s obzirom na vrlo mali sadržaj ugljika. Mikrostruktura je izrazito sitnozrnata i neusmjerena (nema razlike s obzirom na smjer valjanja).
SEM/EDS analiza provedena je s ciljem utvrđivanja morfologije, debljine i elementarnog sastava korozijskih produkata nastalih na površini Corten čelika izloženog ruralnoj, industrijskoj i morskoj atmosferi kroz 200 dana.
Morfološki najujednačeniji i najkompaktniji je sloj korozijskih produkata na čeliku izloženom ruralnoj atmosferi. Prema literaturi, na ovim čelicima nastaju dva sloja korozijskih produkata: vanjski (sadrži α-FeOOH i γ-FeOOH) i unutarnji (sadrži amorfni FeOOH s nešto kristalnog $Fe_3O_4$) [11]. Na slikama 8, 9 i 10 prikazani su rezultati EDS analize.

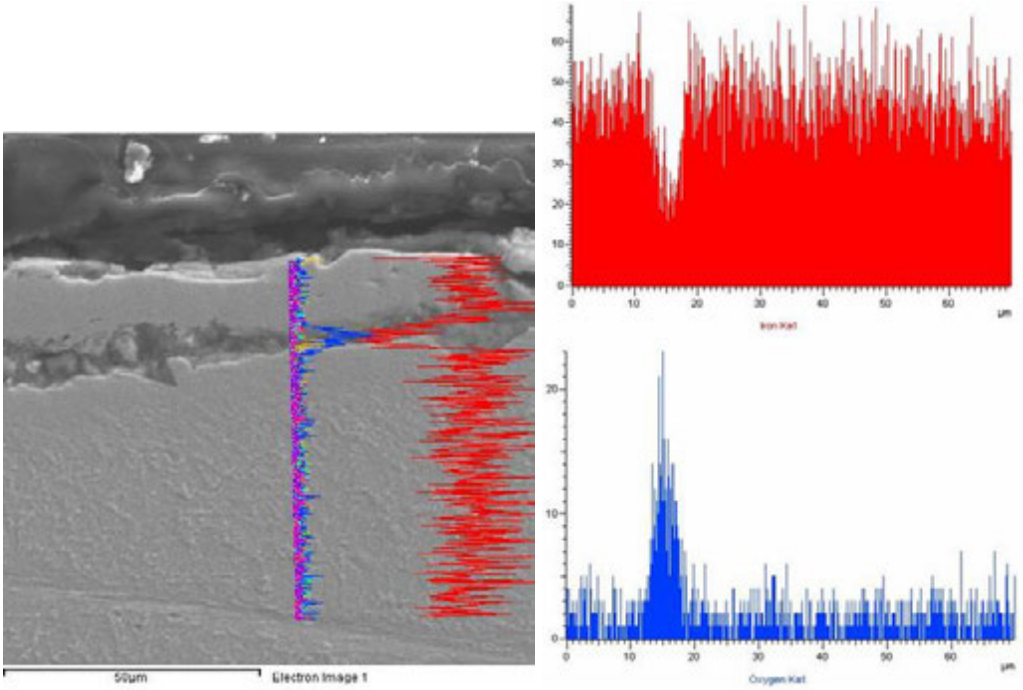


Slika 8. EDS analiza oksidnog sloja (Fe – gore), O – dolje) – ruralna atmosfera

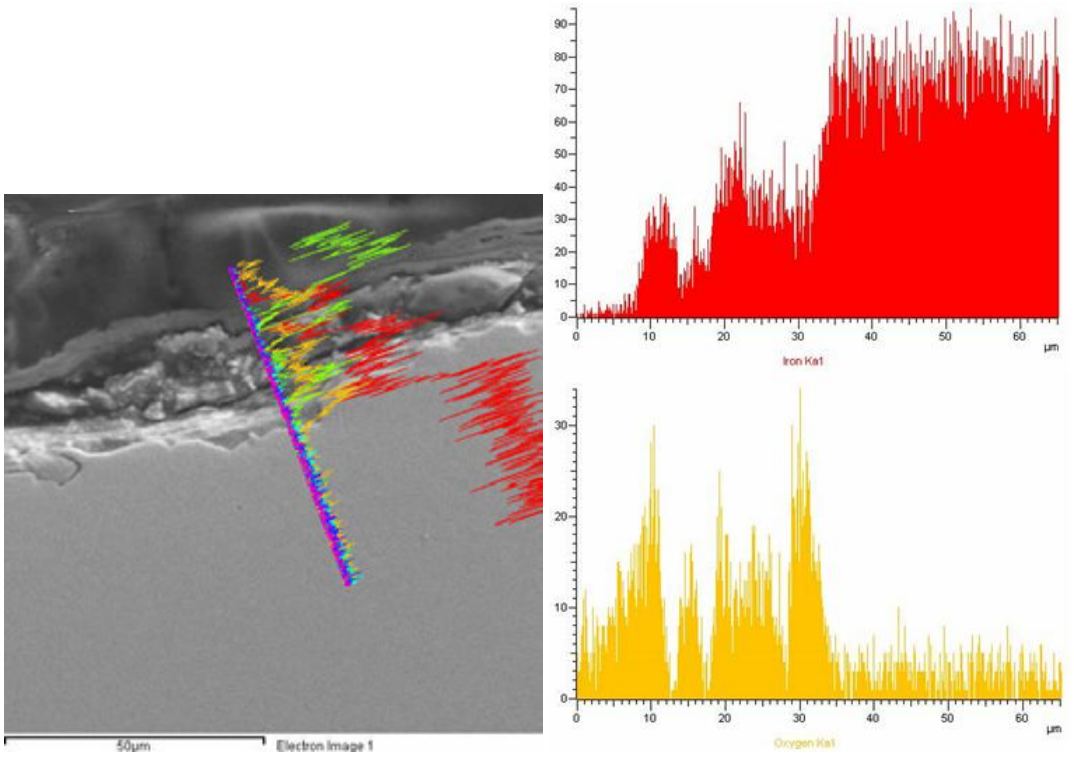


Slika 9. EDS analiza oksidnog sloja ( Fe – gore, O – dolje) – industrijska atmosfera

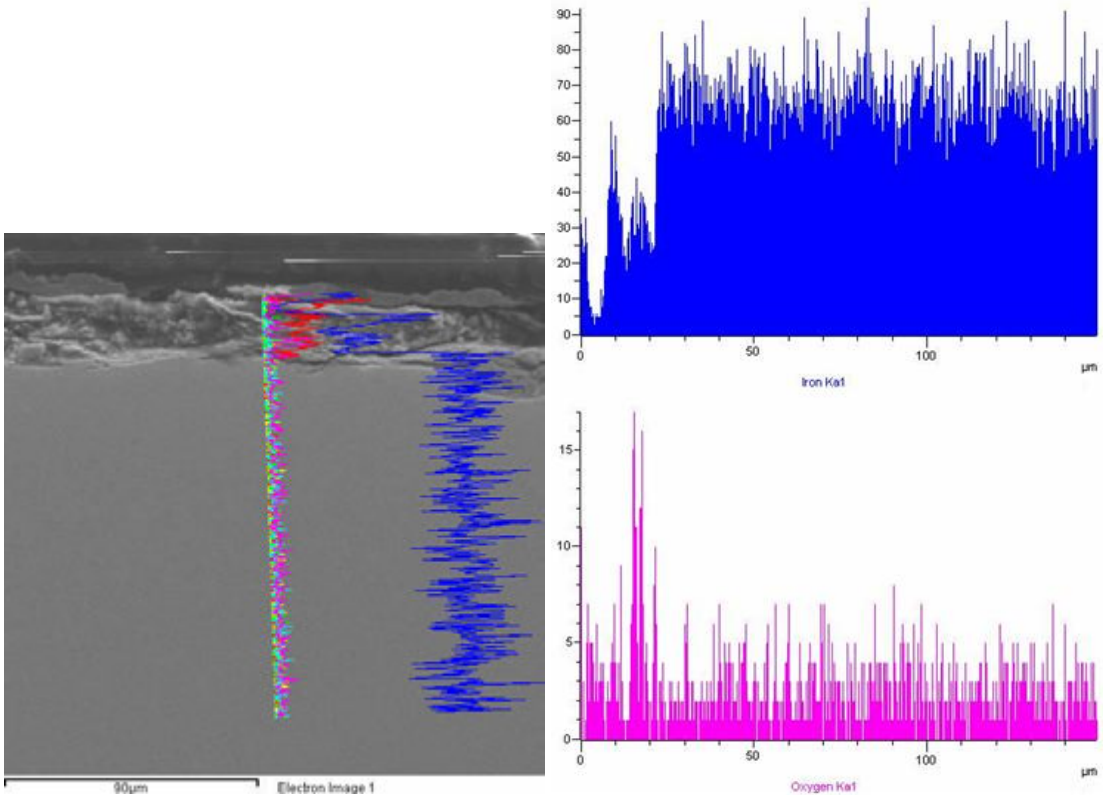


Slika 10. EDS analiza oksidnog sloja (Fe – gore, O – dolje) – morska atmosfera

Na SEM slikama se može uočiti kompaktniji vanjski i amorfni unutarnji sloj. Unutarnji sloj se nalazi na granici između sloja korozijskih produkata i površine čelika te sadrži veliki broj pora i mikropukotina, stoga je oštećen i propusan za daljnje korozijske napade.
Na svim ispitanim uzorcima utvrđena je prisutnost željeza i kisika u površinskom sloju čime je potvrđeno nastajanje korozijskih produkata. Prisutnost kisika u skladu je s određenom debljinom sloja korozijskih produkata.

## ZAKLJUČAK

Na temelju provedenih ispitivanja i pritom dobivenih rezultata može se zaključiti sljedeće:
- postoji velika razlika u intenzitetu korozije i izgledu oksidiranih površina uzoraka s različitih lokacija.
- morska atmosfera je najagresivnije djelovala na materijal, korozija je prodrla duboko, a površina je neravnomjerno prekrivena oksidima.
- površina uzoraka izloženih ruralnoj atmosferi je ravnomjerno prekrivena tankim slojem oksida i ima lijepu crveno–smeđu boju.
- oksidni sloj na uzorcima koji su bili izloženi djelovanju industrijske atmosfere je oko 30 % deblji, a na uzorcima koji su bili izloženi morskoj atmosferi gotovo 100 % deblji u odnosu na uzorke iz ruralne atmosfere.
- kod uzoraka iz morske atmosfere korozija je dublje prodrla zbog čega je površina hrapavija u odnosu na druge uzorke.
- EDS linijskom analizom utvrđena je prisutnost željeza i kisika u površinskom sloju što je u skladu s određenom debljinom oksidnog sloja.

## LITERATURA

[1] Institut Ruđer Bošković, Tehnologije površinske zaštite, Dostupno na internetu: https://tkojetko.irb.hr/documents/8305_1662.pdf, 26.03.2017.
[2] I. Juraga, V. Alar, V. Šimunović, I. Stojanović, Predavanje: Korozija i metode zaštite od korozije, Fakultet strojarstva i brodogradnje u Zagrebu, Dostupno na internetu: https://www.fsb.unizg.hr/korozija/PROIZVODNI_POSTUPCI.pdf
[3] T. Stefanovski, Utjecaj temperature na efikasnost antikorozivne zaštite konstrukcijskog čelika primjenom ekološkog inhibitora, Diplomski rad, Metalurški fakultet u Sisku, 2015., Dostupno na internetu: https://urn.nsk.hr/urn:nbn:hr:115:137233
[4] T. Filetin, Izbor materijala pri razvoju proizvoda, Fakultet strojarstva i brodogradnje u Zagrebu, 2000.
[5] Total Materia, Atmospheric Corrosion Resistant CORTEN Steel, Datum objave: Lipanj 2010., Dostupno na internetu: http://www.totalmateria.com/page.aspx?ID=CheckArticle&site=kts&NM=274, 01.02.2017.

[6] Internet stranica: http://www.gradjevinarstvo.rs/tekstovi/5187/820/estetika-rdje-korten-celik, 02.02.2017.
[7] AZO Materials, Weathering Steel: A Guide to Corten and the A/B Equivalents, Origins & Standards, članak br. 12974, 2016., Dostupno na internetu: http://www.azom.com/article.aspx?ArticleID=12974, 01.02.2017.
[8] H. Otmačić-Ćurković, K. Marušić, E. Stupnišek-Lisac, Zaštita patinirane i čiste bronce ekološki prihvatljivim inhibitorima korozije, Fakultet kemijskog inženjerstva i tehnologije u Zagrebu,
Dostupno na internetu:
http://akm.hkdrustvo.hr/AKM_arhiva/AKM12/AKM2008_radionice/Konz_restaur/AKM2008_Otmacic-Curkovic_Marusic_Stupnisek-Lisac.ppt, 02.02.2017.
[9] H. Mansouri, S. A. Alavi, M. Fotovat, Microbial-Influenced Corrosion of Corten Steel Compared with Carbon Steel and Stainless Steel in Oily Wastewater by Pseudomonas aeruginosa, JOM, 67 (2015) 7, pp. 1594-1600. Dostupno na internetu: https://doi.org/10.1007/s11837-015-1429-1, 26.01.2018.
[10] B. Bašić, Analiza mikrostrukture zavarenog spoja Corten čelika, Diplomski rad, Fakultet strojarstva i brodogradnje u Zagrebu, 2017. Dostupno na internetu: http://repozitorij.fsb.hr/8111/1/Ba%C5%A1i%C4%87_2017_Diplomski.pdf, 27.01.2018.
[11] D. de la Fuente, I. Díaz, J. Simancas, B. Chico, M. Morcillo, Long-term atmospheric corrosion of mild steel, Corrosion Science, 53 (2011) 2, pp. 604-617.

17th INTERNATIONAL FOUNDRYMEN CONFERENCE
Hi-tech casting solution and knowledge based engineering
Opatija, May 16th-18th, 2018
http://www.simet.hr/~foundry/

# COMPARISON OF BRASS YOUNG'S MODULUS TESTING RESULTS OBTAINED THROUGH CONVENTIONAL AND INDENTATION METHODS

# USPOREDBA REZULTATA ISPITIVANJA MODULA ELASTIČNOSTI MJEDI KONVENCIONALNOM I INDENTACIJSKOM METODOM

**Dino Bogdanić, Luka Mahenić, Željko Alar***

University of Zagreb Faculty of Mechanical Engineering and Naval Architecture, Zagreb, Croatia

**Poster presentation**
*Preliminary note*

**Abstract**

Elasticity modulus (Young's modulus) is a constant of the material which depends on bonding strength between atoms and/or molecules in the crystal lattice or amorphous structure. Determination of the elasticity modulus is a very difficult task from the measurer's perspective. In this work, a short overview of the modern applicable methods for the determination of elasticity modulus is discussed. In the experimental part, a comparison between the elasticity modulus testing results of brass samples performed by two different methods is also discussed. Testing methods included a tensile testing method with the use of a contact extensometer and an instrumented indentation method. Testing and statistical analysis of the obtained results showed a significant correlation between the results and several factors, such as extonsemeter's accuracy, load measurement range, sample preparation (material homogeneity) and linearization of elastic (Hook's) line, among others.

***Keywords***: *Young's modulus of elasticity, extensometer, instrumented indentation method, brass*

*Corresponding author (e-mail address): *zeljko.alar@fsb.hr*

**Sažetak**

Modul elastičnosti (Youngov modul) je konstanta materijala koja ovisi o jačini veza između atoma i/ili molekula u kristalnoj rešetci ili amorfnoj strukturi. Određivanje modula elastičnosti je s mjeriteljske strane vrlo zahtjevan postupak. U radu je dan kratki osvrt na danas primjenjive metode za određivanje modula elastičnosti, a u eksperimentalnom dijelu je provedena usporedba rezultata ispitivanja modula elastičnosti mjedi s dvije različite metode. Primijenjene su metoda statičkog vlačnog ispitivanja uz korištenje kontaktnog ekstenzometra te instrumentirana indentacijska metoda. Ispitivanja i statistička analiza dobivenih rezultata su pokazali značajnu ovisnost rezultata ispitivanja o

nekoliko faktora, kao npr. o točnosti ekstenzometra, mjernom području opterećenja, pripremi uzoraka (homogenosti materijala) te o linearizaciji Hook-ovog pravca, između ostalog.

***Ključne riječi**: Youngov modul elastičnosti, ekstenzometar, instrumentirana indentacijska metoda, mjed*

## UVOD

Modul elastičnosti ili Youngov modul jest mehaničko svojstvo materijala koje predstavlja mjeru krutosti materijala i jednak je omjeru vlačnog naprezanja i linijske vlačne deformacije u području Hook-og pravca.

$$E = \frac{\sigma}{\varepsilon} \tag{1}$$

Krutost materijala važna je veličina pri određivanju stabilnosti i sigurnosti neke konstrukcije [1]. Čvrsti materijali će se deformirati ako ih podvrgnemo određenom opterećenju. Ako se zadani materijal nakon opterećenja vrati u početni oblik to znači da je se ostvarila elastična deformacija. Za krute materijale potrebna je znatno veća sila opterećenja da bi se deformirali u odnosu na meke materijale [2].

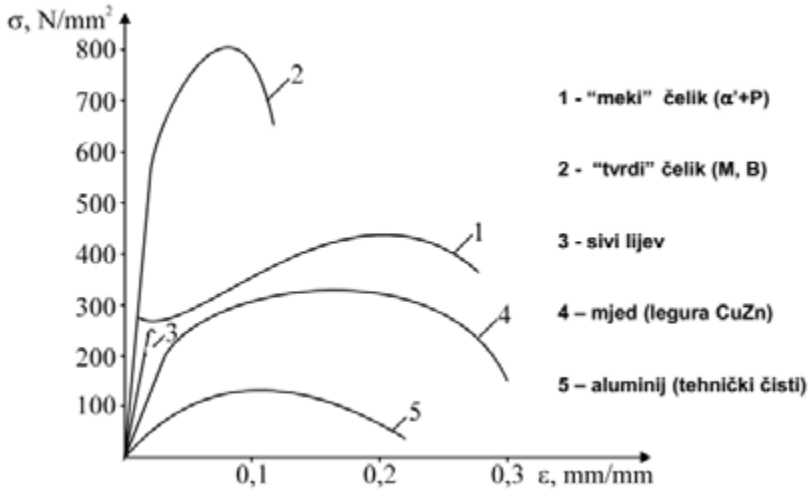


Slika 1. σ-ε dijagram i pripadajuće krivulje za različite vrste materijala [2]

Na slici 1 prikazan je σ-ε dijagram i na temelju njega možemo usporediti materijale prema njihovim elastičnim svojstvima. Prema nagibu Hook-ovog pravca možemo jasno vidjeti razliku u potrebnim silama za određenu veličinu deformacije. Također se iz priloženog σ-ε dijagrama vidi produljenje određenog materijala pod djelovanjem sile. Tako npr. iz slike možemo vidjeti kako je za istu deformaciju kod aluminija potrebna znatno manja sila opterećenja nego kod čelika.

Određivanje modula elastičnosti provodi se u laboratorijskim uvjetima u kojima su poznate točne sile deformiranja i vrijednosti deformacija. Male deformacije koje nastaju tijekom ispitivanja mjere se mjernim instrumentima (ekstenzometri). Postoji više metoda određivanja modela elastičnosti, a u okviru rada su opisane i primijenjene metode statičkog vlačnog ispitivanja uz korištenje kontaktnog ekstenzometra i instrumentizirana indentacijska metoda.

## MATERIJALI I METODE

U okviru rada provedena su ispitivanja na epruvetama izrađenim iz mjedi i dio su jednog šireg istraživanja o utjecajnim faktorima na određivanje modula elastičnosti kod metalnih materijala. Ispitni uzorci su izrađeni iz šipki od mjedi promjera 16 mm uzetih u jednom centru za prodaju metalnih materijala. Namjerno je uzet materijal bez ikakvih podataka o njemu kako tijekom ispitivanja ta saznanja ne bi imala utjecaja. Na ovaj način željelo se simulirati situaciju da netko tko ne poznaje materijale kupi materijal i iz njega izradi ispitne uzorke te provede ispitivanja modula elastičnosti. Na epruvetama je proveden statičko vlačno ispitivanje te su se uz pomoć kontaktnog ekstenzometra na različitim rasponima sile bilježile deformacije i shodno tome izračunat modul elastičnosti. Nakon provođenja statičko vlačnog ispitivanja izrezani su dijelovi epruveta i zaliveni u polimernu masu. Tako pripremljeni uzorci podvrgnuti su ispitivanju pomoću instrumentirane indentacijske metode za mjerenje tvrdoće. U tablici 1 je prikazan plan ispitivanja.

Tablica 1. Plan eksperimentalnog ispitivanja

| Redni broj | Postupak | Opis |
|---|---|---|
| 1. | Priprema uzoraka | - 5 ispitnih uzoraka<br>- izrađeni prema normi HRN EN ISO 6892-1:2016 [3] |
| 2. | Statičko vlačno ispitivanje pomoću kontaktnog ekstenzometra | Provedeno na različitim rasponima sila<br>- 5000 N do 45000 N<br>- 10000 N do 45000 N<br>- 20000 N do 45000 N<br>- 25000 N do 45000 N<br>- 30000 N do 45000 N |
| 3. | Ispitivanje pomoću identora tvrdoće | Provedeno 5 ispitivanja na izrezanim i zalivenim uzorcima sukladno normi HRN EN ISO 14577-1:2015 [4] |
| 4. | Analiza rezultata | Utjecaj izbora raspona i usporedba dobivenih rezultata iz ispitivanja |

U svrhu provođenja statičkog vlačnog ispitivanja prema normi HRN EN ISO 6892-1:2016 pripremljena je kratka cilindrična epruveta promjera tijela 12 mm i mjerne duljine 60 mm (slika 2).

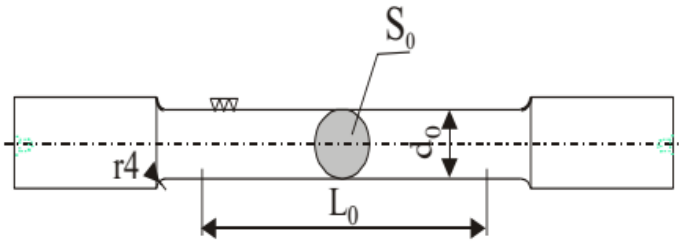


Slika 2. Cilindrična epruveta za provođenje statičkog vlačnog ispitivanja

Statičko vlačno ispitivanje provedeno je na univerzalnoj kidalici (slika 3) sljedećih karakteristika:

- Proizvođač: WEB Werkstoffprüfmaschinen GmbH, Njemačka,
- Vrsta: EU40 mod,
- Mjerno područje: 0 do 400 kN,
- Serijski broj / Oznaka: 990.06/35 / 201/EUmod,
- Klasa: 1 (sukladno normi HRN EN ISO7500:2016).

Slika 3. Kidalica EU40 mod

Na kidalici je bio priključen kontaktni ekstenzometar sljedećih karakteristika:

- Proizvođač: Mess & Feinwerktechnik, Njemačka,
- Vrsta: MFA 2,
- Tip: elektronski,
- Serijski broj: 012872,
- Mjerno područje: 0 – 2 mm,
- Klasa: 1 (sukladno normi HRN EN ISO 9513:2012).

Prilikom ispitivanja primijenjeno je predopterećenje od 2,5 kN a sila i produljenje pri trenutnoj sili su bilježeni u području Hook-ovog pravca za svakih 5 kN.
Drugo ispitivanje modula elastičnosti provedeno je na instrumentiranom indentacijskom tvrdomjeru proizvođača SHIMADZU DUH-211S (slika 4) [5]. Iz slomljene epruvete na kojoj je provedeno statičko vlačno ispitivanje izrezan je uzorak (slika 5) i zaliven u plastičnu masu. Uzorak je zaliven u plastičnu masu zbog ostvarivanja stabilnosti prilikom ispitivanja metodom indentacije.

Slika 4. SHIMADZU DUH-211S

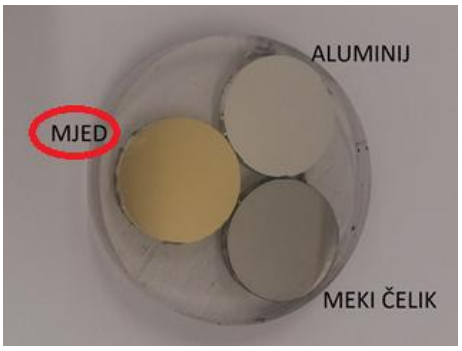


Slika 5. Izrezani i zaliveni uzorci

**REZULTATI I RASPRAVA**

***ISPITIVANJE POMOĆU KONTAKTNOG EKSTENZOMETRA***

U tablici 2 je prikazan rezultat statičkog vlačnog ispitivanja za jedan ispitni uzorak gdje je se u rasponu sile od 5000 N do 45000 N na svakih 5000 N mjerilo trenutno produljenje ispitnog uzorka. Brzina ispitivanja je bila po metodi B sukladno normi HRN EN ISO 6892-2016 i iznosila 60 $N/mm^2$ u sekundi. Vrijednosti modula elastičnosti za određene raspone sila su izračunate i prikazane u tablici 3. Kvaliteta ispitnih uzoraka je u ovom radu ciljano postavljena na donjoj granici prihvatljivosti s obzirom na zahtjeve norme HRN EN ISO 6892-1:2016.

Tablica 2. Rezultati ispitivanja za mjed

| *F*, N | 5000 | 10000 | 15000 | 20000 | 25000 | 30000 | 35000 | 40000 | 45000 |
|---|---|---|---|---|---|---|---|---|---|
| *Δl*, mm | 0,0171 | 0,0428 | 0,0711 | 0,095 | 0,1156 | 0,1343 | 0,1622 | 0,2347 | 0,368 |

Tablica 3. Rezultati modula elastičnosti za mjed

| **Raspon sile, N** | **Modul elastičnosti, N/mm²** | | **Raspon sile, N** | **Modul elastičnosti, N/mm²** |
|---|---|---|---|---|
| 5000-10000 | 86009,07568 | | 10000-15000 | 78107,18180 |
| 5000-15000 | 81867,89796 | | 10000-20000 | 84690,92892 |
| 5000-20000 | 85125,79891 | | 10000-25000 | 91089,28207 |
| 5000-25000 | 89763,78660 | | 10000-30000 | 96630,96153 |
| 5000-30000 | 94301,75960 | | 10000-35000 | 92564,20624 |
| 5000-35000 | 91403,16657 | | 10000-40000 | 69112,03476 |
| 5000-40000 | 71107,68711 | | 10000-45000 | 47580,05140 |
| 5000-45000 | 50394,60233 | | | |
| | | | | |
| 15000-20000 | 92486,74665 | | 20000-25000 | 107302,58470 |
| 15000-25000 | 99345,31438 | | 20000-30000 | 112490,24150 |
| 15000-30000 | 104925,62870 | | 20000-35000 | 98680,05558 |
| 15000-35000 | 97055,24676 | | 20000-40000 | 63290,85884 |
| 15000-40000 | 67556,02827 | | 20000-45000 | 40484,12536 |
| 15000-45000 | 44670,25756 | | | |
| 25000-30000 | 118204,98640 | | 30000-35000 | 79226,99803 |
| 25000-35000 | 94868,37961 | | 30000-40000 | 44032,53476 |
| 25000-40000 | 55678,41927 | | 30000-45000 | 28375,26630 |
| 25000-45000 | 35030,63780 | | | |

***ISPITIVANJE METODOM INDENTACIJE***

Indentacija na posebno izrezanom i ulivenom uzorku provedena je sa silom u iznosu od 1500 N i uz predviđeni Poissonov koeficijent u iznosu od 0,357 [6]. Rezultati ispitivanja prikazani su u tablici 4.

Tablica 4. Rezultati ispitivanja indentacijskom metodom

| Test br. | $F_{max}$ [mN] | $h_{max}$ [um] | $h_p$ [um] | $h_r$ [um] | $HM_s$ [N/mm²] | $H_{it}$ [N/mm²] | $E_r$ [N/mm²] | $C_{it}$ % | $n_{it}$ % | *HV* |
|---|---|---|---|---|---|---|---|---|---|---|
| 1 | 1504,59 | 6,5012 | 5,4422 | 5,7779 | 1124,215 | 1768,565 | 9,51E+04 | 0,561 | 16,87 | 163,42 |
| 2 | 1502,72 | 6,4958 | 5,3741 | 5,7804 | 1229,631 | 1766,077 | 9,35E+04 | 0,503 | 16,967 | 163,19 |
| 3 | 1504,59 | 6,4998 | 5,3514 | 5,7946 | 1236,978 | 1761,365 | 9,24E+04 | 0,495 | 17,234 | 162,75 |
| 4 | 1504,38 | 6,5469 | 5,3884 | 5,8341 | 1176,768 | 1736,969 | 9,29E+04 | 0,481 | 17,386 | 160,5 |
| 5 | 1505,64 | 6,2536 | 4,9983 | 5,5194 | 1212,389 | 1932,113 | 9,31E+04 | 0,571 | 17,921 | 178,53 |

Do informacija o modulu elastičnosti se dolazi uvrštavanjem rezultata ispitivanja (tablica 4) i relevantnih faktora (tablica 5) u sljedeću formulu [4]:

$$E = (1-\nu_m^2)\left[\frac{1}{E_r} - \frac{1-\nu_i^2}{E_{in}}\right]^{-1} \quad (2)$$

Tablica 5. Vrijednosti ostalih faktora za izračunavanje modula elastičnosti za mjed

| | |
|---|---|
| $E_i$ | 890 000 N/mm$^2$ |
| $\nu_i$ | 0,075 |
| $\nu_m$ | 0,0357 |

Tablica 6. Modul elastičnosti za mjed

| Test br. | 1 | 2 | 3 | 4 | 5 |
|---|---|---|---|---|---|
| *E*, N/mm$^2$ | 92869 | 91051 | 89878 | 90436 | 90692 |

**ANALIZA I USPOREDBA REZULTATA**

Problem koji je uočen tijekom ispitivanja jest znatno odstupanje vrijednosti modula elastičnosti. Prilikom računanja modula elastičnosti potrebno je paziti koje vrijednosti sile se uzimaju za računanje, tj. da li se točke nalaze u elastičnom ili plastičnom području deformacija. Slika 6 pokazuje dijagram sila-produljenje iz kojeg se vidi da mjed nema jasno izraženu granicu razvlačenja, tj. granicu prijelaza iz elastičnog u elastično-plastično područje. Zbog toga treba posvetiti posebnu pozornost prilikom odabira relevantnih točaka ispitivanja kod kojih se materijal još uvijek ponaša isključivo elastično.

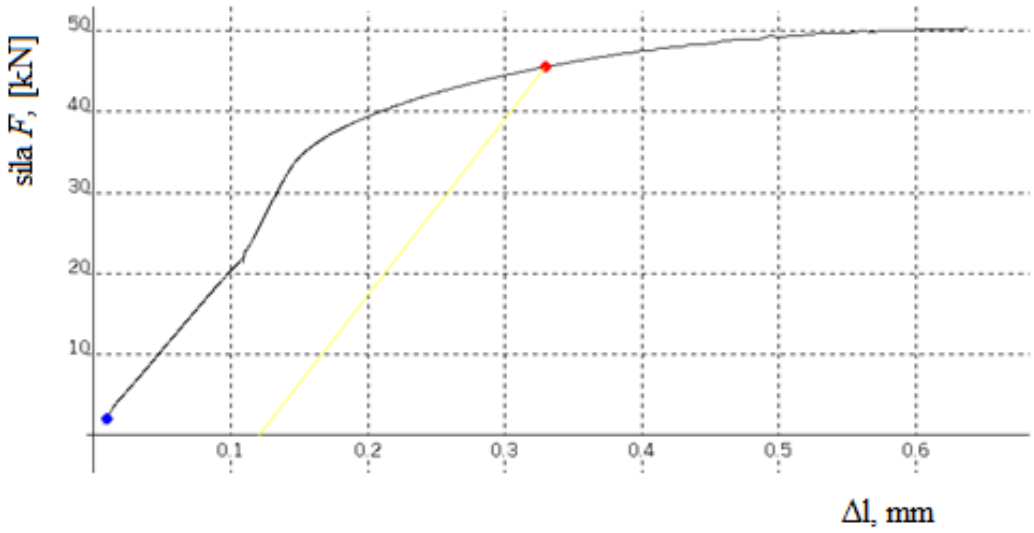


Slika 6. Dijagram sila-produljenje za mjed

Pored toga vidi se i nelinearnost krivulje u elastičnom području koja može biti prouzrokovana različitim utjecajima kao što su: nedovoljna kvaliteta ekstenzometra, klizanje kontaktnog ekstenzometra, pogreške u materijalu, velika nehomogenost materijala, brzina ispitivanja i čitav niz drugih utjecajnih faktora.
Kod metode određivanja modula elastičnosti pomoću instrumentiranog indentacijskog tvrdomjera pojavljuje se također čitav niz utjecajnih faktora. Na slici 7 je dan shematski prikaz metode i određivanja pojedinih geometrijskih veličina a na temelju kojih se kasnije određuje modul elastičnosti. Rezultati ispitivanja kod ove metode značajno ovise o stanju površine na kojoj se provode ispitivanja, kvaliteti same opreme za ispitivanja, homogenosti materijala i njegova odziva na različite brzine ispitivanja. Analizom rezultata iz tablice 6 vide se također dosta velika odstupanja u rezultatima ispitivanja.

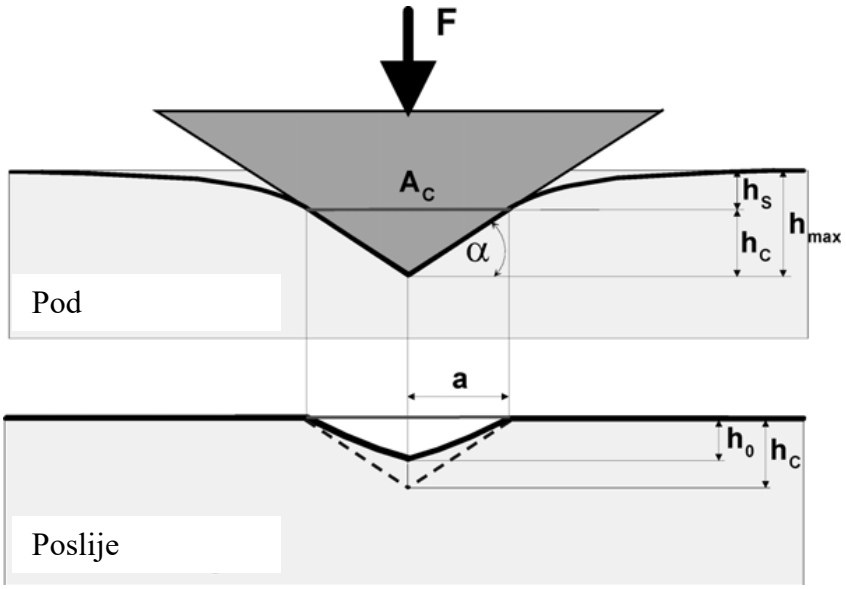


Slika 7. Geometrijske postavke ispitivanja [7]

U tablici 7 prikazane su srednje vrijednosti modula elastičnosti mjedi koje su izračunate metodom statičkog vlačnog ispitivanja (kontaktni ekstenzometar) i indentacijskom metodom. Ovdje je uzet raspon sila od 10 kN do 35 kN pri ispitivanju kontaktnim ekstenzimetrom. Iznosi modula elastičnosti za metodu kontaktnog ekstenzometra i za metodu indentacije su donekle slična iako, gledajući s mjeriteljske strane i ne uzimajući u obzir mjernu nesigurnost, to su dosta velika odstupanja. Ovdje treba naglasiti da su rasipanja vrijednosti modula elastičnosti kod metode indentacije manja nego kod metode s kontaktnim ekstenzometrom.

Tablica 7. Usporedba srednjih vrijednosti rezultata modula elastičnosti za mjed

| Kontaktni ekstenzometar | Metodom indentacije |
|---|---|
| 88616,51 N/mm$^2$ | 90985,2 N/mm$^2$ |

Na slici 8 prikazani su rezultati ispitivanja kontaktnim ekstenzometrom. Rezultati mjerenja su uzeti samo iz područja mjerenje od 10 kN do 35 kN jer ostali rezultati koji su prikazani u tablici 3 imaju preveliko rasipanje što odmah upućuje da izbor mjernog opterećenja ima jako veliki utjecaj na mjerenje.

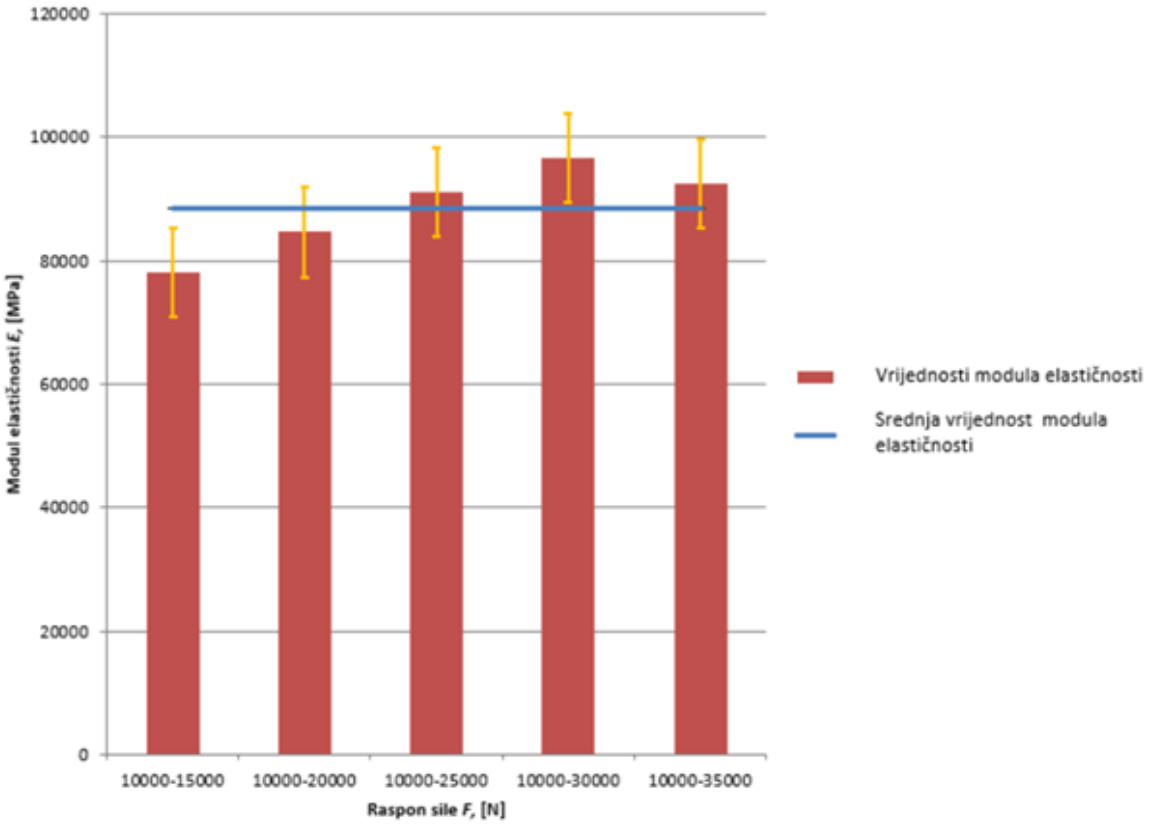


Slika 8. Grafički prikaz dobivenih vrijednosti modula elastičnosti pri mjerenju u rasponu od 10000 N do 35000 N

Iz slike 8 se jasno vidi da u području 10 kN do 30 kN imamo prevelika rasipanja rezultata mjerenja kod klasičnog određivanja modula elastičnosti što možemo pripisati nehomogenosti materijala, nedovoljnoj kvaliteti izrade ispitnih uzoraka posebno s obzirom na hrapavost površine ispitnog uzorka. S obzirom na dobivene rezultate postavlja se pitanje koja je to stvarna vrijednost modula elastičnosti i kako procijeniti pojedine utjecajne faktore kao i njima uzrokovane mjerne nesigurnosti.

## ZAKLJUČAK

Prilikom određivanja modula elastičnosti prisutno je nekoliko čimbenika koji utječu na rezultat. U ovom radu prikazani su samo neki od tih utjecaja jer su ovdje prikazani samo preliminarni rezultati ispitivanja jednog opsežnijeg istraživanja. Na temelju provedenih ispitivanja i analize dobivenih rezultata doneseni su sljedeći zaključci:

- Izbor, metoda, mjerno područje te točnost i kvaliteta mjerne opreme ima veliki utjecaj na rezultate određivanja modula elastičnosti.
- Kod statičkog vlačnog ispitivanja izbor mjernog područja ima veliko značenje. Uzimanjem premalog ili prevelikog raspona sila vrlo lako se može doći u plastično područje materijala a to će se uvelike odraziti na rezultate određivanja modula elastičnosti. Uzimanjem preuskog raspona sila postoji opasnost od lokalne promjene nagiba Hookovog pravca što rezultira krivom vrijednošću modula elastičnosti.
- Prilikom analize rezultata prikazano je da materijali ne pokazuju savršeno linearno – elastično ponašanje u području Hook-ovog pravca pa zbog toga dolazi do odstupanja u rezultatima modula elastičnosti. Ovo može nastati i zbog nehomogenosti materijala od kojeg je izrađena ispitna epruveta. Sama obrada ispitnog uzorka također ima utjecaj na konačne rezultate. Stoga uzorci moraju biti „idealno“ pripremljeni da bi rezultati bili što vjerodostojniji.
- S obzirom na današnji razvoj metoda ispitivanja svakako da treba koristiti i druge metode za određivanja modula elastičnosti s tim da treba biti jako oprezan i znati procijeniti koji sve izvori mjerne nesigurnosti mogu nastati pri ovakvim ispitivanjima.

## LITERATURA

[1] D. Ćorić, Ž. Alar, Odabrana poglavlja iz mehaničkih svojstava materijala, autorizirana predavanja, Fakultet strojarstva i brodogradnje, Zagreb, 2017.
[2] M. Franz, Mehanička svojstva materijala, Fakultet strojarstva i brodogradnje, Zagreb, 1998.
[3] HRN EN ISO ISO 6892-1:2016 Metallic materials – Tensile testing.
[4] HRN EN ISO 14577-1:2015 Metallic materials – Instrumented indentation test for hardness and materials parameters – Part 1: Test method.
[5] Shimadzu DUH 211S, User Manual, 2009.
[6] J. Hay, Introduction to Instrumented Indentation Testing, 66 Experimental Techniques, 2009.
[7] W. C. Oliver, G. M. Pharr, Measurement of hardness and elastic modulus by instrumented indentation: Advances in understanding and refinements to methodology, J. Mater. Res., 19 (2004) 1, pp. 3-20.

17th INTERNATIONAL FOUNDRYMEN CONFERENCE
Hi-tech casting solution and knowledge based engineering
Opatija, May 16th-18th, 2018
http://www.simet.hr/~foundry/

# THE MECHANISM NUCLEATION AND PROPAGATION OF HOT TEARING DUE TO THE FORMATION OF INITIAL MICROPORES ON THE TRIPLE JUNCTION OF GRAIN BOUNDARIES IN THE ALLOY AlMgSi

# MEHANIZAM NUKLEACIJE I ŠIRENJA VRUĆE PUKOTINE USLIJED STVARANJA INICIJALNIH MIKROPORA NA TROJNIM GRANICAMA ZRNA U AlMgSi - LEGURI

**Ivica Buljeta[1]*, Zdenka Zovko Brodarac[2], Ana Beroš[3]**

[1] Elementary School Žepče, Žepče, Bosnia and Herzegovina
[2] University of Zagreb Faculty of Metallurgy, Sisak, Croatia
[3] University of Zenica, Metallurgical - Technological Faculty, Zenica, Bosnia and Herzegovina

**Poster presentation**
*Original scientific paper*

**Abstract**

The formation of pores on the triangular joints of the grain boundaries during the solidification of the aluminum alloy of the billet by the Direct Chill drilling can propagate into the microcrack. The mechanism of propagation of hot cracks for the alloys of the EN AW series 6XXX has described by two superponed processes: (1) the nucleation of the pore at the grain boundaries due to shrinkage during solidification and (2) the thermal contraction due to rapid cooling of the alloy. For this purpose, the areas of early phase formation and morphology of pores were analysed in the EN AW 6060 alloy microstructure in as - cast state produced by Wagsstaff AirSlip. Microscopic investigation using electron microscope confirmed the combined mechanism of the generation and propagation of microcracks from the series of micropores formed on the triple grain boundary joints and micropores along the grain boundaries formed by interdendritic separation before completion of solidification process.

***Keywords**: triple point boundary, hot tearing criteria, pores nucleation, aluminium alloy 6060*

*Corresponding author (e-mail address): *buljeta_ivica@yahoo.com*

**Sažetak**

Stvaranje pora na trojnim spojevima granica zrna tijekom skrućivanja aluminijeve legure pri izradi trupca postupkom Direct Chill lijevanja trupaca može propagirati u mikropukotinu. Mehanizam propagiranja vrućih pukotina u legurama serije EN AW 6XXX, opisuju dva superponirana procesa: (1) nukleacija pora na granicama zrna uslijed stezanja pri skrućivanju i (2) toplinska kontrakcija pri brzom

hlađenju legure. U tu su svrhu analizirana područja ranih faza nastanka i morfologija pora u mikrostrukturi legure uzorka trupca EN AW 6060 proizvedenog postupkom Wagsstaff AirSlip u as - cast (lijevanom stanju). Mikrostrukturna ispitivanja elektronskim mikroskopom potvrđuju kombinirani mehanizam nastanka i propagiranja mikropukotine iz serije mikropora nastalih na trojnim granicama zrna i mikropora duž granica zrna nastalih interdendritnim razdvajanjem prije završetka postupka skrućivanja.

***Ključne riječi**: trojna točka, kriterij nastanka vruće pukotine, nukleacija pora, aluminijska legura 6060*

## UVOD

Predviđanje nastanka toplih pukotina tijekom DC lijevanja je komplicirano zbog složenih uvjeta hlađenja i naknadnog razvoja toplinskih naprezanja. Višegodišnja istraživanja fenomena vrućih pukotina nastalih u trupcima i ingotima proizvedenim Direct Chill (DC) postupkom lijevanja, bila su usmjerena u pravcu razvoja različitih modela koji zahtijevaju detaljno poznavanje procesnih uvjeta i mehanizama inicijacije vrućih pukotina [1-5]. Navedena istraživanja su uključila proizvođače aluminijskih proizvoda i istraživanja na visokosofisticiranoj opremi s ciljem razrješavanja ovog fenomena. Međutim, praktična primjena ovih modela u izboru parametra lijevanja u pogonu ljevaonice, s ciljem sprječavanja nastanka vrućih pukotina, teško je ostvariva.
Drugi pravac istraživanja je izveden u industrijskim uvjetima, a usmjeren je na predviđanje i smanjenje pojave toplih pukotina. Većina ovih istraživanja se uglavnom odnosila na brzinu lijevanja, i to na početku lijevanja trupaca koji je označen kao kritični stadij lijevanja.
Napredna istraživanja su obuhvatila ispitivanja na uzorcima: (1) u lijevanom stanju, (2) uzetim za vrijeme svake od četiri tipične faze AirSlip lijevanja (podešavanje, početak, rad i kraj lijevanja), (3) uzetim po duljini trupca (glava trupca, srednji dio i stopalo trupca). Ispitivanja kemijskog sastava provedena po duljini trupca se proširuju na uzimanje uzorka u višestrukim poprečnim pravcima iz centralnog, središnjeg i površinskog dijela trupca [6]. Rezultati pokazuju grublju površinu trupaca u početnoj i/ili završnoj fazi lijevanja - površinske likvacije što je karakteristika "vrućih uvjeta" lijevanja koje prate pukotine trupca. Isto tako dinamika termal / temporal parametara procesa lijevanja (brzina lijevanja, temperatura taline, protok i temperatura vode, usitnjavanje zrna, nivo taline, pritisak plina i ulja) postupkom Wagstaff Air Slip pokazuje da poremećaj nivoa taline u početnoj ili završnoj fazi lijevanja može otvoriti put ka stvaranju vrućih pukotina [7].
Ipak, u postupku izrade trupaca nužno je uzeti u obzir veliki broj parametra, uključujući složene principe teorije skrućivanja koji ponekad mogu „prekriti“ moguća jednostavnija rješenja. Zato su autori u okviru industrijskih istraživanja ispitivali omjer teških i lakih metala u različitim klasama trupaca (as - cast) aluminijske legure EN AW 6060 u kontekstu istraživanja vrućih pukotina [8]. Ispitivanja su pokazala da izračunati omjer može postati funkcija kriterija u modelu primjenjivom već u fazi pripreme taline što smanjuje mogućnost pojave unutarnje pukotine u slijedećoj fazi lijevanja.

Predloženi mehanizmi su predstavljali problem u postavljanju primjenjivih modela: pojedini mehanizmi nastanka vrućih pukotina nisu primjenjivi za sve ili određene vrste legura, što je kasnije i potvrđeno [9]. Tako, istraživanje provedeno u više serija aluminijskih legura za gnječenje (1XXX, 3XXX, 5XXX i 6XXX), pokazuje različite mehanizme nastanka pukotina na površinama prijeloma koji ovise od intervala skrućivanja, veličine zrna, udjela eutektika, segregacijama metala i precipitaciji sekundarnih faza. Ovi rezultati pokazuju da aluminijska legura EN AW 1050 ima uzak interval skrućivanja (oko 10-20 °C), a vruće pukotine su ponekad potpuno ili djelomično srasle zbog prodiranja taline obogaćene na otopljenim elementima / primjesama u interdendritna područja. Površina prijeloma legure EN AW 3104 pokazuje duktilni lom na spoju dendritnih vrhova, dok legura EN AW 5182 ima nisku tendenciju ka vrućim pukotinama zbog visokog udjela eutektičke faze.
Kod vruće pukotine legura serije 6000 kao što je EN AW 6111, slobodna površina dendrita može ukazati na fenomen razdvajanja prije završetka skrućivanja.
Slična situacija se događa s pronalaženjem odgovarajućih mehanizama: nastanka, propagiranja i otvaranja vruće pukotine. Postoje dva glavna izazova u ovom nastojanju. Prije svega, najznačajnije je nedovoljno poznavanje stvarnih uzroka nukleacije i odgovarajućih uvjeta temperature i naprezanja. Osim navedenog, postoji mogućnost da različiti mehanizmi širenja pukotine i prijeloma djeluju u ovisnosti o udjelu čvrste tvari i specifičnoj mikrostrukturi legure.
Određene postojeće teorije i modele toplih pukotina djelomično opisuju uzroke iniciranja pukotine prikazane morfologijom šupljine ispunjene tekućom fazom ili pore ili oksidnog bifilma oksidnog bifilma [10] pri kojem pukotina napreduje kroz tekući film koji pokriva granice zrna [11], kako je to shematski prikazano slikom 1. Međutim, danas izazov više ne leži u prikladnom opisu makroskopskih i mikroskopskih stanja naprezanje – deformacija, parametara i svojstva kašaste zone, već u pronalaženju stvarnih uzroka nukleacije i širenja tople pukotine: međusobnu povezanost (1) razvoja mikrostrukture, (2) nukleacije i (3) propagiranja vruće pukotine.
Nukleacija vrućih pukotina gotovo je neistražena pojava, a većina istraživanja ne uključuje nukleaciju i širenje vruće pukotine, fokusirajući se više na makro- i mikroskopske uvjete koji mogu uzrokovati prekide.
Na temelju ispitivanja površina vrućih pukotina, kao nukleanti se sugeriraju: tekući film, pore (ili niz pora) i granica zrna smještenih na mjestu koncentracije naprezanja. Na tragu ovih pretpostavki te s idejom da ispitivanja izvedena u laboratorijskim uvjetima ne mogu uvijek osigurati realne uvjete DC lijevanja, industrijska istraživanja su usmjerena na as – cast uzorke trupaca s vrućim pukotinama [12]. Rezultati istraživanja uzoraka po duljini trupca pokazuju inicijalnu i otvorenu pukotinu te diskontinuitet u obliku pojedinačnih pora (slika 2).

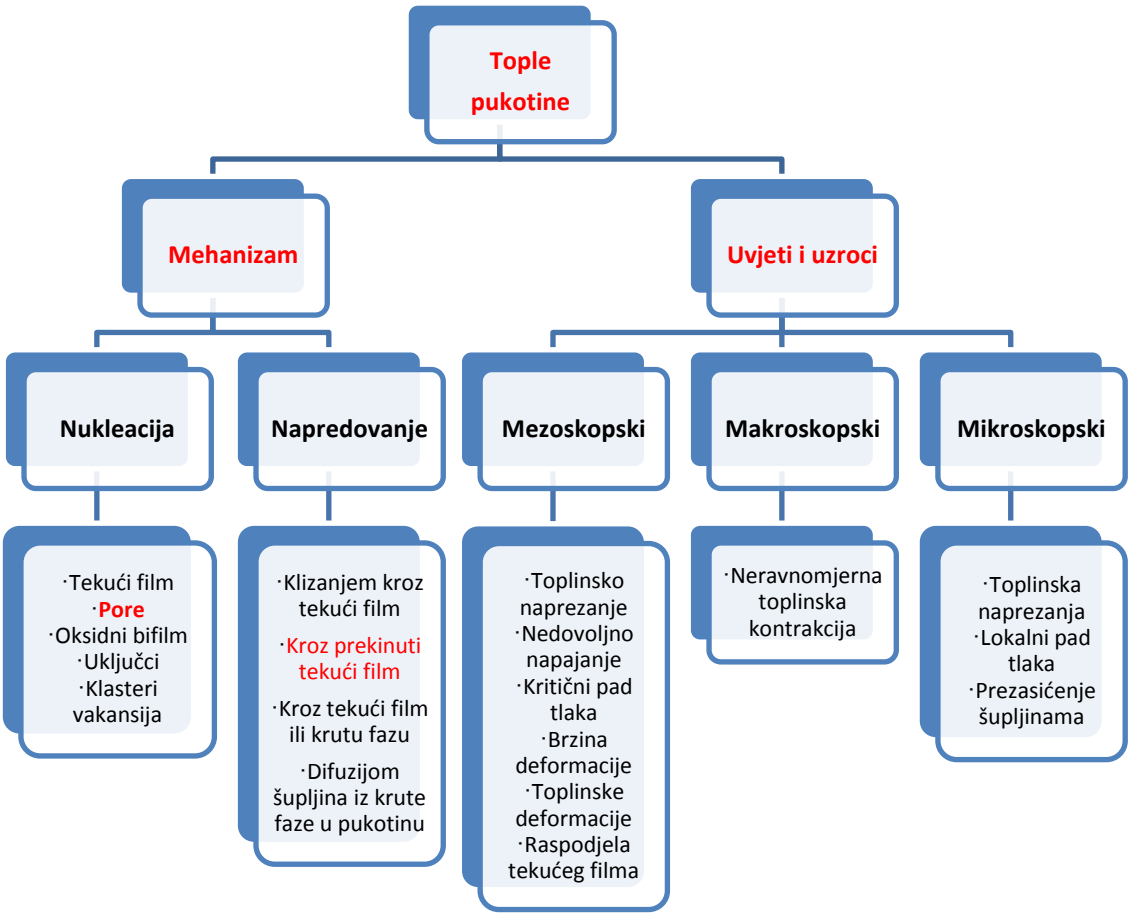


Slika 1. Pregled utjecajnih kriterija na nastanak vrućih pukotina [1]

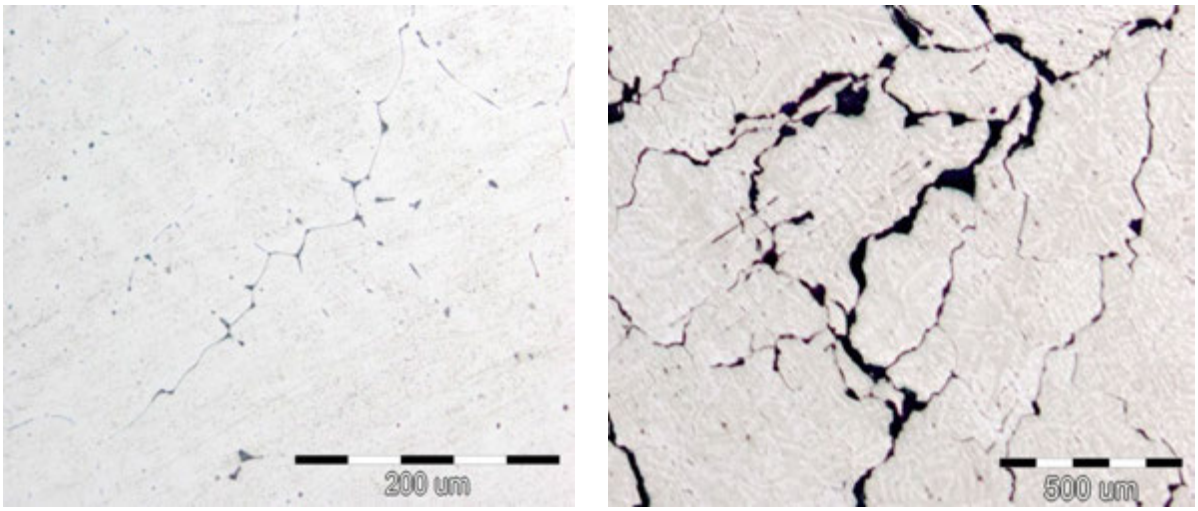


Slika 2. Prikaz propagiranja i otvaranja pukotine [6]

Prikazana preliminarna istraživanja pojedinačnih pora na trojnim spojevima bila su osnova za dalja istraživanja usmjerena na pronalaženje inicijacije fenomena vrućih pukotina.

## MATERIJALI I METODE

Ispitivan je primarni AlMgSi trupac promjera 203 mm, dužine lijevanja 7500 mm legure EN AW 6060 s unutarnjim pukotinama, proizveden u pogonu ljevaonice Aluminij d.o.o. Mostar, BiH po *Direct Chill* postupku lijevanja. Uzorkovanje je provedeno na as – cast uzorcima iz središnjeg dijela stope trupca.
Postignuti kemijski sastav legure ključnih elemenata (Si, Fe, Mg i Ti) prije lijevanja nije imao značajnijih odstupanja od zahtijevanog normom EN 573-3, tablica 1.

Tablica 1. Kemijski sastav legure EN AW 6060

| EN AW 6060 | | Elementi (mas.%) | | | | | | | |
|---|---|---|---|---|---|---|---|---|---|
| | | **Si** | **Fe** | **Cu** | **Zn** | **Mg** | **Mn** | **Ti** | **Cr** |
| Zahtijevano | Min. | 0,41 | - | - | - | 0,38 | - | 0,007 | - |
| | Max. | 0,45 | 0,18 | 0,01 | 0,015 | 0,42 | 0,01 | 0,01 | 0,01 |
| **Postignuto** | | **0,425** | **0,175** | **0,001** | **0,010** | **0,430** | **0,041** | **0,008** | **0,001** |

Ispitivanje mikrostrukture provedeno je na pretražnom elektronskom mikroskopu (SEM) opremljenom energijskim disperzivnim spektrometrom (EDS) Tescan Vega TS 5136 MM i Tescan MAIA3 XMU.
U prvoj fazi, preliminarnim istraživanjima provedena je SEM/EDS analiza pojedinačnih mikro pora na trojnim granicama zrna [10]. Dodatnim ispitivanjima provedena je SEM/EDS analiza serije susjednih mikropora na trojnim spojevima granica zrna i pora uzduž granica zrna mikropukotine.

## REZULTATI I RASPRAVA

### Rezultati

SEM/EDS ispitivanjima ispitivane su pojedinačne pore i susjedne pore na trojnim spojevima granica zrna. Osim navedenih pora, analizirane su serije nepravilnih pora uzduž granica zrna na inicijalnoj mikropukotini s tendencijom propagacije.
U prvoj fazi SEM/EDX ispitivanja (uređaj VEGA TESCAN), u mikrostrukturi prikazanoj na slici 3a, vidi se pojedinačna izolirana pora na trojnom spoju granica zrna (detalj A na slici 3b) na koju se oslanja duga β-AlFeSi čestica (detalj B na slici 3b) i nepravilna pora na granici zrna (detalj C na slici 3b).

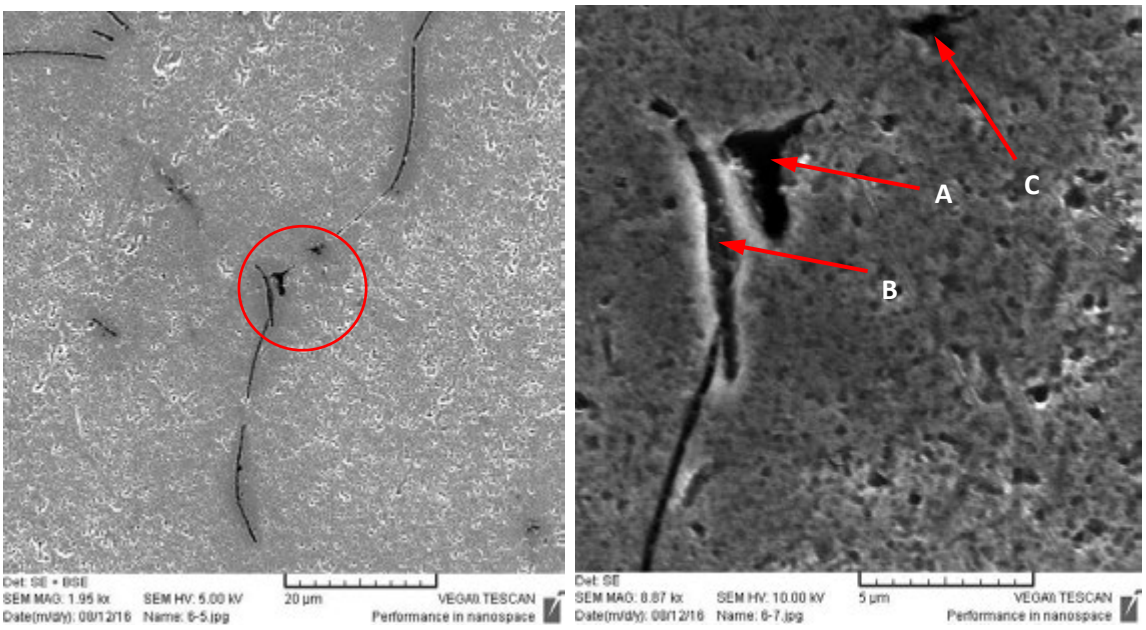


a) b)

Slika 3. Karakteristična mikrostruktura trupca legure EN AW 6060: a) povećanje 1950X i b) povećanje 8870X

Pregled mikrostrukture ukazuje na distribuciju pora po trojnim granicama zrna kako je prikazano na slici 4.

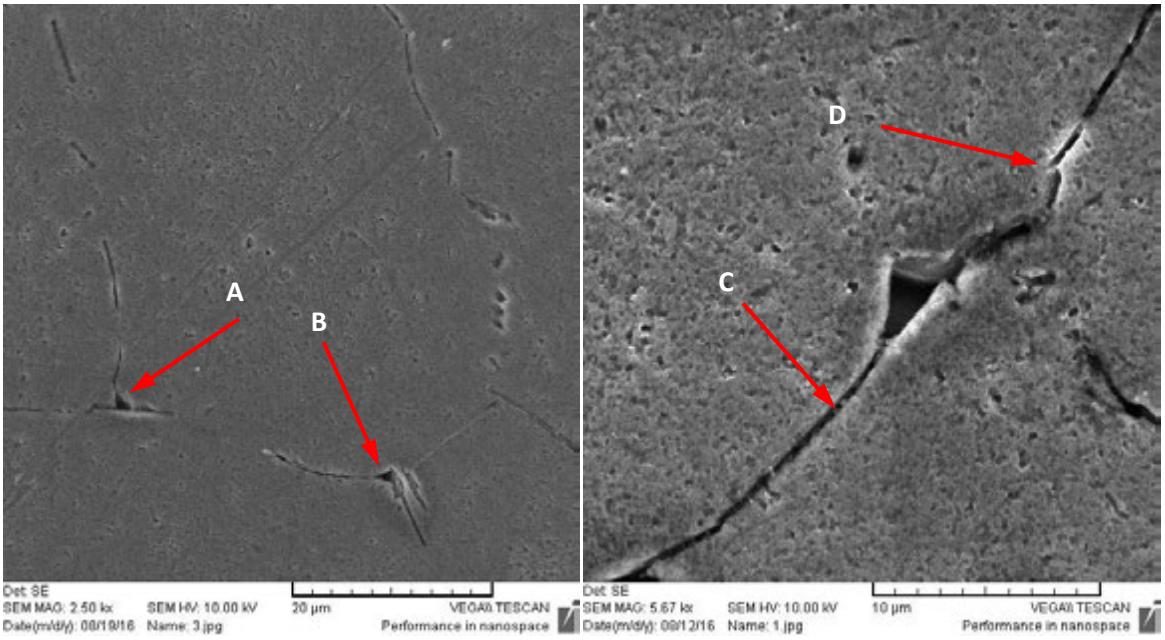


a) b)

Slika 4. Mikrostruktura trupca legure EN AW 6060: a) susjedne pore na granicama zrna i b) pojedinačna pora

Na slici 4 pri povećanju 2500X vidljive su dvije susjedne pore na trojnoj granici zrna (detalji A i B na slici 4a). Pri povećanju 5670X prikazana je jedna pora uz koju se na granici zrna uočavaju igličaste β - AlFeSi čestice (detalji C i D na slici 4b). U odsustvu ovih čestica između trojnih spojeva zrna, nije uočljiva granica zrna i ne dolazi do nukleacije pukotine. U ovom slučaju pore predstavljaju nukleus pukotine, iako se nužno ne moraju razviti u pukotinu. Stoga treba uzeti u obzir razliku između nastanka pore i iniciranja pukotine.
Vruća pukotina i njezina propagacija kroz mikrostrukturu prikazana je na slici 5.

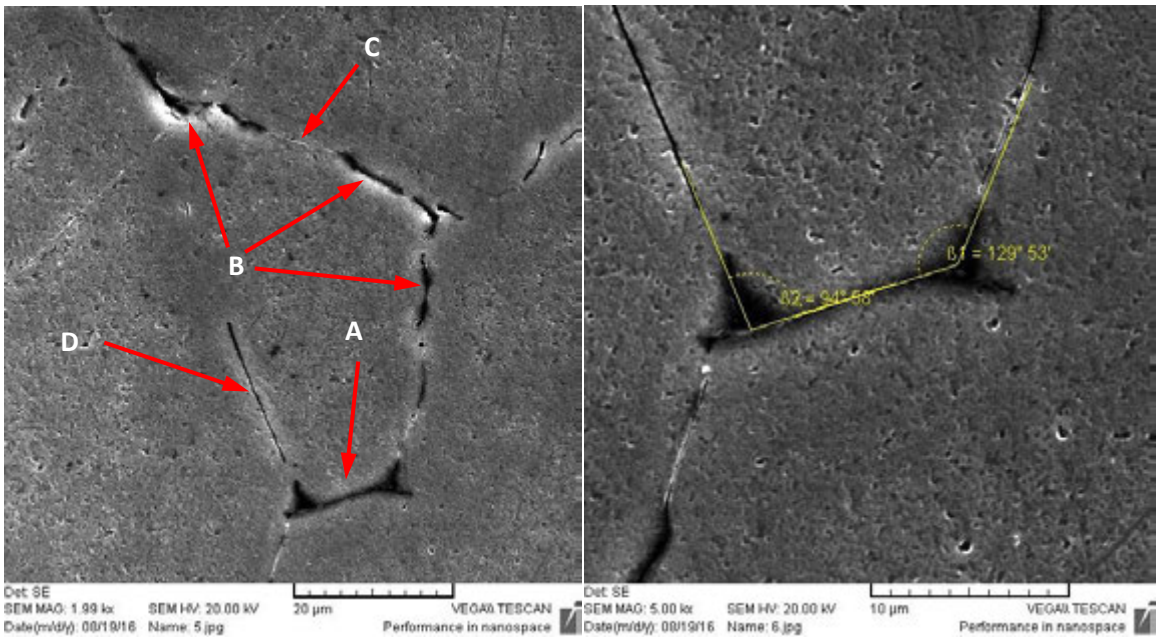


a) b)

Slika 5. Mikrostruktura trupca legure EN AW 6060: nukleacija i napredovanje pukotine preko a) pojedinačnog zrna i b) na trojnim granicama zrna

Na slici 5 prikazana je pukotina propagirana duž granice zrna, a upućuje na dva tipična mjesta nukleacije: detalji A i B. Detalj A slike 5 prikazuje dvije bliske susjedne pore kao pogodna inicijalna mjesta za otvaranje pukotine. Istovremeno za napredovanje pukotine aktiviraju se i drugi mehanizmi uzduž granica istog zrna (detalj B). Dalje, detalj C pokazuje da isključivo toplinska naprezanja neće uzrokovati razdvajanje dva susjedna zrna. Detalj D ukazuje na fenomen da lokalna toplinska naprezanja mogu razdvojiti granice dva susjedna zrna u slučaju prisustva β-AlFeSi čestica. Na slici 5b izmjereni su kutovi orijentacije pora koji se podudaraju s granicama zrna.
Pregled propagacije pukotine s obzirom na okruženje prikazan je slikom 6.

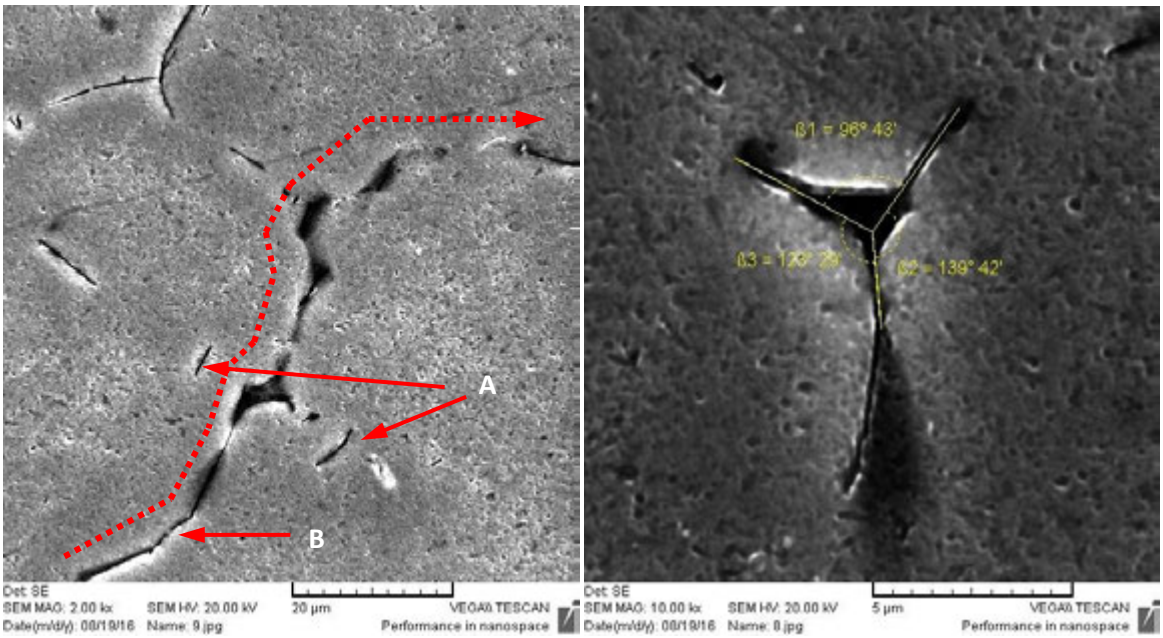


a) b)

Slika 6. Propagacija vruće pukotine u trupcu legure EN AW 6060: a) napredovanje pukotine duž trojnih granica zrna i b) kutovi orijentacije pora

Slika 6 pokazuje još jedan primjer inicijacije pore i napredovanja pukotine: između pora na trojnim spojevima i pora koje se otvaraju po granicama zrna ili na intermetalnim česticama. Detalj A slike 6a, prikazuje poprečno postavljene intermetalne čestice AlFeSi čestice koje su blokirale napajanje talinom interdendritnih kanala i pritom inicirale nastanak pora. Osim navedenog, AlFeSi intermetalne čestice između dvije susjedne granice zrna (detalj B slike 6a), zbog svog zareznog, igličastog oblika, predstavljaju potencijalne smjerove za propagaciju vruće pukotine. Na slici 6b ponovo su izmjereni kutovi orijentacije pore koji odgovaraju trojnoj granici zrna.
Trojna granica zrna detaljnije je ispitana s ciljem utvrđivanja morfologija unutrašnjosti pore i potencijalne inicijacije njezina nastanka, kako je prikazano na slici 7.

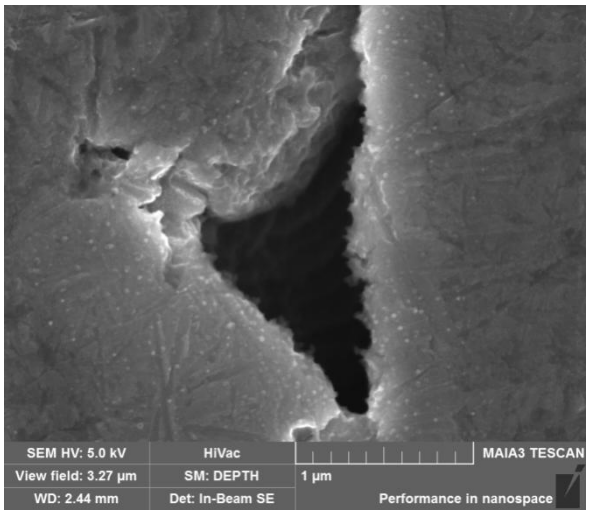


Slika 7. Mikrostruktura uzorka trupca legure EN AW 6060, unutrašnjost pore na trojnoj granici zrna

Mikrostruktura uzorka na trojnoj granici zrna ukazuje na značajnu propagaciju pukotine u z osi koja eksplicitno prati granice pojedinačnih zrna.
Detaljnije istraživanje orijentacije pore / pukotine i granica zrna prikazano je na slici 8.

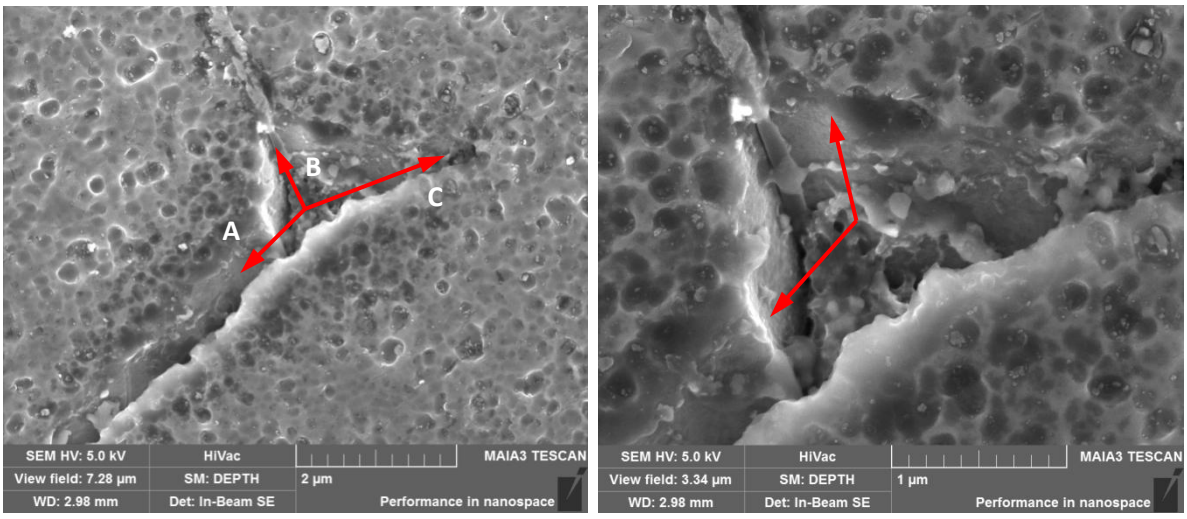


a) b)

Slika 8. Mikrostruktura pore na trojnom spoju granica zrna u uzorku legure EN AW 6060: a) propagacija pukotine po granicama zrna i b) unutrašnjost pore

Pora na slici 8a pokazuje tri karakteristične granice zrna A, B i C te inicijalnu poru na njihovom spoju. Uočava se propagacija pukotine u smjeru A granice zrna, kao i intermetalna čestica na granici zrna (smjer B granice zrna). Dok smjer C ne otkriva propagaciju pukotine niti raslojavanje na granici zrna što upućuje na izostanak grešaka u okruženju. Na slici 8b

prikazana je unutrašnjost pore na trojnoj granici zrna te pravilne i glatke granice / zidovi zrna.
Mikrostruktura unutrašnjosti pore prikazana je na slici 9.

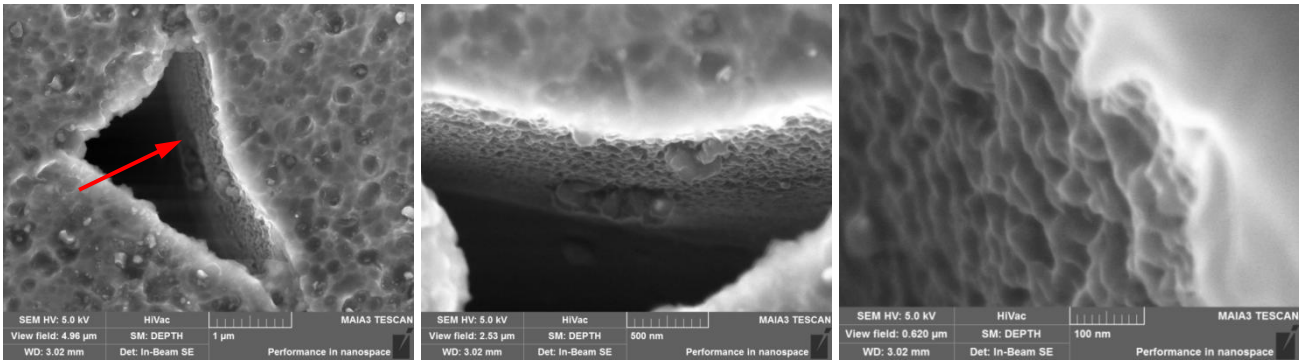


a) b) c)

Slika 9. Mikrostruktura unutrašnjosti pore na trojnoj granici zrna u uzorku legure EN AW 6060: a) unutrašnjost pore, b) detalj „zida“ pore i c) uvećani detalj “zida” pore

Na slikama 9a i b prikazana je unutrašnjost pore na trojnoj granici zrna koja ukazuje na glatke površine primarnih aluminijskih dendrita bez nepravilnosti. Ne uočava se deformacija uslijed toplinskih naprezanja. Morfologija nastale pore upućuje na stezanje pri skrućivanju.
Rezultati ispitivanja kemijskog sastava prikazani su na slici 10.

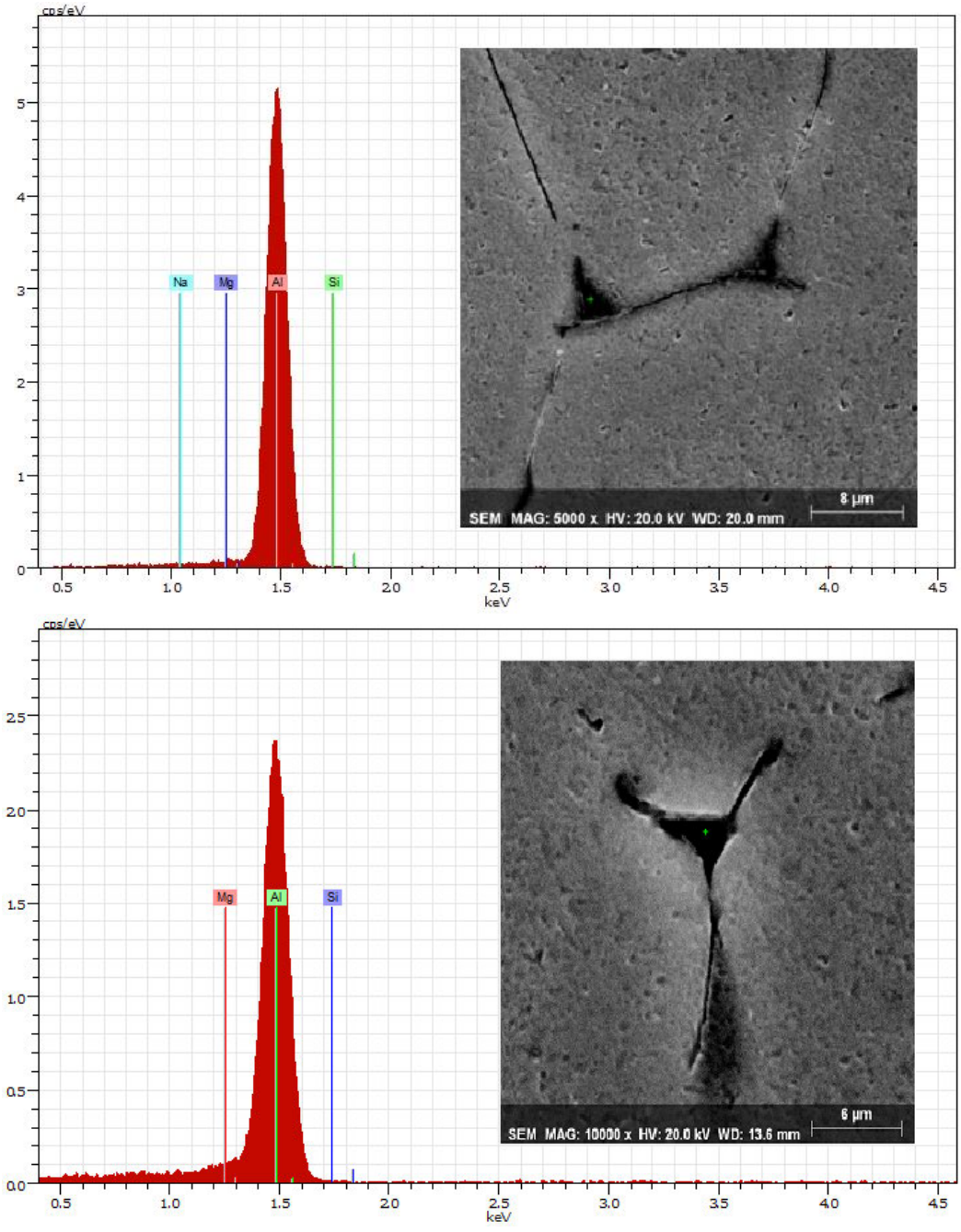


Slika 10. Ispitivanje kemijskog sastava pore na karakterističnim granicama zrna

U cilju potvrđivanja prisutnosti pora / pukotina na trojnoj granici zrna, provedena je usporedna EDS analiza pora nastalih na različitim mjestima. Dobiveni kvalitativni spektri pokazuju visok sadržaj Al, kao odjek pozadine i neznatan sadržaj Mg i Si na oba ispitana mjesta što potvrđuje izostanak faza.

**Rasprava**

Ne postoji univerzalni kriterij za uspješno predviđanje realne pojave vrućih pukotina u ingotima i trupcima u ovisnosti od parametara lijevanja. Postoje dva glavna izazova u ovom nastojanju:

1) Nedovoljno poznavanje stvarnih uzroka nukleacije pora s naglaskom na utjecaj grešaka strukture koje mogu djelovati kao inicijatori pora i nastanak pukotina pod određenim uvjetima temperature i naprezanja.
2) Indicirana je mogućnost utjecaja udjela čvrste faze i karakteristične specifične morfologije na širenje pukotine.

Provedena su mikrostrukturna ispitivanja uzoraka AlMgSi legure s uočenim unutarnjim pukotinama s ciljem otkrivanja uzroka nukleacije pukotina uočenih u preliminarnim istraživanjima [12]. Budući da su istraživanja mikrostrukture ukazala da pojedinačne i udaljene pore na trojnoj granici zrna (slika 3a) ili pore između koji se uočavaju glatke granice zrna ne mogu biti nukleusi vrućih pukotina (slika 4a) indiciran je potencijalni mehanizam nukleacije pukotine iz pora zbog prisustva grešaka ili intermetalnih AlFeSi čestica.

Kako se u EN AW 6060 leguri skrućivanje odvija u širokom temperaturnom intervalu, uslijed nametnutih toplinskih naprezanja, kao nukleusi vrućih pukotina mogu biti dvije ili više susjednih pora na trojnim granicama zrna (slika 5). Istovremeno za napredovanje pukotine uzduž granice dva susjedna zrna, aktivira se i dodatni mehanizam, kojem pogoduje prisustvo AlFeSi intermetalnih faza: čestice koje se nalaze duž granica zrna pomažu njihovom razdvajanju i napredovanju pukotine preko njih, dok poprečno pozicionirane AlFeSi intermetalne čestice mogu blokirati napajanje talinom interdendritnih kanala i stvoriti kritične praznine pogodne za stvaranje pora (slika 6).

Na osnovu preliminarnih istraživanja i dodatnih SEM/EDS istraživanja mikrostukture AlMgSi uzoraka u as – cast stanju, a koja se odnose na nukleaciju i napredovanje vruće pukotine, može se zaključiti:

- primarni uzrok nukleacije su pore na trojnim granicama zrna, nastale pod određenim uvjetima temperature i naprezanja;
- uočeni su različiti mehanizmi napredovanja pukotine koje se može odvijati između: susjednih pora na trojnim granicama zrna, uzduž granica zrna i pod utjecajem intermetalnih čestica izlučenih na granicama zrna.

Idealna mikrostruktura za tvari u polučvrstom stanju, s čvrstom fazom okruženom fazom tekućeg filma u kašastoj (mushy) zoni shematski je prikazana na slici 11a. Naknadno, na slici 11b, u isušenom interdendritnom kanalu (oznaka B), uslijed stezanja pri skućivanju, odvija se nukleacija minimalnog (kritičnog) broja pora na trojnim točkama (oznaka C). Konačno uslijed nametnutih prostornih toplinskih naprezanja $\sigma$, nastupa mehanizam propagiranja mikropukotine (oznaka A).

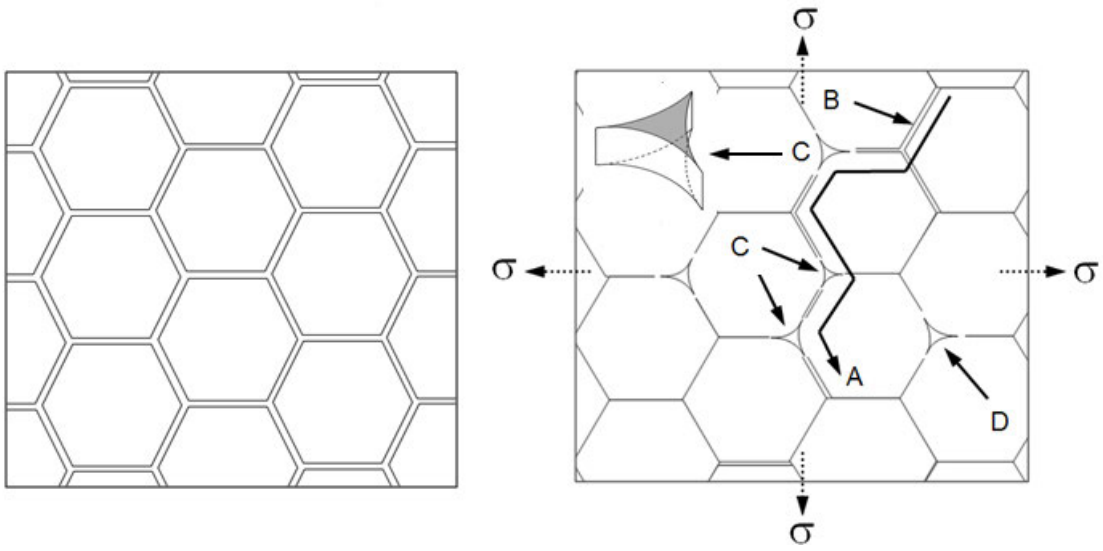


Slika 11. Shematski prikaz nukleacije i napredovanja idealne mikrostrukture

Shema na prethodnoj na slici i rezultati provedenog ispitivanja, opisuju uvjete nukleacije i upućuju na mehanizam rasta mikropukotine za aluminijske legure serije 6XXX. Za ostale aluminijske legure serija 1XXX, 3XXX i 5XXX, provedena su preliminarna istraživanja koja treba dodatno potvrditi [9], a površine prijeloma pokazuju različite mehanizme nastajanja pukotina ovisno o intervalu skrućivanja, veličini zrna, udjelu eutektika, segregacijama metala i precipitaciji sekundarnih faza.

## ZAKLJUČAK

Mikrostrukturna ispitivanja pukotina induciranih u polučvrstom stanju i temperaturnom rasponu, ukazuju da mehanizam nukleacije i propagiranja mikropukotine nastale u toplom stanju, ovisi od tipa legure, ali mnogih drugih faktora. Aluminijske legure serije 6XXX koje se koriste u postupku izrade trupaca postupkom Wagstff AirSlip, imaju široki interval skrućivanja i sklonost ka nastanku vrućih pukotina. Rezultati SEM/EDS ispitivanja uzoraka pokazuju da uvjeti otežanog napajanja i slaba tečljivost u interdendritnim kanalima tijekom skrućivanja iniciraju nukleaciju pora na trojnim granicama zrna. Istovremeno brzo hlađenje kore trupca inducira prostorna toplinska naprezanja uslijed kojih dolazi do nukleacije pora na preostaloj ili zarobljenoj tekućoj fazi uzduž granica zrna. Zaključno, mehanizmu nukleacije, propagiranja i otvaranja pukotine koja kasnije slijedi granice zrna u EN AW 6060 leguri pogoduju blizina:

1) susjednih pora na trojnim granicama zrna te
2) pora i igličaste intermetalne AlFeSi faze na granicama zrna.

**LITERATURA**

[1] D. G. Eskin, Suyitno, L. Katgerman, Mechanical properties in the semi-solid state and hot tearing of aluminum alloys, Progress in Materials Science, 49 (2004), pp. 629-711.
[2] Suyitno, W. H. Kool, L. Katgerman, Hot Tearing Criteria Evaluation for Direct- Chill Casting of an Al-4.5 Pct Cu Alloy, Metallurgical and Materials Transactions A, 36 (2005) pp. 1536-48.
[3] M. Rappaz, J. M. Drezet, M. Gremaud, A New Hot-Tearing Criterion, Metallurgical and Material Transactions, 30 A (1999) pp. 449-455.
[4] N. Hatamia, R. Babaeia, M. Dadashzadeha, P. Davamib, Modeling of hot tearing formation during solidification, The Journal of Materials Processing Technology, 205 (2008) pp. 506-513.
[5] M. Braccini, C. L. Martin, M. Suery, in: P. R. Sahm, P. N. Hansen, J. G. Conley (Eds.), Modeling of Casting Welding and Advanced Solidification Processes IX, Shaker Verlage, Aachen, 2002, pp. 18-24.
[6] I. Buljeta, A. Beroš, Analysis of the Influence of Composition EN AA-6060 (AlMgSi0,5) Aluminum Alloy on the Occurrence of Hot Cracks in the Billets, Proceedings book of 10th International Foundrymen Conference, (Ed. F. Unkić), Faculty of Metallurgy University of Zagreb, 10.-12.06.2010., Opatija, Croatia, No. 14 on CD-ROM, pp. 1-8.
[7] I. Buljeta, A. Beroš, Dynamics of Process AlMgSi DC Casting Billets under the Conditions of Formation of Hot Cracks, Proceedings book of 11th International Foundrymen Conference, (Ed. F. Unkić), Faculty of Metallurgy University of Zagreb, 28. – 30. 04. 2011., Opatija, Croatia, pp. 237-249.
[8] I. Buljeta, A. Beroš, R. Udovičić, Analysis of the internal cracks formation in the aluminum alloy billet EN AW-6060 with the aspect of heavy and light metal contents, Proceedings book of 13th International Foundrymen Conference, (Ed. Z. Glavaš, Z. Zovko Brodarac, N. Dolić), Faculty of Metallurgy University of Zagreb, 16.-17.05.2013., Opatija, Croatia, pp. 31-42.
[9] S. Lin, A study of hot tearing in wrought aluminum alloys, Dissertation, Université du Québec à Chicoutimi (UQAC), 1999.
[10] J. Campbell, Castings, Elsevier, 2003.
[11] D. G. Eskin, L. Katgerman, A quest for a new hot tearing criterion, Metallurgical and Materials Transactions A, 38A (2007) pp. 1511-1519.
[12] I. Buljeta, Z. Zovko Brodarac, A. Beroš, M. Zeko, Mechanism and Morphology of Formation of Micropores in the Structure of DC Cast AlMgSi Alloy, Universal Journal of Materials Science, 5 (2017) 4, pp. 102-110.

**Zahvala**

Svoju zahvalnost autori upućuju inženjeringu tvrtki Aluminij d.o.o., Mostar i Jajce Alloy Wheels d.o.o., Jajce.

17th INTERNATIONAL FOUNDRYMEN CONFERENCE
Hi-tech casting solution and knowledge based engineering
Opatija, May 16th-18th, 2018
http://www.simet.hr/~foundry/

# INFLUENCE OF THE TOOL TRAVEL SPEED AT FRICTION STIR PROCESSING OF ALUMINIUM ALLOY AlCu4Mg1 ON TEMPERATURE FIELD AND MACROSTRUCTURE DEVELOPMENT OF THE WELDED JOINT

**Matija Bušić*, Zoran Kožuh, Ivica Garašić**

University of Zagreb Faculty of Mechanical Engineering and Naval Architecture, Zagreb, Croatia

**Poster presentation**
*Original scientific paper*

**Abstract**

This paper investigates the influence of the tool travel speed on the temperature field developed inside EN AW 2024 plate during the Friction Stir Processing. Different measuring systems were used to obtain temperatures on the tool and processed plates. Measured temperatures differ according to the features and characteristics of the used measuring equipment. The heat input has been calculated and compared with temperatures of the tool and the workpiece using heat input model from the literature. Influence of the tool travel speed on the weld defects was examined using macrostructure analysis of the produced runs. Higher tool travel speed creates less heat input and developed temperatures are lower, but the probability of a wormhole defect in the processed material is high.

***Keywords***: *friction stir processing, friction stir welding, tool speed, temperature measuring system, heat input*

*Corresponding author (e-mail address): *matija.busic@fsb.hr*

## INTRODUCTION

Friction stir welding (FSW) is characterised by a number of advantages when compared to other welding processes, perhaps the most significant of which is the ability to weld alloys that are difficult or impossible to weld using fusion welding techniques [1-5]. Widespread benefits resulting from the application of FSW in, for example, aerospace, shipbuilding, automotive and railway industries have been presented in literature [2, 3]. The most frequently mentioned examples are: longitudinal and circumferential aluminium stiffeners in the Eclipse 500 business class jet aircraft, the central tunnel assembly of the Ford GT, aluminium plate floor in the Mercedes SL R231 and rail carriage structures (side skirt panels) made for Hitachi and Bombardier [3]. FSW is based on Friction Stir Processing (FSP) with a

cylindrical tool of hardened material that rotates and moves along the joint line. The heating is accomplished by friction between the rotating tool and the workpiece [5]. The heat transfer in the material allows the rotating tool to mechanically stir the softened material flowing to the backside of the tool where it is consolidated to form a joint.

During the FSW process there is no melting of the material because joining is performed at temperatures below the melting point (~ 80 % of its melting point) [4]. Generally, since the FSW process development in the 1990s, most attention has been given to the thermal modelling aspect of the FSW process [6-15]. The thermal energy input and temperature gradients experienced during the welding process will affect the quality and mechanical performance of the welds, including the tensile strength, fatigue and corrosion resistance as well as residual stress and distortion within the work piece [6]. The heat input is determined by the process parameters which include tool rotation speed $N$, welding speed (i.e. tool travel speed) $v_s$, tool tilt angle $\alpha$, tool dimensions, vertical force from the tool $F_N$, and the coefficient of friction between tool and metal plates $\mu$ [12]. Tool rotation speed appears to be the most significant process parameter since it also tends to influence the welding speed. When the welding speed is too fast, welding defects can be produced in the joints. Factors feed rate per revolution (*FPR*) and revolutions per feed rate (*RPF*) can give a simple insight into the heat input. The *RPF* gives the information about heat input per weld length [13]:

$$RPF = \frac{N}{v_s} \ [\text{mm}^{-1}] \tag{1}$$

Frigaard *et al.* [9] developed a numerical heat flow model based on the finite differences method and successfully predicted the temperatures during the FSW process. In this model the FSW tool is approximated as a circular shaft which is rotating relative to the upper surface of the plates. If all the shearing work at this interface is converted into frictional heat, the average heat input per unit area and time is [6]:

$$q_0 = \int_0^R 4\pi^2 \mu P N r^2 dr = \frac{4}{3}\pi^2 \mu P N R^3 \ [W] \tag{2}$$

where $q_0$ is the net power (in Watts), $\mu$ is the friction coefficient, $R$ is the surface radius, $P$ is the pressure distribution across the interface and $N$ is the tool rotation speed.

From eq. (2) it is obvious that the heat input depends both on the applied welding parameters and the tool geometry leading to a non-uniform heat generation during welding. In practice, the pressure $P$ cannot exceed the actual flow stress of the material at the operating temperature [9]. The coefficient of sliding friction between aluminium and steel depends on the temperatures produced by welding conditions [9]. Numerical models of FSW have shown that as the welding temperature approaches the solidus temperature of the alloy, the interface between the tool shoulder and workpiece softens, causing the tool to slip which effectively lowers the coefficient of friction and reduces the amount of energy transferred from the tool to the workpiece [10]. Frigaard et al. [9] reasoned that the coefficient of friction between aluminium and mild steel should be set as the average value between 0.5 for sticky friction and 0.25 for dry sliding.

In the FSW a non-uniform and high generated temperature is undesirable [14]. Temperature varies perpendicularly through the workpiece thickness and longitudinally and transversely along the weld centerline, which results in various evolutions of microstructure and hardness. Temperatures can be measured in-situ using thermocouples mounted on the surface or embedded into the plates [6, 9]. Number, location and distribution of the thermocouples are arbitrary but there must be mentioned if the thermocouples are on the retreating side or advancing side of the FSW process.
Temperatures can also be measured on the surface of the welded plates or on the tool body using thermal camera or pyrometer. De Backer and Bolmsjö have invented a novel method for accurate in-process temperature measurements at the interface of the FSW tool and workpiece based on the thermoelectric effect between dissimilar materials, also called Seebeck effect [15]. In FSW process Seebeck effect generates electricity at the interface of the FSW tool steel and material of welded plates depending on the temperature. All of these methods have some advantages and disadvantages and combining of different measuring methods can be usually useful. Real time monitoring of the temperature enables creating thermal profile diagrams for different locations in the material.
In this investigation three different measuring systems were utilized comparatively to obtain temperature plots of the tool and the processed plates. This innovative measuring setup has provided information about measuring precision of applied temperature measuring instruments in the FSP. Influence of the tool travel speed upon the temperatures developed in the process during the FSP has been investigated. Using heat input model from the literature the heat input has been calculated and compared with measured temperatures of the tool and the workpiece. Influence of the tool travel speed on weld defects was examined using macrostructure analysis of the produced runs.

## MATERIALS AND METHODS

Aluminium alloy EN AW 2024 – T4 (AlCu4Mg1) has been used in this experiment. The plates were 140 × 140 × 6 mm in dimensions. Chemical composition of aluminium alloy was verified with X-ray fluorescence analyser OLYMPUS XRF. The results are presented in Table 1. The analysis of the base metal has confirmed chemical composition of the alloy EN AW 2024 according to the EN 573-3:2014 [16]. The main alloying element is copper. Alloys of this series are high strength alloys with poor weldability using fusion welding processes. The strength is achieved by the heat treatment process. The tensile strength is about 400 MPa after hardening. The thermomechanical properties of this alloy according to the literature are presented in Table 2 [17]. When heating this alloy elastic modulus $E$ and thermal expansion coefficient $\alpha_{exp}$ increase, and Poisson's ratio $v$ decreases. The density of the material may be considered to be relatively insensitive to the temperature [6].

Table 1. Chemical composition of used aluminium alloy AlCu4Mg1

| | Mg | Si | Cr | Mn | Cu | Fe |
|---|---|---|---|---|---|---|
| wt. (%) | 1.33 | 0.46 | 0.034 | 0.57 | 3.64 | 0.3 |

Table 2. Thermomechanical properties of EN AW 2024 - T4 sheets [14]

| Temperature (°C) | $E$ (GPa) | $\nu$ | $\alpha_{exp}$ ($10^{-6}$ $C^{-1}$) |
|---|---|---|---|
| 20 | 68 | 0.330 | 21.1 |
| 100 | 64 | 0.334 | 22.9 |
| 150 | 58 | 0.335 | - |
| 200 | 54 | 0.336 | 23.8 |
| 250 | 48 | 0.338 | - |
| 300 | 42 | 0.360 | 24.7 |

Friction stir processing tool was made from X38CrMoV5-1 tool steel quenched and tempered to get the hardness of 62 HRC. Tool geometry is presented in Figure 1. Tool pin was 4 mm long to avoid full penetration in the base metal. A hole was drilled in the upper part of the tool body to reduce a heat transfer from the tool toward the tool chuck.

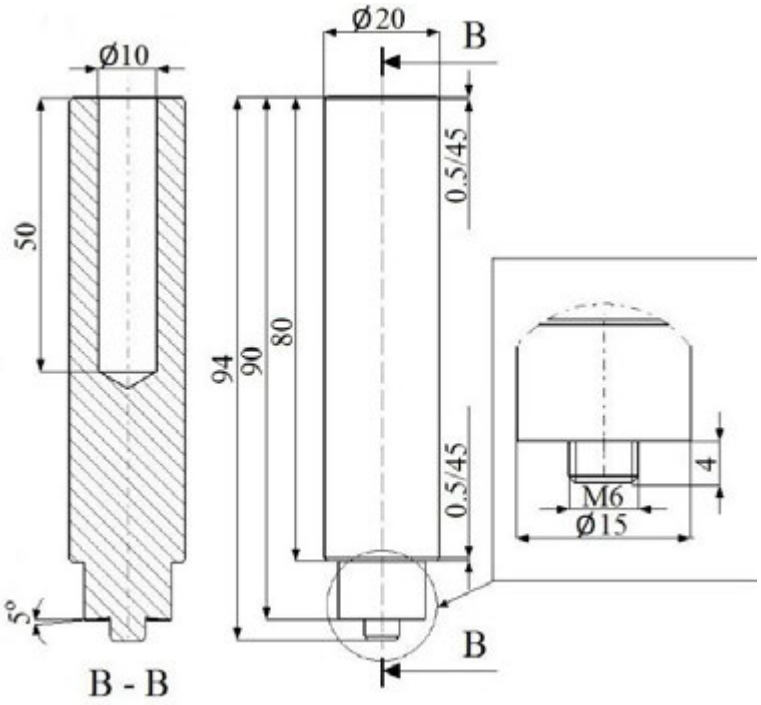


Figure 1. Design of the tool used for FSP

A plan of experiment has been prepared regarding capabilities of a universal milling machine Prvomajska ALG 200B. The tool rotation speed $N$ was constantly 1500 $min^{-1}$. Tool travel speed i.e. processing speed and RPF factor of each pass is presented in Table 3. Axial force of the tool was not a controlled parameter since a used milling machine cannot control z-axis pressure. Other constant parameters were tool material, tool dimensions and design, dimensions and material of aluminium plates, welding equipment and clamping device.

Table 3. Parameters for Friction Stir Processing

| Run | $v_s$ [mm/min] | $N$ [min$^{-1}$] | RPF [mm$^{-1}$] |
|---|---|---|---|
| 1 | 58 | 1500 | 25.9 |
| 2 | 73 | 1500 | 20.5 |
| 3 | 116 | 1500 | 12.9 |

Experimental setup is presented in Figure 2. The same thermal conditions for comparison of the temperatures developed on the tool (1 in Fig. 2.) and base metal (2 in Fig. 2.) were achieved using heat insulation in each FPS run. Clamping was done in a milling vise with backing plate of aluminium alloy EN AW 5083 H111 in dimensions 130 × 130 × 4. Heat insulation has been achieved with 25 mm thick polytetrafluorethylene – TEFLON plate (3 in Fig. 2) under the backing plate and using the same material for sides of the clamping device. Before each FPS run aluminium backing plate, TEFLON plates and FPS tool were cooled in water to temperature of 15 °C. The dwell time for FSP after pin insertion was 10 sec resulting with the same material preheating effect in each run.

In each plate prepared for FPS one K-type thermocouple (6 in Fig. 2) was inserted at a distance of 10.5 mm from the weld centre line and 50 mm far from the FSP start. Thermocouple was inserted into a 3 mm deep hole drilled from the upper side at a position that was found to be located outside the plastically deformed region. Thermocouple was on the advancing side of the weld. The signal from K-type thermocouple was converted from analogue to digital using National Instruments cDAQ-9172 chassis and National Instruments 9215 module (7 in Fig. 2.). This unit transferred digital signals to a personal computer HP ProBook 4510S via USB 2.0 interface (9 in Fig. 2). Signals were processed applying National Instruments Signal Express 2013 software.

Fixed infrared laser thermometer OPTRIS 3MH2-CF4 (4 in Fig. 2.) was used for measuring temperature of the welding tool. The measuring spot was 2 mm above the tool shoulder, at the perimeter in the weld centreline. Time – temperature diagram was recorded in real time using Optris Compact Connect software.

Thermal field of the whole FSP was recorded with FLIR SYSTEMS a thermal camera model ThermaCAM S60 (5 in Fig. 2). For that purpose the FPS tool and aluminium plates were painted with black matt spray paint which is heat resistant to 800 °C. The image was transferred to the PC via USB 2.0 interface (8 in Fig. 2).

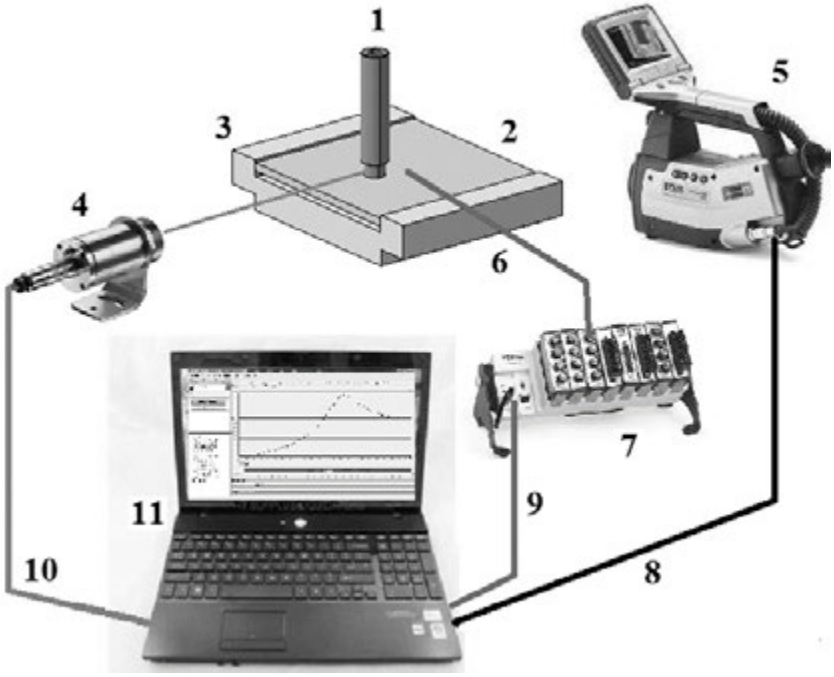


Figure 2. Experimental setup

## RESULTS AND DISCUSSION

Table 4 presents results of measured temperature. $T_{tool}$ is the maximal temperature measured on the tool surface with infrared laser thermometer. $T_{tc}$ is the maximal temperature measured with a thermocouple inserted in the aluminium plate. $T_{cam\text{-}Al}$ is the maximal temperature measured with a thermal camera on the surface of the aluminium plate. $T_{cam\text{-}tool}$ is the maximal temperature measured with a thermal camera on the surface of the tool 2 mm above the shoulder at perimeter. Temperature measurements on the base metal obtained with thermocouples are presented in Figure 3. Figure 4 presents a thermal image of the FSP during the run 1. Heating of the tool, base metal and position of the thermocouple wire is clearly seen.

Table 4. Temperature measurement results

| Run | $T_{tool}$ [°C] | $T_{tc}$ [°C] | $T_{cam\text{-}Al}$ [°C] | $T_{cam\text{-}tool}$ [°C] |
|---|---|---|---|---|
| 1 | 439.9 | 335 | 464 | 429.4 |
| 2 | 402.4 | 312 | 374 | 337.6 |
| 3 | 392.8 | 293 | 331 | 277.6 |

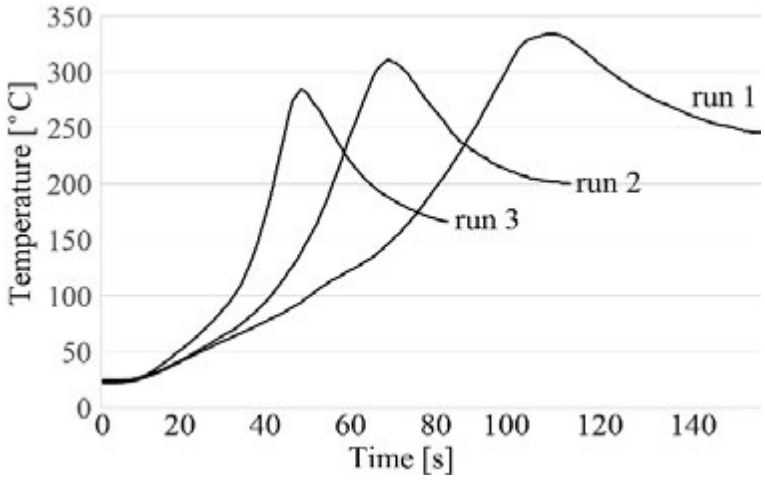


Figure 3. Temperature plots measured with a thermocouple inserted in the aluminium plate

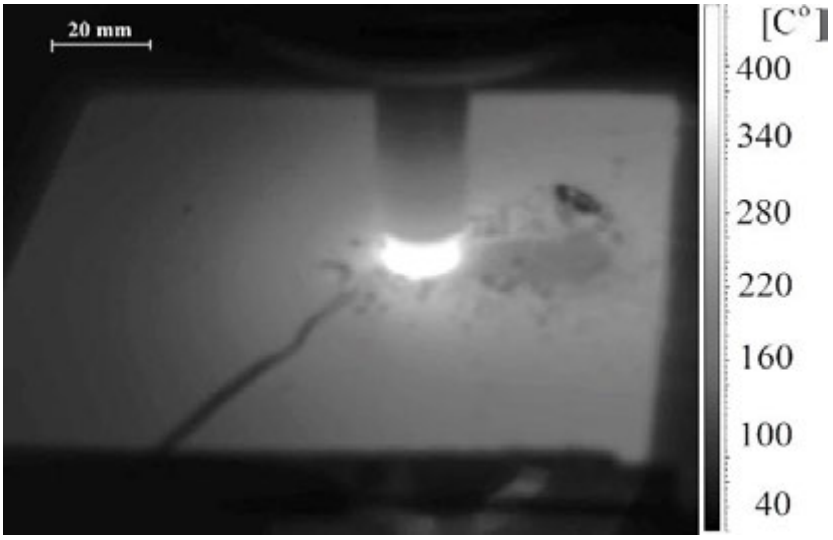


Figure 4. Thermal image of the FSP in run 1

Specimens for macrostructure analysis have been sectioned perpendicular to the welding direction using a band saw. After that, the cut specimens have been grinded and polished using sandpapers: 1) P320, 2) P500, 3) P800, 4) P1000. After that, the polishing specimens were etched with Kroll's Reagen composed of 92 % distilled water; 6 % $HNO_3$ and 2 % HF. The microstructure has been examined using a stereomicroscope LEICA MZ6. Photographs of the macrostructure with magnification of 7.9 are presented in Figure 5.

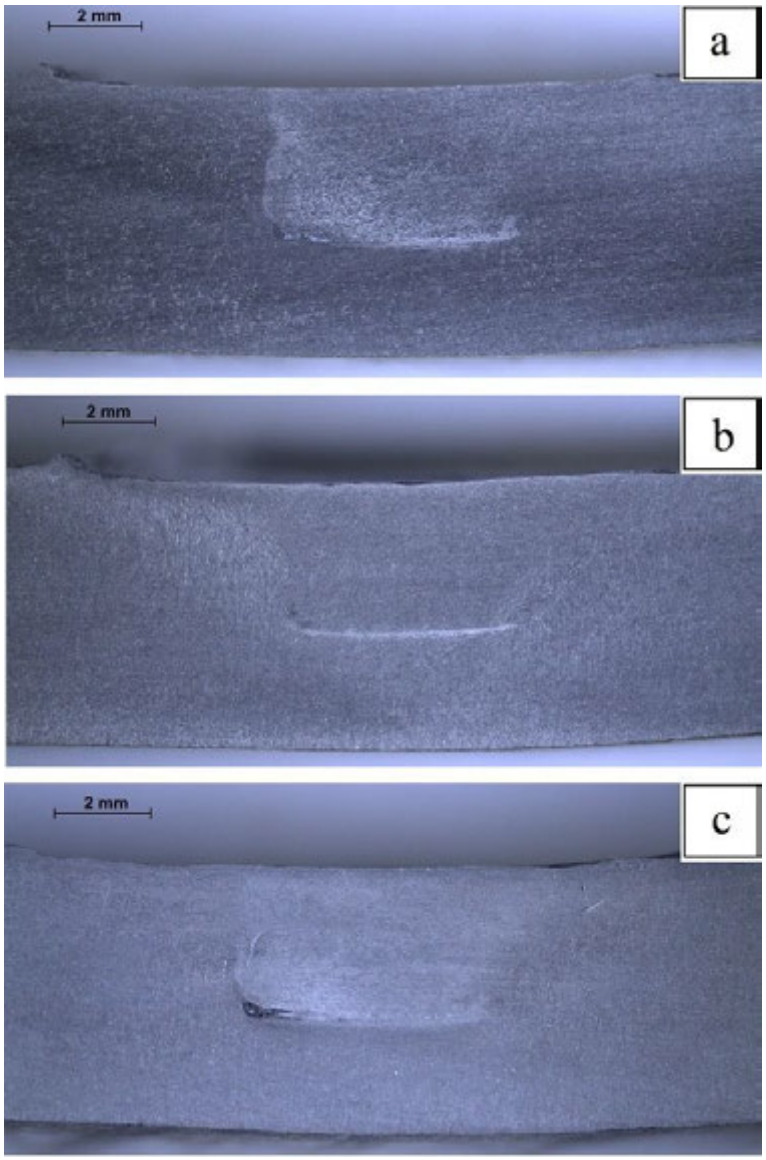


Figure 5. Macrostructure analysis for:
a) run 1 (58 mm/min);
b) run 2 (73 mm/min);
c) run 3 (116 mm/min).

The macrostructure of the welds has been analysed and has confirmed finer structure in thermo-mechanically processed metal compared to the base metal. Horizontal mixing of the material results in a clearly seen footprint of the tool pin profile and absence of mixing under the pin. A weld imperfection called wormhole can be seen in the run 3 (Figure 5). This is the most common defect found in the FSW. It was caused by cold processing conditions due to the combination of travel speed, tool rotation, plunge depth and resulting insufficient axial force [18, 19].

The relationship between the heat input and the process parameters has been calculated using eq. 1. A friction coefficient has been set as 0.375 which is an average value between 0.5 for sticky friction and 0.25 for dry sliding. The heat input for the whole welding trajectory in run 1 is $538.2 \times 10^{-5} \times P$ [J]. The heat input for the whole welding trajectory in run 2 is $427.44 \times 10^{-5} \times P$ [J]. The heat input for the whole welding trajectory in run 3 is $268.94 \times 10^{-5} \times P$ [J]. If it is assumed that the tool pressure $P$ is the same in all of the runs, the difference between heat inputs arises from the difference in tool travel speeds (i.e. 58, 73 and 116 mm/min). Measured temperatures are compared with tool travel speeds in a diagram presented in Figure 6.

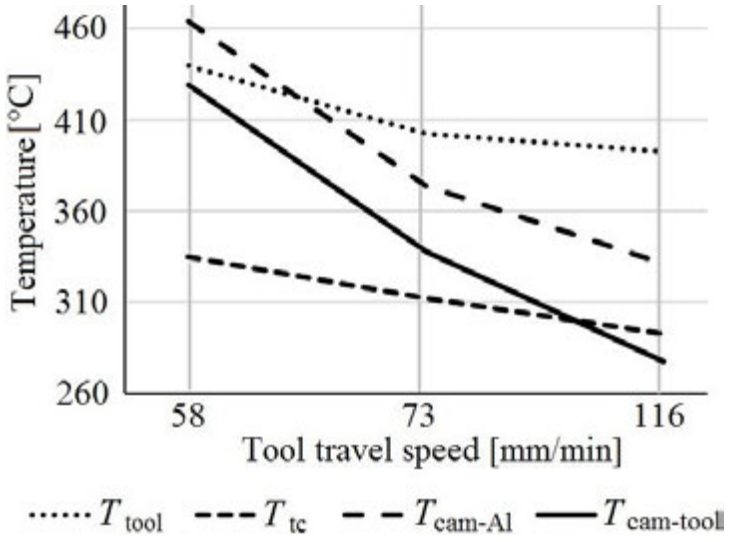


Figure 6. Comparison of measured temperatures and tool travel speeds

## CONCLUSIONS

Based on the analysis of the results the following conclusions can be made:

- The temperature measured using infrared laser thermometer and thermal camera are different due to different surface emissions coefficients adjusted. By correcting the value of surface emission coefficients the temperature fields can be more precisely measured.
- Thermal camera gives a general overview of the temperature fields in the workpiece or the tool, while a thermocouple or infrared laser thermometer gives a value at a particular spot.
- Tool speed progressively influences the heat developed in the tool and the processed plates. Higher tool travel speed in the run 3 has led to less heat input into the processed material and into the tool, since the tool was in contact for shorter time.
- Macrostructure analysis has shown that the low heat input in the run 3 reduced the possibility for deformation and mixing of the material because the material partly remained in a rigid state. In addition, the colder welding condition does not promote the

thermo-mechanical processing. These facts caused the development of the wormhole. The other two runs with a lower processing speed have been free of defects of this type because the heat input was sufficient for deformation and mixing of the processed material.

## REFERENCES

[1] W. M. Thomas, E. D. Nicholas, J. C. Needham, M. G. Murch, P. Temple-Smith, C. J. Dawes, Friction stir butt welding, International Patent Application No. PCT/GB92/02203; 1991.
[2] R. Nandan, T. DebRoy, H. K. D. H. Bhadeshia, Recent advances in friction-stir welding - Process, weldment structure and properties, Progress in Materials Science, 25 (2008) pp. 980-1023.
[3] W. J. Arbegast, Friction stir welding after a decade of development, Welding Journal, 85 (2006) 3, pp. 28-35.
[3] B. T. Gibson, D. H. Lammlein, T. J. Prater, W. R. Longhurst, C. D. Cox, M. C. Ballun, K. J. Dharmaraj, A. M. Strauss, Friction stir welding: Process, automation, and control, Journal of Manufacturing Processes, 16 (2014) pp. 56-73.
[4] M. Aissani, S. Gachi, F. Boubenider, Y. Benkedda, Design and optimization of friction stir welding tool, Materials and Manufacturing Processes, 25 (2010) pp. 1199-1205.
[5] D. Birsan, E. Scutelnicu, F. Stan, Hardness of Friction Stir Welded Joints of AA 6061-T6 Aluminium Alloy The Annals of "Dunarea de Jos" University of Galati, Fascicle XII, Welding Equipment and Technology, 21 (2010) pp. 15-18.
[6] L. Wang, C. M. Davies, R. C. Wimpory, L. Y. Xie, K. M. Nikbin, Measurement and simulation of temperature and residual stress distributions from friction stir welding AA2024 Al alloy, Materials at High Temperatures, 27 (2010) 3, pp. 167-178.
[7] C. C. Rusu, L. R. Mistodie, Thermography used in Friction Stir Welding Processes, The Annals of "Dunarea de Jos" University of Galati, Fascicle XII, Welding Equipment and Technology, 21 (2010) pp. 62-65.
[8] D. Birsan, D. Visan, O. Mircea, Temperature monitoring in Friction Stir Welding using Thermovision method, The Annals of "Dunarea de Jos" University of Galati, Fascicle XII, Welding Equipment and Technology, 20 (2009) 45-49.
[9] Ø. Frigaard, Ø. Grong, O. T. Midling, A Process Model for Friction Stir Welding of Age Hardening Aluminium Alloys, Metallurgical and Materials Transactions A, 32A (2001) pp. 1189-1200.
[10] G. A. Moraitis, G. N. Labeas, Investigation of friction stir welding process with emphasis on calculation of heat generated due to material stirring, Science and Technology of Welding and Joining, 15 (2010) 2, pp. 177-184.
[11] C. S. Wu, W. B. Zhang, L. Shi, M. A. Chen, Visualization and simulation of plastic material flow in friction stir welding of 2024 aluminium alloy plates, Transactions of Nonferrous Metals Society of China, no. 22, (2012) pp. 1445-1451.

[12] S. Vijayan, R. Raju, Process Parameter Optimization and Characterization of Friction Stir Welding of Aluminum Alloys, International Journal of Applied Engineering Research, 3 (2008) 10, pp. 1303-1316.
[13] D. Klobčar, L. Kosec, S. Smolej, J. Tušek, Weldability of aluminium alloy AlSi12 using FSW, Proceedings of conference EUROJOIN 8, HDTZ , Hrvatska, 2012., pp 99-106.
[14] S. A. Hussein, S. Thiru, R. Izamshah, A. S. M. Tahir, Unstable Temperature Distribution in Friction Stir Welding, Advances in Materials Science and Engineering, vol (2014) pp. 1-8.
[15] J. De Backer, G. Bolmsjö, Thermoelectric method for temperature measurement in friction stir welding, Science and Technology of Welding and Joining, 18 (2013) 7, pp. 558-565.
[16] EN 573-3:2014 Aluminium and aluminium alloys -- Chemical composition and form of wrought products - Part 3: Chemical composition and form of products.
[17] G. L. H. G. Lin, Y. T. Zhao, Aluminium alloy application manual, China Machine Press, 2006.
[18] A. H. Plaine, N. Guedes de Alcântara, Prediction of Friction Stir Welding Defect-Free Joints of AISI 304 Austenitic Stinless Steel Through Axial Force Profile Understanding, Materials Research, 17 (2014) 5, pp. 1324-1327.
[19] P. Podržaj, B. Jerman, D. Klobčar, Welding defects at friction stir welding, Metalurgija, 54 (2015) 2, pp. 387-389.

17th INTERNATIONAL FOUNDRYMEN CONFERENCE
Hi-tech casting solution and knowledge based engineering
Opatija, May 16th-18th, 2018
http://www.simet.hr/~foundry/

# HEAT EXCHANGE DURING MELTING OF Al - SCRAP IN SAS FURNACE

**Gustáv Jablonský[1], Augustín Varga[1], Ján Kizek[1], Ladislav Lazić[2]*, Róbert Dzurňák[1]**

[1] Technical University of Košice Faculty of Materials, Metallurgy and Recycling, Košice, Slovakia
[2] University of Zagreb Faculty of Metallurgy, Sisak, Croatia

**Poster presentation**
*Original scientific paper*

**Abstract**

Generally, it is possible to increase the efficiency of the plant through the knowledge and improvement of the heat exchange in the working space of the respective aggregate between flue gases - batch - lining. In this paper, the determination of heat exchange in the Al-scrap melting process as a basis for controlling the melting process, based on information on the amount and composition of the scrap in terms of the batch mass, is described. It was explained how to determine the heat transfer coefficient *K* (W/K) from the data obtained from the operational temperature measurements in the kiln, batch and other necessary parameters of the furnace. The obtained coefficient *K* is used in the mathematical model of heating and melting in order to determine the expected heating time and melting of Al - scrap from the input data and the kiln operation data.

***Keywords**: melting, Al-scrap, SAS furnace, heat exchange*

*Corresponding author (e-mail address): *lazic@simet.hr*

## INTRODUCTION

Fuel melting-fixative furnaces are advised for melting, overheating, temperature maintaining and composition stabilization throughout the volume of the metal. Stabilization of the composition in the volume is carried out due to the mixing of metals from different technologies of production and addition of alloying elements according to the desired properties of the metal [1-3].
The furnace charge consists of several types of aluminium scrap. For large pieces (pins) it is 5 - 6 tons, which can have a diameter of: 152, 178, 203, 228, 254, 279 mm or 15 ton blocks. After tapping the molten metal, a residual melt of 1 to 5 tons remains in the furnace. The total weight of the kiln weighing, which consists of the melt residue from the previous melt, the added scrap of several species, shape and composition, and ultimately two types of molten aluminium, is a maximum of 35-40 tons [2].

The total time of one melt can be divided into 4 time periods, as shown in Figure 1:
$\tau_1$ - charging
$\tau_2$ - the heat of the scrap and the impurities and the partial melting of the batch,
$\tau_3$ - completion of melting and casting of molten metals, doping, maintaining temperature,
$\tau_4$ - metal casting – tapping (empting the furnace).

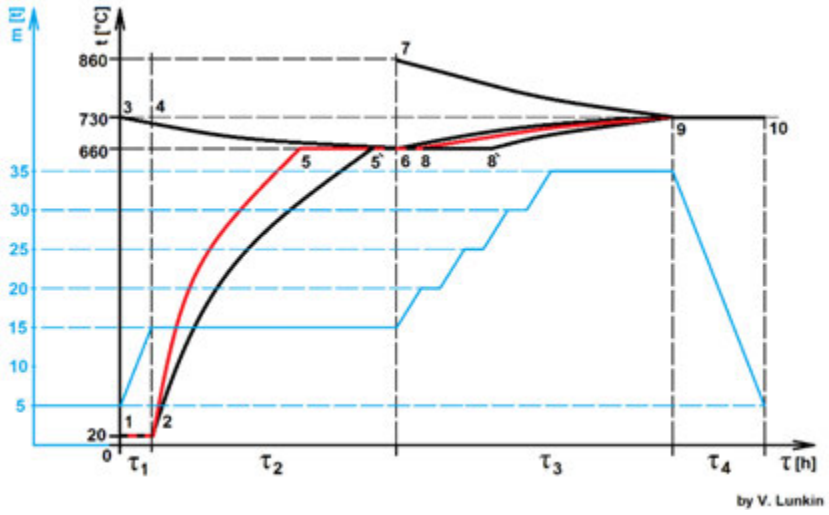


Figure 1. The process of heating and melting of the charge [4]

During the first period, the aluminium scrap is charged, the temperature of which can be considered as constant for a given period of time. Curves in the Figure 1. present only a small heating of the batch of approx. 15 °C (curve 1-2) and cooling the melt (curve 3-4) remained in the aggregate after the previous meltdown. In the second period, the scrap is melted by combustion of natural gases (curves 2-5 and 2-5´) and cooling of the residual melt continues (curve 4-6). The start of the third period is limited to the beginning of the addition of molten aluminium from electrolysis. During the second and third period the heat required to melt the scrap (curve 5-8 and 5´-8´) and to overheat the melt up to the casting temperature (curves 8-9 and 8´-9) takes place. This is done by continuously cooling the melt from the electrolysis to the casting temperature (curve 7-9) and overheating the residual melt to the casting temperature (curve 6-9). The fourth period (curve 9-10) describes the casting of aluminium, but the current running in this period can be considered as constant [4-5].

## MATERIALS AND METHODS

### *Heat exchange in the melting process*

Melting can generally be described as a phase transformation of the substance, whereby the transition from the solid phase to the liquid phase occurs. However, the melting process itself is somewhat more complicated and can be described by mathematical relationships based on the energy balance. The overall process of heating and melting of the Al batch (of

various scrap) can be decomposed into individual periods and these periods are then precisely defined. This was already described in Figure 1.
The calculated useful amount of heat transferred to the batch during the first and second period can be expressed as the functional dependence of the total mean heat transfer coefficient for the specified species and the mass of the scrap [2, 4-6].

$$Q_{užit\_t\_vs} = m_{t\_vs}\left(c_{2\_t\_vs}\, t_{2\_t\_vs} - c_{1\_t\_vs}\, t_{1\_t\_vs}\right) = K_{str\_t\_vs}\, \Delta t_{str\_t\_vs}\, \Delta\tau \quad (1)$$

$$Q_{užit\_m\_vs} = m_{m\_vs}\left(c_{2\_m\_vs}\, t_{2\_m\_vs} - c_{1\_m\_vs}\, t_{1\_m\_vs}\right) = K_{str\_m\_vs}\, \Delta t_{str\_m\_vs}\, \Delta\tau \quad (2)$$

$Q_{užit\_t\_vs}$, $Q_{užit\_m\_vs}$ - heat for heating the thin and massive batch over a period of time $\Delta\tau = \tau_1$, resp. $\tau_2$,
$m_{t\_vs}$, $m_{m\_vs}$ - weight of a thin and massive batch,
$c_{2\_t\_vs}$, $c_{1\_t\_vs}$, $t_{2\_t\_vs}$, $t_{1\_t\_vs}$, $c_{2\_m\_vs}$, $c_{1\_m\_vs}$, $t_{2\_m\_vs}$, $t_{1\_m\_vs}$, - the specific heat capacity and the relevant temperatures of the thin and massive pieces in the batch at the end and start of the relevant time period,
$K_{str\_t\_vs}$, $K_{str\_m\_vs}$, - total average heat transfer coefficient from the kiln to the thin and massive batch during the time period, (W/K),
$\Delta t_{str\_t\_vs}$, $\Delta t_{str\_m\_vs}$ - mean logarithmic temperature differences between the batch and the furnace during the time period (K).

The total heat transfer coefficient for the total batch is valid [7-9]:

$$K_{celk}\, S_{celk} = K_{str\_t\_vs}\, S_{t\_vs} + K_{str\_m\_vs}\, S_{m\_vs} \quad (3)$$

$$K_{celk} = K_{str\_t\_vs}\frac{S_{t\_vs}}{S_{celk}} + K_{str\_m\_vs}\frac{S_{m\_vs}}{S_{celk}} \quad (4)$$

$$S_{celk} = S_{t\_vs} + S_{m\_vs} \quad (5)$$

$S_{t\_vs}$, $S_{m\_vs}$ - heat-exchange surfaces of thin and massive batch, ($m^2$).
$K_{celk}$ is dependent on the thin / massive charge to the total weight of the batch:

$$K_{celk} = f\left(\frac{m_{m\_vs}}{m_{celk}}, \frac{m_{t\_vs}}{m_{celk}}\right) \quad [3, 5] \quad (6)$$

$$m_{šc} = m_{t\_vs} + m_{m\_vs} \quad (7)$$

For the total useful heat transferred to the whole batch, a relationship can be written:

$$Q_{užit\_celk} = K_{celk}\, \Delta t_{str\_celk}\, \Delta\tau \quad (8)$$

$\Delta t_{str\_celk}$ - the mean temperature difference between the batch and the furnace during the period of time,
$Q_{užit\_celk}$ - heat for heating the batch during the period of time.

## RESULTS AND DISCUSSION

### *Determination of heat exchange coefficient*

The first and second periods of the Al-scrap melting process are of interest from the heat engineering point of view.

For the 1st period:

$$Q_{sp} + Q_{ot} = Q_{už} \quad \text{(J)} \qquad (9)$$

$Q_{sp}$ - the heat supplied by flue gases, (J)
$Q_{ot}$ - the heat that brings the melt into the process, (J)
$Q_{už}$ - the heat needed to heat and partially melt the Al-scrap, (J)

$$Q_{sp} = Q_{už} - Q_{ot} \quad \text{(J)} \qquad (10)$$

$$Q_{sp} = K\,\Delta t\,\Delta\tau \quad \text{(J)} \qquad (11)$$

$K$ - the total mean heat transfer coefficient to the batch surface, (W/K)
$\Delta\tau$ - time from 1st period, (s)
$\Delta t$ - the difference between furnace and batch temperature, (°C)

For 2nd period:

$$Q_{sp} = Q_{už} - Q_{ok} - \Delta Q_{nt} \quad \text{(J)} \qquad (12)$$

$Q_{už}$ - the heat needed to melt the scrap and overheating to the casting temperature, (J)
$Q_{ok}$ - the heat delivered by the formation of the aluminium dross, (J)
$\Delta Q_{nt}$ - the heat obtained from the new melt, (J)

The items in the energy balance of the furnace for selected fluxes $Q_{už}$, for the relevant periods, were calculated and the flue gas temperature was determined on the basis of the values of temperature differences.
According to the relations (11) and (12), the $K$ values were calculated for the relevant fluxes. The results of the calculations are included in Table 1.

Table 1. Processing measured data for *K*

| Table | | 947 | 953 | 957 | 962 | 966 | 971 | 969 | 975 | 961 |
|---|---|---|---|---|---|---|---|---|---|---|
| $\tau_1$ | min. | 163 | 73 | 110 | 200 | 218 | 237 | 85 | 19 | 190 |
| $\tau_2$ | min. | 236 | 225 | 174 | 151 | 177 | 95 | 224 | 133 | 87 |
| $\tau_{celk}$ | min. | 399 | 298 | 284 | 351 | 395 | 332 | 309 | 152 | 277 |
| $\tau_{1\_heating}$ | min. | 148 | 62 | 101 | 194 | 207 | 226 | 76 | 12 | 176 |
| | | | | | | | | | | |
| $m_{ot}$ | kg | 3872 | 4495 | 3993 | 4559 | 2819 | 2143 | 4177 | 5703 | 2871 |
| $m_{m\_vs}$ | kg | 9760 | 3750 | 1380 | 10036 | 6950 | 6815 | 5250 | 2665 | 6471 |
| $m_{t\_vs}$ | kg | 3450 | 2439 | 4802 | 0 | 4267 | 5077 | 4025 | 2294 | 5753 |
| $m_{ok}$ | kg | 430 | 325 | 405 | 280 | 405 | 355 | 350 | 560 | 355 |
| $m_{nt}$ | kg | 18390 | 24895 | 23721 | 21585 | 21375 | 22020 | 23290 | 22280 | 21585 |
| $m_{celk}$ | kg | 13210 | 6189 | 6182 | 10036 | 11217 | 11892 | 9275 | 4959 | 12224 |
| $k_m$ | - | 0,739 | 0,606 | 0.223 | 1 | 0.62 | 0,573 | 0.566 | 0.537 | 0.529 |
| | | | | | | | | | | |
| $Q_{užit\_m\_vs}$ | MJ | 6340.21 | 2261.74 | 896.46 | 9103,68 | 7437.21 | 7245.04 | 3166.44 | 209.81 | 0 |
| $Q_{užit\_t\_vs}$ | MJ | 3090.45 | 2168.43 | 4537.57 | 154.15 | 4774.8 | 5491.61 | 2856.99 | 259.94 | 0 |
| $Q_{ot}$ | MJ | -364.23 | -422.84 | -375.61 | -428.86 | -265.18 | -200.66 | -392.92 | -536.47 | -270.07 |
| $Q_{užit\_celk}$ | MJ | 9066.42 | 4007.34 | 5058.42 | 8828.98 | 11946.83 | 12536 | 5630.5 | 0 | 12591.62 |
| | | | | | | | | | | |
| $K_{str\_t\_vs}$ | W/K | 1091 | 1900 | 3042 | 0 | 1154 | 1600 | 1310 | 500 | 3200 |
| $K_{str\_m\_vs}$ | W/K | 1700 | 1266 | 410 | 2287 | 1770 | 1529 | 1657 | 1500 | |
| $K$ *(Figure 2)* | W/K | 2791 | 3166 | 3452 | 2300 | 2924 | 3129 | 2967 | 2000 | |
| $K$ *(Figure 3)* | W/K | 2688 | 2897 | 1915 | 2120 | 2178 | 2268 | 2739 | 2830 | 2830 |
| $K_{\_ot}$ | W/K | 103 | 131 | 167 | 99 | 72 | 62 | 123 | | 60 |

In the analysis of the measurement and the subsequent calculations of the heat flows, the effect of the batch composition (massive charge) on the $K$ value was monitored and the obtained dependence for the 1st period (heating) is shown in Figure 2.

The coefficient $K$ is corrected due to the mass of the batch

$$k_{or} = 1 + 0.02417\, k_m - 0.310468\, k_m^2 \tag{13}$$

$$k_m = \frac{m_m}{m_{šc}} \quad (-) \tag{14}$$

$m_m$ - the weight of the massive batch, (kg)
$m_{šc}$ - total scrap weight, (kg)

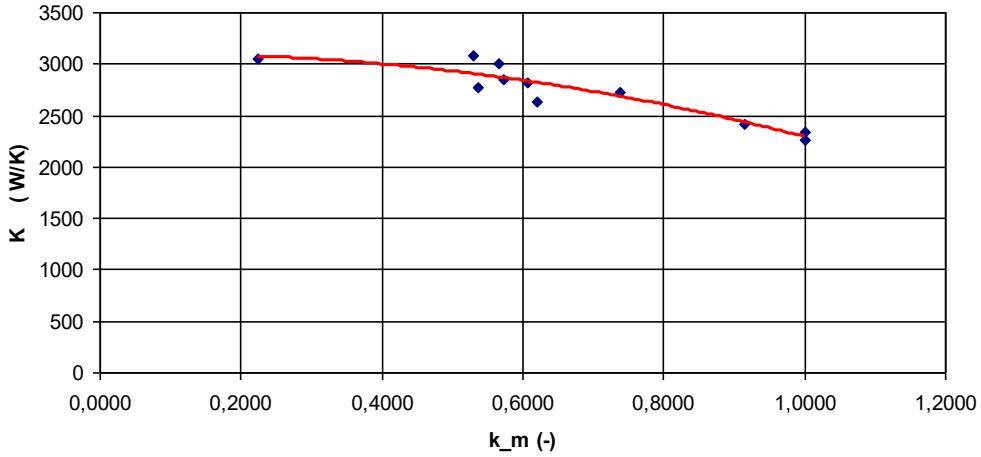


Figure 2. Effect of batch composition on *K* value

The value of the heat transfer coefficient is determined by the relationship:

$$K = K_0 \, k_{or} \tag{15}$$

$K_0$ - mean heat transfer coefficient for a pure thin charge, (W/K)

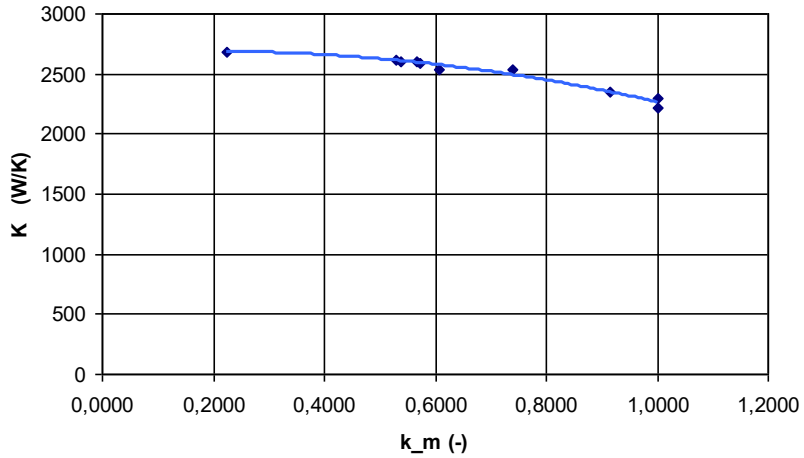


Figure 3. The influence of the batch composition on the $K$ value, taking into account the formation of aluminium dross

If we also take into account the heat release of the aluminium dross in the process (about the same amount of heat for each melt), then the dependence for the $K$ values is adjusted according to Figure 3 and the coefficient value is adjusted:

$$k_{or} = 1 + 0.094878 \, k_m - 0.244 \, k_m^2 \tag{16}$$

$$K = K_0 \, k_{or} \tag{17}$$

where $K_0 = 2659\ W/K$.

In the second period, the $K$ value is constant because the heat exchange area does not change.

***Predictive mathematical model of the melting process***

Based on the knowledge of the energy balance of the processes and knowledge from the determination of the heat transfer coefficient, a mathematical model was developed in the EXCEL program to determine the necessary time for the thermal processes taking place in the respective Al-scrap melting periods. The model is primarily aimed at determining the heat delivered by the flue gas during the heating period.

Based on the melt flow temperature of the mixture, it is possible to model the heating period based on the estimated scrap temperature at the end of the 1st period and the rate of melting of the scrap. The model further provides for the indicative gas consumption for the relevant process period as well as the measured gas consumption ($m^3/h$) and the energy per 1 kg of scrap respectively (MJ/kg). From the model, the values of the individual items of the energy balance in the relevant periods can be obtained.

The proposed model has been verified on the relevant melts. The obtained rates of the batch temperatures during the process from each melt are shown in Figure 4.

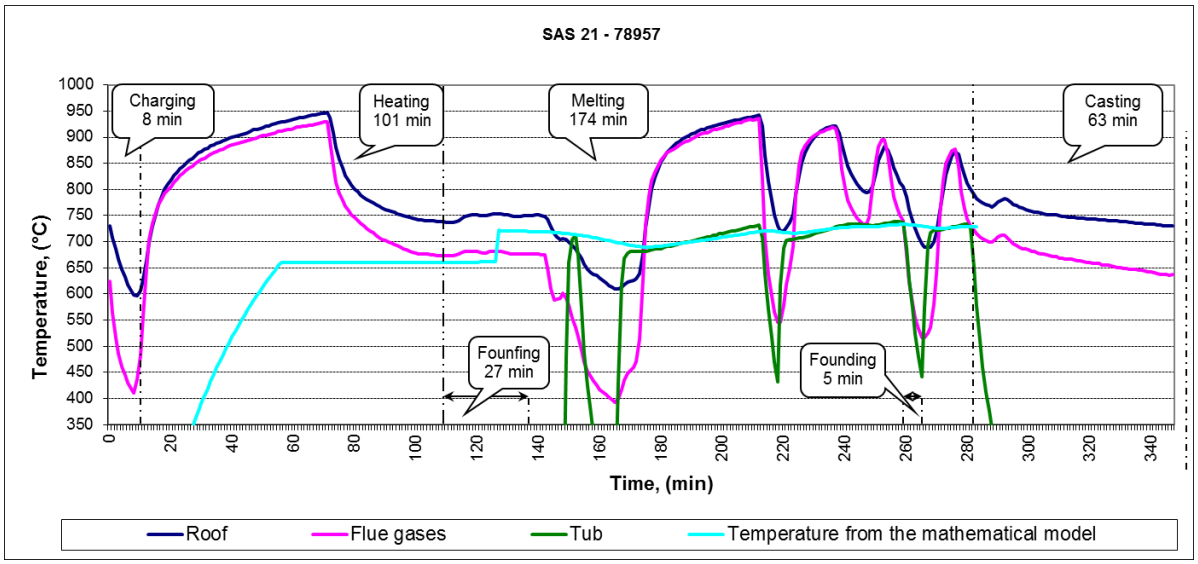


Figure 4. Processes of the batch temperatures during the process

Calculation accuracy can be judged based on the calculated scrap temperature, resp. melt and melt temperature measurements in the certain portions of the 2nd period. On the basis of the measured temperatures, validation of the formulated model was performed.

When applying the model in practice, it is necessary to consider a certain uncertainty of the model, which should not be more than 5% of the calculated time for the respective period. Imprecision is caused by, for example, we cannot pre-define heat loss items for some

technological reasons, the course of the flue gas temperature, which affects the heat exchange between the flue gas and the batch. The process of heat exchange is also influenced by the opening of the door, when it is problematic to specify the exact items: heat by exhausting the flue gases and the heat from the exhaust gases. In the calculation, it is not possible to determine heat items for alloying processes because the exact composition of the legs, admixture and the following chemical chemistry that occurs during alloying. The problem is also the heat input supplied to the formation of aluminium dross, which may be different for each melt and affects the temperature of the mixture after melt application.

## CONCLUSIONS

As can be seen from the presented data, it is possible by the validated model to control the melting process in SAS furnaces. In this model, apart from the energy balance of the process, the heat exchange in the aggregate has important role. The heat exchange calculation in described model is based on determination of the heat transfer between the flue gases and the batch. This model is being used in the Al-Scrap melting process in SAS melting furnaces at SLOVALCO Žiar nad Hronom.

## REFERENCES

[1] Š. Michna et al., Encyklopedie hliníku, Adin, Prešov, 2005.
[2] A. Varga et al., Energetická bilancia pretavovania Al odpadov, Report TUKE, Faculty of Metallurgy, Department Furnace and Thermal Technology, TU of Košice, 2010.
[3] A. Varga, G. Jablonský, L. Lukáč, J. Kizek, Tepelná technika pre hutníkov, TU of Košice, 2013.
[4] V. Lunkin, A. Varga, J. Kizek, L. Lazić, Analysis of aluminium scrap melting, 13th International Foundrymen Conference: Innovative Foundry Processes and Materials, (ed. Glavaš Z., Zovko Brodarac Z., Dolić N.), University of Zagreb, 16. - 17. May, 2013, Opatija, Croatia, pp. 193-198.
[5] A. Varga et al., Energetická analýza rotačnej pece na spracovanie AL šrotov, Report TUKE, Faculty of Metallurgy, Department Furnace and Thermal Technology, TU of Košice, 2011.
[6] J. Fík, Spalovaní plynných paliv a plynové hořáky, GAS s.r.o., Praha, 1998.
[7] M. Dudrík, A. Varga, Vplyv koncentrácie kyslíka v oxidačnom činidle na produkciu emisií NOx, Proceedings of Metalurgia Junior 2013, TU of Košice, 22. - 23. May, 2013, Košice, Slovakia, pp. 7-10.
[8] M. Dudrík, A. Varga, G. Jablonský, Effect of oxidizing agent for co emissions production in process of gaseous fuels combustion, Proceedings of 13th International Scientific Conference - Energy Transformations in Industry, TU of Košice, 25.-27. September, 2013, Vysoké Tatry, Račkova dolina, Slovakia, pp. 28-30.

[9] M. Dudrík, A. Varga, G. Jablonský, Vplyv obohatenia vzduchu na spaľovací proces, Proceedings of the Seminar Energie z biomasy 12, Vysoké učení technické v Brně, 23. - 24. November, 2011, Brno, Czech Republic, pp. 35-40.
[10] L. Lazić, Ž Grubišić, The influence of the emissivity on energy efficiency of foundry aluminium melting furnaces, Proceedings of 13th International Foundrymen Conference: Innovative Foundry Processes and Materials, (ed. Glavaš Z., Zovko Brodarac Z., Dolić N.), University of Zagreb, 16. - 17. May, 2013, Opatija, Croatia, pp. 184-192.

## Acknowledgements

This work was supported by the project VEGA 1/0578/16 and obtained results are part of the solution from this grant project.

17th INTERNATIONAL FOUNDRYMEN CONFERENCE
Hi-tech casting solution and knowledge based engineering
Opatija, May 16th-18th, 2018
http://www.simet.hr/~foundry/

# TESTING OF ABRASION WEAR RATE ON TECHNICALLY PURE ALUMINUM AND Al ALLOY AA 2024

# ISPITIVANJE ABRAZIJSKOG TROŠENJA TEHNIČKI ČISTOG ALUMINIJA I ALUMINIJSKE LEGURE AA 2024

**Antonio Dominik Jelenski[1], Merima Muslić[2]*, Vera Rede[1]**

[1] University of Zagreb Faculty of Mechanical Engineering and Naval Architecture, Zagreb, Croatia
[2] "E-PRO" Ltd. for designing, engineering and technical consulting, Bihać, Bosnia and Herzegovina

**Poster presentation**
*Original scientific paper*

**Abstract**

The purpose of this paper is to determine the influence of abrasive size on wear rate of Al-alloy AA 2024 and technically pure aluminum. Abrasive wear test was performed on Taber abrader, on abrasive papers of different quality (from P80 to P600).
Abrasive wear rate was given like volume lost per abraded surface unit.
It was determined that the abrasive size has a great influence on abrasive wear. Wear rate of technically pure aluminum is higher than the wear rate of Al-alloy AA 2024. Critical particle size – CPS is noticeable for both materials. Due to different microstructures and properties, Al-alloy has a higher value of critical abrasive size (≈ 125μm) than technically pure aluminum (≈ 82μm).

***Keywords**: abrasion, CPS -critical particle size, aluminum, Al alloy 2024, Taber abrader*

*Corresponding author (e-mail address): *dmuslic@bih.net.ba*

**Sažetak**

U radu je istraženo kako veličina abrazivnih čestica utječe na intenzitet abrazijskog trošenja aluminijske legure AA 2024 i tehnički čistog aluminija. Ispitivanje abrazijskog trošenja provedeno je na uređaju Taber abrader, na brusnim papirima različite kvalitete (od P80 do P600).
Intenzitet abrazijskog trošenja je izražen preko potrošenog volumena svedenog na jedinicu abradirane površine.
Utvrđeno je da veličina abrazivnih čestica ima veliki utjecaj na intenzitet trošenja ispitivanih materijala. Intenzitet trošenja tehnički čistog aluminija je viši od Al-legure AA 2024. Kod oba materijala izražena je kritična veličina abrazivnog zrna. Zbog različite mikrostrukture i svojstava, Al-legura ima višu vrijednost kritične veličine abrazivnog zrna (≈ 125 μm) nego tehnički čisti aluminij (≈82 μm).

***Ključne riječi**: abrazija, CPS -kritična veličina zrna, aluminij, Al legura 2024, Taber abrader*

## UVOD

Niska gustoća, dobra oblikovljivost i korozijska postojanost su osnovne prednosti primjene aluminija i njegovih legura, kako u proizvodnji zrakoplova i vozila, tako i drugih lakih dijelova. Legiranjem i toplinskom obradom se dodatno poboljšavaju svojstva poput čvrstoće, tvrdoće i otpornosti na trošenje, te proširuje područje primjene [1].
Tribološka svojstva su od izuzetnog značaja za izbor inženjerskog materijala. Trošenje i zagrijavanje pokretnih dijelova na dodirnim površinama mogu skratiti vijek trajanja proizvoda. Stoga ispitivanje abrazije, kao i drugih mehanizama trošenja materijala [2], ne prestaje biti predmetom znanstvenih istraživanja.
Abrazija je proces odnošenja čestica s površine mekšeg materijala nastao kao posljedica prodiranja vrhova tvrđeg materijala pri njihovom relativnom gibanju. Rezultati abrazivnog djelovanja ovise o nizu faktora. Dinamika relativnog gibanja, tvrdoće materijala u kontaktu, veličina i oblik abrazivnih čestica su najutjecajniji faktori. Također je važno da li su u kontaktu dva ili tri tijela, odnosno da li produkti abrazije ostaju u području dodira površina [2-7].
Istraživanja su pokazala da je gubitak mase trošenog materijala proporcionalan veličini abrazivnog zrna. Međutim, ovaj linearni trend se u određenom trenutku mijenja i ta vrijednost veličine abrazivnog zrna se naziva *kritična veličina abrazivnog zrna*. Nakon dosegnute kritične veličine abrazivnog zrna moguća su tri slučaja: da se gubitak mase nastavi povećavati, ali sa smanjenim intenzitetom, da gubitak mase ostane konstantan, neovisno o daljnjem povećanju veličine zrna ili da se počne smanjivati. U literaturi [6,7] je ovaj fenomen objašnjen preko promjene dominantnog mikro mehanizma trošenja. Do navedene promjene dolazi zbog različite veličine abrazivnih zrna. Krupnije abrazivne čestice pod manjim kutom „napadaju“ abradiranu površinu i dominantni mehanizam trošenja je mikrobrazdanje, odnosno veći je utjecaj plastične deformacije na mikroprocese. Ako su abrazivne čestice sitne, navedeni kut je veći i dominantni mehanizam trošenja je mikrorezanje. Međutim, ovaj zaključak se ne može generalizirati s obzirom na moguće varijacije materijala u kontaktu, te je uvijek zanimljiv predmet istraživanja [5-7].

## MATERIJALI I METODE

Ispitivanje abrazijskog trošenja provedeno je na dvije skupine uzoraka. Prva skupina izrezana je iz tehnički čistog aluminija, a druga iz aluminijske legure oznake AA 2024. Kemijski sastav aluminijske legure AA 2024 prikazan je u tablici 1, a njezina mikrostruktura snimljena na optičkom mikroskopu prikazana je na slici 1. Vrijednosti gustoće oba materijala nalaze se u tablici 2.

Tablica 1. Kemijski sastav aluminijske legure AA 2024 [8]

| Kemijski element | Al | Cu | Mg | Mn | Si max | Fe max | Zn max | Ti max | Cr max | Ostalo |
|---|---|---|---|---|---|---|---|---|---|---|
| Udio, % | 90,7-94,7 | 3,8-4,9 | 1,2-1,8 | 0,3-0,9 | 0,5 | 0,5 | 0,25 | 0,15 | 0,1 | 0,15 |

Uzorci su bili kvadratnog presjeka dimenzija 5×5×45 mm. Sve površine ispitnih uzoraka su obrađene glodanjem, a površina koja je abradirana fino je pobrušena prije samog ispitivanja. U svakoj skupini ispitano je po 5 uzoraka. Na slici 2 prikazani su ispitni uzorci obaju skupina.

Tablica 2. Vrijednosti gustoće ispitanih materijala [8]

| Materijal | Gustoća, kg/m$^3$ |
|---|---|
| Al tehničke čistoće | 2700 |
| AA 2024 | 2780 |

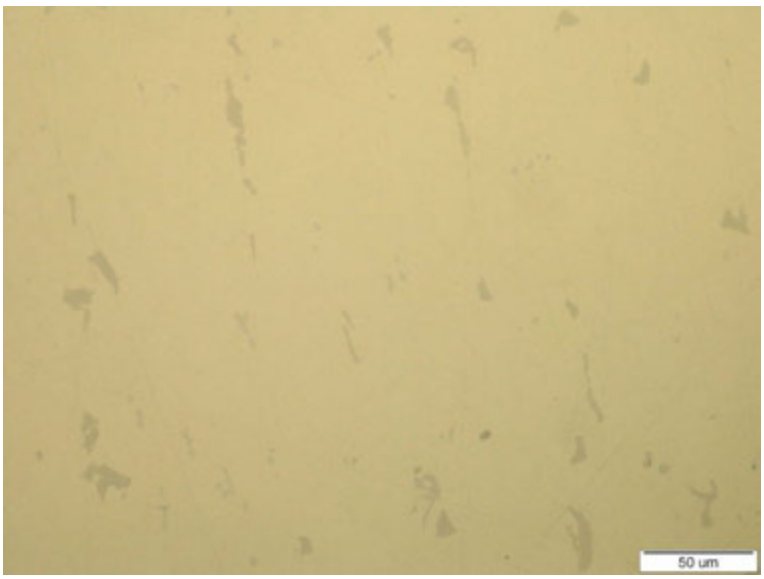


Slika 1. Mikrostruktura aluminijske legure AA 2024

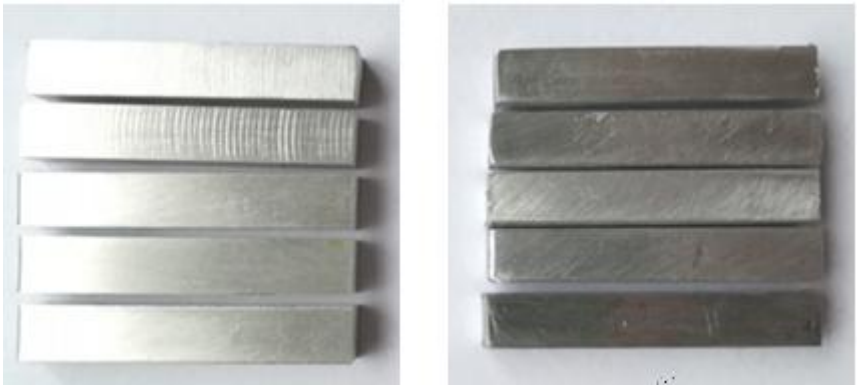

Slika 2. Uzorci za ispitivanje: lijevo - legura AA 2024, desno - čisti tehnički aluminij

Ispitivanje abrazijskog trošenja provedeno je na uređaju *Taber abrader* u Laboratoriju za tribologiju Fakulteta strojarstva i brodogradnje u Zagrebu. Uređaj je prikazan na slici 3.

Promjer abrazivnog diska uređaja iznosi 125 mm, brzina vrtnje je 1 okr/s, a obodna brzina je 0,251 m/s.
Ispitivanja su provedena na brusnom papiru s abrazivnim česticama od aluminijevog oksida $Al_2O_3$. Oznake i kvaliteta korištenih brusnih papira, kao i srednji promjer abrazivnih zrna, prikazani su u tablici 3.

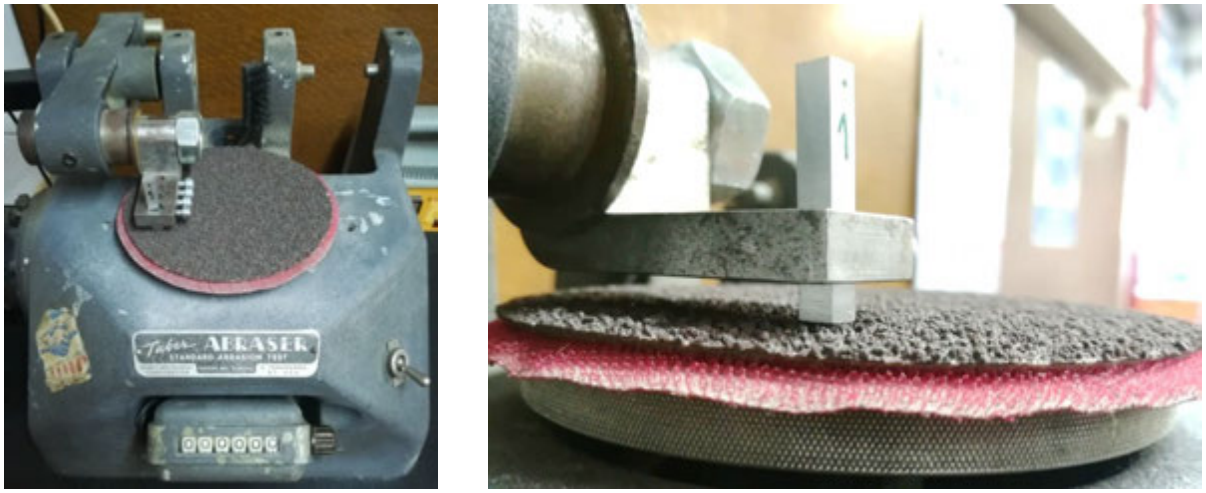


Slika 3. Uređaj za ispitivanje (lijevo) i uzorak u nosaču uređaja (desno)

Tablica 3. Oznake brusnih papira [9]

| Kvaliteta brusnog papira (ISO/FEPA) | Srednji promjer abrazivnog zrna [μm] |
|---|---|
| P80 | 201 |
| P120 | 125 |
| P180 | 82 |
| P240 | 58,5 |
| P600 | 25,8 |

Svaki uzorak podvrgnut je trošenju kroz 400 okretaja brusnog diska, što odgovara duljini od ≈100 m, za svaku kvalitetu brusnog papira. Uzorci su tijekom ispitivanja pritisnuti na brusni papir silom od 4,91 N. Uzorcima je izmjerena masa prije i poslije abradiranja na uređaju *OHAUS Analitycal Plus* u Laboratoriju za analizu metala Fakulteta strojarstva i brodogradnje u Zagrebu. Izračunati gubitak mase (Δm) preveden je u gubitak volumena (ΔV), čime je određeno trošenje svakog uzorka, na svakom brusnom papiru. Intenzitet abrazijskog trošenja (ώ) izražen je preko potrošenog volumena svedenog na jedinicu abradirane površine.

**REZULTATI I RASPRAVA**

Na slici 4 prikazane su srednje vrijednosti intenziteta abrazijskog trošenja oba ispitivana materijala nakon 400 okretaja, za sve kvalitete brusnog papira. Intenzitet abrazijskog trošenja oba ispitivana materijala raste sa smanjenjem kvalitete brusnog papira do brusnog papira s oznakom P120. Kod najgrubljeg brusnog papira oznake P80 uočava se pad intenziteta trošenja aluminijske legure AA 2024, dok se intenzitet trošenja tehnički čistog aluminija i dalje povećava.
Također se može uočiti da je razlika u intenzitetu trošenja između ispitivanih materijala sa smanjenjem kvalitete brusnog papira sve veća.

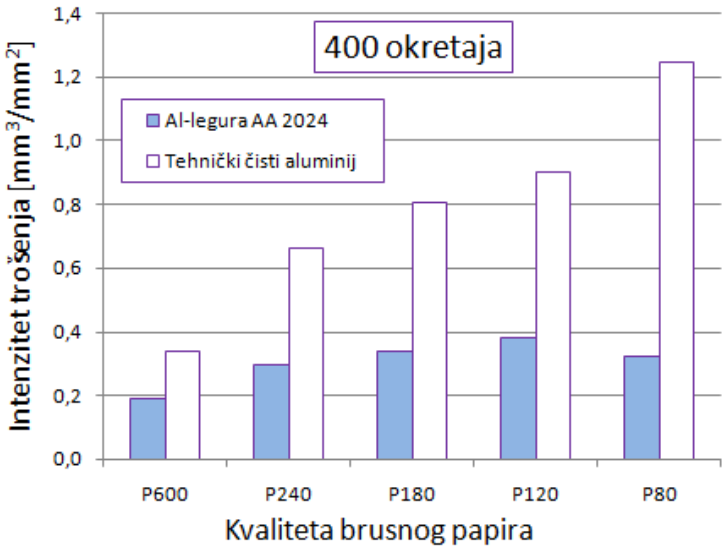


Slika 4. Srednje vrijednosti intenziteta trošenja (ώ) nakon 400 okretaja

Na slici 5 prikazana je ovisnost intenziteta trošenja o srednjem promjeru abrazivnog zrna. Za sitna abrazivna zrna (prva tri brusna papira) ova ovisnost je skoro linearna. Kako abrazivno zrno raste dolazi se do kritične vrijednosti koja je uočena kod oba ispitivana materijala, ali se njihove vrijednosti ne podudaraju. Kod aluminijske legure AA 2024 kritična veličina abrazivnog zrna iznosi oko 125 µm. Kod tehnički čistog aluminija kritična veličina abrazivnog zrna nešto je manja i iznosi oko 82 µm. Također postoji razlika u ponašanju materijala nakon što veličina abrazivnog zrna prekorači kritičnu vrijednost. Tehnički čistom aluminiju se intenzitet trošenja i dalje povećava, ali je stopa rasta niža nego prije kritične vrijednosti, dok se kod legure AA 2024 intenzitet trošenja smanjuje.

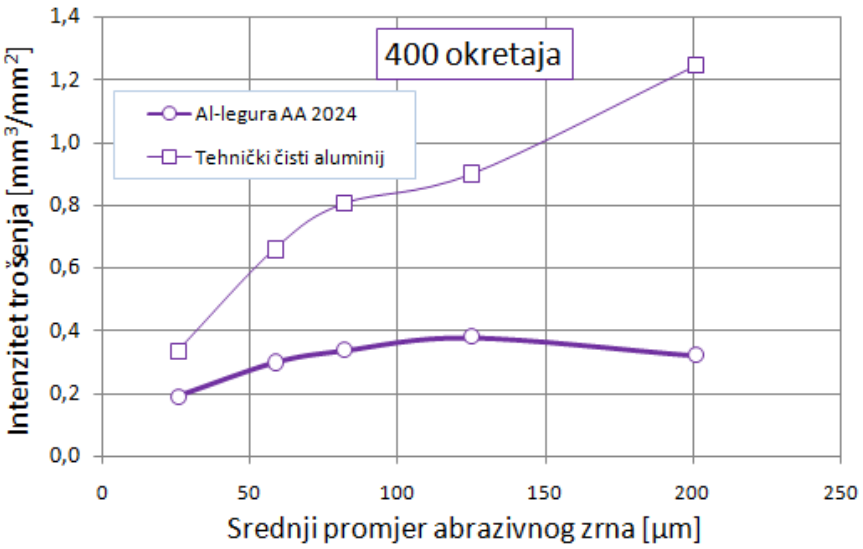


Slika 5. Intenzitet trošenja materijala za različite srednje promjere abrazivnog zrna

Uzrok tome treba tražiti u različitoj mikrostrukturi i svojstvima ovih dvaju materijala. Tehnički čisti aluminij ima puno manju tvrdoću i čvrstoću te bolju duktilnost od legure AA 2024. Njegova mikrostruktura je monofazna za razliku od legure AA 2024 u čijoj se mikrostrukturi osim kristala mješanaca nalazi i određena količina intermetalnih spojeva koji povisuju tvrdoću i čvrstoću.

## ZAKLJUČCI

Na temelju provedenog ispitivanja i dobivenih rezultata može se zaključiti sljedeće:

- Tehnički čisti aluminij se troši više od Al-legure za sve kvalitete brusnog papira.
- Veličina abrazivnih čestica ima veliki utjecaj na intenzitet trošenja oba ispitivana materijala.
- Kod tehnički čistog aluminija intenzitet trošenja raste s porastom abrazivnog zrna za sve korištene kvalite brusnog papira, a kod legure AA 2024 intenzitet trošenja se smanjuje nakon brusnog papira P120.
- Kod oba materijala, za tri najfinija brusna papira, ovisnost između veličine abrazivnih čestica i intenziteta trošenja je gotovo linearna.
- Oba ispitivana materijala imaju izraženu kritičnu veličinu abrazivnog zrna.
- Al-legura ima višu vrijednost kritične veličine abrazivnog zrna (oko 125 µm) nego tehnički čisti aluminij (oko 82 µm).

**REFERENCES**

[1] T. Filetin, F. Kovačiček, J. Indolf, Svojstva i primjena materijala, Fakultet strojarstva i brodogradnje, Zagreb, 2013.
[2] V. Ivušić, Tribologija, Hrvatsko društvo za materijale i tribologiju, Zagreb, 1998.
[3] K.-H. Zum Ghar, Microstructure and Wear of Materials, Elsevier, Amsterdam-Oxford-New York, 1987.
[4] A. Rac, Osnovi tribologije, Mašinski fakultet Univerziteta u Beogradu, Beograd, 1991.
[5] G. K. Nathan, W. J. D. Jones, The empirical relationship between abrasive wear and the applied conditions, Wear, 9 (1966) pp. 300-309.
[6] J. J. Coronado, Effect of Abrasive Size on Wear, Abrasion Resistance of Materials, (Ed. Dr Marcin Adamiak), ISBN: 978-953-51-0300-4, InTech, 2012.
[7] J. J. Coronado, A. Sinatora, Effect of abrasive size on wear of metallic materials and its relationship with microchips morphology and wear micromechanisms: Part 1 and 2, Wear, 271 (2011) p. 1794– 1803 and p. 1804– 1812.
[8] ASM Aerospace Specification Metals Inc., Accessible on Internet: http://asm.matweb.com/search/SpecificMaterial.asp?bassnum=ma2024t4
[9] Dieter Schmid's Fine Tools, Accessible on Internet: https://www.fine-tools.com/G10019.html

17th INTERNATIONAL FOUNDRYMEN CONFERENCE
Hi-tech casting solution and knowledge based engineering
Opatija, May 16th-18th, 2018
http://www.simet.hr/~foundry/

# OPTIMIZATION OF CASTABILITY TEST FOR GRAY IRON USING FEM CALCULATION

**Sebastjan Kastelic[1,2]*, Almir Mahmutovič[1], Mitja Petrič[2], Primož Mrvar[2]**

[1] TC Livarstvo d.o.o., Ljubljana, Slovenia
[2] University of Ljubljana Faculty of Natural Sciences and Engineering, Ljubljana, Slovenia

**Poster presentation**
*Professional paper*

**Abstract**

The aim of investigation was to make and optimize new castability test for grey iron. For this purpose, new measuring test cell for castability test was constructed. The development and construction were based on numerical simulations of casting processes which was calibrated with experiment. In the castability cell also the cup for thermal analysis was integrated. For experimental calibration of the castability test cell spheroidal grey iron EN-GJS-500-7 was used. The geometry in the optimized castability test cell is constructed in this way that we can determine castability for different thermal modulus regarding same pouring conditions. Considering this with this castability test we can determine the casting technology for complex castings with different wall thickness more accurate.

***Keywords***: *castability test, grey iron, ProCAST, FEM*

*Corresponding author (e-mail address): *kastelic.@tc-liv.eu*

## INTRODUCTION

Traditionally for castability test casting in spiral shape is used. Mold can be made from sand or from steel. Usage a casting in spiral shape is because this kind of shape uses less space and the experimental mold can be made in reasonable dimensions. To provide the repeatability of the test all the spiral channels are in same dividing plane to see the influence of channel height. Several different tests were tested [1].
Castability is an important property which is connected with casting wall thickness that can be filled. The research of castability is important especially for automotive industry for making thinner and lighter castings. Castability has an influence on filling of casting cavity, feeding of the casting, porosity and hot cracking. One of the experiments to test thin wall feeding with spiral castability test was made by M. Gorny in 2008. His spiral probe is made

with three different spirals connected with same feeder. All three spirals have same width and has different height – 1 mm, 2 mm and 3 mm [2]. The spiral probe is presented on Figure 1.

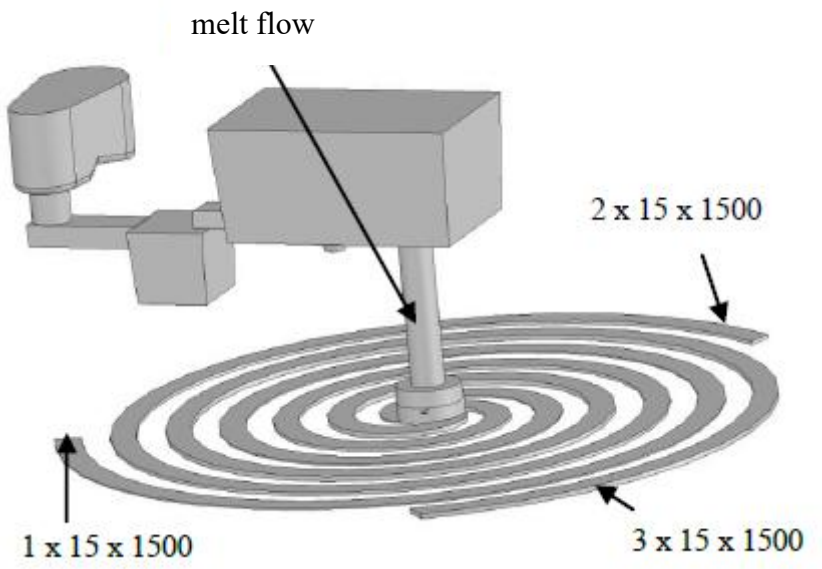


Figure 1. Spiral probe for thin wall casting testing [2]

The goal of new castability probe was to test the influence of cross-section shape on the castability of thin wall castings [3].

## MATERIALS AND METHODS

To test the influence of gating system cross-section shape on the castability several different cross-sections were tested using numerical calculations. At the end three different cross-section were chosen to do the comparison between numerical calculation and with experiment. The cross-section has same cross-section area – 40 $mm^2$ and shape of triangle, semicircle and trapeze. The construction of the probe model was done using CAD program. The used cross-sections are presented on Figure 2.

Figure 2. Cross-section shape of gating system for spiral probe – all have cross-section area 40 $mm^2$ [3]

Cross-section castability test was done using finite element method program for casting processes calculation ProCAST. The alloy using for testing was EN-GJS-500-7 and was used from program standard database. Casting temperature used in numerical simulation was 1250 °C, 1310 °C and 1380 °C. Mold material was green sand also from program standard database.
The sand mold for the experiment was made with 3D printing. The mold is presented on Figure 3. For the experiment the measured purring temperature was 1252 °C and 1311 °C.

Figure 3. Lower part of the mold made with 3D printing

**RESULTS AND DISCUSSION**

Simulation results of castability test are in good correlation with real experiment. On Figure 4 is presented castability in cm for different purring temperatures calculated with numerical calculation. The measured castability is presented on graph on Figure 6.

a) b) c)

Figure 4. Calculated castability with numerical calculation using ProCAST: a) 1250 °C, b) 1310 °C and c) 1380 °C

On Figure 5 are castings from the experiment. On Figure 5a is casting casted with temperature 1252 °C and on Figure 5b the purring temperature was 1311 °C.

a) b)

Figure 5. Measured castability at purring temperature: a) 1252 °C and b) 1311 °C

The castability from calculation and from purring into the printed mold are presented on Figure 6. The calculated castability is higher than castability measured at practically same purring temperature. The difference can be because at the simulation not all the parameters or boundary conditions like roughness were finetuned.

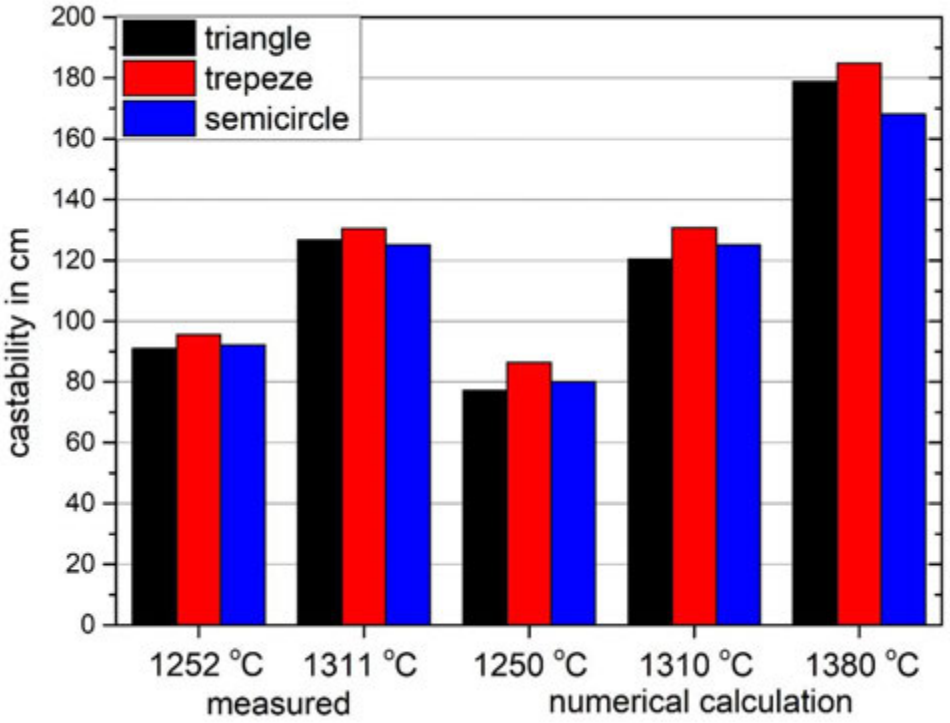


Figure 6. Measured length of castability for experiment and numerical calculation at different temperatures

## CONCLUSION

The comparison of the measured and calculated results of castability obtained at different purring temperatures confirms that the castability is dependent on purring temperature – higher the purring temperature better the castability.
From the measured and calculated results it is clear that the best castability at a constant cross-section has trapeze shape which has best thermal modulus.

## REFERENCES

[1] J. Campbell, R. A. Harding, The Fluidity of molten metals, The University of Birmingham, Birmingham, 1994.
[2] M. Gorny, Castability of ductile iron in thin walled castings, Arcives of Foundry Engineering, 8 (2008) 3, pp. 59-64.
[3] M. Žbontar, Postavitev metode za določanje livnosti sive litine, Bachelor thesis, 2016.

17th INTERNATIONAL FOUNDRYMEN CONFERENCE
Hi-tech casting solution and knowledge based engineering
Opatija, May 16th-18th, 2018
http://www.simet.hr/~foundry/

# PROPERTIES OF CONTINUOUSLY CASTED Cu-Al ALLOY

**Stjepan Kožuh[1]*, Vlado Džomba, Tamara Holjevac Grgurić[1], Ivan Jandrlić[1], Borut Kosec[2], Mirko Gojić[1]**

[1] University of Zagreb Faculty of Metallurgy, Sisak, Croatia
[2] University of Ljubljana Faculty of Natural Sciences and Engineering, Ljubljana, Slovenia

**Poster presentation**
*Original scientific paper*

**Abstract**

In this work are shown properties of continuously casted Cu – 9.1Al alloy before and after heat treatment. The continuously cast cylindrical bar with 8 mm diameter was produced using the device for the vertical continuous casting which is connected with the vacuum induction furnace. Heat treatment was consisted of annealing at 900 °C/30 minutes and water quenching. Microstructural analysis was performed by optical microscopy (OM), scanning electron microscopy (SEM) equipped by device for energy dispersive spectroscopy (EDS) and using differential scanning calorimeter (DSC). Also, hardness and mechanical properties were measured. EDS analysis confirmed that as-cast state of Cu – 9.1Al alloy is successfully done and alloy with homogeneous composition was produced. Optical and scanning electron microscopy showed existence of dual-phase α+β microstructure, which keeps after heat treatment but with certain sporadic changes of α - phase shape. DSC analysis on all samples presented one endothermic change of the heat flow during the heating, which probably represents α→β transformation and one exothermic change of the heat flow during the cooling which probably represents β→α transformation. The effect of heat treatment on the hardness and yield strength values is insignificant, while the tensile strength decreases with annealing.

***Keywords**: Cu-Al alloy, heat treatment, microstructure, mechanical properties, hardness*

*Corresponding author (e-mail address): *kozuh@simet.hr*

## INTRODUCTION

Copper and copper alloys constitute one of the major groups of metals which have commercial application. They are widely used because of their good electrical and thermal conductivities, excellent resistance to corrosion, ease production and favorable strength and fatigue resistance. Copper alloys are generally nonmagnetic and can be readily soldered and brazed [1]. The aluminium bronzes are a group of copper-base alloy with approximately 5 to 11 wt. % aluminium with/without other additions. They have good resistance to atmospheric

corrosion with high strength and often can be used for bearing bushes in aircraft frames. Bronzes which containing only copper and aluminium have microstructure with a single α-phase up to about 8 wt. % aluminium and above that level is formed dual-phase α+β alloy. Aluminium bronzes with α+β microstructure have a similar resistance to general corrosion as α-alloy [2]. Alloy with about 10 wt. % aluminium exhibits the best comprehensive properties [3]. Also, in literature [4-6] was obtained that the heat treatment have interesting effects on mechanical properties and microstructure of aluminium bronzes.

Also, copper alloys can belong to a group of shape memory alloys. Good electrical and thermal conductivity makes shape memory alloys on Cu-basis very interesting for practical application. The main Cu-based alloys with potential for shape memory behavior can be classified in three groups: Cu-Al, Cu-Zn and Cu-Sn systems. Shape memory alloys are characterized by high-temperature stable β-phase. However, the base alloys have bad cold workability and martensite stabilization. Therefore, ternary and quaternary elements have been added to improve upon the properties and remove the drawbacks.

The aim of this paper is characterization of the base Cu-Al alloy, which will be used in the next step for production of quaternary alloy with shape memory effects and favorable properties. Consequently, in this research the microstructure and mechanical properties of Cu-9.1Al alloy, before and after heat treatment were analyzed.

## MATERIALS AND METHODS

The Cu-9.1Al alloy was prepared by melting of pure elements (copper purity 99.9%, aluminium purity 99.5%). Melting was performed in a vacuum induction furnace under protective argon atmosphere. Chemical composition of investigated alloy was estimated by Optical Emission Spectrometer ICP-OES AGILENT 700. Firstly, the ingot (ϕ110 mm x 180 mm) was produced by graphite mould casting and it was then remelted in the same furnace. Afterwards, continuous casting was followed. The continuously cast cylindrical bar with 8 mm diameter of Cu-Al alloy was produced using the device for the vertical continuous casting which is connected with the vacuum induction furnace, Fig. 1. Solid bars were produced directly from about 13.2 kg melt. The temperature of melted alloy during casting was maintained at 1050 °C. The process of remelting was performed in vacuum 1 mbar. During casting, pressure of argon protective atmosphere was set around 500 mbar. Casting speed was constantly 260-265 mm/min.

Heat treatment of samples was performed in laboratory electro-resistance chamber furnace. Solution annealing of samples was carried out at 900 °C for 15 minutes, followed by quenching in the room temperature water.

The microstructure is characterised by optical microscopy (OM) and scanning electron microscopy (SEM) equipped with energy dispersive spectroscopy (EDS). For OM and SEM analysis the samples were ground (from 120 to 1200 grade paper) and polished (0.3 μm $Al_2O_3$). The prepared samples were etched in a solution composed of 2.5 g $FeCl_3$ and 48 ml methanol in 10 ml HCl.

Thermal analysis was carried out using differential scanning calorimeter (DSC) STA 449 F1 Jupiter® Netzsch, in the temperature range from 20 °C to 900 °C, in the inert atmosphere of argon. DSC investigations were done through two cycles of heating and cooling, with heating/cooling rate of 10 °C/min.
Hardness was tested by Vickers method (HV1). Mechanical properties of samples were determined by tensile testing Zwick machine 50 kN.

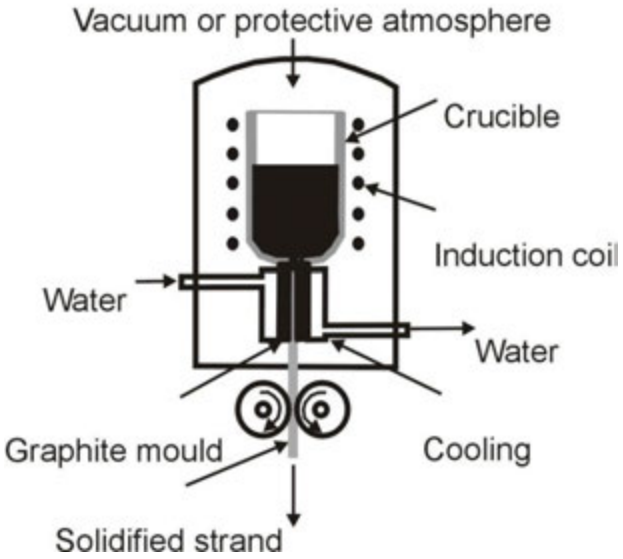


Figure 1. Schematic illustration of casting of Cu-Al alloy by vertical casting technology

## RESULTS AND DISCUSSION

Fig. 2 shows micrographs obtained by optical microscopy of the investigated Cu – 9.1 Al alloy. A more detailed analysis of micrographs obtained by optical microscopy in the as-cast state of Cu – 9.1Al alloy shows the dual-phase α + β microstructure. The dual-phase α + β microstructure is retained after quenching, although there is a certain change in α - phase morphology i.e. more needle shape of the α – phase is formed. According to the literature [4] when the 90% Cu - 10% Al is cooled in the equilibrium conditions α + β phase can be formed. The eutectic reaction takes place at 1037 °C and 8.5% Al and at 565 °C and 11.8% Al and β phase transformed in the $\gamma_2$ phase. During cooling at non-equilibrium conditions β phase can be replaced by a martensite phase β '. Cenoz and Gutierrez [4] mentioned that at the same time there may be present α and β phases in 90% Cu - 10% Al alloy at a temperature of about 500 °C, according to Cu-Al phase diagram. If the β - phase is rapidly cooled it transforms into α - phase of a similar composition. By cooling of the melt firstly is formed solid β – phase. Afterwards, at about 930 °C begins α - phase precipitation from the β - phase. The growth of α - phase is dependent on the rate of heat extraction. Depending on the cooling rate of α - phase there may be existed in two morphological shapes. The

spherical form of the α - phase is formed at some medium rate of cooling and at low and high cooling rates the preferred shape is needle-like [5].

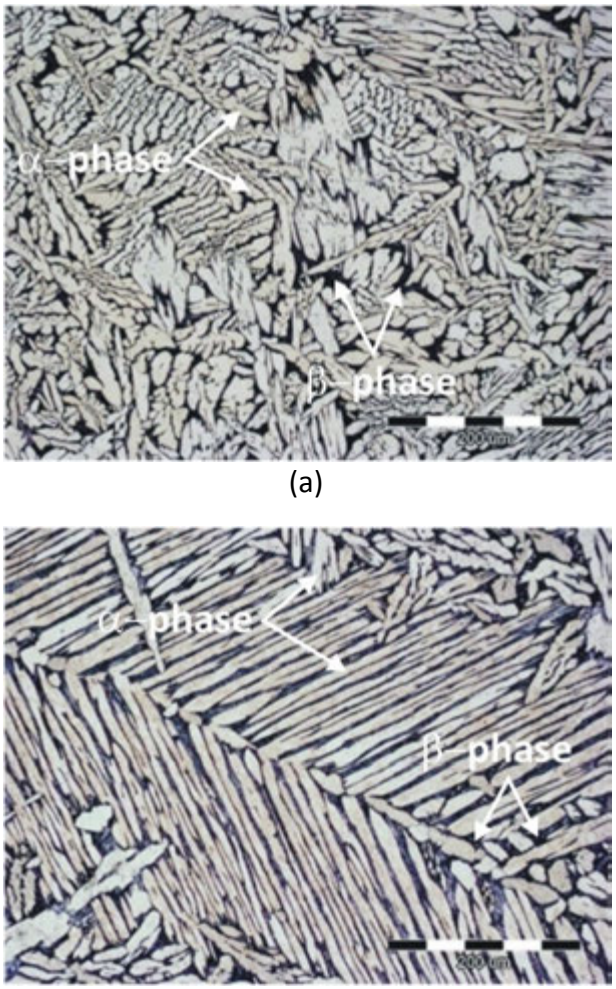


(a)

(b)

Figure 2. Optical micrographs of Cu-9.1Al alloy in as-cast state (a) and as-quenched state (900 °C/15'/$H_2O$) (b)

SEM micrographs can showed a more in detail of the microstructural changes. SEM micrographs of as-cast state Cu-9.1Al alloy show the dual-phase α + β microstructure throughout the cross-section of investigated sample (Figs. 3 and 4). From the results of EDS analysis (Table 1) it can be seen that there is no significant difference in chemical composition in all investigated positions. The as-quenched state (900 °C/15'/$H_2O$) shows a sporadically occurring appearance of properly oriented needles of α - phase which were like martensite shape. With a more detailed analysis of SEM micrographs and EDS results it can be concluded that vertical continuous casting process produced a rod (ϕ8 mm) in the as-cast state with a homogeneous microstructure with a copper content of 92.42 to 93.34 wt. % and aluminum 6.66 to 7.58 wt. % (Table 1). A somewhat lower part of aluminum content obtained by EDS analysis in regards to the chemical composition of Cu – 9.1 Al alloys can be

associated with the error of the EDS measurement i.e. EDS point analysis was performed. Also, SEM micrographs confirmed the presence of dual-phase α + β microstructure and formation of the needle shape α - phase after quenching.


(a)

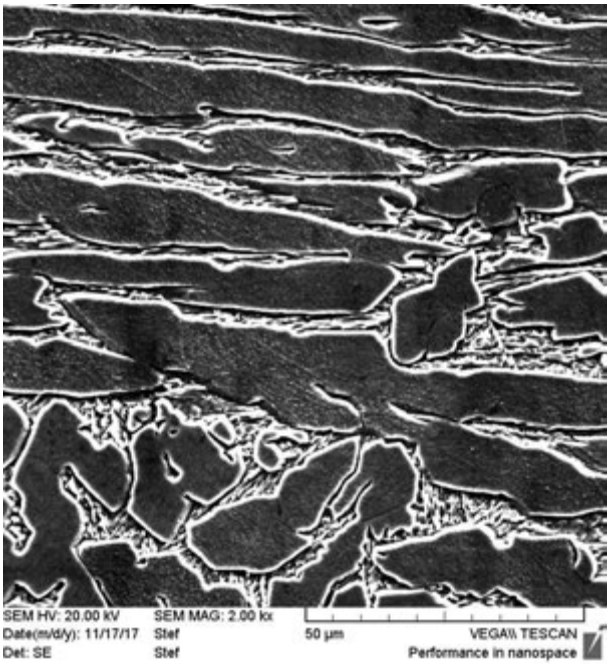


(b)

Figure 3. SEM micrographs of Cu-9.1Al alloy in as-cast state (a) and as-quenched state (900 °C/15'/$H_2O$) (b)

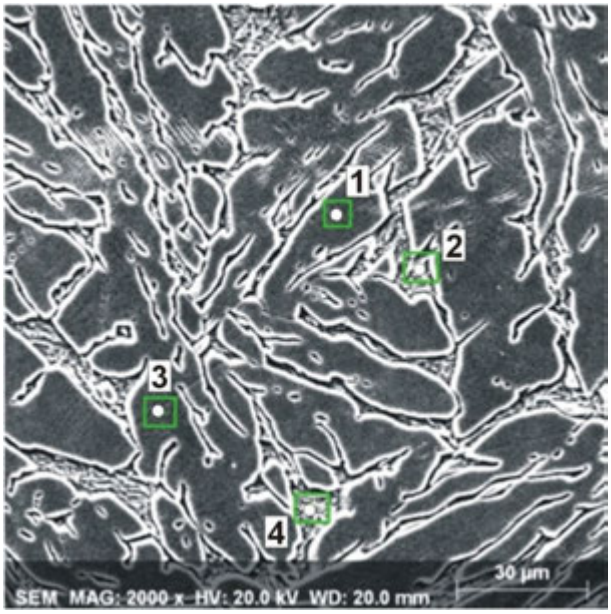


(a)

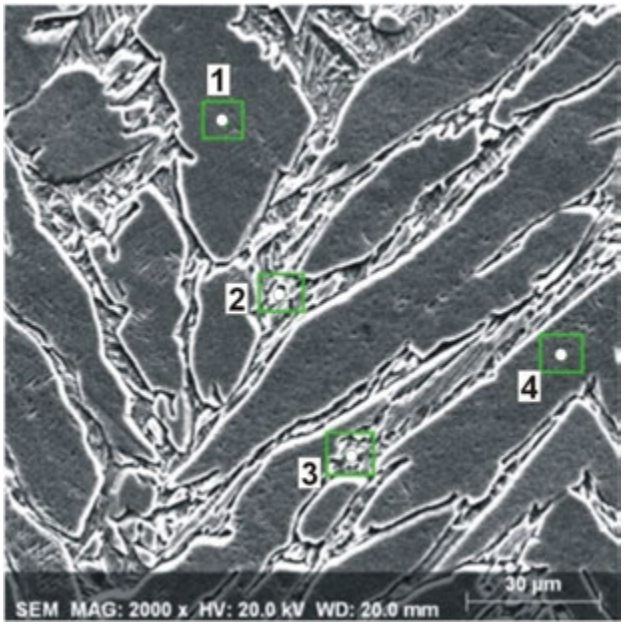


(b)

Figure 4. SEM micrographs of Cu-9.1Al alloy in as-cast state (a) and as-quenched state (900 °C/15'/$H_2O$) (b) with marked positions for EDS analysis

Table 1. The chemical composition of the Cu-9.1Al alloy in as-cast state and as-quenched state (positions marked at the Fig. 3a and 3b), wt.%

| State of samples | Position | Chemical composition, wt.% | |
|---|---|---|---|
| | | Cu | Al |
| As-cast state | 1 | 93.10 | 6.90 |
| | 2 | 93.34 | 6.66 |
| | 3 | 92.42 | 7.58 |
| | 4 | 93.01 | 6.99 |
| As-quenched state (900 °C/15`/$H_2O$) | 1 | 93.50 | 6.50 |
| | 2 | 92.24 | 7.76 |
| | 3 | 87.07 | 12.93 |
| | 4 | 93.57 | 6.43 |

From the results of the DSC analysis it can be seen that in all investigated samples the almost identical changes of the thermal flow at about the identical temperature occurred (Fig. 5). In Fig. 5a it can be seen that the as-cast Cu – 9.1 Al alloy showed endothermic peak at 565.8-581.7 °C (DSC heating curve). One exothermic peak can be observed at the DSC cooling curve at 530.0-506.6 °C. In Fig. 5b it can be seen that on the DSC heating curve of the as-quenched Cu – 9.1Al alloy, the significant change of the thermal flow (endothermic peak) at 566.8-581.1 °C is occurred. Also, one exothermic change can be observed at the DSC cooling curve at 529.2-502.9 °C for as-quenched state. Compared of as-cast to as-quenched state, it can be concluded that there is no change in the temperatures of the endothermic and exothermic reactions. By analyzing the DSC curves obtained during the heating of the investigated samples and microstructures, endothermic reaction probably represents the α → β transformation. In contrast, on DSC cooling curves noted exothermic peak (both samples) at approximately the same temperature, probably represents the β → α transformation.

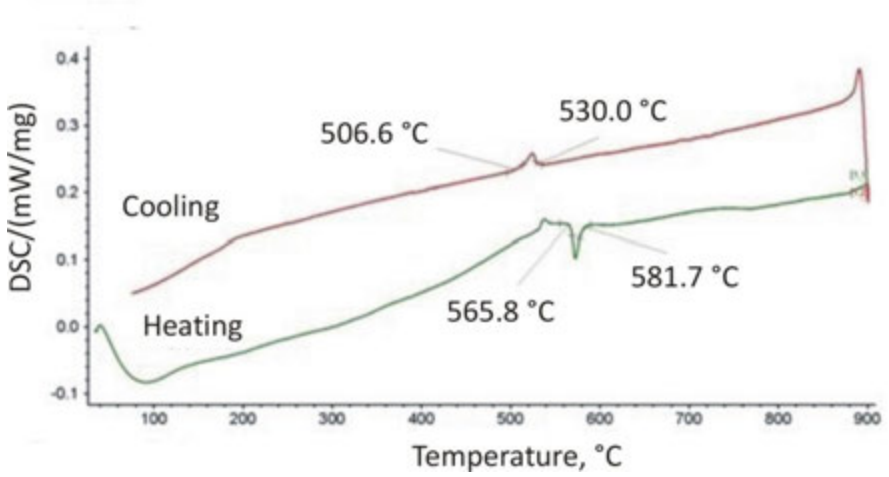


(a)

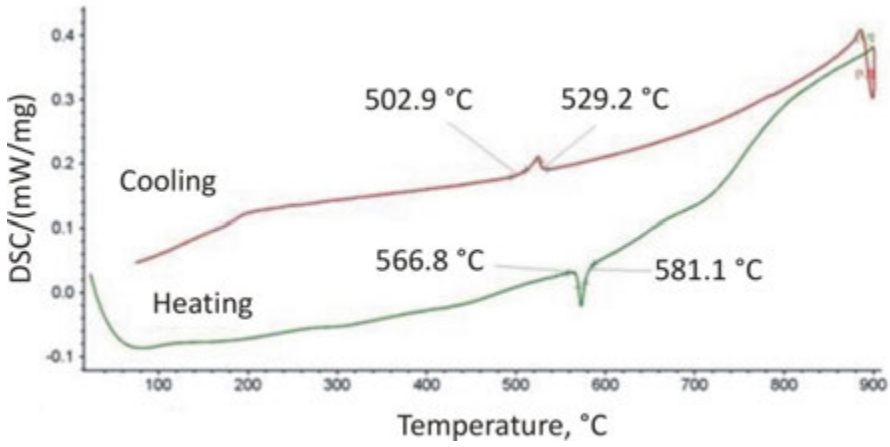


(b)

Figure 5. DSC diagrams of Cu-9.1Al alloy in as-cast state (a) and as-quenched state (900 °C/15'/$H_2O$) (b)

In Fig. 6 it can be seen that the as-cast state of Cu-9.1Al alloy has the lowest hardness value (156.47 HV1), in comparison with hardness value of as-quenched state (169.67 HV1). However, these differences are negligible and can be related to changes in microstructure and to error of measurement. The influence of quenching on the yield strength and tensile strength can be seen on Fig. 7. By the analysis of Fig. 7 it can be seen that the quenching has a low influence on the yield strength (values of 560.78 MPa in as-cast state and 577.67 MPa in as-quenched state). In the contrast, the values of tensile strength show a significant drop after the quenching. In as-cast state the tensile strength value was 1509.9 MPa, while after quenching it decreases to 1082.47 MPa. Fig. 8 shows the influence of quenching on elongation and contraction of Cu-9.1Al alloy. The largest elongation value was observed in the as-cast state (32.31%) and slightly decreased in as-quenched state (30.10%). The

contraction shows the same tendency. As-cast state has contraction value of 50.82% and as-quenched state 45.94%.

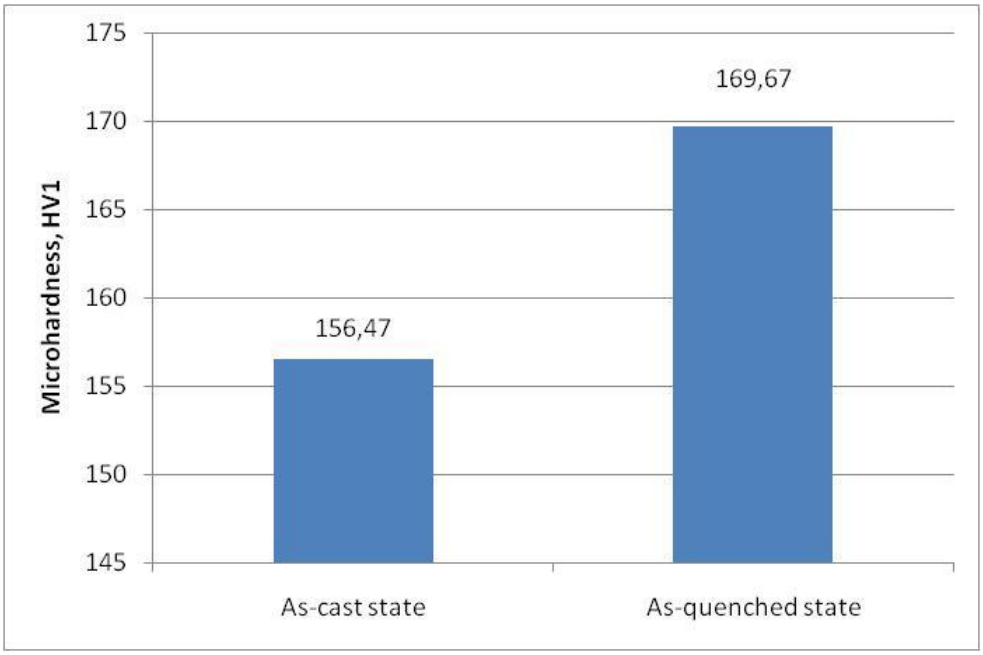


Figure 6. Hardness values (HV1) of investigated Cu-9.1Al alloy in as-cast state and as-quenched state (900 °C/15'/$H_2O$)

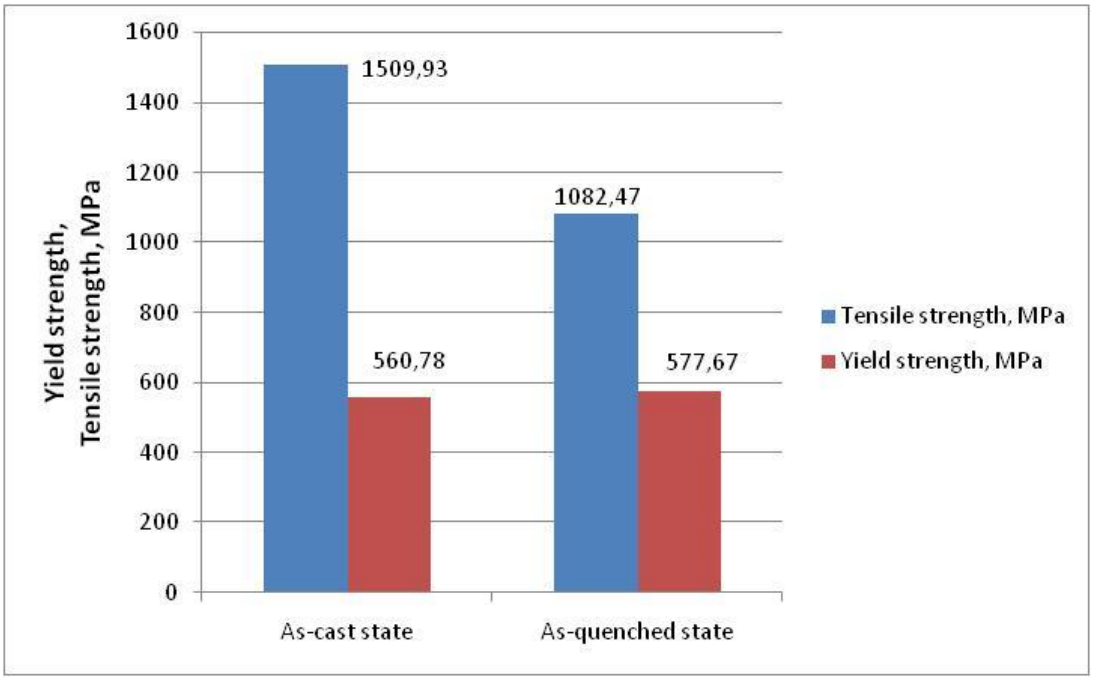


Figure 7. Tensile strength and yield strength of investigated Cu-9.1Al alloy in as-cast state and as-quenched state (900 °C/15'/$H_2O$)

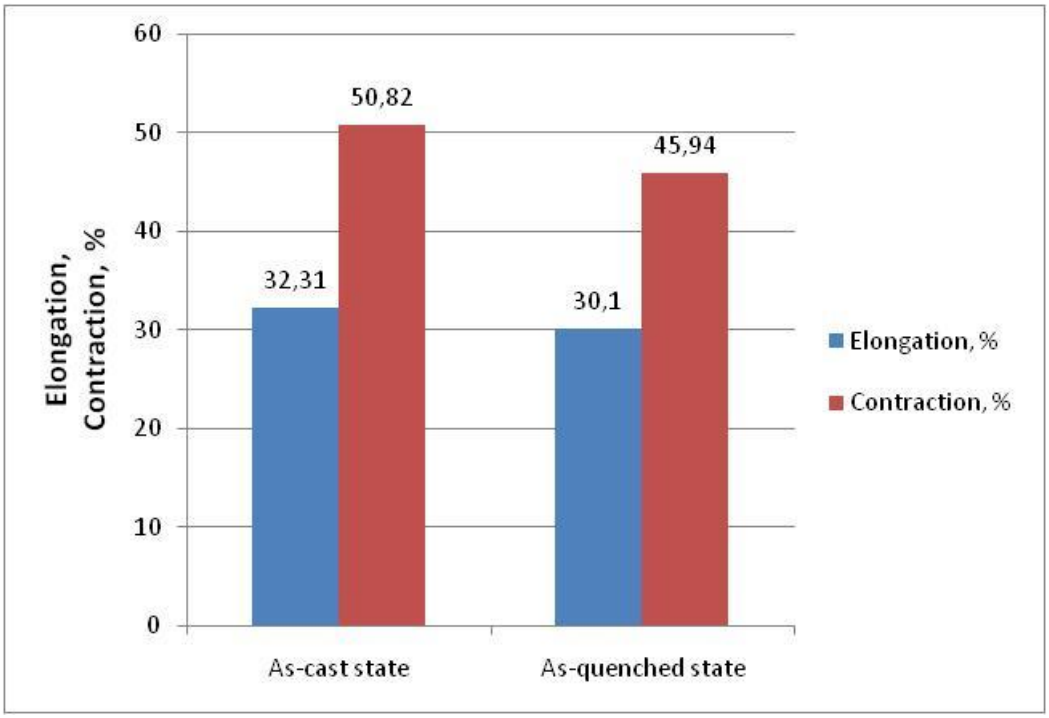


Figure 8. Elongation and contraction of investigated Cu-9.1Al alloy in as-cast state and as-quenched state (900 °C/15'/$H_2O$)

## CONCLUSIONS

The microstructural analysis with hardness and mechanical properties were carried out on bar (ϕ8 mm) of Cu-9.1Al alloy in as-cast state and as-quenched state (900 °C/15`/$H_2O$). From the obtained results we can draw the following conclusions:

- Optical microscopy established the presence of dual-phase α + β microstructure in investigated alloy in the as-cast state. The dual-phase α + β microstructure is retained after quenching but more needle shape of the α - phase is formed. Detailed SEM analysis confirmed the existence of dual-phase α + β microstructure at room temperature in both samples.
- The EDS analysis noted some small differences in the chemical composition in both investigated samples and all analyzed positions. This suggests that high homogeneity of alloy composition in as-cast state was achieved successfully.
- DSC analysis showed no change in the temperatures of the endothermic and exothermic reactions. The endothermic peak (at about 566-582 °C) in both investigated state probably represents the α → β transformation. Also, the exothermic peak in both samples was at approximately the same temperature and probably represents the β → α transformation.
- The as-cast state has the lowest hardness value (156.47 HV1), in comparison with hardness value of as-quenched state (169.67 HV1).

-The quenching has a low influence on the yield strength (values of 560.78 MPa in as-cast state and 577.67 MPa in as-quenched state). The values of tensile strength show a significant drop after the quenching. The largest elongation value was observed in the as-cast state (32.31%) and slightly decreased in as-quenched state (30.10%). The contraction shows the same tendency.

## REFERENCES

[1] ASM Handbook, Materials Characterization-Volume 10, ASM International, 1998.
[2] Aluminium Bronze Alloys-Corrosion Resistance Guide, Publication No 80, Copper Development Association, 1981. Accessible on Internet: http://copperalliance.org.uk/docs/librariesprovider5/resources/pub-80-aluminium-bronze-corrosion-resistance-pdf.pdf (08.03.2018.)
[3] W. S. Li, Z. P. Wang, Y. Lu, Y. H. Jin, L. H. Yuan, F. Wang, Mechanical and tribological properties of a novel aluminum bronze material for drawing dies, Wear, 261 (2006), pp. 155-163.
[4] I. Cenoz, M. Gutierrez, Phase transformation in Cu-Al alloy, Metal Science and Heat Treatment, 53 (2011) 5-6, pp. 265-269.
[5] I. Cenoz, Metallography of aluminium bronze alloy as cast in permanent iron die, Metallurgical&Materials Engineering-Association of Metallurgical Engineers of Serbia, 16 (2010) 2, pp. 115-122.
[6] M. Kaplan, A. K. Yildiz, The effects of production methods on the microstructure and mechanical properties of an aluminium bronze, Materials Letters, 57 (2003) pp. 4402-4411.

## Acknowledgements

This work has been fully supported by Croatian Science Foundation under the project IP-2014-09-3405.

17th INTERNATIONAL FOUNDRYMEN CONFERENCE
Hi-tech casting solution and knowledge based engineering
Opatija, May 16th-18th, 2018
http://www.simet.hr/~foundry/

# INFLUENCE OF GRAPHITE NODULARITY ON PLASTIFICATION AROUND CRACK TIP OF DUCTILE IRON

**Martina Lovrenić-Jugović[1]*, Dragan Pustaić[2**], Ladislav Lazić[1], Jakov Baleta[1]**

[1] University of Zagreb Faculty of Metallurgy, Sisak, Croatia
[2] University of Zagreb Faculty of Mechanical Engineering and Naval Architecture, Zagreb, Croatia

**Poster presentation**
*Original scientific paper*

**Abstract**

The dependence of plastic zone magnitude around crack tip on graphite nodularity of cast iron was considered in this paper. Mechanical properties of four different samples of cast iron as a function of graphite nodularity (21%, 52%, 77% and 95%) were taken from available literature. At plastic deformation, the cast iron is nonlinearly hardened in accordance with the Ramberg-Osgood equation. Those data was fitted with nonlinear Ramberg-Osgood equation, where material parameters were determined using least-squares method. Thin infinite plate with straight crack was loaded perpendicularly to the crack plane. Plastic zone magnitude around the crack tip was determined according to the Dugdale model. A nonlinear isotropic strain hardening of a plate material was assumed. The stress intensity coefficient from the cohesive stresses was calculated using Green functions. The analytical methods, assuming small plastic zone around a crack tip, were used in the analysis. The results were obtained by means of commercial software package and presented in the form of diagrams.

***Keywords**: graphite nodularity, Ramberg-Osgood equation, strain hardening exponent, Dugdale model, plastic zone magnitude around crack tip*

*Corresponding author (e-mail address): *mlovrenic@simet.hr*
** Professor in retirement

## INTRODUCTION

In spite of the fact that numerical methods are widely used in solving engineering problems in different fields of mechanics, in particular the finite element method, the analytical methods will be applied in solving the problems presented in this paper. A straight crack, with the length 2*a*, in a thin infinite plate loaded on its edges, is considered here. The plate is made of a ductile material; therefore cohesive zones around crack tips occur when the plate is loaded. Our aim is to investigate the dependence of the magnitude of the plastic zone

around crack tip $r_p$ on graphite nodularity of cast iron. Mechanical properties of four different samples of cast iron as a function of graphite nodularity are taken from the diagrams in the literature [1].

Since there is a lack of literature data of investigating the dependence of the magnitude of the plastic zone around crack tip $r_p$ on graphite nodularity of cast iron, this paper deals with analytical solution of the posed problem.

A thin, infinite plate with an embedded central straight crack of a length 2*a* was modelled analytically in this paper. A plate is uniaxially loaded in a direction perpendicular to the crack plane by monotonously increasing loading $\sigma_{yy}^{\infty} = \sigma_{\infty}$. A crack surface is unloaded. A plate material has a property of isotropic strain hardening (nonlinear strain hardening). A plane stress state determined by the stress tensor components $\sigma_{xx}(x,y)$, $\sigma_{yy}(x,y)$ and $\sigma_{xy}(x,y)$ is assumed. For an analysis of the elastic-plastic fracture mechanics parameters it is important to consider the stress tensor components and the displacement vector components of the points lying on a direction of a crack plane, i.e. on the *x*-axis. Since there is symmetry with respect to *x*-axis, the shear stresses at the points laying on the *x*-axis will be equal to zero, i.e. the normal stresses $\sigma_{xx}(x,0)$ and $\sigma_{yy}(x,0)$ are the principal stresses. An equivalent stress $\bar{\sigma}$ is determined according to the Tresca or to the Mises yield criteria. The equivalent stress is dependent on the equivalent plastic strain $\bar{\varepsilon}_p$. Because a distribution law of equivalent plastic strain $\bar{\varepsilon}_p$ is not known, the distribution law of the cohesive stresses within a yield zone will be also unknown.

There are a great number of different methods, especially numerical, which can be used for determining the magnitude of the plastic zone around the crack tip. The Dugdale strip yield model [2,3] in the yielding zone around the crack tip is used for that purpose here. According to this model, the plastic zone is a narrow strip extending from the crack tip in the direction of the crack plane, as it is shown in Figures 1a and 1b. The Dugdale model considers, instead of a real, physical crack, an equivalent elastic crack of length 2*b*, as it is shown in Figure 1c. Partial areas of this imaginary elastic crack $a \leq x \leq b$ are subjected to nonlinear cohesive stresses $p(x)$, (Figure 1c).

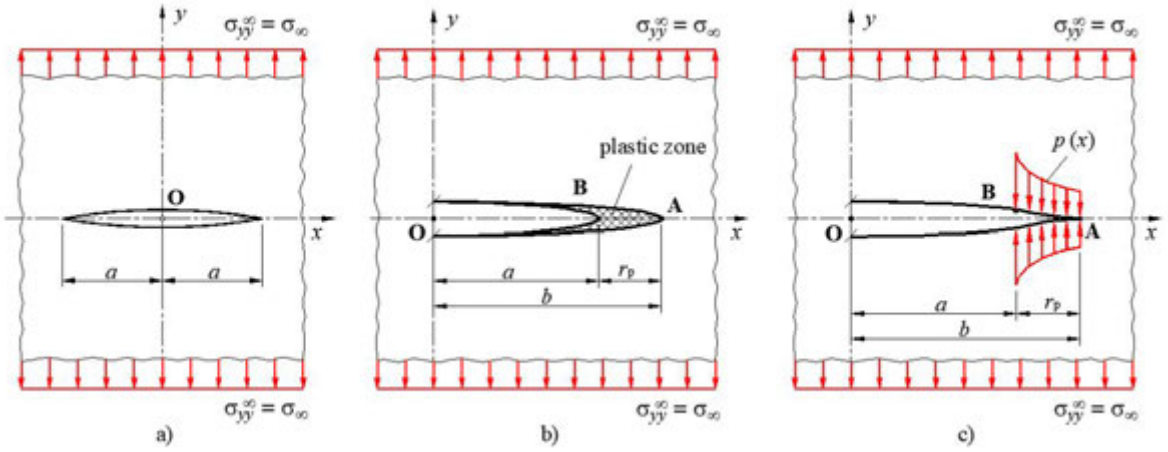


Figure 1. a) Thin, infinite plate with straight crack of a length 2*a* loaded perpendicular to the crack plane, b) fictitious elastic crack including a small plastic zone around crack tip, c) variable cohesive stresses act on a part of fictitious elastic crack

On the edges of plastic zones, or on the tips of an equivalent elastic crack, the normal stress $\sigma_{yy}(b,0)$ will not have singularity, but will have a definite quantity equal to the yield stress of the plate material $\sigma_0$. In other words, the stress intensity coefficient *K* in these points will be equal to zero, i.e.

$$K(a+r_p) = K_{ext}(a+r_p) + K_{coh}(a+r_p) = 0, \quad (1)$$

where $K_{ext}$ and $K_{coh}$ are the stress intensity coefficient of external and cohesive loading of the plate, respectively. The singularity at the tip of the fictitious elastic crack $x = b = a + r_p$, from the external load of the plate, is cancelled with the singularity of the cohesive stresses within the plastic zone.

## STRESS–STRAIN DIAGRAMS OF CAST IRONS

In the literature [1] the samples of cast irons containing different graphite nodularity were analysed. By treating the cast iron of suitable base composition with different amount of spheroidizing (Mg) and antispheroidizing (Ti) elements different degrees of graphite nodularities, from low graphite nodularity of about 21% up to high graphite nodularity of 95%, were produced. It is evident that ferritic fraction for all levels of graphite nodularity has approximately the same values. In this paper the mechanical properties of four different samples of cast iron as a function of graphite nodularity were taken from diagrams, which are presented in the literature [1] (Table 1).

Table 1. Mechanical properties of cast iron [1]

| Nodularity (%) | 0.2% offset yieldstress (MPa) | Ultimate tensile stress (MPa) | Elongation (%) |
|---|---|---|---|
| 21 | 280 | 360 | 3 |
| 52 | 300 | 440 | 5 |
| 77 | 350 | 550 | 8 |
| 95 | 430 | 680 | 12 |

All of the properties related to strength [1] decrease as the proportion of non-nodular graphite increases. As can be seen, the tensile stresses are more affected by the small amount of non-nodular graphite. Due to missing data of modulus of elasticity *E* in reference [1], the mean value of the measured modulus of elasticity of 170 GPa of nodular cast iron with the same chemical composition in reference [4], was taken and included in the further analysis in this paper. The data from Table 1 and the value of mentioned modulus of elasticity are shown in the form of engineering stress-strain diagram in Figure 2.

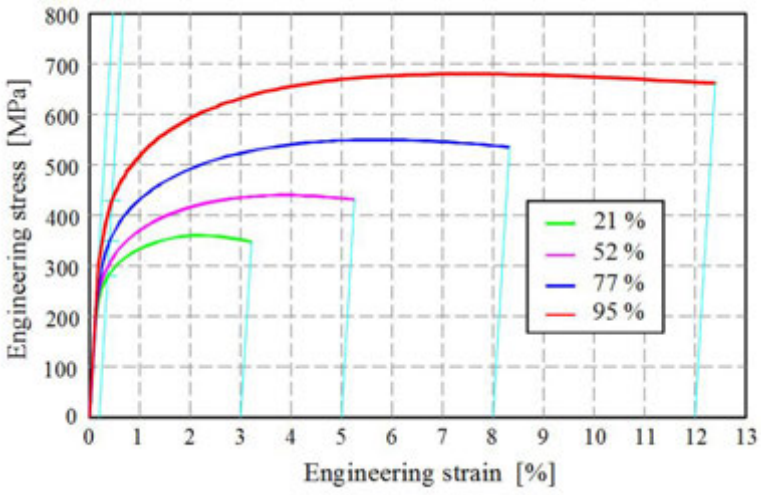


Figure 2. Engineering stress–strain diagram of four graphite nodularity gradations

The relationships between engineering and true values of stresses and strains are presented by expressions

$$\sigma_{\text{true}} = \sigma(1+\varepsilon), \tag{2}$$

$$\varepsilon_{\text{true}} = \ln(1+\varepsilon), \tag{3}$$

where $\sigma$ and $\varepsilon$ are the engineering stress and strain, respectively, and $\sigma_{\text{true}}$ and $\varepsilon_{\text{true}}$ are the true stress and strain, respectively. Using eqs (2) and (3) engineering stress–strain diagram was transformed to the true stress–strain diagram for four graphite nodularity gradations of considered cast iron. Results of transformation are presented in Figure 3.

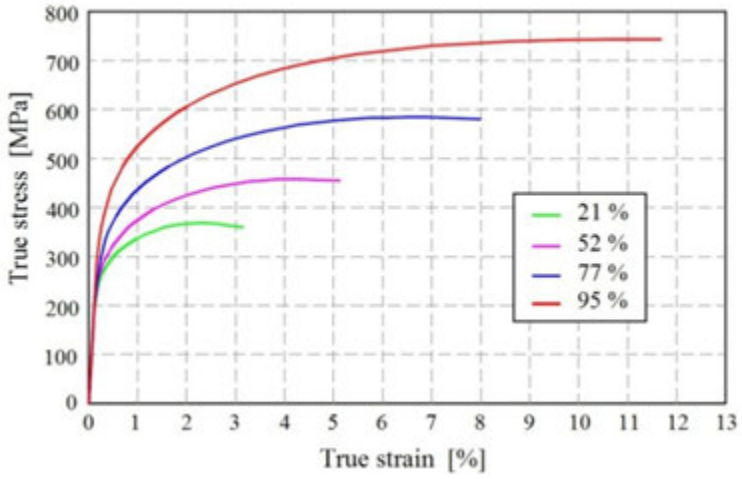


Figure 3. True stress–strain diagram for four graphite nodularity gradations

During the plastic deformation, the cast iron is nonlinearly hardened and the correlation between true stress and true strain could be found in accordance with the Ramberg-Osgood equation, [5]

$$\frac{\varepsilon}{\varepsilon_0} = \frac{\sigma}{\sigma_0} + \alpha \left( \frac{\sigma}{\sigma_0} \right)^n \quad , \tag{4}$$

where $\sigma_0$ and $\varepsilon_0$ denote the material's yield stress and strain, respectively, while $\alpha$ and $n$ denote Ramberg-Osgood's material constant and strain hardening parameter, respectively. If it is taken $\varepsilon_0 = \sigma_0 / E$, the Ramberg-Osgood equation takes the form

$$\varepsilon = \frac{\sigma}{E} + \alpha \frac{\sigma_0}{E} \left( \frac{\sigma}{\sigma_0} \right)^n \quad . \tag{5}$$

According to Table 1, the cast irons have a yield stress of 0.2% offset ($R_{p0.2}$). Instead of the yield stress $\sigma_0$ in equation (5), the 0.2% offset yield stress $R_{p0.2}$ was introduced. Plastic component of the strain tensor $\varepsilon_{pl}$ has an amount of 0.002 for $\sigma = \sigma_0 = R_{p0.2}$. Then equation (5) becomes

$$\varepsilon(\sigma = \sigma_0 = R_{p0.2}) = \frac{\sigma}{E} + \alpha \frac{\sigma_0}{E} = \varepsilon_{el} + 0.002 \, . \tag{6}$$

Fitting data in Figure 3 of four different samples of cast iron by using a least-squares method, the material parameters of nonlinear Ramberg-Osgood equation (5) were found and shown

in Table 2. They are also presented in a form of the diagram in Figure 4. With increasing the graphite nodularity, it was noticed that the material parameters $\alpha$ and $n$ are slightly reduced.

Table 2. Ramberg-Osgood's material parameters

| Nodularity (%) | $\alpha$ | $n$ | $R^2$ |
|---|---|---|---|
| 21 | 1.2142857 | 8.09116 | 0.97994 |
| 52 | 1.1333333 | 6.68551 | 0.97847 |
| 77 | 0.9714286 | 6.30552 | 0.98126 |
| 95 | 0.7906977 | 6.24078 | 0.98782 |

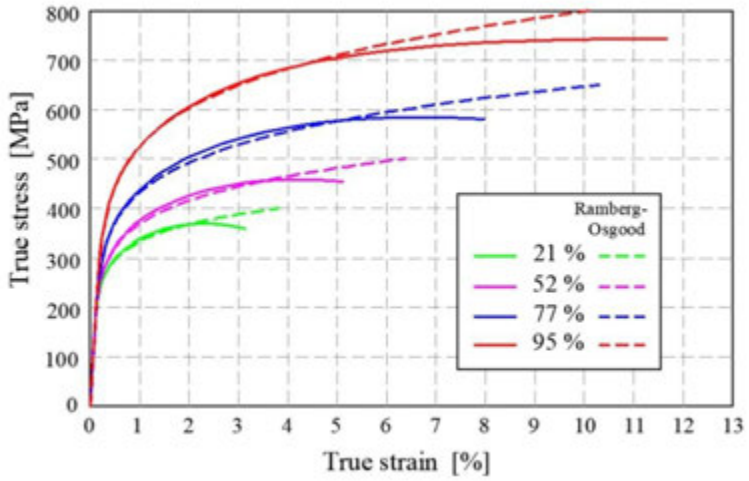


Figure 4. Comparison of Ramberg-Osgood's and true stress–strain curves for four graphite nodularity gradations

## DETERMINATION OF PLASTIC ZONE MAGNITUDE AROUND CRACK TIP

The best approximation of the nonlinear distribution of the cohesive stresses [2,3] is achieved by the analytical expression

$$p(x) = \sigma_0 \left( \frac{r_p}{x - a} \right)^{1/(n+1)} . \tag{7}$$

The physical quantity $p(x)$ is a function of the two parameters, i.e. $r_p$ and $n$. The other researchers suggested in their papers similar analytical expressions for the distribution of cohesive stress within a yield zone, for example, A. Neimitz, [6].
The stress intensity coefficient $K$ and the magnitude of plastic zone around a crack tip $r_p$ can be determined by using the method of weight functions (Green's function). The Green's function for an infinite cracked plate, loaded on stretching in a direction perpendicular to the crack plane, according to D. Pustaić [7] amounts

$$m(x,b)=2\sqrt{\frac{b}{\pi}}\left(b^2-x^2\right)^{-1/2}. \tag{8}$$

The stress intensity coefficient can be calculated using the Green's function [2, 7-8], knowing the distribution of the cohesive stresses (7), as

$$K_{\mathrm{coh}}(b)=\int_a^b p(x)\cdot m(x,b)\,\mathrm{d}x. \tag{9}$$

Introducing a new variable $\xi$, according to [2], the variable $x$ has the form $x=a+r_p(1-\xi)=b-r_p\xi$ ($\xi=1$ for $x=a$, and $\xi=0$ for $x=b$), the expression (7) is transformed in the following form

$$p(\xi)=\sigma_0\left(1-\xi\right)^{-1/(n+1)}. \tag{10}$$

Inserting the expressions (8) and (10) in (9) and after arranging the following expression is obtained

$$K_{\mathrm{coh}}\left(b\right)=\sqrt{\frac{2}{\pi}r_{\mathrm{p}}}\cdot\sigma_0\int_0^1\frac{1}{\left(1-\xi\right)^{1/(n+1)}}\cdot\frac{1}{\left[\xi\left(1-\dfrac{r_{\mathrm{p}}}{2b}\xi\right)\right]^{1/2}}\mathrm{d}\xi. \tag{11}$$

By forming the above expression the assumption about small crack tip plastic zone can be introduced. Under small scale yielding (SSY) condition it could be taken $r_{\mathrm{p}}/2b\approx 0$. After integration, the final result for $K_{\mathrm{coh}}(b)$ has the form

$$K_{\mathrm{coh}}\left(b\right)=\sqrt{\frac{2}{\pi}r_{\mathrm{p}}}\cdot\sigma_0\frac{\Gamma\left(\dfrac{1}{2}\right)\cdot\Gamma\left(\dfrac{n}{n+1}\right)}{\Gamma\left(\dfrac{1}{2}+\dfrac{n}{n+1}\right)}=\sqrt{\frac{2}{\pi}r_{\mathrm{p}}}\cdot\sigma_0\,B\left(\frac{1}{2},\frac{n}{n+1}\right), \tag{12}$$

where $\Gamma(x)$ stands for the gamma function or the Euler's integral of second type and $B(x, y)$ is the beta function or the Euler's integral of first type. This result must be taken with opposite sign because the stress intensity coefficient $K_{\mathrm{coh}}(b)$ takes the negative value if calculations are being conducted for direction of the cohesive tensile stresses. The stress intensity coefficient, corresponding to a remote tension of a plate with an imaginary crack of length $b$, amounts to $K_{\mathrm{ext}}(a+r_{\mathrm{p}})=\sigma_\infty\sqrt{\pi\left(a+r_{\mathrm{p}}\right)}$. Finally, the plastic zone length $r_{\mathrm{p}}$ in front of the crack tip [8], normalized to the initial crack length $a$, is obtained as

$$\frac{r_p}{a}=\frac{\pi}{2}\left(\frac{\sigma_\infty}{\sigma_0}\right)^2\cdot\frac{\left[\Gamma\left(\frac{1}{2}+\frac{n}{n+1}\right)\Big/\Gamma\left(\frac{n}{n+1}\right)\right]^2}{1-\frac{\pi}{2}\left(\frac{\sigma_\infty}{\sigma_0}\right)^2\cdot\left[\Gamma\left(\frac{1}{2}+\frac{n}{n+1}\right)\Big/\Gamma\left(\frac{n}{n+1}\right)\right]^2}. \quad (13)$$

**RESULTS AND DISCUSSION**

On the basis of analytical expression (13), the values of plastic zone magnitude $r_p$ in front of the crack tip, normalized to the initial crack length $a$, are calculated in dependence upon monotonously increasing external load $\sigma_\infty/\sigma_0$, for the four different gradations of graphite nodularity of cast iron. The results were obtained by means of commercial software package *Mathematica* and presented in the form of diagrams in the Fig. 5.
It is important to note that this analysis is valid only for a small plastic zone around a crack tip ( $r_p/a < 0.5$ ) - ( SSY - small scale yielding conditions), i.e. the stress ratio has to be $\sigma_\infty/\sigma_0 < 0.5$ to 0.6.

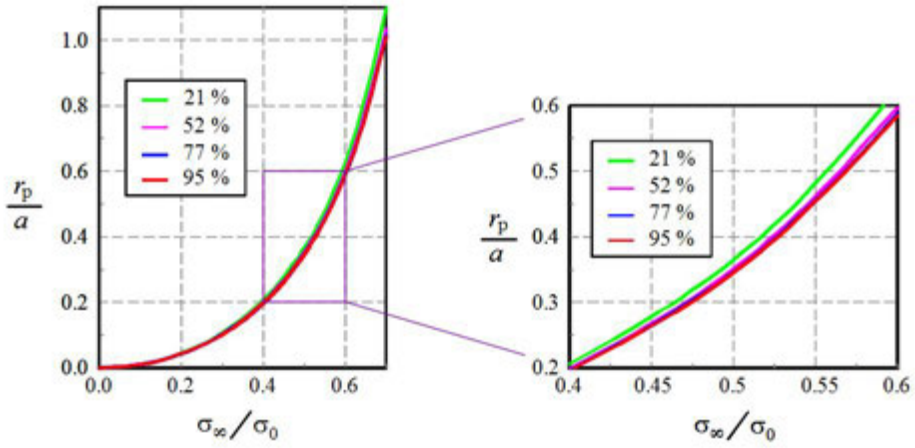


Figure 5. Dependence of plastic zone magnitude $r_p$ on a load $\sigma_\infty/\sigma_0$ of four gradations of graphite nodularity

The results of the magnitude of plastic zone $r_p$ in Fig. 5 are presented as a function of the external load which is normalized to 0.2% offset yield stress ($\sigma_\infty/\sigma_0$). This display of results includes only the strain hardening parameter $n$ of the Ramberg-Osgood equation, which according to Table 2 does not differ too much for four gradations of graphite nodularity. With such depiction of dependence, the results do not differ too much. As it can be seen in Fig. 5, the magnitude of plastic zone $r_p$ becomes greater as nodularity of graphite decreases, for the same level of external load ($\sigma_\infty/\sigma_0$). The diagram in Fig. 5 shows that the sample with the smallest nodularity (21%) gives the largest size of the plastic zone.

In order to include the influence of second material parameter $\alpha$ in the diagram representation, the results should be calculated for particular size of the external load. The material parameter $\alpha$ according to equation (6) is determined for 0.2% offset yield stress. From the Table 1 is evident that with increasing the graphite nodularity, the 0.2% offset yield stress is also increased. For that reason, the plastic zone magnitude was shown and calculated for the particular size of the external load of $\sigma_\infty = 200\,\mathrm{MPa}$. Dependence of the plastic zone magnitude on graphite nodularity at the load of 200 MPa is shown in Fig. 6.

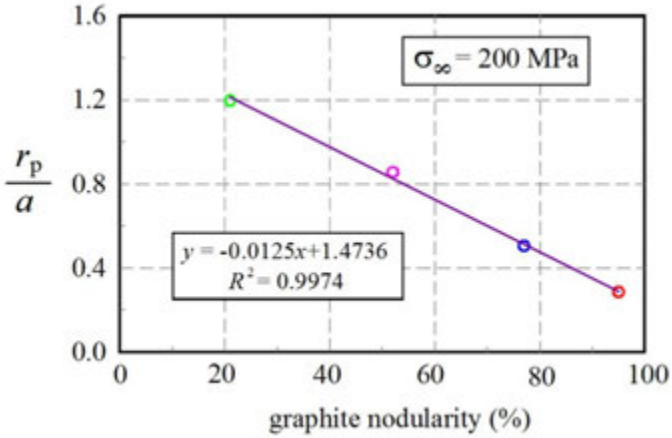


Figure 6. Dependence of plastic zone magnitude $r_p$ at load $\sigma_\infty = 200\,\mathrm{MPa}$ on graphite nodularity

The magnitude of the plastic zone in front of the crack tip at the load of 200 MPa decreases with increasing the graphite nodularity. This dependence can be linearized according to the equation shown in Fig. 6.

## CONCLUSION

The dependence of the magnitude of the plastic zone around the crack tip $r_p$ on the graphite nodularity of cast iron was analytically investigated in this paper. Mechanical properties of four different samples of cast iron as a function of the graphite nodularity of 21%, 52%, 77% and 95% were included in this analysis. The Dugdale model of plastic yielding was used for modelling the narrow yield bands around the crack tips, under the assumption that the cohesive stresses are distributed nonlinearly in the yielded zone. The stress intensity coefficient from the cohesive stresses was determined by the Green function's method.
The magnitude of the plastic zone in front of the crack tip $r_p$ increases as the nodularity of graphite decreases for the same level of external load ($\sigma_\infty/\sigma_0$). This functional dependence becomes linear at the load of 200 MPa.

**REFERENCES**

[1] A. I. Al-Ghonamy, M. Ramadan, N. Fathy, K. M. Hafez, A. A. El-Wakil, Effect of Graphite Nodularity on Mechanical Properties of Ductile Iron for Waterworks Fittings and Accessories, International Journal of Civil & Environmental Engineering IJCCE-IJENS, 10 (2010) 3, pp. 1-5.
[2] X. G. Chen, X. R. Wu, M. G. Yan, Dugdale Model for Strain Hardening Materials, Engineering Fracture Mechanics, 41 (1992) 6, pp. 843-871.
[3] M. Hoffman, T. Seger, Dugdale Solutions for Strain Hardening Materials, The Crack Tip Opening Displacement in Elastic-Plastic Fracture Mechanics, In Proceedings of the Workshop on the CTOD Metodology, Geesthacht, 1985, pp. 57-77.
[4] P. Čanžar, Z. Tonković, J. Kodvanj, Microstructure influence on fatigue behavior of nodular cast iron, Materials Science & Engineering A, 556 (2012) pp. 88-99.
[5] W. Ramberg, W. R. Osgood, Description of stress-strain curves by three parameters, National advisory committee for aeronautics, Technical note no. 902. Accessible on Internet: http://www.apesolutions.com/spd/public/NACA-TN902.pdf, 25.1.2018.
[6] A. Neimitz, Modification of Dugdale model to include the work hardening and in–and out-of-plane constraints, Engineering Fracture Mechanics, 71 (2004) 11, pp. 1585-1600.
[7] D. Pustaić, M. Lovrenić, Analytical and Numerical Investigation of Crack Opening in Strain - Hardening Material, Proceedings of the 5th International Congress of Croatian Society of Mechanics, (F. Matejiček (ed.)), Croatian Society of Mechanics, 21-23.09., 2006, Trogir, Croatia, pp. 141-142.
[8] M. Siratori, T. Miesi and H. Macusita, Numerical Fracture Mechanics, Mir Publisher, Moscow, 1986, [in Russian].

17th INTERNATIONAL FOUNDRYMEN CONFERENCE

Hi-tech casting solution and knowledge based engineering

Opatija, May 16th-18th, 2018

http://www.simet.hr/~foundry/

# MONITORING OF RADIONUCLIDES IN STEEL SCRAP INTENDED FOR RECYCLING IN STEEL MILLS AND FOUNDRIES

# MONITORING RADIONUKLIDA U ČELIČNOM OTPADU NAMIJENJENOM OPORABI U ČELIČANAMA I LJEVAONICAMA

**Don Vito Lukšić[1]*, Tahir Sofilić[2]**

[1] University of Zagreb Faculty of Metallurgy, Sisak, Croatia
[2] Tina Ujevića 25, Sisak, Croatia

**Poster presentation**
*Review*

**Abstract**

Production of steel by the recovery of steel scrap today represents a very important industrial activity worldwide, and its social and ecological utility has been contributed to the preservation of natural sources of ore and energy savings. However, over the last 30 years, a number of unlucky cases have been reported in this activity with radioactive sources that were unintentionally found in recycled steel scrap. The consequences of these incidents were very serious in terms of protecting people and the environment from the harmful effects of ionizing radiation, as well as from an economic point of view.

The purpose of this paper was to point out the need to introduce radionuclide monitoring and monitoring systems in steel and steel casting processes in steel mills and foundries to improve the quality and environmental management system without which no modern steel and steel casting manufacturer can be imagined. The construction of a monitoring system for radionuclide monitoring in steel and casting production processes simultaneously represents a guarantee of the competitiveness of their products on the European and world market which is increasingly demanding in terms of the quality of these products and increasingly requires a certificate of radionuclide content.

This paper presents the basic types of radionuclide monitoring and monitoring system, the most common requirements to be met by such devices, and the process of measurement and imaging monitoring of radionuclide in steel waste.

***Keywords***: *radionuclides, monitoring, steel, steel mill, foundry*

*Corresponding author (e-mail address): *dvluks@simet.hr*

**Sažetak**

Proizvodnja čelika oporabom čeličnog otpada danas predstavlja vrlo važnu industrijsku djelatnost širom svijeta, a čemu je doprinijela njena društvena i ekološka korisnost koja se ogleda u čuvanju prirodnih izvora ruda i štednji energije. Međutim, tijekom posljednjih 30-tak godina u ovoj djelatnosti je zabilježen veći broj nesretnih slučajeva s radioaktivnim izvorima koji su se nehotice našli u prikupljenom čeličnom otpadu namijenjenom recikliranju. Posljedice tih nezgoda bile su vrlo ozbiljne s obzirom na zaštitu ljudi i okoliša od štetnih učinaka ionizirajućeg zračenja, a jednako tako i s gospodarskog stajališta.
Svrha ovog rada je bila ukazati na potrebu uvođenja sustava za nadzor i praćenje radionuklida u procesima proizvodnje čelika i čeličnih odljevaka u čeličanama i ljevaonicama, čime bi se unaprijedio sustav upravljanja kvalitetom i okolišem bez kojeg se ne može zamisliti niti jedan suvremeni proizvođač čelika i čeličnih odljevaka. Izgradnja monitoring sustava za nadzor radionuklida u ovim proizvodnim procesima istovremeno predstavlja jamstvo konkurentnosti njihovih proizvoda na europskom i svjetskom tržištu, koje je sve zahtjevnije glede kvalitete ovih proizvoda i sve češće zahtjeva certifikat ili izjavu proizvođača da proizvod ne sadrži radionuklide.
U radu su prikazani osnovni tipovi sustava za nadzor i praćenje radionuklida, najčešći zahtjevi koje trebaju ispunjavati ovakvi uređaji, te tijek provedbe mjerenja i dojavljivanja pri monitoringu radionuklida u čeličnom otpadu ili pak gotovom proizvodu.

***Ključne riječi:*** *radionuklidi, monitoring, čelik, čeličana, ljevaonica*

## UVOD

Čelik danas predstavlja najvažniji konstrukcijski materijal i koristi se u gotovo svim područjima tehnike, a uglavnom se proizvodi u kisikovim konvertorima, elektrolučnim pećima ili postupcima pretaljivanja. Na ovaj način se dobiva tzv. sirovi čelik koji se različitim postupcima prerađuje u vrlo široki spektar čeličnih proizvoda. Također, vrlo čestu primjenu, posebice u strojogradnji, imaju i različiti proizvodi nastali u ljevaonicama čeličnog lijeva.
Primarne sirovine za proizvodnju čelika su sirovo željezo i produkti procesa direktne redukcije, a kao sekundarna sirovina se koristi čelični otpad obrađivan pretaljivanjem elektropećnim postupku uz uporabu drugih materijala (ferolegure, talitelji, oksidansi, vatrostalni materijali i ljevarski prah). Čelični otpad se prema potrebi, a i zahtjevima elektropeći, usitnjava rezanjem i drobljenjem ili prešanjem okrupnjuje, uz prethodno uklanjanje nepoželjnih primjesa (beton, zemlja, obojeni metali i sl.).
Zbog korisnih svojstava čelika i svekolike uporabe, u svijetu se, prema podacima za razdoblje 2006. do 2016., godišnja proizvodnja čelika kretala od 1,25 mlrd tona do više od 1,67 mlrd tona, a neki od najznačajnijih proizvođača čelika u svijetu su Kina, Japan, Indija, SAD, Rusija i Južna Koreja [1,2]. Istovremeno se, za proizvodnju čelika iz čeličnog otpada, njegova godišnja potrošnja kretala od 500 do 585 mln tona [2]. U procesu proizvodnje čelika pretaljivanjem čeličnog otpada, vrlo važnu ulogu ima kvaliteta otpada, koja uvelike utječe na uspješnost i ekonomičnost same proizvodnje. Stoga se kontroli čeličnog otpada posvećuje velika

pozornost, budući da čelični otpad često može sadržavati neželjene primjese ili onečišćujuće organske i anorganske tvari (npr. Sn, As, Cu, ulja, boje, itd). Navedene primjese iz čeličnog otpada za vrijeme procesa proizvodnje čelika pri taljenju i rafinaciji potpuno prelaze u trosku (Ca, Al, Si, Ti) ili u otpadni plin (Zn, Cd), dok neke samo djelomično prelaze u trosku (Mn, Cr, S, P) ili pak ostaju u talini (Cu, Ni, Mo, Sn…).

Manje je poznato, da čelični otpad može sadržavati i primjese iz grupe radioaktivnih metala, i to najčešće $^{60}$Co, $^{90}$Sr, $^{137}$Cs, $^{192}$Ir, $^{226}$Ra, $^{232}$Th i $^{241}$Am, koji se također sukladno svojim fizikalnim i kemijskim svojstvima za vrijeme trajanja procesa proizvodnje čelika raspodjeljuju između taline, troske i dimnih plinova.

Čelični otpad koji se koristi za potrebe proizvodnje čelika elektropećnim postupkom u čeličanama i ljevaonicama, obično je vlastiti tehnološki otpad tj. povrat iz tehnološkog procesa i čelični otpad nabavljen na tržištu. Stoga se čelični otpad prema podrijetlu dijeli na *vlastiti* (tvornički) otpad koji nastaje prilikom izrade i prerade čelika, relativno je čist, poznatog kemijskog sastava i lako se reciklira; *procesni* (novi) otpad koji potječe od mehaničke obrade tijekom izrade čeličnih proizvoda i koristi se nakon sortiranja i pripreme za recikliranje i *stari* (amortizirani) otpad koji se sastoji od čeličnih proizvoda na kraju životnog vijeka i predstavlja otpad najslabije kakvoće, a često se naziva i *staro željezo* [3].

Otpad koji čeličane i ljevaonice nabavljaju na tržištu, obično ga nabavljaju sukladno tzv. tehničkim uvjetima za prijem i pripremu čeličnog otpada kojeg izrađuje svaki proizvođač prema vlastitim kriterijima ili pak prema međunarodnoj specifikaciji kao što je *European Steel Scrap Specification* [4,5]. Ova specifikacija čeličnog otpada obično razlikuje oblik otpada (tračnice, osovine, dijelovi konstrukcija, karoserije automobila, kućanski aparati, limovi), dimenzije pojedinog komada, najveću dopuštenu težinu pojedinog komada, štetne primjese (obojeni metali, polimeri, nemetali) i nasipnu težinu (za usitnjeni otpad tzv. *šreder*). Osim navedenih značajki ne postoje drugi zahtjevi kojima bi čelični otpad trebao zadovoljavati, a eventualno upozorenje da čelični otpad ne smije sadržavati radioaktivne tvari, više je deklarativne prirode, s obzirom da se, do prije nekoliko godina, kontrola prisutnosti radionuklida uglavnom nije provodila niti pri sakupljanju i pripravi čeličnog otpada za isporuku potrošačima, a isto tako niti kod potrošača pri njegovom prijemu odnosno uporabi u proizvodnim procesima.

S obzirom na kvalitetu, čelični otpad se prema gore navedenoj specifikaciji, dijeli u 11 kategorija i to: s*tari otpad* (E1, E3); *novi otpad* - niži sadržaj primjesa (E2, E6, E8); *zdrobljeni/usitnjeni otpad* ili tzv. *šreder* (E40); *čelična strugotina* (E5H, E5M); *laki legirani otpad s visokim sadržajem primjesa* (EHRB); *otpad s visokim sadržajem primjesa* (EHRM) i *fragmentirani/usitnjeni otpad iz spalionica komunalnog otpada* (E46).

Osim zahtjeva za odgovarajućim dimenzijama pojedinih komada čeličnog otpada koji se ulaže u peć, vrlo važan je i zahtjev za određenom čistoćom čeličnog otpada. Tako onečišćujuće tvari organskog i anorganskog porijekla u čeličnom otpadu ne smiju biti iznad 1,4% težinski za kategoriju označenu kao E1 (laki čelični otpad pripremljen za ulaganje, debljina <6 mm) i EHRB (stari ili novi otpad pripremljen za ulaganje, bez Cu, Sn, Pb i njihovih legura) te 1% za kategoriju označenu sa E3 (teški otpad pripremljen za ulaganje uključujući cijevi, šuplje profile, bez Cu, Sn, Pb i njihovih legura) [6]. Naime, ove primjese, utječu na

kvalitetu proizvedenog čelika smanjujući mu mehanička svojstva, a osim toga sudjeluju u reakcijama pirolize i pirosinteze za vrijeme taljenja, pri čemu nastaju različiti štetni spojevi koji mogu dimnim plinovima biti emitirani u okoliš.

Nadalje, čelični otpad zbog sigurnosnih razloga, ne smije sadržavati posude pod tlakom, zatvorene ili nedovoljno otvorene posude, zapaljive i eksplozivne materijale, vatreno oružje, streljivo, te materijale koji sadrže ili emitiraju onečišćujuće tvari koje mogu negativno utjecati na ljudsko zdravlje, okoliš ili sam proces proizvodnje čelika. Posljednjih 30-tak godina vrlo velika pozornost se pridaje monitoringu radioaktivnih tvari u čeličnom otpadu te se poduzimaju različite mjere kojima se provjerava eventualna prisutnost radioaktivnih tvari u čeličnom otpadu namijenjenom obradi.

## PORIJEKLO RADIOAKTIVNIH TVARI U ČELIČNOM OTPADU

Recikliranje metala danas predstavlja vrlo važnu industrijsku djelatnost širom svijeta, a čemu je doprinijela njena društvena i ekološka korisnost koja se ogleda u čuvanju prirodnih izvora ruda i štednji energije. Međutim, tijekom posljednjih 30-tak godina u ovoj djelatnosti je zabilježen veći broj nesretnih slučajeva s radioaktivnim tvarima koje su se nehotice našle u prikupljenom metalnom otpadu namijenjenom recikliranju. Posljedice tih nezgoda bile su vrlo ozbiljne s obzirom na nastale štete po ljudsko zdravlje usljed štetnih učinaka ionizirajućeg zračenja, a jednako tako i prouzročene štete sa gospodarskog stajališta. Prema podacima Međunarodne agencije za atomsku energiju (engl. *International Atomic Energy Agency*, IAEA) [7], koja između ostaloga bilježi i incidente s radioaktivnim tvarima, utvrđeno je da je tijekom razdoblja od 1993. do kraja 2011., od strane država članica kojih je 169 i nekih država koje nisu članice ili su u postupku učlanjenja, bilo prijavljeno ukupno 2164 incidenata.

Od tog broja, 399 incidenata uključivalo je neovlašteno posjedovanje, kretanje ili pokušaje ilegalnog trgovanja ili uporabe radioaktivnog materijala ili radioaktivnih izvora. Istovremeno je bilo prijavljeno i 588 incidenata koji su uključivali krađu ili gubitak nuklearnog ili drugog radioaktivnog materijala te ukupno 1124 slučaja koji uključuju druge neovlaštene aktivnosti, uključujući neovlašteno odlaganje radioaktivnih materijala ili otkrivanje nekontroliranih izvora [8].

Uzimajući u obzir relativno česte slučajeve nekontroliranog i ilegalnog prometovanja radioaktivnim materijalima i radioaktivnim izvorima kao i vrlo široku primjenu radioaktivnih elemenata u industriji, medicini, nuklearnoj tehnici, vojnoj industriji itd., realna je i pojava niza odbačenih predmeta s radioaktivnim sadržajem, koje nerijetko završe u metalnom otpadu namijenjenom recikliranju metala.

Kako je čelik danas najtraženiji reprodukcijski materijal čija je proizvodnja i nekoliko desetaka puta veća od ukupne proizvodnje svih drugih metala, veliki broj zabilježenih slučajeva pretaljivanja radioaktivnih tvari dogodio se u čeličanama, kao posljedica njihove prisutnosti u čeličnom otpadu namijenjenom termičkoj obradi. Otada je dobro poznato, da ukoliko se radioaktivne tvari dospjele u čelični otpad na različite načine, ne otkriju pravovremeno, mogu taljenjem dospjeti u čeličnu talinu, odnosno preradom tako onečišćenog čelika i u

gotov proizvod, što može prouzročiti različite zdravstvene probleme ne samo radnicima u proizvodnji i preradi čelika, nego i šire te predstavljati opasnost za okoliš u cijelosti.

Niz literaturnih podataka [9-27] o brojnim slučajevima radioaktivnog onečišćenja metalnog otpada namijenjenog uporabi u čeličanama i ljevaonicama, tablica 1, potaknuo je stručnjake da se nakon zabilježenih prvih ozbiljnih incidenata iz 80-tih godina prošlog stoljeća, ozbiljnije pozabave pitanjem onečišćenosti čeličnog i drugog metalnog otpada radionuklidima i njihovim mogućim štetnim djelovanjima na okoliš.

Prema podacima Američke nuklearne regulatorne komisije (engl. *U.S. Nuclear Regulatory Commission*, NRC) u SAD-u se godišnje prijavi oko 200 incidenata s radioaktivnim tvarima i to zbog krađe tih tvari ili gubitkom napuštenih radioaktivnih izvora [27]. U razdoblju od 1997. do 2000. u SAD-u je zabilježeno samo 20 incidenata, dok je samo tijekom 2004. godine bilo zabilježeno više od 5.000 incidenata koji su uključivali različite vrste radioaktivnog metalnog otpada. U razdoblju od 1998. do 2006. godine Bugarska je zabilježila 125 incidenta s radioaktivnim metalnim otpadom, a u Italiji je tijekom razdoblja 1997. do 1999. zabilježeno 113 incidenata. Podaci na globalnoj razini ukazuju da je u razdoblju od 1983. do 1998. godine bilo prijavljeno 62 slučaja pretaljivanja radioaktivnih izvora u različitim zemljama svijeta, a radionuklidi uz koje su najčešće bili vezani ovi incidenti su $^{137}$Cs (48,8%) i $^{60}$Co (26,7%).

Svi brojni zabilježeni slučajevi, od kojih su samo neki navedeni u tablici 1, uglavnom su posljedica nekontroliranog odlaganja otpada koji sadrži radioaktivne tvari različitog porijekla kao i nedovoljnog nadzora nad pripravom i uporabom čeličnog otpada u metalurškim procesima.

Naime, kako se kod priprave čeličnog otpada za potrebe čeličana i ljevaonica primjenjuju različite metode rezanja, drobljenja i prešanja, postoji velika opasnost da eventualno prisutni odbačeni dijelovi opreme koji sadrže radionuklide budu na ovaj način uništeni, a sadržani radionuklidi dispergirani u otpad, što može predstavljati veliku opasnost po okoliš. Mnogi, od do sada zabilježenih incidenata su pokazali da su posljedice onečišćenja radionuklidima u slučaju njihovog pretaljivanja u čeličanama i ljevaonicama vrlo skupi glede sanacije nastalog stanja i vrlo složenih postupaka čišćenja proizvodnih pogona od radioaktivne kontaminacije [28, 29], tablica 2.

Pri pretaljivanju čeličnog otpada, u kojem je moguća prisutnost radionuklida, pri izradi čelika u čeličanama, postoji velika opasnost od njihove moguće disperzije u okoliš. Posebice je to važno napomenuti kada se radi o umjetnim radionuklidima. Naime, najčešće prisutni radionuklidi u zabilježenim incidentima s onečišćenim čeličnim otpadom odnosili su se na umjetne radionuklide i to $^{137}$Cs, $^{60}$Co, $^{226}$Ra, $^{192}$Ir, $^{232}$Th, $^{90}$Sr i $^{241}$Am iako su zabilježeni i slučajevi povišenih aktivnosti prirodnih radioaktivnih izotopa poput $^{40}$K, $^{226}$Ra, $^{232}$Th, i $^{238}$U.

Poznato je da se za vrijeme procesa proizvodnje čelika tj. pri izradi čelične taline u peći, pojedine primjese iz čeličnog otpada prelaze u trosku (Ca, Al, Si, Ti) ili u otpadni plin (Zn, Cd), odnosno neke samo djelomično prelaze u trosku (Mn, Cr, S, P) ili pak ostaju u talini (Cu, Ni, Mo, Sn…). No, jednako tako, a što je manje poznato, i primjese iz grupe prirodnih i umjetnih radionuklida ($^{40}$K, $^{226}$Ra, $^{232}$Th i $^{238}$U te $^{60}$Co, $^{90}$Sr, $^{137}$Cs, $^{192}$Ir, $^{226}$Ra, $^{232}$Th, i $^{241}$Am) za vrijeme procesa izrade čelika imaju različitu sudbinu.

Tablica 1. Neki od zabilježenih incidenata pojave radionuklida u čeličnom otpadu namijenjenom obradi u čeličanama [9-13,15,16,18-27]

| Godina | Država | Radionuklid |
|---|---|---|
| 1983. | SAD | $^{60}Co$ |
| 1984. | SAD | $^{137}Cs$ |
| 1985. | Brazil/SAD | $^{60}Co/^{137}Cs$ |
| 1987. | SAD | $^{137}Cs$ |
| 1988. | SAD/Italija | $^{137}Cs/^{60}Co$ |
| 1989. | Italija/SAD | $^{137}Cs/^{232}Th$ |
| 1990. | Irska | $^{137}Cs$ |
| 1991. | Indija | $^{60}Co$ |
| 1992. | SAD | $^{137}Cs$ |
| 1993. | Kazahstan | $^{60}Co$ |
| 1994. | SAD/Bugarska | $^{137}Cs/^{60}Co$ |
| 1995. | Italija/Češka | $^{137}Cs/^{60}Co$ |
| 1996. | Njemačka | $^{60}Co, ^{137}Cs, ^{192}Ir$ |
| 1997. | SAD/Grčka | $^{60}Co/^{137}Cs$ |
| 1998. | Italija/Španjolska | $^{60}Co/^{137}Cs$ |
| 2000. | Francuska | $^{60}Co$ |
| 2002. | Tajvan | $^{60}Co, ^{137}Cs$ |
| 2004. | Indija/Kina/Švedska | $^{60}Co/^{137}Cs/^{241}Am$ |
| 2005. | Brazil | $^{226}Ra$ |
| 2007. | Finska/Kina | $^{241}Am/^{60}Co$ |
| 2008. | Kina/Njemačka | $^{60}Co/^{137}Cs$ |
| 2009. | Njemačka | $^{60}Co$ |
| 2010. | Nizozemska | $^{137}Cs$ |
| 2012. | SAD | $^{60}Co$ |
| 2016. | SAD | $^{226}Ra$ |

S obzirom na to da radionuklidi imaju različite koeficijente raspodjele između čelične taline, troske i prašine odnosno dimnih plinova [30], a koji ovise o njihovim fizikalnim i kemijskim

svojstvima, to se tijekom procesa proizvodnje čelika različito i raspodjeljuju. Tako se u talini zadržavaju $^{60}$Co i $^{192}$Ir, u elektropećnu prašinu odlazi $^{137}$Cs i manje količine $^{90}$Sr i $^{226}$Ra, a u trosku se izdvajaju $^{226}$Ra, $^{241}$Am, $^{232}$Th i $^{90}$Sr gdje se može pronaći i prirodni radionuklid $^{40}$K.

Tablica 2. Posljedice nekih incidenata nastalih nepropisnim rukovanjem radionuklidima [27-29]

| Lokacija | Godina | Radionuklid | Posljedice |
|---|---|---|---|
| Ciudad Juarez, Meksiko | 1983. | $^{60}$Co | 1 poginuli, 4 ozračena |
| Goiana, Brazil | 1987. | $^{137}$Cs | 4 poginula, 250 ozračenih |
| Jilin, Xinzhou, Kina | 1992. | $^{60}$Co | 3 poginula, 5 ozlijeđenih |
| Tammiku, Estonija | 1994. | $^{137}$Cs | 1 poginuli, 4 ozlijeđena |
| Cadiz, Španjolska | 1998. | $^{137}$Cs | Trošak sanacije 26 mln USD |
| Samut Prakarn, Tajland | 2000. | $^{60}$Co | 3 poginula, 10 ozračenih |
| Nigeria | 2002. | $^{241}$Am | U pošiljci za EU otkriven izvor |
| Canton, Ohio, SAD | 2004. | $^{137}$Cs | Trošak sanacije 30 mln USD |
| Jewit, Teksas, SAD | 2005. | $^{137}$Cs | Trošak sanacije 7 mln USD |
| Mayapuri, Indija | 2010. | $^{60}$Co | 1 poginuli, 8 ozračenih |
| Hueypoxtla, Meksiko | 2013. | $^{60}$Co | Pretpostavljene letalne doze |

## SUSTAVI ZA MONITORING RADIONUKLIDA U ČELIČNOM OTPADU

S obzirom na opasnost od mogućeg štetnog djelovanja proizvedenog čelika, čeličnog odljevka ili pak nastalog proizvodnog otpada, ukoliko ovi sadrže radionuklide, vrlo je bitno spriječiti ulazak radionuklidima onečišćenog čeličnog otpada u čeličane i ljevaonice. Budući da su sakupljanje čeličnog otpada i njegova obrada u čeličanama i ljevaonicama, prilično rasprostranjene djelatnosti, Europska komisija je još 1999. godine donijela niz zaključaka o kontroli i nadzoru metalnog otpada radi određivanja prisutnosti radionuklida, pri čemu je važna suradnja stručnjaka i prerađivača, edukacija rukovatelja metalnim otpadom te razvijanje sustava zaštite od zračenja [9].

U svrhu sprječavanja ulaza radioaktivnog čeličnog otpada u čeličane i ljevaonice, primjenjuju se mjere nadzora i kontrole na samom ulazu u ove proizvodne pogone, kako bi se utvrdila eventualna prisutnost radionuklida u otpadu prije njegove priprave za ulaganje u agregat za taljenje. Jednako tako, a u svrhu zaštite okoliša od širenja radionuklida iz ovih procesa obrade čeličnog otpada, potrebno je provjeriti njihovu prisutnost i u proizvedenim čelicima ili čeličnim proizvodima, kao i u svim vrstama proizvodnih otpada nastalih u spomenutim proizvodnim procesima.

Uvođenjem sustava za monitoring radionuklida i instalacijom odgovarajuće opreme, u „dvorištima“ sakupljača čeličnog otpada kao i u čeličanama i ljevaonicama, osigurava se

zaštita zdravlja ljudi i otklanja mogućnost onečišćenja okoliša distribucijom i obradom čeličnog otpada koji sadrži radioaktivne tvari.

Za nadzor i praćenje radionuklida u čeličnom otpadu, sirovom čeliku, gotovim čeličnim proizvodima, proizvodnim ostatcima (troska, ogorina ili „cunder“, elektropećna prašina, istrošeni vatrostalni materijal) kao i materijalima korištenim u procesu proizvodnje čelika (ferolegure, ugrađeni vatrostalni materijal, nemetalni dodaci i sl.), primjenjuju se obično dva osnovna tipa detektora radioaktivnosti i to *prijenosni* ili ručni, slika 1 i *stacionarni* automatski uređaji, tzv. *portali*, slika 2.


Slika 1. Neki od tipova prijenosnih uređaja za utvrđivanje radioaktivnih tvari u čeličnom otpadu; a) AT6102A Spectrometer, ATOMTEX, Bjelorusija; b) identiFINDER R400, FLIR Systems, SAD; c) ASHKA RS 125 Super SPEC Handheld Gamma Ray Spectrometer, Indija; d) RADTRONICS, RDS – 30 Radiation Survey Meter, Australia [31-34]

Prijenosni ili tzv. ručni uređaji imaju određene prednosti u odnosu na stacionarne, a što se ogleda prije svega u njihovoj cijeni, velikom broju proizvođača i različitih tipova, a posebno njihovoj mobilnosti odnosno mogućnosti njihovog korištenja na raznim mjestima u procesu proizvodnje i prerade čelika kao što su skladišta čeličnog otpada i pratećih materijala, čišćenju sirovog proizvedenog čelika i izdvojenim proizvodnim ostacima (troska, ogorina, prašina), skladištima gotovih proizvoda itd. Prijenosni uređaji imaju i svoje nedostatke u što

se ubraja ograničena mogućnost njihove uporabe tijekom nadzora i kontrole velikih pošiljki čeličnog otpada kada se dopremaju u vagonima, brodovima, kamionima, kontejnerima, itd. Prijenosni uređaji obično moraju ispunjavati određene zahtjeve kako bi se postigla dobra učinkovitost pri njihovom korištenju za monitoring radionuklida u čeličnom otpadu, a ti zahtjevi se odnose na njihovu masu, mjerno područje, vrijeme mjerenja, pogrešku mjerenja itd., tablica 3. Uz ove najčešće zahtjeve koje trebaju ispunjavati prijenosni uređaji za monitoring radionuklida, nerijetko se postavljaju i dodatni zahtjevi koji se uglavnom odnose na mogućnost povezivanja uređaja s računalom, opskrbljenost dodatnom gama spektrometrijskom opremom za spektrometrijsku analizu detektiranih radionuklida sadržanih materijalu kojim je kontaminiran otpad, kao i mogućnost odabira i zamjenjivosti detektora ovisno o vrsti zračenja.

Tablica 3. Zahtjevi koje trebaju ispunjavati prijenosni uređaji za monitoring radionuklida i usporedba s karakteristikama dvaju komercijalnih uređaja [10,35,36]

| **Parametar/ karakteristika** | **Temeljni zahtjev** | **Optimum** | **Komercijalni tip uređaja** | |
|---|---|---|---|---|
| | | | **RADTRONICS, RDS – 30 Radiation Survey Meter** | **LAURUS Systems, Tip RadComm RHandy** |
| Mjerno područje brzine doze zračenja, $\mu Svh^{-1}$ | 0,05-100 | 0,08-10 | 0,01-100 | $0,01\text{-}10^{6}$ |
| Pogreška mjerenja, % | ≤ 20 | ≤ 15 | 10 | 3 |
| Vrijeme mjerenja u jednoj točki, sek. | ≤ 5 | ≤ 2 | 1 | 1 |
| Energija, MeV | 0,05-3,0 | 0,05-2,0 | 0,048-3,0 | 0,03-1,5 |
| Masa, kg | ≤ 5 | ≤ 2 | 0,22 | 0,2 |
| Radna temperatura, ºC | -20 do +50 | -20 do +50 | -20 do +55 | -20 do +70 |

Uz navedene zahtjeve koje trebaju ispunjavati prijenosni uređaji za monitoring radionuklida, nerijetko se postavljaju i dodatni zahtjevi koji se uglavnom odnose na mogućnost povezivanja uređaja sa računalom, opskrbljenost sa dodatkom za γ - spektrometrijsku analizu detektiranih radionuklida u onečišćenom čeličnom otpadu kao i mogućnost odabira i zamjenjivosti detektora ovisno o vrsti zračenja. Integrirani dozimetri odnosno radiometri s izmjenjivim detektorima koji se koriste za bilježenje α -, β -, γ - i neutronskog zračenja kao i identifikaciju γ - emitirajućih nuklida u ovim vrstama materijala danas se na tržištu nalazi veliki broj uređaja različitih proizvođača. U svakom slučaju, ovakvi prijenosni uređaji se izvrsno nadopunjuju sa stacionarnim tipom uređaja, i to za potrebe detaljnog pretraživanja manjih količina otpada, nakon eventualno utvrđene prisutnosti radionuklida stacionarnim uređajem u pošiljci čeličnog otpada na kamionu ili vagonu.

Ukoliko nadzorni monitoring sustavi radioaktivnosti u čeličnom otpadu počivaju na prijenosnim uređajima ne zadovoljavaju potrebe korisnika u čeličanama i ljevaonicama,

uvijek se mogu unaprijediti i nadograditi instalacijom stacionarnih uređaja, kojima je moguće provesti detaljniji nadzor. Stoga se danas, u velikim čeličanama i ljevaonicama, monitoring radionuklida u čeličnom otpadu najčešće i provodi primjenom stacionarnih uređaja u kombinaciji s prijenosnima, što je opravdanim pokazala praksa u velikom broju suvremenih čeličana i ljevaonica te tvrtki koje se bave sakupljanjem i/ili pripravom čeličnog otpada za tržište.

Stacionarni uređaji se najčešće instaliraju na samom ulazu u tvrtkama koje se bave sakupljanjem i pripravom čeličnog otpada ili čeličanama i ljevaonicama gdje se taj otpad obrađuje. Ovi uređaji su obično u obliku portala, kranova ili rampi između kojih se ili ispod kojih se kreće vozilo (kamion, vagon) kojim se doprema čelični otpad, slika 2.

Suvremeni stacionarni monitoring sustavi trebaju biti opremljeni uređajima koji trebaju ispunjavati stroge zahtjeve koji se odnose na brzinu doze zračenja iznad razine prirodnog ili pozadinskog zračenja okoliša, a koja jamči aktiviranje sustava, pouzdanost i osjetljivost detekcije uz odgovarajuću brzinu kretanja kamiona ili vagona s pošiljkom čeličnog otpada. Nadalje, ti sustavi moraju zadovoljavati odgovarajućom točnošću u uvjetima niskih i visokih temperatura zraka, mogućnost automatske obrade podataka uz uračunavanje razine prirodnog ili pozadinskog zračenja okoliša, itd., tablica 4.

Slika 2. Primjer instaliranog stacionarnog sustava/*portala* na ulazu u proizvodni pogon gdje se obrađuje čelični otpad [37]

Osim zahtjeva koje trebaju ispunjavati stacionarni uređaji za monitoring radionuklida, često se postavljaju i dodatni zahtjevi, koji se uglavnom odnose na mogućnost prijenosa informacija telekomunikacijskim sustavima, mogućnost provjere radne zapremnine vozila u kojem se dostavlja pošiljka čeličnog otpada, mogućnost provedbe kvalitativne kemijske analize tj. identificiranja samih radionuklida prisutnih u onečišćenom otpadu i sl.

Danas na tržištu postoji niz razvijenih stacionarnih sustava za monitoring radionuklida u čeličnom otpadu, a vrlo često se koriste sustavi svjetski poznatih proizvođača poput

RadComm Systems, Kanada [38], Thermo Fisher Scientific Inc., SAD [39], PEO Radiation Technology, Belgija [40], LUDLUM Measurement Inc., SAD [41] itd.

Tablica 4. Najčešći zahtjevi koje trebaju ispunjavati stacionarni uređaji za monitoring radionuklida [10]

| Parametar/karakteristika | Temeljni zahtjev | Optimum |
|---|---|---|
| Granica detekcije, $nSvh^{-1}$ | 3-10 | 5-7 |
| Vjerojatnost pojave „lažnog alarma“<br>• Kamioni<br>• Željeznički vagoni | $10^{-3}$-$10^{-4}$<br>< $10^{-5}$ | $10^{-4}$-$10^{-5}$ |
| Energija, MeV | 0,05-3,0 | 0,05-2,0 |
| Brzina kretanja pošiljke, $kmh^{-1}$ | 4-7 | 4-5 |
| Zapremina (kapacitet) vozila, t | 1-60 | 3-60 |
| Radna temperatura, °C | -40 do +50 | -20 do +50 |
| Automatska obrada podataka uz uračunavanje razine prirodnog zračenja u okolišu | + | + |
| Podešavanje sustava s obzirom na brzinu kretanja vozila | + | + |

Oprema stacionarnih sustava/*portala* se sastoji od visoko sofisticirane sprege vrlo osjetljivih detektora za sve vrste zračenja i mikroprocesnu tehnologiju, a u isto vrijeme se odlikuje jednostavnošću rukovanja. Ovi portali, ovisno o namjeni i obujmu proizvodnih pogona za obradu čelika (čeličane i ljevaonice) ili pak o količinama sakupljenog čeličnog otpada kojeg sakupljač priprema za prodaju i distribuciju, mogu imati dva ili više detektora pa čak i do 16 u sustavima za posebne namjene [40], slike 3 i 4.

Pri odabiru sustava za monitoring radioaktivnih tvari u čeličnom otpadu, važnu ulogu ima osjetljivost ugrađenih detektora za mjerenje brzine doze zračenja kao i njihov broj, a što uvijek znatno utječe na cijenu uređaja, slika 5.

Uz osjetljivost, postoje mnogi drugi čimbenici koji određuju lokaciju i raspored opreme u prostoru, a to može biti: veličina i razmak između detektora, razina prirodnog ili pozadinskog zračenja, vrsta izvora zračenja i njegov položaj u pošiljci/vozilu, oblik i veličina pojedinih komada otpada u pošiljci, brzina kretanja vozila/pošiljke kroz zonu mjerenja, dimenzija, oblik vozila itd.

| Model | Izgled | Broj detektora |
|---|---|---|
| 4525-5000 |  | 2 |
| 4525-7500 |  | 3 |
| 4525-10000 |  | 4 |

Slika 3. Primjer stacionarnog sustava za monitoring čeličnog otpada s 2, 3 i 4 detektora, proizvođač *Ludlum Measurements Inc.*, SAD [41]

Raspored pojedinih dijelova monitoring sustava u prostoru obično se izvodi sukladno konfiguraciji i rasporedu pojedinih elemenata sustava (zona nadzora, detektori, monitori, uređaji za zapisivanje, uređaji za dojavu) i u uskoj je vezi s karakteristikama detektora radioaktivnog zračenja (dimenzije, vrste brojača i osjetljivosti) te odabirom softwera.
Stacionarnim monitoring sustavom se najčešće otkrivaju srednje jaki i jaki γ-emiteri poput $^{60}$Co, $^{137}$Cs, $^{192}$Ir, $^{226}$Ra, $^{232}$Th i $^{241}$Am te se prilikom instalacije ovog sustava treba voditi računa da detektori budu što bliže vozilu/transporteru koji se kontrolira. Na takav se način sprječava smanjenje osjetljivosti za određivanje brzine doze zračenja izvora prisutnog u čeličnom otpadu, a koja se kreće od 0,2 μSvh$^{-1}$ do 0,3 μSvh$^{-1}$ ili μGyh$^{-1}$ na udaljenosti od 1m od stjenke vozila (vagona ili kamiona) i jednaka je dvostrukom ili trostrukom višekratniku razine prirodnog zračenja [10].

Na temelju izmjerenih vrijednosti radioaktivnog zračenja i njegove usporedbe s referentnim vrijednostima, monitoring sustav daje korisniku upute za nastavak aktivnosti čiji smjer može biti:

- istovar,
- vračanje pošiljke isporučitelju ili
- dodatna kontrola,

što ovisi o razini eventualno utvrđene i izmjerene brzine doze zračenja. U slučaju pojave radioaktivnog materijala u čeličnom otpadu koji po izmjerenoj razini zračenja predstavlja opasnost za ljude u neposrednoj blizini, to jest pojava radioaktivnog materijala se pretvara u *izvanredni slučaj*, tada se obvezno pokreću aktivnosti za slučaj izvanrednog stanja koje su propisane zakonom. Provođenje propisanih mjera i aktivnosti, određene su opisom posla određenog radnog mjesta i razinom odgovornosti kod svakog gospodarskog subjekta koji se bavi djelatnošću u kojoj se može dogoditi opisani slučaj.

| Model | Izgled | Broj detektora |
|---|---|---|
| 4525-12500 |  | 5 |
| 4525-21000 |  | 6 |

Slika 4. Primjer stacionarnog sustava za monitoring čeličnog otpada s 5 i 6 detektora, proizvođač *Ludlum Measurements Inc.*, SAD [41]

Oprema za monitoring bi inače, prema preporukama Međunarodne agencije za atomsku energiju [43], a koje se odnose na kontrolu radionuklida u čeličnom i drugim metalnim otpadima, trebala biti odabrana u skladu sa tipom industrijskog postrojenja za obradu. Tako velika postrojenja koja rukuju velikim količinama pošiljki čeličnog otpada trebaju koristiti

stacionarne (*portal*) detektore za nadzor radionuklida u prispjelim pošiljkama na ulazu u pogon, kao i svih proizvoda (ingota, metalnih šipki, proizvodnih otpada itd.) koji napuštaju proizvodni proces. Osim toga, ta oprema treba biti dovoljno osjetljiva da detektira i male promjene u razinama zračenja eventualno kontaminiranog otpada u odnosu na prirodno pozadinskog zračenja okoliša.

Imajući na umu opremu koja čini stacionarne sustave, komercijalnu proceduru nabave čeličnog otpada na tržištu, njegovo kretanje od sakupljača/isporučitelja do potrošača kao i kretanje u krugu čeličane ili ljevaonice od ulaza do mjesta istovara, zatim kontrolu zaprimljene pošiljke na kamionu i/ili vagonu, istovar i pripravu za ulaganje u košare te poziciju peći u koju se čelični otpad ulaže i obrađuje, vrlo važno je načiniti precizne upute za rad i korištenje ovih sustava kako bi njihova učinkovitost bila maksimalna. Pri tome, treba u pogonima uzeti u obzir i postojeći raspored građevinskih objekata kao i vaga i prometnica (ceste i željezničke tračnice), te moguće potrebe za primjenom dodatnih nadzornih točaka monitoringa.

Naime, da bi se osigurala što veća sigurnost i zaštita radnika od radioaktivnog zračenja, u čeličanama i ljevaonicama se uvode i dodatne kontrole. Iz ovih razloga se, osim kontrole čeličnog otpada na ulazu u čeličanu pomoću stacionarnih sustava nadzora, u nekim čeličanama otpad kontrolira i dodatno pomoću detektora instaliranih na transportnim uređajima tj. pokretnim trakama i elevatorima, na polipnim grabilicama otpada pri ulaganje otpada u košare, napunjenim košarama na samom ulazu u pećnu halu itd., slika 6.

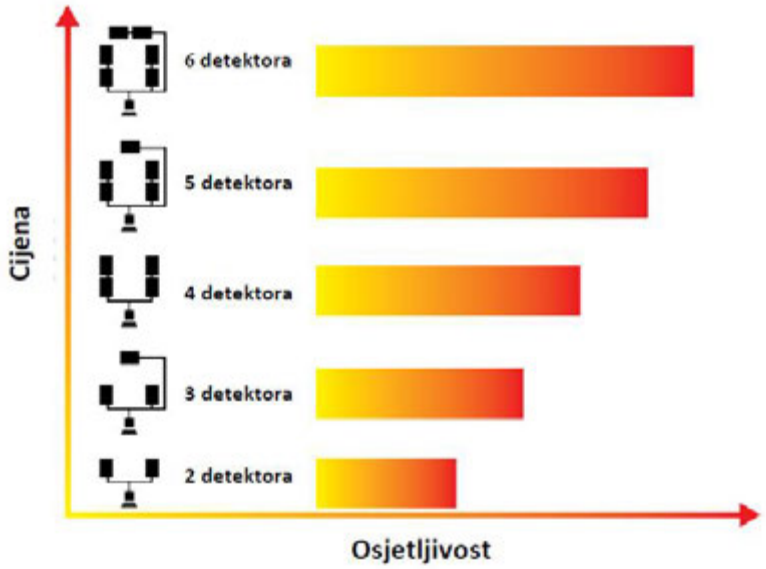


Slika 5. Odnos broja ugrađenih detektora u stacionarni sustav i osjetljivosti samog sustava te njegove cijene [42]

U čeličanama i ljevaonicama relativno velikih proizvodnih kapaciteta, dodatna kontrola se često provodi instaliranjem detektora na mjestima gdje se pune košare pripravljenim

čeličnim otpadom, čime se osigurava utvrđivanje prisutnosti radioaktivnih tvari koje nisu otkrivene na samom ulazu u pogon, a koje su mogle za vrijeme usitnjavanja i drobljenja biti dispergirane u otpadu, npr. kontejneri s oslabljenim radioaktivnim izotopom iz zdravstvenih ustanova i sl. Kako bi se postigla visoka razina sposobnosti otkrivanja radioaktivnog materijala, ovaj oblik dodatne kontrole omogućava brzu obradu signala i analizu alarma istodobno bez prekida postupka praćenja zračenja. Taj je oblik dodatne kontrole testiran u primjeni kod mnogih korisnika te se pokazao vrlo učinkovitim zbog svojih ključnih tehnoloških značajki kao što su visoka osjetljivost, manje „lažnih“ alarma, jednostavno rukovanje, daljinsko upravljanje, itd. Ovakav način postavljanja detektora vrlo je pogodan i za primjenu u tvrtkama koje se bave sakupljanjem čeličnog otpada i njegovom pripravom za uporabu u čeličanama i ljevaonicama.

Dodatna kontrola se može provoditi i instaliranjem posebno dizajniranih detektora koji mogu zadovoljiti potrebe čeličana, ljevaonica, sakupljača i obrađivača čeličnog otpada, utovarnih i istovarnih lučkih i željezničkih punktova. Tako npr. postoji jednostavan dizajn ovakvih detektora koji se pričvršćuje na polipnu grabilicu/*grajfer*, pokazao se vrlo učinkovit za otkrivanja radioaktivnih izvora niskog intenziteta i to na mjestima gdje sustavi otkrivanja zračenja nikada prije nisu postojali. Ovaj način dodatne kontrole pokazao se kao učinkovit i njegova sposobnost otkrivanja radioaktivnosti daleko premašuje bilo koji konvencionalni sustav za otkrivanje zračenja, uključujući i sustave detekcije koji se postavljaju na magnetne dizalice, i to bez obzira na veličinu detektora. U ovom slučaju skeniranje materijala traje duže s boljom preciznošću, jer ovaj način kontrole dodatno nudi tri različite mogućnosti za kontrolu tijekom rukovanja. Prvo, ovakav sustav kontinuirano skenira čelični otpad po cijeloj površini prije nego što ga podigne. Drugo, čelični otpad se skenira dok je u polipnoj grabilici/*grajferu* i treće, otpad se skenira i tijekom ispuštanja iz polipne grabilice/*grajfera*. Ova tri uvjeta skeniranja osiguravaju najviši stupanj učinkovitosti za otkrivanje radioaktivnog materijala niske razine u čeličnom otpadu.

Ponekad se kao dodatna kontrola u čeličanama i ljevaonicama uvode i sustavi za otkrivanje radioaktivnog zračenja tijekom transporta čeličnog otpada na pokretnim trakama i obično se sastoje od dvije glavne komponente - detektora zračenja i kontrolne konzole. Detektori zračenja se postavljaju na transportni prijenosnik do uređaja za usitnjavanje i/ili drobljenje otpada i mjere kontinuiranu, neprekinutu razinu zračenja. Podaci o izmjerenim razinama zračenja pretvaraju se u digitalne signale koji se prenose na računalo, a zatim se analiziraju pomoću mikroprocesorskih sustava s velikom brzinom obrade podataka.

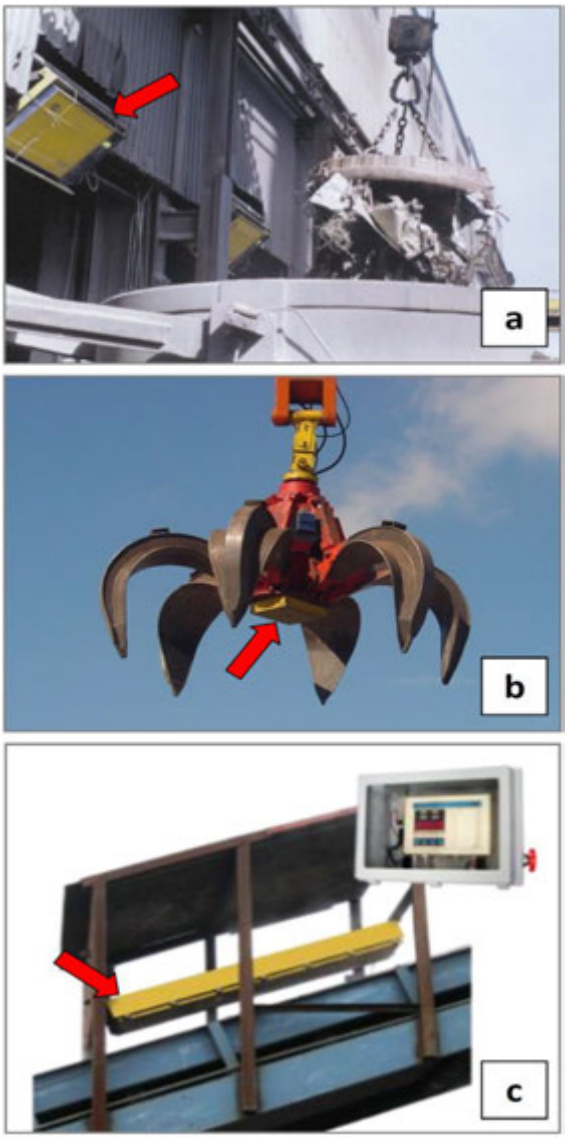


Slika 6. Dodatna kontrola pomoću detektora instaliranih na a) mjestu za ulaganje čeličnog otpada u košare, b) polipnim grabilicama/*grajferima* i c) pokretnim trakama [44-46]

U pogonima za obradu čeličnog otpada, u kojima su instalirani sustavi za monitoring radionuklida, pri svakodnevnom radu koriste se upute ili postupnici za rukovanje ovim sustavima. Naime, u slučaju pojave radioaktivnog zračenja zbog prisutnosti radioaktivne tvari u čeličnom otpadu, a koje po izmjerenoj razini zračenja predstavlja neposrednu opasnost po zdravlje ljudi u neposrednoj blizini, pojava poprima oblik *izvanrednog događaja* te se nužno pokreću zakonom propisane aktivnosti za takav slučaj. Provedba propisanih aktivnosti odnosno mjera određena je aktom svakog korisnika sustava (čeličana, ljevaonica) tj. opisom posla određenog radnog mjesta i razinom odgovornosti. Važno je napomenuti kako je obveza svakog zaposlenika u tim društvima, koji uoči kontaminiranu pošiljku čeličnog

otpada, odmah o tome izvijestiti svog nadređenog te poduzeti prve propisane radnje (za koje je osposobljen) u svrhu sprječavanja širenja izvanrednog događaja. Pri tome se podrazumijeva korištenje svih potrebnih pomoćnih sredstava i opreme, koja mora biti unaprijed osigurana i pripremljena na pristupačnoj i odgovarajućoj lokaciji.

Način zbrinjavanja pronađenih radioaktivnih predmeta ili njihovih dijelova u kontroliranoj pošiljci čeličnog otpada ovisi o kojoj se vrsti i količini radioaktivne tvari radi, a sam postupak zbrinjavanja mora biti u skladu s važećim propisima. Prema tim propisima, a u slučaju kada se u pošiljci čeličnog otpada mjerenjem utvrdi radioaktivnost iznad dopuštene granice, vozilo s pošiljkom je potrebno odmah izdvojiti i na propisnoj udaljenosti staviti pod nadzor te označiti i onemogućiti pristup zaposlenicima i drugim osobama. Kako niti jedna čeličana, valjaonica i druga tvrtka koja obavlja bilo kakve radnje s čeličnim otpadom, nije ovlaštena za promet radioaktivnim materijalom, to je u Republici Hrvatskoj, u slučaju utvrđenog povećanog radioaktivnog zračenja u čeličnom otpadu, dužnost postupati sukladno važećim nacionalnim propisima [47,48].

U svrhu rješavanja ovog važnog problema proizvođači čelika i čeličnih odljevaka na području EU, posljednjih desetljeća su pristupili sustavnom praćenju prisutnosti radionuklida u čeličnom otpadu i sirovom čeliku. Glede normi i propisa kojima bi se odredile granične vrijednosti za dopušten sadržaj odnosno koncentraciju aktivnosti radionuklida u čeličnom otpadu, čeliku i čeličnim proizvodima, Međunarodna agencija za atomsku energiju (IAEA) je izradila i izdala smjernice i preporuke [43].

Kako je bilo nužno uspostaviti ravnomjerne osnovne sigurnosne standarde za zaštitu zdravlja pojedinaca koji su izloženi profesionalnim, zdravstvenim i javnim opasnostima od ionizirajućeg zračenja, pa tako i zračenja koje bi moglo biti posljedica prisutnosti radionuklida u čeliku i čeličnim proizvodima koji nas okružuju, na području EU je donesena Direktiva Vijeća 2013/59/Euratom o osnovnim sigurnosnim standardima za zaštitu od opasnosti koje potječu od izloženosti ionizirajućem zračenju [49]**.** Ova Direktiva pomaže u prevladavanju postojećih razlika među nacionalnim normama/propisima članica EU kojima se uređuje nadzor radioaktivnosti s obzirom da su države članice EU dužne poticati uspostavu sustava otkrivanja prisutnosti radioaktivnih onečišćujućih tvari u metalnim proizvodima uvezenima iz trećih zemalja, a posebice na mjestima kao što su veliki pogoni za uvoz metala ili važna prometna čvorišta. Nadalje, države članice osiguravaju da odgovorne osobe u pogonima za preradu metalnog otpada odmah informiraju nadležno tijelo ako se sumnja ili zna za taljenje ili druge metalurške operacije otpada kontaminiranog radionuklidima te tako spriječe korištenje kontaminiranog materijala kao i njegovo stavljanje na tržište.

S obzirom da je ova Direktiva stupila na snagu, a države članice EU su je bile dužne transponirati u svoje nacionalne propise i to do 6. veljače 2018., a nakon toga i svi gospodarski subjekti koji se bave djelatnostima u čijem radu je moguće stupiti u kontakt s kontaminiranim otpadom, dužne su urediti svoje akte u koje moraju uvrstiti odredbe iz navedene Direktive Vijeća 2013/59/Euratom**.**

## ZAKLJUČAK

S obzirom na zabilježene pojave prisutnosti radioaktivnih elemenata u čeličnom otpadu, gotovim proizvodima metalurške industrije te proizvodnim ostacima, a na temelju iskustva najpoznatijih svjetskih i europskih proizvođača čelika i čeličnog lijeva, nužno je i opravdano u čeličanama i ljevaonicama uvođenje sustava za monitoring radionuklida. Na ovaj način bi se osigurala zaštita zdravlja zaposlenika od posljedica djelovanja radioaktivnih tvari kao i njihovo moguće širenje u okoliš. Na temelju navedenog u ovom radu, može se zaključiti kako slijedi:

- Potpuno poznavanje fizikalnih i kemijskih pa tako i radiokemijskih svojstava čeličnog otpada koji se kao sirovina koristi u proizvodnji čelika i čeličnog lijeva, ima veliki značaj, kada je riječ o ekološki prihvatljivim proizvodnim procesima.
- Radionuklidi kao onečišćujuće tvari mogu na različite načine dospjeti u čelični otpad, a s njim i u procese proizvodnje čelika i čeličnog lijeva, s obzirom da se koriste u mnogim ljudskim djelatnostima iz kojih po prestanku korištenja mogu završiti u ovoj vrsti otpada.
- U svrhu sprječavanja ulaska radioaktivnog čeličnog otpada u čeličane i ljevaonice, primjenjuju se mjere nadzora i kontrole na ulazu u ove proizvodne pogone, kako bi se pravovremeno utvrdila eventualna prisutnost radionuklida u otpadu i spriječila njegovo ulaganje u agregate za taljenje.
- Oprema za monitoring treba biti u skladu sa tipom industrijskog postrojenja za obradu čeličnog otpada na način da pogoni koji pretaljuju velike količine čeličnog otpada koriste stacionarne/*portal* detektorske sustave za nadzor prispjelih pošiljki otpada na ulazu u pogon, kao i svih proizvoda (ingota, metalnih šipki, proizvodnih otpada itd.) koji napuštaju pogon.
- Osim toga, ta oprema treba biti dovoljno osjetljiva da detektira i male promjene u razinama zračenja eventualno kontaminiranog otpada u odnosu na prirodno pozadinskog zračenja iz okoliša.
- Kako bi se osigurala potpuna sigurnost i zaštita radnika od radioaktivnog zračenja, u čeličanama i ljevaonicama se uz monitoring na ulazu, prema potrebi mogu uvesti i dodatne kontrole pomoću detektora instaliranih na transportnim uređajima tj. pokretnim trakama i elevatorima, na polipnim grabilicama pri ulaganju otpada u košare, napunjenim košarama na samom ulazu u pećnu halu itd.

## LITERATURA

[1] The World Steel Assosiation, Steel Statistical Yearbook, 2016.
[2] https://www.statista.com/statistics/270835/world-steel-production-and-scrap-consumption/ (26.1.2018)
[3] M. Gojić, Metalurgija čelika, Sveučilište u Zagrebu, Metalurški fakultet, Sisak, 2005.
[4] http://jbfab.com/custom/euspec.pdf (4.8.2017.)

[5] https://www.scribd.com/document/266413623/EFR-EU27-Steel-Scrap-Specification (4.8.2017.)
[6] T. Sofilić, B. Bertić, V. Šimunić-Mežnarić, I. Brnadić, Soil Pollution as a Result of Temporary Steel Scrap Storage at Melt Shop, Ecologia Balkanica, 5 (2013) 1, 21-30.
[7] https://www.iaea.org/about (28.1.2018.)
[8] E. F. Salem, S. M. Rashad, Statistical treatment of hazards result from radioactive material in metal scrap, XI Radiation Physics & Protection Conference, 25-28 November 2012, Nasr City - Cairo, Egypt. http://www.iaea.org/inis/collection/NCLCollectionStore/_Public/45/099/45099913.pdf (25.1.2018.)
[9] T. Sofilić, A. Rastovčan-Mioč, Š. Cerjan-Stefanović, Radioaktivni materijali u čeličnom otpadu, Strojarstvo, 43 (2001) 1-3, 65-70.
[10] T. Sofilić, T. Marijanović, A. Rastovčan-Mioč, Potreba uvođenja sustava za nadzor radioaktivnosti u procesima proizvodnje čelika Hrvatskih čeličana i ljevaonica, Arh Hig Rada Toksikol, 57 (2006) 45-54.
[11] T. Sofilić, D. Barišić, U. Sofilić, M. Đureković, Radioactivityof some building and raw materials used in Croatia, Polish Journal of Chemical Technology, 13 (2011) 3, 23-27.
[12] https://agmetalminer.com/2009/02/17/radioactive-stainless-steel-found-in-germany/ (8.8.2017)
[13] IAEA – International Atomic Energy Agency, Reducing Risks in the Scrap Metal Industry, Sealed Radioactive Sources, Divisionof Public Information, IAEA Vienna, Austria, 2005.
[14] http://www.thelancet.com/pdfs/journals/lanonc/PIIS1470204510701388.pdf (8.8.2017.)
[15] http://seaisi.org/seaisi2017/file/file/full-paper/Session8B%20Paper5.pdf (8.8.2017.)
[16] T. R. Meena, Anojkumar, R. P. Patra, Vikas, S. S. Patil, M. K. Chatterjee, R. Sharma, S. Murali, Radiological emergencies due to postulated events of melted radioactive material mixed in steel reaching public domain, Radiation Protection and Environment, 37 (2014) 2, 68-70. http://www.rpe.org.in/temp/RadiatProtEnviron37268-4071899_111838.pdf (8.8.2017.).
[17] http://www.wdrb.com/story/31358264/radioactive-scrap-metal-found-at-a-louisville-recycling-centerdropped-off-by-a-competitor (8.8.2017.).
[18] http://www.darkgovernment.com/news/department-of-energy-wants-to-let-radioactive-scrap-metal-back-into-consumer-products/ (9.8.2017.)
[19] http://www.cantonrep.com/news/20160407/radioactive-scrap-forces-closure-of-psc-metals-massillon-facility (9.8.2017.)
[20] T. Sofilić, A. Rastovčan-Mioč, Š. Cerjan-Stefanović, Ž. Grahek, Opravdanost praćenja prisutnosti radionuklida u čeličnom otpadu i sirovom čeliku, Strojarstvo, 43 (2001) 4-6, 203-209.
[21] M. Marseguerra, E. Zio, Monte Carlo approach to the detectability of a gamma source within a scrap-iron truckload, Nuclear Technology, 126 (1999) 279-288.
[22] http://www.cnic.jp/english/newsletter/nit96/nit96articles/nw96.html#basicplan (21.8.2017.)

[23] http://ita.arpalombardia.it/ita/console/files/download/86/radioactivity.pdf (21.8.2017.)
[24] https://www.unece.org/fileadmin/DAM/trans/radiation/docs/brazil.pdf (21.8.2017.)
[25] http://www.iaea.org/inis/collection/NCLCollectionStore/Public/37/004/37004401.pdf (21.8.2017.)
[26] D. Sacco, F. Ruggeri, G. Bindi, A. Bonanni, S. Casciardi, R. Delia, A. Loppa, P. Rossi, E. Venturini, Radioactivity in the Scrap Recycling Process: Radiation Protection Aspects and Experimental Monitoring Problems, Proceedings of Symposium on radiation protection in neighbouring countries in Central Europe, Portorož, Slovenija, 4-8 Sep 1995, pp. 419-426.
[27] BULGARIAN NUCLEAR REGULATORY AGENCY, Prevention, Detection and Response to Radiation Emergency in Case of Discovering of Radioactive Material in Metal Scrap, Safety guide, PP - 4/2010.
[28] United Nations Economic Commission for Europe, Recommendations on Monitoring and Response Procedures for Radioactive Scrap Metal, UN, New York and Geneva, 2006.
[29] https://assets.thermofisher.com/TFS-Assets/CAD/Catalogs/13-10090-RMSI-Industrial-Web.pdf (29.1.2018.)
[30] D. Neuschütz, D. Spirin, U. Quade, J. Meier-Kortwig, L. Holappa, M. Hämäläinen, M. A. Heredia Lozano and M. J. Guio Bonany, Inadvertent Melting of Radioactive Sources in BOF or EAF: Distribution of Nuclides, Monitoring, ISIJ International, 45 (2005) 2, 288-295.
[31] http://www.atomtex.com/en/application/metallurgicheskaya-promyshlennost (13.11.2017.)
[32] http://www.flir.it/threatdetection/display/?id=63333 (13.11.2017.)
[33] https://www.indiamart.com/ashka/radiation-monitoring-instruments.html (28.1.2018.)
[34] http://www.radtronics.com.au/radiation-safety-detection-products-instrumentation/rds-30-radiation-survey-meter (28.1.2018.)
[35] http://www.laurussystems.com/RHandy_Radiation_Contamination_Meter.htm (28.1.2018.)
[36] https://mirion.app.box.com/s/gwdi1fca0qpl9ynze44k (28.1.2018.)
[37] http://www.rivaacciaio.com/en/quality_and_safety/radiometric_detection (30.1.2018.)
[38] http://www.radcommsystems.com/en/products/vehicle-systems (30.1.2018.)
[39]https://www.thermofisher.com/search/browse/results?customGroup=Radiation+Detection+Portals+%26+Monitors (30.1.2018.)
[40] http://www.peo-radiation-technology.com/wp-content/uploads/2015/10/rad_15_rs-300_radiation-portal-monitoring-system_datasheet_peo.pdf (30.1.2018.)
[41] http://ludlums.com/products/all-products/product/model-4525-series (30.1.2018.)
[42] http://ludlums.com/images/stories/catalogs/Medical-Physics_Catalog_Web.pdf (14.11.2017.)
[43] Control of orphan sources and other radioactive material in the metal recycling and production industries, Specific safety guide, International Atomic Energy Agency – IAEA, Vienna, Austria, 2012., pp. 54.
[44] http://www.radcommsystems.com/en/products/charge-bucket (30.1.2018.)

[45] http://www.radcommsystems.com/en/products/cricket/grapple (30.1.2018.)
[46] http://medphys.ludlums.com/products/all-products/product/model-375p-3500 (30.1.2018.)
[47] Zakon o radiološkoj i nuklearnoj sigurnosti (NN broj 141/13, 39/15 i 130/17).
[48] Uredba o mjerama zaštite od ionizirajućeg zračenja te intervencija u slučaju izvanrednog događaja (NN broj 102/12).
[49] Direktiva Vijeća 2013/59/Euratom od 5. prosinca 2013. o osnovnim sigurnosnim standardima za zaštitu od opasnosti koje potječu od izloženosti ionizirajućem zračenju, i o stavljanju izvan snage direktiva 89/618/Euratom, 90/641/Euratom, 96/29/Euratom, 97/43/Euratom i 2003/122/Euratom (Sl. L 13, 17.1.2014., str. 1-73 i Sl. L 137, 25.6.2016., str. 27).

17th INTERNATIONAL FOUNDRYMEN CONFERENCE
Hi-tech casting solution and knowledge based engineering
Opatija, May 16th-18th, 2018
http://www.simet.hr/~foundry/

# MICROSTRUCTURE AND THERMAL ANALYSIS OF THE LOW MELTING Bi–In EUTECTIC ALLOYS

**Ivana Manasijević[1]*, Ljubiša Balanović[1], Tamara Holjevac Grgurić[2], Milan Gorgievski[1], Duško Minić[3], Milena Premović[3]**

[1] University of Belgrade Technical Faculty in Bor, Bor, Serbia
[2] University of Zagreb Faculty of Metallurgy, Sisak, Croatia
[3] University of Priština Faculty of Technical Sciences, Kosovska Mitrovica, Serbia

**Poster presentation**
*Original scientific paper*

**Abstract**

Microstructure and thermal properties of the low melting Bi–In eutectic alloys were investigated in this work. Three eutectic alloys (Bi–47.44 at.% In, Bi–66.33 at.% In, Bi–77.92 at.% In) were prepared by induction melting of pure elements. Microstructure of the alloys was analyzed using scanning electron microscopy (SEM) with energy dispersive X-ray spectrometry (EDS) and identification of co-existing phases was done. Differential scanning calorimetry (DSC) was applied for determination of melting temperatures and latent heats of eutectic melting. Experimentally obtained results were compared with the results of thermodynamic calculation according to CALPHAD (calculation of phase diagram) method and good mutual agreement was observed.

***Keywords***: *Bi-In system, eutectic alloy, latent heat of melting, microstructure*

*Corresponding author (e-mail address): *ivanamanasijevic80@gmail.com*

## INTRODUCTION

Phase change materials (PCMs) are materials with high heat of fusion which undergo melting/solidification process at a constant or nearly constant temperature and absorb/release thermal energy from/to the surroundings [1]. PCMs are extensively used in the field of thermal management and thermal energy storage [1-3], such as electronics cooling [1, 4–6], energy storage for buildings [7], solar energy systems [8] and space systems [9].
Different materials have been investigated so far and commercially applied in the field of PCMs for heat storage [6,10,11]. Commercial nonmetallic PCMs are characterized by low thermal conductivity, which considerably limits the heat transfer in the material [10,11]. In

order to improve the thermal conductivity, intensive research is being carried out on a variety of metals and eutectic alloys as potential PCMs for heat accumulation [1,11]. Low melting point metals (LMPMs) and eutectic alloys represent relatively new category of PCMs [1,6,10,11]. The main advantages of low melting metallic materials usage as PCMs are their high thermal conductivity and high volumetric latent heat [1,10,11].
Low melting eutectic alloys based on bismuth and indium are among the most promising candidates for middle temperature PCMs (with operating temperature from 40 to 200 °C) [6]. However, numerous important thermo-physical properties such as melting point, latent heat of fusion, specific heat capacity, thermal conductivity for many low melting bismuth and indium based eutectics are still unknown [11].
The goal of the present work is experimental investigation of microstructure, melting temperatures and latent heats of fusion for three eutectic alloys from the Bi–In binary system. Experimental work was carried out using SEM-EDS and DSC techniques. Experimentally obtained results were compared with the results of phase equilibria calculation according to the CALPHAD method [12,13].

## MATERIALS AND METHODS

Calculated phase diagram of the Bi–In system from the COST 531 database [14,15], based on the thermodynamic assessment by Boa and Ansara [16], was used for determination of accurate compositions of eutectic alloys. Next, three Bi–In alloys with calculated eutectic compositions were prepared by induction melting of pure elements (Bi 99.995%, In 99.995%, Alfa Aesar) in the graphite crucibles under argon atmosphere. The masses of the prepared samples were about 2 g. The total mass losses of the samples after induction melting were less than 0.2%.
TESCAN VEGA3 scanning electron microscope with energy dispersive spectroscopy (EDS) (Oxford Instruments X-act) was used for microstructure examination and the analysis was carried out at 20 kV. Overall composition and compositions of coexisting phases were determined using EDS area and point analysis. All SEM images of the microstructure were taken on the polished surface of the studied alloy in the backscattered electron mode.
Temperature and latent heats of melting were determined by simultaneous thermal analyzer SDT Q600 (TA Instruments). Before performing DSC experiments, temperature and heat calibrations were performed using the pure metal standards (Bi, In and Zn) under the measurement conditions. Samples weighing about 40 mg were investigated at heating rate of 5 °C/min from room temperature up to 200 °C. The reference material was empty alumina crucible. Every heating run was repeated five times.

## RESULTS AND DISCUSSION

### Microstructure investigation

Microstructures of the prepared eutectic alloys from the binary Bi–In system were studied using scanning electron microscopy (SEM) with energy dispersive X-ray spectroscopy (EDS). Overall compositions of the samples were checked by mapping entire polished surface of the samples and they were in very good agreement with the designed compositions. The compositions of the co-existing phases were determined by observing the surface of the same phase at a different part of the sample (at least five different positions of the same phase are examined per phase). Thus, phase compositions presented in this study represent average values of at least five measurements. Calculated and experimentally determined compositions of co-existing phases are shown in Table 1.

Table 1. Experimentally determined compositions of co-existing phases determined by EDS analysis and related calculated equilibrium compositions for the investigated Bi–In eutectic alloys

| Overall composition (at.%) | Phases at room temperature | | Compositions of phases (at.%) | | | |
|---|---|---|---|---|---|---|
| | Calculation | Experiment | Bi | | In | |
| | | | Calculation | Experiment | Calculation | Experiment |
| $Bi_{52.56}In_{47.44}$ | (Bi) | (Bi) | 100.00 | 100.00 | 0.00 | 0.00 |
| | BiIn | BiIn | 50.00 | 49.94 | 50.00 | 50.06 |
| $Bi_{33.67}In_{66.33}$ | $BiIn_2$ | $BiIn_2$ | 33.33 | 31.55 | 66.67 | 68.45 |
| | $Bi_3In_5$ | $Bi_3In_5$ | 37.50 | 36.75 | 62.50 | 63.25 |
| $Bi_{22.08}In_{77.92}$ | $BiIn_2$ | $BiIn_2$ | 33.33 | 31.34 | 66.67 | 68.66 |
| | (In) | In-rich phase | 6.03 | 5.27 | 93.97 | 94.73 |

As it can be seen from Table 1 there is very good agreement between results of thermodynamic calculation and EDS analysis. Experimentally determined compositions of co-existing phases for all three investigated alloys correspond well to the related calculated compositions.

Characteristic SEM micrograph for the investigated Bi–47.44at.%In eutectic alloy is shown in Fig. 1. Microstructure of the Bi–47.44at.%In alloy reveals many dispersed and interconnected lamellae of the (Bi) phase (bright areas) as the minor phase, and larger grains of the BiIn intermetallic phase (grey areas) as the phase with much higher phase fraction.

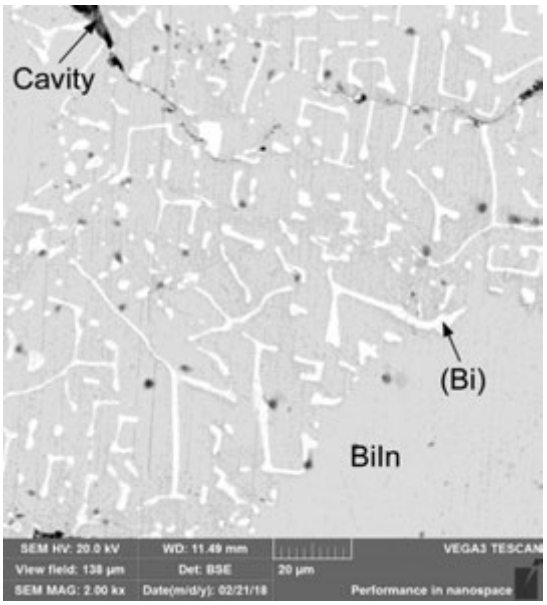


Figure 1. SEM micrograph of the investigated Bi–47.44at.%In eutectic alloy

Microstructure of the Bi–66.33at.%In eutectic alloy (Fig. 2) shows analogous irregular eutectic morphology as the Bi–47.44at.%In eutectic alloy. Using EDS analysis two phases were identified. Phase fraction of the $BiIn_2$ intermetallic phase (dark grey phase) is much larger than the phase fraction of the $Bi_3In_5$ intermetallic phase (bright grey phase).

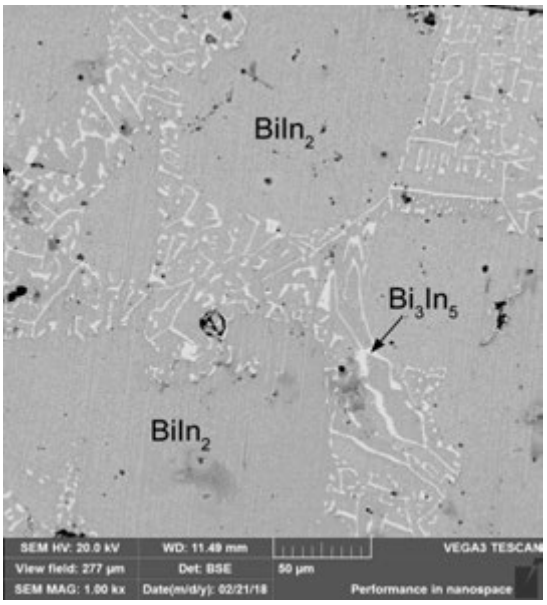


Figure 2. SEM micrograph of the investigated Bi–66.33at.%In eutectic alloy

Characteristic SEM micrograph for the Bi–77.92at.%In alloy is given in Fig. 3. Microstructure of the Bi–77.92at.%In alloy shows typical lamellar-type of eutectic structure. Lamellar eutectic morphology is characteristic for the systems with the approximately equal volume fractions of phases. Lighter lamellae represent $BiIn_2$ intermetallic compound and dark lamellae represent In-rich phase.

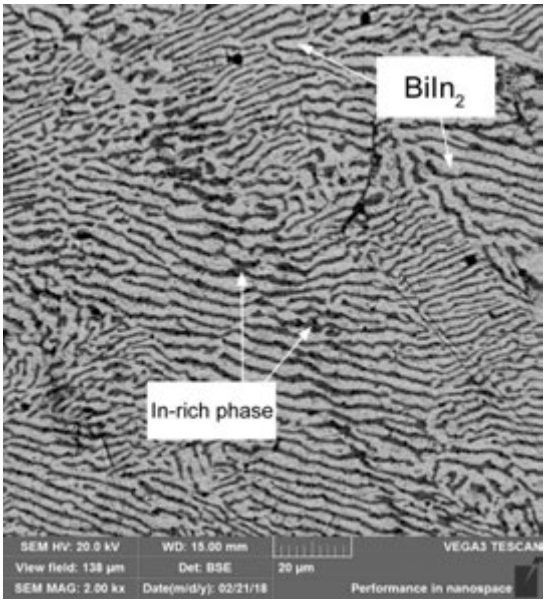


Figure 3. SEM micrograph of the investigated Bi–77.92at.%In eutectic alloy

**Thermal analysis**

Differential scanning calorimetry (DSC) was used for measurements of eutectic temperatures and latent heat of melting for the investigated Bi–In eutectic alloys. The extrapolated temperature of the peak onset was used for determination of eutectic temperature [17].
Examples of DSC heating curves (from the third heating run) for the investigated eutectic alloys are shown in Figs. 4a-c.

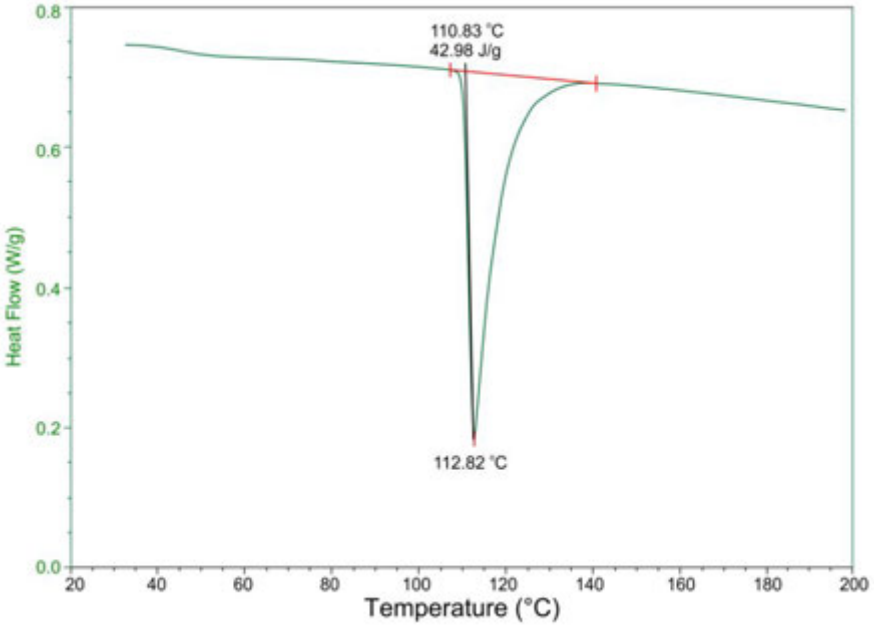
110.83 °C
42.98 J/g
112.82 °C
Heat Flow (W/g)
Temperature (°C)
0.0
0.2
0.4
0.6
0.8
20
40
60
80
100
120
140
160
180
200

(a)

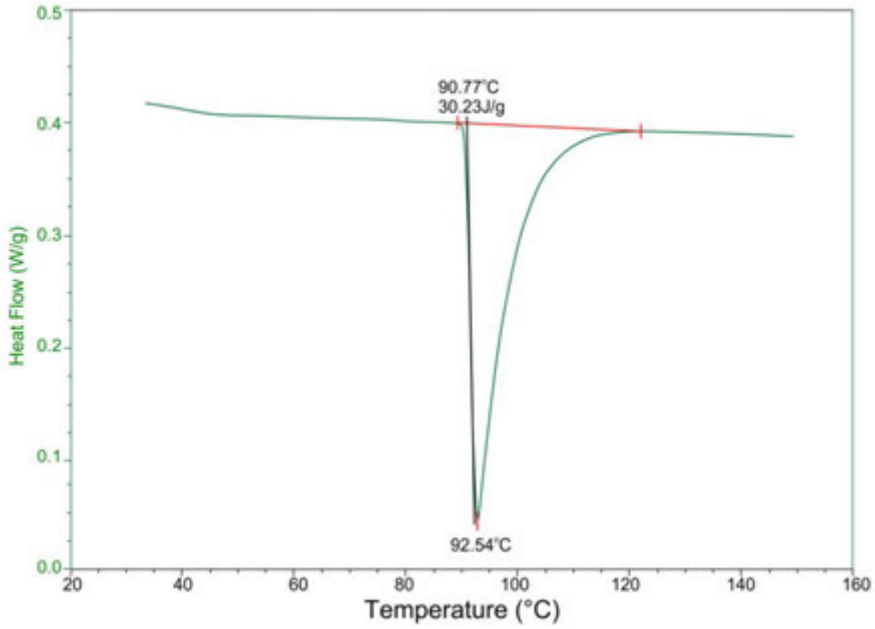
90.77°C
30.23J/g
92.54°C
Heat Flow (W/g)
Temperature (°C)
0.0
0.1
0.2
0.3
0.4
0.5
20
40
60
80
100
120
140
160

(b)

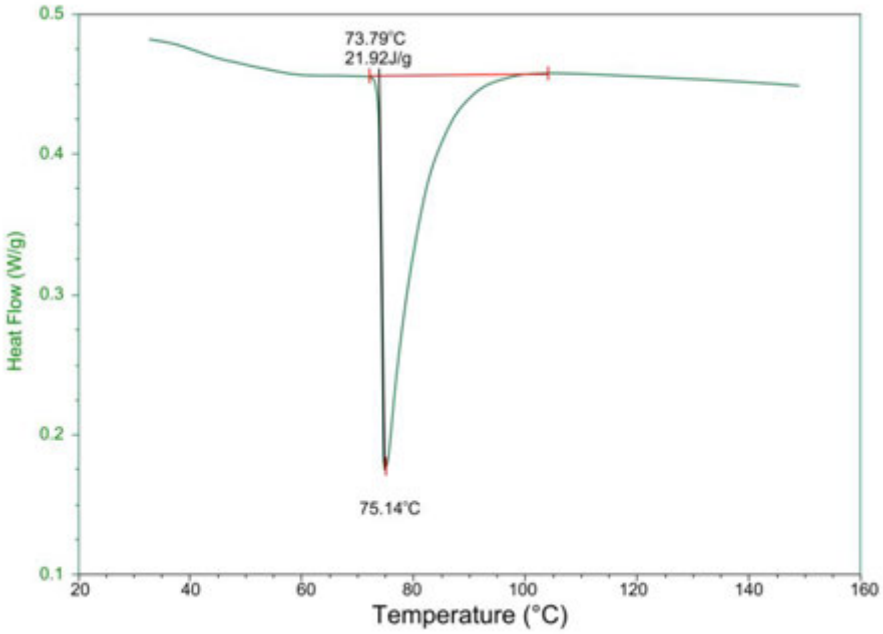


(c)

Figure 4. DSC heating curves from the third heating run:
(a) Bi–47.44at.%In eutectic alloy; (b) Bi–66.33at.%In eutectic alloy;
(c) Bi–77.92at.%In eutectic alloy

Average values of eutectic temperatures and latent heats of melting together with related standard uncertainties obtained from five DSC heating runs are presented in Table 2.

Table 2. Comparison between calculation and DSC results for the investigated eutectic alloys from the Bi–In system

| Alloy composition (at%) | Calculation | | Experimental results | |
|---|---|---|---|---|
| | Eutectic temperature (°C) | Latent heat of fusion (J/g) | Eutectic temperature (°C) | Latent heat of fusion (J/g) |
| Bi–47.44at.%In | 109.2 | 39.4 | 110.7±0.2 | 42.7±0.2 |
| Bi–66.33at.%In | 87.8 | 32.6 | 90.7±0.1 | 30.2±0.1 |
| Bi–77.92at.%In | 71.8 | 23.5 | 73.8±0.2 | 21.8±0.1 |

Experimentally determined melting temperature and latent heat of melting for the Bi–47.44 at.%In eutectic alloy are 110.7 °C and 42.7 J/g. These values are to some extend higher than related calculated values (109.2 °C and 39.4 J/g).
For the Bi–66.33at.%In alloy, measured melting temperature and latent heat of melting are 90.7 °C and 30.2 J/g and corresponding calculated values are 87.8 °C and 32.6 J/g. Experimentally determined melting temperature and latent heat of melting for the Bi–77.92at.%In alloy are 73.8 °C and 21.8 J/g and calculated 71.8 °C and 23.5 J/g.

## CONCLUSIONS

The results of microstructure and thermal analysis of low melting Bi–In eutectic alloys as candidate middle-temperature PCMs are presented in this study. Using CALPHAD technique and optimized thermodynamic parameters from the literature overall compositions and phase equilibria of three eutectic alloys from the binary Bi–In system were calculated. Next, 3 binary Bi–In alloys with target eutectic compositions were prepared by induction melting of pure metals. Microstructure and chemical compositions of the prepared alloys were investigated using SEM-EDS technique. Compositions of co-existing phases, determined by EDS analysis, were compared with the results of thermodynamic calculations and good agreement was found in all cases. It was determined that Bi–77.92at.%In alloy exhibits regular eutectic morphology with typical lamellar-type of eutectic structure. The microstructure includes $BiIn_2$ phase and In-rich phase lamellae with high degree of regularity and periodicity. Bi–47.44at.%In and Bi–66.33at.%In and alloys possess irregular eutectic morphology caused by the large difference in volume fractions of constitutive phases.
Melting temperatures and latent heat of melting were investigated using DSC technique. Five heating runs with the heating rate of 5 °C/min in the temperature interval from room temperature up to 200 °C were performed. It was determined that latent heat of melting strongly depends on alloy composition. The alloy with the largest content of bismuth, Bi–47.44at.%In eutectic alloy, has the highest melting temperature and the largest value of heat of melting. The alloy with the lowest content of bismuth, Bi–77.92at.%In alloy, has the lowest values of melting temperature and heat of melting.
The results of this study represent contribution to the better understanding of microstructure and thermal properties of low melting Bi-In eutectic alloys as candidate metallic PCMs.

## REFERENCES

[1] X. H. Yang, S. C. Tan, J. Liu, Numerical investigation of the phase change process of low melting point metal, International Journal of Heat and Mass Transfer, 100 (2016) pp. 899-907.
[2] X. H. Yang, S. C. Tan, Y. J. Ding, L. Wang, J. Liu, Y. X. Zhou, Experimental and numerical investigation of low melting point metal based PCM heat sink with internal fins, International Communications in Heat and Mass Transfer, 87 (2017) pp. 118-124.
[3] A. S. Fleischer, Thermal Energy Storage Using Phase Change Materials: Fundamentals and Applications, Springer, 2015.
[4] F. L. Tan, C. P. Tso, Cooling of mobile electronic devices using phase change materials, Applied Thermal Engineering, 24 (2004) 2-3, pp. 159-169.
[5] R. Kandasamy, X. Q. Wang, A. S. Mujumdar, Transient cooling of electronics using phase change material (PCM)-based heat sinks, Applied Thermal Engineering, 28 (2008) pp. 1047-1057.

[6] H. Ge, H. Li, S. Mei, J. Liu, Low melting point liquid metal as a new class of phase change material: An emerging frontier in energy area, Renewable and Sustainable Energy Reviews, 21 (2013) pp. 331-346.
[7] S. Mengjie, N. Fuxin, M. Ning, H. Yanxin, D. Shiming, Review on building energy performance improvement using phase change materials, Energy and Buildings, 158 (2018) pp. 776-793.
[8] R. Adinberg, D. Zvegilsky, M. Epstein, Heat transfer efficient thermal energy storage for steam generation, Energy Conversion and Management, 51 (2010) pp. 9-15.
[9] T. D. Swanson, G. C. Birur, NASA thermal control technologies for robotic spacecraft, Applied Thermal Engineering, 23 (2003) pp. 1055-1065.
[10] J. Rodrıguez-Aseguinolaza, P. Blanco-Rodrıguez, E. Risueno, M. J. Tello, S. Doppiu, Thermodynamic study of the eutectic Mg49–Zn51 alloy used for thermal energy storage, Journal of Thermal Analysis and Calorimetry, 117 (2014) pp. 93-99.
[11] A. Sharma, V. V. Tyagi, C. R. Chen, D. Buddhi, Review on thermal energy storage with phase change materials and applications, Renewable and Sustainable Energy Reviews, 13 (2009) pp. 318-345.
[12] N. Saunders, A. P. Miodownik, CALPHAD (A Comprehensive Guide), Elsevier, London, 1998.
[13] H. L. Lukas, S. G. Fries, B. Sundman, Computational Thermodynamics: the Calphad Method, Cambridge University Press, Cambridge, 2007.
[14] A. Kroupa, A. T. Dinsdale, A. Watson, J. Vrestal, A. Zemanova, COST531 PROJECT - STUDY OF THE ADVANCED MATERIALS FOR LEAD FREE SOLDERING, J Min Metall Sect B Metall., 43 (2007) pp. 113-123.
[15] A. Kroupa, A. T. Dinsdale, A. Watson, J. Vrestal, J. Vízdal, A. Zemanova, The development of the COST 531 lead-free solders thermodynamic database, JOM, 59 (2007) pp. 20-25.
[16] D. Boa, I. Ansara, Thermodynamic assessment of the ternary system Bi-In-Pb, Thermochimica Acta, 314 (1998) pp. 79-86.
[17] W. J. Boettinger, U. R. Kattner, K. W. Moon, J. H. Perepezko, DTA and Heat-flux DSC Measurements of Alloy Melting and Freezing, NIST Special Publication 960-15, Washington, 2006.

**Acknowledgements**

This work was supported by the Ministry of Education, Science and Technological Development of the Republic of Serbia, project No. ON 172037.

17th INTERNATIONAL FOUNDRYMEN CONFERENCE
Hi-tech casting solution and knowledge based engineering
Opatija, May 16th-18th, 2018
http://www.simet.hr/~foundry/

# COMMON FAILURES IN ALUMINOTHERMIC WELDING PROCESS AND PROPOSAL FOR THEIR PREVENTION

**Vaso Manojlović[1]*, Milorad Gavrilovski[2], Željko Kamberović[1], Dejan Momčilović[3]**

[1] University of Belgrade Faculty of Technology and Metallurgy, Belgrade, Serbia
[2] University of Belgrade Faculty of Technology and Metallurgy, Innovation Centre, Belgrade, Serbia
[3] IMS Institute, Belgrade, Serbia

**Poster presentation**
*Preliminary note*

**Abstract**

Aluminothermic welding of rail is still a unique method for joining the rails because of its flexibility and ease of performance, both during the reconstruction and construction of a new track, as well as in the ongoing maintenance of the continuity of the track. Although this procedure is applying for almost hundred years with constant improvements, it still has serious shortcomings. The shortcomings primarily relate to quality variability, which directly dependent on the training of the operator and their compliance with the prescribed instructions and procedures, during the welding process. The most common working mistakes are very similar to the casting failures that occur during the usual casting of steel. The process is susceptible because the welded joint is in constant strain condition caused by the structural differences between primary material and filler material (thermite steel). This paper presents some working failures on the samples from the track in exploitation, as well as the analysis of the causes of their formation. Also, the innovative way of performing aluminum welding of the rail was shown, which minimizes working mistakes and prevents working failures. The results of the quality testing of welded joints are done according to the EU standards. They pointed out that the implementation of this procedure provides greater safety of rail transport as well as its coherence because it significantly reduces the impact of faults of welding teams.

***Keywords***: *aluminothermic welding, rails, failures, porosity*

*Corresponding author (e-mail address): *v.manojlovic@tmf.bg.ac.rs*

## INTRODUCTION

The investigation of the faulties in aluminothermic welding process is usually comes down to the determination of the irregularities of the crystallization processes in the mold cavity [1], the inadequate mold geometry and its casting system [2, 3], the choice of different procedures [4, 5, 6], as well as the thermic treatment after welding process [7]. There are

very few studies that examine the impact of the work faulties on the quality of welded joints. Therefore, the aim of this paper is to show the impact of the most common work faulties, primarily inadequate preheating over the rails which often lead to the fractures. They manifest themselves as a unwelded spots, or a lack of fusion, the creation of a cavity and a central crack due to the shrinkage, macro and micro porosity. These errors can be somewhat mitigated by designing of the mold or casting system through which the thermic steel is introduced into the mold cavity.

## MATERIALS AND METHODS

The aluminothermic welding process is done on railways S49-900 or 49E1-216 (Figure 1). Cracks occur in the exploitation and samples marked SKR7-BRG and 10+400 are taken for examination. The chemical analysis and metallographic tests were done on the thermite steel to determine quality of the aluminothermic mixture. Chemical composition of base and weld metal was done by optical emission spectroscopy (OES) on quantometer ARL 3640, according to the standard SRPS C.A1.011:2003. Microstructure was examined on Carl Zeiss Neophot optical microscope.

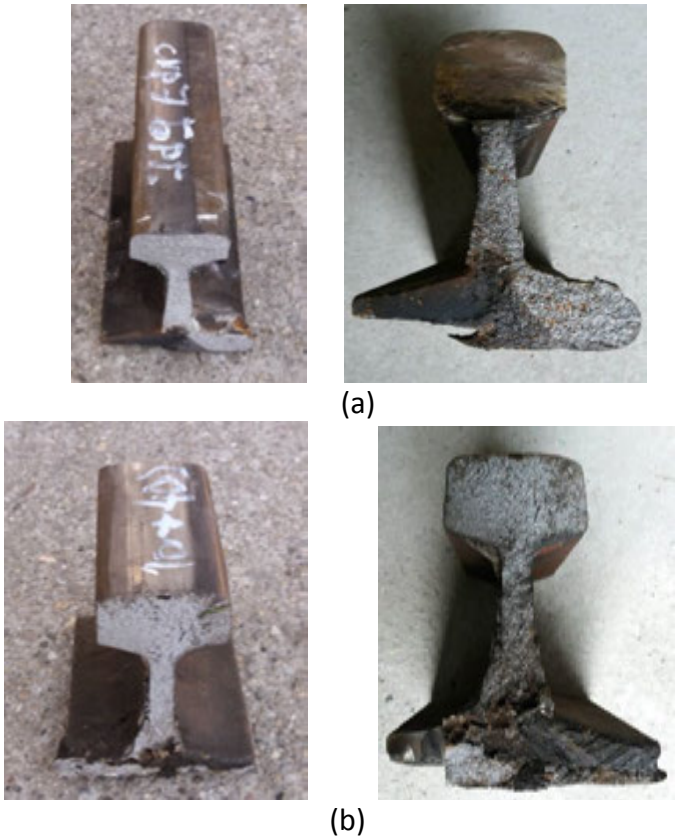

Figure 1. Cross section of cracked samples (a) SKR 7 – BRG and (b) 10+400

(a) (b)

Figure 2. Design of molds geometry – modified aluminothermic method

The new proposed method includes new design of molds geometry shown on Figure 2. The aluminothermic welding was done in the same conditions as previous with the same welding team. The sample is marked as 49-900. Tensile tests were done according to the standard SRPS EN 10002-1:1996, on INSTRON 1330 testing machine. Hardness is tested according to the standard SRPS EN 14730-1:2006 [8-10].

## RESULTS AND DISCUSSION

On the samples SKR 7 – BRG and 10+400 the lack of fusion and asymmetric seam in the lower half of the welded joint are evident (Figure 1). On the sample 10+400 the porosity in the foot of the rail was found (so-called “hot tear”). On the other hand, the microstructure of the thermite steel is pearlite-ferrite with the smaller grains, and chemical analysis meets the required standards EN 14730 (Figure 3 and Table 1).

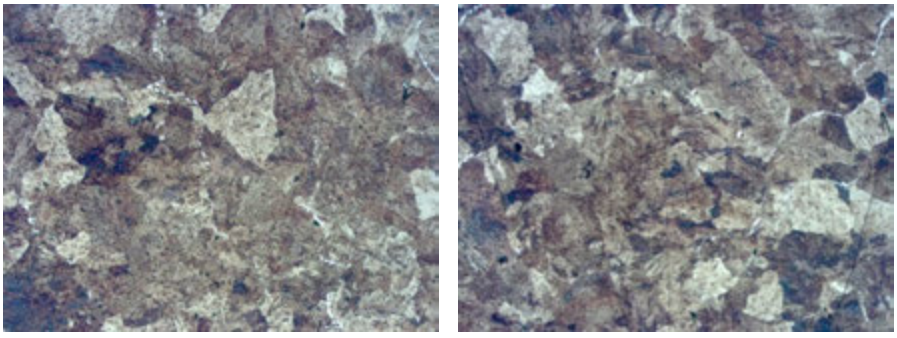

(a) (b)

Figure 3. Microstructure of the thermite steel of samples (a) SKR 7 – BRG and (b) 10+400

The SKR 7-BRG sample was fractured due to the lack of fusion at the base of the rail, which is caused by:

- asymmetrically placed mold halves in relation to the vertical axis of the dilatation gap;
- Inadequate fusion at the ends of the rail base (insufficient temperature, uneven preheating along the entire cross section of the rail);
- Inadequate alignment of the burner with respect to the vertical axis of the dilatation gap;
- Inappropriate gas pressure (particularly oxygen);
- Inadequate width of the dilatation gap.

Table 1. Chemical analysis of the samples SKR 7 – BRG, 10+400 and 49-900

| | SKR 7 – BRG | 10+400 | 49-900 | |
|---|---|---|---|---|
| | | | base metal | thermite steel |
| C | 0.52 | 0.54 | 0.59 | 0.56 |
| Mn | 1.11 | 1.04 | 1.09 | 1.05 |
| Si | 0.34 | 0.304 | 0.24 | 0.22 |
| P | 0.024 | 0.022 | 0.022 | 0.020 |
| S | 0.018 | 0.019 | 0.018 | 0.014 |
| Cr | 0.01 | 0.01 | | |
| Ni | 0.01 | 0.01 | | |
| Cu | 0.02 | 0.03 | | |
| Al | 0.21 | 0.31 | 0.003 | 0.23 |
| V | 0.011 | 0.010 | | |

The 10+400 pattern is characterized by a "hot tear" error at the foot of the rail, which caused fracture. This typical and common mistake, usually followed by porosity and macro inclusion (Figure 3), is the result of:

- The use of large quantities of very moist mass for smudging of the molding halves;
- A water vapor formed during preheating produces hydrogen that is trapped in the metal during solidification of thermite steel. Partial hydrogen pressure increases up to 100 MPa (about 1000 bar). Such an internal pressure leads to the formation of micro and macro cracks as well as porosity, which are clearly visible at the footsteps of this pattern, which necessarily leads to fracture;
- Use of insufficiently heated reaction pot, especially when making the first weld;
- Use of wet molds.

Using the modified molds (Figure 2) the working failures are reduced; this is provided with adequate casting speed of molten metal (without turbulence, erosion, and gas inclusion), degassing of the molding chamber, the preheating of the rails uniformly and evenly, and dissipation of heat throughout the cross section of the seam weld. The mechanical tests were done to prove the quality of the welded joint, where *d* is original diameter of eprouvette; *A* – cross-section area of eprouvette; *F* – force; $R_{p02}$ – yield stress; $R_m$ – ultimate strength; $A_t$ – total elongation, $l_0$ – original gauge length (Table 2).

Table 2. Characteristic points in stress-strain curve

| *d* | *A* | *F* | $R_{p02}$ | $R_m$ | $A_t$ | $l_0$ |
|---|---|---|---|---|---|---|
| mm | $mm^2$ | N | MPa | MPa | % | mm |
| 10 | 78.5 | 63192 | 534 | 805 | 5.66 | 50 |

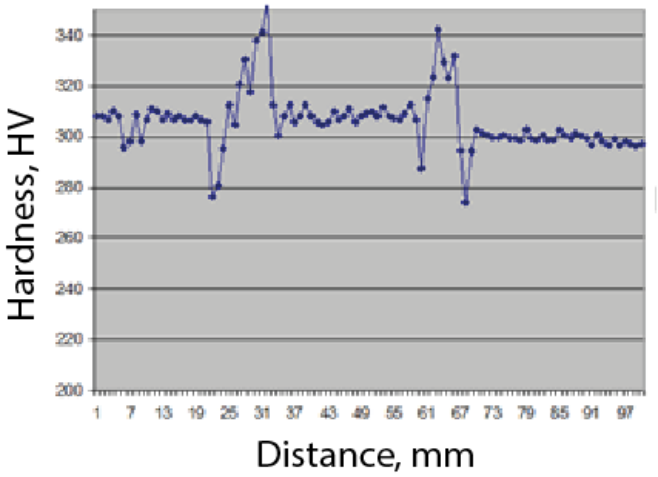


Figure 4. Result of hardness tests for modified aluminothermic welding

Result of hardness tests show the relatively uniform and typical profile for welded joints (Figure 4). The HAZ length was about 101 mm, and the mean hardness was 305 HV.
Microstructure of base metal was fine-grained pearlite-ferrite, and it is very similar to the structure of metal in HAZ, were the grain increase was observed towards to the compound line. Microstructure of the weld metal was also pearlite-ferrite with the smaller grains compared to the structure in the HAZ.

## CONCLUSIONS

Regardless of the fact that aluminothermic welding method is used for several decades, the failures still appear, mainly (95%) as errors of welding teams [7]. The main cause, even with the best-trained team, is a clear failure to comply with the prescribed procedures and guidelines, as well as insufficient attention to details.
Human factor failures can be reduced by frequent training or certification of welding teams as a guarantee for continually repeating the acquired knowledge and experience, which should increase the integrity of the track and avoid expensive repairs.
The most important details that causes the fault can be classified in several areas:
- Preparing the track;
- Assembly and alignment of the mold;
- Moisture in mixture for joining molds;
- Centering accessories, especially heaters;

• Preheating;
• Cleaning and preheating the reaction pot;
• Working with materials that match the quality and type of welding rails.

Performing the aluminothermic welding of rails, using a new form of mold shown in this paper can eliminate the negative effects of welding team errors. The testing results of the welded joint confirm this, which ensures greater safety of the railway traffic, as well as its coherence.

## REFERENCES

[1] L. C. Schroeder, D. R. Poirier, The mechanical properties of thermite welds in premium alloy rails, Materials Science and Engineering 63 (1984) 1, pp. 1-21.
[2] J. P. Cyre, Concepts for improving the fatigue resistance of thermite rail welds, MS Thesis, University of Illinois at Urbana-Champaign, 2002.
[3] E. T. Ross, A statistical study of improved thermite rail welds, MS Thesis, University of Illinois at Urbana- Champaign, 2004.
[4] L. C. Schroeder, D. R. Poirier, Thermite Rail welds, the process, mechanical and metallurgical properties, and possible improvements, Proceedings of Railroad Rail Welding, Memphis, 29–30 November 1983, p. 21.
[5] G. T. Fry, A modified thermite rail welding procedure, MS Thesis, University of Illinois at Urbana-Champaign, 1992.
[6] J. A. Gianetto, E. Es-Sadiqi, K. J. Sawley, M. A. Joos, D. W. Blowatt, Influence of EMS on rail thermite weld structure and properties, Proceedings of the 39th mechanical working and steel processing conference international symposium on rail steels, Indianapolis, IN, 21 October 1997, p. 1091.
[7] B. Jha, Thermite welding of rail steel, PhD Dissertation, Illinois Institute of Technology, 1989.
[8] EN 14730-1, Railway applications - Track - Aluminothermic welding of rails - Part 1: Approval of welding processes; German version EN 14730-1:2006
[9] EN 14732-2, Railway applications - Track - Aluminothermic welding of rails - Part 2: Qualification of aluminothermic welders, approval of contractors and acceptance of welds; German version EN 14730-2:2006
[10] M. Saarna, A. Laansoo, Proceedings of 4th International DAAAM Conference “Industrial engineering – innovation as competitive edge for SME”( Eds. J. Papstel/B. Katalinic) 29 – 30th April, 2004, Tallinn, Estonia, 217-220.

## Acknowledgements

The authors wish to acknowledge the financial support from the Ministry of Science and Technological Development of the Republic of Serbia through the project 34033.

17th INTERNATIONAL FOUNDRYMEN CONFERENCE
Hi-tech casting solution and knowledge based engineering
Opatija, May 16th-18th, 2018
http://www.simet.hr/~foundry/

# ALUMINIUM ALLOY AS CAST MICROSTRUCTURE OBTAINED UNDER THE INFLUENCE OF ELECTROMAGNETIC FIELD

**Branislav Marković[1]*, Aleksandra Patarić[1], Miroslav Sokić[1], Zoran Janjušević[1], Branka Jordović[2]**

[1] Institute for Technology of Nuclear and other Mineral Raw Materials, Belgrade, Serbia
[2] University of Kragujevac Faculty of Technical Sciences, Čačak, Serbia

**Poster presentation**
*Preliminary note*

**Abstract**

Aluminium alloys are characterized by a number of defects that occur during the solidification process such as: porosity, hot cracks, non-uniform grain size and crystal segregation. Since the quality of final product is directly affected by these defects it is necessary to prevent or reduce their appearance by the choice of the appropriate process and optimal parameters of casting. The application of electromagnetic field during the vertical continual casting process can be a very useful tool in reducing these errors. The results presented in this paper were obtained from examination of 7075 Al alloy samples cast with and without electromagnetic field. The microstructure was analyzed by optical microscope. The characterization shows that it is possible to obtain finer and more homogeneous microstructure through the entire cross section of ingots cast with electromagnetic field, compared to ingots cast without electromagnetic field. The grain size measuring is also done and the dependence between grain size and electromagnetic field frequency is given. As the consequence of microstructure-mechanical properties correlation, the use of electromagnetic field improved the mechanical properties, as well.

***Keywords***: *Al alloy, electromagnetic field, microstructure*

*Corresponding author (e-mail address): *b.markovic@itnms.ac.rs*

## INTRODUCTION

The casting under the influence of electromagnetic field is the technology developed by combining the magneto hydrodynamics and casting technique. This casting process provides the opportunity which has never been achieved by conventional casting process. At the beginning, the application of electromagnetic casting has been aimed to obtain the better ingot surface, due to the reduced contact pressure between the mold and the metal. The

reduced contact pressure is the result of potential force acting, as a horizontal component of Lorentz force density, which is being balanced by static pressure of the molten metal, thus resulting in the formation of the convex surface meniscus [1-5].
The other component of the Lorentz force density is a rotational component, resulting in a forced convection in the molten metal, enabling enhanced flow of the melt and homogeneous bulk distribution of alloying elements [6-8]. The researches show that combining the main operating parameters of electromagnetic field, such as frequency and strength of electromagnetic field, this process can efficiently eliminate the other defects of as cast ingots. In this way, the grate savings in energy and time can be achieved. In this paper the special attention was paid to the effect of electromagnetic field on obtained as cast microstructure. Knowing the microstructure-mechanical properties correlation, it is possible to get preferred ingot properties by controlling the main operating parameters and at the same time to avoid needs for additional operations, such as machining and prolonged homogenization.

## MATERIALS AND METHODS

The chemical composition of the used EN AW 7075 alloy is shown in Table 1. Aluminum alloy EN AW 7075 is heat treatable very high strength alloy with wide application in aero and military industry, but it is characterized by a number of defects that occur during the solidification process: porosity, hot cracks, non-uniform grain size and crystal segregation.

Table 1. Chemical composition of alloy EN AW 7075

| Element | Zn | Mg | Cu | Mn | Cr | Fe |
|---|---|---|---|---|---|---|
| Content % | 5.51 | 2.29 | 1.45 | 0.13 | 0.19 | 0.14 |

The experimental equipment consists of medium frequency induction furnace with 100 kg capacity. There is a drainpipe, at the bottom of the furnace, with graphite crystallizer that is intensively cooled with water. The low frequency magnetic field is placed around the crystallizer itself. The testing samples were taken out of ingots with a diameter of 80 mm, obtained by vertical continual casting. The casting temperature was in the range of 710-720°C and the average casting speed was 1.5 mm/s. The frequency of electromagnetic field was 30 Hz, for our previous experience shows that this is the optimal frequency [9]. The current intensity was 200 A.
The microstructure and the frequency of the electromagnetic field are closely related. The sample 1 was obtained from the ingot cast without the presence of electromagnetic field to enable the evaluation of the field effect on the microstructure at sample 2, obtained from the ingot cast in the presence of electromagnetic field with the frequency of 30 Hz.
The microstructure of samples was examined by optical microscopy using the image analysis device Leica Q500MC, after the usual metallographic preparation and etching in Keller's reagent (revealing morphology of Al segregation-solid solution and inter-metallic phase). The grain size measuring is also done.

## RESULTS AND DISCUSSION

Comparing the microstructure of sample 1, obtained without the electromagnetic field effect, and of sample 2 obtained with the effect of electromagnetic field, it is obvious that the structure of sample 1 is more dendritic then the structure of sample 2, which is finer and with more emphasized cells. The characteristic microstructure appearance at the cross section of samples cast under different conditions is shown in Figure 1. As it can be seen, the cellular/dendritic morphology is the result of Al segregation from the solid solution during the solidification process. Nevertheless, the morphology of the sample cast without the electromagnetic field effect, Figure 1a, is more dendritic, in comparison with distinctive cells at Figure 1b, obtained with the electromagnetic field influence.

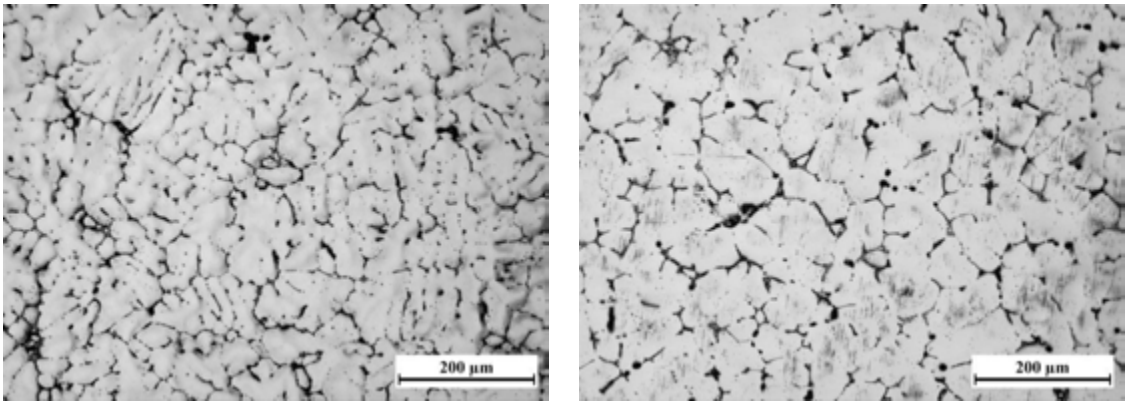


(a) (b)

Figure 1. Microstructure of sample cross section: sample 1 (a) and sample 2 (b), Keller's reagent, 100x

Besides, the presence of shrinkage porosity of interdendritic type was established in sample 1, taken from the ingot cast without the electromagnetic field effect, as can be seen in Figure 2.

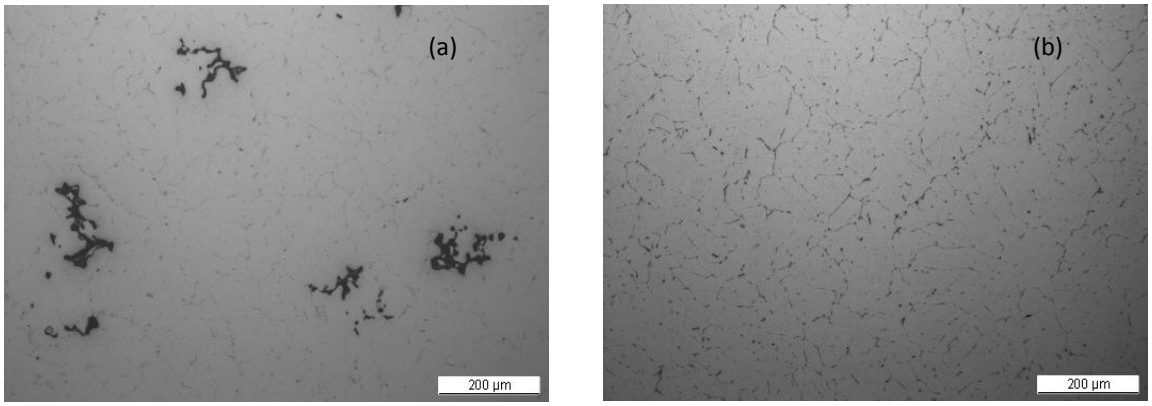


Figure 2. The shrinkage porosity of interdendritic type: sample 1 (a)-without the electromagnetic field effect, and sample 2 (b)-with the electromagnetic field effect, Keller's reagent, 100x

The measured values of grain size of the as cast Al 7075 alloy obtained at the different conditions are given in Table 2.

Table 2. The measured values of grain size of the as cast Al 7075 alloy obtained at the different conditions

| Grain size (μm) / Sample | Min | Max | Average values |
|---|---|---|---|
| Sample 1(0)Hz | 124.96 | 464.96 | 344.41 |
| Sample 2(30)Hz | 87.28 | 189.35 | 101.98 |

Comparing the microstructure of samples it is clear that sample obtained by effect of electromagnetic field with frequency of 30 Hz is finer with the smaller values of gran size. The sample obtained without effect of electromagnetic field has inhomogeneous structure with very uneven grain size. The results of measurement and obtained dependence are shown at Figure 3.

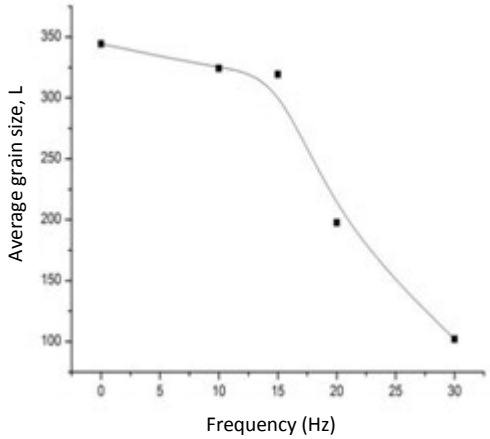


Figure 3. The grain size dependence on electromagnetic field frequency

## CONCLUSIONS

The presented results show the evident influence of the electromagnetic field during casting aluminium alloy 7075. The electromagnetic casting has advantages over conventional casting in terms of obtaining the uniform fine-grained microstructure, and consequently better mechanical properties. The sample obtained by electromagnetic casting process, with a frequency of 30 Hz, have finer and more homogenous microstructure than the sample obtained without electromagnetic field influence, as it was evident on the microstructure figures. The shrinkage porosity of interdendritic type through the entire cross section is reduced in sample 2, obtained using electromagnetic casting process. It is shown that the casting in the electromagnetic field presence, with the previously chosen frequency of 30 Hz,

provide a satisfactory ingots quality. So, there is opportunity to avoid some steps in conventional technological process, such as machining and prolonged homogenization. Namely, the uniform and finer microstructure gives the possibility to shorten the heat treating time.

## REFERENCES

[1] Z. Zhihao, C. Jianzhong, D. Jie, Effect of low-frequency magnetic field on microstructures and macrosegregation of horizontal direct chill casting 7075 aluminum alloy, Journal of Materials Processing Technology, 182 (2007) 1-3, pp. 185-190.
[2] Z. Zhihao, C. Jianzhong, D. Jie, W. Zhefeng, Effect of low- frequency magnetic field on microstructures of horizontal direct chill casting 2024 aluminum alloy, Journal of Alloy and Compounds, 396 (2005) 1-2, pp. 164-168.
[3] Z. Beijiang, L. Guimin, C. Jianzhong, Effect of Electromagnetic Frequency on Microstructures of Continuous Casting Aluminum Alloys, Journal of Materials Science and Technology, 18 (2002) 5, pp. 401-403.
[4] B. Zhang, J. Cui, G. Lu, Q. Zhang, C. Ban, Effect of electromagnetic field on macrosegregation of continuous casting 7075 alloy, Transaction of Nonferrous Metals Society of China, 13 (2003) pp. 158-161.
[5] Q. Zhu, Y. Zhao, J. Cui, B. Zuo, F. Qu, Effect of low-frequency electromagnetic field on the as casting microstructures and mechanical properties of HDC 2024 aluminum alloy, Acta Metallurgica Sinica, 21 (2008) 3, pp. 205-210.
[6] D. Jie, C. Jianzhong, Y. Fuxiao, B. Chunyan, Z. Zhihao, Effect of low-frequency electromagnetic casting on the castability, microstructure and tensile properties of direct chill cast Al-Zn-Mg-Cu alloy, Metallurgical and Materials Transaction A, 35 (2004) pp. 2487-2494.
[7] Z. Yubo, C. Jianzhong, D. Jie, Y. Fuxia, Effect of low frequency electromagnetic field on the constituents of a new super high strength aluminum alloy, Journal of Alloy and Compounds, 402 (2005) 1-2, pp. 149-155.
[8] J. Cui, Z. Zhang, Q. Le, Direct-chilling casting of Mg alloy underelectromagnetic and ultrasonic combined field,Transaction of Nonferrous Metals Society of China, 20 (2010) pp. 297-305.
[9] A. Patarić, Z. Gulišija, S. Marković, Microstructure Examination of Electromagnetic Casting 2024 Aluminum Alloy Ingots, Praktiche Metallographie, 44 (2007) 6, pp. 290-298.

## Acknowledgements

The authors wish to acknowledge the financial support from the Ministry of Science and Technological Development of the Republic of Serbia through the project 34002.

17th INTERNATIONAL FOUNDRYMEN CONFERENCE
Hi-tech casting solution and knowledge based engineering
Opatija, May 16th-18th, 2018
http://www.simet.hr/~foundry/

# EXPERIMENTAL STUDY OF THE TERNARY Ag-Ge-In SYSTEM

**Dušan Milisavljević[1], Duško Minić[1], Milena Premović[1]*, Dragan Manasijević[2]**

[1] University of Priština Faculty of Technical Science, Kosovska Mitrovica, Serbia
[2] University of Belgrade Technical Faculty in Bor, Bor, Serbia

**Poster presentation**
*Original scientific paper*

**Abstract**

Some selected alloys from the ternary Ag-Ge-In system have been experimentally examined by using few different experiment techniques. Used experimental techniques are differential thermal analysis (DTA), scanning electron microscopy (SEM) with energy dispersive spectrometry (EDS), and X-ray powder diffraction (XRD) analysis. Investigated ternary alloys were from three vertical sections Ag-GeIn, Ge-AgIn, and In-AgGe and two isothermal sections at 200 and 400 °C. Temperatures of four invariant reaction and liquid temperatures have been determined with DTA. By EDS and XRD test, phases which are in equilibrium have been determined. By EDS analysis did not detect new compound and large solubility of the third element into the binary compounds.

***Keywords**: ternary system Ag-Ge-In, phase equilibria, DTA, SEM, XRD*

*Corresponding author (e-mail address): *milena.premovic@gmail.com*

## INTRODUCTION

An important task for researchers all over world is to determine a reliable thermodynamic datasets for a description of phase diagrams. The essential part of this approach is a design of key experiments which need to be conducted in order to thermodynamically assess investigated phase diagram. Due to this necessity few alloys from ternary Ag-Ge-In system has been designed. Prepared alloys were from isothermal sections at 200 and 400 °C and three Ag-GeIn, Ge-AgIn, and In-AgGe vertical sections. Used experimental techniques are differential thermal analysis (DTA), scanning electron microscopy (SEM) with energy dispersive spectrometry (EDS) and X-ray powder diffraction (XRD). Reasons for choosing this system are due to technical importance of the system and no other experimental study of the system. Technical importance of the systems is due to special application of the Ge-based alloys as a phase change memory materials (PCM materials) [1-4].

## MATERIALS AND METHODS

All ternary samples with total masses of about 3 g were prepared from high purity (99.999 at. %) Ag, Ge, and In produced by Alfa Aesar (Germany) in an induction furnace under high-purity argon atmosphere. The average weight loss of the samples during induction melting was about 1 mass %. After melting one group of samples were subjected to the SEM-EDS and XRD investigation. Samples were put into quartz glass ampoules, sealed under vacuum and annealed at different temperatures and for different times (200 and 400 °C for four weeks and three weeks, since shorter time did not result equilibrium compositions) and quenched into ice water in order to preserve the equilibrium compositions at a chosen temperatures. The compositions of samples and coexisting phases were determined using JEOL JSM-6460 scanning electron microscope and TESCAN VEGA3 scanning electron microscope both with energy dispersive spectroscopy (EDS) (Oxford Instruments X-act). EDS has been calibrated with the external standard with registration number 7774 and 7775, produced by Micro Analysis Consultants Ltd., Cambridge, UK. Determination of overall compositions of annealed and quenched samples was done by analyzing as large as possible surface of the samples. The compositions of co-existing phases were determined by examining the surface of the same phase at a different parts of the sample (at least five different positions of the same phase are examined per phase). Powder XRD data for phase identification of samples were recorded on a D2 PHASER (Bruker, Karlsruhe, Germany) powder diffractometer equipped with a dynamic scintillation detector and ceramic X-ray Cu tube (KFL-Cu-2K) in a 2θ range from 10° to 75° with a step size of 0.02°. The patterns were analyzed using the Topas 4.2 software, ICDD databases PDF2 (2013) [16]. The instrument was calibrated with Bruker standard, Korundprobe A26-B26-S, beside this standard, ten different powder elements (high purity elements bought from Alpha Acer) were used as a standard in process of calibration. Phase transition temperatures were determined by DTA method. The DTA measurements were performed on an SDT Q600 (TA Instruments). DTA instrument was calibrated with high purity elements Ag, Bi, In, Ge, Sb, Sn, Zn, Ni produced by Alfa Aesar. Alumina crucibles were used and measurements were performed under flowing argon atmosphere produced by MESSER with high purity 6.0 (99.9999 %). Alumina crucible were covered with thin layer of boron-oxide in way to avoid reaction between sample and crucible. Samples with weight about 30 mg were investigated at a heating rate of 5 °C/min with three cycles of heating and cooling. The sample masses and heating rates were determined by analysis of one sample at different testing conditions. The reference material was empty alumina crucible.

## RESULTS AND DISCUSSION

### Vertical sections

Phase transition temperatures of 18 selected alloys from three vertical sections determined by DTA analysis are summarized in Table 1. Temperatures of invariant reactions were

obtained from the beginning of the DTA peak. The liquid temperatures were evaluated from the peak maximum.

Table 1. Experimentally determined phase transition temperatures for the investigated alloys from the ternary Ag-Ge-In system

| Composition of samples (at. %) | Temperatures of phase transformation (°C) | | | | | |
|---|---|---|---|---|---|---|
| | Reaction | | | | Other transformation | Liquidus |
| | * (144.7) | ** (167.6) | *** (204.9) | **** (577.6) | | |
| Vertical section Ge–$Ag_{50}In_{50}$ | | | | | | |
| 47.5 Ag<br>5.0 Ge<br>47.5 In | | 168.2±.3 | 208.6±.4 | | | 485.4±.3 |
| 40.0 Ag<br>20.0 Ge<br>40.0 In | | 169.5±.2 | 203.8±.2 | | 491.6±.2 | 684.3±.5 |
| 30.0 Ag<br>40.0 Ge<br>30.0 In | | 170.3±.1 | 206.8±.5 | | 496.4±.5 | 774.4±.6 |
| 20.0 Ag<br>60.0 Ge<br>20.0 In | | 170.6±.3 | | | 492.6±.4 | 826.8±.3 |
| 10.0 Ag<br>80.0 Ge<br>10.0 In | | 168.8±.4 | 201.6±.2 | | 486.2±.7 | 878.3±.6 |
| Vertical section In–$Ag_{50}Ge_{50}$ | | | | | | |
| 48.0 Ag<br>48.0 Ge<br>4.0 In | | | | | 662.6±.5 | 812.4±.3 |
| 42.5 Ag<br>42.5 Ge<br>15.0 In | | | | 573.4±.8 | 619.6±.8 | 805.5±.6 |
| 40.0 Ag<br>40.0 Ge<br>20.0 In | | | 197.6±.1 | 582.6±.3 | 292.7±.5 | 801.8±.1 |
| 30.0 Ag<br>30.0 Ge<br>40.0 In | | 163.2±.5 | 206.6±.4 | | 445.9±.3 | 737.3±.2 |
| 20.0 Ag<br>20.0 Ge<br>60.0 In | 147.2±.6 | 172.4±.2 | | | 356.6±.2 | 633.3±.3 |
| 10.0 Ag<br>10.0 Ge<br>80.0 In | 147.2±.4 | 171.9±.1 | | | 266.8±.1 | 521.8±.4 |
| 5.0 Ag<br>5.0 Ge<br>90.0 In | 145.6±.3 | | | | | 377.7±.2 |
| Vertical section Ag–$Ge_{50}In_{50}$ | | | | | | |
| 20.0 Ag<br>40.0 Ge<br>40.0 In | | 168.8±.5 | 206.2±.6 | | 395.4±.8 | 753.6±.1 |

| | | | | | | |
|---|---|---|---|---|---|---|
| 40.0 Ag<br>30.0 Ge<br>30.0 In | | 168.2±.3 | 207.6±.7 | | 538.2±.5 | 746.2±.4 |
| 60.0 Ag<br>20.0 Ge<br>20.0 In | | | | 580.9±.4 | | 685.6±.6 |
| 80.0 Ag<br>10.0 Ge<br>10.0 In | | | | | 662.2±.3 | 771.6±.5 |
| 86.0 Ag<br>7.0 Ge<br>7.0 In | | | | | 663.8±.7 | 829.2±.7 |
| 94.0 Ag<br>3.0 Ge<br>3.0 In | | | | | 306.8±.2/837.2±.4 | 926.6±.3 |
| * L→$AgIn_2$+(Ge)+(In)<br>** L+γ($Ag_2In$)→$AgIn_2$+(Ge)<br>*** (Ge)+ζ($Ag_3In$)→L+γ($Ag_2In$)<br>**** L+(Ag)→(Ge)+ζ($Ag_3In$) | | | | | | |

Temperatures of four invariant reactions have been determined. By using thermodynamic parameters for constitutive binary systems of ternary Ag-Ge-In it is determined which reactions is. Based on the DTA results the ternary eutectic reaction L→$AgIn_2$+(Ge)+(In) has been determined on three In-rich samples. Measured temperatures of this ternary eutectic reaction are 145.6 and 147.2 °C and they are close to each other. The occurrence of L+γ($Ag_2In$)→$AgIn_2$+(Ge) invariant reaction has been experimentally detected on ten ternary samples. Measured temperature of invariant reaction vary in the range from 163.2 to the 172.4 °C. The occurrence of the (Ge)+ζ($Ag_3In$)→L+γ($Ag_2In$) invariant reaction has been detected in eight investigated samples. According to the experimental results, this reaction occurs in temperature range from 197.6 to the 208.6 °C. Phase transition temperature related to the L+(Ag)→(Ge)+ζ($Ag_3In$) invariant reaction has been detected in three ternary samples. Experimentally detected temperatures of this reaction are 573.4, 580.9 and 582.6 °C. Other measured temperatures listed in Table 2 are related to the additional phase transitions and liquidus temperatures of the investigated samples. DTA heating curves of some investigated samples from every vertical section with marked temperatures of detected phase transitions are presented in Figure 1 as an illustration.

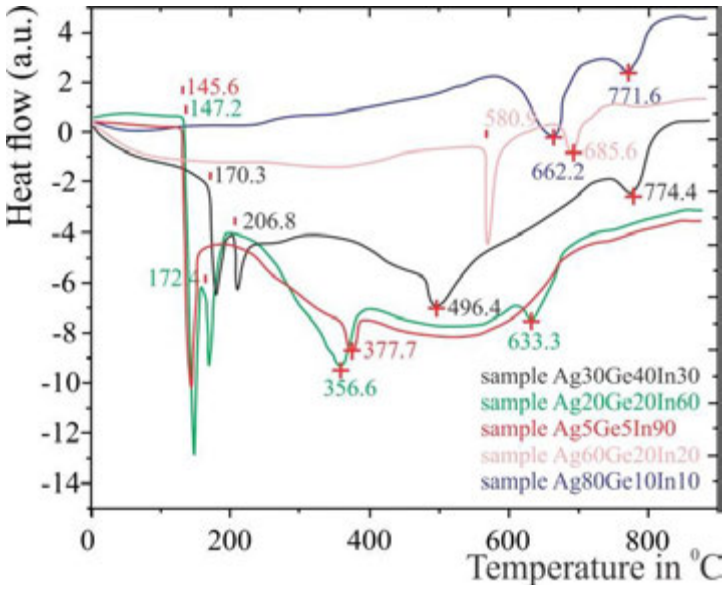


Figure 1. DTA heating curves of few samples

**Isothermal section at 200 °C**

The results of EDS and XRD examination of the seven alloys annealed at 200 °C are presented in Table 2. Data shown in Table 2 includes overall compositions of the examined alloys and compositions of co-existing phases determined by EDS. Since the compositions of β($Ag_3In$), ζ($Ag_3In$), and γ($Ag_2In$) phases obtained by EDS analysis are close to each other additional identification of co-exisitng phases was performed using XRD analysis. Lattice parameters of presented phases are also calculated and shown in Table 2. Determination of lattice parameters was done by using full Rietveld refinement and data for comparison of lattice parameters were used from literature [5-7].

Two co-existing phases are detected in the microstructure of sample I (see Fig. 2a). EDS analysis revealed that dark phase is rich with germanium and the light phase is based on silver which can dissolve 11.1±0.3 at. % of In. Results of XRD analysis confirmed that detected phases correspond to (Ge) and (Ag) solid solution phases. Figure 3 presents XRD pattern of the sample I.

Two co-existing phases were detected in the sample II by EDS analysis. The microstructure of sample II is given in Figure 2b) where two phases are clearly visible. Dark phase is rich with Ge, while the gray phase is binary Ag-rich phase with 23.8±0.4 at. % of In and a 0.3 ±0.2 at. % of Ge. Using XRD analysis detected phases are identified as (Ge) and ζ($Ag_3In$).

Table 2. Experimentally determined phase compositions in the ternary Ag-Ge-In system annealed at 200 °C for four weeks

| N. | Composition of samples (at. %) | Determined phases | | Compositions of phases (at. %) | | | Lattice parameters (Å) | |
|---|---|---|---|---|---|---|---|---|
| | | SEM-EDS | XRD | Ag | Ge | In | *a=b* | *c* |
| I | 62.79 Ag<br>28.91 Ge<br>8.3 In | (Ag)<br>(Ge) | (Ag)<br>(Ge) | 88.2±0.1<br>0.7±0.1 | 0.14±0.2<br>98.9±0.1 | 11.66±0.3<br>0.4±0.2 | 4.1224(9)<br>5.6545(5) | |
| II | 58.92 Ag<br>20.88 Ge<br>20.2 In | (Ge)<br>$\zeta(Ag_3In)$ | (Ge)<br>$\zeta(Ag_3In)$ | 0.3±0.3<br>75.9±0.3 | 99.4±0.1<br>0.3 ±0.2 | 0.3±0.3<br>23.8±0.4 | 5.6560(1)<br>2.9608(8) | 4.7765(7) |
| III | 39.35 Ag<br>17.16 Ge<br>43.49 In | L<br>(Ge)<br>$\gamma(Ag_2In)$ | -<br>(Ge)<br>$\gamma(Ag_2In)$ | 6.4±0.3<br>1.1±0.3<br>65.3±0.4 | 1.2±0.3<br>98.2±0.6<br>0.5±0.4 | 92.4±0.2<br>0.7±0.2<br>34.2±0.1 | -<br>5.6523(2)<br>9.8845(1) | |
| IV | 25.86 Ag<br>12.51 Ge<br>61.63 In | L<br>(Ge)<br>$\gamma(Ag_2In)$ | -<br>(Ge)<br>$\gamma(Ag_2In)$ | 6.7±0.3<br>0.7±0.1<br>65.5±0.4 | 1.5±0.1<br>98.6±0.7<br>1.0±0.2 | 91.8±0.4<br>0.7±0.6<br>33.5±0.3 | -<br>5.6527(8)<br>9.8836(4) | |
| V | 19.23 Ag<br>38.62 Ge<br>42.15 In | L<br>(Ge)<br>$\gamma(Ag_2In)$ | -<br>(Ge)<br>$\gamma(Ag_2In)$ | 6.2±0.3<br>1.0±0.2<br>65.3±0.4 | 0.8±0.2<br>98.1±0.3<br>0.5±0.4 | 93±0.3<br>0.9±0.4<br>34.2±0.5 | -<br>5.6559(3)<br>9.8846(2) | |
| VI | 34.8 Ag<br>36.37 Ge<br>28.83 In | L<br>(Ge)<br>$\gamma(Ag_2In)$ | -<br>(Ge)<br>$\gamma(Ag_2In)$ | 6.4±0.3<br>1.2±0.4<br>64.8±0.5 | 1.6±0.4<br>97.8±0.5<br>1.2±0.5 | 92±0.5<br>1.0±0.3<br>34±0.2 | -<br>5.6557(1)<br>9.8855(8) | |
| VII | 15.38 Ag<br>60.04 Ge<br>24.58 In | L<br>(Ge)<br>$\gamma(Ag_2In)$ | -<br>(Ge)<br>$\gamma(Ag_2In)$ | 5.8±0.6<br>0.5±0.3<br>64.6±0.2 | 1.4±0.3<br>99.2±0.2<br>1.0±0.6 | 92.8±0.6<br>0.3±0.2<br>34.4±0.1 | -<br>5.6535(3)<br>9.8865(5) | |

The experimental results showed that five samples (samples III to VII) have identical three-phase microstructure which includes liquid phase, (Ge) solid solution and binary intermetallic compound $\gamma(Ag_2In)$. Two representative microstructures of samples III and VI are given in Figures 2c and 2d at which three phase regions L+(Ge)+$\gamma(Ag_2In)$ are visible. Detected liquid phase is rich with In with a solubility of Ag in range of 5.8 to 6.7 at. % and a small amount of dissolved Ge. According to the EDS results detected phase can be (In) solid solution or liquid phase. XRD examination helped us to conclude that according to the XRD patterns detected phase cannot be (In) solid solution since there are no peaks which are corresponding to (In) phase and actually detected phase is liquids phase. Second, detected phase on those samples is (Ge) solid solution with a solubility of In from 0.3 to 1 at. % and 0.5 to 1.2 at. % of Ag. Third, detected phase is binary intermetallic compound $\gamma(Ag_2In)$, according to the detected EDS composition this phase can be also $\zeta(Ag_3In)$. Since $\gamma(Ag_2In)$ and $\zeta(Ag_3In)$ phase have a different crystal structure, XRD test confirm that detected phase in samples III to VII is $\gamma(Ag_2In)$. Fig. 2 presents four characteristic microstructures of the ternary samples annealed at 200 °C for four weeks.

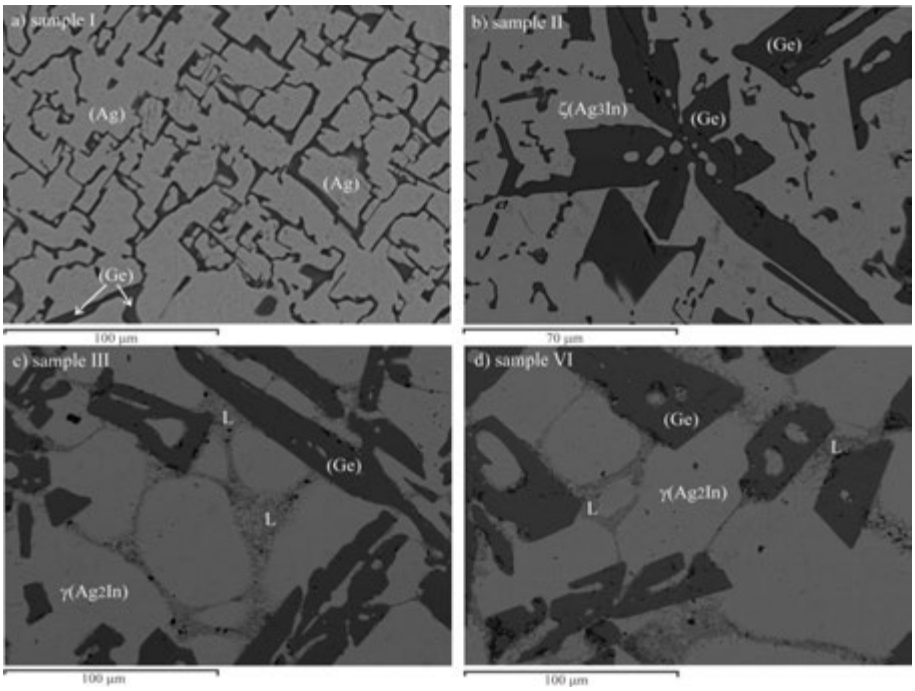


Figure 2. SEM micrographs of the selected alloy samples annealed at 200 °C for four weeks

At all shown microstructures (Ge) solid solution is dark phase, while other phases are lighter in comparison with (Ge) solid solution. In microstructure of the sample I, two phase are visible where one is (Ge) solid solutions detected as a dark phase and (Ag) as a gray phase. Two phases are visible in microstructure of sample II (Figure 2c), dark phase is (Ge) and gray is $\zeta(Ag_3In)$. Beside (Ge) solid solution, liquid phase have been detected in microstructure of samples III and VI. Liquid phase is trapped between grains of (Ge) solution and an intermetallic compound $\gamma(Ag_2In)$ which are detected as a grey phase. Figure 3 presents XRD pattern of the sample I with marked peaks related to the detected phases.

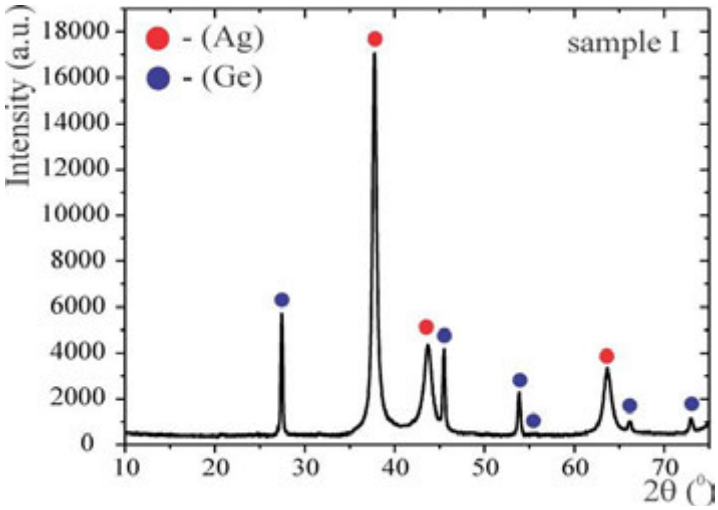


Figure 3. XRD patterns of the selected alloy sample $Ag_{62.79}Ge_{28.91}In_{8.3}$ annealed at 200 °C for four weeks

**Isothermal section at 400 °C**

Experimental results of EDS and XRD analysis for seven samples annealed at 400 °C for three weeks are summarized in Table 3.

Table 3. Experimentally determined phase compositions in the ternary Ag-Ge-In system annealed at 400 °C for three weeks

| N. | Composition of samples (at. %) | Determined phases | | Compositions of phases (at. %) | | | Lattice parameters (Å) | |
|---|---|---|---|---|---|---|---|---|
| | | SEM-EDS | XRD | Ag | Ge | In | *a=b* | *c* |
| 1 | 81.65 Ag<br>8.19 Ge<br>10.16 In | (Ag)<br>(Ge) | (Ag)<br>(Ge) | 87.62±0.4<br>0.7±0.8 | 1.42±0.2<br>98.9±0.5 | 10.96±0.3<br>0.4±0.6 | 4.1198(3)<br>5.6547(4) | |
| 2 | 55.48 Ag<br>28.69 Ge<br>15.83 In | (Ag)<br>(Ge)<br>ζ($Ag_3In$) | (Ag)<br>(Ge)<br>ζ($Ag_3In$) | 79.3±0.3<br>0.8±0.5<br>75.6±0.4 | 2.5±0.1<br>98.7±0.4<br>0.9±0.5 | 18.2±0.1<br>0.5±0.2<br>23.5±0.1 | 4.1314(3)<br>5.6544(8)<br>2.9618(3) | 4.7785(2) |
| 3 | 42.53 Ag<br>32.51 Ge<br>24.96 In | L<br>(Ge)<br>ζ($Ag_3In$) | -<br>(Ge)<br>ζ($Ag_3In$) | 34.41±0.3<br>1.0±0.3<br>65.3±0.4 | 2.54±0.3<br>97.6±0.6<br>0.8±0.4 | 63.05±0.2<br>1.4±0.2<br>33.9±0.1 | -<br>5.6543(3)<br>2.9576(6) | 4.7612(8) |
| 4 | 33.98 Ag<br>52.17Ge<br>13.85 In | (Ge)<br>ζ($Ag_3In$) | (Ge)<br>ζ($Ag_3In$) | 0.7±0.3<br>71.04±0.5 | 98.8±0.2<br>0.6±0.7 | 0.5±0.2<br>28.36±0.6 | 5.6524(5)<br>2.9636(6) | 4.7728(3) |
| 5 | 11.66 Ag<br>77.72 Ge<br>10.62 In | L<br>(Ge)<br>ζ($Ag_3In$) | -<br>(Ge)<br>ζ($Ag_3In$) | 34.51±0.3<br>1.1±0.2<br>66.3±0.4 | 2.37±0.7<br>97.1±0.2<br>0.5±0.4 | 63.12±0.3<br>1.8±0.4<br>33.2±0.5 | -<br>5.6522(2)<br>2.9476(4) | 4.7654(1) |
| 6 | 19.37 Ag<br>15.08 Ge<br>65.55 In | L<br>(Ge) | -<br>(Ge) | 22.48±0.3<br>1.2±0.4 | 6.46±0.4<br>97.8±0.5 | 71.06±0.5<br>1.0±0.3 | -<br>5.6532(2) | |
| 7 | 4.48 Ag<br>51.31 Ge<br>44.21 In | L<br>(Ge) | -<br>(Ge) | 8.96±0.6<br>0.5±0.3 | 2.77±0.3<br>99.2±0.4 | 88.27±0.4<br>0.3±0.7 | -<br>5.6534(1) | |

(Ag) and (Ge) phases are detected in the microstructure od the sample 1. The microstructure of sample 1 is given in Fig. 4.a). EDS results showed that (Ag) solid solution can dissolve 10.96±0.3 at. % of In and 1.42±0.2 at. % Ge.

Sample 2, is from three phase region and microstructure of this sample is given in Fig. 4b. Three detected phases are (Ge) and (Ag) solid solutions and one binary intermetallic compound ζ($Ag_3In$). According to the EDS results (Ag) solid solution can dissolve a 18.2±0.1 at. % of In. On SEM micrograph (see Fig. 4b) (Ag) solid solution appears a light grey phase, intermetallic compound ζ($Ag_3In$) is a grey phase and (Ge) darkest phase.

Similar three-phase microstructure was identified for the samples 3 and 5. Results of EDS and XRD analysis confirmed that those samples belong to the same L+(Ge)+ζ($Ag_3In$) three-phase region. Detected liquid phase consist of ≈ 34.5 at. % of Ag, ≈ 2.5 at. % of Ge, and ≈ 63 at. % of In. One representative microstructure of these samples is given in Fig. 4c, with marked detected phases. The presented microstructure is for sample 3 where the darkest phase is (Ge) solid solution, light phase is ζ($Ag_3In$) binary intermetallic compound, the liquid phase at 400 °C, traped betwine grains of solid phases and holes. Fig. 4c) presents microstructure of sample 4, where two phases are visible. EDS test shows that one of the

detected phases is rich with (Ge) and by XRD test it is confirmed that phase represents (Ge) solid solution. This phase on microstructure appears as a dark phase. The second phase is a binary intermetallic phase ζ($Ag_3In$) detected as a gray phase in the microstructure. Samples 6 and 7 have been detected same two-phase region L+(Ge). Detected liquid phase is rich with In and another phase is (Ge) solid solution.

Fig. 4, presents four characteristic microstructures of the samples annealed at 400 °C for three weeks. XRD pattern of sample 4 is given in Figure 5. Figure 5 shows XRD pattern for the sample 4 annealed at 400 °C for three weeks.

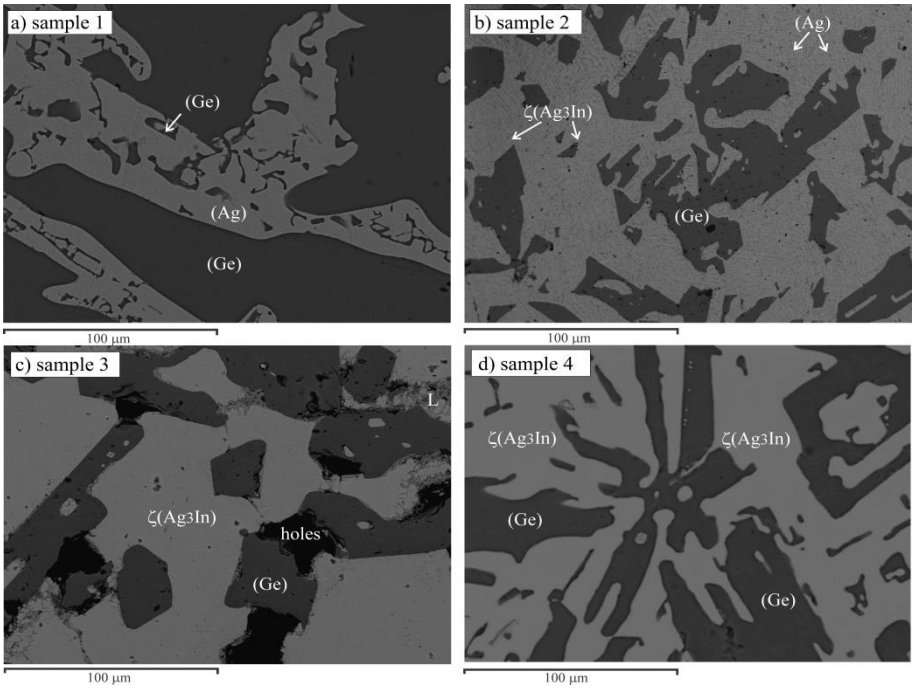


Figure 4. SEM micrographs of the selected alloy samples annealed at 400 °C for three weeks.

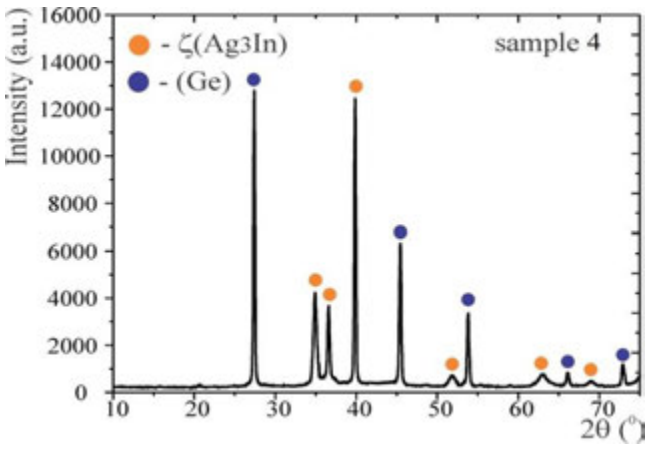


Figure 5. XRD patterns of the alloy sample 4 annealed at 400 °C for three weeks

## CONCLUSIONS

Ternary Ag-Ge-In system has been experimentally examined by DTA, EDS and XRD techniques. DTA results are used for detection phase transition temperatures for ternary samples from three vertical sections. By using this technique, temperatures of four invariant reactions, other phase transitions and liquid phase transitions temperatures are experimentally determined. Measured temperatures of the ternary eutectic reaction $L \rightarrow AgIn_2+(Ge)+(In)$ has been determined to be 145.6 and 147.2 °C. The invariant reaction $L+\gamma(Ag_2In) \rightarrow AgIn_2+(Ge)$ has been experimentally detected on ten ternary samples and the temperature vary in the range from 163.2 to the 172.4 °C. The invariant reaction $(Ge)+\zeta(Ag_3In) \rightarrow L+\gamma(Ag_2In)$ occurs in temperature range from 197.6 to the 208.6 °C. The invariant reaction $L+(Ag) \rightarrow (Ge)+\zeta(Ag_3In)$ has been detected to be 573.4, 580.9 and 582.6 °C. Seven samples per isothermal section at 200 and 400 °C were examined by EDS and XRD method. The EDS analysis did not detect new compound and large solubility of the third element into the binary compounds. With EDS test three different phase regions have been detected with samples annealed at 200 °C and on the samples annealed at 400 °C five different phase regions.

## REFERENCES

[1] E. M. Vinod, R. Naik, R. Ganesan, K. S. Sangunni, J. Non-Cryst. Solids., 358 (2012) pp. 2927-2930.
[2] D. Ielmini, A. L. Lacaita, Mater. Today., 14 (2011) 12, pp. 600-607.
[3] S. Raoux, W. Welnic, D. Lelmini, Chem. Rev., 110 (2010) pp. 240-267.
[4] S. L. Ou, C. P. Cheng, C. Y. Yeh, C. J. Chung, K. S. Kao, R. C. Lin, Adv. Mater. Res., 189-193 (2011) pp. 4430-4433.
[5] E. Jette, F. Foote, J. Chem. Phys., 3 (1935) pp. 605-616.
[6] A. S. Cooper, Acta Crystallogr., 15 (1962) pp. 578-582.
[7] A. N. Campbell, R. Wagemann, R. B. Ferguson, Can. J. Chem., 48 (1970) pp. 1703-1715.

## Acknowledgements

This work has been supported by the Ministry of Education, Science and Technological Development of the Republic of Serbia (Grant No. OI172037).

17th INTERNATIONAL FOUNDRYMEN CONFERENCE
Hi-tech casting solution and knowledge based engineering
Opatija, May 16th-18th, 2018
http://www.simet.hr/~foundry/

# CASTING AN Al ALLOY 2024 + 4% FLY ASH COMPOSITE SUITABLE FOR PROCESSING BY PLASTIC DEFORMATION

# LIJEVANJE KOMPOZITA NA BAZI Al-LEGURE 2024 S DODATKOM 4% LEBDEĆEG PEPELA PRIKLADNOG ZA OBRADU PLASTIČNOM DEFORMACIJOM

**Merima Muslić[1]*, Vesna Maksimović[2], Ilija Bobić[2]**

[1] "E-PRO" Ltd. for designing, engineering and technical consulting, Bihać, Bosnia and Herzegovina
[2] University in Belgrade, "Vinča" Nuclear Institute, Belgrade, Serbia

**Poster presentation**
*Original scientific paper*

**Abstract**

Fly ash appears as a by-product of the coal combustion in thermal plants and it presents a serious ecological problem. It is a low density material that consists of spherical micro particles, which are by its constitution basically metal oxides. Fly ash micro-particles can be incorporated as reinforcement into a metal matrix based on aluminium or Al alloy. Developing this composite achieves two basic aims: a) resolving the problem of disposal of the fly ash, and b) providing a lower price material suitable for production of light components which are usually made from Al or Al alloys.
This paper describes producing an Al alloy 2024 + 4% fly ash composite by casting method. The gained composite as well as the non fly ash aluminum alloy 2024 was subsequently subjected to plastic deformation of 25%. We performed a comparison of microstructure of cast and deformed composites, and 2024 alloy without fly ash by *Olympus GX51F-5* microscope.

***Keywords**: composite, fly ash, Al alloy 2024, casting, deformation*

*Corresponding author (e-mail address): *dmuslic@bih.net.ba*

**Sažetak**

Lebdeći pepeo se pojavljuje kao nusprodukt pri izgaranju ugljena u termoelektranama i predstavlja ozbiljan ekološki problem. Radi se o materijalu male gustoće, koji sadrži pune i djelimično šuplje sferične čestice, a koje su po sastavu uglavnom metalni oksidi. Mikročestice lebdećeg pepela mogu se ugraditi kao ojačalo u metalnu matricu baziranu na aluminiju ili Al leguri. Razvojem ovakvog kompozita postižu se dva osnovna cilja: a) rješavanje problema odlaganja lebdećeg pepela i b) dobivanje jeftinijeg materijala pogodnog za proizvodnju lakih dijelova koji se uobičajeno izrađuju od aluminija i njegovih legura.

U ovom radu opisana je proizvodnja kompozita na bazi aluminijske legure sa 4wt.% masenog udjela lebdećeg pepela lijevanjem. Dobiveni kompozit, kao i legura 2024 bez pepela naknadno su podvrgnuti plastičnoj deformaciji od 25%. Provedena je usporedba mikrostuktura lijevanog i gnječenog kompozita te ugnječene legure bez lebdećeg pepela pomoću svjetlosnog mikroskopa *Olympus GX51F-5*.

***Ključne riječi**: kompozit, lebdeći pepeo, aluminijska legura 2024, lijevanje, deformacija*

## UVOD

Kompozitni materijali s metalnom matricom i različitim ojačalima, zbog varijacija materijala, predstavljaju trajno zanimljiv predmet proučavanja. Radi njihovih pozitivnih svojstava, u istraživanjima su kao materijal za metalnu osnovu kompozita često korišteni aluminij ili njegove legure. Kao ojačalo u aluminijsku matricu se može dodati određena količina lebdećeg pepela.

Lebdeći pepeo, koji nastaje kao nusprodukt pri izgaranju ugljena u termoelektranama, je nehomogena mješavina sferičnih čestica promjera 1-250 µm. Nastaje pri temperaturama 920-1200 °C, a sadrži $SiO_2$, $Al_2O_3$, $Fe_2O_3$, CaO i druge okside, ovisno o vrsti ugljena i termoelektrani iz koje potječe. Prikuplja se u filterima, pri ulasku dimnih plinova u dimnjak [1, 2].

Iako ovaj izuzetno jeftin materijal, niske gustoće, nalazi svoju primjenu kao dodatak u proizvodnji konstrukcijskih materijala u građevinarstvu, to je nedovoljno za rješavanje problema njegovog sigurnog odlaganja. Samo u SAD-u skupi se godišnje oko 80 milijuna tona lebdećeg pepela kojeg je potrebno zbrinuti na siguran i zakonit način [1].

Uobičajeno se za izradu kompozita koriste sitnije čestice lebdećeg pepela usljed čega kompozit s lebdećim pepelom može imati bolja svojstva nego bazna legura. Ispitivanja su pokazala da fine sferične čestice pepela dovode do boljeg povezivanja kompozita i povećanja čvrstoće, tvrdoće i otpornosti prema trošenju s povećanjem udjela pepela [3-5]. Aluminijske legure s manje od 10 % lebdećeg pepela pokazuju dobre karakteristike pri lijevanju dijelova primijenjenih u autoindustriji, što im uz nižu cijenu materijala, energije i pozitivnog efekta na okoliš daje prednost pred drugim materijalima [5]. Istovremeno nije uočena veća razlika između kompozita i bazne legure prilikom izvođenja testova starenja materijala [6]. Ispitivan je i utjecaj predgrijavanja pepela na njegovu distribuciju unutar matrice gdje se pokazalo da viša temperatura predgrijavanja i manja brzina dodavanja pepela dovode do povećanja tvrdoće, smanjenja poroznosti i općenito poboljšanja svojstava kompozita [7].

Dosadašnja istraživanja su orijentirana prema postupku lijevanja kompozita uz miješanje (eng. stir casting), gdje su ustanovljeni optimalni parametri: temperatura taljenja (700 °C), brzina miješanja (1200 o/min), vrijeme miješanja (6 min) i maseni udio lebdećeg pepela (13 %), pri kojima je vlačna čvrstoća povećana i do 50 % [8-10]. U pogledu smanjenja potrošnje energije i produljenja vijeka trajanja alata za lijevanje, te poboljšanja strukture materijala interesantni su postupci lijevanja kompozita u poluočvrsnutom stanju (eng. rheocasting, thixocasting, compocasting) [11, 12]. Ovi postupci podrazumjevaju lijevanje kompozita i

miješanje ojačala pri nižim temperaturama, gdje usljed sila smicanja dolazi do "razbijanja" dendrita, odnosno nastanka nedendritne strukture [11-14].

## MATERIJALI I METODE

Pri lijevanju kompozita korištena je aluminijska legura 2024, čiji je sastav naveden u tablici 1 i koja pripada u legure namijenjene za obradu deformacijom.
Lebdeći pepeo je porijeklom iz termoelektrane "Kolubara", Srbija, a njegova svojstva su određena kombiniranjem metoda. Rendgenskom difrakcijskom analizom (XRD) određen je fazni sastav pepela. Optičkom emisijskom spektrometrijom s induktivno spregnutom plazmom (ICP-OES) određivan je kemijski sastav pepela. Ovom metodom nije bilo moguće odrediti sve elemente zbog korištenih rastvarača i pojave nerastvorenog ostatka. Preračunavanjem je određen sadržaj oksida u pepelu, dan u tablici 2.
Mjerenje raspodjele veličine čestica izvršeno metodom difrakcije laserske svjetlosti. Ne može se sav pepeo koristiti u proizvodnji kompozita jer su moguće različite nepoželjne reakcije [11-14]. Stoga je pepeo prosijan te je korištena samo frakcija koja sadrži čestice manje od 45 µm.

Tablica 1. Kemijski sastav aluminijske legure 2024

| Kemijski element | Al | Cu | Mg | Mn | Si | Fe | Zn | Ti | Cr | Ti+Zr max |
|---|---|---|---|---|---|---|---|---|---|---|
| *w*, % | Ostatak (do 93,57) | 4,2 | 1,06 | 0,53 | 0,14 | 0,34 | 0,10 | 0,05 | 0,01 | 0,2 |

Kompozit na bazi legure 2024 i 4 % lebdećeg pepela izliven je sa slijedećim parametrima:
- da bi se riješili vlage, pepeo je predgrijavan na temperaturu 150°C u trajanju od 2h,
- lijevanje kompozita je izvedeno pri temperaturi 680°C,
- pepeo je dodan postupno s brzinom miješanja od 800 o/min,
- vrijeme miješanja: 4 min,
- kokila u koju je kompozit uliven predgrijana je na temperaturu 300°C, te je nakon lijevanja ostavljeno da se postupno ohladi.

Pri navedenom postupku korištena je sljedeća oprema:
- Za taljenje legure korišten je keramički lonac s grijačima te ugrađenim senzorom za praćenje temperature. Grijači su povezani na izvor električne energije pomoću kojeg se može regulirati temperatura kokile.
- Za predgrijavanje pepela i kokile korištena je električna peć koja također posjeduje mogućnost regulacije temperature.
- Kokila je čelična, dimenzija 20 × 30 × 120 mm
- Mješalica s plosnatom lopaticom kojoj se može podešavati broj obrtaja.

Slika 1 pokazuje dio korištene opreme.

Slika 1. Oprema za lijevanje

**REZULTATI I RASPRAVA**

Obzirom na sastav lebdećeg pepela, kao i njegovu morfološku, mineraloški i drugu strukturu moguće su različite štetne pojave pri lijevanju kompozita koji sadrži pepeo. U nekim slučajevima može doći do različitih kemijskih reakcija između komponenti pepela i matrice zbog kojih lijevanje može biti neuspješno. Vrlo često može doći do isplivavanja čestica pepela na površinu odljevka. Također je poznat problem aglomeracije čestica pepela, odnosno neravnomjerne distribucije unutar matrice.

Tablica 2. Sadržaj oksida u korištenom lebdećem pepelu

| $SiO_2$ (%) | $Al_2O_3$ | $Fe_2O_3$ | $TiO_2$ | MnO | CaO | MgO |
|---|---|---|---|---|---|---|
| 6,8±0,4 | 22,5±0,4 | 17,4±0,2 | 0,80±0,02 | 0,109 ±0,003 | 12,42±0,08 | 3,06±0,06 |

Sadržaj oksida u korištenom lebdećem pepelu je dat u tablici 2, dok slika 2 pokazuje difraktogram uzorka lebdećeg pepela. Glavne mineralne komponente u lebdećem pepelu su: hematit ($Fe_2O_3$), kvarc ($SiO_2$), kalcijev karbonat ($CaCO_3$) i gehlenit ($CaAl_2Si_2O_3$). Rezultati analize veličine čestica lebdećeg pepela prikazani su na kumulativnom dijagramu, slika 3.

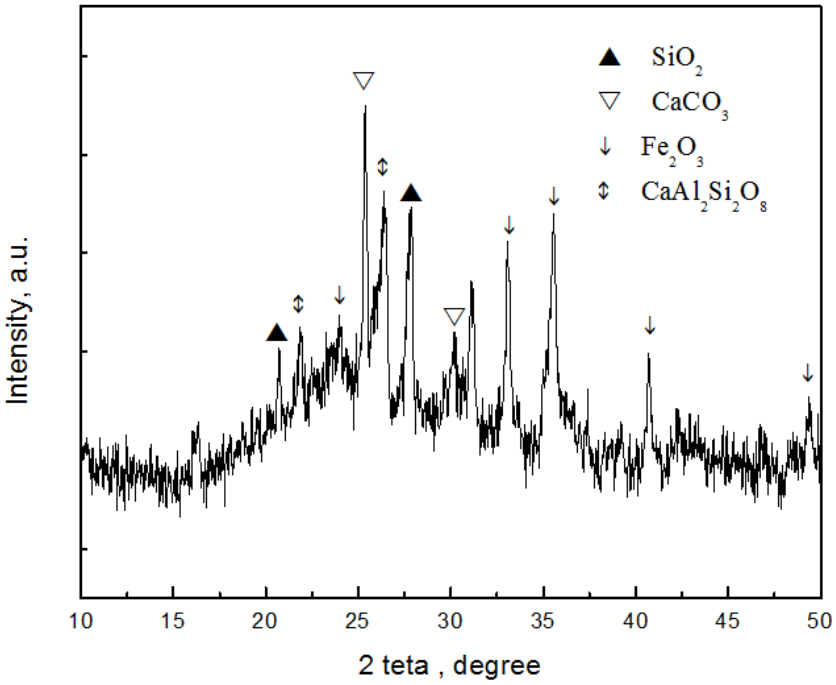


Slika 2. Difraktogram lebdećeg pepela

U ovom radu je pokazano da se primjenom postupka lijevanja s miješanjem može uspješno proizvesti kompozit na bazi Al 2024 legure s lebdećim pepelom kao ojačalom. Neželjene pojave su spriječene pravilnim izborom parametara lijevanja.

Slika 4 pokazuje mikrostrukturu kompozita sa 4% lebdećeg pepela. Na slici se vide krupnije nakupine lebdećeg pepela (tamna površina). Unatoč određenoj aglomeraciji pepeo je dobro distribuiran u matricu i kompozit ima zadovoljavajuću mikrostrukturu. Tijekom materijalografske pripreme uzoraka površina kompozita je brušena i polirana, usljed čega je mjestimice došlo do površinskog "čupanja" čestica pepela. Na slici su ta mjesta također tamnija i teško ih je razlučiti od aglomerata.
Kako lebdeći pepeo ima manju gustoću od Al legure u koju je umiješan dobiveni kompozit ima manju gustoću nego osnovna legura.
Obzirom da je legura 2024 namijenjena obradi plastičnom deformacijom u svrhu daljih istraživanja ista je podvrgnuta hladnom gnječenju sa stupnjem deformacije od 25%.

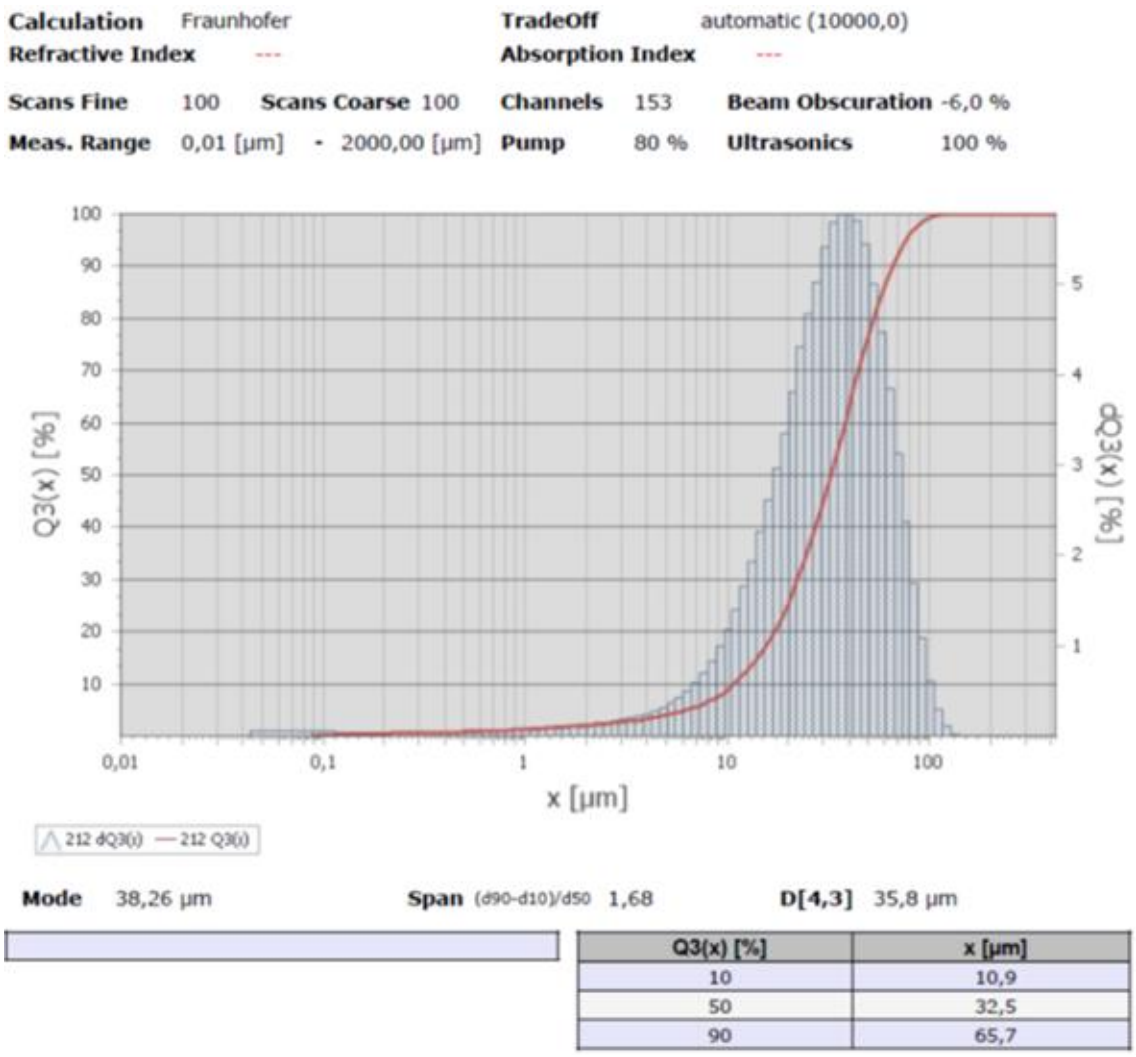


| Q3(x) [%] | x [µm] |
|---|---|
| 10 | 10,9 |
| 50 | 32,5 |
| 90 | 65,7 |

Slika 3. Rezultati analize veličine čestica

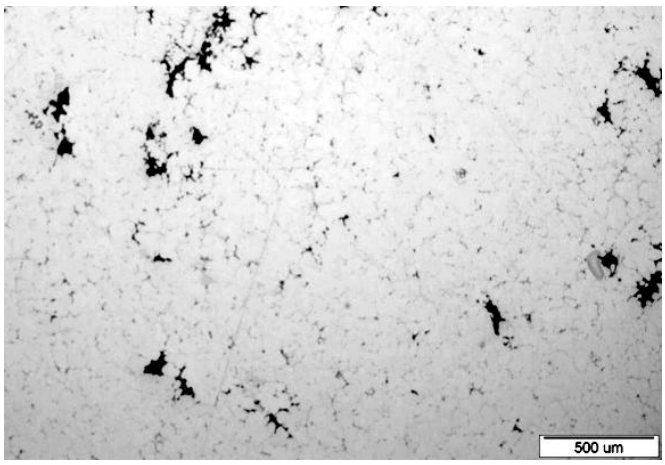


Slika 4. Mikrostruktura kompozita sa 4% lebdećeg pepela u lijevanom stanju

Slike 5 i 6 pokazuju mikrostrukturu ugnječene legure i kompozita. Usljed plastične deformacije došlo je do ugnječenja mikrostrukture u oba uzorka, zbog čega se očekuje poboljšanje mehaničkih svojstava.

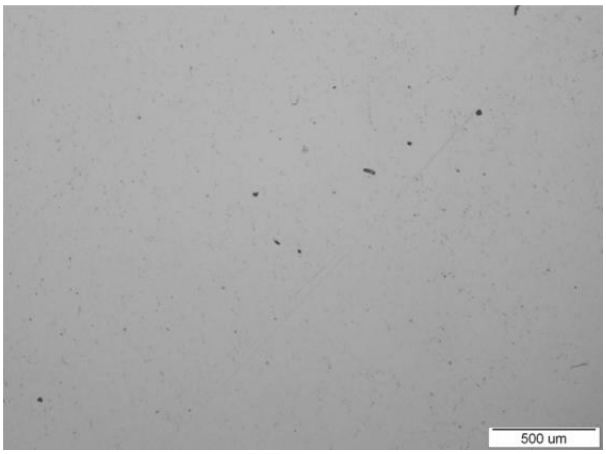


Slika 5. Mikrostruktura ugnječene Al legure 2024

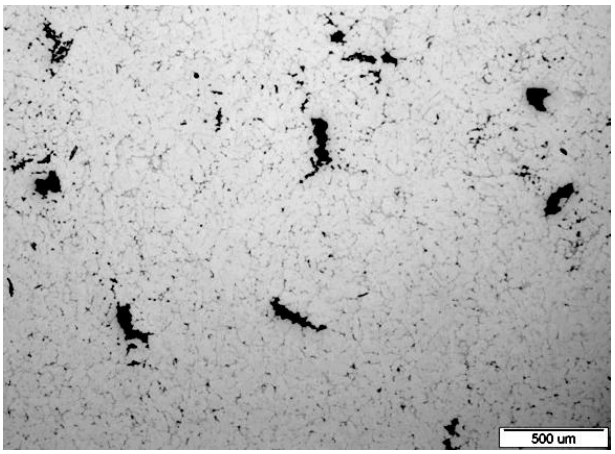


Slika 6. Mikrostruktura kompozita s 4% lebdećeg pepela u ugnječenom stanju

## ZAKLJUČAK

Na temelju provedenih ispitivanja i dobivenih rezultata može se zaključiti da je moguće uspješno sintetizirati kompozit na bazi Al legure s lebdećim pepelom kao ojačalom. Prethodno je potrebno provesti detaljnu analizu kako pepela, tako i legure kako bi se spriječile neželjene reakcije, te pažljivo odabrati parametre lijevanja. Dobiveni kompozit ima zadovoljavajuću distribuciju pepela i manju gustoću od osnovne legure. Pri deformaciji i kompozita i čiste legure dolazi do ugnječenja i usitnjavanja mikrostrukture.
Do izrade ovog rada nisu detaljno ispitana svojstva uzoraka, a pri budućim istraživanjima ispitat će se poroznost, mehanička i tribološka svojstva kompozita.

## LITERATURA

[1] J. Sobczak, N. Sobczak, P. K. Rohatgi, Using Fly Ash for the Production of Light Weight Composites, (Ciach R), Advanced Light Alloys and Composites, NATO ASI Series, 59, Springer Netherlands, 1998.
[2] J. Huang, M. Fang, Z. Huang, Y. Liu, J. Yang, S. Huang, et al, Preparation, Microstructure, and Mechanical Properties of SpinelCorundum-Sialon Composite Materials from Waste Fly Ash and Aluminum Dross, Advances in Materials Science and Engineering, 2014 (2014) pp. 1-10.

[3] S. Selvi, E. Rajasekar, Theoretical and experimental investigation of wear characteristics of aluminum based metal matrix composites using RSM, J. Mech. Sci. Technol., 29 (2015) 2, pp. 785-92.
[4] D. Luong, N. Gupta, P. Rohatgi, The high strain rate compressive response of Mg-Al alloy/fly Ash cenosphere composites, JOM, 63 (2011) 2, pp. 48-52.
[5] P. K. Rohatgi, D. Weiss, N. Gupta, Applications of fly ash in synthesizing low-cost MMCs for automotive and other applications, JOM, 58 (2006) 11, 71-6.
[6] P. K. Rohatgi, J. K. Kim, R. Q. Guo, D. P. Robertson, M. Gajdardziska-Josifovska, Age-hardening characteristics of aluminum alloy-hollow fly ash composites, Metallurgical and Materials Transactions A-Physical Metallurgy and Materials Science, 33 (2002) 5, pp. 1541-7.
[7] S. H. Juang, L-J. Fan, HPO Yang, Influence of Preheating Temperatures and Adding Rates on Distributions of Fly Ash in Aluminum Matrix Composites Prepared by Stir Casting, International Journal of Precision Engineering and Manufacturing, 16 (2015) 7, pp. 1321-7.
[8] Y. Sun, Y. Lyu, A. Jiang, J. Zhao, Fabrication and characterization of aluminum matrix fly ash cenosphere composites using different stir casting routes, Journal of Materials Research, 29 (2014) 2, pp. 260-6.
[9] A. Bhandakkar, K. Singh, P. K. Limaye, S. M. L. Sastry, Wear behaviour of Equal chanel Angular Pressed Aluminium AA 20204 Fly Ash Metal Matrix Composites, International Journal of Trend Reasearch and Development, 3 (2016) 6, pp. 688-695.
[10] D. Mohana Rao, M .E. Bapi Raju Bandam, Preparation and Characterisation of Al-Fly Ash Metal Matrix Composite by Stir Casting Method, International Journal of Innovative Science and Modern Engineering, 3 (2014) 1, pp. 1-5.
[11] M. Flemings, Behavior of metal alloys in the semisolid state, Metall. Trans. A, 22A (1991) pp. 957-980.
[12] B. Bobić, Ispitivanje uticaja procesa korozije na strukturne i mehaničke karakteristike odlivaka Zn27Al1,5Cu0,02Mg legure ojačane česticama silicijum-karbida, doktorska disertacija, Univerzitet u Beogradu, Tehnološko metalurški fakultet, Beograd, 2011.
[13] I. Bobić, J. Ružić, B. Bobić, M. Babić, A. Vencl, S. Mitrović, Microstructural characterization and artificial aging of compo-casted hybrid A356/SiCp/Grp composites with graphite macroparticles, Materials Science & Engineering A, 612 (2014) pp. 7–15. Contents lists available at ScienceDirect, journal homepage: www.elsevier.com/locate/msea
[14] V. Maksimović, A. Devečerski, A. Došen, I. Bobić, M. Erić, T. Volkov-Husović, Comparative Study on Cavitation Erosion Resistance of A356 Alloy and A356FA5 Composite, Trans Indian Inst Met, 70 (2017) 1, pp. 97-105.

17th INTERNATIONAL FOUNDRYMEN CONFERENCE
Hi-tech casting solution and knowledge based engineering
Opatija, May 16th-18th, 2018
http://www.simet.hr/~foundry/

# A COST EFFECTIVE APPROACH TO PRODUCTION OF INVESTMENT CASTING WAX MODELS BY ADDITIVE MANUFACTURING

**Daniel Novoselović[1]*, Štefanija Klarić[2], Damien J. Hill[2]**

[1] Josip Juraj Strossmayer University of Osijek Mechanical Engineering Faculty in Slavonski Brod, Slavonski Brod, Croatia
[2] Charles Darwin University College of Engineering, IT and Environment, Casuarina, Australia

**Poster presentation**
*Professional paper*

**Abstract**

Production of precise cast parts is often be accomplished by investment casting process. Within this process molten metal is poured into molds produced around wax models of the final part. In this process models and molds, which may be costly or time consuming to create, can be used one time only.
Investment casting is well established process in production of metal castings with complex or thin walled shapes or patterns. In this paper application of desktop size 3D printer for production of wax models is presented as fast and low-cost method of model production. The goal of this investigation was to test the possibility of the use of open source printer and software for wax pattern manufacturing for educational and training purposes. The use of a 3D printer allows rapid production of a part from a CAD image as well as the ability to create many copies of the same wax model. The surface quality of models was analyzed regarding to print parameters (layer thickness vs time) and some of typical wax models' defects and reparation method are shown.

***Keywords**: investment casting, rapid prototyping, 3D printing, additive manufacturing*

*Corresponding author (e-mail address): *daniel.novoselovic@sfsb.hr*

## INTRODUCTION

The investment casting process allows the production of complicated shape parts when production with some other manufacturing processes would be difficult and non-cost effective. Castings produced by this process have precise dimensions and good surface appearance so usually final processing requires only small scale operations for the final dimension achievements (i.e. just sawing off or grinding of the gating system). This is very important for production of complex shapes castings as machining of those parts would be almost impossible [1, 2].

Investment casting allows production of items from a variety of metals: different steel grades, aluminum, copper, tin, titanium etc. In a production of smaller size iron castings investment casting is used for weighing from a few grams to 20 kg and for aluminum castings up to 10 kg [1]. Casting size and weights are defined by model and/or ceramic shell production limitations. Larger castings are usually produced as one-off parts in individual production. Although this process is typically used for quantities from 10 – 1000 products [2] it is considered cost-effective for the series of at least 50 castings in industrial applications [1].

## WAX MODEL PRODUCTION

Wax is considered as the oldest thermoplastic material [3] and today majority of investment casting models are produced form wax.
Wax models can be produced from wax blocks or cylinders manually (with saws, shredders, grinding machines, carving tools and tools that use heat). Wax can be cut, melted or welded and these processes allow production of different model shapes. However that method is slow, demands higher level of workers' skills and production of precise parts with dimensional consistency across the parts is not possible. Due to the above, manual production of wax models is not utilized for industrial production. Its application is generally for one of a kind jewelry production, production of wax master models and in dental laboratories [1].
Industrial production usually includes the application of metal dies into which wax is injected [2]. This allows higher productivity and dimensional and shape consistency (with narrow tolerances). Besides the above mentioned, models can be produced by machining of wax material on wood or metal processing machines or by application of additive manufacturing technologies. Production of models with these technologies usually take hours while injection of model in dies can be done in minutes. Due to that, machining and 3D printing is also in limited use in individual production or for the small model series [1].
Like in all production processes, defects are possible in the production of wax models. Every step of the wax model production process can influence error occurrence.
Some of the most common defects in wax model production are [4,5,6]:

- Gas porosity – gas inclusions,
- Incomplete filling of the mould,
- Excessive filling of the mould,
- Sticky wax pattern that is easily bent,
- Excessive shrinkage,
- Sinks (depressions in large patterns),
- Poor surface finishing,
- Fins,
- Wax model breaking tendency,
- Deformations – warping.

Model defects can be caused by poor model design, incorrect production parameters, incorrect handling/storage of models or by unskilled staff.

Due to the complexity of the model production process, one type of model defect can have more than one source and each could produce many types of defects. Due to this complex relationship every step of the production process needs to be controlled so the number of defects can be minimized.

## RAPID PROTOTYPING IN CASTING

Rapid prototyping and/or 3D printing belongs to the group of additive manufacturing technologies. Objects are produced by computer controlled machines from CAD models. Material is added in layers to form the desired object. With this method it is possible to produce tridimensional object almost without shape limitations.
There are number of 3D printing technologies available and for the production of wax models usually photo-polymerization process or material extrusion of wax is used.
Photo-polymerization technique includes photo-reactive material that polymerize due to UV light exposure (one layer at the time) [7]. Production of models by wax extrusion printers works in a similar way, to inkjet printers extruding melted material instead of ink. The printer head includes a heated nozzle that extrudes melted wax and build the part one layer at the time. The printing head moves along the x and y axes and builds the material layers. Then the printing surface is lowered and the process is repeated for the next layer (Figure 1) [8].

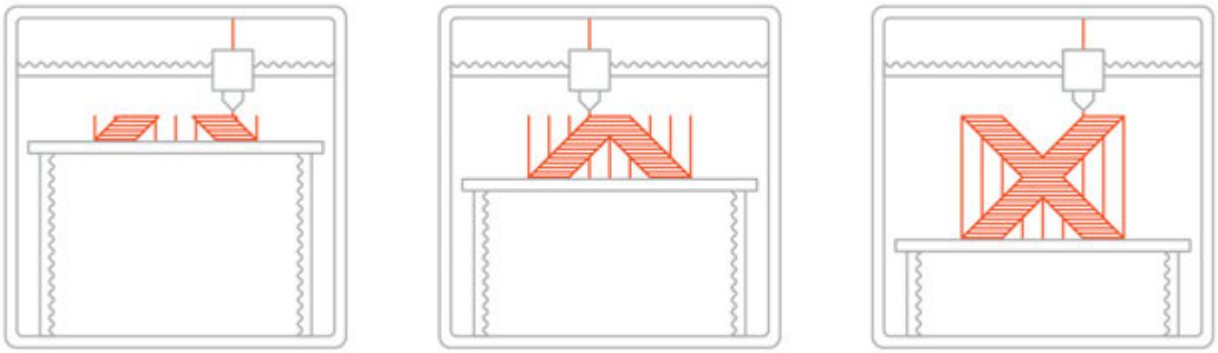

Figure 1. 3D printing process [8]

## PRINTING OF WAX MODELS

In order to produce wax models for the tests described in this paper, a Duinotech Mini 3D Printer L4076 with MachinableWax 1.75 mm Print2Cat Wax Filament was used (Figure 2). According to the manufacturer this filament produces extremely clean burnout in comparison with plastic filaments [10]. The goal was to test the possibility of production of wax models with appropriate quality as cost effective and quickly as possible. Although there are more precise industry solutions for wax 3D printing on a market today, this method would allow fast and cost efficient printing of wax samples for educational and training purposes.

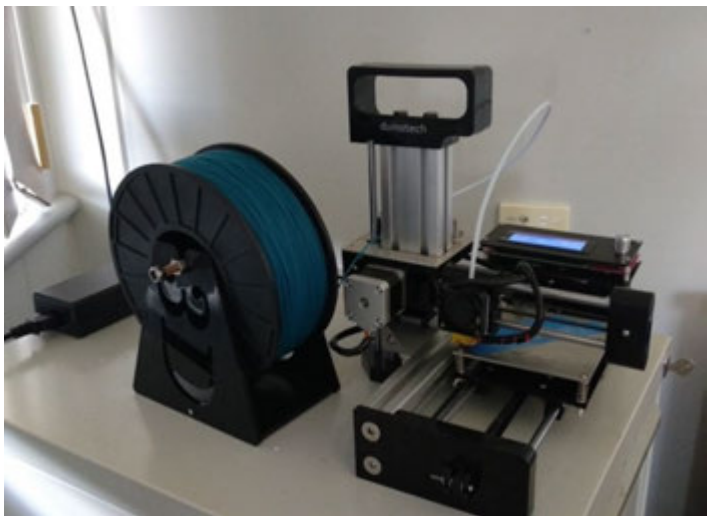

Figure 2. Duinotech Mini 3D Printer (with wax filament)

Tensile testing specimen shape 5A (according to ISO 527-2 standard) with 3 mm thickness was selected for this test (Figure 3a). The Duinotech printer used in this experiment is a relatively low price desktop printer (around 150 €) originally designed for printing PLA models (Figure 3b).
For printing of Print2Cast Wax Filament, the producer suggest extrusion temperature of 140 - 150 °C, heating of bed on 80-90 °C, the application of 2-3 shells during model print and print speeds of 20 to 70 mm/s [10].

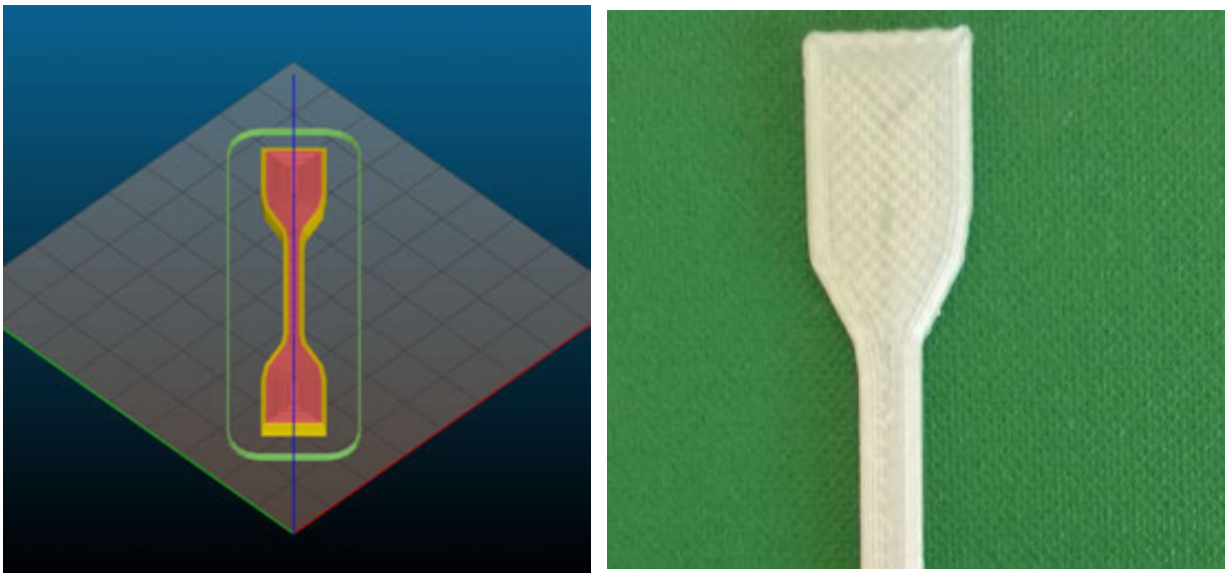

a) b)

Figure 3. a) Test specimen model in G-code generator software (SLic3r [9]),
b) PLA print of the model

As heating of the bed was not possible with this printer, selection of different printing parameters was tried in order to achieve an appropriate quality of specimen (Table 1). For all specimens, the extruder temperature was 200 °C for the first layer and 175 °C for subsequent layers. The infill density was 50 %. A skirt of 6 layers and print speed of 15 mm/s for infill and 30 mm/s top solid infill was used. Horizontal shells had a thickness of 2 layers.

Table 1. Printing parameters

| No. | Layer height, mm | Fill pattern | Printing time |
|---|---|---|---|
| 1 | 0.1 | Concentric | 1.3 h |
| 2 | 0.1 | Rectilinear | 1.3 h |
| 3 | 0.2 | Concentric | 0.5 h |
| 4 | 0.2 | Rectilinear | 0.5 h |
| 5 | 0.3 | Concentric | < 20 min |
| 6 | 0.3 | Rectilinear | < 20 min |

After printing it was evident that certain types of defects appeared on wax models (Figure 4). Those defects can be categorized as:

- Gas porosity – gas inclusions,
- Excessive shrinkage,
- Deformations - warping.

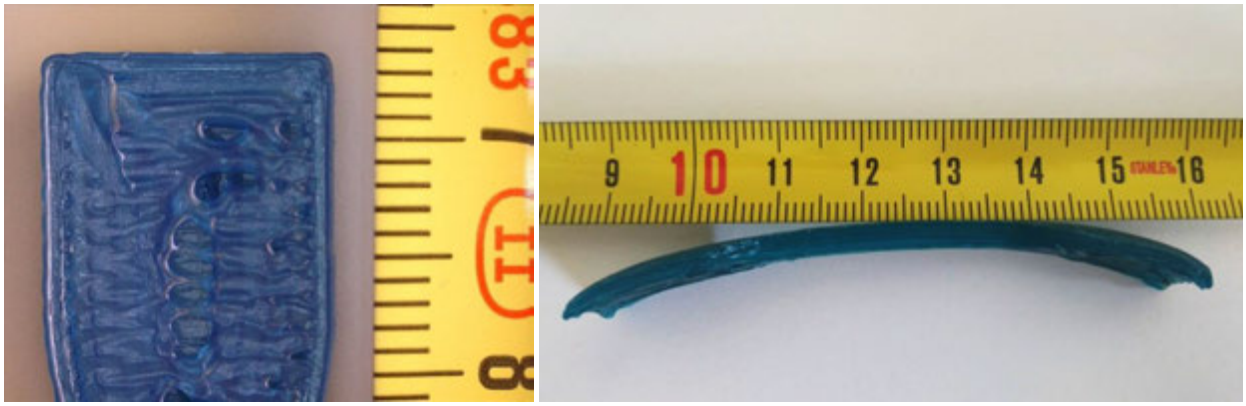


a) gas inclusions b) deformations (warping)

Figure 4. Wax model defects

The top and side surface of all specimens from Table 1 are shown in Table 2.

Table 2. Surface quality of specimens

| No. | Top surface | Side surface |
|---|---|---|
| 1 | 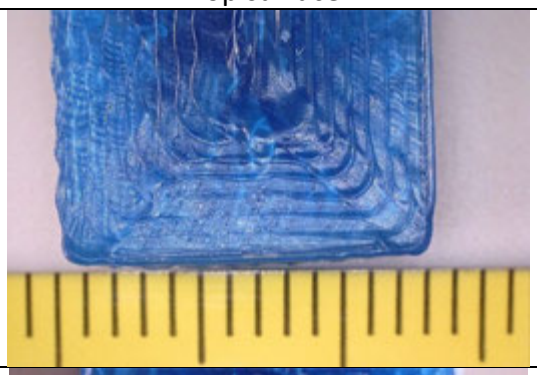 | 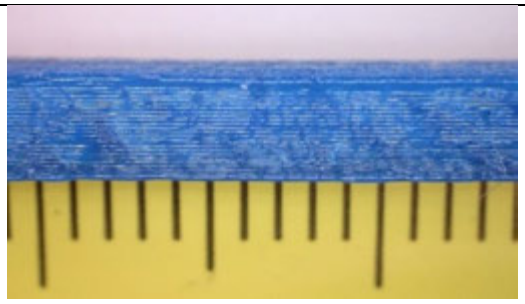 |
| 2 | 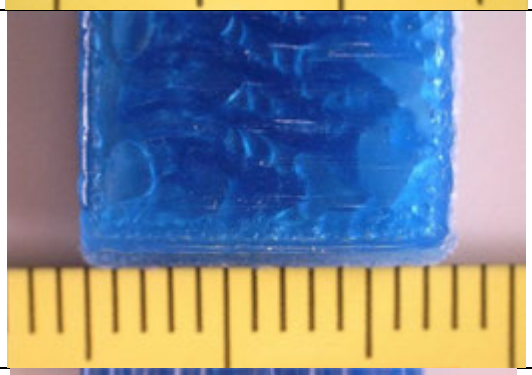 | 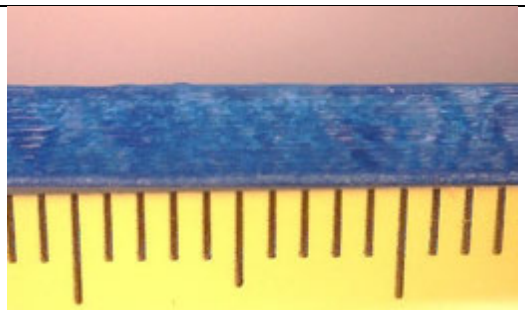 |
| 3 | 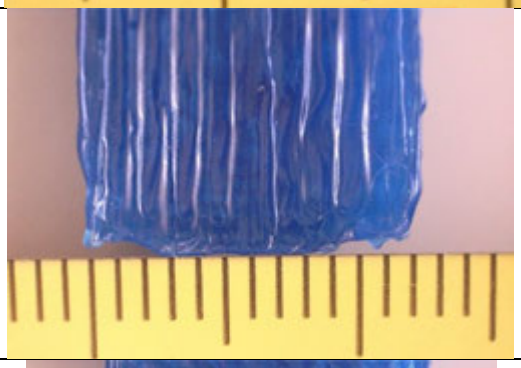 | 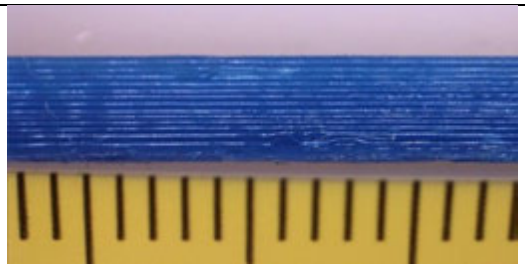 |
| 4 | 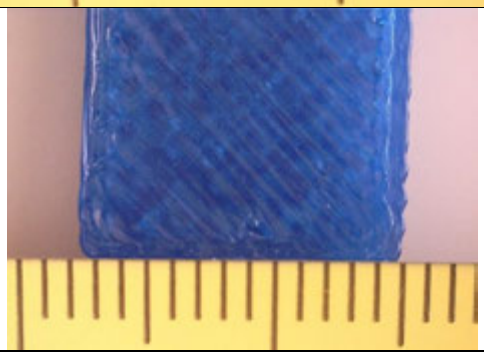 | 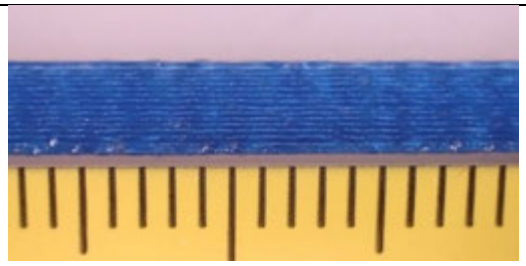 |

| | | |
|---|---|---|
| 5 | 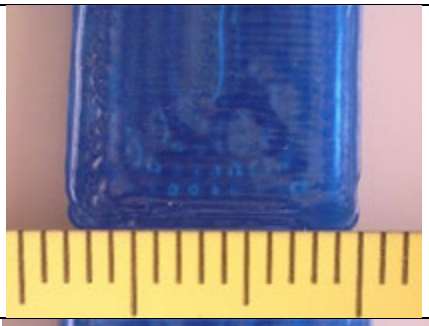 | 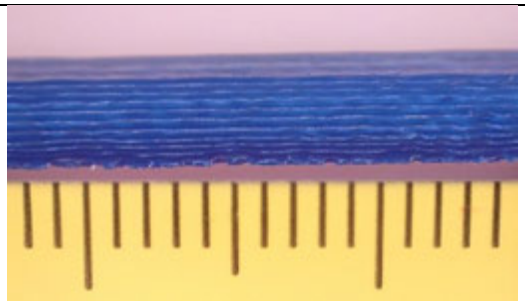 |
| 6 | 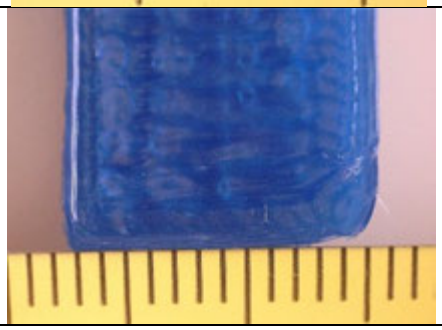 | 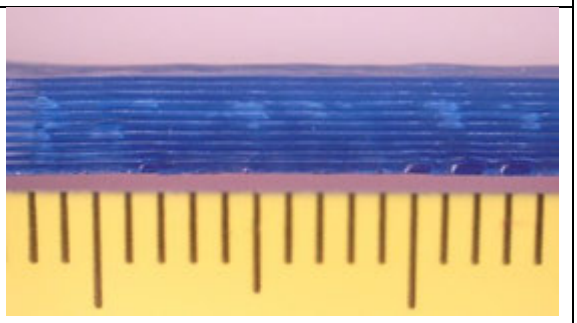 |

Samples 1 and 2 were printed with the smallest layer thickness (0.1 mm) with different fill pattern inside the specimen (concentric or rectilinear). The change of fill pattern however did not influence the printing time that was around 1.3 hours.
There are some defects visible on the models 1 and 2: excessive shrinkage and gas inclusions in the middle of sample are created during the printing of final concentric layers and on connection lines of fill and outer layer on sample 2.
Samples 3 and 4 are printed with 0.2 mm layer thickness and printing time for both fill patterns (concentric and rectilinear) was 0.5 hours. There are some deformations of wax models and excessive shrinkage and gas inclusions on samples where fill is joined with outer layers.
Samples 5 and 6 are printed with 0.3 mm layer thickness and printing time was less than 20 minutes. Samples are well deformed but with good fill trough, and excessive shrinkage and gas inclusions are minimal.
After the analysis of the model defects it can be concluded that layer thickness (printing time) can significantly influence model deformation. This can be explained by the fact that thinner layers are printed slowly so heat input is reduced.
Appearance of the excessive shrinkage and gas inclusions can be related to fill pattern. It seems that the concentric fill pattern produced smaller amount of this defects. It can be related back to a smaller number of printing path interruptions in concentric fill patterns as printing path is not interrupt at the outer line of the sample by a rapid moves to a new location, but instead extrudes continuously.
Although the wax models produced during this testing show some of characteristic defects, additive manufacturing of wax models can be justified by the production costs and time. Additionally, the described defects can be repaired by additional post processing.
According to the wax filament producer, this material can be polished, machined, and carved much easier than plastic filaments usually used in 3D printing [10]. Also surfaces can be

modified by heat. Figure 5 shows model repaired manually by carefully heating the damaged area with a soldering iron tip set to a temperature high enough to melt the wax. For this repair trial Hakko 926 soldering station was used with Hakko 900 soldering iron with the temperature set on 350 °C. Heat was applied by a flat chisel-type solder tip and care was taken to only melt small amounts of the wax at a time.

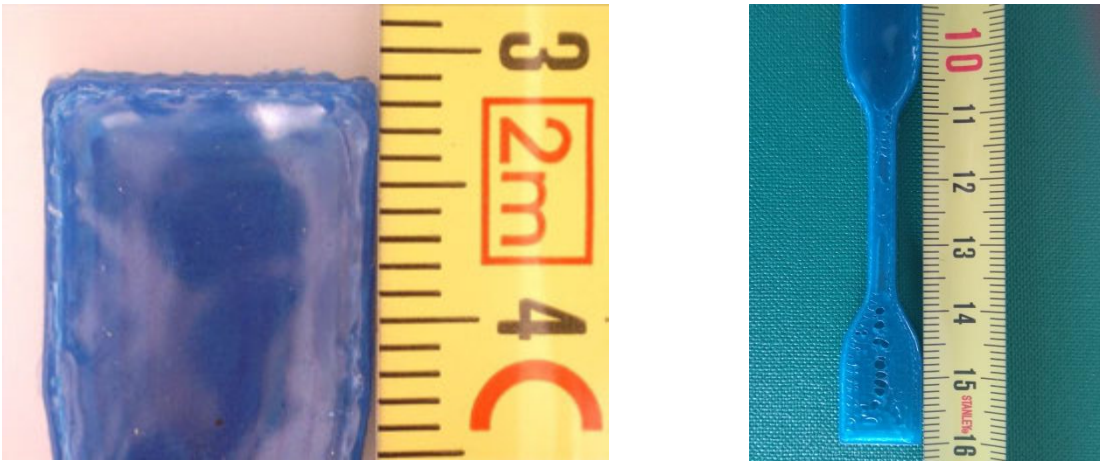


Figure 5. Wax model reparation

## CONCLUSIONS

Wax model production is one of the most demanding steps in the investment casting procedure. Wax is a sensitive material and demands careful handling, and as wax model defects cause casting defects, the quality of wax models is very important.
In this paper the influence of the printing parameters of the low cost 3D printing equipment, on wax model quality is analyzed. It can be concluded that layer thickness can influence model warping as thinner layers produce less deformations.
Additionally, fill pattern effect is considered and in general, a concentric fill pattern selection resulted in less excessive shrinkage type defects and gas inclusions due to more continuous printing path.
Despite the mentioned defects that appeared on the wax models, this method of production has obvious advantages in production costs and time and in the ability to repair the models.
In the future, the investigation scope will be focused on the influence of print wax model quality and defects on casting surface appearance.

**REFERENCES**

[1] I. Budić, Z. Bonačić-Mandinić, Osnove tehnologija kalupljenja: Jednokratni kalupi II. dio, Strojarski fakultet u Slavonskom Brodu, Slavonski Brod, 2004.
[2] CustomPartNet, Investment Casting, Accessible on Internet: http://www.custompartnet.com/wu/investment-casting, 19/04/2018.
[3] H. A. Youssef, H. A. El-Hofy, M. H. Ahmed, Manufacturing Technology: Materials, Processes, and Equipment, CRC Press, Taylor and Francis Group, Boca Raton, 2012.
[4] V. Faccenda, Handbook on investment casting, The lost wax casting process for carat gold jewellery manufacture, World Gold Council, London, 2003.
[5] D. Ott, Handbook on casting and other defects, In Gold Jewellery Manufacture, World Gold Council, London, 2001.
[6] CFS, Causes & Prevention Methods of Common Investment Casting Defects, Accessible on Internet: http://www.investmentcastchina.com/causes-prevention-methods-of-common-investment-casting-defects/, 19/01/2018.
[7] B. Redwood, Jewelry 3D Printing Applications, Accessible on Internet: https://www.3dhubs.com/knowledge-base/jewelry-3d-printing-applications, 19/01/2018.
[8] A. B. Varotsis, Introduction to FDM 3D printing, Accessible on Internet: https://www.3dhubs.com/knowledge-base/introduction-fdm-3d-printing, 19/01/2018.
[9] Slic3r G-code generator for 3D printers, Accessible on Internet: http://slic3r.org/, date 22/02/2018.
[10] MachinableWax.com, Inc, 3D Printing Filament, Accessible on Internet: http://www.machinablewax.com/product.php?product=52, date 22/02/2018.

17th INTERNATIONAL FOUNDRYMEN CONFERENCE
Hi-tech casting solution and knowledge based engineering
Opatija, May 16th-18th, 2018
http://www.simet.hr/~foundry/

# EFFECT OF ANNEALING ON HARDNESS AND TOUGHNESS OF DUPLEX STAINLESS STEEL

# UTJECAJ ŽARENJA NA TVRDOĆU I ŽILAVOST DUPLEKS NEHRĐAJUĆEG ČELIKA

**Zrinka Švagelj[1]*, Iva Karačić[2], Damir Muslić[3]**

[1] University of Zagreb Faculty of Mechanical Engineering and Naval Architecture, Zagreb, Croatia
[2] Ivičeki 21, Lučko, Croatia
[3] "E-PRO" Ltd. for designing, engineering and technical consulting, Bihać, Bosnia and Herzegovina

**Poster presentation**
*Original scientific paper*

**Abstract**

The aim of this work was to investigate the effect of 475 °C embrittlement on microstructure and properties of duplex stainless steel X2CrNiMoN 22-5-3 (1.4462). Microstructural changes that occur by annealing at 475°C for 3 hours cannot be clearly visible under a light microscope. The maximum magnification of 1000x and the maximum resolution of 0.4 µm are not enough to clearly distinguish small clusters of alpha-prime-phase formed in Fe-Cr alloys with 13%-90% Cr during ageing at temperature between 350 and 525 °C.
It was observed that the sample annealed for the longest time (3 hours) had 2 % higher austenite content in comparison with the untreated sample and the sample annealed for 1 hour. It was found that the hardness increases with increasing annealing time at 475 °C and decreasing load. The toughness of duplex stainless steel decreases with increasing annealing time.

***Keywords**: duplex stainless steel, embrittlement 475, hardness, toughness*

*Corresponding author (e-mail address): *zsvagelj@fsb.hr*

**Sažetak**

Cilj ovog rada bio je istražiti utjecaj žarenja na temperaturi 475 °C, na mikrostrukturu i svojstva nehrđajućeg dupleks čelika oznake X2CrNiMoN 22-5-3 (1.4462). Mikrostrukturne promjene koje nastaju žarenjem na navedenoj temperaturi u trajanju do 3 sata ne mogu se posve jasno determinirati na svjetlosnom mikroskopu. Maksimalno povećanje (do 1000×) i sposobnost razlučivanja svjetlosnog mikroskopa (0,4 µm) nije dovoljno da se jasno vide vrlo sitne nakupine alfa-prim-faze koja nastaje u Fe-Cr legurama s 13 do 90% Cr, kada se dulje vrijeme zadrže na temperaturi između 350 i 525 °C.

Kod uzoraka koji su najdulje žareni (3 sata) izmjeren je za 2 % veći udio austenita nego kod nežarenih i 1 sat žarenih uzoraka. Tvrdoća je veća što je dulje vrijeme žarenja na 475 °C, a prirast tvrdoće je veći što je primijenjeno opterećenje manje. S produljenjem vremena žarenja pada žilavost dupleks čelika.

***Ključne riječi**: dupleks nehrđajući čelik, krhkost 475, tvrdoća, žilavost*

## UVOD

Nehrđajući dupleks čelici su stručnoj javnosti poznati još od tridesetih godina prošlog stoljeća, a u širu uporabu ulaze posljednjih dvadesetak godina. Njihovo glavno obilježje jest izvanredno dobra otpornost prema interkristalnoj, napetosnoj i rupičastoj koroziji u kombinaciji s odličnim mehaničkim svojstvima - visokom vlačnom čvrstoćom, visokom granicom tečenja i dobrom žilavošću te dobrom zavarljivošću [1-3]. Posebni su po tome što nemaju monofaznu mikrostrukturu kao ostali nehrđajući čelici, nego bifaznu strukturu sastavljenu od ferita (α) i austenita (γ). Kod idealne dvofazne dupleks strukture volumni udjeli α i γ faze su jednaki i iznose 0,5 [4]. Parametar dupleks strukture, koji predstavlja odnos između gustoće kristalnih granica αα i γγ, ima vrijednost 1, a parametar disperzije koji predstavlja odnos između gustoće faznih (ραγ) i kristalnih granica (ργγ, ραα) treba imati vrijednost 2. Dvofazna struktura u realnim dupleks čelicima razlikuje se od idealne dupleks strukture. Premda sličnu dupleks strukturu imaju još neki čelici, naziv ˝dupleks čelici˝ odnosi se samo na visokolegirane nehrđajuće feritno-austenitne čelike [5].
Optimalna mikrostruktura kod dupleks čelika postiže se balansiranjem kemijskog sastava i režima toplinske obrade. Za određeni kemijski sastav podešava se brzina ohlađivanja tako da između 1050 i 1150 ˚C u strukturi bude podjednaka količina ferita i austenita. Kad se postigne fazna ravnoteža, hlađenje se nastavlja gašenjem u vodi, čime se osigurava zadržavanje postignutog faznog omjera i na sobnoj temperaturi.
Primjena dupleks čelika ograničena je na temperaturni raspon od -80 do 300 °C [2, 6-8]. Kako u strukturi sadrži veliku količinu feritne faze, na temperaturama nižim od - 80 °C dupleks čeliku značajno pada žilavost. Ako se dupleks čelik zagrije i duže vrijeme ostane na temperaturi višoj od 300 °C u njegovoj mikrostrukturi mogu se formirati neke faze koje loše utječu na njegovu korozijsku postojanost i mehanička svojstva [6, 9-11]. Jedna od tih nepoželjnih faza je i alfa-prim-faza, koja izaziva pojavu krhkosti 475 ˚C.
Alfa-prim-faza nastaje u Fe-Cr legurama s 13 do 90% Cr, kada se dulje vrijeme zadrže na temperaturi između 350 i 525 °C [12]. Ima istu kristalnu strukturu (bcc rešetka) kao feritna faza uz neznatno veći parametar rešetke. Sadrži oko 80 % Cr, nemagnetična je i ekstremno sitna, promjera oko 15 do 30 nm. Teško se detektira optičkim mikroskopom, eventualno se nešto šire granice zrna i tamnija unutrašnjost feritnog zrna mogu pripisati njezinom formiranju.
Formiranje ove faze izaziva povećanje tvrdoće feritne faze koje se može registrirati mjerenjem mikrotvrdoće i nanotvrdoće. Povisuje se i vlačna čvrstoća, a padaju žilavost, istezljivost i korozijska postojanost [1, 2, 6, 13] . Pad žilavosti i istezljivosti najjače je izražen grijanjem na oko 475 ˚C pa se ova pojava naziva ''krhkost 475 ˚C''. Količina izlučene alfa-prim-

faze raste s povećanjem sadržaja kroma i ugljika. Na isti način djeluju molibden, vanadij, titanij, niobij i dušik, [1]. Ova pojava je reverzibilna. Alfa-prim-faza može biti otopljena, a dobra svojstva čelika vraćena žarenjem na temperaturi iznad 675 °C.
Cilj ovog rada je odrediti kako formiranje alfa-prim-faze pri žarenju na temperaturi 475 °C ovisi o vremenu te kako njezin nastanak utječe na tvrdoću i žilavost dupleks čelika oznake X2CrNiMoN 22-5-3.

## MATERIJALI I METODE

Sva ispitivanja su provedena na uzorcima dupleks nehrđajućeg čelika X2CrNiMoN 22-5-3 (1.4462) izrezanima iz valjane ploče dimenzija 8503 x 1807 x 13 mm. Nakon otapajućeg žarenja na 1080 °C i gašenja u vodi, provedeno je dekapiranje površine.
U tablici 1 prikazan je kemijski sastav čelika dobiven u Laboratoriju za analizu metala na Fakultetu strojarstva i brodogradnje u Zagrebu. Analiza kemijskog sastava provedena je na uređaju LECO GD-OES 850A (engl. *Glow Discharge Optical Emission Spectrometry*) koji radi na principu optičke emisijske spektrometrije.
U tablici 2 prikazane su srednje vrijednosti mehaničkih svojstava dobivenih pri statičkom vlačnom ispitivanju u Laboratoriju za ispitivanje mehaničkih svojstava na Fakultetu strojarstva i brodogradnje u Zagrebu. Ispitivanje je provedeno na pet uzoraka na kidalici EU 40mod, proizvođača WPM, Njemačka u mjernom području od 0 - 400kN.

Tablica 1. Rezultati analize kemijskog sastava čelika X2CrNiMoN 22-5-3, u % mase

| C | Cr | Ni | Mo | N | Si | Mn | P | S | Fe |
|---|---|---|---|---|---|---|---|---|---|
| 0,024 | 22,78 | 5,27 | 3,00 | 0,156 | 0,26 | 1,62 | 0,027 | - | ostatak |

Tablica 2. Granica razvlačenja, vlačna čvrstoća i istezljivost čelika X2CrNiMoN 22-5-3

| | |
|---|---|
| Konvencionalna granica razvlačenja, $R_{p0,2}$ (N/mm$^2$) | 582 |
| Vlačna čvrstoća, $R_m$ (N/mm$^2$) | 768 |
| Istezljivost, $A_5$ (%) | 42 |

Iz ploče je izrezano devet uzoraka za ispitivanje udarnog rada loma i tri uzorka za analizu mikrostrukture. Uzorci za ispitivanje udarnog rada loma bili su dimenzija 10 × 10 × 55 mm, s „V“ utorom, a ispitivanje je provedeno pri sobnoj temperaturi na uređaju Charpyjev bat UT30 proizvođača AVK, Mađarska, nazivne energije 300 J. Tri uzorka ostavljena su u početnom stanju, tri uzorka žarena su 1 sat na 475 °C, a preostala tri uzorka žarena su 3 sata na 475 °C. Uzorci su žareni u vakuum peći, koja se nalazi u Laboratoriju za toplinsku obradbu i inženjerstvo površina Fakulteta strojarstva i brodogradnje u Zagrebu. Nakon određivanja udarnog rada loma na uzorcima je izmjerena makrotvrdoća po Vickersu s opterećenjem 10x9,81N, metoda HV10. Mjerenje Vickersove mikrotvrdoće uz opterećenje 0,2x9,81N (HV0,2) provedeno je na metalografskim uzorcima u poliranom stanju. Ispitivanje mikrotvrdoće provedeno je u Laboratoriju za materijalografiju Fakulteta strojarstva i

brodogradnje u Zagrebu na mikrotvrdomjeru PMT–3. Tvrdoća HV10 izmjerena je na uređaju proizvođača Zwick u Laboratoriju za ispitivanje mehaničkih svojstava Fakulteta strojarstva i brodogradnje u Zagrebu, gdje je izmjeren i udarni rad loma.

## REZULTATI I RASPRAVA

### *Karakterizacija mikrostrukture*

Kemijski sastav naveden u tablici 1 odgovara standardnom nehrđajućem dupleks čeliku oznake X2CrNiMoN 22-5-3.

Na slikama 1 - 3 prikazana je mikrostruktura uzoraka nakon završnog poliranja i nagrizanja u otopini LB I (*Lichtenegger und Bloech*). Ova otopina nagriza austenitnu fazu, a površina feritnih zrna ostaje nenagrižena. Temperatura otopine tijekom nagrizanja bila je 30 °C, a uzorci su uranjani u otopinu neposredno nakon završnog poliranja jer se tako postižu najbolji rezultati nagrizanja. Svi uzorci su zajedno uronjeni u sredstvo za nagrizanje i zajedno izvađeni. Trajanje nagrizanja određeno je vizualnom metodom i iznosilo je oko 30 sekundi. Uzorci su nakon nagrizanja isprani u vodi, a zatim u alkoholu, te osušeni u struji toplog zraka. Pri promatranju na optičkom mikroskopu nagrižena austenitna zrna su tamna, a nenagrižena feritna zrna su svijetlija. Njihov oblik, raspored i volumni udio odgovaraju dupleks strukturi. Osim austenita i ferita nisu uočene nikakve druge faze ni pri najvećem povećanju (1000×).

U tablici 3 prikazani su rezultati mjerenja volumnih udjela ferita i austenita, određenih pomoću računalnog programa *ImageJ*. Žarenje čelika na 475 °C neznatno utječe na izbalansirani omjer austenit/ferit i to tek nakon 3 sata žarenja.

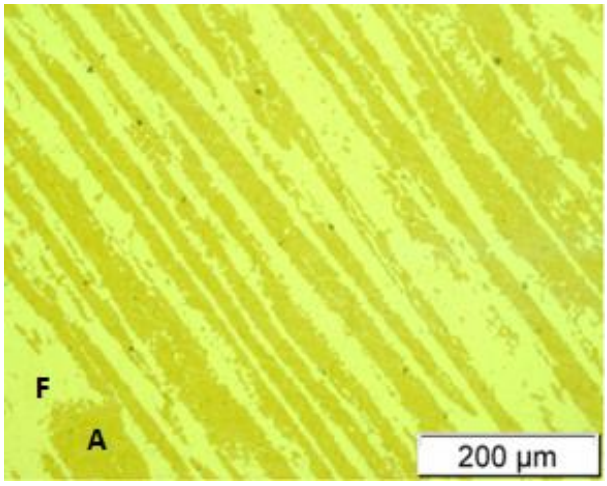


Slika 1. Mikrostruktura nežarenog uzorka

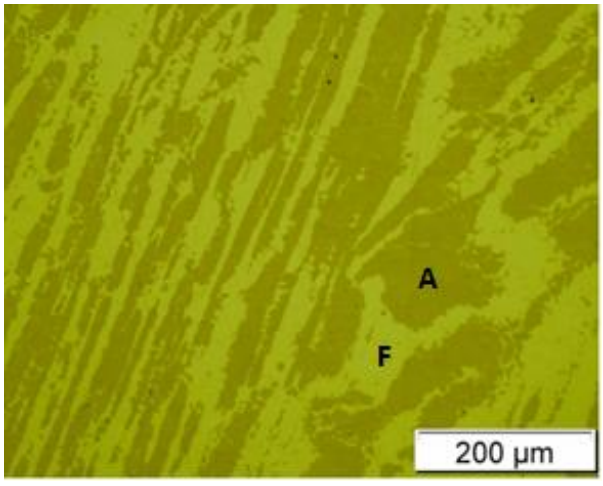


Slika 2. Mikrostruktura uzorka žarenog 1 sat

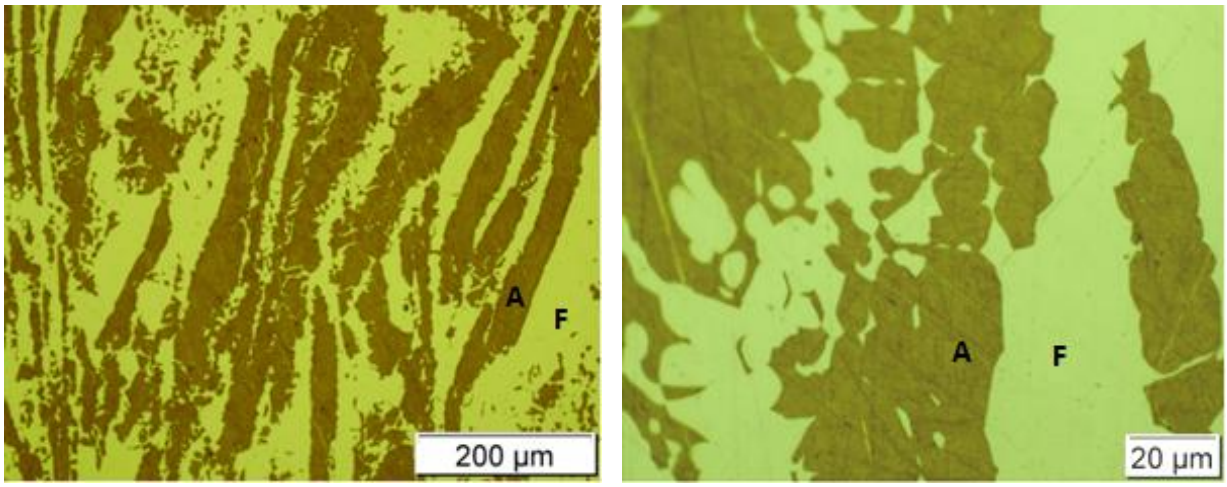


Slika 3. Mikrostruktura uzorka žarenog 3 sata pri manjem (lijevo) i većem povećanju (desno)

Tablica 3. Volumni udjeli faza u uzorcima

| | austenit | ferit |
|---|---|---|
| nežareni uzorak | 51 | 49 |
| žareni uzorak 475°C/ 1 sat | 51 | 49 |
| žareni uzorak 475°C/ 3 sata | 53 | 47 |

***Tvrdoća i žilavost uzoraka***

U dijagramu na slici 4 prikazane su srednje vrijednosti izmjerene mikrotvrdoće HV0,2 te tvrdoće HV10 u ovisnosti o vremenu žarenja. Dobiveni rezultati pokazuju da su vrijednosti tvrdoće mjerene s opterećenjem od 10×9,81 N niže od vrijednosti izmjerenih pri opterećenju od 0,2×9,81 N. Također je jasno vidljivo da žarenje na 475 °C u trajanju od jednog sata podjednako povisuje tvrdoću HV10 i mikrotvrdoću HV0,2. Produljenjem vremena žarenja na tri sata tvrdoća HV10 raste i dalje, ali vrlo malo, dok mikrotvrdoća HV0,2 raste puno intenzivnije. Zbog toga razlika između vrijednosti HV10 i HV0,2 s produljenjem vremena žarenja postaje sve veća.

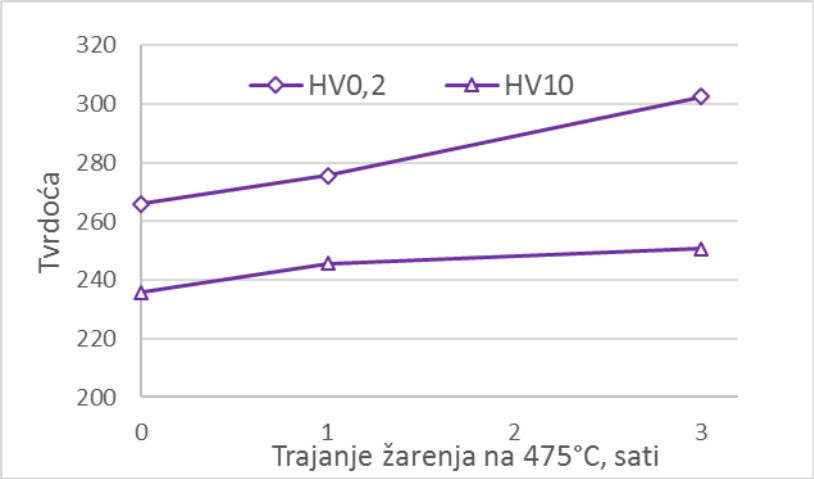


Slika 4. Promjena tvrdoće s vremenom žarenja na 475 °C

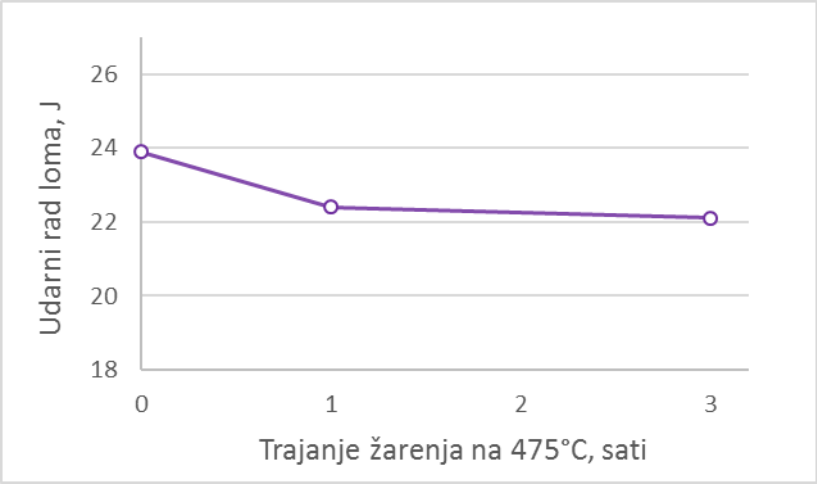


Slika 5. Promjena udarnog rada loma s vremenom žarenja na 475 °C

U dijagramu na slici 5 prikazane su srednje vrijednosti udarnog rada loma u ovisnosti o vremenu žarenja.
Uzorak koji nije toplinski obrađen ima najvišu vrijednost udarnog rada loma, dok se žarenjem na 475 °C žilavost smanjuje. Produljenjem žarenja s 1 na 3 sata vrijednost udarnog rada loma još više pada, ali taj pad nije tako jako izražen kao između nežarenih uzoraka i uzoraka koji su 1 sat žareni na 475 °C. Također je potrebno napomenuti, da niti jedan ispitni uzorak pri ispitivanju nije do kraja slomljen, nego su svi „provučeni“ između oslonaca nosača, slika 6.

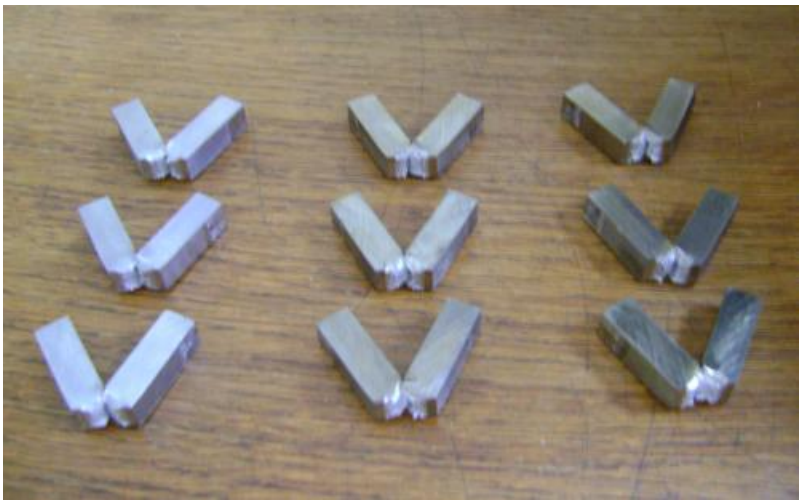

Slika 6. Ispitni uzorci nakon ispitivanja na Charpyjevom batu

## ZAKLJUČAK

Na temelju rezultata dobivenih tijekom ispitivanja može se zaključiti sljedeće:

- Žarenjem uzoraka na 475 °C u mikrostrukturi nehrđajućeg dupleks čelika X2CrNiMoN 22-5-3 nastupaju promjene koje izazivaju promjenu mikrotvrdoće, makrotvrdoće i žilavosti.
- Analizom mikrostrukture na svjetlosnom mikroskopu ne mogu se uočiti razlike između žarenih i toplinski neobrađenog uzorka. Mikrostruktura svih uzoraka sastoji se od ferita i austenita u podjednakoj količini, nešto je veći udio austenita kod uzorka žarenog 3 sata (2 %).
- Žarenje dupleks čelika na 475 °C izaziva prirast mikrotvrdoće i makrotvrdoće koji je to veći što je primijenjeno opterećenje manje i što je dulje vrijeme žarenja.
- Rezultati mjerenja žilavosti na Charyjevom batu pokazuju da s produljenjem vremena žarenja na 475 °C udarni rad loma pada. Uzorci su nakon žarenja ipak dovoljno žilavi da ne dođe do potpunog loma epruvete već one bivaju provučene između oslonaca na batu.

## LITERATURA

[1] J. R. Davis, Stainless Steels (Asm Specialty Handbook), ASM International, 1994.
[2] A. J. Sedriks, Corrosion of Stainless Steels, John-Wiley and Sons, New York, 1996.
[3] V. Muthupandi, P. Bala Srinivasan, S. K. Seshadri, S. Sundaresan, Effect of weld metal chemistry and heat input on the structure and properties of duplex stainless steel welds, Materials Science and Engineering A, 358 (2003) 1-2, pp. 9-16.

[4] R. N. Gunn, Duplex Stainless Steels - Microstructure, Properties And Applications, Abington Publishing, Cambridge, 2003.
[5] C. Brock, E. Hornbogen, P. Stratmann, H. Thommek, Die Herstellung von duplexgefügen in Stählen, Steel research international, 47 (1976) 8, pp. 513-518.
[6] J. Charles, Super duplex stainless steels: Structure and properties, Proceedings of 3rd International Conference on Duplex stainless Steels, (J. Charles, S. Bernhardsson), Les Editions de Physique, 1991, Les Ulis Cedex A, France, pp. 3-48.
[7] J. Charles, 10 years later, obviously duplex grades in industrial applications look like a success story, Proceedings of 6th World Duplex Conference and Expo 2000, (P. Bufalini), Associazione Italiana di Metallurgia, 2000, Venezia, Italy, pp. 1-12.
[8] B. Leffler, H. Groth, A. Bergquist, Advantages and limitations of 2205 and other duplex stainless steels for the transport of chemicals, Proceedings of 5th World Duplex Conference, KCI Publishing, 1997, Maastricht, The Netherlands, pp. 785-792.
[9] J. E. Truman, K. R. Pirt, Properties of a duplex (austenitic – ferritic) stainless steel and effects of thermal history, Proceedings of ASM Conference on Duplex Stainless Steels, (ASM), ASM Ohio, 1983, Metals park, Ohio, pp. 113-142.
[10] G. Herbsleb, P. Schwaab, Precipitation of Intermetallic Compounds, Nitrides and Carbides in AF 22 Duplex Steel and Their Influence on Corrosion Behavior in Acids, Proceedings of ASM Conference on Duplex Stainless Steels, (ASM), ASM Ohio, 1982, Metals park, Ohio, pp. 25-26.
[11] L. Duprez, B. C. De Cooman, N. Akdut, Microstructure evolution during isothermal annealing of a standard duplex stainless steel type 1.4462, Steel Research, 71 (2000) 10, pp. 417-422.
[12] S. Hertzman, R. Pettersson, K. Frisk, T. Jerwin, The relation between alloy composition and kinetics of intermetallic phase formation, Proceedings of 6th World Duplex Conference and Expo 2000, (P. Bufalini), Associazione Italiana di Metallurgia, 2000, Venezia, Italy, pp. 347-354.
[13] J. V. S. Matias, S. Tavares, J. Pardal, A. Ribeiro, Embrittlement and Corrosion Decay of a Cast Duplex Stainless Steel, Materials research, 20 (2017) 2, pp. 279-283.

17th INTERNATIONAL FOUNDRYMEN CONFERENCE
Hi-tech casting solution and knowledge based engineering
Opatija, May 16th-18th, 2018
http://www.simet.hr/~foundry/

# INFLUENCE OF GRAIN REFINEMENT STRUCTURE ON THE INOCULATION EFFICIENCY IN WROUGHT AA 6182 ALLOY

**Maja Vončina[1]*, Jožef Medved[1], Lina Jerina[1], Irena Paulin[2], Peter Cvahte[3], Matej Steinacher[3]**

[1] University of Ljubljana Faculty of Natural Sciences and Engineering, Ljubljana, Slovenia
[2] Institute of Metals and Technology, Ljubljana, Slovenia
[3] Impol Group, Slovenska Bistrica, Slovenia

**Poster presentation**
*Preliminary note*

**Abstract**

Al–Ti–B refiners perform adequately for wrought aluminium alloys whereas the efficiency is various. It is in general believed that the poisoning elements interact with the grain refining constituents of the Al–Ti–B master alloys ($Al_3Ti$ and $TiB_2$) and make them ineffective or less effective. Also, the quality of grain refiner is utmost important, whereas the size, shape and distribution of particles influence on the inoculation efficiency.
In our case three different grain refiners were investigated using thermal analysis (TA) to establish the inoculation efficiency in AA6182 alloy. Furthermore, optical microscopy and scanning electron microscopy (SEM) with energy dispersive spectroscopy (EDS) was used in order to analyse the structure of $TiB_2$ and $Al_3Ti$ particles in the microstructure of grain refiners for three different manufacturers.
The potency of $TiB_2$ and $Al_3Ti$ particles changed regarding the size, shape and distribution of particles in the grain refinement master alloy. It was established that the most favourable refinement was shown for a grain refiner with more evenly distributed $Al_3Ti$ particles with a flake-like shape and smaller $TiB_2$ particles fragmented in-between $Al_3Ti$ particles.

***Keywords**: grain refinement structure, nucleation potential, $TiB_2$ particles, $Al_3Ti$ particles*

*Corresponding author (e-mail address): *maja.voncina@omm.ntf.uni-lj.si*

## INTRODUCTION

The vast majority of grain refining applications employ Al–Ti–B alloys which typically contain 2–10 wt.% Ti and 0.1–2 wt.% B [1].
There are many benefits from the use of grain-refiners in aluminium alloy castings. For example, mechanical properties can be improved and the susceptibility tendency to hot

cracking is reduced while fluidity is improved [2]. However, it is important to design the addition process to achieve the most effective grain-refinement, e.g. finding the contact time with the highest grain-refinement efficiency. If the contact time is too short, the finest grain size may not be achieved. On the other hand, if the contact time is too long, effectiveness of the grain-refiner will be lowered [3, 4]. Many researchers have made an assumption that the fading time resulted from the higher density of $TiB_2$ and $Al_3Ti$ comparing to that of molten aluminium so they settled down at the bottom of the furnace after long contact time.

The very popular Al–Ti–B refiners are known to perform adequately for wrought aluminium alloys except when the alloy to be inoculated contains one or more of the elements whose borides are more stable than $TiB_2$. The mutual presence of $Al_3Ti$ and $AlB_2$ particles in Al–Ti–B alloys, on the other hand, could offer to maximize the grain-refining efficiency for aluminium foundry alloys [5,6]. A popular grain-refinement mechanism has been proposed as $TiB_2$ which acts as a substrate for the nucleation of $Al_3Ti$, which then nucleates α-Al grains, i.e., via two steps of heterogeneous nucleation. Without the covering $Al_3Ti$ layer, $TiB_2$ are easily contaminated by impurities that have a high tendency to form eutectic microstructures with aluminium and therefore being poor in nucleating α-Al grains. However, the $Al_3Ti$ layer must be thinner enough and dynamic to avoid agglomeration to form compounded particles [7].

The ratio between Ti/B in master alloy and the way of processing conditions leads to a different morphologies of the $Al_3Ti$ particles which may be resulted from different growth mechanisms. In various Al-Ti-B grain-refines the morphology of $Al_3Ti$ particles could be as large blocky $Al_3Ti$ particles in the α-Al grain centres while smaller $TiB_2$ particles being pushed into the grain boundaries (Al-5 wt.% Ti-1 wt.% B) or as flake-like when the Ti/B ratio is reduced (Al-3 wt.% Ti-1 wt.% B) [8, 9]. Ti/B weight ratio corresponding to $TiB_2$ stoichiometry is 2.215; refining performance improves sharply as this ratio is exceeded, but wanes at higher titanium contents [9].

By considering why the grain-refiners of different manufactures show various inoculation efficiency, the quality of three different grain refiners from various manufacturers was investigated in this study.

## MATERIALS AND METHODS

The composition of experimental AA6182 alloy is listed in Table 1. In this study three different grain-refiners (GR) were used, whereas the chemical composition, made by Optical emission spectrometer with inductively coupled plasma ICP-OES (Agilent 720), is listed in Table 2. Base alloy AA6182 was melted in an induction furnace using a steel crucible. The experimental alloy was preheated at 700 °C and when it was melted, the Al-Ti-B master alloy was added into the melt, at either 1.2 or 1.5 g/kg, depending of the recommendations from the manufacturers. The melt was held for two minutes (contact time) before casting in an Croning measuring cell at a temperature of 680 – 690 °C, whereas the cooling rate was ~ 7 K/s. Furthermore cooling curves were recorded.

Table 1. Chemical composition (wt. %) of the experimental alloy AA6182

| Element | Zr | Pb | Zn | Cu | Fe | Mn | Cr | V | Ti | Si | Mg | Al |
|---|---|---|---|---|---|---|---|---|---|---|---|---|
| **AA6182** | 0.209 | 0.003 | 0.024 | 0.046 | 0.229 | 0.731 | 0.341 | 0.016 | 0.030 | 1.149 | 0.859 | rest |

Table 2. Grain-refiner Al-Ti-B master alloy designations and its chemical composition

| Designation | Master alloy | Addition /g/kg Al | Chemical element /wt.% | | | | | |
|---|---|---|---|---|---|---|---|---|
| | | | Si | Cr | Fe | B | Ti | Al |
| **GR1** | Al-3Ti-1B | 1.2 | 0.20 | <0.01 | 0.17 | 0.75 | 3.1 | rest |
| **GR2** | Al-3Ti-1B | 1.2 | 0.13 | <0.01 | 0.12 | 0.83 | 3.1 | rest |
| **GR3** | Al-5Ti-1B | 1.5 | 0.20 | <0.01 | 0.12 | 0.92 | 4.8 | rest |

The samples for grain size assessment were taken from the specimens after thermal analysis and analysed in the centre region. Specimens were prepared using a standard metallographic technique. Electropolishing was performed with Barker's reagent (4% $HBF_4$) to show the grain boundaries. All the samples were examined under polarized light, using Leica MeF4M at 25x magnification. The mean linear intercept technique according to ASTM E112 was used to quantify the grain size.
In addition, the grain-refiners were also analyzed using JEOL JSM-6500F equipped with energy dispersive spectrometer (EDS), which enabled the microchemical analysis of investigated grain-refiners. Furthermore, the size, shape and distribution of $Al_3Ti$ and $TiB_2$ particles in investigated grain-refiners was estimated.

## RESULTS AND DISCUSSION

Thermal analysis was used in order to analyse the inoculation efficiency of experimental grain-refiners and to establish whether the contact time is sufficient. From Fig.1 can be established that all three grain-refiners were effective; liquidus temperature has risen, contact time was suitable.

In order to establish the grain refiner's efficiency, micrographs of experimental samples taken in polarized light after etching are presented in Fig.2. The results of grain size measurements are presented in Table 3. These results are showing that the most effective grain refiner is GR2, whereas the grain size is the smallest 237 µm.

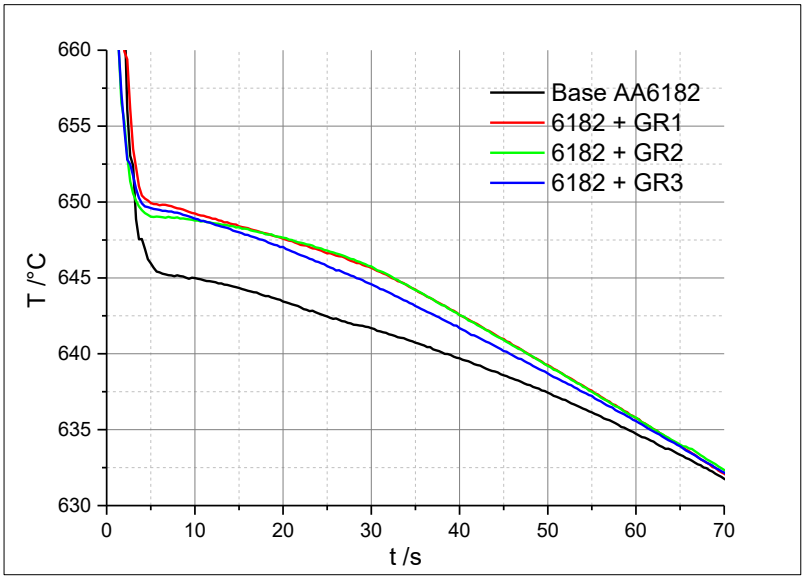


Figure 1. Cooling curves of experimental alloys with various grain refiner additions

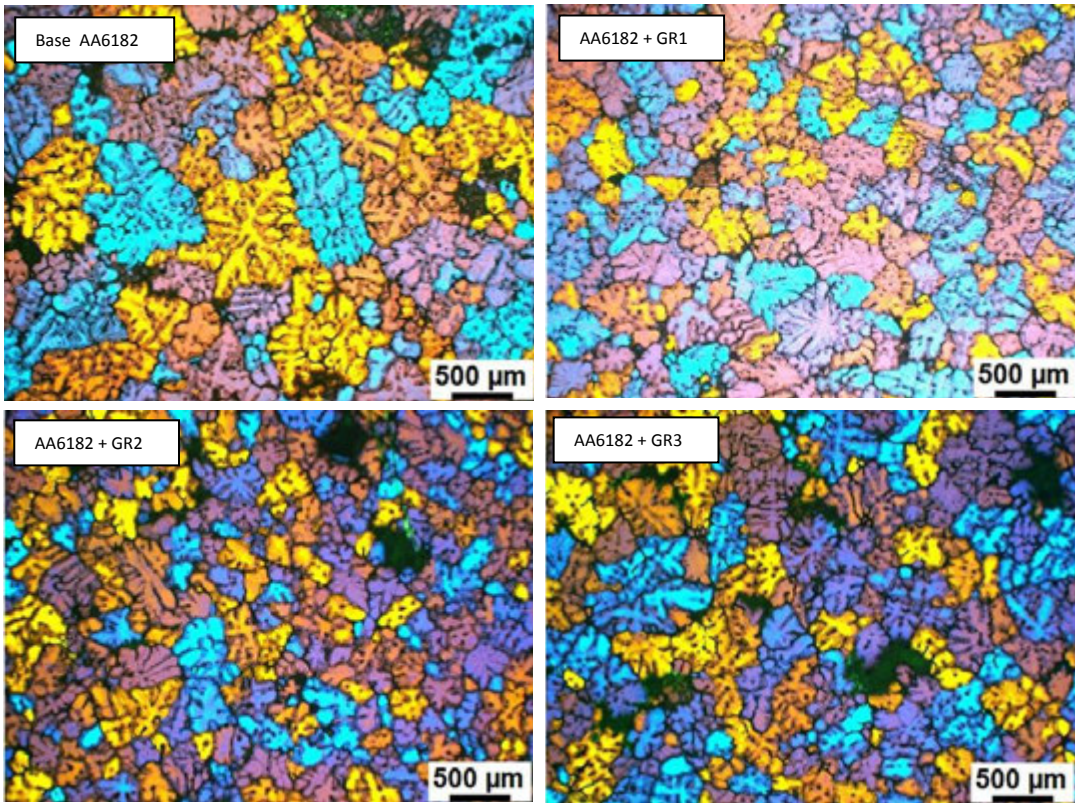


Figure 2. Micrographs taken in a polarized light for base AA6182 alloy and grain-refined samples at contact time 2 min

Table 3. Liquidus temperature ($T_L$) /°C and the grain size ($D_{grain}$) /µm

| Sample | $T_L$ /°C | $D_{grain}$ |
|---|---|---|
| **Base AA6182** | 649 | 416 |
| **AA6182 + GR1** | 651 | 264 |
| **AA6182 + GR2** | 653 | 237 |
| **AA6182 + GR3** | 652 | 243 |

Figs.3a–c present s typical micro-images of the as-cast grain-refiners. Fig.3a is from the Al-3 wt.% Ti-1 wt.% B alloy (GR1) showing large blocky- and flacky-like $Al_3Ti$ particles which are unevenly distributed in the matrix, while smaller $TiB_2$ particles are fragmented in-between. Fig.3b shows microstructure of a grain-refiner GR2 showing that the morphology of the $Al_3Ti$ particles is much different from grain-refiner GR1. Here $Al_3Ti$ particles in a flake-like shape are much more evenly distributed in the microstructure. In case of grain-refiner GR3 (Fig.3c), Al-5 wt.% Ti-1 wt.% B, the $Al_3Ti$ particles change from blocky to flake-like shape when the Ti/B ratio is reduced. All three grain refiners were analysed using SEM, presented in Fig.4a-c. When $Al_3Ti$ and $TiB_2$ particles were analyzed using EDS, many more impurities were detected in grain refiner GR1 and GR3, whereas beside Al, Ti and B also traces of F, Na, K and Ca were detected.

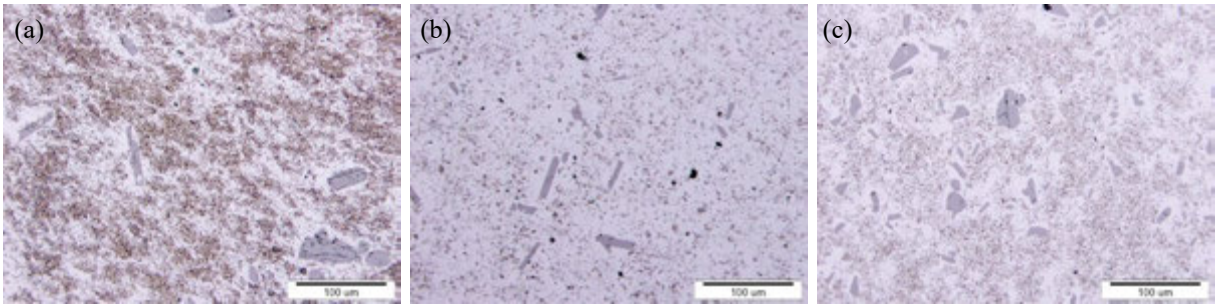


Figure 3. Micrographs of investigated grain-refiners: GR1 (a), GR2 (b) and GR3 (c)

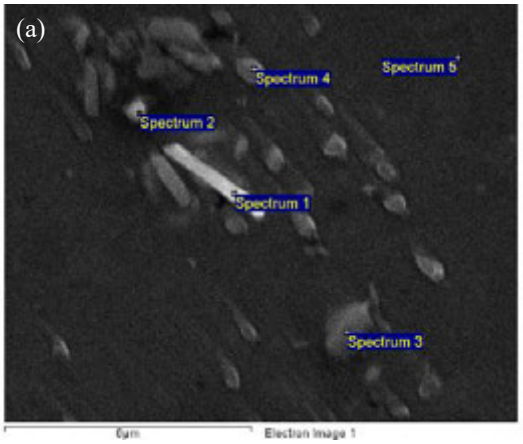


| Spectrum | B | O | F | Na | Al | K | Ca | Ti |
|---|---|---|---|---|---|---|---|---|
| Spectrum 1 | | 34.56 | 2.12 | | 58.85 | 2.48 | | 1.99 |
| Spectrum 2 | | 25.44 | | 2.55 | 62.60 | | 5.86 | 3.55 |
| Spectrum 3 | 42.30 | | | | 35.44 | | | 22.25 |
| Spectrum 4 | 31.61 | | | | 63.15 | | | 5.25 |
| Spectrum 5 | | 0.91 | | | 98.17 | | | 0.92 |

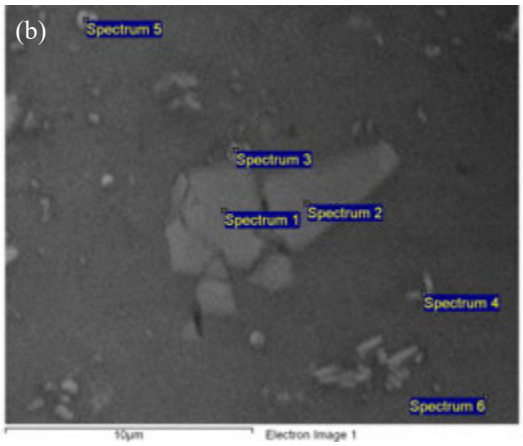


| Spectrum | B | Al | Ti |
|---|---|---|---|
| Spectrum 1 | | 64.73 | 35.27 |
| Spectrum 2 | | 67.03 | 32.97 |
| Spectrum 3 | 44.46 | 40.95 | 14.59 |
| Spectrum 4 | 28.09 | 50.97 | 20.94 |
| Spectrum 5 | 42.86 | 49.57 | 7.57 |
| Spectrum 6 | | 100.00 | |

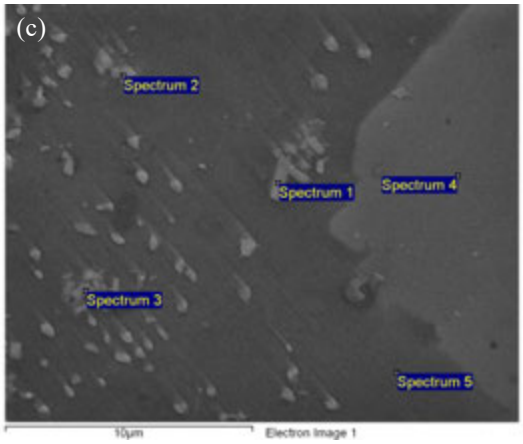


| Spectrum | B | F | Al | K | Ti | Fe |
|---|---|---|---|---|---|---|
| Spectrum 1 | 39.31 | | 30.89 | | 29.81 | |
| Spectrum 2 | 40.51 | 2.16 | 38.90 | 0.78 | 16.13 | 1.52 |
| Spectrum 3 | | | 72.21 | | 22.82 | 4.97 |
| Spectrum 4 | | | 62.08 | | 37.92 | |
| Spectrum 5 | | | 95.31 | | 4.69 | |

Figure 4. SEM-images with corresponding EDS analysis of $Al_3Ti$ and $TiB_2$ particles in GR1 (a), GR2 (b) and GR3 (c) in wt.%

## CONCLUSIONS

From the presented experimental results the following conclusions can be made:

- A very small fine equiaxed grains were achieved when GR2 was added in the AA6182 alloy at holding time of 2 min.
- The two different morphologies of the $Al_3Ti$ particles analyzed in this investigation may result from different growth mechanisms and also from different processing conditions. For most effective inoculation insoluble $TiB_2$ and the soluble $Al_3Ti$ particles in suitable shapes and sizes are needed and are present in GR2.
- Without the covering $Al_3Ti$ layer, $TiB_2$ are easily contaminated by impurities that have a high tendency to form eutectic microstructures with aluminium and therefore being poor in nucleating α-Al grains. In our case presumably latest occurred when GR1 and GR3 were added due to impurities analysed in these two grain refiners.

## REFERENCES

[1] Y. Birol, A novel Al–Ti–B alloy for grain refining Al–Si foundry alloys, Journal of Alloys and Compounds, 486 (2009) pp. 219-222.
[2] C. Limmaneevichitr, W. Eidhed, Fading mechanism of grain refinement of aluminum/silicon alloy with Al/Ti/B grain refiners, Materials Science and Engineering A, 349 (2003) pp. 197-206.
[3] Z. Fan, Y. Wang, Y. Zhang, T. Qin, X. R. Zhou, G. E. Thompson, T. Pennycook and T. Hashimoto, Grain refining mechanism in the Al/Al–Ti–B system, Acta Materialia, 84 (2015) pp. 292-304.
[4] P. Schumacher, A. L. Greer, J. Worth, P. V. Evans, M. A. Kearns, P. Fisher, A. H. Green, New studies of nucleation mechanisms in aluminium alloys: implications for grain refinement practice, Materials Science and Technology, 14 (1998) 5, pp. 394-404.
[5] Z. Fan, Y. Wang, Y. Zhang, T. Qin, X.R. Zhou, G.E. Thompson, T. Pennycook and T. Hashimoto, Grain refining mechanism in the Al/Al–Ti–B system, Acta Materialia, 84, 2015, pp. 292-304.
[6] S. A. Kori, B.S. Murty, M. Chakraborty, Development of an efficient grain refiner for Al–7Si alloy and its modification with strontium, Materials Science and Engineering A, 283 (2000) pp. 94-104.
[7] B. S. Murty, S. A. Kori, M. Chakraborty, Grain refinement of aluminium and its alloys by heterogeneous nucleation and alloying, International Materials Reviews, 47 (2002) pp. 3-29.
[8] X. Wang, J. Song, W. Vian, H. Ma, Q. Han, The Interface of $TiB_2$ and $Al_3Ti$ in Molten Aluminum, Metallurgical and Materials Transactions B, 47 (2016) 6, pp. 3285-3290.
[9] P. Schumacher, A. L. Greer, J. Worth, P. V. Evans, M. A. Kearns, P. Fisher, A. H. Green, New studies of nucleation mechanisms in aluminium alloys: implications for grain refinement practice, Materials Science and Technology, 14 (1998) 5, pp. 394-404.

**Acknowledgements**

This work was supported by A Republic of Slovenia, Ministry of Education, Science and Sport and by European Commission, European Regional Development. This work was made in a frame of program Materials and Technologies for New Applications (MARTINA, grand number: C3330-16-529008).

17th INTERNATIONAL FOUNDRYMEN CONFERENCE
Hi-tech casting solution and knowledge based engineering
Opatija, May 16th-18th, 2018
http://www.simet.hr/~foundry/

# ANCIENT LEAD METALLURGY AND THE APPLICATION OF LEAD ARTIFACTS IN ANCIENT TIMES

**Irena Žmak*, Krešimir Grilec**

University of Zagreb Faculty of Mechanical Engineering and Naval Architecture, Zagreb, Croatia

**Poster presentation**
*Review*

**Abstract**

The paper describes the typical applications of lead and its compounds, which have been used since 8 000 years by many civilizations. Products such as cosmetics, a medicine, pottery glazing, and as a food additive were commonly accepted for far too many centuries. Different engineering applications were made possible due to the easily available large amounts of the lead-containing ore, and to the simple metallurgical production technology, with lead having a relatively low melting point. The remains of one of the first human attempts to melt the lead-rich ore galena was found in today's Bosnia, which is described in the paper. Lead is a soft and easily malleable metal, which has allowed lead to be used in many engineering applications that require high plasticity. Besides art figures, and value-expressing Roman tesserae, one of the lead usage examples explained in the paper is the Roman water supply system found in the Sisak area in Croatia. In addition, numerous lead engineering applications found on ancient Roman ships are discussed in the paper.

***Keywords**: lead, melting, ancient Rome, applications.*

*Corresponding author (e-mail address): *irena.zmak@fsb.hr*

## INTRODUCTION

Lead is probably best known as a heavy metal, denser than most commonly used materials. With the density of 11 340 kg/m$^3$, it is one of the densest common materials, with only the gold surpassing it with 19 300 kg/m$^3$. As for its mechanical properties, it is soft and easily malleable, which has allowed lead to be used in many applications that require high plasticity. Moreover, lead has a reasonably low melting point of 327.5 °C. This physical property was also favorable in the early historical applications of lead.

Lead is an amphoteric metal, i.e. the metal and its oxides react with both acids and bases. This chemical property has induced many historically known health issues. Unfortunately, only at the end of the 19th century, the toxicity of lead was officially accepted. Since then, many efforts have been made in order to reduce its areas of application, and the maximum allowed amounts of lead in different products.

**THE USE OF LEAD IN ART IN ANCIENT WORLD**

Ancient civilizations have been processing lead ores for at least 8 000 years, which is confirmed by numerous artefacts stored in museums, and by ancient writings, such as the biblical Book of Exodus. Lead beads, as it was originally thought, dated to about 6 500 BC were discovered in current area of Turkey. They belonged to the people, which inhabited the large Neolithic settlement of Çatal Hüyük, Level IX (c. 6400 BC.) in in southern Anatolia. The presupposed lead beads were later identified as lead-rich minerals cerussite and galena, i.e. not as lead metal [1].
One of the oldest lead findings was found in a jar belonging to the Vinča culture. The jar was found near the town of Donja Tuzla in Bosnia and Herzegovina, and is traced back to more than 5 000 years BC (Figure 1). It is assumed that the metallic remains on the bottom of the jar are molten lead. Although, some claim this finding too is not pure metal but lead-rich mineral galena, what is very interesting is that the jar was used for melting the ore. The metallic remains on the jar bottom, heat cracks and traces of high temperature exposure on the jar outside clearly indicate it was used as a melting pot. The Neolithic people were not yet familiar with all the required metallurgical processes to separate sulphur and oxides from the metal. Such complex metallurgical processes will only be known and applied in the so-called Eneolithic Age (or Chalcolithic period or Copper Age). This example of a failed galena-melting attempt is understandable considering the very early stages of the metallurgical development at the time. Therefore, the fascinating jar of Donja Tuzla may be considered as the oldest preserved artefact showing first human attempts in solving the complex melting process of sulfide-rich ores [2].

Figure 1. Jar with remains of molten mineral galena, Donja Tuzla (Bosnia and Herzegovina) around 5 000 BC (courtesy of Dr. Andrijana Pravidur)

In ancient Egypt lead was used for glazing pottery, for soldering, and for casting ornamental artifacts as far as 5 000 BC [3]. The British Museum is said to be storing a lead statuette, probably found in the temple of Osiris in the ancient city of Abydos, dating from 3500-3800 BC [4]. Whether the city Abydos refers to Abydos in the Dardenelles or to the Abydos in Upper Egypt is uncertain. The statuette is not in exhibit in the Museum, but an old scanned photograph of the statuette may be seen on Figure 2 on the right-hand side. The limestone figurine on the left-hand side originates form the same archeological spot [5].

Figure 2. The oldest lead artefact from the Temple of Osiris at Abydos, around 3800 BC [5]

The height of the figurine is only about 5 cm, and it has visible traces of wear and tear. The whole figurine is covered with a thin hard brownish layer, which is probably the tetragonal laced lead-oxide. The style and size make it comparable to the several carved limestone female figurines, found during the excavation of the Osiris Temple at Abydos [5].
Although the artistic modelling of the lead figurine is not as refined as the comparable limestone figurines (Figure 2, left), with a too large head, facial features crudely worked, with the whole surface being quite rough, and unfortunately, with the right arm missing, the value of this little lead statue is remarkable. The chemical analysis by the British Museum's laboratories showed there are not any noticeable impurities in the lead figurine. The composition of the figurine of remarkably pure lead. It was also determined that the figurine was not cast, but carved [5].
Similar small lead figurines were found in 1912 in the river Kupa near the city of Sisak, Croatia. Figure 3 a. presents a very simplified model of a man. The facial expressions are primitively modelled by simple lines. The form of the head was determined simply by a small fillister, the arm length is dissimilar, and the legs are not in proportion with the body. There are hardly any distinct physical characteristics, except for the extremely highlighted penis. The figurine weighs 21.60 g; it is 50 mm high, 26 mm wide and 9 mm thick. A similar, yet even more simplified figurine was also found in the river Kupa in 1913, Figure 3 b. The figurine, whether male or female, is flat as if carved from a plate, with the arms stretched on

the sides and the legs starting right below the arms. The bended ends of the extremities indicate hands and feet. The dimensions of the figurine are 65 mm height, 57 mm width, 8 mm thickness and it weighs 41.90 g. These two figurines were also not cast, but hand carved. Any analogue figurines to these were not found on any other historical locations [6].

a) b)

Figure 3. a) Very simplified model of a man, and b) Flat, plate-like figurine, both the oldest lead figurines found in Sisak area (Croatia) [6]

**EVERYDAY ANCIENT LEAD ITEMS**

Roman used lead plates called tesserae for, among others, marking value of goods and for declaring the composition of goods too. They were usually in the form of irregular rectangles, having one hole in the angle for easier using a rope or wire. They usually had inscription of both sides, often being reused, i.e. rewritten several times. About 1200 pieces were found in the area of the Croatian city of Sisak. Most of these tesserae have inscriptions regarding the type of textile clothing, its composition, color, length, etc. The ancient Roman lead declarations are dated to the 1st and early 2nd c AD. Some of them have names written on them, listing in total around 950 different persons form the area. Some of the articles were interpreted as personal belongings being delivered for washing or dying (coloring) clothes [7]. Figure 4 presents a photograph of an array of Sisak's tesserae, and the chart on Figure 5 shows a distribution of the value stated on the lead plates, as expressed in the Roman currency, denarius. Most of the goods were of low value, having a continuous drop in frequency as the value increased.

Figure 4. Lead Roman tesserae for trading textile (Sisak area) [8,9]

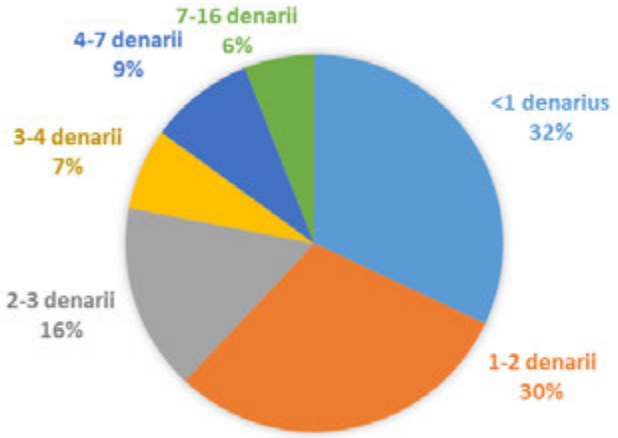


Figure 5. Values imprinted on the lead tesserae for trading textile (Sisak area) [8,9]

**SIMPLE LEAD PRODUCTION FROM THE ORE**

Lead production is related to the discovery of the cupellation process. This metallurgical process was primarily used for the separation of precious metals, like gold or silver from the base metals, like lead or copper, from the ore. The process is based on the fact that precious metals do not react chemically, unlike the base metals. So when the ore is heated, precious metals remain stable, while the base metals oxidize, thus forming the slag. This process is still being used in the modern times; the ore melted in the blast furnace produces the melt with 25 % to 50 wt. % of silver in the silver-lead alloy. The lead is being separated from the silver using a bottom-blown furnace, Figure 6. The lead is oxidized, and forms lead monoxide (PbO), also called the litharge, which is usually poured off the top. Lead is oxidized into litharge until the silver is more than 98 wt. % purity. [10].

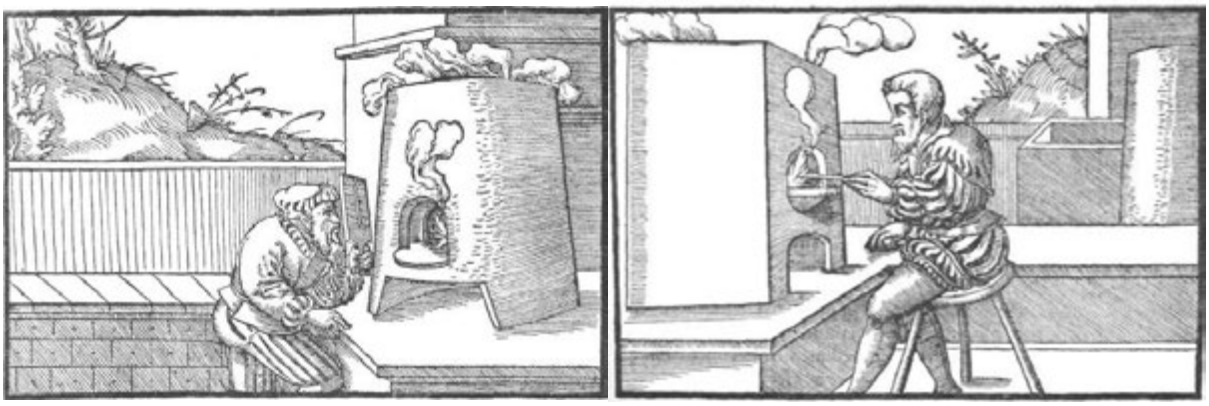

Figure 6. 16th century cupellation furnaces (round and rectangular) [11]

Roasting the ore called galena, which is composed of lead sulphide, PbS produces lead oxide in the following manner [12]:

$$2PbS + 3O_2 \rightarrow 2PbO + 2SO_2 \quad (1)$$

The next step is smelting of lead oxide for producing the lead as follows:

$$2PbO + C \rightarrow 2Pb + CO_2 \quad (2)$$

**TOXICITY OF LEAD COMPOUNDS USED IN ANCIENT TIMES**

The lead monoxide was widely used throughout the history as a pigment, for making glass and for pottery coloring. Ancient Egyptians used lead compounds in cosmetics for both decorative and medical applications. The black eye-paint was made of galena, which is a grey lead compound; white lead-carbonate, and lead compounds, such as laurionite, PbCl(OH) and phosgenite, $Pb_2(CO_3)Cl_2$, all powder ground, were used for decorating the face, nails and feet. The Egyptian medical documents written on papyrus contain also several recipes for the treatment of eye infections using lead based eye paint [13]. This tradition was later adopted by ancient Greeks and Romans too.
Unfortunately, many believed that lead had positive health properties, such as scars removal, anti-bacterial plasters for ulcers and the eyes, as for Pliny, who was also a notable Roman scholar from the 1st century AD [4].
Although there is a general conception that the ancient Rome has declined because of the lead water pipes, studies have shown that the lead levels in ancient Roman skeletons were not as high as presupposed. For instance, the median of determined lead levels in pre-Roman skeletons in Britain was 0.08 mg/kg, 1.23 mg/kg in Roman Britain, 3.61 during Imperial Rome. The post-Roman data include: median of 0.39 mg/kg between 5th and 7th c AD, 8th-11th c AD 1.93 mg/kg, and 4.69 mg/kg in late Medieval [25,14], Figure 7.

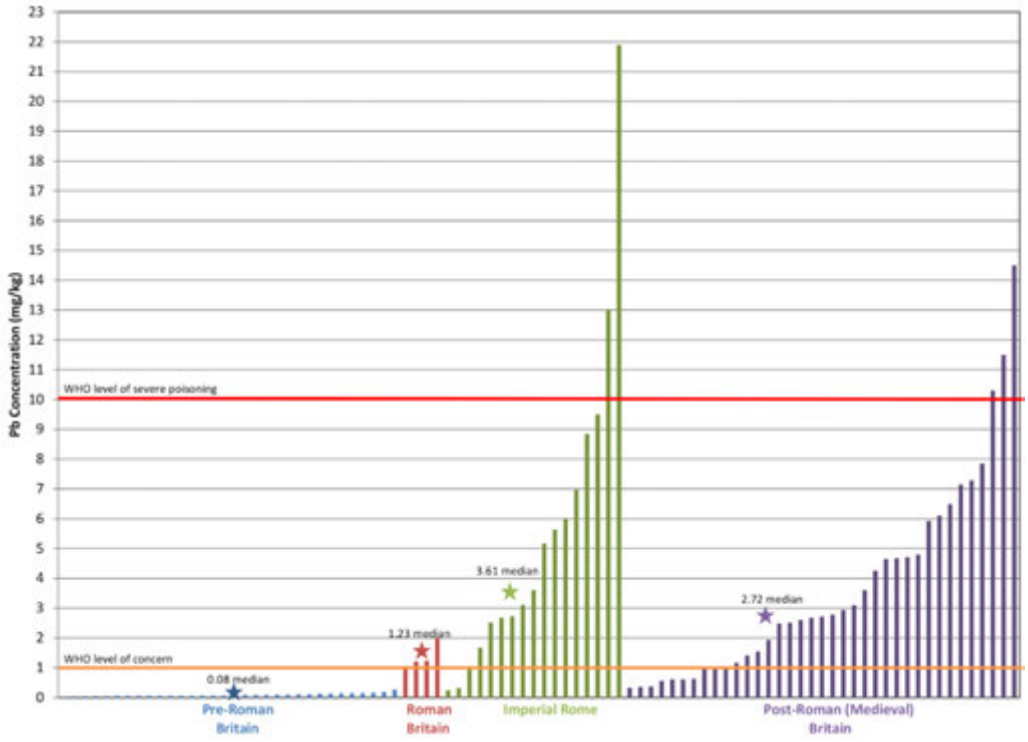


Figure 7. Lead concentration from skeletons from Britain and Rome [25]

The sources of lead that most influenced the poisoning of humans in different historic times were different. Most probable examples include drinking soft water from lead cups, storing soft water in lead cisterns, drinking acid drinks such as wine from lead cups, swallowing different lead compounds as believed to be a medicine or using it as cosmetics, using lead-glazed pottery, pans and different storage containers [14].

One of the benefits of the higher society members was the opportunity to indulge in wine, which is a corrosive medium for lead. Roman winemakers produced an artificial sweetener known as *defrutum* or *sapa* by boiling unfermented grape juice specifically in lead vessels, with bronze pots or cooking bowls being not adequate, and not having a pleasant taste. This sweet liquid was used to sweeter the liquids, especially wine, for improving the flavor of Roman foods, to preserve the fruits, and to preserve the food for the Roman soldiers. Recreating the Roman *sapa* in lead vessels using antique recipes produced a liquid with a lead content of 2.9 mg/kg [15]. As a comparison, current maximum levels in the European Union allow up to 0.02 mg/kg of lead in milk, 0.1 mg/kg in fresh meat and leaf vegetables, and 0.3 mg/kg in the muscle meat of fresh fish [16]. The tradition of sweetening wind using the ancient sweetener continued well into the history, which is associated for example with the death of Pope Clement II in 1047. The study of his remains done in 1959 confirmed lead poisoning. One of the possible sources was the wine that the often pope drunk, which was still at the time sweetened the way the ancient Romans did. Ludwig van Beethoven is suggested to have died from the same cause and the same source of lead [17].

**LEAD WATER PIPES IN ANCIENT ROME**

Perhaps one of the most widely used lead products in history were the Roman water pipes, Figure 11. Lead pipes of 3 m length and in 15 standard diameters were commonly produced. Many of these pipes are still in excellent condition and may be found throw-out Europe where the Romans once reigned. The Latin word *plumbum*, meaning lead is connected to the English word plumbing and plumber, as well as the very symbol of the chemical element, Pb [24].

The Romans used the lead pipes widely. An archeological study at the end of the nineteenth century revealed a lead pipe system for supplying the Roman Forum, which was 1 750 meters long, and weighed 232 752 kg [22]. Most of the ancient Roman lead pipes were recycled during the history, eventually. One example includes the Croatian island of Veliki Brijun, where the last 16 m if the remaining Roman lead pipes were removed by archeologists in 1979. Being a small and uninhabited island between the Roman times and the beginning of the 20th c, the entire ancient lead water supply system was well preserved until the end of the World War II, when it was devastated [18].

A more recent example of the Roman lead pipes tragic recycling was recorded in the Croatian city of Sisak, which lies on the remains of the Roman town of Siscia. In November 2006 a total of 1303 kg lead pipes was declared missing from the courtyard of the "Veliki kaptol" palace in Sisak, where they were temporarily stored. Figure 8 and Figure 9 show one of the remaining water pipes that the burglars left behind. Although the two perpetrators were identified, the ancient lead had already been sold and exported, and thus lost for the authorities. The way this very large amount of Roman lead pipes was discovered in the first place is also fascinating. The water pipes along with the very well preserved supporting wooden pillars were accidentally found in the 1980s during ship dragging of the bottom of river Kupa near Sisak. Unfortunately, the pipes ended twisted and twined by the dragger at the time [19,20], Figure 10. The founding of such a large water supply system confirmed the high importance of the city of Siscia in the Roman times.

Figure 8. A piece of the remaining lead water pipe (Sisak area, Croatia),
(courtesy of Ivana Miletić Čakširan)

Figure 9. Roman lead pipe inscriptions raised in high-relief on the surface (Sisak area, Croatia), (courtesy of Ivana Miletić Čakširan)

Figure 10. Roman lead water pipes after being accidentally rolled up by a dragger ship in river Kupa (Sisak area, Croatia) [20]

A commonly accepted opinion is that of the Roman ignorance towards the lead toxicity, but the fact is the an important Roman architect and engineer, Marcus Vitruvius Pollio, from the 1st century BC, did warn about the toxic use of lead pipes for conveying water. Vitruvius recommended clay pipes to be used instead of lead. Vitruvius is known for his multi-volume work entitled De architectura, where he wrote about the poor skin color of the workers in lead foundries of those times. He noticed in fact that the fumes from the molten lead destroyed the “vigor of the blood” [4,21].

Lead water pipes may be dangerous to the humans if used for accumulating still water, and especially water with low carbon content. Intense lead corrosion may occur in soft water with dissolved oxygen, or when both the dissolved oxygen and carbon dioxide are present. In the latter case, the corrosion rate depends predominantly on the carbon dioxide content. On the other hand, lead is corrosion resistant in high-hardness water (above 120 mmol/L) with low amounts of dissolved $CO_2$ and the pH-value slightly above 7, since lead pipes get passivated via a thin layer of lead carbonate. Very hard water with high amounts of $CO_2$ is corrosive to lead. The corrosion product of lead hydroxycarbonate does not adhere strongly, so it does not afford good protection. When the water contains also some phosphates, the produced layer of hydroxyphosphate, which is more adhesive, hence giving a much better protection [22,23].

Figure 11. Set of lead pipes from river Rhone [24], and lead pipes from a Roman bath [25]

**LEAD USED ON ROMAN SHIPS**

Roman ships used lead in abundance, as lead was one of the best available metals concerning the specific requirements and the available technologies at ancient times. The material had to be easily malleable, corrosion-resistant, of reasonable price and low maintenance costs [26].
One important characteristics of lead is that it easily fitted curved ship hulls; holes were easily punched using copper and bronze nails, the corrosion resistance was satisfactory, and it also and provided ballast weight without consuming any cargo space. Romans used also Lead bilge-pumps (Figure 12, detail no. 5), which pipes were easily bent, cut and joined, even in tight environments, such as the ship hull. What is interesting to notice is that the Romans used lead brailing-rings (Figure 12, detail no. 4), which were heavy, but more easily formed than comparable iron or bronze rings. Since lead has a low friction coefficient, the wear of the ropes and sails was minimized [26].
Considering its density and corrosion resistance, lead was also used for making anchors and anchor parts (Figure 12, detail no. 3) or for fishing gear (Figure 12, detail no. 10 and 11). Lead sheathing was used since the Roman times to protect the under-water hull of the ship from the salt-water corrosion and partially against biofouling [27]. Lead plates were attached to

the hull outside (Figure 12, detail no. 1), offering also great protection against worms destroying the wood and more easily cleaned [28].

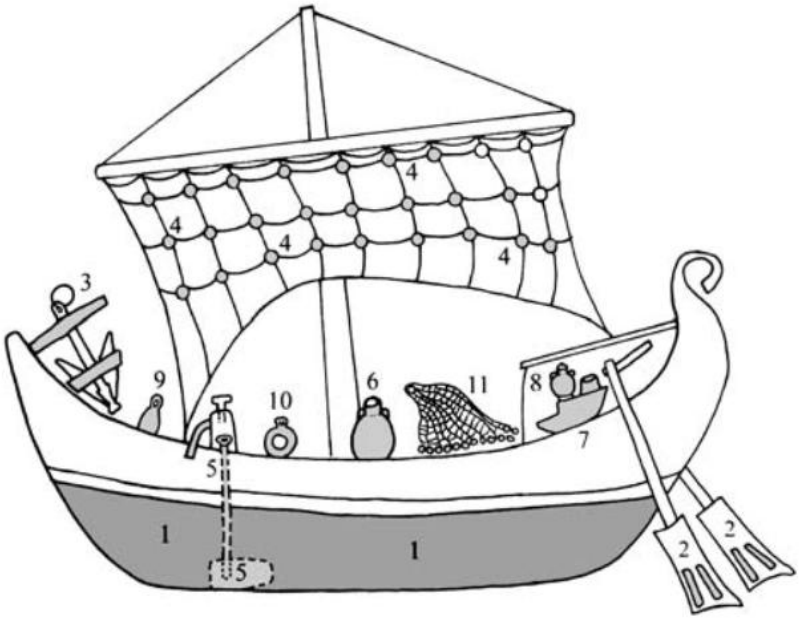


Figure 12. Different parts made of lead on the ancient roman ship [26]

Lead weights were also used for estimating the sea depth and the type of the seabed (Figure 12, detail no. 9). Rudder-oars and rowing-oars were also balanced using lead weights (Figure 12, detail no. 2). Lead braziers were probably the only cooking devices on board of the Roman ships (Figure 12, detail no. 7). They were portable, tough and easy to repair. The Roman pottery glazed with lead based paint, was also a source of lead that romans took with them on their naval expeditions (Figure 12, detail no. 6 and 8) [26].

## HISTORICAL RECORD OF THE LEAD PRODUCTION

The production of lead more than began 5 000 years ago, and its production has been increasing throw-out most of the history. Figure 13 presents a timeline with the global production of lead, with a noticeable decrease during the fall of the Roman Empire, and with a later recovery during the medieval times.

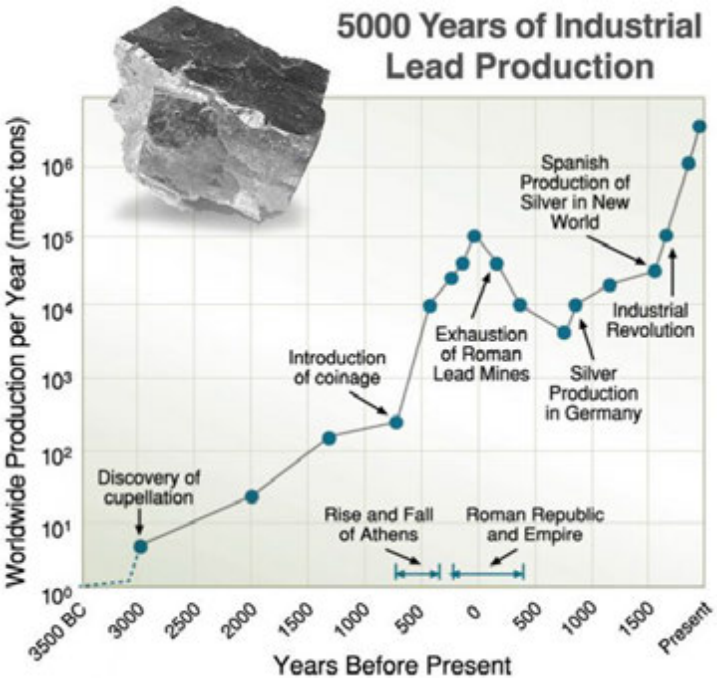


Figure 13. Historical record of industrial lead production in last 5,000 years [29]

The production has increased significantly again during the industrial revolution, which lead to a new massive contamination of the environment. The use of lead in paints, cosmetics, pottery glazing has been limited only recently in the developed part of the word, while still being allowed in many developing countries.

## CONCLUSIONS

Lead is one of the most commonly used heavy materials. It has been used since 7 000 years, by ancient civilizations. Humans have used lead in many different everyday applications, starting from medicine and cosmetics, and to glazing pottery. Many engineering applications were made feasible and were at the time advanced solutions, thanks to the easily malleable lead.

Unfortunately, the toxicity of lead was underestimated through times, even when the health side effects were known or at least suspected. The toxicity of lead was accepted only at the end of the 19th century. Numerous efforts have been made to reduce the areas of application and to lower the allowed lead levels in different products.

**REFERENCES**

[1] I. Hodder (ed.), Substantive Technologies at Çatalhöyük: Reports from the 2000–2008 Seasons: Çatalhöyük Research Project Volume 9 (Monumenta Archaeologica): Chapter 17, T. Birch, T. Rehren, E. Pernicka, The Metallic Finds from Catalhoyuk: A Review and Preliminary New Work, Accessible on Internet: http://discovery.ucl.ac.uk/1474072/1/Birch%20et%20al%202013%20Catal%20Hoyuk%20copper%20a%20review%20and%20new%20work%20plus%20Appendices.pdf, April 29, 2018.
[2] A. Pravidur, Metal u životu prapovijesnih zajednica na tlu Bosne i Hercegovine, doktorski rad, Sveučilište u Zagrebu, Filozofski fakultet, Zagreb, 2014.
[3] B. A. Fowler, Measuring Lead Exposure in Infants, Children, and Other Sensitive Populations, 1993, Accessible on Internet: https://books.google.hr, April 3, 2018.
[4] A. L. Ponikvar, F. E. Goodwin, Lead processing, Accessible on Internet: https://www.britannica.com/technology/lead-processing, April 3, 2018.
[5] W. W. Krysko, Comments on the oldest known lead figurine, Accessible on Internet: http://hist-met.org/images/Journal_PDFs/20_2_p_109_Krysko.pdf, April 3, 2018.
[6] A. Bauer, Rimska olovna plastika s osobitim obzirom na materijal pohranjen u Hrvatskom narodnom muzeju. Zaklada tiskare Narodnih novina, Zagreb, 1939., Accessible on Internet: https://hrcak.srce.hr/file/80785, April 4, 2018.
[7] Gradski muzej Sisak, Sisak u svjetlu novih arheoloških istraživanja, zbornik sažetaka, Accessible on Internet: https://bib.irb.hr/datoteka/751341.Gradski_muzej_Sisak_zbornik.pdf, April 4, 2018
[8] D. Prerad, N. Čutuk, Je li se u Sisciji i prije rafinerije živjelo teško, Accessible on Internet: https://www.vecernji.hr/kultura/je-li-se-u-sisciji-i-prije-rafinerije-zivjelo-tesko-986876/galerija-122666?page=2, April 4, 2018.
[9] I. Radman-Livaja, Olovne tesere iz Siscije, osvrt Vendi Jukić Buča, Accessible on Internet: http://www.arheologija.hr/?p=7176, April 4, 2018.
[10] Precious Metal Recovery, Silver Recovery, Gold Refining and Platinum Refining, West Bromwich, UK, Accessible on Internet: http://www.jbr.co.uk/process-cupellation.html, April 5, 2018.
[11] G. Agricola, 16th century cupellation furnaces, Cupellation, Wikipedia, Accessible on Internet: https://en.wikipedia.org/wiki/Cupellation, April 5, 2018.
[12] A. McCartney, Ancient and Marvellous Metallurgy – GooseyGoo, Accessible on Internet: https://www.gooseygoo.co.uk/ancient-and-marvellous-metallurgy-2/, April 5, 2018.
[13] A. Hallmann, Was Ancient Egyptian Kohl a Poison?, Proceedings of the Third Central European Conference of Young Egyptologists, Egypt 2004, Accessible on Internet: https://www.academia.edu/1824180/Was_Ancient_Egyptian_kohl_a_poison, April 5, 2018.
[14] J. Montgomery, J. A. Evans, S. R. Chenery, V. Pashley, K. Killgrove, Gleaming, white and deadly': using lead to track human exposure and geographic origins in the Roman period in Britain, Journal of Roman archaeology, Suppl. 78(2010), pp. 199-226,

Accessible on Internet: https://www.yorkarchaeology.co.uk/wp-content/uploads/2015/08/Janet-Montgomery-Text-%E2%80%9CGleaming-white-and-deadly%E2%80%9D-using-lead-to-track-human-exposure-and-geographic-origins-in-the-Roman-period-in-Britain.-1.pdf, April 5, 2018.

[15] The first artificial sweetener poisoned lots of Romans, Accessible on Internet: https://io9.gizmodo.com/5877587/the-first-artificial-sweetener-poisoned-lots-of-romans, April 6, 2018.

[16] CELEX 02006R1881-20150521 EN, Accessible on Internet: http://eur-lex.europa.eu/legal-content/EN/TXT/HTML/?uri=CELEX:02006R1881-20150521&from=EN, April 6, 2018.

[17] J. Rhodes, Sugar of Lead, A Deadly Sweetener, Arts & Culture. Smithsonian, Accessible on Internet: https://www.smithsonianmag.com/arts-culture/sugar-of-lead-a-deadly-sweetener-89984487/, April 6, 2018.

[18] A. Vitasović, Opskrba vodom i rimski vodovod na brdu Gradina na otoku Veliki Brijun, Histria archaeologica, 37(2008), pp. 47-82, Accessible on Internet: https://hrcak.srce.hr/34472, April 7, 2018.

[19] Olovne rimske cijevi prodali za 3000 kuna, Jutarnji list, published: November 10, 2006, Accessible on Internet: https://www.jutarnji.hr/arhiva/olovne-rimske-cijevi-prodali-za-3000-kuna/3237173/, April 29, 2018.

[20] Sisak: Ukrali rimske cijevi stare 2000 godina, Jutarnji list, published: November 7, 2006, Accessible on Internet: https://www.jutarnji.hr/arhiva/sisak-ukrali-rimske-cijevi-stare-2000-godina/3236582/, April 30, 2018.

[21] Vitruvius, Wikipedia, Accessible on Internet: https://en.wikipedia.org/wiki/Vitruvius, April 7, 2018.

[22] Aqueducts of Rome, Italy, Building the World, Accessible on Internet: http://blogs.umb.edu/buildingtheworld/waterworks/aqueducts-of-rome-italy/, April 7, 2018.

[23] Lead corrosion in water treatment, SUEZ's Degremont water handbook, Accessible on Internet: https://www.suezwaterhandbook.com/water-and-generalities/corrosion-in-metal-and-concrete/corrosion-in-metallic-materials/lead, April 7, 2018.

[24] Aqua Clopedia, a picture dictionary on Roman aqueducts Pipes, Accessible on Internet: http://www.romanaqueducts.info/picturedictionary/pd_onderwerpen/pipe.htm, April 7, 2018.

[25] K. Killgrove, Lead Poisoning in Rome - The Skeletal Evidence, Accessible on Internet: http://www.poweredbyosteons.org/2012/01/lead-poisoning-in-rome-skeletal, April 7, 2018.

[26] B. Rosen, E. Galili, Lead use on roman ships and its environmental effects, International Journal of Nautical Archaeology, 36(2007)2, pp. 300 –307, Accessible on Internet: https://onlinelibrary.wiley.com/doi/pdf/10.1111/j.1095-9270.2007.00145.x, April 9, 2018.

[27] The History of the Prevention of Fouling, Marine Fouling and Its Prevention, Contribution No. 580 from the Woods Hole Oceanographic Institute, U. S. Naval Institute, Annapolis, Maryland, George Banta Publishing Co., Menasha, WI, 1952, Accessible on Internet: https://darchive.mblwhoilibrary.org/bitstream/handle/1912/191/chapter%2011.pdf?sequence=20, April 9, 2018.
[28] L. Bruzelius, An Account of Lead Sheathing, Formerly used for the Protection of Ships' Bottoms, Extracted from a work published in 1695, Accessible on Internet: http://www.bruzelius.info/Nautica/Shipbuilding/Lead_sheathing(1695).html, April 9, 2018.
[29] Lead, Canadian Environmental Health Atlas, Accessible on Internet: http://www.ehatlas.ca/environmental-contaminants/lead, April 9, 2018.

**Acknowledgements**

The authors wish to thank Prof Aleksandar Durman from the University of Zagreb, Faculty of Philosophy, Department of Archaeology for the vast knowledge he unselfishly shared. The authors also wish to thank Dr. Andrijana Pravidur, a curator from The National Museum of Bosnia and Herzegovina for the images and dissertation excerpt shared through Prof Aleksandar Durman. Special thanks go to Ms Ivana Miletić Čakširan from the Ministry of Culture of the Republic of Croatia, Conservation Department in Sisak for the area of the Sisak – Moslavina County for sharing the photographs of Roman water pipes found in the city of Sisak.

17th INTERNATIONAL FOUNDRYMEN CONFERENCE
Hi-tech casting solution and knowledge based engineering
Opatija, May 16th-18th, 2018
http://www.simet.hr/~foundry/

# COMMERCIAL PAGES

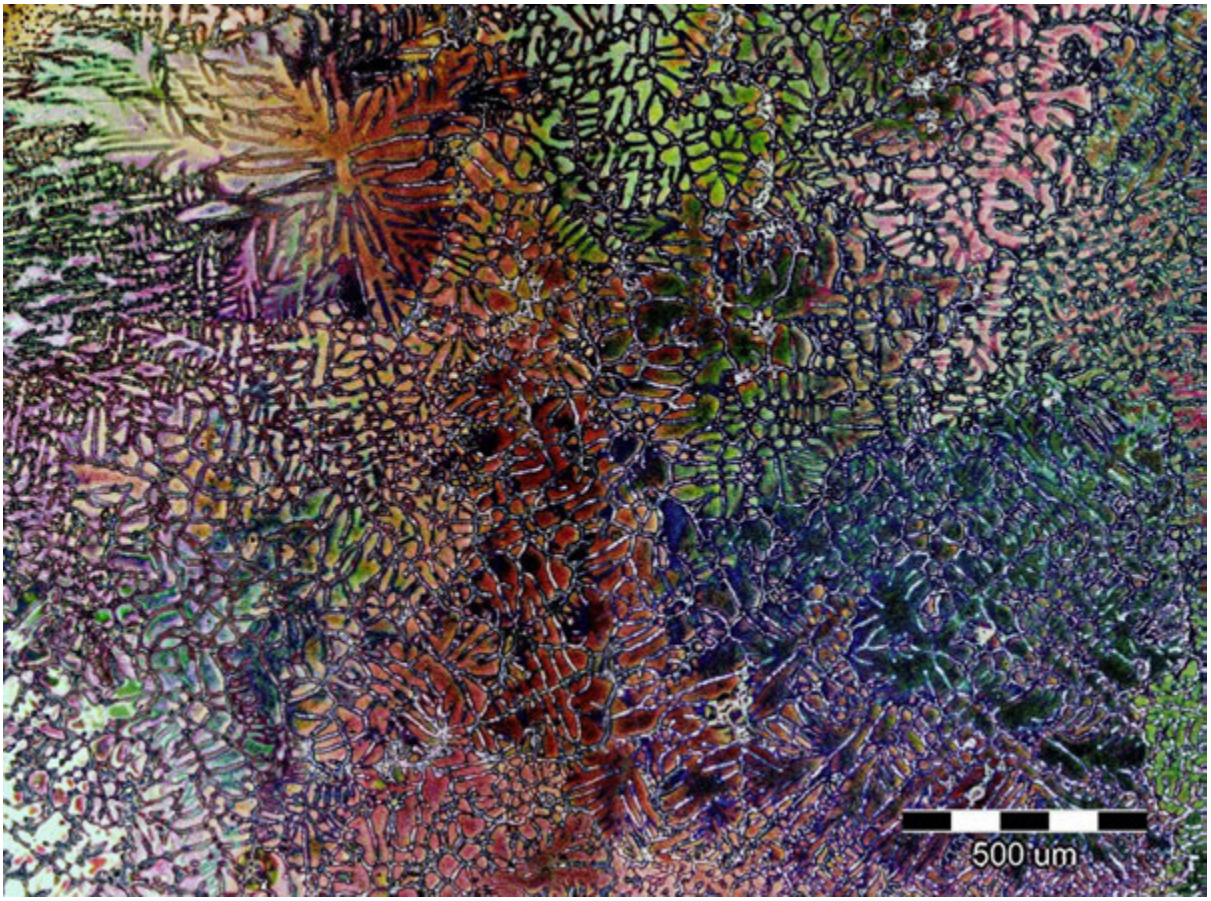


**Dendritic network development in Al-2.5Mg-0.7Li alloy**
F. Kozina, Z. Zovko Brodarac, M. Petrič, P. Mrvar, T. Rupčić,
Innovative Al-Mg-Li alloy with improved properties for aero - and space industry,
15. International fair of innovation ARCA 2017, October, 19 - 21, 2017, Zagreb

# 17th INTERNATIONAL FOUNDRYMEN CONFERENCE

## Hi-tech casting solution and knowledge based engineering

**Opatija, May 16th-18th, 2018**

http://www.simet.hr/~foundry/

By the order of appearance:

| SPONSORSHIP CATEGORY | COMPANY |
|---|---|
| CO-ORGANIZER | ELKEM AS (NO) |
| GOLDEN SPONSOR | COMET d.o.o., Novi Marof (HR) & SWATYCOMET d.o.o., Maribor (SI) |
| | KONTROLTEST INTERNATIONAL d.o.o., Zagreb (HR) |
| | LABTIM ADRIA d.o.o., Sesvete (HR) |
| | MIKROLUX d.o.o., Zaprešić (HR) |
| BRONZE SPONSOR | ANALYSIS d.o.o., Beograd (RS) |
| | BL METAL d.o.o., Črnomelj (SI) |
| | EDC d.o.o., Zagreb (HR) |
| | EKW – KREMEN d.o.o., Šentjerej (SI) |
| | HAGI GmbH, Pyhra (AT) |
| | HEINRICH WAGNER SINTO MASCHINENFABRIK GmbH, Bad Laasphe (DE) |
| | IDEF d.o.o., Zagreb (HR) |
| | INDUCTOTHERM EUROPE Ltd., Worcestershire (UK) |
| | LABEKO d.o.o., Zagreb (HR) |
| | MECAS ESI s.r.o., Plzen (CZ) & TC LIVARSTVO d.o.o., Ljubljana (SI) |
| | SCAN d.o.o, Kranj (SI) |
| | TCT TESIC GmbH, Iserlohn (DE) |
| | TOPOMATIKA d.o.o., Zagreb (HR) |
| MEDIA COVERAGE | IRT 3000 |
| | Foundry Lexicon |
| | Foundry Planet |
| SUPPORTING ASSOCIATION AND COMPANIES | Croatian Foundry Association, Zagreb (HR) |
| | Slovenian Foundry Association, Ljubljana (SI) |

Elkem

# Five steps to **high quality castings**

1. Base iron preparation
2. Metal treatment of Grey Iron and Ductile Iron
3. Grey Iron and Ductile Iron Inoculation
4. Focus on ductile iron production
5. Optimisation of Cast Iron Production

**Stable and well nucleated base iron**

Production of sound and cost effective iron castings begins with the selection of good quality raw materials and additives. Yet the best materials can deliver a poor quality iron unless there is sufficient nucleation carried through the process to give the graphite morphology, chill control and mechanical properties required.

Preconditioning with a long-lasting material, such as Elkem´s unique Preseed ™ preconditioner is the optimal way to ensure that the nuclei, once created in the melt, are stable enough to survive subsequent treatment processes prior to casting.

Essential to the process is a means of measuring the graphite activity with a melt and the thermal analysis system EPIC™ is able to quickly and accurately give and indication of whether the iron is suitable for pouring or requires correction.

www.elkem.com/foundry

## **Optimise** your ductile iron production **in partnership** with **Elkem**

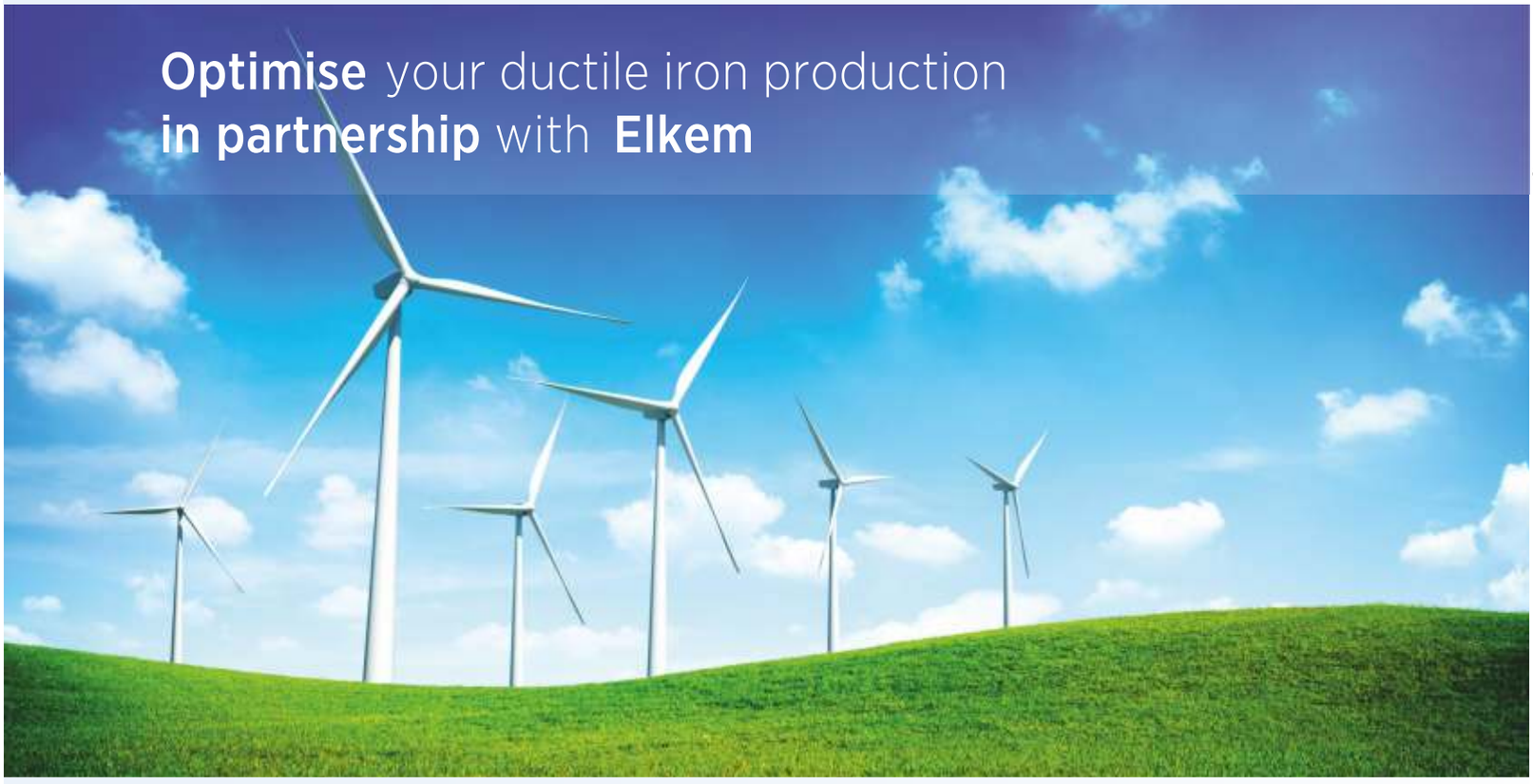

Business areas:

**Silicon Materials**

**Silicones**

**Foundry Products**

**Carbon**

Representative office:
**Elkem AS**
J.J. Strossmayer 176, Sisak Croatia · Tel. +385/44/659-065 · Fax +385/44/659-067 · gordana.gojsevic@elkem.com · zoran.kovacic@elkem.com

Elkem

# **Innovative** Metal Treatment Solutions

## **More then 100 reasons** to have a partnership

Getting the best value from nodularising alloys can be a big saving for foundries. The trend towards low Mg alloys, which have lower reactivity and hence higher recovery, continues. Elkem´s extensive range of over 100 MgFeSi chemistries, coupled with Topseed® cover alloy, means that together we can optimizes your total treatment alloy package. Please contact your local Elkem representative for more details or visit us at www.elkem.com/foundry.

*Conventional Mg Treatment*

*® cover alloy*

Our Partner: **Ferrosad Low Carbon Steel Shot**

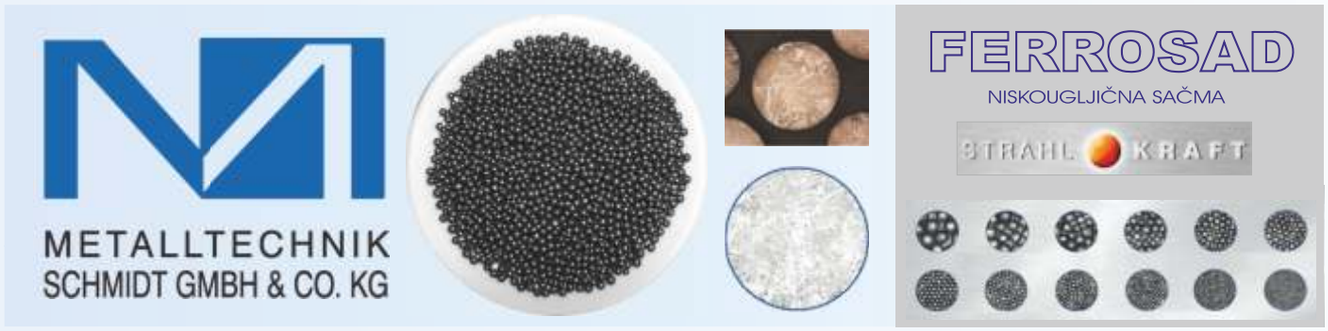


Representative office:
**Elkem AS**
J.J. Strossmayer 176, Sisak Croatia · Tel. +385/44/659-065 · Fax +385/44/659-067 · gordana.gojsevic@elkem.com · zoran.kovacic@elkem.com

# COMET

Karnasch PROFESSIONAL TOOLS

**Visokokvalitetan alat za obradu metala**

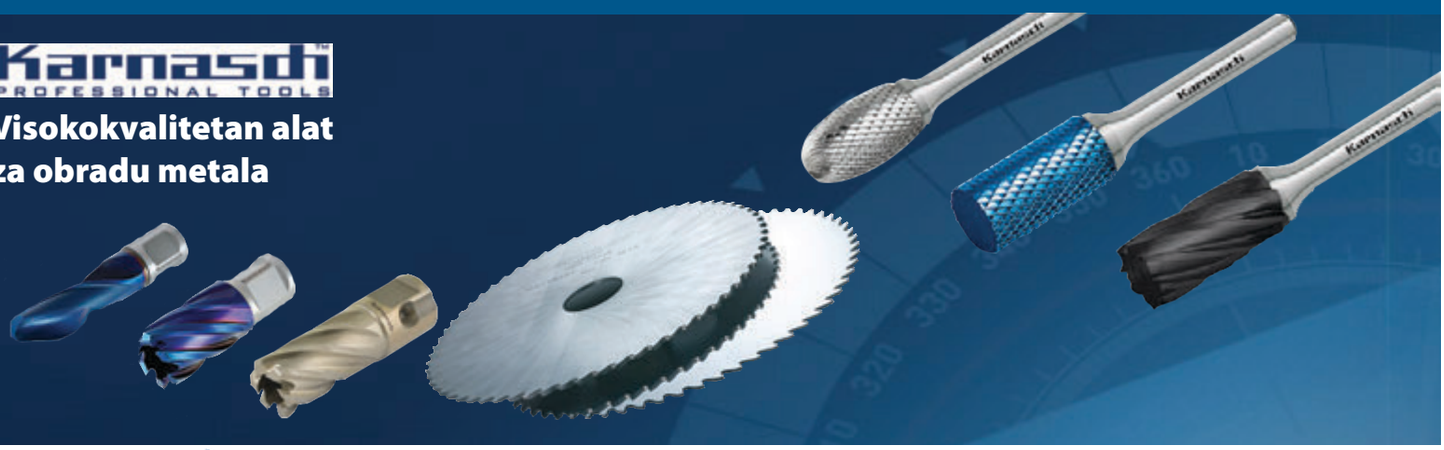

HELIOS · PREISSER

**Profesionalni mjerni alati**

Mikrometri

Mjerne ure

Pomična mjerila

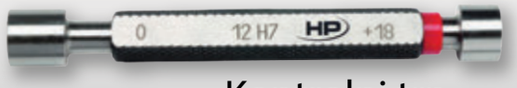

Kontrolni trn

Chicago Pneumatic

**Industrijski pneumatski alati**

COMET

**Ekskluzivni uvoznik za Hrvatsku:**
**COMET d.o.o.**
**Varaždinska 40c, Novi Marof, Hrvatska**
**T:+385 (0)42 408 500**
**www.comet.hr**


SWATYCOMET, umetni brusi in nekovine, d.o.o.
Titova cesta 60, 2000 Maribor, Slovenija - www.swatycomet.si

QUALITY IS DEFINED BY STANDARD, OUR ADVANTGE IS THAT WE FOLLOW INOVATIONS

# Trokut Test Group

## YOUR SOLUTION PROVIDER AND SUPPLIER OF CONSUMABLES AND DEVICES FOR QUALITY CONTROL AND PREDICTIVE MAINTENANCE FOR FOUNDRY INDUSTRY

**TROKUT TEST GROUP** is active in the following countries:

*Slovenia,*
*Croatia,*
*Bosnia and Herzegovina,*
*Serbia,*
*Bulgaria,*
*Montenegro,*
*Macedonia,*
*Albania,*
*Kosovo*

QUALITY IS DEFINED BY STANDARD, OUR ADVANTGE IS THAT WE FOLLOW INOVATIONS

# SOLUTIONS FOR FOUNDRY

## Non-Destructive Testing

Visual Testing

Penetrant Testing
Magnetic Particle Testing

Ultrasound Testing

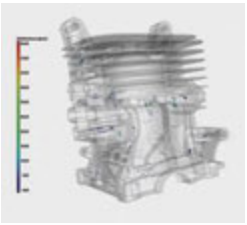

Radiography Testing

## Laboratory equipment

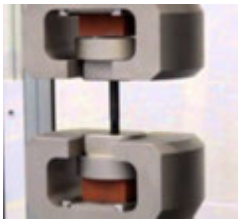

Material Testing

Hardness Testing

Metallography

Elemental Analysis

Macro scopes

Microscopes, SEM

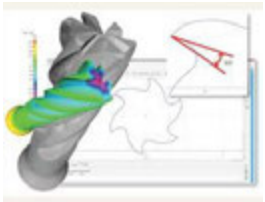

Metrology

Stress analysis

## Preventive Maintenance

Ultrasonic Devices for Preventive Maintenance *(Leak detection, Tightness Testing, Bearing Monitoring and lubrication, Steam trap and Valve Inspection, detection of Partial Discharges)*

Monitoring the condition of equipment driven by an electric motor *(maintenance program on critical pumps, presses, compressors and waterjet cutters)*

Labtim

**Labtim d.o.o.** is a laboratory equipment supplier & service company with a 25 years tradition.

Tinius Olsen

The First Name In Materials Testing

**Tinius Olsen is the leading specialist manufacturer and supplier of static tension and/or compression materials testing machines.**

Our machines are designed for use in Research and Quality Control to measure material's strength and performance.

Using Tinius Olsen equipment it is possible to perform such tests on raw materials such as metals, polymers, textiles, rubbers, adhesives, food as well as finished components.

A whole series of tests are available including tension, shear, compression, flex / bend, puncture / burst, tear, peel, melt flow, Charpy and Izod impact, friction, stiffness, heat distortion temperature, Vicat penetration, and torsion.

Horizon Software has a comprehensive selection of pre-defined testing programs which includes powerful analysis of testing data, complex control, and sophisticate reporting.

Horizon software - Tinius Olsen

**Labtim d.o.o. is an official distributor for Tinius Olsen and ATS Systems for Slovenia, Croatia, Serbia and BIH.**

ATS APPLIED TEST SYSTEMS

THE MARK OF RELIABILITY

**ATS Creep Testing Systems** are precision lever arm testers that incorporate a number of enhanced design features, making them far superior to those of our competitors.

Lever Arm Creep Testing Systems


Labtim d.o.o.
Ziherlova ulica 6,
1000 Ljubljana, Slovenia
E info@labtim.si
W www.labtim.si
T + 386 1 428 36 84

Labtim Adria d.o.o.
Av. V. Holjevca 40
10000 Zagreb, Croatia
E info@labtim.hr
W www.labtim.hr
T +385 1 662 3883

**Labtim d.o.o.** is an official distributor for TA Instruments for Slovenia, Croatia and BIH.

**Quenching Dilatomers -** Characterization of steel and metal alloys at Heating Rates up to 4000 °C/sec and Quenching Rates up to 2500 °C/sec permits optimization of processing conditions

**Optical Dilatometry** - Heating microscopy as a non-contact technique, based upon an advanced image analysis of a specimen subjected to a thermal treatment reproducing industrial firing conditions, identifies several characteristic shapes and related temperatures for the optimization of manufacturing processes in ceramics, metals, alloys.

**TA Instruments high technology products**, quality manufacturing and unbeatable after sales support is why more customers recommend TA products to their colleagues around the world.

**NEW Discovery DSC/TGA/SDT systems** deliver the purest real-time simultaneous heat flow and weight data possible.

**TA Instruments offers**

**thermal analysis instruments, rheology, microcalorimetry, and mechanical analysis instrumetation.**

**ElectroForce Mechanical Test Instruments**

We start with your specific testing needs and combine unique ElectroForce motor technologies with our test applications engineering expertise to create a tailored test solution that meets your testing objective.


Labtim d.o.o.
Ziherlova ulica 6,
1000 Ljubljana, Slovenia
E info@labtim.si
W www.labtim.si
T + 386 1 428 36 84

Labtim Adria d.o.o.
Av. V. Holjevca 40
10000 Zagreb, Croatia
E info@labtim.hr
W www.labtim.hr
T +385 1 662 3883

μikrolux
advantageous technologies consulting

general representative

TESCAN
PERFORMANCE IN NANOSPACE

# 17th International Foundrymen Conference

"Hi-tech casting solution and knowledge based engineering"

## Opatija, May 16th-18th, 2018

It is our pleasure to invite you to come and visit us at the 17th International Foundrymen Conference in Opatija, Croatia
Check out for the latest news at our booth
TESCAN'S S8000G is one of them...


TESCAN S8000G
The TESCAN S8000G is the first member of a new family of TESCAN microscope – The S8000 series.
Key features
New BrightBeam™SEM column technology for uncompromised UHR
· New BrightBeam™ SEM column with proprietary 70° combined electrostatic-magnetic objective lens for maximum universality.
· Field-free ultra-high resolution imaging for maximum versatility in imaging and analysis including the analysis of magnetic samples and live SEM imaging during FIB operations.
· New detection system including In-Beam Axial detector and Multidetector for angle-selective and energy-selective signal collection gives complete control on surface sensitivity and the option to explore with different contrast for sharpening your senses and deepening your insight.
· New generation of electronics with up to 8 live signal channels simultaneously.
· New Field Emission Schottky electron gun now enabling beam currents up to 400 nA and rapid beam energy changes.
· EquiPower™ lens technology for efficient thermal power dissipation and excellent electron column stability.
· Beam Deceleration Technology (BDT) for further improved resolution at low and ultra-low electron beam energies with simultaneous detection of SE and BSE signals. (optional)

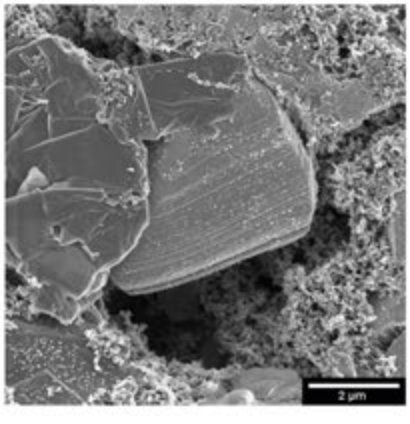


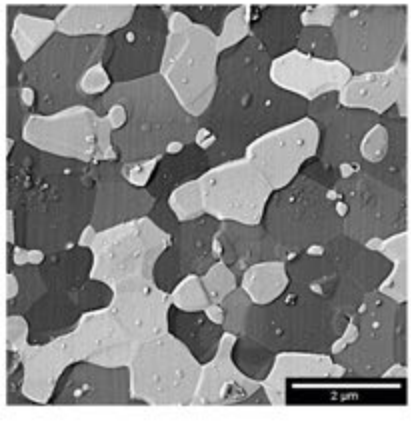


μikrolux
advantageous technologies consulting

representative

# 17th International Foundrymen Conference

"Hi-tech casting solution and knowledge based engineering"

Opatija, May 16th-18th, 2018

We will give you a better insight into the technological news
We are looking forward to Your visit!

---

OXFORD INSTRUMENTS

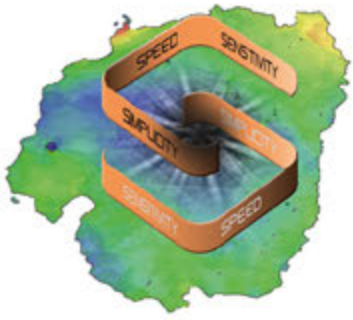


**EBSD Detector: Symmetry**

EBSD – electron backscatter diffraction – is a powerful microanalysis technique that enables rigorous characterisation of the microstructural properties of crystalline materials. A high-performance EBSD detector is critical for the effectiveness of the technique, influencing both speed and data quality.

Quorum TECHNOLOGIES

**Q300T D Dual Target Sequential Sputtering System**

The Q300T D is a fully automatic, large chamber, dual-head sputter coater ideally suited for thin film applications and for conductive coating of scanning electron microscopy (SEM) specimens. The dual-head configuration allows two different oxidising or non-oxidising metals to be sequentially sputtered without the need to 'break' vacuum. A dual channel film thickness monitor option is available.

BRUKER

**QUANTAX Micro-XRF**

QUANTAX Micro-XRF with the XTrace micro-spot X-ray source adds the capabilities of a complete micro-XRF spectrometer to a scanning electron microscope. XTrace fits on a free inclined chamber port of almost any SEM. The user benefits from both the trace element sensitivity and the higher information depth of XRF analysis.

MEIJI TECHNO


**ML8100 Halogen Trinocular Metallurgical Microscope**

ML8000 Metallurgical Microscopes by Meiji Techno are available in binocular or trinocular models. Authorized Meiji Techno Dealers can also integrate additional optional equipment to tailor a system to meet your specific needs.

17th INTERNATIONAL FOUNDRYMEN CONFERENCE
Hi-tech casting solution and knowledge based engineering
Opatija, May 16th-18th, 2018
http://www.simet.hr/~foundry/

# SUPPORTING ASSOCIATION AND COMPANIES

**Croatian Foundry Association, Zagreb (HR)**

---

**Slovenian Foundry Association, Ljubljana (SI)**

---

# MEDIA COVERAGE

**IRT 3000**

**Foundry Lexicon**

**Foundry Planet**